

Lecture Notes in Mechanical Engineering

Andrey A. Radionov
Vadim R. Gasiyarov *Editors*


Proceedings of the 7th International Conference on Industrial Engineering (ICIE 2021)

Volume I

 Springer


Lecture Notes in Mechanical Engineering

Series Editors

Francisco Cavas-Martínez , Departamento de Estructuras, Universidad Politécnica de Cartagena, Cartagena, Murcia, Spain

Fakher Chaari, National School of Engineers, University of Sfax, Sfax, Tunisia

Francesca di Mare, Institute of Energy Technology, Ruhr-Universität Bochum, Bochum, Nordrhein-Westfalen, Germany

Francesco Gherardini , Dipartimento di Ingegneria, Università di Modena e Reggio Emilia, Modena, Italy

Mohamed Haddar, National School of Engineers of Sfax (ENIS), Sfax, Tunisia

Vitalii Ivanov, Department of Manufacturing Engineering, Machines and Tools, Sumy State University, Sumy, Ukraine

Young W. Kwon, Department of Manufacturing Engineering and Aerospace Engineering, Graduate School of Engineering and Applied Science, Monterey, CA, USA

Justyna Trojanowska, Poznan University of Technology, Poznan, Poland

Lecture Notes in Mechanical Engineering (LNME) publishes the latest developments in Mechanical Engineering—quickly, informally and with high quality. Original research reported in proceedings and post-proceedings represents the core of LNME. Volumes published in LNME embrace all aspects, subfields and new challenges of mechanical engineering. Topics in the series include:

- Engineering Design
- Machinery and Machine Elements
- Mechanical Structures and Stress Analysis
- Automotive Engineering
- Engine Technology
- Aerospace Technology and Astronautics
- Nanotechnology and Microengineering
- Control, Robotics, Mechatronics
- MEMS
- Theoretical and Applied Mechanics
- Dynamical Systems, Control
- Fluid Mechanics
- Engineering Thermodynamics, Heat and Mass Transfer
- Manufacturing
- Precision Engineering, Instrumentation, Measurement
- Materials Engineering
- Tribology and Surface Technology

To submit a proposal or request further information, please contact the Springer Editor of your location:

China: Ms. Ella Zhang at ella.zhang@springer.com

India: Priya Vyas at priya.vyas@springer.com

Rest of Asia, Australia, New Zealand: Swati Meherishi at swati.meherishi@springer.com

All other countries: Dr. Leontina Di Cecco at Leontina.dicecco@springer.com

To submit a proposal for a monograph, please check our Springer Tracts in Mechanical Engineering at <https://link.springer.com/bookseries/11693> or contact Leontina.dicecco@springer.com

Indexed by SCOPUS. All books published in the series are submitted for consideration in Web of Science.

More information about this series at <https://link.springer.com/bookseries/11236>

Andrey A. Radionov · Vadim R. Gasiyarov
Editors

Proceedings of the 7th International Conference on Industrial Engineering (ICIE 2021)

Volume I

 Springer

Editors

Andrey A. Radionov
South Ural State University
76, Lenin ave.
Chelyabinsk, Russia

Vadim R. Gasiyarov
South Ural State University
76, Lenin ave.
Chelyabinsk, Russia

ISSN 2195-4356

ISSN 2195-4364 (electronic)

Lecture Notes in Mechanical Engineering

ISBN 978-3-030-85232-0

ISBN 978-3-030-85233-7 (eBook)

<https://doi.org/10.1007/978-3-030-85233-7>

© The Editor(s) (if applicable) and The Author(s), under exclusive license to Springer Nature Switzerland AG 2022

This work is subject to copyright. All rights are solely and exclusively licensed by the Publisher, whether the whole or part of the material is concerned, specifically the rights of translation, reprinting, reuse of illustrations, recitation, broadcasting, reproduction on microfilms or in any other physical way, and transmission or information storage and retrieval, electronic adaptation, computer software, or by similar or dissimilar methodology now known or hereafter developed.

The use of general descriptive names, registered names, trademarks, service marks, etc. in this publication does not imply, even in the absence of a specific statement, that such names are exempt from the relevant protective laws and regulations and therefore free for general use.

The publisher, the authors and the editors are safe to assume that the advice and information in this book are believed to be true and accurate at the date of publication. Neither the publisher nor the authors or the editors give a warranty, expressed or implied, with respect to the material contained herein or for any errors or omissions that may have been made. The publisher remains neutral with regard to jurisdictional claims in published maps and institutional affiliations.

This Springer imprint is published by the registered company Springer Nature Switzerland AG
The registered company address is: Gewerbestrasse 11, 6330 Cham, Switzerland

Preface

International Conference on Industrial Engineering took place on May 17–21, 2021. The spread of the coronavirus COVID-19 made adjustments to our lives that year, including the organization of the ICIE conference. ICIE was held as a traditional conference as a virtual conference. Both oral sections and poster sections were organized by on-line. Oral sections were implemented as video conferences. Poster sections were in a chat mode. The conference was organized by 4 universities—South Ural State University (national research university), Moscow Polytechnic University, Platov South-Russian State Polytechnic University and Volgograd State Technical University.

The conference was carried out under financial support of the South Ural State University (national research university).

The conference was really large-scaled and international. The international program committee has selected more than 370 reports. The conferees represented 86 Russian cities from the western and central parts to the Far East regions. International participants represented 38 cities and 17 countries. These are countries such as Azerbaijan, Belarus, Bolivia, China, Germany, India, Iraq, Kazakhstan, Lebanon, Morocco, Poland, South Korea, Tajikistan, Turkey, Vietnam, Uzbekistan, Ukraine.

The conference participants submitted papers reflecting recent advances in the field of Industrial Engineering, in Russian and English. The conference was organized in 13 sections, including:

Part 1. Mechanical Engineering (Machinery and Mechanism Design; Dynamics of Machines and Working Processes; Friction, Wear, and Lubrication in Machines; Design and Manufacturing Engineering of Industrial Facilities; Transport and Technological Machines; Mechanical Treatment of Materials; Industrial Hydraulic Systems; Green Manufacturing);

Part 2. Materials Engineering and Technologies for Production and Processing (Polymers, Composites and Ceramics; Steels and Alloys, Metallurgical and Metalworking Technologies; Chemical and Hydrometallurgical Technologies; Surface Engineering and Coatings; Processing and Controlling Technologies).

The international program committee has selected totally 203 papers for publishing in the Lecture Notes in Mechanical Engineering (Springer International Publishing AG).

The organizing committee would like to express our sincere appreciation to everybody who has contributed to the conference. Heartfelt thanks are due to authors, reviewers, participants and to all the team of organizers for their support and enthusiasm which granted success to the conference.

Chelyabinsk, Russia

Prof. Andrey A. Radionov
Conference Chair

Contents

The Effect of Longitudinal Diffusion on the Operation Parameters of the Packed Distillation Column in Emulsification Mode	1
A. B. Golovanchikov, N. A. Prokhorenko, and O. A. Zalipaeva	
Theoretical Study of the Force Heterogeneity of Airless Tires Made of Elastic Polyurethanes	13
V. V. Mazur	
Heating System for Rigid Wedge Valves	21
A. A. Bazarov, N. V. Bondareva, and A. A. Navasardyan	
Research of the Modified Tooth-Belt Drive for the Machining Center	32
S. Shevchenko, A. Mukhovaty, and O. Krol	
Modified Belt Transmission with Enhanced Technical Characteristics	42
O. Krol	
Improvement of the Timber Supply Flow at Syktyvkar Plywood Mill LLC by Upgrading KKS-10	52
F. V. Svoykin, V. A. Sokolova, and A. A. Borozna	
On the Issue of Designing Cantilever Shafts with Joint Consideration of Strength, Endurance and Rigidity	60
B. N. Akramov and I. A. Ismatov	
Features of the Use of Structural Polymer-Composite Materials for the Manufacture of Complex-Shaped Parts in Small-Scale Production	68
V. M. Medunetskiy, S. Yu. Perepelkina, and Yu. S. Andreev	
Evaluation of the Accuracy of Gears Made of Polymer Composite Materials	76
M. V. Abramchuk, V. M. Medunetskiy, and V. A. Zinkov	

Lifetime Prediction for the Jaw Crusher by the Criterion of Toggle Fatigue Strength Based on the Application of the Kinetic Concept of Material Destruction	83
M. Slobodianskii	
Development of a Necessity and Sufficiency Scheme for the Use of Different Types of Car Tire Radii in Different Car Modeling Tasks	92
E. V. Balakina and I. V. Sergienko	
Assessment of the Influence of Inclined Wheel Installation on the Vehicle Lateral Stability	100
E. V. Balakina, M. S. Kochetov, and D. S. Sarbaev	
Improvement of Computer Methods of Designing Gears with High Load Capacity	109
K. Syzrantseva and V. Syzrantsev	
Evaluating the Influence of Perforated Baffle on Hydraulic Resistance of Impeller Machine Diffuser Channels	118
A. Bobkov and S. Chepurnykh	
Investigation of String Vibrations of a Transporting Device	126
M. U. Musirov and N. Yu. Kholmanov	
Experimental Thermal Performance Double-Sided Face Grinding Machine	134
I. P. Nikitina and A. N. Polyakov	
Calculating the Flexure of Circular Plates with Stiffening Rings	143
S. V. Konev, A. S. Fainshtein, and I. E. Teftelev	
Research and Analysis of Rational Parameters for a Conveying Mechanism of a Multi-operation Roller Machine	154
G. A. Bahadirov and M. I. Nosirov	
Design of a Fault-Tolerant Sliding Formwork Complex	166
T. Kruglova	
The Methodology of Resource Forecasting on Working Rolls of the Final Stands of the Widestrip Hot Rolling Mill	174
A. A. Fedulov, V. P. Antsupov, and A. V. Antsupov	
Monitoring the Technical Condition of the Mass Air Flow Sensors and the Cylinder-Piston Group in Test Modes	181
A. V. Gritsenko, V. D. Shepelev, and F. N. Grakov	
Normalization of the Support Coefficient Values at Vibration of a Straight Multi-Span Beam	189
I. V. Kudryavtsev, O. I. Rabetskaya, and A. E. Mityaev	

Animation Modeling as a Method of Structural and Kinematic Synthesis of Mechanisms	197
Yu I. Brovkina, T. S. Rabcicheva, and E. A. Petrakova	
Normalization of the Effective Length Factor Values at Buckling of a Straight Multi-Span Beam	205
I. V. Kudryavtsev, A. V. Kolotov, and A. E. Mityaev	
Analysis of the Relationship Between the Transfer of the Mechanism of the Multi-operating Machine	213
G. A. Bahadirov and F. R. Rakhimov	
Formation of Contact Thermal Resistance Based on the Analysis of the Characteristics of the Pseudo-Medium	221
A. F. Denisenko, R. G. Grishin, and L. Y. Podkruglyak	
Method of Calculating of the Heat-Stressed State of the Cylinder Head of a Liquid-Cooled Diesel Engine	230
A. N. Gots and V. S. Klevtsov	
Applying Morphing Wing for Optimization of Small-Size Unmanned Aircraft Wing	238
T. A. Mitashova	
Using a Chipper Without Felling Wood When Improvement Cutting Middle-Aged Plantings	245
A. A. Karelina, D. V. Chernik, and A. Y. Karnauhov	
Modeling of the Heat Setting Process in Order to Eliminate Defects in the Obtained Part	253
E. G. Demyanenko, I. P. Popov, and A. S. Kuznetsov	
Study and Improvement of Operation of the Planetary Gear Reducers of the Cold Rolling Mill Tension Leveler	261
G. Kornilov, O. Filatova, and I. Abdulvelev	
The Development and Study of a General-Service Automatically Controlled Weighing Batcher	270
I. M. Shandybina, A. M. Makarov, and M. P. Kukhtik	
A Study of the Technical Condition of Mass Airflow Sensors in Test Modes at Varying ICE Crankshaft Speeds	278
A. V. Gritsenko, V. D. Shepelev, and V. N. Nikolaev	
Feature of Predicting the Thermal Characteristics of Machine Tools Using Feedforward Neural Networks	286
A. N. Polyakov, V. V. Pozevalkin, and I. P. Nikitina	
Experimental Determination of the Kinematic Accuracy of a Planetary Oblique-Toothed Cycloidal Gearbox	295
E. Shirokikh, D. Sinitsyn, and A. Popov	

Developing a Mathematical Model of Interaction of a Conveyor-Bottom Bucket Working Body with the Soil	302
Yu. M. Lyashenko, E. A. Revyakina, and G. V. Lukyanova	
A Study of Vacuum Assisted Resin Injection for Molding Hard-To-Reach Locations in the Manufacture of Parts	311
N. S. Chashchin, A. P. Koval, and A. S. Gruzdev	
Physicochemical Properties of Natural Gas and Oxygen Combustion Products at Diffusion and Kinetic Burning	318
G. V. Voronov and I. V. Glukhov	
Development of the Solar Collector Orientation Mechanism Design	325
V. V. Boldyrev and M. A. Gorkavyi	
Simulation and Calculation of Stress–strain State of Thin-Walled Structures Strengthened Under Load	332
M. N. Ubaydullov and M. N. Serazutdinov	
Assessment of the Quality of the Coupling Billet for Tubing	341
A. V. Vladimirov and G. A. Orlov	
Numerical Modeling of Steel Structures Connections	348
N. Buzalo, B. Chernykhovskiy, and A. Alekseeva	
Natural Gas Burning with Process Oxygen in Up-to-Date Arc Steel Furnace Operating Space	358
G. V. Voronov and I. V. Glukhov	
Methods for Minimum Clearances Calculating in a Multiple-Teeth Contact of Straight Bevel Precessional Gears	366
V. Syzrantsev and A. Pazyak	
Design of the Robotic Arm Using 3D Printed Parts	373
I. Bzhikhatlov and P. Simonov	
Influence of the Fuel Injection Advance Angle on the Technical and Environmental Performance of a Diesel Engine (21/21) with a Turbocharger	383
D. S. Shestakov and L. V. Plotnikov	
Evaluation of the Effect of Longitudinal Forces on the Stability of Straight Line Movement of a Tractor Unit	391
A. Startcev, S. Romanov, and I. Storozhev	
Fluctuations of a Simplified Railway Vehicle Model as a System with One Degree of Freedom with a Nonlinear Restoring Force	398
A. N. Savoskin and A. P. Vasilev	

Evaluation of the Main Indicators of Piston Engine with an Improved Gas Exchange System by Modeling	405
L. V. Plotnikov, Yu. M. Brodov, and L. E. Osipov	
Energy-Efficient Vertical Kiln for the Firing of Ceramic	413
I. V. Dolotovskij	
Identification of Parameters of a Sub-Rail Base in the Computer System “Wheel-Railway Track”	420
E. S. Evtukh and G. A. Neklyudova	
Aerodynamic and Numerical Studies of the Flow in the Relief Surface Seals	428
G. E. Evtukh, A. Yu. Androsov, and V. V. Gorbachev	
A Mathematical Model for the Asynchronous Drive of the Overhead Traveling Crane	435
V. A. Krutova and I. A. Yaitskov	
Study of Asphalt Milling Workflow Dynamics	442
D. V. Furmanov, N. E. Lysakov, and L. M. Shamahov	
Environmental Properties Evaluation of Spark-Ignition Engines Running on Water/Fuel Mix	451
S. Plotnikov, Sh. Buzikov, and A. Birukov	
Trinkler Cycle Analysis with Maximum Pressure Limitation	461
A. Malozemov, A. Naumov, and A. Shavlov	
Simulation of Different Vibration Modes of a Drum in Continuous Compaction Control Systems of Soil by Vibratory Rollers	469
I. S. Tyuremnov and A. S. Morev	
The Dynamic Model of Unbalanced Grinding Wheel	477
E. N. Kashirskaya, S. V. Antonov, and I. A. Ganichev	
Combined Extraction of Liquid from Wet Leather Semifinished Products	486
A. M. Nabiev	
Experimental Determination of the Influence of Fibrous Material on the Dehydration of Wet Semifinished Leather Product	496
G. N. Tsoy	
Modeling Nonlinear Oscillations for the Wall of a Narrow Channel Interacting with Viscous Liquid	505
A. V. Christoforova, V. S. Popov, and A. A. Popova	
Study of the Base Plate Motion Between the Pairs of Shafts	514
Z. A. Rakhimova	

Study of the Influence of Body Roll on Lateral Stability When Maneuvering and Cornering 524
Tint Naing Win and V. M. Alakin

Improvement of Turbocharger Aeroacoustic Performance When Opening Wastegate 533
R. I. Rakhmatov, V. E. Krutolapov, and A. G. Vetoshnikov

Cooling System Axial Fan Design Calculation and Optimization in Terms of Tonal Noise 545
R. I. Rakhmatov, V. E. Krutolapov, and R. H. Kurmaev

Research and Improvement of Muffler Acoustic Characteristics with Regard to Thermodynamic Characteristics of Exhaust Gas Flow with Aeroacoustic Sources 553
R. I. Rakhmatov, V. E. Krutolapov, and G. G. Nadareishvili

System Views on the Features of the Dynamics of Elements of Oscillatory Structures 567
A. V. Eliseev, N. K. Kuznetsov, and A. S. Mironov

Study of the Vibration Separation of Mineral Raw Materials 575
A. D. Bardovsky, I. I. Basyrov, and L. M. Valeeva

Influence of the Incoming Flow Velocity to the Error of the Orientation Angle of a Horizontal-Axial Wind Turbine 583
A. Terekhin, A. Martyanov, and D. Ismagilov

Some Features of Measurements of Dynamic Characteristics of Heavy Machinery Objects During Operation in the Far North 592
M. O. Sinitsa, E. V. Tumakova, and A. S. Komshin

Dynamic Coupling Between Links of Articulated Transport Systems 603
E. Bazhenov, A. Zelenin, and D. Chernyshev

Comparative Evaluation of the Compressor-Ejector Unit’s Designs for Gas Evacuation During Repair of the Main Gas Pipeline 611
A. R. Buranshin, D. A. Godovskiy, and A. P. Tokarev

The Algorithm of Calculation of the Four-Stroke Turbocharged Diesel Engine Cycle Using the Compressor Efficiency Map 619
A. Yu. Abalyaev, A. A. Gavrilov, and A. N. Gots

Analysis of the Possibility and Feasibility of Using the Clocking Effect in the Design of Compressors and Turbines of Gas Turbine Engines 627
I. A. Krivosheev, N. B. Simonov, and K. E. Rozhkov

Analysis of the Smooth Running of Wheeled Suspensionless Vehicles in Various Operating Conditions	637
A. V. Pozdeev, I. M. Ryabov, and N. V. Timoshin	
Improvement of the Performance Properties of the Wheel with a Pneumatic Tire Due to the Internal Elastic Damping System	647
I. M. Ryabov, A. V. Pozdeev, and V. V. Erontaev	
Drive Axle of Vehicle and Environment Impact	656
A. Yu. Barykin, M. M. Mukhametdinov, and R. Kh. Takhaviev	
Numerical and Experimental Research of Intentional Mistuning of an Academic Bladed Disk Using Sensitivity Analysis	663
O. V. Repetckii, V. V. Nguyen, and Bernd Beirrow	
Reducing Fuel Consumption During Diesel Engine Operation on Idle Mode	672
A. N. Gots and V. F. Guskov	
Numerical Analysis of Dynamics and Fatigue Life of the Turbomachine Impeller with Mistuning	682
I. N. Ryzhikov, O. V. Repetckii, and V. V. Nguyen	
Fatigue Crack Growth Estimation in Low-Alloy Steel Under Random Loading in Middle Section of Fatigue Diagram	690
A. N. Savkin, A. A. Sedov, and K. A. Badikov	
Mathematical Simulation of Car Dynamics with Account of Air Conditioning System	698
M. Yu. Elagin and R. N. Khmelev	
Determination of the Hydrodynamic Vibration Frequencies in the Main Pump Pipings	705
A. P. Tokarev, S. E. Spirin, and A. R. Valeev	
Mathematical Planning of the Experiment in Product Design	712
K. V. Zhegera, N. A. Petuhova, and E. A. Samigullina	
Modeling the Laying Material Trajectory on the Technological Mandrel Surface Specified by an Irregular Spatial Point Set	721
E. Ustinova	
Estimation of the Total Road Load Coefficient for a Road Train	731
D. N. Dem'yanov and I. M. Hazipov	
Artificial Intelligence in the Problems of Organizational Control and Planning of Electric Power Consumption in Oil Pipeline Transportation	740
N. Gabdrakhmanova	

Control of a Mobile Cart with Two Traction Rear Wheels and a Free Front Wheel	751
S. Kochetkov	
Predictive Algorithm for Tuyere Areas' Parameters and Control Over the Distribution of Blast Parameters Around a Blast Furnace	764
I. A. Gurin, N. A. Spirin, and V. V. Lavrov	
Research of a Nonlinear Vibration Isolation System with a Controlled Magnetorheological Damper	773
D. Randin, A. Abakumov, and A. Goryachkin	
Estimating the Level of Friction and Wear in Gas-Powered Diesel Engines	784
A. V. Muratov and V. V. Lyashenko	
The Analysis of New Manufacturing Methods Dry Friction Powder Articles with Fe-Based Materials	791
Y. I. Krykhtin and V. I. Karlov	
Welding Technology in the Manufacture, Repair, and Restoration of Large Castings Made of High-Manganese Steel	801
A. Davydov and V. Broido	
Influence of the Rate Composition for the Chemical Elements in the Steel Parts on the Serviceability of the Pairs of Friction	810
A. Esbulatova and K. Voinov	
The Influence of Agricultural Production Factors on the Rate of Changing the Radial Clearance in the Electric Motor Bearings When Working with V-belt Transmission	818
R. V. Banin, V. A. Butorin, and I. B. Tsarev	
The Influence of Structural Components of Diamond-Bearing Mineral Ceramic Abrasive Material on Its Cutting Ability and the Treated Surface Quality	826
A. Bolotov, O. Novikova, and V. Novikov	
Mathematical Model of a Lubricant in a Bearing with a Fusible Coating on the Pilot and Irregular Slider Profile	834
M. A. Mukutadze and E. O. Lagunova	
Micropolar Lubricants in a Bearing with a Low-Melting Base Ring Coating and a Porous Slider Surface Coating	841
A. M. Mukutadze, A. N. Opatskikh, and V. M. Prikhodko	
Experimental Evaluation of the Influence of Microgeometry on the Tribological Characteristics of a Radial Plain Bearing	851
K. Gavrilov, A. Doikin, and M. Izzatulloev	

Modeling the Magnetorheological Fluid Flow Between Parallel Plates Under an External Magnetic Field	860
A. Fetisov, A. Kornaev, and V. Tyurin	
Surface Modification of AISI 321 Steel by Solid Lubricants	867
D. V. Tsukanov, G. S. Sevalnev, and N. N. Zubkov	
Technical Requirements for Lubricating Flanges Devices of Locomotive Wheelsets	875
I. A. Mayba	
Improving the Reliability of the Sliding-Current Assembly for Electrical Machines by Using a Non-conductive Grinding Brush	883
A. Izotov, V. Timoshenko, and S. Izotov	



The Effect of Longitudinal Diffusion on the Operation Parameters of the Packed Distillation Column in Emulsification Mode

A. B. Golovanchikov, N. A. Prokhorenko^(✉), and O. A. Zalipaeva

Volgograd Technical University, 28, Lenin Prospekt, Volgograd 400005, Russia

Abstract. The operation parameters of the packed distillation column operating in the emulsification mode are compared taking into account longitudinal diffusion along the boiling solution and ideal displacement by steam bubbles moving from the bottom up in the ideal displacement mode. Using the binary mixture “methyl alcohol–ethyl alcohol” as an example, the necessity of increasing the nozzle height in both parts of the column is shown in comparison with the standard calculation algorithm, which assumes that the continuous phase of the boiling solution and the dispersed phase of the vapor bubbles move along the height of both parts of the column in the ideal displacement mode. This need to increase the height of the nozzle is ensured by a jump in the concentration of reflux at the entrance to the strengthening part of the column and a similar jump in the concentration of the initial mixture at the entrance to the exhaustive part of the column and the nonlinearity of the working lines in both parts of the column, which leads to a decrease in local and average driving forces in the concentration of the flows.

Keywords: Longitudinal diffusion · Peclet number · Rectification · Packing · Emulsification mode · Equilibrium and working lines · Concentration jumps in the liquid phase · Local and average driving forces

1 Introduction

Until recently, a typical algorithm for calculating a packed distillation column was based on the structure of ideal displacement flows in the vapor and liquid phases [1, 2].

However, in the middle of the last century, in the calculations of mass transfer and reactor processes, including the calculations of the rectification process, they began to take into account not the ideality of flow structures in both phases and reflect it in cell, diffusion, and combined models. This led to nonlinearity of the working lines, a decrease in local and average driving forces, and a decrease in mass transfer coefficient [3, 4].

2 Methodology

The authors in articles [5, 6], based on the differential equations of material balance and mass transfer, taking into account longitudinal diffusion in the vapor phase when

they are a continuous phase, and ideal displacement in a liquid dispersed phase when it moves along both parts of the column in the form of droplets or it flows down the film on the surface of the packed bodies, obtained calculation equations, developed a calculation algorithm, and gave examples of such calculations for binary mixtures “ethyl alcohol–water” and “chloroform–benzene,” which confirmed the concentration jumps at the input RA cubic comprehensive parts and the lower part of the reinforcement of the column, the nonlinearity of the working lines, reduction of local and secondary driving forces in both parts of the column, and as a consequence, the related need to increase the height of the nozzle and the volume of the column.

In articles [5–7], also based on the differential equations of material balance and mass transfer, but already taking into account the longitudinal diffusion along the boiling liquid solution in both parts of the column and ideal displacement for vapor bubbles, which corresponds to the emulsification regime behind the phase inversion point. Equations of working lines are derived that explains the jumps in the concentrations of the volatile component at the phlegm inlet to the strengthening part of the column and at the outlet of the initial boiling solution, at the inlet to the exhausting part of the column, nonlinearity of the working lines in both parts of the column and, as a result, a decrease in local and average driving forces [8–11].

For example, working lines take the form (Fig. 1) [12]:

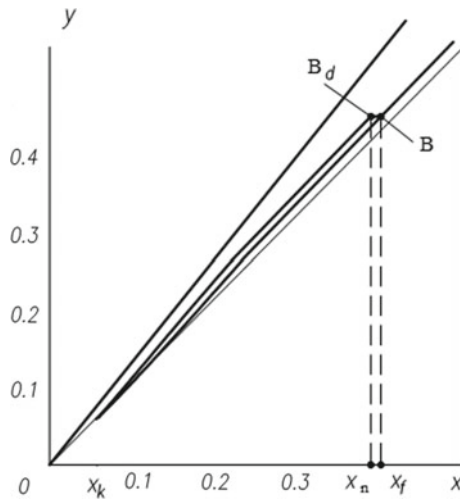


Fig. 1 Graphs of the dependences of the concentrations of the volatile component A in the exhaustive part of the column: 1—equilibrium line; 2—working line for a typical calculation algorithm, when both phases move in the ideal displacement mode; 3—working line when longitudinal diffusion is taken into account for a boiling solution at $Pe = 82, 259$ ($x_f = 0, 4035$; $x_n = 0, 3983$)

- for the exhaustive part of the column:

$$y = x_k + \left(\frac{F + R}{R + 1}\right)(x - x_k) - \left(\frac{F + R}{R + 1}\right) \cdot g/Pe; \tag{1}$$

- with the boundary condition at the entrance to the exhaustive part: $x_f = x_n - \frac{1}{Pe} g_n$

$$y = \frac{x_w + R_x}{R + 1} - \frac{1}{Pe} \left(\frac{R}{R + 1} \right) g; \quad (2)$$

- with a boundary condition at the entrance to the reinforcing part: $x_w = x_d - \frac{1}{Pe} g_d$, and the mass transfer equation:

$$\frac{1}{Pe} \frac{d^2x}{dh^2} = \frac{dx}{dh} + k_v \tau \left(\frac{M_j}{\rho_j} \right) (x - x^*); \quad (3)$$

(designation of parameters is given in Table 1.

However, in these articles, the authors set the Pecle numerical values of the longitudinal diffusion without their calculations, as a function of the Reynolds numbers of the boiling solution in the strengthening and exhaustive parts of the column given in [1] for packed columns. In this article, the Pecle numbers of longitudinal diffusion for a boiling solution were calculated using the approximate criterion equation given in [13, 14]:

$$Pe = 7.58 \times 10^{-3} Re_l \frac{H}{d_n}$$

and separately for the strengthening and exhaustive parts of the column, since the Reynolds number in the liquid phase Re_l and the height of the nozzle in these parts of the column are not the same.

The aim of the work is to carry out numerical calculations for the binary methanol–ethanol mixture according to the developed algorithm when the liquid boiling solution moves in the packed column in the back mixing mode (taking into account longitudinal diffusion) and the dispersed vapor stream in the form of bubbles in the ideal displacement mode, which corresponds to the emulsification mode behind the phase inversion point and comparing the results of these calculations with the calculations according to the standard algorithm, which assumes that both flows move in the ideal displacement mode.

3 Results and Discussions

Tables 1 and 2 show the initial and reference data and the calculation results of the technological and geometric parameters of the packed distillation column, designed to separate the binary mixture “methanol–ethanol”, according to the developed algorithm, taking into account longitudinal diffusion according to a boiling solution and a typical algorithm.

Thus, taking into account longitudinal diffusion along the boiling solution reduces the local and average driving mass transfer forces in both parts of the column. This leads to an increase in the nozzle height in both parts of the column by 16–19%, and the total nozzle volume by 17% compared to calculations using the standard algorithm, which assumes that both phases move in the ideal displacement mode (Fig. 2).

Table 1 Initial and reference data, for the binary mixture “methanol–ethanol”

Parameter Name	Designations	Value taking into account longitudinal diffusion $Pe = 82.259$
Initial data		
Stock solution performance, kg/h	G_f	15,000
Absolute mass concentration of volatile A: in stock solution, kg A/kg (A + B)	x_f	0.32
in the distillate, kg A/kg (A + B)	x_d	0.95
in cubed, kg A/kg (A + B)	x_k	0.02
Column pressure, at	P	1.033
Reference data		
Initial boiling point of the stock solution, OC	t	20
Boiling point of stock solution, OC	t_f	73.2
Distillate boiling point, OC	t_d	65.2
The boiling point of the bottoms liquid, OC	t_k	78
Heat capacity of the initial solution, kJ/kg	c_f	1.79
Heat capacity of the distillate, kJ/kg	c_d	1.05
The heat capacity of the bottom solution, kJ/kg	c_k	2.21
The specific heat of boiling of the distillate, kJ/kg	r_d	250
Specific surface of the nozzle, m^2/m^3	σ	87.5
The average viscosity of the vapor in its entirety, Pass	μ_u	4.2×10^{-5}
The average viscosity of the steam in the strengthening part, Pass	μ_y	5.1×10^{-4}
The average viscosity of the boiling solution in the column, Pass	μ_l	4.4×10^{-4}
The average density of the boiling solution in the column, kg/m^3	ρ_l	727
Outer diameter of the nozzle ($50 \times 50 \times 3$), m	d_n	0.05

Table 2 Initial and reference data and parameters

Parameter name	Designations	Value taking into account longitudinal diffusion $Pe = 82.259$
<i>Design parameters</i>		
The absolute molar concentration of the volatile component in the starting mixture, kmol A/kmol (A + B)	x_f	0.404
The absolute molar concentration of the volatile component in the distillate, kmol A/kmol (A + B)	x_d	0.965
The absolute molar concentration of the volatile component in the bottom liquid, kmol (A + B)	x_k	0.029
The molecular weight of the distillate, kg d/kmol d	M_d	32.5
The molecular weight of the cubic solution, kg K/kmol K	M_k	45.6
Coefficient in the approximating equation	k	0.595
	n	1.024
The average temperature in the strengthening part of the column, °C	t_y	69.2
The average temperature in the exhaustive part of the column, °C	t_u	75.6
Distillate consumption, kg/h	G_d	4838.7
	G_k	10,161.3
Bottoms flow rate, kg/h	M_{cy}	36.4
The average molecular weight of volatile in the strengthening part, kg A/kmol A	M_{cu}	43.0
Exhaustive average molecular weight of volatile, kg A/kmol A		
The average density of steam in the strengthening part of the column, kg/m ³	ρ_y	1.3
The average density of the vapor in the exhaustive part of the column, kg/m ³	ρ_u	1.5

(continued)

Table 2 (continued)

(a) Calculated parameters of the packed distillation column for the binary mixture “methanol–ethanol”		
The equilibrium concentration of volatile in steam, corresponding to its working concentration in a boiling still solution, kmol A/kmol (A + B)	y_w^*	0.043
The equilibrium concentration of volatile in vapor, corresponding to its working concentration for the distillate, kmol A/kmol (A + B)	y_d^*	0.980
Power number	F	2.496
Equilibrium concentration of volatile in vapor, corresponding to its working concentration in the initial solution, kmol A/kmol (A + B)	y_f^*	0.53
Minimum reflux ratio	R_m	3.446
The average tangent of the angle of inclination of the equilibrium line in the strengthening part of the column	m_y	0.803
The average tangent of the angle of inclination of the equilibrium line in the exhaustive part of the column	m_u	1.297
Optimum reflux ratio	R_0	5.034
The number of theoretical plates in the strengthening part of the column	N_y	10.75
The number of theoretical plates in the exhaustive part of the column	N_u	13.17
The working concentration of volatile in steam at the optimum reflux ratio in the initial solution, kmol A/kmol (A + B)	y_f	0.4965
Column thermal power, kw	Q_w	2457
Steam flow in column height, kg/h	G	29,197.5
The flow rate of the boiling solution in the strengthening part of the column, kg/h	L_y	24,358.8
The flow rate of the boiling solution in the exhaustive part of the column, kg/h	L_u	39,358.8
Archimedes number for steam in the exhaust part of the column	Ar_u	1.52×10^8

(continued)

Table 2 (continued)

Parameter Name	Designations	Value taking into account longitudinal diffusion $Pe = 82.259$
Total nozzle volume in the column, m^3	V	65.56
The number of transfer units in the reinforcing part of the column in pairs	CH_y	10.62
The number of transfer units in the exhaustive part of the column in pairs	CH_u	13.73
The mass transfer coefficient of steam in the strengthening part of the column, $kmol A / m^3 \cdot s$	K_y	0.0696
The mass transfer coefficient of the steam in the exhaustive part of the column, $kmol A / m^3 \cdot s$	K_u	0.0846
The average residence time of the steam in the nozzle for the strengthening part of the column, s	τ_y	4.5
The average residence time of the steam in the nozzle for the exhaustive part of the column, s	τ_u	7.1
Input absolute molar concentration of volatile component A in phlegm, taking into account longitudinal diffusion, $kmolA / kmol (A + B)$	x_{η}	0.962
The number of transfer units in the strengthening part of the column, taking into account longitudinal diffusion	CH_{yd}	12.28
The height of the nozzle in the reinforcing part of the column, taking into account longitudinal diffusion, m	H_{yd}	14.50

(continued)

Table 2 (continued)

Parameter Name	Designations	Value taking into account longitudinal diffusion $Pe = 82.259$
(b) Calculated parameters of the packed distillation column for the binary mixture "methanol-ethanol"		
The coefficient of increase in height of the nozzle in the reinforcing part, taking into account longitudinal diffusion	y_d	1.156
Input absolute molar concentration of volatile component A in the initial mixture, taking into account longitudinal diffusion, kmolA/kmol (A + B)	x_{fd}	0.398
Gradient of absolute molar concentration of volatile component A in the initial mixture, taking into account longitudinal diffusion along dimensionless height, kmolA/kmol (A + B)	g_{fd}	-0.429
The number of transfer units in the exhaustive part of the column, taking into account longitudinal diffusion	CH_{ud}	16.36
The height of the nozzle in the exhaustive part of the column, taking into account longitudinal diffusion, m	H_{ud}	14.7
The coefficient of increase in height of the nozzle in the exhaustive part, taking into account longitudinal diffusion	u_d	1.19
Total nozzle height with longitudinal diffusion, m	H_d	29.2
The coefficient of increase in height of the nozzle, taking into account longitudinal diffusion	u_d	1.17
The coefficient of increase volume taking into account longitudinal diffusion	y_{vd}	1.18

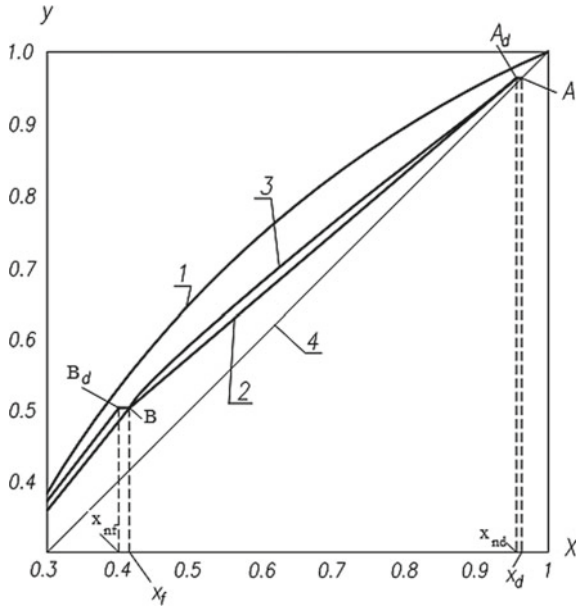


Fig. 2 Graphs of the dependencies of the concentrations of the volatile component A in the strengthening part of the column; 1—equilibrium line; 2—working line for a typical algorithm, when both phases move in the ideal displacement mode; 3—working line, when longitudinal diffusion is taken into account for a boiling solution at and the diagonal $y = x$

4 Conclusion

In addition, for comparison, the calculations of the numbers of units of the CEP transfer in the liquid phase were carried out taking into account the back mixing without using formulas (1–3) according to the algorithm described for packed absorption columns in the manual [15–20]. The numbers of transfer units amounted to $CH = 12.26$. Correspondingly, the coefficient of increase in nozzle height in the reinforcing part of the column is $k_{oy} = 1.15$, for the exhaustive part of $CH_u = 16.56$, $k_{ou} = 1.21$. Accounting for longitudinal diffusion in both boiling solution and vapor bubbles according to the above algorithm [1] leads to an increase in the coefficients of increasing the nozzle height to $k_y = 1.16$ and $k_u = 1.22$. That is, the longitudinal diffusion of vapor bubbles in both parts is practically zero and cannot be taken into account in a distillation column operating in the emulsification mode. Thus, the proposed algorithm for calculating the packed distillation column operating in the emulsification mode, taking into account longitudinal diffusion and related to the calculation of working lines and mass transfer according to Eqs. (1–3) for the strengthening part of the column practically coincides with the results of calculations by the algorithm for the packed absorption column given in the manual [1]. Calculations using both algorithms show the need to increase the nozzle height with longitudinal diffusion by 15% compared with ideal displacement. For the exhaustive part of the column, this increase is different: according to the proposed algorithm by 19%; according to the textbook algorithm [1]—21%. But longitudinal diffusion along

the vapor bubbles is practically absent, and its effect on increasing the height of the nozzle and its volume in both parts does not exceed 1%.

The reported study was funded by RFBR, project number 19-38-90002.

References

1. Pavlov KF (2013) Examples and tasks on the course of processes and apparatuses of chemical technology. Alliance, Moscow, Russia
2. Romankov PG (1974) Hydrodynamic processes of chemical technology. Chemistry, Russia
3. Romanov PG (2013) Guide to practical exercises in the laboratory of processes and apparatuses of chemical technology. Chemistry, Russia
4. Laptev AG (2018) Modeling and modernization of tray towers for reactive distillation. *Process Theor Foundations Chem Eng* 52(1):3–12
5. Levenshpil O (1969) Engineering design of chemical processes. Chemistry, Russia
6. Kafarov VV (1985) Methods of cybernetics in chemistry and chemical technology. Chemistry, Russia
7. Zakheim AYu (1982) Introduction to the modeling of chemical-technological processes. Chemistry, Russia
8. Tyabin NV (1983) Methods of cybernetics in rheology and chemical technology: a training manual. Publishing house, Volgograd
9. Bagaturov SA (1974) Fundamentals of the theory and calculation of distillation and rectification. Chemistry, Russia
10. Nikolaev PI (1987) Processes and apparatus of chemical and petrochemical technology. Chemistry, Moscow
11. Ramm VM (1976) Absorption of gases. Chemistry, Russia
12. Timonin AS (2002) Basics of calculation and design of chemical-technological and environmental protection equipment. Bochkareva Publishing House, Russia
13. Dytner'sky YI (2008) The main processes and apparatus of chemical technology. Alliance, Russia
14. Golovanchikov AB, Prokhorenko NA, Karev VN (2016) Algorithm for calculating the packed distillation column with allowance for longitudinal mixing in the liquid phase. *Izvestiya VolgGTU, Volgograd* 3(182):14–17
15. Golovanchikov AB, Reshetova AA, Ostroukhova AS, Fetisov EG (2011) Approximation of tabular dependencies in equilibrium of binary mixtures by a power equation. *News of the Volgograd State Technical University. Series Rheology, processes and devices of chemical technology*", vol 1, issue 74, pp 37–39
16. Golovanchikov AB, Vasilyeva EV, Ostroukhova AS, Reshetnikov AA (2011) Improving the accuracy of approximation of tabular dependencies on the equilibrium of binary mixtures. *Series "Actual problems of computer management and informatics in technical systems"*, vol 11, issue 84, pp 9–12
17. Golovanchikov AB, Prokhorenko NA (2018) Material balance modeling taking into account longitudinal diffusion in a distillation column. *News of VolgGTU. Ser. Actual problems of management, computing and computer science in technical systems*, vol 5, issue 215, pp 18–21
18. Golovanchikov AB, Prokhorenko NA (2016) Calculation of the dispersion of reproducibility in the absence of parallel experiments *News of VolgGTU. Ser. Actual problems of control, computational engineering and computer science in technical systems*, vol 11, issue 190, pp 13–16

19. Golovanchikov AB, Prokhorenko NA (2015) Simulation of rectification process in a packed column with a diffusion structure of the flow in the liquid phase. News of VolgGTU. Ser. Actual problems of management, computing and information technology in technical systems, vol 14, issue 178, pp 12–16
20. Golovanchikov AB (2015) Modeling the operation of a two-pipe heat exchanger taking into account the heat diffusion of the gas coolant. Izvestiya Vuzov Chem Chem Technol 58(9):58–62



Theoretical Study of the Force Heterogeneity of Airless Tires Made of Elastic Polyurethanes

V. V. Mazur^(✉)

Bratsk State University, 40, Makarenko, Bratsk 665709, Russia

Abstract. The advent of airless automobile tires that rival traditional pneumatic tires in performance is an important step toward improving the safety of vehicles and the survivability of military vehicles. However, by the time of the qualitative leap in the development of the design of airless tires, a sufficient number of published scientific works had not been accumulated, which contain theoretical generalizations and make it possible to judge the optimality of the designs. Despite this, airless tires from well-known companies such as Uniroyal, Michelin, Resilient Technologies, Polaris, Yokohama, Bridgestone, Hankook, Toyo, Boeing, Amerityre, Sumitomo, and Goodyear have scientifically based technical solutions obtained as a result of theoretical research at the design stage. However, the methods and mathematical models they propose are intended to scientifically substantiate their original technical solutions for airless wheels and tires. Therefore, the task of the study is to develop a new structural scheme of an airless tire and create its mathematical model to assess the influence of the mechanical properties of elastic polyurethanes and the geometric parameters of structural elements on the force heterogeneity of the wheel.

Keywords: Polyurethane tires · Characteristic of normal rigidity · Coefficient of variation · Solid model · Mechanical characteristics · Flexible spoke · Support ring

1 Relevance

The irremovable shortcomings of pneumatic tires are associated with the loss of excess air pressure and force to look for fundamentally new design solutions for wheeled movers that can improve the safety of civilian vehicles and the survivability of wheeled armored vehicles. One of these solutions are wheels with airless tires made of elastic polymeric materials.

2 Literature Review

A very large contribution to the research and development of airless tires was made by scientists at Clemson University (USA), working in conjunction with Michelin, Oshkosh, Gibbs Sports Amphibians, scientists at the University of North Texas, University of

North Carolina at Charlotte, and Saint Louis University. In their scientific papers, the finite element method is widely used for numerical modeling of airless tires.

Thus, the article [1] presents the results of a theoretical study of hysteresis losses and rolling resistance of an airless tire with flexible spokes and a support ring with hexagonal axial cavities and an elastic layer, working in shear and made of a material with a low elastic modulus.

The scientific article [2] simulates the dynamic interaction of the Michelin Lunar Wheel with sandy soil and stone obstacles. The developed model makes it possible to assess the deformations and local stresses of structural elements of an airless tire, tire deflection and deformation of the bearing surface, longitudinal reactions and the nature of the distribution of normal pressure in the tire-ground contact patch, and vertical acceleration of the wheel hub when driving through obstacles at different speeds.

The joint scientific work of scientists from Clemson University, the University of North Texas, and Gibbs Sports Amphibians [3] is aimed at studying the rolling resistance of an airless tire with flexible radial spokes and the nature of the pressure distribution in the patch of its contact with the supporting surface. Based on the results of theoretical studies using the developed viscoelastic finite element mathematical model, it was found that in order to reduce the rolling resistance and pressure in contact of an airless tire with the support surface, it is necessary to increase the thickness of the support ring and the shear modulus of elastic polyurethane from which this support ring is made.

The work of scientists at the University of Clemson and the University of North Carolina at Charlotte [4] is devoted to the study of the force heterogeneity of an airless tire, as well as vibration and noise during its rolling.

In a joint work of scientists from Clemson University and the University of North Texas [5], an airless tire with flexible spokes and a support ring with an elastic layer of porous material, which works in shear and is reinforced with carbon fiber, is modeled. The paper presents the results of theoretical studies of elastic properties and rolling resistance of an airless tire.

The article [6] proposes a model of an airless tire with flexible spokes and a support ring with axial cavities, which is shear and is made of *AL7075-T6* aluminum alloy.

An equally significant contribution to the methodology for calculating and designing airless tires was made by scientists from the Korea Aerospace University, working in conjunction with scientists from the Hankook company, the Korea Aviation University, the University of North Texas, and the Shanghai University of Transport. For example, in their scientific work [7], the finite element method was applied for numerical modeling of airless tires with axial cavities of a hexagonal shape, and in work [8] with axial cavities of a trapezoidal shape.

Russia's research on airless wheeled movers are conducted by Vescom Research Centre for Tire Industry LLC [9], Bauman Moscow State Technical University [10], and others.

3 Formulation of the Problem

The flexible spokes of an airless tire are discretely arranged, which causes the radial force to oscillate as the wheel rolls. Reducing radial force oscillations and reducing

wheel vibration is an important scientific-technical challenge. Theoretical studies make it possible to scientifically substantiate a new technical solution.

4 Design of a Wheel with an Airless Tire

The successes of foreign companies and the accumulated experience in the creation of non-traditional wheels [11] served as an impetus for inventive activity aimed at creating new designs of airless tires. Based on the results of patent research, a new scientifically grounded technical solution [12–14] was proposed and implemented in the original design of a wheel with an airless tire, and the structural scheme of which is shown in Fig. 1.

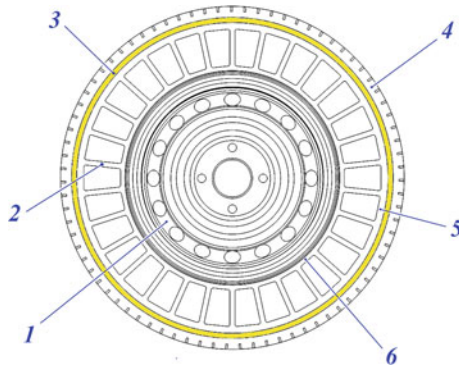


Fig. 1 Automobile wheel with airless tire of elastic polymeric materials: (1) disk wheel; (2) flexible spokes; (3) supporting ring; (4) protector; (5) fitting ring; (6) mounting ring

The elastic resistance and load-bearing capacity of the airless tire are provided by flexible radial spokes and a support ring. In this case, the flexible polyurethane spokes are bent in the longitudinal direction under the influence of the weight load in the contact area of the wheel with the supporting surface and in the upper semicircle of the airless tires that are in a stressed state under the influence of tensile forces.

It is known that a decrease in the total normal rigidity of flexible spokes allows one to reduce the force heterogeneity of an airless tire caused by its cyclic symmetry, but in response this also reduces the wheel bearing capacity [15].

We assume that in order to compensate for the elastic resistance of the flexible spokes of an airless tire, which is insufficient to ensure the required bearing capacity, and also to reduce the force of wheel heterogeneity during rolling, it is possible to use a support ring made of a polyurethane elastomer with a high modulus of elasticity compared to the material of flexible spokes.

5 Electronic Geometric Solid Model of Airless Tire

A theoretical study using an electronic solid-state geometric model [16] has shown that the tread significantly affects the force heterogeneity of an airless tire, since the tread and

flexible spokes have different characters of cyclic symmetry. This circumstance does not allow to fully assess the influence of the geometric parameters of the structural elements of an airless tire and the physical and mechanical properties of elastic polyurethanes on the force heterogeneity.

The results of an experimental study of pneumatic tires in the well-known work [17] showed that the tread has very little effect on the value of the coefficient of normal rigidity of the tire and the parameters of its contact with the supporting surface. Therefore, to justify the adopted technical solution, an electronic solid-state geometric model [18] of an airless tire without a tread was used, shown in Fig. 2. The electronic model allows the use of up to two grades of polyurethane elastomers for structural elements of an airless tire. The main attributes of the model, which remain constant in the study, are given in Table 1.

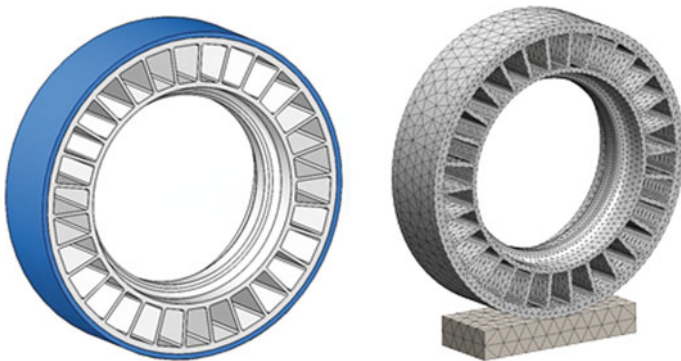


Fig. 2 Electronic solid-state dual-material airless tire model

Table 1 Constant attributes of a two-material airless tire model

Parameter	Value
Number of flexible needles	30
Angle between flexible needles, deg	12
Length of flexible needles, mm	57
Width of the tire profile, mm	120
Height of the tire profile, mm	100
Overall tire diameter, mm	530
Landing diameter of the tire, mm	330

To calculate the output characteristics of airless tires by the finite element method, we used the characteristics of the mechanical properties of Russian-made polyurethane elastomers: *SKU-PFL-100*, *SUREL TF-235*, *SUREL TF-228*, and *SUREL TF-682*.

For nonlinear static analysis with large displacements and deflections of structural elements, nonlinear elastic isotropic models of airless tire materials and a linear elastic isotropic model of the base plate material were adopted.

For example, Fig. 3 shows the mechanical characteristics of polyurethanes. The dependence of the stress σ on the relative deformation ε in tension [19] has negative values and positive values in compression [20].

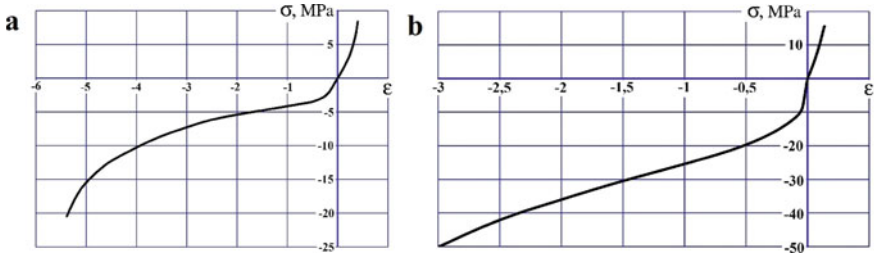


Fig. 3 Mechanical characteristics of elastic polyurethanes: **a** SUREL TF-228 with MOCA hardener; **b** SUREL TF-682 with Urelink-107 hardener

To shorten the notation of sets of variable attributes, alphanumeric designations were adopted in the following format:

$$ST/M \text{ RT}/M, \quad (1)$$

where S as flexible spoke; R as support ring; T as thickness of the flexible spoke or support ring, mm; M as material of the flexible spoke or support ring.

When using the characteristics of mechanical properties of the selected polyurethane elastomers in the calculations of the output characteristics of an airless tire, the M can take the following values: 100 for *SKU-PFL-100*, 228 for *SUREL TF-228*, 235 for *SUREL TF-235*, and 682 for *SUREL TF-682*.

To reduce the number of finite elements and nodes and reduce the calculation time, the stereometric two-material model was converted into a flat model. The calculation was carried out by the iterative Newton–Raphson method with a constant ($\Delta t = 0.01$ s) pseudo-time interval.

Normal loading of the airless tire was carried out in different positions relative to the central transverse plane. These positions were set by the angle between the central transverse plane and the longitudinal axis of one of the flexible spokes. The angular range $\sigma_\kappa = 0 \dots 360^\circ/N$, where the number of spokes of the airless tire is $N = 30$.

6 Results of Theoretical Study

As an example, Fig. 4 shows the calculated characteristics of the normal rigidity of an airless tire with different attributes of the electronic model.

The analysis of the characteristics of normal rigidity showed that for all variations of the sets of attributes of the electronic model, loading an airless tire with a normal load

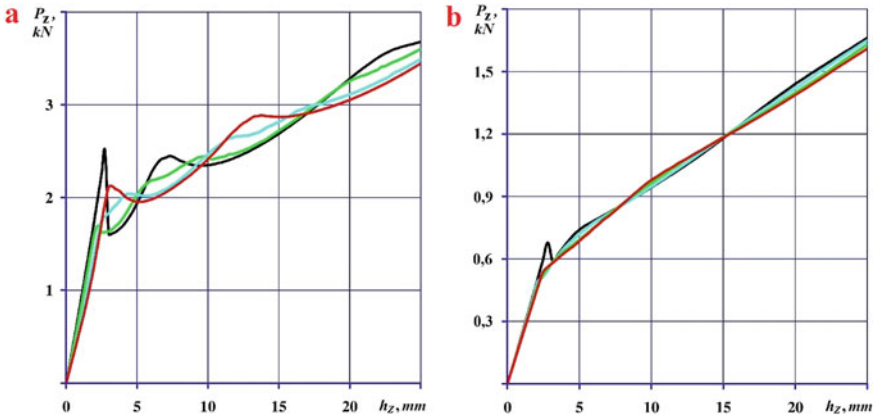


Fig. 4 Calculated characteristics of normal rigidity of airless tires: **a** S5/100 R4/682; **b** S5/228 R8/682

in each position relative to the central transverse plane is accompanied by oscillations in this load due to the discrete arrangement of flexible spokes and loss of stability of the spokes.

The largest mutual deviations of the normal load oscillation curves are observed at loading angles $\alpha_k = 0^\circ$ and $\alpha_k = 6^\circ$, which is explained using Fig. 5. These deviations with sufficient accuracy can be characterized as antiphase with increasing phase shift and period. The extreme points of these curves correspond to the onset of deformation of the flexible spokes, which is characterized by an increase in the normal load, or to the loss of their stability, which leads to a sharp decrease in deforming forces.

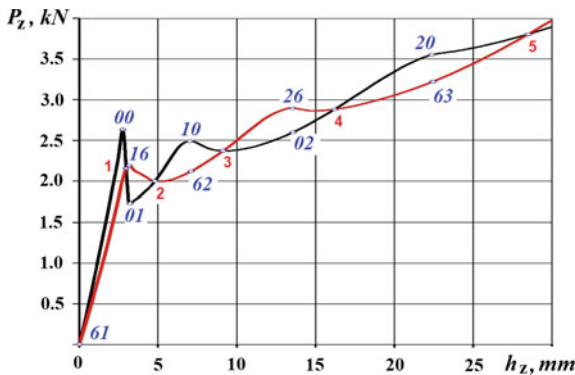


Fig. 5 Calculated characteristics of the normal rigidity of the airless tire S5/100 R8/682: **1–5** as the smallest mutual deviations of the normal load oscillation curves; **61** as beginning of tire deformation **01** and **02** as load at $\alpha_k = 0^\circ$ and h_z corresponding to the loss of stability of the spokes at an angle $\alpha_k = 6^\circ$; **62** and **63** as load at $\alpha_k = 6^\circ$ and h_z corresponding to the buckling of the spokes at $\alpha_k = 0^\circ$

At the loading angle $\alpha_\kappa = 0^\circ$, point **61** on the graph corresponds to the beginning of deformation of an airless tire and a spoke, whose longitudinal axis before loading coincides with the normal to the bearing surface. At point **00**, with a normal deflection of $h_z = 2.8$ mm, this spoke loses its stability and the normal load drops sharply. At point **01** ($h_z = 3.2$ mm), the first pair of flexible spokes begins to deform (angle between the spokes $\alpha_C = 24^\circ$), and the load increases again. At **10** ($h_z = 7$ mm), the spokes of the first pair also lose stability. The second pair of flexible spokes ($\alpha_C = 48^\circ$) loses stability at **20** ($h_z = 22$ mm). At a loading angle $\alpha_\kappa = 6^\circ$, point **16** ($h_z = 3.2$ mm) corresponds to the moment of loss of stability of the first pair of flexible spokes ($\alpha_C = 12^\circ$). In turn, the second pair of flexible spokes ($\alpha_C = 36^\circ$) loses stability at point **26** ($h_z = 13.7$ mm).

The assessment of the force heterogeneity of airless tires was carried out according to the graphs of oscillation in normal load using the coefficient of heterogeneity (coefficient of variation):

$$K = \frac{100}{\bar{P}_z} \sqrt{\frac{\sum_{i=1}^n (P_z(\alpha_i) - \bar{P}_z)^2}{n - 1}} \quad (2)$$

where $P_z(\alpha_{\kappa i})$ as the normal load on an airless tire at the i -th point of the oscillation curve, N ; \bar{P}_z as arithmetic mean of normal load, N ; n as number of points on the normal load oscillation curve.

For all sets, the highest value of the coefficient K does not exceed 4.87% (set of attributes *S5/235 R8/228*). The smallest value of K (points **I-5** as in Fig. 5) is in the range from 0.023% to 1.65%. The average over the range of K is 0.691%.

7 Conclusion

The analysis of the given characteristics showed that the change in the weight load on the wheel or the selection of the geometric parameters of the structural elements of the airless tire and the mechanical properties of the structural materials in accordance with the weight load makes it possible to ensure the minimum calculated force heterogeneity close to zero.

References

1. Ju J et al (2009) Design of honeycomb meta-materials for high shear flexure. IDETC/CIE 2009. San Diego, California. <https://doi.org/10.1115/DETC2009-87730>
2. Ma J et al (2011) Dynamic impact simulation of interaction between non-pneumatic tire and sand with obstacle. SAE 2011. <https://doi.org/10.4271/2011-01-0184>
3. Veeramurthy M et al (2014) Optimisation of geometry and material properties of a non-pneumatic tyre for reducing rolling resistance. Int J Vehicle Des <https://doi.org/10.1504/IJVD.2014.064567>
4. Narasimhan A et al (2011) Effects of material properties on static load-deflection and vibration of a non-pneumatic tire during high-speed rolling. SAE 2011. <https://doi.org/10.4271/2011-01-0101>
5. Ju J et al (2013) Rolling resistance of a non-pneumatic tire having a porous elastomer composite shear band. Tire Science and Technology

6. Ma J, Summers J (2011) Numerical simulation of tread effects on the interaction between cellular shear band based non-pneumatic tire and sand. IDETC/CIE 2011. Washington. <https://doi.org/10.1115/DETC2011-47044>
7. Lee C et al (2012) Vibration analysis of non-pneumatic tires with hexagonal lattice spokes. IDETC/CIE 2012. Chicago, Illinois. <https://doi.org/10.1115/DETC2012-70538>
8. Kim K et al (2015) Optimization of non-pneumatic tire with hexagonal lattice spokes for reducing rolling resistance. SAE 2015. <https://doi.org/10.4271/2015-01-1515>
9. Veselov IV et al (2016) Calculation and computer optimization of an airless tire. Rubber industry: raw, materials, technology
10. Kartashov AB (2010) Development of large wheeled propulsions from composite materials based on fiberglass. Dissertation. Bauman Moscow State Technical University
11. Mazur VV (2004) Improving the smooth running of vehicles by internal springing of the wheels. Dissertation. Bratsk State Technical University
12. Mazur VV (2008) Vehicle wheel with flexible spokes. RU Patent 2336178, 27 February 2007
13. Mazur VV (2015) Airless tire. RU Patent 2538472, 30 April 2013
14. Mazur VV (2010) Car tyre of elastic polyurethane with elastic deformable spokes. RU Patent 2397877, 08 July 2009
15. Tychina KA (2001) Development of a numerical method for calculating and designing metal-elastic wheels. Dissertation. Bauman Moscow State Technical University
16. Mazur VV (2020) Modeling and calculation of airless tires made of elastic polyurethanes. Scientific and technical bulletin of the Bryansk State University. <https://doi.org/10.22281/2413-9920-2020-06-01-93-108>
17. Knoroz VI et al (1976) Car tire work. Moscow
18. GOST 2.052-2015 Unified system for design documentation. Electronic model of the product. General Provisions
19. GOST 270-75 Rubber. Method for determination of elastic-strength properties in tension
20. GOST ISO 7743-2013 Rubber and thermoplastic elastomers. Determination of elastic-strength properties in compression



Heating System for Rigid Wedge Valves

A. A. Bazarov^(✉), N. V. Bondareva, and A. A. Navasardyan

Samara State Technical University, st. Molodogvardeyskaya, 244, Samara 443100, Russia
epp@samgtu.ru

Abstract. The problems of electromagnetic, thermal, and hydraulic processes of the valve with liquid to eliminate jamming during the heating are considered. This effect is the characteristic of rigid wedge valves with an ambient temperature decrease. Heating the valve body is used to eliminate jamming. The use of induction heaters is applied for local heating with a specified intensity. This heating method does not require the tight fitting of the heater to the valve body. The power and location of the heat source are determined by taking into account the limitations of the maximum value of the liquid temperature. Overheating can lead to vaporization and pressure increasing. The analysis of convective flow inside the cavity of the valve body which shows the mixing processes near the lower surface of the wedge is less intense and limited by a small volume. The movement of fluid at the side walls occurs along with the entire height of the valve body. This difference leads to local overheating of liquid in the lowers areas. The designing of the induction heater's location of the heating zones is provided. This is necessary to prevent eddy currents in the areas of the housing where overheating is dangerous. The design of the inductor's cup-shaped magnetic core is made of ferrite to reduce the magnetic dispersion field and increase the power factor. The lateral protrusions of the magnetic core limit the area with eddy currents.

Keywords: Valve · Rigid wedge · Thermal–hydraulic processes · Induction heating

1 Introduction

The flow control of the pumped-over liquids and gases is carried out by means of shut-off elements, one of which is a wedge gate valve. It is used as a blocking structure and is not intended to regulate flow. Wedge gate valves are considered the most reliable type of valves. Their area of application is pipelines with various working media. The contact surfaces of the valve body (seat) are located at a slight angle of inclination to each other, and the valve has the shape of a wedge, which in the closed position fits tightly between them. There are several types of steel gate valves [1]. In gate valves with a solid wedge made of one-piece, good tightness is ensured; but with a significant decrease in the ambient temperature, jamming is possible [2]. This problem is solved in valves with a two-disk integral locking element or a rubber wedge. Nevertheless, in spite of the advantages of constructions with a composite or rubberized wedge, gate valves with a rigid wedge are in operation. A rigid wedge ensures reliable tightness of

the shut-off element, which is achieved by increased precision of processing the surfaces of the wedge and the body seat [2, 3].

Figure 1 shows a simplified design of a rigid wedge gate valve. Sealing surfaces are welded with high-alloy steel, which allows long-term maintenance of the specified tightness during operation. The valve body is made of A732 (2A) steel.

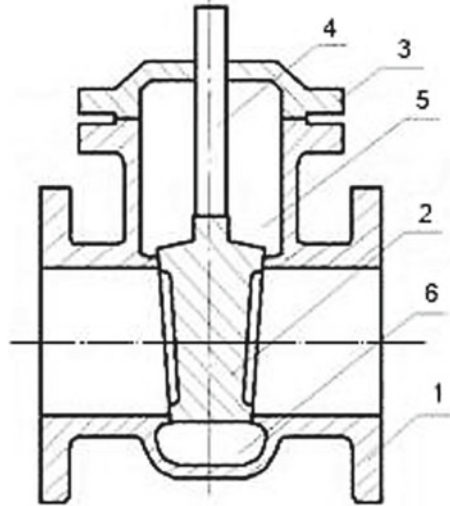


Fig. 1 Valve section: 1—body; 2—wedge; 3—cover; 4—rod; 5—cavity under the cover; 6—lower cavity

A tight fit of the wedge with the body is ensured when a significant force is created. For this, motors with a power of 0.025–7.5 kW are used with a nominal diameter of 50–1200 mm. The gate valve drive contains a reducer that reduces the rotation speed and increases the torque. All this leads to an increase in the forces created when the wedge is lifted, which, when jammed, can lead to a stem (spindle) breakage [4].

2 Task Formulation

Deformations of the body and components of the valve with temperature changes occur disproportionately due to the difference in physical properties and geometric non-symmetry.

A lot of works [2–9] are devoted to the problems of reliable operation of valves and, in particular, jamming, where the issues of improving calculation methods [6, 9], analysis of the causes of failure [7], modeling of deformation processes [10, 11] and improvement of operational characteristics [12].

To explain this problem in [10], an analysis of the deformation processes of gate valves with different body designs was carried out. The reason for the occurrence of significant compressive forces in the lower part of the wedge is revealed. This phenomenon occurs in valves in which the body is tapered at the bottom. In valves with a

cylindrical body shape, no deformations occur during cooling that can lead to seizure. Theoretically, it is possible to create a control system for the state of the valve. To do this, it is required, when external conditions change, to apply short-term control actions to the electric drive for opening and subsequent closing, so that the voltage in the valve is always at an acceptable level. A similar approach is implemented in the drilling rig [13].

In practice, the use of heating gate valves using a steam generator requires manual labor and time-consuming equipment transportation to the location. It is more convenient to use electric heating. The complex shape of the bottom of the case makes the induction method preferable to the resistive method.

Calculation of the parameters of an induction heater, including power, dimensions, and location, requires taking into account the limitation on the maximum temperature of the liquid inside the valve body, which depends on the thermophysical characteristics and on convective processes. Thus, when designing a heater, it is necessary to develop electromagnetic, thermal, and hydraulic models of the “gate valve—liquid” system, carry out calculations and determine the parameters.

3 Development of Mathematical Models

When designing gate valve structures, a lot of work has been devoted to determining the parameters of thermal deformation processes [10, 11, 14, 15].

Induction heating systems have been used for quite a long time, competing with other types of heating with great success. At the same time, such features of the technological process as high temperature and increased frequency of the supply voltage significantly limit the use of magnetic cores in the manufacture of inductors. This has a negative effect on the energy characteristics of induction heating devices, mainly due to the large stray magnetic fields. Recently, the use of magnetic cores made of new materials, such as magneto dielectrics, has somewhat expanded, which has a positive effect on the control of the distribution of the magnetic field and internal heat sources in the load. The proposed work is aimed at expanding the capabilities of induction devices through the use of magnetic circuits. The ultimate goal of such a solution is to increase the controllability of the process of forming internal sources. The peculiarity of the problems under consideration is the complexity of the mathematical apparatus and the significant resource consumption of computations [16–21].

Modeling thermal processes in itself is not so resource intensive. However, taking into account the increase in the sizes of the vectors of sources and stiffness matrices when combining electromagnetic and thermal problems, this procedure significantly complicates the calculation. It is much more economical and faster to identify the path of the current flow and determine the heat release power, in order to transfer it to the heat problem. Of course, it is unprofitable to do this in a one-time solution or in a two-dimensional setting.

Induction heating systems usually use higher voltage frequencies, which, together with low power factors, cause increased voltage and power losses in the network. The solution to the problem of designing an induction system should be focused on achieving such indicators as the minimum weight of the equipment complex, maximum autonomy from engineering systems, and high accuracy of temperature control [5].

Studies of deformation processes in the valve, occurring when the ambient temperature decreases, revealed the main reason for jamming of valves with a rigid wedge [10]. The narrowing of the body in the lower part leads to the appearance of forces directed along the horizontal axis of the valve. In the upper part of the wedge, the forces are directed to tension and in the lower part to compression. The tensile forces are not strong enough to create a visible gap, but the compressive forces are sufficient to prevent the valve actuator from seizing or breaking the stem. Thus, in order to eliminate the jamming phenomenon in this situation, it is necessary to eliminate the cause, that is, to warm up the valve. The complex design of the valve does not allow to act selectively on individual elements, since heat fluxes in different areas are due to thermal conductivity and convection processes in the liquid. To determine the effective design of the heater, studies of thermal and hydraulic processes are required [22].

The use of industrial frequency currents makes it possible to use laminated iron as a material for the magnetic circuit, but the lack of electrical conductivity in one direction is not enough for the disk structures of the inductor. Therefore, for the magnetic circuit, the use of ferrites is more profitable.

Two inductors for heating the vertical part of the housing are made in the form of multi-turn coils located in an annular groove. The use of numerical calculation methods makes it possible to obtain efficient heating systems for bodies of complex shapes [23, 24]. For the design of the induction heater, the software packages.

Ekcut, Comsol were used, which make it possible to calculate the electromagnetic and thermal processes [19–21].

To describe the electromagnetic field, a combination of vector magnetic potential A and electric scalar potential V is used to ensure the closure of magnetic fluxes and currents when the direction of movement is changed.

$$j\omega\sigma A + \nabla \times \left(\frac{\nabla \times A}{\mu_0\mu_r} \right) + \sigma \nabla V = J^e; \quad (1)$$

$$-\nabla(j\omega\sigma A + \sigma \nabla V - J^e) = 0; \quad (2)$$

There: ∇ —nabla, $\nabla = \frac{\partial}{\partial x} \vec{i} + \frac{\partial}{\partial y} \vec{j} + \frac{\partial}{\partial z} \vec{k}$, where \vec{i} , \vec{j} , \vec{k} —unit vectors along the axes x , y , z , respectively, μ_0 , μ_r —vacuum magnetic permeability and μ relative magnetic permeability of the media.

The zero equality of the potential combination on a surface far from the structure is used as boundary conditions

$$A = 0; V = 0. \quad (3)$$

A three-dimensional region is used to describe thermal processes. The equation of thermal conductivity with internal heat sources has the form

$$\rho C_P \frac{\partial T}{\partial t} + \nabla \cdot (-k \nabla T) = Q - \rho C_P \mathbf{u} \cdot \nabla T; \quad (4)$$

There: ρ —material density; k —coefficient of conductivity; T —temperature; Q —specific heat input, \mathbf{u} —vector of the displacement velocity.

The speed of movement is provided for the liquid filling the body.

Convective heat transfer in the formula is used as boundary conditions on surfaces

$$k \frac{\partial T}{\partial n} = \alpha(T - T_{\text{ext}}); \quad (5)$$

n —normal line in relation to the surface under consideration.

The condition of thermal insulation is set on the line of symmetry

$$k \frac{\partial T}{\partial n} = 0. \quad (6)$$

The initial temperature value is assumed to be equal to the ambient temperature $T_0 = T_{\text{ext}} = 253 \text{ K}$.

The fluid velocity is determined in the application for calculating hydraulic processes and imported into the thermal model

$$\mathbf{u} = [u \ v]^T. \quad (7)$$

coefficient of conductivity $k = 0.11 \text{ W/(m K)}$, density $\rho = 880 \text{ kg/m}^3$, heat capacity $C_p = 1700 \text{ J/(kg K)}$.

The Navier–Stokes equation for an incompressible fluid is used to simulate hydraulic processes

$$\rho(u \cdot \nabla)u = \nabla \cdot [-pI + \eta(\nabla u + (\nabla u)^T)] + F, \quad (8)$$

$$\nabla \cdot u = 0. \quad (9)$$

coefficient of dynamic viscosity $\eta = 0.005 \text{ Pa s}$.

The vertical component of the lift force is set for the formation of convective fluid transfer flows

$$\begin{aligned} F_y &= -9.81 \cdot (880 - 0.6 \cdot (T - 253)), \\ F_y &= -g \cdot (\rho - k_V \cdot (T - T_0)). \end{aligned} \quad (10)$$

There $k_V = 0.6 \text{ kg/(m}^3\text{K)}$ —coefficient of decrease in fluid density due to temperature increases.

The zero velocity on the line corresponding to the wall is set as the boundary conditions

$$u = 0, \quad (11)$$

The velocity is set as a scalar value in the sections of axial symmetry U_w and the condition prescribes.

$$n \cdot u = 0, \quad u \cdot t = U_w. \quad (12)$$

There: t —vector value $t = (-n_x, n_y)$.

Thus, the boundary condition is written.

$$n \cdot u = 0, \quad t \cdot \left[-pI + \eta (\nabla u + (\nabla u)^T) \right] n = 0 \quad (13)$$

Simulation of hydraulic processes in this problem has features associated not only with heating, but also with the complex shape of the internal cavity of the valve, which complicates the calculation [25].

Thus, a complex of mathematical models for two- and three-dimensional formulation has been formed, which makes it possible to calculate electromagnetic and thermal processes when studying the properties of an induction heater with a magnetic core.

4 Calculation of the Heating System Parameters

Heat sources are provided in the lower part of the housing under the wedge, in the vertical part in the area, from the base to the horizontal center line.

Modeling of thermal processes without taking into account hydraulic processes was carried out on a three-dimensional model. One inductor is located in the lower part of the housing and two inductors in the vertical part at a height not exceeding the point of the centerline of the valve. The simulation implemented a temperature control system that limits the maximum value.

When calculating thermal processes, the required heat release power in each zone was determined. The power of the lower inductor is 2 kW, for vertical 1 kW. The total power is 4 kW.

The considered approach to solving the heating problem has a large error in the calculations due to the lack of consideration of hydraulic processes. The complexity of the design, the size of the computational domain, and the combination of solid and liquid media make it difficult to use a three-dimensional thermohydraulic model. To study the processes of convective heat transfer, a two-dimensional model for a liquid medium is used. Heat supply is specified using boundary conditions of the third kind. The heat transfer coefficient is taken equal to 500, which allows one to correctly approximate the real process of heat transfer from a metal wall into a liquid. In a real heating process, the increase in the wall temperature and the heating of the liquid occur simultaneously. To speed up the computational process, taking into account the duration of the heating process of the walls of the valve body, it is assumed in the calculations that the wall temperature is 100 °C. The temperature and velocity distributions shown in Fig. 2 for times 2 s and 12 s illustrate the rapid formation of a convective fluid flow, which leads to the rise of a thin layer along the outer surface, followed by lowering along the surface of the wedge.

The small thickness of the liquid layer in the lower part does not allow the formation of large vortices. At time 12 s, a large number of small moving vortices are formed in the entire volume. Because of this, the density of the heat flux into the liquid from the wall is unstable (Table 1). At the time of 10 s, there is some stabilization of the heat exchange process and the movement of the liquid. After that, the density of the lower section flow q_2 changes within 3% and for the upper section q_1 —5%. The maximum velocity of the liquid near the wall increases to 4 sm/s. This leads to the fact that the density of the heat

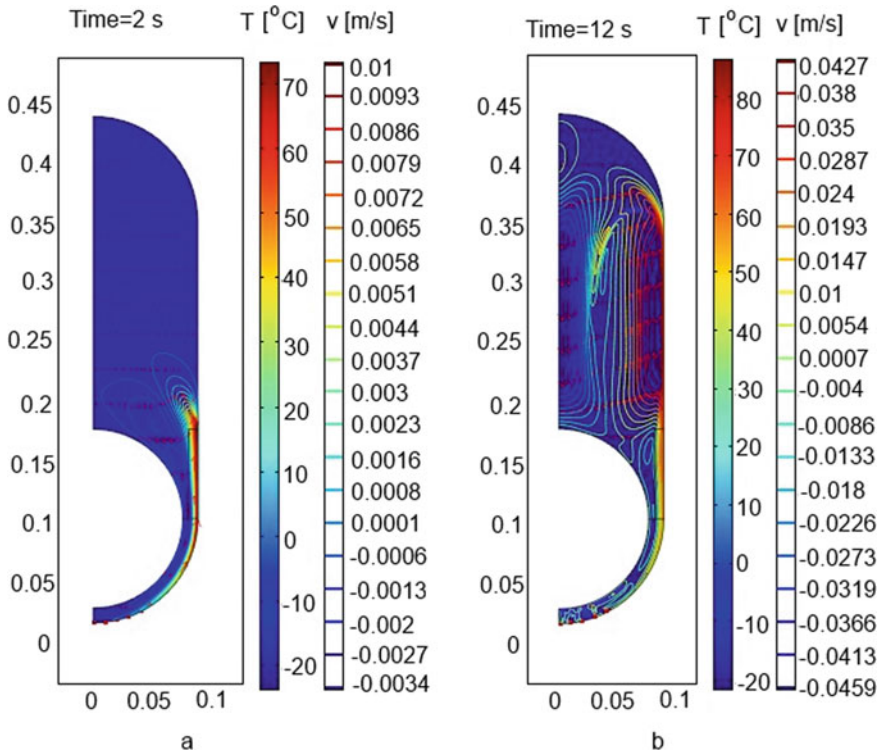


Fig. 2 Temperature and velocity distributions of the liquid in the valve in the wedge subspace: **a** at time 2 s; **b** at time 12 s

flux from the wall in comparison with the transfer of heat to a stationary fluid is more than ten times. As can be seen from Table 1, the density of the heat flux q_3 absorbed by the wedge is only 24–34 W/m. This is much less than the flux absorbed by the liquid.

Table 1 Heat flux density from the walls

t (s)	4	6	8	10	11	12	14	16	18
q_1 (W/m)	1009	875	823	799	806	819	841	839	855
q_2 (W/m)	1988	2115	2238	2239	2220	2277	2232	2171	2170
q_3 (W/m)	10	4	5	23	18	24	27	26	34

The results obtained show that heat transfer to the “saddle-wedge” connection with a limitation on the maximum value of the wall temperature is more efficient due to convective flows in the liquid. A significant part of the heat is absorbed by the upper layers of the liquid above the wedge. Therefore, the heating of the wedge, when only the convective heat transfer is taken into account, is a long process.

The calculated value of the heater power can be determined based on the heat flux density and the area of the side and bottom surfaces of the case, which are available for placing the induction heaters. Based on the values of the surface area of the base and a fragment of the vertical surface and heat flux densities, the heat release power in the load is 800 W and 2×100 W. 1800s.

5 Determination of Inductor Parameters

The calculation of inductors for heating the lower bowl-shaped surface and the sector of the frontal cylindrical surface is performed using two-dimensional models, which, with some assumptions, provides an acceptable error. The appearance of the first inductor is shown in Fig. 3. The multilayer coil is bounded on the lower side by a magnetic circuit, which reduces stray fields and serves as a support structure.

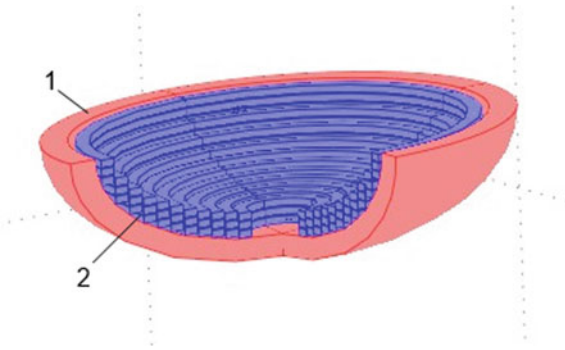


Fig. 3 Inductor for the lower surface of the valve body

Two variants of the inductor design are considered—without cooling when using power frequency voltage and with cooling when using increased frequency. At 50 Hz, the limitation is the inductor temperature. Increasing the number of layers increases the magnetic field strength and loading power. Each additional layer reduces the efficiency and worsens the conditions for heat exchange between the coil and the environment. As a result, due to the limitation on the current density, the power value in the load was obtained $P_2 = 500$ W instead of the required 800 W. The coil contains 135 turns of a copper bus with a cross section of 1.5×3 mm². The inductor current is 45 A, and the voltage is 220 V. The power factor is 0.278, and the efficiency is 0.927.

The variant with the use of an increased frequency is more attractive from the point of view of the reliability of the inductor, since the required power in the load is provided without overheating of the conductors. However, the need for a semiconductor frequency converter and an inductor cooling system reduces the reliability of the heating system, which is unacceptable in the case of maintenance-free installations.

When calculating the parameters of the inductor, a profiled tube with sides equal to 10 mm is provided as conductors of the inductor coil. The calculation results given show (Table 2) that a step-down transformer is required to match the frequency converter.

Table 2 Parameters of inductors at different current frequencies

F (Hz)	2400	4000	10,000	20,000
I (A)	195	155	104	75
U (V)	27	31	43	54
P_2 (W)	781	801	814	780
ΔP_{ind} (W)	387	365	203	142
P_{ind} (W)	1188	1154	1017	922

In general, a high-frequency heater is inferior to a low-frequency heater in terms of costs and implementation complexity.

The inductor for heating the sector of the vertical front surface of the valve body has a design with one annular groove in the magnetic circuit, in which a multi-turn coil has the shape of a rectangle. With the power in the load increased to 200 W, the voltage is 220 V, the current is 71 A, the number of turns is 51, and the conductor cross section is 10 mm². The dimensions of the inner window are 10 × 10 mm, which is filled with a core. Research has shown that without a central core, the performance of an inductor degrades dramatically.

6 Conclusion

The development of an induction heating system for individual sections of the valve body allows solving an important problem—eliminating jamming and ensuring operational control of pipelines with oil products. Studies of electromagnetic, thermal, and hydraulic processes in the “inductor–valve body–oil” system made it possible to determine the parameters of induction heaters and the location of temperature sensors that guarantee trouble-free operation.

Acknowledgements. Work on the article was supported by the Russian Federal Property Fund (project No. 19-06-00212)

References

1. Shegelman IR, Vasilyev AS, Shchukin PO (2015) Zadvizhka zapornaya dlya truboprovoda (Gate valve for the pipeline). *Nauka i biznes: puti razvitiya* (Science and business: ways of development). *Fond razvitiya nauki i kultury Publ* 8(50):36–38
2. Podrezova IS, Shutova LV, YuYe U, Pugacheva OYu, Yelzhov YuN (2014) Analiz prichin zaklinivaniya i obryvov shtokov truboprovodnoy elektropriwodnoy armatury (Analysis of the causes of jamming and breaks in the rods of electric pipeline valves). *Globalnaya yadernaya bezopasnost* (Global nuclear security) 4(13):32–37
3. Zhuk DI, Gaffanov RF, Shchenyatskiy AV (2016) Analiz vliyaniya mekhanicheskikh vozdeystviy na uplotnitelnye poverkhosti zaporno-reguliruyushchey armatury (Analysis of the influence of mechanical stresses on the sealing surfaces of shut-off and control valves). *Vestnik IZhGTU imeni M.T. Kalashnikova* 19(2):27–29

4. Kakuzin VB et al (2008) Problemy nastroyki elektroprivodov zadvizhek (Problems of setting up electric actuators of valves). *Armaturostroenie* 4(55):74–76
5. Berniker YeI (1966) Posadki s natyagom v mashinostoenii (Fixing tight in mechanical engineering). *Mashinostroenie Publ.*, Moscow, Leningrad, p 168
6. Kuznetsova NV (2010) Truboprovodnaya armatura. Konstruirovaniye i raschet zadvizhek stalnykh klinovykh (Pipe fittings. Design and calculation of wedge gate valves). *Sputnik Publ.*, Moscow, p 175
7. Muratayev FI (2017) Issledovaniye razrusheniya litogo korpusa zadvizhki magistralnogo nefteprovoda (Investigation of the destruction of the molten body of the valve of the main oil pipeline). *Professionalnye kommunikatsii v nauchnoy srede – faktor obespecheniya kachestva issledovaniy* (Professional communication in the scientific environment—a factor in ensuring the quality of research). In: Yudinoy SV (ed) *Proceedings of the All-Russian Scientific and Practical Conference*, Pero Publ, Moscow, pp 27–32
8. Zakirnichnaya MM, Kulsharipov IM (2016) Osobennosti rascheta resursa bezopasnoy ekspluatatsii klinovykh zadvizhek s uchetom rabochikh parametrov v tekhnologicheskikh truboprovodakh (Features of calculating the resource for the safe operation of wedge gate valves, taking into account operating parameters in process pipelines). *Neftegazovoe delo* (Oil and gas business) 14(4):121–125
9. Zhukovskiy VK, Gokhman AR (2009) Svyaz koeffitsienta lineynogo temperaturnogo rasshireniya s ostatochnymi napryazheniyami (The relationship of the coefficient of linear thermal expansion with residual stresses). *Gurnal tekhnicheskoy fiziki [J Tech Phys]* 79(4):90–96
10. Bazarov AA, Bondareva NV, Navasardyan AA (2019) Modelirovaniye protsessov deformatsii v zadvizhke (Modeling of deformation processes in a valve) *Sbornik statey “EurasiaScience” XXV Mezhdunarodnaya nauchno-prakticheskaya konferentsiya. 15 noyabrya 2019* (Proceedings of the “EurasiaScience” XXV International Scientific and Practical Conference. November 15, 2019). *Aktualnost RF Publ Part I*:69–72
11. Barbotko MA (2018) Chislennoye modelirovaniye termicheskikh napryazheniy i deformatsiy v tsilindre s uprugoplasticheskoy obolochkoy i vyazkoupругim zapolnitelem (Numerical simulation of thermal stresses and strains in a cylinder with an elastoplastic shell and a viscoelastic filler) *Vestnik inzhenernoy shkoly Dalnevostochnogo federalnogo universiteta* 4(37):16–23
12. Mayskiy RA, Chernova AYu (2014) Vozmozhnosti programmnykh kompleksov na osnove metoda konechnykh elementov pri otsenke rabotodosobnogo sostoyaniya elementov truboprovodnoy armatury (Possibilities of software systems based on the finite element method in assessing the operational state of pipeline fittings). *Informatsionnye tekhnologii. Problemy i resheniya* (Information technologies. Problems And solutions) 1–2:47–49
13. Ma W, Ma F (2016) Modeling and experimental study on drilling rig anti-jamming valve with BP neural network. *Eng Rev* 36(2):99–106
14. Sathishkumar S, Hemanathan R, Gopinath R, Dilipkumar D (2017) Design and analysis of gate valve body and seat ring. *Int J Mech Eng Technol* 8(3):131–141
15. Glukhov VI, Shalay VV, Grinevich VA, Panin YuN (2018) Geometricheskoye modelirovaniye detaley klinovogo zatvora dlya obespecheniya germetichnosti zadvizhek (Geometrical modeling of wedge gate parts to ensure valve tightness) *Tekhnika i tekhnologiya neftekhimicheskogo i neftegazovogo proizvodstva. Materialy 8-y mezhdunarodnoy nauchno-tekhnicheskoy konferentsii* (Equipment and technology of petrochemical and oil and gas production. In: Proceedings of the 8th International Scientific and Technical Conference), Omsk State Technical University, pp 193–194
16. Zenkevich O (1975) Metod konechnykh elementov v tekhnike (Finite element method in engineering). *Mir Publ*, Moscow, p 541

17. Khalifa M, Barka N, Brousseau J, Bocher P (2019) Optimization of the edge effect of 4340 steel specimen heated by induction process with flux concentrators using finite element axis-symmetric simulation and experimental validation. *Int J Adv Manuf Technol* 104, 9–12(1):4549–4557
18. Alferov BI, Steshenkova NA (2010) *Primenenie MKE dlya resheniya teplovoy i deformatsionnoy zadach rascheta svarochnykh deformatsiy sudovykh korpusnykh konstruksiy (FEM for solving thermal and deformation problems of calculation of welding deformations of ship hull structures)*. *Proc Trans Krylov State Res Centre* 56(340):147–162
19. Nemkov VS, Demidovich VB (1988) *Teoriya i raschet ustroystv induktsionnogo nagreva (Theory and calculation of induction heating devices)*. *Energoatomizdat Publ, Leningrad*, p 280
20. Kuvaldin AB (2005) *Matematicheskie modeli dlya issledovaniya elektromagnitnogo polya v ferromagnitnykh sredakh (Mathematical models for the study of electromagnetic fields in ferromagnetic environment)*. *Electricity* 11:56–61
21. Gnatov AV, Argun Shch V, Chaplygin EA, Sabokar OS (2015) *Induktsionnyy nagrev ferromagnetikov ploskim krugovym mnogovitkovym solenoidom (Induction heating of ferromagnets with a flat circular multi-turn solenoid)*. *Vestnik Kharkovskogo natsionalnogo avtomobilno-djrozhnogo universiteta (Report of the Kharkiv National Automobile and Road University)* 70:113–118
22. Hinov N, Petkov T, Ibrishimov H (2019) *Modeling of the thermal and electromagnetic processes in the induction water heating system*. In: *Proceedings of the 28th international scientific conference electronics, ET 2019, September 2019, Bulgaria*: 8878577
23. Mannanov, Galunin S, Yermekova M, Nikanorov A, Nacke B (2019) *Numerical simulation, investigation and development of induction systems for heating of disks with complex profile*. In: *Proceedings of the 2019 IEEE Conference of Russian Young Researchers in Electrical and Electronic Engineering, ElConRus 201928 February 2019, Saint Petersburg and Moscow, Russian Federation*; 28–30 January 2019, 8656912, pp 606–608
24. Tong Q, Hu L (2019) *Optimal design and finite element simulation of induction cooker magnetic circuit*. In: *Proceedings of 2019 IEEE 3rd Information Technology, Networking, Electronic and Automation Control Conference, ITNEC 2019 March 2019, 3rd; Chengdu, China*; 15–17 March 2019, 8729552, pp 2545–2548
25. Temirbekov N, Malgazhdarov Y, Tokanova S, Amenova F, Baigereyev D, Turarov A (2019) *Information technology for numerical simulation of convective flows of a viscous incompressible fluid in curvilinear multiply connected domains*. *J Theor Appl Inf Technol* 97(22):3166–3177



Research of the Modified Tooth-Belt Drive for the Machining Center

S. Shevchenko¹, A. Mukhovaty¹, and O. Krol²(✉)

¹ Volodymyr Dahl Lugansk State University, 20-a, Kvartal Molodezny, Lugansk 91000, Ukraine

² Volodymyr Dahl East Ukrainian National University, 59-a Central Pr, Severodonetsk 93400, Ukraine

krolos@snu.edu.ua

Abstract. The article discusses the drive of the main movement for the machining center with a modified toothed-belt drive. A three-dimensional model of the drive in the environment of the integrated CAD KOMPAS-3D is built. The main parts such as a stepped shaft, a belt pulley, and gears in the 3D-representation in the special application “Shafts and mechanical transmissions-3D” are implemented. A procedure for parametric modeling of the toothed-belt drive elements in CAD APM WinMachine is proposed, intended for the design of both standard and modified versions. The article presents the results of the two variants study with toothed-belt drive constructive modification—with convex and concave in the longitudinal direction of the belt teeth. The main parameters of both modifications teeth, which showed their advantage over standard toothed belts in terms of load capacity, have been obtained. The possibility of self-adjusting for the proposed variants of belts with a curved shape of the working teeth surfaces is noted.

Keywords: Toothed belt · Convex · Concave belt · Base area · Tooth parameters · Belt self-adjusting

1 Introduction

In the structure of universal CNC machines and machine-tool complexes, drives of the main movement with a DC motor of the 2P series with two-zone regulation are often used. For some technological operations performed on machine tools, the control range must be increased, which is carried out by the introduction of an additional gearbox and belt transmission [1–3]. The widespread use of toothed-belt drive (TBD) for these machine configurations is associated with the ability to maintain the gear ratio when the external load changes and reasonably high efficiency. TBD performance is determined through the main criterion—belt tractive ability, which is estimated by the permissible reduced specific force transmitted by 1 mm of the belt width [4–6].

Some design and performance improvements aim at increasing tractive ability and reliability of the TBD drive.

The patent [7] proposes a new design TBD, the belt teeth of which have a convex profile, and the pulley grooves are concave. The height of the belt teeth exceeds the

depth of the pulley groove. The disadvantages of this patent solution include increased deformation of the belt teeth and the presence of flanges on the end surfaces of the pulleys, which leads to significant losses of friction power. It is impossible to discount the additional costs for the technology of manufacturing the tooth profile.

In [8], the study of the process of increasing the toothed belt pitch and the change in its length, which occur during operation and remains after unloading the belt is carried out. It is proved that the maximum value of the transmitted power depends on the shape and much less on the frictional forces in the contact zone. The main mechanism of this phenomenon, according to the authors, is the plastic deformation of the belt (tape)—about 70%. In [8], the analysis of the factor associated with rolling on the side surface of the belt was carried out. Impact, sliding, and rolling within the confines of tribo-mechanical systems are considered as the main movements of the toothed belt. Of interest is the phenomenon of rolling with linear contact between the belt tooth which occurs in the contact zone. During an engagement, an interference (preload) occurs when the belt tooth cuts into the flank of the pulley tooth. In contrast to the gear transmission, this phenomenon leads to a sharp increase in belt deformation, but with a simultaneous increase in the contact surface of the belt with the pulley [8]. The authors point out the importance of taking into account the friction force on the sides of the belt and pulley. Besides, the frictional forces on the flange surfaces of the belt can also change the pitch of the belt. Together, these processes lead to a disruption function of the toothed belt, which is expressed in a change in load distribution, a decrease in carrying capacity and uneven operation. There is a need for additional belt tension, which directly affects the durability of the transmission. It was noted in [9] that the belt tension force has a constant component (initial tension force) and periodic, caused by the contact of the belt teeth and the pulley in the process of torque transmission. Moreover, a change in the last component can cause the operating state to fall into the region of instability.

Modification of the belt design affects the specified service life. The condition of TBD elements and their basic mechanical properties must be monitored online. In this regard, the mechanism for measuring the thickness of the belt (conveyor tape) and assessing the change in its transverse and longitudinal profile is promising. [10]. Evaluation of the operability condition is carried out along the belt axis, and control is carried out by the specialized DiagBeltSonic application. This information about the belt's cross-section along the entire length, as well as its longitudinal and transverse profiles, provides feedback to the designer of mechanical transmissions and, as a result, contributes to rational design decisions aimed at increasing the reliability of the TBD. Along with the geometric characteristics, it is important to evaluate the level of loads arising in the belt drive. In [11], algorithms for calculating the forces, arising in the transmission, taking into account the parameters of the belt and the structural characteristics of the TBD elements were developed. For these purposes, the authors have developed a specialized information system for collecting complex data (technical and operational). The processing of statistical data allows to give a reliable assessment of the transmission elements state and is used for simulation calculations.

Another aspect of the influence of the tension layer on the mechanical properties of toothed belts is considered in [12]. The analysis of materials, type of fibers, and the number of the carrier layer fibers on the mechanical characteristics of the belt are

carried out. The current study concerned T10 and AT10 trapezoidal toothed belts. It is noted that in addition to the composition of the rubber compound, an important aspect is the so-called mechanical stabilization and orientation of the structure, which reduces energy losses caused by internal friction and increases the mechanical strength of the belt material in tension and intensions.

Analysis of the above works showed the importance of research related to the search for modified designs of belt drive elements, taking into account their correct orientation in the working space of the machine.

Formulation of the problem. The purpose of this work is to improve a toothed-belt drive design by finding a rational geometry of the belt teeth and the corresponding geometry of the pulleys, as a result of which it is expected to increase the load capacity of the transmission by the toothed belt.

2 Three-Dimensional and Parametric Modeling of a Toothed-Belt Drive for Machining Center

A typical representative of CNC machines with an extended control range is the machining center model MC200PF4V. This machine has a portal layout with a longitudinally movable cross slide, along which a portal rack moves transversely, carrying a vertically movable spindle head [13–15]. The torque from the engine to the input shaft of the gearbox is transmitted by TBD, which is characterized by the module $m = 4$ mm and the gear ratio $u = 1.4$. In this work, a three-dimensional model of the main motion drive with a toothed-belt drive (Fig. 1) is developed in an integrated CAD KOMPAS-3D [16–18]. Models of mechanical transmissions and drive shafts are created in the specialized application “Shafts and mechanical transmissions-3D” [19–21]. In a separate section of the appendix, the design calculation of the TBD is carried out, and solid models of the driving and driven pulleys are built.

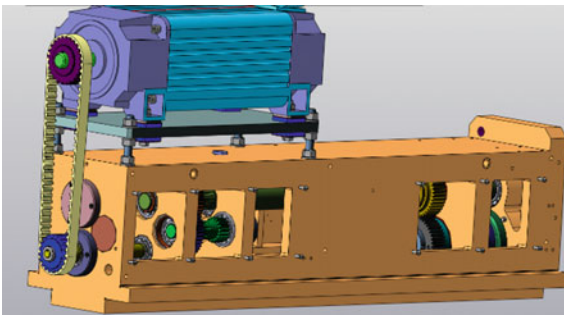


Fig. 1 3D model of the main motion drive of the MC200PF4 machine

A large nomenclature of metal-cutting equipment predetermines a variety of types and designs of belt drives [22–24]. This increases the time required to design workable gear options. One way to improve the productivity of the design process is to use a

parameterization mechanism. CAD/CAE APM WinMachine [25–27], which is compatible with the CAD system KOMPAS-3D, is efficient in terms of constructing parametric models of mechanical transmissions. The resulting parametric mechanical transmission models will allow to streamline the design process in the 2D editor and modeling in the 3D system editor. In the process of parameterization, the syntax of the APM Graph module is used [28, 29]. Figure 2 shows the window of variables (Fig. 2a), in which the input of the initial and derived variables, as well as logical expressions for building in the command window a parametric model of the TBD belt and pulleys, is carried out. The developed program is focused both on the classical design of the toothed-belt transmission and on the modified versions (Fig. 2c). To do this, use the “Command execution condition” option in the command window of the APM Graph module. Figure 2b shows a drawing of the TBD design, made based on the constructed parametric model.

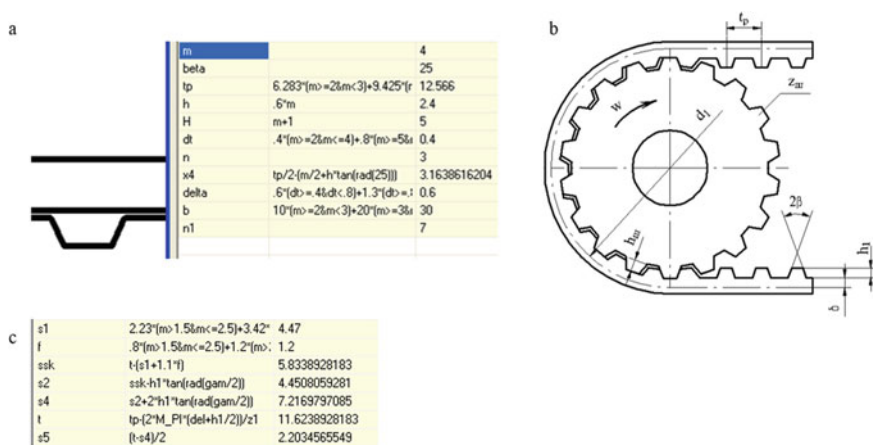


Fig. 2 **a** Parametric modeling of a pulley: fragment of the program; **b** drawing; **c** modification of the tooth profile

3 Modification of Toothed-Belt Drive

To improve the technical and economic characteristics of the TBD and, first of all, to increase the load capacity and reduce the friction of the lateral sides of the belt on the flanges, this article discusses two new design varieties of toothed-belt transmission [4, 30].

The task is achieved by the fact that the shape of the lateral sides of the teeth in the longitudinal direction changes in the toothed-belt transmission. The research is aimed at finding opportunities to increase the contact length of the belt and pulley by using a convex shape, outlined by an arc of a circle with a radius R and a central angle β .

There are two options for the modified design of the TBD.

Convex belt teeth—option (I).

In this design of the toothed-belt transmission, the sides of the belt teeth convex in the longitudinal direction contact with the sides of the pulley teeth concave in the same direction. Figure 3 shows a fragment of the developed 3D model of the modified design TBD—option (I):

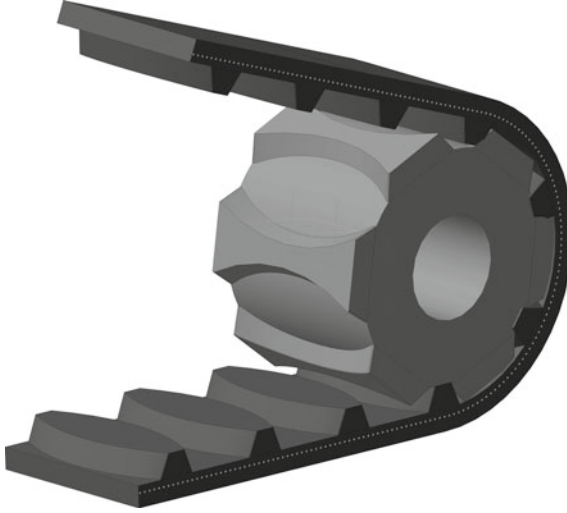


Fig. 3 Modified belt drive with convex teeth

Specified transmission parameters (Fig. 4): belt width b , module m , pitch $P = \pi m$ and height of teeth h , and the angle between the lateral sides of the teeth $\gamma = 40^\circ$. The numerical values of these parameters are determined from the known dependencies from [6]. The parameter S is also considered a given value, and we take $S = 0.75P$.

To identify the shape, we define three parameters (Fig. 4): the radius of the circular arc of the convex tooth R , the central angle β , and the width of the belt teeth tip at its end S_T .

From Fig. 4a, two obvious relationships follow (1):

$$\begin{cases} \sin(\beta/2) = 0.5 \cdot b/R; \\ \cos(\beta/2) = \sqrt{R^2 - 0.25 \cdot b^2}/b. \end{cases} \quad (1)$$

Solving these equations together, we find the values of two unknown parameters of the belt teeth: $R = b$; $\beta = 60^\circ$. After simple geometric constructions, the third desired parameter of the belt teeth is determined—the width of their tooth tip at the ends of the belt S_T (2):

$$S_T = 0.75 \cdot P - 2 \cdot [R - R_a \cdot \cos(\beta_a/2)], \quad (2)$$

where $R_a = R - h \cdot \operatorname{tg}(\gamma/2)$; $\beta_a = 2 \cdot \arcsin\{0.5b/[R - h \cdot \operatorname{tg}(\gamma/2)]\}$.

The longitudinally convex shape of the belt tooth lengthens its lateral surface to a value $L = R \cdot \beta = b \cdot 60 \cdot \pi/180 = b \cdot \pi/3$. This will lead to an increase in

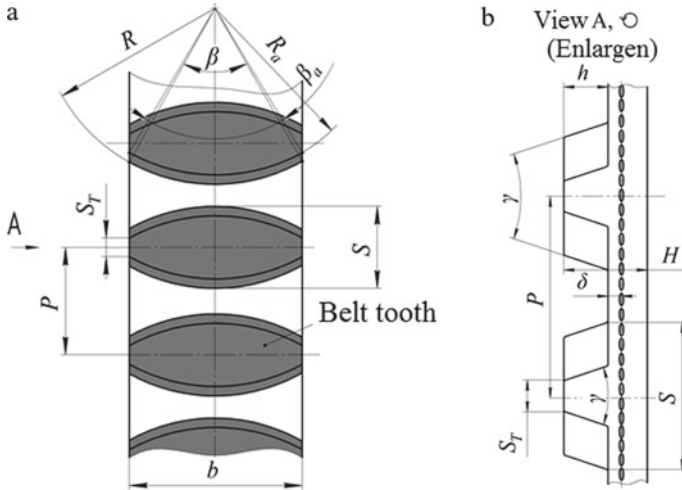


Fig. 4 **a** Modified transmission parameters with convex teeth; **b** cross-section

the total area of the side surfaces of the belt teeth on the arc of the belt contact for the smaller pulley by at least a factor of $(\pi/3) \cdot z_{1\min}$, where $z_{1\min} = 3 \div 4$ —the minimum number of belt teeth on this arc, which corresponds to the most unfavorable combination of transmission parameters, when their values have maximum permissible values: $a = a_{\min}$, $d_1 = d_{1\min}$, $u = u_{\max}$. Side surfaces of each convex tooth in comparison with straight teeth from [6], all other things being equal, are ~5%. This, in turn, will reduce the specific pressure on the teeth and, as a result, will increase the load capacity of the toothed-belt transmission with its unchanged dimensions.

Besides, the convex longitudinal shape of the belt teeth increases the tooth base area A_I , which increases their resistance to shear stress. The value A_I (3) is determined by the equality:

$$A_I = b^2 \cdot (\beta - \sin \beta) + b \cdot \{0,75 \cdot P - 2 \cdot b \cdot [1 - \cos(\beta/2)]\}. \quad (3)$$

The base area of standard straight teeth A_0 (4):

$$A_0 = 0,5 \cdot P \cdot b = 0,5 \cdot \pi \cdot m \cdot b \quad (4)$$

which is significantly less area A_I . For example, for a toothed-belt transmission with parameters: $m = 5$ mm, $b = 25$ mm, $\beta = 60^\circ$, numerical values A_I and A_0 will be (5):

$$A_I = 25^2 \cdot [\pi/3 - \sin(\pi/3)] + 25 \cdot \{0.75 \cdot 15.7 - 2 \cdot 25 \cdot [1 - \cos(\pi/6)]\} \approx 240 \text{ mm}^2; \\ A_0 = 0.5 \cdot 15.7 \cdot 25 \approx 196 \text{ mm}^2. \quad (5)$$

That is, the area A_I exceeds the value A_0 by 22%, which shows the potential superiority of convex teeth over straight teeth in shear resistance.

Finally, another advantage of belts with modified teeth is the ability to self-adjusting on pulleys, which is impossible with standard timing belts [6] due to the straight-line shape of their teeth in the longitudinal direction.

4 Discussion

(II) Concave belt teeth, Fig. 5.

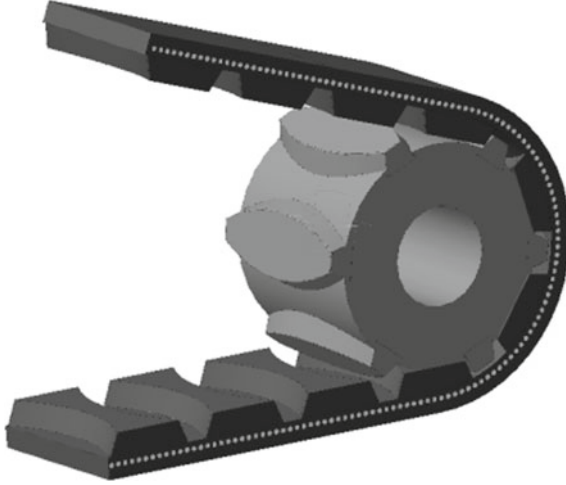


Fig. 5 Modified belt drive with concave teeth

In comparison with (I), structural modification (II) is its mirror opposite—the lateral sides of the belt teeth concave in the longitudinal direction contact with the lateral sides of the pulley teeth convex in the same direction.

The values of R and β remain the same as in (I): $R = b$; $\beta = 60^\circ$.

The fundamental difference in calculations (II) and (I) is that for concave belt teeth, we set the minimum transverse dimension of the belt tooth—the width of its tips S_a in the middle section of the belt, Fig. 6, b: $S_a = 0.25P$.

Omitting intermediate actions using the data in Fig. 6, a; b, we present the final analytical dependences for calculating the remaining parameters belt teeth according to option (II) taking into account the accepted value $S_a(6)$:

$$\begin{aligned}
 S &= 0.25p + 2h \cdot \operatorname{tg}(\gamma/2); \\
 S_T &= 2R[1 - \cos(\beta/2)] + 2h \cdot \operatorname{tg}(\gamma/2) + 0.25P; \\
 S_{TP} &= 0.75P - 2R[1 - \cos(\beta/2)] - 2h \cdot \operatorname{tg}(\gamma/2); \\
 A_{II} &= b \cdot \{2R[1 - \cos(\beta/2)] + 2h \cdot \operatorname{tg}(\gamma/2) + 0.25P\} - R^2(\beta - \sin \beta). \quad (6)
 \end{aligned}$$

Find the numerical value A_{II} and compare it with $A_I(7)$:

$$\begin{aligned}
 A_{II} &= 25 \cdot [2 \cdot 25(1 - \cos 30^\circ) + 2 \cdot 3.5 \cdot \operatorname{tg} 20^\circ = 0.25 \cdot 15.7] \\
 &\quad - 25^2 \cdot \left(60^\circ \cdot \frac{\pi}{180} - \sin 60^\circ\right) \approx 216 \text{ mm}^2. \quad (7)
 \end{aligned}$$

The area A_{II} is less than $A_I \approx 240 \text{ mm}^2$, but more than $A_O \approx 196 \text{ mm}^2$, that is, $A_{II} > A_I > A_O$. Therefore, both new design versions of the toothed belt are superior

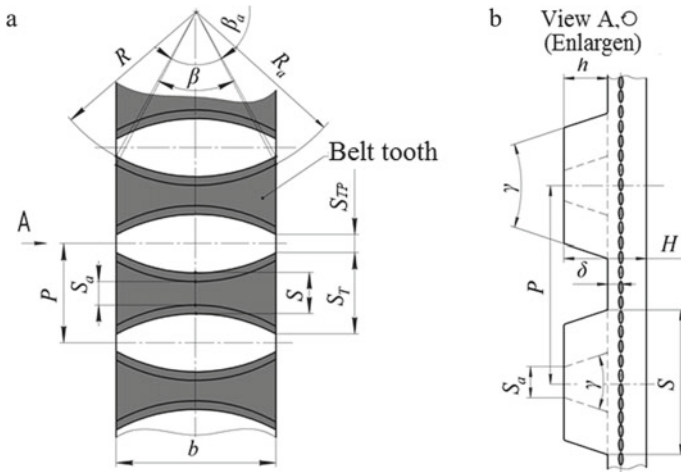


Fig. 6 **a** Modified transmission parameters with concave teeth; **b** cross-section

to the standard toothed belt in shear resistance but to a different extent. As for the areas of the flank surfaces of the teeth, they are the same in versions (I) and (II), since the parameters R , β , h defining them have the same numerical values.

At the same time, the method of designing modified belts does not differ from the generally accepted one, [4–6], but taking into account the replacement of the parameter b with an increased length of the teeth $L = b \cdot \pi/3$.

Like belts with the modification (I), belts (II), due to the curved flank of the teeth, have the ability to self-adjusting on the pulleys.

5 Conclusion

In the work, the 3D model of the assembly structure of the machine-tool drive was created in the KOMPAS-3D computer-aided design system, consisting of more than 300 parts. This project became the winner of the International competition “Future Aces of Computer 3D Modeling” held by the ASCON group of companies. A program for parametric modeling of toothed-belt drives of standard and modified designs has been developed. This program, written in the CAD / CAE APM WinMachine environment using the syntax of the APM Graph module, provides a more efficient design of mechanical transmissions of various modifications.

Two constructive modifications of drive toothed belts with the curved shape of working surfaces of teeth have been developed. The proposed designs make it possible to increase the contact length of the belt by about 5%, which, in turn, will reduce the specific pressure on the teeth and, as a consequence, increase the load capacity of the toothed belt transmission with its unchanged dimensions. This modified design is patented.

An analytical model for determining the geometric parameters of modified toothed-belt drives has been developed. Based on this model, it has been proved that the base area of a modified convex belt exceeds the corresponding value of a standardized belt by

about 22%. It shows the potential superiority of convex teeth over straight teeth in shear resistance. This makes it possible to increase their traction capacity or, at a constant level of external load, to increase the resource of the belts in comparison with standard transmission toothed belts. The proposed new design modifications of the teeth allow the toothed belts to self-adjusting on the pulleys, which eliminates the displacement of the belts to the ends of the pulleys, which occurs with standard toothed-belt drives.

References

1. Bushuev VV, Eremin AA, Kakilo AA (2012) *Metallorėzhuschie stanki: Uchebnik (Metal-cutting machines: Textbook)*. Mashinostroenie, Moscow
2. Avramova TM, Bushuev VV, Gilova LYa (2012) *Metallorėzhuschie stanki: Uchebnik (Metal-cutting machines: Textbook)*. Mashinostroenie, Moscow
3. Solomentsev YuM, Svitkovsky FYu (2001) *Metallorėzhuschie stanki I stanochnyie sistemyi (Metal cutting machine tools and machine tool systems)*. Izhevsk State Technical University, Izhevsk
4. Mashinostroenie-ehnciklopediya T. IV-1. Detali mashin, konstrukcionnaya, prochnost, trenie, iznos, smazka (1995) (Mechanical engineering. Encyclopedia. Machine parts. Structural strength. Friction, Wear, Lubrication). In: Reshetov DN (ed) *Mashinostroenie*, Moscow
5. Andrienko LA, Baikov BA, Zakharov MN (2014) *Detali mashin (Machine parts)*. Moscow State Technical University N.E.Bauman, Terra mechanica series. Mashinostroenie, Moscow
6. OST 38 05114-76. Toothed belt transmissions. Calculation Methods
7. US Patent (1997) 21337485, cl. 73-229, 21 July 1977.
8. Stojanović B, Miloradović N, Marjanović N, Blagojević M, Ivanović L (2011) Length variation of toothed belt during exploitation. *Strojniški vestnik. J Mech Eng* 57(9):648–654. <https://doi.org/10.5545/sv-jme.2010.062>
9. Belyaev AK (2010) Dinamicheskaya ustojchivost zubchato-remennykh peredach (Dynamic stability of toothed belt drives). *Izvestiya Vuzov. Instrument making* 53(2):20–23
10. Iążej B, Jurdziak L, Kirjanow A, Kozłowski T (2017) A device for measuring conveyor belt thickness and for evaluating the changes in belt transverse and longitudinal profile. *J Diagnostyka* 18(4):97–102
11. Gładysiewicz L, Kawalec W, Krol R (2016) Selection of carry idlers spacing of belt conveyor taking into account random stream of transported bulk material. *J Eksploatacja i Niezawodność—Maintenance Reliability* 18(1):32–37. <https://doi.org/10.17531/ein.2016.1.5>
12. Wilczyński M, Domek G (2019) Influence of tension layer quality on mechanical property of timing belts Matec Web of Conferences 254, 05010, pp 1–8. <https://doi.org/10.1051/mateconf/201925405010>
13. Kolka IA, Kuvshinsky VV (1983) *Mnogooperacionnye stanki (Multioperational machines)*. Mashinostroenie, Moscow
14. Krol O, Sokolov V (2019) Parametric modeling of transverse layout for machine tool gearboxes. In: Gapiński B, Szostak M, Ivanov V (eds) *Advances in Manufacturing II. Manufacturing 2019. Lecture Notes in Mechanical Engineering* vol 4, pp 122–130. https://doi.org/10.1007/978-3-030-16943-5_11
15. Sokolov V, Krol O, Baturin Y (2019) Dynamics research and automatic control of technological equipment with electrohydraulic drive. In: 2019 International Russian Automation Conference (RusAutoCon). IEEE (2019) <https://doi.org/10.1109/RUSAUTOCON.2019.8867652>

16. Ganin NB (2012) Trekhmernoe proektirovanie v KOMPAS-3D (Three-dimensional designing in KOMPAS-3D). DMK, Moscow
17. Krol O, Sokolov V (2019) 3D modelling of angular spindle's head for machining centre. J Phys Conf Ser VSPID-2018, 1278: 012002. <https://doi.org/10.1088/1742-6596/1278/1/012002>
18. Sokolov V, Krol O (2017) Installations criterion of deceleration device in volumetric hydraulic drive. Proc Eng 206:936–943. <https://doi.org/10.1016/j.proeng.2017.10.575>
19. Fomin EP (2007) Ispolzovanie-parametricheskikh-vozmozhnostej KOMPAS-3D (Using the parametric capabilities of KOMPAS-3D). J CAD Graphics 10:70–74
20. Sokolov V, Rasskazova Y (2016) Automation of control processes of technological equipment with rotary hydraulic drive. Eastern-Eur J Enterprise Technol 2(80):44–50. <https://doi.org/10.15587/1729-4061.2016.63711>
21. Sokolov V (2019) Diffusion of circular source in the channels of ventilation systems. In: Advances in engineering research and application. ICERA 2018. Lecture Notes in Networks and Systems, vol 63. Springer, Cham, pp 278–283. https://doi.org/10.1007/978-3-030-04792-4_37
22. Sokol I, Savchenko Yu, Shanin D, Rosinsky S (2002) Baza dannykh “APM DATA”—svyazuyushchij ehlement v structure sistemy ARM WinMachine (Data Base “APM Data”—connecting element in structure APM WinMachine). J CAD Graphics 9:9–12
23. Zamriy AA (2007) Prakticheskij uchebnyj kurs CAD/CAE APM WINMACHINE. Uchebno metodicheskoe posobie (Practical training course CAD/CAE APM WinMachine. Teaching aid). APM Publishing house Moscow
24. Sokolov V (2020) Transfer functions for shearing stress in nonstationary fluid friction. In: Proceedings of the 5th international conference on industrial engineering. ICIE 2019. Lecture Notes in Mechanical Engineering. Springer, Cham, pp 707–715. https://doi.org/10.1007/978-3-030-2241-9_76
25. Shelofast VV (2004) Osnovy proektirovaniya mashin (Bases of the designing machine). APM Publishing house, Moscow
26. Krol O, Sokolov V (2018) Modeling carrier system dynamics for metal-cutting machines international russian automation conference, RusAutoCon-2018. IEEE, 2018. <https://doi.org/10.1109/RUSAUTOCON.2018.8501799>
27. Sokolov V (2021) Hydrodynamics of flow in flat slot with boundary change of viscosity. In: Proceedings of the 6th International Conference on Industrial Engineering (ICIE 2020). Lecture Notes in Mechanical Engineering
28. Sokolov V (2021) Increase measurement accuracy of average velocity for turbulent flows in channels of ventilation systems. In: Proceedings of the 6th International Conference on Industrial Engineering (ICIE 2020). Lecture Notes in Mechanical Engineering
29. Bondarenko I, Lunys O, Neduzha L and Keršys R (2019) Dynamic track irregularities modeling when studying rolling stock dynamics. In: Proceedings of the 23rd international science Conference Transport Means 2019 pt. II (Palanga, Lithuania: Kaunas Univ. of Technology), pp 1014–1019
30. Shevchenko SV, Mukhovaty OA, Krol OS (2020) Toothed-belt drive. UA Patent Application u 2020 04697 24 July 2020



Modified Belt Transmission with Enhanced Technical Characteristics

O. Krol(✉)

Volodymyr Dahl East Ukrainian National University, 59-a Central Pr, Severodonetsk 93400,
Ukraine
krolos@snu.edu.ua

Abstract. The drive of the main movement for the multioperational machining center with a modified V-belt and poly-V-belt drives is considered. A three-dimensional model of the drive in the environment of the integrated CAD KOMPAS-3D is built. The 3D-representation of stepped shaft and belt pulley in the special application “Shafts and mechanical transmissions-3D” is implemented. A procedure of parametric modeling for the V-belt drive elements in CAD APM WinMachine intended for the design of both standard trapezoidal and modified versions is proposed. The two design variants research results of V-belt transmission with a profile variable geometry in the form convex and concave in the longitudinal direction of the modified belt are presented. The main parameters, of both modifications’ teeth, which showed their advantage over standard V-belts in terms of load capacity, have been obtained. The possibility of self-adjusting for the proposed variants of belts with a curved shape of the working teeth surfaces is noted.

Keywords: Poly-V-belts · Modified section · Arch contour · Durability belts

1 Introduction

In modern mechanical engineering, there is a problem of a rather short service life of CNC machine tool drives with various designs of belt transmissions. The V-belt transmissions in drilling-milling-boring machines of the second and third standard sizes are widely used. One of the research directions for designs of main motion drives is associated with increasing their operational reliability.

One of the stages in determining the parameters of operational reliability is the assessment the level of the belt drive elements stress–strain state. For this, an effective finite element method, used in studies on three-dimensional modeling is intended [1–3]. Analysis of various approaches to assess the reliability of mechanical transmissions [4–6] showed the main directions to which the discussed below works are devoted.

Impact analysis of loads on the intensity of belt wear with the subsequent allocation of deterioration parameters is presented in the work [4]. It is shown that the result of wear in the belt cross section is decreased. As a consequence, the stress level is increased, and the service life is shortened. A classification of a number of factors affecting belt

wear is given. Research shows that the main factors relate the design features of the belt transmission, including the shape and geometric characteristics of its elements. The authors of [4] point out the importance of early detection of possible damage, which allows researchers a more accurate schedule of current repairs is prepared. For this, an effective device for measuring the thickness of the belt is proposed and, as a result, assessing changes in the transverse and longitudinal profile of the belt.

The level of the stress state directly depends on the spatial system of forces arising in the belt drive. The method for calculating the characteristics of the primary resistance to the movement of the conveyor belt, as well as the design and operational parameters of the conveyor are developed [5]. An automated system for collecting complex data (technical, operational, diagnostic), and on this basis, a method for determining energy characteristics has developed and implemented in [5].

The problem of belt lengthening associated with an increase in its pitch, which occurs during operation and which remains after unloading the belt is considered in work [6]. The authors argue that the greatest amount of movement and power is transmitted by the form, and much less—by friction. At the same time, the mechanisms of this phenomenon, the main factor of which (about 70%) is the plastic deformation of the belt are discovered.

At the same time, the improvement of the belt construction and its impact on traction characteristics and durability in these works insufficient attention is paid.

The purpose of this work is to improve the design of the V-belt transmission of the metal-cutting machine drive, which ensures increased durability of the machine.

2 3D and Parametric Modeling of V-belt Transmission (VBT)

The drive of the main forming movement (rotation of the tool in the spindle head) in drilling-milling-boring machines for highly efficient processing by various technological operations when changing cutting conditions in a wide range is designed. These capabilities of the equipment can be realized by introducing several mechanical transmissions into the drive to increase the range of speeds and torque. The main advantages of such a drive are the ability to implement various technological operations of semi-finishing and finishing. Besides, it becomes possible to flexibly regulate the range of changes in technical characteristics, and its configuration can be changed by choosing another engine or a different gear ratio of the VBT.

To analyze the design features and assess the stress–strain state of the designed elements [7–9], a three-dimensional model of the drive of a drilling-milling-boring machine was built in the CAD KOMPAS-3D environment [10–12]. Figure 1a shows a three-dimensional assembly of the main motion drive, developed using the specialized application “Shafts and mechanical transmissions-3D.” [13, 14]. The kinematics of this drive using a V-belt transmission are shown in Fig. 1b. Similarly, using the above application, 3D-models of VBT-elements were built.

The pulleys used in machine tools in their shape in many cases do not differ from the pulleys common in other machines. The variety of the nomenclature of pulleys used in drives, on the one hand, and the availability of normative documentation regulating the shape and size of their structures, makes it promising to use the parameterization mechanism [15–17].

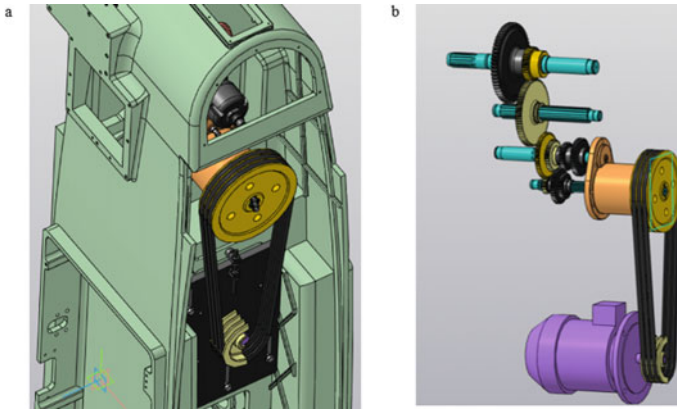


Fig. 1 a 3D-modeling assembly of the drive; b 3D-kinematics

For a wide range of V-belt pulleys, design forms have been developed that are used in the “Variable windows” of the APM Graph module [18–20] (Fig. 2a). At the first stage of the design calculation of the belt transmission, the belt section is selected. By the syntax of parametric modeling in CAD “APM WinMachine,” a calculation form for choosing a belt section, consisting of a set of logical selection conditions has been developed (Fig. 2b).

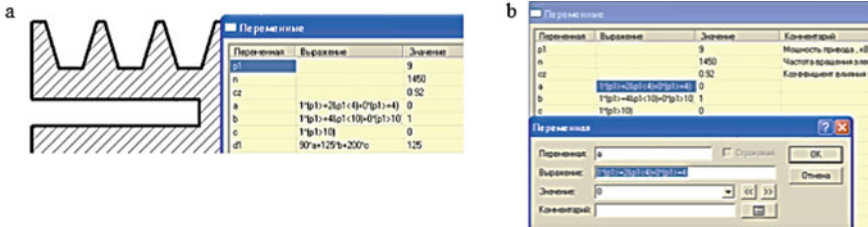


Fig. 2 a Variable windows; b selection belt section

To determine the dimensions of the pulleys and the dimensions of the belt, a corresponding algorithm presented in the window of variables (Fig. 3a) has been developed. Algorithms for determining the kinematic and power characteristics of the VBT are determined similarly [21–23]. Based on the calculation form, a graphical procedure for constructing a parametric model of VBT-pulleys (the command window of which is shown in Fig. 3b) was developed.

3 Modification of V-belt Transmission

The ultimate goals of any frictional belt drive modernization are to improve belt traction and durability. One of the reasons for the insufficient durability of V-belts and poly-V-belts is the significant bending stress caused by the relatively large thickness of these

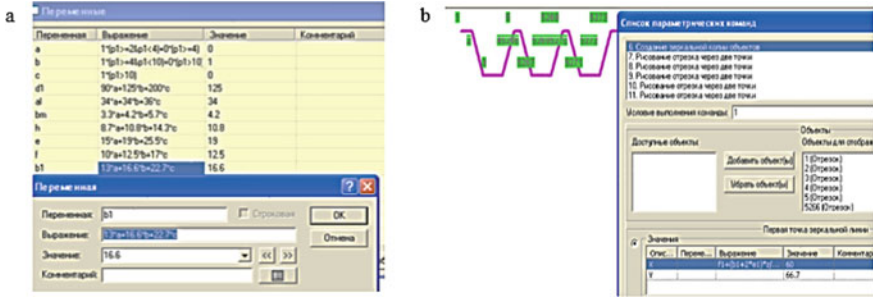


Fig. 3 a Variable window; b command window

belts. In this regard, the task: to develop modifications to the designs of V-belts and poly-V-belts with increased durability was formulated. At the same time, their traction capacity should not be lower than that of standard V-belts and poly-V-belts [21, 22]. A fundamental solution to this problem is proposed in [23].

To solve the problem of identifying the shape of the proposed modified design, the following procedure has been developed.

The cross-sectional contour of the modified V-belt is outlined by an arch that turns into a rectangle [23]. That is, the cross section is a combination of a circle segment of radius R with a central corner β and a rectangle with dimensions $[S \times y]$, Fig. 4.

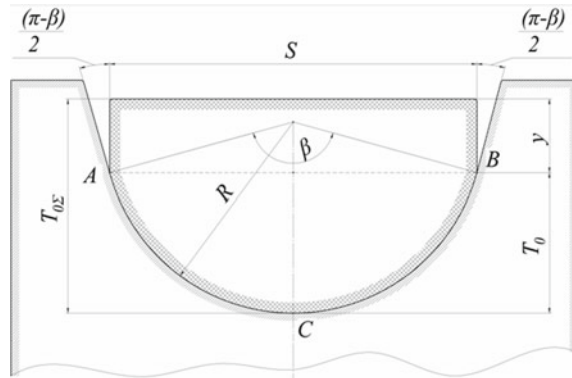


Fig. 4 The contour of the cross section of the modified V-belt

Modification of V-belts is based on 3 conditions:

1. equality of the contact areas with the pulleys of standard V-belts [21] and modified [23] belt transmission;
2. equality of the arch width S , where the cord of the modified belt is located, Fig. 1, and the cross-sectional widths of a standard V-belt W ;
3. equality of the cross-sectional areas of the standard belts [21] and modified [23].

The first condition is realized when the total length of the two lateral sides of the belt section [21]— L_{Σ} and the length of the arch of the belt section [23]— $\cup ACB$ is equal, Fig. 4, that is: $\cup ACB = L_{\Sigma}$.

This condition is expanded (1):

$$2T / \cos(\alpha/2) = R \cdot \beta, \quad (1)$$

hence follows (2):

$$R = \frac{2T}{\beta \cdot \cos(\alpha/2)}, \quad (2)$$

here T and $\alpha = 40^\circ$ —the height and angle between the lateral sides of the V-belt section [21].

The implementation of this condition will provide equal areas of contact of these belts with the pulleys. This, in turn, ensures the equality of the friction forces in the contact between belts and pulleys [24–26], which means that it retains the same pretensioning forces for modified belts as in standard V-belt transmissions.

According to the second condition $S = W$ that is (3):

$$2R \cdot \sin(\beta/2) = W \rightarrow R = \frac{0,5W}{\sin(\beta/2)}. \quad (3)$$

Equating the right-hand sides of Eqs. (1) and (2), we obtain a transcendental equation with one unknown (4)—the angle β

$$\beta \cdot W \cdot \cos(\alpha/2) - 4 \cdot T \cdot \sin(\beta/2). \quad (4)$$

The value β found from Eq. (3) ensures that the first and second conditions for modifying the V-belts are performance. Condition (3) modification of standard belts [21] lays in the design of modified belts [23] the equality of their cross-sectional areas, that is: $A_1 = A_0$. It follows that such stresses as: σ_0 —from pretension, σ_t —from the circumferential force, σ_V —from centrifugal forces, these belts will be the same, which means that they will have the same traction capacity [27–29].

The section of a belt with an arched profile, as mentioned above, consists of two shapes—a segment (seg.) of a circle and a rectangle (rec.). Accordingly, the total area of such a section (A_0) will be (5):

$$A_0 = A_{0(\text{seg})} + A_{0(\text{rec})} = R[0,5 \cdot R \cdot (\beta - \sin \beta) + 2 \cdot y \cdot \sin(\beta/2)]. \quad (5)$$

From the equality of areas: $A_1 = A_0$, the desired value of y is found (6), for where this equality holds:

$$y = \frac{A_1 - 0,5 \cdot R^2 \cdot (\beta - \sin \beta)}{2 \cdot R \cdot \sin(\beta/2)}. \quad (6)$$

Height of the segment section (7) of the arch belt:

$$T_0 = R \cdot [1 - \cos(\beta/2)]. \quad (7)$$

The total height of the modified section ($T_{0\Sigma}$) with an arched contour will be the sum of the heights of its segment (T_0) and rectangular (y) parts that is $T_{0\Sigma} = T_0 + y$, Fig. 4. As a result (8):

$$T_{0\Sigma} = R \cdot [1 - \cos(\beta/2)] + \frac{A_1 - 0.5 \cdot R^2 \cdot (\beta - \sin \beta)}{2 \cdot R \cdot \sin(\beta/2)}. \tag{8}$$

Since the parameters of the sections of standard V-belts [21]— T, W, α are used in calculating the parameters of the arched sections of the modified belt [23], the designations for the latter are taken as in [21], but with the addition of a 0-index, for example, B_0 .

The calculation results of the main parameters of modified belts with an arched section are given in Table 1 (for comparison, it gives the corresponding parameters for standard V-belts).

Table 1 Cross section designation Belts: Standard/Arched

Cross section parameters	Cross section designation Belts: Standard/Arched					
	Z/Z ₀	A/A ₀	B/B ₀	C/C ₀	D/D ₀	E/E ₀
$T/T_{0\Sigma}$	6/5.6	8/7.5	11/9.8	14/12.6	19/17.8	23.5/21.9
$W = S$	10	13	17	22	32	38
R	5.4	6.9	8.7	11.4	17.5	20.1
β (°)	134.3	140.9	152.8	149.0	131.5	142.1
$A_1 = A_0$	47	81	138	230	476	692

For a comparative assessment of the belts durability with standard and modified sections, we use (9) the well-known relationship [24, 30]:

$$\frac{L'_h}{L_h} = \left(\frac{\sigma_{\max}}{\sigma'_{\max}} \right)^8 = \frac{1}{[1 - k \cdot (1 - c)]^8}, \tag{9}$$

where L_h and σ_{\max} —durability and maximum stress in a standard V-belt, L'_h and σ'_{\max} —the same in a belt with a modified section;

$k = \sigma_b/\sigma_{\max} \approx 0.7$ —bending stress in a standard V-belt at the arc of the girth of the smaller pulley);

$c = \sigma'_b/\sigma_b = T_{0\Sigma}/T$ —calculated according to Table 1.

Calculations based on dependence (5) showed that replacing standard V-belts Z, A, B, C, D, E with their modified versions with an arched profile Z₀, A₀, B₀, C₀, D₀, E₀ gives an increase in durability from 6 to 11%.

4 Discussion

Belts modification is based on one condition: equality of the areas of contact with the pulleys [30] and modified (coincides with condition 1 for modifying V-belts [21]). To

do this, it is enough to equate the total length of the two lateral sides of the section— L_{Σ} and the length of the belt section arch $\cup ACB$, Fig. 5, that is: $\cup ACB = L_{\Sigma}$:

$$2 \cdot h / \cos(\alpha/2) = R \cdot \beta. \tag{10}$$

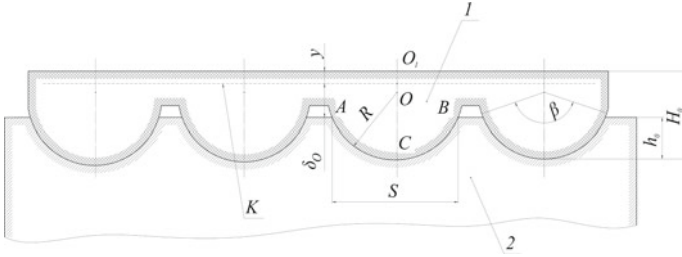


Fig. 5 The contour of the cross section of the modified poly-V-belt

From here, given the angle of the arch β , we find its radius R (11):

$$R = \frac{2 \cdot h}{\beta \cdot \cos(\alpha/2)}. \tag{11}$$

As a result, the total height of the modified profile will be (12):

$$H_O = h_O + \delta_0 + y = R \cdot [1 - \cos(\beta/2)] + H - h + 0.5 \cdot \delta, \tag{12}$$

where the dimensions: $H, \delta, h, y = H - (h + \delta)$ – taken from the belt [30].

The width of the modified belt segment S (13) was determined using the same algorithm as for the modified V-belt [23]:

$$S = 2 \cdot R \cdot \sin(\beta/2). \tag{13}$$

To compare the dimensions of the belts, we find the width of one wedge (14) of a poly-V-belt [30]:

$$S_1 = 2 \cdot h \cdot \text{tg}(\alpha/2). \tag{14}$$

Let us compare the areas of one edge (15) of a poly-V-belt [30]— A_1 and one edge of a modified belt— A_O :

$$\begin{aligned} A_1 &= 2 \cdot h \cdot (H - 0,5 \cdot h) \cdot \text{tg}(\alpha/2); \\ A_O &\approx R \cdot [0,5 \cdot R \cdot (\beta - \sin \beta) + 2 \cdot (H - h + 0,5 \cdot \delta) \cdot \sin(\beta/2)]. \end{aligned} \tag{15}$$

The calculation results for dependencies (11)–(15) are summarized in Table 2 (for all sections of the belt, the angle of the arch β is taken the same: $\beta = 140^\circ$).

Table 2 Cross section designation Belts: Standard/Arched

Section	R	S / S_0	H/H_0	A/A_0
K/K_0	2.0	1.7/3.8	4/3	4.8/10.1
L/L_0	4.2	3.5/7. 3.5/7.9	9.5/7.4	25/53
M/M_0	9.0	7.5/16.9	16.7/12.3	86.8/180.7

5 Conclusion

The article deals with the problems of constructing and researching three-dimensional and parametric models of V-belt and poly-V-belt transmissions for the drive of metal-cutting machines. Three-dimensional solid models of the main motion drive for a drilling-milling-boring machine of the second standard size, consisting of more than 500 parts and assembly units, have been built. The toolkit for creating solid models in the environment of the integrated CAD KOMPAS-3D was used, in particular, the specialized application “Shafts and mechanical transmissions-3D.” The 3D-project of this drive became the winner of the International Competition “Future ASe of COMPUter 3D Modeling”-2014, held by the ASCON group of companies. The method and algorithms for parametric modeling of the belt transmission basic elements in the syntax of the APM Graph module have been developed—the choice of the V-belt section and poly-V-belt section, the determination of the type of pulley construction (monolithic, disk), the calculation of energy parameters. The proposed toolkit provides an enlargement in the productivity of a designer, and the level of design decisions is increased.

To increase the technical and economic parameters of drives and enlargement the tractive capacity of the belt transmission, modified designs of V-belt and poly-V-belt drives are proposed. The patent solutions for which have been obtained. An analytical calculation of their main geometrical and energy characteristics is carried out. The obtained numerical results make it possible to assert that they have an advantage over standardized belt drives in terms of traction capacity and durability. At the same time, their dimensions are about twice as wide. These advantages are provided by a decrease in stress (with an increase in the cross-sectional area of the order of 2.1 times) from the pretension (σ_0) and the circumferential force (σ_t) in the proposed modified designs of the sections K0, L0, M0. A lower cross-sectional height of the modified belts will create lower bending stresses σ_b compared to standard belts, which, in turn, will lead to an increase in the durability of the modified belts by 6–11%.

Based on the structural similarity of a V-belt and one wedge in a poly-V-belt, it is assumed that the bending stress in the latter is directly proportional to the height of the belt cross section. Therefore, the obtained dependence (5) for a comparative assessment of the V-belts durability with standard and modified sections can be used in the first approximation to compare the durability of poly-V-belts.

Thus, if, according to the condition of the drive layout, the width of the belt transmission is not a limiting factor, replacing the standardized poly-V-belt with a modified

one will be one of the possible solutions to the problem of increasing the resource of the belt transmission.

References

1. Ganin NB (2012) Trekhmernoe proektirovanie v KOMPAS-3D (Three-dimensional designing in KOMPAS-3D). DMK Press, Moscow
2. Ganin NB (2011) Proektirovanie i prochnostnoj raschet v sisteme-KOMPAS-3D (Design and Strain Calculation in KOMPAS-3D System). DMK Press, Moscow
3. Magomedov A, Alehin A (2010) Integrirovannyj konechno ehlementnyj analiz v KOMPAS-3D (Integrated finite element analysis in KOMPAS-3D). J CAD/CAM/CAE Observer 8(60):1–5
4. Iañej B, Jurdziaek L, Kirjanow A, Kozłowski T (2018) A device for measuring conveyor belt thickness and for evaluating the changes in belt transverse and longitudinal profile. J Diagnostyka 18(4):97–102
5. Gładysiewicz L, Kawalec W, Krol R (2016) Selection of carry idlers spacing of belt conveyor taking into account random stream of transported bulk material. J Eksploatacja i Niezawodność—Maintenance and Reliability 18(1):32–37. <https://doi.org/10.17531/ein.2016.1.5>
6. Stojanović B, Miloradović N, Marjanović N, Blagojević M, Ivanović L (2011) Length Variation of Toothed Belt During Exploitation. J Strojniški vestnik. J Mech Eng 57(9):648–654. <https://doi.org/10.5545/sv-jme.2010.062>
7. Platonov L (2013) Mashinostroitelnoe proektirovanie v KOMPAS-3D na novom vitke razvitiya (Machine-building design in KOMPAS-3D at a new round of development). J CAD Graphics 10:6–12
8. Sokolov V (2021) Hydrodynamics of flow in flat slot with boundary change of viscosity. In: Proceedings of the 6th International Conference on Industrial Engineering (ICIE 2020). Lecture Notes in Mechanical Engineering
9. Malyukh VN (2013) Novyj KOMPAS-3 D V14 (New KOMPAS-3 D V14). J Isicad.ru 102:76–81
10. Sokolov V, Rasskazova Y (2016) Automation of control processes of technological equipment with rotary hydraulic drive. J Eastern-European J Enterprise Technol 2, 2(80):44–50. <https://doi.org/10.15587/1729-4061.2016.63711>
11. Malyukh VN (2012) Vvedenie v sovremennye SAPR kurs lekcij (Introduction to modern CAD systems. The course of lectures). DMK Press, Moscow
12. Mukhovannaya EYu, Mikhailov MA, Kholin MI, Novoselov VI (2000) Otkrytyj SolidWorks: edinstvo i borba protivopolozhnostej (Open SolidWorks: unity and struggle of opposites). J CAD Graphics 3:59–63
13. Sokolov V (2019) Diffusion of circular source in the channels of ventilation systems. In: Advances in engineering research and application. ICERA 2018. Lecture Notes in Networks and Systems, vol 63 pp 278–283. https://doi.org/10.1007/978-3-030-04792-4_37
14. Sokolov V, Krol O (2017) Installations criterion of deceleration device in volumetric hydraulic drive. Proc Eng 206:936–943. <https://doi.org/10.1016/j.proeng.2017.10.575>
15. Fomin EP (2007) Ispolzovanie-parametricheskikh-vozmozhnostej KOMPAS-3D (Using the parametric capabilities of KOMPAS-3D). J CAD Graphics 10:70–74
16. Sokolov V (2020) Transfer functions for shearing stress in nonstationary fluid friction. In: Proceedings of the 5th international conference on industrial engineering. ICIE 2019. Lecture Notes in Mechanical Engineering. Springer, Cham, pp 707–715. https://doi.org/10.1007/978-3-030-2241-9_76

17. Sokolov V (2021) Increase measurement accuracy of average velocity for turbulent flows in channels of ventilation systems. In: Proceedings of the 6th International Conference on Industrial Engineering (ICIE 2020). Lecture Notes in Mechanical Engineering
18. Kurov AV (2017) Modelirovanie I inzhenernyj analiz konstrukcij mostovykh kranov s pomoshchyu APM WinMachine (Modeling and engineering analysis of overhead crane structures using APM WinMachine). *J Polytechnic Youth J MSTU NE Bauman* 72(17):1–9
19. Sokolov V, Krol O, Baturin Y (2019) Dynamics research and automatic control of technological equipment with electrohydraulic drive. In: 2019 International Russian Automation Conference (RusAutoCon). IEEE (2019). doi:<https://doi.org/10.1109/RUSAUTOCON.2019.8867652>
20. Sokol I, Savchenko Yu, Shanin D, Rosinsky S (2002) Baza dannykh “APM DATA”—svyazuyushchij ehlement v structure sistemy ARM WinMachine (Data Base “APM Data”—connecting element in structure APM WinMachine). *J CAD Graphics* 9:9–12
21. GOST 1284.1-89 (2001) V-belt. Driving of normal sections. Basic dimensions and methods of control. Standard Press, Moscow
22. Krol O, Sokolov V (2018) Modeling carrier system dynamics for metal-cutting machines international Russian Automation Conference, RusAutoCon-2018. IEEE, <https://doi.org/10.1109/RUSAUTOCON.2018.8501799>
23. Shevchenko SV, Mukhovaty OA, Krol OS (2020) Toothed-belt Drive. UA Patent 113816 10 Febr 2017
24. Mashinostroenie-ehnciklopediya T. IV-1. Detali mashin, konstrukcionnaya, prochnost, trenie, iznos, smazka (1995) (Mechanical engineering. Encyclopedia. Machine parts. Structural strength. Friction, Wear, Lubrication). In: Reshetov DN (ed) Mashinostroenie, Moscow
25. Krol O, Sokolov V (2019) 3D modelling of angular spindle’s head for machining centre. *J Phys Conf Ser VSPID-2018*, 1278:012002. <https://doi.org/10.1088/1742-6596/1278/1/012002>
26. Krol O, Sokolov V (2019) Parametric modeling of transverse layout for machine tool gear-boxes. In: Gapiński B, Szostak M, Ivanov V (eds) *Advances in Manufacturing II. Manufacturing 2019. Lecture Notes in Mechanical Engineering*. Springer, Cham, vol 4, pp 122–130. https://doi.org/10.1007/978-3-030-16943-5_11
27. Andrienko LA, Baikov BA, Zakharov MN (2014) Detali mashin (Machine parts). *J Moscow State Technical University N.E.Bauman, Terra mechanica series. Mashinostroenie, Moscow*
28. Pronin BA, Ovchinnikova VA (1982) Raschet klinoremennykh peredach (Calculation of V-belt transmissions). *J Vestnik mashinostroeniya* 3:23–28
29. Vorobiev II (1971) Peredachi s gibkoj svyazyu v privodakh stankov (Transmission with flexible coupling in machine tool drives). Mashinostroenie, Moscow
30. TU 38-105763-89. Poly-V-belts drive. Specifications



Improvement of the Timber Supply Flow at Syktyvkar Plywood Mill LLC by Upgrading KKS-10

F. V. Svoykin¹(✉), V. A. Sokolova², and A. A. Borozna²

¹ Syktyvkar Forest Institute (branch) of the Federal State Budgetary Educational Institution of Higher Professional Education “St. Petersburg State Forest Technical University Named After S. M. Kirov” (SLI), 39, Lenin St., Komi Republic, Syktyvkar 167982, Russia

² St. Petersburg State Forest Technical University Named After S. M. Kirov, 5, Institutsky Per., St. Petersburg 194021, Russia

Abstract. The article proposes a solution to a problem of a reduced flow of round timber in the production conditions of Syktyvkar Plywood Factory LLC (Syktyvkar, Komi Republic) located in the North-West Federal District of the Russian Federation. The solution involves modernizing an element of loading and unloading operations, an electric double-girder gantry crane KKS-10-26-8.5, based on the improved design of the grapple jaw in the open state. Specifically, we propose installation of a hydraulic grapple with a lifting capacity of 6000 kg, model DGMg-3-10-L1-2.1 with a lifting swing beam DPT-10-0/1-83-U1U of a new design, the boxes of which are made on the basis of FDM technologies on a 3D printer to reduce the weight of the structure and energy consumption for movement. In the article, the design diagram of the jaw strength (i.e., calculation of the main structural elements) is presented, the strength of the metal structure of the jaw checked, and the structural diagram of technological flows at Syktyvkar Plywood Factory LLC taking into account the modernization of KKS-10 provided. The possibility of scaling up the proposed solution in the conditions of the North-West Federal District of the Russian Federation has been assessed. In the analytical part of the article, the technological aspects of the operation of the enterprise (including technical equipment) are discussed in the context of the general requirements of the technological process in the timber warehouse, but with an emphasis on lifting mechanisms. As a result of the research, the productivity of the KKS-10 crane has been increased and working conditions in winter improved.

Keywords: Gantry crane · Jaw strength · Hydraulic grapple · Traverse · 3D printer based · FDM technologies · Technological streams

1 Introduction

Forest industries are the major contributor to the economy of the Komi Republic. The forest sector of the republic is a leader in terms of the volume of commercial products, gross revenue, and the contribution to the regional budget. Thus, it largely determines the overall economic and social state of the region. Syktyvkar Plywood Factory LLC

is one of the largest manufacturers of wood-based panels in Russia and one of the leading enterprises in the Komi Republic. The company processes over 540,000 m³ of raw materials annually. It produces 220,000 m³ of different types of plywood and 300,000 m³ of laminated chipboard with various decors and unique embossing. The technological process of the enterprise starts with the raw material being supplied in packages. Unloading of raw material is performed by cantilever gantry cranes which then stack the unloaded timber for storage. Timber is supplied by two streams. In the first stream, there are 12 pools, and in the second, 14 pools. Loading of timber and feeding it to the tables is performed by gantry cranes, three in each stream. Timber is lifted by cranes from the pools to the rolling tables. In total, the enterprise has six cranes: two KKE-12.5, one KKD-12.5, and three KKS-10 (with an electric grapple with a lifting capacity of 4700 kg).

2 Problem

The KKS-10-26-8.5 electric double-girder gantry crane is an old piece of equipment and has insufficient productivity in the conditions of an increased load turnover. However, due to the limited investment capacity of the enterprise, it is not possible to replace the crane with a modern, more productive piece of equipment. Therefore, it is advisable to modernize the existing equipment. It should be noted that the KKS-10 crane is a specialized piece of equipment. It is a bridge-type lifting unit on supports; it moves on wheels and has a fully electric control [1–4]. The KKS-10-26-8.5 electric double-girder gantry crane is a universal crane with a medium operating mode. This crane is widely used in cargo yards for lifting and transporting a wide range of goods. This is a double-cantilever self-erecting equipment with a specific span length, which could be placed outdoors or indoors [5]. So far, a substantial body of experience in the analysis of operation [6, 7] and repair of KKS-10 [8, 9] has been accumulated; however, there is a shortage of publications on the issue of its modernization.

3 Methodology

Taking into account [10–12], we will design the grapple jaw in the open state. The design diagram of the jaw strength is shown in Fig. 1.

O_{1P} axis coordinate is determined by:

$$Y_{1P} = 0.5Y_1. \quad (1)$$

From the point O_{1P} to the point of contact with the X axis, we will draw a segment $O_{1P}H_P$ of the length Y_1 . To determine the position of the point B_P , we will draw a segment $H_P B_P = HB$ from the point H_P in the direction to the point O_{1P} . Then, we will draw a perpendicular with the height of $B_P B'_P = BB'$ from the point B_P . Let us draw a horizontal segment $B'_P O_{BP} = R_B$ starting from the point B'_P and stretching from right to left; it will define the position of the center O_{BP} . After that, let us build the inner contour of the jaw.

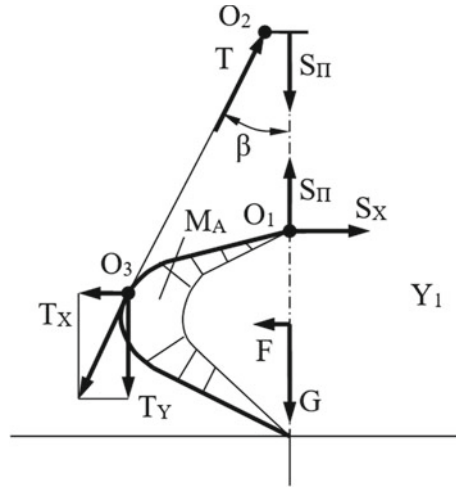


Fig. 1 Scheme for calculating the jaw strength

Let us measure the angle α from the contour of the left jaw in Fig. 1. On the contour of the right jaw, let us draw a segment of the length $H_P H'_P = HH'$ at an angle α from the point H_P to the segment $B_P B'_P$. From the point H'_P , let us draw a segment $H'_P O_{HP} = R_H$ perpendicular to the straight line $H_P H'_P$, defining the position of the center O_{HP} . From the center O_{HP} , let us draw an arc of the outer contour of the jaw with the radius R_H . Then, let us perform conjugation of the arc with a circle with the center O_{1P} and the diameter d .

The position of the point O_{3P} will be found at the intersection of the serifs with the radii C and E drawn from the centers O_{1P} and H_P , respectively.

To determine the angle β of the inclination of the connecting rod in the open position of the jaws, let us determine the position of the point O_{2P} using the known length of the connecting rod L_T . Let us connect the points O_{2P} and O_{3P} . The position of the upper traverse when the grapple is open conditionally coincides with the position when the grapple is closed. The angle β of inclination of the connecting rod is assumed to be the same as when the grapple is closed.

The second projection of the grapple (view on the left in Fig. 1) is built according to the known dimensions and the rules of the IG.

The jaw width:

$$b_{ch} = d. \tag{2}$$

The grapple width:

$$V_{GR} = 1.52R + 1.2D_B \tag{3}$$

When opening the grapple, the O_1 axis travel is determined by the difference in heights of the point O_1 in the closed and in the fully opened grapple:

$$h_{zakr} = Y_1 - Y_{1P} + Y_{2P} - Y_2 \tag{4}$$

The length of the rope drawn in when closing the grapple is:

$$L_K = h_{zakr}u. \quad (5)$$

The jaw span with the grapple fully opened (distance between the edges of the jaws):

$$L = 2Y_1 \cos 30^\circ. \quad (6)$$

Let us check the strength of the jaw metal structure.

The jaw is acted upon by the force in the connecting rod T , the force in the closing polystap S_p , the horizontal reaction S_X in the joint O_1 , as well as half of the gravity of the timber pack G and the thrust force F (Fig. 1).

The angle of inclination of the thrust axis to the vertical:

$$\beta = \text{arctg}\left(\frac{X_3 - X_2}{Y_2 - Y_3}\right). \quad (7)$$

The total effort in one closing polystap:

$$S_\Pi = S_{\max}. \quad (8)$$

The traction effort in the connection rod:

$$T = \frac{S_\Pi}{\cos \beta} \quad (9)$$

The force T components:

$$T_X = T \sin \beta. \quad (10)$$

$$T_Y = T \cos \beta. \quad (11)$$

The sum of the moments of forces acting on the jaw, relative to the axis O_1 :

$$T_X(Y_1 - Y_3) - T_Y X_3 + F(Y_1 - Y_B) = 0. \quad (12)$$

Therefore,

$$F = \frac{T_Y X_3 - T_X(Y_1 - Y_3)}{Y_1 - Y_B}. \quad (13)$$

The sum of the projections of all forces acting on the jaw along the horizontal X axis:

$$T_X - S_X + F = 0. \quad (14)$$

Therefore,

$$S_X = T_X + F. \quad (15)$$

The maximum bending moment in the section A–A:

$$M_A = S_{\Pi}X_3 - S_X(Y_1 - Y_3) \quad (16)$$

The bending *moment* acting in the section of one jaw segment, taking into account the uneven distribution of the load:

$$M = 0.7M_A \quad (17)$$

The section height is taken as:

$$h_C \approx R_H - R_B. \quad (18)$$

The wall thickness:

$$\delta_C = 0.025h_C. \quad (19)$$

The belt thickness:

$$\delta_{\Pi} = \delta_C. \quad (20)$$

The moment of inertia of the section without taking into account the moments of inertia of the wall elements:

$$J = 0.5b_{Ch}\delta_{\Pi} \left[(h_C + \delta_{\Pi})^2 + (d_O + \delta_{\Pi})^2 \right]. \quad (21)$$

The section resistance moment:

$$W = \frac{2J}{h + 2\delta_{\Pi}}. \quad (22)$$

The bending stress:

$$\sigma = M/W. \quad (23)$$

The resulting bending stress is $\sigma = 113.1$ MPa.

The permissible stress can be taken as $[\sigma] = 170$ MPa.

The cross-sectional strength is provided when the following condition is met:

$$\sigma \leq [\sigma] \quad (24)$$

Taking into account (24), we propose to install a hydraulic grapple with the lifting capacity of 6 tons, model DGMg-3-10-L1-2.1. However, taking into account the mechanism of movement of the trolley, it is necessary to improve the proposed grapple by making the traverse box on a 3D [13–16] printer based on FDM technologies [17–22], to reduce the weight of the structure and energy consumption for movement. A load gripping body of such a design (a load-lifting rotary traverse DPT-10-0/1-83-U1U) is shown in Fig. 2.

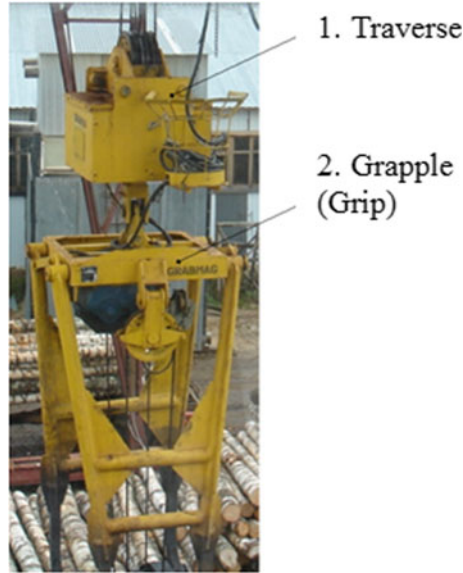


Fig. 2 Load gripping body DPT-10-0/1-83-U1U. (1) Traverse; (2) Grapple (Grip)

4 Conclusions and Recommendations

Based on the results of our research aimed to increase the productivity of the KKS-10 crane and improve working conditions in winter, we propose to modernize the equipment by replacing the electric grapple with the lifting capacity of 4700 kg with a hydraulic grapple with the lifting capacity of 6000 kg (model DGMg-3-10-L1-2.1 improved through FDM technology).

Taking into account the modernization of KKS-10, the structural diagram of technological streams at Syktyvkar Plywood Plant LLC will take the following form (Fig. 3).

5 Conclusion

The experience of modernizing the structural diagram of the technological flow of Syktyvkar Plywood Plant LLC by improving the KKS-10 crane can be scaled up in the North-West Federal District of the Russian Federation, the forest sector enterprises of which have a comparable infrastructure.

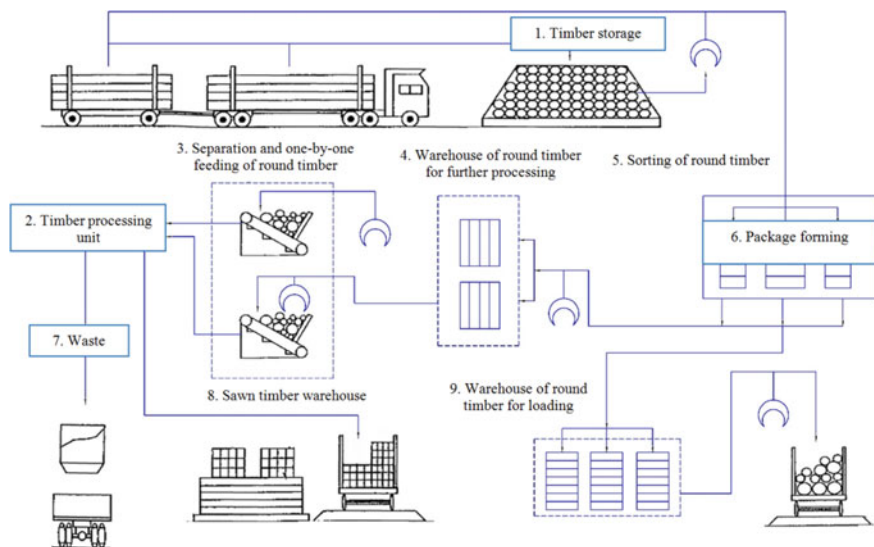


Fig. 3 Block diagram of the process flow of Syktyvkar Plywood Plant LLC, taking into account the modernization of KKS-10. (1) Timber storage; (2) Timber processing unit; (3) Separation and one-by-one feeding of round timber; (4) Warehouse of round timber for further processing; (5) Sorting of round timber; (6) Package forming; (7) Waste; (8) Sawn timber warehouse; (9) Warehouse of round timber for loading

References

1. Zhuravlev NP, Malikov OB (2006) Transport and cargo systems: a textbook for railway transport universities. Marshrut, Moscow, p 368
2. Timoshin AA et al (2003) Complex mechanization and automation of loading and unloading operations: a textbook for higher educational institutions of the railway transport. Marshrut, Moscow, p 400
3. Kurochkin VA (2019) Transport and cargo systems. Machinery and equipment. Study guide. Saratov
4. Kulikova NN, Alexandrov MP, Gokhberg MM, Kovin AA et al (1988) Cantilever and gantry cranes, bridge cranes (Handbook of cranes: in 2 volumes. v 2). Mashinostroenie, Moscow, p 559
5. Boyko NI, Cherednichenko SP (2011) Loading and unloading operations and warehouses of the railway transport: a textbook for higher educational institutions of the railway transport UMC on education in the railway transport, Moscow, p 292
6. Kulkov M, Gulin N, Solyakov O, Ambartsumyan L (2015) Features of the monorail crane KKS-10. Regulations 6(44):77
7. Akulin OI, Sekachev VA, Sorokin GE, Nikolaev AP, Berdnikov AG (2015) The main stages of assessing the causes of destruction of cylindrical shanks of a single-horn forged hook on the example of an electric gantry crane KKS-10-3K. Young Scientist 17(97):74–76
8. Kulkov M, Gulin N, Solyakov O, Ambartsumyan L (2016) Repair of the traveling monorail KKS-10 crane made of I-beams. TechNadzor, 30M, 1(110): 55
9. Nikolaev AF, Burlakova EV, Khalikov IK, Semenikhin NA (2018) Restoration of the working capacity of the cargo beams of the gantry cranes in operation. Constr Mech Structures 2(17):111–116

10. Karpenko GV (1976) The influence of the environment on the strength and durability of metals. Naukova Dumka, Kiev, p 128
11. Barchenkova NA, Minaeva NV (2011) Analysis of the stress-strain state of an elastically reinforced strip taking into account the initial imperfections. *Build Mech Structures* 1(2):24–26
12. Belsky MR (1975) Strengthening metal structures under tension. *Budivel'nik*, Kiev, p 120
13. Aravind Raj S, Muthukumaran E, Jayakrishnaa K (2018) A case study of 3D printed PLA and its mechanical properties. *Materials Today: Proceedings* 5(5), part 2:11219–11226. <https://doi.org/10.1016/j.matpr.2018.01.146>
14. Gantenbein S, Masania K, Woigk W et al (2018) Three-dimensional printing of hierarchical liquidcrystal-polymer structures. *Nature* 561(7722):226
15. Gibson I, Rosen DW, Stucker B (2010) Additive manufacturing technologies. In: *Rapid prototyping to direct digital manufacturing*. Springer, New York. <https://doi.org/10.1007/978-1-4419-1120-9>
16. Gibson I, Rosen D, Stucker B (2015) Additive manufacturing technologies. *3D Printing, Rapid prototyping, and direct digital manufacturing*. Springer, New York. <https://doi.org/10.1007/978-1-4939-2113-3>
17. Afrose MF (2016) Mechanical and viscoelastic properties of Polylactic Acid (PLA) Materials Processed Through Fused Deposition Modelling (FDM). B.Sc. (Hons) in Mechanical Engineering. Hawthorn, Australia, Swinburne University of Technology, p 81
18. Samykano M, Selvamani SK, Kadirgama K, Ngui WK, Kanagaraj G, Sudhakar K (2019) Mechanical property of FDM printed ABS: influence of printing parameters. *Int J Adv Manuf Technol* 102:2779–2796. <https://doi.org/10.1007/s00170-019-03313-0>
19. Hmeidat NS, Kemp JW, Compton BG (2018) High-strength epoxy nanocomposites for 3D printing. *Compos Sci Technol* 160:9–20
20. Hill N, Haghgi M (2014) Deposition direction-dependent failure criteria for fused deposition modeling polycarbonate. *Rapid Prototyping J* 20(3):221–227. <https://doi.org/10.1108/RPJ-04-2013-0039>
21. Petrova GN, Larionov SA, Sorokin AE, Sapego YuA (2017) Modern methods of processing thermoplastics. In: *Proceedings of VIAM: electron. Scientific and Technical Zhurn.* 11(59) Art. 07. <https://doi.org/10.18577/2307-6046-2017-0-11-7-7>
22. Platonov MM, Petrova GN, Larionov SA, Barbotko SL (2017) Optimization of the composition of the polymer composition with a reduced fire hazard based on polycarbonate for the technology of 3D-printing with molten polymer filament. *Izvestiya Vuzov Ser: Chem Chem Technol* 60(1):87–94



On the Issue of Designing Cantilever Shafts with Joint Consideration of Strength, Endurance and Rigidity

B. N. Akramov and I. A. Ismatov^(✉)

Tajik Technical University Named After Academic M.S. Osimi, 10, Street ac. Rajabovho,
Dushanbe 734042, Tajikistan

Abstract. The article considers a method for calculating cantilever shafts, which simultaneously takes into account both the strength and endurance of the shaft, and its rigidity. For this purpose, a so-called rigid shaft model is used. Usually, the strength calculation is carried out as a design, and then the stiffness calculation is carried out as a test, that is, separately from each other. In this case, it may turn out that the design does not fully meet all the requirements. These requirements are usually related to the parts mounted on the shaft, including the type of shaft supports. Gears, variable gear pulleys and rolling and sliding bearings have strict requirements for shaft deformations at the point of their landing. Adjusting the stiffness of the shaft when calculating its strength allows you to simultaneously take into account these requirements. This adjustment is possible because it depends on the design of the shaft. If there is a need to change the stiffness of the shaft in a certain section, the technique allows you to adjust its value to take into account the need for this section. A concrete example is given for a cantilever shaft with a rigid seal.

Keywords: Cantilever shaft · Strength · Stiffness · Deformation parameters · Joint accounting · Adjustment

1 Introduction

The calculation of the shafts is carried out taking into account their strength for power load and endurance, determined by the operating conditions. Very often, it is also necessary to calculate the shaft stiffness [1, 2], which is determined by the design of the shaft, that is, the parts mounted on the shaft.

These calculations are performed independently of each other separately, and if the shaft does not meet the conditions of rigidity, then its design is usually developed anew (calculations for strength and endurance) [3–5]. In the article, it is proposed to adjust the design of the shaft taking into account the required changes in its rigidity.

Cantilever, double-support and multi-support shafts with protruding elements, have strong bending deformations in the cantilever sections (Fig. 1a, b) [6]. The diagram of the cantilever shaft (Fig. 1a) shows the parameters of the shaft deformation: α —the

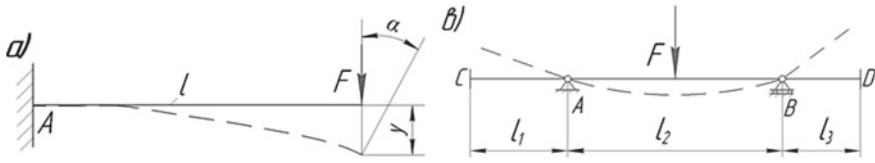


Fig. 1 **a** Deformations of the cantilever shaft; **b** deformations of the cantilever sections of the support shaft

angle of rotation of the section, y —the deflection (along the line of action of the power load F). Figure 1b shows the deformations of the cantilever sections.

AC (length l_1) and BD (length l_3) over the action of the force F acting on the two support shaft CABD. Since the shaft is designed to maintain and simultaneously transmit the torque M of rotating parts (bearings, gears, belt pulleys, etc.) in order to ensure their normal operation, the following conditions must be met: $y \leq [y]$, $\alpha < [\alpha]$, where α and y are the deformation parameters at the landing site of the part to be fitted, $[y]$ and $[\alpha]$ are the permissible values of the deformation parameters α and y at the landing site. They depend on the type of part to be fitted [1, 5, 10–15]: $[y] = (0,005 \div 0,01) \cdot m$ [millimeter]—under the worm wheel, $[y] = (0,01 \div 0,03) \cdot m$ —under the cylindrical gear wheel (here- m -modulus in mm), $[\alpha] = 0,01$ [radian]—under the deep groove ball bearing, $[y] = 0,001$ —under the plain bearing, and so on. Failure to comply with these condition leads to the violation of normal operation of the stick part and its rapid failure, as well as reduced quality performance of the whole mechanism (machine) in general. For example, the condition $y > [y]$ under the gear wheel leads to incorrect engagement of the teeth (the condition of uniform load distribution along the tooth length is violated), that is, it leads to increased wear of the tooth profiles and an increase in friction losses. Failure to meet the condition $\alpha < [\alpha]$ under the bearing (in the shaft supports) leads to a violation of the conditions of normal operation of the bearing, namely, the possibility of jamming of the rolling elements in the separator, increased wear of the raceways, bursting of the separator, and so on. Therefore, it appears that the account of rigidity of the shaft (restrictions on the deformation) is an important objective in the design of rational design of the shaft that is under the min weight of the shaft and the material consumption for its production, and at the max considering the conditions of work planting parts, technology, its structure and providing strength and endurance of the shaft [7]. Currently, cantilever shafts (however, like all other shafts) are designed according to a method that does not take into account the rigidity of the shaft and is based only on taking into account its strength and endurance. The calculation is carried out in two stages. In step 1 based on the known from the kinematic calculation of a drive torque M and kind of stick parts (including bearings) are designed based on strength at a reduced allowable stress in torsion, design of shaft, that is, determined by the diameter d and length l of the plots every plot is suitable for planting individual stick details. Then, landing and transition elements and sections (chamfers, keyways, collars, etc.) are introduced into the shaft structure. Phase 2—the known loads from the stick components (obtained from calculation of gear which includes these details) D the power P , radial and axial P_r , P_a forces—tested margin of safety in a dangerous

(critical) cross section, the condition: $n > [n]$, where $[n]$ permissible (min) margin of safety [4]. These plots are the bending M_1 and torsional M moments for the critical section (cross section where the maximum load $M_{\max} = \overline{M}_1 + \overline{M}$ and where the section is the weakest—keyway, press fit parts, and the like) calculated effective coefficients of stress concentration K_σ and K_τ (for normal from M and tangential for M_1 stresses) and calculate the value of n . The stiffness (and therefore the values of α and γ parameters of its deformation) depends on the shaft material (usually the same for all sections of the shaft), from its geometrical moment of inertia I (determined by the shaft diameter and the presence of stress concentrators—the keyways, fillets and the like—in the considered cross section), but also from the power load on the shaft. The force load can be represented by a concentrated force P , a distributed load with intensity q , or a moment of forces M_2 usually, the distributed load q is represented as a concentrated force applied at the center of mass of the plot q [8].

2 Method

In order to take into account, the rigidity of the shaft already at the stage of its design, it is necessary to make a so-called “rigid” model of the cantilever shaft (or cantilever sections of a two support or multi-support shaft). Instead of calculating the shaft for strength and endurance, it is proposed to introduce changes in its design (correcting its rigidity in the right areas), instead of calculating the shaft design anew, taking into account the newly discovered circumstances [9–14].

Let us have a cantilever shaft $ACDE$ (Fig. 2), which has different stiffness EI in different sections (with the same material and moment of inertia of the cross section I for all sections of the shaft).

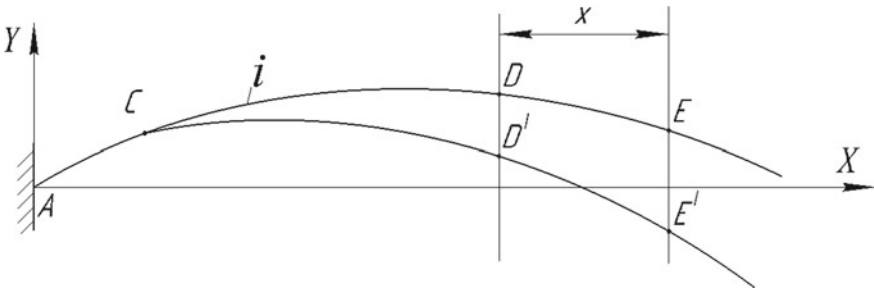


Fig. 2 Cantilever shaft with rigid pinching

Assume that the sections to the left of section C (section AC in Fig. 2) retain their position (for them, neither the power load Q_y and M_x nor the shaft stiffness EI change). Let on the plot with the number “ i ” (plot CD in Fig. 2), we changed the stiffness from $E_i J_i$ to $E'_i J'_i$. This will cause a rotation of the shaft section by an angle $\Delta\alpha_D$ and a deflection (additional) Δy_D , respectively. Then, the new position of the flexible axis of the cantilever shaft will be $ACD'E'$, respectively (see Fig. 2). Sections of the shaft to the right of section “ i ” (to the right of point D of the modified section CD) will be subjected

to deformation (deflections and turns of the section) as a rigid body, that is, without changing the configuration [15].

In this case, their deformations can be found by dependencies:

$$\Delta\alpha_E = \Delta\alpha_D \tag{1}$$

$$\Delta y_E = \Delta y_D + \Delta\alpha_D \cdot x \tag{2}$$

where: x is the distance of the considered (arbitrary) section from the right end of the section “ I ” (section D). The values of $\Delta\alpha_D$ and Δy_D are determined by known methods depending on the changed parameters of the section “ I ”.

Consider their definition:

Figure 3a is showed a section of the shaft bounded by sections C and D , and Fig. 3b shows the deformation parameters of the CD section.

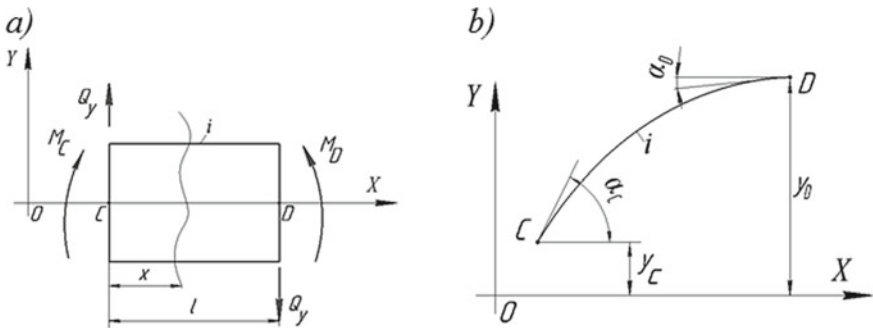


Fig. 3 a Section CD of the shaft; b deformation parameters of the CD section

The section is affected by the transverse force Q_y (constant in the section), the bending moment M_x (variable in the section: M_C in section C , M_D —in section D). According to [2], the differential equation of a curved shaft axis in an arbitrary cross section with the coordinate x has the form:

$$EJ_x \cdot \frac{d^2y}{dx^2} = EJ_x \cdot y'' = M_x = M_C + Q_y \cdot (l - x) \tag{3}$$

We integrate this equation twice with respect to the variable x , taking into account the boundary conditions of $G. U.$ for the section “ i ”:

$$\begin{aligned} x = 0 : \alpha &= \alpha_C, y = y_C \\ x = l : \alpha &= \alpha_D, y = y_D \end{aligned} \tag{4}$$

equation of the angles of rotation of the section;

$$EJ\alpha_D = EJ\alpha_C + M_C \cdot l + Q_y \cdot l^2$$

the deflection equation.

$$EJy_D = EJy_C + EJ\alpha_C \cdot l + \frac{M_C l^2}{2} + Q_y \cdot \frac{l^3}{3} \tag{5}$$

Let us introduce the notation:

$$B = \frac{M_C l^2}{2} + \frac{Q_y l^3}{3}, A = M_C \cdot l + \frac{Q_y l^2}{2} \tag{6}$$

Then the dependencies (5), taking into account (2) and (6), will take the form:

$$EJ\alpha_D = EJ\alpha_C + A, EJy_D = EJy_C + EJ\alpha_C \cdot l + B \tag{7}$$

After changing the shaft stiffness in the section “i” from EI to (EI’), the dependencies (7) will take the form:

$$(EJ)'\alpha'_D = (EJ)'\alpha'_C + A, (EJ)'y'_D = (EJ)'y'_C + (EJ)'\alpha'_C \cdot l + B \tag{8}$$

Subtracting pairwise (7) from (8) and performing some transformations, we find:

$$\begin{cases} \Delta y_D = y'_D - y_D = (k - 1) \cdot (y_D - y_C - \Delta\alpha_C \cdot l) \\ \Delta\alpha_D = \alpha'_D - \alpha_D = (k - 1) \cdot (\alpha_D - \alpha_C) \end{cases} \tag{9}$$

where $k = \frac{(EJ)}{(EJ)}$ —coefficient of change in shaft stiffness.

3 Results

Below is an example of calculating the shaft according to the proposed method.

Example. Let the cantilever shaft consisting of 3 sections—AC (length 2 l), CD (length 2 l) and DE (length l) act in the cross section E force P. The stiffness of the cross section of the shaft EI is the same in all sections. Graphoanalytic methods or the method of initial parameters determine the parameters of deformation of sections 0, 1, 2, 3 of the shaft (Fig. 4).

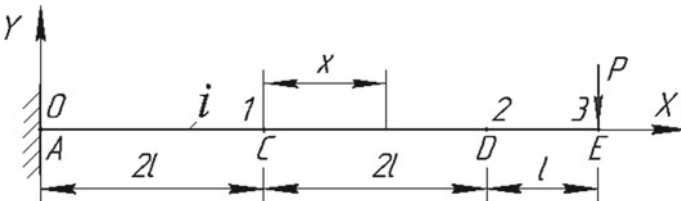


Fig. 4 Design scheme of the cantilever shaft

The calculation results are presented in Table 1.

Table 1 Parameters of shaft deformation in calculated cross sections

N	0	1	2	3
α , [P12]	0	-8.0	-12.0	-12.5
y , [P13]	0	-8.667	-29.334	-41.667

For example, for section C , we have the deformation parameters:

$$\alpha_C = \alpha_1 = -8.0 \cdot \frac{Pl^2}{EJ}$$

$$y_C = y_1 = -8.667 \cdot \frac{Pl^3}{EJ}$$

Let us now change the stiffness EI on the sections AC and DE . Take $(EJ)' = 2 \cdot EJ$ (increased the stiffness twice). We will determine the new values of α'_E and y'_E according to the proposed method (after changing the stiffness on the “ i ” section). By the dependencies (9), we find (for $x = 2l$ for the section D):

$$\Delta\alpha_C = (k - 1) \cdot (\alpha_D - \alpha_C) = -0.5 \cdot (-12 + 8.0) \cdot \frac{Pl^2}{EJ} = +2 \cdot \frac{Pl^2}{EJ}$$

$$\Delta y_C = (k - 1) \cdot (y_D - y_C - \Delta\alpha_C \cdot 2l)$$

$$= -0.5 \cdot (-29.334 + 8.667 + 8.0 \cdot 2)$$

$$\cdot \frac{Pl^3}{EJ} = +2.334 \cdot \frac{Pl^3}{EJ}$$

where $k = \frac{(EJ)}{(EJ)'} = 1/2$.

By dependencies (1) and (2) for the section E ($x = l$) under consideration, we find:

$$\Delta\alpha_E = \Delta\alpha_D = +2 \frac{Pl^2}{EJ'}$$

$$\Delta y_E = \Delta y_D + \Delta\alpha_D \cdot l = (2.334 + 2 \cdot 1) \cdot \frac{Pl^3}{EJ} = 4.334 \cdot \frac{Pl^3}{EJ}$$

Now, we find the deformation parameters for the section E [9]:

$$y'_E = y_E + \Delta y_E = (-41.667 + 4.334) \cdot \frac{Pl^3}{EJ} = -37.333 \cdot \frac{Pl^3}{EJ}$$

$$\alpha'_E = \alpha_E + \Delta\alpha_E = (-12.5 + 2) \cdot \frac{Pl^2}{EJ} = -10.5 \cdot \frac{Pl^2}{EJ}$$

Let us check the result obtained using the Mohr integral, which is convenient (quick calculation and minimum calculations) for determining the parameters of the shaft deformation in a small number of design points. Figure 5b shows the design scheme for calculating the shaft deflection, and Fig. 5c—for calculating the angle of rotation of the section.

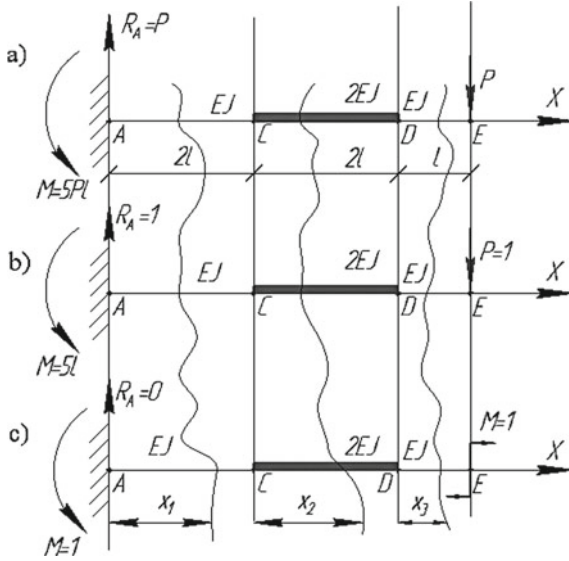


Fig. 5 Calculation scheme of the Mohr integral method

The calculation of the deformation parameter Δ (the angle of rotation of the section α or the deflection of the section y) is carried out according to the formula:

$$\Delta = \sum \int_0^{l_i} \frac{M_w \cdot M_3 \cdot dx}{EJ} \tag{10}$$

where M_w —the value of the moment from the working load (force P), M_3 —the value of the moment from a unit load (unit force $P = 1$ when calculating the deflection of the section y or a unit moment $M = 1$ when calculating the angle of rotation of the section α).

When calculating the deflection y'_E in section E , we obtain for 3 sections of the shaft AC , CD and DE :

- Plant section AC : $M_w = P \cdot (x - 5 \cdot l)$, $M_3 = x - 5 \cdot l$ and $\Delta_1 = \frac{98}{3 \cdot EJ} P \cdot l^3$.
 - Plant section CD : $M_w = P \cdot (x - 3 \cdot l)$, $M_3 = x - 3 \cdot l$ and $\Delta_2 = \frac{13}{3 \cdot EJ} P \cdot l^3$.
 - Plant section DE : $M_w = P \cdot (x - l)$, $M_3 = x - l$ and $\Delta_3 = \frac{1}{3 \cdot EJ} P \cdot l^3$.
- Now the deflection in section E is found by the formula:

$$y'_E = \Delta_1 + \Delta_2 + \Delta_3 = \frac{112}{3 \cdot EJ} P \cdot l^3$$

We perform a similar calculation for the angle of rotation α'_E of the section E :

$$\alpha'_E = \Delta_1 + \Delta_2 + \Delta_3 = \frac{21}{2 \cdot EJ} P \cdot l^3$$

Verification confirms the correctness of the proposed method.

4 Conclusions

1. Verification of the obtained results (values of y'_E and α'_E) by the method of the Mohr integral confirmed the correctness of the obtained results.
2. The proposed dependencies (1) and (2) establish a relationship between the parameters of the original (having insufficient stiffness for this shaft design) and the corrected (having sufficient stiffness for this shaft design) shafts. Thus, these dependencies significantly reduce the amount of work and simplify the calculation of the shafts (there is no need to re-design the shaft according to the condition of strength and endurance), while taking into account their strength and stiffness.
3. The example shows that the proposed method of adjusting the stiffness of the beam, taking into account the strength and endurance of the shaft, gives results, the reliability of which is confirmed by other methods of calculating the stiffness of the shaft (the Mohr integral method) and allows you to significantly simplify the design of cantilever shafts or cantilever elements of support shafts.

References

1. Markhel II (1986) Machine parts. Mashinostroenie, Moscow, p 448
2. Darkov AV, Shapiro GS (1975) Resistance of materials. Higher School, Moscow, p 657
3. Serensen SV, Groman MB, Nadarevic RM, Chagaev VP (1970) Shafts and axles. Design and calculation. Mashinostroenie, Moscow, p 320
4. Birger IA (1993) Calculation of the strength of machine parts: Handbook I. A. Birger, B. F. Shorr, G. B. Iosilevich. - 4th ed., reprint. Mashinostroenie, Moscow, p 640
5. Lelikov OP (2006) Shafts and bearings with rolling bearings. Calculation and construction. Constructor library. Mashinostroenie, Moscow, p 639
6. Potapova LB (2003) Complex resistance. Static and dynamic calculation of the shaft: Methodological guidelines for the implementation of computational and graphical work on the course "Resistance of materials" for students of mechanical specialties. Khabarovsk State Technical University. University press, Khabarovsk, p 31
7. Borisov EA, Kadermyatova DSh, Lobyntseva OA (2007) Verification calculation of KP DP-37 shafts. Synergy of Sciences. ISSN: 2500-0950 12:1010–1024
8. Kuzmin AA, Pavlova EA (2016) Calculation of shafts for torsional stiffness on the basis of a method for determining the positions of fixed sections. Modern Sci-Intensive Technol 8–1:64–67
9. Zhernakov VS, Mardimasova TN, Gazizov HSh (2013) Calculation of shafts for static, fatigue strength and stiffness: Textbook UGATU. Ufa. p 76
10. Acherkan NS (1968) Machine parts. In: Acherkan NS (ed) Calculation and construction. Guide., vol 1. Mashinostroenie, Moscow, p 440
11. Ivanov MN, Finogenov VA (2008) Machine parts: textbook for machine-building specialties of universities. Higher School, Moscow, p 408
12. Iosilevich GB (1988) Details of machines: textbook for students of engineering specialties of universities. Mashinostroenie, Moscow, p 368
13. Kuzmin AV, Chernin AB, Kozintsev BS (1986) Calculations of machine parts. Reference manual. Higher School, Moscow, p 400
14. Guzenkov PG (1986) Machine parts. Higher School, Moscow, p 359
15. Ryakhovskiy OA, Klypin AV (2002) Machine parts. Drofa, Moscow, p 288



Features of the Use of Structural Polymer-Composite Materials for the Manufacture of Complex-Shaped Parts in Small-Scale Production

V. M. Medunetskiy^(✉), S. Yu. Perepelkina, and Yu. S. Andreev

ITMO University, 49, Kronverkskiy prospekt, St. Petersburg 197101, Russia

Abstract. The article provides a brief overview of structural polymer-composite materials with an indication of their main properties. It is noted that these materials are advisable to be used in the manufacture of complex-shaped products, in particular gears with complex configuration of gear rims. To illustrate this, a drawing of a tapered gear rim of a cylindrical wheel is shown. For small-scale production of gear wheels, made of polymer-composite materials, it is recommended to use shaping matrices, which should also be made of composite materials with a metal shell. The technology of their manufacture is briefly described and a variant of the structural diagram of such a shaping matrix is given as an example. The authors recommended the use of composite thermosetting plastics as a filler for forming matrices. The experiment was performed via the equipment of the universal friction machine MTU-1 and SHIMAZU AGS-500X and the respective results are consequently presented in this article. Research polymer samples were made by using FDM technologies. The resulting graphs demonstrate the relation between the friction coefficient and ultimate tensile strength on the percentage ratio of polymer samples, which must be taken into account when designing and manufacturing gears.

Keywords: Complicated products · Gear drives · Polymer materials · Shell matrices

1 Introduction

As practice shows, polymer materials are widely used in various fields of technology [1]. It should be noted that at present there is a steady tendency to use structural polymer-composite materials (PCM) for the manufacture of gears, that are used in mechanical, electromechanical and mechatronic devices for various purposes. The advantages and disadvantages of composite and plastic gears are well known [2–5]. The advantages of polymer-composite products are reduced friction, wear and weight. In addition, the use of polymers will increase the strength and reliability, which directly affects the cost of the product [6–10]. The practical use of polymers has shown that these materials are low noise and corrosion resistant compared to metal products. It is recommended

to use structural polymer-composite materials for the manufacture of complex-shaped products in small-scale production. For example, it is difficult to make profile gear rims of cylindrical gears. Figure 1 illustrates a complex-profile cylindrical gear rim with tapered teeth.

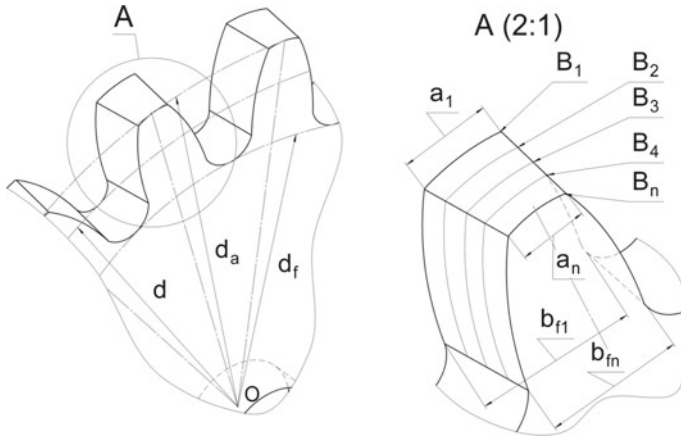


Fig. 1 Fragment of a ring gear with tapered teeth

Thus, this arises an objective need to analyze existing and practically applied structural polymer materials, as well as to study their properties and characteristics during the operation. The issue of manufacturing complex-profile parts from PCM in pilot, individual and small-scale production is also topical.

2 A Brief Overview of Non-Metallic Gear Materials

It is known that composite materials (composites) are materials that usually contain a base a plastic matrix and a filler with high strength and rigidity. The filler and the base must be chemically inert to each other. A wide range of materials with the required set of properties can be obtained by varying the composition of the matrix, filler, their ratio, and the orientation of the filler. Polymer matrix composites are one of the most numerous and varied types of materials. PCM with low density have high physical and mechanical characteristics. In particular, the coefficient of thermal expansion of polymer composites is significantly lower than that of metals and simple polymers. This allows PCM products to be used in a wide temperature range.

The variety of polymer-composite materials has led to the creation of various databases and programs for their modeling [11–14]. By selecting fillers, resins, using different layouts or winding schemes, it is possible to create materials for different operating conditions.

It is noted that for the manufacture of complex-profile gear rims of cylindrical wheels, polymeric materials of various technological, physical, mechanical, tribological and chemical properties are used. For example, there are such materials as polyamide and

its variety—polyamide 6, better known as caprolon, and fluoroplast, both pure and with various fillers. Polyamides have high strength, hardness, elasticity, wear resistance and heat resistance.

Caprolon can also be used for the manufacture of complex-shaped parts in small-scale production, since it has a high tensile strength. This material has a low friction coefficient in a pair with any metals. It is also well and quickly running in, and it is 6–7 times lighter than bronze and steel, which can be used instead. Apart from that, it possesses high manufacturability. There are also known composite materials based on this: glass-filled and mineral-filled.

The second common polymer is fluoroplast. Fluoroplast has extremely low surface energy, and therefore, it can be used as a release material. It is resistant to aging under normal conditions and has high antifriction properties, an extremely low coefficient of friction (under certain conditions and in pairs, the coefficient of friction is up to 0.02) [15]. Compositions based on fluoroplasts are also widely used. When fillers are introduced into the fluoropolymer, it increases wear resistance, strength, hardness, or elasticity [16].

It should be noted that the advantage of composite polymer gears over metal gears is not only a reduced noise level, but also a greater efficiency (efficiency) due to lower friction losses.

It is known from practice that 3D printers are widely used for the manufacture of prototypes of gear wheels. The most used materials in this variant for the manufacture of such gears are ABS and PLA plastics [17].

To take into account the friction of surfaces made of PLA plastic, tribological studies were carried out with various filling factors, using MTU-1 friction machine [18].

3 Results of the Study of Polymeric Materials for the Manufacture of Gear

Recently, a wide range of measurement machines and methods have been developed for the estimation of tribological behavior in various conditions. 3D printing technology allows us to manufacture parts with varying accuracy and degree of filling of the inner layers of the part. Deviations of the shape and roughness of the surface have significant influence on various properties of the part, including its reliability and wear [13].

Roughness of the surface layers normally does not depend on the filling factor. Therefore, it is interesting to investigate the tribological properties of tribopairs after abrasion of the surface layers. A universal friction machine MTU-1 was used for testing. (Fig. 2).

In Fig. 2, the following parts of the universal friction machine “MTU-1” are presented, where: 1—the part used for the control of rotation speed; 2—the power button; 3—the speed control button; 4—the friction torque measurement system with the elastic sensing element; 5—the strain gauge for axial load measurement; 6—the handle for fast loading; 7—the handle for fine loading; 8—the chuck for the upper sample; 9—the lubricant reservoir; 10—the handle for the displacement of coordinate table.

The structure of the universal friction machine “MTU-1” allows us to save the parallelism of the contacted surfaces, which increases the accuracy of measurements. The

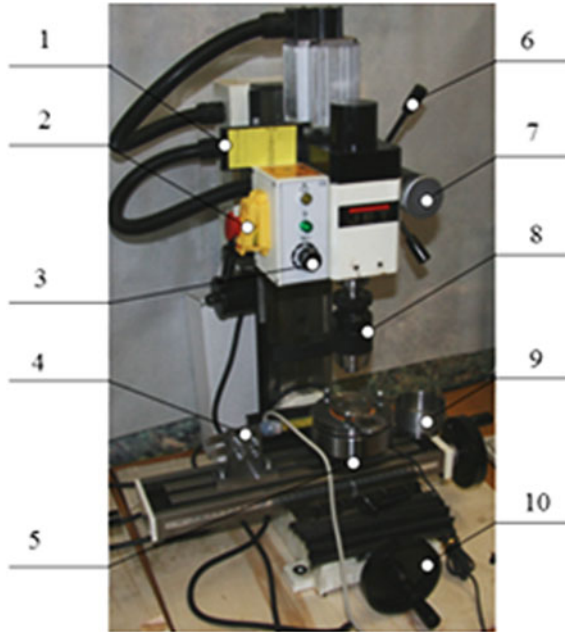


Fig. 2 Universal friction machine “MTU-1”

machine is resistant to the environmental influence, such as vibration, electromagnetic interference, dust, humidity and temperature fluctuations.

The testing method for “MTU-1” is based on a relative rotational movement of the upper sample to the lower stationary sample with or without lubricants using different test schemes, such as disc to disk, sphere to ring, pin to disk motion, etc.

The upper sample rotation speed without the load is adjustable up to 2500 rpm, the load on the samples can be varied from 50 to 1000 N.

Figure 3 shows the dependence of the maximum coefficient of friction on the filling factor (given porosity) of the samples under study.

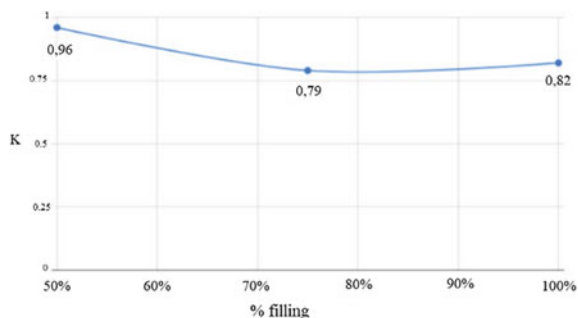


Fig. 3 Dependence of the maximum friction coefficient on the sample filling factor

As it can be seen from Fig. 3, specimens with 50% infill have the highest maximum coefficient of friction. Perhaps, this happens due to the absence of equilibrium of the surface layer and the presence of voids. With such a ratio between pores and areas of overlap of threads, the contact area of two pairs of samples is uneven and maximally “spotted”, which increases the coefficient of friction. The minimum coefficient of friction is observed at 75% coverage, which can be explained by the optimal distribution of areas with intersecting filaments in 3D printing. In the process of friction, the surface layer is smoothed due to the plastic flow of the polymer. However, an increased coefficient of friction is observed by 75% during friction of samples, treated with fine-grained abrasive and dichloromethane, which occurs due to an increase in surface energy after chemical treatment. In this regard, a non-equilibrium structure with a small number of pores is created on the surface. For the same reason, the coefficient of friction of samples of 100% filling increases slightly, while for 50% it decreases significantly.

Strength studies were carried out on a tensile testing machine SHIMAZU AGS-500X. Figure 4 demonstrates a diagram of the SHIMAZU AGS-500X tensile testing machine.

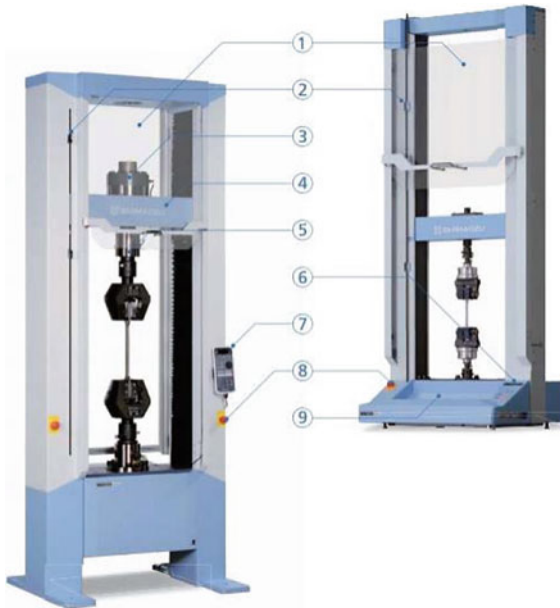


Fig. 4 Tensile testing machine SHIMAZU AGS-500X. Protective glass is used to protect against flying debris (1) One-touch travel stops (2) Load cell (3) Crosspiece (4) General gripper for tensile and compression tests (frame 20–300 kN) (5) Built-in main control panel (6, 7) Emergency stop button (8) Multipurpose Tray (Table Frame) (9)

Figure 5 shows the relation between the ultimate strength and the filling factor of the samples.

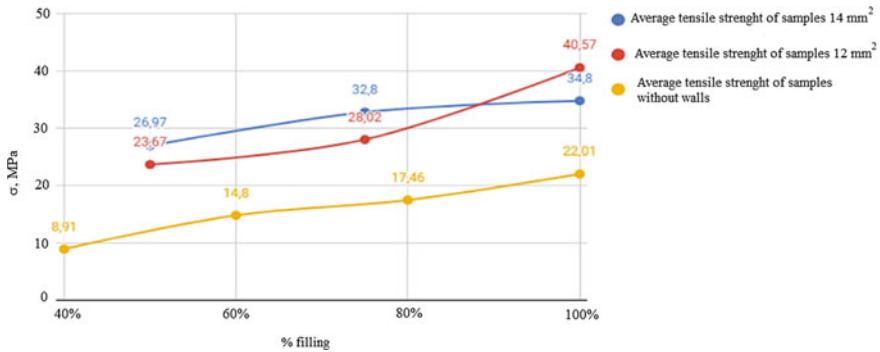


Fig. 5 The dependence of ultimate strength on sample filling factor

The figure shows that the increase in ultimate strength is directly proportional to the increase in the filling factor. As the fill factor increases from 40 to 100%, additional adhesive molecular bridges appear, which provides the viscous fluidity of the material.

4 Recommendations for the Manufacture of Gear Links in Small Batch Production

For small-scale production of gears with a complex gear rims configuration, it is possible to propose shaping matrices, which are also expedient to be made of composite materials. Finished products can have different physical and mechanical properties: rigid, imitating the properties of ABS, semi-rigid, elastic, heat-resistant, transparent, as well as combined.

The crucial factor for the reliable operation of the gear transmission, made of composite polymer materials, is the maximum compliance of the operational requirements with the properties of the selected material. For example, a high load defines the choice of hard rigid plastics, in particular, reinforced thermoplastics.

Studies have shown that to ensure a high-quality working surface of gear wheels, it is recommended to make them of composite thermoplastics by casting or molding into shell forming matrices [15, 19]. The matrix for their manufacture is made of thermosetting plastics, for example, from phenol–formaldehyde and epoxy polymers. This design of the shell shaping matrix is shown in Fig. 6.

Reactoplasts have a sufficiently high stability of physical and mechanical properties when the environment changes. Due to their strength and electrical insulating properties, as well as the ability to operate at high temperatures, phenolic strips are successfully used for the manufacture of structural, frictional, and antifriction products [20]. In this case, the inner surfaces, that form the cavity, should be made of metal in the form of a shell. This is possible if the metal shell gear rim is made of a thin strip, bent along the contour of the master model. For this option, it is recommended to use cold rolled mild steel strip, which is usually used when parts are bent. It is also recommended to make a master model for the formation of the shell on a 3D printer.

It should be noted that on one side of the metal strip it is necessary to create a microrelief with the specified functional parameters. In addition, it is necessary to set

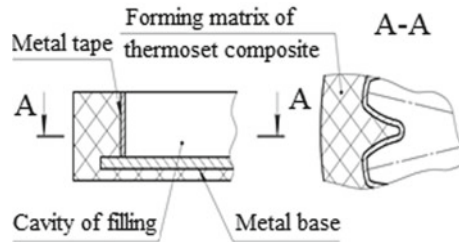


Fig. 6 Fragment of a shaping matrix made of polymer-composite materials

a sufficiently rough roughness for a strong connection with the material of the forming matrix on the other surface, since an increase in roughness leads to an increase in adhesion strength.

5 Conclusion

Thus, as a result, it can be noted that structural polymeric materials are considered, which are recommended for the manufacture of complex-shaped products in small-scale production using the example of tapered gear rims. Furthermore, a shell structure of a forming matrix made of thermosets for their manufacture is proposed. Apart from that, the results of studies on the strength and tribological characteristics of polymer samples obtained by the FDM technology with different filling factors are presented, which makes it possible to use them for the manufacture of complex-shaped products (parts).

References

1. González-Henríquez CM, Sarabia-Vallejos MA, Rodríguez-Hernández J (2019) Polymers for additive manufacturing and 4D-printing: Materials, methodologies, and biomedical applications. *Prog Polym Sci* 94:57–116. <https://doi.org/10.1016/j.progpolymsci.2019.03.001>
2. Ghosh R, Ghosh S, Srivastava T, Barman RN (2017) Design and manufacturing of laminated spring: a new approach based on composites. *Int J Eng Technol* 9(2):1438–1451. <https://doi.org/10.21817/ijet/2017/v9i2/170902285>
3. Chatterjee S, Gupta K (2018) Advances in modelling and analysis C 73(3):79–83. *Journal Homepage: http://iieta.org/Journals/AMA/AMA_C*. https://doi.org/10.18280/ama_c.730301
4. Pawar PB, Utpat AA (2015) Analysis of composite material spur gear under static loading condition. *Mater Today Proc* 2:2968–2974. <https://doi.org/10.1016/j.matpr.2015.07.278>
5. Thirugnanam A, Sathish J, Rakesh L (2014) Contact analysis of spur gear using composite material (NYLO CAST). *Middle-East J Sci Res* 20(8):966–968. <https://doi.org/10.5829/idosi.mejsr.2014.20.08.114144>
6. Mao K, Greenwood D, Ramakrishnan R, Goodship V, Shrouti C, Chetwynd D, Langlois P (2019) The wear resistance improvement of fibre reinforced polymer composite gears. *Wear* 426:1033–1039. <https://doi.org/10.1016/j.wear.2018.12.043>
7. Catera PG, Mundo D, Gagliardi F, Treviso A (2020) A comparative analysis of adhesive bonding and interference fitting as joining technologies for hybrid metal-composite gear manufacturing. *Int J Interactive Des Manuf (IJIDeM)* 1–16. <https://doi.org/10.1007/s12008-020-00647-y>

8. Catera PG, Mundo D, Treviso A, Gagliardi F, Visrolia A (2019) On the design and simulation of hybrid metal-composite gears. *Appl Compos Mater* 26(3):817–833. <https://doi.org/10.1007/s10443-018-9753-6>
9. Gauntt SM, Campbell RL (2019) Characterization of a hybrid (steel-composite) gear with various composite materials and layups. In: *AIAA Scitech 2019 Forum*, 0146. <https://doi.org/10.2514/6.2019-0146>
10. Singh AK, Yadav S, Singh PK (2019) A comparative study for transmission efficiency of ABS, POM, and HDPE spur gears. In: *Advances in engineering design*. Springer, Singapore, pp 269–277. https://doi.org/10.1007/978-981-13-6469-3_24
11. Total Materia. The most extensive database of materials in the world. <https://www.totalmateria.com/page.aspx?ID=Home&LN=RU>. Accessed: 28 Oct 2020
12. Material Data Center. Data on materials and their applications. <https://www.materialdatacenter.com/mb/>. Accessed: 28 Oct 2020
13. Base of polymer materials. Material Data Center. <https://plastinfo.ru/m-base/>. Accessed: 28 Oct 2020
14. Kryazhev YuA, Andreev MV, Shituk AA (2018) Analysis of machining regimes and their influence on surface roughness while high-speed turn-milling. *Innovations in mechanical engineering*, pp 491–497 (in Russian)
15. Friedrich, K, Walter R (eds) (2020) *Structure and properties of additive manufactured polymer components*. Woodhead Publishing. <https://doi.org/10.1016/C2018-0-03664-6>
16. Goh GD, Yap YL, Tan HKJ, Sing SL, Goh GL, Yeong WY (2020) Process–structure–properties in polymer additive manufacturing via material extrusion: a review. *Crit Rev Solid State Mater Sci* 45(2):113–133. <https://doi.org/10.1080/10408436.2018.1549977>
17. Milisavljević J, Petrović E, Ćirić I, Mančić M, Marković D, Đorđević M (2012) Tensile testing for different types of polymers. In: *DAS-29, 29th Danubia-Adria symposium*, University of Belgrade, Serbia, pp 266–269
18. Perepelkina S, Kovalenko P, Pechenko R (2017) Investigation of tribological properties of metallic materials with the use of the universal friction machine “MTU-1”. *Proc Eng* 176:301–309
19. Directory of polymers. *Polymer materials: products, equipment, technologies*. <http://www.polymerbranch.com/catalogp.html>. Accessed: 28 Oct 2020
20. Vitkalova IA, Torlova AS, Pikalov ES (2018) Technology of preparation and properties of phenol-formaldehyde resins and compositions based on them. *Sci Rev Techn Sci* 2:15–28 (in Russian)



Evaluation of the Accuracy of Gears Made of Polymer Composite Materials

M. V. Abramchuk^(✉), V. M. Medunetskiy, and V. A. Zinkov

ITMO University, 49, Kronverksky Pr., bldg. A, St. Petersburg 197101, Russia

Abstract. The paper briefly describes and justifies the need to evaluate the accuracy of gears that are made of polymer composite materials. The production of gears is recommended using specific databases of polymer composite materials, which are given in the article, to select materials for the required physical and mechanical parameters. An example of manufacturing a gear wheel from composite polymer materials with an asymmetric tooth profile and an internal reinforcing gear ring is given. A sequence of dependencies is proposed that can be used to evaluate the accuracy of gears made of polymer composite materials. The paper deals with the calculation of the maximum and minimum values of the tangential composite deviation and kinematic backlash of gears, taking into account the installation the mounting radial and axial runout of the gear, the total reduced mounting error and options for the location of the gears on the transmission shaft.

Keywords: PCM gears · PCM databases · Gear accuracy · Composite deviation · PCM

1 Introduction

It is known that structural polymer materials are widely used for the manufacture of mechanisms for various purposes [1]. Currently, there is a steady trend of using structural composite polymer materials (PCM) for the manufacture of gears in the actuators of various devices. The advantages and disadvantages of composite and plastic gears are well known [2–5]. The advantage of products made of polymer composites is to reduce the weight of products, reduce friction and wear, which significantly affects the quality and cost of products [6–10].

A special feature of the use of polymer composites [11–14] is that it is possible to simultaneously create the material itself and form the technology for its processing into a product. Selecting fillers, resins, as well as using various schemes of laying out or winding, you can get samples for different operating conditions. Today, there are extensive databases of polymer composites:

- (1) Total Material of the Swiss company Key to Metals AG [15];
- (2) Material Data Center of the German developed by M-Base Engineering + Software GmbH [16];

(3) Plastinfo.ru localized for processors in Russia and CIS countries material Data Center database of the Russian Plastinfo LLC.ru [17].

The Material Data Center database combines a set of different characteristics of polymer materials for developers, with fairly detailed curves of properties depending on temperature and/or time. It is possible to superimpose functional curves of different materials on a single diagram to visually compare the manufacturability of materials or their various properties [18].

Thus, it is possible to produce gears from PCM with improved properties [19–23].

The design of the polymer gear wheel largely determines the efficiency of the gear train. The chosen ratio of the crown dimensions, the reliability of the interfaces, and the location of the reinforcing elements depend on the manufacturing accuracy and strength of the transmission. In practice, PCM gears are divided into all-polymer and reinforced according to their design [14].

It can be noted that in many structures of mechanisms, gears made of such materials are used with reverse, and the so-called dead stroke occurs due to the presence of gaps in the joints and elastic deformations [24]. Often, in some cases, there is a need to increase the load capacity of gears from PCM. As an example of solving this problem, we can give a non-standard gear crown with an asymmetric profile and a reinforcing symmetrical gear crown made of metal (Fig. 1).

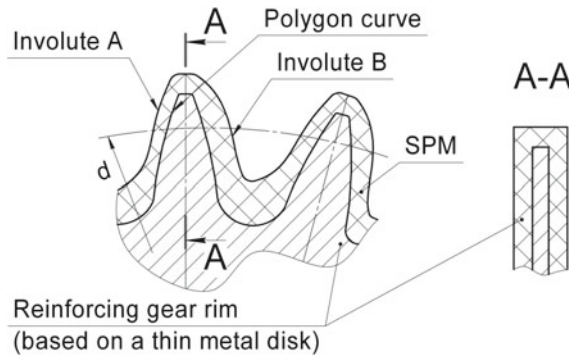


Fig. 1 Cross-section of a non-standard toothed reinforced crown with an asymmetric external profile (the internal reinforcing toothed crown is symmetrical)

The reinforcing metal-toothed crown can be made both symmetrical and asymmetric according to the profile of the tooth.

It is important to note that in single or small-scale production, the reinforcing toothed crown can be made on universal equipment with a disk tool with straight cutting edges. This can be implemented using the discrete bending method, that is, without the use of gear-cutting tools and equipment [23]. In this case, the profile of the internal reinforcing teeth on the metal disk will be represented as a polygonal curve relative to the involute, and the external working surface of the teeth of the crown is represented by a composite material. The reinforcing metal-toothed crown can be made both with a symmetrical profile and asymmetric according to the profile of the tooth.

This method of forming a reinforcing metal-toothed crown is illustrated in Fig. 2, which shows two positions of the relative position of the toothed crown being manufactured and the disk tool. At position 1 and position 2, a metal reinforcing disk is drilled with a disk tool along the axis of the workpiece. The transition from position 1 to position 2 is achieved by discrete rotation by an angle ($\Delta\varphi$) and discrete displacement of the disk tool by an amount (Δ). The angle of rotation of the metal disk and the linear displacement of the tool must be such that the point “a” and point “b” belong to the calculated involute. In this case, the formed surface on the tooth of the metal disk will be a sequence of flat cuts that encircle the involute. In order to form one side of the tooth (left according to this figure), it is enough, for example, 5–6 positions with a corresponding discrete change in the angle (φ) and a discrete movement of the disk tool along the axis of its rotation. Next, all the right sides of the subsequent manufactured teeth should be formed in the same way. After that, the workpiece should be turned over and perform the same operations to profile the other side of each tooth.

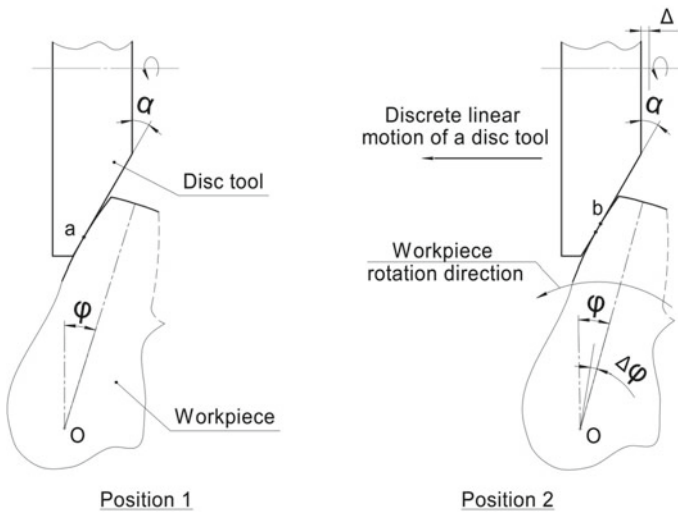


Fig. 2 Formation of a toothed reinforcing crown by the method of discrete bending

It is important to note that gear links from PCM also have shrinkage during their manufacture, and they are subjected to warping (uneven shrinkage).

Therefore, based on the above, the issue of evaluating the accuracy of gears from PCM is very relevant, since the accuracy of gears is the main indicator of their quality.

Without departing from the standard (GOST 1643-81) for gears with a tooth module $m \geq 1$ mm, 12 degrees of accuracy, 6 types of coupling are set for gears with a tooth module $m \geq 1$ mm: A, B, C, D, E, H and 8 types of T_{jn} tolerance for the backlash: x, y, z, a, b, c, d, h . The manufacturing accuracy of each gear wheel and then the actual transmission is set by the degree of accuracy, while the backlash requirement is set by the type of coupling according to the backlash standards.

For cylindrical gears that are mainly involute, taking into account mounting errors, the values of the minimum and maximum tangential composite deviation are determined by the expressions:

– for degrees of accuracy 3–6:

$$F'_{i0 \min} = 0.62K_s(F'_{i1} + F'_{i2}).$$

– for degrees of accuracy 7–8:

$$F'_{i0 \min} = 0.71K_s(F'_{i1} + F'_{i2}).$$

For all degrees of accuracy (the same applies to other gears)

$$F'_{i0 \max} = K \left[\sqrt{(F'_{i1})^2 + E_{\Sigma M_1}^2} + \sqrt{(F'_{i2})^2 + E_{\Sigma M_2}^2} \right],$$

where K , K_s —phase compensation coefficients, i.e., coefficients that take into account the degree of change in the tangential composite deviation from the initial position of the links; F'_{i1} , F'_{i2} —tangential composite deviations of the driving and driven gears, respectively, $E_{\Sigma M_1}$, $E_{\Sigma M_2}$ —the total reduced installation error (in GOST 21098-82 is determined by Appendix 2).

Tolerance for the tangential composite deviation of the gear:

$$F'_i = F_p + f_f$$

where F_p is the tolerance for the accumulated error of the gear pitch and f_f is the tolerance for the error of the tooth profile.

The value of the minimum kinematic backlash of the gear transmission:

$$j_{i \min} = \frac{j_{n \min}}{\cos \alpha \cos \beta},$$

where $j_{n \min}$ is the allowance backlash (normal), α is the pressure angle of the standard basic rack tooth profile, and β is the helix angle.

The value of the maximum kinematic backlash for a cylindrical gear transmission:

$$j_{i \max} = 0,7(E_{H_{S1}} + E_{H_{S2}}) + \sqrt{0,5(T_{H1}^2 + T_{H2}^2 + 2f_a^2 + G_{r1}^2 + G_{r2}^2)},$$

where $j_{i \max}$ —the maximum circular backlash in the gear transmission, E_{H_S} is the smallest additional bias source circuit, T_H —tolerance on the basic racks tooth profile modification, $\pm f_a$ is the center distance limit error, and G_r is the radial clearance in the bearings of rotation and is equal to the radial runout (in GOST 21098-82 is defined in Annex 2).

The total reduced mounting error for cylindrical gears is calculated based on the relationship:

$$E_{\Sigma M} = \sqrt{\left(\frac{e_r \operatorname{tg} \alpha}{\cos \beta}\right)^2 + (e_a \operatorname{tg} \beta)^2},$$

where e_r and e_a are the mounting radial and axial runout of the gear, respectively (indicators of the accuracy of mounting gears). The values of e_r and e_a are calculated using the formulas:

$$e_r = 0,85 \sqrt{\sum_{i=1}^n e_i^2}, \quad e_a = 0,85 \sqrt{\sum_{j=1}^n e_j^2}$$

where e_r and e_a are the error tolerances that create the primary radial and axial runouts of the gear wheel, respectively.

It is assumed that the value of G_r is equal to e_r . It is clear that e_r and e_a depend on the type of connection or smooth cylindrical coupling of the part with the shaft.

The mounting radial runout of the gear can be calculated using the following expression:

$$e_r = \left(F_r + e_C + e_B + K_{i\alpha} \frac{a + b}{l} \right),$$

where F_r is the tolerance for the radial runout of the gear ring. Determined by GOST 1643-81; e_C —clearance in the gear fit on the shaft, depending on the design of the connection and the fit used; e_B —tolerance for radial runout of the fit stage of the shaft under the gear wheel relative to the shaft pin, and for smooth shafts $e_B = 0$, is determined by GOST 24643-81; $K_{i\alpha}$ —radial runout of the inner ring of the assembled bearing is determined according to GOST 520-2011.

Dimensions a , b , l are based on the wheel arrangement on the shaft according to Fig. 3.

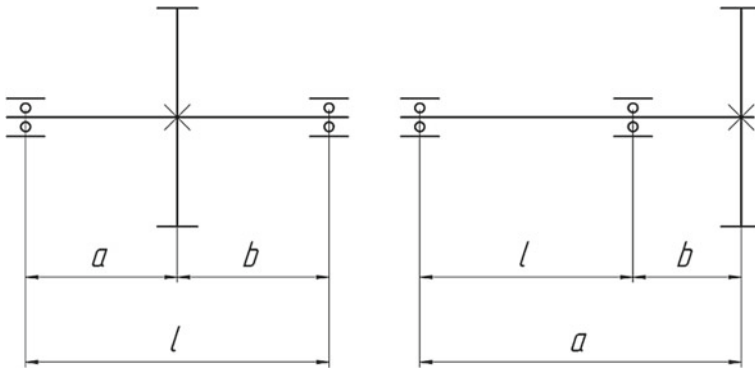


Fig. 3 Inter-support (left) and cantilever arrangement of the gear wheel on the shaft

For spur gears, axial runout can be neglected, i.e., $e_a = 0$.

You can also use the probabilistic method for calculating the accuracy—the Monte Carlo method, in which the components of the tangential composite deviation and backlash will be random values in certain intervals [25, 26].

2 Conclusion

Thus, as a conclusion, it should be noted that this paper offers a specific sequence of dependencies that can be used to evaluate the accuracy of gears made of polymer composite materials that are intended for use as transmission mechanisms in devices for various purposes.

References

1. González-Henríquez CM, Sarabia-Vallejos MA, Rodríguez-Hernández J (2019) Polymers for additive manufacturing and 4D-printing: Materials, methodologies, and biomedical applications. *Prog Polym Sci* 94:57–116. <https://doi.org/10.1016/j.progpolymsci.2019.03.001>
2. Ghosh R, Ghosh S, Srivastava T, Barman RN (2017) Design and manufacturing of laminated spring: a new approach based on composites. *Int J Eng Technol* 9(2):1438–1451. <https://doi.org/10.21817/ijet/2017/v9i2/170902285>
3. Chatterjee S, Gupta K (2018) Advances in modelling and analysis C. 73(3):79–83 Journal homepage. http://iieta.org/Journals/AMA/AMA_C. https://doi.org/10.18280/ama_c.730301
4. Pawar PB, Utpat AA (2015) Analysis of composite material spur gear under static loading condition. *Mater Today Proc* 2(4–5):2968–2974. <https://doi.org/10.1016/j.matpr.2015.07.278>
5. Thirugnanam A, Sathish J, Rakesh L (2014) Contact analysis of spur gear using composite material (NYLO CAST). *Middle-East J Sci Res* 20(8):966–968. <https://doi.org/10.5829/idosi.mejsr.2014.20.08.114144>
6. Mao K, Greenwood D, Ramakrishnan R, Goodship V, Shrouti C, Chetwynd D, Langlois P (2019) The wear resistance improvement of fibre reinforced polymer composite gears. *Wear* 426:1033–1039. <https://doi.org/10.1016/j.wear.2018.12.043>
7. Catera PG, Mundo D, Gagliardi F, Treviso A (2020) A comparative analysis of adhesive bonding and interference fitting as joining technologies for hybrid metal-composite gear manufacturing. *Int J Interactive Des Manuf (IJIDeM)* 1–16. <https://doi.org/10.1007/s12008-020-00647-y>
8. Catera PG, Mundo D, Treviso A, Gagliardi F, Visrolia A (2019) On the design and simulation of hybrid metal-composite gears. *Appl Compos Mater* 26(3):817–833. <https://doi.org/10.1007/s10443-018-9753-6>
9. Gauntt SM & Campbell RL (2019) Characterization of a hybrid (steel-composite) gear with various composite materials and layouts. In: *AIAA Scitech 2019 Forum* 0146. <https://doi.org/10.2514/6.2019-0146>
10. Singh AK, Yadav S, Singh PK (2019) A comparative study for transmission efficiency of ABS, POM, and HDPE spur gears. In: *Advances in engineering design*. Springer, Singapore, pp 269–277. https://doi.org/10.1007/978-981-13-6469-3_24
11. Goh GD, Yap YL, Tan HKJ, Sing SL, Goh GL, Yeong WY (2020) Process–structure–properties in polymer additive manufacturing via material extrusion: a review. *Crit Rev Solid State Mater Sci* 45(2):113–133. <https://doi.org/10.1080/10408436.2018.1549977>
12. Friedrich K, Walter R (eds) (2020) *Structure and properties of additive manufactured polymer components*. Woodhead Publishing. <https://doi.org/10.1016/C2018-0-03664-6>
13. *Directory of polymers* [Internet]. Polymer materials: products, equipment, technologies. Available at: <http://www.polymerbranch.com/catalogp.html>. Accessed: 28 Oct 2020
14. Karapetyan AN, Scharf G (2007) The choice of polymeric materials in the design of gear wheels. *Proc NAS RA SEUA: Tech Sci* 60(2):266–271 (in Russian)
15. Total Materia [Internet]. The most extensive database of materials in the world. <https://www.totalmateria.com/page.aspx?ID=Home&LN=RU>. Accessed 28 Oct 2020

16. Material Data Center [Internet]. Data on materials and their applications. <https://www.materialdatacenter.com/mb/>. Accessed 28 Oct 2020
17. Base of polymer materials [Internet]. Material Data Center. <https://plastinfo.ru/m-base/>. Accessed 28 Oct 2020
18. Kryazhev YuA, Andreev MV, Shituk AA (2018) Analysis of machining regimes and their influence on surface roughness while high-speed turn-milling. In: Innovations in mechanical engineering, pp 491–497 (in Russian)
19. Starzhinsky VE, Shalobaev EV, Shilko SV (2012) Elements of drive devices. calculation, design, technology. Belaruskaya Navuka, Minks, p 769 (in Russian)
20. Starzhinsky VE, Shilko SV, Shalobaev EV (2018) Production technology of gears from thermoplastic polymer materials (review). Polimernye materialy i tekhnologii. Polym Mater Technol 4(2):6–31 (in Russian)
21. Starzhinsky VE, Shalobaev EV (2005) Designing molds for precision plastic wheels using rapid prototyping technology. Progressive technologies in machine and instrument engineering NSTU-API, pp 28–29 (in Russian)
22. Vitkalova IA, Torlova AS, Pikalov ES (2018) Technology of preparation and properties of phenol-formaldehyde resins and compositions based on them. Sci Rev Tech Sci 2:15–28 (in Russian)
23. Medunetskiy VM (2002) Ensuring quality indicators of combined cylindrical gears. St. Petersburg, p 160 (in Russian)
24. Dong YQ, Yang XC (2006) Experimental application of gapless gear pairs to noise reduction of an automobile engine. J Nanchang Univ (Engineering & Technology) 3
25. Abramchuk MV (2014) Improvement of calculations of accuracy parameters of gears, gearings and multi-link gear mechanisms (Abstract of the thesis of Doctoral dissertation). Saint Petersburg, p. 20. <https://dlib.rsl.ru/01005558497>. Accessed 06 Nov 2020 (in Russian)
26. Abramchuk MV (2018) Calculation of accuracy parameters of evolvent cylindrical gear transmissions. J Instrument Eng 61(2):118–122. <https://doi.org/10.17586/0021-3454-2018-61-2-118-122>



Lifetime Prediction for the Jaw Crusher by the Criterion of Toggle Fatigue Strength Based on the Application of the Kinetic Concept of Material Destruction

M. Slobodianskii^(✉)

Nosov Magnitogorsk State Technical University, 38, Lenin Street, Magnitogorsk 455000, Russia

Abstract. A toggle, which performs a safety function in case of getting uncrushable material into the chamber, is shown to be one of the elements determining the lifetime of a complex swing jaw crusher. It was determined that the toggle failure prior to the scheduled overhaul period under the conditions of crusher stationary operation is unacceptable (not in case of getting uncrushable material into), since it leads to the economic costs from reduced productivity of the enterprise and increased time for equipment breakdown maintenance. The known approaches were analysed in order to assess the durability of the jaw crusher toggles; the results revealed that their performance is assessed according to the static strength condition, and the lifetime is assessed by the criterion of cyclic strength using the experimental SN-Curve (Wöhler curve). The article proposes a mathematical model for failures by the criterion of material kinetic strength in order to solve the problem of analytical assessment of the toggle lifetime. An algorithm has been developed, based on the failure model proposed, to determine the average toggle lifetime under given operating conditions. The theoretical studies of the toggle durability of the PE 1200 × 1500 jaw crusher under operating conditions at Orenburg Minerals JSC were carried out with the use of the algorithm. The verification of the proposed failure model showed that the prediction error in the average toggle lifetime does not exceed 18%. This indicates a fairly high level of the mathematical model reliability.

Keywords: Failure model · Jaw crusher · Toggle · Lifetime · Prediction

1 Introduction

The following types of crushers, such as jaw, roll, cone and impact, are used to crush various solid bulk materials [1]. Complex swing jaw crushers for crushing materials, having a tensile strength of not more than 300 MPa, are the most common in construction, mining and metallurgical industries. They are widely used in various complex production processes due to their compactness, the ease of operation and maintainability.

Unplanned failures of jaw crushers can lead to significant economic costs from reduced productivity of the enterprise and increased time for equipment breakdown maintenance.

Breakdowns of the following elements can lead to failures of complex swing jaw crushers:

- worn or damaged crushing plates;
- a broken swing jaw;
- eccentric shaft bearings;
- a broken eccentric shaft;
- toggle fatigue damage.

In practice, the toggle is the most important element of the crusher which failure leads to significant breakdown maintenance. It prevents the material which is hard to be crushed on this equipment from getting into the crusher. On the one hand, when the uncrushable material gets into the chamber, it is the toggle that must be broken first, thereby preventing the destruction of the movable jaw which restorations and repairs are more expensive. On the other hand, the toggle lifetime under stationary operating conditions should be not less than the assigned one, after which it has to be replaced.

Thus, the toggle is an element which determines the durability of the entire crusher, and its lifetime prediction at the design and operation stages will allow one to establish the most rational structure of the repair cycle. Mathematical description of the material destruction process according to the cyclic strength criterion is needed for an analytical assessment of the toggle average lifetime.

An analysis of the scientific literature showed that most of the works are dedicated to simulation of the crushing process [2], examination of the toggle reliability [3] and study the kinematics of the crusher operation. However, the issue of ensuring the required reliability level of complex swing jaw crusher toggles is still open.

The jaw crusher toggle performance is determined by the static strength condition [4, 5]:

$$\sigma_c \leq [\sigma_c], \quad (1)$$

where σ_c is the maximum compressive stress in the toggle and $[\sigma_c]$ is the allowable compressive stress depending on the toggle material and its physical and mechanical characteristics.

At the same time, it is believed that if condition (1) is fulfilled, the crusher toggle will be in a state of operability for any length of time. Compressive stresses σ_c , arising in the body of the toggle, can be assessed using the methods described in [4–6], but the use of the finite element method in computer-aided design systems (Autodesk Inventor, SolidWorks, Ansys, Abaqus, Nastran, and others) has become relevant to assess the stress state of loaded parts. In this case, this method allows one to calculate the stress state in the toggle taking into account all design features, including σ_c in condition (1).

Thus, if the stresses σ_c , calculated according to the conditions described in [4–6] or by the finite element method, satisfy the condition (1), then it is assumed that the toggle is in the state of operability for any length of time. This is in conflict with operational practice. In this case, in order to assess the toggle lifetime based on the calculated value of compressive stresses σ_c , the SN-Curve (Wöhler curve) is used that resulted from a large number of laboratory tests of samples from various structural materials. This approach

has a significant drawback that is in the limited data on the fatigue curves of materials used for the toggle manufacture. There is also no possibility to evaluate the complex effect of temperature power factors, physical and mechanical properties of materials on durability indicators.

However, the issue of analytical prediction of the jaw crusher toggle lifetime by the criterion of cyclic strength is not considered in the literature. In our opinion, this problem can be solved on the basis of modern achievements of the physical reliability theory for machine parts [7, 8] and the kinetic concept of solid destruction process interpretation [9–14].

Thereby, the aim of this research is to develop an analytical model for jaw crusher failures on the criterion of toggle cyclic strength, which does not require additional experimental studies.

2 A Model for Jaw Crusher Failures by the Criterion of Toggle Cyclic Strength Based on the Kinetic Concept of Material Destruction

The basic principles of the reliability prediction theory for machine parts are used to build a model of failures [7, 11, 12]. The energy density $u_{e\tau}$ of structural defects of the most stressed material volumes is taken for the parameter of the toggle state. If we assume that the toggle load conditions are stationary, then the failure by the cyclic strength criterion will occur if the value $u_{e\tau}$ reaches the critical value u_{e*} [7, 11, 12]:

$$u_{e\tau} = u_{e0} + \dot{u}_e \cdot t = u_{e*}. \quad (2)$$

The initial value u_{e0} for the density of the latent energy of defects in the structure of the material is determined as a function of Vickers hardness HV and a shear modulus G [10, 15–19]:

$$u_{e0(vk)} = \left((0.071 \cdot HV)^{1,2} \right)^2 / \left(6 \cdot G_{vk} \cdot \left(6.47 \times 10^{-6} \cdot HV + 0.12 \times 10^{-2} \right)^2 \right). \quad (3)$$

Solving Eq. (2) in relation to $t = t_{np}$, we determine the average lifetime expectancy of the toggle by the cyclic strength criterion:

$$t = (u_{e*} - u_{e0}) / \dot{u}_e. \quad (4)$$

The average rate of damage in the structure of the contact material volumes can be determined according to [8, 10] using the equation:

$$\dot{u}_e = \frac{k_{\text{cmp}} \cdot k \cdot T_f \cdot U(\sigma_0, T_f)}{h} \cdot \left(\exp\left(-\frac{\vec{U}(\sigma_i, T_f) \cdot V_{\text{am}}}{k \cdot T_f}\right) - \exp\left(-\frac{\overleftarrow{U}(\sigma_i, T_f) \cdot V_{\text{am}}}{k \cdot T_f}\right) \right), \quad (5)$$

where $k_{\text{cmp}} = 2 \cdot (u_{e*} - u_{e0}) / (3 \cdot u_{e*} - u_{e0})$ is Le Chatelier's principle taking into account the material resistance to its structural damage [17];

k, h, V_{am} are the Boltzmann constant, the Planck constant and the atomic volume of the toggle material;

$\sigma_0 = (\sigma_1 + \sigma_2 + \sigma_3)/3$ is the average hydrostatic stress [20]; $\sigma_2 = -0.288 \cdot \sigma_c$ and $\sigma_3 = -0.78 \cdot \sigma_c$ are principal stresses determined with the use of the function of the maximum stresses arising in the body [20];

$\sigma_i = \sqrt{((\sigma_1 - \sigma_2)^2 + (\sigma_2 - \sigma_3)^2 + (\sigma_1 - \sigma_3)^2)}/2$ is the normal stress intensity factor [20];

$T_f = T_0 + (T_* - T_0)/(44 \cdot v_0)$ is the average heating-up temperature through the entire volume of the surface layer [17];

$T_* = T_0 \cdot (3 \cdot \sigma_T)^2 / ((3 \cdot \sigma_T)^2 - \sigma_c^2)$ is the heating-up temperature in the local volumes [17];

σ_T is the yield strength of the toggle material;

σ_c is the maximum compressive stress of the toggle;

$U(\sigma_0, T_f) = U(p_{T,0}) - \Delta U_T(T_f) - A_V(T_f)$ is the height of the symmetrical energy barrier [15, 17];

$U(p_{T,0})$ is the initial activation energy of the destruction in the structure with allowance for the thermal pressure at T_0 and $\sigma_c = 0$, determined using the methods described in works [15, 17];

$\Delta U_T(T_f) = 1.5 \cdot \alpha_0 \cdot K \cdot T_f$ is a change in the activation energy from the self-heating temperature in the local volumes from $T = 0^\circ\text{C}$ to $T = T_f^\circ\text{C}$ [11, 15];

$A_V = M_r^2 \cdot \phi_\sigma^2 \cdot \sigma_0^2 / (2 \cdot K)$ is the specific energy per unit volume change of a real crystal under conditions of equivalent static tension [15, 17];

$M_r^2 = (\sigma_T \cdot (65 + 0, 46 \cdot HV)) / \sigma_r^2$ is the coefficient of cyclic and static stress state equivalence [15, 17];

$\vec{U}(\sigma_i, T_f) = U(\sigma_0, T_f) - 0.5 \cdot A_f$ is the activation energy for defect nucleation (in the direction of σ_c) [15, 17];

$\overleftarrow{U}(\sigma_i, T_f) = U(\sigma_0, T_f) + 0.5 \cdot A_f$ is the $M_r^2 = (\sigma_T \cdot (65 + 0, 46 \cdot HV)) / \sigma_r^2$ activation energy for defect destruction (in the opposite direction σ_c) [15, 17];

$A_f = M_r^2 \cdot \phi_\sigma^2 \cdot \sigma_i^2 / (6 \cdot G)$ is the specific energy per unit volume forming of a real crystal under conditions of equivalent static tension [15, 17];

α_0 is the coefficient of linear thermal expansion of the toggle material;

K is the bulk modulus of material elasticity;

σ_r is the material fatigue limit;

$\varphi_\sigma = k_\sigma \cdot v_0^{0.5}$ is the coefficient of interatomic bonding overstress [15, 17];

v_0 is the coefficient of the uneven distribution of the internal energy density over the deformable volume [17];

k_σ is a complex structural parameter of the material [17].

The system of Eqs. (2)–(5) and dependencies for calculating the parameters included in them is a mathematical model for the formation process of design failures of the jaw crusher toggle.

The model proposed makes possible the analytical evaluation of the average lifetime of the jaw crusher toggle by the cyclic strength criterion with allowance for loading conditions, geometric parameters and physical and mechanical properties of the material as a function of temperature.

3 Verification of Theoretical Research Results and Their Practical Implementation

We use the PE 1200 × 1500 series jaw crusher to verify the developed mathematical model for failures under operating conditions at Orenburg Minerals JSC by comparing the calculated lifetime t with the assigned one $t_p = 180$ days according to the technological instruction. Figure 1 shows a general view of the PE 1200 × 1500 series jaw crusher (Fig. 1a) and its structural scheme (Fig. 1b).

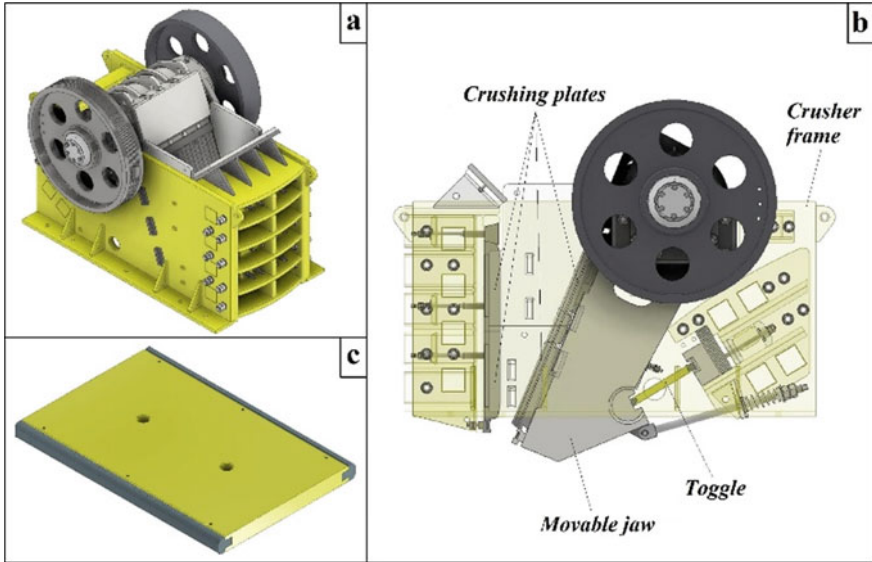


Fig. 1 General view of the PE 1200 × 1500 jaw crusher (a), a structural diagram of the crusher (b), a three-dimensional model of the toggle (c)

The average lifetime of the jaw crusher toggle can be determined by two methods: with the use of the failure model developed (2)–(5) and on the basis of SN-Curves [20–22]. The following conditions were taken into account while performing calculations:

- when calculating the power loading parameters for the toggle, we took chrysotile-asbestos with the tensile strength $\sigma_B = 290$ MPa as a crushed material;
- grey cast iron of SC-36–56 grade (EN-GJL-360) was accepted as the toggle material;
- the forces acting on the toggle were determined by the known method published in works [4, 5];
- the stress–strain state of the toggle was assessed using the Autodesk Inventor Nastran software for the finite element calculation. When determining the stresses arising in the material volume, this method allows one to take into account all possible design features of the toggle, a three-dimensional model of which is presented in Fig. 1c;
- we determined the critical number to the toggle destruction using the data on the SN-Curves in the Autodesk Inventor Nastran software.

Figures 2 and 3 show the assessment results of the toggle stress state (Fig. 2a, b) and its cyclic strength based on the SN-Curves of grey cast iron of SC-36–56 grade (EN-GJL-360) (Fig. 3a, b).

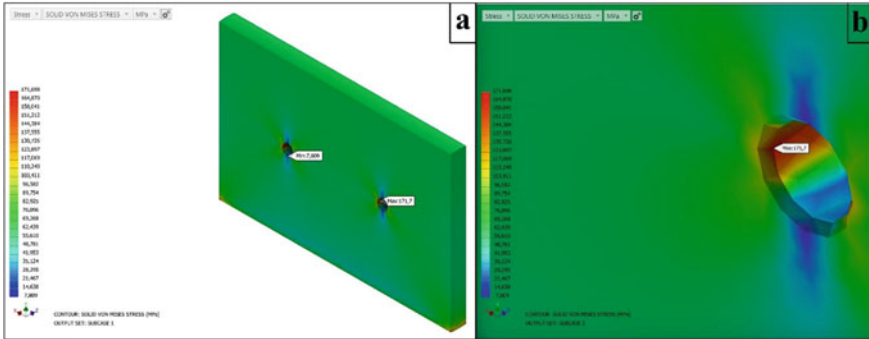


Fig. 2 Results of modelling the toggle stress state (a), the site of the maximum stress concentration (b)

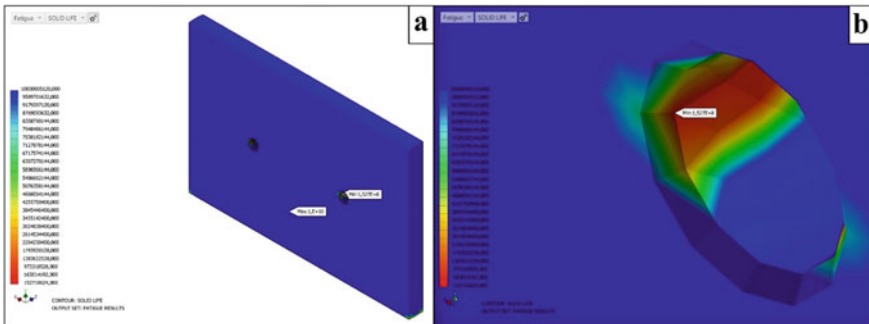


Fig. 3 Results of calculating the cyclic strength of the toggle (a), the site of fatigue crack nucleation in the toggle (b)

The generalised results of theoretical studies of the PE 1200 × 1500 jaw crusher toggle durability are presented in Table 1. Studies were conducted for three grades of grey cast iron used in the toggle manufacturing. The average toggle lifetime was estimated by the criterion of cyclic strength based on the SN-Curves (row 4 of Table 1) and by the criterion of kinetic strength with the use of the failure model developed (row 5 of Table 1).

The calculation of the average toggle lifetime with the use of the first method showed that it is possible to recommend the toggles made of SC-30 (EN-GJL-300) and SC-36–56 (EN-GJL-360) grades for operation under given conditions. The prediction error in the lifetime for these materials is in the range from 27 to 70%, respectively. However, according to the operating experience and recommendations of the crusher manufacturer, the use of SC-30 grade (EN-GJL-300) for the toggle manufacture under these operating

Table 1 Results of calculating the average lifetime of the toggle

The toggle material (Cast Iron grade)		SC-36-56 (EN-GJL-360)	SC-30 (EN-GJL-300)	SC -20 (EN-GJL-200)
Assigned toggle lifetime t_p , days		180		
Estimated number of cycles to failure (Inventor Nastran)		152,710,624	52,796,032	59,442
Average estimated lifetime t , days	By the criterion of cyclic strength based on the SN-Curve	583	245	0,23
	By the criterion of kinetic strength based on the failure model	218	93,7	7,77
Calculation Error δ_t , %	By the criterion of cyclic strength based on the SN-Curve	69,13	26,53	-
	By the criterion of kinetic strength based on the failure model	17,43	92,10	-

conditions is not recommended. Thus, we can conclude that, on the one hand, this method confirms the possibility of using cast iron of SC-36-56 grade (EN-GJL-360); on the other hand, it overstates the estimated toggle lifetime made of cast iron of SC-30 grade (EN-GJL-300). This can be explained by the fact that in order to obtain the most accurate data on the SN-Curves, a sufficiently large number of experimental studies are necessary, since the main physical and mechanical characteristics, such as compressive strength, have a wide range of possible values. The data on the SN-Curves of the materials in question are very limited in the literature; therefore, an analytical assessment of the average lifetime of the jaw crusher toggles by this method is impossible without the need for additional experimental studies.

The results of the analytical assessment of the average lifetime analysed by the second method (by the criterion of kinetic strength with the use of the failure model developed) showed that the prediction error for the toggle made of SC -36-56 (EN-GJL-360) cast iron is 17.43%. This, in turn, suggests that the second calculation method allows us to recommend the toggle made of SC-36-56 (EN-GJL-360) cast iron that fully confirms the operating experience and manufacturer's instructions. The theoretical average lifetime of toggles made of SC-30 (EN-GJL-300) and SC-20 (EN-GJL-200) grades of cast iron turned out to be much lower than the assigned one $t_p = 180$ days, so their operation is impractical.

In our opinion, the results obtained indicate an acceptable reliability and adequacy of the mathematical model developed for failures.

4 Conclusion

1. An analytical model is developed for complex swing jaw crusher failures by the criterion of kinetic strength of the toggle material based on the modern achievements in the reliability theory, physics and mechanics of machinery damage and destruction. The failure model takes into account the technological parameters of loading, geometric dimensions and physical and mechanical properties of the toggle material and does not require additional experimental studies.
2. The results of theoretical studies on the durability of the PE 1200 × 1500 jaw crusher toggle under the working conditions at Orenburg Minerals JSC showed that the manufacturing of toggles made of SC-36-56 (EN-GJL-360) cast iron is the most appropriate. The results obtained are fully confirmed by the operating experience of these crushers and the manufacturer's recommendations.
3. The failure model can be used for searching effective solutions to increase the durability of jaw crushers by changing the operating conditions, design and toggle material matching.

References

1. Gupta A, Yan D (2016) Mineral processing design and operations 2nd edn. Elsevier. <https://doi.org/10.1016/C2014-0-01236-1>
2. Johansson M, Bengtsson M, Evertsson M, Hulthén E (2017) A fundamental model of an industrial-scale jaw crusher. *Miner Eng* 105:69–78. <https://doi.org/10.1016/j.mineng.2017.01.012>
3. Olawale John O, Ibitoye Simeon A (2018) Failure analysis of a crusher jaw (Chapter 10), *Handbook of materials failure analysis*. Butterworth-Heinemann, pp 187–207. <https://doi.org/10.1016/B978-0-08-101928-3.00010-0>
4. Klushantsev BV, Kosarev AI, Muzeimneck VA (1990) The crushers. Construction, calculation, application features. Mashinostroenie, Moscow
5. Sharipov L (2016) Jaw crushers. Constructions and calculations. Tutorial. Voronezh State Technical University
6. Kuzbakov ZhI (2013) Determination of loads in the spacing plate of a jaw crusher taking into account the ramp loading. *Vestnik of Nosov Magnitogorsk State Technical University* 41(1):5–7
7. Pronikov A (2002) Parametric reliability of machines. Publishing House of Bauman Moscow State Technical University, Moscow
8. Antsupov A, Antsupov A, Antsupov V (2017) Analytical method for project resource estimation of metallurgical machinery parts. *News of Higher Educational Institutions. Ferrous metallurgy*, pp 62–66. <https://doi.org/10.17073/0368-0797-2017-1-30-35>
9. Regel V, Slutsker A, Tomashevsky E (1974) The kinetic nature of the strength of solids. The publishing house “Science”, Moscow
10. Fedorov V (1985) Kinetics of damaging and breakdown of solid bodies. Publishing center “Fan” UzSSR, Tashkent

11. Antsupov A Jr, Antsupov A, Antsupov V (2015) Theory and practice of assurance of machine element reliability according to criteria of material kinetic strength and wear resistance. Nosov Magnitogorsk State Technical University Publ, Magnitogorsk
12. Antsupov AV, Antsupov AV Jr, Antsupov VP (2013) Designed assessment of machine element reliability due to efficiency criteria. Vestnik of Nosov Magnitogorsk State Technical University 45(5):62–66
13. Zhurkov S (1957) The problem of the strength of solids. Bull Acad Sci 11:78–82
14. Zhurkov S, Nurzullaev B (1953) The time dependence of the strength under different loading conditions. ZhTF 10:1677–1689
15. Antsupov A, Antsupov V, Antsupov A (2016) Estimation and assurance of machine component design lifetime. Proc Eng 150:726–733. <https://doi.org/10.1016/j.proeng.2016.07.094>
16. Antsupov Alexey V, Antsupov Alexander V, Antsupov VP (2020) Development of analytical methodology for detail durability test while arranging metallurgical machines. Lecture Notes in Mechanical Engineering, pp 83–90. https://doi.org/10.1007/978-3-030-22041-9_10
17. Fedorov V (2014) Fundamentals of ergodynamics and synergetics of deformable bodies. Publishing house FGBOU VPO “KSTU”, Kaliningrad
18. Fedorov V (1979) Thermodynamic aspects of strength and fracture of solids. Publishing House “Fan” UzSSR, Tashkent
19. Fedorov S (2003) The basics of triboergodynamics and the physic chemical background of the compatibility theory. KSTU, Kaliningrad
20. Belyaev N (1976) Resistance of materials. “Science”, Moscow
21. Zhukova A, Sherman A (1968) Materials in mechanical engineering. Matching and application. V.4. Cast iron., Publishing house Engineering
22. Ruditsyn M, Artemov P, Lyuboshits M (1979) Reference guide on the strength of materials. Higher School Publishing House, Minsk



Development of a Necessity and Sufficiency Scheme for the Use of Different Types of Car Tire Radii in Different Car Modeling Tasks

E. V. Balakina^(✉) and I. V. Sergienko

Volgograd State Technical University, Lenin Avenue 28, Volgograd 400005, Russian Federation

Abstract. A car wheel equipped with an elastic tire and oriented in a certain way has a significant effect on such car properties as driving stability, handling, braking dynamics. Therefore, when modeling these properties, an elastic wheel is also modeled: its geometric dimensions, elastic and friction properties, and its deformation. In this case, the calculated parameters of the simulated phenomena are related to the type of wheel radius used for calculations. For example, the value of the wheel radius is used when calculating: the contact patch length, slip, moments about the axis of the wheel rotation, moments about the axis of the controlled wheel rotation, sliding in contact, etc. An elastic wheel loaded with a radial load does not have a uniform radius in the geometric sense due to a change in the shape of the circle. Approximate theoretical dependences are obtained for calculating the relative rolling radii of the wheel. The scheme of necessity and sufficiency for the use of wheel radii types in different tasks has been developed.

Keywords: Car tire · Types of radii · Relative radii · Calculation method · Application scheme

1 Introduction

A car wheel equipped with an elastic tire and oriented in a certain way has a significant effect on such car properties as driving stability, handling, braking dynamics [1–24]. Therefore, when modeling these properties, an elastic wheel is also modeled: its geometric dimensions, elastic and friction properties, and its deformation. In this case, the calculated parameters of the simulated phenomena are related to the type of wheel radius used for calculations. For example, the value of the wheel radius is used when calculating: the contact patch length, slip, moments about the axis of the wheel rotation, moments about the axis of the controlled wheel rotation, sliding in contact, etc. An elastic wheel loaded with a radial load does not have a uniform radius in the geometric sense due to a change in the shape of the circle. There are different radius types of the deformed elastic wheel: free R_0 , rolling R_r , static R_{st} , dynamic R_d [1, 4, 8, 9, 12, 15, 16, 18, 21].

The radii of an elastic wheel (tire) can have different values. At the same time, always $R_{st} < R_0$; $R_d \leq R_0$. Depending on the radial deformation of the tire, $R_d <> R_{st}$ $\wedge R_d = R_{st}$; $R_r \leq R_0$; $R_r > R_{st}$; $R_r \geq R_d$.

Not all types of wheel radii are equivalent when used for model calculations of the indicated phenomena and properties. In particular, a lot of controversy in the scientific community is caused by the use of types of radii when calculating: 1—the friction moment and 2—sliding in contact of the tire with a solid support surface.

From our point of view, task 1 was closed by the author of [10], who experimentally proved the legality of using only the rolling radius for calculating the friction moment. Task 2 remains open. Also, there are no recommendations on the use of types of wheel radii when calculating the contact patch length, even if there are formulas [22].

2 Purpose of Research

The purpose of the study is to develop a scheme of the necessity and sufficiency for the use of wheel radii types in different tasks.

To achieve the research purpose, it is required to solve the following tasks.

1. Obtain expressions for calculating the relative radii of the elastic wheel. Explore the relationship between the relative radii and the relative tire deformation.
2. Determine the influence of the types of radii on the shape of the calculated $\varphi_x - s_x$ -diagrams.
3. Develop a scheme of the necessity and sufficiency for the use of types of wheel radii in different tasks.

3 Research Method

To solve task 1, the authors obtained an approximate expression for calculating the rolling radius of a wheel:

$$R_r \approx R_0 \left[\left(1 - \frac{\arcsin(\sqrt{n(2-n)})}{\pi} \right) + \frac{\sqrt{n(2-n)}}{\pi} \right], \quad (1)$$

where n —relative radial deformation of the tire ($n = \frac{z}{R_0}$).

In this expression (1) at $n = 0$ (no radial tire deformation), $R_r = R_0$. At $n = \text{const}$, $R_r = \text{const}$.

As

$$R_d = R_0 - z = R_0 - n \cdot R_0 = R_0(1 - n), \quad (2)$$

then

$$\frac{R_r}{R_d} \approx \frac{1 - \frac{\arcsin(\sqrt{n(2-n)})}{\pi} + \frac{\sqrt{n(2-n)}}{\pi}}{1 - n}. \quad (3)$$

This equation has no explicit solution. Therefore, it was decided to use the MATLAB environment for these purposes. In the MATLAB environment, the following relations are obtained:

$$\frac{R_r}{R_0} \approx 1 - 0.075 \cdot n; \quad (4)$$

From formula (2) \Rightarrow

$$\frac{R_d}{R_0} = 1 - n. \tag{5}$$

Their joint solution made it possible to find the ratio

$$\frac{R_r}{R_d} \approx \frac{\frac{1}{n} - 0,075}{\frac{1}{n} - 1}. \tag{6}$$

Figure 1 shows the relative radii calculated using formulas (4) and (5): dynamic and rolling at different relative deformations of the tire, and Fig. 2 shows their ratio in accordance with the formula (6).

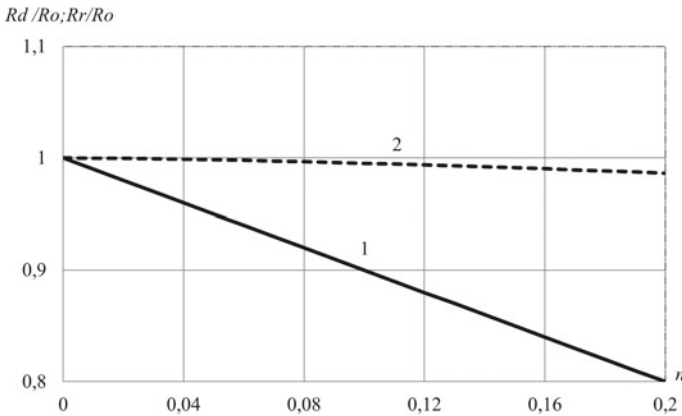


Fig. 1 Calculated relative radii: 1—dynamic and 2—rolling

Figure 1 shows that at working deformations of the tire and the rolling radius decreases by no more than 2%. Figure 2 shows that at working deformations of the tire, the rolling radius is greater than the dynamic one by 0...23%.

$\varphi_x - s_x$ —diagrams are constructed to solve task 2. $\varphi_x - s_x$ —diagram is the dependence of the friction coefficient φ_x of a car tire to the supporting surface on the longitudinal wheel sliding coefficient s_x . The type and numerical characteristics of these dependencies have a significant impact on the estimated parameters of stability, controllability, and braking dynamics of a car.

$$s_x = \frac{V_s}{\omega \cdot R_r}, \tag{7}$$

where V_s —longitudinal wheel sliding speed ($V_s \approx V_x - \omega \cdot R_r$); ω —wheel angular velocity; R_r —wheel rolling radius; V_x —longitudinal component of the translational speed of the wheel axis.

Range of change $s_x = 0 \dots 100\%$. In the denominator of formula (7) in practical calculations of the longitudinal wheel sliding in the braking mode, V_x is set to exclude division by zero when the wheel is blocked.

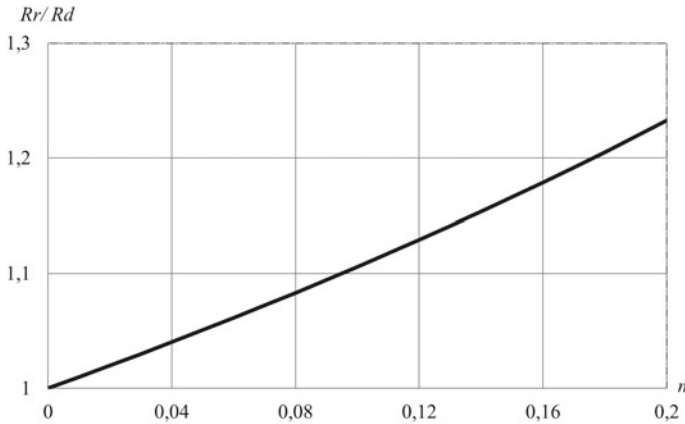


Fig. 2 Rolling radius to dynamic ratio

Many authors calculate the value s_x according to the indicated dependence (7), i.e., through the rolling radius, for example [2, 5, 6, 12, 14, 15, 19, 21, 23].

Some authors, due to the lack of data on the rolling radius, replace it with other values: free radius [7, 17, 24], etc., dynamic radius [8, 13], etc. Therefore, in this article, the authors analyzed the influence of the used radius type when calculating the longitudinal wheel sliding on the shape of the obtained $\varphi_x - s_x$ -diagrams.

A computational analysis of the influence of the radius type when calculating sliding s_x according to dependence (7) on the shape of the resulting $\varphi_x - s_x$ -diagrams was carried out, the results of which are shown in Fig. 3. For the calculation φ_x a well-known method was used [4, 17].

Based on the analysis, it was concluded that it is advisable to use the tire rolling radius (but not the dynamic one!) when calculating sliding s_x . When calculating $\varphi_x - s_x$ -diagrams, instead of the rolling radius value, we can use a free radius close to it. Of course, from the point of view of mechanics, it would be more correctly to use the rolling radius. But, since it differs from the free radius, even with the maximum permissible tire deformations, by no more than 2%, and this discrepancy does not have a visible effect on the calculated $\varphi_x - s_x$ -diagrams at different values of the lateral force that appeared before or after the start of wheel braking, then no the need to complicate the task by calculating the rolling radius at each moment of movement, since this increases the counting time, and the use of the free radius gives the same result. And, it is possible to approximately calculate the rolling radius with an accuracy sufficient for practical calculations using the above dependence (2).

The contact patch length is calculated from geometric considerations using the free radius and radial tire deformation, or, which is the same, free and dynamic radii [22].

To solve task 3, the authors have developed a scheme of the necessity and sufficiency for the use of wheel radii types in various tasks related to modeling the properties of active safety of cars. It is shown in Fig. 4. The properties of active safety of a car and the main phenomena that determine the parameters of these operational properties are listed. This is the sliding of the elastic wheel, large and small oscillations of the steered

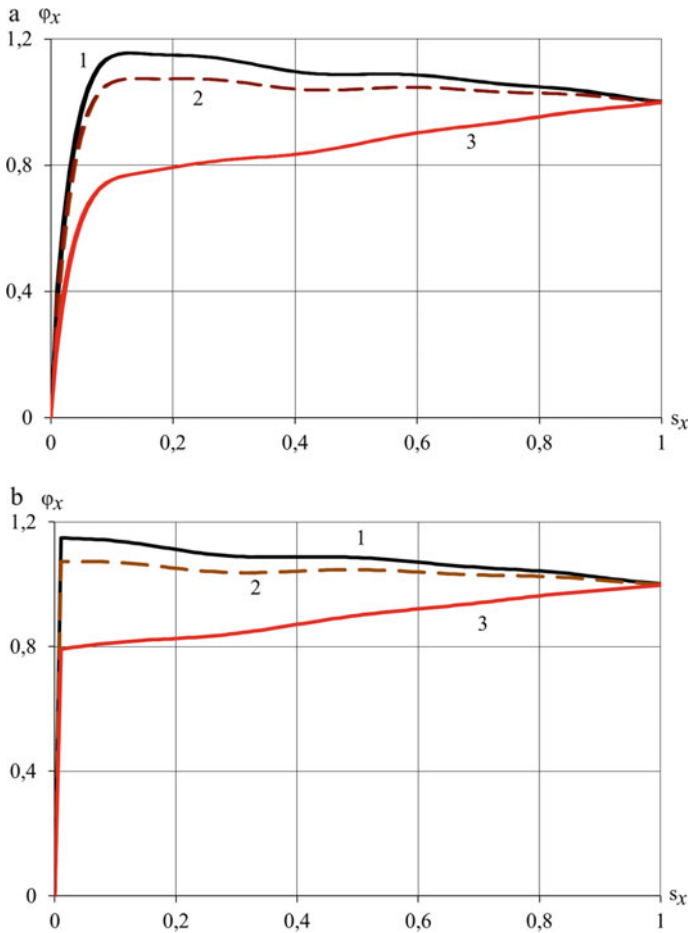


Fig. 3 Calculated $\varphi_x - s_x$ -diagrams for different values of the lateral force that appeared before the start of braking, obtained when calculating the value s_x : **a** free radius and rolling radius and **b** dynamic radius: 1— $\frac{P_y}{P_z} = 0$; 2— $\frac{P_y}{P_z} = 0.5$; 3— $\frac{P_y}{P_z} = 1$

wheels, longitudinal and lateral redistribution of loads on the wheels, longitudinal and lateral sliding in the contact patch. The intensity of these phenomena is associated with many parameters of the first and second levels, but this scheme of Fig. 4 shows not all, but only those of them that in one way or another depend on one of the wheel radii!

4 Conclusion

Expressions for calculating the relative radii of the elastic wheel are obtained. The relationship between the relative radii and the relative tire deformation has been investigated. Shown that:

- at working deformations of the tire, the rolling radius is reduced by no more than 2%;

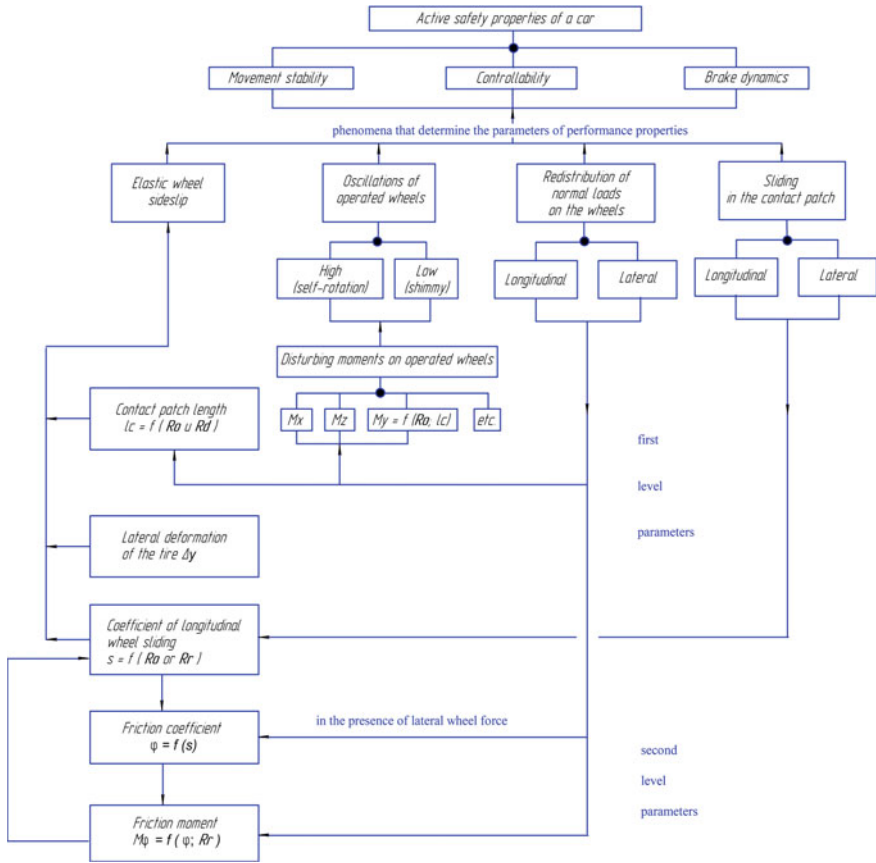


Fig. 4 Scheme of the necessity and sufficiency for the use of wheel radii types in various tasks

- at working deformations of the tire, the rolling radius is greater than the dynamic one by 0...23%.

It has been established that the rolling radius should be used when calculating the sliding in contact of the tire with a solid support surface. We can also use a free radius close to it. When calculating the friction moment, only the rolling radius. The length of the contact patch should be determined from geometric considerations using free and dynamic radii.

The scheme of necessity and sufficiency for the use of types of wheel radii in different tasks of a car modeling has been developed.

Acknowledgements. The reported study was funded by RFBR according to the research project № 20-31-90001.

References

1. Balabin IV et al (2012) Automobile and tractor wheels and tires. MGTU MAMI, Moscow, p 920
2. Balakina EV, Sergienko IV (2019) The use of different wheel radii in the problems of modeling the properties of active vehicle safety. *Automot Ind* 5:16–19
3. Balakina EV (2017) Calculation of the geometric position and the sizes of the static friction and sliding friction zones at the point of contact between an elastic wheel and a firm surface. *J Frict Wear* 38(2):144–149. <https://doi.org/10.3103/S1068366617020039>
4. Balakina EV (2019) Calculation of the friction coefficient between a steady elastic wheel and a solid support surface in the presence of a lateral force. *J Frict Wear* 40(6):573–579. <https://doi.org/10.3103/S1068366619060047>
5. Boiko AV, Fedotov AI (2016) Spatial mathematical model of the car braking process on a full-support roller stand. *Automot Ind* 3:8–15
6. Dik AB (2020) About the radius of the elastic wheel. *Automot Ind* 10:21–28
7. Zadornov VN et al (2020) Protector wear forecasting on elastic characteristics of tires. *J Frict Wear* 41(4):354–358. <https://doi.org/10.3103/S1068366620040145>
8. Kravec VN, Selifonov VV (2011) *Automobile theory: university textbook*. Greenlight, Moscow, p 884
9. Pozhidaev SP (2014) On the theory of rolling an elastic wheel from a position of mechanics. *Automotive industry* 11:16–17
10. Pozhidaev SP, Shkarovskij GV (2019) Experimental verification of the relationship of torque and total circumferential force of the elastic wheel. *Automot Ind* 9:8–13
11. Ryzhih LA et al (2019) Determination of the longitudinal realizable friction force of the automobile wheel with the supporting surface from the torsional deformation of the tire and its rigidity. *Automot Ind* 5:16–19
12. Tarasik VP (2006) *Automobile movement theory: university textbook*. BHV-Peterburg, ST. Peterburg, p 478
13. Turenko AN et al (2010) Methods for calculating the implemented friction coefficient when rolling the wheel in the brake mode. *Automob Trans* 27:7–12
14. Fedotov AI (2015) *Dynamic diagnostic method for pneumatic brake drive of automobiles: monograph*. IRNITU, Irkutsk, p 514
15. Balakina EV et al (2020) Advantages of using wheel rolling radius for calculating friction characteristics in wheel-to-road contact patch. *Lecture Notes in Mechanical Engineering*, Springer Nature Switzerland AG, Cham, Switzerland I:1015–1022
16. Balakina EV et al (2020) Analysis of various types of elastic wheel radii and establishing necessity and sufficiency of their application for various problem solving. *Lecture Notes in Mechanical Engineering*, Springer Nature Switzerland AG, Cham, Switzerland
17. Balakina EV (2018) Forms of diagrams of an automobile tire. *Proceedings of 9th International Scientific Conference “Balttrib’2017”*, Aleksandras Stulginskis University Akademija, Kaunas, Lithuania, 16–17 November 2017, pp 110–116
18. Jimenez E, Sandu C (2020) Experimental investigation of the tractive performance of pneumatic tires on Ice. *Tire Sci Technol* 48(1):22–45
19. Pacejka HB (2012) *Tire and vehicle dynamics*. Published by Elsevier Ltd., USA, p 672
20. Sarkisov P et al (2019) Physical understanding of transient generation of tire lateral force and aligning torque. *Tire Sci Technol* 47(4):308–333
21. Jazar RN (2008) *Vehicle dynamics: theory and application*. Springer Science + Business Media, LLC, p 1015
22. Balakina EV et al (2019) The calculation method of the length of contact of car tires with the road surface. In: *IOP conference series: materials science and engineering*, IOP Publishing, Irkutsk, Russia, vol 632, p 9. <https://doi.org/10.1088/1757-899X/632/1/012022>

23. Marco Viehweger et al (2020) Vehicle state and tyre force estimation: demonstrations and guidelines. *Vehicle System Dynamics*, p 1–28. <https://doi.org/10.1080/00423114.2020.1714672>
24. Zotov NM, Balakina EV (2007) Using the nomogram in calculating the dynamics of a braked wheel. *J Mach Manuf Reliab* 36(2):193–198



Assessment of the Influence of Inclined Wheel Installation on the Vehicle Lateral Stability

E. V. Balakina^(✉), M. S. Kochetov, and D. S. Sarbaev

Volgograd State Technical University, 28, Lenin Avenue, Volgograd 400005, Russia

Abstract. The properties of active vehicle safety include: stability, controllability, braking dynamics. They are influenced by many design parameters of the chassis: unsprung weight, wheel radii, steering geometry, stiffness and damping of suspensions, tires, steering gear, machine configuration, etc. To improve these properties, the listed parameters are optimized or their on-board regulation is carried out. The search for control parameters is one of the important tasks of ensuring vehicle trajectory stabilization. This study relates to the field of vehicles wheels installation, namely, to the issue of their inclination angles in the transverse vertical plane and the influence of this angle on the tire properties and the performance properties of the vehicle. A calculated assessment of the relationship between the inclined wheel setting and the vehicle stability in side sliding and side rollover is carried out. Approximate dependences are obtained to determine the influence of the wheel inclination angle on the indicated properties. Changing the vehicle stability when the wheels are inclined requires additional research.

Keywords: Car · Wheel incline · Outer incline · Inner incline · Stability assessment · Side sliding · Side rollover

1 Introduction

The incline of the vehicle wheel in a transverse vertical plane is called camber, and its values are small on modern vehicles. At the same time, a camber is considered to be a positive camber, in which the distance between the upper parts of the wheels of the same axle is greater than between the lower ones. This is how the front controlled wheels are installed to reduce the rolling arm (in order to reduce the horizontal angular oscillations of the controlled wheels) and to promote vehicle understeer, with positive camber values from 0 to $+2^\circ$. A negative (inner) camber is currently considered camber, in which the distance between the upper parts of the wheels of the same axle is less than between the lower ones. This is how the rear wheels are sometimes installed to slightly improve the estimated controllability parameters, with negative camber values from 0 to 2.5° .

When the left and right wheels of the same axle are inclined, they incline in opposite directions in any case, so it is illogical to call camber, which refers to two wheels of the same axle (left and right), positive or negative. Therefore, it is proposed to clarify the terminology associated with wheel incline and to apply the terms “outer incline” and “inner incline” as shown in Table 1.

Table 1 Suggested terminology for inclined wheel

Term	Definition
Wheel incline	Non-perpendicularity of the wheel rotation plane of the supporting plane
Design wheel incline	Wheel inclination embedded in the vehicle design
Operational wheel incline	Additional wheel incline that occurs during vehicle operation: <ul style="list-style-type: none"> • when the sprung wheel moves along the unevenness of the supporting surface; • when the sprung body rolls from lateral force; • when the controlled wheel is turned around an axis inclined in the transverse vertical plane; • with forced on-board automatic wheel incline control
Wheel incline angle	The angle between the rotation plane and the longitudinal plane of the wheel
Design wheel incline angle	Wheel inclination angle provided by the design documentation
Wheel operating angle	Additional wheel inclination angle that appears during vehicle operation
Outer inclination of the wheels of the vehicle axle	The inclination of the wheels, in which the axes of their rotation intersect above the vehicle axis, within the vehicle's track
Inner inclination of the wheels of the vehicle axle	The inclination of the wheels, in which the axes of their rotation intersect below the vehicle axis, within the vehicle track
Multidirectional inclination of the wheels of the vehicle axle	The inclination of the wheels in which the axes of their rotation intersect above or below the vehicle axis, outside the vehicle's track, or do not intersect
Single inclination of the wheels of the vehicle axle	Inclination of one wheel of the vehicle axle
Wheel toe-in	Non-perpendicularity of the wheel rotation plane of the transverse plane, embedded in the vehicle design
Wheel toe-in angle	The angle between the wheel rotation plane and the longitudinal vehicle plane, provided in the design documentation

(continued)

Table 1 (continued)

Term	Definition
Outer toe-in of the wheels of the vehicle axle	Toe-in of the wheels, in which their central longitudinal axes intersect behind the vehicle axis, within the vehicle's track
Inner toe-in of the wheels of the vehicle axle	Toe-in of the wheels, in which their central longitudinal axes intersect in front of the vehicle axis, within the vehicle's track
Multidirectional toe-in of the wheels of the vehicle axle	Toe-in of the wheels, in which their central longitudinal axes intersect in front or behind the vehicle axle, outside the vehicle's track, or do not intersect
Single toe-in of wheels of the vehicle axle	Toe-in of one wheel of the vehicle axle

It is known that wheel inclination up to 3° has no visible effect on fuel consumption and tire wear, but affects driving stability and controllability, which creates the prerequisites for its use as a control parameter in movement control systems. However, the question arises of the invariability of this angle when the vehicle is moving.

During the vehicle movement, its wheels can incline at an angle that is additional in relation to the constructive one. The reasons are:

- the presence of a given suspension kinematics to ensure the direction of impacts on elastic and damping elements;
- the presence of a lateral incline angle of the rotation axis of the controlled wheel to ensure its weight stabilization and to reduce the running arm.

The total wheel inclination angle is defined as

$$\alpha = \alpha_0 \pm \alpha_s \pm \alpha_\Theta, \quad (1)$$

where α_0 —design wheel incline angle; α_s —the angles of the operating wheel inclination that appear when the sprung wheel moves along the unevenness of the supporting surface and when the sprung body rolls from the action of lateral force; α_Θ —the angle of the operational wheel inclination that appears when the controlled wheel is turned.

There are numerous studies of tire properties [1–26], including those related to wheel inclination.

Previously, Kozlov Yu.N. and Balakina E.V. performed experimental studies of the angle's values of the operational wheel inclination α_s . The experiments were carried out on the auto-polygon [9]. The object of research was a front-wheel drive passenger car with independent rear suspension. It was found that when driving on a road with asphalt concrete pavement, both the front and rear wheels of a passenger car, when moving over irregularities, incline by an angle less than 30 times the angle α_0 (3°) of the design inclination of the wheels. Calculations of the component α_Θ of the operational incline angle of the wheel during its rotation are carried out. It is up to 3 times less than

the design inclination of the wheels α_0 . This makes it expedient to solve the problem of optimizing the inclination angle of the rear wheels to improve the characteristics of vehicles controllability.

2 Purpose of Research

The purpose of the study is to determine the influence of the wheel inclination angle on the vehicle stability in side sliding and side rollover.

3 Research Method

The calculated assessment of the influence of the inclined wheel installation on the vehicle stability in transverse sliding is carried out.

Lateral sliding start condition

$$P_y = R_y, \quad (2)$$

where R_y —lateral reaction of the supporting surface.

$$R_y = P_z \cdot \cos^2 \alpha \cdot f_{sl} + P_z \cdot \cos \alpha \cdot \sin \alpha, \quad (3)$$

where f_{sl} —sliding friction coefficient.

The ratio of the lateral force to the normal load at which the vehicle side sliding of the vehicle with the wheels inclined at an angle α begins is defined as

$$\left(P_y/P_z \right)_{sl\alpha \neq 0} = \cos \alpha \cdot (\cos \alpha \cdot f_{sl} + \sin \alpha). \quad (4)$$

At $\alpha = 0$ side sliding starts at

$$\left(P_y/P_z \right)_{sl\alpha=0} \approx f_{sl}. \quad (5)$$

Let us denote by $K_{\alpha sl}$ the specific ratio of the lateral force to the normal load according to the criterion of the beginning of the side sliding of the vehicle with inclined wheels

$$K_{\alpha sl} = \frac{\left(P_y/P_z \right)_{sl\alpha \neq 0}}{\left(P_y/P_z \right)_{sl\alpha=0}}. \quad (6)$$

Then,

$$K_{\alpha sl} = \cos \alpha \cdot \left(\cos \alpha + \frac{\sin \alpha}{f_{sl}} \right). \quad (7)$$

The results of calculating the coefficient $K_{\alpha sl}$ are shown in Fig. 1.

It follows from the figure that with the inner inclination of the wheels, and the passenger car becomes more resistant to transverse (side) sliding. At $\alpha = 5^\circ$, it becomes more resistant to transverse sliding by about 10%. In this case, the value of the sliding

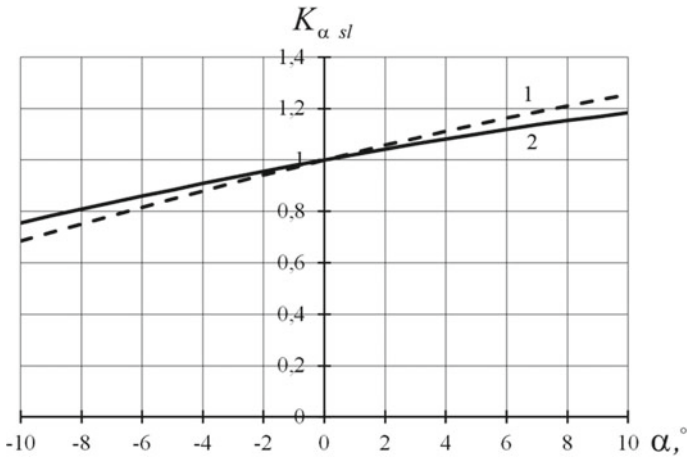


Fig. 1 The results of calculating the coefficient $K_{\alpha sl}$: 1— $f_{sl} = 0,8$; 2— $f_{sl} = 0,6$

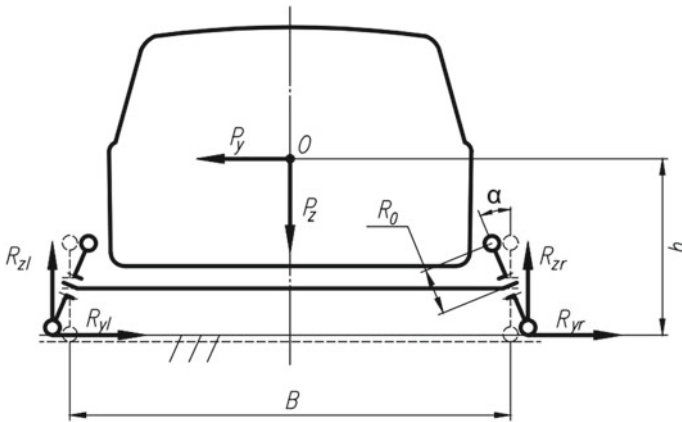


Fig. 2 The calculated scheme for assessment the tendency of the vehicle with inclined wheels to side rollover

friction coefficient affects the propensity of a passenger car with inclined wheels to side sliding by no more than 5%.

A calculated assessment of the influence of inclined wheel installation on the vehicle stability in side rollover is carried out. Figure 2 shows the calculated scheme.

The calculated assessment is approximate, since it does not take into account the suspension kinematics, i.e., the location of the roll axis.

$$R_{zr} \cdot (B + 2R_0 \cdot \sin \alpha) + P_y \cdot (h - \Delta h_\alpha) - P_z \cdot \left(\frac{B}{2} + R_0 \cdot \sin \alpha \right) = 0; \quad (8)$$

$$\Delta h_\alpha = R_0 \cdot (1 - \cos \alpha). \quad (9)$$

where B —track of the vehicle with wheels whose rotation planes are perpendicular to the reference one; h —center mass height; Δh_α —change in the center of mass height when the wheels are inclined; R_0 —free wheel radius; P_z —normal load; P_y —lateral force; R_{zr} —normal reaction to the right wheel.

When the wheel loses contact with the supporting surface ($R_{zr} = 0$).

Then,

$$P_y \cdot (h - \Delta h_\alpha) = P_z \cdot \left(\frac{B}{2} + R_0 \cdot \sin \alpha \right). \quad (10)$$

The ratio, of the lateral force to the normal load, at which the side rollover of the vehicle with the wheels inclined at an angle α begins, is defined as:

$$(P_y/P_z)_{\text{til}\alpha \neq 0} = \frac{\frac{B}{2} + R_0 \cdot \sin \alpha}{h - R_0 \cdot (1 - \cos \alpha)}. \quad (11)$$

At $\alpha = 0$ side rollover begins (without taking into account the design features of the suspension)

$$(P_y/P_z)_{\text{til}\alpha=0} \approx \frac{B}{2h}. \quad (12)$$

That is, the wider the vehicle, the more stable it is. The lower the vehicle's center of mass, the more stable it is.

Let us denote by $K_{\alpha\text{til}}$ the specific ratio of the lateral force to the normal load according to the beginning criterion of the side rollover of the vehicle with inclined wheels

$$K_{\alpha\text{til}} = \frac{(P_y/P_z)_{\text{til}\alpha \neq 0}}{(P_y/P_z)_{\text{til}\alpha=0}}. \quad (13)$$

After algebraic transformations, the final expression is obtained

$$K_{\alpha\text{til}} = \frac{1 + (2R_0/B) \cdot \sin \alpha}{1 - (R_0/h) \cdot (1 - \cos \alpha)}. \quad (14)$$

The obtained expressions take into account the change in the center of mass height when the wheels are inclined Δh_α , but the change in the height of the center of mass during roll, associated with the suspension kinematics Δh_N (location of the roll center), is not taken into account. This value should be calculated in dynamics. At maximum suspension deformation during roll $\Delta h_N = 0$.

The results of calculating the coefficient $K_{\alpha\text{til}}$ are shown in Fig. 3 for different wheel inclination angles α .

It follows from the figure that with an inner inclination of the wheels, and a passenger car becomes more resistant to side (sliding) rollover. At $\alpha = 5^\circ$, it becomes more resistant to side rollover by approximately 3...3.5%. This process is practically not influenced by the existing values of the ratio R_0/h . The ratio R_0/B affects the propensity of the vehicle with inclined wheels to side rollover no more than 1% at $\alpha = 5^\circ$. It can be assumed that the free wheel radius has practically no effect on the propensity of the vehicle with inclined wheels to side rollover.

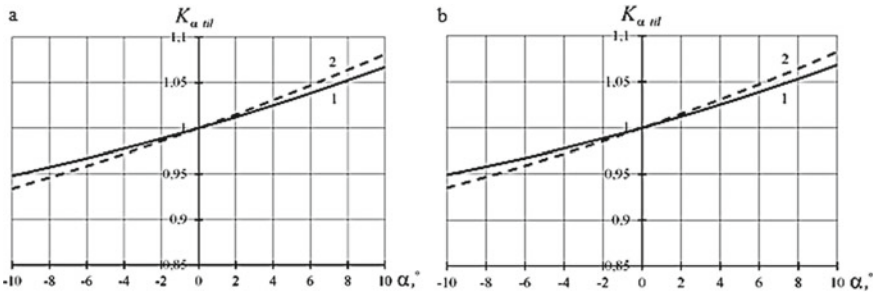


Fig. 3 The results of calculating the coefficient $K_{\alpha \text{til}}$: **a**— $R_0/h = 0.5$; **b**— $R_0/h = 0.58$; 1— $R_0/B = 0.17$; 2— $R_0/B = 0.21$

4 Conclusion

1. The inclination of the vehicle wheels up to 3° does not have a visible effect on fuel consumption and tire wear, but affects the driving stability and controllability. This creates the prerequisites for its use as a control parameter in movement control systems. However, the question arises of the invariability of this angle when the vehicle is moving.
2. It has been established that when driving on a road with asphalt concrete, and the wheels of a passenger car when crossing irregularities are inclined at an angle that is less than 30 times the angle of the design inclination of the wheels. It was found that when turning the controlled wheels, and they incline at an angle less than 3 times the angle of the design inclination of the wheels. This makes it expedient to solve the problem of optimizing the inclination angles of the rear wheels to improve the characteristics of vehicles controllability.
3. When the wheels are inner inclined, a passenger car becomes more resistant to transverse (side) sliding. At an inclination angle of 5° , it becomes more resistant to transverse sliding by about 10%. In this case, the value of the sliding friction coefficient affects the tendency of a passenger car with inclined wheels to transverse sliding by no more than 5%.
4. When the wheels are inner inclined, the passenger car becomes more resistant to transverse (side) rollover. At an inclination angle of 5° , it becomes more resistant to transverse rollover by approximately 3...3.5%. This process is practically not affected by the ratio of the free radius to the center of mass height. The ratio of the free radius to the track affects the tendency of a vehicle with inclined wheels to transverse rollover by no more than 1%. It can be assumed that the free wheel radius has practically no effect on the tendency of the vehicle with inclined wheels to transverse rollover.

Acknowledgements. The reported study was funded by RFBR according to the research project № 19-08-00011.

References

1. Dik AB (2020) About the radius of the elastic wheel. *Automot Ind* 10:21–28
2. Fedotov AI (2015) Dynamic diagnostic method for pneumatic brake drive of automobiles: monograph. IRNITU, Irkutsk, p 514
3. Turenko AN et al (2010) Methods for calculating the implemented friction coefficient when rolling the wheel in the brake mode. *Automobile Trans* 27:7–12
4. Boiko AV, Fedotov AI (2016) Spatial mathematical model of the car braking process on a full-support roller stand. *Automot Ind* 3:8–15
5. Balakina EV (2017) Calculation of the geometric position and the sizes of the static friction and sliding friction zones at the point of contact between an elastic wheel and a firm surface. *J Friction Wear* 38(2):144–149. <https://doi.org/10.3103/S1068366617020039>
6. Balakina EV (2018) Forms of fx-sx-diagrams of an automobile tire. Proceedings of 9th International Scientific Conference “Balttrib’2017”, Aleksandras Stulginskis University Akademija, Kaunas, Lithuania, 16–17 November 2017, p 110–116
7. Balakina EV (2019) Calculation of the friction coefficient between a steady elastic wheel and a solid support surface in the presence of a lateral force. *J Frict Wear* 40(6):573–579. <https://doi.org/10.3103/S1068366619060047>
8. Balakina EV, Sergienko IV (2019) The use of different wheel radii in the problems of modeling the properties of active vehicle safety. *Automot Ind* 5:16–19
9. Balakina EV et al (2016) Changing the angles of design inclination of the wheel when driving a passenger car. *Automot Ind* 12:16–19
10. Balakina EV et al (2019) The calculation method of the length of contact of car tires with the road surface. In: IOP conference series: materials science and engineering, IOP Publishing, Irkutsk, Russia, vol 632, p 9. <https://doi.org/10.1088/1757-899X/632/1/012022>
11. Balakina EV et al (2020) Advantages of using wheel rolling radius for calculating friction characteristics in wheel-to-road contact patch. Lecture notes in mechanical engineering, Springer Nature Switzerland AG, Cham, Switzerland, vol I, pp 1015–1022
12. Balakina EV et al (2020) Analysis of various types of elastic wheel radii and establishing necessity and sufficiency of their application for various problem solving. Lecture Notes in Mechanical Engineering, Springer Nature Switzerland AG, Cham, Switzerland
13. Jimenez E, Sandu C (2020) Experimental Investigation of the Tractive Performance of Pneumatic Tires on Ice. *Tire Science and Technology* 48(1):22–45
14. Balabin IV (2016) Angles of controlled wheels installation and their quantitative influence on resistance to vehicle movement. *Automot Ind* 9:21–24
15. Balabin IV (2020) Improving the stability of a mobile machine by using negative camber. *Automot Ind* 7:8–9
16. Ryzhih LA et al (2019) Determination of the longitudinal realizable friction force of the automobile wheel with the supporting surface from the torsional deformation of the tire and its rigidity. *Automot Ind* 5:16–19
17. Viehweger M et al (2020) Vehicle state and tyre force estimation: demonstrations and guidelines. *Veh Syst Dynam* 1–28. <https://doi.org/10.1080/00423114.2020.1714672>
18. Zotov NM, Balakina EV (2007) Using the nomogram in calculating the dynamics of a braked wheel. *J Mach Manuf Reliab* 36(2):193–198
19. Pacejka HB (2012) *Tire and Vehicle Dynamics*. Published by Elsevier Ltd., USA, p 672
20. Sarkisov P et al (2019) Physical understanding of transient generation of tire lateral force and aligning torque. *Tire Sci Technol* 47(4):308–333
21. Reza N Jazar (2008) *Vehicle dynamics: theory and application*. Springer Science + Business Media, LLC, p 1015

22. Pozhidaev SP (2014) On the theory of rolling an elastic wheel from a position of mechanics. *Automot Ind* 11:16–17
23. Pozhidaev SP, Shkarovskij GV (2019) Experimental verification of the relationship of torque and total circumferential force of the elastic wheel. *Automot Ind* 9:8–13
24. Kravec VN, Selifonov VV (2011) *Automobile theory: university textbook*. Greenlight, Moscow, p 884
25. Zadvornov VN et al (2020) Protector wear forecasting on elastic characteristics of tires. *J Friction Wear* 41(4):354–358. <https://doi.org/10.3103/S1068366620040145>
26. Tarasik VP (2006) *Automobile movement theory: university textbook*. BHV-Peterburg, ST. Peterburg, p 478



Improvement of Computer Methods of Designing Gears with High Load Capacity

K. Syzrantseva^(✉) and V. Syzrantsev

Tyumen Industrial University, 38, Volodarskogo street, Tyumen 625000, Russia

Abstract. The article deals with a new variational approach to the development of algorithms and programs for designing cylindrical gears, which starts with optimization synthesis of lines of action. The developed synthesis methodology allows to avoid teeth undercutting during cutting, as well as to design gears with increased load capacity. The paper describes processing the results of computer modeling of the teeth stress–strain condition to obtain a two-parameter basic formula for calculating maximum tensile stresses in the root of involute teeth (depending on the place of force application and the tool shifting coefficient). The solution of this problem is required for further optimization synthesis of the root fillet curves on the teeth, which allows providing maximum bending endurance of the teeth at the gear design stage. A comparative assessment of tensile stresses in the root of the tooth for the involute and proposed full-strength tooth profile performed by means of the finite element analysis in the ANSYS software package has been presented.

Keywords: Cylindrical gears · Variational approach · Full-strength tooth profile · Optimization synthesis · Load capacity · Stress–strain condition · Bending endurance

1 Introduction

Gears are used in metal-cutting machines, automobiles, tractors, lifting and transporting equipment, marine installations, helicopters, drilling equipment, and other machines. They operate at surface velocity of up to 275 m/s, capacity of up to 65,000 kW, and gear ratios of up to several thousands.

To provide quality and reliability of the gears, it is necessary to develop methods of cutting tooth gears, characterized as highly accurate in manufacturing, having good strength features during operation and high manufacturing performance [1].

This article is dedicated to the research aimed at improving computer methods of designing high-load-capacity gears [2–4]. The work is carried out in coordination and close cooperation with ASKON, one of the leading companies in the scope of development and maintenance of computer design software, which has developed and supports KOMPAS, a well-known CAD system.

The currently used methods and algorithms of gears synthesis used in cutting tooth gears by means of modern NC machines have a number of disadvantages. The fact is

that the classical methods of conjugate mesh formation are focused on finding conjugate surfaces in gears and in machine gearing [1, 5–7]. In [5, 8] eight classical methods of forming conjugate meshes have been presented, where teeth surfaces are formed by using the form-generating method and the very gears synthesis is started with a choice of a generating element. In such cases, the issues of location, shape, and size of the teeth instantaneous contact areas, i.e., the parameters having a decisive impact on the performance of manufactured gears, are not touched upon.

An alternative option is to develop a synthesis method as a variational problem. The variational approach was apparently first used by Lebek [9] when searching for tooth profiles, and later on this approach started developing in the Ukraine [10, 11] and in the Tyumen Industrial University [12–14] with the assistance of [15] the Institute for Machine Tools University of Stuttgart (Germany). The peculiarity of the synthesis methodology using the proposed approach is that first, we aim at synthesizing an optimal line of action, and then at finding conjugate profiles (Fig. 1). This can significantly reduce the time spent on the synthesis by simplifying algorithms and programs of the very synthesis. Besides, the new synthesis method allows avoiding the problems of teeth undercutting. During undercutting on the profile formed by the classical form-generating method, a return point (singularity) appears, as a rule, followed by a section formed inside the body of the producing element [6]. Using the proposed method, the shape of the line of action can be set such that there will be no undercutting on the teeth profiles. And this can be reliably stated even before the conjugate tooth profiles contacting on this line of action are found. This is a strong argument for feasibility of starting synthesis of gear tooth actions in a plane with the synthesis of lines of action rather than with the synthesis of any conjugate profiles.

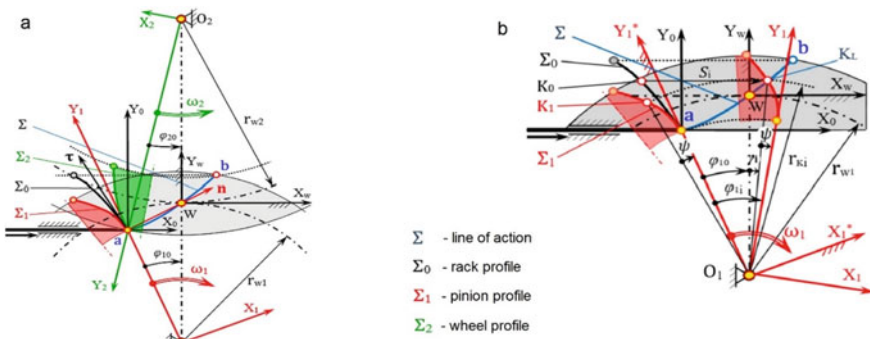


Fig. 1 Generating of teeth profiles for pinion and wheel: **a** coordinate systems of machine and working meshing; **b** generating of pinion profile Σ_1 at obtained rack profile Σ_0

The basis of the proposed concept and methodology of the synthesis of gears (with teeth point contact) includes [12, 14]:

1. setting the shape, location, and dimension ratio of the teeth contact instantaneous area (areas) in the design point (points) and setting the required change law of these area (areas) parameters along the line (lines) of action;

2. synthesizing the lines of action and teeth surfaces which provide the target parameters of the contact instantaneous areas;
3. calculation and estimation of the quality indicators of the designed gear and its optimization by the group of indicators.

2 Task Definition

To optimize the gear synthesis, it is necessary to vary a number of parameters of the instantaneous contact area (from four to seven) [16], and for each set of parameters to build relationships and diagrams of quality indicators. If each of the four main parameters has 4–5 values, the total number of diagrams for one quality indicator will be $4^4 \dots 5^4 = 256 \dots 625$ which is quite a lot. Therefore, it is necessary to plan computer experiments and perform calculation results processing with provision of approximation results in the form of formulas and graphs.

The aim of this work is recovery of the tensile stress function in the root of the tooth depending on the geometric parameters of the tooth profile and the place of force application. The function is required in order to take into account the teeth bending strength criterion [17, 18] at the stage of gear optimization synthesis using the proposed variational approach.

To achieve this goal the following tasks have been solved:

1. to perform computer modeling by the method of spur gear set involute tooth finite element, varying the place of force application as well as the profile shape corresponding to a tool shifting during tooth cutting;
2. to obtain a family of one-parameter functional relationships of maximum tensile stresses in the root of the teeth and the tool shift coefficient value and the number of the load application point, as well as to evaluate the accuracy of the one-parameter stress approximation;
3. to obtain a two-parameter functional relationship of the maximum tensile stresses in the root of the teeth and the place of load application and the tool shift value, as well as to estimate the accuracy of the one-parameter and two-parameter approximations;
4. to illustrate the increased bending strength of the full-strength tooth profile in comparison with the involute one it is necessary to perform a computer engineering analysis of the both teeth 3D models by means of the ANSYS software.

3 Computer Simulation

The main criterion of the gear efficiency is strength estimated by contact and bending stresses. In this case, the loss of bending strength leading to a tooth fracture causes much more significant problems during the gear operation [2, 4, 18], as it causes failures of not only the gear itself, but also of other elements of the gear drive (shafts and bearings).

The most modern and accurate method of stress studies in parts of complex geometry is currently the finite element method, implemented in a number of industrial, quite powerful, and software packages.

Task 1. Computer modeling of teeth 2D models by the finite element method performed in the APM system jointly with Golovanyov [19]. A fragment of the results of this computer experiment is shown in Fig. 2 for the profile with the tool shift value equal to zero and load application to the top of the tooth.

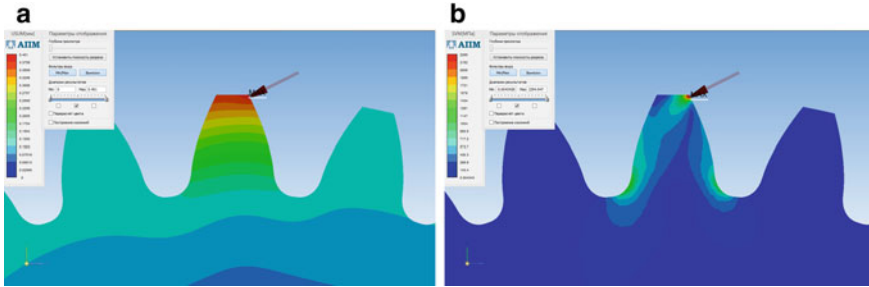


Fig. 2 Results of the finite element analysis (**a**—total displacement, **b**—equivalent stresses by Mises)

The pattern of total shifts distribution illustrates tooth compliance which decreases with descending the force application point to the root of the tooth. In the picture of equivalent stress distribution, two zones of stress concentration in the root of the tooth are clearly visible: on the left (on the compressed side) and on the right (on the stretched side). As it is known, equivalent stresses σ_{eq} (in this case, according to the fourth strength theory stresses are equivalent by Mises) are the resultant for all types of deformation. But in the model under study, tensile stresses σ_1 are the most important for assessing gear reliability because they are responsible for an occurrence and development of fatigue cracks [18, 20]. Despite the fact that compression stresses take higher values, they are not dangerous for the gear drive operation. For an analysis of a 2D problem, they are the most informative, so it is customary to use σ_1 as a criterion.

Task 2. Obtaining a family of one-parameter functional relationships to calculate maximum tensile stresses in the root of the teeth. To obtain the functional relationships of stresses, it is most rational to use polynomial regression in terms of further processing the results. We perform this task in the Mathcad mathematical processor.

As recommended in work [21], a minor polynomial degree should be selected to avoid oscillation of the polynomial function. It is revealed that in our task with the polynomial degree equal to two, the required approximation accuracy is not achieved. The third and fourth degrees of polynomials give similar in accuracy results, so the approximations stopped at the third degree.

Task 3. Obtaining a two-parameter functional relationship (basic formula) to calculate the maximum tensile stresses in the root of the teeth.

To obtain a two-parameter functional relationship, it is necessary to have coefficients that take into account the second parameter variation: the shift coefficient. The polynomials coefficients obtained during the second task solution are reduced to separate matrices, and then, a polynomial regression of the final cubic polynomial coefficients is performed.

Then, the basic formula for tensile stresses function approximation can be written:

$$\text{Stress}(x, y) = F_A(x) \cdot y^3 + F_B(x) \cdot y^2 + F_C(x) \cdot y + F_D(x) \tag{1}$$

where functions:

$$\begin{aligned} F_A(x) &= 0.242127x^3 - 0.074454x^2 - 0.005236x + 0.063353; \\ F_B(x) &= -6.64295x^3 + 0.712885x^2 + 1.357548x - 0.377994; \\ F_C(x) &= 27.687417x^3 + 31.557322x^2 - 19.539916x - 36.17424; \\ F_D(x) &= 215.0387x^3 - 203.091x^2 - 258.37037x + 1002.0103. \end{aligned}$$

The 3D image and basic formula values contours are shown in Fig. 3a and b, respectively.

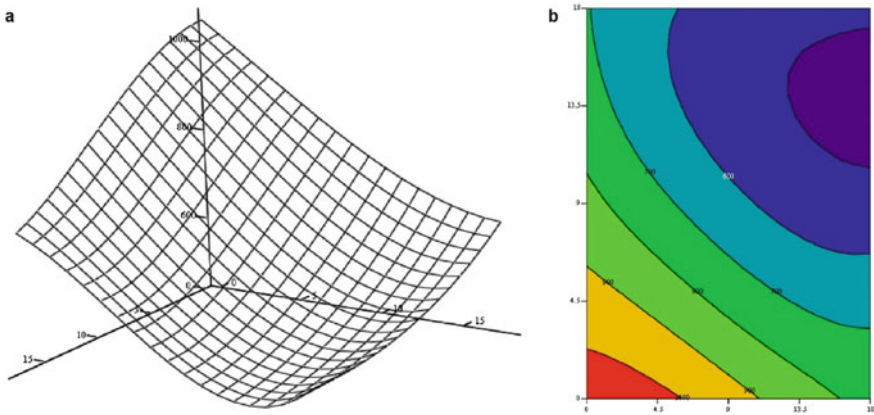


Fig. 3 3D image of the two-parameter function (1) of maximum tensile stresses in the root of the tooth

One of the indicators assessing the quality of a built model in statistics is determination coefficient R^2 , which is also called the value of approximation reliability [21]. It can be used to determine a level of accuracy of a model. It is calculated by the formula:

$$R^2 = 1 - SS_{\text{res}}/SS_{\text{tot}}. \tag{2}$$

As the table shows, the obtained relationships provide a very good approximation for the data of the computer experiment: the determination coefficients for all the relationships take values of more than 99%.

For example, in Fig. 4, the agreement of the basic formula with the source experimental data for two values of shifting coefficient is illustrated. Symbols “+” show the computer experiment data; thin lines are the implemented one-parameter function; thick green lines are the two-parameter function cross section with a fixed corresponding shifting coefficient (i.e., the values calculated by the obtained basic formula (1)).

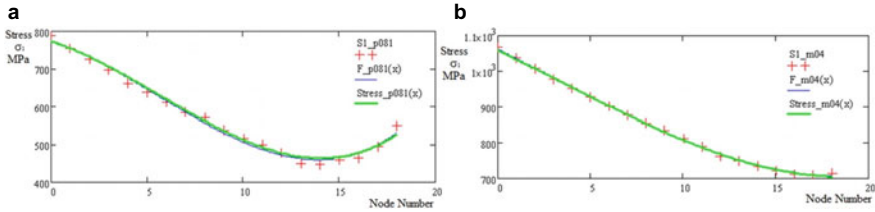


Fig. 4 1D approximation and 2D approximation cross section (1) of experimental data with the shifting coefficients of -0.4 (a) and $+0.81$ (b)

Task 4. We illustrate the results of the full-strength gears synthesis on the example of comparative evaluation of bending endurance of the teeth with involute and full-strength profiles.

Since a three-dimensional model is to be analyzed, the most powerful finite element package ANSYS has been chosen by the authors as a tool to evaluate additionally edge effects [3, 4, 22]. The geometry is built bottom-up; the SOLID186 quadratic element has been selected for discretization. The root of the tooth is tightly constrained; an evenly distributed force is applied to the upper edge of the tooth addendum. Figure 5 shows the results of calculation of total shifts in involute (Fig. 5a) and full-strength (Fig. 5b) teeth in a single scale. The maximum values are 0.0095 mm for the involute tooth and 0.0074 mm for the full-strength tooth. The deformed shape is 500 times exaggerated for clarity.

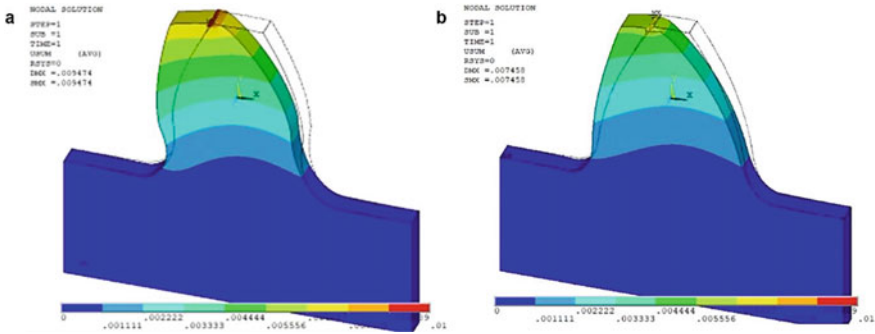


Fig. 5 Total displacements of involute tooth (a) and full-strength tooth (b)

The patterns of distribution of equivalent stresses by Mises are shown in Fig. 6 also in a single scale. The maximum values of tensile stresses σ_1 : in the involute tooth is 62.44 MPa and in the full-strength tooth is 46.67 MPa which proves a higher bending endurance of the teeth with the full-strength profile.

4 Conclusions

- The variational approach to solving the problem of gear synthesis allowed to develop scientific bases, as well as algorithms and programs for designing cylindrical gears

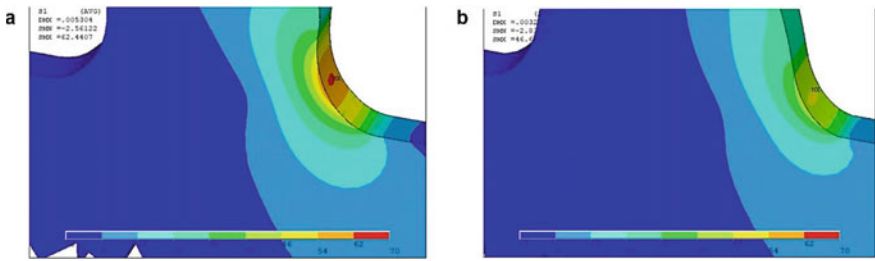


Fig. 6 Stress of involute tooth (a) and full-strength tooth (b)

based on the analysis and synthesis of gears with initial setting a line of action rather than a type of curve for tooth profiles or generating profiles. The created algorithms and programs do not require time-consuming calculations, because the solution of the problem does not require solving trigonometric or algebraic equations of meshing

- Based on the 2D computer modeling the teeth stress–strain state by the finite element method, a basic formula for calculating the greatest tensile stresses in the tooth root fillet of the involute spur gears cut with the standard rack tool has been obtained. This is necessary for the optimization synthesis of root fillet curves by the criterion of minimum tensile stresses in the root of the teeth
- The results of processing the developed algorithms and programs for designing full-strength profiles of the spur gear teeth have been confirmed by a comparative finite element analysis of the teeth bending strength: the tensile stresses in the root of the full-strength tooth, leading to its fracture, are 1.34 times lower than for the involute tooth

Table 1 Assessment of 2D function experimental data approximation quality

Tool shifting coefficient	1D function determination coefficient	2D function determination coefficient
−0.4	0.99904911	0.99886547
−0.2	0.99977062	0.99912358
0	0.99722972	0.99923105
+0.2	0.99584726	0.99912011
+0.4	0.99048152	0.99900598
+0.6	0.99231412	0.99872141
+0.81	0.99052032	0.99865205

Acknowledgements. This work was performed within the governmental assignment from the Ministry of Education and Science of the Russian Federation for the period of 2017–2019 in Tyumen Industrial University (project N9.6355.2017/BCh).

References

1. Litvin FL, Gutman Y (1981) Methods of synthesis and analysis for hypoid gear-drives of fifi formate and “helixform”: Part 1. Calculations for machine settings for member gear manufacture of the formate and helixform hypoid gears. *J Mech Des, Trans ASME* 103(1):83–88. <https://doi.org/10.1115/1.3254890>
2. Yilmaz TG, Dogan O, Yuce C, Karpat F (2017) Improvement of loading capacity of internal spur gear with using asymmetric trochoid profile. In: *Proceedings of the ASME international mechanical engineering congress and exposition, (IMECE) vol 11*. <https://doi.org/10.1115/IMECE2017-71009>
3. Syzrantseva K, Syzrantsev V, Babichev D (2020) Comparative analysis of stress-strain condition of cylindrical gears arc teeth and spurs. *Lect Notes Mech Eng* 101–108. https://doi.org/10.1007/978-3-030-22041-9_12
4. Syzrantseva K, Syzrantsev V (2017) Estimation of Novikov gearing loading capacity on a base of Integral Strain Gauges application. *Proc Eng* 206:1081–1086
5. Litvin FL, Fuentes A (2004) *Gear geometry and applied theory*. Cambridge University Press, Cambridge, UK
6. Litvin FL, Hsiao C-L, Wang J-C, Zhou X (1994) Computerized simulation of generation of internal involute gears and their assembly. *J Mech Des Trans ASME* 116(3):683–689. <https://doi.org/10.1115/1.2919436>
7. Park N (2017) A generalized hypoid gear synthesized with common crown rack positioned between pinion and gear blanks. *J Mech Des Trans ASME* 139(8):085001. <https://doi.org/10.1115/1.4036779>
8. Litvin FL, Fuentes A, Zanzi C, Pontiggia M (2002) Design, generation, and stress analysis of two versions of geometry of face-gear drives. *Mech Mach Theory* 37(10):1179–1211. [https://doi.org/10.1016/S0094-114X\(02\)00050-2](https://doi.org/10.1016/S0094-114X(02)00050-2)
9. Lebeck AO, Radzimovsky EJ (1970) The Synthesis of profile shapes and spur gears of high load capacity. *Trans ASME* 92(3):543–553
10. Shishov VP, Nosko PL, Fil PV (2006) *Theoretical bases of synthesis of gear transmissions*. Volodymyr Dahl East Ukrainian National University, Lugansk, p 408
11. Pavlov AI (2005) *Modern theory of gear meshing*. Kharkiv National Automobile and Highway University, Kharkiv, p 100
12. Babichev D, Storchak M (2015) Synthesis of cylindrical gears with optimum rolling fatigue strength. *Prod Eng Res Dev* 9(1):87–97
13. Babichev DT, Babichev DA, Lebedev SY (2018) Calculation of tooth profile radiuses of curvature into line of contact parameters. *IOP Conf Ser Mater Sci Eng* 393:681–692
14. Babichev DT, Babichev DA, Lebedev SY (2018) Concept of gear synthesis based on assignment of instant contact areas for loaded teeth. *Int Rev Mech Eng (IREME)* 12(5):420–429
15. Babichev DT (2013) The report on grant of the German scientific organization on training in Institute of machines of the University of Stuttgart (from 1.10.2012 till 31.12.2012), p 23 [Entwicklung eines Konzepts zur Synthese zylindrischer Verzahnungen mit optimaler Wälzfestigkeit, Ergebnis des Forschungsaufenthalts eines Wissenschaftlers aus Russland, Arbeits- und Ergebnisbericht zum Vorhaben HE 1656/164–1, Uwe Heise, Institut für Werkzeugmaschinen Universität Stuttgart].
16. Vimercati M (2007) Mathematical model for tooth surfaces representation of face-hobbed hypoid gears and its application to contact analysis and stress calculation. *Mech Mach Theo* 42(6):668–690. <https://doi.org/10.1016/j.mechmachtheory.2006.06.007>
17. Gdanskij NI (1997) Calculation of optimum geometrical characteristics in epicycloidal lantern gear. *J Mach Manuf Reliab* 2:29–34

18. Syzrantseva KV (2009) Development of a method to calculate the strength reliability of tooth gears based on the fatigue resistance when the teeth bend. *J Mach Manuf Reliab* 38(6):552–556. <https://doi.org/10.3103/S1052618809060065.10>
19. Golovanev V, Babichev D (2014) Using of block contours at designing of involute spurs: state, problems, prospects. https://support.ascon.ru/source/info_materials/2014/V.%20Golovanev_and_D.Babichev.pdf
20. Syzrantseva KV (2009) Predicting the failure of gear transmissions by nonparametric statistics. *Russ Eng Res* 29(2):1206–1208. <https://doi.org/10.3103/S1068798X09120028>
21. Bakhrushin VE (2011) Methods of estimation of characteristics of nonlinear statistical communications. *Syst Technol* 2(73):9–14
22. Syzrantseva K, Syzrantsev V (2016) Reliability estimation of machine parts with complicated geometry on a base of methods of nonparametric statistics. *J Eng Appl Sci* 11(2):204–209. <https://doi.org/10.3923/jeasci.2016.204.209>



Evaluating the Influence of Perforated Baffle on Hydraulic Resistance of Impeller Machine Diffuser Channels

A. Bobkov^(✉) and S. Chepurnykh

Komsomolsk-na-Amure State University, 27, Lenin Prospect, Komsomolsk-on-Amur 681013,
Russia
bobkov@knastu.ru

Abstract. The paper studies one of the methods of increasing boundary layer stability in “separation” diffuser channels of impeller machines: compressors, pumps, and turbines. Such channels include diffusers with expansion angle $\varphi \geq 15^\circ$. The flow in them occurs with boundary layer separation. The option of installing a perforated baffle at the separation diffuser outlet is considered as a way to localize the separation. The localization mechanism is as follows: Due to the uneven approach flow velocity field caused by the separation, the baffle resists the flow unevenly at the channel cross section with formation of negative static pressure gradient directed at the separation area. As the result, convection current appears at the diffuser outlet from the high-energy flow core and goes to the separation area, facilitating its localization. This paper presents experimental data on measuring the flow duct hydraulic resistance for an impeller machine comprising a separation diffuser and a perforated baffle at the outlet. The objects of the study are three conic diffusers with expansion angles φ 30° , 60° , and 90° as well as two variations of perforated baffle with nets 014 and 045 with flow section coefficients 0.37 and 0.479, correspondingly. The purpose of the study is to evaluate the energy balance between two processes: decreasing diffuser’s hydraulic resistance due to separation localization and increasing duct’s hydraulic resistance due to perforated baffle resistance. The results of the study show that hydraulic resistance of a diffuser with angle $\varphi = 30^\circ$ increased by 1.0...1.3% with the installation of perforated baffle, depending on Re. Installation of perforated baffle at the outlet of diffusers with $\varphi = 60^\circ$, 90° does not lead to a change in hydraulic resistance of diffusers.

Keywords: Diffuser · Separation area · Perforated baffle

1 Introduction

The reserve for improving energy efficiency of impeller machines (IM): pumps, compressors, and turbines lies in perfecting the diffuser channel design of these machines’ impellers as well as supply and outflow of fluid [1–10].

Diffuser channels with expansion angle over 15° are the so-called “separation” diffusers as they are where boundary layer separation occurs. Efficient pressure restoration in such diffusers is observed only in the area before the separation point [11–14]. Zero-gradient current continues after this point with energy losses due to separation support.

As a consequence, separation flow mode in the channels reduces energy conversion efficiency, facilitates flow duct self-oscillation, and reduces the reliability of the device. This is why localizing separation areas in the IM diffuser channels are a current concern for improving flow hydrodynamics of their flow cavity [15–19].

2 Separation Area Localization Mechanism

There is a way to localize separation areas in the channels by creating negative static pressure gradient in the flow which is transverse to the basic flow. A 3D or flat perforated obstruction is installed on the way of the flow [20–23]. The latter may be represented by a system of rods, perforated plate, net, etc., and will be hereinafter referred to as perforated baffle (PB). The use of PB is especially important for small impeller machines intended for outer space [24, 25] where small full size of working elements does not allow using 3D obstructions. Figure 1 shows two examples of PB installation in the cavity of a low-flow centrifugal pump which is part of spacecraft temperature control system. In Fig. 1a, baffle is installed at the curvilinear diffuser outlet which is the end of pump diverter’s spiral collector. In Fig. 1b, baffle is attached at the periphery of the wheel with curvilinear diffusers as inter-impeller channels.

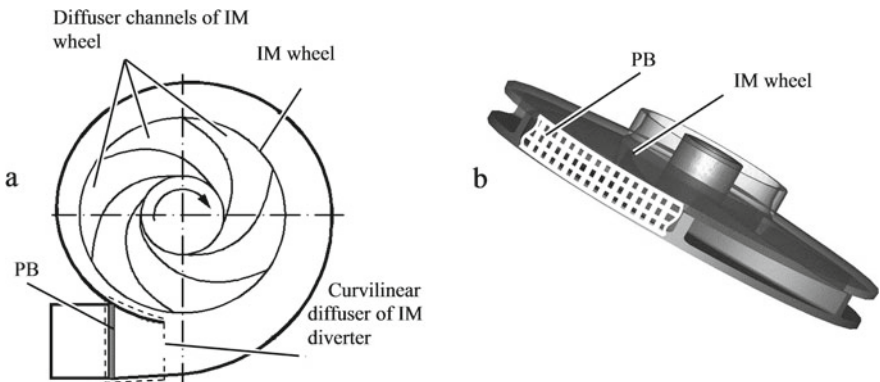


Fig. 1 Options of PB installation into the diffuser channels of impeller machines: **a** stationary diffuser channel; **b** rotating diffuser channels of IM wheel

Separation localization mechanism is as follows: Due to separation, uneven approach flow velocity field W is formed in separation diffusers [26, 27] with positive gradient directed to the side from the separation point to the flow core; see Fig. 2a. The baffle installed on the way of the fluid flow gives resistance to the current which is proportional to the squared velocity of approaching streams. Due to the uneven approach flow velocity

field, PB gives uneven resistance Δp_{pb} to the current at the frontal side; see Fig. 2b. Along the channel's cross section, static pressure gradient is formed before PB due to Δp_{pb} which is opposite in sign to approach flow velocity gradient. This gradient facilitates the convection current of fluid along the PB frontal side from the high-energy area to the separation area. Thus, due to a combination of two factors: uneven approach flow velocity field and uneven frontal resistance of PB, a mechanism of energy redistribution in the flow is formed which facilitates separation area localization.

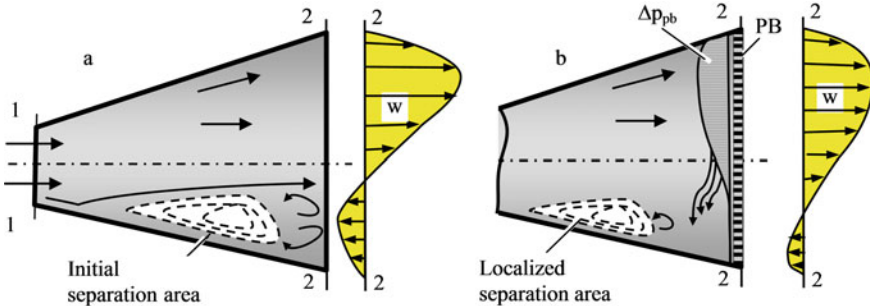


Fig. 2 Separation area localization mechanism in “Separation” diffuser: **a** diffuser without PB; **b** diffuser with PB

This mechanism is accompanied by an additional type of energy loss. The energy is spent on overcoming PB resistance and is evaluated Δp_{pb} . To evaluate the energy balance between two processes: decreasing diffuser's hydraulic resistance due to separation area localization and increasing duct's hydraulic resistance due to PB resistance Δp_{pb} , experimental studies of hydraulic resistance for a diffuser with perforated baffle installed at the outlet are required.

3 Experimental Unit Description

A model of IM stationary diffuser channel comprising a conical diffuser and a perforated baffle installed at the diffuser's outlet became the test object. The measurements of model's hydraulic resistance were performed at a hydraulic test stand using water as fluid.

Three conical diffusers were manufactured with expansion angle meeting the requirement of “separating” $\varphi \geq 15^\circ$. Figure 3 shows test stand flow duct with a diffuser installed.

The unevenness of boundary layer (separation area size) was changed by increasing diffuser expansion angle by 30° from $\varphi = 30^\circ$ to $\varphi = 90^\circ$. Table 1 shows the geometry of diffusers.

Two variations of PB made of net 014 and 045 (designations as per GOST 6613-86 Wire Cloth Nets with Square Mesh. Specifications) with two different flow section coefficients were installed at the diffuser outlet. Net geometric parameters: mesh size σ_m , wire diameter d_w and flow section coefficient \bar{f} are given in Table 2.

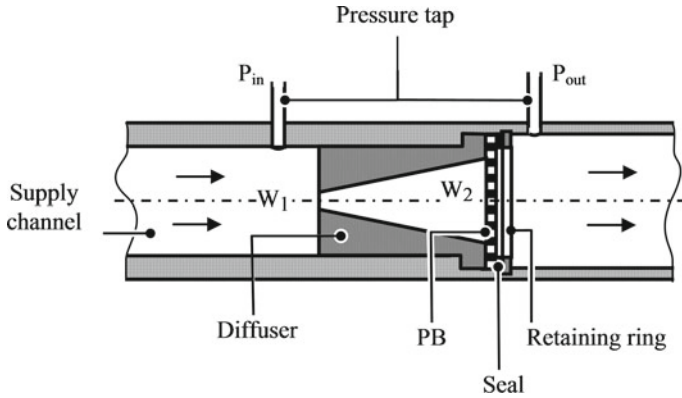


Fig. 3 Test stand flow duct scheme

Table 1 Diffuser geometric parameters

φ (°)	d_{throat} (mm)	$L_{\text{dif}}/d_{\text{throat}}$
30	2.8	8.8
60	3.03	3.7
90	3.04	2.1

Table 2 Net geometric parameters

Net	σ_m (mm)	d_w (MM)	\bar{f}
014	0.14	0.09	0.37
045	0.45	0.2	0.479

Two parameters were measured during the tests: volumetric flow of fluid through the diffuser Q (m³/s) and diffuser pressure gradient $\Delta p_{\text{dif}} = p_{\text{out}} - p_{\text{in}}$ (Pa) where p_{out} and p_{in} are static pressure at the diffuser's inlet and outlet.

Based on the results of measurements, diffuser resistance coefficient ξ_{dif} was calculated:

$$\xi_{\text{dif}} = \frac{2 \cdot \Delta p_{\text{dif}}}{\rho \cdot W_m^2}, \quad (1)$$

where ρ is fluid density, kg/m³; W_m is fluid velocity per PB mesh, m/s.

Fluid velocity per mesh was calculated based on the following formula:

$$W_m = W_2 / \bar{f}, \quad (2)$$

where W_2 is middle-flow velocity by [5], see Fig. 3.

4 Results of Experimental Study

Figure 4 shows the results of experiments as dependence diagrams $\xi_{dif} = f(Re_{w2})$. Here, Reynolds number was calculated by formula:

$$Re_{w2} = \frac{W_2 \cdot d_{2dif}}{\nu}, \tag{3}$$

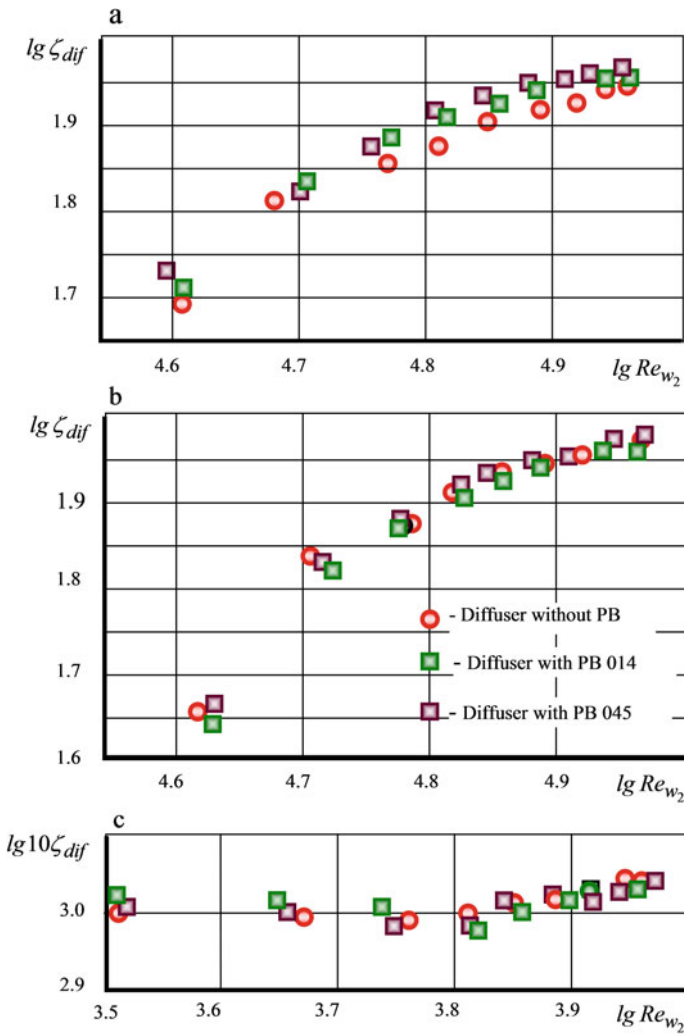


Fig. 4 PB influence on diffuser hydraulic resistance: **a** $\varphi = 30^\circ$; **b** $\varphi = 60^\circ$; **c** $\varphi = 90^\circ$

where d_{2dif} is diffuser’s diameter at the outlet, m ; ν is kinematic viscosity coefficient of fluid, m^2/s .

PB installation did not affect hydraulic resistance of diffusers with expansion angles $\varphi = 60^\circ$ and $\varphi = 90^\circ$. Increased energy losses due to PB resistance with coefficient $\xi_{\text{net}} = 0.4 \dots 0.6$ [26–28] in diffusers with large expansion angles were compensated by reducing separation losses. Nets 014 and 045 have significantly differing flow section coefficients $\bar{f} = 0.37$ and $\bar{f} = 0.479$, correspondingly, as well as resistance coefficients at the same Reynolds numbers, but they ensured the same energy results after PB installation: stable ξ_{dif} within the tolerances for hydraulic test stand system of measurement.

Installing nets 014 and 045 at the outlet of diffuser with expansion angle $\varphi = 30^\circ$ led to an insignificant increase of hydraulic resistance. Here, increased ξ_{dif} is explained by reduced initial level of separation losses (diffuser losses) due to increased relative length $L_{\text{dif}}/d_{\text{throat}}$ achieved by reducing expansion angle to $\varphi = 30^\circ$. The share of friction losses is increased in the balance of losses for such diffuser. Their mechanism does not change with PB installation. Estimated power loss N_{PB} due to PB installation at the outlet of a diffuser with $\varphi = 30^\circ$ and fluid flow $Q = 2 \times 10^{-4} \text{ m}^3/\text{s}$ constituted the range of values $N_{\text{PB}} = (0.1 \dots 0.5) W$.

5 Conclusion

The obtained results confirmed the viability of installing PB at the outlets of IM separation diffuser channels and the lack of any significant additional power loss due to overcoming baffle resistance. The latter factor is especially important for rotating diffuser channels of impeller machine wheels. The efficiency of the latter is evaluated with the use of hydraulic energy conversion efficiency.

The stability of flow duct hydraulic resistance after PB installation allows predicting that IM hydraulic energy conversion efficiency will stay the same, in particular, for a low-flow centrifugal pump with perforated baffle installed on the wheel. In this case, the effect from PB installation will be the increased pump pressure coefficient due to the decreased flow “slippage” at the wheel outlet caused by increased static pressure gradient at its blades due to PB resistance.

References

1. Gostelou Dzh (1987) Aerodinamika reshetok turbomashin (Aerodynamics of turbomachine grilles). Mir, Moskva
2. Kampasti N (2000) Aerodinamika kompressorov (Aerodynamics of compressors). Mir, Moskva
3. Leshchiner LB, Ulyanov IE, Tvertsky VA (1991) Proyektirovaniye toplivnykh sistem samolota (Design of aircraft fuel systems). Mashinostroyeniye, Moskva
4. Arinushkin LS, Abramovich RB, Polinovskiy AyU, Leshchiner LB, Glozman YeA (1967) Aviatsionnyye tsentrobezhnyye nasosnyye agregaty (Aircraft centrifugal pumping units). Mashinostroyeniye, Moskva
5. Deych ME, Zaryankin AY (1970) Gazodinamika diffuzorov i vykhlopnykh patrubkov turbomashin (Gas dynamics of diffusers and exhaust pipes of turbomachines). Energiya, Moskva
6. Ershov VN, Menshikov VA, Skob YuA, Ugryumov ML (1988) Features of the formation of spatial separated flows in flat diffuser grids. Prob Mech Eng 29:17–24

7. Gerasimenko VP, Shelkovsky MJ, Dmitriev SA (2014) Aerodynamic improvement of an axial compressor. *Eng Build Bull* 2:27–33
8. Falaleev SV, Belousov AI (2017) Development of gas and hydrodynamic seals for turbomachine supports. *Pumps Turbines Syst* 4(25):6–17
9. Beeck AR (2012) U.S. Patent No. 8,313,286. Washington, DC: U.S. Patent and Trademark Office
10. Kim JH, Kim KY (2012) Analysis and optimization of a vaned diffuser in a mixed flow pump to improve hydrodynamic performance. *J Fluids Eng.* 134(7):071104-1–071104-10
11. Chzhen P (1979) *Upravleniye otrvyvom potoka* (Managing the Separator). Mir, Moskva
12. Idelchik IE (1948) Equalizing action of the resistance placed behind the diffuser. *TsAGI Proc Issue* 662:25–52
13. Idelchik IE (1947) Aerodynamics of flow and head loss in diffusers. *Ind Aerodynam* 3:132–209
14. Davletshin IS, Mingazov BG, Yavkin VB, Kesel BA, Voskoboinikov DV (2011) Features of turbulent flow modeling in diffuser channels of simple and complex configuration. *Samara University Bulletin. Aerospace Eng, Tech Mech Eng* 3–2:11–15
15. Grigoriev EYu, Zaryankin AE, Noskov VV, Buzulutskiy DE, Trukhin OA (2012) New methods of flow stabilization in flat, conical, annular diffuser channels of turbomachines. *Bull Ivanovo State Power Eng Univ* 5:5–9
16. Zaryankin AE, Rogalev AN, Grigoriev EYu, Garanin IV, Padashmoganlo MT, Cherkasov MA (2015) Circumferential irregularity of flow parameters in conical diffusers and a method of damping. *Bullet Ivanovo State Power Eng Univ* 6:9–16
17. Osipov AV, Perevezentsev VT, Gorbachev VV, Tikhonovsky VI (2020) Experimental static stand for studying the aerodynamics of the flow in the channels and branch pipes of turbomachines. *Modern science in the context of modernization processes: problems, realities, prospects*, pp 42–49
18. Subbotovich VP, Yudin YA, Lapuzin AV, Yudin AYu (2013) Aerodynamic studies of the section of the outlet diffuser of a turbine with a special flow injection. *Bulletin of NTU “KhPI”* 12:30–35
19. Yudin AYu (2011) Investigation of axisymmetric diffusers of the outlet pipes of turbomachines with a special flow injection. *Aerospace Eng Tech* 3:80–84
20. Shapiro AS, Neklyudov LV, Ovsyannikov BV (1968) *Tentrobezhny nasos* (Centrifugal Pump). A.s. 240480 USSR, March 21, 1969
21. Bobkov AV, Kraev MV, Lukin VA, Ovsyannikov BV (1982) *Rabocheye koleso tsentrobezhnogo nasosa* (Centrifugal Pump Wheel). A.s. 1138544 USSR, February 7, 1985
22. Tereshchenko YM, Doroshenko EV, Volyanskaya LG (2013) Modeling the flow in a diffuser channel with turbulators. *Eastern Eur J Adv Techn* 4–7:36–38
23. Yaroslavtseva NA, Ivanov NG, Kirillov AI (2018) Evaluation of the effectiveness of the use of vortex cells to control the separation of a turbulent flow in an axial radial diffuser. *SPbPU Science Week*, pp 58–60
24. Kraev MV, Lukin VA, Ovsyannikov BV (1985) *Maloraskhodnyye nasosy aviatsionnykh i kosmicheskikh sistem* (Low-Flowrate Pumps of Aviation and Space Systems). *Mashinostroyeniye*, Moskva
25. Bobkov AV (2003) *Tsentrobezhnyye nasosy sistem termoregulirovaniya kosmicheskikh apparatov* (Spacecraft Thermal Regulation Systems Centrifugal Pumps). *Dal'nauka*, Vladivostok
26. Idelchik IY (1983) *Aerogidrodinamika tekhnologicheskikh apparatov*. (Podvod, otvod i raspredeleniye potoka po secheniyu apparatov) *Aerohydrodynamics of technological devices*. (Inlet, outlet and distribution of flow over the section of the apparatus). *Mashinostroyeniye*, Moskva

27. Altshul AD (1970) *Gidravlicheskiye soprotivleniya* (Hydraulic resistance). Nedra, Moskva
28. Idelchik IY (1992) *Spravochnik po gidravlicheskim soprotivleniyam* (Hydraulic resistance reference). Mashinostroyeniye, Moskva



Investigation of String Vibrations of a Transporting Device

M. U. Musirov¹(✉) and N. Yu. Kholmanov²

¹ Academy of Sciences of the Republic of Uzbekistan, 33, Durmon Yuli Street, Tashkent, Uzbekistan100047

² National University of Uzbekistan Named After Mirzo Ulugbek, 4, University street, Tashkent, Uzbekistan100174

Abstract. String and belt conveyors are widely used in the light industry and agriculture to transport products and flat goods, in particular, leather products, to the processing area of the technological machines. For these conveyors to work effectively and efficiently for a long time, it is necessary to correctly select the geometrical and kinematic parameters at the process of their design. The technological processing of leather semi-finished products affects the quality of leather products. Therefore, it is necessary to analyze the conditions of the processed material after each technological operation. Experimental research in the leather industry is aimed at solving complex many-sided problems, revealing rational solutions to technological processes in leather raw materials processing. The motion of the conveyor strings, stretched on cylindrical shafts with the grooves, is determined by the Mathieu equation. The parameters of the Mathieu equation depend on the speed of the conveyor strings and geometrical parameters of the system. To limit the amplitude of the transverse vibrational motion of the conveyor strings, it is necessary to select the kinematic and geometrical parameters so that they fall into the stability zone. These parameters are determined depending on the geometrical and kinematic parameters of the device.

Keywords: Conveying device · Strings · Flat material · Variable mass · Lateral vibrations · Uniform feed

1 Introduction

Earlier, we developed a transporting device for feeding flat materials into the processing zone between rotating working shafts [1]. It was stated from the literature publications that the physical and mechanical properties of semi-finished leather products vary depending on their moisture content [2–7].

It is known that smooth and uniform feed of the processed material to the working area is one of the important tasks in various industries. Owing to it, substantial amounts of raw materials are saved when solving the issue of eliminating defective materials and losses in the process of feeding into the processing zone on transporting devices [8].

Articles [9–12] are devoted to solutions of contact interaction in two-roll modules. Mathematical models of roll contact curves, friction stresses, and contact stress distribution patterns are obtained in these publications.

In [13], the deformation properties of a semi-finished leather product processed between the squeezing rollers covered with moisture-extracting materials were experimentally determined. The influence of the feeding speed and the pressure of the squeezing rollers on the deformation of a leather semi-finished product in its topographic sections (shoulder, belly, and butt) was determined.

2 Research Methods

Four analytical methods were used to determine the parameters, typical for the conveyor belts, and to analyze the test results when determining the elastic modulus; they are Euler–Bernoulli methods and finite element methods for determining the flexural modulus of unstretched belts, and the Timoshenko and Mindlin–Reissner methods [14].

It was determined that the conveyor belt slippage depends on the diameter of the driveshaft and vertical stress in the contact area, and that the belt resistance to its vibration is low [15].

It is known that the process of the conveyor belt splice is based on the Mooney–Rivlin law [16].

In problems of this type, the change in string velocity with time plays an important role in dynamic behavior. The transverse vibrations of the belt were calculated by the Kirchhoff method using the differential equations of motion of the system [17, 18].

Velocity control in belt conveyors results in energy efficiency and stable operation of basic units of conveyor equipment [19].

A virtual energy storage model was proposed to reduce the energy consumption of belt conveyors. This model studied the reduction in energy consumption over time by controlling the speed of the conveyor belt, feeding speed of the product, and the speed of other parts of the equipment [20].

Mechanical damage can occur after a certain time of conveyor operation. This process was considered and the methods to assess the damage probability during the operation were described using existing statistical models [21].

3 Research Results

Let us consider the problem of the transverse vibration of a conveyor belt with uneven gravity.

Non-uniformly distributed vertical forces of gravity of flat material being transported along the conveyor strings stretched on cylindrical shafts of radius R act on a transporting belt. Consider small vibrations of this system (Fig. 1).

We obtain the law of mass distribution of flat material in the conveyor as:

In the device under consideration, the conveyor strings move at a constant speed.

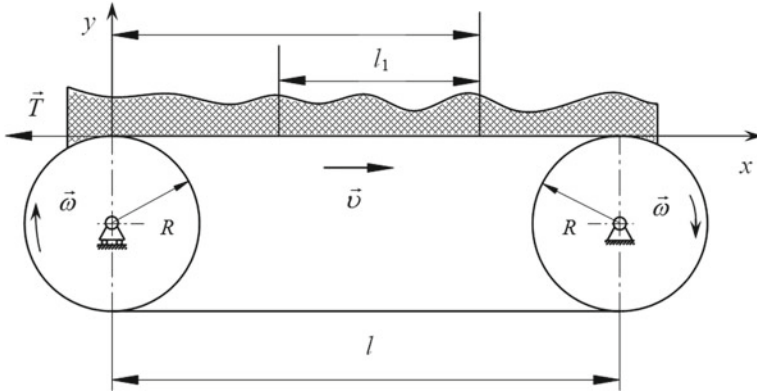


Fig. 1 Scheme of a device that moves flat materials to the processing area

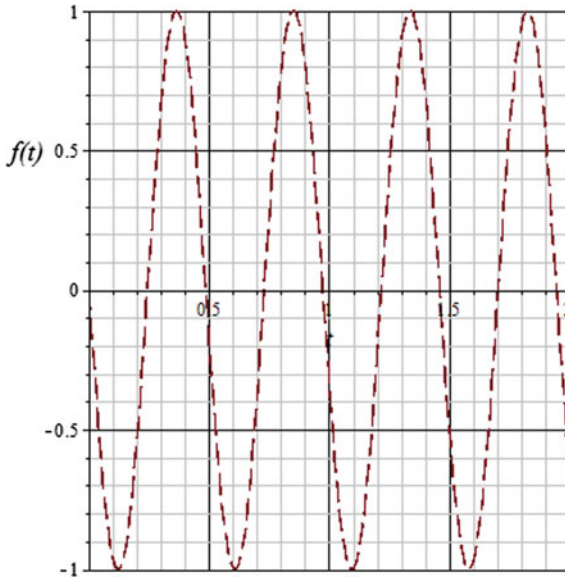


Fig. 2 Graphical solution of the Mathieu equation as a function of time

When solving problems of this type, it is convenient to consider them in the Euler coordinate system.

$$\frac{dy}{dt} = \frac{\partial y}{\partial t} + v \frac{\partial y}{\partial x}, \quad \frac{d^2y}{dt^2} = \frac{\partial^2 y}{\partial t^2} + 2v \frac{\partial^2 y}{\partial x \partial t} + v^2 \frac{\partial^2 y}{\partial x^2}$$

Using the D’alembert principle, we write the following expression as [22, 23].

$$m \left(\frac{\partial^2 y}{\partial t^2} + 2\omega R \frac{\partial^2 y}{\partial x \partial t} + \omega^2 R^2 \frac{\partial^2 y}{\partial x^2} \right) = T \frac{\partial^2 y}{\partial x^2}.$$

In this case, m is the mass corresponding to the unit length

$$m = m_2 + m_0 + m_1 \sin\left(\frac{2\pi}{l_1}(x - vt)\right)$$

where m_0 is the average value of the mass of the transported product per unit length of the conveyor strings (kg/m); m_1 —variable amplitude of the function of flat material mass (kg/m); m_2 —mass per unit length of conveyor strings (kg/m); l_1 —stepwise change in the variable mass of raw materials; T —tension of the working strings of the conveyor.

Since it is difficult to find a general analytical solution to the problem, we will use the Taylor series [24].

Assuming that m_1 , i.e., the deviation of the non-uniformly distributed mass from m_0 is small, and then expanding the linear part $\frac{1}{m}$ around the point $m_1 = 0$ in the Taylor series, we obtain the equation of transverse motion in the following form

$$\frac{\partial^2 y}{\partial t^2} + 2\omega R \frac{\partial^2 y}{\partial x \partial t} + (\omega R)^2 \frac{\partial^2 y}{\partial x^2} = \frac{T}{m_0 + m_2} \left(1 - \frac{m_1}{m_0 + m_2} \sin\left(\frac{2\pi}{l_1}(x - \omega R t)\right)\right) \frac{\partial^2 y}{\partial x^2} \quad (1)$$

The initial and boundary conditions for the resulting partial product equation are as follows.

$$\begin{cases} y(0, t) = 0 \\ y(l, t) = 0 \end{cases}$$

Let us consider the problem of the small vibrations predominance by the Galerkin method.

$$y = f(t) \sin \frac{\pi x}{l} \quad (2)$$

It is easy to see that the approximating function from this point of view satisfies the boundary conditions. Substituting the relation (2) into the equation of motion (1), we obtain a simple second-order differential equation for the function $f(t)$.

$$\begin{aligned} \ddot{f} \sin\left(\frac{\pi x}{l}\right) + \frac{2\nu\pi}{l} \dot{f} \cos\left(\frac{\pi x}{l}\right) + \left(\frac{\pi}{l}\right)^2 \left(\frac{T}{m_0 + m_2} \left(1 - \frac{m_1}{m_0 + m_2} \sin\left(\frac{2\pi}{l_1}(x - \omega R t)\right)\right) - \omega^2 R^2\right) \\ \dot{f} \sin\left(\frac{\pi x}{l}\right) = 0 \end{aligned} \quad (3)$$

To solve the differential Eq. (3), we construct the following system of differential equations.

$$\begin{cases} \frac{2\nu\pi}{l} \dot{f} = 0 \\ \ddot{f} + \left(\frac{\pi}{l}\right)^2 \left(\frac{T}{m_0 + m_2} \left(1 - \frac{m_1}{m_0 + m_2} \sin\left(\frac{2\pi}{l_1}(x - \omega R t)\right)\right) - \omega^2 R^2\right) f = 0 \end{cases} \quad (4)$$

The first equation of the system of Eq. (4) always satisfies Eq. (1). We solve the second equation of the system

$$\ddot{f} + \left(\frac{\pi}{l}\right)^2 \left(\frac{T}{m_0 + m_2} \left(1 - \frac{m_1}{m_0 + m_2} \left(a_{11} \cos \frac{2\pi \omega R t}{l_1} - a_{12} \sin \frac{2\pi \omega R t}{l_1}\right)\right) - \omega^2 R^2\right) f = 0 \tag{5}$$

Here

$$a_{11} = \frac{l_1^2}{\pi^2 \omega^2 R^2} \int_0^l \sin \frac{2\pi x}{l_1} \sin^2 \frac{\pi x}{l} dx = -\frac{l_1^2}{\pi^2 \omega^2 R^2} \frac{l_1}{4\pi} \frac{l_1^2}{l^2 - l_1^2} \left(1 - \cos \frac{2\pi l}{l_1}\right)$$

$$a_{12} = \frac{l_1^2}{\pi^2 \omega^2 R^2} \int_0^l \cos \frac{2\pi x}{l_1} \sin^2 \frac{\pi x}{l} dx = -\frac{l_1^2}{\pi^2 \omega^2 R^2} \frac{l_1^2}{4\pi(l - l_1)} \sin \frac{2\pi l}{l_1}$$

The resulting equation is written as:

$$\ddot{f} + \left(a - b \sin\left(\frac{2\pi \omega R t}{l_1} + \beta\right)\right) f = 0 \tag{6}$$

Here

$$a = \left(\frac{\pi}{l}\right)^2 \left(\frac{T}{m_0 + m_2} - \omega^2 R^2\right), b = \frac{T m_1}{(m_0 + m_2)^2} \left(\frac{\pi}{l}\right)^2 \sqrt{a_{11}^2 + a_{12}^2}, \beta = \text{arctg}\left(\frac{a_{11}}{a_{12}}\right).$$

Let us introduce the following substitution:

$$\frac{2\pi \omega R t}{l_1} = 2\tau - \frac{\pi}{2} - \beta$$

After this substitution, we compose the Mathieu equation.

$$\ddot{f} + (a + 2q \cos 2\tau) f = 0 \tag{7}$$

where

$$2q = b.$$

The general solution of the differential Eq. (7) is as follows:

$$f(t) = C_1 \text{MathieuC}(a, -q, \tau(t)) + C_2 \text{MathieuS}(a, -q, \tau(t))$$

Here.

MathieuC—is the Mathieu cosine, MathieuS—is the Mathieu sine;

C_1 and C_2 are the Mathieu’s constant coefficients of differentiation, defined as follows:

$$C_1 = \frac{\text{MathieuC}(\text{MathieuA}(n, q), q, x)}{\text{MathieuCE}(n, q, x)}, C_2 = \frac{\text{MathieuS}(\text{MathieuB}(n, q), q, x)}{\text{MathieuSE}(n, q, x)}.$$

Here $n = 1, 2, 3, \dots$

4 Discussion of Results

Problems of this type are reduced to the Mathieu equation by various methods. Solving the Mathieu equation obtained (6), it is convenient to determine and select the rational parameters of the working bodies of the transporting device of the technological machine.

We obtain a graphical solution of differential Eq. (6) for the given values $l_1 = 0.3$ m, $l = 1$ m, $T = 300$ N, $v = 0.2$ m/s, $m_0 = 0.15$ kg/m, $m_1 = 0.2$ kg/m, $m_2 = 0.3$ kg/m.

As seen from the obtained graphical solution of the Mathieu equation, the vibration amplitude of the conveyor strings does not change. If the amplitude does not change, the motion is stable. This ensures long-term and efficient operation of the working bodies of the transporting device.

5 Conclusions

The solution of the equation of motion (6) of the conveyor obtained for feeding flat materials to the processing zone is described by parametric vibrations depending on the values of the constants belonging to the system, considered in Fig. 1, where the amplitude of vibrations changes uniformly. An increase in the amplitude of vibrations with time leads to the occurrence of a parametric resonance state, and this process is considered undesirable for the mechanisms of the device. The movement of the conveyor strings stretched over the shafts, after several replacements, is determined by the Mathieu equation.

The parameters of the Mathieu equation depend on the speed of the conveyor strings and the geometrical parameters of the system. Since the amplitude of the oscillatory motion of the conveyor strings is limited, the kinematic and geometrical parameters must be selected so that they fall into the stability zone. These parameters depend on the geometry and speed of the device.

The values of the Mathieu equation solutions, representing the lateral vibrations of a mechanical system, were obtained using the Maple 18 programming package.

The computations obtained allow calculating the parameters of the transporting device of flat materials into the processing zone. They are useful for engineers when stating the operating modes of the conveyor in design of conveyors for various purposes. With technological requirements, we can set the speed and geometrical parameters of the transporting device. Its rational parameters can be chosen using the resulting equations.

References

1. Bahadirov GA, Rizaev AA, Bakhadirov KG, Abdukarimov A, Makhmudov KA (2008) Device for straightening and feeding sheet material into the processing zone. Patent RUz No. FAP 00405, State Patent Office of the Republic of Uzbekistan, Official Bulletin No. 9
2. Burmistrov AG (2006) Machines and devices for the production of leather and fur. Moscow
3. Bahadirov G, Musirov M, Bakhadirov K (2020) Parameters substantiation of guide surface of flat material into the processing area. Int J Eng Adv Technol (IJEAT), 962–966. <https://doi.org/10.35940/ijeat.D7655.049420>

4. KhurramovShR, Khalturaev FS, Kurbanova FZ (2020) Mathematical models of the character of deformation of semi-finished leather products. Proceedings of the international scientific conference, volume 6 “Mathematical methods in engineering and technology”, St. Petersburg
5. Bahadirov GA, Sultanov TZ, Abdukarimov A (2020) Comparative analysis of two gear-lever differential inter-roller transmission mechanisms. IOP Conf. Ser.: Earth Environ. Sci. 614:012102. <https://doi.org/10.1088/1755-1315/614/1/012102>
6. Bahadirov GA, Sultanov TZ, Abdukarimov A (2020) Kinematic analysis of tooth-lever differential transmission mechanisms. IOP Conf. Ser.: Earth Environ. Sci. 614:012101. <https://doi.org/10.1088/1755-1315/614/1/012101>
7. Bahadirov G, Sultanov T, Umarov B, Bakhadirov K (2020) Advanced machine for sorting potatoes tubers. IOP Conf Ser: Mater Sci Eng. 883:012132. <https://doi.org/10.1088/1757-899X/883/1/012132>
8. Bahadirov G, Tsoy G, Nabiev A (2021) Study of the efficiency of squeezing moisture-saturated products. EUREKA: Physics and Engineering 1:86–96. <https://doi.org/10.21303/2461-4262.2021.001606>
9. Khurramov ShR (2020) Simulation of the form of contact curves rolls in two-roll modules IOP Conf. Series: Earth Environ Sci 614:012096. <https://doi.org/10.1088/1755-1315/614/1/012096>
10. Khurramov ShR (2020) Some questions of the contact interaction theory in two-roll modules. J Phys: Conf Ser 1546:012132. <https://doi.org/10.1088/1742-6596/1546/012132>
11. Khurramov ShR, Kurbanova FZ (2020) Distribution of contact voltages in asymmetric two-roll module. IOP Conf. Series: Earth and Environmental Science 614:012098. doi:<https://doi.org/10.1088/1755-1315/614/1/012098>
12. Khurramov ShR, Khalturayev FS (2020) Simulation of contact voltages in two-roll modules. IOP Conf. Series: Earth and Environmental Science 614:012097. <https://doi.org/10.1088/1755-1315/614/1/012097>
13. Amanov AT, Bahadirov GA, Amanov TY, Tsoy GN, Nabiev AM (2019) Determination of Strain Properties of the Leather Semi-Finished Product and Moisture-Removing Materials of Compression Rolls. Journal Materials. Basel, Switzerland. <https://doi.org/10.3390/ma12213620>
14. Zamiralova ME, Lodewijks G (2016) Review of the troughability test ISO 703 for quantifying a uniform transverse bending stiffness for conveyor belts. Archiv. Civ. Mech. Eng 17:249–270. <https://doi.org/10.1016/j.acme.2016.10.007>
15. Chen H, Zhang K, Piao M et al (2018) Dynamic analysis of indentation rolling resistance of steel cord rubber conveyor belt. J MechSciTechnol 32:4037–4044. <https://doi.org/10.1007/s12206-018-0803-7>
16. Mazurkiewicz D (2009) Problems of numerical simulation of stress and strain in the area of the adhesive-bonded joint of a conveyor belt. Archiv. Civ. Mech. Eng 9:75–91. [https://doi.org/10.1016/S1644-9665\(12\)60061-2](https://doi.org/10.1016/S1644-9665(12)60061-2)
17. Suweken G, van Horssen WT, (2003) On the Weakly Nonlinear, Transversal Vibrations of a Conveyor Belt with a Low and Time-Varying Velocity. Nonlinear Dyn 31:197–223. <https://doi.org/10.1023/A:1022053131286>
18. Hedrih K (2007) Transversal vibrations of the axially moving sandwich belts. Arch ApplMech 77:523–539. <https://doi.org/10.1007/s00419-006-0105-x>
19. He D, Liu X, Zhong B (2020). Sustainable belt conveyor operation by active speed control. <https://doi.org/10.1016/j.measurement.2019.107458>
20. Mu Y, Yao T, Jia H, Yu X, Zhao B, Zhang X, Ni C, Du L (2020) Optimal scheduling method for belt conveyor system in coal mine considering silo virtual energy storage. <https://doi.org/10.1016/j.apenergy.2020.115368>
21. Semrad K, Draganova K, Koscak P, Cernan J (2020) Statistical prediction models of impact damage of airport conveyor belts, pp 11–19. <https://doi.org/10.1016/j.tpro.2020.11.003>

22. Dobrov IV (2015) Development of scientific bases of the dynamics of machines as a section of applied mechanics. Proc Eng 863–872 <https://doi.org/10.1016/j.proeng.2015.12.108>
23. Małkowski P, Ostrowski Ł (2017) The methodology for the young modulus derivation for rocks and its value. Proc Eng 134–141. <https://doi.org/10.1016/j.proeng.2017.05.164>
24. Groza G, Razzaghi MA (2013) Taylor series method for the solution of the linear initial–boundary-value problems for partial differential equations. Comput Math Appl 1329–1343. <https://doi.org/10.1016/j.camwa.2013.08.004>



Experimental Thermal Performance Double-Sided Face Grinding Machine

I. P. Nikitina and A. N. Polyakov(✉)

Orenburg State University, 13, av. Pobedy, Orenburg 460018, Russia

Abstract. The paper presents a description of the experimental thermal characteristics of a double-sided face grinding machine. Thermal characteristics in the form of time dependences of temperatures and displacements were obtained when the machine was idling, as well as under load. The analysis of experimental studies showed that for a face grinding machine, the thermal characteristics differ significantly at idle and when operating under thermal load. First of all, this is due to different heating of the machine components during idling and when operating under thermal load. It was experimentally found that the highest temperatures during idling are at the faces of the spindle heads and the bed. When working under a thermal load, the greatest heating was recorded for structural elements of the bed located near the fence of the grinding zone, as well as for the faces of the spindle heads facing the grinding zone. The design features of the machine led to a significant difference in the magnitude of the thermal displacements of the right and left grinding wheels. The grinding wheels moved in the direction “wider at the bottom” under the influence of thermal deformations when the machine was idling. When working under heat load, the relative position of the grinding wheels gradually changed from “it is wider at the bottom” to “it is narrower at the bottom.” Changing the position of the grinding wheels led to distortions in the relative position of the grinded faces of the workpiece on the machine.

Keywords: Double-sided face grinding machine · Grinding wheels · Thermal characteristics · Thermal deformations · Spindle heads · Thermal deformations · Thermal displacements

1 Introduction

Grinding is of great importance as a finishing operation in mechanical engineering. Therefore, grinding and grinding machines are still an active area of research today. A fairly large volume of research covers the implementation of new grinding technologies to guarantee the achievement of high-quality surfaces of bearing rings and roller end faces with a roughness parameter R_a not exceeding $0.04 \mu\text{m}$ [1, 2]. It has been experimentally shown that improving the surface quality significantly increases the service life of roller bearings due to the stabilization of the friction torque values over time [2]. In [3], the authors proposed a method for calculating the parameters of roughness, grinding forces and the thickness of the dark layer on the machined surfaces of the bearing rings.

The proposed dependencies took into account the design and technological parameters of the grinding process. This made it possible to optimize the grinding process with control of the output parameters of the machined bearing rings. For a more accurate determination of the grinding temperature in the work area, the heat flux transferred to the workpiece was calculated. The calculation of the dark layer thickness is based on the known temperature of 150 °C at which the phase transformation begins in the bearing steel. During this phase transformation, a dark surface layer forms on the bearing rings. In [4], a thermal model of grinding the bearing inner ring, implemented in the Ansys CAE system, is presented. The developed model, taking into account the design parameters of the bearing and the technological parameters of grinding, allows optimization of the cutting process. In [5], a progressive method of ultrasonic plunge grinding is considered. The method provides a more than 20% increase in the efficiency of the grinding process, a decrease in roughness by more than 25%.

Grinding technology and grinding machines are not limited to their use in the bearing industry. So in [6, 7] the thermal characteristics of gear grinding and worm grinding machines were investigated. The thermoelasticity problem for the supporting system of the gear grinding machine and the bed of the worm grinding machine have been implemented in the Ansys CAE system. The calculated data have been confirmed experimentally. In [8, 9], the thermal processes of deep grinding are investigated. In [8], a thermal finite element model of deep grinding is presented, since the main limitation of this technology is thermal damage to the workpiece and rapid wear of the grinding wheel. In [9], the results of experimental studies are shown, obtained using a new machine tool that implements deep grinding. In [10], a developed simplified theoretical model of thermal deformations of a gear grinding machine is presented, based on solving the bending problem for a beam. The efficiency of the model was confirmed experimentally with an error not exceeding 5%.

In [11], a model for calculating the temperature field in the grinding zone based on the finite difference method is presented. The developed model of heat generation allows taking into account the technological modes of grinding: feed, depth of cut and cutting speed. It has been shown that the effect of feed on the grinding temperature is more significant than the grinding speed and depth of cut.

Thus, a review of modern research carried out for grinding machines over the past five to seven years has shown that one of the most important factors determining the accuracy and quality of machined surfaces are thermal processes in the grinding zone. Works in which the thermal processes occurring in the supporting system of the grinding machine are comprehensively investigated are rarely encountered today. In the presented work, the features of the course of thermal processes in the bearing system of a double-sided face grinding machine, identified experimentally, are considered.

2 Experimental Research

The experiments were carried out on a machine model 3A343ADF2 (manufactured in 1990 year) with an individual cooling tank. The temperature of the characteristic points of the machine was measured according to the technique proposed in [12]. The change in the angular position of the circles was estimated using the principle of a pneumatic

stop, according to the technique also proposed in [12]. The temperatures of the ambient and the cutting fluid (coolant) leaving the machine were monitored. The temperatures were measured at the points shown in Fig. 1.

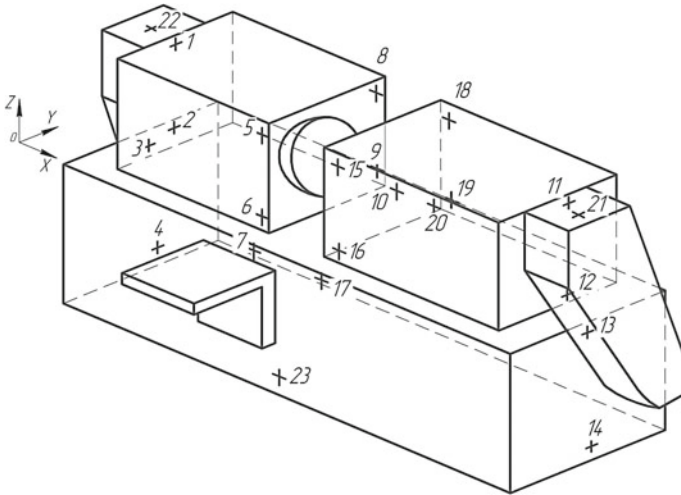


Fig. 1 Scheme of distribution of characteristic points of temperature measurement

2.1 Idling of the Machine

Within the scope of the article, individual graphs of experimental thermal characteristics are presented. However, their volume allows you to form an idea of the features of the course of thermal processes in the machine. For example, temperature changes in individual nodes of the machine depending on the duration of the machine idling are shown in Fig. 2.

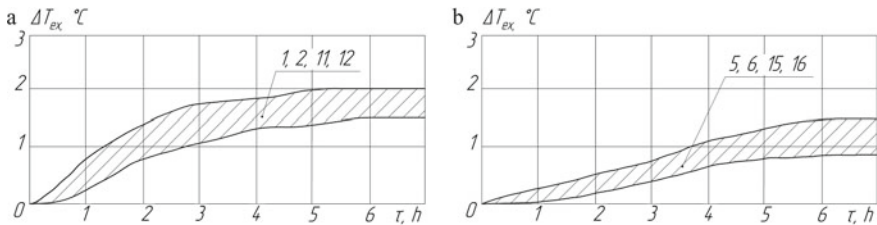


Fig. 2 Changes in the temperatures of the characteristic points of the spindle headstocks of the machine during idling: **a** excess temperatures of the outer ends (points 1, 2, 11, 12); **b** excess temperatures of the front walls (points 5, 6, 15, 16)

Excessive temperatures of the housings (rear and front walls) of the spindle headstock (Fig. 2) at points 5, 6, 15, 16, 8, 9, 18, 19 were determined by the excess temperatures

of the barrels in the area of the front bearings of the spindle units, and ranged from 0.8 to 1.5 °C. Excessive temperatures of the faces of the spindle headstocks (points 1, 2, 11, 12) were determined by the excess temperatures of the barrels in the area of the rear bearings of the spindle units and the release of heat from the drive pulleys and electric motors. The excess temperature of the faces of the spindle headstocks at points 1, 2, 11, 12 was in the range from 1.5 to 2 °C.

The excess temperature of the end faces of the bed was determined by the release of heat from the barrels of the spindle headstocks, drive pulleys and electric motors [12]. Excessive temperatures of the upper and lower parts of the surface of the bed end faces were the same. This is because a plurality of partitions that remove heat from the end face surface are adjacent to the inner upper surface of each end face. There are no partitions in the lower part of the surface of each end face of the bed, therefore, heat accumulates. The excess temperature at points 3, 13, 4, 14 ranged from 0.8 to 1.3 °C. The upper part of the bed, near the fence (points 7, 17, 10, 20), had an excess temperature in the range from 0.5 to 0.9 °C, determined by the excess temperatures of the barrels in the area of the rear bearings of the spindle units and coolant. The lower part of the bed (point 23) had the lowest excess temperature—0.1 °C, as the most distant from the heat sources. The excess temperature under the pulley casings (points 21, 22) was 3.9 °C, coolant—4 °C.

The performed measurements of the displacements of the spindle flanges when the machine is idling showed that the thermal displacements of the grinding wheels relative to the plane of the workpiece feed occur unequally (Fig. 3). The main percentage of displacements occurred in the first two hours of machine operation and was: for the left grinding wheel—8 μm, for the right one—22 μm. This means that the left grinding wheel changes its position relative to the feed disk by an amount almost three times less than the right wheel. The position of the flange of the right grinding wheel stabilized after 6–7 h of operation, while the position of the left wheel remained practically stable. Thus, during the operation of the machine, the grinding wheels took a position called “it is wider at bottom.” This is due to the fact that the main elements of the machine that are deformed under the influence of thermal processes are the outer end faces of the grinding heads and the bed, since the center of the bed was heated much weaker.

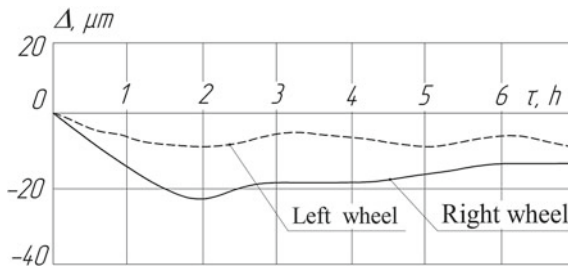


Fig. 3 Thermal displacements of grinding wheels at idling

2.2 Simulation of a Working Stroke

Changes in the temperatures of machine nodes depending on the duration of operation of electric heaters with a power of 6 kW, used to simulate the operation of the machine during grinding, are shown in Fig. 4.

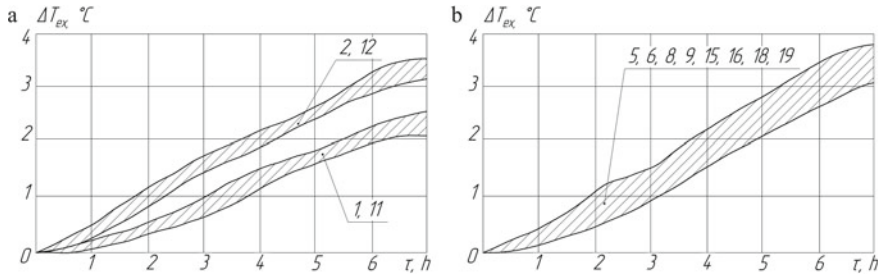


Fig. 4 Changes in the temperatures of the characteristic points of the spindle headstock of the machine during operation under thermal load ($N = 6$ kW): **a** excess temperatures of the upper (points 1, 11) and lower (points 2, 12) parts of the outer end faces of the spindle headstocks; **b** excess temperatures on the front (points 5, 6, 15, 16) and rear (points 8, 9, 18, 19) walls of the spindle headstocks

So the excess temperatures on the front and rear walls of the spindle headstock (points 5, 6, 15, 16, 8, 9, 18, 19), as well as at their end faces below (points 2, 12), had values in the range from 3.1 to 3.7 °C. At the end faces of the headstock from above (points 1, 11), the excess temperatures were in the range from 2.1 to 2.5 °C. The excess temperatures of the headstock housings at the corresponding points turned out to be practically the same and had an equal rate of rise. The upper part of the bed near the fence (points 7, 17, 10, 20) had the highest excess temperature—the temperature range was from 4.3 to 4.8 °C. The lowest excess temperature had the lower part of the bed (points 4, 14, 23)—the temperature range was from 1 to 1.2 °C. The end faces of the bed in its upper part (points 3, 13) had excess temperatures in the range from 2.3 to 2.9 °C. The excess temperature of the coolant was 14 °C.

The excess temperatures of the end faces of the bed at points 3, 13 and the end faces of the spindle heads at points 2, 12 ranged from 3.5 to 5 °C. In the upper part of the ends of the spindle heads (points 1, 11), the range of excess temperatures from 3 to 3.4 °C was recorded. Excessive temperatures on the headstock housings near the fence ranged from 5.6 to 6.7 °C. The middle part of the bed near the fence had the highest excess temperature—in the range from 12.5 to 13.5 °C. In this case, the excess temperature of the coolant was fixed at 32 °C. The lower part of the bed had the lowest excess temperature—in the range from 1 to 1.5 °C.

The nature of the temperature distribution shows that the coolant is the dominant source of heat generation during the operation of the machine under thermal load.

3 Discussion

Studies have shown that the thermal displacements of the flanges of the grinding wheels occurred unequally relative to the plane of the workpiece feed at idle speed of the machine. The change is even more striking when the machine is operating under load. The experiments showed that the stabilization of the position of the right grinding wheel did not occur in 7 h, but the rate of change of its angular position was significantly reduced. So, if at the end of the second hour of the experiment under load ($N = 6 \text{ kW}$), the change in the angular position of the right circle was $14 \text{ }\mu\text{m}$ in one hour, then after seven hours of the experiment, the hourly change was only $7 \text{ }\mu\text{m}$. In this case, the absolute values of changes in the angular positions of the grinding wheels amounted to 7 h of operation: for the right— $82 \text{ }\mu\text{m}$, for the left— $5 \text{ }\mu\text{m}$.

When the machine was operating under a load of 18 kW , changes in the angular positions of the grinding wheels were in 7 h of machine operation: for the right— $152 \text{ }\mu\text{m}$, for the left— $45 \text{ }\mu\text{m}$ (Fig. 5a).

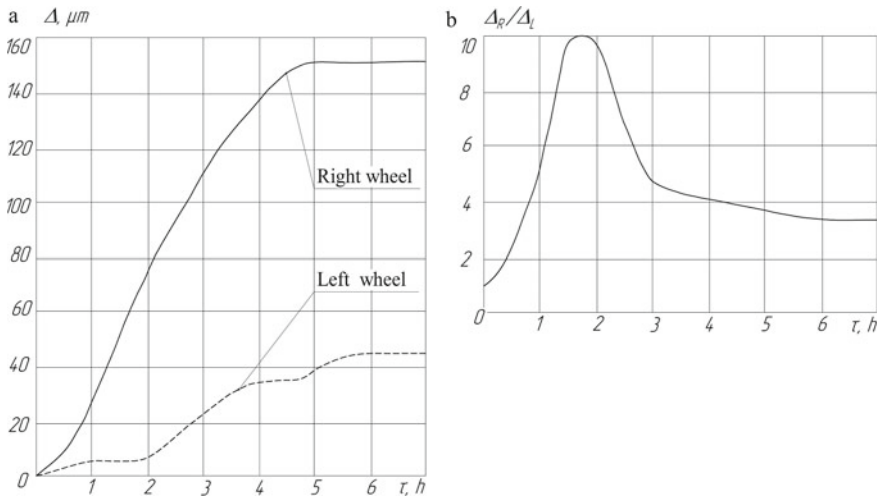


Fig. 5 Absolute and relative displacements of grinding wheels during operation under heat load ($N = 18 \text{ kW}$)

The heat released in the middle of the machine has led to a complete asymmetry of the position of the wheels relative to the plane of the workpiece feed, thereby violating one of the basic requirements for high-quality grinding. The position of the flanges of the grinding wheels stabilized after 5–6 h of heating.

The change in the asymmetry of the displacements of the grinding wheels Δ_R/Δ_L (the ratio of the displacement of the right grinding wheel Δ_R to the left Δ_L) is shown in Fig. 5b at a heat load of 18 kW . The graph shows that asymmetry had a maximum value after 1.5 h of machine operation— $\Delta_R/\Delta_L = 10$, in contrast to the initial value—1.

When the machine was operating under a thermal load, the bed in its central part warmed up more than the ends, which led to a change in the relative position, called “it

is narrower at the bottom.” When the machine was operating under a thermal load, the bed in its central part warmed up stronger than the end faces. This led to a change in the relative position called “it is narrower at the bottom.”

Thus, it was experimentally found that during the operation of the machine, thermal deformations varied in a wide range, both in magnitude and in direction.

The elimination of the time factor made it possible to obtain the dependences: changes in the angular positions of grinding wheels on the excess temperature of the coolant (Fig. 6); changes in the values of the end faces runouts of the machined rollers from the values of the angular displacements of the grinding wheels (Fig. 7).

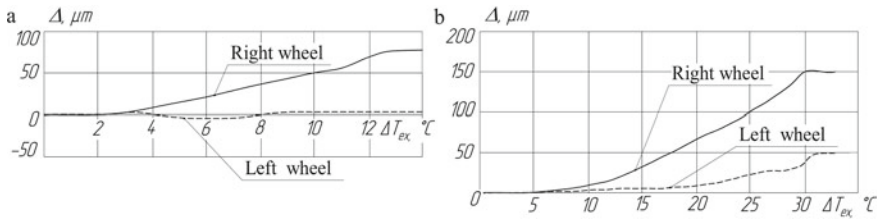


Fig. 6 Changes in the angular positions of the grinding wheels depending on the excess temperature of the coolant: **a** when the machine is operating under a thermal load $N = 6$ kW; **b** when the machine is operating under a thermal load $N = 18$ kW

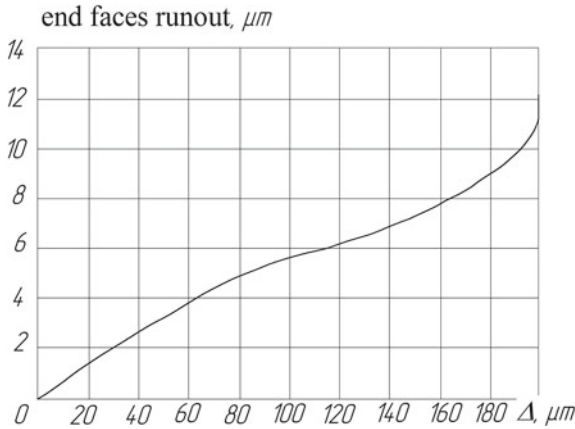


Fig. 7 Influence of thermal displacements of grinding wheels on the end runout of the roller

4 Conclusion

1. The thermal characteristics of the machine when idling and when operating under thermal load are different. This is due to the fact that the units of the face grinding machine when idling and when operating under heat load are heated unequally. The highest temperatures when the machine is idling are at the end faces of the spindle

headstocks and the bed, and when working under thermal load, the parts of the bed are located near the fence of the grinding zone and the endfaces of the spindle headstocks facing the fence.

2. The temperature displacements of the wheels are not the same. The displacement of the right grinding wheel relative to the workpiece feed disk is three times greater than that of the left one at idling and five times greater when working under heat load.
3. When the machine is idling, the grinding wheels due to thermal deformations move in the direction “it is wider at the bottom,” which deprives the work area of the workpiece calibration area and leads to a deterioration in the grinding accuracy.
4. When working under heat load, the machine gradually warms up, and the relative position of the circles gradually changes from “it is wider at the bottom” to “it is narrower at the bottom,” i.e., the setting of the machine, its work area, changes spontaneously. At the same time, these changes continue with varying intensity over the entire operating spindle time.
5. Grinding wheels change their position in the vertical plane in proportion to the value of excess coolant temperatures and the operating time of the machine.
6. The face runout of the machined rollers increases in proportion to the magnitude of the angular displacements of the grinding wheels.
7. The grinding wheels move relative to the feed disk by different amounts, which creates an asymmetry of the work area relative to the feed disk (it is technological base of the workpiece). This creates an asymmetry of the power loads on the workpiece, which violates the laws of rotation of the workpiece up to a complete stop.
8. The absolute value of the changing non-parallelism of the grinding wheels was 0.13 mm after 3 h of operation. This can be considered quite large, since during grinding the entire removable allowance is 0.05–0.07 mm. A rational machining allowance is associated with the relative position of the grinding wheels. Consequently, if this position changes (increases), and the specified allowance remains constant, then the processing conditions deviate from the specified ones.

The performed studies have shown that thermal deformations of double-sided face grinding machines with an arc trajectory of the workpiece feed can violate the main requirement for the precise operation of the machine—the symmetry of the processing conditions at both end faces of the workpiece. Consequently, in order to further improve the quality of the work of machines of this type, it is necessary to use measures that would reduce thermal deformations and ensure the symmetry of the machine in all temperature–time ranges.

References

1. Luk'yanov KY (2011) More efficient grinding of conical roller-bearing surfaces by the end of a discontinuous wheel. *Russ Engin Res* 31:185–186. <https://doi.org/10.3103/S1068798X11020158>
2. Jurko J, Panda A, Valíček J et al (2016) Study on cone roller bearing surface roughness improvement and the effect of surface roughness on tapered roller bearing service life. *Int J Adv Manuf Technol* 82:1099–1106. <https://doi.org/10.1007/s00170-015-7449-8>

3. Jiang J, Ge P, Sun S et al (2017) The theoretical and experimental research on the bearing inner ring raceway grinding process aiming to improve surface quality and process efficiency based on the integrated grinding process model. *Int J Adv Manuf Technol* 93:747–765. <https://doi.org/10.1007/s00170-017-0462-3>
4. Yu G, Wang Q, Song Z et al (2019) Toward the temperature distribution on ball bearing inner rings during single-grit grinding. *Int J Adv Manuf Technol* 102:957–968. <https://doi.org/10.1007/s00170-018-03238-0>
5. Zhao B, Guo X, Yin L et al (2020) Surface quality in axial ultrasound plunging-type grinding of bearing internal raceway. *Int J Adv Manuf Technol* 106:4715–4730
6. Shi X, Zhu K, Wang W et al (2018) A thermal characteristic analytic model considering cutting fluid thermal effect for gear grinding machine under load. *Int J Adv Manuf Technol* 99:1755–1769. <https://doi.org/10.1007/s00170-018-2562-0>
7. Shi X, Wang W, Mu Y et al (2019) Thermal characteristics testing and thermal error modeling on a worm gear grinding machine considering cutting fluid thermal effect. *Int J Adv Manuf Technol* 103:4317–4329. <https://doi.org/10.1007/s00170-019-03650-0>
8. Ortega N, Bravo H, Pombo I et al (2015) Thermal analysis of creep feed grinding. *Proc Eng* 132:1061–1068. <https://doi.org/10.1016/j.proeng.2015.12.596>
9. Batako ADL, Morgan MN, Rowe BW (2013) High efficiency deep grinding with very high removal rates. *Int J Adv Manuf Technol* 66:1367–1377. <https://doi.org/10.1007/s00170-012-4414-7>
10. Wang S, Zhou B, Fang C et al (2017) Research on thermal deformation of large CNC gear profile grinding machine tools. *Int J Adv Manuf Technol* 91(1–4):577–587. <https://doi.org/10.1007/s00170-016-9442-2>
11. Wang X, Yu T, Sun X et al (2016) Study of 3D grinding temperature field based on finite difference method: considering machining parameters and energy partition. *Int J Adv Manuf Technol* 84:915–927. <https://doi.org/10.1007/s00170-015-7757-z>
12. Nikitina IP, Polyakov AN (2019) Experimental study of double-sided face grinding machine tool. *J Phys Conf Ser* 1399(4):044026. <https://doi.org/10.1088/1742-6596/1399/4/044026>



Calculating the Flexure of Circular Plates with Stiffening Rings

S. V. Konev¹, A. S. Fainshtein¹(✉), and I. E. Teftelev²

¹ Nosov Magnitogorsk State Technical University, 38, Lenin pr., Magnitogorsk 455000, Russia

² Magnitogorsk Hardware-Metallurgical Plant—United Joint Stock Company “MMK-Metiz”,
5, Metiznikov st., Magnitogorsk 455002, Russia

Abstract. The authors performed calculation for thin rigid circular plates with stiffening rings by using the Ritz-Timoshenko variational energy method. The flexure of rings with symmetrical cross-sectional shape gives rise to strain fields that are symmetric about the middle plane of the plate. However, when there is a stiffening ring, the radial stresses existing within the section of the plate will be asymmetric. This fact must be double-checked by calculating the potential strain energy of the stiffening ring more precisely. The calculation was based on the assumption that the middle plane curvature of the ring element was the same as that of the carrier plate, subject to the Kirchhoff hypothesis on normal middle plane element. The approximating function is defined as a beam function for a stepped beam with unit thickness. The obtained findings allowed us to calculate the rigidity of a welding wire spool flange. The analysis of the obtained relationships showed that the addition of one or two stiffening rings resulted in the reduction of spool flange flexure by 29–64%. The effect of the stiffener on the flange flexure when it is arranged within the first (from the side of the inner radius) one-third part of the flange is 2.5–3 times higher than the effect resulting when the stiffener is arranged within the second one-third part of the flange.

Keywords: Circular plate · Stiffening rings · Flexure · Potential energy · Approximating function · Spool flange

1 Introduction and Problem Statement

Strain of thin rigid circular plates with radial stiffeners was earlier calculated by the authors using the variational energy method [1]. However, when applying the above method to make calculations for plates with stiffening rings, the potential strain energy of the stiffening ring must be known.

The potential flexural energy of the ring as a circular plate depends on its cross-sectional shape. The flexure of rings with symmetrical cross-sectional shape is well-studied [2–5]. Such flexure gives rise to strain fields that are symmetric about the middle plane of the plate. When there is a stiffening ring arranged someway on the carrier plate, the radial stresses existing within the section of the plate will be asymmetric. This fact must be double checked by calculating the potential strain energy of the stiffening ring more precisely.

The general case of strain calculation at any loading of the plate was studied by Timoshenko [6]. To calculate the potential strain energy of a stiffening ring, which is somehow attached to the flexed carrier plate, special solutions must be obtained under certain loading conditions.

2 Research Goal

The goal of this research is to calculate the stress–strain behavior of a round-shaped circular plate with stiffening rings by using the variational method.

3 Research Methodology

The calculation is made based on the variational Ritz–Timoshenko method. For this purpose, the known value of potential strain energy for a round-shaped thin rigid plate was used in combination with the formula for finding the potential energy of flexed stiffening ring of the plate that was obtained by the authors. Calculations were narrowed down to circular plates (flanges) of monolithic plastic spools used for welding wire winding [7].

4 Problem Solution

According to the Ritz–Timoshenko method, solving the problem of determining the stress–strain behavior of a stiffened plate comes down to find the minimum of the composite function

$$En = U + V$$

where U and V are the potential strain energy and the external load potential. Let us write down the potential strain energy as the sum of potential energies of the flexed carrier plate and stiffening rings as follows:

$$U = U_1 + U_2$$

The potential strain energy of a circular axisymmetrically loaded and symmetrically deformed plate [6, 8] can be written down as follows:

$$U_1 = \frac{D}{2} \int_a^b \int_0^{2\pi} \left[\left(\frac{\partial^2 w}{\partial r^2} + \frac{\partial w}{r \partial r} \right)^2 - \frac{2(1-\nu)}{r} \left(\frac{\partial^2 w}{\partial r^2} \frac{\partial w}{\partial r} \right) \right] r dr d\theta \quad (1)$$

where D is the flexural rigidity of the plate, a and b

are the inner and the outer circular plate diameters, $w(r)$ is the function of plate flexures, r is the radius, and ν is the Poisson's ratio that is equal to 0.3.

Let us define the procedure for calculating the potential strain energy of a plate with stiffening rings. For this purpose, we shall compare the calculation of potential energy

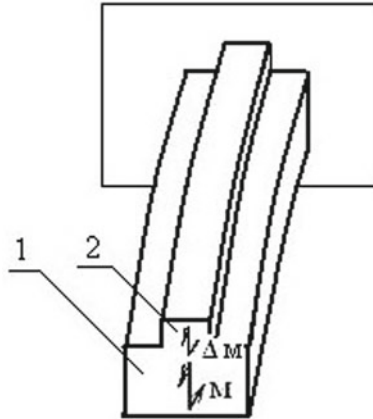


Fig. 1 Flexure of composite section

in a flexed beam whose section is comprised of the main element 1 and the additional element 2 (Fig. 1) with a plate that is flexed together with a monolithically attached stiffener.

When the beam is flexed as shown in Fig. 1, the potential energy of the main element that corresponds to the internal momentum M is added to the potential energy of the additional element, which corresponds to the partial internal momentum ΔM . The values M and ΔM are determined based on the values of actual stresses in the elements. As opposed to the beam, the flexure of a circular plate gives rise to two different types of momenta including the radial M_r and the circumferential M_θ momenta whose values depend on the stresses σ_r and σ_θ , respectively. Therefore, let us assume that the potential strain energy of a stiffened plate will correspond to the sum of individually calculated potential strain energies of the main plate body and the stiffening rings. We shall not take into account the potential energy of the transverse force Q .

Let us analyze the pattern and the level of stresses in the stiffening ring. Due to the fact that the stiffening ring of the given flange forms an integral part of the plate, the strains of the stiffener on the interfacing surfaces of the stiffener and the plate will be exactly the same as the strains of the plate. In other words, the middle plane curvature of the plate and the stiffener, the flexure w , and the rotation angle θ of radial section perpendicular to the radius of the stiffener will be the same at the point lying on the radius r (Fig. 2).

The stiffener height is normally consistent with the plate thickness. For example, the stiffener height h_r for the above-mentioned plastic wire winding spool D200 (Fig. 2) is 0.8–1.5 mm when the plate (flange) thickness h_f is 2–3 mm. Therefore, the plate thickness together with the stiffener height still remains less than one fifth of the plate diameter. In addition, any spool flange flexures exceeding one fourth of its thickness are not acceptable from technological perspective. Thus, we believe that the Kirchhoff hypothesis is respected in case with the stiffening ring as is the case with the circular carrier plate [9].

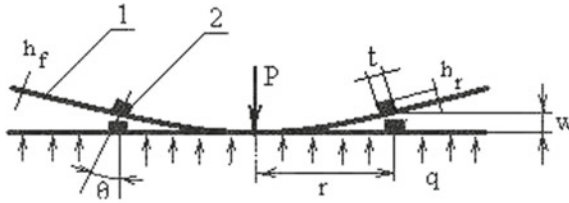


Fig. 2 Radial section of a flexed plate with a stiffening ring 1—plate, 2—stiffener

The level of stresses existing in a thin rigid plate that is symmetric about the middle plate was determined by Germain [10, 11] and linearly depends on the distance to the middle layer z :

$$\sigma_r = \frac{Ez}{1 - \nu^2} \left(\frac{\partial^2 w}{\partial r^2} + \frac{\nu}{r} \frac{\partial w}{\partial r} \right) \tag{2}$$

The formula for finding flexures (2) for a plate that is loaded with uniformly distributed stress q and fixed along the inner peripheral surface is presented in [2].

Distribution of stresses σ_r across the height of the stiffener will have a linear pattern (Fig. 3) under the above-made assumptions. The values of these stresses will vary from

$$\sigma_r = \frac{E \frac{h_f}{2}}{1 - \nu^2} \left(\frac{\partial^2 w}{\partial r^2} + \frac{\nu}{r} \frac{\partial w}{\partial r} \right) \text{ to } \sigma_r = \frac{E \left(\frac{h_f}{2} + h_r \right)}{1 - \nu^2} \left(\frac{\partial^2 w}{\partial r^2} + \frac{\nu}{r} \frac{\partial w}{\partial r} \right).$$

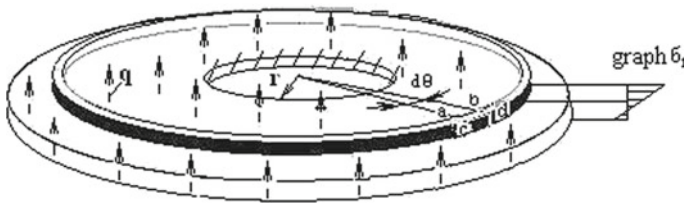


Fig. 3 Radial stresses existing in a stiffened plate

Stresses σ_θ (Fig. 4) will be formed in the stiffener at the same time with stresses σ_r . Their distribution across the height of the stiffening ring will follow the same pattern. The level of these stresses existing in the same plate loaded with uniformly distributed stress q and fixed along the inner peripheral surface is

$$\sigma_r = \frac{Ez}{1 - \nu^2} \left(\frac{1}{r} \frac{\partial w}{\partial r} \frac{\partial^2 w}{\partial r^2} + \frac{\partial^2 w}{\partial r^2} \right).$$

Due to the fact that the ring is in the plane stress condition under the above-made assumptions, the specific potential energy of elastic change in volume and shape of stiffener points at the principal stresses [12]

$$u = \frac{1}{2E} (\sigma_1^2 + \sigma_2^2 - 2\nu\sigma_1\sigma_2).$$

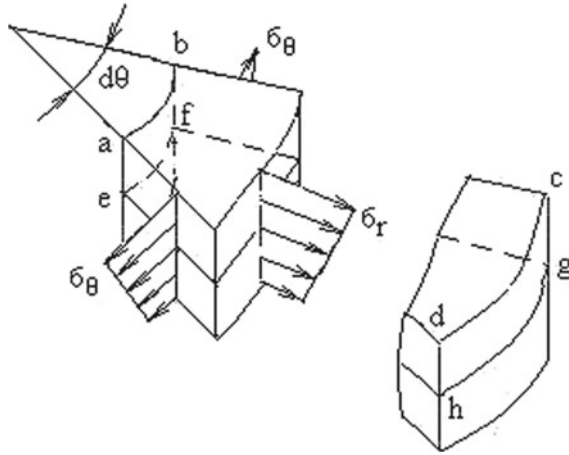


Fig. 4 Element of the stiffener shown in Fig. 3

Using polar coordinates and taking into account the symmetrical loading of the stiffener, the above formula can be written as

$$u = \frac{1}{2E} [(\sigma_r \cos^2 \theta + \sigma_\theta \sin^2 \theta)^2 + (\sigma_r \sin^2 \theta + \sigma_\theta \cos^2 \theta)^2 - 2\nu(\sigma_r \cos^2 \theta + \sigma_\theta \sin^2 \theta)(\sigma_r \sin^2 \theta + \sigma_\theta \cos^2 \theta)].$$

Let us write down the total potential flexural energy of the stiffening ring taking the integration limits into account:

$$\int_{r_i}^{r_i+t} \int_0^{2\pi} \int_{\frac{h_f}{2}}^{\frac{h_f}{2}+h_r} u dr d\theta dz, \tag{3}$$

where r_i is the radius on the inner edge of the i -th stiffener and t is the width of the stiffener (Fig. 2). Hence,

$$U_2 = \sum_{i=1}^n \int_{r_i}^{r_i+t} \int_0^{2\pi} \int_{\frac{h_f}{2}}^{\frac{h_f}{2}+h_r} u dr d\theta dz,$$

where n is the number of stiffening rings.

The load behavior (the potential reverse load) when the stiffened plate is loaded with uniformly distributed stress q applied by the even surface of the circular plate (flange) (Figs. 2 and 3) can be expressed as an integral taken for the area F of the plate by

multiplying the elementary force $qrdrd\theta$ by the flexure w [12]. Given the constant value of q

$$A = q \iint_F w(r)rdrd\theta. \tag{4}$$

The total energy in the system $En = U_1 + U_2 - A$. Thus, our problem can be narrowed down to defining the minimum of the composite function made up of Eqs. (1), (3), and (4):

$$En = \frac{D}{2} \int_a^b \int_0^{2\pi} \left[\left(\frac{\partial^2 w}{\partial r^2} + \frac{\partial w}{r \partial r} \right)^2 - \frac{2(1-\nu)}{r} \left(\frac{\partial^2 w}{\partial r^2} \frac{\partial w}{\partial r} \right) \right] rdrd\theta + \sum_{i=1}^n \int_{r_i}^{r_{i+1}} \int_0^{2\pi} \int_{\frac{h_f}{2}}^{\frac{h_f}{2}+h_r} udrd\theta dz - q \iint_F w(r)rdrd\theta. \tag{5}$$

The n number of stiffening rings dividing the radius of the plate into $n + 1$ equal parts is described in the Eq. (7). Individual stress state defined by the function w is determined for every stiffener marked under the summation symbol.

According to the Ritz-Timoshenko method [13], the approximating function $w(r)$ of flexure for a plate with stiffening rings must be defined to obtain the approximate solution of the problem. When the problem is solved to a first approximation (with the leading coefficient of the series a_1), the selected approximating function must be as close to the exact problem solution as practical provided that all the boundary conditions are met. Let us follow the recommendations [13–15] to define this function as a beam function, which is based on the stepped radial section configuration of a plate with stiffening rings. The procedure described in the study [16] was applied in this case where a stepped beam was replaced by an equivalent beam with uniform section, applying additional momenta and transverse forces at the points of changing sectional dimensions of the original stepped beam:

$$w_1(r) = \frac{qa_1}{EI} \left[-\frac{(b-a)^2(r-a)^2}{4} + \frac{(b-a)(r-a)^3}{6} - \frac{(r-a)^4}{24} + A_1(r) + A_2(r) \right], \tag{6}$$

where $I = \frac{h_f^3}{12}$ is the inertia moment of the strip beam of dimensionless unit thickness, with profile height equal to the plate thickness h_f .

The origin of coordinates in the formula (6) is defined on the symmetry axis of the ring and corresponds to the Figs. 2 and 3. The first terms of the sum are written using the method of initial parameters [17]. $A_1(r)$ and $A_2(r)$ are the terms corresponding to even and odd sections of the beam, which are based on the effect of additionally applied momenta and concentrated forces on beam flexure and taken into account when the coordinate of the selected point is greater than the coordinate of the applied load.

For example, for two stiffeners that divide the radius into three equal segments inside the ring:

$$w(r) = \begin{cases} w_1(r), & \text{if } a \leq r \leq r+l, \\ w_1(r) + w_2(r), & \text{if } a+l \leq r \leq r+l+t, \\ w_1(r) + w_2(r) + w_3(r), & \text{if } a+l+t \leq r \leq r+2l+t, \\ w_1(r) + w_2(r) + w_3(r) + w_4(r), & \text{if } a+2l+t \leq r \leq r+2l+2t, \\ w_1(r) + w_2(r) + w_3(r) + w_4(r) + w_5(r), & \text{if } a+2l+2t \leq r \leq b, \end{cases}$$

where

$$\begin{aligned} w_1(r) &= \frac{q}{EI} \left[-\frac{(b-a)^2(r-a)^2}{4} + \frac{(b-a)(r-a)^3}{6} - \frac{(r-a)^4}{24} \right], \\ w_2(r) &= \frac{-\mu q}{EI} \left[\left[-\frac{(b-a)^2}{2} + (b-a)l - \frac{l^2}{2} \right] \frac{(r-a-l)^2}{2} + (b-a-l) \frac{(r-a-l)^3}{6} \right] \\ w_3(r) &= \frac{\mu q}{EI} \left[\left[-\frac{(b-a)^2}{2} + (b-a)(l+t) - \frac{(l+t)^2}{2} \right] \frac{(r-a-l-t)^2}{2} \right. \\ &\quad \left. + (b-a-l-t) \frac{(r-a-l-t)^3}{6} \right], \\ w_4(r) &= \frac{-\mu q}{EI} \left[\left[-\frac{(b-a)^2}{2} + (b-a)(2l+t) - \frac{(2l+t)^2}{2} \right] \frac{(r-a-2l-t)^2}{2} \right. \\ &\quad \left. + (b-a-2l-t) \frac{(r-a-2l-t)^3}{6} \right], \\ w_5(r) &= \frac{\mu q}{EI} \left[\left[-\frac{(b-a)^2}{2} + (b-a)(2l+2t) - \frac{(2l+2t)^2}{2} \right] \frac{(r-a-2l-2t)^2}{2} \right. \\ &\quad \left. + (b-a-2l-2t) \frac{(r-a-2l-2t)^3}{6} \right], \end{aligned}$$

t is the width of the stiffener, $l = \frac{b-a-2t}{3}$, $\mu = \frac{k-1}{k}$ and k is equal to the ratio between the inertia moment of the section of a strip beam with unit width near the stiffener and the inertia moment of the section of the same strip beam whose stiffener height is equal to the plate thickness. Calculations are based on $k = 5$, which corresponds to the parameters used in this research. Calculations are performed in Mathcad [18].

The formula (6) meets the following kinematic boundary conditions: $w|_{r=a} = 0$ and $\frac{\partial w}{\partial r}|_{r=a} = 0$.

Let us define the coefficient a_1 based on the following condition of the minimum of the composite function (7): $\frac{\partial En}{\partial a_1} = 0$. Let us note that when $w(r)$ (6) is substituted into the formula (7), En represents a quadratic function with relation to a_1 . Moreover, for the first two terms of the sum (7) defining U , a_1 occurs quadratically; whereas for the third term of the sum defining A , it occurs to the power of one, and its point of minimum can be found using the following formula [19]:

$$a_1 = \frac{A}{2U}. \tag{7}$$

As a result, the flexure of a plate with n number of stiffening rings is expressed in the formula (6) into which from (7) is substituted, and we obtain the following formula for the flexure of a plate with n number of stiffening rings:

$$w_1(r) = \frac{qA}{2U} \left[-\frac{(b-a)^2(r-a)^2}{4} + \frac{(b-a)(r-a)^3}{6} - \frac{(r-a)^4}{24} + A_1(r) + A_2(r) \right],$$

Graphs representing the obtained relationships for the two commercially used models of plastic spools D200 and D300 for welding wire winding are illustrated in Figs. 6a, b, respectively, together with the parameters provided in Table 1. Stiffening rings with width $t = 3$ mm and various heights are arranged on the flange between the radii a and b as shown in the diagram below (Fig. 5):

Table 1 Parameters of monolithic spools for welding wire winding

Parameter	Inner radius	Outer radius (wire winding radius)	Flange thickness	Elasticity modulus of the material (high-impact polystyrene, [20]) at flexure	Stiffener height	Stiffener width	Load intensity
Designation, unit	$a, \text{ m}$	$b, \text{ m}$	$h_f, \text{ m}$	$E, \text{ N/m}^2$	$h_r, \text{ m}$	$t, \text{ m}$	$q, \text{ N/m}^2$
Value, D200	5×10^{-2}	8.5×10^{-2}	3×10^{-3}	26.5×10^8	$0.8\text{--}2 \times 10^{-3}$	5×10^{-3}	1×10^4
Value, D300	8.5×10^{-2}	13.5×10^{-2}			$3\text{--}5 \times 10^{-3}$		

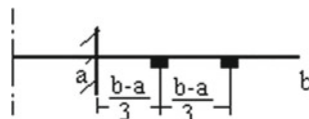


Fig. 5 Arrangement of three stiffeners

As we can see from the graphs, the flange flexure is significantly reduced with the arrangement of stiffening rings. For example, the flexure is reduced from 3.1×10^{-4} m to 2.2×10^{-4} m at the 0.085 m radius of the D200 spool (Fig. 6a) and from 3.05×10^{-4} m to 1.1×10^{-4} m at the 0.13 m radius of the D300 spool (Fig. 6b). Therefore, the elastic strains of the ribbed spool flange are reduced by 29–64% depending on stiffener dimensions and spool model.

The obtained formula allows to examine the optimum arrangement of stiffening rings at the spool flange. This is most clearly demonstrated when the position of a single stiffener is changed. Figure 6 illustrates the graph of behavior for D200 spool

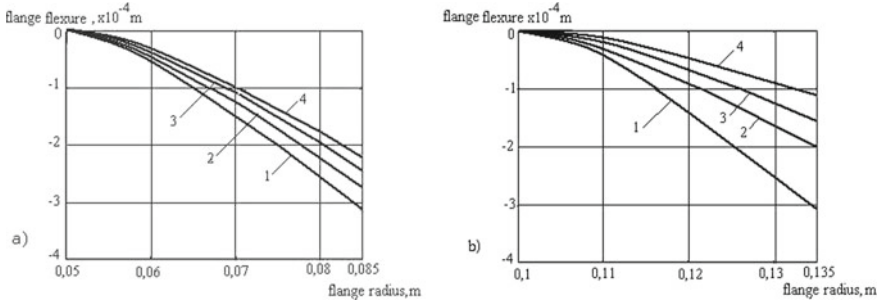


Fig. 6 **a** Flexures of D200: 1—flexure of a ribless flange; 2—flexure of a flange with stiffener height $h_r = 0.0008$ m; 3—flexure of a flange with stiffener height $h_r = 0.0015$ m; 4—flexure of a flange with stiffener height $h_r = 0.002$ m. **b** Flexures of D200 (**a**) and D300 (**b**) spool flanges: 1—flexure of a ribless flange [2] 2—flexure of a flange with stiffener height $h_r = 0.003$ m; 3—flexure of a flange with stiffener height $h_r = 0.004$ m; 4—flexure of a flange with stiffener height $h_r = 0.005$ m.

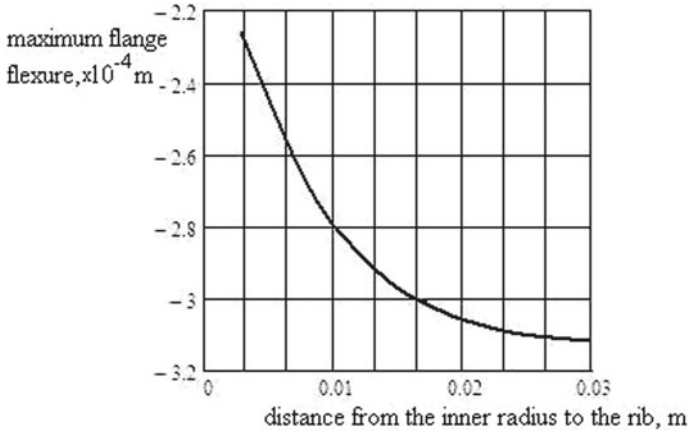


Fig. 7 Effect of the stiffening ring position on the flexure of spool flange

flange flexures when the stiffening ring is “shifted” from the inner flange radius a to the outer flange radius b flange stiffener parameters selected for the analysis are as follows: stiffener width = 0.005 m and stiffener height = 0.008 m. All the other parameters correspond to the data provided in Table 1.

The analysis of the graph (Fig. 7) shows that the effect of the stiffener on the flexure of flange when it is arranged within the first (from the side of the inner radius) one-third part of the flange is 2.5–3 times higher than the effect resulting when the stiffener is arranged within the second one-third part of the flange. The average slope ratio of the graph between 0.003 m and 0.01 m from the inner flange radius is equal (at the selected coordinates) to $2.7/2 = 1.35$; whereas between 0.01 and 0.02 m, such average slope ratio is equal to $1.3/3 = 0.43$, which is three times smaller. The slope ratio of the graph within the third segment between 0.02 and 0.03 m approaches zero, which indicates minimal

effect of the stiffening ring arranged in that position on the flexure of the flange. Thus, it is preferred to arrange stiffening rings on the inner one-third part of the flange.

5 Conclusions

1. Formulas for calculating flexures of thin rigid circular plates with stiffening rings were obtained using the variational Ritz-Timoshenko method.
2. It was found that the arrangement of two stiffening rings—whose width and height were equal to the thickness of the spool flange—at the flange of a monolithic welding wire spool reduced the flexure of spool flange by 29–64% depending on technologically acceptable stiffener dimensions and spool model.
3. The obtained relationships were applied during the design of plastic spools used for welding wire winding. It was recommended to arrange stiffening rings at the first (from the side of the inner radius) one third of the distance between the inner and the outer spool flange diameters.

References

1. Konev SV, Fainshtein AS, Teftelev IE (2021) Calculating the flexure of circular plates with radial stiffening ribs. In: Proceedings of the 6th international conference on industrial engineering (ICIE 2020), Springer
2. Weinberg DV, Weinberg ED (1970) Plate calculations. Budivel'nik, Kiev
3. Murakami Y (2016) Theory of elasticity and stress concentration. Kyushu University, Japan
4. Timoshenko SP, Goodier J (1959) Theory of elasticity. Nauka, Moscow
5. Timoshenko SP, Voinovsky-Krieger S (2021) Theory of plates and shells. McGraw-Hill Book-Company, New York, Proceedings of the 6th international conference on industrial engineering (ICIE 2020), Springer
6. Konev SV, Mikhaylets VF, Fainshtein AS, Teftelev IE (2018) Analysis of the characteristics of the stress state of the flange of the winding device as the annular plate. Vestnik of Nosov Magnitogorsk State Technical University 3(16):98–102
7. GOST RF 25445 (2018) (CMEA standard 2735). Welding wire reels, spools and cores. Basic dimensions
8. Dokshinin SG, Mityaev AE, Troshin SI (2017) Structural machinery mechanics. Publishing house of the Siberian Federal University, Krasnoyarsk
9. Rabotnov YN (1988) Deformable solid mechanics. Nauka, Moscow
10. https://en.wikipedia.org/wiki/Sophie_Germain
11. Pisarenko GS (ed) (1975) Resistance of materials. Vyscha Shkola, Kiev
12. Darkov AV, Shpiro GS (1975) Strength of materials. Vysshaya shkola, Moscow
13. Gots AN (2010) Numerical method of calculation in power plant engineering. Training manual. Part 2. Publishing house of Vladimir State University, Vladimir
14. Donnell LH (1976) Beams, plates and shells. McGraw-Hill Book-Company, Ohio
15. Ivanov VN (2004) Variational principles and problem-solving techniques related to the elasticity theory. Publishing house of the People's Friendship University of Russia, Moscow
16. Konev SV, Fainshtein AS, Teftelev IE (2020) Application of Kantorovich-Vlasov method for shaped plate bending problem. In: Proceedings of the 6th international conference on industrial engineering (ICIE 2019) vol 1, pp 91–100

17. Belyaev NM (1976) Strength of materials. Nauka, Moscow
18. Kiryanov DV (2012) Mathcad 15/Mathcad Prime 1.0. BHV-Peterburg, S.- Peterburg
19. Zobin NM, Krein SG (1978) Mathematical analysis of smooth functions. Voronezh State University, Voronezh
20. GOST USSR 20282-86 (1991) General purpose polystyrene. Izdatelstvo standartov, Moscow



Research and Analysis of Rational Parameters for a Conveying Mechanism of a Multi-operation Roller Machine

G. A. Bahadirov and M. I. Nosirov(✉)

Institute of Mechanics and Seismic Stability of Structures, Academy of Sciences of the Republic
of Uzbekistan, 33, Durmon yuli street, Tashkent, Uzbekistan100125

Abstract. The relation of forces in the process of feeding of a semi-finished leather product into the working area of a multi-operation machine by a conveying device is studied. The relations between the pulling force and the radius of the drive shaft, and the friction coefficient and the angle of contact of the semi-finished leather product with the drive shaft are determined. It was determined that with an increase in the angle of contact and an increase in the friction coefficient, the pulling force increases. Therefore, the radius of the drive shaft must be large enough to pull in the semi-finished leather product. In order to develop a rational design of the conveying mechanism, an inequality was derived, including the parameters of transportation and retraction of a semi-finished leather product into the processing zone; it allows choosing the rational parameters of the conveying mechanism by setting the parameters of the processed leather semi-finished product. The use of the results obtained will increase the productivity of the technological process of extracting moisture from the leather semi-finished product, taking into account its physical and mechanical properties. The results of the research will be used in research and development work in the design of new roller machines and conveying mechanisms.

Keywords: Conveying mechanism · Tractive force · Semi-finished leather product · Angle of contact · Free roller · Spreading table · Machining · Planing · Buffing · Average thickness · Passage width

1 Introduction

It is known that in every country, leather resources are scattered throughout the territory; therefore, the presence of small- and medium-sized enterprises in regions makes it possible to efficiently and economically use leather raw materials. This requires the development and creation of compact machines and equipment for the primary mechanical processing of the semi-finished leather product in small batches.

In modern large tanneries, numerous mechanical and physical–mechanical operations require the use of a whole range of appropriate equipment. To meet the needs of the leather industry, up to 90 types of technological equipment are required [1–5].

Despite the wide variety of types of machines and mechanisms used in the leather industry, there is still a substantial number of non-mechanized operations, especially in small enterprises. The level of mechanization, i.e., the share of mechanized labor in the total work time expenditures is 50–80%. In addition, even in mechanized operations, the worker has to perform manual heavy and monotonous auxiliary operations. Most of the technological operations in leather and fur production are, in essence, machine-manual operations [6–11].

At small enterprises, it is impractical to use expensive, specialized high-performance technological machines for mechanical processing of the semi-finished leather products, because due to the small volume of production, they will stand idle for a long time and occupy production areas.

Consequently, the development of a machine that performs several technological operations is relevant.

2 Development of a Design of Multi-operation Machine

We have developed the design of a multi-operation machine for the mechanical processing of the semi-finished leather product [12–19]. The machine is designed to perform several mechanical operations in sequence, such as squeezing, setting, planing, softening, rolling, and buffing (Fig. 1).

The multi-operation machine contains a working roller 1 cantilevered on an axle 2, conveying the roller 3, mounted on an axle 4 interacting with an adjustable spring 5; a pressure shaft 6 is mounted on an axle 7. A lever 8 has a common axle 9 with a lever 10, and the lever 10 is equipped with a lock of the initial position (not shown in the figure), and the lever 8 is equipped with a stop 11 for interaction with the lever 10. A supporting roller 12 is installed on lever 8. Between the pressure roller 6 and the supporting roller 12, there is a spreading table 13 rigidly connected to the pressure roller 6. When pedal 14 is pressed, the stops 19 and 20 move to their extreme positions, and the lever 8 by stop 21 moves to the extreme position by means of rod 15, the lever 8 moves to the area of processing leather or skin 18. After finishing the treatment, pedal 14 is lowered, and under the springs 16 and 17, the conveying roller 3 and the pressure roller 6 are folded back and stopped.

The multi-operation machine contains a set of working rollers 1 for fleshing, gouging, setting, wringing, rolling, and buffing [20].

3 Study of the Process of Material Feeding

Consider the force relation between the shaft of the conveying mechanism and the leather semi-finished product. The conveying device consists of a drive shaft 1 and a driven shaft 2, with a spreading table 3 located between them. The drive shaft 1 rotates forcibly, and the driven shaft 2 rotates due to the friction between the leather semi-finished product 4 and the driven shaft 2 (Fig. 2).

The drive shaft 1 pulls in and feeds the semi-finished leather product 4 into the machining zone. To pull in the leather semi-finished product by the drive shaft, the condition $T_2 \geq T_1$ must be met (Fig. 3).

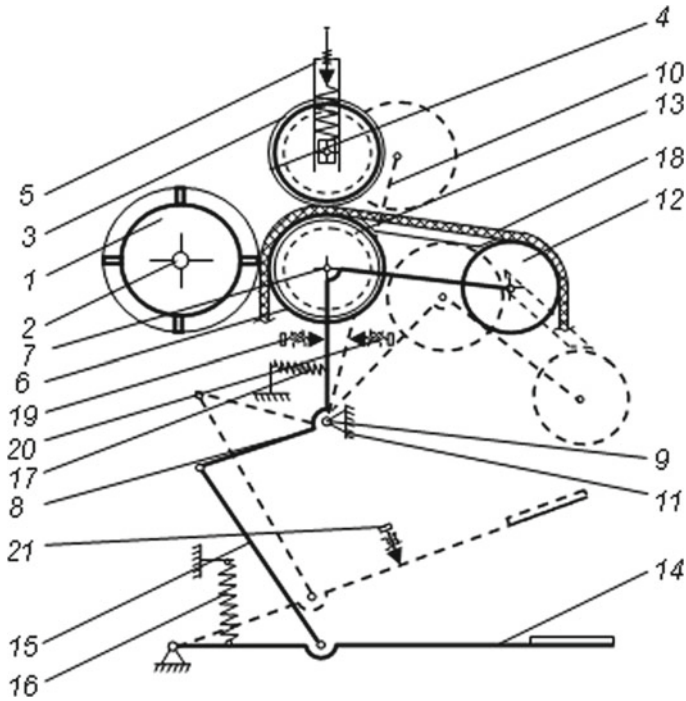


Fig. 1 Scheme of a multi-operation machine for mechanical processing of the semi-finished leather product

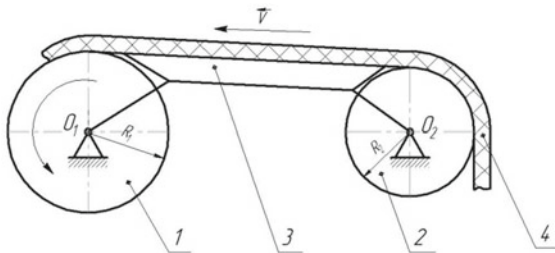


Fig. 2 Scheme of the conveying mechanism. 1—drive shaft; 2—driven shaft; 3—spreading table; 4—semi-finished leather product

Figure 2 shows an expression for the pulling force:

$$T_2 = \mu N_1 \cos(90 - \alpha) = \mu N_1 \sin \alpha. \tag{1}$$

Let us conditionally divide the semi-finished leather product into four sections.

Here, N_1 is the normal response of the drive shaft to an element of the leather semi-finished product, μ is the coefficient of friction between the leather semi-finished product and the drive shaft. Considering that $\alpha = \frac{\pi}{2}$, then

$$T_2 = \mu N_1. \tag{2}$$

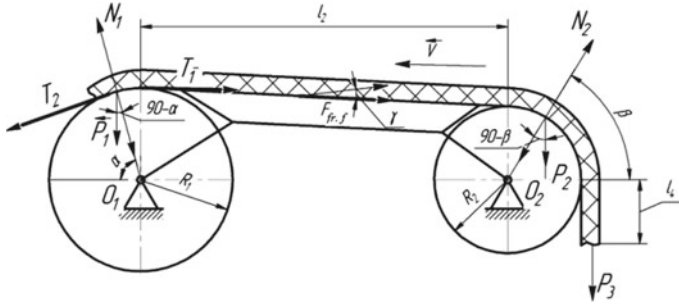


Fig. 3 Scheme of forces acting on the conveying mechanism

The average density of the leather semi-finished product is $\rho_{av} = \frac{m_1}{V_1}$, hence

$$m_1 = \rho_{av} V_1, \quad (3)$$

where m_1 is the mass of the section at the front end of the leather semi-finished product and V_1 is the volume of this section. V_1 is defined as follows

$$V_1 = l_1 \delta_{av} l_{wid} \quad (4)$$

where δ_{av} is the average thickness of the leather semi-finished product, l_{wid} is the passage width of the leather semi-finished product, and l_1 is the length of the arc determined as

$$l_1 = R_1 \alpha \quad (5)$$

Here, R_1 —is the radius of the drive shaft and α is the central angle of contact at which the semi-finished leather product touches the shaft.

Substituting expressions (4), (3), and (5) into (2), we obtain

$$T_2 = \mu m_1 g = \mu \rho_{av} V_1 g = \mu \rho_{av} l_1 \delta_{av} l_{wid} g = \mu \rho_{av} R_1 \alpha \delta_{av} l_{wid} g. \quad (6)$$

On the other hand, the force T_1 consists of three components, i.e., these forces create braking of the semi-finished leather product passage,

$$T_1 = F_1 + F_2 + F_3, \quad (7)$$

where F_1 is the friction force arising (at friction coefficient μ_1) between the surface of the spreading table and the semi-finished leather product, $F_1 = F_{fr,f} \sin \gamma$.

Similarly, for $\alpha = \frac{\pi}{2}$ we obtain

$$F_1 = F_{fr,f} \sin \gamma = \mu_1 N_1. \quad (8)$$

The volume of section V_2 is determined from,

$$\rho_{av} = \frac{m_2}{V_2} \Rightarrow m_2 = \rho_{av} V_2, \quad (9)$$

where m_3 is the mass of the section at the front end of the leather semi-finished product at the distance between the driving and driven shafts

$$V_2 = l_2 \delta_{av} l_{wid}, \quad (10)$$

where δ_{av} is the average thickness of the leather semi-finished product and is the distance between the driving and driven shafts.

Substituting expressions (10) and (9) into (8), we obtain

$$F_1 = \mu_1 N_1 \sin \gamma = \mu_1 m_2 g = \mu_1 \rho_{av} l_2 \delta_{av} l_{wid} g. \quad (11)$$

In the second section of the leather semi-finished product, the driven shaft works according to the brake wheel scheme. The braking moment M_m acts on it

$$M_m = R_2 F_2, \quad F_2 = \frac{M_m}{R_2}, \quad (12)$$

where F_2 is the friction force; N_2 is the force of normal pressure of a leather semi-finished product; P_2 is the response of supports.

From the equality of the shaft work in one revolution, we write

$$2 \pi R_2 F_2 = 2 \pi r_{st.ax} f_{st.ax} N_2 \cos(90 - \beta) = 2 \pi r_{st.ax} f_{st.ax} N_2 \sin \beta, \quad (13)$$

where $f_{st.ax}$ is the coefficient of friction in the stub axles of the driven shaft supports; $r_{st.ax}$ is the radius of the stub axle.

For $\beta = \frac{\pi}{2}$, formula (13) implies

$$F_2 = f_{st.ax} \frac{N_2 r_{st.ax}}{R_2} \quad (14)$$

After some transformations, we get

$$F_2 = f_{st.ax} \frac{m_3 g r_u}{R_2} = f_{st.ax} \rho_{av} l_3 \delta_{av} l_{wid} \frac{g r_{st.ax}}{R_2} \quad (15)$$

In the third section of the leather semi-finished product, the following equation holds:

$$F_3 = P = m_4 g. \quad (16)$$

m_4 is determined as

$$\rho_{av} = \frac{m_4}{V_4} \Rightarrow m_4 = \rho_{av} V_4, \quad (17)$$

where m_4 is the mass of the free end of the semi-finished leather product, $V_4 = l_4 \delta_{av} l_{wid}$ is the volume of this area, δ_{av} is the average thickness of the semi-finished leather product, and l_4 is the length of the free end.

Substituting expression (17) into (16), we obtain

$$F_3 = P = m_4 g = \rho_{av} l_4 \delta_{av} l_{wid} g, \quad (18)$$

To meet the condition, taking into account (11), (15), (19), and (7), the following must hold

$$\mu \rho_{av} R_1 \alpha \delta_{av} l_{wid} g \geq \mu_1 \rho_{av} l_2 \delta_{av} l_{wid} g + f_{st.ax} \rho_{av} l_3 \delta_{av} l_{wid} \frac{g r_{st.ax}}{R_2} + \rho_{av} l_4 \delta_{av} l_{wid} g. \quad (19)$$

Let us assume that the parameters in all sections of a semi-finished leather product (average thickness δ_{av} , width l_{wid} and average density ρ_{av}) are the same. Then, we get the following expression

$$\mu R_1 \alpha \geq \mu_1 l_2 + f_{st.ax} l_3 \frac{r_{st.ax}}{R_2} + l_4. \quad (20)$$

To ensure the maximum oncoming force, μ_1 should have the maximum value, i.e.:

$$f_{st.ax} \frac{N_2 r_{st.ax}}{R_2} > \mu_2 N_2, \quad (21)$$

where μ_2 is the coefficient of friction between the leather semi-finished product and the driven shaft.

Hence, we obtain the following condition

$$f_{st.ax} \frac{r_{st.ax}}{R_2} > \mu_2, \quad (22)$$

It is seen that to pull in the auxiliary shaft of the leather semi-finished product μ_2 , it becomes necessary that the coefficient of friction should be greater than expression $f_{st.ax} \frac{r_{st.ax}}{R_2}$.

4 Numerical Results of the Study

In the condition (21) obtained for the pulling of the semi-finished leather product by the driving roller of the conveying device, we substitute the most close values to real conditions: the minimum coefficient of friction between the semi-finished leather product and the driving roller $\mu_1 = 0.1$; the length of the semi-finished leather product located on the table $l_2 = 800$ mm; the length of the semi-finished leather product located on the auxiliary roller $l_3 = 100$ mm; the remaining length of the semi-finished leather product $l_4 = 200$ mm; constructional dimensions of the auxiliary roller are: $f_{st.ax} = 0.9$, $r = 10$ mm, $R_2 = 100$ mm.

Taking these values into account, Fig. 4 shows the relationship between the drive roller R_1 of the conveying device and the coefficient of friction of the leather semi-finished product located on the drive roller μ .

Figure 5 shows the relationship between the drive roller R_1 of the conveying device and the angle of contact μ of the leather semi-finished product by the drive roller.

After the calculations, the parameters of the radius of the driving roller, the coefficient of friction of the leather semi-finished product located on the driving roller, and the angle of the contact of the leather semi-finished product by the driving roller were obtained.

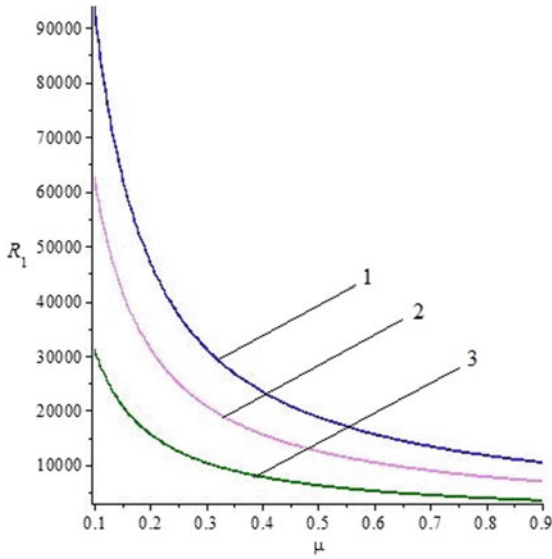


Fig. 4 Graph of dependence of R_1 on μ : for (1) $\alpha_1 = \frac{\pi}{6}$; (2) $\alpha_2 = \frac{\pi}{4}$; (3) $\alpha_3 = \frac{\pi}{2}$

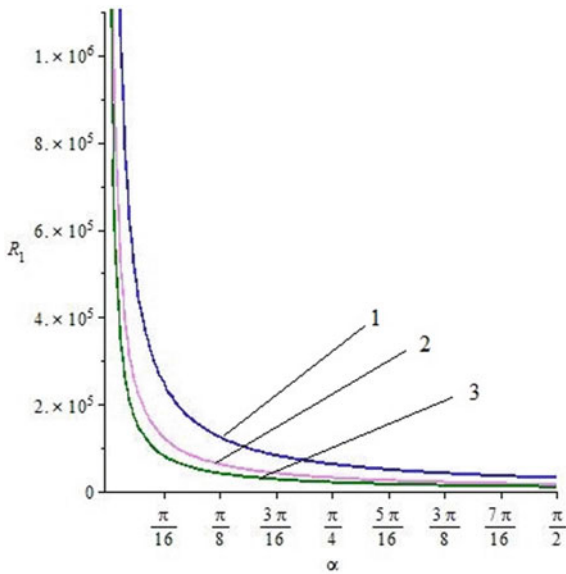


Fig. 5 Graph of dependence of R_1 on α : for (1) $\mu_1 = 0.1$; (2) $\mu_2 = 0.2$; (3) $\mu_3 = 0.3$

5 Discussion of Results

The dependencies of radius R_1 of the driving roller of the conveying device on the angle of the contact of the semi-finished leather product by the driving roller for three

conventional values are plotted in Fig. 4. Here, one can observe that with an increase in the angle of the contact, the radius of the drive roller and the coefficient of friction decrease. The dependencies of the radius of the driving roller R_1 on the angle α in Fig. 5 show the change in the coefficient of friction over the table surface with the semi-finished leather product on it, for three conventional values. It is also observed here that with an increase in the coefficient of friction, the radius of the drive roller and the angle of contact decrease.

From the graphs, we can conclude that condition (21) satisfies the technological requirement of pulling the leather semi-finished product by the driving roller of conveying device, i.e., at large values of the angle of contact and low values of the coefficient of friction, a greater pulling force is provided. So, to conduct the pulling-in of the leather semi-finished product, the value of the radius of the drive roller R_1 increases. Consequently, this leads to an increase in the consumption of materials, the mass of the working elements of conveying devices, etc. Therefore, it is recommended to make changes in the design of the conveying device.

The force generated by the pressure roller is not enough to pull the leather semi-finished product into the processing zone. To increase the pulling-in force, we proposed to install a freely rotating additional roller of radius R_3 on top of the drive roller of the conveying device, due to which the required friction force is provided, and therefore, the required force for the semi-finished leather product pulling-in is reached (Fig. 6).

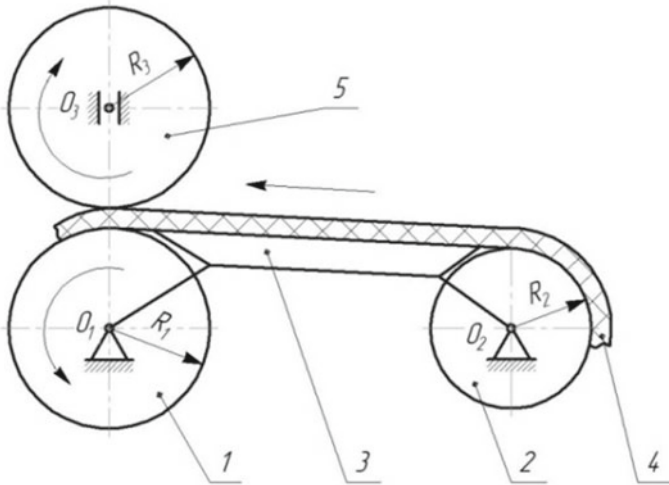


Fig. 6 Scheme of the conveying mechanism with a free upper working roller. 1—drive shaft; 2—driven shaft; 3—spreading table; 4—semi-finished leather product, 5—freely rotating shaft

The forces are plotted in the same way as above, and the fulfillment of condition $T_2 \geq T_1$ is checked (Fig. 7).

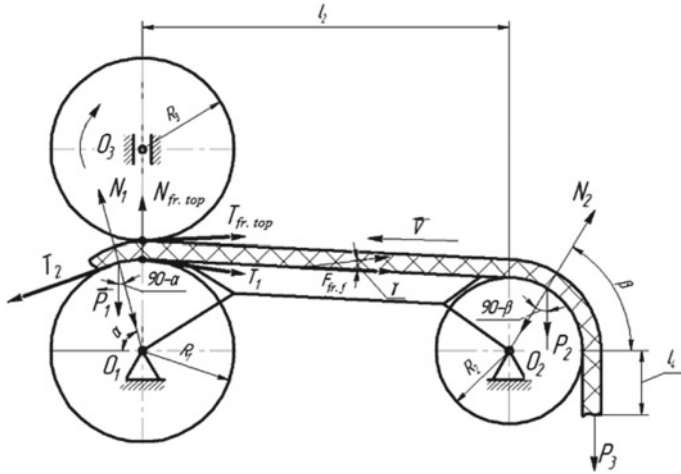


Fig. 7 Scheme of forces acting on the conveying mechanism

On the other hand, the force T_1 consists of several components, i.e., these forces brake the semi-finished leather product movement,

$$T_1 = T_{fr.top} + F_1 + F_2 + F_3, \tag{23}$$

The values of $T_{fr.top}$ —the friction force of the free upper transporting roller, F_1 —the friction force, F_1 —the brake force of the supporting roller, F_3 —the response of gravity, enter formula (24).

Now let us start studying each value separately.

In the second section of the leather semi-finished product, the driven shaft works according to the brake wheel scheme. The braking moment M_m acts on it

$$M_{fr} = P_3 T_{fr.top}, \quad T_{fr.top} = \frac{M_m}{R_3}, \tag{24}$$

where $T_{fr.top}$ is the friction force; P_3 is the response of supports.

From the equation of the shaft work in one revolution, we write,

$$2\pi R_3 T_{fr.top} = 2\pi r_{st.ax}^{fr} f_{st.ax}^{fr} N_{fr.top} \tag{25}$$

where $f_{st.ax}^{fr}$ is the coefficient of friction in the stub axles of the support rollers; $r_{st.ax}^{fr}$ is the radius of the stub axle; $N_{fr.top}$ is the force of normal pressure of the leather semi-finished product;

$$T_{fr.top} = f_{st.ax}^{fr} \frac{N_{fr.top} r_{st.ax}^{fr}}{R_3}, \tag{26}$$

here $\rho_{av}^{fr} = \frac{m_{fr}}{V_{fr}}$, hence $m_{fr} = V_{fr} \rho_{av}^{fr} = \rho_{av}^{fr} \pi R_3^2 l_{wid}$.

where ρ_{av}^{fr} is the average density, m_{fr} is the mass, and V_{fr} is the volume of the supporting rollers.

$$N_{fr.top} = m_{fr} g = \rho_{av}^{fr} \pi R_3^2 l_{wid} g \tag{27}$$

After some transformations, we obtain

$$T_{fr.top} = f_{st.ax}^{fr} \frac{\rho_{av}^{fr} \pi R_3^2 l_{wid} g r_{st.ax}^{fr}}{R_3} = f_{st}^{fr} r_{st}^{fr} \rho_{av}^{fr} \pi R_3 l_{wid} g. \tag{28}$$

Similar to (8)–(19), consider the forces F_1, F_2, F_3 .

To meet the condition $T_2 \geq T_1$, taking into account (6), (15), (19), and (29), the following inequality should hold

$$\begin{aligned} \mu \rho_{av} R_1 \alpha \delta_{av} l_{wid} g &\geq f_{st.ax}^{fr} r_{st.ax}^{fr} \rho_{av}^{fr} \pi R_3 l_{wid} g + \mu_1 \rho_{av} l_2 \delta_{av} l_{wid} g + \\ &+ f_{st.ax} \rho_{av} l_3 \delta_{av} l_{wid} \frac{g r_{st.ax}}{R_2} + \rho_{av} l_4 \delta_{av} l_{wid} g \end{aligned} \tag{29}$$

Then, after simplification, we get the following expression

$$\mu R_1 \alpha \geq \frac{f_{st.ax}^{fr} r_{st.ax}^{fr} \rho_{av}^{fr} \pi}{\rho_{av} \delta_{av}} R_3 + \mu_1 l_2 + \frac{f_{st.ax} r_{st.ax}}{R_2} l_3 + l_4. \tag{30}$$

From the inequality obtained, it is seen that the inequality δ_{av} is the average thickness of the leather semi-finished product, which affects the changes between the shafts spacing in technological processes.

6 Conclusion

From the above, it is seen that the advantages of a multi-operation machine for processing the leather semi-finished products are evident. The issue of conveying the semi-finished leather product in the developed machine to its working area is very important. Therefore, first of all, we consider the transportation of semi-finished leather products to the working area. Here, the sliding of the leather semi-finished product on the table, the resistance of the driven and pressure rollers, and the traction force of the driving roller were taken into account. From the graphs obtained, it can be seen that, as noted above, the radius of the drive roller is very important.

This causes problems in the design and manufacture of the machine. Therefore, in addition to the design, we have placed a freely rotating roller on top of the drive shaft. This has two main functions for conveying the leather semi-finished product to the working area: firstly, it causes the pulling pressure and increases the coefficient of friction, and, secondly, it prevents the damage of the product quality as a result of the rotational force of the working roller. This dramatically affects the quality of the product and maintains it at a high level.

Drawing an analogy with the work done above, we obtained an inequality. The inequality obtained includes all the parameters involved in the conveying and pulling-in of the semi-finished leather product into the processing zone. The rational parameters of

the mechanism are selected setting the parameters of the processed leather semi-finished product.

It is advisable to make the identical radii of the shafts R_1 and R_3 , since this is one of the factors influencing the quality of the semi-finished leather product. It is also necessary to take into account the fact that during the squeezing process, the rubber cushions and cuffs are put on the rollers.

In conclusion, we can say that the rational parameters of the device are selected with the expressions obtained for the parameters of the processed leather semi-finished product.

References

1. Covington AD, Wise WR (2020) Current trends in leather science. *J Leather SciEng* 2:28. <https://doi.org/10.1186/s42825-020-00041-0>
2. Riguetto CVT, Rosseto M, Krein DDC et al (2020) Alternative uses for tannery wastes: a review of environmental, sustainability, and science. *J Leather SciEng* 2:21. <https://doi.org/10.1186/s42825-020-00034-z>
3. Navarro D, Wu J, Lin W et al (2020) Life cycle assessment and leather production. *J Leather SciEng* 2:26. <https://doi.org/10.1186/s42825-020-00035-y>
4. Appiah-Brempong M, Essandoh HMK, Asiedu NY et al (2020) An insight into artisanal leather making in Ghana. *J LeatherSciEng* 2:25. <https://doi.org/10.1186/s42825-020-00039-8>
5. Olle L, Sorolla S, Casas C et al (2013) Design of a Prototype to produce a new collagen material by dehydration. *J Soc Leather Technol Chem* 97(6):244–250. https://www.nitidae.org/files/85e09496/161018045211_161011_carbon_footprint_of_smallholder_farms_in_central_madagascar_rakotovao_et_al.pdf
6. Burmistrov AG (2006) Machines and apparatus for the production of leather and fur. KolosS, Moscow
7. Sokolovsky AR (2010) Development of methods and improvement of means for studying the physical and mechanical properties of fibrous-porous materials of light industry. Dissertation, Moscow
8. Korotchenko YuN (2007) Improvement of the parameters of roller leather machines. Dissertation, Moscow
9. Kolychev MV (2015) Improvement of contact interaction in pressing zones to increase the efficiency of the press parts of paper machines. Dissertation, St. Petersburg
10. Ershov SV (2013) Dynamic loading of the roller pair to intensify the spinning process. Dissertation, Ivanovo
11. Darda IV (2004) Development of theoretical foundations for improving the technological equipment of leather and fur production. Dissertation, Moscow
12. Bahadirov GA, Barakaev NR, Nosirov MI (2018) Interaction of retraction and braking forces in the roller conveyor. In: Mechanical engineering and technosphere of the XXI century. Proceedings of the XXV international scientific and technical conference in Sevastopol, 10–16 September. *Donetsk* 2:349–353
13. Amanov AT, Bahadirov GA, Amanov TY, Tsoy GN, Nabiev AM (2019) Determination of strain properties of the leather semi-finished product and moisture-removing materials of compression rollers. *J Mater* 12(21), Basel, Switzerland. <https://doi.org/10.3390/ma12213620>
14. Bahadirov GA, Sultanov TZ, Abdukarimov A (2020) Comparative analysis of two gear-lever differential inter-roller transmission mechanisms. *IOP Conf Ser: Earth Environ Sci* 614:012102. <https://doi.org/10.1088/1755-1315/614/1/012102>

15. Bahadirov GA, Sultanov TZ, A Abdukarimov A (2020) Kinematic analysis of tooth-lever differential transmission mechanisms. IOP Conf Ser: Earth Environ Sci 614:012101. <https://doi.org/10.1088/1755-1315/614/1/012101>
16. Bahadirov GA, Sultanov T, Umarov B, Bakhadirov K (2020) Advanced machine for sorting potatoes tubers. IOP Conf Ser: Mater Sci Eng 883:012132. <https://doi.org/10.1088/1757-899x/883/1/012132>
17. Khurramov ShR (2020) Simulation of the form of contact curves rollers in two-roll modules. IOP Conf Ser Earth Environ Sci 614:012096. <https://doi.org/10.1088/1755-1315/614/1/012096>
18. Khurramov ShR (2020) Some questions of the contact interaction theory in two-roll modules. J. Phys: Conf. Ser 1546:012132 <https://doi.org/10.1088/1742-6596/1546/012132>
19. Buchgolts NN (2013) Basic course of theoretical mechanics. Part 1. Kinematics, statics, dynamics of a material point. Moscow
20. Bahadirov GA, Rizaev AA, Barakaev NR, Bahadirov KG, Umarov AA, Atazhanova NB (2010) Machine for mechanical processing of leather. Patent of RUz for a utility model, No. FAP 00675, Tashkent



Design of a Fault-Tolerant Sliding Formwork Complex

T. Kruglova^(✉)

Platov South-Russian State Polytechnic University (NPI), Prosveshcheniya 132, Novocherkassk
346428, Russian Federation

Abstract. This article is about fault-tolerant sliding formwork complex using technical condition executive drives prediction diagnosis system design. The relevance of the use of diagnostic systems in monolithic construction is substantiated. The device and principle of operation of the sliding formwork complex for the monolithic construction of residential and office buildings and industrial structures are considered. The basic requirements for the sliding formwork complex servos technical condition *predictive diagnosis* methods are formulated. The diagnostic parameters meet these requirements are selected. A method for predictive diagnostics of technical condition is proposed. The diagnostic method is based on the coefficients of the envelope straight line approximating calculating coefficients for the wavelet coefficients on the characteristic scales. Long-term technical condition prediction is realized using a hierarchical neural network with flexible feedback for the servo's residual resource. The results of the experimental researches for predictive diagnostics methods which showed its adequacy and efficiency are presented.

Keywords: Sliding formwork · Servos · Predictive diagnosis · Wavelet transformation · Envelope approximation · Artificial intelligence

1 Introduction

Construction is one of the main actively developing sectors of the national economy. Every year the number of high-rise buildings and structures is growing steadily. The requirements for the quality and speed of the structures being built are constantly changing, which leads to the emergence of innovative construction technologies. It is necessary to automate the main construction operations and erect facilities of proper quality for the new technological complex implementation. During the operation, construction equipment is strongly influenced by weather conditions, uneven loading throughout the year, constant changes in operating conditions and the presence of dust, moisture, noise and vibration. All this negatively affects its technical condition, causing failures and long downtime. Resilient construction equipment is needed to solve this problem. The least reliable elements of building complexes are DC or AC servo drives, the correct operation of which largely determines the quality of buildings and structures being erected. Failure or incorrect operation one of the drives can lead to a malfunction of the entire

complex, damage to building materials and the receipt of a structure of inadequate quality. Therefore, the urgent task is to ensure the reliable functioning of all servos included to the complex. This problem can be solved by using the built-in system of diagnostics and forecasting [1–6], which implements control of the complex servo drives technical condition.

2 Sliding Formwork Complex

The most common method of high-rise buildings and structures is monolithic construction. Technology this method provides a continuous supply and laying of concrete, installation of rebar, formwork hoist, regulation of project sizes and control settings of the building. The modern method of automation of monolithic construction is the use of sliding formwork complex (SFC) (Fig. 1), which is a spatial form installed on the perimeter of the structures and moved up by lifting jacks (LJ).

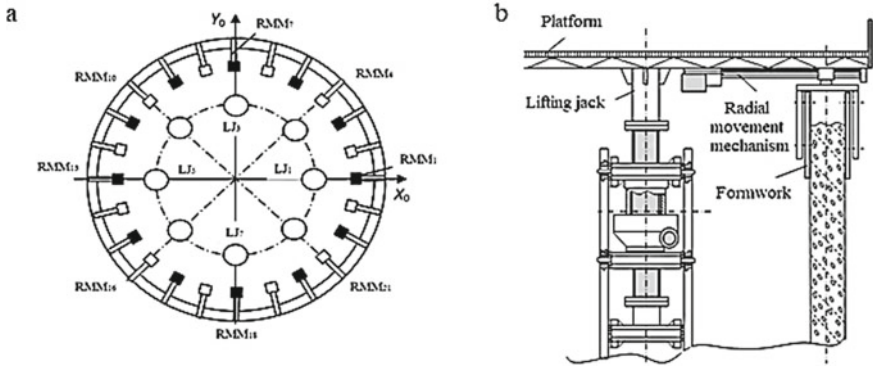


Fig. 1 a longitudinal and vertical section of the SFC; b the distribution of LJ and RMM in the plane of the complex platform

The position of the formwork panels is fixed by Jack frames that accept the loads of the laid concrete. Lifting of the formwork is carried out by electromechanical lifting jacks based on DC or AC servo motors. Jacks should provide high load capacity, synchronous movement of the formwork, lifting speed regulation and ease of maintenance. It also includes adjustment mechanisms, dynamic properties, design and technological features that determine the structure of control algorithms and the choice of control laws. For example, for structures of conical shape, these are radial movement mechanisms (RMM), which are located along the radius with a uniform step (Fig. 1a). Their task is to move the formwork panels in the process of lifting it. Changing the position of the boards should be synchronized with the LJ. To do this, the number of RMM mechanisms (m) is chosen as a multiple of the number of LJ (n). This will allow the platform radial beams to be distributed evenly with angular pitch $2\pi/m$ and used for the RMM installation. Important conditions for the quality of construction work are the continuity of the technological process and maintaining a constant movement speed of

the formwork not less than 1 cm/min, as well as the need to strictly horizontal platform. To implement these requirements, it is necessary to ensure consistent operation of all servo motors included in the complex. This problem can be solved by using methods and tools for predictive diagnosis of LJ and RMM servo motor with its operation mode subsequent optimization. For this purpose, it is necessary to provide the technical condition control of all servo motors which are a part of the SFC, information exchange between drives and decision-making for SFC operation mode changing.

The implementation of this approach involves the integration of the predictive diagnostics system into the structure of the sliding formwork complex at the design stage. This implies the inclusion of special hardware and software in the design of the servo actuators. Sensors, equipment and information systems interact throughout the life cycle of the FSC and information exchange is carried out using standard Internet protocols. This allows performing self-tuning and SFC adaptation to changing operating conditions and technical condition of the equipment. Therefore, the development of predictive diagnostic methods of the SFC servos technical condition to improve its fault tolerance is very important.

3 Technical Condition Predictive Diagnostics Method

The construction equipment extreme operating conditions cause significant dynamic alternating loads on its executive servos using existing methods cannot be distinguished from faults which can lead to significant diagnostic errors. Therefore, it is necessary to develop new methods that meet the following requirements:

- minimum range of measured parameters;
- the absence of complex bulky measuring equipment installed on the servo drive body, affecting its operation;
- the ability to use on a moving object in conditions of high humidity and dustiness of the working environment;
- possibility of the measured automatic analysis.

Analysis of the existing methods of predictive diagnostics shows that the only servos current analysis method is most requirements for its main electrical and mechanical fault identification.

The classical method for analyzing this parameter is spectral analysis using the Fourier transform [7], which involves converting a time signal into a frequency form, identifying characteristic frequencies for drive faults (Table 1), and analyzing them by comparing them with similar frequencies of a new serviceable servo taken as a standard.

This method is very laborious. It does not allow distinguishing the faulty state of a servo drive from a change in its operating mode and also requires the involvement of an experienced specialist—an expert to interpret the diagnostic results; therefore, it cannot be used in the design of a sliding formwork complex. An alternative is the wavelet transform. It provides a two-dimensional scanning of the signal in frequency and time, focusing on certain local features of the analyzed processes that cannot be detected by traditional Fourier and Laplace transforms.

Table 1 Fourier transformation characteristic frequencies

Motors faults	Fourier transformation characteristic frequencies
<i>DC-motor</i>	
Commutation defects	$2 \cdot k \cdot p \cdot f_{rot}$
Rotor defects	$2 \cdot p \cdot f_{rot}, (k \pm 2 \cdot p) \cdot f_{rot}$
Voltage ripple	$k \cdot f_s$
Stator defects	$k \cdot f_{rot}$
<i>AC-motor</i>	
Stator defects	$k \cdot f_{rot}$
Bearing defects	$1/4 \cdot f_{rot}, 1/2 \cdot f_{rot}, f_{rot}, 1.5 \cdot f_{rot}$
Misalignment or no parallelism of the motor shafts and the mechanism	$f_{rot}, 3 \cdot f_{rot}, 5 \cdot f_{rot}$

where f_s —frequency of the network supplying the rectifier, (Hz); f_{rot} —motor rotor speed, (Hz); $k = 1, 2, 3$ —number of current harmonic; p —the number of poles.

Wavelet signal transformation is a representation in the form of generalized Fourier series and integral system of basic functions constructed from the original wavelet $\psi(t)$, with certain properties due to a time shifting operation (b) and changes in the time scale (a)

$$\psi_{ab}(t) = 1/\sqrt{a} \cdot \psi((t - b)/a), \tag{1}$$

The factor $1/\sqrt{a}$ ensures the independence of the norms of these functions in the scaling of a . For given values of the parameters a and b , function $\psi_{ab}(t)$ is the wavelet generated by the original wavelet $\psi(t)$. Small parameter (a) corresponds to the smaller scale $\psi_{ab}(t)$ or to the high frequency ($\omega \approx 1/a\omega \sim 1/a\omega \sim 1/a$), large parameter (a) is for large scale $\psi_{ab}(t)$, the stretching of the original wavelet $\psi(t)$.

There is an inverse proportional relationship between the Fourier harmonics and the wavelet scale, weighted by a certain conversion factor

$$a = K \cdot \omega^{-1} \tag{2}$$

where ω —natural frequency (Table 1), K —conversion factor, which is determined depending on the selected mother wavelet [8, 9].

For each characteristic scale, a continuous wavelet transform function $\psi_{ab}(t)$ is defined, from which an analytically conjugate signal $\hat{\psi}_{ab}(t)$ is formed, the mathematical form of which has the following form:

$$\hat{\psi}_{ab}(t) = \int_{-\infty}^{\infty} \frac{\psi_{ab}(\tau)}{t - \tau} = \Gamma[\psi_{ab}(t)] \tag{3}$$

The Hilbert transform makes it possible to form an analytical signal from the analyzed signal of a real function of time $\psi_{ab}(t)$:

$$s(t) = \psi_{ab}(t) + j\widehat{\psi}_{ab}(t) \quad (4)$$

from which you can find the instantaneous amplitude (signal envelope):

$$A(t) = |s(t)| = \sqrt{\psi_{ab}(t)^2 + \widehat{\psi}_{ab}(t)^2} \quad (5)$$

For a formal description of the envelope obtained, it is advisable to choose a first degree polynomial, the generalized formula of which has the following form:

$$A(t) = k \cdot t + b \quad (6)$$

Analysis of the coefficients k and b of the approximating straight envelope of the wavelet coefficients at characteristic scales showed that a working servo corresponds to a $k < 0$, and the approximating straight line descends to the abscissa axis, $k \geq 0$ is typical for a faulty state of the servos. Coefficient b is always positive; however, with an increase in load on a serviceable drive, coefficient b increases and k decreases.

For a faulty servo motor, an increase in load will lead to an increase in all the parameters of the approximation line [10–16]. Thus, the sign of the coefficient k of the approximating direct envelope at the characteristic scales of the wavelet coefficients will determine the current servos technical condition.

A method for servo motor technical condition prediction [17–20] using neural networks is proposed. The forecasting initial data are the trend of the coefficients k of the approximating direct envelope of the wavelet coefficients of the current signals at characteristic scales for previous periods of operation, distributed over equal time intervals. The forecasting process includes three levels. At the first level, the values of the coefficients k for the straight line which envelope the wavelet coefficients on the characteristic wavelet scale approximate are predicted. A direct signal transmission network with three inputs and one output is simulated.

The input vector of the neural network

$$P = [k(t_1), \dots, k(t_{N-3}); k(t_2), \dots, k(t_{N-2}); k(t_3), \dots, k(t_{N-1})]$$

The target vector H , the values of the determining parameter are set, which should be obtained at the output.

$$H = [k(t_4), \dots, k(t_N)].$$

For a given input P , the neural network calculates the output value of the predicted parameter C corresponding to a given target vector H .

$$C = [k(t_{N-2}); k(t_{N-1}); k(t_N)]$$

To train the neural network, the back propagation algorithm is used.

Similar calculations are performed for each scale of wavelet coefficients. If during the calculation all the coefficients are negative, then the servomotor will remain operational

in the next period of operation. If at least one is zero or positive, then in the next period of operation, the object will fail.

The forecast at the next levels is an approximation of the values obtained at the previous level. To determine the cause of the failure and motor, it is necessary to approximate the outputs of the previous levels coefficients values. The outputs of the first level consist of values of the coefficients k , negative values of which indicate a working condition, and zero or positive ones indicate a faulty state of the servo, the result of the next level of forecasting can be obtained by maximizing the previous level. Then, the development factors of faults and servo states are performed as follows:

$$K_{\text{FAULT}j} = \max(k_i), K_{\text{MOTOR}} = \max(K_{\text{FAULT}j}),$$

To determine the servo motor failure time, it is necessary to add the predicted coefficients values of the approximation direct envelope of the wavelet coefficients in the training set and repeat the entire forecasting process until the coefficient determining the state of the servo motor becomes $K_{\text{MOTOR}} \geq 0$. The number of iterations passed will be equal to the number of time intervals T during which the servomotor remains operational. The implementation structure of the above method is shown in Fig. 2

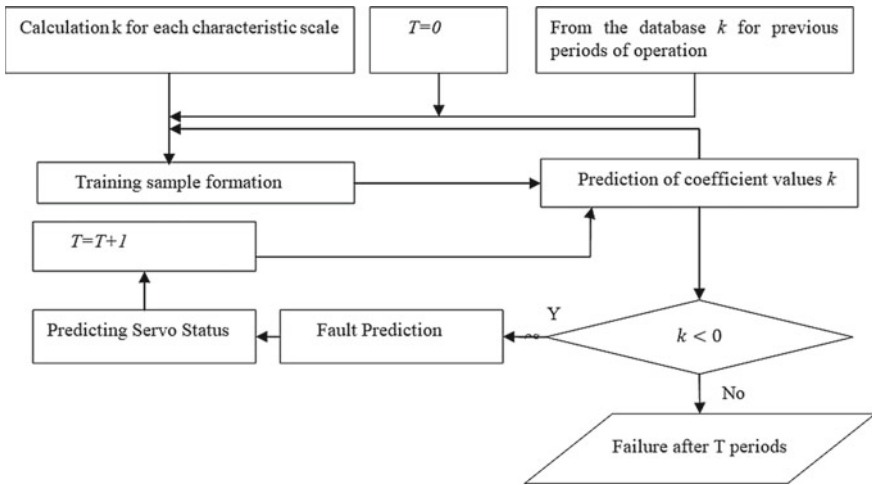


Fig. 2 Structure of the implementation of the method for predicting the technical condition of SFC servo motors

The proposed method for forecasting the technical condition will allow short-term and long-term forecasting of defects of each SFC servos. The results will be used for subsequent optimization of the operating mode of SFC.

4 Experimental Researches

The prediction diagnosis method research has been performed. For servo motor, KY110AS0415-15B-D2-2000 was carried out according to the measurement of the current signal from January 2008 to January 2015.

The obtained records of the supply current signals were processed using the proposed diagnostic method. The coefficients of the approximation straight envelope are found for each scale. According to the data obtained, it is clear that in January 2015, this servo motor was in the boundary state, since the approximation coefficient k for the rolling bearing malfunction is close to 0. According to the record in the equipment maintenance journal, the KY110AS0415—15B—D2—2000 servo drive failed on 27.02.2015 due to wear of the bearings, which confirms the accuracy of the proposed diagnostic method. According to the values of the coefficients k for the period from 2008 to 2012, the values of these coefficients are predicted for 2013–2015. A comparison of the results of diagnosis and forecasting is shown in Fig. 3.

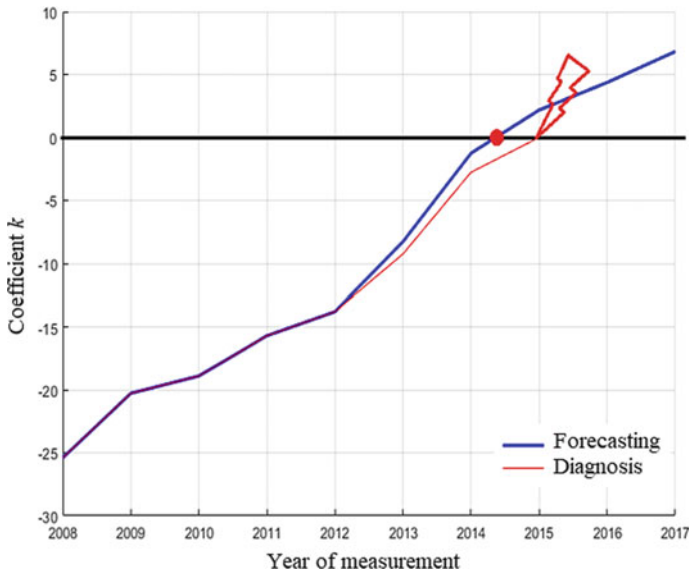


Fig. 3 Comparative analysis of the diagnosis and forecasting results

It can be seen from this graph that, according to the forecast, the failure of the servo drive occurred earlier than in fact, which will prevent a sudden failure of the equipment.

The analysis of the effectiveness and reliability of the predictive diagnostic method is proposed. It is established that the use of these methods will increase the coefficient of technical use by 16%. The reliability of the diagnosis is 93%. The accuracy of short-term forecasting is 1.7% and long-term forecasting does not exceed 10%. Prediction accuracy can be increased by increasing the volume of the training sample, as well as adding it to the current values of the diagnostic parameters.

5 Conclusion

The article presents a system for predictive diagnostics of the technical state of the servo drives of the sliding formwork complex. The innovative methods of diagnostics

and forecasting of the technical condition are described. These methods use wavelet transform of the servo current signal in conjunction with a hierarchical neural network. These methods allow the design of fault-tolerant sliding formwork complexes with 16% higher reliability.

References

1. Nandi S, Hamid A et al (2005) Condition monitoring and fault diagnosis of electrical motors—a review. *J. Magaz.* 20(4):719–729
2. Lee Y-S, Kim K-T et al (2015) Finite-element analysis of the demagnetization of IPM-type BLDC motor with stator turn fault. *IEEE Trans Magn* 2:7022004–7022004
3. Zhang J, Rizzoni G et al (2015) Structural analysis for FDI of PMSM drive system in electric vehicles. In: *IEEE Transportation electrification conference*, pp 1–7
4. Liu B, Ling SF (1999) On the selection of informative wavelets for machinery diagnosis. *Mech Sys Signal Proc* 13(1):145–162
5. Peter W et al (2004) Machine fault diagnosis through an effective exact wavelet analysis. *J Sound Vib* 277:1005–1024
6. Andersen TJ (1995) A modified regression algorithm for fast one layer neural network training. *World Cong Neural Netw* 1:687–690
7. Körner TW (1988) *Fourier analysis*. Cambridge University Press 377
8. Daubechies I (1992) The wavelet transform time-frequency localization and signal analysis. *IEEE Trans Inform Theo* pp 961–1004
9. Daubechies I (1990) Ten lectures on wavelets. *Soc Ind Appl Math* 357
10. Kruglova T, Bulgakov A et al (2017) Artificial intelligence method for electric drives mode operating and technical condition determination. *DTS-2017* 132:04017
11. Kruglova T, Shaykhtudinov D et al (2016) Intelligent sensorless fault diagnosis of mechatronics module wavelet transformation. *Asian J Inf Technol* 15(22):4694–4697
12. Kruglova TN (2015) Intelligent diagnosis of the electrical equipment technical condition. *Proc Eng* 129:219–224
13. Kruglova T (2016) Wavelet analysis for fault diagnosis of electrical machines using current signals. *ICIEAM*, pp 1–5
14. Kruglova TN (2019) Investigation of the electric drive technical condition under various loading conditions. *Bull Belgorod State Technol Univ* 3:112–113
15. Kruglova TN (2019) Intellectual decision - making in the cyber-physical system for diagnosing electric motors of process equipment. *Vestnik UGATU* 23(1)(83):97–103
16. Bulgakov A, Kruglova T et al (2018) Synthesis of the AC and DC drives fault diagnosis method for the cyber-physical systems of building robots. *MATEC Web Conf* 251:03060
17. Kruglova T et al (2017) Smart sensorless prediction diagnosis of electric drives. *IOP Conf Series: Earth Environ Sci* 87
18. Kruglova TN et al (2017) Forecasting of the electrical actuators condition using stators current signals. *IOP Conf Ser: Mat Sci Eng* 177(1)
19. Bulgakov A, Kruglova T et al (2019) Fuzzy logic and neural networks for insulation fault diagnosis in construction robots drives. *CCC 2019*, pp 55–60
20. Travush V, Erofeev V et al (2020) Cyber-physical predictive diagnostics system for servos of mobile construction robots. *J Phys: Conf Ser* 1687:012014



The Methodology of Resource Forecasting on Working Rolls of the Final Stands of the Widestrip Hot Rolling Mill

A. A. Fedulov¹, V. P. Antsupov², and A. V. Antsupov³(✉)

¹ Ural Federal University (UrFU), 19, Mira street, Yekaterinburg 620002, Russia

² Magnitogorsk State Technical University, 38, Lenin street, Magnitogorsk, Chelyabinsk Region
455000, Russia

³ Bauman Moscow State Technical University, 5, 2nd Baumanskaya street, Moscow 105005,
Russia

Abstract. In the article, the methodology for a calculated evaluation of sequential distortion of the working roll's profile during the serial widestrip rolling was presented. The function to evaluate the average resource of working rolls was obtained by the criterion of the cross-section gage variation of strip. The gage variation for each rolled strip in the batch was defined by summing up values on active generatrices of the upper and bottom rolls. The active generatrices of each roll in the moment of rolling of each following strip in turn was defined as the difference between the value of the roll radius in the middle of the barrel and under (or above) the edge of a strip. To evaluate the rate of the roll distortion in the conditions of the rolling of each following batch of strip, there was used the basic equation of the structural energy concept of a stationary friction unit wear. The moment of failure (the expected lifetime) of working rolls was defined from the condition of the gage variation reaching the limit value for the current batch of strip.

Keywords: Main equipment · Broadband mill · Low-reliable elements · Design assessment · Life expectancy · Annual productivity · Production efficiency

1 The Problem Statement

The main problem in the theory and practice of the sheet rolling industry is the question of the forecasting durability of working rolls by the criterion of the limit distortion of a profile of their active generatrix due to the non-uniform wear of the barrel surface in the deformation zone [1–3]. The possibility of mathematical description of the current profile change for the known schedule of the rolling allows not only to control the cross-section profile of each strip but to predict the moment of failure of the rolls (their lifetime) by the time when the cross-section gage variation will be beyond the restricted value for the following batch of strip.

The design evaluation of the roll source for the prescribed assortment allows to plan the schedule of the roll change, forecast the mill productivity, calculate the excess

material for regrinds, the roll expenses, and its annual requirement, and also to analyze possible methods to increase the durability and quality of final product.

However, the current profile of the wear of the work rolls determines many technological and design factors that change during maintenance in sequential rolling of various standard sizes of strips per a set of the rolls into the stand. These include the power, temperature and velocity conditions of rolling, the number, sizes and properties of rolled strips, geometric dimensions, initial profiling, roughness, and physical and mechanical characteristics of the roll material. The large volume of the listed characteristics makes complicated the construction of analytical dependences for prediction of the wear in profiles of rolls during rolling.

Therefore, the empirical dependences known in the literature make it possible to predict the maximum wear in the middle of the roll barrel ΔR by the value of only one factor—the weight G of the rolled metal $\Delta R = L_G \cdot G$ or the length L of the rolled strips $\Delta R = L_L \cdot G$ [1–3]. The weight L_G or geometric L_L coefficients of proportionality are determined by statistical processing of a large number of worn rolls for the working conditions of a particular rolling mill and are not universal. To establish similar dependencies in other conditions of roll operation, it is necessary to carry out special long-term experimental studies.

Known [1, 2] empirical dependencies, where the current wear in the middle of the roll barrel is determined by the value of the specific work of friction forces performed in the deformation zone at the current moment $\Delta R = I_{en} \cdot A_{fr}$. The energy index I_{en} is determined by statistical processing of the ratio of the measured wear values ΔR of the investigated rolls to the calculated work A_{fr} of friction forces. The calculation of A_{fr} additionally takes into account the influence on wear of the following factors: the weight of the rolled strips, the diameter of the rolls, the width and thickness of the rolled strips, their mechanical and physical characteristics, reduction and angle of engagement, temperature and rolling velocity, and the friction coefficient.

However, in the light of modern concepts [4–7] on modeling the processes of friction and wear of solids, the usage of the indicator of the energy intensity of wear and the work of friction forces (work of external forces) in the initial equations are incorrect since most of it dissipates in the form of heat. The total work of external forces per unit of the worn-out volume of the material, and, accordingly, the integral index I_{en} , are not a property of the material to be worn but determine the critical energy level established upon destruction of the surface layer only for given conditions of frictional interaction. They are imaginary (conditional) characteristics of the process, as they change when external conditions change. By their value, it is impossible to estimate the share of energy spent on distorting the structure of materials of the surface layers leading to a critical degree of damage and separation of wear particles.

The amount of wear material of the friction surface is determined by the critical value of the accumulated inner energy. This energy is the characteristic of the material—its energy intensity [4]. In addition, the well-known empirical dependencies, obtained only to evaluate the wear of the rolls, do not allow to control the quality of the rolled strips, in particular, their transverse thickness variation. In our opinion, for the correct problem statement of prediction of the reliability of rolls, these conditions must be taken into account simultaneously.

The authors could not find any analytical solution of the problem in the literature. Therefore, the alternative physical analytical model of the working rolls failure by the criterion of profile accuracy disturbance of the cross-section of a rolled strip is presented below.

2 The Methodology of the Design Evaluation of the Working Rolls Lifetime

The expected lifetime of working rolls for an anticipated schedule of the rolling of the j th batch of strip could be defined using the solution of the one-parameter boundary problem of the physical theory of technical object reliability [4–7]. In that case as a controlled parameter of working rolls state in the maintenance, the current value of cross-section gage variation $\delta_{hj} = h_{cj} - h_{ej} > 0$ of the rolled strip could be chosen. Here, h_{cj} and h_{ej} are the thickness of the j th strip in the middle of the width and on the edge. The change of the value δ_{hj} in the process of the upper and bottom rolls wear defines the process of their aging during maintenance.

The moment of failure of the working roll (their lifetime) in that case is defined by the condition of the attainment of the current value δ_{hj} to the limit δ_{hj}^* set by the standard:

$$\delta_{hj} = \delta_{hj}^* \tag{1}$$

The equation of the cross-section gage variation in the serial rolling of the j th batch of strip in the stationary thermal and load condition could be described by the evolution operator [8, 9]:

$$\delta_{hj} = \Delta_{wj}^u + \Delta_{wj}^b = \left(\sum_{j=1}^j \Delta_{w(j-1)}^u + \dot{\Delta}_{wj}^u \cdot t_j \right) + \left(\sum_{j=1}^j \Delta_{w(j-1)}^b + \dot{\Delta}_{wj}^b \cdot t_j \right) \tag{2}$$

where Δ_{wj}^u , $\dot{\Delta}_{wj}^u$ and Δ_{wj}^b , $\dot{\Delta}_{wj}^b$ —the values of the current profile active generatrix of the upper and bottom working rolls and the rate of change, retrospectively, in the rolling process of the j th batch of strip along their width ($j - 1, 2, 3, \dots, j$)*; j^* —the batch number during the rolling of which the condition (1) is fulfilled);

$\Delta_{w(j-1)}^u = \Delta_{w0}^u$ and $\Delta_{w(j-1)}^b = \Delta_{w0}^b$ for $j = 1$ are the values of the profile active generatrix of the upper and bottom working rolls along the width of the first rolled strip $B_{j=1}$ taking into account the initial grinding profile, thermal distortion, roll’s bending, and counter bending.

$t_j = G_j / (\rho_j \cdot b_j \cdot h_j \cdot V_{nj})$ —the time of the j th batch rolling with the strip weight G_j and the cross-section $b_j \cdot h_j$, and the density ρ_j ; V_{nj} —the rolling velocity of the j th batch.

The expected resource of the working rolls is defined by the solution of the Eq. (1) for $t_j = t_{\delta j^*}$:

$$t_{\delta j^*} = \frac{\delta_{h j^*} - \sum_{j=1}^{j^*-1} \Delta_{w(j-1)}^u - \sum_{j=1}^{j^*-1} \Delta_{w(j-1)}^b}{\dot{\Delta}_{wj}^u + \dot{\Delta}_{wj}^b}, \tag{3}$$

where $j = j^*$ when $(\delta_{hj^*} - \sum_{j=1}^{j+1} \Delta_w^u(j-1) - \sum_{j=1}^{j+1} \Delta_w^b(j-1)) \leq 0$.

The rate of the current strip batch profile distortion $\dot{\delta}_{hj} = \dot{\Delta}_{wj}^u + \dot{\Delta}_{wj}^b$ (as the sum of rates of profile distortion of the active generatrices for both rolls along the width of the j th strip in the condition (3)) could be defined thought rates of wear process $\dot{R}_w(x, t_j)$ of the upper and bottom working rolls above (or under) the middle ($x = 0$) and the edge $x = B_j$ of the strip, retrospectively:

$$\dot{\delta}_{hj} = \dot{\Delta}_{wj}^u + \dot{\Delta}_{wj}^b = (\dot{R}_w^u(0, t_j) - \dot{R}_w^u(B_j, t_j)) + (\dot{R}_w^b(0, t_j) - \dot{R}_w^b(B_j, t_j)). \quad (4)$$

The distribution of rates of wear of the upper and bottom working rolls in points along the contact with a rolled strip $\dot{R}_w(x, t_j)$ (by the coordinate x counted from the middle of the barrel) could be obtained with the usage of the wear process model of the stationary friction unit [10–14]:

$$\dot{R}_w(x, t) = \frac{v_w}{u_{ew*}} \cdot \left(\sum_{k=1}^2 N_{fr(mech)k}^{sp}(x, t_j) + \sum_{k=4}^5 N_{fr(mech)k}^{sp}(x, t_j) \right) \quad (5)$$

where v_w —the coefficient of the external energy absorption of the surface layer material of the working roll:

$$v_w = \varepsilon_w / (1 + \varepsilon_w); \quad (6)$$

$\varepsilon_w = (\theta_w)^{2/3} \cdot Ra_w^{1/3} / (\theta_s)^{2/3} \cdot Ra_s^{1/3}$ —the coefficient of the external energy distribution $(N_{fr(mech)}^{sp})$ between the working roll and the strip in the deformation zone;

$\theta_w = (1 - \mu_w^2(T_w)) / E_w(T_w)$ и $\theta_s = (1 - \mu_s^2(T_s)) / E_s(T_s)$ —the elastic constants of materials of the working roll and the strip (the temperature of the surface layer of the working roll could be evaluated by the methodology) [15];

$\mu_w(T_w), \mu_s(T_s), E_w(T_w), E_s(T_s)$ —their Poisson coefficient and elastic modulus by the temperature T_w of the surface layer of the working roll and T_s of the strip, retrospectively;

Ra_w, Ra_s —the arithmetic mean value of the profile surface microroughness of the working roll and the strip, retrospectively;

in hot rolling $v_w \approx 1$;

u_{ew*} —the critical power intensity of the working roll material:

$$u_{ew*} = \Delta H_{Sw} - u_{e0w} - u_{Tw}; \quad (7)$$

ΔH_{Sw} —the enthalpy of the working roll material melting in the liquid state;

$u_{e0w} = \frac{(0,071 \cdot HV_w)^{2,4}}{6 \cdot G_w \cdot (6,47 \cdot 10^{-6} \cdot HV_w + 0,12 \cdot 10^{-2})^2}$ —the density of the latent energy of the material in the initial state; HV_w and G_w —Vickers hardness of the roll’s surface and shear modulus;

$u_{Tw} = \rho_w \cdot c_w \cdot T_w$ —the thermal component of the density of the latent energy of the working roll material by the temperature T_w ; ρ_w, c_w —the density and the heat capacity of the material by the temperature T_w ;

$k = 1 \dots 5$ —the number of the elastic–plastic area in the deformation zone [16];

$N_{\text{fr(mech)}k}^{\text{SP}}(x, t_j)$ (in Eq. (5))—the distribution along the width of the strip (by the coordinate x) of the specific power of the mechanical component of the friction force in each k th area of slippage in the contact zone between the working roll and the strip in the period of time t_j of the j th strip rolling:

$$N_{\text{fr(mech)}k}^{\text{SP}}(x, t_j) = \tau_{\text{mech } k}(x, t_j) \cdot V_{\text{sl } k}(x, t_j); \quad (8)$$

$\tau_{\text{mech } k}(x, t_j)$ —the distribution along the width of the strip (by the coordinate x) of the mechanical component of contact shear stresses in the k th area of the deformation zone in the period of time t_j :

$$\tau_{\text{mech } k}(x, t_j) = p_{m k}(x, t_j) \cdot f_{\text{mech } k}(x, t_j) \quad (9)$$

$p_{m k}(x, t_j)$ —the distribution along the width of the strip (by the coordinate x) of the mean pressure in each k th area in the deformation zone in the period of time t_j defined for the worn-out profile of active generatrices of the working rolls $R_w^u(x, t_{j-1})$ and $R_w^b(x, t_{j-1})$ defined after the rolling of the previous $(j-1)$ th batch of strips;

$f_{\text{mech } k}(x, t_j)$ —the distribution along the width of the strip (by the coordinate x) of values of the mechanical component of the friction coefficient in each k th area of the strip slippage relative to rolls in the period of time t_j that could be found:

- in areas of the elastic slippage of the strip in lag and advance zones of deformation (for $k = 1,5$)—by the methodology of I.V. Kragelsky [17, 18]:

$$f_{\text{mech } 1,5}(x, t_j) = \frac{(1 \div 1.5) \cdot (\tau_{0w} \cdot \theta_w(T_w) \cdot \alpha_{ef w}) + \beta_w \cdot (\tau_{0w} \cdot \theta_w(T_w) \cdot \alpha_{ef w})^{0,5}}{3 \cdot (\tau_{0w} \cdot \theta_w(T_w) \cdot \alpha_{ef w})^{0,5} + \beta_w}; \quad (10)$$

τ_{0w} , β_w and $\alpha_{ef w}$ —the shear stress of intermolecular interaction of the friction unit “roll—strip,” the coefficient of cohesion hardening, and the coefficient of hysteretic losses of the working roll material;

- in the areas of plastic slippage of the strip in the lag and advance zones of deformation (for $k = 2,4$)—by the dependency [19, 20]:

$$f_{\text{mech } 2,4}(x, t_j) = m \cdot \sqrt{\xi \cdot R_{\text{max}(w)} / r_{(w)}}; \quad (11)$$

$m = \sigma_{\text{sc}} / \sigma_s$ —the coefficient of the contact layer hardening [19]; σ_{sc} and σ_s —the flow stress of material in the contact layer and in the main volume according to [19, 20]; in the hot rolling $\sigma_{\text{sc}} \approx \sigma_s$;

ξ —the coefficient of surfaces relative approach according to [19];

$R_{\text{max}(w)}$, $r_{(w)}$ —the maximum peak-to-valley height of the profile and the mean radius of curvature of the surface heights of the working roll;

$V_{\text{sl } k}(x, t_j)$ —the distribution of the slippage velocity of the strip and working roll in each k th area of the slippage according to [16].

The expected lifetime of the working rolls could be calculated using the preset value P of the planned pauses:

$$t_{n*} = t_{\delta*} \cdot (1 + P); \quad (12)$$

Therefore, the sequence of the calculations with a usage of Eqs. (3)–(5), (6)–(11) represents the methodology of design evaluation of the lifetime of the working rolls in the final stands of the widestrip hot rolling mills by the criterion of rolled strip profile accuracy. During this term, the required level of the cross-section gage variation is provided based on the forecast which could be made on the stage of design decision, improvement, and maintenance with the time advance.

3 Conclusion

On the basis of the general methodological approach to the mechanical system element reliability forecasting and of the energy mechanical concept of the stationary friction unit wear, the methodology of the lifetime calculation (resource) of the working rolls was designed taking into account the advanced methods of the evaluation of the kinematic, energy-power, temperature, and friction parameters of sheet rolling. The derived system of equations allows to simulate the changes in the deformation zone of the working roll's worn profile; therefore, the cross-section of the strip which could be used to evaluate the design resource by the moment of the gage variation reaching the restricted value.

The evaluation of the roll lifetime on the stage of design gives the possibility not only to plan the roll change schedule but to analyze the possible methods of their durability increasing to expand the efficiency of the mill with the simultaneous preservation of the rolled strip quality.

References

1. Konovalov YuV, Ostapenko AL, Ponomarev VI (1986) The calculation of sheet rolling parameters. a reference book. Metallurgiya, Moscow
2. Nazaibekov AB, Talmazan VA, Krivtsova ON (1999) The study on the reasons of failure and wear of working rolls of CBBRM 1700. Proc. on KarMetI. Almaty, pp 128–134 (In Russian)
3. Kozhevnikova IA, Garber EA (2010) The rolling production, vol 1. The development of the theory of thin-sheet rolling to increase efficiency of widestrip rolling work, book 2. Teplotechnik, Moscow, p 225
4. Antsupov AV, Antsupov AV, Antsupov VP (2017) Analytical method for project resource estimation of metallurgical machinery parts. Izvestiya Vysshikh Uchebnykh Zavedenij. Chernaya Metallurgiya 1(30):62. <https://doi.org/10.17073/0368-0797-2017-1-30-35>
5. Antsupov AV, Antsupov AV, Antsupov VP (2014) The development of the theory for the reliability of the machine parts prediction. Mach Build: Netw e-J Sci 2:26–32 (In Russian)
6. Antsupov AV, Antsupov VP (2016) Estimation and assurance of machine component design lifetime. Proc Eng 150:726–733. <https://doi.org/10.1016/j.proeng.2016.07.094>
7. Antsupov AV, Slobodyansky MG, Antsupov VP, Antsupov AV (2018) The evaluation of parts and nodes lifetime of metallurgical machines on the stage of design and maintenance: a tutorial. Magnitogorsk. State tech. University of them. G.I. Nosova, p. 211
8. Khazov BF, Didusev BA (1986) A reference book about calculation of the reliability of machines on the stage of design. Mashinostroenie, Moscow, p 224
9. Pronikov AS (2002) The parametric reliability of machines. The Publishing House of Bauman Moscow State Technical University, Moscow, p 560

10. Antsupov AV, Antsupov AV, Antsupov VP, Slobodianskii MG, Rusanov VA (2016) Energy-mechanical concept of the durability prediction of friction units on the wear resistance criterion of elements. *J Frict Wear* 37(5):494–499. <https://doi.org/10.3103/S1068366616050032>
11. Antsupov VP, Antsupov AV, Antsupov AV Jr, Slobodianskii MG (2012) Forecasting on the reliability of parts and nodes of metallurgical equipment during their design and maintenance: a tutorial. Magnitogorsk. State tech. University of them. G.I. Nosova, p 114
12. Antsupov AV, Antsupov AV, Slobodyansky MG (2010) The model of the wear process of friction units on the basis of thermodynamic analysis of their state. In: *Proceeding 68th scientific technology conferences on actual problems of modern science, engineering and education, Magnitogorsk, vol 1. Magnitogorsk. state tech. University of them. G.I. Nosova, pp 264–268*
13. Antsupov AV, Antsupov AV, Antsupov VP (2009) The choice of the wear-resistant materials for the design of friction units. In: *Proceeding 67th scientific technology conferences on actual problems of modern science, engineering and Education (Magnitogorsk) vol 1. Magnitogorsk. State tech. University of them. G.I. Nosova, pp 197–200*
14. Antsupov AV, Antsupov VP, Slobodianskii MG (2016) Analytical model of wear-out failures of working rolls at wide-strip rolling mills *Proc Eng* 150:411–415. <https://doi.org/10.1016/j.proeng.2016.06.754>
15. Garber EA, Klopotin MV (2013) Simulation and upgrading of the thermal mode and caliber of rolls of the widestrip mills of hot rolling. Teplotechnik, Moscow
16. Garber EA, Kozhevnikova IA (2013) The theory of rolling. Teplotechnik, Moscow
17. Antsupov AV et al (2008) The model of the thermal state of the CBMHR in its cooling by air-water flux. In: Frolov KV (ed) *The modern tribology Resume and prospect. LKI publishing, Moscow, pp 158–164*
18. Kragelsky IV, Dobychin MN, Kombalov VS (1977) The basics of calculation on friction and wear. Mashinostroenie, Moscow
19. Gorenstein MM (1972) Friction and technological lubricants in rolling. Tekhnika, Moscow
20. Levanov AN, Kolmogorov VL, Burkin SP (1976) Contact friction in processes of metal-forming. Metallurgiya, Moscow



Monitoring the Technical Condition of the Mass Air Flow Sensors and the Cylinder-Piston Group in Test Modes

A. V. Gritsenko^{1,2}, V. D. Shepelev¹ (✉), and F. N. Grakov²

¹ South Ural State University (National Research University), 76, Lenin prospect, Chelyabinsk 454080, Russia

shepelevvd@susu.ru

² South Ural State Agrarian University, 13, Gagarin St, Troitsk 457100, Russia

Abstract. All modern automobiles and tractors produced by manufacturers are equipped with mass air flow sensors (MAFS). Electronic systems in automotive vehicles are among the first in the number of failures, in particular MAFS. Analysis of the causes of MAFS failure showed the presence of many operational factors contributing to the reduction of its resource. As a promising method, the MAFS test diagnostics method is proposed by forming a load due to complete and partial cylinder shutdown and certain internal combustion engine (ICE) fuel supply cycles. During the experiments, the controlled parameters were selected as follows: mass air flow, the voltage from the MAFS control terminal, crankshaft speed of the ICE, and hourly fuel consumption with varying throttle position from 0 to 100%. The use of the DBD-4 device and the MAFS diagnostic test methods allows getting an annual savings of up to 590,000 rubles per diagnostic post per year.

Keywords: Engine · Intake system · Mass air flow sensor · Shutdown · Monitoring · Fuel consumption

1 Introduction

The merging of electronics and mechanical actuators for automotive applications is driven by environmental and societal influences, quality and reliability [1–3]. Modern MAFS designs continuously control the air flow in the ICE taking into account its temperature, pressure, and reverse oscillations [4–6]. The more accurately the air flow control is carried out, the more efficiently the ICE modes are maintained with the minimum fuel consumption [7–9]. But despite the significant improvement in the modern MAFS, according to a number of works, this element of the microprocessor control system occupies one of the leading places in the number of failures, among which it should be noted: MAFS wire breaks and damaged connectors, poor contact, low or high signal level, and wire short to ground or positive wire [10–12]. However, the self-diagnostic system does not recognize the distortion of the output data from the MAFS, changes in the signal at individual points, and significant variations in the signals [13–15]. The

reason for the ambiguity in assessing the technical condition of the MAFS is the absence of specially provided actions, called test influences, to recognize the correct operation of the MAFS and assess its real technical condition [15, 16]. Thus, there is a need to develop test actions for recognizing latent MAFS failures that are not recorded by the standard self-diagnostics system [17–20].

With this in mind, the goal of this study is to develop a new test method for monitoring the technical condition of the MAFS on a working ICE to register hidden failures.

2 Methods

Let us consider the theoretical aspects of the application of the test diagnostics method and its features when used on modern automotive vehicles. In our case, the focus of consideration of the diagnostic process is placed on monitoring the technical condition of the MAFS and cylinder-piston group (CPG). When implementing test actions, only one of the four cylinders will be left in operation. A single cylinder, when other cylinders are switched off, is loaded with the power of mechanical losses of other cylinders. Already at this stage of disabling the cylinders, several ratios can be written [17, 20]:

$$K_1 = \frac{Q_1}{Q_2}, K_2 = \frac{U_1}{U_2}, K_3 = \frac{n_1}{n_2}, K_4 = \frac{V_1}{V_2} \quad (1)$$

where K_1 —coefficient taking into account the ratio of the amount of air entering the intake when all four cylinders are running Q_1 (kg/h) to the amount of air during the operation of one cylinder Q_2 (kg/h); K_2 —coefficient taking into account the ratio of the voltage value at the control terminal of the MAFS during the operation of all four cylinders U_1 (V) to the voltage value at the control terminal of the MAFS during the operation of one cylinder U_2 (V); K_3 —coefficient taking into account the ratio of the speed of the crankshaft of an ICE with all four cylinders n (min^{-1}) to crankshaft speed of an ICE with one cylinder n (min^{-1}); K_4 —coefficient taking into account the ratio of the value of the hourly fuel consumption when all four cylinders are running V_1 (kg/h) to the value of the hourly fuel consumption during the operation of one cylinder V_2 (kg/h).

Theoretical studies show that the coefficients K_1 , K_2 , K_3 , and K_4 for the ICE reference state lie within: $K_1 < 1$, $K_2 < 1$, $K_3 < 1$, and $K_4 < 1$. However, the values of all four coefficients are close to 1 and differ by 5–15% depending on the ICE parameters. With a change in the technical state of the ICE systems, in particular MAFS and CPG, all coefficients sharply tend to zero: $K_1 \rightarrow 0$, $K_2 \rightarrow 0$, $K_3 \rightarrow 0$, and $K_4 \rightarrow 0$. The ICE electronic control unit seeks to compensate for the deterioration in technical condition by correcting and maintaining an operable condition, including switching to emergency mode (emergency ICE algorithm). At system limit states and failures, there comes a point where an ICE cannot function on one cylinder.

Let us consider the change in the voltage value at the control terminal of the MAFS from the air flow rate (Fig. 1).

The analysis of the data in Fig. 1 shows that the maximum deviations from the reference voltage at the MAFS test pin lie within small limits, which are 5–10% at some points. When monitoring the technical condition in test modes, it is necessary to capture this deviation with high sensitivity.

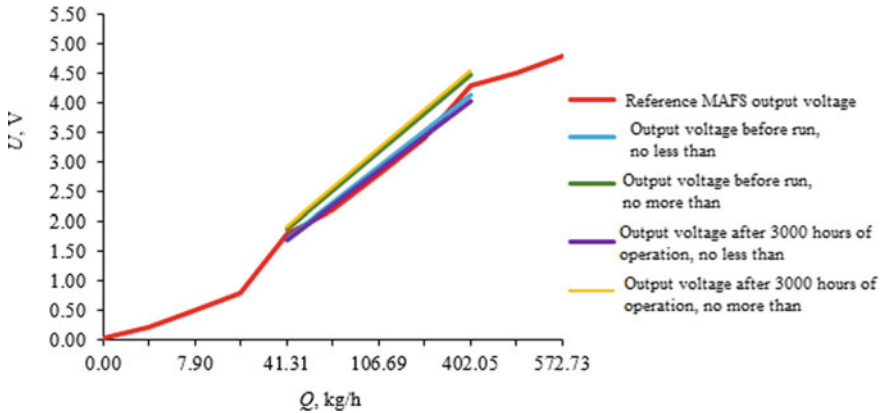


Fig. 1 Dependency between the voltage value at the control terminal of the MAFS U on the mass air flow rate Q

A general methodology for MAFS research was developed in the formation of test influences on a working ICE. All experimental studies were carried out at the stand with the ability to provide loading modes with instrumental methods and an electric motor in its design (Fig. 2).



Fig. 2 Stand with the ability to provide loading modes by instrumental methods and an electric motor in its design

The output parameters of MAFS can be significantly influenced by CPG. Therefore, during the preparation of the stand, separate cylinders of the ZMZ-4062 engine were

specially prepared. To assess the technical condition of the cylinders, the method of compression testing was used (pneumotester device K-69 M).

An electronic device DBD-4 was used to form the load on the ICE. This electronic device DBD-4 was used as the main tool in the formation of test influences in the process of experimental research. The CPG monitoring results were summarized in Table 1.

Table 1 Results of CPG control using the compression test method

Control output indicators	Checked cylinder number			
	1	2	3	4
U_2 (end-of-compression leak) (%)	32	22	29	14
U_2 at the limit state of the ICE (%)	28			
U_2-U_1 (leakage difference) (%)	8	4	9	3
U_2-U_1 at the limit state of the ICE (%)	20			
U_1 (early compression leak) (%)	24	18	20	11
U_1 at the limit state of the ICE (%)	14			

From the data presented in Table 1 for monitoring the CPG of the cylinders of the ZMZ-4062 engine, it can be seen that the limiting leakage value at the end of the compression stroke U_2 is observed in 1 and 3 ICE cylinders. The analysis of the leakage at the beginning of the compression stroke of U_1 shows the limit value of this parameter in 1, 2, 3 ICE cylinders. In addition, from Table 1 it follows that the parameter U_2-U_1 (leakage difference) does not exceed the limit value anywhere from the cylinders.

3 Results

The results of the experimental work were examined for excessive emissions of individual indications and non-conformities and were also verified by repeated experiment. Based on the refined output data, the dependencies of the mass air flow (Q) on the position of the throttle valve (R) were built (Fig. 3).

The analysis of the data in Fig. 3 shows that the growth dynamics of the mass air flow rate during the operation of the second and fourth cylinders somewhat differs from the first and third. Thus, the maximum value of the mass air flow rate is observed in the fourth cylinder and is 361 kg/h. A slightly lower value of Q is observed when the second cylinder is in operation—355 kg/h, whereas the maximum values of Q for the first and third cylinders are significantly lower and amount to 321 and 315 kg/h, respectively. The maximum difference in air flow values for the fourth and third cylinders is: $\Delta Q_{4,3} = Q_4 - Q_3 = 361 - 315 = 46$ kg/h. (12.7%).

The analysis of the data in Table 1 shows that the least CPG wear was found in the fourth cylinder and amounted to 14%. It is for this cylinder that the highest mass air flow

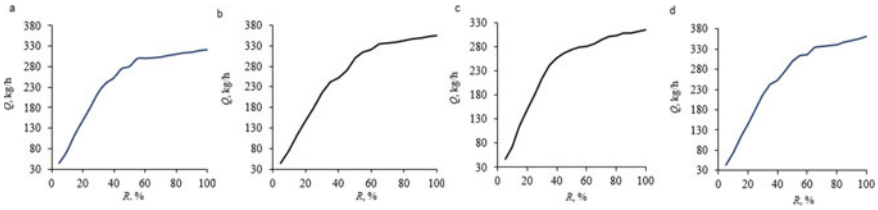


Fig. 3 Dependency of the mass air flow Q on the throttle position R during operation: **a** on the first cylinder (2, 3, 4 off); **b** on the second cylinder (1, 3, 4 off); **c** on the third cylinder (1, 2, 4 off); **d** on the fourth cylinder (1, 2, 3 off)

rate is observed - 361 kg/h. The wear of the second cylinder is slightly more than the fourth (22%), and this explains the slightly lower value of the mass air flow - 355 kg/h. The wear of the first and third cylinders is 32 and 29%, and for these wear values, the maximum mass air flow rate was 321 and 315 kg/h.

Simultaneously with fixing the value of the mass air flow, another very important diagnostic parameter was monitored—the voltage value from the MAFS control terminal (Fig. 4).

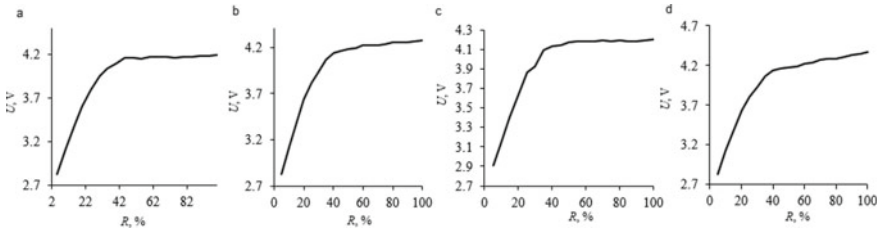


Fig. 4 Dependency of the voltage value from the MAFS control terminal U on the throttle position R during operation: **a** on the first cylinder (2, 3, 4 off); **b** on the second cylinder (1, 3, 4 off); **c** on the third cylinder (1, 2, 4 off); **d** on the fourth cylinder (1, 2, 3 off)

The analysis of the data in Fig. 4 confirms the conclusions formulated in Fig. 3—the voltage value from the MAFS control output U changes in proportion to the value of the mass air flow Q . For example, in the most sealed cylinders 4 and 2, respectively, large voltage values are fixed—4.37 and 4.27 V. While in the extremely worn cylinders of the first and third, the following results are observed—4.19 and 4.20 V. The maximum difference in voltage values occurs between the results of monitoring the fourth and first cylinders $\Delta U_{4,1} = U_4 - U_1 = 4.37 - 4.19 = 0.28$ V (6.4%).

Of significant value for assessing the technical condition of the intake system and MAFS is the parameter—the speed of the ICE crankshaft during the implementation of test modes. As a result of the experiments, data were obtained on the control of the speed of the crankshaft ICE depending on the position of the throttle valve (Fig. 5).

The analysis of the data in Fig. 5 shows that the most sealed cylinder (fourth) develops the highest maximum ICE crankshaft speed of 4230 min^{-1} at the maximum throttle valve opening. Next in terms of the degree of wear is the second cylinder with a leak at the end

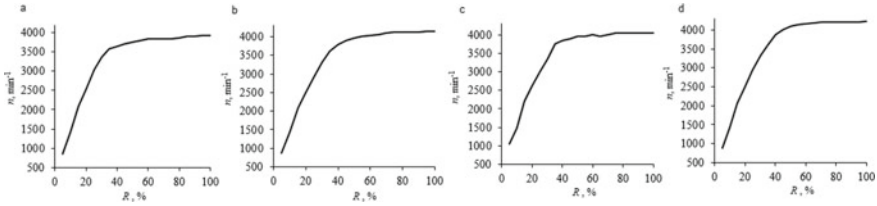


Fig. 5 Dependency of the crankshaft speed of the ICE n on the throttle position R during operation: **a** on the first cylinder (2, 3, 4 off); **b** on the second cylinder (1, 3, 4 off); **c** on the third cylinder (1, 2, 4 off); **d** on the fourth cylinder (1, 2, 3 off)

of the compression stroke—22%. The control of the crankshaft speed developed by the second cylinder at the maximum throttle valve opening showed a value of 4140 min^{-1} . And the control of the most worn out cylinders of the third and the first revealed the result: 4040 and 3930 min^{-1} . The maximum difference in the rpm of the crankshaft of the ICE arises between the results of monitoring the fourth and first cylinders $\Delta n_{4,1} = n_4 - n_1 = 4230 - 3930 = 300 \text{ min}^{-1}$ (7%). A rather sensitive parameter is the crankshaft rotation speed, on condition of the measurement accuracy is $1\text{--}3 \text{ min}^{-1}$.

And at the final stage of the experimental work, the hourly fuel consumption (V) from the throttle position (R) was estimated (Fig. 6).

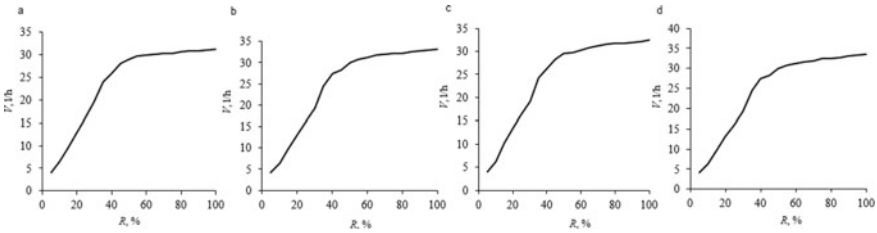


Fig. 6 Dependency of the hourly fuel consumption V on the throttle position R during operation: **a** on the first cylinder (2, 3, 4 off); **b** on the second cylinder (1, 3, 4 off); **c** on the third cylinder (1, 2, 4 off); **d** on the fourth cylinder (1, 2, 3 off)

The analysis of the results of monitoring the hourly fuel consumption (Fig. 6) showed that the highest value at the maximum degree of opening of the throttle valve is observed for the fourth cylinder 33.5 l/h . When controlling the hourly consumption of the second cylinder, the result was recorded— 33.1 l/h . The measurement of the parameters of the hourly fuel consumption in the third and first cylinders showed the data, respectively— 32.4 and 31.3 l/h . The presented result shows that with increasing CPG wear, the mass air flow value decreases and, accordingly, the fuel supply decreases. Thus, the cylinder with the best tightness will always show the maximum hourly fuel consumption. The maximum difference in hourly fuel consumption occurs between the results of monitoring the fourth and first cylinders $\Delta V_{4,1} = V_4 - V_1 = 33.5 - 31.3 = 2.2 \text{ l/h}$ (6.5%). This parameter is the result of a set of various input parameters and can additionally be used to clarify the technical condition of the intake system and CPG.

4 Conclusion

The experiment showed that the maximum difference between the air consumption values for the fourth and third cylinders is 46 kg/h (12.7%). The maximum difference in voltage values arises between the results of monitoring the fourth and first cylinders 0.28 V (11.8%). The maximum difference in rpm of the crankshaft of the ICE occurs between the results of monitoring the fourth and first cylinders 300 min^{-1} (7%). The maximum difference in hourly fuel consumption occurs between the results of monitoring the fourth and first cylinders of 2.2 l/h (6.5%). The economic effect of diagnosing one passenger car per year will amount to 3880 rubles.

References

1. Fleming WJ (2001) Overview of automotive sensors. *IEEE Sens J* 1(4):296–308. <https://doi.org/10.1109/7361.983469>
2. Schatz O (2004) Recent trends in automotive sensors. In: Rocha D, Sarro PM, Vellekoop MJ (eds) *IEEE Sensors 2004*, Vienna, 24–27 October 2004 proceedings of IEEE sensors, vol 1, no M3L-D.1, pp 236–239
3. Hourdakis E, Sarafis P, Nassiopoulou AG (2012) Novel air flow meter for an automobile engine using a Si sensor with porous Si thermal isolation. *Sensors (Switzerland)* 12(11):14838–14850. <https://doi.org/10.3390/s121114838>
4. Horning MA, Shakya R, Ida N (2018) Design of a Low-Cost Thermal Dispersion Mass Air Flow (MAF). *Sens Sens Imaging* 19(21). <https://doi.org/10.1007/s11220-018-0204-0>
5. Grimes MR, Verdejo JR, Bogden DM (2005) Development and usage of a virtual mass air flow sensor. *SAE Technical Papers* 2005–01–0074. <https://doi.org/10.4271/2005-01-0074>
6. Yu BL, Gan ZY, Liu S, Cao H, Xu JP (2007) Modeling and design of a new type air mass flow sensor. *Chin J Sens Actuators* 20(7):1517–1521
7. Buehler PJ, Franchek MA, Makki I (2002) Mass air flow sensor diagnostics for adaptive fueling control of internal combustion engines. In: *ASME international mechanical engineering congress and exposition*, New Orleans, 17–22 Nov 2002, pp 585–593. <https://doi.org/10.1115/IMECE2002-32023>
8. Park BK, Lee JS (2009) Measurements of thermal characteristics for a micro-fabricated thermal mass air flow sensor with real-time controller. *Trans Korean Soc Mech Eng B* 33(8):573–579. <https://doi.org/10.3795/KSME-B.2009.33.8.573>
9. Betta G, Capriglione D, Pietrosanto A (2006) Fault accommodation of mass air flow sensors in diesel automotive engines. In: *18th IMEKO world congress 2006: metrology for a sustainable development*, Rio de Janeiro, 17–22 Sept 2006, vol 1, pp 738–743
10. Buehler PJ, Franchek MA, Makki I (2002) Mass air flow sensor diagnostics for adaptive fueling control of internal combustion engines. In: *Proceedings of the American control conference*, Anchorage, 8–10 May 2002, vol 3, issue 62, pp 2064–2069. <https://doi.org/10.1109/ACC.2002.1023940>
11. Capriglione D, Liguori C, Pianese C, Pietrosanto (2003) A On-line sensor fault detection, isolation, and accommodation in automotive engines. *IEEE Trans Instrum Measur* 52(4):1182–1189. <https://doi.org/10.1109/TIM.2003.815994>
12. Komorska I, Woczyski Z, Borczuch A (2018) Fault diagnostics in air intake system of combustion engine using virtual sensors. *Diagnostyka* 19(1):25–32. <https://doi.org/10.29354/diag/80972>

13. Höckerdal E, Frisk E, Eriksson L (2011) EKF-based adaptation of look-up tables with an air mass-flow sensor application. *Control Eng Pract* 19(5):442–453. <https://doi.org/10.1016/j.conengprac.2011.01.006>
14. Suematsu K, Nosaka K, Okazaki T (2020) Development of a method to predict performance of sensing system with air mass flow sensor by CFD. *SAE Technical Papers Part F163706*
15. Desantes JM, Galindo J, Guardiola C, Dolz V (2010) Air mass flow estimation in turbocharged diesel engines from in-cylinder pressure measurement. *Exp Thermal Fluid Sci* 34(1):37–47. <https://doi.org/10.1016/j.expthermflusci.2009.08.009>
16. Gritsenko A, Shepelev V, Zadorozhnaya E, Shubenkova K (2020) Test diagnostics of engine systems in passenger cars. *FME Trans* 48(1):46–52. <https://doi.org/10.5937/fmet2001046G>
17. Gritsenko A, Shepelev V, Salimonenko G, Cherkassov Y, Buyvol P (2020) Environmental control and test dynamic control of the engine output parameters. *FME Trans* 48(4):889–898. <https://doi.org/10.5937/fme2004889G>
18. Dąbrowski Z, Zawisza M (2012) Investigations of the vibroacoustic signals sensitivity to mechanical defects not recognised by the OBD system in diesel engines. *Solid State Phenomena* 180:194–199. doi:<https://doi.org/10.4028/www.scientific.net/SSP.180.194>
19. Gritsenko AV, Shepelev VD, Shepeleva EV (2019) Optimizing consumption of gas fuel using static method of tuning automobile gas-cylinder equipment. In: Radionov A, Kravchenko O, Guzeev V, Rozhdestvenskiy Y (eds), *Proceedings of the 4th international conference on industrial engineering. ICIE 2018. Lecture notes in mechanical engineering*. Springer, Cham. https://doi.org/10.1007/978-3-319-95630-5_233
20. Gritsenko A, Shepelev V, Lukomsky K, Grakov F, Kostyuuchenkov N, Kostyuuchenkova O (2020) Control of the exhaust gas tract resistance of modern engines by the run-down time during testing. *Tribol Indus* 42(4):627–640. <https://doi.org/10.24874/ti.966.09.20.11>



Normalization of the Support Coefficient Values at Vibration of a Straight Multi-Span Beam

I. V. Kudryavtsev^(✉), O. I. Rabetskaya, and A. E. Mityaev

Siberian Federal University, 79, Svobodny Pr, Krasnoyarsk 660041, Russia
i.kudryavcev@sfu-kras.ru

Abstract. One of the most important parameters determining the dynamic behavior of an extended structure is the value of the first natural frequency of vibration, which usually must be equal to or greater than some certain value. Modeling extended structures with a beam model allows the engineer to quickly evaluate its first natural frequency of vibration, that is, to perform a check calculation, using the appropriate theory and reference literature. However, existing scientific techniques do not allow for design calculations, for example, selecting supports to obtain the certain value of the first natural frequency of beam vibration. An effective way to ensure the first natural frequency of beam vibrations is to choose the appropriate method of its fixation: the type of the end supports and, if necessary, intermediate supports. This paper proposes a method of normalizing support coefficients, which enables to obtain convenient comparable values when choosing supports and, as a result, to develop a method for reasonable selection of a support arrangement system for a straight beam. The obtained results can be used in the calculation and design of any beam structures for control of their first natural frequency of vibration by means of the arrangement of supports.

Keywords: Vibration · Beam · Support · Coefficient of support · First natural frequency · Normalizing

1 Introduction

Most structural elements in mechanical engineering are subject to forced vibrations from various periodic machines: engines, electric motors, various actuators, etc. In these cases, all elements of these structures are required to avoid resonances, in which their fatigue destruction is possible. Usually, at the first frequency of natural $[f_1]$, maximum stresses and deformations of the structure material are observed, so the task of ensuring the fatigue strength of the structural elements is largely reduced to the requirement to provide the necessary value of the first natural vibration frequency:

$$f_1 \geq [f], \quad (1)$$

where $[f]$ is acceptable first natural frequency value.

Mathematically, the problem of calculating the natural frequencies of vibrations is reduced to the compilation of differential equations of state with boundary conditions

reflecting the conditions of fixation [1–26]. Due to the difficulty of obtaining an analytical solution to such a problem, various numerical calculation methods are used and implemented in a number of specialized computer programs, which are usually based on FEA (Ansys, Nastran, etc.), which eliminates the problem of obtaining solutions for the design in question. However, numerical methods make it possible to obtain only individual private solutions and the problem of extrapolation and interpolation of calculation results arises, for example, in design calculations to evaluate the influence of the arrangement scheme and the type of supports on the dynamic behavior of the design when choosing the most rational solution [27, 28].

To solve this problem, reference literature [29, 30] has been developed, allowing the engineer to carry out the required calculations without the need to compile and solve differential equations. However, almost all of this literature are compiled in the form of universal tables and diagrams that do not explain the applicability of the proposed solutions. Another problem of such directories is their research approach; that is, they are designed to use them to evaluate the dynamic parameters of existing structures with given supports.

One effective way to ensure the value of the first natural frequency of vibrations of the extended structure is a reasonable choice of the type and arrangement of supports. Therefore, in practice, engineers usually need to solve the inverse problem of determining a system for arranging supports, for which the construction will have the necessary values of the first natural frequency of vibrations. In these cases, they have to design the structure by calculating many versions of its implementation, from which the most suitable option is then selected since in the existing literature there are no methods that would allow such a design task to be completed.

In this paper, a method is proposed that allows, on the basis of initial requirements, to make a reasonable selection of the support arrangement system, which provides the required values for the first natural vibration frequency. In order to obtain an explicit analytical solution, beam theory is used, which makes it possible to clearly evaluate the contribution of various factors (supports, geometric shapes and dimensions, material, etc.) to the obtained results. The basis of the method is the normalization of the support coefficient values, which makes it possible to bring the calculated equations to a convenient comparable form.

2 Criterion for Selecting a Support Arrangement System

The method of reasonable selection of the supports scheme requires the use of some criterion that will provide the required values for the first frequency of natural vibrations. As such a natural criterion, we choose the support coefficient, which is formed when solving the differential equation of beam vibrations and is determined only by the conditions of its fixations.

2.1 Derivation of the Original Support Coefficients

Consider the harmonic vibrations of the straight hinged beam, since this scheme allows modeling the most real structures as well as external periodic loads (Fig. 1).

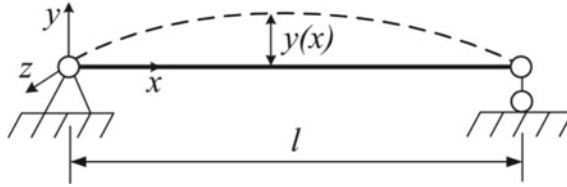


Fig. 1 Harmonic vibrations of the hinged beam

In this case, the first form of natural vibrations is the transverse vibrations in the plane of the least stiffness, around the z -axis in Fig. 1. Such transverse vibrations are the most dangerous since they occur with the largest part of effective beam mass and lead to maximum bending stresses. According to the accepted scheme in Fig. 1, the equation of free vibrations by the theory of vibration has the form [26]:

$$EJ_{\min} \frac{\partial^4 y}{\partial x^4} + m \frac{\partial^2 y}{\partial t^2} = 0, \tag{2}$$

where $y = y(x)$ is the beam deflection; E is the elastic modulus of the beam material; J_{\min} is the minimum moment of inertia of the beam cross section; m is the mass per beam length.

As the deflection function $y(x)$ for bending vibrations, we take the equation in the form:

$$y_1(x, t) = A \sin\left(\frac{x\pi}{l}\right) \sin(\omega t), \tag{3}$$

where A is the amplitude and ω is the circular frequency.

To solve Eq. (2), you must specify four boundary conditions that conform to the beam fixation conditions in the supports. Substituting the deflection Eq. (3) into the free vibration Eq. (2) and taking into account the boundary conditions, we obtain a system of linear equations. The first eigenvalue of this system will determine the solution for the first vibration frequency of the beam, which has the form [30]:

$$f_1(\Delta T) = \frac{\alpha^2}{2\pi l^2} \cdot \sqrt{\frac{EJ}{m}}, \tag{4}$$

where α is the support factor, which takes into account the method of beam fixation at vibrations. For the case under consideration (Fig. 1), it is equal to:

$$\alpha = 3.1416. \tag{5}$$

The coefficient of supports α is determined only by the fixing conditions, which makes it possible to set the inverse task and control the first natural frequency of beam vibrations by choosing the arrangement scheme of supports with the required value of the coefficient α . Consider the three most common straight beam fixation schemes (Fig. 2) and associated reference coefficient values (Table 1), which can be determined from reference literature [30] or from the solution of Eq. (2).

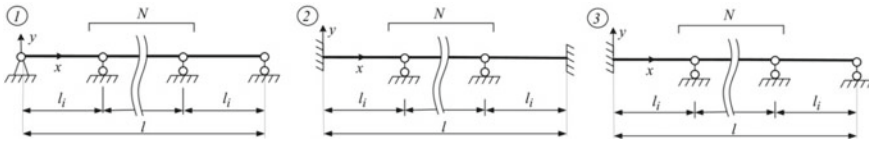


Fig. 2 Straight beam fixation schemes

Table 1 Original values of support coefficients α

Scheme №	Number of intermediate supports N											
	0	1	2	3	4	5	6	7	8	9	10	
1	3.1416											
2	4.730	3.927	3.557	3.393	3.310	3.260	3.230	3.210	3.196	3.186	3.180	
3	3.927	3.393	3.261	3.210	3.186	3.173	3.164	3.159	3.156	3.153	3.151	

Schemes in Fig. 2 differ in the types of end supports and the number of intermediate supports N . At $N = 0$, we obtain a single-span beam as a special case of a multi-span structure. We believe that in the above diagrams all supports are equally spaced from each other, and in this case, the length of each span is defined as:

$$l_i = \frac{l}{N + 1}. \tag{6}$$

The maximum number of intermediate supports in this paper is 10, which is enough in most practical cases. If necessary, it is possible to obtain values for any number of intermediate supports, but from the analysis of Table 1, it follows that at $N > 7$ the number of intermediate supports weakly affects the value of coefficients α and is less and less dependent on the type of end supports.

2.2 Normalizing of the Support Coefficients

The use of original values of the support coefficients α (Table 1) is difficult when designing the support arrangement schemes due to the lack of rationing and accounting for the number of spans. For example, they do not allow you to explicitly estimate how much the value of the first natural vibration frequency will change when the number of intermediate supports changes or the type of fixation scheme changes. For the convenience of calculations, we convert the initial values of the support coefficients α so that their values become normalized. As the basis of normalizing, we take the coefficient of supports of a free beam at its vibrations at the first natural frequency. We divide all original values of support coefficients in Table 1 by the free beam support coefficient, which, taking into account (5), will lead to the following conversion equation:

$$\alpha' = \left(\frac{\alpha \cdot (N + 1)}{\pi} \right)^2. \tag{7}$$

Table 2 New values of support coefficients α'

Scheme №	Number of intermediate supports N										
	0	1	2	3	4	5	6	7	8	9	10
1	1	4	9	16	25	36	49	64	81	100	121
2	2.267	6.251	11.54	18.66	27.75	38.77	51.80	66.82	83.83	102.8	124.0
3	1.562	6.288	9.697	16.71	25.72	36.72	49.70	64.71	81.75	100.7	121.7

New values of support coefficients α' are given in Table 2.

The proposed method of normalizing (7) made it possible to establish a direct dependence for the first natural frequency of vibration on new values of support coefficients, while the type of recording of Eq. (4) for the first vibration frequency practically do not change:

$$f_1(\Delta T) = \alpha' \frac{\pi}{2l^2} \cdot \sqrt{\frac{EJ_{\min}}{m}}. \tag{8}$$

In Eq. (8), the first natural frequency of vibration is now linearly determined by the new support coefficient, and the total beam length l is used, since the number of intermediate supports is already taken into account by the new values of the support coefficients α' . Also, from the values in Table 2, it is possible to easily set how many times the first natural frequency will change depending on the type of end supports and the number of intermediates supports N since the new coefficients α' are directly determined. Finally, the new values of the support coefficients α' can be taken as a criterion for the reasonable selection of the support arrangement scheme, which will ensure the fulfillment of its operability conditions (1) and implement the design method for calculating the beam.

3 Selection Method of Fixation Scheme

Normalization of support coefficients allows obtaining a simple procedure of reasonable selection of straight beam fixation scheme, for which the first frequency of natural vibration f_1 will not be lower or higher than the specified value $[f_1]$. To do this, we express from Eq. (8) the required minimum value of the support coefficient:

$$\alpha_{\min} = \frac{2l^2[f_1]}{\pi} \sqrt{\frac{m}{EJ_{\min}}}. \tag{9}$$

To meet the operability condition (1), it is necessary to select from Table 2 such a fixation scheme and the number of intermediate supports for which the values of the coefficient α' will not be less than the calculated value according to the expression (9), that is:

$$\min(\alpha') \geq \alpha_{\min}. \tag{10}$$

The selected scheme will ensure that the operability condition of the beam (1) is met, as can be seen by checking the actual frequency value with the selected coefficient value α' by Eqs. (8) or (4). Similarly, the calculation is carried out for the case when the first natural frequency of the beam should be below the specified value $[f_1]$.

4 Discussion

The proposed approach to the normalizing of support coefficients and the use of the well-known theory of beam vibrations without changes allow us to argue that the developed technique is workable and does not introduce any deviations. A new version of the representation of coefficients α' allowed obtaining their values convenient for comparison. We set how many times the coefficients α' increase, that is, actually the first natural frequency, depending on the type of end supports and the number of intermediates supports N compared to an absolutely free beam. In this case, the new values of the beam support coefficients α' and will be the desired values, which plotted in Fig. 3.

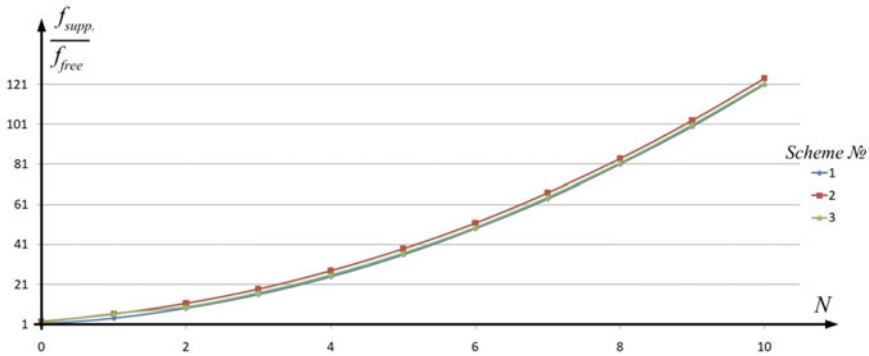


Fig. 3 Relation of the natural vibration frequency of the supported and free beam

Also of practical interest is the relative dependence of the values of the support coefficients α' , which shows how many times the first natural frequency will change when one intermediate support is added or removed (Table 3).

Table 3 Relative change of values of support coefficients α' from scheme and number of intermediate supports N

Scheme №	Number of intermediate supports N										
	0	1	2	3	4	5	6	7	8	9	10
1	1	4	2.25	1.778	1.563	1.44	1.361	1.306	1.266	1.235	1.21
2	1	2.757	1.846	1.617	1.487	1.397	1.336	1.299	1.255	1.226	1.206
3	1	4.025	1.542	1.723	1.539	1.428	1.353	1.302	1.263	1.232	1.209

The obtained relative changes of values of coefficients α' from the number of intermediate supports are also represented in the form of graphs, which are given in Fig. 4.

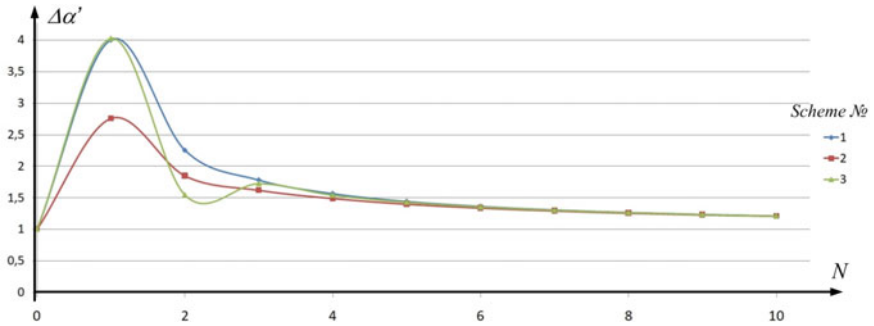


Fig. 4 Relative change of values of support coefficients α' from scheme and number of intermediate supports N

Graphs show that intermediate supports effectively affect the first natural frequency of vibration, increasing their values. It can also be seen that with a large number of intermediate supports, an increase in their number weakly affects the change in the value of the coefficient α' . For example, at $N > 7$, adding new support increases the first natural frequency of vibration by only 1.21 times, that is, by about 21%. It can also be noted that at $N > 5$, the values of the coefficients α' are weakly dependent on the type of end supports and are determined only by the type of intermediate supports.

5 Conclusion

The paper proposes the development of the theory of beam vibrations in the form of normalization of support coefficients, which made it possible to obtain explicit comparative values for them, as well as to develop a method for the reasonable selection of the scheme for fixing straight beams, which provides the given requirements for the minimum frequency of natural vibrations. The proposed approach can be used in designing any extended structures to provide their first natural frequency of vibration by selecting the method of fixation.

Acknowledgements. The research was funded by RFBR, Krasnoyarsk Territory and Krasnoyarsk Regional Fund of Science, project number 20-48-242922.

References

1. Krein MG (1933) Vibration theory of multi-span beams. Vestnik Inzhenerov i Tekhnikov 4:142–145
2. Miles LW (1956) Vibration of beams on many supports. ASCE J Eng Mech 82:1–9

3. Lin YK (1962) Free vibration of a continuous beam on elastic supports. *Int J Mech Sci* 4:409–423
4. Sen Gupta G (1970) Natural flexural wave and the normal modes of periodically-supported beams and plates. *J Sound Vib* 13:89–101
5. Zhu L, Elisacoff I, Lin YK (1994) Free and forced vibrations of periodic multispan beams. *Shock Vib* 3:217–232
6. Balachandran B (2009) *Vibrations*. Cengage Learning, Toronto, Canada
7. Benaroya H, Nagurka M, Han S (2017) *Mechanical vibration*. CRC Press, Taylor & Francis Group
8. Bottega WJ (2006) *Engineering vibrations*. CRC Press, Taylor & Francis Group
9. Clough RE (1995) *Dynamics of Structures*. McGraw-Hill College, USA
10. Geradin M, Rixen DJ (2015) *Mechanical vibrations*. Wiley, UK
11. Hartog JP (1985) *Mechanical vibrations*. McGraw-Hill, New York
12. Hagedorn P (2007) *Vibrations and waves in continuous mechanical systems*. Wiley, NJ
13. Inman DJ (2014) *Engineering vibration*. Pearson Education, NJ, USA
14. Kelly SG (2007) *Advanced vibration analysis*. CRC Press, Taylor & Francis Group, LLC, USA
15. Jazar RN (2013) *Advanced vibrations. A modern approach*. Springer, NY. <https://doi.org/10.1007/978-1-4614-4160-1>
16. Kelly SG (2012) *Mechanical vibrations. Theory and applications*. Cengage Learning, USA
17. Leissa AW (2011) *Vibration of continuous systems*. McGraw-Hill, New York
18. Meirovitch L (1967) *Analytical methods in vibrations*. The Macmillan Company, New York
19. Meirovitch L (2001) *Fundamentals of vibrations*. McGraw-Hill, Book Co, New York
20. Rades M (2010) *Mechanical vibrations II. Structural dynamic modeling*. Printech Publisher, Turin
21. Rao S (2018) *Mechanical vibrations*. Pearson Education Limited, UK
22. Shabana AS (2019) *Theory of vibration*. Springer, New York
23. Blekhman II (2004) *Selected topics in vibrational mechanics*. World Scientific Publishing Co. Pte. Ltd, Singapore
24. Magnus K (1965) *Vibrations*. Blackie & Son, UK
25. Baddour N (2011) *Recent advances in vibrations analysis*. INTECH open. Croatia
26. Weaver W, Timoshenko SP, Young DH (1992) *Vibration problems in engineering: solutions manual*. Wiley, UK
27. Shrihande M (2008) *FEM and computational structural dynamics*. PHI Learning Private Limited, New Delhi
28. Moaveni S (2015) *Finite element analysis*. Pearson, USA
29. Biedermann VL (1980) *Applied theory of mechanical vibrations*. M.VSH, Russia
30. Blevins RD (2016) *Formulas for dynamics, acoustics and vibration*. Wiley, UK



Animation Modeling as a Method of Structural and Kinematic Synthesis of Mechanisms

Yu I. Brovkina^(✉), T. S. Rabicheva, and E. A. Petrakova

Moscow Polytechnic University, 38, Bolshaya Semenovskaya Street, Moscow 107023, Russia

Abstract. Any mechanism's design begins with choosing its structural and kinematic layout. The length of the links, the location of the hinges relative to each other, the choice of the initial link rotation direction outline the dimensions of the future output link working area, and the trajectories of the mechanisms' joints and bearing points. By visualizing the design process as early as at the initial stages, one can reduce the number of options for structural schemes, and, consequently, the time spent on the mechanism development. The use of modern CAD tools allows both visualizing the mechanism movement and optimizing the selection of parameters used to determine the best conditions for obtaining the desired structural and kinematic properties. The visual design method allows identifying the dependencies, including those inexplicit, between the mechanism geometric parameters, and finding a solution in a short time. The paper discusses the application of this technique to the mechanism with a double rocker arm stroke. Using this technique in synthesis, the authors determine the dimensions affecting the angular pitch of the output link. This technique is applicable when a single kinematic scheme is used to solve various technological problems, for example, to implement a certain movement trajectory or to fit the mechanism moves into a certain working area.

Keywords: Mechanisms · Design · Synthesis · Animation · Visualization

1 Introduction

The mechanisms' synthesis has been relevant since the first machines appeared. Artobolevsky [1], Levitsky [2], Chebyshev [3], and other authors considered the methods for determining the lengths of links and the resulting trajectories. Currently, when a non-standard mechanism scheme is designed or an existing design is optimized, a designer is to determine the overall dimensions of the mechanism that meet the specified requirements in the shortest possible time.

For lever mechanisms featuring one and two degrees of mobility, the known methods of basic hinge mechanisms calculation are based on graphical and analytical methods. The graphical method provides good visualization, but it requires multiple construction iterations and numerous calculations to obtain the desired result. The analytical method shows the coordinate relationships between the links' lengths and the angles of their slopes. This technique requires the designer to be a confident user of specialized software and to have certain programming skills. Above that, finding a specific solution requires solving fairly complex equations.

The use of the structural-parametric synthesis method featuring an animation modeling function (it combines the advantages of graphical and analytical methods) to identify the dependencies between geometric and kinematic parameters, and the output function of mechanisms; as well as to optimize the design process is an urgent practical task.

2 Relevance, Scientific Significance of the Issue with Brief Overview of Literature

Modern mechanical engineering is very much concentrated on the development and research of new mechanisms. The search for simple solutions gives a new impetus to the development of lever mechanisms. The use of new materials and innovative methods of additive manufacturing allows for the expansion of the scope of such mechanisms. The main and the most important stage of creating a mechanism is structural and kinematic synthesis, i.e., designing the mechanism movement scheme with the account to the specified geometric characteristics. The development of automatic design systems entails a transition from a parametric synthesis to a structural-parametric one [4]. The main peculiarity of the structural-parametric synthesis is that the structure is defined during the synthesis, as well as that it can be changed at various stages of design. This helps to design a mechanism that most accurately meets the specified requirements. 3D modeling can significantly simplify the design process [5–18], but it is more convenient to solve kinematic analysis and synthesis problems in 2D. The constraints or qualitative indicators in the synthesis of mechanisms used are as follows:

- the condition of the links rotatability, i.e., ensuring that the input and (or) output links can be rotated at an angle of more than 360° ;
- acceptable pressure angles, i.e., the angle between the vector of the driving force from the driving member to the driven one, and the velocity vector at the point of application must not exceed certain permissible values in order to eliminate unacceptably large values of reactions in kinematic pairs, the low efficiency of the mechanism, the possibility of jamming (the impossibility of movement at any value of the driving force on the input link);
- design restrictions on the mechanism dimensions; i.e., the links size must ensure that the mechanism fits into the specified dimensions;
- accurately ensured specified law of motion or the specified positions of the mechanism links;
- other conditions and requirements determined by the conditions of operation and operation of the mechanism.

Kinematic mobility cannot be determined only by the type and number of links and kinematic pairs; it is necessary to consider the location of links and dimensional measurements. The scheme, which represents the mechanism's structure and kinematic mobility, is called a structural–kinematic scheme. The method of structural–kinematic synthesis through fitting structural units is considered in (6).

3 Formulation of the Problem

Lever mechanisms allow getting various trajectories of the output link—from a straight line to a perfect circle. When designing lever mechanisms, the use of CAD tools for solving synthesis problems very much simplifies finding optimal solutions. The ability to visualize the result of the synthesis using animation allows seeing the synthesized mechanism in operation and adjusting the necessary dimensions. This technique is instrumental when the structure of the mechanism is initially unknown, but there are, for example, restrictions on the trajectory of the output link.

The study describes the visual animation method used for structural and kinematic synthesis illustrated by the example of a mechanism with a double output link stroke. A feature which distinguishes the developed mechanism from the Chebyshev prototype is the difference in the values of the rocker arm span. The mechanism proposed by Chebyshev performs two equal strokes of the output link; see Fig. 1. For some automatic machines types, it is required to provide a rocker arm with double stroke, but unequal angular steps, for example, 180° and 20° per a crank rotation. The main objective of the study was to identify geometric dependencies that affect the value of the angular step. The CAD program of parametric modeling T-FLEX CAD (Russia) was chosen for the study.

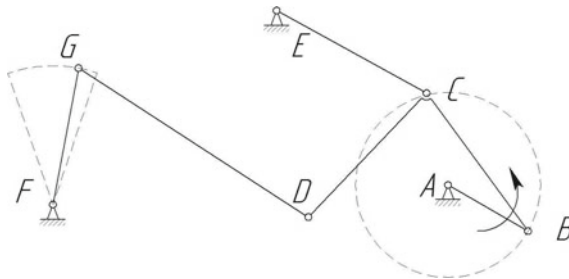


Fig. 1 Chebyshev mechanism with double rocker arm GF

The main developments in parametric design concern 3D modeling. Parameterization has not previously been used to study the mechanisms structural and kinematic properties. Parameterization is instrumental to determine both the working area of a mechanism and its kinematic and dynamic characteristics.

4 Theoretical Part

The main task of a designer is to identify the parameters that can affect the mechanism links movement trajectory. In some cases, changing one or two dimensions can have a significant impact on the operation of the entire mechanism. For example, adjusting the length of the crank in a hinged four-link chain allows getting either two-arm or crank-rocker mechanisms. Determining dimensions, which affect the trajectory of the output link thus helping to obtain the angles of the rocker arm span $\gamma_{51} = 15 \dots 25^\circ$ and

$\gamma_{52} \simeq 180^\circ$ per rotation of the crank, is the task of this paper. In the course of the study, a scheme of a six-branched mechanism with one degree of freedom was obtained; see Fig. 2. The technique of animation parametric modeling showed that in order to obtain the required angles of the rocker arm span, it is necessary to place the hinges D and E on the same vertical line. The use of the parametric T-FLEX CAD model made it possible both to visualize the operation of the mechanism and to control the dimensions (synthesis parameters).

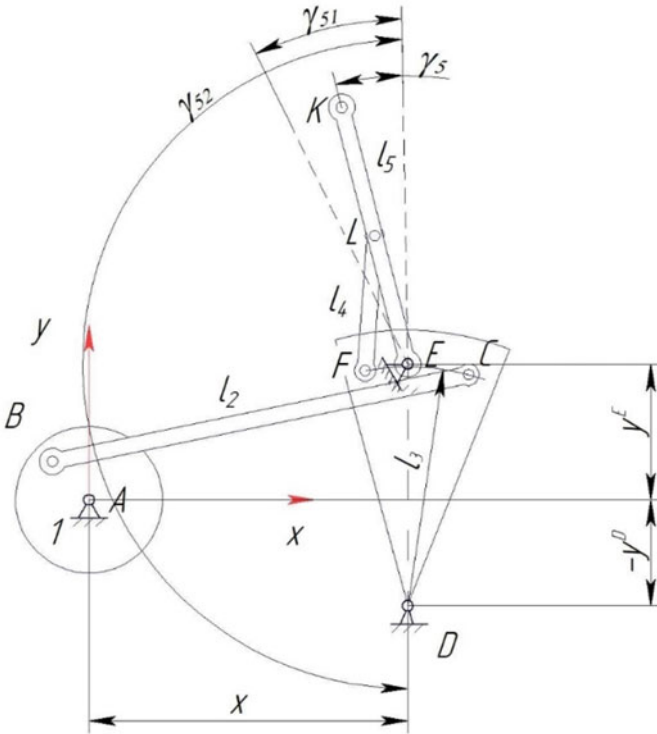


Fig. 2 Scheme of the synthesized mechanism with a double stroke of the KE rocker arm

Analytical design, for example, when MATLAB, Matlab, or GeoGebra software are used, requires the application of the coordinate method. The geometric approach gives a better visualization, but until recently it was considered an approximate method due to the construction error. Parametric mechanism synthesis with the help of CAD software allows solving the problem of the resulting design error.

In the course of the study, it was found that the desired output angles are functions that depend on the following variables Fig. 3:

- the length of the rocker $DC = DF$;
- connecting rod length FL ;
- the ordinate of the hinge $E - y_E$;

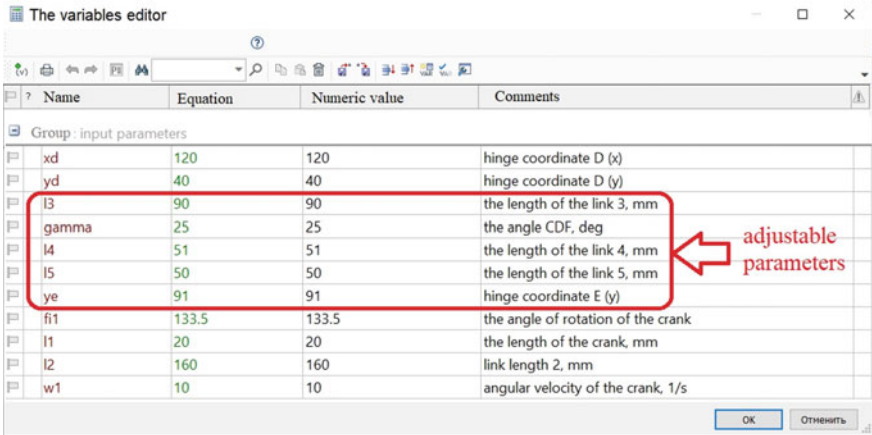


Fig. 3 Variable editor in T-Flex CAD software

- the length of the rocker arm EL .

The synthesis task was reduced to finding dependencies between the given parameters that would provide the required values of the output coordinate, namely the unfolded angle when the rocker arm 5 moves in the second phase of operation with minimal deviations in the first phase.

5 Practical Significance, Offers, Results of Experiments, and Implementation

The structural–kinematic synthesis performed with the help of the animation modeling method (see Fig. 4) revealed the following patterns:

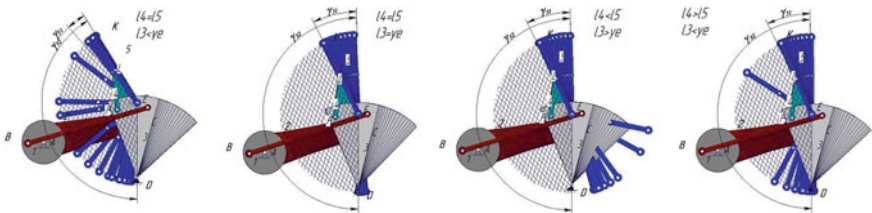


Fig. 4 Structural-parametric synthesis of a double-stroke rocker arm mechanism with the help of animation modeling

- when lengths FL and EL grow, there is an increase in the second phase and a reduction in the short travel time;
- when a DC size is larger than y_E , the second phase direction changes: The rocker arm rotates clockwise (see Fig. 4), as also indicated by the deflection in the graph in Fig. 5;

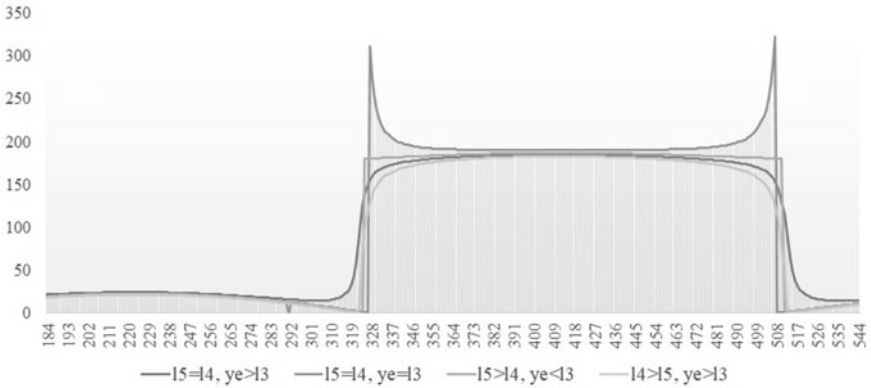


Fig. 5 Change in the swing angle of the rocker arm 5 at different ratios of lengths of the designed mechanism

- when equal values of the parameters are chosen, $FL = EL$, the obtained values of the angles γ_{51} and γ_{52} are close to the desired ones, but when the rocker arm 5 is operating, shocks may occur, due to a sharp change in the value of the angular velocity (see Fig. 7);
- when the length of the segment CF grows, it leads to an increase in the angular velocity of the rocker arm 5;
- the smoothest operation of the mechanism is achieved when and $y_E > DC$;
- to obtain the specified values of the angular step, the ratio of lengths must be at least $FL = 0,55y_E$, provided that $y_E > DC$;
- when $FL \neq EL$ and $y_E = DC$, the mechanism is not feasible.

The obtained functions showing the change in the angle of the rocker arm swing and its angular velocity at different ratios of length segments are shown in the graphs in Figs. 5 and 6.

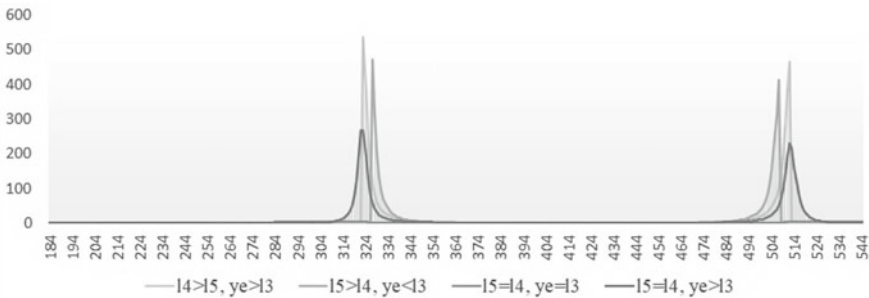


Fig. 6 Changing the angular velocity of the rocker arm 5

As a result of the synthesis, a double-stroke mechanism with the following geometric parameters was obtained: $l_1 = 0.02$ m, $l_2 = 0.16$ m, $l_3 = 0.088$ m, $l_4 = 0.052$ m,

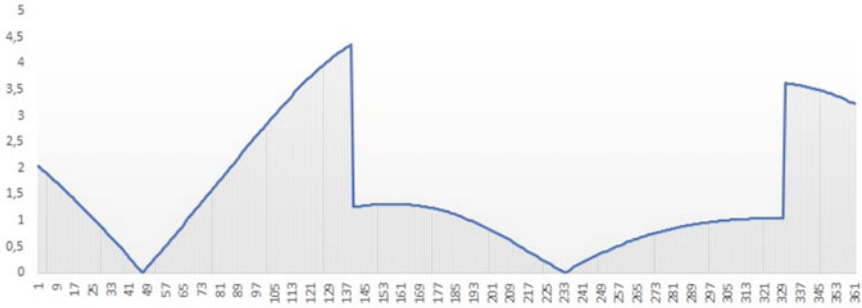


Fig. 7 Peak values of the angular velocity of the rocker arm 5

$l_5 = 0.05$ m, $y_E = 0.09$ m, $x_D = 0.12$ m, $y_D = -0.04$ m, $\angle FDC = 25^\circ$. The obtained values of the angles: $\gamma_{51} = 20, 5^\circ$, $\gamma_{52} = 180^\circ$.

The output link of the designed mechanism has two acceleration phases, which are characterized by an increase in the angular velocity. The rest of the time it moves almost uniformly. But a sharp increase in the angular velocity can affect the forces in kinematic pairs, so it is necessary to study the dynamic parameters of the designed mechanisms separately.

6 Conclusions

Thus, the block diagram of a two-circuit flat lever mechanism developed by the method of visual-parametric synthesis makes it possible to implement the law of motion of the output link in a double stroke with a different angle of swing per a crank rev. The animation modeling method reduces the time to determine the best possible parameters of the mechanism and can be used for the design of mechanisms both in the field of mechanical engineering and other industrial areas, for example, in furniture production. This technique allows for the metric, kinematic, and dynamic analysis.

References

1. Artobolevsky II (1988) Theory of mechanisms and machines. Nauka, Moscow
2. Levitsky NI (1967) Theory of mechanisms and machines. Nauka, Moscow
3. Chebyshev PL (1955) Selected Works. Paradoxical Mechanism. Publisher of the USSR Academy of Sciences, Moscow
4. Dzhuraev AD, Madrakhimov ShKh, Mansurova MA, Umarova ZM (2016) Analysis of the influence of connecting rod and rocker link lengths on the position function of a flat four-link mechanism. *Theor Mech Mach* 29:21–29. <https://doi.org/10.5862/TMM.29.2>
5. Verkhovod VP (2013) Kinematic geometry and synthesis of rectilinear guiding mechanisms in the GeoGebra system. *Theor Mech Mach* 2:100–112
6. Brovkina YI, Petrakova EA (2020) Structural-parametric synthesis of mechanisms in CAD-systems. *J Phys Conf Ser* 1515(4). <https://doi.org/10.1088/1742-6596/1515/4/042014>
7. Kong X, Gosselin C (2007) Type synthesis of parallel mechanisms. Springer, Heidelberg, pp 21–27

8. Brovkina YI, Reznikov SS, Sobolev AN, Nekrasov AY (2020) Theory of mechanisms and Machines in examples and problems. Kurs, Moscow
9. Brovkina YuI, Strizheus VA and Shipilov PA (2020) Experimental study on parameters of Fabbster and Picaso 3D personal printers with XZ-Head Y-Bed and XY-Head Z-Bed kinematics Journal of Physics: Conference Series 1679:042049. <https://doi.org/10.1088/1742-6596/1679/4/042049>
10. Evgrafov AN, Petrov GN (2018) The effect of self-braking of linkage mechanisms. Modern mechanical engineering: science and education MMESE-2018. Publishing House of the Polytechnic University, Saint Petersburg, pp 111–121
11. Pramanik S, Thipse SS (2020) Kinematic synthesis of central-lever steering mechanism for four wheel vehicles. Acta Polytechnica 60:252–258: <https://doi.org/10.14311/ap.2020.60.0252>
12. Sobolev AN, Nekrasov AYa (2016) The automated design of ratchet mechanisms. Messenger MSTU STANKIN 3(38):38–41
13. Glazunov VA (1991) Kinematic analysis of manipulators of parallel structure taking into account special provisions. Solid Mech 4:54–61
14. Sobolev AN, Nekrasov AY, Arbuzov MO (2017) The modeling of noncircular gears. Messenger MSTU STANKIN 1(40):48–51
15. Brovkina YuI, Sobolev AN, Nekrasov AYa (2017) An analytical method of the calculation of positional error of links of mechanisms of machines with parallel kinematics. Messenger MSTU STANKIN 1(40):52–56
16. Sobolev AN, Nekrasov AYa, Yagolnitsa OV (2017) An upgrade of the methodology of the design of harmonic reducers and of its using in construction preparation of students of engineering. Messenger MSTU STANKIN 2(41):23–26
17. Nekrasov AY, Sobolev AN, Arbuzov MO (2016) An innovate interactive software product as a means of the advancement of the efficiency of engineering devices design. Innovation 8(214):104–107
18. Yagolnitsa OV, Butrimova EV, Sobolev AN et al (2016) An information-measuring complex for the investigation of factors affecting for the ergonomics of production environment of machine-building enterprise. Life safety 9(189):11–14



Normalization of the Effective Length Factor Values at Buckling of a Straight Multi-Span Beam

I. V. Kudryavtsev^(✉), A. V. Kolotov, and A. E. Mityaev

Siberian Federal University, 79, Svobodny Pr, Krasnoyarsk 660041, Russia
i.kudryavcev@sfu-kras.ru

Abstract. This paper proposes a method of reasonable selection of the fixation scheme, and the number of intermediates supports for straight multi-span beams in order to ensure the given values of the critical load from the compressive axial force. This axial force may be an external load or may occur, for example, as a result of a change in beam temperature. An effective way of providing the first critical force of the beam is to choose the appropriate method of fixing it: the type of the main supports and, if necessary, intermediate supports. This paper proposes a method of normalizing effective length factors, which enables to obtain convenient comparable values when choosing a fixation method and, as a result, to develop a method for a reasonable selection of a support arrangement system for a straight beam. The technique is based on the well-known theory of beam stability and uses effective length factors as a criterion for selecting the fixation scheme, which is formed after solving the corresponding differential equations of the beam state and is determined only by the fixing conditions. The obtained results can be used in calculations and design of any extended beam structures to control their stability by selecting the appropriate fixation scheme.

Keywords: Stability · Beam · Support · Effective length factor · The first critical load · Normalizing

1 Introduction

Extended tubular elements of structures are widespread in mechanical engineering and usually serve to transport various liquid and gaseous substances; these include pipelines, oil pipelines, steam pipelines, railway rails, rods, cables, waveguides, etc. The appearance of axial forces, for example, from a change in the temperature of the material of such structures, causes a change in its geometric dimensions, which, if there are obstacles, for example in the form of fixed supports, leads to the appearance of temperature forces that can cause a loss of their stability. According to the theory of stability, the beam has an infinitely large number of critical loadings, but the most dangerous is the first critical force of loss of stability P_{cr1} . Then the condition for the operability of such extended multi-support beam structures is to provide the given minimum acceptable value of the first critical force P_{cr1} :

$$P_{cr1} \geq [P], \quad (1)$$

where $[P]$ is the acceptable value of the external force.

The mathematical problem of critical load calculation is reduced to compilation and solution of differential equations of state with boundary conditions reflecting conditions of fixation and loading [1–16]. The analytical solution to this problem is usually complex and uses various numerical calculation methods implemented in a number of specialized computer programs, which are usually based on FEA. However, numerical methods allow you to obtain only individual private solutions and there is a problem of extrapolation and interpolation of calculation results, for example, in design calculations to evaluate the effect of the arrangement scheme and the type of supports on the stability of the design when choosing the most rational solution [17, 18].

The existing reference literature [19, 20] allows the engineer to carry out stability calculations without the need to compile and solve differential equations. However, almost all of this literature is oriented towards a research approach; that is, it is designed to calculate the stability of existing structures with given fixations. However, in practice, engineers usually need to solve the inverse problem of determining the system for arranging structural supports, for which the design will have the necessary values of the first critical force. In these cases, they have to use a method of search, which is extremely ineffective.

In this work, a technique is proposed that allows, on the basis of initial requirements, to make a reasonable choice of the support arrangement system, which provides the required values for the first critical load. In order to obtain an explicit analytical solution, the theory of stability of beams is used, which makes it possible to clearly assess the contribution of various factors to the results. The basis of the technique is the rationing of the values of the support coefficients, which makes it possible to bring the calculated equations to a convenient comparable form.

2 Criterion for Selecting a Support Arrangement System

The development of a reasonable scheme selection technique that will provide the desired value for the first critical force requires the assignment of a scheme selection criterion. We choose as such a criterion the support coefficient also called the effective length factor, which is formed when solving the differential equation for the stability problem of the beam and is determined only by the conditions of its fixations.

2.1 Derivation of the Effective Length Factor

Figure 1 shows the loss of stability of the straight hinge beam under the compressive axial force.

According to the accepted scheme in Fig. 1, the equation of state at the moment of stability loss has the form [1]:

$$EJ_{\min} \frac{\partial^2 y}{\partial x^2} = -P \cdot y, \quad (2)$$

where $y = y(x)$ is the beam deflection; E is the elastic modulus of the beam material; J_{\min} is the minimum moment of inertia of the beam cross section; P is the external axial force.

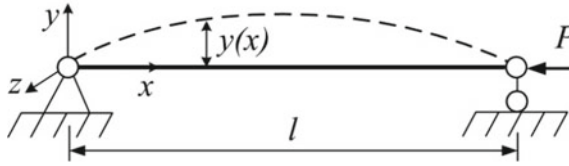


Fig. 1 Loss of beam stability under compression

The solution of this equation has a general form:

$$y = C_1 \cdot \sin(kx) + C_2 \cdot \cos(kx), \tag{3}$$

where C_1, C_2 are the coefficients determined from conditions of beam fixation and loading, k is the value calculated by formula:

$$k = \sqrt{\frac{P}{EJ_{\min}}}, \tag{4}$$

To solve Eq. (2), you must specify two boundary conditions that reflect the beam fixations conditions in the supports. As a result, for the first critical force, we get a solution in the form [1]:

$$P_{cr} = \frac{\pi^2 EJ_{\min}}{\mu^2 \cdot l^2}, \tag{5}$$

where μ is the effective length factor, which takes into account the method of beam fixation. In the case of fixing (Fig. 1), it is:

$$\mu = 1. \tag{6}$$

The effective length factor μ is defined by fixing conditions that give the opportunity to set the inverse task and to control the first critical force of a beam by means of the scheme of arrangement of support with the required value of this coefficient. We will consider the three most widespread schemes of fixing of a rectilinear beam (Fig. 2) and values of effective length factors corresponding to them μ (Table 1). You can determine the values of the coefficients μ from the reference literature [19, 20] or directly from the solution of Eq. (2).

The schemes of fixation in Fig. 2 differ only by end supports, and if there are no intermediate supports ($N = 0$), then we obtain a single-span beam. We accept that for multi-support beams all supports are equally spaced from each other and then the length of each span is:

$$l_i = \frac{l}{N + 1}. \tag{7}$$

The maximum number of intermediate supports in this paper is 10, but if necessary, values can be obtained for any number of intermediate supports. However, from Table 1 follows that at $N > 7$ the values of effective length factor slightly depend on the quantity of intermediate support and a type of end support.

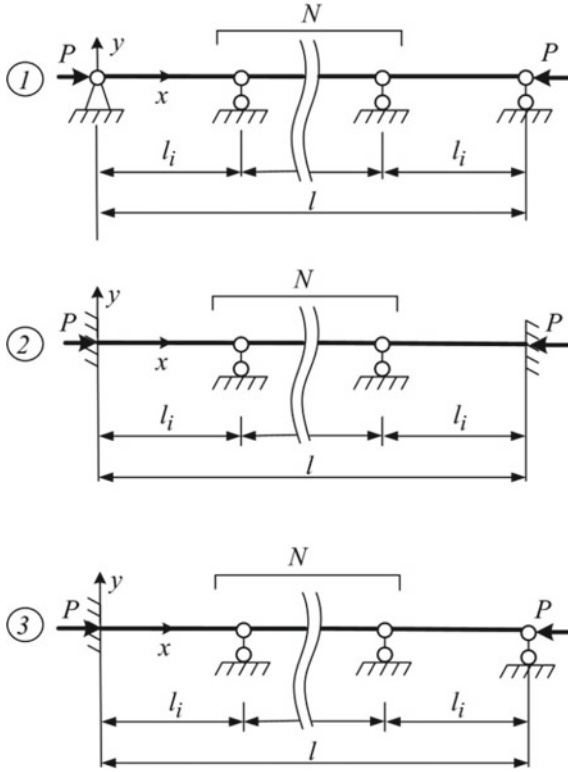


Fig. 2 Options of beam support arrangement scheme

Table 1 Original values of effective length factors μ

Scheme №	Number of intermediate supports N										
	0	1	2	3	4	5	6	7	8	9	10
1	1										
2	0.5	0.699	0.814	0.879	0.917	0.939	0.954	0.964	0.971	0.977	0.978
3	0.7	0.879	0.939	0.964	0.977	0.983	0.988	0.99	0.992	0.994	0.996

2.2 Normalizing of the Effective Length Factors

The original values of the effective length factors (Table 1) make it difficult to design the support arrangement schemes due to the lack of normalizing and accounting for the number of spans. For example, they do not allow you to explicitly estimate how much the value of the first critical force will change when you change the number of intermediate supports or change the type of fixation scheme. For convenience, we normalize the initial values of the effective length factors with respect to the unfixed, free beam support coefficient at its axial compression. We divide all original values

of epy effective length factors in Table 1 by the free beam support coefficient by the equation:

$$\mu' = \left(\frac{N + 1}{\mu} \right)^2. \tag{8}$$

New values of the effective length factors μ' for schemes in Fig. 2 are given in Table 2.

Table 2 New values of the effective length factors μ'

Scheme №	Number of intermediate supports N										
	0	1	2	3	4	5	6	7	8	9	10
1	1	4	9	16	25	36	49	64	81	100	121
2	4	8.187	13.58	20.71	29.73	40.83	53.84	68.87	85.91	104.8	126.5
3	2.047	5.177	10.21	17.22	26.19	37.26	50.2	65.3	82.31	101.2	122.0

The proposed method of normalizing (8) made it possible to establish a direct dependence for the first critical force on the new values of the effective length factors, while the form of writing of the equation for the first critical force (5) practically did not change:

$$P_{cr} = \mu' \cdot \frac{\pi^2 EJ_{min}}{l^2}. \tag{9}$$

In Eq. (9), the first critical force now depends linearly on the new values of the effective length factor and the total beam length l is used, since the number of intermediate supports is already taken into account according to Eq. (8). Also, the values in Table 2 determine how many times the first critical force will change depending on the type of edge supports and the number of intermediates supports N since the new values of the effective length factor directly determine it. Finally, the new values of the effective length factor can be taken as a criterion for the reasonable selection of the support arrangement scheme, which will ensure that its operability conditions (1) are met and allow the design method of calculating the beam to be implemented.

3 Selection Method of Fixation Scheme

Normalization of support coefficients allows obtaining a simple procedure of reasonable selection of scheme of fixation of a straight beam, for which the first critical force of P_{cr1} will not be lower or higher than specified value $[P]$. To do this, we express from Eq. (9) the required minimum value of the effective length factor:

$$\mu_{min} = \frac{P_{cr} \cdot l^2}{\pi^2 EJ_{min}}. \tag{10}$$

To meet the operability condition (1), it is necessary to select from Table 2 such a fixing scheme and the number of intermediate supports for which the values of the effective length factor μ' will not be less than the calculated value according to the expression (10), that is:

$$\min(\mu') \geq \mu_{\min}. \tag{11}$$

The selected scheme will ensure that the operability condition of the beam (1) is met, as can be seen by checking the actual value of the first critical force with the selected value of the effective length factor μ' according to Eqs. (9) or (5). Similarly, the calculation is carried out for the case when the first critical beam force should be below the specified value [P].

4 Discussion

The proposed approach to normalize the effective length factors made it possible to obtain their values convenient for comparison. For example, we can easily determine how many times the factors increase, that is, actually the first critical force, depending on the type of end supports and the number of intermediates supports N compared to an absolutely free beam. In this case, the new values of the beam effective length factors in Table 2 will be the desired values. Let us plot a graph from them, which clearly shows this dependence (Fig. 3).

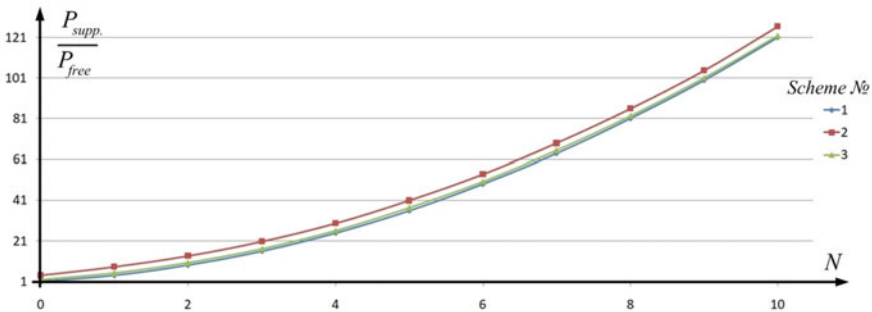


Fig. 3 Relation of the first critical force of the supported and free beam

Also of practical interest is the relative dependence of the values of the effective length factors μ' , which shows how many times the first critical force will change when adding or removing one intermediate support. We calculate this dependence separately within the limits of each attachment scheme in Fig. 2, the results are given in Table 3. The obtained relative changes of the values of the coefficients $\Delta\mu'$ from the number of intermediate supports are also presented in the form of graphs, which are given in Fig. 4.

Graphs show that the introduction of intermediate supports effectively affects the first critical force, increasing their values. It can also be seen that with a large number of intermediate supports, an increase in their number weakly affects the change in the value of the effective length factor μ' . For example, at $N > 7$, adding a new support increases the first critical force by only 1.21 times, that is, by about 20%.

Table 3 Relative change of effective length factor values $\Delta\mu'$ from scheme and number of intermediate supports

Scheme №	Number of intermediate supports N										
	0	1	2	3	4	5	6	7	8	9	10
1	1	4	2.25	1.778	1.563	1.44	1.361	1.306	1.266	1.235	1.21
2	1	2.047	1.659	1.525	1.436	1.373	1.319	1.28	1.247	1.219	1.208
3	1	2.53	1.972	1.687	1.521	1.422	1.347	1.301	1.261	1.23	1.206

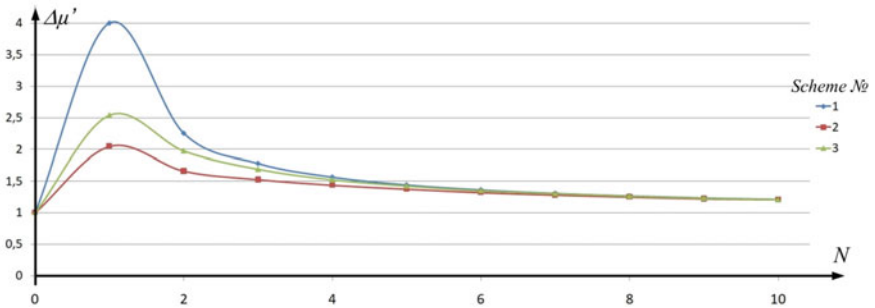


Fig. 4 Relative change of effective length factor values $\Delta\mu'$ from scheme and number of intermediate supports N

5 Conclusion

The paper proposes the development of the theory of stability of beams by normalizing the effective length factors, which made it possible to obtain visual comparative values for them, as well as to develop a method for the reasonable choice of the fixing scheme, which provides the given requirements for the minimum first critical force. The proposed approach can be used in designing any extended structures to provide their first critical force by choosing the method of fastening.

Acknowledgements. Research was funded by RFBR, Krasnoyarsk Territory and Krasnoyarsk Regional Fund of Science, project number 20-48-242922.

References

1. Timoshenko SP, Gere JM (2009) Theory of elastic stability, 2nd edn. Dover Publications, USA
2. Thomsen JJ (2003) Vibrations and stability. doi:<https://doi.org/10.1007/978-3-662-10793-5>
3. Farshad M (1994) Stability of structures. Elsevier Science & Technology, Oxford, p 434
4. Wang CM (2005) Exact solutions for buckling of structural members. CRC Press, p 212
5. Ziemian RD (2010) Guide to stability design criteria for metal structures. Wiley, p 1117

6. Ingerle K (2018) Non-conservative systems: new static and dynamic stability criteria. CRC Press
7. Jerath S (2020) Structural stability theory and practice: buckling of columns, beams, plates, and shells. Wiley
8. Dubin&acaron D (1999) Stability and ductility of steel structures (SDSS'99). In: Proceedings of the 6th international colloquium, first session, SDSs'99. Elsevier Science
9. Abramovich H (2017) Stability and vibrations of thin-walled composite structures. Woodhead Publishing
10. Gambhir ML (2004) Stability analysis and design of structures. Springer
11. Wiggers SL, Pedersen P (2018) Structural stability and vibration: an integrated introduction by analytical and numerical methods. Springer
12. Vinson JR (2012) The behavior of thin walled structures: beams, plates, and shells: beams: plates and shells. Springer
13. Pignataro M (2013) Stability, bifurcation and postcritical behaviour of elastic structures. Elsevier Science
14. McKenzie WMC (2013) Design of structural elements. Red Globe Press
15. He W, Liu L (2018) Active vibration control and stability analysis of flexible beam systems. Springer
16. Narayanan R (2007) Beams and beam columns: stability and strength. Applied Science Publisher
17. Shrikhande M (2008) FEM and computational structural dynamics. PHI Learning Private Limited, New Delhi
18. Moaveni S (2015) Finite element analysis. Pearson, USA
19. Biedermann VL (1980) Applied theory of mechanical vibrations. M.VSH, Russia
20. Blevins RD (2016) Formulas for dynamics, acoustics and vibration. Wiley, UK



Analysis of the Relationship Between the Transfer of the Mechanism of the Multi-operating Machine

G. A. Bahadirov and F. R. Rakhimov(✉)

Institute of Mechanics and Seismic Stability of Structures named after M.T.Urazbaev of the Academy of Sciences of the Republic of Uzbekistan, Durmon yuli Street, 33, Tashkent 100125, Uzbekistan

rahimov-furqat1992@inbox.ru

Abstract. This article discusses the problem of ensuring a stable motion of the feed mechanism of multi-operation machines for mechanical processing of semi-finished leather products. The given calculations determine some conditions, such as the lifting height of the pedal height limited by the movement of the operator's foot. The relation between the pressing forces and the pressure force on the working shaft shows that to create large values of the pressure force, the values of the pressing forces must also be large. It is shown that the strength of the human foot is insufficient to create large pressing force, so, additional devices and equipment are required. The graphs of the dependence of the force arising on the transporting roll on the angle between the pedal and the horizon, and on the angle between the lever holding the pedal and the vertical axis, and the force acting on the pedal were plotted and analyzed. Based on the results of theoretical studies obtained, research is underway to manufacture an experimental bench for a multi-operation roller machine

Keywords: Conveying mechanism · Tractive force · Semi-finished leather · Angle of contact · Free roller · Spreading table · Machining · Planning · Buffing · Average thickness · Passage width

1 Introduction

It is known that in many countries there are small and medium-sized enterprises for the processing of raw hides. These enterprises try to use the available leather raw materials efficiently and economically. This requires compact machines and equipment for the primary mechanical processing of leather semi-finished products in small batches.

Currently, there is a growing need for energy-saving and resource-saving equipment for the production of high-quality leather semi-finished products. For the needs of the tannery, up to 90 units of technological equipment are required [1–5].

Despite the variety of machines and mechanisms used in small enterprises in the leather industry, most of the technological operations in these enterprises are performed

manually. The mechanization level is 50–80%. In addition, even with mechanized operations, the operator is forced to manually perform heavy and monotonous auxiliary operations [6–11].

Due to low production capacity, small businesses do not use expensive, high-performance technological machines specializing in the mechanical processing of semi-finished leather products, since they are not used regularly and occupy production areas [12–18].

Consequently, the development of a machine that performs several technological operations is very relevant today.

2 Research Methods

A multi-operation machine was developed for the mechanical processing of semi-finished leather products [19]. The use of such a machine in small tanneries is economical and energy-efficient for the manufacturer. In this multi-operation machine, the feeder is made up of some links (Fig. 1). When the OA axis is pressed vertically by the force F_A , the OA lever moves the DE lever with the BC lever. In turn, the moving shaft E acts on the working shaft with the force F_2 . After that, the process of mechanical processing of the semi-finished leather product begins. Consider the problem of determining the pressure on the working shaft F_2 , created by the lever OA [20].

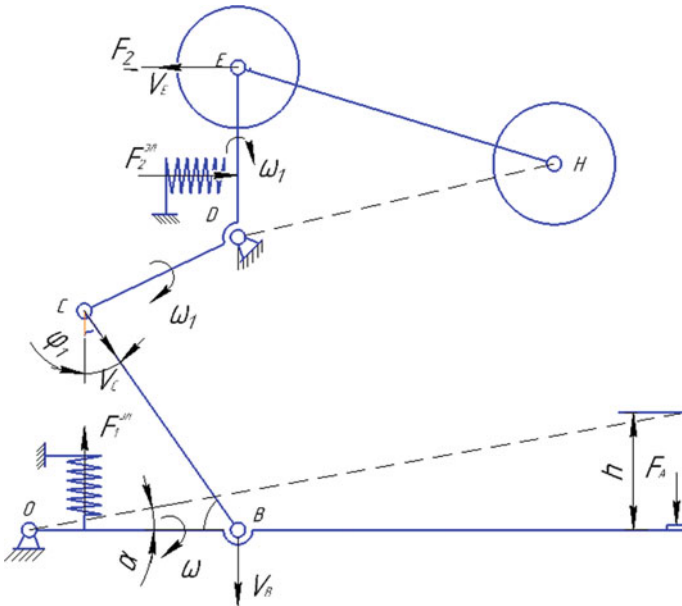


Fig. 1 Conventional scheme of the feeding mechanism of a multi-operation machine

To ensure the motion stability of this feeding mechanism, the force F_A applied to point A of the pedal, by the operator, should be sufficiently less, and the maximum lifting

height h from the ground to point A should be small enough so that the operator can easily create required pressure by pressing the pedal. For this, we investigated the regularity of the pressure acting on the working shaft, the angle of inclination of the OA lever to the horizontal axis and the vertical angle of rotation of the BC lever.

Let us consider the definition of the force parameters of the feeding mechanism of a multi-operation machine (Fig. 1).

First, determine the velocities of points A , B and C in Fig. 1. Since the BC lever moves plane-parallel, the projections of the velocities of points B and C are mutually equal relative to the axis directed along the length of the lever. i.e:

$$V_C = V_B \cdot \cos \varphi_1 \tag{1}$$

here φ_1 is the angle formed by the BC lever with the vertical axis.

DC and ED rotate about point D . Therefore, the velocities of points C and E are:

$$V_C = \omega_1 \cdot CD, V_E = \omega_1 \cdot ED \tag{2}$$

where ω_1 —is the angular velocity of the axis of rotation of the lever EH about point D .

From the first equation of the system of Eqs. (2) we find ω_1 :

$$\omega_1 = \frac{V_C}{CD}$$

From the system of Eq. (2), we determine the relation between the velocities of points C and D .

$$V_E = \frac{ED}{CD} \cdot V_C \tag{3}$$

Since OA rotates about point O , the velocities of points A and B are:

$$V_B = \omega \cdot OB, V_A = \omega \cdot OA \tag{4}$$

where ω —is the angular velocity of the axis of rotation OA about the axis O . From (4), we find

$$\omega = \frac{V_B}{OB}$$

Substituting ω into the second equation of the system of Eq. (4), we can relate the velocities of points A and B .

$$V_A = \frac{OA}{OB} \cdot V_B \tag{5}$$

Substitute Eq. (1) into (5):

$$V_A = \frac{OA}{OB \cos \varphi_1} \cdot V_C \tag{6}$$

According to the Theorem on variation in the quantity of motion, we can write the following:

$$\begin{aligned} M \cdot V_E &= (F_2 - F_2^{el}) \cdot t \\ M_1 \cdot V_A &= (F_A - F_1^{el}) \cdot t \end{aligned} \tag{7}$$

where M, M_1 —are the weights of the levers EH and OA , respectively.

F_1^{el}, F_2^{el} —are the elastic forces of the spring in the levers OA and EH , t —is the motion duration.

We derive expression $t = \frac{MV_E}{F_2 - F_2^{el}}$ from the first equation of the system of Eq. (7). Replacing t in the second equation of this system of equations, we obtain the following equation:

$$\begin{aligned} \frac{MV_E}{F_2 - F_2^{el}} &= \frac{M_1 \cdot V_A}{F_A - F_1^{el}} \Rightarrow \frac{M \cdot \frac{ED}{CD} \cdot V_C}{F_2 - F_2^{el}} = \frac{M_1 \cdot \frac{OA}{OB \cos \varphi_1} \cdot V_C}{F_A - F_1^{el}} \\ M \cdot \frac{ED}{CD} \cdot (F_A - F_1^{el}) &= M_1 \cdot \frac{OA}{OB \cdot \cos \varphi_1} \cdot (F_2 - F_2^{el}) \end{aligned}$$

where F_A —is the external force acting on the pedal.

Let us find F_2 from the last equation:

$$F_2 = \frac{M \cdot ED \cdot OB \cdot \cos \varphi_1}{M_1 \cdot CD \cdot OA} (F_A - F_1^{el}) + F_2^{el} \tag{8}$$

Suppose there is no spring on the pedal and ED lever. Then Eq. (8) has the following form:

$$F_2 = \frac{M \cdot ED \cdot OB \cdot \cos \varphi_1}{M_1 \cdot CD \cdot OA} \cdot F_A \tag{9}$$

Figure 1 shows that if we set the angle α between the initial position and the horizontal position of the pedal, then the angle α is:

$$tg \alpha = \frac{h}{OA} \tag{10}$$

here h —is the height of the pedal from the ground, α —is the angle formed by the pedal with the horizon.

From (10) we determine OA :

$$OA = \frac{h}{tg \alpha} \tag{11}$$

Given Eq. (11), we can write Eq. (9) as follows:

$$F_2 = \frac{M \cdot ED \cdot OB \cdot \cos \varphi_1 \cdot tg \alpha}{M_1 \cdot CD \cdot h} \cdot F_A \tag{12}$$

These expressions determine the relationship between the forces F_2 and F_A .

3 Discussion of Results

Let us introduce the numerical values of the developed machine (closer to the real ones) into Eq. (9): $M_1 = 2$ kg, $ED = 253$ mm, $CD = 140$ mm, $OB = 250$ mm, $OA = 690$ mm, $F_A = 1$ N, then we obtain the equation of the dependence of the force F_2 on the angle φ ($0 \dots \frac{\pi}{10}$). According to this equation, we can plot the following graph (Fig. 2).

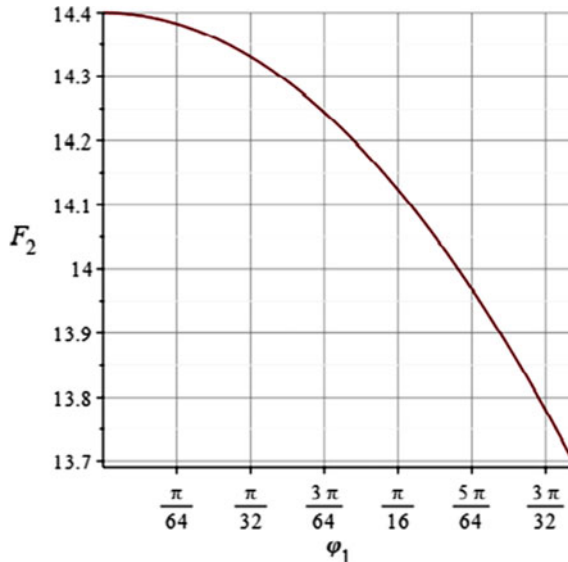


Fig. 2 Graph of dependence of force F_2 on angle φ_1

As seen from Fig. 2, when the force F_2 reaches a small value, the angle φ_1 takes the greatest value.

If we substitute the numerical values of the developed machine $M = 44$ kg, $M_1 = 2$ kg, $\cos\varphi_1 = 0.95$, $ED = 253$ mm, $CD = 140$ mm, $OB = 250$ mm, $OA = 690$ mm into Eq. (9), we obtain the equations of the dependence of the force F_2 on the force F_A . According to this equation, we get the following graph (Fig. 3).

Substituting the numerical values of the developed machine $M = 44$ kg, $M_1 = 2$ kg, $ED = 253$ mm, $CD =$ mm, $OB = 250$ mm, $\cos\varphi_1 = 0.95$ into Eq. (12), a dependence of the force F_2 on the angle α and height h is plotted.

The graph shows the change in the force F_2 at the values of the lever lifting height— h , taken as 100, 200 and 300 mm, when the angle α changes in the range from 0 to $\pi/6$.

As seen from Fig. 3, the force F_A , applied by an operator to the pedal OA is directly proportional to the force F_2 applied to the working shaft E . That is, the less F_A , the less F_2 .

Figure 4 shows three different graphs of force F_2 depending on angle α . It is necessary to determine such h and α at which the force F_2 has a small value. According to Formula (12), for the force F_2 to have a small value, it is enough for h to have the greatest value

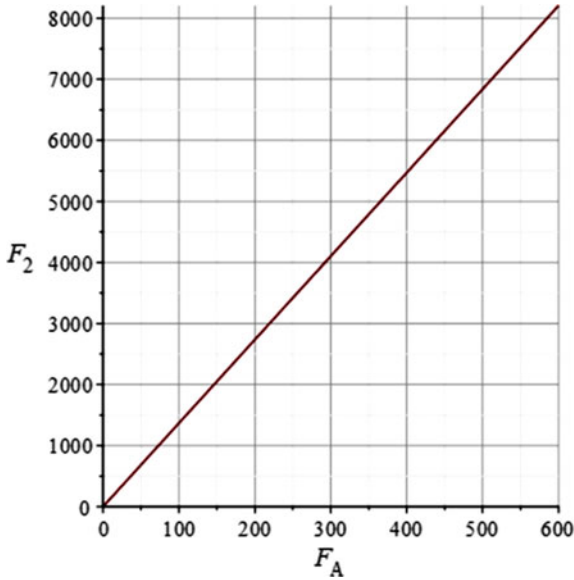


Fig. 3 Graph of dependence of force F_2 on force F_A

or for $\text{tg}\alpha$ to be the least. For $\text{tg}\alpha$ to be less than the angles, $\sin\alpha$ must be the least value, and $\cos\alpha$ —the maximum value of the angles, that is, the less the value of the angle α , the greater the value of the created pressure in the working area of machine.

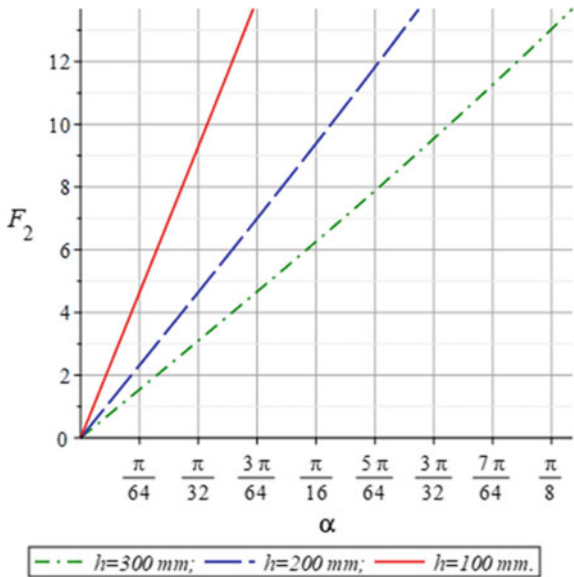


Fig. 4 Graph of dependence of force F_2 on angle α

4 Conclusions

According to the above calculations, the stable operation of the considered machine mechanisms can be ensured under the following conditions:

From the relation (9) between F_2 and α , it is seen that the force F_2 increases with an increase in the angle of pedal rotation α , however, it is recommended to limit the lift of the pedal height h because the movement of the operator's foot is limited.

The compressive force F_2 reaches its maximum value when the angle φ_1 is 00° . This means that it acts on the working shaft with the greatest force in the vertical position of the lever BC .

From the ratio between the forces F_A and F , it is seen that to create large values of the force F_2 , the values of the forces F_A must also be large. But the human foot strength is limited. Therefore, to create a sufficiently large force F_A , additional devices and equipment are required.

References

1. Golovteeva AA, Kutsidi DA, Sankin LB (1982) Laboratory workshop on chemistry and technology of leather and fur. Moscow
2. Sokolovsky AR (2010) Development of methods and improvement of means for studying the physical and mechanical properties of fiber-porous materials of light industry. Dissertation, Moscow
3. Amanov AT, Bahadirov GA, Amanov TY, Tsoy GN, Nabiev AM (2019) Determination of strain properties of the leather semi-finished product and moisture-removing materials of compression rolls. *J Mater.* <https://doi.org/10.3390/ma12213620>
4. Bahadirov GA, Sultanov TZ, Abdukarimov A (2020) Kinematic analysis of tooth-lever differential transmission mechanisms. *IOP Conf Ser Earth Environ Sci* 614:012101. <https://doi.org/10.1088/1755-1315/614/1/012101>
5. Bahadirov G, Sultanov T, Umarov B, Bakhadirov K (2020) Advanced machine for sorting potatoes tubers. *IOP Conf Ser Mater Sci Eng* 883:012132. <https://doi.org/10.1088/1757-899X/883/1/012132>
6. Covington AD, Wise WR (2020) Current trends in leather science. *J Leather Sci Eng* 2:28. <https://doi.org/10.1186/s42825-020-00041-0>
7. Riguetto CVT, Rosseto M, Krein DDC et al (2020) Alternative uses for tannery wastes: a review of environmental, sustainability, and science. *J Leather Sci Eng* 2:21. <https://doi.org/10.1186/s42825-020-00034-z>
8. Navarro D, Wu J, Lin W et al (2020) Life cycle assessment and leather production. *J Leather Sci Eng* 2:26. <https://doi.org/10.1186/s42825-020-00035-y>
9. Ershov SV (2013) Dynamic loading of the roller pair to intensify the spinning process. Dissertation, Ivanovo
10. Darda IV (2004) Development of theoretical foundations for improving the technological equipment of leather and fur production. Dissertation, Moscow
11. Tikhomirov VA (1974) Experiment planning and analysis. Moscow
12. Beghetto V (2013) The leather industry: a chemistry insight part I: an overview of the industrial process. In: *Sciences at Ca' Foscari*, pp 12–22. <https://doi.org/10.7361/SciCF-448>
13. Amanov TYu, Bahadirov GA, Tsoy GN, Nabiev AM (2011) Method of extracting moisture from wet leather. Patent RUz for invention No. IAP 04451, Published in Patent Bulletin No. 12

14. Farooqa MA, Nóvoa BH, Araújo A, Tavares SMO (2016) An innovative approach for planning and execution of pre-experimental runs for design of experiments. *Euro Res Manage Bus Econ*. <https://doi.org/10.1016/j.iedee.2014.12.003>
15. Bahadirov GA, Sultanov TZ, Abdulkarimov A (2020) Comparative analysis of two gear-lever differential inter-roller transmission mechanisms. *IOP Conf Ser Earth Environ Sci* 614:012102. <https://doi.org/10.1088/1755-1315/614/1/012102>
16. Appiah-Brempong M, Essandoh HMK, Asiedu NY et al (2020) An insight into artisanal leather making in Ghana. *J Leather Sci Eng* 2:25. <https://doi.org/10.1186/s42825-020-00039-8>
17. Bakhadirov GA, Khusanov K (2020) Construction of automatic lines connecting several mechanical operations in processing leather semi-finished product. *Int J Psychosoc Rehabil*. <https://doi.org/10.37200/IJPR/V24I4/PR201318>
18. Bahadirov G, Tsoy G, Nabiev A, Umarov A (2020) Experiments on moisture squeezing from a leather semi-finished product. *IJRTE*. <https://doi.org/10.35940/ijrte.E6125.018520>
19. Jeff Wu CF, Michael S Hamada (2009) *Experiments: planning, analysis, and optimization*, 2nd edn. USA
20. Mavlonov T, Akhmedov A, Saidakhmedov R, Bakhadirov K (2020) Simulation modelling of cold rolled metal strip by asymmetric technology. *IOP Conf Ser Mater Sci Eng*. <https://doi.org/10.1088/1757-899X/883/1/012194>



Formation of Contact Thermal Resistance Based on the Analysis of the Characteristics of the Pseudo-Medium

A. F. Denisenko^(✉), R. G. Grishin, and L. Y. Podkruglyak

Samara State Technical University, 244, Molodogvardeyskaya St, Samara 443100, Russia

Abstract. When designing metal-cutting machines, the temperature criterion is taken into account on the basis of calculation models created with various degrees of detail. In this case, a characteristic feature of such models is the presence of connections of parts that make up the assembly in question. In contrast to thermal modeling of solid bodies using FEM, modeling of joints requires the introduction of parameters that determine contact thermal resistance into the calculation model. The directional formation of contact thermal resistance during design is determined by the implementation of design and technological measures. This makes it possible to evaluate, along with the design options associated primarily with the shape and dimensions of the joints, also the influence of the quality requirements of the contacting surfaces, determined by the deviations of the mating surfaces from the ideal shape. The article proposes the results of numerical modeling of the formation of contact thermal resistance and assessment of the influence of the parameters of the intermediate layer (pseudo-medium), which occurs in the contact zone of surfaces with microdeviations, on the passage of the heat flow.

Keywords: Contact thermal resistance · Nominal contact area · Actual contact area · Pseudo-medium · Finite element model

1 Introduction

The increasing requirement for the accuracy of processing on metal-cutting machines puts thermal processes among the main factors that determine the quality of products. Analysis of the balance of errors in metalworking shows that the thermal error is 40–70% of the total manufacturing error.

In this regard, there are reasonable recommendations that limit the values of the temperature criterion for the main subsystems of the machine tool, which determine the processing accuracy.

Heat flows in machine tools are very complex due to the large number of heat sources (electric motors, rolling bearings, cutting zone, gear and belt drives, hydraulic system, etc.), as well as the large number of parts included in their design. Therefore, the formation of heat fluxes in machine tools is determined not only by the spread of

heat from sources through solid parts, but, to a large extent, through the contacts of parts with each other [1, 2].

The passage of a heat flux through real contacting surfaces of parts is very different from its movement through a solid material and through an ideal joint, when the heat flux practically does not encounter significant resistance on its way. The reason is that in real joints, due to the presence of macrodeviations, waviness and roughness, which depend on the structure and nature of technological processing, continuous contact along the joint is broken. This leads to the appearance of contact thermal resistance (CTR), which must be taken into account in the thermal models used.

Thus, the need to reasonably control heat fluxes, particularly precise units of metal-cutting machine tools due to design and technological measures, makes the task of forming a CTR very urgent.

2 Formation of Pseudo-Medium Characteristics

Previous studies by a number of authors [3–6] have shown that the conditions of contact have a very significant effect on such characteristics of the joint as the convergence of surfaces, contact stiffness, the nature of contact deformation (elastic, elastoplastic, plastic) and electrical conductivity of the contact. There are significantly fewer works considering the influence of contacting conditions on the passage of heat flux in machine tool designs [7–14].

The modern theory of contacting surfaces is based on the position that the presence of roughness, waviness and macrodeviations leads to discreteness of their interaction, as well as the division of contact areas into nominal A_a , contour A_c and actual A_r (Fig. 1).

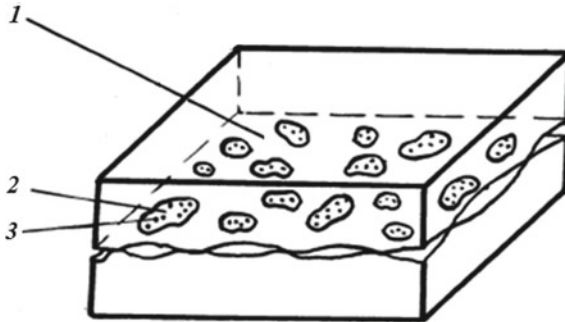


Fig. 1 Contact areas: 1—nominal; 2—contour; 3—actual

The nominal contact area A_a is determined by the dimensions of the contacting bodies, is always known and is used in all calculations. The contoured contact area A_c is associated with the presence of waviness, and the actual A_r is associated with the presence of roughness on the contacting surfaces.

In work [3], it is indicated that the contour area of contact is the area that limits the area of the location of the areas of actual contact. The distribution of such contact

zones over the nominal area depends primarily on the shape and degree of waviness, which determines the area and density of the actual contact areas. Macro unevenness of surfaces will also affect the size of the contour area.

In the case of elastic interaction of a surface with spherical waves with a rigid smooth plane and when the wave tops are at the same level, the formula [3] is given

$$A_c/A_a = 2.5 \cdot (1 - \mu^2)^{2/3} \cdot (R/L)^{2/3} \cdot (q_a/E)^{2/3}, \tag{1}$$

where μ is Poisson’s ratio; R —radius of spherical waves; L —wavelength; $q_a = P/A_a$ —nominal pressure; P —load; E —modulus of normal elasticity.

Khokhlov [6] gives a simpler dependence, containing only two initial parameters, for the relative contour area

$$A_c/A_a = (q_a/\sigma_T)^{1-q_a/\sigma_T}, \tag{2}$$

where σ_T is the yield point.

To determine the actual area in [6], the dependence was obtained

$$A_r = k \cdot A_a \cdot q_a = k \cdot P, \tag{3}$$

where depending on the accuracy of calculations

$$k = 0.48075/\sigma_T \approx 0.48/\sigma_T \approx 1/(2 \cdot \sigma_T). \tag{4}$$

The linear dependence of the actual contact area on the load is also indicated in [4, 15].

At the contact of rough bodies, one more parameter should be taken into account, connected with the fact that not all protrusions are elastically deformed by the amount of y , due to their different heights. As a result, a layer (pseudo-medium) is obtained, consisting of areas of actual contact and cavities filled with air or oil (Fig. 2).

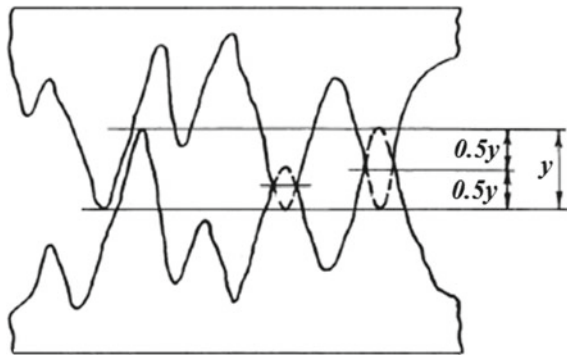


Fig. 2 Scheme of contact of surfaces with the same roughness

The thickness of this layer in the case of elastic contact of surfaces with the same physical and mechanical properties and roughness [6]:

$$h_3 = 2 \cdot R_p \cdot \left\{ 1 - (1/2) \cdot [q_a/\sigma_T]^{[1-q_a/\sigma_T]} - 0.18 \cdot [q_a/\sigma_T]^2 \cdot [1-q_a/\sigma_T] \right\}. \quad (5)$$

Theoretical analysis showed that at $q_a/\sigma_T \leq 0.1$ and the calculation error is not more than 6.5%, the pseudo-layer thickness can be determined as

$$h_3 \approx 2 \cdot R_p, \quad (6)$$

where R_p is the smoothing height (the distance from the line of protrusions to the middle line).

For surface treatment methods with chip removal, the value can be calculated using the formula [6, 16]

$$R_p = 2.6 \cdot R_a = 0.5 \cdot R_z, \quad (7)$$

where R_a and R_z are roughness parameters.

3 Development of a Finite Element Model of Contacting Two Rectangular Plates

In order to assess the effect of the characteristics of the intermediate layer upon contact of two solid bodies that do not have macrodeviations, a flat finite element model of contacting two rectangular plates 1 mm thick was developed on the conditions for the formation of CTR (Fig. 3).

In this case, the change in thermal conductivity in the contact zone will be determined only by microdeviations, which can be conventionally taken to be the same throughout the entire connection zone. Thus, the interlayer between the parts can be represented in the form of a continuous pseudo-medium having a thermal conductivity coefficient and a thickness that depend on the roughness of the contacting parts.

Since the thermal conductivity coefficient of the pseudo-medium is formed as a result of direct contact of micro-roughnesses with the thermal conductivity coefficient of the base material and the presence of cavities filled with oil or air, it can vary from $\lambda = 0.025$ W/(m K) (air) to $\lambda = 50.0$ W/(m K) (steel).

The dimensions of the contacting parts and the thickness of the pseudo-medium for the used design model are shown in Table 1.

Plates material—steel (thermal conductivity coefficient $\lambda = 50$ W/(m K)).

The power of each of the five heat sources is 20 W/m.

The boundary conditions along the edges of the model were taken as follows: Convection $F_n = \alpha(T - T_0)$ along the side edges and along the upper edge was equal to zero ($\alpha = 0$ and $T_0 = 0$), and along the lower edge $\alpha = 50$ W/K m² and $T_0 = 293$ K.

The finite element mesh was built at discretization steps: at the lower nodes (No. 1 and 11)—0.005 m; in heat sources (No. 4–8)—0.004 m; in the nodes of the pseudo-medium (No. 2, 3, 9, 10)—0.001 m.

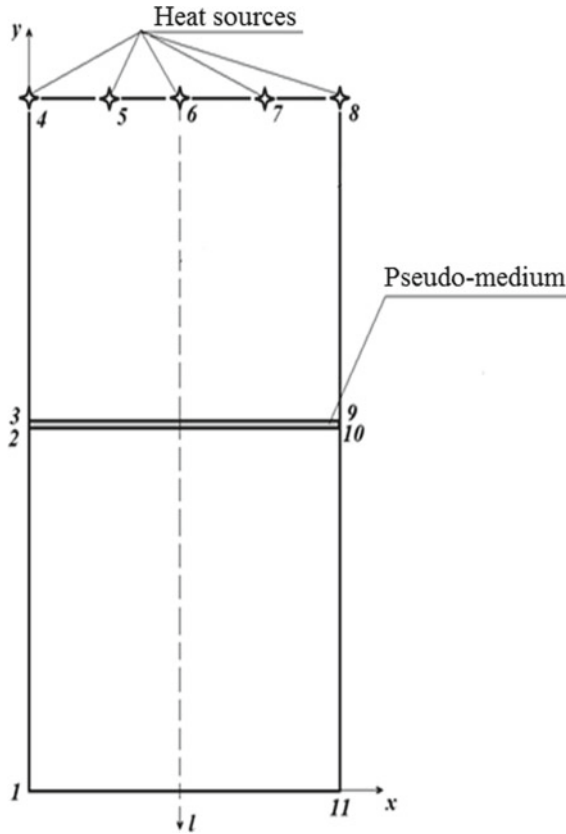


Fig. 3 Plane model of contacting two plates

Table 1 Coordinates of vertices (nodes) of the plane model of contacting plates

Points	1	2	3	4	5	6	7	8	9	10	11
<i>x</i> , mm	0	0	0	0	0.005	0.01	0.015	0.02	0.02	0.02	0.02
<i>y</i> , m	0	0.02	0.0205	0.04	0.04	0.04	0.04	0.04	0.0205	0.02	0

Numerical experiments with the developed finite element model were carried out using the ELCUT package [17–21].

The effect of the pseudo-medium was estimated by the temperature difference ΔT (see Fig. 4), where l is the distance from the upper edge of the upper part in the direction indicated in Fig. 3.

Knowing the value of ΔT , °K, it is easy to determine the thermal resistance of the compound R , K m²/W as follows:

$$R = \frac{\Delta T}{q} \tag{8}$$

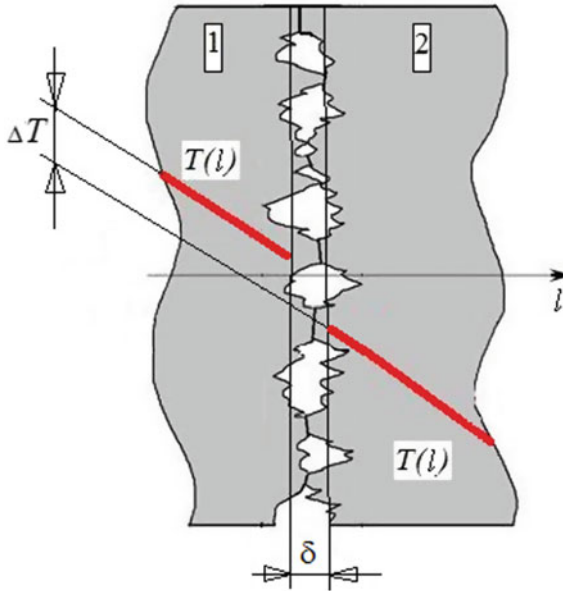


Fig. 4 Influence of a pseudo-medium with a thickness of δ on a temperature drop ΔT

or

$$R = \frac{\delta}{\lambda}, \tag{9}$$

where q is the heat flux, W/m^2 ; δ —thickness of the layer that overcomes the heat flux, m ; λ —coefficient of thermal conductivity, $W/(m\ K)$.

4 Numerical Simulation Results

Figure 5 shows examples of graphs of temperature changes along the axis l at various values of λ , constructed from the simulation results.

The values of ΔT obtained by processing graphs ΔT (Fig. 5) are shown in Fig. 6.

To assess the effect of the thickness of the pseudo-medium δ , which differs in thermal conductivity from the base material, graphs of dependence $\Delta T = f(\delta)$ were plotted. As the material of the pseudo-medium, the material with $\lambda = 5\ W/(m\ K)$ and $\lambda = 0.025\ W/(m\ K)$ (air).

The simulation results are presented in Table 2.

5 Conclusion

The studies carried out have confirmed the possibility of using a contact pneumatic medium when modeling the propagation of heat fluxes over the structures of metal-cutting machines. Varying the characteristics of the pseudo-medium makes it possible,

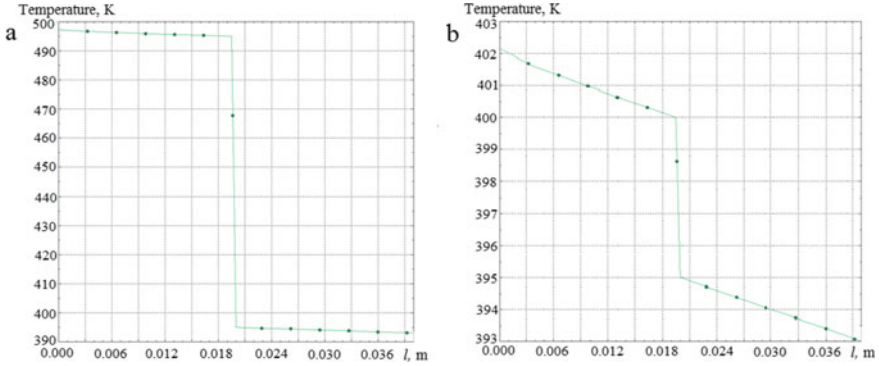


Fig. 5 Graphs of temperature changes along the axis l at various values of λ , obtained from the simulation results in the ELCUT environment: $a - \lambda = 0.025$ W/(m K); $b - \lambda = 0.5$ W/(m K)

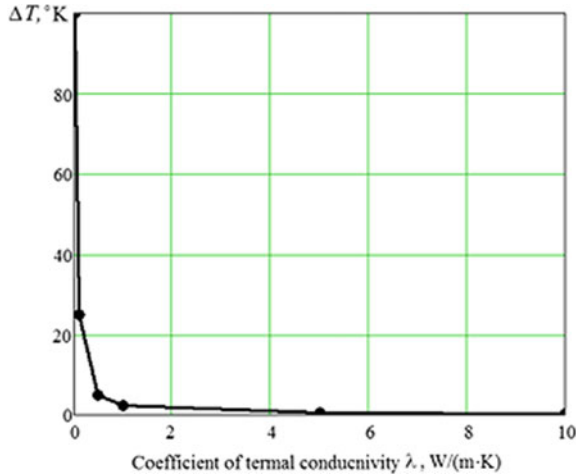


Fig. 6 Change ΔT depending on the thermal conductivity of the pseudo-medium

even at the design stage, to evaluate the adopted design decisions by the temperature criterion. From the performed numerical experiments, it can be concluded that with a decrease in the thickness of the pseudo-medium and an increase in the thermal conductivity coefficient, i.e., by improving the quality of the contact, the temperature drop in the contact ΔT decreases, and the contact thermal resistance decreases accordingly. Moreover, the CTR depends linearly on the pseudolayer thickness, and the effect of the thermal conductivity coefficient of the pseudo-medium has a pronounced nonlinear character. The range of possible change in the thermal conductivity coefficient of the pseudo-medium was established from the condition for the occurrence of CTR.

Table 2 Dependence of temperature on the thickness and quality of the pseudo-medium

δ , mm	ΔT	
	$\lambda = 5 \text{ W/(m K)}$	$\lambda = 0.025 \text{ W/(m K)}$
0.5	0.45	100
0.4	0.35	80
0.3	0.27	60
0.2	0.18	40
0.1	0.09	20
0.07	0.06	14

References

- Denisenko AF, Podkruglyak LY (2020) Development of a thermal model of a spindle support for a metal-cutting machine. *Bull Samara Sci Center Russ Acad Sci* 22(3):49–55
- Denisenko AF, Podkruglyak LY (2020) Heat model of a spindle support of a precession metal cutting machine. *IOP Conf Ser Mater Sci Eng* 971:022020. <https://doi.org/10.1088/1757-899X/971/2/022020>
- Ryzhov EV (1966) Contact stiffness of machine parts. Mechanical Engineering, Moscow
- Demkin NB (1962) The actual contact area of solid surfaces. AN SSSR, Moscow
- Suslov AG (2000) The quality of the surface layer of machine parts. Mechanical Engineering, Moscow
- Khokhlov VM, Khokhlova SV, Petrakov DI (2007) Calculation of connections. VIMAKHO LLC, Bryansk
- Mesnyankin SYu, Vikulov AG, Vikulov DG (2009) Modern view on the problems of thermal contacting of solids. *Adv Phys Sci* 179(9):945–970
- Kamenev S (2018) Method for automated building of spindle thermal model with use of CAE system. *IOP Conf Ser Mater Sci Eng* 327:022055
- Lipov A, Bolshakov G, Panchurin V (2014) Model of thermal deformations of the spindle drilling machine unit. *Models Syst Netw Econ Technike Nat Soc* 4(12):124–128
- Raja PV, Moorthy SR (2019) Thermal modelling of a high speed motor spindle. *Arab J Sci Eng*. <https://doi.org/10.1007/s13369-019-03732-x>
- Li Y et al (2015) A review on spindle thermal error compensation in machine tools. *Int J Mach Tools Manuf* 95:20–38
- Li Wu, Tan Q (2016) Study of a spindle-bearing system. *Entropy* 18(271):1–25
- Izmailov V, Chaplygin S (2016) Electrothermal analogy and calculation of the conductivity of discrete contact of machine parts. *Int J Sci* 8(2). <https://doi.org/10.15862/26TVN216>
- Denisenko A, Nazarov N (2017) Formation of a regression model of contact thermal resistance of flat joints of spindle assemblies. *Assembly Mech Eng Instrum Mak* 7:325–329
- Moore D (1978) Basics of using tribonics. Peace, Moscow
- Ryzhov EV, Khokhlov VM (1976) Calculation of surface roughness in the conditions of selective transfer. In: *Application of selective transfer in friction units of machines*. Moscow, pp 35–40
- Salova IA, Khrushchev VV (2007) Simulation in ELCUT. Saint Petersburg State University of Aerospace Instrumentation, Saint Petersburg

18. ELCUT (2013) Simulation of electromagnetic, thermal and elastic fields by the finite element method. Version 6.0. User's manual. LLC "Tor", Saint Petersburg
19. Semernin AN, Urvanov AA (2016) Application of the "ELCUT" software for modeling magnetic fields in electric machines. *Energy Syst* 1:289–291
20. Tatevosyan AS et al (2015) Solution of the problem of optimum control of electromagnetic drive of vibratory motion based on application of the "ELCUT" program. *Int J Appl Basic Res* 11–1:19–24
21. Andreeva EG, Tatevosyan AA, Semina IA (2009) Study of the magnetic field of the open-type system using the ELCUT programs complex. *Dyn Syst Mech Mach* 1:111–114



Method of Calculating of the Heat-Stressed State of the Cylinder Head of a Liquid-Cooled Diesel Engine

A. N. Gots and V. S. Klevtsov^(✉)

Vladimir State University named after Alexander Grigorievich and Nikolay Grigorievich
Stoletov, 1, Universitetskaya St, Vladimir 600005, Russia

Abstract. The method of calculating the heat-stressed state of the individual cylinder head of a liquid-cooled diesel engine, which is not only subjected to mechanical loading, but also the main type of load, especially on the firing surface, is the thermal load. Based on the study of the loading modes of the cylinder head of similar engines, a loading cycle is proposed, and the numerical values of which can be determined by the results of the study of cars in operation. The problem of choosing kinematic boundary conditions when calculating the cylinder head by the finite element method is considered. The boundary conditions for calculating the stress state and especially the thermal boundary conditions for the firing surface of the cylinder head, intake and exhaust channels, as well as valves and cooling systems are analyzed. When calculating the thermal state, it is necessary to coordinate the temperature fields of the valve chamfer and the landing surface of the cylinder head, since heat flows change their direction during the entire working cycle. Mathematical modeling by finite element method of the thermal state of the cylinder head, as well as the stressed and heat-stressed state, taking into account the accepted boundary conditions, is considered. When calculating the heat-stressed state of the cylinder head, the estimated parameters of the firing bottom of the cylinder head are proposed in order to ensure its durability.

Keywords: Internal combustion engine · Diesel · Cylinder head · Thermal state · Boundary conditions · Heat-stressed state

1 Introduction

One of the main trends in the development of internal combustion piston engines is to increase their power and efficiency, while ensuring environmental indicators adopted for all years of their production and operation. Analysis of statistical data on the production of foreign-made piston engines for various purposes shows that the capacity of new modifications produced increases by an average of 60, ..., 80% for every 10 years [1]. Manufactured engines, as a rule, boost by the average effective pressure, which inevitably causes an increase in heat stress in parts that contact with hot gases: cylinder heads (CH), valves, turbines, cylinder liners, and pistons. CH experiences mechanical loading in the fabrication process (the contact pressure at the firing surface of CH from the pressing

seat and the valve), and in the assembly process (loading force from tightening the studs CH and tighten the mounting nuts to the injectors) [2, 3]. Under the influence of these loads, the stress–strain state (SSS) of CH is determined. When operating a diesel engine, significant stresses arise mainly from thermal loads [3–7] caused by temperature fluctuations on the firing surface of the CH. Obtaining information about the temperature fields of the CH at the design stage is important for evaluating its performance and reliability, modeling the thermal stress–strain state, correct selection of materials, design optimization, and design of the cooling system. Thus, the calculation of the thermal stress–strain state is the main one in the calculation of CH. According to research [3, 8, 9], heating and cooling cycles in the combustion chamber (CC) during operation of the diesel engine cause temperature differences on the firing surface of the CH. This “thermal load” leads to significant temperature stresses that can cause cracks on the bottom side of the inter-valve lintels, as well as on the lintels between the nozzle opening and the inlet or outlet valve opening [2, 10–12]. In [2, 3], the method of calculating the stress–strain state of CH under the influence of power loads that occur during manufacture and assembly was considered in detail. For 4CHN10.5/12 diesel (D-145 T) due to a significant temperature difference on the firing surface of the CH, the finite element method (FEM) calculation showed that the stress intensity σ_1 in the inter-valve jumper is 108.1 MPa. At the same time, σ_1 under the action of the mounting load and gas pressure forces is only 31.1 MPa, so the temperature stresses are almost 3.5 times higher than the stresses from the action of the mounting forces [3, 8]. The calculation confirms that it is the heat-stressed state of the CH that determines its durability.

Let us consider the procedure for calculating the heat-stressed state of the CH of a liquid-cooled transport diesel, taking into account the heating and cooling cycles in the combustion chamber during its operation.

2 Purpose of Research

To develop a method for analyzing the thermal and stress–strain state of the CH of the 8CHN12/13 liquid-cooled transport diesel engine under the influence of the mounting load and gas pressure forces, as well as thermal loads, which will allow calculating the CH for durability and predicting its reliability in operation.

3 Materials and Methods of Research

Consideration of mounting loads caused by pressing the seats and valve bushings during assembly; tightening the nut for mounting the nozzle during assembly; tightening bolts or studs for attaching the CH to the block crankcase; gas force during diesel operation was considered in [2].

Only low-frequency temperature fluctuations caused by changes in the engine operating mode are calculated for the calculation of T_{SSS} [3]. High-frequency temperature fluctuations of CH caused by changes in the temperature of gases in the cylinder have, as a rule, an amplitude of 5, ..., 8 °C at a depth of 1 mm from the firing surface, and do not significantly affect the T_{SSS} of the CH [13–16].

When studying the modes of YAMZ-238 diesels installed on KrAZ-257 and KrAZ-256B trucks, it turned out that about 50, ..., 89% of the time they work in the zone of external speed characteristics at a speed of 0.7, ..., 1 of the nominal crankshaft [17]. On an international highway with an asphalt-concrete surface, the number of speed switches, and therefore the change of mode, is 15, ..., 16 switches per 100 km of mileage, in heavy urban traffic, such switches are already about 400 [17]. It can be recognized that similar mode changes occur in diesel 8CHN12/13.

Therefore, when modeling the thermal state of CH, only low-frequency temperature fluctuations caused by changes in the engine operating mode should be taken into account.

In this regard, the cycle of thermal loading of CH can be represented as a loading cycle, from which it follows that the transition to a new mode leads to a sharp increase in temperatures in the inter-valve jumper, while the temperature level T_{max} is stabilized for $\tau = 2, \dots, 3$ min after the diesel enters the steady state (Fig. 1) that the transition to the new mode leads to a sharp increase in temperatures in the inter-valve cross-piece, while the temperature level T_{max} is stabilized for $\tau_{heating}$ load = 2, ..., 3 min after the diesel engine enters the steady state mode (Fig. 1). Vehicle movement at T_{max} during $\tau_{time\ del.1}$ (Fig. 1) it is accompanied by a load fluctuation (the speed of rotation of the crankshaft is not constant), but this phenomenon practically does not have a significant impact on the thermal mode of the diesel engine. Stopping the car leads to a decrease in temperature to the level T_{min} for $\tau_{cool} = 2, \dots, 3$ min and subsequent exposure $\tau_{time\ del.2}$.

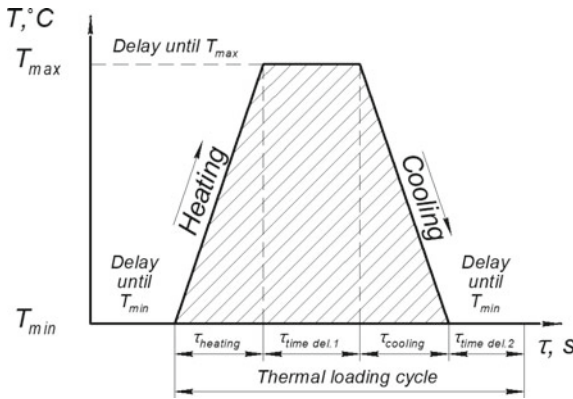


Fig. 1 Thermal loading cycle

To calculate the FEM, it is necessary to create a three-dimensional model of the CH based on the drawings (Fig. 2) using the solid-state modeling program SolidWorks, Catia, Pro/Engineer, ANSYS, etc.

According to reference data [18], the physical and mechanical properties of CH materials (aluminum alloy AK5M7 (AL10V)), guide bushings, valve seats, and cylinder liners are determined and set depending on the temperature. On the basis of the created three-dimensional model, a finite element model (FEM) is constructed using the SolidWorks Simulation and ANSYS finite element modeling software packages,

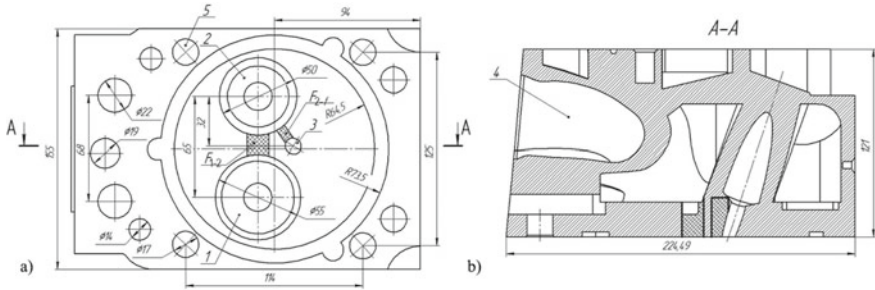


Fig. 2 Cylinder Head of diesel 8CHN12/13: **a** view from the firing surface of the CH: 1—inlet valve; 2—exhaust valve; 3—hole for installing the nozzle, 4—inlet channel; 5—holes for mounting pins CZ; F_{1-2} —inter-valve jumper; F_{2-f} —jumper between the exhaust valve and the nozzle cup; **b** cross section along the line A–A

and boundary conditions are assigned. The most successful is the use of a FEM based on three-dimensional twenty-node isoparametric finite elements (FE) when building a FEM, it is necessary to use a thick design grid and reduced CE in the junction sections, for example, in the inter-valve jumpers or in the jumpers between the nozzle hole and the valve hole of the CH. The size of the FE side is selected based on the condition of ensuring the required accuracy of calculation and the cost of machine time.

When choosing kinematic boundary conditions for the FEM, it is necessary to take into account the possibility of moving surfaces associated with the block case. According to [19], the exclusion of lateral movements of the surface of the FEM CH causes an increase in the stresses in the inlet valve jumper by 3, ..., 4 times. If there is no gasket between the CH and the cylinder block, then it can be assumed that only the friction force limits the free lateral expansion of the CH [3].

To display the conditions of thermal interaction between the environment and the surface of the CH body, the following boundary conditions are assigned.

4 Matching the Temperature Field of the Valve Chamfer and the Landing Surface of the Cylinder Head

When calculating, it is necessary to coordinate the temperature fields of the valve chamfer and the landing surface of the CH, since heat flows change their direction during the entire operating cycle [4]. When the diesel engine is running, when the valves are closed, heat is transferred from the exhaust valve to the CH or from the CH to the intake valve via the chamfer and the valve seat. During the intake cycles, the intake valves are washed with fresh charge, and when the exhaust valves are released, and they are washed with exhaust gases. The parameters of heat exchange can be determined by the boundary conditions of the third kind: the gas temperature and the coefficient of heat transfer in the valve slot.

The heat transfer coefficient of the contact of two bodies α_k W/(m² K), depending on the material properties of the contacting parts, the quality of processing of the contacting surfaces, as well as the contact pressure can be determined by the formula [20].

$$\alpha_k = 2.12 \times 10^4 \lambda_m \left(\frac{p}{E_m} B_p \right)^{0.8} + \frac{\lambda_c}{(h_{m1} + h_{m2})(1 - m)d}, \quad (1)$$

where $\lambda_m = 2\lambda_1\lambda_2/(\lambda_1 + \lambda_2)$ is the average coefficient of thermal conductivity of materials of contacting bodies; p —contact pressure; $E_m = 2E_1E_2/(E_1 + E_2)$ —the average modulus of elasticity of materials of contacting bodies (in this case, aluminum alloy and cast iron); $B_p = 0.15, \dots, 0.25$ dimensionless coefficient characterizing the geometrical properties of contact surfaces, depending on the amount of average heights of asperities h_{m1} and h_{m2} of the contacting bodies (the greater the amount of $h_{m1} + h_{m2}$, the less B_p); $\lambda_c \approx 0.35$ —thermal conductivity of the medium in the volume of the asperities (when the temperature in the contact zone $T_k = 420$ °K and pressure $p = 10$ MPa $\lambda_c \approx 0.35 \times 10^{-3}$ W/(m K)); m —coefficient of filling of the profile of the asperities (for sanded surfaces $\mu = 0.5$); $d \approx 1.2, \dots, 1.6$ —coefficient characterizing the maximum influence of the protrusions of asperities that depend on the ratio p/E [19].

In accordance with the recommendations [4, 21], when determining the thermal and stress–strain state of the CH, a separate calculation of its and valves is used with iterative matching of their temperatures. In the first iteration, when calculating CH, an arbitrary temperature of the valve seat is set, and then the coefficient of heat transfer from the valve to the seat. When the valve is open, the time-average temperature and heat transfer coefficient are calculated.

4.1 Boundary Conditions on the Firing Bottom of the Cylinder Head

To determine the average value of the heat transfer coefficient over the firing surface of the CH, the Voshni or Hohenberg formulas can be used. In [22], it is shown that none of the dependencies allows us to obtain satisfactory results. In this regard, the Zapf formula [22] is used to calculate the average coefficient of heat transfer of α_{ch} in CH during gas exchange:

$$\alpha_{cc_h} = CD^{-0.22} T_\infty^{-0.52} p^{0.78} c_m^{0.78}, \quad (2)$$

where $C = 535$; T_∞ —current temperature of the working fluid in the cylinder, K; c_m —average piston speed, m/s; p —current cylinder pressure, MPa.

The temperature of the medium is averaged over the entire surface of the combustion chamber and is assumed to be equal to the temperature obtained by thermodynamic calculation averaged over the cycle time. The distribution of the heat transfer coefficient over the radius in the first approximation can be assumed to be similar to the temperature distribution on the firing bottom of the piston [23].

4.2 Boundary Conditions in Inlet and Outlet Channels

When the engine is running, a significant amount of heat, in addition to the firing bottom, is supplied to the walls of the exhaust channel. The boundary conditions in the inlet

and outlet channels can be represented by the Nusselt number [22, 23], which is a dimensionless heat transfer coefficient:

$$\text{Nu}_{\text{in}.k.} = 0.214\text{Re}^{0.68} \left(1 - 0.765 \frac{h_{\text{in}.k.}}{d_{\text{in}.k.}} \right); \quad (3)$$

$$\text{Nu}_{\text{out}.k.} = 2.58\text{Re}^{0.5} \left(1 - 0.797 \frac{h_{\text{out}.k.}}{d_{\text{out}.k.}} \right). \quad (4)$$

In expressions (3, 4), h and d are the valve stroke and valve diameters (with corresponding indexes: in. $k.$ —inlet; out. $k.$ —outlet). To calculate the Reynolds number, the determining dimensions are the hydraulic diameters of the channels and the average flow rate in the inlet and outlet channels:

$$\text{Re} = \frac{QD_g}{\nu A} = \frac{\nu D_g}{\nu}, \quad (5)$$

where Q is the volumetric flow rate of gas, m³/s; D_g —hydraulic diameter of channel, m; ν —kinematic viscosity of gas, m²/s; A —area of section, m²; ν —the characteristic velocity of m/s.

The transition to the heat transfer coefficients α is carried out according to a known dependence, where λ is the thermal conductivity of the gas. The calculation is based on the parameters of the working body averaged over the working cycle.

The calculation of stresses in the coupling of the seat and cylinder head, taking into account the tension and heating, was discussed in detail in [2].

4.3 The Heat Transfer from the Coolant

At moderate forcing levels, the Sonneken formula can be used to calculate the heat transfer coefficient as much as, $W/(m^2 \text{ K})$ [24]

$$\alpha_1 = (300 + 1800\sqrt{w_1})1.163 \quad (6)$$

where w_1 is the speed of the coolant.

In [2, 24], dimensionless parameters are proposed for calculating as much as, since the cooling of CH can occur in the mode of forced convection and surface boiling; therefore, the calculation based on the dependence (12) leads to large errors.

5 Performance Indicators

Since the most typical types of CH failures are cracks on the side of the firing bottom on the inter-valve jumpers, as well as on the jumpers between the nozzle hole and the inlet or outlet channels (zones F_{12} and F_{21} , see Fig. 2).

Within each finite element (FE), the scalar temperature field and the vector displacement field are described by second-order polynomials; the stresses change linearly. The FE form function is parabolic, which makes it possible to use significantly fewer elements with the same calculation accuracy than when using tetrahedral elements [23].

A fourteen-point cubator numerical integration formula can be applied to obtain the thermal conductivity and stiffness matrices of the bulk CE, as well as the corresponding vectors of the right parts. This formula reduces the counting time by 20% compared to the twenty-seven-point one.

To solve the problem of thermal conductivity, the thermal conductivity matrix and the heat load vector of each element are calculated, and on the basis of this matrix, the general matrix and the “heat load” vector of the entire design scheme are formed. The temperature at all nodal points of the calculation scheme is determined after solving the resulting system of linear equations.

Since the aluminum alloy AK5M7 (AL10V), from which the CH is made, changes its physical and mechanical characteristics depending on temperature [21], to clarify the thermal conductivity coefficient λ and the elastic modulus E , they were recalculated depending on temperature. Variables $\lambda(T)$ and $E(T)$ can be calculated at nodes and then interpolated using form functions. To implement this method, the temperature range of CH was divided into ten intervals, for which one can take $\lambda = \text{const}$, $E = \text{const}$.

6 Calculation Results and Conclusions

Despite a fairly significant number of studies on determining the heat transfer coefficient [22], their values obtained from empirical dependencies differ greatly. More accurate calculations and refinement of formulas can be carried out using numerical methods based on the results of experimental studies. When calculating the thermal problem in a non-stationary setting, the only way to solve the problem is to average temperatures and heat transfer coefficients over time.

According to the results of calculations based on the above dependencies, the heat transfer coefficient on the firing bottom of the CH is about $\alpha_{\text{ch}} = 800 \text{ W}/(\text{m}^2 \text{ K})$ (in the area of the inter-valve jumper— $775 \text{ W}/(\text{m}^2 \text{ K})$).

In the maximum torque mode, the highest temperature of the firing surface of the 8CHN12/13 CH diesel engine is $345 \text{ }^\circ\text{C}$ in the inter-valve jumper. The temperature of the cooling side CH is equal to $175 \text{ }^\circ\text{C}$. The temperature of the seat surface of the exhaust valve seat is $450 \text{ }^\circ\text{C}$. When further boosting the diesel engine by the average effective pressure, it is necessary to provide measures to improve the design of the CH.

References

1. Gots AN (2019) Kinematics and dynamics of the crank-rod mechanism of piston engines, 3rd edn. FORUM-INFRA-M Moscow, p 384
2. Gots AN, Klevtsov V S (2019) Method of calculating the thermal and stress state of the cylinder head of a liquid-cooled transport diesel engine. *Izvestiya MSTU “MAMI” Transp Mach Transp Technol Means Power Plants* 1(39):2–8
3. Gots AN, Ivanchenko AB, Prygunov MP, Frantsuzov IV (2013) Modeling of the heat-stressed state of the cylinder head of a tractor diesel engine of air cooling. *Fundam Res* 6–5:1061–1067
4. Onishchenko DO, Pankratov SA (2013) Modeling of the thermal state of the cylinder cover and valves of a diesel engine. *Vestnik MGTU named after N. E. Bauman, Mech Eng* 4:95–108

5. Grishin DK, Alejamiento PR, Chynov ND, Lodna VA (2010) Mathematical modeling of the thermal state of head high-speed small diesel engine with direct injection. *Tractors Agricult Mach* 8:28–30
6. Gots A, Klevtsov V (2018) Method of determining the durability of diesel cylinder heads. Collection of reports technical and scientific conference with international participation. *Transp Ecol Sustain Dev* 24:73–77
7. Prygunov MP (2013) Research and development of an assessment of the durability of cylinder heads of air-cooled tractor diesels. Vladimir State University, Dissertation
8. Isaev EV, Milshtein LG (1985) Calculation analysis of the thermal stress-strain state of the bottom of block cylinder heads taking into account the influence of structural factors. *Engine Build* 10:28–31
9. Myagkov SP (2009) Improving the strength reliability of cylinder covers for transport diesels. Dissertation, Moscow
10. Chainov ND, Raenko MI, Ryzhov VA (2015) Strength of heat-stressed base parts of medium-speed internal combustion engines. *Machinery Building Publ, Moscow*
11. Trofimov VB (2003) Improving the reliability of the engine cylinder head 8CHVN15/16. *Engine Build* 3:19–21
12. Fomin VM, Koshelenko AS, Zhed OV (2005) Distribution of stresses in the bottom of the cylinder heads of diesels. *Tract Agricult Mach* 3:21–24
13. Chaynov ND, Raenko MI, Myagkov SP (2008) Questions of strength of cylinder covers of medium-speed diesels. *All-Ukrainian Sci Tech J Int Combust Engines* 1:68–71
14. Chaynov ND, Raenko MI, Myagkov SP, Ryzhov VA (2008) Mathematical modeling of the stress-strain state of the cylinder cover of a forced diesel engine. *Trucks* 3:32–35
15. Raenko MI, Ryzhov VA (2012) Evaluation of the strength reliability of cylinder covers of transport diesels by the criterion of durability. *Engine Build* 1:7–17
16. Raenko MI, Ryzhov VA, Myagkov SP (2010) Estimation of durability of cylinder covers of medium-speed transport diesels. *Engine Build* 2:3–6
17. Kostin AK, Pugachev BP, Kochenev YuYu (1989) Work of diesel engines under operating conditions. *Machinery Building, Leningrad*, p 284
18. Non-ferrous metals and alloys (2001) In Friedlander IN (ed), *Engineering. Encyclopedia*, No II-3, *Machinery Building, Moscow*, p 880
19. Milshtein LG, Isaev EV (1985) Determination of kinematic boundary conditions when calculating thermal stresses in block cylinder heads. *Engine Build* 9:22–26
20. Popov VM (1971) Heat transfer in the contact zone of detachable and non-removable connections. *Energia Publ, Moscow*, p 214
21. Chaynov ND, Ivashchenko NA, Krasnokutskaya, AN, Miagkov LL (2008) *The Design of internal combustion engines. Machinery Building, Moscow*, p 494
22. Kavtaradze RZ (2016) *Local heat exchange in piston engines. Publishing House of MGTU, Moscow*, p 516
23. Gots AN, Glinkin SA (2017) *Forecasting the durability of internal combustion engine pistons. LAP LAMBERT Academic Publishing, Saarbrücken*, p 149
24. Onishchenko DO (2002) *Investigation of the thermal state of diesel parts in a three-dimensional setting using experimental boundary conditions: dissertation*, p 137



Applying Morphing Wing for Optimization of Small-Size Unmanned Aircraft Wing

T. A. Mitashova^(✉)

Filial PAO Kompaniia “Sukhoi” “KnAAZ Im.Iu.A.Gagarina”, 1, Sovetskaya Str,
Komsomolsk-on-Amur 681018, Russia

Abstract. One of the perspective trends of improving aerial vehicle design, including small-size unmanned aircrafts is the morphing wing technology that is based on principles of adapting the wing configuration to aircraft flight conditions. For small-size aircrafts, this problem is still open because airflow over the wing corresponds to low Reynolds numbers $Re \leq 300\,000$ due to the main factors: small shape and low speed. As a result, the boundary level is separated at the upper surface of the aerofoil and transitions to turbulent flow and then reattaches to the surface forming a laminar separation bubble. A small-size aircraft shows a worse lift force and the aircraft performance. This article analyzes a possibility for increasing the lift force of a small-size unmanned aircraft by morphing the aerofoil configuration: in the wing plane, outside the wing plane and in the transverse plane of the wing. This required an analysis of acceptable morphing wing concepts of morphing by changing the wing area, sweep and changing the area together with sweep.

Keywords: Small-size unmanned aircraft · Morphing wing

1 Introduction

The aviation engineering includes enhanced design studies for small-size unmanned aircrafts (SUA) that are now widely used by military forces for reconnaissance and striking functions [1–5].

Specific aerodynamic characteristics of SUA include flow around the wing with low Reynolds numbers calculated by the profile chord $Re = 2 \times 10^5, \dots, 1.5 \times 10^6$ due to the small shape: wing span 0.6, ..., 2, 3 m, body length 0.3, ..., 1.8 m and low speed: 100, ..., 150 km/h.

The Reynolds numbers correspond to the laminar-to-turbulent transition when the boundary level is separated at the upper surface of the aerofoil and transitions to turbulent flow and then reattaches to the surface forming a laminar separation bubble, Fig. 1 [6, 7]. An excluded part of the wing is formed in the bubble and does not generate the lift force. The sketch in Fig. 1c shows that this is the wing part with the lift force coefficient $C_f = 0$ and lateral dimension up to 17% of the chord length [8].

A laminar separation bubble is a strap extended along the wing, and it therefore considerably reduces the lift force.

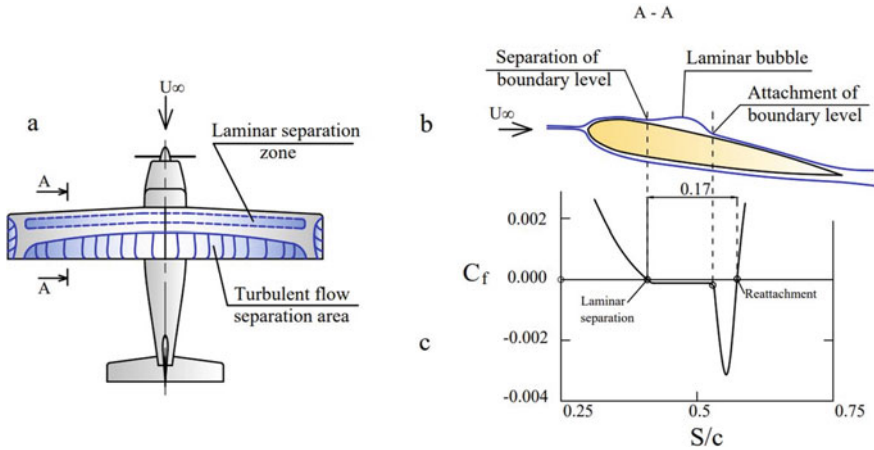


Fig. 1 Separation flow above aerofoil. **a** Plan view of wing flow; **b** profile view of wing flow; **c** change conditions C_f on the chord

There are methods for controlling the separation-vortex shedding that are based on typical principles of the boundary layer control [9, 10].

The three main methods: blow, suction and transition to turbulent flow of the boundary layer give kinematic energy to the boundary layer due to mass exchange between the boundary layer and non-stagnant flow layers when the wing configuration is constant. Other options for controlling the boundary layer are morphing wing concepts that generate favorable conditions for the flow by modifying the wing configuration to adapt it to the flight conditions.

2 Task

Morphing wing is a technology of morphing the wing configuration in order to improve its aerofoil and minimize flow-induced losses in flight conditions. The parents of the concept are Wright brothers whose Flyer-1 had no hinge high-lift devices as modern aircrafts have. Instead, its wings were bending and twisting with the help of rods and sheaves.

This technology has two main trends. Trend one: applying the lift force generation mechanism is similar to bird's or insect's wings. Trend two: applying either option instead of the uniform rigid profile wing with hinge high-lift devices. Option one: rigid morphing wing with telescopic sections, see Fig. 2a, b. Option two: flexible morphing wing that can change the aerofoil configuration and twisting, see Fig. 2c–e.

The morphing wing designers understand the associated issues and this allows believing that a small-size unmanned morphing aircraft will be created. This requires an analysis of good design solutions of the morphing wing technology for such aircrafts.

For small-size aircrafts, the rigid morphing wing would be a choice as it does not require complicated and energy-consuming drive systems. The rigid morphing wing allows reducing dimensions, number or getting rid of hinge high-lift devices that create

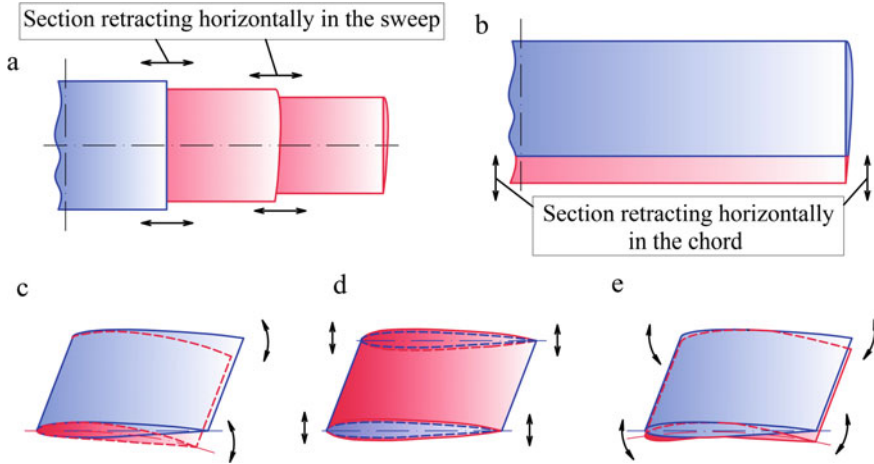


Fig. 2 Morphing wing options. **a** telescopic wing; **b** additional aerofoil retracted; **c** chord-wise bending; **d** profile thickness change; **e** profile curvative change

wing edge gaps with turbulence and higher drag. Moreover, the high-lift reduces stealth capability which is not good for military purposes for SUA. Below is review of rigid morphing wing options for SUA.

3 Review of Rigid Morphing Wing Options

The morphing wing technology provides for two options of morphing the rigid wing [10, 11]:

- In the wing plane (area, span, chord);
- Outside the wing plane (folding, bending, twisting);
- And combinations thereof.

Earlier options of the in the wing plane morphing that gave the greatest variation of aerodynamic performance yet simple design are:

- Area change (Fig. 3);
- Sweep change (Fig. 4);
- Area and sweep change.

The variable wing area gives high speed and short wing maneuverability, greater flight duration and range and fuel efficiency of the long wing. Depending on the wing outline changing line, Fig. 3 shows the following options for changing the wing area: telescopic sections, telescopic lead and trail, deflections and twists of the wing edges, up/down retracting additional aerofoils, wing retracting from the body and twisting around the vertical rotation line. The telescopic wing with sections capable of moving

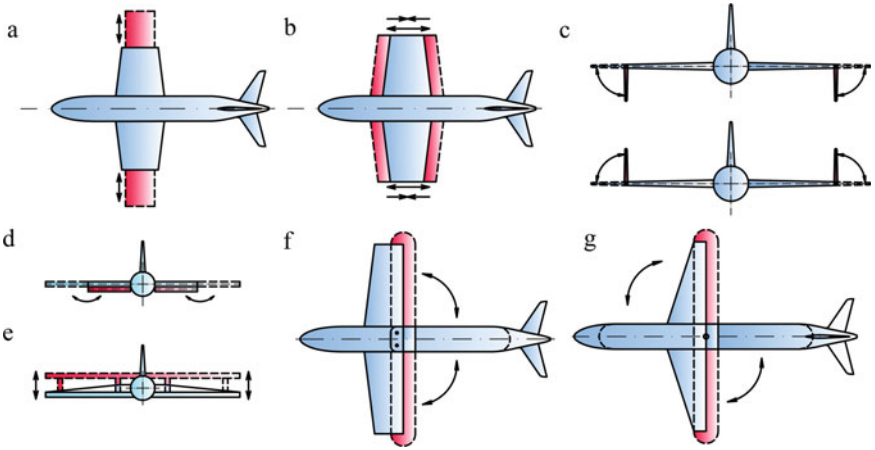


Fig. 3 Main ways of changing the wing area. **a** telescopic wing; **b** wing lead and trail retracting; **c** up/down deflection of the wing edges; **d** wing edges' twist by 180°; **e** up/down retracting additional aerofoils; **f** wing retracting from the body and twisting around the vertical rotation line; **g** additional aerofoil twist by 90° to the vertical line

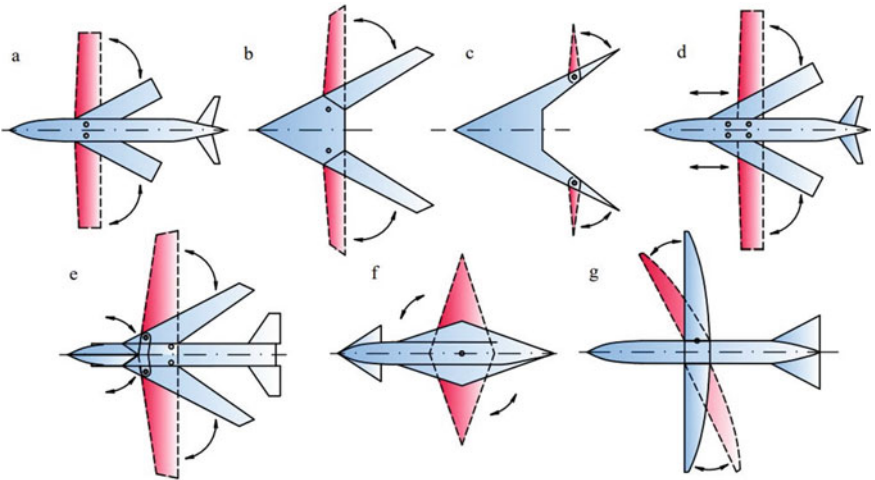


Fig. 4 Main ways of changing the sweep. **a–d** twisting wing panels with changing the sweep relatively the vertical rotation line; **c** twisting wing edges; **f** diamond wing twist by 90°; **g** asymmetrical change of the wing plane sweep (oblique airfoil)

back can considerably reduce SUA transverse dimensions in the start condition and therefore make transportation and launching thereof easier.

The main ways for changing the sweep are illustrated in Fig. 4.

Changing the sweep is changing the sweep angle during a flight to improve the lift force-drag ratio. For low-speed stages: climbing and lowering, using the reduced sweep wing more effectively. The high-speed cruise mode requires a larger sweep. Sweep

change affects changes of the wing extraction; therefore, the wing flow aerodynamics as this reduces the wave resistance and improves the aircraft maneuverability [12–36]. This morphing type is mainly used in fighting aircrafts and not good for SUA due to low speed. Moreover, changing the sweep will not be good for SUA that cannot take-off and landing stages by itself. They are container-type SUA with a starter for take-off (catapult or accelerator) and single-use SUA with no landing stage.

4 Justification of Practical Rigid Morphing Wing Option for SUA

For this, use the data on Fig. 1c and “effective wing area” S_{ef} definition. This is the wing surface area where the lift force is generated. Therefore, the wing lift force will be proportional to its effective area and calculated by formula:

$$S_{ef} = S \cdot (1 - k_{ex}) \quad (1)$$

where S —is geometrical wing area, m^2 . For a rectangular wing, $S = b \cdot l$, where b —is wing chord, m ; l —is wing span, m ; k_{ex} —wing exclusion coefficient, $k_{ex} = S_{ex}/S$, where S_{ex} —is excluded wing area.

If the rectangular laminar bubble axis length is 17% of the chord [8], then $k_{ex} = 0.17$. From Formula (1), $S_{ef} = 0.83S$.

Let us study the optimal wing chord. In order to ensure separation-free flow, the chord must be equal to the separation-free shedding $0.38 \cdot b$, that is, the wing must be narrow.

Let us find the effective wing span $l_{ef} = S_{ef}/0.38 \cdot b = 0.83 \cdot b/0.38 \cdot b = 2.18 \cdot l$. Therefore, the effective wing must be more than two times narrower and longer of a typical wing.

The conclusion is that aerodynamics improvement of a rigid wing of SUA should consider a longer and narrow wing free of high-lift devices. The most practical option from the above is a telescopic wing. Differentially retracted sections enable it to function as ailerons, while symmetrical retracting can change the lift force required for the flight conditions.

5 Conclusions

The morphing wing study aimed at justification of practical options for small-size aircrafts shows that SUA design reduces generation of the lift force of the wing with typical profiles and span and eventually does not allow applying the options for SUA to full extent.

Wing aerodynamics with low Reynolds number and separation of laminar boundary level are deemed to be critical factors because in this case most of the morphing wing options cannot be used when flow conditions are characterized with high Re typical for full-size aircrafts.

Small-size unmanned aircraft engineering takes the priority position in aviation and that is why aerodynamic modeling and study of optimal SUA configurations should proceed.

References

1. Burenok VM, Ivlev AA, Korchak VY (2009) Development of military technologies in 21st century, problems, planning, implementation. OOO Kupol, Tver
2. Makarenko SI (2016) Military robotics: nowadays status and perspectives. *Syst Control Commun Secur* 2:73–132
3. Buzhinskii EP (2013) Prioritized development of unarmed aircrafts from military science to economics. *Secur Index* 3(106); 19:123–132
4. Verlebnyy VV (2020) Methodology the selection of the rational aerodynamic layout and the basic characteristics of the single-use unmanned aircraft. *VKS-teoriya-i-praktika* 14:161–174
5. Ananov AV, Filatov SV (2020) Metod for determining the required orders of small-class unmanned aerial vehicles to delay the advance of enemy columns. *VKS-teoriya-i-praktika* 13:11–20
6. Kozlov VV (1998) Physics of flows structure. *Flow Separation*. Soros Edu J 4:86–94
7. Krasnov NF, Koshevoi VN, Kalugin VT (1988) Aerodynamics of separation flows. *Vysshaia Shkola, Moscow*
8. Schlichting G (1974) Boundary layer theory (Teoriya pogrannichnogo sloya) Nauka, Moscow
9. Ananda GK, Sukumar PP, Selig MS (2015) Measured aerodynamic characteristics of wings at low Reynolds numbers. *Aerosp Sci Technol* 42(2015):392–406. <https://doi.org/10.1016/j.ast.2014.11.016>
10. Chzhen P (1979) *Upravleniye otryvom potoka (Managing the Separator)*. Mir, Moscow
11. Barbarino S, Bilgen O, Ajaj RM, Friswell MI, Inman DJ (2011) A review of morphing aircraft. *J Intell Mater Syst Struct* 22(9):823–877
12. SyU S (1969) *Transporting airplanes with morphing wing*. Transport, Moscow
13. Sofla AYN, Meguid SA, Tan KT, Yeo WK (2010) Shape morphing of aircraft wing: status and challenges. *Mater Des* 31(3); 1:284–1292
14. Ajaj RM, Friswell MI, Flores EIS, Little O (2012) Span morphing : a conceptual design study. In: *AIAA/ASME/AHS adapted structure conference*, No April, pp 1–12
15. Neal DA, Good MG, Johnston CO, Robertshaw HH, Mason WH, Inman DJ (2004) Design and wind-tunnel analysis of a fully adaptive aircraft configuration. In: *Proceeding of 45th AIAA/ASME/ASCE/AHS/ASC structures, structural dynamics and materials conference*, Palm Springs, California, p 1727
16. Zverkov ID, Krukov AV, Grek GR (2014) Prospects of studies in region of low-sized aircraft (Review) *Vestnik NSU. Ser Phys* 9(2):95–115
17. Voronich IV, Kolchev SA, Panchuk DV, Pesetskii VA, Silkin AA, Tkachenko VV, Nguen Tkhan Tung (2019) On the peculiarities of aerodynamics of a small-sized aircraft of a normalschem. *Trudy MAI No 109*. <https://doi.org/10.34759/trd-2019-109-8>
18. Voronich IV, Kolchev SA, Konshin VN, Tkachenko VV (2010) On small-sized unmanned aircraft for area monitoring. *Aerosp MAI J* 17(5):24–33
19. Parkhaev ES, Semenchikov NV (2018) Wings aerodynamic optimization technique for small-sized unmanned aerial vehicles. *Aerosp MAI J* 2593:7–16
20. Airapetov AB, Katunin AV, Timerbulatov AM (2019) Aerodinamic design of multi-purpose miocro-UAV airframe. *Vestnik UGATU* 23(2):81–89
21. Brusov VS, Petruchik VP, Morozov NI (2010) Flight aerodynamics and dynamics of small-size unarmed aircrafts. MAI, Moscow
22. Parkhaev ES, Semenchikov NV (2015) Some aspects of airfoil optimization process for small size unmanned aerial vehicles application. *Trudy MAI, No 80*
23. Supekar AH (2007) Design, analysis and development of a morphable wing structure for unmanned aerial vehicle performance augmentation. Masters thesis, The University of Texas at Arlington

24. Ismail NI, Zulkifli AH, Abdullah MZ, Basri MHM, Arif M, Hamid A (2012) Evolution of monoplane fixed wing micro air vehicle's shape and design review. In: 2nd international conference on arts, social sciences and technology (ICAST2012)
25. Ajaj RM, Flores ES, Friswell MI, Allegri G, Woods BKS, Isikveren AT, Dettmer WG (2013) The Zigzag wingbox for a span morphing wing. *Aerosp Sci Technol* 28(1):364–375
26. Thill C, Etches J, Bond I, Potter K, Weaver P (2008) Morphing skins/the aeronautical journal. March, 2008. Paper no. 3216
27. Bobkov AV, Mitashova TA (2020) Feasibility review of substitution a high-lift device by a telescopic wing with self-similarity of Reynolds. *IOP Conf Ser Mater Sci Eng* 939(2020); 012013:1–6. <https://doi.org/10.1088/1757-899X/939/1/012013>
28. Blondeau J, Richeson J, Pines DJ (2003) Design, development and testing of a morphing aspect ratio wing using an inflatable telescopic spar. In: *Proceeding of 44th AIAA/ASME/ASCE/AHS structures, structural dynamics, and materials conference*, Norfolk, Virginia, p 1718
29. Brusov VS, Petruchik VP, Kuznetsov AV (2013) Investigation of wing airfoils for low-speed high-altitude unmanned aerial vehicles. *Aerosp MAI J* 20(3):19–31
30. Spedding GR, McArthur J (2010) Span efficiencies of wings at low Reynolds numbers. *J Aircr* 47(1). <https://doi.org/10.2514/1.44247>
31. Mo H, Kim T, Suk J, Kim S (2019) Modeling and desing of automatic landing system for variable span morphing wing UAV. *J Inst Control Robot Syst* 25(5):353–362. <https://doi.org/10.5302/J.ICROS.2019.19.0035>
32. Ozel C, Ozbek E, Ekici S (2020) A Review on applications and effects of morphing wing technology on UAVs. *Int J Aviat Sci Technol* 1(1):30–40
33. Ajaj RM, Jankee GK (2018) The Transformer aircraft: a multimission unmanned aerial vehicle capable of symmetric and asymmetric span morphing. *Aerosp Sci Technol* 76:512–522
34. Gamboa P, Aleixo P, Vale J, Lau F, Suleman A (2007). Design and testing of a morphing wing for an experimental UAV. *University Of Beira Interior Covilha (Portugal)*
35. Di Luca M, Mintchev S, Heitz G, Noca F, Floreano D (2017) Bioinspired morphing wings for extended flight envelope and roll control of small drones. *Interface focus* 7(1):20160092
36. King Sutton Woods B, I. Friswell M (2014) The adaptive aspect ratio morphing wing: design concept and low fidelity skin optimization. In: *Proceedings of the ASME 2014 conference on smart materials, adaptive structures and intelligent systems*, Newport, Rhode Island, USA, pp 1–11



Using a Chipper Without Felling Wood When Improvement Cutting Middle-Aged Plantings

A. A. Karelina^(✉), D. V. Chernik, and A. Y. Karnauhov

Reshetnev Siberian State University of Science and Technology, Krasnoyarsky Rabochy Av. 31,
Krasnoyarsk 660037, Russia

Abstract. Logging is an integral part of the Russian economy. However, with significant forest reserves, timber extraction is ineffective, and the economic benefit is only 1.3% of GDP. In this context, it is necessary not only to take into account the harvesting methods and equipment, but also the methods of reforestation. Thinning is one of the most important reforestation operations. Currently, the equipment used for planting maintenance is either large-sized machines such as harvesters, forwarders, skidders or a hand-held motorized tool. They, in turn, have a number of restrictions on their use. For example, harvesters, when working, cause great damage to undergrowth and unnecessarily compact the soil, and hand tools are ineffective and labor-intensive. This is a sufficient reason not to carry out care measures. In this regard, it is important to develop a device that combines the maneuverability of a hand tool and the performance of a large machine. Based on these conditions, the article provides a proposal for the development of a wheelless shredder based on the Bobcat mini-loader. A description of its work is given, as well as the characteristics of wood, in accordance with which the parameters of the base machine and the wheelless grinder were selected. As a result, the article outlines the positive results that are achieved during felling.

Keywords: Improvement cutting · Forest restoration · Mechanization · Logging · Chopping without felling wood

1 Introduction

Improvement cutting—is the most important forestry activity aimed at the formation of stable highly productive economically valuable plantations, the preservation and enhancement of their useful functions and the timely use of wood. They are carried out by removing unwanted trees from plantations and creating favorable conditions for the growth of the best trees of the main species [1].

The following types of felling are: admitting light, cleaning, thinning, passage felling, regeneration felling, re-forming felling, landscape felling, selective sanitary felling [2].

2 Relevance

The Krasnoyarsk Territory is one of the leaders among the regions of Russia in terms of forest resources; therefore, it is strategically important to maintain a balance between

felling and restoring forests. The area of its forest fund is 168.1 million hectares, and the forested area is 69% of the territory. More than half of the forests are larch, about 17%—spruce and fir, 12%—pine and 9%—cedar. Forests are 88% coniferous. Every year, on the territory of the Krasnoyarsk Territory, reforestation activities are carried out on an area from 50.4 to 57.0 thousand hectares, forest cultures are created in forest areas from 4.8 to 7.3 thousand hectares, and measures are taken to promote natural forest regeneration in an area from 45.5 to 49.8 thousand hectares. As a result of work on forest reproduction, land covered with forest vegetation on an area of 77.6–83.6 thousand hectares is being carried out, which allows ensuring a balance between forest felling, forest fires, other negative impacts and reforestation [3].

Russia has a wide variety of resources, one of which is forest. The timber industry occupies an insignificant part of the country's economy, only 1.3% of GDP. This indicates an ineffective use of forest potential [4].

Taking into account the low efficiency of forest use in Russia, it is necessary to choose a type of reforestation that, at minimal cost, will provide good results in the long term.

Thinning can be seen as one of the most effective methods of reforestation. It requires a minimum inclusion of additional equipment or even the use of forestry machines. The use of various fertilizers or specially grown trees is not required.

3 Problem Statement

Improvement cutting is an effective forest restoration operation [5]. However, even here, there are disadvantages that force the neglect of forest care measures. Large-sized machines, such as harvesters, skidders [6, 7], are mainly used in felling. They have high productivity, but their use in young and mid-aged forests does more harm than good. Because the machines are large, they often destroy healthy undergrowth and small trees. In addition, with their weight, they unnecessarily compact the soil. Hand power tools, in turn, are effective with a large density of plantations; however, labor productivity is low. In addition, there is a need to deliver the brigade to the site of felling, additional accommodation arrangements [8]. The main disadvantage of felling with the help of large-sized machines and manual power tools is the need to deliver the felled trees from the felling site to the warehouse. These are additional economic and time costs. In this regard, there is a need to develop a device that is able to combine the efficiency of the harvester and the maneuverability of a person. At the same time, it is also important to solve the problem of utilization of felled plantations in order to exclude their transportation to the place of storage.

4 Theoretical Part

One of the reasons for the low efficiency and low applicability of improvement cutting in forestry is the unsettled system for conducting maintenance activities, as well as a great variety and orderliness of equipment for felling [9]. This, in turn, leads to additional costs for equipment maintenance and labor organization. However, it is very important to carry out forest restoration measures, since in the long term they allow to improve

the quality of the grown timber, increase the growth per unit area, improve the sanitary conditions in the forest, and much more.

When choosing equipment for felling, it is necessary to be guided by environmental and economic indicators. So, if you carry out forest restoration using large machines, there is a risk of damaging growing and healthy young trees, as well as unnecessarily compacting the soil. In addition, when cutting with harvesters, it is necessary to take the removed trees to a warehouse and further process them. This, in turn, adds to the cost of such an operation [10].

In the case, when improvement cutting is carried out with a hand motorized tool, for example, a motorized hedge trimmer, labor productivity are reduced in comparison with machine felling. But at the same time, it is environmentally safer, since a person removes damaged trees more thoroughly and accurately. Also, with a high density of plantations, a person will cause less harm to trees, since he is more mobile [11]. Another nuance when conducting felling with a hand-held motorized tool is the need to deliver the crew to the cutting site, as well as organize additional accommodation and food points for them, which in turn adds cost to the process. It is important to note that after manual felling, it is also necessary to deliver the remote trees to the warehouse or immediately process them.

The existing equipment for grinding small trees and felling waste is quite diverse. It includes mechanisms with both internal combustion engines and electric ones, as well as driven from the power take-off shaft of a wheeled tractor. Cutting products can be scattered, fed into the car body, collected in a special container. Implementation of mechanisms hinged or trailed.

Usually, special shredders are used for wood processing. These shredders can be mounted in the body of a truck or stationary. Among such devices, one can single out a disk chipper with the ability to attach it to various vehicles [12]. There is also a way to remove felling residues, which involves the use of a modernized forwarder trailer. When collecting trees, they are sorted, and then they are processed into chips using a rotary knife mill [13].

It is important to take into account that processed wood should not be left in the cutting area or warehouse, as it is a factor that increases the fire hazard. It is necessary to immediately send it for further processing. However, wood chips can also be left in the forest as fertilizer.

Such an integrated approach has its advantages, but in conditions of limited mobility, it is not relevant. In addition, this option requires additional financial investments.

In this situation, it is necessary to put into operation such a device that will combine good cross-country ability, high productivity, maneuverability and efficiency. To do this, you need to understand what the subject of labor is.

Basically, when choosing, an economic and biological classification are used in accordance with which trees are divided into I—the best, II—auxiliary (useful), III—unwanted (to be removed). Externally, defects can be divided into the following categories: bimodality, root curvature, trunk curvature, knotty, apex curvature and the presence of lateral shoot [14]. Such a classification takes into account the sum of economic and biological indicators for assigning a tree to a certain category. In addition, each category uses additional classifications according to Kraft, Nesterov, Shedelin, etc. During

falling, it is necessary to strive to level the vertical structure of the stand and to evenly distribute the stands over the entire area of the site [15, 16].

Since larch, pine and spruce II ... IV categories are the most common tree species in the forests of Eastern Siberia, consider the geometric parameters of these tree species, which are presented in Table 1, while focusing on the maximum diameter at chest height, that is, 20 cm [17].

Table 1 Geometric parameters of Siberian conifers of II ... IV categories

Species	Bonitet					
	II		III		IV	
	Height (m)	Volume (m ³)	Height (m)	Volume (m ³)	Height (m)	Volume (m ³)
Larch	23	0.360	20	0.320	17	0.280
Spruce	21	0.320	19	0.294	17	0.268
Pine	21	0.300	19	0.282	17	0.264

Assuming the density of spruce 550 kg/m³, pine—600 kg/m³, and larch 700 kg/m³, determine the mass of trees by the following formula:

$$m_t = V_t * \rho_t, \quad (1)$$

where V_t —volume of tree, m³, ρ_t —density tree, m³.

We also determine the force of gravity of the plantings by multiplying the mass by the acceleration of gravity. We will summarize the obtained data in Table 2.

Table 2 Mass and weights of Siberian conifers of the II ... IV categories

Species	Bonitet					
	II		III		IV	
	Mass (kg)	Weight (N)	Mass (kg)	Weight (N)	Mass (kg)	Weight (N)
Larch	252	2475	224	2200	196	1925
Spruce	176	1728	161,7	1588	147	1447
Pine	180	1768	169,2	1662	158	1555

Based on the data obtained, it can be concluded that the largest weight, with a diameter at a chest height of 20 cm, has a larch of 23 m, which corresponds to the II category and a weight of a tree of 2475 N. In accordance with this, it is necessary to select such a basic machine, which, taking into account the weight working equipment will carry out thinning, meeting all safety standards.

Taking into account the fact that the trees must to be cut subsequently be transported and disposed of, it is rational to offer such a device that will simultaneously cut and chop the removed tree.

As a base machine, we will take a Bobcat T770 mini-track loader (Fig. 1), and as a working body, we will use a chipper without felling wood [18].



Fig. 1 Mini-track loader Bobcat T770

Since the loader is crawler-type, it makes it stable when working on clay soil as well as on rocky roads, and the hydrostatic transmission increases its flotation, even when fully loaded. The machine boom rises to a height of 3.3 m, which makes it possible to bring the attachment to the tree in a convenient position, even on a small slope. The glazed cabin allows for safe felling in high-density stands. It will also eliminate injury if the severed parts of a tree accidentally hit a person.

The main features are the rated lifting capacity of 1611 kg and the tipping load of 4602 kg. This, in turn, will allow for the unhindered use of devices that not require to felling for improvement cutting and provide a reserve of power for tipping the tree [19].

Chipper without felling wood is an open cylindrical casing in which a logarithmic knife is installed at an angle to the shaft. The device is equipped with a hydraulic gripper and pressure rollers. The cutting disk (Fig. 2) has a maximum diameter of 25 cm to fully penetrate the wood. The cutting disk radius is reduced by 5 mm every 18°.

The chipper is powered by the hydraulic system of the existing machine.

The work cycle looks like this:

1. A tree is selected for removal;
2. The approach and aiming of attachments is made;
3. The tree is captured;
4. Cutting and chopping wood;

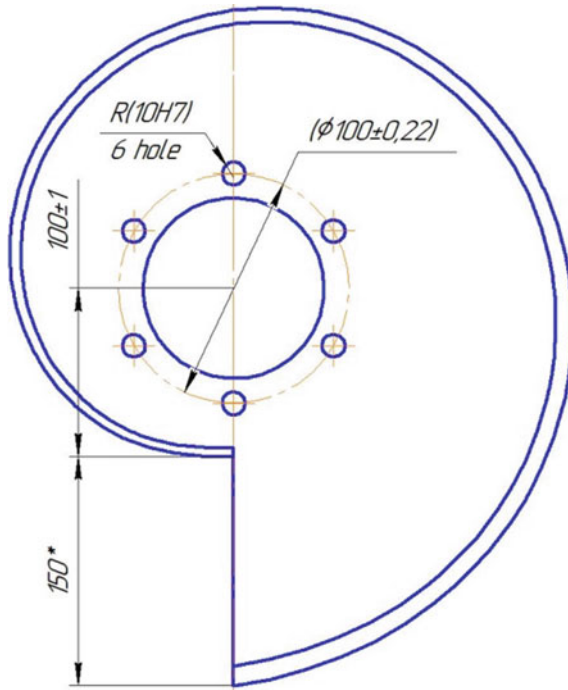


Fig. 2 Cutting disk

5. Moving to the next tree.

The existing equipment for chopping small trees and felling waste is diverse, but none of the devices performs the function of cutting trees. In addition, the use of such mechanisms is difficult due to the difficulty of their delivery to the place of work [20].

5 Practical Significance

Using a chipper without felling wood in improvement cutting will reduce environmental damage by reducing the number of accidental visits to healthy plantations, since the base machine is smaller. In addition, it compresses the soil less. The use of the proposed device will eliminate the need to deliver the cut trees to another place, and will allow them to be processed immediately. This, in turn, will reduce the cluttering of the warehouse, which means it will reduce the fire hazard. In comparison with manual labor, productivity will increase, because most of the time in the working cycle will be spent only on moving from tree to tree. The need to organize the labor of additional workers will disappear. Cutting will be safer for the operator.

6 Conclusion

Improvement cutting is an important forestry measure, which is aimed at the formation of highly productive, biologically sustainable plantations with specified parameters, as well as at the preservation and enhancement of their useful functions, the timely use of wood. They are made by cutting down some of the trees from the plantations and creating favorable conditions for the growth of the remaining best trees of the main species. Thinning is one of the most time consuming and challenging forestry operations. Therefore, the widespread use of thinning is difficult to implement with a low level of mechanization.

With the correct technology chosen, as well as with regular thinning, the following positive results occur:

1. Changing the composition of forest stands in the direction desirable for the economy;
2. Selection of the fastest growing and most valuable forms of tree species;
3. Reduction of the period of growing technically mature wood;
4. Improving the quality of the grown timber;
5. Increase in total growth per unit area. Increase in the productivity of plantations by 5–15%;
6. Improving the sanitary situation in the forest and increasing the resistance of forest stands against harmful factors;
7. Strengthening water protection, water regulation, soil protection and other values of the forest [21, 22].

The machines used in improvement cutting must meet the requirements for productivity and economy, as well as for the implementation of programs with minimal damage to the growing stand and soil.

References

1. Ministry of Nature of Russia (2017) Rules for the care of forests. Russia
2. Rogozin MV (2015) Perm Univ Bull 3:207–218
3. Puzanova OA, Smolina LV (2019) Proceedings of the BrSU. Ser Nat Eng Sci 238:157–162
4. Petrov AP (2013) LesPromInform 2:28–31
5. Chibisov GA, Nefedova AI (2003) Forest J 5:11–17
6. Kondratyuk VA (2016) Forestry machine for improvement cutting of forests, RF 167259 U1, 27 Dec 2016
7. Zinin VF, Prokhorov LN, Blinov EK (1998) Machine for improvement cutting, RF patent 2101925 C1, 25 Mar 1998
8. Gerts EF, Terinov NN (2019) Forestry J 2:86–94. <https://doi.org/10.17238/issn0536-1036.2019.2.86>
9. Schwartz E, Shmatkov N, Kobayakov K (2019) LesPromInform 4:156–157
10. Sukhanov YV (2004) Actual problems of the forestry complex 8:205–207
11. Pasyura AG, Pasyura AG, Malyukov SV (2014) Actual directions of scientific research of the 21st century: theory and practice 2–2:121–125
12. Syromyatnikov SV, Zyryanov MA, Leiman SP (2017) Innovations in the chemical-forestry complex: trends and development prospects 186:153–155

13. Zyryanov MA, Syromyatnikov SV, Borin KV (2019) Innovations in the chemical and forestry complex: trends and development prospects 250:179–183
14. Stanko Jan (2010) Wood species and main wood defects. Moscow
15. Danilenko OK, Sukhikh AN (2019) Syst Methods Technol 3:105–110. <https://doi.org/10.18324/2077-5415-2019-3-105-110>
16. Markovsky AV (2018) Improvement cutting in young stands: how to build a forestry enterprise. A Practical Guide, Moscow
17. Groshev BI (1980) Forest taxation reference book. Moscow
18. Oryol SN (2018) Forest J 5:135–150. <https://doi.org/10.17238/issn0536-1036.2018.5.135>
19. Mini-track loader Bobcat T770 (2015) Trivial HTTP. <https://bobcatrussia.ru/upload/iblock/0e2/0e2973ba312cdf1839c232fcf0c587fb.pdf>. Access 2015
20. Mikhailov MG, Ovsyannikov SI, Andreeva DV (2018) Modern technologies of the wood-working industry 320:244–251
21. Oskorbin PA, Bugaeva KS (2007) Conifers of the boreal zone 4–5:408–413
22. Kryuk VI, Magasumova AG, Pulnikov AP, Zalesova EC (2009) Agrarian Bull Urals 8:103–105



Modeling of the Heat Setting Process in Order to Eliminate Defects in the Obtained Part

E. G. Demyanenko^(✉), I. P. Popov, and A. S. Kuznetsov

Samara National Research University, 34, Moskovskoye shosse, Samara 443086, Russia

Abstract. This paper investigates the mechanics of the heat setting process of the ‘cup’ part. There is a certain difficulty in forecasting the behavior during manufacturing of thin-walled parts out of sheet blanks, so there is a possibility of losing their stability due to the presence of unwanted stresses, which leads to additional expenses on negating these defects. Obtaining thin rods, flat membranes, rings and even more complex parts of various configurations often leads to a necessity of lengthy reworks of stamps and tooling, which leads to additional material expenses, which significantly increases the manufacturing cost. In order to estimate the possibility of negating defects, related to the size of gaps between the workpiece and the stamp tooling elements, the simulation of the heat setting process was performed using ANSYS/LS-DYNA software for different sizes of tooling elements. During the heat setting, due to the temperature and duration of the process the stress state of the workpiece changes, so the choice of the desirable gap variant is determined by the close values of intensities of residual stressed and strains in the entire workpiece volume.

Keywords: Heat setting · Metal · Model · Modeling · Stress · Warping · Wrinkling · Corrugation

1 Introduction

Nowadays, titan alloys took the leading place among other high-strength construction materials. Many parts of modern airplanes, rockets and jet engines are made by using hot sheet stamping out of alloys like OT4-1 [1–5], which allows the creation of strong and rigid, but lightweight structures with low material consumption [6, 7]. The considerable drawbacks of stamping these alloys, which are particularly prominent in the case of thin-walled products, are wrinkling and corrugation of their parts [8–10]. In order to remove these negative effects and manufacture a part with designed parameters and dimensions, a costly heat setting operation is usually performed.

2 Methods and Theoretical Foundations

The main condition defining the choice of material for the heat setter tooling is the linear thermal expansion coefficient, which must be 1.5–2 times higher than that of the part’s material (for OT4-1 it is $9 \times 10^{-6} 1/^\circ\text{C}$). In this study, we also use 12X18H10T

(GOST 5632—72) stainless steel alloy with the coefficient of linear thermal expansion of $17 \times 10^{-6} 1/^\circ\text{C}$.

In Fig. 1, the form of the part and its cross-section after the hot stamping is presented. Warpage in the form of deflection and corrugation appeared on the flat portion of the part with the $205 \times 10^{-3}\text{m}$ diameter.

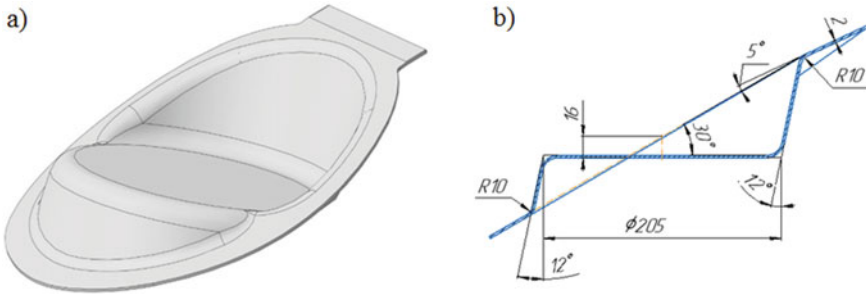


Fig. 1 a The form of the part ‘cup’; b Cross-section of the part ‘cup’

The presence of the defects during heat setting operation could be detected using the results of simulation [11, 12] of the distribution of residual stresses and deformations after cooling the workpiece to 20°C . The geometry of the tooling was modeled using KOMPAS-3D software (see Fig. 2) and later imported into ANSYS/LS-DYNA workspace (see Fig. 3).

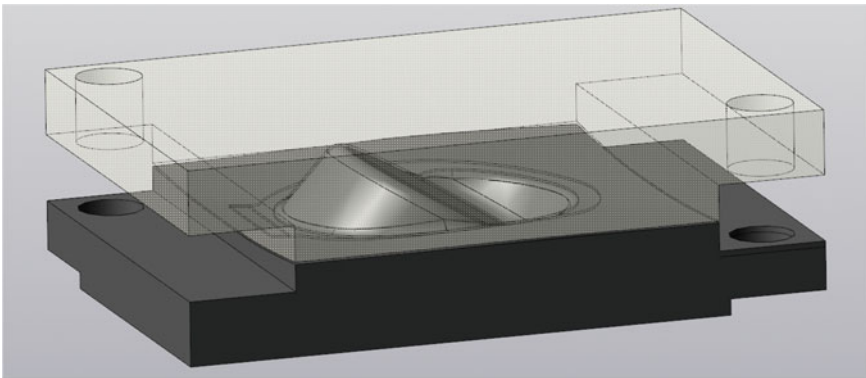


Fig. 2 The geometry of the tooling in KOMPAS-3D software

In Figs. 4 and 5, we present the movement graph of the tooling and the workpiece. The following contacting surfaces were chosen: workpiece—punch, workpiece—die. The coefficient of friction was taken equal to 0.12, RBUZ displacement restrictions were imposed on the entire die tooling—only Z-axis movement is permitted.

In our simulation, we used the 4-node shell element SHELL 163, which accounts for bending and spring back. Its constants, material properties for the tooling and the

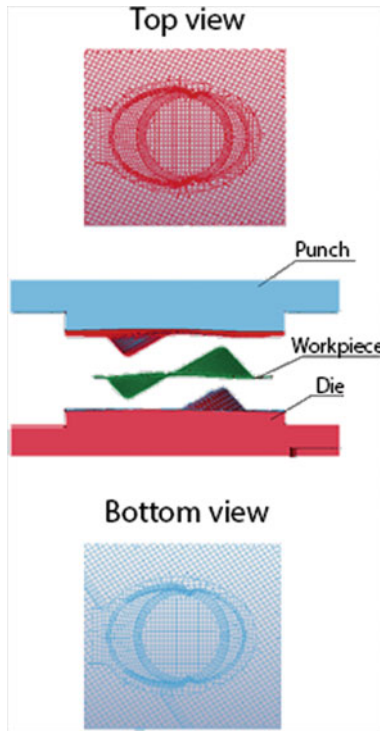


Fig. 3 Tooling mathematical model in ANSYS / LS-DYNA software

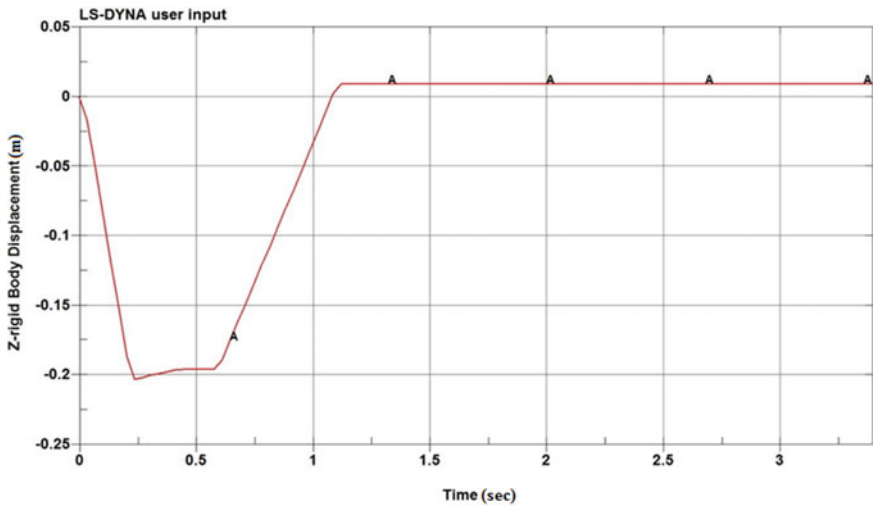


Fig. 4 The movement of the punch and the die

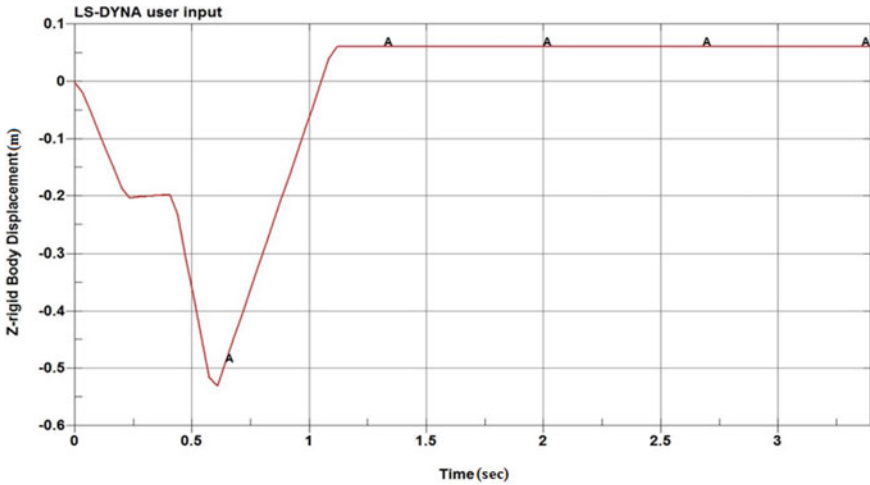


Fig. 5 The movement of the workpiece

workpiece, movement constraints, as well as other parameters: Shearfactor (SHRF) = 0.83 (a factor affecting the type of mathematical analysis when setting a problem), No. of integration pts. (NIP) = 5 (number of nodes along with the thickness of the SHELL 163 element), Thickness at node 1 (T1) = 0.0062 (thickness at the node).

The mechanical properties of the OT4-1 samples for the creation of a transverse anisotropic hardening model (see Fig. 6) were established using the Tinius Olsen H5KT machine. The data was processed by Horizon Startub Wizard software and printed out as graphs.

In Fig. 7, we present the hardening curve for OT4-1 titan alloy from ANSYS/LS-DYNA, derived at the following material properties: density = 4.54×10^{-3} kg/m³ Young modulus = $1.12 \cdot 10^5$ MPa, Poisson's ratio = 0.32, yield point = 2.5×10^8 Pa.

3 Experimental Technique and Results

An adequate mathematical model could allow us to predict the development and degradation of the system, evaluate its performance and durability under specified conditions, check hypotheses about the causes of the observed phenomena and undesirable changes in the state of the system [13].

The model provided us with features of the stress–strain state of the workpiece [4, 14, 15] after applying three modes of the heat setting and varying the gap between the punch and the workpiece ($0; 0.1 \times 10^{-3}$ m).

In Fig. 8, we present the distribution of intensity of residual stresses and intensity of deformation after complete cooling down to $T = 20$ °C.

It was discovered, that the mathematical model of the heat setter, with the gap set to, yields the highest observed irregularities of the residual stresses and deformations after cooling down to. With the gap between the tooling and the workpiece set to, the stresses and deformations had the lowest and most consistent values. Therefore, in

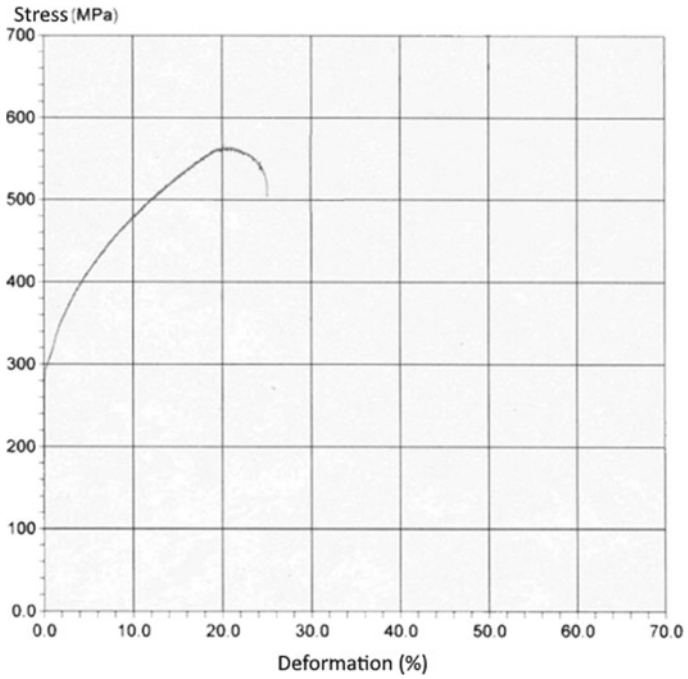


Fig. 6 Hardening curve of OT4-1 titan alloy

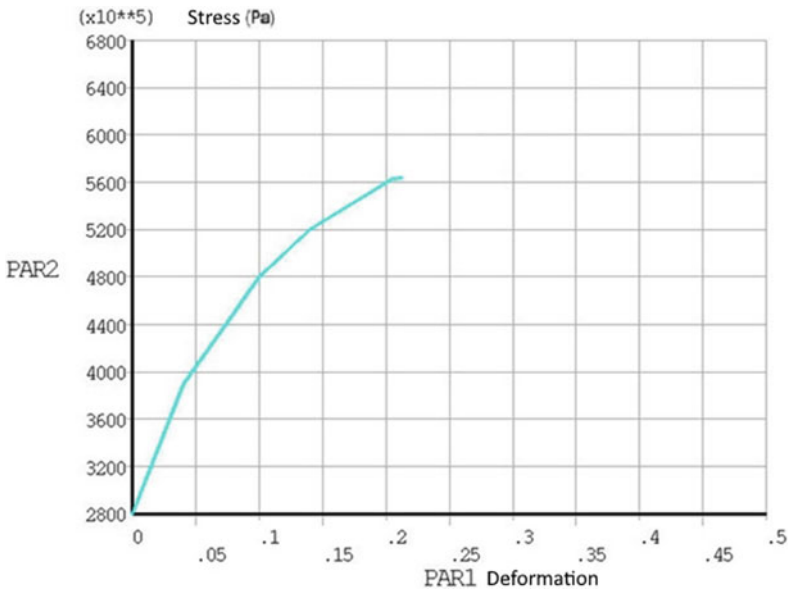


Fig. 7 Hardening curve of the modeled material from ANSYS/LS-DYNA

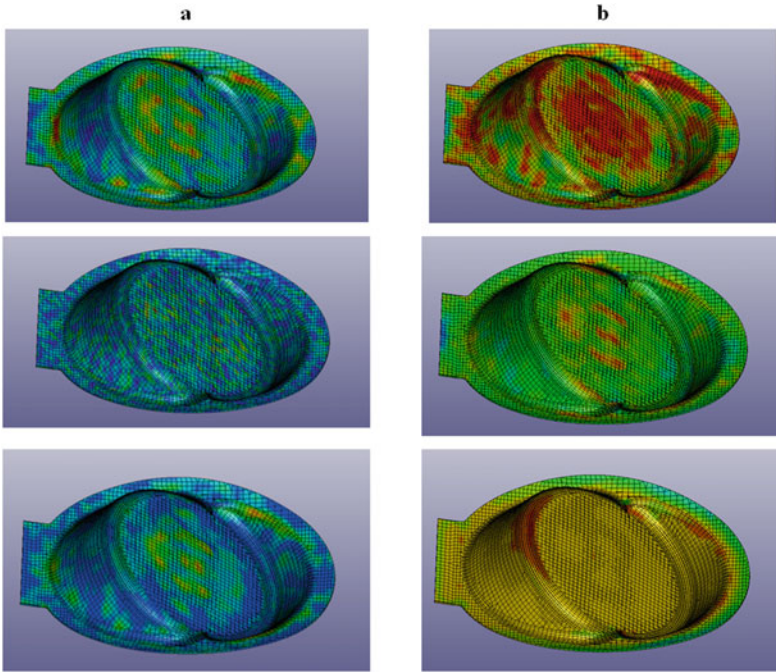


Fig. 8 **a** Distribution of the intensity of the residual stresses; **b** Distribution of the intensity of the residual deformations after the heat setting

order to eliminate warpage and corrugation of the ‘cup’ part, the optimal gap size of is considered the best.

4 Conclusions

In this paper, the constructive and technological analysis of the hot-stamped part was performed. Two kinds of defects (warpage and corrugation) were discovered, which could be eliminated by heat setting operation during manufacturing of the ‘cup’ part.

The efficiency of the developed technology is determined by the fact that the downtime in the manufacture, including the ‘cup’ part, is significantly reduced due to the increase in the number of usable parts (see Fig. 9).

Thanks to the inclusion of the heat setting operation in the technological process of manufacturing of this part the number of defective parts was reduced from 80 to 20%.

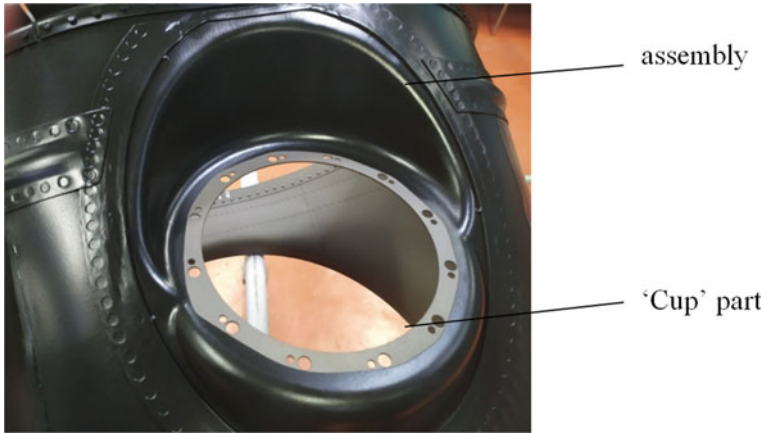


Fig. 9 The part in the assembly

References

1. Avdeev VV, Bystrov VB, Kazakov PA (2014) Sposob izgotovleniya shtampovok lopatok iz dvukhfaznogo titanovogo splava (A method of manufacturing engine blade forgings from a two-phase titanium alloy). Ru Patent 2525961:20
2. Pervov ML, Skobeleva AS, Golovkin SA (2017) Sposob izgotovleniya shtampovok lopatok iz titanovykh splavov. (Method of manufacturing titanium alloy engine blade forgings). Ru Patent 2614294, 24 Mar 2017
3. Khaimovich AI, Khaimovich IN (2018) Methods and algorithms for computer-aided engineering of die tooling of compressor blades from titanium alloy. IOP Conf Ser Mat Sci Eng 302(1):012062
4. Shtrikman MM, Kolednikov AS et al (2019) O snizhenii ostatochnykh napryazheniy v svarykh soyedineniyakh listovykh konstruksiy iz titanovykh splavov (On reducing residual stresses in welded joints of sheet titanium structures). Aviation Indus 1:57–62
5. Lavrov AF, Dubrovsky ES et al (2003) Sposob polucheniya polykh zagotovok iz vysokoprochnykh materialov (Method for producing hollow workpieces from high strength materials). Ru Patent 2204449:20
6. Melnikov EN, Schekaturov YI et al (2000) Ustroystvo dlya termofiksatsii detaley dlya lista (The device for heat setting sheet parts. Ru Patent 2155235:27
7. Melnikov EN, Shport IE et al (2001) Ustroystvo dlya termofiksatsii detaley dlya lista (The device for heat setting sheet parts. Ru Patent 2170770:20
8. Mitin AS, Mitin AA (2010) Sposob izgotovleniya pustotelykh izdeliy (A method of manufacturing hollow parts). Ru Patent 2386719:20
9. Baburin MA, Baskakov VD et al (2019) Sposob izgotovleniya segmentnykh obolochek dlya sharovykh yemkostey (Method of manufacturing segmental shells for spherical containers). Ru Patent 2710619:30
10. Demyanenko EG (2012) Issledovaniye protsessa formovki v ustroystve s ispol'zovaniyem vozmozhnostey razzhimnykh sektorov (Investigation of the capabilities of the forming process in a device using expansion sectors). Izvestia RAS SamSC T14-6:182–186
11. Kolesnikov AV, Mironenko VV, Cheslavskaya AA, Shmakov AK (2013) Optimizatsiya tekhnologicheskikh protsessov izgotovleniya detaley iz lista sredstva virtual'nogo tekhnologicheskogo modelirovaniya (Optimization of technological processes for the manufacture

of parts from a sheet by means of virtual technological modeling). Proc Irkutsk State Tech U Tech Sci 12:73–77

12. Khaimovich IN, Khaimovich AI (2017) Computer-aided engineering of the process of injection molding articles made of composite materials. Key Eng Mater 746(KEM):269–274
13. Larin SN, Yakovlev SS, Platonov VI, Leonova EV (2014) Shtampovaya osnastka dlya izotermicheskoy pnevmoformovki listovykh vysokoprochnykh materialov v rezhime kratkovremennoy polzuchesti (Die tooling for isothermal pneumoforming of sheet high-strength materials in the mode of short-term creep). Izvestiya TulGU Tech sci 11:124–125
14. Golenkov VA, Yakovlev SP et al (2009) Teoriya obrabotki metallov davleniya: uchebnik dlya vuzov (Theory of pressure working of metals: a textbook for universities). Aviation Indus 1:57–62
15. Ponomarev VA (2018) O napryazhennom sostoyanii obladayushchey polzuchest'yu krugloy membrany v protsesse termofiksatsii (On stress state of a creeping circular membrane during heat setting). Bul of the Siberian St Ind U 2:4–7



Study and Improvement of Operation of the Planetary Gear Reducers of the Cold Rolling Mill Tension Leveler

G. Kornilov, O. Filatova, and I. Abdulveleev^(✉)

Nosov Magnitogorsk State Technical University, 38, Lenin Avenue, Magnitogorsk 455000, Russia

i.abdulveleev@magtu.ru

Abstract. The paper analyzes generating tensions in a tension leveler (TL) of a continuous strip pickler of a broad-strip cold rolling mill of a large-scale metallurgical enterprise. The research objective is to ensure stable TL operation based on the correct settings of the electric drive torque and speed for various strip gauges. The novelty comprises developing a mathematical description of the actual strip extension depending on the bridle roller diameters, and a mathematical model linking the strip tension with a given strip thickness and loads of the main and extension drives. It has been found that the actual strip extension may vary within a wide range of 1.5–3.1%. An average value of 2.3% can be achieved by changing the roller diameters within a quite narrow range. A 1 mm change in diameter was found to cause a change in actual extension of approximately 0.1%. It has been established that the strip tension upstream of the TL is directly determined by the extension drive load. The dependencies obtained to calculate the electric drive speed and power parameters allow adjusting the TL drive speed and torque settings to maintain the target extension and avoid unacceptable loads on the planetary gear elements at various strip gauges, thereby improving the strip resource and stability of operation.

Keywords: Continuous strip pickler · Tension leveler · Strip tension · Planetary gears · Extension drive

1 Introduction

The continuous strip pickler (CSP) is located at the start of the cold rolling mill production line. While passing through the CSP, the strip undergoes the following procedures: unwinding, scale breaking, end welding, debarring, pickling, rinsing, drying, and coiling. The tension leveler is designed to straighten the strip profile and break up the scale emerging on the strip surface after the hot rolling [1–3]. The stable TL operation impacts significantly on the operation of the entire CSP unit [4–7]. The paper studies the TL developed and supplied to process a wide range of strips. A feature of its design (Fig. 1) is the use of planetary gear reducers in the bridle drives. Operating experience has shown that in the planetary gear elements, excessive forces occur, causing their failure.

In our opinion, the main reasons may include an insufficient safety margin of mechanical equipment and incorrect adjustment of drives in the case of a complex planetary gear [8, 9].

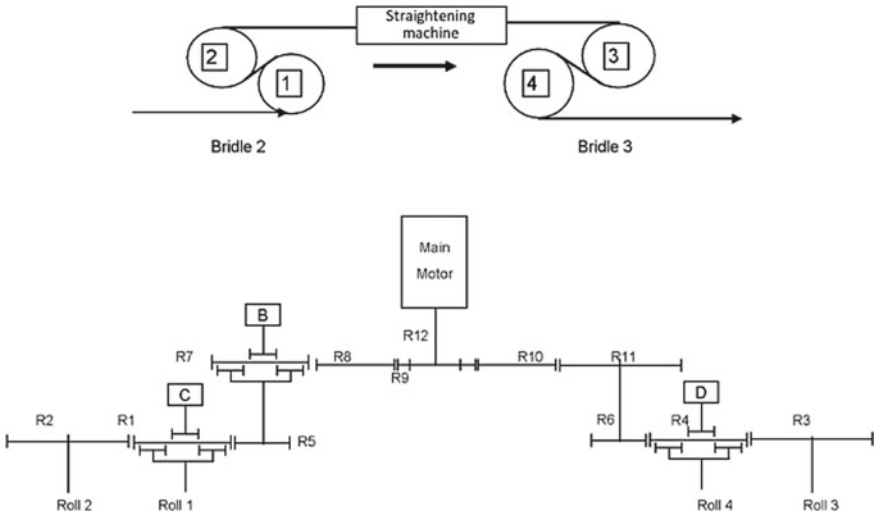


Fig. 1 The layout of the TL reducer gear wheels (*B*—extension drive motor; *C*—the motor of bridle No. 2; *D*—the motor of bridle No. 3; *1*—roller connected to the *C* motor through the planetary gear reducer; *2*—the TL input roller; *3*—the TL output roller; *4*—roller connected to the *D* motor through the planetary gear reducer)

The paper is aimed at ensuring the stable TL operation based on the correct setting of the electric drive torque and speed for various strip gauges. Achieving this goal requires solving the below problems:

- deriving formulas linking the drive rotation speeds with the speed of the strip on the TL rollers,
- analyzing the impact of unequal roller diameters on the actual extension,
- deriving formulas linking the drive shaft torques with the strip tension upstream and downstream of the TL,
- analyzing changes in the rear and front strip tension as a function of loading the main and extension drive motors.

2 Determining Dependencies to Calculate the TL Drive Speeds

In the TL, the planetary gear is used to more accurately set the speed of the roller located upstream of the cassettes. The main drive sets 90% of the rear roller speed, the extension drive adds the remaining 10%, while to change the extension by 0.1%, and the extension drive speed should be changed by 10%. Thus, the use of a planetary gear reduces the speed control accuracy requirements for the drive.

Figure 2a shows simplistically the gear ratios between the center and countershafts and the outer gear. Here, $i = z_o/z_c$ is the gear ratio represented as the ratio of the outer gear teeth number z_o to the central gear teeth number z_c . The planetary gear of bridle No. 3 has the following teeth number: $z_o = 72$ and $z_c = 18$.

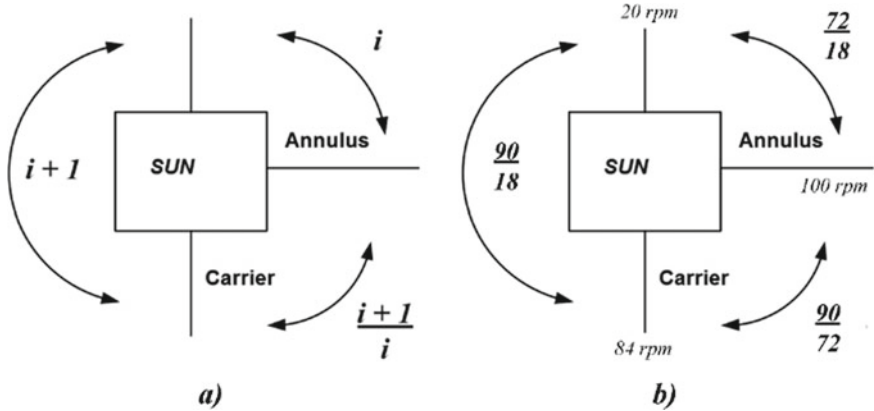


Fig. 2 a gear ratios and b rotation speeds in the planetary gear reducer of bridle No. 3

At the first stage of the study, experimental data on the distribution of tension in the TL and adjacent bridles have been gathered and processed using the electric drive torque and speed oscillography [10, 11]. Analysis of the oscillograms obtained for different strip gauges has shown that the actual strip extension varies within 2.6–2.9%, while the target extension is 1.2%. It has been found that such a significant difference is caused by the lack of consideration of the actual roller diameters of bridles 2 and 3 in the main and extension drive speed settings.

To determine the exact drive settings, the dependence between their rotation speed and the speed of the strip on the TL rollers should be determined. Using the known teeth numbers of the TL drive tooth and planetary gears, the gear ratios of the speeds of the motor A and rollers 1–4 (Table 1) and those linking the speeds of the motors B, C, D, and A have been calculated [12]:

$$\begin{aligned}
 n_A &= 5.9469 \cdot \frac{V_3}{D_3}, \\
 n_B &= 58.6297 \cdot \left(\left(1 - \frac{E_{\%}}{100} \right) - \frac{D_2 \cdot 5.9469}{D_3 \cdot 6.4140} \right) \frac{V_3}{D_2}, \\
 n_C &= 47.0988 \cdot 5.9469 \cdot \frac{V_3}{D_3} \cdot \left(\frac{D_2/D_1}{6.4140} - \frac{1}{7.0853} \right) \\
 &+ 47.0988 \cdot 58.6297 \cdot \left(\left(1 - \frac{E_{\%}}{100} \right) - \frac{D_2 \cdot 5.9469}{D_3 \cdot 6.4140} \right) \cdot \frac{V_3}{D_2} \cdot \left(\frac{D_2/D_1}{58.6297} - \frac{1}{64.7658} \right), \\
 n_D &= (77.6994 - 73.9995 \frac{D_4}{D_3}) \cdot \frac{V_3}{D_4}
 \end{aligned} \tag{1}$$

Table 1 Gear ratios between motor & roller speeds

Roller No	Motor			
	A	B	C	D
1	22.259	203.468	147.965	276.978
2	20.150	184.191	133.947	250.736
3	18.683	170.777	124.192	232.476
4	19.617	179.316	130.402	244.100

Here, $E\%$ is the calculated strip extension; $V1, V2, V3, V4$ are the linear strip speed (m/min) on the 1st, 2nd, 3rd, and 4th roller, respectively; $D1, D2, D3, D4$ are diameters (m) of the 1st, 2nd, 3rd, and 4th roller, respectively; nA, nB, nC, nD are the rotation speeds (rpm) of the A, B, C, and D motors, respectively.

3 Analysis of the Impact of Inequality of Roller Diameters on Actual Extension

At this stage, the authors have analyzed the impact of actual roller diameters on the strip extension. The motor speeds have been calculated by the formulas programmed in the controller without considering the diameters (k), and the extension has been calculated considering the inequality of the roller diameters. The calculation results (Table 2) show that for a target (t) value of 1.2%, and the actual (a) extension is 2.64%, while the strip speed does not affect the actual extension.

Table 2 Impact of roller diameters on extension

Parameter	Value		
Target extension, %	1.2	1.2	1.2
Linear strip speed (t), m/min	300	200	100
The 2nd roller diameter (k), mm	1250	1250	1250
The 3rd roller diameter (a), mm	1245	1245	1245
The 2nd roller diameter (a), mm	1227	1227	1227
Motor A rotation speed, rpm	1427.3	951.5	475.8
Motor B rotation speed, rpm	854.8	569.9	284.9
The 2nd roller linear speed (a), m/min	290.93	193.95	96.98
The 3rd roller linear speed (a), m/min	298.80	199.20	99.60
Actual extension, %	2.64	2.64	2.64

The actual strip extension $E_{23\%}$ is determined through the speeds of the 2nd and 3rd rollers by formula:

$$E_{23\%} = \frac{V3 - V2}{V2} \cdot 100 \tag{2}$$

To determine the extension by the above formulas, the roller speeds should be known. These speeds are proposed to be determined through the TL motor speeds already available in the control system. The dependence between the roller and motor speeds is described by previously obtained formulas (1). Let us calculate how the roller diameter affects the actual extension. To do this, we vary the diameters of the 2nd and 3rd rollers within the range of the average value ± 4 mm, which is 1229 and 1245 mm for the 2nd and 3rd rollers, respectively.

Analysis of the data obtained shows that the actual extension may vary in a quite wide range of 1.6 (diameters 1.240/1.235 mm) to 3.1% (diameters 1.249/1.225 mm). An average value of 2.3% is achieved at different diameter ratios, e.g., 1.240/1.226 mm or 1.249/1.235 mm. In general, a 1 mm change in diameter may be considered to cause a change in actual extension of about 0.1%.

4 Calculation of the TL Strip Tension

As part of the continuous strip pickler line, two groups of drives should be distinguished: those regulating the strip speed (speed master drive) and those regulating the strip tension. Tension control motors make up the majority. Since direct tension control requires installing a tension sensor, which is not always possible due to the compact pickler design, the indirect method of regulating the drive torque, proportional to the tension, is often used in practice [13]. The designation of strip tensions used by the TL manufacturer is shown in Fig. 3.

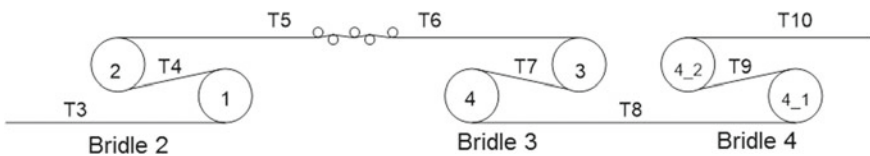


Fig. 3 Designation of tensions for the section of bridle No. 2—bridle No.4 (T_3 —the strip tension downstream of the buffer; T_4 —the strip tension between the rollers of bridle No. 2; T_5 —tension upstream of the TL; T_6 —tension downstream of the TL; T_7 —the tension between the rollers of bridle No. 3; T_8 —the tension between bridles Nos. 3 & 4; T_9 —the tension between the rollers of bridle No. 4; T_{10} —tension downstream of bridle No. 4 upstream of the baths)

By their joint action, the input buffer, bridle No. 2, and the extension drive set the rear tension T_5 upstream of the TL. The main drive and bridles Nos. 3 and 4 pull the strip out of the TL rollers and provide the required tension upstream of the baths.

According to the process mode proposed by the TL manufacturer, the main controlled coordinate is not the strip tension but the extension. Information about the TL strip

tension is very critical since when the tension is too high, accelerated wear and failure of mechanical equipment occur [14]. The situation is also complicated by the presence of several planetary gears and the interconnection of the drives of bridles Nos. 2 and 3 through them.

The strip tension at the TL output (front tension) is made up of those created by bridles Nos. 3 and 4 and the strip upstream of the *T10* baths:

$$T6 = T_{\Sigma 3} + T_{\Sigma 44} + T10 \quad (3)$$

The strip tension upstream of the TL (rear tension) is made up of those created by bridle No. 2 and the input buffer:

$$T5 = T_{\Sigma 2} + T3 \quad (4)$$

According to the technical documents, the maximum front tension is 600 kN, while the maximum rear tension is only 300 kN. The maximum front tension is 2 times more than the rear one; therefore, it is logical to install two bridles Nos. 3 and 4 downstream of the TL, which, with their four rollers, are capable of creating twice as much force as two rollers of bridle No. 2 located upstream of the TL.

The formulas to calculate the rear and front tensions created by the TL's 1st, 2nd, 3rd, and 4th rollers are given below:

$$\begin{aligned} T_2 &= (Mb \cdot 184.191 + Mc \cdot 14.01)/(D/2), \\ T_3 &= (Ma \cdot 18.683 + Mb \cdot 170.777)/(D/2) + T_{34} \cdot (1 - 18.683/19.617) \end{aligned} \quad (5)$$

An analysis of these formulas shows that the planetary gear between the TL's 2nd and 3rd rollers allow transmitting 92% of the energy ($170.777/184.191 \cdot 100\%$) of the rear tension created by the extension drive forward through the mechanical transmission and converting it into the front tension through the 3rd roller. This explains why a change in the extension drive load does not affect the main drive load: the main drive only adds front tension, but most of it is created by the rear tension mechanically transmitted forward. The front tension also changes simultaneously with the rear tension, but this change cannot be fixed due to the lack of a direct sensor.

When the extension drive is overloaded due to the incorrect process mode, the load on the planetary gear also increases significantly since it transmits the rear tension energy, which increases multiply. Obviously, this situation leads to accelerated wear and failure of the planetary gear.

5 Analysis of the Change of the Rear and Front Strip Tension as a Function of Motor Load

At the final stage of the study, the authors analyze separately the action of each of three bridles Nos. 2, 3, and 4. Further material summarizes the results obtained above and gives a general picture of the strip tension distribution in the TL. To do this, four sections were identified for which the below parameters were calculated:

- the strip tension $T3$ downstream of the buffer,

- the strip tension $T5$ upstream of the TL,
- the strip tension $T6$ downstream of the TL,
- the strip tension $T10$ upstream of the baths.

The strip tensions downstream of the buffer and upstream of the baths were calculated by the TL manufacturer’s formulas. The strip tension upstream of the TL was made up of those in the buffer and from bridle No. 2. The strip tension downstream of the TL was made up of those upstream of the baths and from bridles Nos. 3 and 4. The formulas to calculate the strip tension in the TL section are given below:

$$\begin{aligned}
 T3 &= 2.6449 \cdot H^{-0.6405} \cdot H \cdot B, \\
 T10 &= 1.111 \cdot H^{-0.0606} \cdot H \cdot B, \\
 T5 &= T3 + T_2 = T3 + (Mb \cdot 184.191 + Mc \cdot 14, 01)/(D/2), \\
 T6 &= T10 + T_3 + T_4 = T10 + (Ma \cdot 18.683 + Mb \cdot 170.777)/(D/2) \\
 &\quad + T_{34} \cdot (1 - 18.683/19.617) + T_4.
 \end{aligned} \tag{6}$$

where H, B are the strip thickness and width (mm).

Table 3 shows the tension calculation results for several options. The extension and main drive loads and the strip thickness were varied. The strip width was taken equal to 1.850 mm.

Table 3 Calculation of strip tensions in the TL section

Parameter	Value							
Thickness, mm	2.2	2.2	2.2	2.2	4.0	4.0	4.0	4.0
Main drive load, %	10	20	10	20	10	20	10	20
Extension drive load, %	20	30	40	50	20	30	40	50
Tension-input buffer, kN	64.9	64.9	64.9	64.9	80.5	80.5	80.5	80.5
Tension upstream of the TL, kN	134.8	169.7	204.6	239.6	150.3	185.3	220.2	255.1
Tension downstream of the TL, kN	337.0	401.9	401.8	466.7	419.3	484.2	484.1	548.9
Tension upstream of the baths, kN	43.1	43.1	43.1	43.1	75.6	75.6	75.6	75.6

The results obtained allow drawing the below conclusions:

- the strip tension upstream of the TL is directly determined by the extension drive load; with an increase in the load from 20 to 50% at a strip thickness of 2.2 mm, the tension increases from 134.8 to 239.6 kN, at a strip thickness of 4.0 mm-from 150.3 to 255.1 kN, and in both cases the difference is 105 kN;
- at minimum main and extension drive loads (10 and 20%, respectively), the strip tension upstream of the TL is approximately 2 times higher than in the input buffer, i.e., bridle No. 2 additionally creates the same tension as in the input buffer;

- when the extension drive is loaded by 50%, the strip tension upstream of the TL is approximately 4 times higher than in the input buffer;
- the ratio between the strip tensions downstream and upstream of the TL is about 2.0–2.5; approximately half of the front tension balances the rear tension, and the other half goes to the plastic bending deformation of the strip between the rollers;
- when comparing the strip tension downstream of the TL with that upstream of the baths, it should be noted that for thin strips of 2.2 mm, this ratio reaches about 10, and for thick strips of 4.0 mm, and it is about 7. Such a high-tension ratio obviously required installing two bridles Nos. 3 and 4. For comparison, upstream of the TL, this indicator does not exceed 4; therefore, a single bridle No. 2 is sufficient.

6 Conclusion

As a result of the analysis of the TL drive operation, the dependencies to set the motor speeds have been obtained considering the TL roller diameters. The dependence of the strip extension on the actual roller diameters has been found. The dependencies of the front and rear tensions on the main and extension drive torques have been obtained. It has been found that the strip tension upstream of the TL is directly determined by the extension drive load; at the load of 50%, the strip tension upstream of the TL is approximately 4 times higher than in the input buffer. It is shown that the ratio between the strip tensions downstream and upstream of the TL is about 2.0–2.5; approximately half of the front tension balances the rear tension, and the other half goes to the plastic bending deformation of the strip between the rollers.

The planetary gear between the TL's 2nd and 3rd rollers allows transmitting 92% of the energy of the rear tension created by the extension drive forward through the mechanical transmission and converting it into the front tension through the 3rd roller. Thus, the main drive only adds front tension, but most of it is created by the rear tension mechanically transmitted forward.

The dependencies obtained to calculate the electric drive speed and power parameters allow adjusting the TL drive speed and torque settings to avoid the extension drive and the planetary gear overloads and maintain the target strip extension. The study allows preventing the overload of the planetary gear elements and thereby improving the strip resource and stability of operation.

References

1. Sufianov D et al (2012) Theoretical research of the passing a hot-rolled strip process through a tension-bending scale breaker of a continuous pickling line. *Manufacture of hire* 10:31–34 (In Russ.)
2. Devyatchenko L, Mayachenko E (2013) Operation of an extension and bending machine in scale removal from hot-rolled strip. *Steel in translation* 43(2):59–63. <https://doi.org/10.3103/S0967091213020071>
3. Magura D, Fedák V, Sanjeevikumar P, Kyslan K (2018) Tension controllers for a strip tension levelling line. In: Konkani A, Bera R, Paul S (eds) *Advances in systems, control and automation* vol. 442, Springer, Singapore, p 33–44. doi: https://doi.org/10.1007/978-981-10-4762-6_4

4. Kornilov V et al (2009) Settings optimization of the straightening machine for efficient scale breaking. *Steel* 10:77–78 (In Russ.)
5. Poletskov P (2011) On the change in profile and flatness of sheet iron during flattening by stretching and bending. *Vestnik of Nosov magnitogorsk state technical university* 3(35):60–62 (In Russ.)
6. Rumyantsev M, Zelinov I, Novitsky I, Zelinova Ju (2015) Improving model for settings the scale breaker in automatical computer-assistant engineering of working pattern of speed n continuous pickling line combined with the rolling mill”. *Engineering - from theory to practice* 53:122–130 (In Russ.)
7. Zhang J et al (2017) Influence of tension leveling parameters on the microstructure and mechanical properties of steel strip. *JOM* 69:937–941. <https://doi.org/10.1007/s11837-017-2272-3>
8. Selivanov I et al (2013) Research of control systems of continuous rolling mill using a mathematical model. *Vestnik of Nosov magnitogorsk state technical university* 3(35):11–13 (In Russ.)
9. Nigam A, Jain S (2015) Modelling and structural analysis of planetary geared winch. *International Journal of Science and Research (IJSR)* 4:330–333
10. Kornilov G, Abdulveleev I, Khramshin T, Shokhin V (2020) Advanced electric drive control system of continuous hot-dip galvanizing line. *International Conference on Industrial Engineering, Applications and Manufacturing (ICIEAM)*. doi: <https://doi.org/10.1109/ICIEAM48468.2020.9111905>
11. Gasiyarov V et al (2018) Correcting electric motor drive speed of plate mill stand in profiled sheet rolling. *IEEE International Conference on Power Electronics, Drives and Energy Systems (PEDES)*. doi:<https://doi.org/10.1109/PEDES.2018.8707442>
12. Kornilov G et al (2020) Improving the drive of the tension-bending machine continuous pickling unit, cold rolling mill. *Vestnik of Nosov Magnitogorsk State Technical University* 18(1):71–79. <https://doi.org/10.18503/1995-2732-2020-18-1-71-79>.(InRuss.)
13. Magura D, Kyslan K, Padmanaban S, Fedák V (2019) Distribution of the strip tensions with slip control in strip processing lines. *Energies* 12:3010. <https://doi.org/10.3390/en12153010>
14. Mathieu N, Potier-Ferry M, Zahrouni H (2017) Reduction of flatness defects in thin metal sheets by a pure tension leveler. *Int J Mech Sci* 122:267–276. <https://doi.org/10.1016/j.ijmecs.2017.01.036>



The Development and Study of a General-Service Automatically Controlled Weighing Batcher

I. M. Shandybina, A. M. Makarov, and M. P. Kukhtik^(✉)

Volgograd State Technical University, 28, Lenina Av., Volgograd 400005, Russia

Abstract. A general-purpose automatically controlled weighing batcher has been developed, which refers to the field of packaging equipment, and it is intended to weigh and batch food and non-food granular products. The existing designs have been studied, and a patent search for similar inventions has been carried out. A kinematic diagram of the mechanism has been drawn on the basis of the analysis of the inventions similar to the study object. The design of the batching unit and a schematic block diagram of the automatic control system of the batcher have been developed. The modeling and study of the device design have been carried out. Being equipped with an automated control system, this mechanism can be used by machine-building enterprises, which are engaged in the development, production, and operation of devices for product batching and filling.

Keywords: Weighing batcher · Automatic control · Filling food products · Filling non-foods products

1 Introduction

One of the main challenges at the current stage of development of the food industry is improving the operation efficiency of automated batching and filling devices due to an increase in the filling accuracy [1, 2].

As shown by the patent search carried out, no global changes have been introduced into designs of batching devices since 1986 [3–8].

The analysis of the existing designs of automatically controlled batchers has shown that so far the main goal of Russian designers has been to increase the efficiency. The batching accuracy of the filling mechanisms has been, however, decreasing [9–14]. As it has been revealed, this manifests itself particularly pointedly when vegetable products like potatoes are filled in small containers.

Therefore, when a design of a general-purpose automatically controlled weighing batcher is developed, a crucial task is to meet the criterion of optimality, i.e., to simultaneously improve the production efficiency and increase the filling accuracy. A weighing batcher, which meets the operational standards, has been modeled to solve the task set [15–19].

The following tasks were set and solved when the batching device was being developed:

- studying the existing designs;
- carrying out a patent search for similar inventions;
- creating a kinematic diagram of this mechanism on the basis of the analysis of inventions similar to the study object;
- developing the design of the batching unit;
- developing a block diagram of the automatic control system;
- determining the technical parameters of the device.

2 The Configuration and Operating Principle of the Weighing Batcher

The analysis carried out of the existing designs and the patent search have allowed to find out the designs, which are the most analogous to the design proposed. Several batching and filling devices for bulk materials can be referred to as such [3–5]. Those devices consist of units, such as a hopper with a feeding funnel, a vibratory feeder, which is equipped with a motor-driven gate, and a weighing unit. The weighing unit contains a weighing tank with a strain gauge, which is connected to the drive of the vibratory feeder gate through a feedback control unit.

The configuration of an automatically controlled weighing batcher is known [6]. The batcher has the case with a cup inside in the form of a cylinder with a beveled surface. There are spindles with bearings pressed into the case at the ends of the cup on the longitudinal axis of the cylinder. Two fittings are attached to the case: one above the cup and the second one under the cup. A drive is installed on the case, in line with the cup cylinder, and it turns the cup 180° to empty a batch weighed. The case and the drive mechanism are installed on sensors.

However, the disadvantages of this device are that it is only intended to weigh bulk materials and that the weight of the entire structure, including the drive, enters the calculation of the scale capacity of the sensors. This weight is much bigger in comparison with the weight of a batch. Such correlation reduces the batching accuracy in small portions.

The configuration of a combination weighing batcher is known [7]. The batcher consists of a vibratory feeder, which is made as a system of radial vibratory trays intended to supply a product to the weighing modules, which are located around the circumference. The weighing modules contain accumulation baskets, which are connected to the weighing baskets equipped with strain gauges through the first motor-driven gates. The weighing baskets are connected to the tank for a batch of a product through the second motor-driven gates. The strain gauge of each weighing basket is connected to a microprocessor, which analyzes the signals from the strain gauges. The microprocessor is connected to the control units, which are intended to control the motion of both the gate and the vibratory tray drives. The tank for a batch of a product contains outlet slopes, which are intended to feed batches of a product from the weighing baskets to the intake funnel. Each vibratory tray has a tray, a platform, a base, an electromagnet with its armature, and at least two plate springs.

A disadvantage of this device is that the batcher is only intended to operate with medium fraction bulk products, i.e., it cannot batch small and large products such as

potatoes, carrots, apples, etc. When the device is used, a product, e.g., potatoes, will change its position and orientation in space in a random way by moving along the vibratory tray. Also, if a product is stuck at a certain stage of batch forming, it can influence the weighing accuracy, and thus the accuracy of the subsequent filling, in a negative way.

The configuration of a discrete automatically controlled weighing batcher is known [8]. The batcher consists of a supporting frame with a load receptor, which is installed on it in order to turn on a tray and a weight sensor; a discharge device with a drive, and a control unit. The discharge device equipped with a drive has a tray rollover bar, which is connected to the supporting frame, with the frame being supported by a weight sensor. The bar is mounted with gaps in relation to the bottom of the tray and to a clamp, which is attached to the external part of the tray. The bar can impact on the bottom of the tray in the point, which corresponds to the center of gravity of the supporting frame.

A disadvantage of this device is the impossibility to weigh raw materials with large dimensions, i.e., when raw materials with large dimensions are loaded in this weighing batcher, a decrease in the batching accuracy of small batches will occur as the raw material will bump against the bottom of the tray, which will result in a damage to the units and, consequently, a decrease in the reliability and service life of the entire machine.

All the above-listed alternatives have a common disadvantage. It is the impossibility to fill large objects at a high speed and with a high productivity. A combination batcher was taken as a prototype when developing the device [7].

A kinematic diagram of the mechanism was developed by analyzing the alternatives of the study object (Fig. 1).

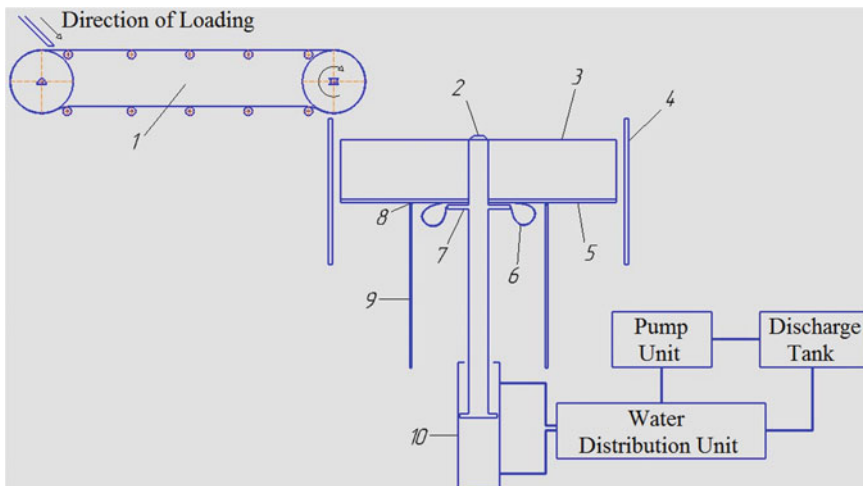


Fig. 1 A Kinematic diagram of mechanism: 1—loading belt, 2—rod, 3—mobile walls, 4—housing walls, 5—“petals”, 6—flexible catching, 7—opening disk, 8—joints, 9—vibrating supports, 10—hydraulic drive

Figure 2 represents a 3D model of the general-purpose weighing batcher developed, the design of which is free from this disadvantage [20]. A cross section of the batcher is set out in Fig. 3.

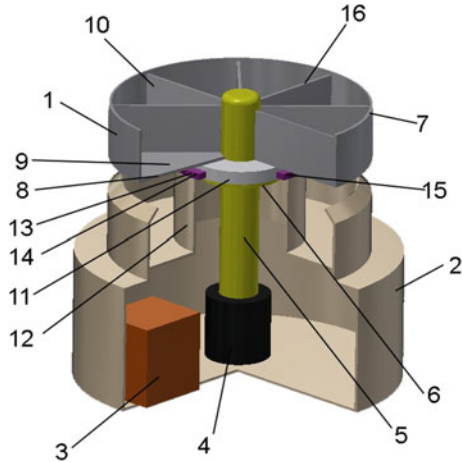


Fig. 2 3D model of the batcher

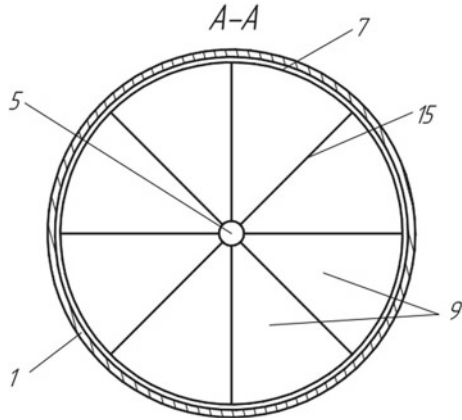


Fig. 3 Cross section of the batcher

The batcher consists of housing 1 (the back wall is not displayed in Fig. 2), which is set on supporting frame 2; control unit 3, drive 4, rod 5, which is rigidly coupled with opening disk 6; ribs 7, mobile disk 8, which is equipped with damping coating 9 (e.g., food rubber or silicon) and divided into sectors forming eight radial trays 10, which are connected to opening disk 6 by means of flexible catching 11. Load frame 12 is connected to mobile disk 8 through joints 13, and it is put in motion by means of vibration motor 14. An angle is formed therewith between the surface of radial trays 10 and the level axis for unloading products. Weight sensor 15 is installed under each radial

tray 10 of mobile disk 8. Guiding ribs 16 allow a product to enter directly a container. Drive 4 is rigidly connected to rod 5.

A block diagram of the automatic control system of the batcher is set out in Fig. 4.

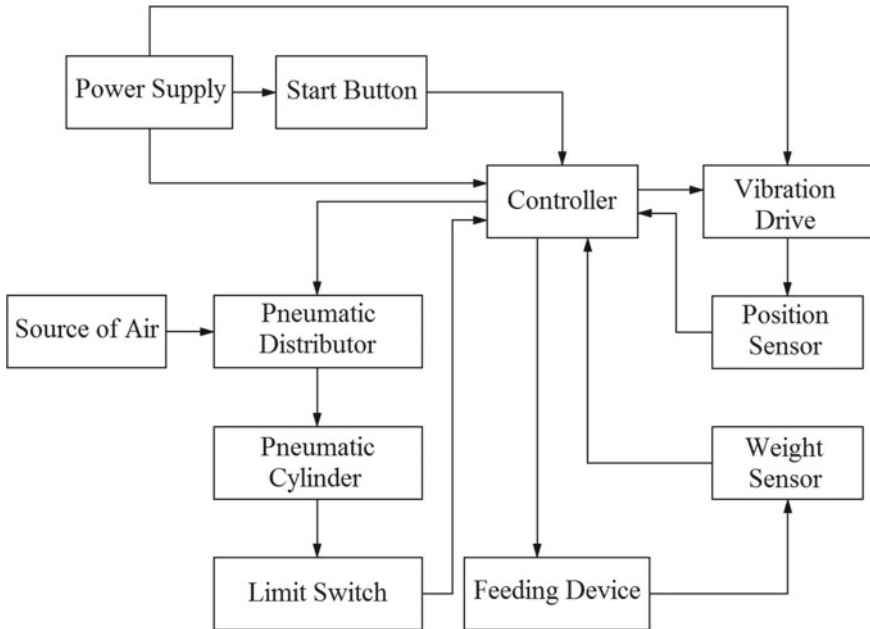


Fig. 4 Block diagram of the automatic control system of the batcher

The operation principle of the general-purpose automatically controlled weighing batcher is as follows. A command to start loading can come from an external control device, e.g., an automated technological process control system or from a button at a remote control panel. As the target weight is achieved, weight sensor 15 sends a signal to control unit 3, which forms a command to turn off the loading mechanisms.

Control unit 3 sends a signal to turn on vibration motor 14, in order to uniformly distribute the product along the surface of mobile disk 8. On distributing the product in a uniform way, drive 4 lifts up rod 5 together with ribs 7, thereby dividing all the mass equally. Rising together with rod 5, opening disk 6 pushes radial trays 10 of mobile disk 8, which turn on joints 13, thus creating an angle for unloading the product.

In order to return rod 5 and ribs 7 to the start position, control unit 3 forms a command to drive 4, which lowers rod 5 and radial trays 10 of mobile disk 8 by means of flexible catching 11. New loading starts on a signal from control unit 3.

All the necessary components were selected to implement the automatic control system on the basis of a comparative analysis. A control program was written for the programmable logic controller (PLC).

The batcher drive can be implemented in two variants. In the first case, a double-acting pneumatic cylinder can be used as the drive. This pneumatic cylinder is put in

motion by a source of compressed air and controlled by the PLC via an electropneumatic control valve. The advantage of this type of a drive is fast response time and high torque when a product is moved, batched, and distributed. In the second case, a linear electric drive (actuator) can be used, which is controlled by the PLC directly or via a converter. The advantage of this variant of implementation is the absence of a necessity for a source of compressed air and lower operation costs of the batching equipment.

The technical result of the design proposed is an improvement in the accuracy of batching small portions of a product. This is achieved by the fact that the batcher consists of a supporting frame, a weight sensor, a discharge mechanism with a drive, a control unit, a loading frame, a vibration motor, a rod, a flexible catching, and eight radial trays in the form of sectors, which are located at a mobile disk and mounted on joints, with the mobile disk being equipped with a damping coating.

The vibration motor allows to uniformly distribute a product along the surface of the mobile disk owing to vibration and thus improve the accuracy of batching small portions of a product.

The rod lifts the mobile disk, thus enabling the uniformly distributed product to divide into equal batches, which also improves the accuracy of batching small portions of a product.

The presence of a flexible catching in the design contributes to a uniform distribution of a product along the surface of the mobile disk as a result of vibration and, therefore, improves the accuracy of batching small portions of a product.

The installation of eight radial trays in the form of sectors, which are mounted on the mobile disk and turn on joints, allows to form an angle between the surface of the radial tray and the level axis so as to unload a product, so that the entire product should directly enter a container while rolling down the inclined surface along the guiding ribs.

The design with eight radial trays is optimal, and it is due to the fact that when a greater number of radial trays is set, sharp angles are formed between their vertically located guiding ribs. These angles do not allow to fill in the capacity of the radial tray, thus creating an inactive area in it and reducing the accuracy of batching small portions of a product. When the number of radial trays is less than eight, the efficiency decreases in terms of packets filled.

Equipping the mobile disk with a damping coating allows to increase the storage time of the products packed, as their surface will not be crumpled and broken when a product is bumped against the mobile disk. The damping coating will, in its turn, reduce the impact loads on the weight sensor, which will extend the service life of the machine in a whole and result in an increase in the accuracy of batching small portions of a product.

The operation of the general-purpose automatically controlled weighing batcher is performed in several stages.

Stage one. The device is ready for loading, i.e., the walls and the rod are on the same level with the petals, creating a level ground. After that, the vibratory supports are turned on, which will distribute the product all over the surface.

Stage two. The rod and the walls are pulled out by means of the drive. They divide, in their turn, the product into eight equal parts.

Stage three. The petals are lifted up relative to the support elements by means of the disk, which is attached to the rod. During this, some gaps appear between the wall of the housing and the petals. The product drops into these gaps and enters eight special containers.

The technical parameters of the device were obtained during calculations and simulation modeling. The preliminary dimensions of the device elements:

- the radius of the mobile disk: 0.37 m;
- the length of the rod: 0.8 m.

The anticipated productivity of the mechanism developed shall be about 3 tons per hour, i.e., approximately 1000 bags of finished products will be packaged in an hour. The planned efficiency of the project is determined under the following parameters:

- an improvement in the operational properties of batching devices due to the jam prevention;
- an increase in the batching speed;
- enabling uniform distribution of a product on trays;
- an increase in the operation convenience.

3 The Results and Discussion

The results obtained have allowed to conclude that the device developed is suitable to perform the tasks set. Its use will raise considerably the quality and accuracy of filling.

The mechanism developed is characterized by simplicity and generality of its design. It allows to use the device, with minimum costs for its adaptation, for filling and packaging items, which are close to the study object in their shape and configuration. Such a reprofiling of the automated batcher developed will allow to expand its application field.

Consumers of the results of the project can be machine-building enterprises, which develop, produce, and operate devices used for batching, filling, and packaging food and non-food products. The performance of the device was confirmed by the approval at the All-Russian Scientific and Creative Competition “Mechatronics and Robotics Forward!”, which was held at the venue of the large machine-building enterprise “Taurus-Fenix”, which specializes in developing and manufacturing equipment for packaging, filling, and batching liquid, paste-like, solid, and bulk foodstuffs.

Acknowledgements. The authors would like to acknowledge the administrative and technical support, which was provided by Volgograd State Technical University.

References

1. Tummala R (2019) Fundamentals of device and systems packaging: technologies and applications. McGraw-Hill Education, New York
2. Natarajan S, Govindarajan M, Kumar B (2014) Fundamentals of packaging technology. PHI Learning, Delhi

3. Ratushenko GV, Genel VA, Semjonov VA, Tarnavskij OV, Luzhetskij VN (1969) Device of dosing of powder materials. Inventor's certificate USSR 259688, 12 Dec 1969
4. Sherstobitov VI, Bychkovskij VN (1992) Device for dosing and packaging of bulk materials. Inventor's certificate USSR 1706916, 23 Jan 1992
5. Khansen KI (2011) Weighing device. Patent RF 2435145, 27 Nov 2011
6. Belonosov AI, Hajkinson YM (2001) Weighting batcher with automatic control. Patent RF 2163357, 20 Feb 2001
7. Grebenshnikov AV (2007) Weighting combinative batcher. Patent RF 60714, 2007
8. Men'shchikov VA, Akimov VK, Vorob'ev AP (2010) Weighting batcher of sampling action with automatic control. Patent RF 96957, 20 Aug 2010
9. Rodionov DA, Suvorina IV, Makeev PV, Knjazev YV (2015) Classification and purpose of batchers. *Molodoj uchenyj* 11(91):409–413
10. Deeva VS, Romanishin AE, Slobodjan SM (2015) The analysis of flow measuring hoppers for heterogeneous loose media. *Vestnik AGAU* 8(130):135–139
11. Chumanov IV, Anikeev AN, Sergeev DV (2015) Development of a dispenser for supplying fine particles. *Vestnik JuUrGU. Serija: Metallurgija* 3:80–83
12. Abramova IS, Kochegarov AV (2011) Analysis of constructions of loading and dosing devices in forestry and agriculture. *Lesotekhnicheskij zhurnal* 4:76–82
13. Abramova IS, Kochegarov AV (2011) Analysis of constructions of devices, which operate with bulk materials. *Lesotekhnicheskij zhurnal* 4:82–89
14. Kaloshin YA, Shamshurko SM (2010) New classification of packing devices. *Pishhevaja promyshlennost'* 1:20–21
15. Lapikov MA, Makarov AM, Vaganov AV, Zhupikov AE (2018) Automated system of dosing for bulk materials in flexible containers. In: Paper presented at the XXIX International conference "Mechanical Engineering and Innovation. Conference of Young Scientists and Students" (MEICYSS-2017), Moscow, 6–8 Dec 2018
16. Melashhenko OI, Tverdokhlebov SA, Azarjan DK, Shagal'djan SS (2017) Automated device for dosing and prepacking of potatoes. In: Paper presented at the review-competition of scientific, design and technological student works of the Volgograd State Technical University, Volgograd, 16–19 May 2017
17. Azarjan DK, Shagal'djan SS (2017) Automated unit for dosing and prepacking of potatoes. In: Paper presented at the XXII Zonal conference of Volgograd region young scientists, Volgograd, 21–24 Nov 2017
18. Melashhenko OI, Tverdokhlebov SA, Shagal'djan SS (2019) General-service batcher for weighting dosing of food and non-food production. In: Paper presented at the XXIII Zonal conference of Volgograd region young scientists, Volgograd, 11–14 Dec 2019
19. Melashhenko OI, Tverdokhlebov SA, Shagal'djan SS, Shandybina IM (2019) Weight batcher with automatic control for packing oval products. In: Paper presented at the XXX International Innovation Conference of Young Scientists and Students (MEICYSS-2018), Moscow, 20–23 Nov 2019
20. Azarjan DK, Melashhenko OI, Tverdokhlebov SA, Shagal'djan SS, Shandybina IM, Makarov AM, Romanenko MD (2020) General-service weighting batcher with automatic control. Utility model RF 195251, 21 Jan 2020



A Study of the Technical Condition of Mass Airflow Sensors in Test Modes at Varying ICE Crankshaft Speeds

A. V. Gritsenko^{1,2}, V. D. Shepelev¹(✉), and V. N. Nikolaev²

¹ South Ural State University (National Research University), 76, Lenin prospect, Chelyabinsk 454080, Russia

shepelevvd@susu.ru

² South Ural State Agrarian University, 13 Gagarin St, Troitsk 457100, Russia

Abstract. Electronic systems of cars and tractors operate in various conditions: the operating temperature ranges from -45 to 125 °C, the airflow temperature ranges from -40 to 110 °C, the operating pressure ranges from 80 to 108 kPa, high dust content and pollution of mass airflow sensors (MAFSs) with dust particles, fuel, and oil. A brief analysis of MAFS configurations showed their significant variety. However, high response time, low accuracy and reliability of airflow control, and low operational reliability resulted in the rejection of imperfect configurations and their replacement with film-type sensors. An analysis of modern means and methods to control the technical condition of MAFSs showed that there are no methods for their in-place control under operating conditions. This research is based on the use of the DBD-4 tool for the formation of test modes. As a result of the experimental research during the formation of test inputs, we developed the MAFS control modes, which consist in the cutout of three cylinders and loading one cylinder remaining in operation with the power of mechanical losses of the dead cylinders. The annual economic effect of diagnosing one passenger car amounted to 3880 rubles.

Keywords: Engine · Failure · Mass airflow sensor · Diagnostics · Test method

1 Introduction

Automotive electronics is currently developing at a significant pace. There appear new systems, sensors, and elements [1–3]. Let us consider the aspects of improving modern intake systems and their components [4–7], in particular, the configuration of mass airflow sensors [8–10]. One of the earliest mass airflow sensors is a pivoted flap flowmeter with a sensitive damper in the air flow. However, due to their significant response time and low sensitivity, they are not used in modern systems of cars and tractors [11–13]. There is also a vortex MAFS also called a Karman meter. The element base of this MAFS uses the ultrasonic principle of signal detection. An analysis shows that these sensor configurations have disappeared from the intake systems of modern cars and tractors, but they are widely used in industry [14–17].

The most widespread MAFS configuration over the last decade is a thermometric or threadlike mass airflow sensor [18–22]. However, its cost and self-cleaning ability raised doubt, which led to its replacement with more up-to-date technologies.

2 An Analysis of the MAFS Control Means and Methods

In the initial part of the analysis, we should note that modern mass airflow sensors belong to non-repairable and non-recoverable electronic devices [23–26]. Specifications indicate the MAFS control method using a regulated power supply unit and a control voltmeter (it is also possible to control the resistance of the terminals) (Fig. 1a).

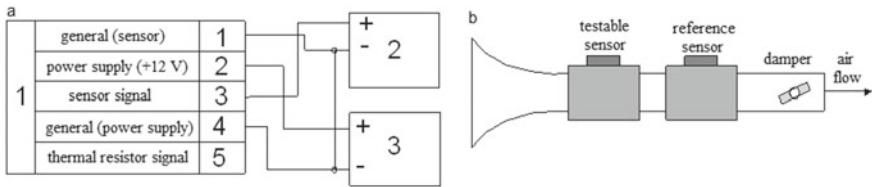


Fig. 1 a MAFS control method using a regulated power supply unit and a control voltmeter: 1—controlled MAFS, 2—measuring voltmeter, 3—regulated power supply unit; b MAFS control method when comparing its parameters with the reference ones

However, this method shown in Fig. 1a does not allow us to detect deviations of the MAFS from the correct operation.

The literature also mentions the MAFS control method when its parameters are compared with the reference ones (Fig. 1b) [15–20].

This method provides for the need to dismantle the controlled MAFS from the automotive vehicle. The modes set on the device do not correspond to the operating ones. The method is very laborious and ineffective.

Factory laboratories and ordinary enterprises propose the MAFS control method taking into account the influence of the direct and reverse air flow (Fig. 2).

This method has basically the same disadvantages as the previous one; besides, it is even more laborious and complicated.

A wide range of diagnostic scanners, testers, motor testers, and digital oscilloscopes are used to control the technical condition of mass airflow sensors [17, 19, 21, 22]. However, control is local and focused on a specific connector or lead. As the MAFS diagnosing practice shows, only the following MAFS failures are reliably distinguished: open circuits, short circuits to plus, or ground fault. The deviation from the MAFS correct operation is not registered in any way.

Thus, it becomes necessary to develop a diagnostic method without dismantling the mass airflow sensor from the vehicle, taking into account its actual operating conditions. This method is proposed for test control of MAFSs during the formation of load actions and recording the response of the MAFSs’ output parameters to the performed tests.

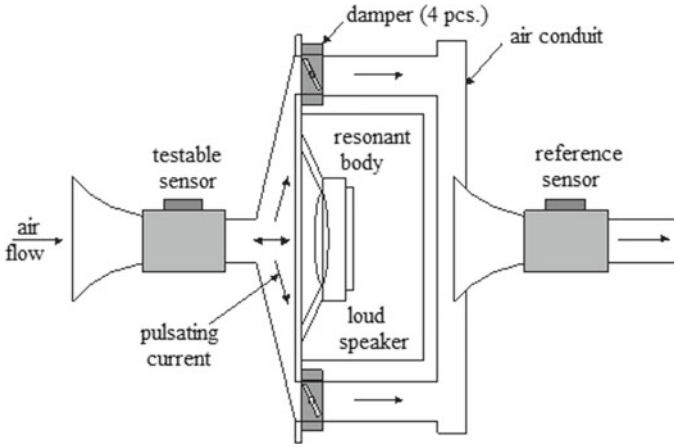


Fig. 2 MAFS control method taking into account the influence of the direct and reverse air flows

3 Methods

Let us consider the theoretical aspects of applying the testing method and its characteristics when used on modern motor vehicles. Ordinary practice faces frequent malfunctions causing a significant deviation of the air supply [23–26]. Let us determine the total head loss at the cylinder inlet, the amount of passing air, and the cyclic airflow rate. To this end, we compose Bernoulli’s equation [10, 11]:

$$\frac{P_k}{\rho_k} + \frac{W_k^2}{2} + g \cdot Z_k = \frac{P_a}{\rho_a} + \beta^2 \frac{W_{IN}^2}{2} + \xi_{IN} \frac{W_{IN}^2}{2} + g \cdot Z_a \quad (1)$$

where P_k and P_a are the air pressures at the inlet and directly in the cylinder; ρ_k and ρ_a are the air densities at the inlet and in the cylinder, respectively; W_k and W_{IN} are, respectively, the air velocity at the inlet to the intake system and the average air velocity in the valve during the intake process (m/s); Z_k and Z_a are the elevations from the axis of the intake system and the axis of the intake valve, respectively; β is the coefficient of the charge velocity attenuation in the considered cylinder section, $\beta = W_C/W_{IN}$ (W_C is the average air velocity in the considered cylinder section); ξ_{IN} is the coefficient of the intake system resistance referred to its narrowest section.

Taking the conditional assumption that $W_k = 0$ and the elevations of the elements of the intake system and individual cylinders are identical $Z_k = Z_a$, and, at the same time, neglecting the change in the density of air and the air–fuel mixture during their movement in the intake system ($\rho_k = \rho_a$), we obtain:

$$\frac{P_k}{\rho_k} = \frac{P_a}{\rho_a} + (\beta^2 + \xi_{IN}) \frac{W_{IN}^2}{2} \quad (2)$$

Transforming Eq. 2 and expressing the head loss from it in the form of the difference $\Delta P_a = P_k - P_a$ in the considered section, we obtain:

$$\Delta P_a = P_k - P_a = (\beta^2 + \xi_{IN}) \frac{W_{IN}^2}{2} \rho_k \quad (3)$$

Let us present the equation of the air–fuel mixture flow continuity taking into account the smallest values of the cross sections in the ICE intake system and cylinder:

$$W_{IN} \cdot f_{IN} = C_{P \max} \cdot F_p \tag{4}$$

where f_{IN} is the area of the working section of the intake valve (the narrowest section of the intake system) (m^2); $C_{P \max}$ is the maximum piston velocity (m/s); F_p is the total area of the piston crown (m^2).

Using the known expression, we determine the maximum piston speed:

$$C_{P \max} = R \cdot \omega \cdot \sqrt{1 + \lambda^2} \tag{5}$$

where R is the crank radius (m); ω is the angular speed of the ICE crankshaft, which can be determined from the expression $\omega = 2\pi n$ (n is the ICE crankshaft speed, rpm); λ is the ratio of the crank radius R to the crank length L , $\lambda = R/L$.

Jointly solving Eqs. 4–5 and expressing W_{IN} we obtain:

$$W_{IN} = C_{P \max} \frac{F_p}{f_{IN}} = 2\pi \cdot R \cdot n \cdot \sqrt{1 + \lambda^2} \frac{\pi \cdot D^2}{4} \cdot \frac{1}{f_{IN}} = A_1 \frac{n}{f_{IN}} \tag{6}$$

Further, substituting the value of the air velocity in the valve W_{IN} into expression (2), we obtain:

$$\Delta P_a = (\beta^2 + \xi_{IN}) \rho_k \cdot A_1^2 \frac{n^2}{2} \frac{1}{f_{IN}^2} = A_2 \frac{n^2}{f_{IN}^2} \tag{7}$$

Thus, taking into account all the transformations, we determined the head losses at the inlet to the ICE cylinder, the air velocity, and the cyclic airflow rate. These models (5, 6, 7) can be used to determine the actual amount of air, the pressure drop of the air entering the ICE cylinders, and the air velocity in the valve section.

4 Experimental Research Procedure

During the research, the basis for the load formation was the DBD-4 electronic device used as a loading device for the ICE. This device provided loading by a sequential complete and partial cutout of the working cylinders and individual pulses of an electromagnetic injector [17–19]. As a result, one cylinder remained on, loaded with mechanical losses of other dead cylinders [20–22]. Besides, when this loading scheme was used, the throttle valve was opened sequentially with 5% discreteness. In these modes, the following output parameters were controlled: mass airflow rate Q (kg h); voltage from the test lead of the MAFS U (V); throttle valve opening R (%); and hourly fuel consumption V (l/h) at a smooth change in the ICE crankshaft speed n (rpm).

5 Results

According to the experiment program, we obtained the dependences of the mass airflow rate Q , the voltage from the test lead of the MAFS U , the throttle valve opening R , and the hourly fuel consumption V (l/h) on the ICE crankshaft speed n (rpm). Let us analyze each dependence in the order of the experiments. At the first stage, we built the dependences of the mass airflow rate Q (kg/h) on the ICE crankshaft speed n (rpm) (Fig. 3).

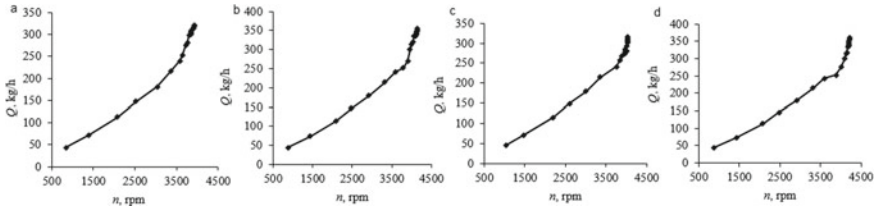


Fig. 3 Dependence of the mass airflow rate on the ICE crankshaft speed: **a** when the first cylinder is on (cylinders 2, 3, 4 off); **b** when the second cylinder is on (cylinders 1, 3, 4 off); **c** when the third cylinder is on (cylinders 1, 2, 4 off); **d** when the fourth cylinder is on (cylinders 1, 2, 3 off)

An analysis of the data in Fig. 3 shows an obvious maximum when testing the fourth cylinder, where we recorded the minimum air leakage of 14% from the cylinder. The maximum mass flow rate in the fourth cylinder reaches 361 kg/h at the simultaneous maximum ICE crankshaft speed of 4,230 rpm. The minimum mass flow rate in the third cylinder reaches 315 kg/h at the simultaneous maximum ICE crankshaft speed of 4,040 rpm.

And at the final stage of the experiment, we assessed the hourly fuel consumption depending on the ICE crankshaft speed (Fig. 4).

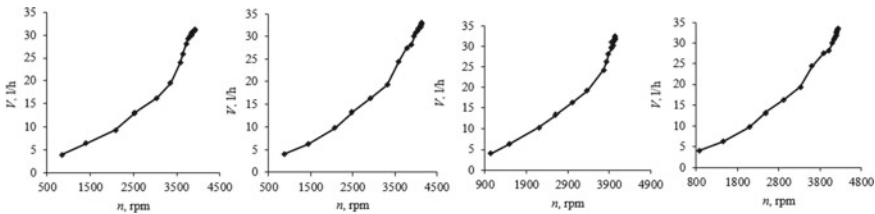


Fig. 4 Dependence of the hourly fuel consumption V on the ICE crankshaft speed n : **a** when the first cylinder is on (cylinders 2, 3, 4 off); **b** when the second cylinder is on (cylinders 1, 3, 4 off); **c** when the third cylinder is on (cylinders 1, 2, 4 off); **d** when the fourth cylinder is on (cylinders 1, 2, 3 off)

An analysis of the hourly fuel consumption monitoring results (Fig. 4) showed that the highest value of 33.5 l/h at the maximum ICE crankshaft speed is observed for the fourth cylinder. When monitoring the hourly consumption of the second cylinder,

we recorded the result of 33.1 l/h. Measurements of the parameters of the hourly fuel consumption in the third and first cylinders showed 32.4 and 31.3 l/h, respectively.

The presented result shows that with an increase in cylinder-piston group wear, the value of the mass airflow rate drops and, accordingly, the fuel supply decreases. Thus, the cylinder with the best tightness will always show the maximum fuel consumption per hour. There appears the maximum difference in the hourly fuel consumption between the control results of the fourth and first cylinders $\Delta V_{4,1} = V_4 - V_1 = 33.5 - 31.3 = 2.2$ l/h. In percentage terms, this value reaches 6.5%. This parameter results from a set of various input parameters and can be additionally used to clarify the technical condition of the intake system and the cylinder-piston group.

6 Conclusion

We analyzed numerous works dealing with the design, research, and diagnostics of mass airflow sensors and identified the most promising ones among them.

We carried out a brief analysis of the MAFS configurations, from which it follows that the basis of the modern intake system is film technology-based sensors, which have replaced all other options. The considered modern means and methods to control the technical condition of mass airflow sensors should be supplemented by developing a testing method.

As a result of a comprehensive study of the practical methods to control the technical condition of mass airflow sensors, we developed a new method for testing the MAFS on an operating automotive vehicle. The method is based on the use of the DBD-4 tool for the formation of test modes.

As a result of the experimental research during the formation of test inputs, we developed the MAFS control modes, which consist in the cutout of three cylinders and loading one cylinder remaining in operation with the power of mechanical losses of the dead cylinders. Besides, further loading consists in a smooth stepwise formation of the load on the cylinder remaining in operation. The controlled parameters included the mass airflow rate, voltage from the test lead of the MAFS, the ICE crankshaft speed, the hourly fuel consumption when the throttle position varies from 0 to 100%. The most sensitive parameters are the mass airflow rate and its duplicating voltage at the test contact of the MAFS.

References

1. Gritsenko A, Shepelev V, Zadorozhnaya E, Shubenkova K (2020) Test diagnostics of engine systems in passenger cars. *FME Transactions* 48(1):46–52. <https://doi.org/10.5937/fmet2001046G>
2. Galkin A, Lobashov O, Capayova S, Hodakova D, Schlosser T (2018) Perspective of decreasing of road traffic pollution in the cities. In: 18th International Multidisciplinary Scientific GeoConference-SGEM 4.2(18):547–554. doi:<https://doi.org/10.5593/sgem2018/4.2/S19.071>
3. Startcev A, Romanov S, Vagina O (2019) Increasing Engine Power by Applying Water Injection. In: Radionov A, Kravchenko O, Guzeev V, Rozhdestvenskiy Y (eds) *ICIE 2018: Proceedings of the 4th International Conference on Industrial Engineering, Lecture Notes in Mechanical Engineering* 9783319956299:2071–2078

4. Startcev A, Romanov S, Romanova G (2019) Influence of Water Injection on Performance of Diesel Engine, In: Radionov A, Kravchenko O, Guzeev V, Rozhdestvenskiy Y (eds) ICIE 2018: Proceedings of the 4th International Conference on Industrial Engineering, March 2019, Lecture Notes in Mechanical Engineering 9783319956299 2089–2095
5. Gritsenko A, Shepelev V, Lukomsky K, Grakov F, Kostyuchenkov N, Kostyuchenkova O (2020) Control of the Exhaust Gas Tract Resistance of Modern Engines by the Run-Down Time during Testing. *Tribology in Industry* 42(4):627–640. <https://doi.org/10.24874/ti.966.09.20.11>
6. Gritsenko A, Shepelev V, Salimonenko G, Cherkassov Y, Buyvol P (2020) Environmental Control and Test Dynamic Control of the Engine Output Parameters. *FME Transactions* 48(4):889–898. <https://doi.org/10.5937/fme2004889G>
7. Startcev A, Romanov S, Vagina O (2020) Interaction of Elastic Wheel with Bumps of Rectangular Shape. In: Radionov A, Kravchenko O, Guzeev V, Rozhdestvenskiy Y (eds) ICIE 2019: Proceedings of the 5th International Conference on Industrial Engineering, Lecture Notes in Mechanical Engineering, p 621–629
8. Ageev EV, Kudryavtsev AL, Sevastiyarov AL (2012) The algorithm for diagnosing a cylinder-piston group using the technical endoscope. *World of Transport and Technological Machinery* 1:116–122
9. Gritsenko AV, Zadorozhnaya EA, Shepelev VD (2018) Diagnostics of friction bearings by oil pressure parameters during cycle-by-cycle loading. *Tribology in Industry* 40(2):300–310
10. Plaksin A, Gritsenko A, Glemba K (2016) Experimental studies of cylinder group state during motoring. In: Radionov AA (ed) *Procedia Engineering*, Chelyabinsk, 19 – 20 May 2016, p 1188–1191
11. Kukov SS (2006) Stands with training simulators for electrical vehicles. *Bulletin of SUSAU* 47:67–69
12. Fleming WJ (2001) Overview of automotive sensors. *IEEE Sensors J* 1(4):296–308
13. Gritsenko AV, Shepelev VD, Shepeleva EV (2019) Optimizing consumption of gas fuel using static method of tuning automobile gas-cylinder equipment. In: Radionov A, Kravchenko O, Guzeev V, Rozhdestvenskiy Y (eds), Proceedings of the 4th International Conference on Industrial Engineering. ICIE 2018. Lecture Notes in Mechanical Engineering. Springer, Cham. doi:https://doi.org/10.1007/978-3-319-95630-5_233
14. Marek J, Illing M (2000) Microsystems for the automotive industry. In: *Technical Digest - International Electron Devices Meeting*, San Francisco, 10 –13 December 2000, p 3–8
15. Sazhin OV, Pervushin YuV (2011) Mikrosensor potoka teplovogo tipa dlya datchika massovogo raskhoda vozdukh (Heat flow microsensor for a mass air flow sensor). *Nauchnoye priborostroyeniye* 21(3):52–61
16. Mel'nikov AA (2010) Ul'trazvukovyye preobrazovateli v sredstvakh izmereniya (Ultrasonic transducers in measuring instruments). Sputnik, Moscow
17. Teremyakin PG (2011) Opredeleniye tsiklovogo napolneniya vozdukhom tsilindrov gazovogo dvigatelya (Determination of the cyclic filling of gas engine cylinders with air). *Transport na al'ternativnom toplive* 1(19):19–21
18. Yerokhov VI (2011) Proyektirovaniye i raschet raskhodomera vozdukh elektronnykh sistem vpryskivaniya topliva (Design and calculation of air flow meter for electronic fuel injection systems) 6(24):20–27
19. Nabokikh VA, Safronov AV (2013) Sposoby diagnostirovaniya datchikov avtomobil'nykh elektronnykh sistem upravleniya s gibridnoy silovoy ustanovkoy (Methods for diagnosing sensors of automotive electronic control systems with a hybrid power plant). *Izvestiya MGTU MAMI* vol. 1, 2(16):185–188
20. Brodov YM, Grigoryev NI, Zhilkin BP, Plotnikov LV, Shestakov DS (2015) Increasing Reliability of Gas-Air Systems of Piston and Combined Internal Combustion Engines by Improving Thermal and Mechanic Flow Characteristics. *Therm Eng* 62(14):1038–1042

21. Senapati U, McDevitt I, Hankinson A (2011) Vehicle Refinement Challenges for a Large Displacement Engine with Cylinder Deactivation Capability. SAE Technical Paper 2011-01-1678
22. Muhamad Said M, Abdul Aziz A, Abdul Latiff Z, Mahmoudzadeh Andwari A (2014) Investigation of Cylinder Deactivation (CDA) Strategies on Part Load Conditions. SAE Technical Paper 2014-01-2549
23. Bech A, Shayler P, McGhee M (2016) The Effects of Cylinder Deactivation on the Thermal Behaviour and Performance of a Three Cylinder Spark Ignition Engine. SAE Int J Engines 9(4):1999-2009
24. Connolly F (1994) Direct Estimation of Cyclic Combustion Pressure Variability Using Engine Speed Fluctuations in an Internal Combustion Engine. SAE Technical Paper 940143
25. Ramesh A, Gosala D, Allen C, Joshi M (2018) Cylinder Deactivation for Increased Engine Efficiency and Aftertreatment Thermal Management in Diesel Engines. SAE Technical Paper 2018-01-0384
26. Flierl R, Lauer F, Breuer M, Hannibal W (2012) Cylinder Deactivation with Mechanically Fully Variable Valve Train. SAE Int J Engines 5(2):207-215



Feature of Predicting the Thermal Characteristics of Machine Tools Using Feedforward Neural Networks

A. N. Polyakov^(✉), V. V. Pozevalkin, and I. P. Nikitina

Orenburg State University, 13, av. Pobedy, Orenburg 460018, Russia

Abstract. The paper presents a method for predicting the thermal characteristics of machine tools using a feedforward neural network. The method was based on the results of full-scale and computational tests. Experimental modal analysis is a feature of the proposed mathematical description of the thermal behavior model of the machine tool. This made it possible to use an analytical description for the thermal characteristics of the machine tool and analytically link the values of the input vector and the predicted values of the thermal characteristics. The conducted research on predicting the thermal characteristics of machine tools using neural networks revealed the multivariance of the predictive characteristics. To select one solution, it was proposed to use two criteria for the discrepancy between the predicted and calculated values of thermal characteristics. The results of the machine experiment are presented for four variants of the varied parameters of the mathematical model. The use of a feedforward neural network to predict the thermal characteristics of machine tools has shown high efficiency in reducing the duration of a full-scale experiment.

Keywords: Thermal characteristics · Machine tool · Feedforward neural network · Temperature displacements · Modal analysis

1 Introduction

Today, all spheres of the economy are permeated with the idea of using artificial intelligence. In [1], the main trends in the development of intelligent manufacturing are presented. In [2], a cement production control system is presented, built on the use of fuzzy logic. In [3], an effective application of the multi-objective optimization algorithm is shown to solve the multi-objective data clustering problem based on the pigeon behavior algorithm. In [4], a methodology for controlling a swarm of drones based on swarm algorithms is presented. In [5], a modular method for creating modern CNC machine tools based on artificial neural networks and cloud technologies is presented. In [6], a serial–parallel hybrid polishing machine tool is presented. To achieve the required machining quality, a multi-objective optimization problem is formulated, solved using a genetic algorithm based on an artificial neural network. In [7], a solution to the problem of constructing a flexible manufacturing system with optimal characteristics using an integrated model combining an artificial neural network and a fuzzy analytical network

process is presented. Research in the field of systems for compensating the temperature error of machine tools, created on the basis of artificial neural networks, occupies a special place in achieving machining accuracy on CNC machine tools [8–17]. According to various estimates, the use of such systems makes it possible to reduce the temperature error of the machine tool by up to 80%, and in some cases, their efficiency is even higher. So in [9], the result of compensation for the temperature error of a turning machining center is given, which made it possible to reduce the temperature displacements of the spindle from 19 to 1 μm.

Along with this, artificial neural networks are characterized by three basic problems: an experimental database for network training; optimization procedure for finding the weights of neurons; variety of artificial neural network architecture. These problems raise doubts about the effectiveness of artificial intelligence methods compared to traditional methods. Therefore, from time to time, there are studies devoted to the comparative analysis of the effectiveness of neural network models in relation to, for example, regression ones [18].

The need to use neural network technologies in real time to control machine tools imposes strict restrictions on the unambiguity of the results generated by the neural network. Therefore, in this work, a study of the stability of the resulting solutions for constructing the thermal characteristics of a CNC machine tool based on a neural network model was carried out.

2 Methods for Solving the Problem

Despite the diversity of artificial neural network architectures, the practice of their application to solving problems of approximation and forecasting has shown that feedforward networks with one hidden layer of neurons are quite effective.

We have adopted the below described neural network architecture. A multi-layer feedforward network consists of three layers: input, one hidden, and one output. The input signal propagates in the forward direction only. The backpropagation algorithm is used to train the network. Each neuron in the hidden layer has a sigmoidal activation function.

A description of the features of the implementation of the thermal model of the machine tool is presented below. To solve the problem of thermal stability of a particular machine tool, its thermal model can be represented by its thermal characteristics [19]. Without taking into account the lag, the thermal characteristic at a specific point of the bearing system of the machine tool for temperature displacements can be represented as

$$\delta_n(t_j) = \sum_{k=1,4,\dots,3m-2} x_{k,n}(1 - e^{-t_j/x_{k+1,n}}) + \sum_{k=1,4,\dots,3m-2} x_{k+2,n}e^{-t_j/x_{k+1,n}}, n \rightarrow X, Y, Z, j = 1, \dots, L \tag{1}$$

where $x_{k,i}$, $x_{k+1,i}$, $x_{k+2,i}$ are modal parameters, amplitude, thermal time constant, and initial level, respectively; m is number of temperature modes; t_j is separate time interval; L is number of time intervals; $\delta_n(t_j)$ is coordinate displacement along the n -th axis.

Equation (1) explains the choice of input and output signals for the neural network. We represent the set of observed and predicted time intervals as a single vector t

$$t = \{0, t_1, \dots, t_m, t_{m+1}, \dots, t_L\} \quad (2)$$

where t_m is the limiting moment in time for which the training sample is formed; t_L is limiting moment of forecasting time.

Similar vectors can be generated for temperatures and temperature displacements

$$T = \{0, T_1, \dots, T_m, T_{m+1}, \dots, T_L\} \text{ and } \delta = \{0, \delta_1, \dots, \delta_m, \delta_{m+1}, \dots, \delta_L\} \quad (3)$$

Sliding window. Obviously, the temperatures or displacements vector can be taken as an input signal in the form

$$T = \{0, T_1, \dots, T_m\} \text{ and } \delta = \{0, \delta_1, \dots, \delta_m\} \quad (4)$$

and as an output signal, respectively, take vectors of the form

$$T = \{T_{m+1}, \dots, T_L\} \text{ and } \delta = \{\delta_{m+1}, \dots, \delta_L\} \quad (5)$$

For the practical implementation of (4) and (5), it was proposed to use the sliding window method [20]. The idea of the method is that a certain time interval is set during which the process is monitored, in the form

$$t = \{0, t_1, \dots, t_m\} \quad (6)$$

During this time interval, a data vector of the form (4) is formed. Using the concept of a sliding window, we introduce the width of the sliding window p , its offset b and the forecasting horizon Γ , that is, the time interval for which the desired function is predicted. The width of the sliding window corresponds to the length of the input data vector as known values of temperature displacements. The size of the window offset determines the length of the target vector or output signal in the neural network architecture. The generalized vector X of length m , taking into account the parameters, can be represented as a matrix of size $[(p + b)q]$. Thus, the available sample of experimental data of length m is divided into q -pairs of vectors: length p and b . The used data structure leads to a change in the network architecture: the input layer of the network will be represented by p -neurons; output layer – by b -neurons. After training the neural network, it is possible to form a forecasting horizon Γ outside the training sample of length m .

Results of experimental studies. To obtain a training sample, full-scale tests were carried out at two spindle speeds of two HAAS TM-1P and 400 V CNC machine tools: 2500 and 4000 rpm.

Smoothing thermal characteristics. A feature of using electronic measuring devices in field tests is the formation of step thermal characteristics. This is explained by the fact that the polling and recording of the measured data to the file is performed with a fixed time step. Therefore, the direct use of this data for training the network can create an additional error not related to the implementation of thermal processes on the machine tool. To minimize this error, it is proposed to use the thermal characteristics smoothing procedure.

Software tool. The solution to the problem posed in the work of studying the stability of a solution based on a neural network model for the thermal characteristics of a machine tool was carried out from a machine experiment. To solve this problem, a software tool (ST) “Neural network thermal modeling of machine tools” was developed in the Matlab system. The architecture of the developed ST can be referred to as layered. Each of the layers is a set of programs of the same functionality and in practice implemented as a single working window with controls.

As the initial data for training a neural network, either experimental or software-generated data can be used in accordance with (1). Then, (1) takes the form

$$\delta_n(t_j) = \sum_{k=1,4,\dots,3m-2} x_{k,n}(1 - e^{-t_j/x_{k+1,n}}) + \sum_{k=1,4,\dots,3m-2} x_{k+2,n}e^{-t_j/x_{k+1,n}} + k \cdot \Delta_r \cdot t_j \tag{7}$$

where Δ_r is a random data error generated randomly, $\Delta_r \in [0, 1][0, 1]$; k is a scale factor.

3 Discussion

A machine experiment was carried out for two variants of the input data. For the first variant of the input data, the time vector in the form (6) was fed to the input of the neural network. The network output took the form (5). In the second version, the sliding window method was investigated, so the input and output vectors had the same physical meaning: temperature displacements.

For each variant of the input data of the network, the following parameters were varied: the number of neurons in the hidden layer; the size of the input and output vectors; input vectors error; the size of the training, validation, and test sample; functional features of thermal characteristics supplied to the network input or their multimodality; the presence and absence of normalization of the input vector.

A feature of the construction of an artificial neural network (ANN) was their cyclic generation. The presence of various ANN variants is due to the fact that synaptic weights and bias for each neuron in the network are determined from the solution of the optimization problem. An ANN simulation in relation to predicting the thermal characteristics of machine tools showed that it is difficult to find stable, slightly different solutions. Therefore, to select one ANN option, it is proposed to use two similar criteria of the form

$$Kp_1 = \frac{1}{N_\lambda} \sum_{\zeta=1}^N [(\delta_{np,\zeta} - \delta_{\lambda,\zeta})/\delta_{\lambda,\zeta}] \cdot 100 \tag{8}$$

$$Kp_2 = \max([\delta_{np,\zeta} - \delta_{\lambda,\zeta})/\delta_{\lambda,\zeta}] \cdot 100, \zeta = \overline{1, N_\lambda} \tag{9}$$

where $\delta_{pr,\zeta}, \delta_{\lambda,\zeta}$ are predicted (by ANN) and calculated values of temperature displacement; N_λ is the number of predicted elements of the vector $\delta_{pr,\zeta}$.

Analytical studies and practice of thermal testing have shown that after 100 min of continuous operation of the machine, all high-frequency modes characterized by a small value of the thermal time constant no longer affect the kinetics of the formation of the thermal characteristic [19]. Therefore, at any point of the thermal characteristic, the record is valid

$$y = A_1(1 - e^{-\lambda_1 t}) + B_1 e^{-\lambda_1 t} + C + \varepsilon \quad (10)$$

where A_1 , B_1 is the amplitude and the initial level of the first temperature mode in physical coordinates of the function under study y ; λ_1 is the reciprocal of the thermal time constant of the first mode; C is the sum of the amplitudes of all high-frequency modes; ε is a small error caused by the processes of stabilization of high-frequency modes continuing in time.

Considering the small value of ε for machine tools with a temperature error significantly greater than one micron, this value can be neglected. Then, it is possible to analytically determine the thermal time constant of the thermal characteristic as the reciprocal of λ_1 by the known values of the ordinate of the thermal characteristic at times t_1 and t_2

$$\begin{aligned} \lambda_1 &= \ln(Y_1/Y_2)/(t_2 - t_1), \\ Y_1 &= (A_1 + C - y_1)/(A_1 - B_1), \\ Y_2 &= (A_1 + C - y_2)/(A_1 - B_1) \end{aligned} \quad (11)$$

The times t_1 and t_2 are selected on the section of the thermal characteristic used for training the network, and the moment in time t_2 delimits this section from the prediction section. In this case, any predicted value of the investigated function y_3 at time t_3 has the form

$$y_3 = A_1 + C - e^{\ln((A_1+C-y_2)/(A_1-B_1))-\lambda_1(t_3-t_2)}(A_1 - B_1) \quad (12)$$

Thus, when calculating criteria (8) and (9), the components of the output vector of the trained ANN are used as predicted values of the thermal characteristic $\delta_{pr,\zeta}$, and the calculated values $\delta_{\lambda,\zeta}$ are determined by dependencies (11) and (12).

The ANN modeling made it possible to establish the following results and patterns.

For the first variant of the ANN input data:

- for a single-modal function, the best results of ANN modeling are achieved when using one neuron in the hidden layer;
- in the presence of two modes, it is preferable to use several neurons for the hidden layer; at the same time, no strict regularities were revealed about the correspondence between the growth of the number of neurons in the hidden layer and the stability of the results of ANN modeling;
- for a unimodal function, the forecasting efficiency is insignificant, but higher, since the size of the input vector was formed in a time less than one thermal time constant (stable results were recorded when constructing a predictive characteristic according to the input vector obtained from observations, for a duration of 90% of the thermal time constant of the test thermal characteristic); when modeling a bimodal function,

stable results were recorded when constructing a predictive characteristic using an input vector obtained from observations, for a duration of 130% of the thermal time constant of the first mode of the test thermal characteristic;

- the use of normalized input data did not improve the stability of the ANN modeling;
- when studying the ratios of the sizes of the training, validation, and test samples, it was found that the minimum size of the training sample was 60% of the length of the input data vector; the minimum size of the validation and test samples cannot be less than 10% of the length of the input data vector.

As an illustration of the efficiency of ANN simulation, Fig. 1 shows four indexed curves for two variants of variation of ANN simulation parameters. Curve 1 is a noisy initial vector with known modal parameters, formed in accordance with (7). Curve 2 is a theoretical thermal characteristic formed in accordance with (1). Curve 3 is predicted thermal characteristic as the result of ANN modeling, isolated from the set of solutions by criterion (9). Curve 4 is also a predicted thermal characteristic representing the result of ANN modeling and highlighted by criterion (8). Figure 1a illustrates the efficiency of ANN simulation for a single-modal thermal characteristic, Fig. 1b – for a two-modal one. Figure 1a shows that depending on the selected criteria (8) or (9), you can get a different result. However, to date, there is no justified decision on the priority of criteria (8) relative to (9). Therefore, other things being equal, it is necessary to achieve close modeling options when using criteria (8) and (9), for example, by choosing the duration of the basic experiment, during which the training sample is formed. For the thermal characteristics shown in Fig. 1 b, the duration of the basic experiment was 130% of the thermal time constant of the first mode of the test thermal characteristic.

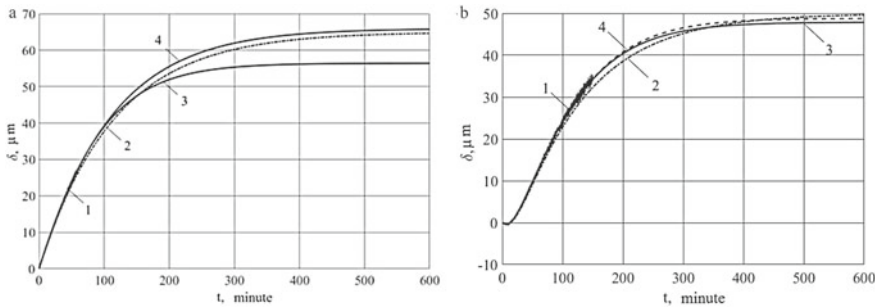


Fig. 1 ANN simulation results: **a** 1 mode, duration of the experiment is 0.5τ , 1 neuron (in the hidden layer), $\Gamma > 3\tau$; **b** 2 modes, 1.3τ , 3 neurons, $\Gamma > 3\tau$

For captions for Fig. 1, the following designations were used: Γ – forecast horizon; τ is the thermal time constant of the first mode of the test thermal characteristic.

For the second variant of the ANN input data, using the sliding window method, invariant results and patterns were also obtained:

- regardless of the modality of the investigated thermal characteristic, the best results of ANN modeling are achieved when more than two neurons are used in the hidden

layer, but a stable decrease in the modeling error with an increase in the number of neurons in the hidden layer was not established;

- for a unimodal thermal characteristic with a comparable error in predicting a bimodal thermal characteristic, the forecast horizon is larger, but comparable with the thermal time constant of the first mode;
- for a single-modal thermal characteristic, more stable results of ANN modeling are achieved with a larger sliding window; for a two-modal thermal characteristic, the optimal ratios for the size of the sliding window, the forecasting horizon, and the duration of the base experiment are ambiguous and are selected experimentally.

Figure 2 shows five indexed curves. Curves 1 are noisy thermal characteristics over the length of the base experiment. The duration of the basic experiment in Fig. 2 a was one thermal time constant of the first mode, and in Fig. 2b – 130% of the thermal time constant of the first mode of the test thermal characteristic. An excessive increase in the duration of the base experiment automatically leads to a decrease in the efficiency of ANN simulation, since it is known from the theory of thermal conductivity that the duration of the base experiment equal to determines more than 95% of the amplitude of the thermal characteristic. Curve 2 is a theoretical thermal characteristic formed in accordance with (1). Curves 3 and 4 are the predicted thermal characteristics obtained from the results of ANN modeling using criteria (8) and (9), respectively. Curve 5 is approximated functions.

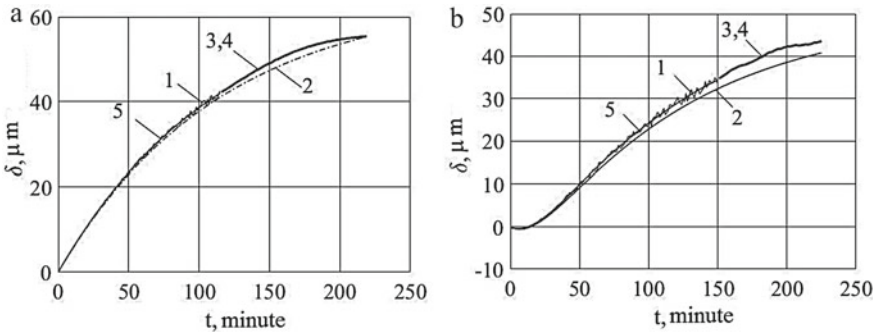


Fig. 2 Results of ANN modeling: **a** 1 mode, $\Gamma = 0.9\tau$, 4 neurons; **b** 2 modes, $\Gamma = 0.65\tau$, 10 neurons

4 Conclusion

A new procedure for studying the stability of ANN modeling for the thermal characteristics of a machine tool is presented. The new procedure has made it possible to form a generalized concept of studying the effectiveness of the use of neural network technologies in thermal modeling of machine tools. This concept defines a typical set of variable modeling parameters, a basic mathematical model based on a modal approach, and a typical software architecture that can be developed to study the effectiveness of ANN

modeling. In this work, only one type of ANN architecture has been investigated, and taking into account their diversity, the presented methodology shows the prospects of ANN research in thermal modeling of machine tools.

The practical result of using a neural network of direct propagation in solving the problem of predicting thermal characteristics is the possibility of further reducing the duration of the full-scale experiment of the machine; this reduction is estimated at approximately 30% of the duration of a full-scale experiment, implemented in accordance with an approach based on experimental modal analysis, in which stable predictive solutions are obtained with a duration of a full-scale experiment equal to twice the time of the thermal time constant of the first mode.

Acknowledgements. The reported study was funded by RFBR according to the research project № 20-38-90045.

References

1. Li Bh, Hou Bc, Yu Wt et al (2017) Applications of artificial intelligence in intelligent manufacturing: a review. *Frontiers Inf Technol Electronic Eng* 18:86–96. <https://doi.org/10.1631/FITEE.1601885>
2. Zermane H, Mouss H (2017) Development of an internet and fuzzy based control system of manufacturing process. *Int J Autom Comput* 14:706–718. <https://doi.org/10.1007/s11633-016-1027-x>
3. Chen L, Duan H, Fan Y et al (2020) Multi-objective clustering analysis via combinatorial pigeon inspired optimization. *Sci China Technol Sci* 63:1302–1313. <https://doi.org/10.1007/s11431-020-1587-y>
4. Dentler J, Rosalie M, Danoy G et al (2019) Collision Avoidance Effects on the Mobility of a UAV Swarm Using Chaotic Ant Colony with Model Predictive Control. *J Intell Robot Syst* 93:227–243. <https://doi.org/10.1007/s10846-018-0822-8>
5. Kabaldin YG, Shatagin DA, Kolchin PV et al (2019) Modular Design of Machine-Tool Equipment as Cyberphysical Systems on the Basis of Artificial Intelligence and Cloud Technology for Digital Production. *Russ Engin Res* 39:288–295. <https://doi.org/10.3103/S1068798X19040099>
6. Wang G, Wang Y, Zhao J et al (2012) Process optimization of the serial-parallel hybrid polishing machine tool based on artificial neural network and genetic algorithm. *J Intell Manuf* 23:365–374. <https://doi.org/10.1007/s10845-009-0376-5>
7. Sadeghian R, Sadeghian MR (2016) A decision support system based on artificial neural network and fuzzy analytic network process for selection of machine tools in a flexible manufacturing system. *Int J Adv Manuf Technol* 82:1795–1803. <https://doi.org/10.1007/s00170-015-7440-4>
8. Li B, Tian X, Zhang M (2019) Thermal error modeling of machine tool spindle based on the improved algorithm optimized BP neural network. *Int J Adv Manuf Technol* 105:1497–1505. <https://doi.org/10.1007/s00170-019-04375-w>
9. Yang J, Shi H, Feng B et al (2015) Thermal error modeling and compensation for a high-speed motorized spindle. *Int J Adv Manuf Technol* 77:1005–1017. <https://doi.org/10.1007/s00170-014-6535-7>
10. Li Y, Zhao J, Ji S (2018) Thermal positioning error modeling of machine tools using a bat algorithm-based back propagation neural network. *Int J Adv Manuf Technol* 97:2575–2586. <https://doi.org/10.1007/s00170-018-1978-x>

11. Ziegert JC, Kalle P (1994) Error compensation in machine tools: a neural network approach. *J Intell Manuf* 5:143–151. <https://doi.org/10.1007/BF00123919>
12. Zhang Y, Yang J, Jiang H (2012) Machine tool thermal error modeling and prediction by grey neural network. *Int J Adv Manuf Technol* 59:1065–1072. <https://doi.org/10.1007/s00170-011-3564-3>
13. Ma C, Zhao L, Mei X et al (2017) Thermal error compensation of high-speed spindle system based on a modified BP neural network. *Int J Adv Manuf Technol* 89:3071–3085. <https://doi.org/10.1007/s00170-016-9254-4>
14. Shi H, Jiang C, Yan Z et al (2020) Bayesian neural network-based thermal error modeling of feed drive system of CNC machine tool. *Int J Adv Manuf Technol* 108:3031–3044. <https://doi.org/10.1007/s00170-020-05541-1>
15. Guo Q, Yang J, Wu H (2010) Application of ACO-BPN to thermal error modeling of NC machine tool. *Int J Adv Manuf Technol* 50:667–675. <https://doi.org/10.1007/s00170-010-2520-y>
16. Fu G, Gong H, Gao H et al (2019) Integrated thermal error modeling of machine tool spindle using a chicken swarm optimization algorithm-based radial basic function neural network. *Int J Adv Manuf Technol* 105:2039–2055. <https://doi.org/10.1007/s00170-019-04388-5>
17. El Ouafi A, Guillot M, Barka N (2013) An Integrated Modeling Approach for ANN-Based Real-Time Thermal Error Compensation on a CNC Turning Center. *Advanced Materials Research* 664:907–915. <https://doi.org/10.4028/www.scientific.net/AMR.664.907>
18. Majumder H, Maity KP (2018) Predictive Analysis on Responses in WEDM of Titanium Grade 6 Using General Regression Neural Network (GRNN) and Multiple Regression Analysis (MRA). *SILICON* 10:1763–1776. <https://doi.org/10.1007/s12633-017-9667-1>
19. Polyakov AN, Goncharov AN, Parfenov IV (2020) Method for Predicting Thermal Characteristics of Machine Tools Based on Experimental Modal Analysis. In: *Proceedings of the 5th International Conference on Industrial Engineering (ICIE 2019)*. ICIE 2019. Lecture Notes in Mechanical Engineering. Springer, Cham, pp 85–93. https://doi.org/10.1007/978-3-030-22063-1_10
20. Chou J-S, Truong TTH (2019) Sliding-window metaheuristic optimization-based forecast system for foreign exchange analysis. *Soft Comput* 23:3545–3561. <https://doi.org/10.1007/s00500-019-03863-1>



Experimental Determination of the Kinematic Accuracy of a Planetary Oblique-Toothed Cycloidal Gearbox

E. Shirokikh^(✉), D. Sinitsyn, and A. Popov

Kolomna Institute (Branch) Moscow Polytechnic University, 408, Oktyabrskoy revoliutsii str,
Kolomna, 140402, Russia

Abstract. The relevance of the creation and research of planetary cycloidal gears is due to the increasing needs of the industry in servo drives of actuators with high-precision positioning of the final link. Currently, a wide variety of planetary cycloidal gearboxes are used in industry, made according to different design schemes, but equally containing cycloidal gears with straight teeth. Gears with straight-toothed gears do not fully realize their potential in terms of the bearing capacity of the gears and dynamic characteristics, in particular, in terms of smoothness and noise. This problem can be solved by the use of helical gears that can improve the specified performance of planetary cycloidal gears. However, the possibility of their application is largely constrained by the lack of effective industrial technologies for manufacturing skew-toothed cycloidal gears with high accuracy, assembling gearboxes based on them and evaluating their kinematic errors. To date, there is not enough research on real samples of planetary skew-toothed cycloidal reducers. The developed and created skew-toothed cycloidal gearbox of the original design and a special stand for experimental studies with a measuring system capable of registering the kinematic errors of the gearbox in automatic mode are presented. The method of experimental determination of the kinematic error is described, some results of the study of the kinematic error of the presented gearbox are presented, their evaluation is performed, and conclusions are formulated.

Keywords: Cycloidal gearbox · Experimental bench · Kinematic accuracy · Methodology · Research results

1 Introduction

Comprehensive automation of modern mechanical engineering is now becoming a serious incentive for the creation and production of servos of a wide range of applications, which are increasingly used in tracking systems of various machines, in particular, modern machine tools, actuators of robotic devices, remote control systems (e.g., high-precision positioning systems of narrow-directional antennas), mechatronic drives, etc., and which are subject to increasingly high requirements for the quality of motion transmission, response to the control signal and working out the accuracy of movement (positioning) of the executive link [1–3].

To increase the clarity of the control signal processing (to minimize the delay in the reaction to it and the accuracy of the movement of the executive link), servomechanisms are usually equipped with various amplifiers, most often of the mechanical-type reducers, which have high kinematic rigidity. The most preferred in this respect are the planetary cycloidal gears (PCG) [4–6] characterized, first of all, by the multi-pair engagement, as well as the possibility of gas-free coupling of the interacting gears.

Compared to traditional involute gears, PCG are characterized by significantly higher [7]: compactness; kinematic rigidity; gear ratios realized in a single reduction stage with a small number of gears; transmitted torques and resistance to mechanical overloads; accuracy of the phase positioning of the output shaft, as well as: in 2.0.4 times less weight at the same gear ratios; the possibility of a more convenient layout of the designed devices, thanks to the alignment of the input and output shafts; the possibility of using PCP as a differential mechanism; higher efficiency [8, 9].

2 Relevance of the Topic

Currently, in mechanical engineering, a wide variety of planetary cycloidal gearboxes (PCGB) are used, made according to different design schemes, but equally containing cycloidal gears with straight teeth.

For these PCG, methods for selecting design schemes [10] and calculating all parameters have been developed, their manufacturing technologies are well developed by industry, and a large number of theoretical and experimental scientific studies have been devoted to evaluate the effectiveness of their characteristics [11–14].

At the same time, PCG with straight-toothed gears do not fully realize their potential in terms of the bearing capacity of the gear rings and dynamic characteristics, in particular, in terms of smoothness and noise. However, the possibility of using helical gears that can improve these indicators of planetary cycloidal gears is currently largely constrained by the lack of effective industrial technologies for manufacturing helical cycloidal gears with high accuracy, assembling gearboxes based on them and evaluating their kinematic errors. To date, there is not enough research on real samples of planetary oblique-toothed cycloidal reducers (POTCR), which puts the topic under consideration in the category of relevant.

3 Problem Statement and Solution Methods

For comprehensive studies of the kinematic accuracy, as well as the performance indicators of the POTCR, it is necessary to have a prototype of such a gearbox, a special stand for experimental studies of its characteristics and a methodology for conducting them.

The kinematic error of PCG is determined by the set of production (primary) manufacturing errors of its kinematic links (elements), their rigidity, the accuracy of their assembly, as well as operating conditions characterized by the magnitude and type of thermal and mechanical loads [15, 16].

Therefore, for greater objectivity, both calculated and experimental studies of the kinematic accuracy of PCG should allow simulating its operation under adequate operating conditions [17].

The object of the study was an original prototype of a promising PCG with oblique gears, made according to patents [18, 19], the 3D model, see Fig. 1.

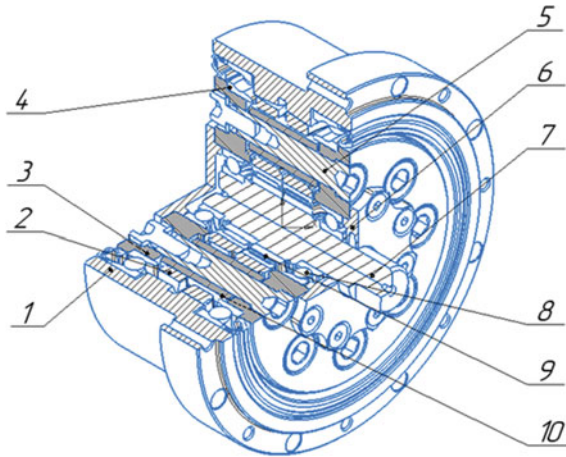


Fig. 1 3D model of the POTCR 1—housing; 2—satellite; 3—output flange of the coupling; 4—bearing; 5—pin of the parallel crank mechanism; 6—cover; 7—eccentric shaft; 8—angular contact bearing; 9—eccentric shaft bearing; 10—pin bushing

Studied POTCR has the following main characteristics: number of gears transmission—1; the angle of inclination of the teeth of gear wheels $\beta = 12^{\circ}$; total gear ratio $U_p = 102$; the torque on the output shaft of the reducer $M = 250 \text{ N} \cdot \text{m}$; frequency of rotation of the shafts, respectively, the input $n_{in} = 6000 \text{ min}^{-1}$ and output $n_{out} = 59 \text{ min}^{-1}$; backlash of not more than $\Delta\varphi = \pm 2.5 \text{ s of arc. min}$; dimensions: $\text{Ø}380 \times 186 \text{ mm}$.

Before assembly, the manufactured kinematic elements of the gearbox were subjected to a metrological examination on a control and measuring machine, which made it possible to determine and evaluate their primary errors [20].

For experimental studies of the POTCR to determine its kinematic and dynamic characteristics, a special stand was designed and created. The block diagram of stand is shown in Fig. 2.

The stand is also equipped with a specially developed control and measurement system that can automatically perform: measurement and registration of kinematic errors in the form of spectrograms, followed by their processing by a special analytical computer program, errors in the overall gear ratio, as well as simulate test conditions that are close to real operating conditions.

At the beginning of the process of measuring the kinematic accuracy POTCR mounted on the stand, see Fig. 3, checked for free rotation of the input shaft, and then to the PC runs a special program “Diakin – 4” for processing the experimental data

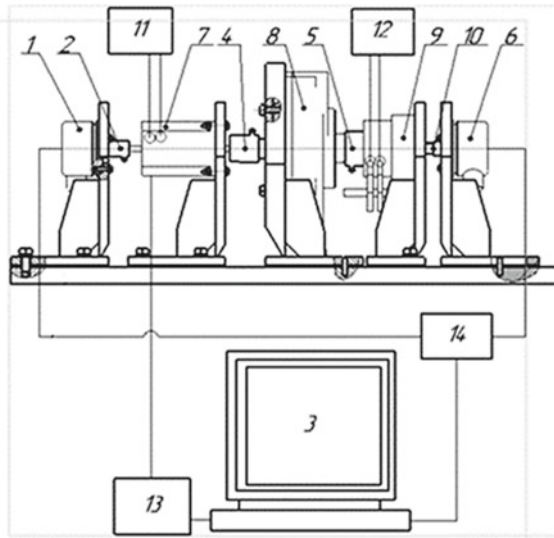


Fig. 2 Block diagram of the stand 1—gearbox input motion sensor (LIR-158A); 2—elastic coupling; 3—PC; 4,5—diaphragm couplings; 6—gearbox input motion sensor (LIR-190A); 7—stepper motor ST57-76D; 8—POTCR; 9—load device (electromagnetic coupling EAT 20); 10—elastic coupling; power sources: 11—stepper motor and 12—electromagnetic coupling; 13—stepper motor driver; 14—the converter of signals of the input and output sensors

obtained in the study of kinematic precision POTCR, which at the same time in online mode on the PC monitor output the measurement results. The kinematic error of the gearbox chain was recorded at three full revolutions of the output shaft of the gearbox at the rotational speeds of the input shaft $n_{in} = 100 \text{ min}^{-1}$ and the output shaft $n_{out} = 0.98 \text{ min}^{-1}$ at idle, respectively. As a result of the study of the POTCR under the program “Diakin – 4” at idle, the graph of the kinematic error and the spectrum of the kinematic error of the POTCR were obtained.

4 Results of Experimental Studies

The maximum value of the kinematic error of the gearbox under study is defined as the difference between the highest and lowest peak values within one revolution of the output shaft. From the graph, see Fig. 4, it can be seen that the largest kinematic error $\Delta\varphi$ does not exceed 144 arcseconds or 2.4 arcmin with a gear ratio error not exceeding 0.011%.

The spectrum of the kinematic error allows you to identify the angles rotation of the output shaft of the gearbox, on which there are noticeably high (spikes) errors, at the corresponding harmonics. These errors are primarily caused by assembly defects (shaft misalignments, etc.), inherent defects in standard products (bearing runouts, etc.), as well as the possible presence of contamination, etc.

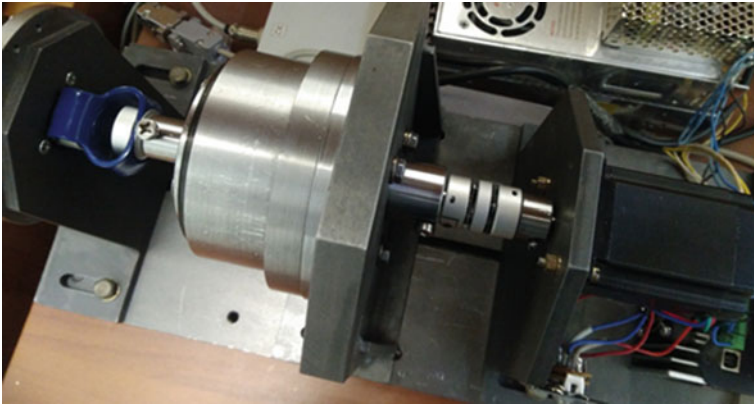


Fig. 3 Appearance of the POTCR on the stand

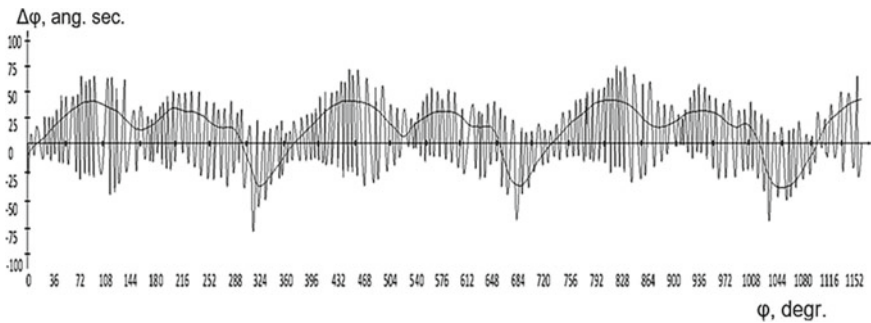


Fig. 4 Kinematic error graph

Comparing the spectrogram with the kinematic error graph, it is possible to determine in which phase position of the output shaft, which harmonic h introduces the greatest error.

The error, characterized by small and almost identical harmonic amplitudes, is usually caused by defects in the geometry of the mating gears and the quality of the actuating surfaces of the kinematic elements [21].

From the spectrogram of the gearbox under study, see Fig. 5, it can be seen that the most significant spikes in the amplitudes of the phase errors $\Delta\varphi$ are observed at the harmonics: $h = 1.0.3$ (38...60 angular min); $h = 58...62$ (6...27 angular min); $h = 100...106$ (8...17 angular min).

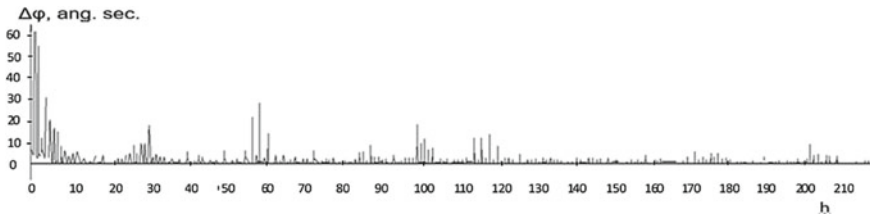


Fig. 5 Spectrogram of the kinematic error of the PCCR

5 Conclusion

Analysis of the results obtained spectral components showed that the main sources of kinematic error POTCR are not sufficiently tight tolerances on geometrical parameters (size, shape Executive of surfaces and their relative location) of the kinematic elements, the lack of quality surfaces cycloidal gear rims and provide the required precision Assembly of the gearbox.

Compliance with the conditions for achieving the appropriate manufacturing quality of kinematic elements by production methods and their assembly with maintaining the required gaps in the interfaces of kinematic links will ensure a high level of kinematic accuracy and uniformity of the gear ratio, which will allow the use of planetary skew-toothed cycloidal reducers as the main type of drives in high-precision actuators with high smoothness.

References

1. Siritsyn AI, Bashkirov VN, Shirokikh EV et al (2016) Kinematic Precision of a Planetary Cycloid-Pin Machine Tool Drive. *J Russian engineering research* 36(2):89–92
2. Sinitsyn DA, Shirokikh EV (2014) Problematic issues of the technology of cutting internal oblique hypocycloidal wheels of antenna drives. *J Natural and Technical Sciences*. 11–12(78):205–211
3. Sinitsyn DA, Siritsyn AI, Shirokikh EV (2014) Prospects for the use of cycloid drives in robotic systems of rocket technology objects. *J Defense Technology* 12:6–12
4. Sinitsyn DA, Shirokikh EV (2016) Cycloidal transmission-the basis of high-precision machine drives. *J Scientific and practical Journal* 1(8):64–70
5. Sinitsyn AI, Sinitsyn DA, Khandogin VA (2017) The influence of accuracy factors on the performance of guidance drives for missile launchers. *J Defense technology* 10:34–38
6. Sinitsyn DA, Shirokikh EV (2012) Problems and prospects of production of planetary cycloidal-tsevochny gears. In: *Prospects of development of science and education-collection of scientific papers on the materials of the International Scientific and Practical Conference*. Tambov, p 84–87
7. Planetary and differential mechanisms. <https://present5.com/planetarnye-i-differencialnye-mexanizmy-planetarnymi-nazyvayut-peredachi-imeyushhie>. Accessed 08 February 2021
8. Siritsyn AI, Sinitsyn DA, Bashkirov VN et al (2015) Kinematic accuracy of the planetary cycloidal-tsevochny drive of the machine. *J Bulletin of Mechanical Engineering* 11:28–31
9. Siritsyn AI, Bashkirov VN, Shirokikh EV et al (2016) Kinematic Precision of a Planetary Cycloid-Pin Machine Tool Drive In *Russian Engineering Research* Allerton Press. Inc 36(2):89–92

10. Sinitsyn DA, Shirokikh EV (2016) Factors of choice of structural planetary cycloidal gears. *J Nauchno-prakticheskiy Zhurnal* 2(a):60–70
11. Mamaev IM, Morozov VV, Fedotov OV et al (2015) Experimental studies of the accuracy of the roller transmission of the radio telescope actuator. *J Bulletin of Mechanical Engineering* 9:59–63
12. Kapitonov AV, Nepsha DV, Goncharov MV et al (2014) The study of the kinematic error of a planetary eccentric reducer. *J Bulletin of the Belarusian-Russian University* 3(44):14–24
13. Kapitonov AV, Chernyakov SG (2011) Investigation of the kinematic accuracy of planetary roller gears by methods of harmonic analysis and assembly control. *J Bulletin of the Belarusian-Russian University* 4(33):40–50
14. Pashkevich MF, Pechkovskaya OE (2006) Kinematic accuracy and vibration activity of the 2K-N planetary transmission with modified satellite teeth. *J Bulletin of the Mogilev State Technical University* 1(10):221–225
15. Rodikov AV (2010) Influence of primary errors of planetary pinion gearing on the kinematic accuracy of output shaft rotation In: *Materials of the AAI International scientific and Technical conference. Automobile and Tractor Construction in Russia: Development Priorities and Personnel Training, dedicated to the 145th anniversary of MSTU MAMI, November 2010, Moscow*, p 106–109
16. The kinematic error of the planetary mechanisms. <https://studfile.net/preview/5992626/page/4/>. Accessed 08 February 2021
17. Kapitonov AV, Chernyakov SG, Soskovets KV et al (2016) Methods of experimental studies of the kinematic accuracy of planetary gears with intermediate rolling bodies and control of the treadmill profile. *J Bulletin of the Belarusian-Baltic University* 2(51):41–50
18. Shirokikh EV, Siritsyn AI, Sinitsyn DA (2016) Planetary cycloidal reducer. *RF PM* 173 084, 23 June
19. Sinitsyn DA, Popov AA, Khandogin VA (2019) Planetary oblique transmission. *RF PM* 195739, 03 October
20. Sinitsyn DA, Shirokikh EV (2015) Choosing the type of end mill for cutting cycloidal gears of internal gearing. *J Scientific and practical Journal/KI (F) MPU N* 1(6):193–204
21. Pashkevich AM (2006) Kinematic accuracy of planetary cam-plunger gears. *J Bulletin of the Belarusian-Russian University* 4(13):129–139



Developing a Mathematical Model of Interaction of a Conveyor-Bottom Bucket Working Body with the Soil

Yu. M. Lyashenko¹(✉), E. A. Revyakina², and G. V. Lukyanova³

¹ Platov South Russia State Polytechnic University (NPI), 132, Prosveschenia Str., Novocherkassk, Russia346428

² Don State Technical University, 1, Gagarina Sq., Rostov-na-Don, Russia346000

³ Rostov State University of Economics, 69, Bolshaya Sadovaya str., Rostov-on-Don, Russia346000

Abstract. The paper describes the developed models of conveyor-bottom buckets solving the problem of reducing the coefficient of friction of rocky soils on the working body bottom through the transition from sliding to rolling friction while forming a new structural and technological group of bucket loading bodies, which can be used on excavators, bucket loaders, and other loading equipment. The paper discusses technical solutions represented by a combination of two bottom structures with a roller surface and in the form of a closed belt. The developed mathematical model of interaction of a conveyor-bottom bucket working body with the soil allows simulating the working process and analyzing the results. Based on the developed analytical tool, the optimal parameters of the structural conveyor-bottom components can be determined for specific operating conditions, considering the minimization of power consumption for loading the soil as a target function of the problem being solved.

Keywords: Conveyor-bottom bucket · Mechanization of loading · Penetration resistance · Minimization of power consumption

1 Introduction

Studying the interaction of the bucket working body with the rock mass has revealed the factors affecting the efficiency of mechanized loading rocky soils [1–21]. It has been established that the design of the bucket working body is mainly improved by reducing resistance to the bucket penetrating the stockpile [22]. Herewith, the resistance to the bucket working body penetrating the stockpile significantly depends on the coefficient of friction of the material loaded on the bucket component surfaces [23, 24].

The conveyor-bottom bucket models developed, solving the problem of reducing the coefficient of friction of rocky soils on the working body bottom through the transition from sliding to rolling friction, form a new structural and technological group of bucket loading bodies, which can be used on excavators, bucket loaders, and other loading

equipment [25]. These technical solutions are represented below (Fig. 1) by a combination of two bottom structures with a roller surface and in the form of a closed belt. In turn, the closed-belt models are structurally divided into the non-driven ones and those with a belt drive mechanism. There can be various versions of the conveyor-bottom belt drive: a motor with a mechanical transmission and various hydraulic power cylinders.

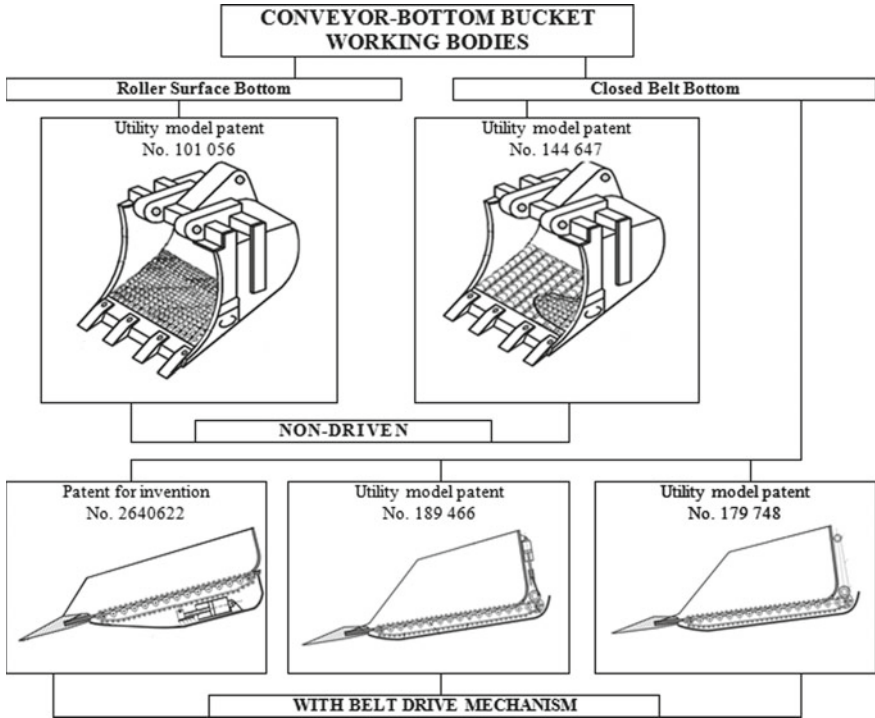


Fig. 1 Systematics of conveyor-bottom bucket working bodies

The excavation of bedrock or filled soil in a stockpile is performed mechanically by introducing a bucket loading body into the loosened material. In the study, the impact of the conveyor-bottom bucket working body parameters on the forces of rocky soil interaction with the stockpile is evaluated by a comparative analysis of the processes occurring when conventional flat and roller surface bottoms penetrate it.

The analysis of studying the bucket loading body interaction with the soil allowed summarizing the methodological approaches to the mathematical description of the resistance to the bucket working body W_{wb} penetrating the stockpile (excluding the side walls) (Fig. 2):

$$W_{po} = W_l + W_{dn}, \tag{1}$$

where W_l —is the drag force of resistance to the penetration of the leading bottom edge; W_{dn} —is the force of resistance to bottom penetration.

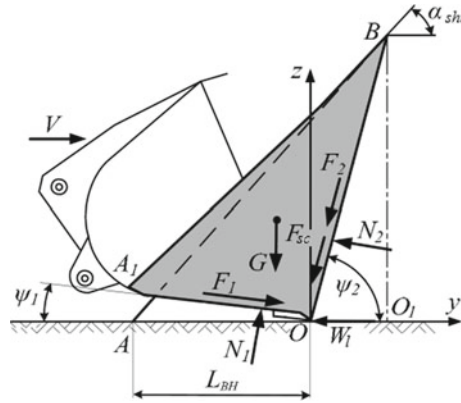


Fig. 2 Diagram of generating forces of resistance to the bucket working body bottom penetrating the stockpile

In this study, shoving the bucket loading body bottom to the ground face or bulk material has been considered based on the *S. Coulomb* theory of adhesion and ultimate rock equilibrium (Fig. 2).

It is considered that when the material is loaded with external shear forces, shear planes emerge in its mass, where shear τ and normal σ stresses and adhesion C act, analytically related according to the *S. Coulomb* law:

$$\tau = Ctg \rho_0 \tag{2}$$

When developing an analytical tool, the methodological approach described in [19] has been used.

2 Determining the Resistance to the Bucket Bottom Edge Penetration

When the bucket bottom is shoving to the ground face or bulk material before the leading edge with the height b_3 and the length equal to the internal bucket width B_k , a compacted core emerges in the form of a soil wedge with an internal friction angle ρ_o (Fig. 3). The soil wedge width coincides with the bucket width B_k . Normal forces N and tangential soil-on-soil friction forces F act on the wedge edges, creating shear stresses τ .

The drag force of resistance to the penetration of the bucket bottom edge W_d is determined by the equation of the sum of the force projections on the horizontal axis:

$$W_l = 2(N \cdot \sin \rho_o + F \cdot \cos \rho_o) \tag{3}$$

The normal force N is defined as the force of pressure on the wedge side surface:

$$N = \frac{b_\varepsilon B_o}{2 \sin \rho_{0r}} \tag{4}$$

where σ_r are the normal stresses on the inclined sliding faces of the soil wedge.

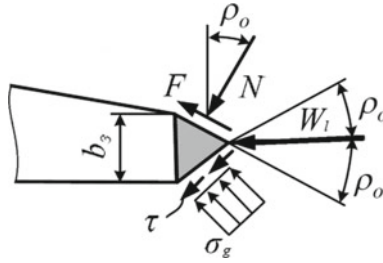


Fig. 3 Diagram of generating forces of resistance to the bucket bottom edge penetration

Tangential friction force is given by $F = \mu_2 N$; where $\mu_2 = \operatorname{tg} \rho_0 - \rho_0$ is the coefficient of soil friction on the soil, and ρ_0 is the internal friction angle.

For bulk materials, the internal friction angle is equal to the stockpile slope angle: $\rho_0 = \alpha_{\text{шт}}$.

Thus, the force of resistance to the bucket bottom edge penetration $W_{\text{л}}$ is determined as follows:

$$W_l = (\sin \rho_0 + \mu_2 \cos \rho_0) \frac{b \varepsilon b_0}{\sin \rho_0} \sigma_g \quad (5)$$

3 Determining the Resistance to the Bucket Bottom Penetration

The bucket bottom under an angle of inclination to the soil ψ_1 penetrates the stockpile with the natural soil slope angle $\alpha_{\text{шт}}$. When the bucket bottom penetration starts, a shear plane emerges under an angle ψ_2 , and a loosened material prism is formed with a cross section OA_1B , a weight G , and slide planes: OA_1 —the plane of soil sliding against the bottom; OB —the plane of soil sliding against the ground. In the slide plane OA_1 , the force of resistance to the soil motion F_1 and the normal force N_1 act on the prism from the bucket bottom side, and Coulomb forces arise in the slide surface OB : the force F_2 of the soil-on-soil friction, the soil adhesion force F_{CII} , and the normal force N_2 .

The total force of resistance to horizontal bottom motion when penetrating a stockpile is

$$W_{dn} = F_1 \cdot \cos \psi_1 + N_1 \cdot \sin \psi_1 \quad (6)$$

When the soil moves along the fixed rollers of the conveyor bottom, rolling friction of the material on the rollers and sliding or rolling friction emerges in the roller bearings [11].

Thus, the force of resistance to the soil motion F_1 is equal to the total force of resistance to soil motion along the conveyor bottom in the form of a roller surface in the plane OA_1 :

$$F_1 = F_{1P} = F_{1P1} + F_{1P2} + F_{1P3} \quad (7)$$

where F_{P1} is the resistance to the material rolling along the rollers, F_{P2} is the resistance to friction in the roller pins, F_{P3} is the resistance to the material sliding along

the rollers and imparting kinetic energy to them. The resistance to the material rolling along the rollers F_{1P1} :

$$F_{P1} = 2k \cdot N_{1P}/D_P \tag{8}$$

where k is the coefficient of rolling friction of the material on the rollers; D_P is the roller diameter, m;

The resistance F_{1P2} is a consequence of friction in the roller pins if the material lies on z_P rollers:

$$F_{1P2} = \mu_P \cdot d_P \cdot (N_{1P} + P_P \cdot z_P) / D_P \tag{9}$$

where P_P is the gravity of the rotating roller parts; μ_P is the coefficient of friction in the roller neck; d_R is the roller neck diameter, m.

The resistance to the material sliding along the rollers and imparting kinetic energy to them F_{1P3} :

$$F_{1P3} = K_P \cdot P_P \cdot z_P \cdot v_P^2 / (g \cdot L) \tag{10}$$

where $K_P < 1$ is a coefficient considering that not the entire mass of the rotating roller part is concentrated along its circumference (in practice $K_P = 0,8 \div 0,9$); v_P is the circumferential roller rotation speed, m/s; g is the free-fall acceleration, m/S^2 ; L is the load path ($L = L_{\theta H} / \cos\psi I$), m.

For the normal force N_I , the functional dependence is described by the equilibrium equations of the concurrent force system:

$$N_1 = f(F_1, F_2, N_2, F_{sc}, \psi_1, \psi_2, \mu_1, \mu_2) \tag{11}$$

In the problem being solved, the prism of the material with the cross section $OAIB$ is considered as a solid body performing a translation motion and being in equilibrium under the action of a system of three concurrent forces: R_1, R_2 (Fig. 4).

The resulting forces of R_1, R_2 are considered as vectors:

$$\vec{R}_1 = \vec{F}_1 + \vec{N}_1. \tag{12}$$

$$\vec{R}_2 = \vec{F}_2 + \vec{F}_{sc} + \vec{N}_2 \tag{13}$$

The concurrent force system equilibrium equations are written in the form of the projections of these forces on the O_y and O_z axes and are supplemented by the equations of friction and adhesion forces.

$$\begin{aligned} \sum_{i=1}^n F_{ij} &= 0; \\ \sum_{i=1}^n F_{iy} &= 0; \\ N_1 \sin \psi_1 + F_1 \cos \psi_1 - (F_2 + F_{sc}) \cos \psi_1 - N_2 \sin \psi_1 &= 0 \end{aligned} \tag{14}$$

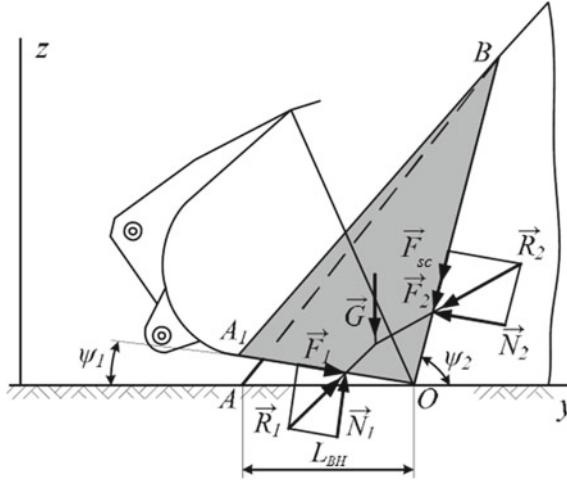


Fig4 Concurrent force system equilibrium diagram

$$\sum_{i=1}^n F_{iz} = 0 \quad (15)$$

$$-G + N_1 - \cos \psi_1 - F_1 \sin \psi_1 - (F_2 + F_{sc}) \sin \psi_2 + N_2 \cos \psi_2 = 0$$

Solving Eqs. (14) and (15) gives the below formulas. Normal force N_1 for the plane bottom penetration:

$$N_1 = N_{1P} = F_{sc} \cdot K_{10} + G \cdot K_{11}. \quad (16)$$

Normal force N_1 for the roller surface bottom penetration:

$$N_1 = N_{1P} = F_{sc} \cdot K_{12} + G \cdot K_{13} + \mu_p \cdot d_p \cdot P_p \cdot z_p \cdot K_{14}/D_p + K_p \cdot P_p \cdot z_p \cdot v_p^2 \cdot K_{14}/(g \cdot L), \quad (17)$$

where K_i is the coefficients

$$K_1 = \frac{(\sin \Psi_1 \cos \Psi_1 + \sin \Psi_2 \cos \Psi_2)}{(\sin^2 \psi_1 + \cos^2 \Psi_1)}; K_2 = \frac{(\sin \Psi_1 \sin \Psi_2 - \cos \Psi_1 \cos \Psi_2)}{(\sin^2 \psi_1 + \cos^2 \Psi_1)}$$

$$K_3 = \frac{\cos \psi_1}{(\sin^2 \psi_1 + \cos^2 \psi_1)}; K_4 = \frac{(\cos \Psi_1 \sin \Psi_2 + \sin \Psi_1 \cos \Psi_2)}{(\sin^2 \psi_2 - \cos^2 \Psi_2)}$$

$$K_5 = \frac{(\sin \psi_1 \sin \psi_2 - \cos \psi_2 \cos \psi_2)}{(\sin^2 \psi_2 + \cos^2 \psi_2)}; K_6 = \mu_2 \cdot K_1 + K_2;$$

$$K_7 = \frac{K_1}{1 - K_5 \cdot K_6}; K_8 = \frac{K_3}{1 - K_5 \cdot K_6}; K_9 = \frac{K_4 \cdot K_6}{1 - K_5 \cdot K_6}; K_{10} = \frac{K_7}{(1 - \mu_1 \cdot K_9)};$$

$$K_{11} = \frac{K_7}{(1 - \mu_1 \cdot K_9)}; K_{12} = \frac{K_7}{(1 - 2 \cdot k \cdot K_9/D_p - \mu_p \cdot d_p \cdot K_9)};$$

$$K_{13} = \frac{K_8}{(1 - 2 \cdot k \cdot K_9/D_p - \mu_p \cdot d_p \cdot K_9)}; K_{14} = \frac{K_9}{(1 - 2 \cdot k \cdot K_9/D_p - \mu_p \cdot d_p \cdot K_9)};$$

The adhesion force in the slide plane OB is determined by the formula:

$$F_{sc} = B_k \cdot L_{vn} \cdot \sin \psi_2 \cdot tga_{st} \cdot C / (tg \psi_2 - tga_{st}). \quad (18)$$

where C is the adhesion, specific tangential adhesion force per unit of slide plane area, Pa.

Weight G of the loosened sliding prism OA_1B hanging over the working area of the inclined bottom:

$$G = 0.5 \cdot \rho_m \cdot L_{vn}^2 \cdot B_k \cdot tg \psi_2 \cdot tga_{st} / (tg \psi_2 - tga_{st}). \quad (19)$$

where ρ_M is the soil density, kg/m^3 .

Simulation of loading the soil with a conveyor-bottom bucket working body will allow evaluating the efficiency of reducing the coefficient of friction of rocky soils on the working body bottom through the transition from sliding to rolling friction and determining the optimal parameters of the structural conveyor-bottom components for specific operating conditions.

4 Conclusion

1. To reduce the power consumption for loading the soil, technical solutions have been proposed for conveyor-bottom buckets solving the problem of reducing the coefficient of friction of rocky soils on the working body bottom through the transition from sliding to rolling friction while forming a new structural and technological group of bucket loading bodies. Developing this area may serve as an impetus for the development of new efficient machines and technologies.
2. A mathematical model of interaction of a conveyor-bottom bucket working body with the soil has been developed, which allows simulating the working process and analyzing the results.
3. Based on the developed analytical tool, the optimal parameters of the structural conveyor-bottom components can be determined for specific operating conditions, considering the minimization of power consumption for loading the soil as a target function of the problem being solved.

References

1. Kalmykov SG (1948) Kinematic and dynamic study of the scooping organ of a loading machine with a rolling handle. *Gorn zhur* 3
2. Ivanov OP (1952) Determination of the required weight of loading machines. *Tr NPI* t 23:22–27
3. Rodionov GV (1957) Some questions of the theory of the working cycle of rock loading machines of periodic action. *Questions of mechanization of rock loading: Sb. tr., GGI ZSF of the USSR Academy of Sciences-Novosibirsk* 19:177–201
4. Rodionov GV, Miherev PA (1957) Basic laws in the interaction of a bucket with a stack of bulk cargo. *Questions of mechanization of rock loading: Sb. tr., GGI ZSF of the USSR Academy of Sciences-Novosibirsk* 19:7–18

5. Kostylev AD (1957) Influence of the geometry of the bucket with the resistance to digging. Issues of mechanization of loading of rock: Sat. Tr., GGI ZSF OF THE USSR 19:55–70
6. Solov'ev AA (1958) Application of the mechanics of loose bodies to the determination of the forces of resistance to the introduction of a plane into a stack. bugle. in - ta, Kharkiv VI:279–297
7. Stogov VN (1959) Odnokovshovye loading machines. Metallurgizdat, Moscow, p 20
8. Silnya VG, Mikhailov VG (1961) On the theory of operation of the bucket loading body in the slope. Tr. NPI. Novocherkassk 130:5–17
9. Gagin OL, Ivanov OP (1970) Justification of the calculation model for describing the process of interaction of the working body of the loading machine with the bulk material stack. Research the loadin-sochnyh machines, transport facilities and their calculation: Sat. nauch. Tr. / NPI. Novocherkassk 214:122–124
10. Ereyskiy VD, Polezhaev VG, Ivanov OP (1975) K opredeleniyu resistantsii vnutrennii kovsha v sypuchiy material (To determine the resistance to the introduction of a bucket into a bulk material). Novocherkassk 313:93–95
11. Spivakovskiy AO, Dyachkov VK (1983) Transporting machines: a textbook for machine-building universities. Mashinostroenie, Moscow, p 487
12. Mushin SS (1984) Loading of ore self-propelled vehicles. Nauka, Alma-Ata, p 224
13. Balovnev VI (1994) Modeling of processes of interaction with the environment of working bodies of road-building machines. Mashinostroenie, Moscow, p 432
14. Lukin AM (2001) Formation of a compacted core on the frontal face of a knife in the process of scooping bulk material with a loader bucket. Trudy SibA-DI, SibADI Publishing House, Omsk, Issue 4, Ch. 4. Road and construction machines (research, testing and calculation), p 85–92
15. Komissarov AP, Sovershenstvovanie konstruktsii karyernykh hydrauliceskikh excavatorov (Improvement of designs of hydraulic mining excavators). Gorny informatsionno-analiticheskiy bulletin' 3:118–119
16. Tarasov VN, Boyarkina IV, Kovalenko MV (2004) Methods of analytical design of front-end loader working equipment. Constr Road Veh 4:37–41
17. Poderni RYu (2007) Mechanical equipment of quarries: textbook for universities, 6th ed., reprint. and extra. Moscow state mining University, Moscow, p 680
18. Ananin VG (2007) Determination of optimal parameters of working equipment of a quarry excavator with a mechanical drive. Constr Road Mach 6:36–38
19. Boyarkina IV (2011) Technological mechanics of single-bucket front loaders: monograph. SibADI, Omsk, p 336
20. Pavlov VP (2013) Methodology of automated design of excavators: models, methods, technologies: Monograph. LAP LAMBERT, Saarbruchen, Academic Publishing, Deutschland (printed by Schalungsdienst Lange o. H. G., Berlin), 2013, p 336
21. Sergeev VV, Kusov ZM, Marzoev TF (2014) Classification of methods and means of combating the sticking and freezing of minerals in the process of loading, transportation and delivery. Mining Equipment Electr Eng 8:21–30
22. Lyashenko YuM, Revyakina EA, Lyashenko AYu (2014) Loading bodies with a roller working surface of loading and transport complexes of non-metallic materials quarries. Mir Transp Technol Mach J Orel GUNPK 3(46):60–71
23. Lyashenko YuM, Shurygin DN, Revyakina EA (2017) Application of the laws of mechanics of granulated solids in studies to loader bucket interaction with bulk material stack. Procedia Eng 1388–1394

24. Lyashenko YuM, Revyakina EA (2018) Methodological approaches to modeling the system “loose body-working element” in the research of the process of loading rocks. *Mining Equipment Electr Eng* 3(137):15–20
25. Lyashenko YuM, Revyakina EA, Lyashenko AYu (2020) Bucket working bodies with a conveyor bottom: systematics and design features. *Adv Eng Res* 20(3):302–310



A Study of Vacuum Assisted Resin Injection for Molding Hard-To-Reach Locations in the Manufacture of Parts

N. S. Chashchin^(✉), A. P. Koval, and A. S. Gruzdev

Irkutsk National Research Technical University, 83, Lermontov Street, Irkutsk, Russia664074

Abstract. An increase in the share of composite materials is due to the possibility of obtaining mechanical properties superior to those of metals. One of the problems of the widespread application of composite materials is difficulties arising when choosing optimal reinforcement schemes and expensive manufacturing technologies. The most effective manufacturing technology is autoclave molding, but its disadvantage is high cost of manufacturing equipment. Therefore, many manufacturers use the vacuum infusion technology: the filler is impregnated with a binder composition, which makes it possible not to limit the duration of stack assembly, which is especially important when manufacturing large-sized and thick-walled products. The disadvantage of this technology is possible insufficient penetration of the binder into the fabric of hard-to-reach elements. This article discusses problems arising in the manufacture of products from the composite materials by the vacuum infusion method. Attention is paid to the problems of molding and impregnation of the leading and trailing edges of the product. The elements carry the base plane for joining two products. High requirements are applied to the geometry, accuracy, and rigidity of these elements.

Keywords: Vacuum assisted resin injection · Carbon fiber · Defects · Resin transfer molding

1 Introduction

The use of products made of composite materials is due to the development of manufacturing technologies, machining [1–3], and repair [4, 5] of these materials. Particular attention is paid to the process of manufacturing, as it facilitates the replacement of products from traditional materials with the composite ones. Currently, the following methods of manufacturing products from carbon fiber-reinforced polymer (carbon fiber) are used: autoclave molding [6–8] and vacuum assisted resin injection. Autoclave molding [9] is a process of manufacturing composites used in the aerospace industry. It ensures the process and material reliability by using high volume fiber components from the pre-manufactured materials. Autoclave molding has not become a mass production process due to the high labor intensity, long cycle duration, and high capital cost [10]. Therefore, the vacuum infusion technology [11] has become widespread in the manufacture of large-sized products, such as aircraft wings and boat hulls.

Vacuum infusion [12, 13] is complicated by hard-to-reach locations for binder compositions [14, 15], which cause voids and other defects [16, 17]. Various software modules are being developed and implemented to simulate the impregnation process [18, 19]. In [20], the author describes a technique for improving the process of laminating the material using magnetic clamps. This method is suitable for molding corners and edges. However, it is only applicable when working with the metal tooling. To reduce the share of scrap, additional operations such as the resin degassing technology [21] and the method of double vacuum bags [22, 23] are used.

2 Objectives

The research object is the manufacture technology for the center section of the flying wing using the monolithic mold of a negative type. For the convenience of manufacturing, the center section (Fig. 1a) is divided into upper and lower panels. When assembling the center section, the panels are connected to each other by an adhesive seam applied to the mating surfaces located along the leading and trailing edges.

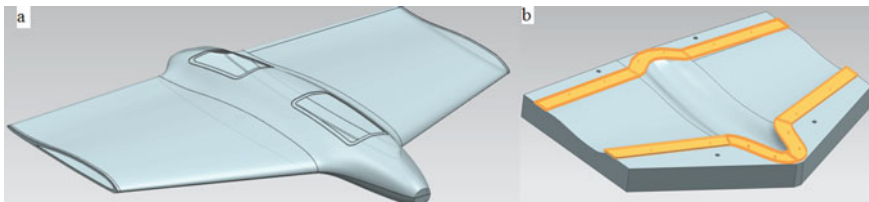


Fig. 1 a Central section, b mold overlays

Structurally, molding elements of the leading and trailing edges are flat overlays located along the leading and trailing edges of the working mold surface. The overlays have holes to install them on the mold block. The overlays installed on the mold are shown in Fig. 1b.

To obtain a mating surface, it is necessary to ensure that the fabric adheres to the working overlay surface. The outer contours of the panel are formed by a theoretical profile, which is dependent on the geometry of profiles that form it. The aerodynamic contour has a greater height in the center wing symmetry plane and a smaller one in the end chord plane. As a result, the distance from the interface is variable and decreases as the section plane moves away from the center wing symmetry plane. Thus, there is such a distance between the working overlay surface and the mold, at which it is necessary to use an additional element to ensure the adherence of the fabric to the working overlay surface due to the limited access for the tool used for straightening the fabric. To use the filler, the distance between the working overlay surfaces and the mold should be less than 10 mm. A geometric analysis of the tooling identified coordinates of the sections, limiting the areas of application of the filler for molding mating surfaces of the panel edges.

3 Experimental Details

The purpose of the experimental study is to develop a technology for laying materials in complex zones (Fig. 2) to form molding elements used for joining. Structurally, molding elements are flat overlays located along the leading and trailing edges of the working surface of the mold.

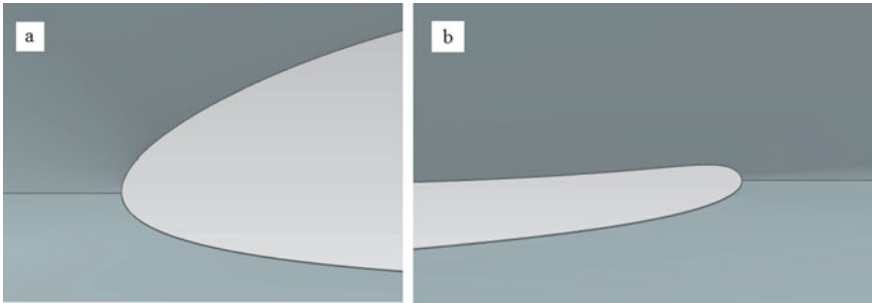


Fig. 2 a Mold interface along the leading edge, b mold interface along the trailing edge

Figure 2a shows the configuration of the profile in the leading edge region; the interface goes in such a way that there are no closed zones that impede the manufacture of the mold, as well as the recess of the finished part; the minimum radius of curvature of the surface is larger compared to that of the trailing edge surface shown in Fig. 2b. The configuration of the trailing edge was chosen in the same way as that of the leading edge. When laying the fabric and molding the panel, the tooling blocks were divided along the section plane and used separately from each other. Overlays installed on the mold blocks were used as carriers of the separation plane along the leading and trailing edges. The stages in the process of laminating fabric layers, installing ancillaries, and comparing panel molding approaches are described below.

Figures 3, 4 and 5 show the stages in the process of laminating fabric layers and installing the overlays in the manufacture of test edges of the panels. Initially, a layer of carbon fabric is laid on the mold surface (see in Fig. 3a). A layer retainer was used to temporarily fix the fabric layers to the mold.

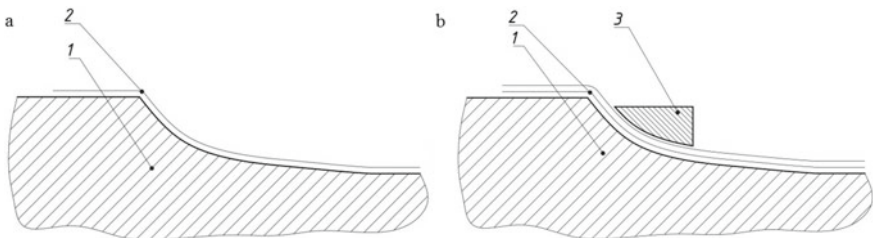


Fig. 3 1—mold, 2—carbon fabric, 3—foam filler a Lamination of carbon fabric layers, b lamination of the filler

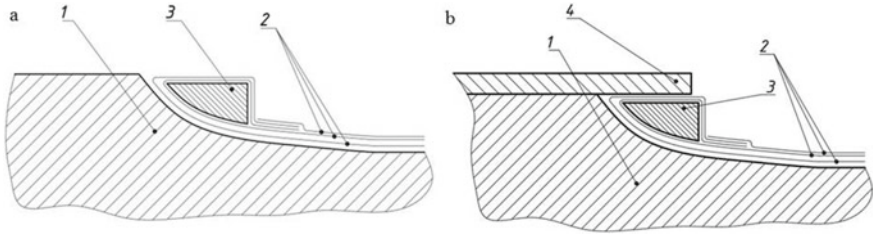


Fig. 4 1—mold, 2—carbon fabric layers, 3—foam filler, 4—overlay **a** Lamination of carbon fabric on the filler top, **b** installation of the overlay

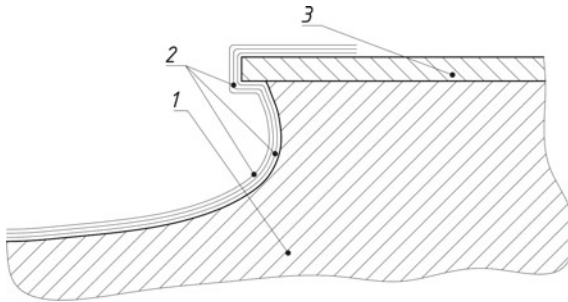


Fig. 5 1— mold, 2—carbon fabric layers, 3—overlay Lamination of carbon fabric along the leading edge

At the second stage, the foam filler was laminated along the trailing edge (see Fig. 3b). The overlays were removed.

At the third stage, the carbon fiber layer was laminated on the mold surface. The first and second layers were wrapped around the filler (Fig. 4a). The overlays were removed.

At the final stage, the overlays were installed, and the foam filler was fixed (Fig. 4b).

When molding the leading edge region, the carbon fabric layer was laminated on the mold surface (see Fig. 5). The layers were temporarily fixed with glue, sprayed locally in a thin layer on the most significant places (edges, locations where the radius of curvature of the surface is smallest).

4 Results

It was revealed that the areas of the edges under study were hard-to mold. Thus, to obtain a joint surface of the panels, two different methods were used (Fig. 6a, b) for each area. Under the limited access for the tool (Fig. 6a), impregnation with a binder composition (Fig. 6a, position 4) was partial due to the capillary effect of fabric fibers. This was an ineffective method which caused the occurrence of areas with a low content of epoxy resin (Fig. 6a, position 6). In the second option, several holes were made in the flat overlays for better passage of the binder composition (Fig. 6b). Thus, under the limited tool access, the edge area was impregnated more homogeneously.

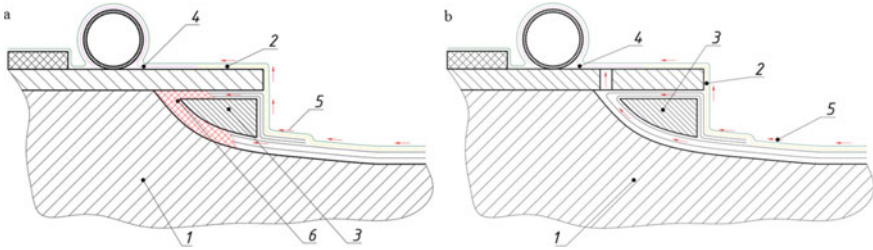


Fig. 6 1—mold, 2—conductive mesh+peel ply, 3—foam filler, 4—peel ply, 5—binder flow, 6—non-impregnated area of carbon fabric. Trailing edge impregnation pattern **a** using the capillary effect **b** using a perforated overlay

The filler is not laminated when molded areas of the edge are 10 mm (about 0.39 in) in height, as the edge geometry allows all layers to be conveniently compressed when assembling the stack. In Fig. 7a, the fabric is directly compressed by the vacuum bag under the influence of a pressure difference in the bag and in the environment. However, due to the insufficient compression of the fabric, mold defects occur at the edge (Fig. 7a, position 1). This is due to the insufficient supply of fabric needed for the full adherence to the mold. However, excess fabric can distort the weave structure and create folds, which have a negative effect on the properties of the laminate.

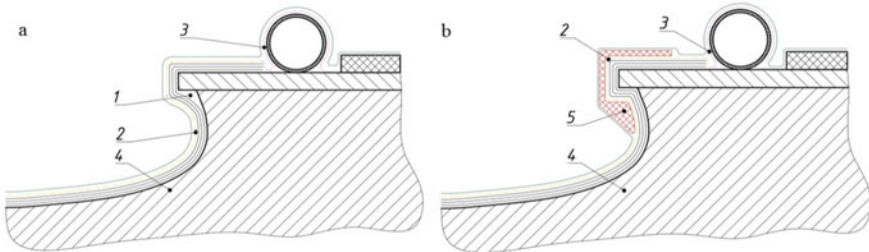


Fig. 7 1—Non-adherence of fabric to the mold, 2—conductive mesh+peel ply, 3—peel ply, 4—mold, 5—molding profile The scheme of molding edge sections and access for the tool without **a** and with **b** the molding profile

The second method is devoid of this drawback (Fig. 7b), since the fabric is supported by the molding profile (Fig. 7b, position 1), produced with the use of additive technologies. The molding profile ensures better adherence of fabric to the mold and reduces the likelihood of folds. The molding profile is curved around the edge and located under the vacuum bag, allowing pressure to be transferred from the vacuum bag to the fabric. The profile is fastened to the mold by three L-shaped clips, located at equal distances along the profile.

The scheme of molding edges providing tool access is shown in Fig. 7.

5 Discuss

When comparing different approaches to the molding of edges in hard-to-reach locations, it was found that the use of perforated overlays ensures better passage of the binder at the trailing edge of the panel. The use of specialized shaped profiles contributes to better adherence of fabric to the mold in the impregnation and polymerization of the binder composition of the leading edge.

References

1. Chashchin NS, Ivanov YN, Pashkov AE, Sturov AA (2018) Precise holes machining in multicomponent stacks from metals and CFRP. In: International conference “Aviamechanical engineering and transport”. <https://doi.org/10.2991/avent-18.2018.13>. Accessed 12 May 2018
2. Bobarica IO (2019) Elementy zcifrovoyh dvoynikov pri proektirovanii bespilotnogo letatel'nogo apparata (Elements of digital twins in the design of an unmanned aerial vehicle) Modern materials and advanced manufacturing technologies 2019. Abstracts of the international scientific conference, pp 94–95
3. Bobarica IO, Gruzdev AS, Koval AP (2018) Razrabotka sbornoy osnastki dlya isgotovleniya malozhestkih kompozitsionnyh detaley metodom vakuumnoy infoozii pri prototipirovanii (Development of prefabricated equipment for the manufacture of low-rigid composite parts by vacuum infusion during prototyping). In: All-Russian conference “Aviamechanical engineering and transport” (AVENT 2018), pp 5–10
4. Ivanov YN, Pashkov AE, Chashchin NS (2017) Optimization of hole generation in Ti/CFRP stacks 2018. IOP Conf Ser Mater Sci Eng 327(4):042043. <https://doi.org/10.1088/1757-899X/327/4/042043>
5. Sturov AA, Chashchin NS, Ivanov YN, Makaruk AA (2020) Ocenka vliyaniya rassloeniy na resurs detalej iz ugleplastika (Assessment of the delamination influence on the life limit of parts made of carbon fiber reinforced plastics) Modern technologies. Syst Anal Model 68:32–40. [https://doi.org/10.26731/1813-9108.2020.4\(68\).32-40](https://doi.org/10.26731/1813-9108.2020.4(68).32-40)
6. Stringer LG (1987) Optimization of the wet lay-up/vacuum bag process for the fabrication of carbon fibre epoxy composites with high fibre fraction and low void content. Composites 20(5):441–452
7. Sherwin GR (1999) Non-autoclave processing of advanced composite repairs. Adhes 155–159
8. Niggemann C, Song YS, Gillespie JW, Heider D (2008) Experimental investigation of the controlled atmospheric pressure resin (CAPRI) process J Compos Mater 42(11):1049–1061
9. Patel N, Lee LJ (1996) Modeling of void formation and removal in liquid composite molding part II: model development and implementation. Polym Compos 17(1):104–114
10. Afendi M, Banks WM, Kirkwood D (2005) Bubble free resin for infusion process. Compos Part A Appl Sci Manuf 36(6):739–746
11. Khan LA, Mahmood AH, Ahmed S (2013) Day Effect R.J of double vacuum bagging (DVB) in quickstep processing on the properties of 977–2A carbon - epoxy composites. Polym Compos 34(6):942–952
12. Andersson HM, Lundstrom TS, Gebaki BR, Ergren PSY (2003) To measure thickness variations in the vacuum infusion process. Polym Compos 24(3):448–455
13. Correia NC, Robitaille F, Long AC, Rudd CD, Šimáček P, Advani SG (2005) Analysis of the vacuum infusion moulding process: I analytical formulation. Compos Part A Appl Sci Manuf 36(12):1645–1656
14. Shih C, Lee LJ (2002) Analysis of void removal in liquid molding using microflow models, vol. 2, no. 1, Google Scholar

15. Kang KAI, Koelling K (2004) Void transport in resin transfer molding. *Polym Compos* 25(4):417–432
16. Chong HM, Liu SL, Subramanian AS, Ng SP, Tay SW, Wang SQ (2018) Out-of-autoclave scarf repair of interlayer toughened carbon fibre composites using double vacuum debulking of patch. *Compos Part A* 107:224–234
17. Moon C, Bang B, Choi W (2005) A technique for determining fiber content in FRP by thermogravimetric analyzer. *Polym Test* 24:376–380
18. American A, Standard N Standard test method for ignition loss of cured reinforced resins 1. Google Scholar, p 1–2
19. Sturov AA, Chashchin NS, Ivanov YN (2019) Service life testing of composite material. *IOP Conf Ser Mater Sci Eng* 632(1):012110 <https://doi.org/10.1088/1757-899X/632/1/012110>
20. Chashchin NS, Pashkov AE, Ivanov YN, Sturov AA (2019) Roughness of holes in metal and polymer composite bags. *IOP Conf Ser Mater Sci Eng* 632(1):012089 <https://doi.org/10.1088/1757-899X/632/1/012089>
21. Amirkhosravi M, Pishvar M, Altan MC (2017) Improving laminate quality in wet lay-up/vacuum bag processes by magnet assisted composite manufacturing (MACM). *Compos Part A* 98:227–237
22. Krehl WL, Gillespie J, Heider D (2004) Process and performance evaluation of the vacuum-assisted process. *J Compos Mater* 38(20):1803–1814
23. Beckwith Resin SW (2007) Infusion technology: Part 3 – a detailed overview of RTM and VIP infusion processing technologies. *SAMPE J* 6(4):66–70



Physicochemical Properties of Natural Gas and Oxygen Combustion Products at Diffusion and Kinetic Burning

G. V. Voronov and I. V. Glukhov^(✉)

First President of Russia B. Yeltsin Ural Federal University, 19, st., Mira, Yekaterinburg 620002, Russia

Abstract. The work provides comparison results of flare physicochemical properties of VG, Etalon Research and Production Company, VAI FUCHS and SMS DEMAG burners, ensuring diffusion burning at external natural gas mixing with process oxygen and kinetic burning at their premixing in the burner volume. The rapid burning length, variation of the temperature field and velocity, the maximum methane, hydrogen, carbon oxide concentrations throughout the flare length were defined using computer simulation in ANSYS 17.2 software, module CFX. Identical boundary parameters were stated for all burners. It was established that gas-oxygen burners used at the state-of-the-art operating arc steel furnaces are not meant for burning of the initial premixed blend as gaseous combustion is accompanied by the flare drawing into the burner interior with its subsequent failure. The burning conditions of natural gas with process oxygen in the state-of-the-art arc steel furnace operating space were proposed; they ensure rational heating of cold charge material and the melt with due account for the combustion product properties.

Keywords: Methane · Oxygen · Flare · Conditions · Diffusion · Mixing · Kinetic

1 Introduction

Diffusion burning of natural gas with process oxygen is considered provided that the gas mixture is generated in the furnace free space outside the burner. At the diffusion burning, the gas and the oxidizer are fed separately until they meet at the gas and oxidizer flow boundary; due to molecular diffusion, a mixture characteristic of laminar diffusion flame is formed at low flow rates or molar diffusion, contributing to large-scale turbulence formation inherent to turbulent diffusion flame at the Reynolds number of over 2310. The gas and oxidizer mixture is partially generated prior to its ignition and in the course of burning what causes significant difficulties at the process review. The combustion product temperature, composition, physical and thermophysical properties in the burning area separated from the initial mixture by the border, impact both the initial mixing stage and the chemical reaction velocity. The temperature in the diffusion flame front at equal diffusion heat (thermal conductivity) and gas and oxidizer mix

interdiffusion is the same with the burning temperature of the stoichiometric premixed blend. Such result is possible provided equal mass and thermal diffusivities with no heat losses to atmosphere. Basic concepts of the diffusion burning theory were developed and published in works [1–8]. At the current open flame furnaces, kinetic burning of natural gas with oxygen is implemented considering their design features, the process, heating and temperature conditions; the special feature of such burning consists in preparation of well-premixed blend. The mix preparation for burning is practically excluded from the cycle of subsequent physicochemical processes.

Burning conditions may be defined based on the distribution analysis of the combustible mixture components, particularly CH_4 , CO and H_2 , in the flare volume. In view of complicated experimentation to study the element distribution in the furnace operating space, the researchers increasingly tend toward the burning process computer simulation. For this purpose, the computational fluid dynamics (CFD) simulation software ANSYS CFX developed by ANSYS Inc. is well proven [9–12].

Let us illustrate natural gas diffusion and kinetic burning with oxygen in an arc steel furnace using the corresponding design burners.

2 Computer Simulation of Burning Process

To plot the combustible mixture component distribution field in the operating space, the ANSYS CFX Software Package is used; the analysis there is based on solution of the simultaneous transient equations for mass conservation, impulse and energy as well as the stream component transfer equations [13–19]. The burning process in the turbulent stream was analyzed using the extended coherent flamelet model (ECFM) on the preliminary developed 3D model of the furnace burner and the operating space. The heat transfer model was defined as the total energy. The equations were closed with the k - ε turbulence model. The ECFM model choice was determined by the most accurate analysis of the premixed fuel and oxidizer blend burning process [19]. The combustible mixture was generated using the CFX-RIF tool with determination of the fuel and oxidizer composition. The fuel and oxidizer temperature was preset at 288 K, and pressure in the furnace operating space was 1 atm. Heat transfer in the burner housing was neglected.

3 Comparison of Flare Properties at Kinetic and Diffusion Burning

Figure 1 shows burners of the Etalon Research and Production Company, SMS DEMAG, VAI FUCHS and VG burner with natural gas and oxygen mixing in the diffuser. The stated boundary parameters for all burners were identical:

- Process oxygen flow—0.553 kg/s with oxygen concentration of 95%, mas.;
- Methane flow—0.092 kg/s. (with methane concentration of 100%, mas.). Natural gas hydrocarbon composition was factored into the equivalent methane concentration.

Figures 2, 3, 4, 5 and 6 show evaluation results of the maximum CH_4 , CO , H_2 concentration, temperature and velocity variation throughout the flare length.

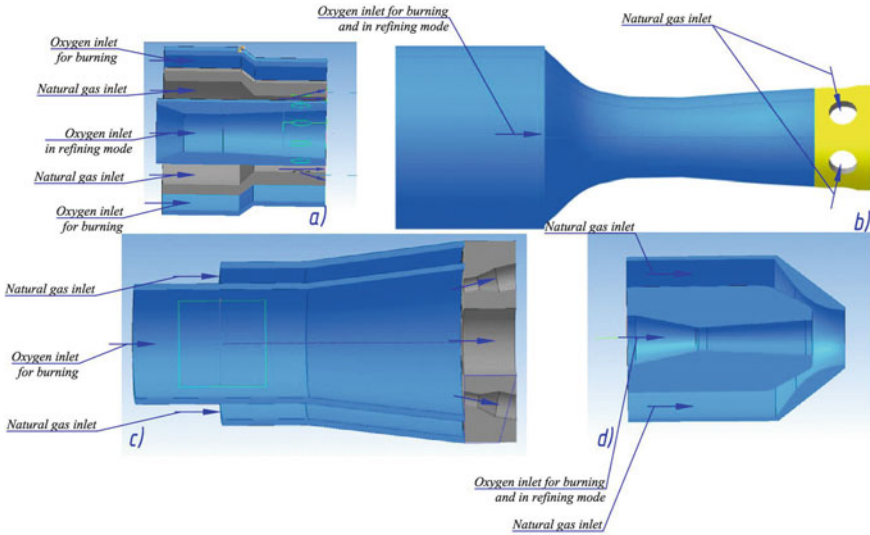


Fig. 1 Design versions of gas-oxygen burners evaluated by the computational method **a** VAI FUCHS burner, **b** VG version burner, **c** etalon research and production company burner; **d** SMS DEMAG burner

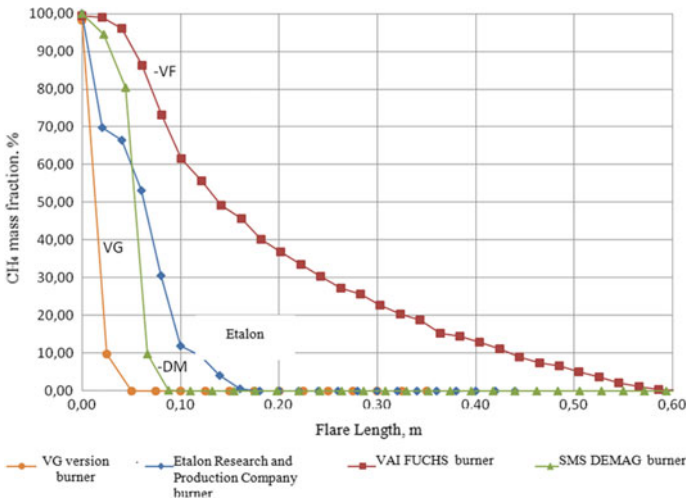


Fig. 2 Variation of the maximum CH₄ mass fraction in cross section of combustion product volume throughout the flare length of VG, etalon research and production company, VAI FUCHS and SMS DEMAG burners

In the flare rapid burning zone with the length of 100—200 mm of the VG burner in Figs. 2, 3, 4, the CH₄, CO and H₂ concentrations reach the minimum and indicate completion of the initial blend burning.

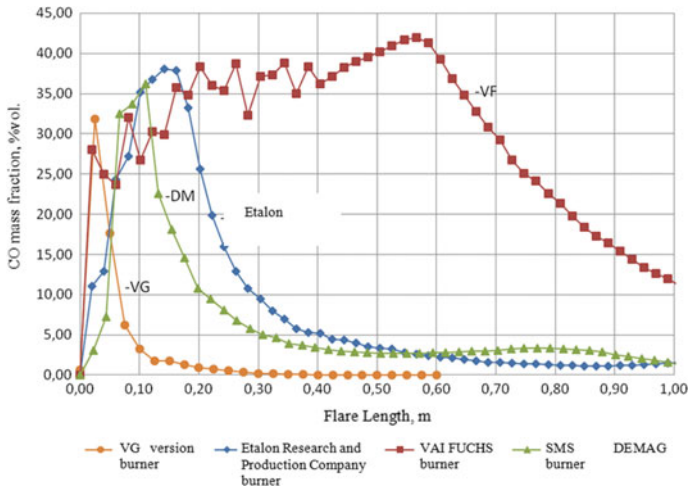


Fig. 3 Variation of the maximum CO mass fraction in cross section of combustion product volume throughout the flare length of VG, etalon research and production company, VAI FUCHS and SMS DEMAG burners

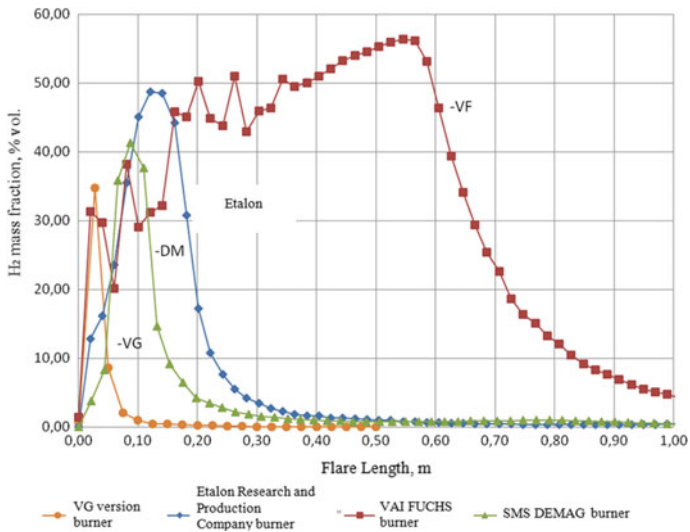


Fig. 4 Variation of the maximum H2 mass fraction in cross section of combustion products throughout the flare length of VG, etalon research and production company, VAI FUCHS and SMS DEMAG burners

The maximum temperature of the combustion products in the burner flare varies within 2757–2792 °C while the gas-dynamic flow velocity is measured in a broad range (Table 1). It should be noted that the VG burner combustion product temperature of 2776 °C corresponds to the gas-dynamic flow with the velocity of 1.15–3.75 times higher as compared to the burners creating the diffusion burning.

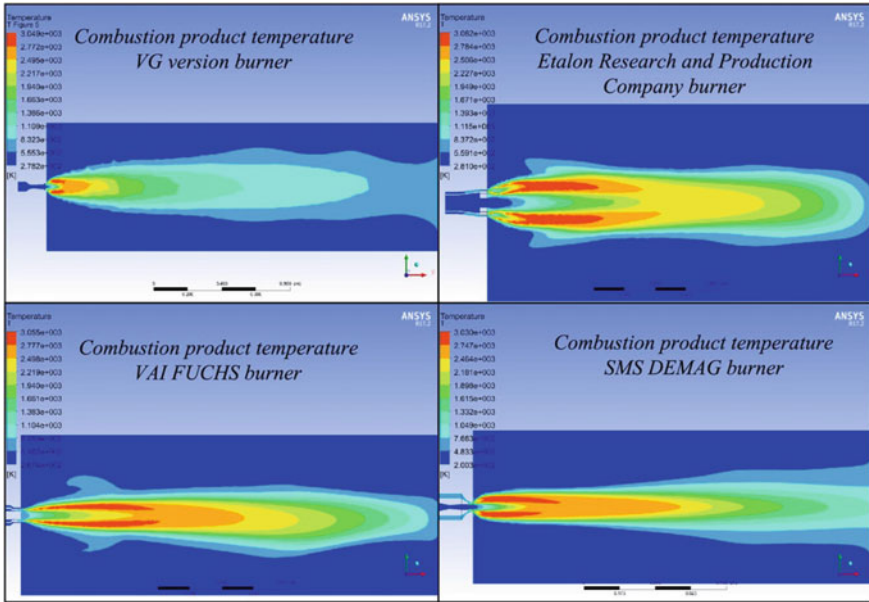


Fig. 5 Temperature fields of VG, etalon research and production company, VAI FUCHS and SMS DEMAG burner combustion products at natural gas burning with oxygen (O₂-95%)

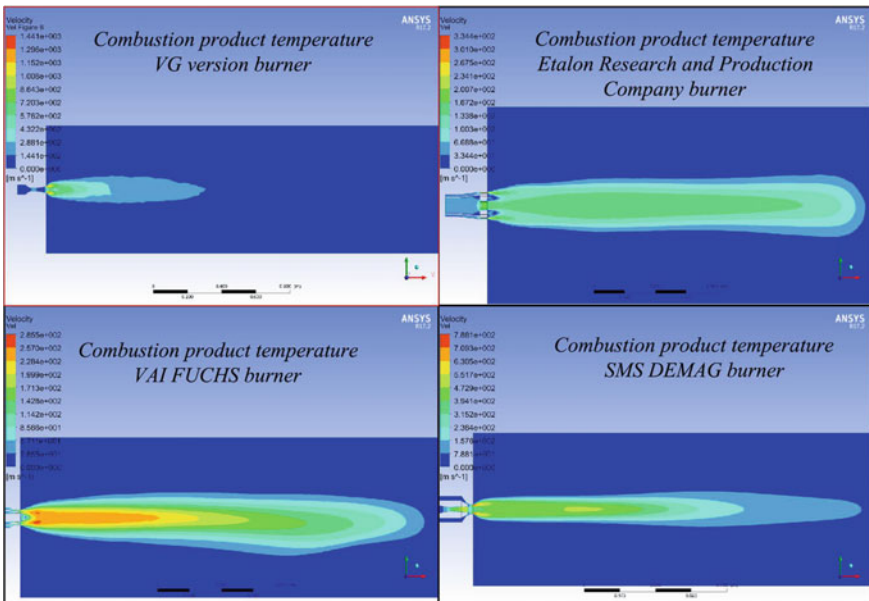


Fig. 6 Velocity fields of VG, etalon research and production company, VAI FUCHS and SMS DEMAG burner combustion products at natural gas burning with oxygen (O₂-95%)

Table 1 Burner performance

Parameter	VG version burner	Etalon research and production company burner	SMS DEMAG Burner	VAI FUCHS Burner
Maximum velocity of combustion products, m/sec	750	200	650	250
Rapid burning length, mm	100	500	300	Over 1000
Maximum temperature, K (°C)	3049 (2776)	3062 (2789)	3030 (2757)	3065 (2792)
Maximum hydrogen (H ₂) mass fraction in combustion products, %vol	35	49	41	56
Maximum carbon monoxide (CO) mass fraction in combustion products, % vol	32	38	36	42

4 Summary

The VG burner creating the kinetic burning of natural gas with oxygen ensures complete burning of the initial blend and rapid heating of charge materials just with combustion products with high temperature and gas-dynamic flow velocity.

References

1. Burke SP, Schumann TE (1928) Diffusion flames. . Ind Eng Chem 20(10):998–1004
2. SHvab VA (1948) Svyaz' mezhdru temperaturnymi i skorostnymi polyami gazovogo fakela (Relationship between temperature and velocity fields of a gas flare). Issledovanie processov gorennya natural'nogo topliva. Gosenergoizdat, Moscow-Leningrad, pp 231–248
3. YaB Z (1949) K teorii gorennya neperemeshannyh gazov (The theory of combustion gases unturned). ZHurnal teoreticheskoy fiziki 19:1199–1210
4. Hottel HC and Hawthorne WR (1949) Diffusion in Laminar Flame Jets. In: Third international combustion symposium, the combustion institute, Pittsburgh, PA, pp 254–266
5. Zel'dovich YaB (1944) Teoriya gorennya i detonacii gazov (Theory of combustion and detonation of gases). Izdatel'stvo akademii nauk SSSR, Moscow-Leningrad, p 71
6. Hitrin LN (1957) Fizika gorennya i vzryva (Physics of combustion and explosion). Izdatel'stvo Moskovskogo universiteta, Moscow, p 442
7. SHCHetinkov ES, (1965) Fizika gorennya gazov (Physics combustion of gases). Nauka, Moscow, p 739

8. YaB Z, Barenblat GI, Librovich VB, Mohviladze GM (1980) *Matematicheskaya teoriya goreniya i vzryva* (The mathematical theory of combustion and explosion). Nauka, Moscow, p 479
9. SHabliij LS, Zubanov VM and Stepanov DV (2016) Simulation methods of a burning process inside a rocket engine chamber. *Problemy i perspektivy razvitiya dvigatelestroeniya. Materialy dokladov mezhdunarodnoj nauchno-tehnicheskoy konferencii*, Samara, Jun, pp 95–96. (In Russ.)
10. Zohra KF, Mounir A, Salah C (2017) Numerical simulation of CH₄-H₂-AIR non-premixed flame stabilized by a bluff body. *Energy Procedia* 139:530–536. <https://doi.org/10.1016/j.egypro.2017.11.249>
11. Yeom J (2014) Diagnosis of the behavior characteristics of natural gas jet. *J Mech Sci Technol* 28(1):127–135. <https://doi.org/10.1007/s12206-013-0948-3>
12. Santosh Kumar TV, Alemela PR, Kok JBW (2012) Dynamics of flame stabilized by triangular bluff body in partially premixed methane-air combustion, in *Turbo Expo: Power for Land, Sea and Air*, pp 1017–1026. <https://doi.org/10.1115/GT2011-46241>
13. Voronov GV and Glukhov IV (2020) Thermal and physical properties of methane family hydrocarbon and oxygen combustion products. State-of-the-art arc steel furnace. In: *IOP conference series: materials science and engineering*, vol 969, no 1, pp 012043
14. Voronov GV, Glukhov IV and Plesakin IV (2020) Arc steel furnace operation at changing working space aerodynamic flows. *Mater Eng Technol Prod Process* 664–669
15. Gluhov IV, Mekhryakov DV, Voronov GV, Vdovin KM, Rybak AA, Taranov VV (2020) Energy saving in a modern arc steelmaking furnace DSP-120. *Stal' 5*:21–23 (In Russ.)
16. Limited Liability Company “Scientific and Technical Production Company” Etalon. http://www.ntpf-etalon.ru/gorelochnie_ustroystva. Accessed 21 Desem 2020
17. SMS GROUP. <https://www.sms-group.com>. Accessed 20 Desem 2020
18. Starcev VA (2004) Skrap karbyuratornyj process pri proizvodstve stali v martenovskih pechah (Scrap carburetor process in the production of steel in open hearth furnaces). *Iz-vo UGTU-UPI, Yekaterinburg*, p 225 (In Russ)
19. ANSYS CFX-Solver Theory Guide, Release 12.1. Canonsburg: Release 12.1, 2009, p 270



Development of the Solar Collector Orientation Mechanism Design

V. V. Boldyrev^(✉) and M. A. Gorkavyi

Federal State-Financed Educational Institution of Higher Learning Komsomolsk-Na-Amure State University, 27, prospect Lenina, Komsomolsk-Na-Amure, Russia681013

Abstract. The article proposes a new modular design of a vacuum solar collector with additional salt panels that are part of a common work surface, adapted to operating conditions in areas with low temperatures, rare but abundant precipitation in the form of snow, and a high building density of low-rise and mid-rise buildings, near which it is possible to place an array of vacuum collectors with a minimum length of the pipeline for transporting the heated coolant when they are fully located relative to each other. A configuration of a new vacuum manifold with design features aimed at adapting to external factors typical of the operating area with severe climatic conditions and high levels of insolation is proposed to ensure the maximum temperature of the coolant inside the vacuum tubes and reduce the losses of converted energy. A holder of the work surface of the collector is proposed, which provides the functionality of changing the direction of its center in nine directions, based on which it is possible to implement a tracking system for direct, scattered, and reflected solar radiation. The results of the study of the effectiveness of the developed functional model in real operating conditions on the territory of the settlement of the Far East of Russia in winter and spring are presented.

Keywords: Machine designs · Technological inheritance · Design adaptation · Solar collector · Modular design · Quality improvement · Manufacturability

1 Introduction

The available data on the increasing amount of energy produced using solar techniques indicate their growing spread, which stimulates research in the area of improving the solar technique efficiency, aimed at unlocking their potential. Solving the problem of insufficient use of the vacuum collector efficiency potential is one of the solar energy research areas. Vacuum collectors convert heat generated by any heat source and are suitable for energy sources other than the Sun. For such collectors, the issue of adapting the design to the operating conditions remains relevant since non-optimal configuration not only reduces the rated efficiency but also increases the risk of malfunctions, which is unacceptable, especially for solar systems forming the basis of the heat supply system.

In Russia, the practice of using vacuum collectors is most common in the positive temperature areas, which is largely due to the configurations of available industrial

prototypes adapted to mild operating conditions. According to the Global Engagement—Areas of Work—IEA study results, the number of solar hours and the level of solar radiation are higher in the low-temperature territories of Russia, where the heating cost issue is especially urgent. The vacuum collector potential is better unlocked just in cold climates, but this requires adapting the technology to the typical conditions of Russian low-temperature territories [1]. Earlier [2], a configuration has been proposed for the solar collector work surface holder adaptable to the position of the natural IR radiation source (the Sun), featuring a hemispheric base acting as a support for the reflector (and an element containing a heat-insulating layer with a heat exchanger inside) and pneumatic actuators setting the reflector inclination angle in nine directions. The holder proposed has a modular design, which allows changing the configuration to ensure the highest efficiency when working under certain operating conditions [3]. The northern populated areas of Russia are characterized by low temperatures and a high density of low- and mid-rise buildings, the roofs of which host many various heat radiation sources (e.g., surfaces heated by the Sun, heating mains, exhaust pipes, surfaces reflecting the Sun's rays, etc.). In [4, 5], the concept of a position-controlled vacuum solar collector control system is proposed, ensuring automatic orientation of its work surface's center toward the greatest total heat radiation from available sources.

In conjunction with the configuration of the holder providing the collector surface orientation in nine directions, such a control system [6] will be the most effective implementation of a vacuum solar collector to be operated in cities of the northern regions of Russia [7] and territories with similar climatic conditions. Since the collector work surface holder adaptable to the position of the natural infrared radiation source (the Sun) has a modular design, it can be adapted to operate under the conditions of low temperature, snow precipitation, and icing of the work surface to ensure the highest heat conversion efficiency and easy maintenance.

2 The Work Surface Design

The new vacuum manifold assumes support for reorienting the work surface center. Each reorientation is associated with additional energy consumption for the operation of the actuators adjusting the collector center rotation angle relative to the initial position. Therefore, it is advisable to ensure hardware support for energy-saving modules. Since the Sun is the main source of energy converted, solar panels will be used as energy-saving modules. They are suitable to convert radiation into electrical energy, which will be used by actuators, and the excess energy will be accumulated by other elements of the solar system the collector is coupled with. Solar panels are auxiliary modules aimed at minimizing the additional energy consumption for reorienting the collector's work surface and should take up a smaller part of the work surface. Figure 1 shows the design of the work surface of a vacuum manifold with energy-saving modules [8].

The work surface perimeter is built of four solar panels being separate monolithic blocks, which allows their prompt replacement in the case of failure. The block thickness allows accommodating electrical wiring and measuring device subsystems (in particular, IG22 series InGaAs photodiodes operating within the electromagnetic wavelength range of 500–2200 nm). The figure shows that the work surface has a concave shape required

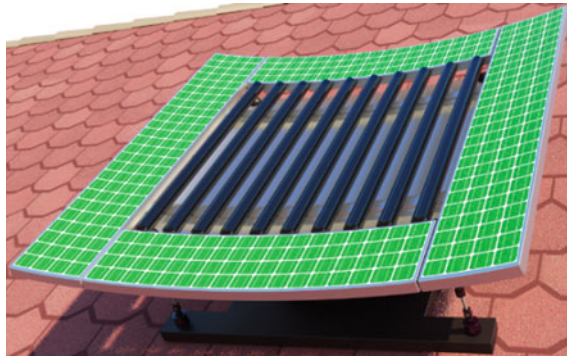


Fig. 1 Work surface design

to ensure an inclination angle of 45° —the recommended value for the best surface insolation in the Russian Far East. Also, such a shape allows accumulating sediments in a certain work surface zone and dumping them when the work surface center orientation changes.

The solar panels are mounted on a metal profile attached to the reflector located under the vacuum tubes. The reflector has a concave shape; the bending radius corresponds to the hemispheric base radius. Figure 2 shows the work surface mounts.

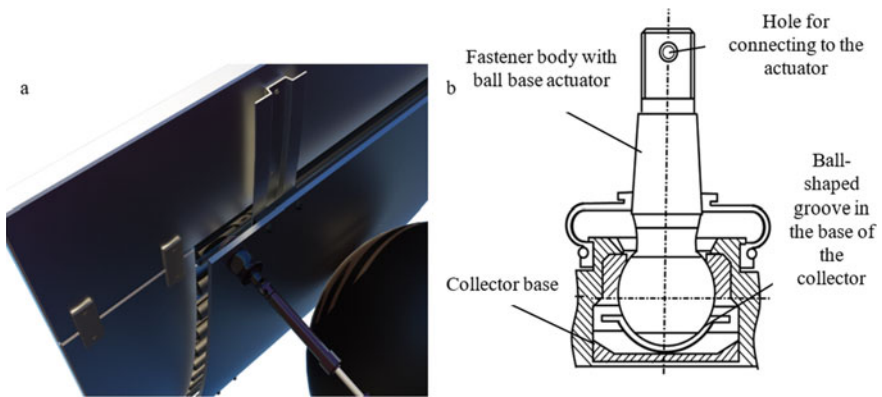


Fig. 2 a Work surface mounts, b fastener scheme

The mounting option proposed allows not disassembling the entire structure but replacing the individual elements, which, among other things, simplifies the device cleaning during operation. The figure also shows a massive hemispheric base. It is the main work surface support, which may weigh up to 70 kg (considering the weight of the work surface itself and the potential accumulation of precipitation).

3 The Base Design

The main vacuum collector purpose is converting thermal energy; therefore, the main part of the work surface should be occupied by vacuum tubes, while to minimize heat loss, the heating main length [10] (from vacuum tubes to the heat exchanger) should be minimal. To comply with these criteria, it has been proposed to arrange the tubes in the holder surface center and make them symmetrical and place the bulb with a heat pipe connected to the heat exchanger [11] to the center of the structure (Fig. 3).

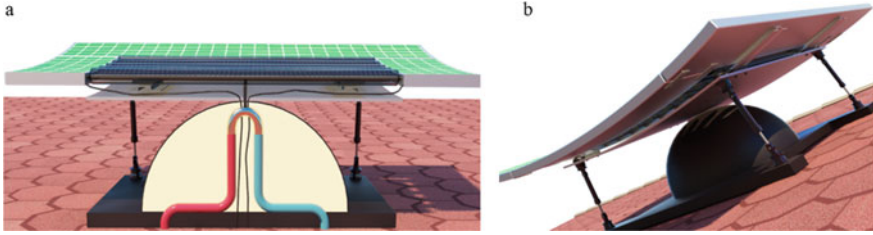


Fig. 3 a Base in section, b general base

The vacuum tube structure and operation principle correspond to the heat pipe type with the only difference in [12] the location of the heat pipe bulb. Such a solution allows inclining the work surface in any direction, in contrast to standard vacuum collectors with heat pipes, the inclination angle of which is limited to a single direction since the heat exchanger is placed at one of the tube ends, and to ensure effective thermodynamics inside the vacuum tube, the coolant should accumulate in its lower part. Such a vacuum tube structure assumes connecting to the heat exchanger through the central part of the structure.

In standard vacuum collectors, the heat exchanger [13] is placed outside the work surface and has an own heat-insulating layer (the thickness of which is adapted to certain operating conditions). This paper solves the problem of adapting vacuum collectors to operating conditions of low-temperature areas, so the heat-insulating layer thickness should be as large as possible. The zone of an interface between the bulb and the heat pipe and the heat exchanger is also important since the main transfer of the converted energy to the coolant inside the heated room occurs there. The new design integrates a heat-insulating layer with a heat exchanger in the base, ensuring the smallest energy transfer interface (heating main) length. The design proposed is also suitable for installing new vacuum collectors on the heated object roofs (Fig. 4).

The new vacuum solar collector configuration proposed supports various actuators [14, 15] (pneumatic, hydraulic, or electric linear actuators) ensuring the work surface orientation in nine directions. Orienting the surface center allows converting the energy of total heat radiation from all available sources (e.g., surfaces heated by the Sun, heating mains, exhaust pipes, surfaces reflecting the Sun's rays, etc.). To study the efficiency of the solutions proposed, a functional prototype was implemented, supporting the work surface orientation using an automated system of tracking the heat radiation sources (Fig. 5).

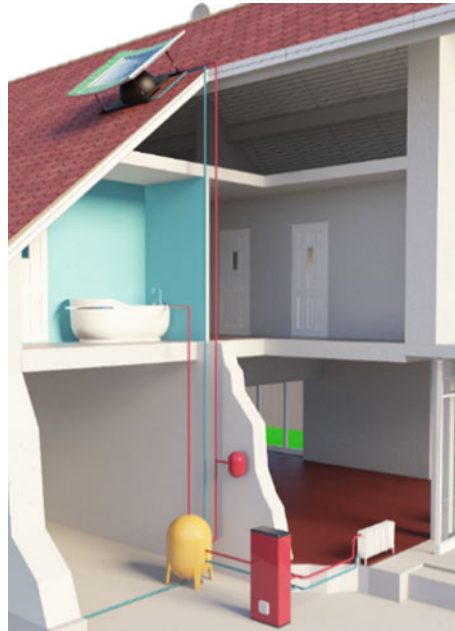


Fig. 4 Heating system connection

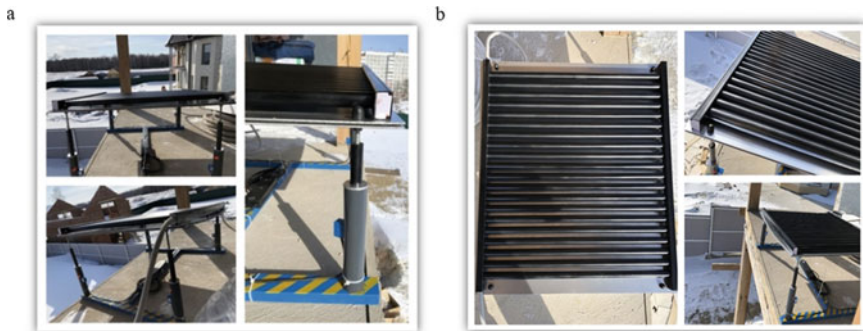


Fig. 5 Photos of the functional prototype

The studies have shown that the proposed solutions ensure the efficient operation of the solar system based on a new vacuum manifold under the following conditions:

The design proposed is a development of the solutions implemented in the collectors supporting the tracking system, where the work surface consists of solar panels only (not requiring heating main for a liquid coolant) and is suitable to ensure a similar functionality in terms of orienting the work surface toward the heat radiation source while considering the thermodynamics. The functional ability to orient toward any potential heat radiation sources allows converting thermal energy even in short solar days since some sources' temperature (exhaust pipes, windows, heated walls of premises, heating

mains, etc.) is independent of the Sun, and they provide additional heat radiation. The design proposed is modular and suits better to adapt collectors to certain conditions; it also simplifies the maintenance of the entire solar system. Per the totality of its characteristics, this solution surpasses its analogs on the market and can better unlock the potential of vacuum collectors in cold areas.

Table 1 Experimental conditions

Experiment conditions	Options
The geographic location of the reservoir	50°33' North 137°00' East
Duration	from January 5 to March 25
Ambient temperature range	from -35 °C to + 5 °C
Wind speed range	from 9 m/s to 27 m/s
The average level of insolation	4.5 kW/m ² per day
Average day length	7 h 21 min
Available heat sources	Sun, living room window (less than 1 m distance), chimney (1.5 m distance), reflected sunlight
Length of heating main	The collector is installed close to the heated room, the length of the heating main is less than 1 m
Tube material	Copper coated with an absorbent layer [7]
Number of tubes	20 pieces
Tube parameters	Diameter 38 mm, length 1000 mm, without insulation layer
Heat exchanger parameters	A similar tube is used as a heat exchanger connected to a hose going to the radiator located in the heated room
Reflector	Two aluminum sheets, 5 mm thick
Executive mechanisms	4 electric rods (work surface weight 11 kg)
The construction basis	Aluminum profile
Controller for ensuring the operation of an automated tracking system	Raspberry Pi 4 Model B 4 GB

References

1. Rakhmatulin IR, Kirpichnikova IM (2017) Analysis of the economic efficiency of the use of solar energy in the process of development of electrical and heat energy using the steam turbine in the territory of Russian federation. Cherepovets

2. Boldyrev VV (2018) Adaptable to the position of the natural source of infrared radiation (Sun), the holder of the work surface of the solar collector. RU patent 2018101835, 17 Jan 2018
3. Mohd MN, Jumaat SA, Jawa RA (2020) Dual-axis solar tracker with IoT monitoring system using Arduino. <https://doi.org/10.11591/ijpedes.v11.i1.pp451-458>
4. Boldyrev VV, Gorkavyy MA, Solovev DB (2019) Designing an adaptive software and hardware complex for converting solar energy. *Ind Eng Modern Technol Vladivostok*. <https://doi.org/10.1109/FarEastCon.2019.8934085>
5. Gorkavyy MA, Gudim AS, Efimov AY, Solovev DB (2018) Intelligent system for prognostication and optimization of power expenses of technological processes at robotized productions. *Ind Eng Modern Technol Vladivostok*. <https://doi.org/10.1109/FarEastCon.2018.8602503>
6. Boldyrev VV, Gorkavyy MA (2021) Development of an intelligent control system for an autonomous hybrid solar system. *Lecture Notes in Networks and Systems*. https://doi.org/10.1007/978-3-030-69421-0_11
7. Knysh LI (2014) Accounting method for absorber heat conductivity in a flat solar collector. *Life and Ecology*
8. Emmi G, Zarrella A, De Carli M (2017) A heat pump coupled with photovoltaic thermal hybrid solar collectors: A case study of a multi-source energy system. *Energy Convers Manag*
9. Solovyov AA, Solovyov DA, Shilova LA (2017) Solar converters of energy of atmospheric vortex flows
10. Fedosov SV, Fedoseev VN, Petrukhin AB, Oparina LA, Martynov IA (2018) Analysis of conditions when designing energy-saving heat pump systems for autonomous textile manufactures. *Volga*
11. Iwafune Y, Kanamori J, Sakakibara H (2017) A comparison of the effects of energy management using heat pump water heaters and batteries in photovoltaic -installed houses. *Energy ConversManag*
12. Bush KA, Palmstrom AF, Checharoen R, Moghadam MW (2017) 23.6%-efficient monolithic perovskite/silicon tandem solar cells with improved stability. *Nature Energy*. <https://doi.org/10.1038/nenergy.2017.9>
13. Falter CP, Pitz-Paal R (2017) A generic solar-thermochemical reactor model with internal heat diffusion for counter-flow solid heat exchange. *Sol Energy*. <https://doi.org/10.1016/j.solener.2017.01.063>
14. Burkov AF, Zaychenko IV, Goncharova SA (2019) Development of a comprehensive criterion for evaluating the ergonomics configuration of the seat. *Ind Eng Modern Technol Vladivostok*. <https://doi.org/10.1109/EastConf.2019.8725313>
15. Efimov A, Gorkavyy M, Gorkavyy A (2020) Predicting power consumption of robotic complex based on neuro-fuzzy system. *Appl Manuf Sochi*. <https://doi.org/10.1109/ICIEAM48468.2020.9112066>



Simulation and Calculation of Stress–strain State of Thin-Walled Structures Strengthened Under Load

M. N. Ubaydullov^(✉) and M. N. Serazutdinov

Kazan National Research Technological University, 68, K. Marks st., Kazan 420015, Russia

Abstract. This article presents a mathematical model and method for defining a stress–strain state of the thin-walled structures strengthened under load with the account of elastoplastic strains. The peculiarity of this paper is the fact the assessment of a stress–strain state of the strengthened structure is conducted with the account of changes in the section dimensions under load, the availability of the initial stresses and plastic strain occurrence in the system components. The presented model allows avoiding quite complex theoretical ratios occurring at the calculation of rods with a curvilinear longitudinal axis or a curvilinear profile. Are provide the results of the calculation of strengthening for the cantilever beam under the bending strain with torsion. The results obtained showed that when calculating without taking into account the warping of the cross sections of the bar, the resulting deformations and stresses are only elastic. In case the calculation was conducted with taking into account the warping, in the lower side flange of the rod I-section, a significant region of plastic strains occurs.

Keywords: Mathematical model · Thin-walled structures · Strengthening · Variational method · Warping of cross sections · Elastoplastic deformations · Stress–strain state

1 Introduction

It is known that damages and changes of the computational schemes of the objects under operation occurring in the structures during their strengthening causing the occurrence of constrained torsion of thin-walled components [1–9]. Note that mechanical engineering, aviation and construction industries are increasingly using thin-walled structures [10]. Therefore, to calculate the strengthening of thin-walled rod systems, it is relevant to develop a mathematical model and the method for defining a stress–strain state taking into account the characteristics of a strained thin-walled rod.

Simulating the processes of strain–stress state change at the strengthening is quite a complex problem especially if nonlinear processes occur. This is explained by the need to consider the changes in geometry, structure computational scheme and additional stresses occurring during strengthening [11–13]. For the foregoing reasons, the relevant issues are those that concern developing a mathematical model to assess the strain–stress state of the strengthened rod systems at linear and nonlinear strains.

2 Mathematical Model and Calculation Method

This article describes a variational method for defining a stress–strain state of the thin-walled structures strengthened under load with the account of elastoplastic strains. The peculiarity of this paper is the fact the assessment of a stress–strain state of the strengthened structure is conducted with the account of changes in the section dimensions under load, the availability of the initial stresses and plastic strain occurrence in the system components.

At the calculation, the author uses the basic assumptions and the relationships of the rod theory [14] and assumptions adopted in the theory of thin-walled rods, taking into account shifts [15].

The application of the presented model allows avoiding quite complex theoretical ratios occurring at the calculation of rods with a curvilinear longitudinal axis or a curvilinear profile. Also, it eliminates the need to apply any additional transformations or use any other methods to take into account eccentricities related to the selection of the coordinate origin of the ways of load application or structural components' connection.

As it is known, at the torsion of thin-walled rods, cross-sectional warping occurs. In the longitudinal axis Ox direction, additional displacement occurs from the warping of the section $u_k(x)$ which has the following form in compliance with the theory of thin-walled rods with the account of shifts.

$$u_k(x) = -\beta(x)\omega(y, z), \quad (1)$$

where $\beta(x)$ —function of measure of the warping; $\omega(y, z)$ —sectorial profile area.

To describe the rod strain, a local coordinate system $Oxyz$ is introduced into its cross sections. It has the axis Ox perpendicular to the cross-sectional plane (Fig. 1). It is assumed that the torsion center coincides with the coordinate origin $Oxyz$, while \bar{i} , \bar{j} , \bar{k} —unit vectors of the coordinate system.

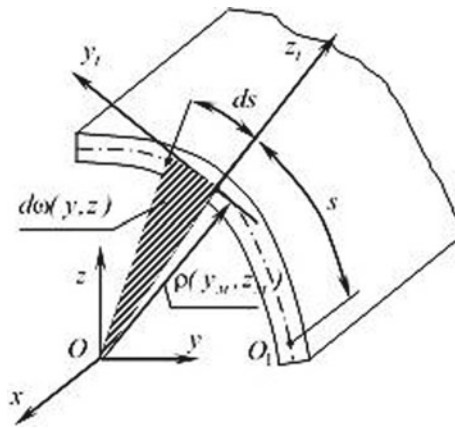


Fig. 1 Cross section of a thin-walled bar

To calculate the components of a stress–strain state, an additional local rectangular coordinate system [16] is introduced on a median surface of the rod cross section in the points $M(y_M, z_M)$. The system axes My_t, Mz_t are directed tangentially and flatwise to the rod section profile, and the axis Mx_t is perpendicular to the section (Fig. 1).

The strains of some point M in a local coordinate system My_tz_t are calculated by the formula

$$\bar{\varepsilon} = [L]\bar{u}^*, \tag{2}$$

where the displacement vector for thin-walled rod is written in the following form $\bar{u}^*(x, y, z) = \{u_1(x), u_2(x), u_3(x), \varphi_1(x), \varphi_2(x), \varphi_3(x), u_k(x)\}^T$.

The theory of thin-walled rods includes the hypotheses on the torque-free and no-pressure nature of longitudinal fibers. In compliance with these hypotheses, it is assumed $\gamma_{xz_t} = 0, \tau_{xz_t} = 0$, as well as stresses $\sigma_{y_t}, \sigma_{z_t}$ in the direction of axes My_t, Mz_t are equal to zero.

Therefore, in the cross sections of a thin-walled rod only, the stresses σ_x and τ_{xy_t} occur that is why a differential operator $[L]$ is made in the form

$$[L] = \begin{bmatrix} \frac{d}{dx} & 0 & 0 & 0 & z \frac{d}{dx} & -y \frac{d}{dx} & -\omega \frac{d}{dx} \\ 0 & t_y \frac{d}{dx} & t_z \frac{d}{dx} & (\rho(y, z) + 2z_t) \frac{d}{dx} & t_z & -t_y & -\rho(y, z) \end{bmatrix} \tag{3}$$

here $\rho(y_M, z_M) = y_M t_z - z_M t_y$ —length of a perpendicular line from the coordinate origin $Oxyz$ to the tangential line O_1M ; $\omega(y, z) = \omega(s) = \int_0^s \rho ds$; $\omega(y, z)$ —sectorial profile area; $t_y = dy/ds, t_z = dz/ds$ —directional cosines of the axes My_t, Mz_t ; $y = y_M + y_t t_y + z_t t_z, z = z_M + y_t t_z - z_t t_y$.

In case the strains occurring in the material are elastic, the stresses $\bar{\sigma}(x, y, z) = \{\sigma_x(x, y, z), \tau_{xy_t}(x, y, z)\}^T$ and strains $\bar{\varepsilon}(x, y, z) = \{\varepsilon_x(x, y, z), \gamma_{xy_t}(x, y, z)\}^T$ are interconnected by linear ratios:

$$\bar{\sigma}(x, y, z) = [D]\bar{\varepsilon}(x, y, z), \tag{4}$$

where

$$D = \begin{bmatrix} E & 0 & 0 \\ 0 & G & 0 \\ 0 & 0 & G \end{bmatrix}, \bar{\varepsilon} = [L]\bar{u}^*. \tag{5}$$

In case of occurring elastic–plastic strains, it is assumed that the structure material complies with the Prandtl diagram (Fig. 2). The authors apply the Huber-Mises-Hencky plasticity condition: $\sigma_i = E\varepsilon_i$ at $\varepsilon_i \leq \varepsilon_y$ and $\sigma_i = \sigma_y$ at $\varepsilon_i \geq \varepsilon_y$, where

$$\sigma_i = \sqrt{\sigma_x^2 + 3(\tau_{xy}^2 + \tau_{xz}^2)}, \varepsilon_i = \frac{1}{3} \sqrt{4\varepsilon_x^2 + 3(\gamma_{xy}^2 + \gamma_{xz}^2)}. \tag{6}$$

The displacement of components of the reinforced rod structure consisting of the N rod components (Fig. 3) is defined from the solution of the Lagrange variation equation in the form

$$\sum_{i=1}^N (\delta U_i^{el} + \delta U_i^{pl} - \delta W) = 0, \tag{7}$$

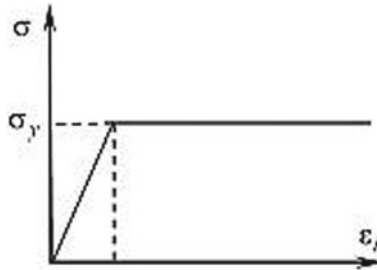


Fig. 2 Prandtl's diagram

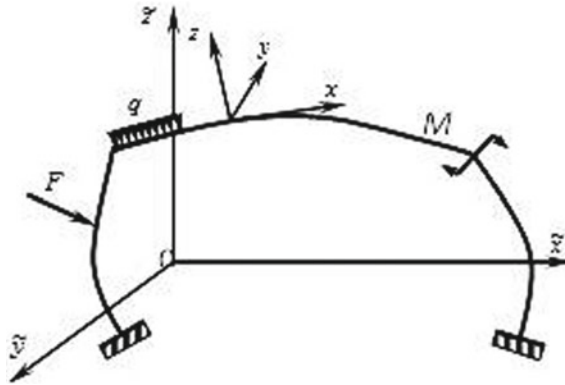


Fig. 3 Computational model of a bar system

where δU_{el} —variation of the potential energy of the rod system strain in the area of elastic strains; δU_{pl} —variation of the potential energy of the rod system strain in the area of plastic strains; δW —variation of the work of external forces.

To define the unknown components of the displacement vector $u_1(x)$, $u_2(x)$, $u_3(x)$, rotation angles' vector $\varphi_1(x)$, $\varphi_2(x)$, $\varphi_3(x)$ and warping measure $\beta(x)$ of rod cross-sections, the authors introduce a local xyz and a global orthogonal coordinate system $\tilde{x}\tilde{y}\tilde{z}$. The axis x of a local coordinate system is directed tangentially to the rod axis. The components of rod points' displacement in a global coordinate system are expressed in the form $\bar{u} = \{\tilde{u}_1(x), \tilde{u}_2(x), \tilde{u}_3(x)\}^T$; $\bar{\varphi} = \{\tilde{\varphi}_1(x), \tilde{\varphi}_2(x), \tilde{\varphi}_3(x)\}^T$; $\bar{\beta} = \tilde{\beta}(x)$, defined in the system of coordinates $0\tilde{x}\tilde{y}\tilde{z}$.

At the definition of the stress–strain state, the rod structure is divided into N sections in such a way that the rod longitudinal axis is not bifurcated at each section [17, 18]. At each of these displacement sections \tilde{u}_1 , \tilde{u}_2 , \tilde{u}_3 , both rotation angles $\tilde{\varphi}_1$, $\tilde{\varphi}_2$, $\tilde{\varphi}_3$ and the warping measure β are represented in the form of rows in a global coordinate system:

$$\tilde{u}_k(x) = \tilde{u}_k^i(t) = \sum_{m=1}^M C_{km}^i f_m(t), \tilde{\varphi}_k(x) = \tilde{\varphi}_k^i(t)$$

$$= \sum_{m=1}^M D_{km}^i f_m(t), \beta^i(x) = \beta^i(t) = \sum_{m=1}^M B_m^i f_m(t) \tag{8}$$

where $t = x/l_i$ ($0 \leq t \leq 1$); x —coordinates of the rod longitudinal axis measured from the section beginning; l_i —length of the section longitudinal axis with the number i ; C_{km}^i , D_{km}^i , B_m^i —unknown constants, $f_m(t)$ —approximating functions; $k = 1, 2, 3$; $i = \overline{1, N}$, N —number of the specified sections of the rod system, M —number of the row members.

To obtain the solution, the authors use the approximating function systems.

$$f_1(t) = 1 - t, f_2(t) = t, f_m(t) = (1 - t)t^{(m-2)}, m = \overline{3, M}. \tag{9}$$

The representation of vector components \bar{u} , $\tilde{\varphi}$ and $\tilde{\beta}$ in the form of the ratios (4) allows easily conducting geometrical interface conditions and the joining conditions of the required displacements, rotation angles and the twist measure of rods at the interfaces of rod system sections. To obtain a high-precision solution, one does not require to divide the rod structure into a large number of sections; instead, one should include a necessary number of the members of the row M members into (8).

The calculation for the structure strengthened under load consists of two stages.

At the first stage using the method [19, 20], the author defines the displacements and stresses occurring during the strengthening because of the action of initial loads.

Further, at the second stage, the author defines the stress–strain state of a thin-walled structure after strengthening. To do this, the variations from (7) δU_i^{el} and δU_i^{pl} are written with the account of repair (initial) stresses $\bar{\sigma}_r = \{\sigma_x^r, \tau_{xy}^r\}T$ in effect during strengthening

$$\delta U^{el} = \int_{l_{el}} \left[\iint_{A^s} (\bar{u}^{*T} [L]^T [D][L] \delta \bar{u}^*) dA + \iint_{A^d} (\bar{\sigma}_r^T [L] \delta \bar{u}^*) dA \right] dx, \tag{10}$$

$$\delta U^{pl} = \int_{l_{pl}} \left(\iint_{A_{el}^s} (\bar{u}^{*T} [L]^T [D][L] \delta \bar{u}^*) dA + \iint_{A_{el}^s} (\bar{\sigma}_p^T [L] \delta \bar{u}^*) dA + \iint_{A_{pl}^s} (\bar{\sigma}_{\pi\pi}^T [L] \delta \bar{u}^*) dA \right) dl, \tag{11}$$

where l_{el} , l_{pl} —lengths of the rod system sections where only elastic and elastic–plastic strains occur, correspondingly; A_{el}^s , A_{pl}^s —correspondingly, the areas of the sections of elastic and plastic strains of the strengthened rod section; A_{el}^d —areas of the sections of the damaged structure components; $\bar{\sigma}_{pl}^T = \{\sigma_x^{pl}, \tau_{xy}^{pl}\}$ —vector of the stresses occurring in the area of plastic strains, where $\sigma_x^{pl} = \sigma_x/K$, $\tau_{xy}^{pl} = \tau_{xy}/K$, $K = \sigma_i/\sigma_y$; σ_y —material yield strength.

Variation of the work of external forces

$$\delta W = \int_{l_q} \bar{q}^T \delta \bar{u}^* dl + \sum_{j=1}^J \bar{F}_{ij}^T \delta \bar{u}^*(x_{ij}^*), \quad (12)$$

where $\bar{q}^T = \{q_1(x), q_2(x), q_3(x), m_1(x), m_2(x), m_3(x),\}$ —external load distributed over the section l_q ; $\bar{F}_{ij}^T = \{F_{1j}, F_{2j}, F_{3j}, M_{1k}, M_{2k}, M_{3k}\}$ —concentrated forces and moments acting in the points with the coordinates x_j^* and x_k^* .

Substituting the expressions (10)–(12) into a variation condition (7) with the account of the ratios (8 and 9) and the satisfaction of the joining conditions $\bar{u}(x)$, $\bar{\varphi}(x)$, $\beta(x)$ on the interfaces of the rod system sections, obtain the system of algebraic equations

$$[K] \bar{C} = \bar{F}, \quad (13)$$

where $[K]$ —matrix of the rod structure stiffness; \bar{C} —vector of unknown coefficients $C_{km}^i, D_{km}^i, B_m^i$; \bar{F} —vector depending on external loads.

Using the solution of the system of Eq. (13), the author defines unknown displacements of the strengthened structure components. Further, applying the ratios (4 and 5), the author calculates the strains $\varepsilon_x, \gamma_{xy_i}$ and stresses σ_x, τ_{xy_i} . After that, the author defines the internal forces and moments occurring in the cross sections of a thin-walled rod after strengthening.

To calculate the integrals in (10 and 12), the author conducts numerical integration along the length and the area of sections of the rod system components. The cross sections of the structure components can be complex and consisting of various forms in the form of a circumference, rectangle and rolled sections. That is why, to define the integrals included in (10 and 12), the author applies special methods [18, 20].

The application of the numerical integration algorithm allows numerically defining the areas of plastic and elastic strains in a strengthened rod system. As the position of the plastic strain regions in the rods is unknown in advance, to obtain the regions, one should use the iteration method. At the first iteration, the strains are considered elastic. During the further iterations, each integration point (y_j, z_j) is checked for the fulfillment of the plasticity condition $\sigma_x < \sigma_y$. The iteration process is finished at the fulfillment of the condition $(\varepsilon(n)_{\max} - \varepsilon(n-1)_{\max}) / \varepsilon(n)_{\max} 100\% \leq \Delta$, where Δ —given error.

3 Results of Calculations

Provide the results of the calculation of strengthening for the cantilever rod under the bending strain with torsion (Fig. 4). The section of a strengthened rod is provided in Fig. 5.

The material of the main and strengthening elements—St. 3 ($\sigma_y = 240 \text{ m}\Pi\text{a}, E = 2 \cdot 10^5 \text{ m}\Pi\text{a}, G = 8 \cdot 10^4 \text{ m}\Pi\text{a}$). Before strengthening, a torque moment $M^r = 4 \text{ kNm}$ and concentrated force $F^r = 100 \text{ kN}$ were affecting the rod. After the strengthening, the additional moment $\Delta M = 6 \text{ kNm}$ and additional load $\Delta F = 50 \text{ kN}$ are applied to the

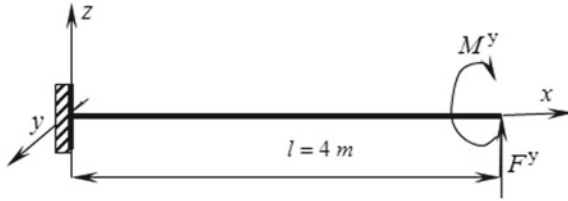


Fig. 4 Computational model of a rod

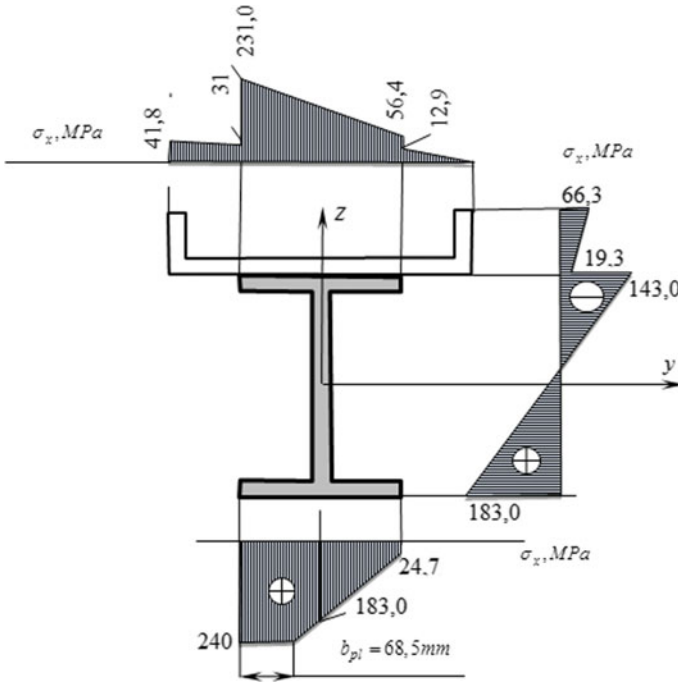


Fig. 5 Normal stress diagram σ_x

specified rod. Total loads on the rod after strengthening will correspondingly be equal to $N^s = 10\text{ kNm}$ and $F^s = 150\text{ kN}$.

The results of the calculations conducted both with/without the account of rod section twist are provided in Table 1 as well as in the form of the diagram of normal stresses in the most loaded rod section (Fig. 5).

4 Conclusions

The data presented show that, when calculating without taking into account the warping of the cross sections of the bar, the resulting deformations and stresses are only elastic ($A_{pi} = 0$). In case the calculation was conducted with taking into account the warping

Table 1 Results of calculations

The results of calculations for the rod at the action of repair loads $M^r = 4 \text{ kN m}$, $F^r = 100 \text{ kN}$				
Calculated parameters	Rotation angle	Measure of the warping	Bimoment	Area of the plastic strain region
	φ_1 , radian	β , 1/m	B , $\text{kN} \cdot \text{m}^2$	A_{pl} , m^2
Without taking into account the warping of the section	0.0781	–	–	0
Taking into account the warping of the section	0.0495	0.0169	5.85	0
The results of calculations after rod strengthening at load action $M^s = 10 \text{ kN} \cdot \text{m}$, $F^s = 150 \text{ kN}$				
Calculated parameters	φ_1 , radian	β , 1/m	B , $\text{kN} \cdot \text{m}^2$	A_{pl} , m^2
	Without taking into account the warping of the section	0.102	–	0
Taking into account the warping of the section	0.0703	0.0232	11.6	0.00137

of the section, as it is seen from the stress diagram (Fig. 5), a significant region of plastic strains occurs in the lower side flange of the rod I-section ($A_{pl} = 0,00137 \text{ m}^2$).

Therefore, the account of the rod section warping has a significant impact on the characteristics of the stress–strain state of thin-walled rods. It appears that in the cases, similar to the one considered in the example, without taking into account the warping, it is even impossible to forecast plastic strains in a strengthened rod.

References

1. Astakhov IV (2006) Prostranstvennaya ustojchivost' elementov konstrukcij iz holodnognutyh profilej (Spatial stability of the components of structures made of cold formed profiles). Dissertation, Saint-Petersburg
2. Belyi GI (1983) Raschet uprugoplasticheskikh tonkostennyh sterzhnej po prostranstvenno-deformirovannoj skheme (Calculation of elastic-plastic thin-walled rods on spatial-strained model). Structl Mech Constructions 42:40–48
3. Belyi GI (1985) O raschete uprugoplasticheskikh tonkostennyh sterzhnej po prostranstvenno-deformirovannoj skheme s uchetom kasatel'nyh napryazhenij i deformacii sdviga (On the calculation of elastoplastic thin-walled rods according to a spatially deformed scheme taking into account shear stresses and shear deformation). Steel structures and testing of structures, pp 10–23
4. Tusnin AR (2003) Raschet i proektirovanie konstrukcij iz tonkostennyh sterzhnej otkrytogo profilya (Calculation and design of structures from thin-walled rods of an open profile). Dissertation, Moscow

5. Tusnin AR (2009) Chislennyj raschet konstrukcij iz tonkostennyh sterzhnej otkrytogo profilya (Numerical calculation of structures from thin-walled rods of an open profile). Publishing house ASV, Moscow
6. Cheng Y, Schafer BW (2007) Simulation of cold-formed steel beams in local and distortional buckling with applications to the direct strength method. *J Constr Steel Res* 63:581–590
7. Hancock GJ (2009) Compression tests of high strength cold-formed steel channels with buckling interaction. *J Constr Steel Res* 65:278–289
8. Pyatkin PA (2000) Prochnost' i prostranstvennaya ustojchivost' usilennyh pod nagruzkoy sterzhnevyyh elementov konstrukcij otkrytogo profilya (Strength and spatial stability of open profile bar elements strengthened under load). Dissertation, St. Petersburg
9. Rybakov VA (2012) Primenenie polusdvigovoj teorii V.I. Slivkera dlya analiza napryazhenno-deformirovannogo sostoyaniya sistem tonkostennyh sterzhnej (Application of the semi-shear theory of V.I. Slivker for analysis of the stress-strain state of systems of thin-walled rods). Dissertation, Saint-Petersburg
10. Vatin NI, Popova EN (2006) Termoprofil' v legkih stal'nyh tonkostennyh konstrukciyah (Thermoprofile in light steel thin-walled structures). Publishing House of Polytechnic University, Saint-Petersburg
11. Serazutdinov MN, Ubaydulloyev MN (2012) Modelirovanie usileniya nagruzhennyh sterzhnevyyh sistem (Modeling of amplification of loaded rod systems). In: Abstracts of the IV International Symposium, SUSU
12. Serazutdinov MN, Ubaydulloyev MN (2012) Usilenie nagruzhennyh sterzhnevyyh konstrukcij s uchetom vliyaniya remontnyh i montazhnyh sil (Amplification of loaded bar structures taking into account the influence of repair and assembly forces). *Inzhenerno-stroitelnyj zhurnal* 1(27):98–105
13. Serazutdinov MN, Ubaydulloyev MN (2016) Method of calculation of strengthening of the loaded rod structures taking into account plastic deformations. *Procedia Eng* 150:1741–1747
14. Tymoshenko SP, To Hera J (1976) Mekhanika materialov (Mechanik of materials). Mir, Moscow
15. Slivker VI (2005) Stroitel'naya mekhanika. Variatsionnyye osnovy. Uchebnoye posobiye. (Structural mechanics. Variation bases. Manual). Izdatelstvo Assotsiatsii stroitelnykh vuzov, Moscow
16. Serazutdinov MN (2013) Variacionnye sootnosheniya teorii tonkostennyh sterzhnej otkrytogo profilya (Variational ratios of theory of thin-walled open profile rods). *Bull Kazan Technol Univ* 5:216–223
17. Serazutdinov MN, Khairullin FS (1991) Metod rascheta krivolinejnyh sterzhnej (Method for calculating curved bars) *Izv. universities. Constr Archit* 5:104–108
18. Serazutdinov MN, Ubaydullov MN (2016) Variatsionnyy metod rascheta pryamolineynykh i krivolineynykh tonkostennykh sterzhney: monografiya (Variational method for calculating rectilinear and curvilinear thin-walled rods: monograph). *Kazan Nat. Research Technol. Un-t., Kazan*
19. Serazutdinov MN, Ubaydulloyev MN, Abragim KhA (2011) Povyshenie nesushchej sposobnosti usilivaemyh nagruzhennyh konstrukcij (Increasing the bearing capacity of the strengthened loaded structures). *Struct Mech Eng Constructions Build* 3:23–30
20. Ubaydulloyev MN, Serazutdinov MN (2012) Modelirovanie napryazhenno-deformirovannogo sostoyaniya usilivaemyh sterzhnevyyh sistem (Modeling of the intense deformed condition of the strengthened rod systems). *Struct Mech Eng Constructions Build* 43–51



Assessment of the Quality of the Coupling Billet for Tubing

A. V. Vladimirov^(✉) and G. A. Orlov

Ural Federal University named after the first President of Russia B.N. Yeltsin, 19, st. Mira,
Yekaterinburg 620002, Russia

Abstract. The article uses an approach to assessing quality using complex quality indicators. The calculation of complex indicators of the quality of hot-rolled sleeve billet for tubing is considered. Comparison of weighted average arithmetic and geometric complex indicators is carried out. In the modern world, an integrated approach to assessing the quality of metal products, based on the principles of a relatively new science—qualimetry, has been significantly developed. For a comprehensive assessment of quality, two approaches are most often used: the first provides for the standardization of quality indicators in the interval (0 ... 1), corresponding to the spread of permissible values of properties. This approach was implemented by us earlier to analyze the quality of some types of metal products. The second approach estimates the probability of properties falling into the required range and is not considered in this article yet, since the analysis of significant arrays of production data is required. This article implements the first approach and is devoted to identifying the reserves for improving the quality of the coupling billet for tubing.

Keywords: Tubing · Pipe rolling unit · Sleeve billet · Comprehensive quality assessment · Quality indicators

1 Introduction

On the pipe rolling unit of JSC Sinarsky Pipe Plant with a tandem automatic mill, pipes made of carbon and alloy steel grades of critical use are rolled: pumping, compressor, drilling, casing, for power engineering with a diameter of 73–168 mm with a wall thickness of 5–20 mm. The pipe rolling mill-140 (PRM-140) includes an automatic tandem mill, which consists of two successive longitudinal rolling stands (SPP-1 and SPP-2).

The technological process for the production of seamless hot-deformed pipes at PRM-140 is a series of sequential operations. The main ones are: preparation of metal for rolling; heating the metal before rolling; stitching the workpiece into the sleeve; rolling pipes on an automatic tandem mill; rolling in rolling machines; metal heating; calibration or reduction of pipes, their cooling; finishing; acceptance and delivery of suitable pipes in finished goods warehouses [1]. Further, to obtain the required properties, the pipes are heat-treated. After heat treatment, the pipes are straightened on a straightening mill.

Then, the pipes go for ultrasonic testing. Pipes that comply with the normative and technical documentation are delivered to the T-4 workshop for cutting couplings. A distinctive feature of modern tube-rolling plants and mills is their increasing productivity and high level of automation. The desire to increase productivity is combined with the demand for high-quality products.

In the modern world, an integrated approach to assessing the quality of metal products, based on the principles of a relatively new science—qualimetry, has been significantly developed [2]. For a comprehensive assessment of quality, two approaches are most often used: the first provides for the standardization of quality indicators in the interval (0 ... 1), corresponding to the spread of permissible values of properties [2, 3]. This approach was implemented by us earlier to analyze the quality of some types of metal products [4–6]. The second approach estimates the probability of properties falling into the required range [7] and is not considered in this article yet, since the analysis of significant arrays of production data is required. This article implements the first approach and is devoted to identifying the reserves for improving the quality of the coupling billet for tubing.

2 Subject to Research

As an object of research, we chose a sleeve blank for tubing with an outer diameter of 108 mm and a wall thickness of 19.5 mm; steel grade—32Cr3; strength group L80, type 1, acceptance level PSL-1. Normative documentation: API Spec 5CT (Casing and tubing. Technical conditions), which contains requirements for mechanical properties, surface quality, chemical composition; technological regulations (features of the production of casing and tubing pipes with new types of threaded connections) TR 161-0-1486-2019, which sets out the requirements for the accuracy of pipes [8].

To select the nomenclature of quality indicators in accordance with GOST 22851-77, we select the type of industrial products: materials and products and the All-Russian classifier of industrial products OKPD-2: base metals 24.20.11.000: seamless steel pipes for oil and gas pipelines. For these products, according to API 5CT, we select the nomenclature of quality indicators: indicators of purpose, manufacturability, and transportability. Transportability indicators are not considered in this article, since they do not have a significant effect on product quality [9].

3 Indexes of Quality

According to methodology of complex evaluation test [1, 2], hierarchical structure of indexes of quality (“a tree of properties”) was constructed and 17 simple indexes of quality located at the last level was defined (refer with Fig. 1).

For the selected single quality indicators, the reference $x_{\text{reference}}$ and rejection x_{reject} values of properties in natural terms were determined according to the recommendations [2]. The reference values of the properties correspond to a higher quality category, or are taken 20–30% better than the limit values allowed by the regulatory documentation. The rejection values were chosen slightly worse than the permissible values according to the regulatory documentation.

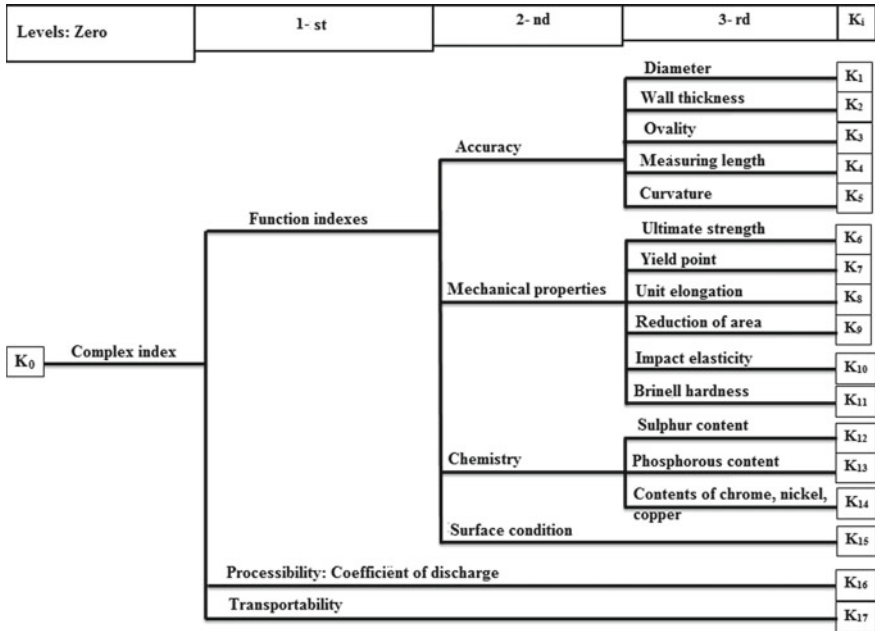


Fig. 1 “Wood” quality indicators of pipe billet for couplings

Normalization of quality indicators is carried out according to the following formulas: if an increase in the value of a property leads to an increase in quality (for example, mechanical properties), $x_{reference} > x_{reject}$:

$$k = \frac{x - x_{reject}}{x_{reference} - x_{reject}} \tag{1}$$

When calculating by formula (1), the following limiting conditions are met:

At $x = x_{reject}$ $k = 0$ (reject); At $x = x_{reference}$ $k = 1$ (great quality)

When calculating accuracy indicators, you can take $x_{reference} = 0$ and use formula (1) in the form:

$$k = 1 - \frac{x}{x_{reject}} \tag{2}$$

If an increase in the property value leads to a decrease in quality (for example, the content of harmful impurities in the alloy), $x_{reference} < x_{reject}$

$$k = \frac{x_{reject} - x}{x_{reject} - x_{reference}} \tag{3}$$

Formula (3) gives the same limiting conditions as formula (1).

Let us consider examples of using formulas (1)–(3) for standardizing quality indicators.

For example, the ultimate tensile strength of pipe billets for couplings of strength group L80, type 1 in accordance with API 5 CT must be at least 655.0 MPa. We select the rejection value of 650 MPa, and the reference value is taken as 800 MPa, given that the fur. properties are determined with an accuracy of 5 units. For normalization, we use formula (1).

The accuracy of the outer diameter according to TR 161-0-1486-2019 is estimated by the maximum deviations, which for the outer diameter of 108 mm should be $+1.0/-0.0\%$. For accuracy indicators, the reference value in the formula (1) is chosen $x_{\text{reference}} = 0$. The rejection values are chosen a little worse than the allowable ones, the normalized value is calculated by the formula (2), and the results are entered in Table 1.

Table 1 List of individual properties for assessing the quality of round steel

No.	Property		$x_{\text{reference}}$	x_{reject}	Formula for calculating ki
1	Accuracy diameter	Tolerance “+”	0	1.2%	$1 - \frac{x}{1.2}$
		Tolerance “-”	0	0.1%	$1 - \frac{x}{0.1}$
2	Accuracy walls	Tolerance “+”	0	13%	$1 - \frac{x}{13}$
		Tolerance “-”	0	11%	$1 - \frac{x}{11}$
3	Ovality		0	1.5 MM	$1 - \frac{x}{1.5}$
4	Accuracy of measured length 9.6 m		0	100 MM	$1 - \frac{x}{100}$
5	Curvature		0	20	$1 - \frac{x}{20}$
6	Temporary resistance		800 MIIa	650 MIIa	$\frac{x-650}{800-650}$
7	Yield point		655 MIIa	545 MIIa	$\frac{x-545}{655-545}$
8	Relative extension		30%	10%	$\frac{x-10}{30-10}$
9	Hardenability		55%	40%	$\frac{x-40}{55-40}$
10	Hardness value		18	25	$\frac{25-x}{25-18}$
11	Sulfur content		0.0%	0.02%	$\frac{0.02-x}{0.02-0.0}$
12	Phosphorus content		0.0%	0.02%	$\frac{0.02-x}{0.02-0.0}$
13	Silicon content		0.17%	0.50%	$\frac{0.50-x}{0.50-0.17}$
14	Oxide content		2	4	$\frac{4-x}{4-2}$
15	Sulfide content		1.5	2.5	$\frac{2.5-x}{2.5-1.5}$
16	Depth of surface defects		0	2.2%	$1 - \frac{x}{2.2}$
17	Metal utilization rate		0.9	0.5	$\frac{x-0.5}{0.9-0.5}$

We perform the normalization of the content of harmful impurities according to the formula (3). For example, the sulfur content in accordance with API 5 CT should be no more than 0.015%. The rejection value is taken as 0.02%, the reference value—0.0%.

The content of the main elements in steel of strength group L80, type 1: carbon C no more than 0.43%; chromium Cr not more than 1.5% manganese Mn not more than 1.90%, nickel Ni not more than 0.25%, copper Cu not more than 0.35%. If real chem., the composition goes beyond these ranges, the rental is rejected, and the complex indicator is reset to zero $k_0 = 0$.

The quality of the outer surface of rolled products is assessed as follows: certain types of defects are allowed without stripping that do not bring the profile dimensions beyond the minus deviation, i.e., 2% of the diameter (see property 1) [10]. The reference value in this case is 0 (no defects), the rejection value is 2.2%. For normalization, the formula (1) was used.

The expense ratio was estimated by the formula:

$$K_{um} = \frac{G_{u3\partial}}{G_{ucx}} \quad (4)$$

as the ratio of the mass of the product to the mass of the original metal (workpiece). In this case, we will accept the rejection value of 0.5, the reference value—0.9, and formula (1) was used for normalization.

Allowable intervals for changing the selected properties, their reference, and rejection values, as well as formulas for their normalization are given in Table 1.

Further, to calculate a complex quality indicator, the coefficients of significance (importance) of single properties were determined by an expert method based on a survey of 10 experts—specialists in this field on a 10-point assessment of the importance of the selected properties. The coefficient of significance of the i -th property was determined by the formula

$$a_i = \frac{B_i}{\sum B_i} \quad (5)$$

where B_i the average score for the significance of the i -th property; $\sum B_i$ —the sum of the average scores of all experts [2].

4 Complex Indexes

The complex indicator of product quality K_0 was calculated according to the formulas of the weighted average arithmetic and the weighted average geometric for the intermediate values of the unit properties given in Table 2.

Table 2 Values of single properties for calculating a complex quality index of a sleeve blank for tubing

No.	Property	X	k_i	a_i
1	Outside diameter, mm	108.5	0.616	0.052
2	Wall, mm	20	0.79	0.052
3	Ovality, mm	0.3	0.8	0.048
4	Accuracy of measured length 9.6 m, Mm	0	1.0	0.048
5	Curvature, mm	10	0.5	0.048
6	Ultimate resistance, MPa	769	0.304	0.072
7	Yield strength, MPa	619	0.672	0.067
8	Relative extension, %	26	0.8	0.067
9	Material hardenability, mm	50.4	0.69	0.072
10	Hardness value, HRC	21.3	0.53	0.061
11	Sulfur content, %	0.0029	0.855	0.065
12	Phosphorus content, %	0.010	0.5	0.066
13	Silicon content, %	0.28	0.66	0.051
14	Content of oxides, %	2.5	0.75	0.063
15	Sulfide content, %	1.78	0.72	0.068
16	Depth of surface defects, % of diameter	1	0.545	0.046
17	Metal utilization rate	0.75	0.625	0.049

The weighted average arithmetic complex quality indicator is calculated by the formula:

$$\begin{aligned}
 k_0 = \sum_{i=1}^{17} k_i \cdot a_i &= 0.616 \cdot 0.052 + 0.79 \cdot 0.052 + 0.8 \cdot 0.048 \\
 &+ 1 \cdot 0.048 + 0.5 \cdot 0.048 + 0.304 \cdot 0.072 + 0.672 \cdot 0.067 \\
 &+ 0.8 \cdot 0.067 + 0.69 \cdot 0.072 + 0.53 \cdot 0.061 + 0.855 \cdot 0.065 \\
 &+ 0.5 \cdot 0.066 + 0.66 \cdot 0.051 + 0.75 \cdot 0.063 + 0.72 \cdot 0.068 \\
 &+ 0.545 \cdot 0.046 + 0.625 \cdot 0.049 = 0.66
 \end{aligned} \tag{6}$$

The weighted average geometric complex quality indicator is calculated by the formula:

$$\begin{aligned}
 k_0 = \prod_{i=1}^{17} k_i^{a_i} &= 0.0616^{0.052} \cdot 0.79^{0.052} \cdot 0.8^{0.048} \cdot 1^{0.048} \cdot 0.5^{0.048} \\
 &\cdot 0.304^{0.072} \cdot 0.672^{0.067} \cdot 0.8^{0.067} \cdot 0.69^{0.072} \cdot 0.53^{0.061} \\
 &\cdot 0.855^{0.065} \cdot 0.5^{0.066} \cdot 0.66^{0.051} \cdot 0.75^{0.063} \cdot 0.72^{0.068} \\
 &\cdot 0.545^{0.046} \cdot 0.625^{0.049} = 0.64
 \end{aligned} \tag{7}$$

5 Conclusions

Thus, the indicators differ insignificantly, and both methods of calculation are legitimate.

The values obtained were assessed using the Harrington scale: the range of values 0.64 ... 0.8 corresponds to good quality [11].

Thus, on the basis of the qualimetric assessment, it was possible to identify reserves for improving the quality of the coupling billet for tubing, such as: accuracy of the outer diameter of pipes, curvature of pipes, and depth of surface defects on the outer surface of pipes. Further work will be aimed at improving the quality indicators described above.

References

1. Danilov AF, Gleiberg AZ, Balakin VG (1972) The hot rolling and extrusion of pipes, 3rd ed, And revised. Moscow
2. Azgaldov GG, Kostin AV, Sadov VV (2012) Qualimetry for all: textbook. Allowance, ID InformZnanie, Moscow
3. Gong GS (1984) Quality management of high-precision profiles. Moscow
4. Orlov GA, Orlov AG (2018) Comprehensive assessment of the quality of steel rolling. *Proizvodstvo prokat* 4:3–8
5. Orlov GA, Loginov YuN, Orlov AG (2018) Complex assessment of the quality of hot-rolled steel pipes. *Chernye Metally* 4:41–45
6. Orlov GA, Gorbunova YuD, Orlov AG (2018) Development of a methodology for a comprehensive assessment of the quality of hot-stamped elliptical bottoms. *Bull Sci Tech Econ Inform* 12:97–102
7. Steblov AB (2017) Complex indicator of metal rolling quality and its application. *Cast Metall* 86:97–102
8. Shveykin VV (1987) Pipe production on machines with automatic mills. Sverdlovsk
9. Ostrenko VYa, Vatutin PI (1958) Pipe production on automatic machines. Kharkov
10. Potapov IN, Kolikov AP, Druyan VM (1991) Theory of pipe production. Moscow
11. Novik FS, Arsov YaB (1980) Optimization of metal technology processes by methods of planning experiments. Moscow



Numerical Modeling of Steel Structures Connections

N. Buzalo^(✉), B. Chernykhovskiy, and A. Alekseeva

Platov South-Russian State Polytechnic University (NPI), 132, st. Prosveshcheniya,
Novocherkassk 346428, Russia

Abstract. This article is presented in the way to determine the stress distribution in the connection of the beam and column. That structure was previous researched experimentally under cyclic loads, and now, based on experimental data, the numerical model was made for the evaluation of the influence of the geometric parameters of the assembly parts on the bearing capacity of the assembly and on the stress concentration factor. The way of the calculation is finite element analysis using CAE package. This method helps to more accurately determine the bearing capacity of the connection and identify weakened zones of increased stress. In order to increase the bearing capacity of the connection, reduce the stress concentration factors, it is necessary to make changes in the design of the connection by installing additional stiffening diaphragms. The development of options for the structural solution of the connection is the goal of further research. This work shows the way for future researches for improvement of steel structure connections and its successful using in the civil engineering industry.

Keywords: Numerical modeling · Steel structures · Connections · Concentration factors · Equivalent stresses

1 Introduction

In the steel frames of multi-storey civil and industrial buildings, one of the most critical and important places is the connections of columns with beams [1], which are carried out mainly during assembly. Improvement of the frame connections aimed at reducing the steel consumption is achieved, as a rule, through the use of materials of increased strength, the development of new effective types of structural connections, and the introduction of optimal design methods [2].

Designing connections of steel structures need a large amount of information for an objective assessment of the influence of the connection parameters on the force resistance of the frame elements [3]. Adopting a goal of reducing the consumption of materials and the cost of construction, it cannot be discount the requirements for improving the reliability and durability of structures, improving the design technology and manufacturing structures, which is directly related to the refinement of design schemes and the creation of sufficient design models [4]. Accuracy of the design model is based on the results of physical studies of the actual operation of structures and numerical studies

of design models, the study of real acting loads, especially seismic ones. The research results make it possible to reveal the real operating conditions, to study the processes of deformation and destruction of the structure and to set the permissible limits for the idealization of design models [5].

The introduction of numerical modeling of the nodes of the steel frames of structures makes it possible to refine the design schemes, take into account the spatial work of structures, the real properties of materials, including the behavior of the material beyond the elastic limit, and nonhomogeneities that cause stress concentration (stresses increase in small areas adjacent to the places of nonhomogeneity) [6].

2 Numerical Model

2.1 Description of the Work

In this article, the objective is to determine the stress distribution in the node of the rigid connection of the I-beam with the square column, made of four corners (Fig. 1). This constructure was researched and analyzed in the work [7]. All elements of the connection are made of steel C235. Mechanical properties of steel are taken in accordance with the standard [8]: $\sigma_t = 235$ MPa; $\sigma_w = 360$ MPa.

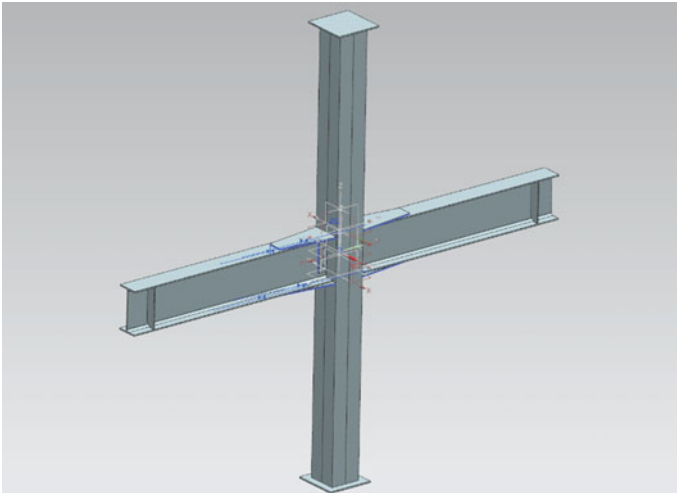


Fig. 1 Rigid connecting of the beam and column

2.2 Model Characteristic

The design model is presented in the form of a three-dimensional thin-walled body. The model is made in a CAE package compatible with the Nastran solver. The model uses two-dimensional four-node plate-elements of appropriate thickness for beam and

column parts and one-dimensional rigid elements (RBE-2 in terms of the Nastran solver) to simulate welded connections. The use of two-dimensional elements for modeling steel parts in this work seems to be rational, since the ratio of the thicknesses of the parts to the overall dimensions of the sections is more than ten, which makes it possible to accept these parts as thin-walled. The use of plate-elements in this task is possible, since the thicknesses of all used parts is not variable (as, for example, in I-beams with varying thickness flanges). The use of RBE-2 elements for modeling welded joints introduces errors into the weld-affected zones of the design model. To assess the strength of welded structures modeled using rigid elements, the hot-spot stresses technique is used, since incredible stress spikes appear in the finite stiffeners adjacent to RBE-2 elements under load.

According to the stresses acting at the distance of such an offset in the finite element model, it is possible to correctly estimate the strength of the weld-affected zone. The strength of the weld body can be assessed by classical analytical calculations using well-known standard methods [9]. Despite the significant disadvantages of using rigid elements in modeling welds, this modeling method seems to be reasonable for several reasons:

- modeling of welded joints with elements of finite stiffness is a much more time-consuming process;
- a design model of welded structures, in which welds are modeled by similar elements of final stiffness, is more resource-intensive (this is especially noticeable for models made with volumetric elements);
- there is no universal method for modeling welded joints that would reliably show the stressed state of parts, taking into account the inhomogeneity of the shape and elastic properties of the weld and residual welding stresses, using only the design shape of the weld.

2.3 Model Connections

At the base of the column for the assembly in the center of the base plate, translational degrees of freedom are limited, which makes it a spherical hinge. This node does not belong to the elements of the base plate, and the boundary conditions from the node to the plate are transmitted by the interpolating element RBE-3. Two diametrically opposite nodes of the base plate are limited in translational movement along the X -axis, which limits rotation for the entire structure around its vertical axis (Z -axis in the model).

In the upper support, one of the nodes is constrained by displacements in the horizontal XY -plane. These displacement constraints ultimately provide sufficient restraints for the model to compute.

2.4 Loading Conditions

The loads on the transom and column are modeled similarly to the spherical hinge of this model—using an interpolation element.

Determination of stresses in elements of sections of structures by known methods of resistance of materials for various types of stress state is valid only if the section under

consideration is at a sufficiently large distance from the places of abrupt changes in the shape of the section, internal corners, holes, cracks, mechanical damage, welds, etc. [10]. Practically in all the elements of operated structures, there are zones of structural or technological stress concentrators (Fig. 2), in which local stress concentrations are manifested; it is in them that fracture is initiated [11]. The appearance of stress concentration in some cases (at variable loads, when using high-strength steels) can lead to a decrease in the strength of the element and an increase in the probability of its brittle fracture [12].

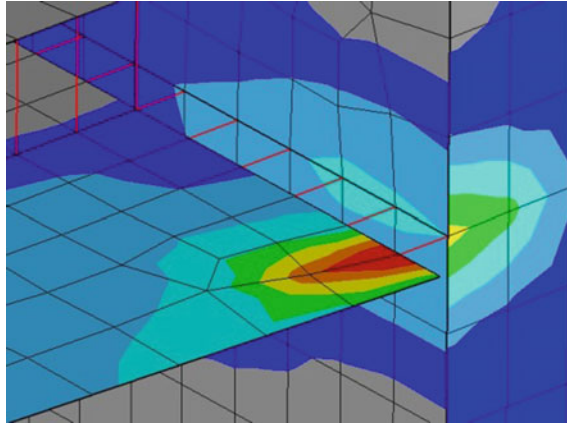


Fig. 2 Local surge of tension in the beam at the edge of the column

In places of stress concentration, the hypothesis of flat sections is false, and the formulas for the resistance of materials are not applied [13]. Stresses near stress concentrators must be determined by methods of elasticity theory, computer modeling or experimentally.

3 Experiment

For the numerical experiment as the primary methodology was selected full factorial experiment type 2^k , allowing for known among the factors to find the number of experiments required to implement all possible levels of the factors of $N = 2^k$, where N —is the number of experiments, k —the number of factors, and 2—the number of levels. The factors that determine the process are: the thickness of the lining t , the length of the lining b , the force on the column P , and the force on the beam S (Fig. 3). When considering a problem in which the number of factors under study is 4, it is necessary to perform $2^4 = 16$ different combinations of experiments.

For the research, the levels and intervals of variation are presented in Table 1.

The conditions for conducting experiments in the natural values of the factors are presented in Table 2.

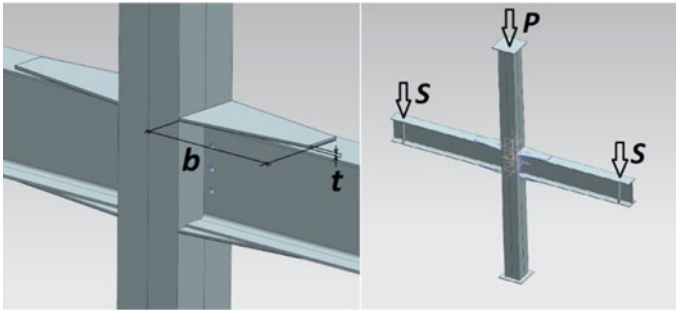


Fig. 3 Parameters of the numerical model

Table 1 Variation levels and intervals

Level	<i>t</i> (mm)	<i>b</i> (mm)	<i>P</i> (kN)	<i>S</i> (kN)
Main	8.0	40	700	40
Upper	10.0	50	800	50
Lower	6.0	30	600	30
Range of variation	2.0	10	100	20

As a result of the calculation, the distributions of equivalent stresses in the elements of the node were obtained. The general nature of the distributions is similar for all variants of the experiment and varies only in the values of the stresses (Fig. 4).

The numerical values of stresses in the cross section of the beam (σ_{\max}^b) and in the column cross section (σ_{\max}^c), vertical displacement of the end of the console (*z*) are presented in Table 3. Bold text in selected options satisfies the condition of strength.

Analysis of the destruction of elements of steel structures shows that the overwhelming majority of them, the formation of brittle or fatigue cracks, and other reasons for the loss of bearing capacity occur, as a rule, near stress concentrators. The phenomenon of stress concentration is explained by the fact that in a solid body, the forces are transmitted along the shortest possible path, which ensures a minimum of the body’s internal energy under a given loading. As a result, the material adjacent to the weakened area perceives additional forces transmitted from the material surrounding the hole or cut [14].

The maximum stress in the weakened section in the classical setting will be written as in [15]:

$$\sigma_{\max} = \alpha_{\sigma} \cdot \sigma_n \tag{1}$$

here σ_{\max} is the maximum elastic stress in the weakened section; σ_n —is the nominal voltage determined in the most weakened section located at a sufficiently large distance from the weakening without taking into account the effect of stress concentration, and α_{σ} —is the theoretical stress concentration coefficient, which depends on the shape and size of the holes, on the ratio of the size of the damage that weaken the section and the transverse dimensions of the body.

Table 2 Natural values of factors

Experiment number	t (mm)	b (mm)	P (kN)	S (kN)
1	10	50	600	20
2	10	50	600	30
3	10	50	800	20
4	10	50	800	30
5	10	30	600	20
6	10	30	600	30
7	10	30	800	20
8	10	30	800	30
9	6	50	600	20
10	6	50	600	30
11	6	50	800	20
12	6	50	800	30
13	6	30	600	20
14	6	30	600	30
15	6	30	800	20
16	6	30	800	30

As a result of a numerical experiment, the stress distribution near the point of weakening was obtained (Fig. 5).

The numerical values of the calculated theoretical stress concentration factors in the node for the factors considered are given in Table 4.

4 Results

The stresses obtained in the first, second, and fifth of sixteen numerical experiments satisfy the condition of strength in terms of the yield point of the material; in all variants, the stiffness condition is met (Table 3), and the values of the stress concentration factors in the near-weld zone of the beam exceed 2.7. In order to increase the bearing capacity of the connection, reduce the stress concentration factors, it is necessary to make changes in the design of the connection by installing additional stiffening diaphragms. The development of options for the structural solution of the connection is the goal of further research.

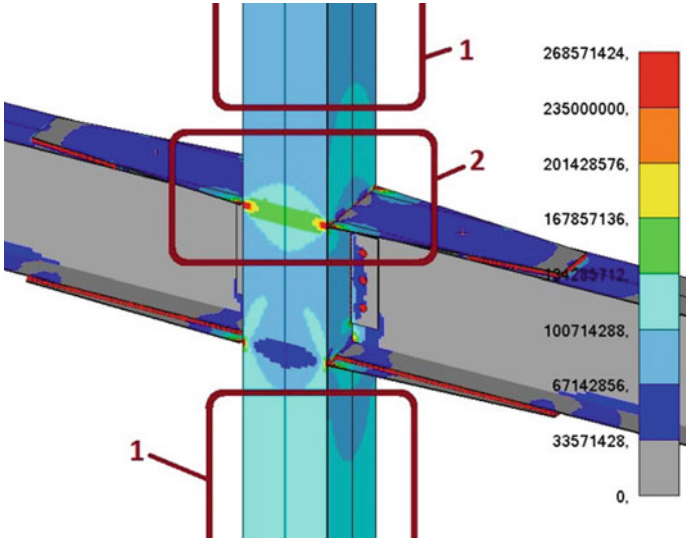


Fig. 4 Distribution of equivalent stresses (Pa) in the connection. 1—the compressed zone of the column; 2—the zone of influence of the bending moment in the beam on the stress state of the column at the place of the connection

Table 3 Numerical values of the calculated parameters

Experiment number	σ_{\max}^b (MPa)	σ_{\max}^c (MPa)	z (mm)
1	153.6	206.6	3.4
2	148.5	231.1	3.6
3	238.4	276.2	4.7
4	233.1	298.2	5.0
5	189.6	230.0	3.5
6	187.6	253.1	3.8
7	294.8	313.4	4.9
8	287.8	334.0	5.2
9	255.1	235.6	4.1
10	249.8	258.2	4.3
11	390.6	322.7	5.7
12	187.6	253.1	3.8
13	294.8	313.4	4.9
14	287.8	334.0	5.2
15	255.1	235.6	4.1
16	249.8	258.2	4.3

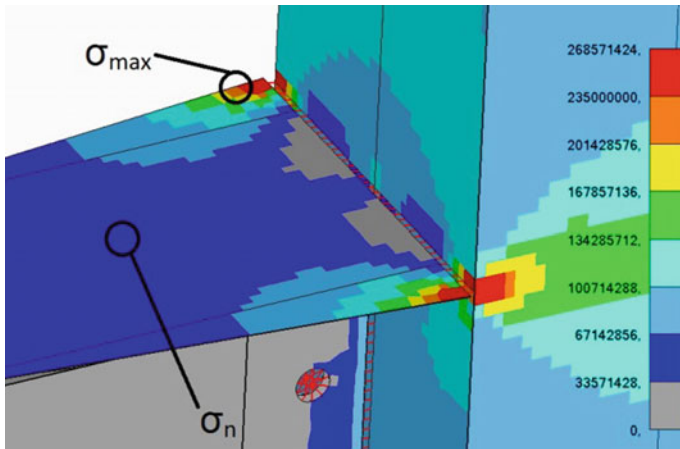


Fig. 5 Distribution of equivalent stresses (Pa) in the node and location of measurement points to determine α_σ

Table 4 Values of theoretical stress concentration factors

Experiment number	α_σ	σ_{\max} (MPa)	σ_n (MPa)
1	2.96	153.6	51.9
2	2.778	148.5	53.5
3	3.128	238.4	76.2
4	3.014	233.1	77.3
5	3.777	189.6	50.2
6	3.684	187.6	50.9
7	3.943	294.8	74.8
8	3.817	287.8	75.4
9	2.971	255.1	85.9
10	2.874	249.8	86.9
11	3.062	390.6	127.6
12	2.999	385.3	128.5
13	4.012	319.4	79.6
14	3.959	313.2	79.1
15	4.037	488.5	121
16	4.017	482.2	120

Acknowledgements. The report study was funded by RFBR, project number 20-38-90046\20.

References

1. Itskov IE (2008) Estimated seismic loads on high-rise buildings erected in the Republic of Kazakhstan. *Seismic Constr Saf Struct* 2:32–35
2. Zlochevsky AB (1983) *Experimental methods in structural mechanics*. Stroyizdat, Moscow, p 192
3. Pavlov AB (2002) Accounting the real behavior of connections in the calculation of steel frames. *Ind Civil Constr* 6:37–39
4. Polyakov SV (1984) *Seism-resistant buildings and development of the theory of seismic resistance*. Moscow, p 254
5. Svyatoshenko AE (2006) Increasing the reliability of frame units of steel frames in multi-storey buildings. Novgorod, p 25
6. Martemyanov AI (1985) *Design and construction of buildings and structures in seismic regions*. Stroyizdat, Moscow, p 255
7. Polyakov SV (1983) *Earthquake-resistant structures of buildings*. Higher School, Moscow, p 304
8. GOST 27772-88
9. SP 16.13330.2017
10. Trufyakova VYa (ed) (1990) *Strength of welded joints at variable loads*. Naukova Dumka, Kiev, p 256

11. Neuber G (1947) Stress Concentration. OGIZ, I.-L, p 114
12. Odessa PD, Vedyakov II, Gorpichenko VM (1998) Prevention of brittle destruction of steel building structures. SP "Internet Engineering", Moscow, p 220
13. Lampsii BB (1979) Steel thin-walled supporting structures under local loads: theory of local stresses. Stroyizdat, Moscow, p 272
14. Novozhilov VV On the basics of the theory of equilibrium cracks in elastic bodies. PMM 33(5):797–812
15. Savin GN (1968) Distribution of stresses around holes. Naukova Dumka, Kiev, p 887



Natural Gas Burning with Process Oxygen in Up-to-Date Arc Steel Furnace Operating Space

G. V. Voronov and I. V. Glukhov^(✉)

First President of Russia B. Yeltsin Ural Federal University, 19, Mira str, Yekaterinburg 620002, Russia

Abstract. In recent years, modern electrometallurgy has shown a trend towards the integrated use of various methods of intensifying the thermal performance of up-to-date arc steel furnaces. Thus, wall gas-oxygen burners and refining tuyers have become increasingly common to reduce electric power consumption. They are used to burn natural gas with process oxygen. The paper outlines the design of the burners of operating furnaces (*VAI FUCHS*, *SMS DEMAG*, and Research Production Company *Etalon*) and describes the design options for mixing natural gas with oxygen in the burner space, as well as in the divergent nozzle. ANSYS CFX software has been applied to study temperature fields and possible flashback, which resulted in the development of a burner design precluding flashback during kinetic combustion of natural gas in oxygen. The study revealed that the gas-oxygen burners used at the state-of-the-art operating arc steel furnaces are not designed for combustion of the initial premixed blend, as gaseous combustion is accompanied by the flare being drawn into the space inside the burner with a subsequent failure of the burner.

Keywords: Burner · Flare · Design · Kinetic · Diffusion · Mixture

1 Introduction

In recent years, modern electrometallurgy has shown a trend towards the integrated use of various methods of intensifying the thermal performance of up-to-date arc steel furnaces. Wall gas-oxygen burners and refining tuyers have become increasingly common [1].

A gas burner is designed to form a flare under preset conditions for combustion of gas with an oxidizer. Its geometry (l_f —full length, l_{rb} —rapid burning length, aperture angle, etc.), as well as temperature and chemical composition of the combustion products at a minimum rate of incomplete combustion are predetermined [2–7].

Simulation of fuel burning processes demonstrated a good possibility to determine optimal parameters of a burner. Bobrov and Loshkarev [8] applied the ANSYS CFX software to generate the temperature field, as well as CO, CO₂, and H₂ distribution in the operating space. Druzhinin carried out the burner mathematical simulation for the Borovich Refractory Plant to evaluate the optimal design solutions [9]. Mathematical

simulation allowed Vereshchetin to determine the impact of the furnace design on the natural gas burning behaviour and NO_x formation [10, 11]. The obtained results enabled the researchers to determine an optimal design for a burner.

Gas-oxygen burners in an arc steel furnace are primarily designed to expedite the heating of the charge contained in the first basket. It facilitates the feeding of the final charge amount into the operating space. Preheating of the complete charge amount to the melting temperature should be uniform throughout the total space without any local overheated or fluxed zones. The formation of the liquid phase on the surface results in reduced porosity and gas permeability when filling the voids in the bottom layers of the charge.

Maximum level of the heat transfer created in the charge layers leads to positive fusion. Gas is burnt with oxygen in the diffusion mode, which means that it is mixed with an oxidizer after their outflow from the burner. It can also be carried out in the kinetic mode provided that the premixed gas and oxidizer blend are of high quality. Thus, we need to define the most efficient mode for an arc steel furnace.

During the turbulent diffusion combustion, the flare is characterized by the individual extensional areas with increased oxygen content. This reduces the temperature and heat exchange. It also increases the charge component waste, thus influencing mass exchange.

The turbulent flare during the kinetic combustion is characterized by homogeneity of the chemical composition, temperature homogeneity in the adjacent spaces, and uniform dispersion of heat and mass transfer processes. The elimination of the mixing of gas with oxygen from the burning process changes the flare geometry.

Such burning conditions make it essential to determine which part of the burner should be used to prepare the mixture, and how this mixture should be fed to the flare; as at certain conditions of the mixture outflow from the burner, its burning spreads into the burner, i.e. backflash occurs [12–14].

2 Design of Gas-Oxygen Burners Used in Arc Steel Furnaces

The VAI FUCHS 6.5/120t burner is shown in Fig. 1. Its specifications are given in Table 1.

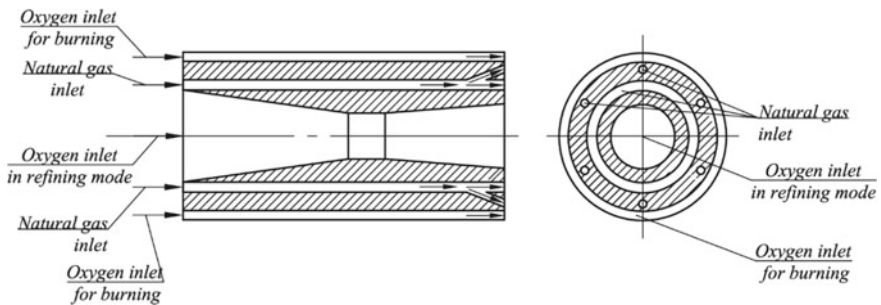


Fig. 1 Design of VAI FUCHS 3.5 MW heat power gas-oxygen burner for arc steel furnaces

Table 1 Wall gas-oxygen burner specifications

Parameter	Value
Number of furnace wall burners, pcs	4
Heat power per 1 burner, MW	3.5
Natural gas flow per 1 burner (at a constant pressure of 6 bar), m ³ /h (m ³ /s)	100–350 (0.028–0.097)
Oxygen flow per 1 burner (at a constant pressure of 7–14 bar), m ³ /h (m ³ /s)	200–800 (0.056–0.222)
Compressed air flow per 1 tuyere (at a constant pressure of 7–14 bar), m ³ /h (m ³ /s)	80–150 (0.022–0.042)
Range of adjustment of the burner tilt in the vertical and horizontal planes, (°)	±10

Figure 2 shows a burner designed by Research Production Company *Etalon* [15]. The burner consists of a central duct (1) for oxygen supply, a peripheral duct (5) for natural gas supply, and an external duct (3) for cooling water supply. The burner head has six angular holes (6) and one central hole for oxygen outflow, as well as six flat peripheral ducts for natural gas outflow [15].

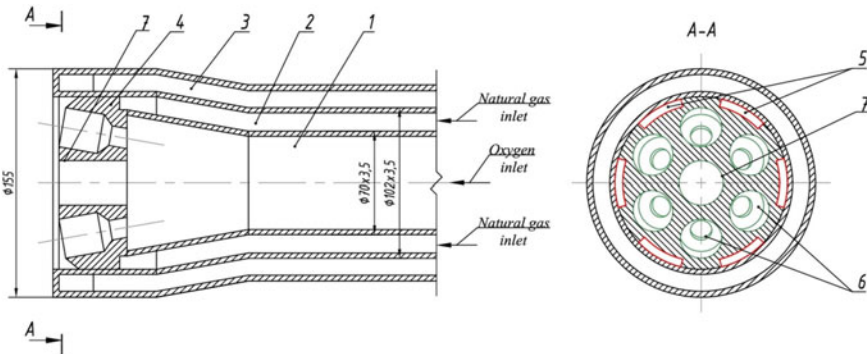


Fig. 2 Design of the *Etalon* gas-oxygen burner for arc steel furnaces: 1—oxygen supply duct, 2—natural gas supply duct, 3—water jacket, 4—head, 5—holes for natural gas outflow, 6—holes for oxygen outflow, 7—central duct

Figure 3 shows the burner designed by *SMS DEMAG* [16, 17].

In this case, natural gas is mixed with oxygen in the unconfined space at the burner outlet. The burner creates the diffusion combustion that oxidizes natural gas combustible components outside the burner. The burning spreads in the charge layer or above the melt surface.

Kinetic combustion of natural gas with oxygen is preferable. The premixed blend burns in a flare of a smaller length as compared to diffusion combustion under equal

SMS DEMAG burner design

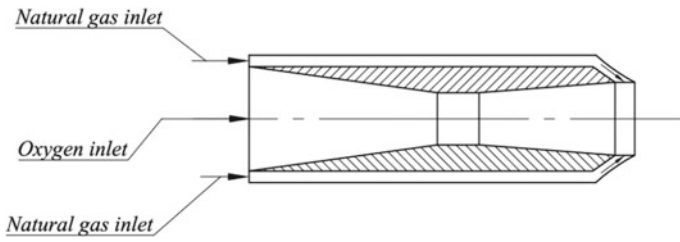


Fig. 3 Design of the SMS DEMAG gas-oxygen burner for arc steel furnaces

initial conditions. There is no burning of the initial fuel components in the charge layer. The temperature of the combustion products reaches its maximum at the entry of the charge layer.

This paper covers various options for combustion of natural gas with oxygen in the kinetic mode (Figs. 4 and 5).

Options with mixing in divergent nozzle

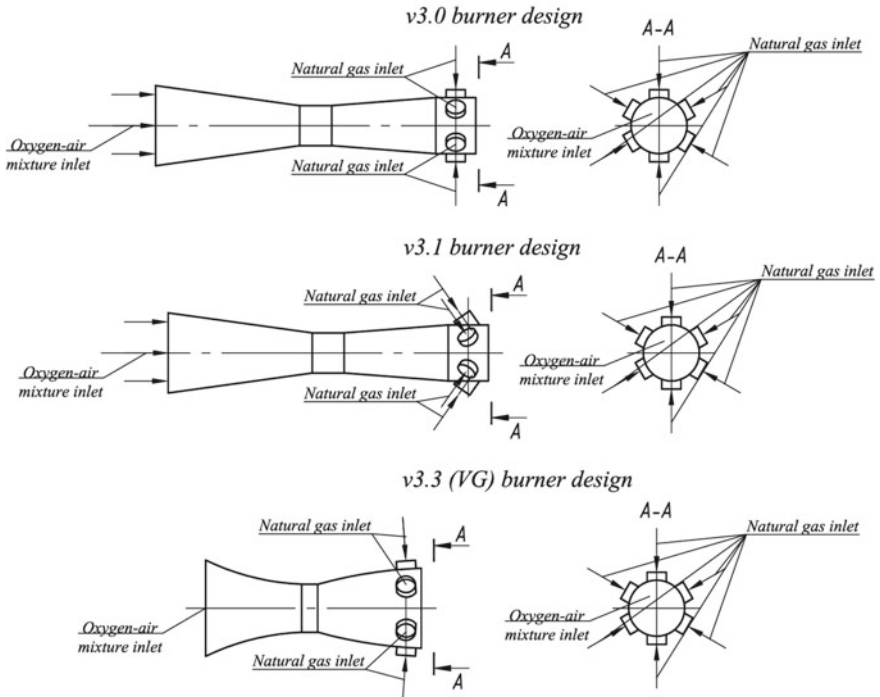


Fig. 4 Options for gas-oxygen burner designs under study (options with mixing in the divergent nozzle)

Options with mixing in the burner

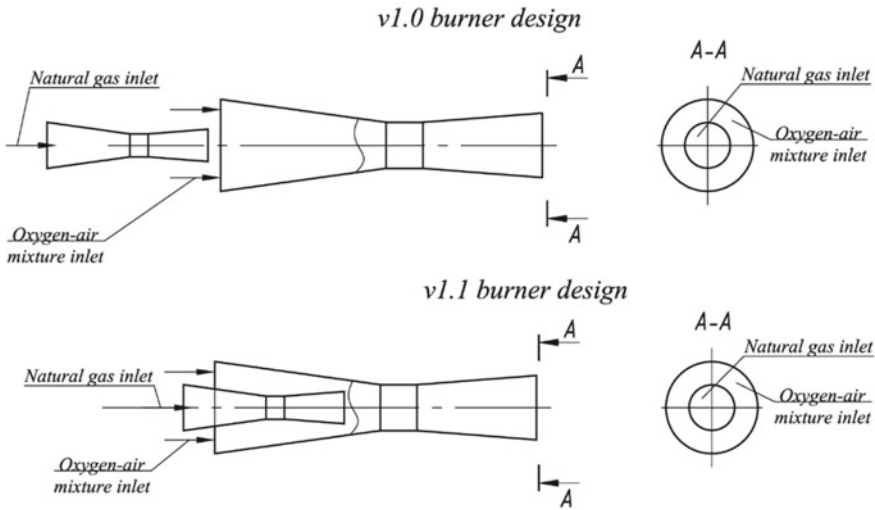


Fig. 5 Options of gas-oxygen burner designs under study (options with mixing in the burner)

3 Computer Simulation of Burner Designs

Experimental research requires high costs for the development of the guidelines and tools for sample testing. Computer simulation applied for the development of the most efficient burner design allows us to avoid intermediate designs and to evaluate the influence of any design changes on the flare characteristics [18, 19].

We used ANSYS CFX software to evaluate combustion of natural gas with various oxygen concentrations in an oxidizer.

At the first stage, a 3D burner model was created in KOMPAS-3D software on the basis of the results of the de Laval nozzle analysis.

At the second stage, the geometry model was imported into Ansys Design Modeller. ANSYS Meshing generated a mesh with a pitch of 2 mm for the burner space and 5 mm for the flare burning space. This created 1,423,425 nodes and 7,607,414 elements at the maximum length of the hexagonal mesh rib of 3.16 mm.

At the third stage, a design model and boundary parameter conditions were specified in setup. We used the Extended Coherent Flamelet Model (ECFM) to calculate combustion, the Total Energy model to calculate heat transfer, and the k-Epsilon model to calculate turbulence.

The ECFM model is the most precise model to calculate combustion of the premixed fuel and oxidizer blend, as it provides calculations for two separate patterns, namely the premixed or partially premixed combustion model and the burning velocity model (BVM) [20].

To generate the combustion reaction, a flammable mixture and an oxidizer were specified in the CFX-RIF tool. Initial conditions for oxidizer and fuel were as follows:

temperature of 288 K and pressure of the arc steel furnace operating space equal to atmospheric.

The boundaries for the burner housing were specified as *No Slip Wall*. *Inlet* was chosen for the oxidizer and natural gas inlet areas and *Outlet* for the combustion product outlet area. The natural gas and oxidizer flow rate was specified at the inlet.

4 Evaluation of the Burner Temperature Field to Avoid Flashback

We failed to avoid flashback (flame spreading into the burner) in the burner designs which imply that the internal mixing of natural gas with oxygen begins in the convergent nozzle (Fig. 6a) or in front of the cylindrical mixer (Fig. 6b). The combustion started in the burner internal space.

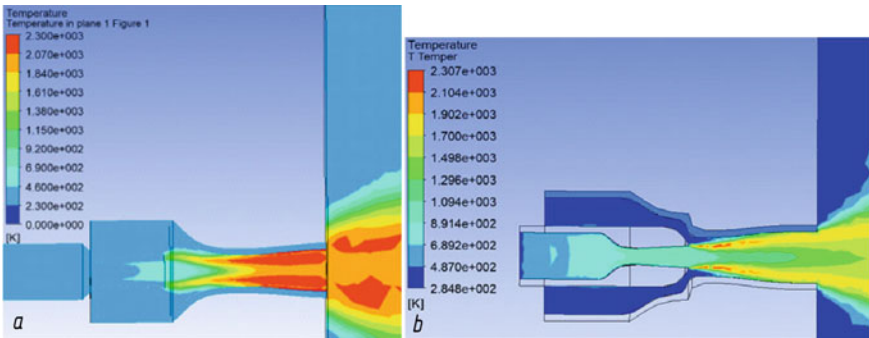


Fig. 6 **a** Temperature distribution in v1.0 burner with mixing of natural gas and oxygen starting in the convergent nozzle; **b** Temperature distribution in v1.1 burner with mixing of natural gas and oxygen starting in front of the cylindrical mixer

The combustion of natural gas with compressed air showed similar results (see Fig. 7).

In the burners with the option of mixing inside the burner, flame flashback also occurred, therefore the burning spread into the burner space.

During simulation, the v.3.3 burner design (VG) proved to be the most efficient for kinetic combustion of natural gas with oxygen. Figure 8 shows the burner design where natural gas is mixed with oxygen in the divergent nozzle with an external supply of natural gas. The supply of natural gas to the oxidizer flow occurs through the holes in the divergent nozzle without creating any hydraulic resistance to the oxidizer flow, which is a distinctive feature of this design.

5 Conclusions

The study of the kinetic combustion of natural gas with oxygen revealed that flame backflash is possible at any concentration of oxygen in the oxidizer in the existing burner designs. No flare backflash is observed during kinetic combustion when natural gas is mixed with oxygen in the divergent nozzle.

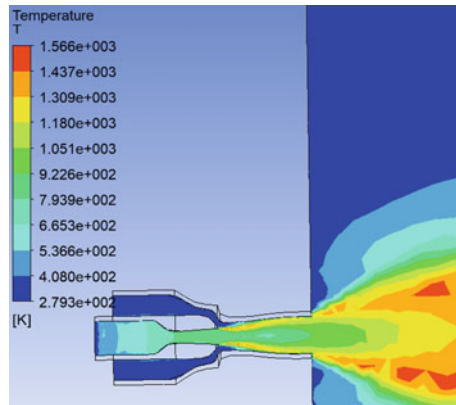


Fig. 7 Temperature distribution in v1.1 burner mixing of natural gas and air in the cylindrical mixer

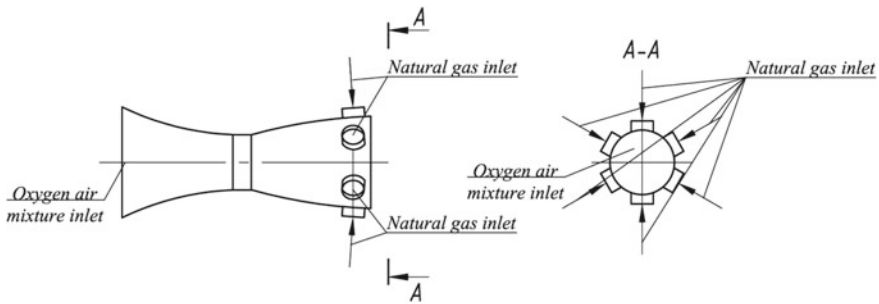


Fig. 8 Burner design under study

References

1. Mokson P (2004) Use of oxygen injection process with RCB system, particularly for stainless steel production in arc steel furnace. *REV Met* 101(4):309–316
2. Arseev AV (1963) *Natural gas burning*. Metallurgizdat, Moscow
3. Vintovkin AA, Ladygichev MG, Gusovsky VL, Kapinova TV (2008) *Burner devices of industrial furnaces and combustion appliances (Design and specification)*. Reference Book. Teplotekhnik, Moscow
4. Lisienko VG, Voronov GV, Kitayev BI, Kokarev NI (1970) Study of natural gas torch in steel melting furnaces. In: *Abstracts of the 11th international gas conferences*, Moscow, June 1970
5. Vintovkin AA, Dengub VV, Voronov GV (2015) *Fuel, its combustion and explosion safety*. Interregional Research Center, Ekaterinburg
6. Lisienko VG, Kitaev BI, Kokarev NI (1977) *Improvement of natural gas burning methods in steel furnaces*. Metallurgy, Moscow
7. Startsev VA et al (2004) *Scrap and coke practice at steel manufacture in open hearth furnaces*. USTU-UPI, Ekaterinburg
8. Bobrov KO, Loshkarev AN (2016) Computer simulation of natural gas combustion in the GPS-0,4 Burner. In: *Collection of reports of the V All-Russian scientific-practical conference of*

- students, graduate students and young scientists (TIM'2016) with international participation, UrFU, Yekaterinburg, 12–13 May 2016
9. Druzhinin GM et al (2020) Analytical determination of the burner jet characteristics for Rotary Kilns. *Stal'* 5:44–46
 10. Vereshchetin VA et al (2006) Experience of research and adjustment of the slagless mode of operation of gas-burning devices located in the zone of the fluidized bed of the solid waste incineration device. *Electric Stations. Special issue*, p 34–37
 11. Vereshchetin VA (2005) Research, mathematical modeling and adjustment of the slagless mode of operation of gas-burning devices located in the zone of the fluidized bed of the incinerator of special Plant No. 4 In: *Materials of the all-Russian conference on the results of the competition for young specialists of NPK organizations of RAO UES of Russia, VTI, Moscow*
 12. Glinkov MA (1962) *General theoretical framework of furnaces*. Metallurgizdat, Moscow
 13. Volk K, Shipman K (1961) *Ch. diffusion flames. Burning processes*. State Publishing House of Physico-Mathematical Literature, Moscow
 14. Krivandin VA (1977) *Metallurgical furnaces: university textbook*. Metallurgy, Moscow
 15. Limited Liability Company Scientific and Technical Production Company Etalon. http://www.ntpf-etalon.ru/gorelochnie_ustroystva. Accessed 21 December 2020
 16. SMS GROUP. <https://www.sms-group.com>. Accessed 20 December 2020
 17. Glukhov IV et al (2020) Energy saving in state-of-the-art arc steel furnace DSP-120. *Steel* 5:21–23
 18. Voronov GV et al (2015) Gas dynamics in the working space of a modern electric-arc steelmaking furnace. *Refract Ind Ceram* 55(6):498–500. <https://doi.org/10.1007/s11148-015-9752-1>
 19. Voronov GV et al (2016) Aerodynamics and thermal state of state-of-the-art arc steel furnace. *Ferrous Metall Mater Sci Issues* 1:28–34
 20. Ansys (2009) *Ansys CFX-Solver Theory Guide Canonsburg: Release 12.1*



Methods for Minimum Clearances Calculating in a Multiple-Teeth Contact of Straight Bevel Precessional Gears

V. Syzrantsev and A. Pazyak^(✉)

Industrial University of Tyumen, 38, Volodarskogo Street, Tyumen 625000, Russia

Abstract. Various types of gearboxes are used in most of the drilling and oilfield equipment. Gearboxes make it possible to obtain the torques and rotation speeds necessary for the implementation of the technological drilling processes or oil production. In addition to the traditional requirements for load capacity and durability, the gear mechanisms should have a high overload capacity and small radial dimensions that ensure placement in the drill string of pipes (submersible gearboxes for screw pumps and gearboxes for downhole drilling motors) and allow high reduction at high efficiency in harsh climatic conditions (valves actuators). These requirements are met by gearboxes that use straight precessional bevel gears with a small shaft angle and a small difference in the gear and pinion teeth quantity, making a precessing motion. The article provides formulas for determining the minimum clearances in the gearing required to determine the contact strength of straight precessional bevel gears with a small shaft angle. The resulting formulas and methods will allow develop and manufacture gearboxes with adjusted performance characteristics necessary for harsh conditions.

Keywords: Precessional gearbox · Straight precessional bevel gears with a small shaft angle · Gears minimum clearances

1 Introduction

Mechanical drives, created on known modifications of spur and bevel gears, worm [1–4] and spiroid [5–15] gears, do not correspond to oil and gas industry needs in some cases. The oil and gas industry makes high demands on the gearboxes such as high efficiency, low weight and dimensions, low torque, due to the operating conditions of gearboxes drives in the Far North. An effective way to solve the problem is to develop a new generation of drives [16–22] based on a straight precessional bevel gears (SBPG). Due to the small difference in the numbers of pinion and gear teeth, drives based on SBPG [16–22] can be manufactured with a gear ratio from 10 to 65. Their radial dimensions in comparison with traditional drives are much less at high efficiency ($\eta \approx 0.9$). Multiple-teeth contact is implemented in straight bevel precessional gears, as a result drives load capacity with straight bevel precessional gears significantly exceed other types of drives. Figure 1a, b shows ball valve drive DN-300 and the screw pump gearboxes for the heavy oils production based on a straight bevel precessional gear with a small shaft angle.

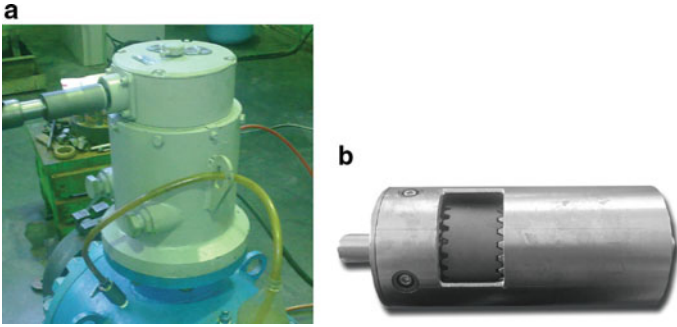


Fig. 1 a, b Ball valve DN 300 and screw pump gearboxes based on a bevel precessional gear with a small shaft angle

Works [16, 17, 19, 20] describe straight precessional bevel gears geometry and mathematical models of the gear’s teeth forming processes. Also, problems of gearing teeth optimal geometric characteristics determination are solved based on varying tools parameters and gear cutting machine settings.

Straight precessional bevel gears distinctive feature is that teeth pairs surfaces of the pairs adjacent to the contacting pair are located close enough in any gearing phase and multi-pair engagement is realized with the external torque application to the external torque transmission.

2 Determination of Minimum Clearances in a Multi-Pair Gear Meshing of Straight Bevel Precessional Gears

Distinctive feature of straight precessional bevel gears is that the teeth pairs adjacent to the one pair there is a geometric contact in an engagement certain phase ($\psi_1 = \text{const}$) are located rather close. In this regard, when torque is applied to the transmission, chosen clearance will be “selected”, and several gear teeth pairs will be in contact. This fact allows us to assume that straight precessional bevel gears will be, in terms of the load capacity, due to the multi-pair engagement, higher than the usual bevel gear with an axle angle $\Sigma = 90^\circ$.

Let us consider the procedure for determining the minimum clearances function in multiple-teeth contact of straight bevel precessional gears. To solve this problem, let us turn to Fig. 2, which shows gears scheme and coordinate system $S_1 = (x_1, y_1, z_1)$, $S_2 = (x_2, y_2, z_2)$, which describe gear and pinion teeth surfaces.

We define the elements of the transition matrix $\tilde{A}_{12}(\psi_1, \psi_2)$ from the coordinate system $S_2 = (x_2, y_2, z_2)$ to the coordinate system $S_1 = (x_1, y_1, z_1)$

$$\begin{aligned}
 b_{11} &= \cos \psi_1 \cdot \cos \Sigma \cdot \cos \psi_2 + \sin \psi_1 \cdot \sin \psi_2; \\
 b_{12} &= -\cos \psi_1 \cdot \cos \Sigma \cdot \sin \psi_2 + \sin \psi_1 \cdot \cos \psi_2; \\
 b_{13} &= \cos \psi_1 \cdot \sin \Sigma; \quad b_{14} = d \cdot \cos \psi_1 \cdot \sin \Sigma; \\
 b_{21} &= -\sin \psi_1 \cdot \cos \Sigma \cdot \cos \psi_2 + \cos \psi_1 \cdot \sin \psi_2;
 \end{aligned}$$

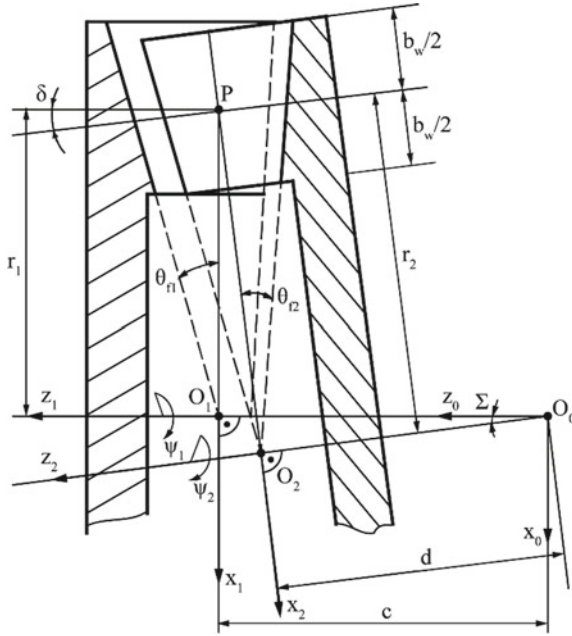


Fig. 2 Designed scheme of bevel gears with a small shaft angle with a non-generated gear and a generated pinion and used coordinate systems

$$\begin{aligned}
 b_{22} &= \sin \psi_1 \cdot \cos \Sigma \cdot \sin \psi_2 + \cos \psi_1 \cdot \cos \psi_2; \\
 b_{23} &= -\sin \psi_1 \cdot \sin \Sigma; \quad b_{24} = -d \cdot \sin \psi_1 \cdot \sin \Sigma; \\
 b_{31} &= -\sin \Sigma \cdot \cos \psi_2; \quad b_{32} = \sin \Sigma \cdot \sin \psi_2; \\
 b_{33} &= \cos \Sigma; \quad b_{34} = d \cdot \cos \Sigma - c; \\
 b_{41} &= b_{42} = b_{43} = 0; \quad b_{44} = 1.
 \end{aligned}
 \tag{1}$$

where the angles ψ_1 and ψ_2 determine the rotation, respectively, of the gears and wheels around their axes of rotation in the gears.

Following the gears theory [23, 24], the condition of the gear and pinion teeth surfaces, considering the matrix $\tilde{A}_{12}(\psi_1, \psi_2)$, has the form

$$\begin{cases} \tilde{r}_1(u_1, h_1, \phi_1, V_1) = \tilde{A}_{12}(\psi_1, \psi_2) \cdot \tilde{r}_2(u_2, h_2, V_2); \\ \tilde{m}_1(u_1, h_1, \phi_1, V_1) = \tilde{A}_{12}(\psi_1, \psi_2) \cdot \tilde{m}_2(u_2, h_2, V_2); \\ f_1(u_1, h_1, \phi_1, V_1) = 0, \end{cases}
 \tag{2}$$

where \tilde{r}_1, \tilde{m}_1 —column matrices composed of the vector radius projections \bar{r}_1 and the normal of the gear tooth surface \bar{m}_1 ; \tilde{r}_2, \tilde{m}_2 —column matrices composed of the vector radius projections \bar{r}_2 and the normal of the pinion tooth surface \bar{m}_2 ; f_1 —gearing equation.

In expanded form, Eq. (2) is called the inverse problem of gear theory [23, 24] and is a system of six transcendental equations (the coincidence of the normal unit vectors projections is determined not by three, but by two independent equations) with seven

unknowns: $u_1, h_1, \phi_1, u_2, h_2, \psi_1$ and ψ_2 . System (24) is solved by numerical methods for a fixed phase of the engagement ($\psi_1 = \text{const}$).

As shown in the works [17, 18, 21], to solve load distribution problem between teeth pairs, it is necessary to know the function of the minimum clearances changing in adjacent (geometrically) contacting teeth pairs at an angle $\psi_1 = \text{const}$. This problem, based on dependencies obtained in article [20] and developed program for studying geometric characteristics of the straight precessional bevel gears with a localize contact, is solved as follows.

Let us set the gear engagement phase $\psi_1 = \text{const}$. By solving the engagement inverse task [23–30] (system transcendental Eq. (2)), we define the pinion rotation angle ψ_2 operatively engaged.

Let us designate found angles with a superscript 0 (ψ_1^0, ψ_2^0) indicating that a teeth pair with No. 0 is contacting.

Consider the next teeth pair numbered $N = 1$. In the same engagement phase, angle ϕ_1 , corresponding to a teeth pair with No. 1, is

$$\psi_1^1 = \psi_1^0 + \frac{2\pi \cdot N}{z_1^*}, \tag{3}$$

where z_1^* —pinion teeth quantity, and N —teeth pair number (0, $\pm 1, \pm 2, \pm 3$, etc.).

From expression (3), it follows that the gear teeth angular pitch is added to the angle ψ_1^0 .

With a help of $\psi_1 = \psi_1^1$, we will solve equations system (2) and set the gear rotation angle in the working gears $\psi_2^1 = \psi_2$, at which geometric contact will be provided in a teeth pair with No. 1.

If studied gears were conjugate, then angle ψ_2^1 would be equal to the expression

$$\psi_2^1 = \psi_2^0 + \frac{2\pi \cdot N}{z_2^*}, \tag{4}$$

where z_2^* —gear teeth quantity.

At the same time, taking into account modification of the gear tooth surface, formula (4) will be not applicable, because studied gears are approximate. Using obtained angle ψ_2^1 , we can determine angle $\delta\psi_2^1$ (gear compensating angle). Using this angle, teeth pair $N = 1$ will start gear meshing:

$$\delta\psi_2^1 = \psi_2^1 - \psi_2^0 - 2 \cdot \pi \cdot N / z_2^*. \tag{5}$$

Solving the system of Eq. (2), the parameters $h_1, h_2, u_1, u_2, \phi_1, \psi_2$ and coordinates projections x_2, y_2, z_2 of the vector radius \vec{r}_2 of the gear and pinion teeth surfaces contact point are determined, and also using $\delta\psi_2^1$, it is possible to calculate the value of the minimum clearance in a teeth pair $N = 1$:

$$\Delta_r^1 = \delta\psi_2^1 \cdot \vec{r}_2 = \delta\psi_2^1 \cdot \sqrt{x_2^2 + y_2^2 + z_2^2} \tag{6}$$

Proceeding in the same way for the pairs with $N = \pm 1; \pm 2, \dots$, a set of turns $\delta\psi_2^N$ and minimum clearances values Δ_r^N are established:

$$\Delta_r^N, N = 0; \pm 1 \pm 2, \dots$$

As an example of the considered algorithm implementation, in Fig. 3, for the engagement phase $\psi_1 = 0$, minimum clearances in five teeth pairs ($N = 0; \pm 1; \pm 2$, paired with $N = 0$ and clearance equal to zero) of straight precessional bevel gears with a localized contact are presented with the following parameters: $z_1^* = 64$, $z_2^* = 65$, $\Sigma = 2^\circ$, $m_n = 5.0$ mm; $b_w = 25$ mm. The parameters defining the law of gear tooth surface longitudinal modification are taken as follows: $a_u = 10$ mm, $b_u = 80$ mm and $\vartheta_{up} = 0.0$.

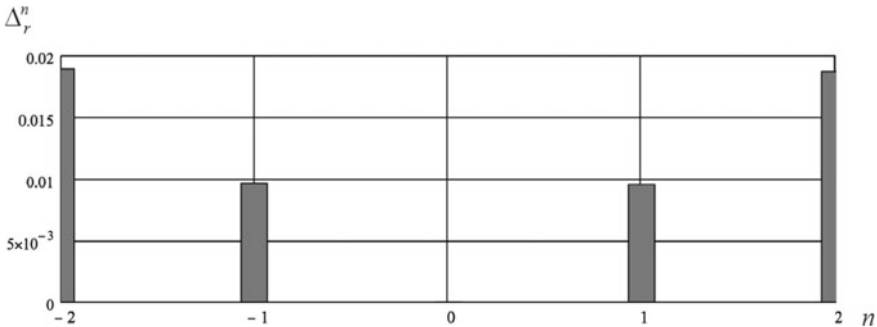


Fig. 3 Values of the minimum clearances in the gear pairs adjacent to the contacting

3 Main Results

The advantages of using straight precessional bevel gears with a small shaft angle in various designs of oil and gas equipment are described. The new scientific results of the article are methods and formulas for determining the minimum clearances—one of the most important geometric characteristics for solving the problems of load capacity and calculating contact strength.

References

1. Nabiev RM (2010) Chervyachnyy reduktor elektroprivoda – perezhitok proshlogo ili aktual'naya klassika (Screw gear motor is a relic of the past or current classical). *Territoria neftegaz (Oil and gas territory)* 6:100–102
2. Litvin FL, Yukishima K, Hayasaka K et al (2007) Geometry and investigation of Klingelnberg-type worm gear drive. *J Mech Des Trans ASME* 129 (1):17–22
3. Gurevich DF (2008) Raschet i konstruirovaniye truboprovodnoy armatury. *Promyshlennaya truboprovodnaya armatura. Konstruirovaniye truboprovodnoy armatury (Calculation and design of pipeline valves. Industrial pipeline valves. Construction of pipeline valves)*. LKIPubl

4. Gavrilenko VA (1962) *Zubchatyye peredachi v mashinostroyenii* (Gears in mechanical engineering). Mashgiz Publ
5. Goldfarb VI (2011) *Spiroidnyye reduktory truboprovodnoy armatury* (Spiroid gearboxes for pipeline valves). Veche Publishing, Moscow
6. Litvin FL, Fuentes A, Zanzi C et al (2002) Face gear drive with spur involute pinion: geometry, generation by a worm, stress analysis. *Comput Methods Appl Mech Eng* 191:2785–2813
7. Goldfarb VI, Trubachev ES (2004) Manufacturing synthesis of spiroid gearing. In: Huang T (ed) *Proceeding of the 2004 the eleventh world congress in mechanism and machine science*, Tianjin, China, 1 April 2004 through 4 April 2004 Code 63248, pp 901–904
8. Goldfarb VI, Trubachev ES, Savelieva TV (2005) Unification of the hobs in spiroid gears. In: *VDI Berichte, Issue 1904 II*. VDI Verlag GMBH, pp 1755–1759
9. Goldfarb VI, Reshetnikov SM, Trubachev ES et al (2015) Slip bearing and lubricants in low-speed heavy-duty spiroid gears. *Russ Eng Res* 35(8):584–588
10. Trubachev E (2016) Several issues of tooth generating process by two-parametric families of generating lines. *Mech Mach Sci* 34:97–116
11. Saari OE (1954) Speed-reduction gearing. US Patent 2,696,125, 7 Dec 1954
12. Nelson WD (1961) Spiroid gearing. *Mach Des* 3:136–144
13. Nelson WD (1961) Spiroid gearing. *Mach Des* 4:93–100
14. Nelson WD (1961) Spiroid gearing. *Mach Des* 5:165–171
15. Bohle F (1955) Spiroid gear. *Machinery* 62(2):155–161
16. Syzrantsev V, Kotlikova V (2000) Mathematical and program provision of design of bevel gearing with small shaft angle. In: *Proceedings of the international conference on gearing, transmissions, and mechanical systems*, Nottingham Trent University, UK, July 2000, pp 3–6
17. Syzrantsev V, Denisov J, Wiebe V, Pazyak A (2015) The design and production of drives based on pan precess gear for oil and gas machinery. In: *ASME 2015 international design engineering technical conferences and computers and information in engineering conference*, vol 10, Boston, USA, 2–5 August 2015. <https://doi.org/10.1115/DETC2015-47096>
18. Syzrantsev V, Syzrantseva K, Pazyak A (2015) Method of loading capacity calculation of bevel precessional gear for pipeline valve drives. 10(8):243–246
19. Syzrantsev V, Syzrantseva K, Pazyak A, Milanovic M (2017) Research on geometrical characteristics of straight bevel gears with a small shaft angle with a non-generated gear and generated pinion. *FME Trans* 45(4):661–669. <https://doi.org/10.5937/fmet1704661S>
20. Syzrantsev VN, Pazyak AA (2017) Precessional gears for drives of stop valves of oil and gas pipelines and gearboxes of pumps to produce heavy crude oil. *Bull Tomsk Polytech Univ Geo Assets Eng* 328(2):15–27
21. Syzrantsev VN, Pazyak AA (2017) Calculating loading capacity of bevel gears with a small shaft angle with a non-generated gear and a generated pinion for drives of stop valves. *Bull Tomsk Polytechnic Univ Geo Assets Eng* 328(3):64–74
22. Denisov JG, Syzrantsev VN, Vibe VP (2014) Soosnyy reduktor (Coaxial gearbox). RF Patent 2,529,943, 10 Oct 2014
23. Litvin FL, Fuentes A (2004) *Gear geometry and applied theory*. University Press, Cambridge, UK, p 800
24. Litvin FL (1998) *Development of gear technology and theory of gearing*. NASA Reference Publication, Cleveland, Ohio, USA, p 124
25. Sheveleva GI (1999) *Teoriya formoobrazovaniya i kontakta dvizhushchikhsya tel* (Theory of formation and contact of moving bodies). Stankin Publishing, Moscow
26. Ginzburg EG (1980) *Zubchatyye peredachi* (Gears). Mashinostroyeniye Publishing, Leningrad
27. Airapetov EL (1990) Static loading of multi-pair toothed transmissions. *Sov Eng Res* 5(12):4–7

28. Airapetov EL (1985) Calculation of contact stresses in gear transmissions with localized tooth contact. *Sov Eng Res* 101:8–17
29. Airapetov EL (1985) Contact loads in gear engagement. *Sov Eng Res* 210:3–5
30. Medvedev VI, Sheveleva GI (1993) Method of contact and bending stresses determination in gear-wheels. *Problemy Prochnosti i Nadezhnos'ti Mashin* 6:35–40



Design of the Robotic Arm Using 3D Printed Parts

I. Bzhikhatlov^(✉) and P. Simonov

ITMO University, pr. Kronverkskij, 49, 197101 Saint-Petersburg, Russia
bia@itmo.ru

Abstract. This paper presents the development of a 6-DOF spatial robot using 3D printed parts and low-cost electronic components to be used as a research and teaching tool in robotics. The main purpose of this work is to give students a general platform for making it possible to emphasize some disadvantages and improve mechanical and electrical parts. The secondary purpose is the development of a research platform that could be used as a basis for the development of industrial robots using the latest additive technologies and other economically efficient methods of manufacturing mechanical components for robots. The requirements for the new design were formulated after analysis of existing solutions. The general concept of the spatial robot with integrated electronic components was developed as the result. The control system was developed in addition. The prototype of the developed spatial robot was produced and tested to verify the correspondence of achieved results to the requirements.

Keywords: Manipulator · Robot for higher education · Robot for teaching · 3D-printed spatial robot · Low-cost robotics platform

1 Introduction

The modern education process in robotics at the university makes demands from the hardware and software. The use of tools like Lego MINDSTORMS [1] became common only for primary school. As one of the most widespread robots for teaching, consider KUKA YouBot [2]. This solution was developed for high education in robotics, but the mechanical parts could not be modified. The price of this robot is very high at the same time. In this work, authors look for cheaper and still industrial-like solutions. Based on the mentioned reason, next research was continued in the direction of using 3D printed parts and other manufacturing methods to provide more efficient education during the study of robotics at the university.

The students at the university need the tools which are more flexible systems to be improved during education not only for the purpose of control algorithms design but in terms of mechanical (physical) components. Such requirements come from the limitations of the hardware that impose restrictions on the software, which today is practically unlimited, since new algorithms and control methods are implemented as software.

Hardware limitations are reduced since the use of 3D printers has become widespread. Many parts today can be printed at home or in a university laboratory as 3D printers and filament have become cheap. Analysis of requirements for robotic manipulators to be used as educational tools is an important stage to make the education more effective.

There are many useful projects that used 3D printed parts in various robotics applications. Today, only a few of them could be related to scientific or industrial solutions in some approximation level. The most important difference between an industrial solution and DIY projects is reliability and durability. Solutions available in the market are not intended for long-term work, and they are suitable only for short-time working on for demonstration purposes. Their functional parts wear out, and the driven parts must be replaced in several hours of intensive work.

The original open-source project named “Thor” [3] made a huge contribution to the evolution of robotics solutions with the 3D printed parts. Since 2016, many manipulators have been developed inspired by the Thor project. The open-source project MOVEO [4] is one of the best versions of Thor project which is a simplified version of the original project but without a few lacks. This solution could be adapted for educational purposes, but still, it requires a lot of efforts from teachers.

The solution presented in the paper [5] is the most affordable robot for teaching purposes, but some limitations on the kinematics do not allow work with full-rank kinematics because it has the kinematics like SCARA robots. Such type of robot has important feature—kinematic redundancy—but the kinematics is still simple because the mechanics is planar. Other big problem is pointing on the side of control. Most solutions have no control systems, and development of a general control system takes too much time for users in the education process. The use of simulations is widely used in education, but the simulation does not provide equivalent skills because it has only scripting and skipping huge skills on the control of real motors.

The next requirements have been formulated based on the analysis of available solutions:

- Spatial six degrees of freedom kinematics
- Dimensions 0.5 m in each direction
- Low-cost stepper motors
- Low-cost and reliable gear reduction
- Low-cost links
- Repeatability ± 2 mm
- Radius of the workspace 0.3 m
- General control system that provides low-level control of joints
- Driven components must provide accuracy and reliability during a long time.

The structure of the paper is arranged as follows. In the introduction, we analytically derived the general requirements for the new concept of the robotic manipulator to make it more suitable for teaching robotics. The second section delivers the design of mechanical parts that provides all the requested abilities for control functionality. The features of control implementation on high and low levels are presented in the third section, including software architecture. Authors in this section also explained how

physically implemented the control system, which provides the required functions. The fourth section concludes the achieved results with the key points.

2 Design of the Robotic Arm

The kinematics structure of the robot is important since this feature determines most abilities of the robot to manipulate the objects in space. The kinematic structure is shown in Fig. 1. The kinematics was selected according to requirements formulated in the previous section.

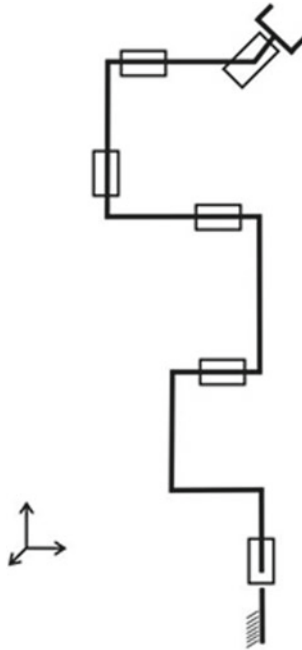


Fig. 1 Kinematics scheme of the robotic arm

The proposed kinematics provides high accessibility for object manipulation. Also, the location of the joints allows reducing the inertial effects on the robot. This kinematics provides a lot of singularities which is a common problem in robotics, and students should face such problems and get skills in solving them.

The workspace was checked using Jacobian analysis for different configurations to verify the manipulability of the robot.

2.1 Choice of Materials

The design of the robotic arm was supposed to be lightweight and affordable to manufacture in university laboratories. Thus, key materials for the design were chosen as follows.

Load-bearing elements of the robotic arm were decided to be made from polymethylmethacrylate or PMMA, as this material has a lot of advantages. Available processing of PMMA implies cutting with saws, water or laser, drilling, milling, turning and sanding [6].

PMMA has the following mechanical properties:

- Compressive (crushing) strength is 120 MPa
- Elastic (Young's, tensile) modulus is 3.2 GPa
- Flexural strength is 110 MPa
- Tensile strength: ultimate (UTS) is 71 MPa [7].

Properties listed make this material applicable for constructional elements. PMMA plates can be made using laser cutting and serve as stiffeners.

Parts that are not as loaded as PMMA plates were designed to house motors, encoders, rolling bearings and to be 3D printed. Parts were decided to be made of polylactic acid (PLA). This material was chosen over other popular printing material due to several reasons. It is widely spread, has relatively low cost [8], has low requirements for printing conditions and is biodegradable. PLA shows better operational characteristics compared to its closest competitor—acrylonitrile butadiene styrene (ABS) [9].

PLA has the following mechanical properties:

- Elastic (Young's, tensile) modulus is 3.5 GPa
- Flexural strength is 80 MPa
- Tensile strength: ultimate (UTS) is 50 MPa [10].

ABS has the following mechanical properties:

- Elastic (Young's, tensile) modulus is 2.0–2.6 GPa
- Flexural strength is 72–97 MPa
- Tensile strength: ultimate (UTS) is 37–110 MPa [11].

PLA is rather resistant to deformations and has high tensile strength.

2.2 Hardware

Any robotic system requires actuating hardware, and the most suitable one for the robotic arm is stepper motors. These allow control motion via pulses and change their position by steps, instead of rotating them for a given time at a given speed. Stepper motors' main advantages are ruggedness, high reliability and ability to maintain a given shaft position while keeping full torque. On the other hand, there are several disadvantages. Stepper motors have low efficiency, rapidly decreasing torque with increasing speed, the difficulty of control on high speeds, but listed disadvantages are insufficient, as no batteries are used, and the arm operates at relatively low speed.

There are plenty of stepper motors manufactured according to standards of the US National Electrical Manufacturers Association (NEMA). Thus, these can be easily

obtained and replaced. NEMA 17 motors are very popular among prototyping community, as it show the best quality to price ratio. This makes them an optimal choice for the described project's purposes.

2.3 Motion Transmission

There are several principles of actuation to choose from. The first and the most obvious way of connecting motors to joints is direct but comes with several downsides. Motors' speed is too high to operate joints accurately; at the same time, motors' torque is relatively low, thus leading to the necessity of using reducers to optimize actuators characteristics. Chosen NEMA drivers have a step resolution of 1.8 degrees which is rather low and can benefit from a reducer. Not to mention that a reducer can serve as a safety measure and prevent bending of a driver's shaft.

The other option to transmit motion from motors to arm's joints is to use gears. Unfortunately, plastic-printed gears are difficult to manufacture; they have high tolerances and wear out quickly. It is virtually impossible to overcome a backlash without using specific spring-loaded gears; thus, pulleys and timing belt were considered as a suitable choice.

In this scenario, the backlash can be compensated by tensioning elements. Pulleys can be both bought or manufactured via laser cutting or 3D printing as tolerance requirements are lower. Furthermore, interaxial pulley distance can be varied without reduction ration modifications, which provides more constructional freedom.

HTD 3 M standard profile was chosen because of its high operating torques [13]. HTD belts are highly resistant to stretching and are suitable for high-load scenarios.

2.4 Feedback Hardware

To control the robotic arm with high accuracy, feedback utilities must be taken into consideration. Positioning inaccuracies are caused by mechanical imperfections, which come from motors' ability to miss steps and belts' stretching under load. To get information about the real position of arm's joints, sensors are used. The choice was made between several types of ones, but two were tested.

Firstly, optical incremental encoders were tried out. Incremental encoders turned out to have a lot of disadvantages as faced given purposes. The necessity to home the robotic arm before every use and after any step misses decreases the robot's robustness, impossibility to easily register the direction of rotation and incompatibility with used materials make such optical encoders inapplicable. Infrared light used by optical encoders passes through PMMA and PLA encoding perforated disks and makes registering its values impossible.

Then, on-axis magnetic encoders turned out to be the best choice. Those are easily used for absolute joint position tracking, do not require bulky encoding disks, occupying little space and make homing unnecessary.

2.5 Design Synthesis

The main guidelines for design synthesis were established as follows. The robotic arm must be easy to assemble and follow similar design principles within joints.

Each joint must contain a stepper motor, a metallic axis, a pair of rolling bearings, an on-axis magnetic encoder, a load-bearing PMMA plate and a PLA housing, a bigger pulley to receive motion from a previous joint and a smaller one to transmit it to the next joint through a timing belt. Stepper motors must have access to environmental air to prevent overheating and, more importantly, avoid deformation of parts made of PLA and PMMA, as these are thermoplastics.

Load-bearing PMMA parts hold stepper motors and let the construction of the robotic arm be stiff. PLA parts are meant to be connected to the plates and house bearing and encoders. Magnetic encoders are held in place with printed caps (Fig. 2) on each joint axle.

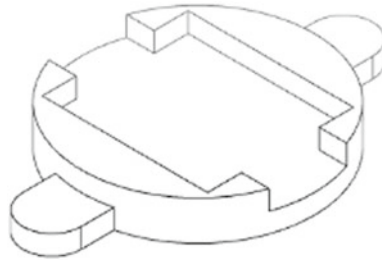


Fig. 2 3D-printed cap to be used as encoder holder

The first joint of the robotic arm is intended to have the highest lifting capacity as it moves all the following joints and a cargo. Furthermore, this joint has the most impact on end-effector’s positioning accuracy as is the furthest from one and multiplies positioning errors due to longer lever.

The multi-stage gearbox was designed. It has four synchronous pulley stages with a transmitting ratio of 40/12 each and a total ratio of 123.5. The positioning of pulleys can be seen in Fig. 3. Each belt is tensioned with eccentric nuts with rollers.

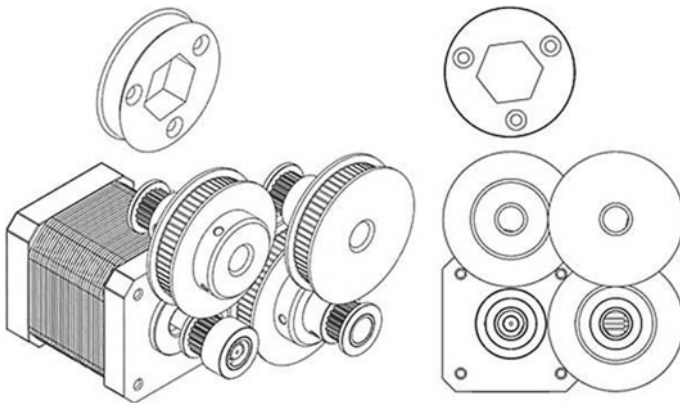


Fig. 3 Pulleys’ positions

There are two different types of joints possible ones that have parallel in-and-out axles and those, which have axles perpendicular. The second joint of the arm had to be the parallel type and is shown in Fig. 4a.

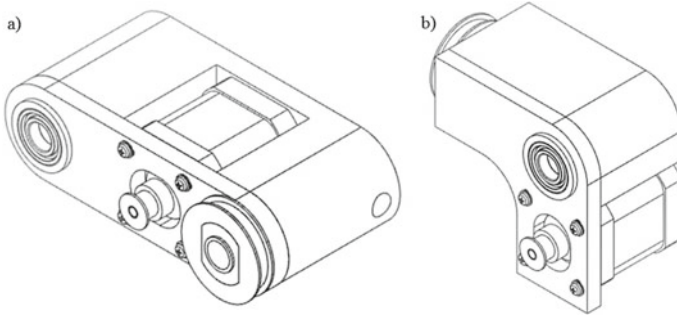


Fig. 4 a Joint with parallel axles; b joint with perpendicular axles

Belt tensioning is achieved by configurable motor mounting which represents a group of slots for a motor and screws. The same applies to the rest of the joints.

Joints from third to fifth were designed with perpendicular in-and-out axles. The third and the fifth joints have the exact same design, the fourth is their opposite-hand version. Unlike parallel axles joint, these ones are L-shaped as shown in Fig. 4b.

The robotic arm's grip was designed to be able to hold objects or their elements which are up to 100 mm wide. The grip uses a single servomotor as an actuator and a geared two-fingered mechanism (Fig. 5). The maximum holding force of the grip can be tuned by the amount of current dedicated to the motor.

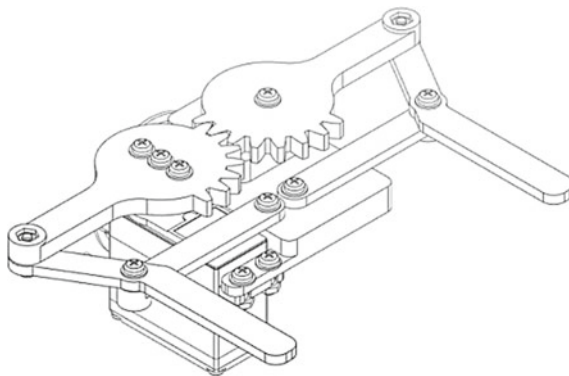


Fig. 5 Grip of the robotic arm

The general view of the robotic arm assembled is shown in Fig. 6. The construction remains in established dimensions and corresponds to the requirements of the project.

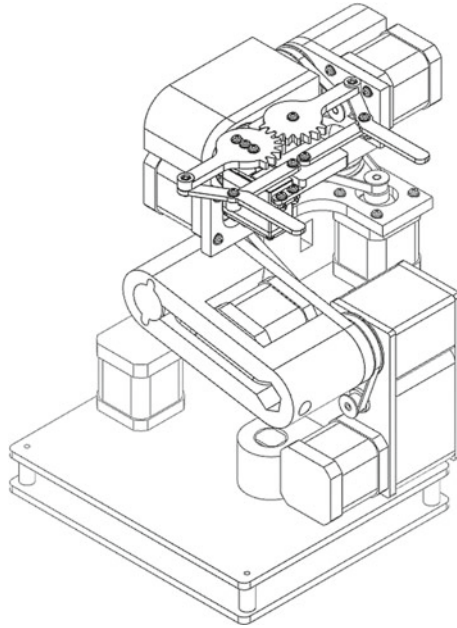


Fig. 6 All joints put together

3 Design of the Software

The main goal of the manipulator is proper following of the end-effector to desired trajectory. In addition to the mechanical system, the control system is required. The architecture of the software is proposed to be separated into two parts: low level and high level. The low-level control subsystem receives the desired velocity and error. It was implemented to minimize the error with the desired velocity. Such a control subsystem works if the motor can provide enough torque value for maximum velocity, which is restricted by hardware.

The high control level must provide the formulation of the task for the manipulator and transform it into an appropriate form to be implemented by low-level control. The graphical user interface is a common solution for high-level part of robot software, but the authors decided to use some initial scripts [14] to be useful for students. In case of using those scripts, the graphical interface could be prepared by students in a simple and quick way. The authors actively used in the scripting part the Python library presented by Kevin Lynch in the [15], so it is strongly recommended literature for teachers, who are going to use described tools in the education process as described in this paper.

The architecture of the software presented is shown in Fig. 7. The main part of the control system was implemented on the microcomputer Raspberry Pi; the low-level control was implemented using microcontroller ATmega on Arduino mega 2560 board with the extension board ramps 1.6 to make easier connection of the drivers for stepper motors. Since the ramps 1.6 has only 4 sockets for drivers, the other two drivers could be connected using one additional board ramps 1.6, or the scheme of the PCB could

be downloaded from the project repository and produced by any available methods on the market or by students in the electronics course. The last one is cheaper and more recommended by authors. The encoders are connected to the Arduino through the extension board. The local controller on the Arduino is processing the digital signal from magnetic encoders updating the data used by local controller. At the same time, the local controller communicates with the high-level control system to send new values from encoder and get new data about the next part of instruction to be implemented on the electromechanical side of the system.

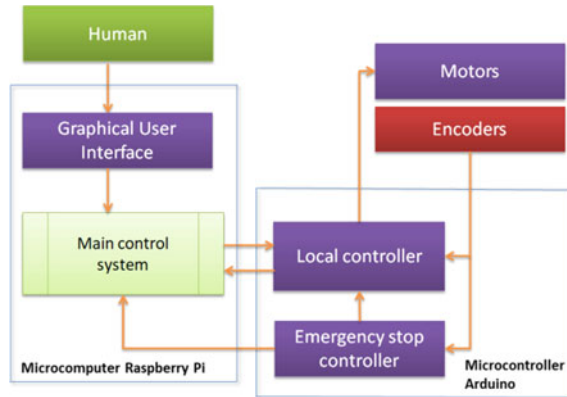


Fig. 7 Illustration of the software architecture

4 Conclusion

In this paper, the authors formulated the main requirements for the robot to be used as a teaching tool in robotics courses at the university. The new mechanical design was developed based on the requirements. The control system with the electronic components was implemented to provide the control algorithms for the mechanical parts. The main feature of the developed robot is financial affordability, keeping it like industrial robots. The results were published on GitHub repository and could be used in education purposes.

Acknowledgements. Authors wishing to acknowledge encouragement from administration of ITMO University for financial support of this project.

References

1. LEGOMINDSTORMS, the official web page of the company. <https://www.lego.com/ru-ru/themes/mindstorms/> Accessed 29 September 2020

2. Bischoff R, Huggenberger U, Prassler E (2011) KUKA youBot—a mobile manipulator for research and education. In: Proceedings—IEEE international conference on robotics and automation
3. Thor project original materials by authors. <https://hackaday.io/project/12989-thor/>. Accessed 15 November 2020
4. Open-source project BCN3D MOVEO. <https://github.com/BCN3D/BCN3D-Moveo>. Accessed 17 November 2020
5. Ivan C, Valentin N, Bozhidar N, George B (2019) Design and control of an educational redundant 3D printed robot. In: International conference on software, telecommunications and computer networks (SoftCOM), Split, Croatia
6. Plexiglas fabrication manual. <https://www.plexiglas.com/export/sites/plexiglas/.content/medias/downloads/sheet-docs/plexiglas-fabrication-manual.pdf>. Accessed 19 November 2020
7. Polymethylmethacrylate (PMMA, Acrylic). <https://www.makeitfrom.com/material-proper-ties/Polymethylmethacrylate-PMMA-Acrylic>. Accessed 19 November 2020
8. 3D Printer material cost: the real cost. <https://all3dp.com/2/3d-printer-material-cost-the-real-cost-of-3d-printing-materials/>. Accessed 5 January 2021
9. Dimić A, Mišković Ž, Mitrović R, Ristivojević M, Stamenić Z, Danko J, Bucha J, Milesich T (2018) The influence of material on the operational characteristics of spur gears manufactured by the 3D printing technology. *Strojnícky časopis J Mech Eng* 68(3)
10. Farbman D, McCoy C (2016) Materials testing of 3D printed ABS and PLA samples to guide mechanical design. In: ASME 2016 11th international manufacturing science and engineering conference
11. Jayanth N, Senthil P, Prakash C (2018) Effect of chemical treatment on tensile strength and surface roughness of 3D-printed ABS using the FDM process. *Virtual Phys Prototyping* 13(3):155–163
12. Stepper motor: construction, working, types and its applications. <https://www.elprocus.com/stepper-motor-types-advantages-applications/>. Accessed 15 January 2021
13. Timing belt drive selection procedure. <https://www.sdp-si.com/D265/PDF/D265T146.pdf>. Accessed 17 January 2021
14. Project repository on Github services. <https://github.com/industrial-robotics-lab/small-manipulator>. Accessed 18 January 2021
15. Lynch KM, Park FC (2017) *Modern robotics: mechanics, planning, and control*. Cambridge University Press



Influence of the Fuel Injection Advance Angle on the Technical and Environmental Performance of a Diesel Engine (21/21) with a Turbocharger

D. S. Shestakov and L. V. Plotnikov(✉)

Ural Federal University named after the first President of Russia B.N. Yeltsin, 19, Mira str, Ekaterinburg 620002, Russia

Abstract. Diesel engines are used in all branches of engineering and technology. The modern market of the diesel locomotive, automobile and power plants based on diesel engines imposes strict requirements on the values of specific fuel consumption and the amount of harmful emissions. Therefore, improving the technical and environmental performances of diesel engines remains the primary task in the development of piston engine building. A brief overview of modern trends in the improvement of diesel engines is presented in the article. The description of the investigated diesel engine and the conditions of the experiments is given in the article. The authors studied the influence of the fuel injection advance angle on the technical and environmental performances of an engine with a turbocharger for a diesel locomotive through experimental studies. The studies were carried out at the stands of the LLC “Ural Diesel Motor Plant” in accordance with the regulatory documents. It is shown that the fuel injection advance angle has a significant effect on the performance of a diesel engine. It was found that the specific fuel consumption is reduced to 10%, the amount of NO_x emissions is reduced to 50% and the maximum cycle pressure is reduced to 25% by selecting the optimal fuel injection advance angle at low crankshaft speeds.

Keywords: Diesel engine · Fuel injection advance angle · Bench tests · Technical and economic indicators · Environmental friendliness of engines

1 Introduction

Internal combustion engines are common energy converters. The important advantages of engines are that they can be used in various climatic conditions, engines are mobile power plants and engines are sufficiently reliable and maintainable [1, 2]. The modern market of diesel locomotive, automobile and power plants based on internal combustion engines puts forward stringent requirements for the values of specific fuel consumption and the amount of harmful emissions of diesel engines in all operating modes [3, 4].

Today, there are many ways to improve the technical and environmental performances of diesel engines. Some of these methods are discussed below. One of the most common

methods is to set the optimum values for fuel injection pressure, injection time and the amount of fuel supplied [5–8]. Optimal setting of the considered parameters for a gasoline or diesel engine can significantly improve fuel efficiency and environmental friendliness. Also, positive effects can be achieved by adjusting the composition of the fuel–air mixture [9]. The design of the piston (combustion chamber) and materials for their manufacture have a noticeable effect on the technical performance of the engine [10, 11]. The modern way to improve the performance of engines is to use multiple and stratified fuel injection [12, 13]. This method affects both the efficiency and the environmental friendliness of engines. Moreover, it has been established that the type of fuel used (biofuel, hydrogen, etc.) and the thermal state of the engine significantly affect the performance of engines [14–17]. A separate direction for improving the performance of engines is to improve the processes of gas exchange [18–20]. Scientists and engineers have also investigated the effect of boost and variable compression ratio on engine efficiency and environmental friendliness [21, 22]. Another effective way to improve the efficiency of diesel engines is the introduction of regulation of the fuel injection advance angle depending on the power and crankshaft speed [23, 24]. According to the authors, this direction of improving diesel engines has not exhausted its potential and should be studied in more detail.

In this article, the influence of the fuel injection advance angle on the technical and environmental performances of an engine with a turbocharger (cylinder diameter—210 mm and piston stroke—210 mm) for a diesel locomotive was experimentally investigated using bench tests.

2 Research Object and Problem Statement

The research engine has the factory designation 8DM-21. It is an eight-cylinder V-shaped turbocharged diesel engine (Fig. 1). The 8DM-21 diesel can be used in all types of power plants with minor design changes. In this study, a modification of the 8DM-21 engine was selected for use on diesel locomotives.

The high-pressure fuel pump has a mechanical drive in the form of a spring with double-sided splines (Fig. 2). The pump is driven via a bevel gear transmission from the engine crankshaft. The number of splines at the ends of the spring is made unequal (external—31, and internal—26) to ensure the setting of the fuel injection advance angle φ_{inj} with an accuracy of $\pm 1^\circ$. This design has high reliability and the ability to set the fuel injection advance angle during the assembly of the diesel engine without the possibility of changing it during operation. The design and manufacturability of this drive have proven themselves over several decades of operation.

The fuel injection advance angle φ_{inj} was 34° (degrees of crankshaft rotation) to top dead center (TDC) for the base 8DM-21 diesel engine. The value of the φ_{inj} remained constant for the base diesel engine at all operating modes. In the course of the study, the value of the fuel injection advance angle varied from 12° to TDC to 40° to TDC for the modernized engine. The step of changing the φ_{inj} was 2° .

The diesel engine was tested at the test benches of LLC “Ural Diesel Motor Plant” in accordance with the regulations of the Russian Federation. The studies were carried out at a crankshaft speed from 520 to 1500 rpm and at an engine load from 0 to 100%. The

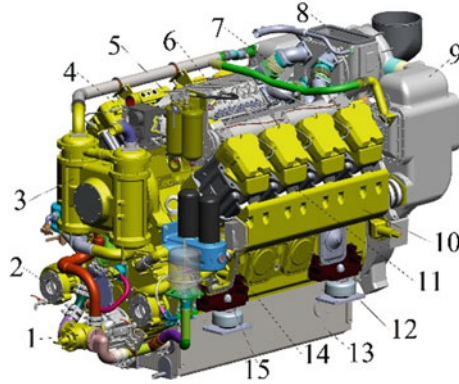


Fig. 1 Layout of the 8DM-21 diesel engine: 1— temperature regulator; 2—water pump; 3— water–oil cooler; 4—executive device of the speed regulator; 5—water collector; 6—high-pressure fuel pump; 7—compensator; 8—turbocharger; 9—charge air cooler; 10—intake manifold; 11— cylinder head; 12—shock absorber; 13—pallet; 14—crankcase; 15—oil filter

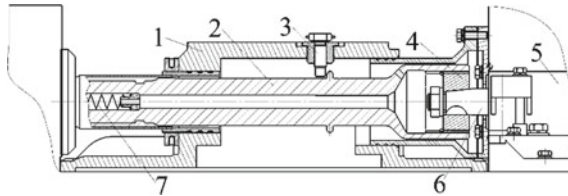


Fig. 2 High-pressure fuel pump drive: 1—drive housing; 2—spring of the fuel pump drive; 3— bolt for limiting the movement of the spring; 4—splined bushing; 5—high-pressure fuel pump; 6—high-pressure fuel pump drive shaft; 7—spring

main efficiency criteria of the modernized diesel engine was specific fuel consumption, NO_x emissions and maximum cycle pressure. Additional condition: The values of power and torque of a diesel engine with new values of the fuel injection advance angle must correspond to the values of the base engine (8DM-21) with deviations of no more than ±5%.

3 The Results of Bench Tests of a Diesel Engine

The influence of the fuel injection advance angle φ_{inj} on the economic performance of a diesel engine is shown in Fig. 3.

It was revealed that the specific fuel consumption g_e significantly decreased at the fuel injection advance angles φ_{inj} from 40 to 24° at a load of up to 25% of the rated power. At the same time, g_e had almost the same values at φ_{inj} from 24 to 12°. This is due to the fact that the autoignition delay period increased with an increase in the crankshaft speed, and this led to a delay in the start of fuel ignition. Accordingly, the heat release from fuel combustion occurred during the expansion process, so the efficiency became worse at high φ_{inj} and at a low crankshaft speed with a small load on the diesel engine. The

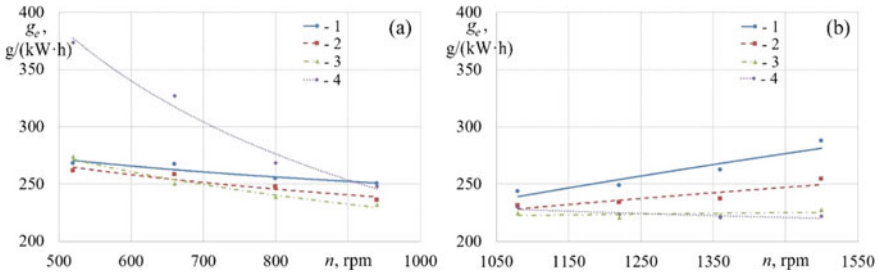


Fig. 3 Dependence of specific fuel consumption g_e on the crankshaft speed n at a load of up to 50% of the rated power **a** and up to 100% **b** for different φ_{inj} : 1—12°; 2—20°; 3—30°; 4—40°

duration of fuel injection and heat release decreased with a drop in load. This led to an increase in the cycle fuel supply and, as a consequence, to an increase in the specific fuel consumption. For the same reason, a significant difference was observed in the values of g_e at angles φ_{inj} equal to 40 and 34°. It should be noted that the nature of the change in the specific fuel consumption from the crankshaft rotation speed was identical for all values of the fuel injection advance angle.

The efficiency of the 8DM-21 diesel engine significantly improved at high values of φ_{inj} (40–36°) with an increase in the crankshaft speed from 660 to 940 rpm and an increase in the engine load up to 50% of the rated power (Fig. 3). Also, efficiency continued to improve slightly at low values of φ_{inj} (34–12°). This can be explained by the fact that there is an optimal fuel injection advance angle for each combination of crankshaft speed and cyclic fuel supply, at which the highest values of efficiency and average pressure of the engine cycle are achieved. The specific fuel consumption g_e of the 8DM-21 diesel reached its minimum value at $\varphi_{inj} = 12\text{--}22^\circ$ at a crankshaft rotation speed of 1080 rpm and a load of 50 to 75% of the rated power (Fig. 3). This can be explained by the fact that there is an increase in the filling ratio and the excess air ratio, and as a result, a more complete combustion of the fuel takes place. It should be noted that there was a deterioration in efficiency at all φ_{inj} values at $n > 1250$ rpm (i.e., at a load from 75 to 100% of rated power). This is due to the fact that the filling of the cylinder with the working fluid deteriorated with increasing fuel supply. This was also accompanied by a proportional decrease in the excess air ratio, which led to a decrease in efficiency and average cycle pressure.

The influence of the fuel injection advance angle φ_{inj} on the amount of NOx emissions in the exhaust gases can be traced in Fig. 4. Figure 4 shows that the amount of NOx emissions increased proportionally with increasing values of φ_{inj} . NOx production slowed down significantly with decreasing φ_{inj} due to the lower combustion temperature. However, it should be noted that the smoke of the exhaust gases increased with decreasing φ_{inj} . The maximum amount of NOx emissions occurred at low rotational speeds n and low diesel power (Fig. 4). This is due to the low fuel injection pressure, which leads to deterioration of atomization and mixing of fuel with air, an increase in the temperature in the cylinder due to the formation of separate zones in the combustion chamber with a lack of oxygen. A noticeable decrease in the amount of NOx emissions took place with an increase in the crankshaft speed n , which was typical for all fuel

injection advance angles φ_{inj} . This can be explained by the improvement in the mixture formation and combustion conditions due to the increase in fuel injection pressure.

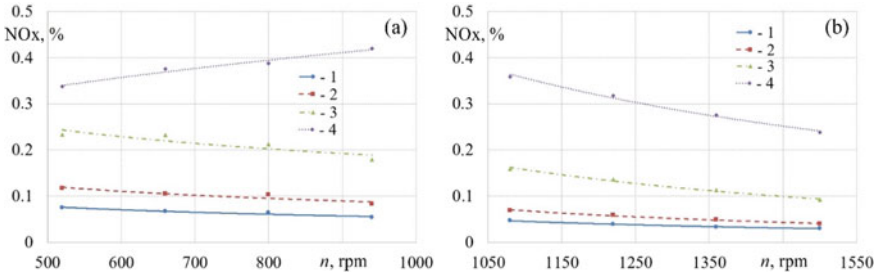


Fig. 4 Dependence of the amount of NOx emissions on the crankshaft speed n at a load of up to 50% of the rated power **a** and up to 100%, **b** for different φ_{inj} : 1—12°; 2—20°; 3—30°; 4—40°

The influence of the fuel injection advance angle φ_{inj} on the maximum cycle pressure p_z of the 8DM-21 diesel is shown in Fig. 5. Figure 5 shows that there is an increase in the maximum cycle pressure of the diesel engine with increasing φ_{inj} . This indicates the increasing mechanical stress on the main engine parts. It has been experimentally established that the maximum possible values of p_z are 15 MPa for a given diesel engine. The conditions of strength and reliability are met with these parameters.

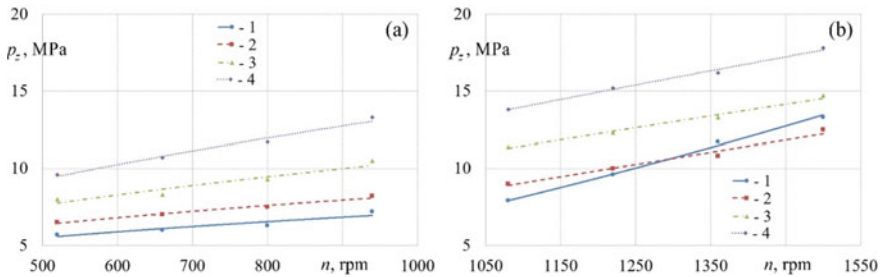


Fig. 5 Dependence of the maximum cycle pressure p_z on the crankshaft speed n at a load of up to 50% of the rated power **a** and up to 100%, **b** for different φ_{inj} : 1—12°; 2—20°; 3—30°; 4—40°

The dependences of the specific fuel consumption, the amount of NOx emissions and the maximum cycle pressure for the base diesel engine ($\varphi_{inj} = 34^\circ$) and for the modernized engine with new values of the fuel injection advance angle are shown in Fig. 6. On the basis of bench tests, it was found that the fuel injection advance angle had an optimal value of 24° at $n = 520$ rpm, and the other optimum was $\varphi_{inj} = 26^\circ$ at $n = 660$ rpm. In other modes of engine operation, the fuel injection advance angle was equal to the base one, i.e., 34°.

Specific fuel consumption of the modernized engine was decreased by 7–10% compared to the base diesel engine at low crankshaft speeds (Fig. 6a). The amount of NOx emissions from the modernized engine was decreased by up to 50% compared to the base

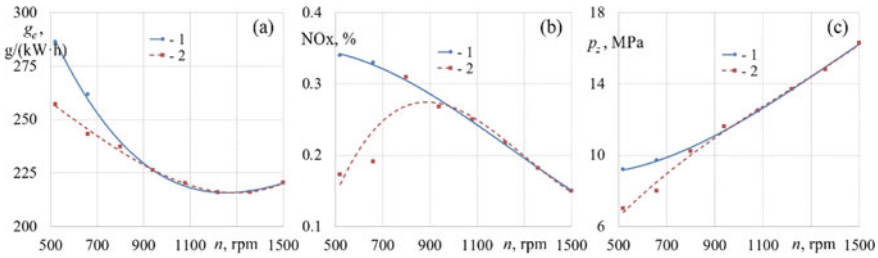


Fig. 6 Dependences of the specific fuel consumption g_e **a** amount of NOx emissions, **b** and the maximum cycle pressure p_z , **c** on the crankshaft speed n for the base diesel engine (1) And the modernized engine (2)

diesel (Fig. 6b). Moreover, the maximum values of the cycle pressure of the modernized engine were decreased by 17–24% than that of the base diesel engine (Fig. 6c). Considering that the 8DM-21 diesel engine mainly operates at low crankshaft speeds, this will have a positive impact on the technical, economic and environmental performances of the locomotive.

4 Conclusion

The following conclusions can be drawn from the experiments carried out:

1. It is shown that the fuel injection advance angle has a significant effect on the technical, economic and environmental performances of a turbocharged diesel engine.
2. It was found that the specific fuel consumption is reduced to 10%, the amount of NOx emissions is reduced to 50% and the mechanical loads are reduced to 25% by choosing the optimal fuel injection advance angle at low crankshaft speeds of the 8DM-21 diesel engine.
3. It is necessary to continuously adjust the fuel injection advance angle, taking into account the load and the crankshaft speed, in order to ensure the optimal performance of the diesel engine.
4. For the 8DM-21 diesel engine, the fuel injection advance angle should be controlled in the range from 24 to 34° at a crankshaft rotation speed from 520 to 1500 rpm by using a fuel injection advance clutch or by introducing a fuel pump with solenoid valves.

References

1. Virubov DN, Ivaschenko NA (1983) Internal combustion engines: theory of piston and combined engines. Engineering, Moscow
2. Taylo AMKP (2008) Science review of internal combustion engines. *Energ Pol* 36(12):4657–4667. <https://doi.org/10.1016/j.enpol.2008.09.001>

3. Knecht W (2008) Diesel engine development in view of reduced emission standards. *Energy* 33(2):264–271. <https://doi.org/10.1016/j.energy.2007.10.003>
4. O'Driscoll R, Stettle MEJ, Molden N, Oxley T, ApSimon HM (2018) Real world CO₂ and NO_x emissions from 149 Euro 5 and 6 diesel, gasoline and hybrid passenger cars. *Sci Total Environ* 621:282–290. <https://doi.org/10.1016/j.scitotenv.2017.11.271>
5. Lan Q, Bai Y, Fan L, Gu Y, Wen L, Yang L (2020) Investigation on fuel injection quantity of low-speed diesel engine fuel system based on response surface prediction model. *Energy* 211:118946. <https://doi.org/10.1016/j.energy.2020.118946>
6. Jain A, Porpatham E, Thipse SS (2020) Emission reduction strategies for small single cylinder diesel engine using valve timing and swirl ratio. *Int J Eng Trans B Appl* 33(8):1608–1619. <https://doi.org/10.5829/ije.2020.33.08b.19>
7. Kiplimo R, Tomita E, Kawahara N, Yokobe S (2012) Effects of spray impingement, injection parameters, and EGR on the combustion and emission characteristics of a PCCI diesel engine. *Appl Therm Eng* 37:165–175. <https://doi.org/10.1016/j.applthermaleng.2011.11.011>
8. Sener R, Yangaz MU, Gul MZ (2020) Effects of injection strategy and combustion chamber modification on a single-cylinder diesel engine. *Fuel* 266:117122. <https://doi.org/10.1016/j.fuel.2020.117122>
9. Jeon J (2020) Spatiotemporal flame propagations, combustion and solid particle emissions from lean and stoichiometric gasoline direct injection engine operation. *Energy* 210:118652. <https://doi.org/10.1016/j.energy.2020.118652>
10. Vijaya Kumar K, Shailesh P, Srinivasa Raghavan K, Ranga Babu JA, Ravi Kumar P (2020) Performance and emission analysis of diesel engine with design modifications on piston crown. *Int J Ambient Energ* 41(12):1336–1341. <https://doi.org/10.1080/01430750.2018.1517664>
11. Thibblin A, Olofsson U (2020) A study of suspension plasma-sprayed insulated pistons evaluated in a heavy-duty diesel engine. *Int J Engine Res* 21(6):987–997. <https://doi.org/10.1177/1468087419879530>
12. Zhang M, Derafshzan S, Richter M, Lundgren M (2020) Effects of different injection strategies on ignition and combustion characteristics in an optical PPC engine. *Energy* 203:117901. <https://doi.org/10.1016/j.energy.2020.117901>
13. Mathivanan K, Mallikarjuna JM, Ramesh A (2016) Influence of multiple fuel injection strategies on performance and combustion characteristics of a diesel fuelled HCCI engine—an experimental investigation. *Exp Therm Fluid Sci* 77:337–346. <https://doi.org/10.1016/j.expthermflusci.2016.05.010>
14. Shojae K, Mahdavian M (2018) Influences of spray angle and bowl center depth on power and exhaust emissions in a dual fuel direct injection engine. *Int J Engine Res* 19(6):643–652. <https://doi.org/10.1177/1468087417727425>
15. Hoang AT, Le AT, Pham VV (2019) A core correlation of spray characteristics, deposit formation, and combustion of a high-speed diesel engine fueled with Jatropha oil and diesel fuel. *Fuel* 244:159–175. <https://doi.org/10.1016/j.fuel.2019.02.009>
16. Guardiola C, Climent H, Pla B, Reig A (2017) Optimal Control as a method for Diesel engine efficiency assessment including pressure and NO_x constraints. *Appl Therm Eng* 117:452–461. <https://doi.org/10.1016/j.applthermaleng.2017.02.056>
17. Olmeda P, Martín J, Novella R, Blanco-Cavero D (2020) Assessing the optimum combustion under constrained conditions. *Int J Engine Res* 21(5):811–823. <https://doi.org/10.1177/1468087418814086>
18. Plotnikov LV, Zhilkin BP, Brodov YM (2020) Physical and numerical modeling of thermo-mechanical processes in gas-air systems of piston engines under gasdynamic-nonstationarity conditions. *J Eng Phys Thermophys* 93(3):594–604. <https://doi.org/10.1007/s10891-020-02157-w>

19. Plotnikov LV, Zhilkin BP (2018) Influence of gas-dynamical nonstationarity on local heat transfer in the gas–air passages of piston internal-combustion engines. *J Eng Phys Thermophys* 91(6):1444–1451. <https://doi.org/10.1007/s10891-018-1879-8>
20. Plotnikov LV, Zhilkin BP, Brodov YM (2020) Thermomechanical improvement of gas–air systems of turbocharged piston internal-combustion engines. *J Eng Phys Thermophys* 93(6):1557–1566. <https://doi.org/10.1007/s10891-020-02260-y>
21. Chen J, Wang B, Liu D, Yang K (2019) Study on the dynamic characteristics of a hydraulic continuous variable compression ratio system. *Appl Sci* 9(21):4484. <https://doi.org/10.3390/app9214484>
22. Tang Q, Fu J, Liu J, Boulet B, Tan L, Zhao Z (2016) Comparison and analysis of the effects of various improved turbocharging approaches on gasoline engine transient performances. *Appl Therm Eng* 93:797–812. <https://doi.org/10.1016/j.applthermaleng.2015.09.063>
23. Yoon SH, Kim HJ, Park S (2018) Study on optimal combustion strategy to improve combustion performance in a single-cylinder PCCI diesel engine with different combustion chamber geometry. *Appl Therm Eng* 144:1081–1090. <https://doi.org/10.1016/j.applthermaleng.2018.09.003>
24. Raeie N, Emami S, Karimi Sadaghiyani O (2014) Effects of injection timing, before and after top dead center on the propulsion and power in a diesel engine. *Propul Power Res* 3(2):59–67. <https://doi.org/10.1016/j.jprr.2014.06.001>



Evaluation of the Effect of Longitudinal Forces on the Stability of Straight Line Movement of a Tractor Unit

A. Startcev¹(✉), S. Romanov², and I. Storozhev³

- ¹ South Ural State Agrarian University, 75, Lenin Avenue, Chelyabinsk 454080, Russia
² State Agricultural University of the Northern Trans-Ural Region, 7, Republic Street, Tyumen 625003, Russia
³ Ural State University of Railway Transport, 66, Kolmogorov Street, Sverdlovsk Region, Yekaterinburg 620034, Russia

Abstract. The article presents a mathematical model that allows us to evaluate the effect of longitudinal forces on the stability of straight line movement of a all-wheel drive machine-tractor unit. The use of all-wheel drive machine-tractor units that have a free hinge between the tractor and trailer allows you to change the longitudinal force of interaction between these kinematic links. It is obvious that the magnitude and direction of this interaction force can affect the stability of the rectilinear motion of such machines. However, this factor has not been sufficiently studied and requires the creation of new theoretical approaches. The proposed theoretical approach is based on Lagrange equations of the second kind with indefinite multipliers. The application of this theoretical approach was dictated by the presence of nonholonomic constraints in the system. As a result of the research, it was found that the deviation of a single-axle tractor trailer from the line of movement of a all-wheel drive machine-tractor unit, which determines its stability, depends on the size and direction of the longitudinal component of the traction force on the tractor hook and the construction parameters of the trailer, the properties of wheel tires and the support surface. The results of experimental studies confirmed the possibility of using the proposed mathematical model for practical calculations.

Keywords: Machine-tractor unit · Mathematical model · Stability of straight line movement

1 Introduction

Increasing the productivity of tractor units in the production of transport works can be achieved by using trailers with driving axles [1–5]. However, the use of drive axles on the trailer leads to a decrease in the longitudinal component of the traction force on the tractor hook, which negatively affects the stability of the straight line movement of the trailer. Nevertheless, the influence of the longitudinal component of the traction force on the tractor hook on the stability of the straight line movement of the trailer has not been sufficiently studied and requires further theoretical and experimental studies.

2 Theoretical Studies

In order to study the stability of the rectilinear movement of a single-axle trailer with driving wheels, calculation schemes were compiled (Fig. 1). When drawing up the calculation schemes, the recommendations were taken into account [6–15].

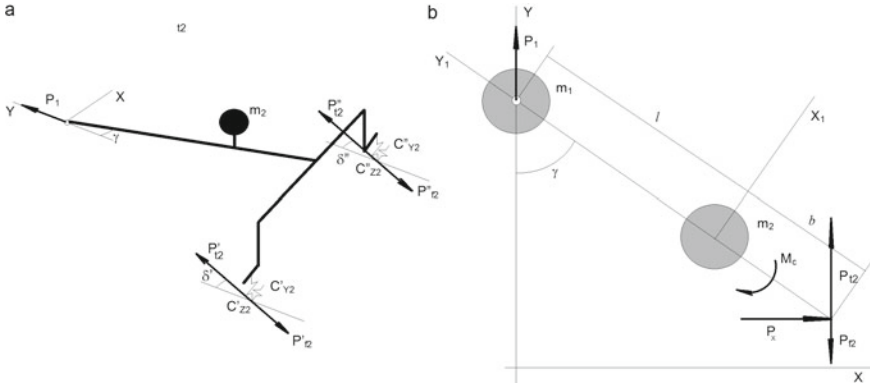


Fig. 1 **a** Actual calculation scheme; **b** equivalent calculation scheme

When developing the mathematical model, only small angles of deviation of the trailer from the line of movement of the tractor were considered. In the process, the actual calculation scheme was replaced with an equivalent one. The equivalent calculation scheme was a system of two bodies with masses m_1 and m_2 , connected by a rigid connection having a hinge with one degree of freedom. The movement of the machine-tractor unit was considered on a flat horizontal surface. The movement of the tractor is straight and uniform with a speed of V_1 .

To create equations of motion for a machine-tractor unit with nonholonomic constraints, we used Lagrange equations of the second kind with indeterminate multipliers [11–20]:

$$\frac{d}{dt} \left(\frac{\partial T}{\partial \dot{q}_i} \right) - \frac{\partial T}{\partial q_i} = Q_i + \lambda_1 A_{1i} + \dots + \lambda_m A_{mi},$$

$$i = 1 \dots s \quad i \in \{1, s\} \tag{1}$$

s —number of generalized coordinates; m —number of nonholonomic constraints; $\lambda_1 \dots \lambda_m$ —indeterminate multipliers; $A_{1i} \dots A_{mi}$ —coefficients of the nonholonomic constraints; T —kinetic energy of the system.

The formula for the kinetic energy of a machine-tractor unit, taking into account the accepted assumptions, has the form

$$T = \frac{(m_1 + m_2)}{2} \dot{y}^2 + \frac{m_2}{2} l^2 \dot{\gamma}^2 + m_2 l \dot{y} \dot{\gamma} \sin \gamma + \frac{J_2 \dot{\gamma}^2}{2}, \tag{2}$$

J_2 —moment of inertia of the trailer relative to its center of mass.

The work of external forces on elementary movements

$$dA = (P_1 + P_{T2} - P_{f2})dy + [((P_{T2} - P_{f2}) \cdot (l + b)) \cdot \sin \gamma + P_x(l + b) \cdot \cos \gamma - M_c] \cdot d\gamma, \tag{3}$$

P_{T2} —total tangential traction force of the driving wheels of the trailer; P_{f2} —total resistance force to rolling of wheels of the trailer; P_1 —traction force on the tractor hook; P_x —lateral force; M_c —moment of resistance to turning the trailer.

A wheel loaded with lateral force performs a complex movement. The movement of the wheel relative to the plane of motion can be described by the dependency

$$\operatorname{tg} \delta = \frac{\dot{X}}{\dot{Y}}, \quad \text{or, taking } \operatorname{tg} \delta \approx \delta, \quad \delta = \frac{\dot{X}}{\dot{Y}}. \tag{4}$$

Then, the constraint equation has the form

$$\dot{y}\delta - \dot{\gamma}(l + b) = 0. \tag{5}$$

Based on the above, we will make up the equations of motion of the all-wheel drive machine-tractor unit

$$\begin{cases} (m_1 + m_2)\ddot{y} + m_2l(\ddot{\gamma} \sin \gamma + \dot{\gamma}^2 \cos \gamma) = P_1 + P_{T2} - P_{f2} + \delta\lambda_1 \\ (m_2l^2 + J_2)\ddot{\gamma} + \ddot{y}m_2l \sin \gamma = P_x(l + b) \cos \gamma \\ \quad + (P_{T2} - P_{f2})(l + b) \sin \gamma - M_c - (l + b)\lambda_2 \\ \dot{y}\delta - \dot{\gamma}(l + b) = 0. \end{cases} \tag{6}$$

Analysis of the resulting system of Eq. (6) shows that the first equation describes the traction dynamics of a machine-tractor unit and does not affect the stability of straight line movement. To study the stability of straight line motion, the last two equations that describe the movement of a all-wheel drive tractor unit in a transverse plane are of interest. Taking into account the accepted assumptions about the smallness of the deviation angles, these equations can be written as

$$\begin{cases} (m_2l^2 + J_2)\ddot{\gamma} + \ddot{y}m_2l\gamma + ((P_{T2} - P_{f2})(l + b) + C_\phi n)\gamma = P_x(l + b) - (l + b)\lambda_2 \\ \dot{y}\delta - \dot{\gamma}(l + b) = 0. \end{cases} \tag{7}$$

C_ϕ —angular stiffness of the pneumatic tire of the trailer wheel; n —number of trailer wheels.

In the system of Eq. (7), the indeterminate multiplier λ_2 is the resultant of the lateral forces that leads to tire slip of the trailer wheels. Thus, there is a mathematical expression

$$\delta = \frac{\lambda_2}{k_{ts}n}, \tag{8}$$

k_{ts} —coefficient of resistance to lateral tire slip of trailer wheels.

Taking into account (8), we get

$$\begin{cases} (m_2l^2 + J_2)\ddot{\gamma} + \ddot{y}m_2l\gamma + ((P_{t2} - P_{f2})(l + b) + C_{\phi}n)\gamma = P_x(l + b) - (l + b)\lambda_2 \\ \dot{y}\frac{\lambda_2}{k_{ts}n} - \dot{\gamma}(l + b) = 0. \end{cases} \tag{9}$$

Solving the system of Eq. (9), we obtain the equation of motion of a all-wheel drive machine-tractor unit with a single-axle trailer for uniform movement ($V = \text{const}$)

$$(m_2l^2 + J_2)\ddot{\gamma} + \frac{k_{ts}n(l + b)^2}{V_1}\dot{\gamma} + ((P_{t2} - P_{f2})(l + b) + C_{\phi}n)\gamma = P_x(l + b) \tag{10}$$

or

$$\ddot{\gamma} + \frac{k_{ts}n(l + b)^2}{V_1(m_2l^2 + J_2)}\dot{\gamma} + \frac{(P_{t2} - P_{f2})(l + b) + C_{\phi}n}{(m_2l^2 + J_2)}\gamma = \frac{P_x(l + b)}{(m_2l^2 + J_2)}. \tag{11}$$

Thus, the motion of a single-axle trailer with driving wheels can be described by a linear non-uniform second-order differential equation with constant coefficients of the form

$$\ddot{\gamma} + 2n\dot{\gamma} + \omega^2\gamma = M, \tag{12}$$

$2n$ —dissipative coefficient; ω^2 —quasi-elastic coefficient.

The stability of the straight line movement of the trailer can be judged by the signs of the dissipative ($2n$) and quasi-elastic (ω^2) coefficients. In a steady motion, both coefficients should be positive.

Analysis of Eq. (12) shows that the dissipative coefficient will always be positive. However, its value is largely determined by the value of the coefficient of resistance to lateral tire slip of trailer wheels and the speed of movement of the machine-tractor unit.

The quasi-elastic coefficient will be positive only if there is a pulling force on the tractor hook. According to the accepted assumption ($V = \text{const}$), the magnitude and direction of the traction force on the tractor hook can be defined as

$$P_1 = P_{t2} - P_{f2}. \tag{13}$$

Taking into account (13), the equation of motion (11) takes the form

$$\ddot{\gamma} + \frac{k_{ts}n(l + b)^2}{V_1(m_2l^2 + J_2)}\dot{\gamma} + \frac{P_1(l + b) + C_{\phi}n}{(m_2l^2 + J_2)}\gamma = \frac{P_x(l + b)}{(m_2l^2 + J_2)}. \tag{14}$$

At the same time, the presented analysis of Eq. (12) allows obtaining only a qualitative solution. We can say whether the movement is stable or not. In order to find a quantitative solution to the equation of motion (14), it is necessary to carry out experimental studies aimed at finding the parameters of the rigidity of pneumatic tires of trailer wheels.

3 Results of Experimental Researches

Experimental studies to determine the elastic characteristics of pneumatic tires of trailer wheels were carried out at a special stand. Tires 8.25–15 and 9.00–16, which are usually equipped with model 855 tractor trailers, were used as the object of research. When carrying out measurements and processing the results of experimental studies, recommendations were taken into account [21, 22].

Considering the limited scope of the article, as a fragment of experimental studies, the dependence of the angular stiffness of pneumatic tires 8.25–15 and 9.00–16 on the radial load on the wheel is presented (Fig. 2).

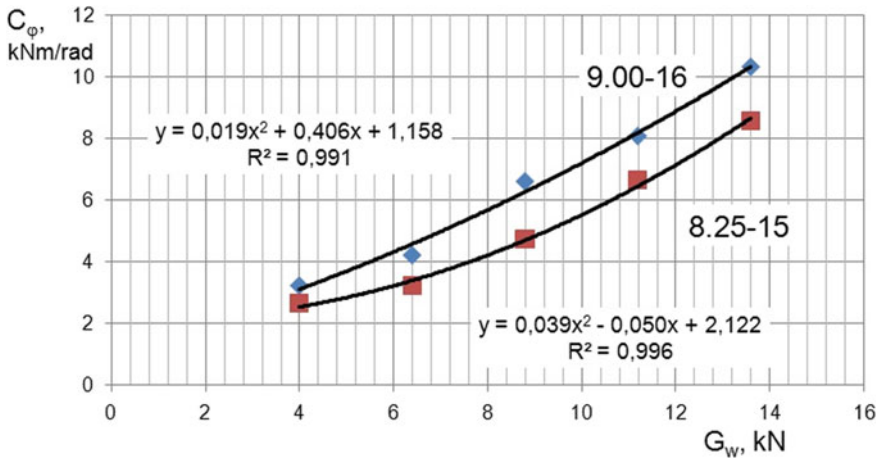


Fig. 2 Angular stiffness of pneumatic tires 8.25–15 and 9.00–16 on the radial load on the wheel

The analysis of the data presented in Fig. 2 shows that the angular stiffness of pneumatic tires is highly dependent on the radial load on the wheel. The dependence is complex and nonlinear. The experimental data obtained with a 95% confidence level were described by a second-order regression equation.

The data obtained as a result of experimental studies were subsequently used in carrying out mathematical modeling of the movement process of a single-axle trailer model 855. The drive axle of the trailer was equipped with wheels with pneumatic tires 9.00–16. The specific folding angle of the all-wheel drive machine-tractor unit was used as the output parameter of the mathematical model. The results of mathematical modeling are presented in Fig. 3.

The analysis of the data presented in Fig. 3 shows that the traction force on the tractor hook has a significant effect on the stability of the straight line motion of a single-axle trailer with driving wheels. This effect is especially evident when the trailer is moving without load.

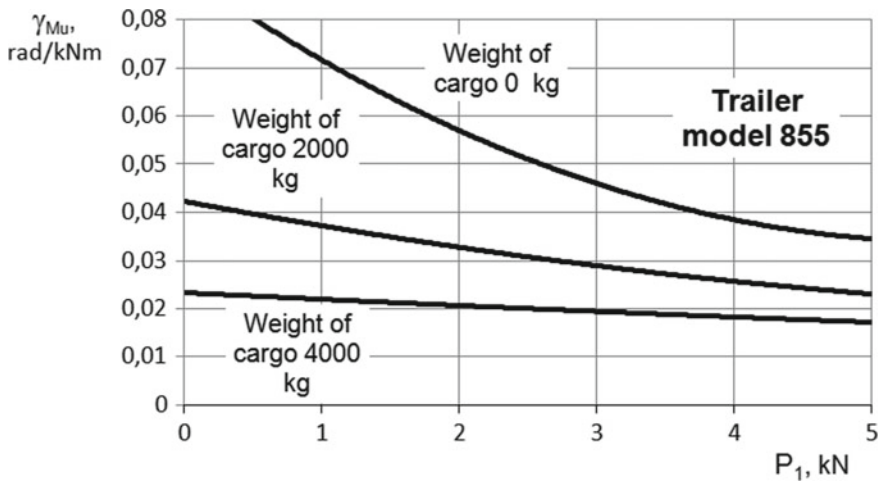


Fig. 3 Change in the specific folding angle of the machine-tractor unit depending on the magnitude of the traction force on the tractor hook

4 Conclusions

The angular stiffness of pneumatic tires is highly dependent on the radial load on the wheel. The dependence is complex and nonlinear. The proposed mathematical model statistically significantly describes the results of experimental studies.

When designing and using trailers with driving wheels, it is necessary to remember about the stabilizing effect of the longitudinal component of the traction force on the tractor hook on the stability of the straight line motion of the all-wheel drive machine-tractor unit.

References

1. Bekker MG (1956) Theory of land locomotion. The University of Michigan Press, p 277
2. Bekker MG (1969) Introduction to Terrain-vehicle systems. University of Michigan Press, Ann Arbor, MI
3. Grytsenko AV (2013) Concept of development of methods and means of diagnosis of cars. In: The collection: achievements of science-agro-industrial production LII international scientific and technical conference, pp 42–49
4. Abdel Hady MBA, Crolla DA (1992) Active suspension control algorithms for a four-wheel vehicle model. *Int J Veh Des* 13(2):144–158
5. Startcev AV, Storozhev II (2009) Efficiency of using machine-tractor units with engines operating on multi-component fuel. In: Communication 1. Economic assessment. Science and production: CHRO RAEN, Chelyabinsk, pp 10–17
6. Benzit P (1982) Transient dynamic behaviour of a vehicle by mathematical simulation. *ISAE Tech Paper Ser 820764*:1–9
7. Bulgakov V, Pascuzzi S, Nadykto V, Ivanovs S (2018) A mathematical model of the plane-parallel movement of an asymmetric machine-and-tractor aggregate. *Agriculture* 8(10):151

8. Franken G, Glass Z (2007) Advanced state estimation and control of an autonomous ground vehicle using a priori knowledge of vehicular dynamics. Princeton University Junior Independent Project. Princeton, NJ, May 2007, p 40
9. Olson BJ (2001) Nonlinear dynamics of longitudinal ground vehicle traction. M.S. thesis defense, Michigan State University, p 53
10. Olson BJ, Shaw SW, Stepan G (2004) Nonlinear dynamics of longitudinal vehicle traction. In: Proceedings of the 9-th mini-conference on vehicle system dynamics, identifications and anomalies, Budapest, p 537–545
11. Pushkin AV (2004) Simulations of the effects of the micro-profile of roads on the movable ground object. *Tula Instrum Control* 2:81–85
12. Short M, Pont MJ, Huang Q (2004) Simulation of vehicle longitudinal dynamic. Technical report ESL 04–01, Embedded Systems Laboratory, University of Leicester, p 18
13. Startcev AV (1997) Results of experimental studies of the micro-profile of roads. *Chelyabinsk Bull ChSAU* 22:32–35
14. Startcev AV (2001) Justification of the possibility of using the linear characteristics of tyres in the study of the movement of wheeled vehicles with speeds up to 10 m/s. *Chelyabinsk Bull ChSAU* 34:93–95
15. Wong JY (2001) *Theory of ground vehicles*, 3rd edn. Wiley, New York, p 488
16. Bellman R (1953) *Stability theory of differential equations*. New York, Toronto, London, p 216
17. Chetaev NG (1965) *Stability of movement*. Nauka, Moscow, p 176
18. Lukashuk OA, Akulova AA, Stroganov YuN (2018) Movement stability of tractor unit. In: ICMRE 2018—proceedings of 4th international conference on mechatronics and robotics engineering. Part F137690 Association for Computing Machinery (ACM), pp 117–120
19. Lyapunov AM (1959) *Collected works*, vol 1. Akad. Nauk SSSR, Moscow, p 446
20. Malkin IG (1966) *Theory of motion stability*. Nauka, Moscow, p 530
21. Freedman DA (2005) *Statistical models: theory and practice*. Cambridge University Press
22. Upton G, Cook I (2008) *Oxford dictionary of statistics*. OUP



Fluctuations of a Simplified Railway Vehicle Model as a System with One Degree of Freedom with a Nonlinear Restoring Force

A. N. Savoskin^(✉) and A. P. Vasilev

Russian University of Transport, 9b9, Obrazcova Street, Moscow 127994, Russia

Abstract. The power characteristics of the various spring suspension elements of the rolling stock have nonlinear dependencies on deformation and the rate of its change. Air springs, rubber parts, and vibration dampers have such characteristics. The nonlinear dependencies also appear due to the suspension gaps and tightness. All these effects must be taken into account when creating a mechano-mathematical model of the rolling stock—railway track system. There are no general methods of analytical solution and research for such complex systems. In this case, the analysis of the properties of the system is performed by numerical methods. This article deals with a study of the dynamic properties of a simplified vehicle model as a system with one degree of freedom with a nonlinear restoring force. It is shown that the fluctuations of a system with a nonlinear restoring force will be nonharmonic—periodic even with a harmonic disturbance force. The frequencies and amplitudes of the ultraharmonic components that make up the solution of such a system have been determined. The considered approach can be used to solve the problems of random fluctuations of a railway rolling stock with nonlinear characteristics of a spring suspension.

Keywords: Vehicle model · Nonlinear restoring force · Rolling stock fluctuations · Spring suspension

1 Introduction

A nonlinear dynamical system includes the nonlinear restoring (positional) and (or) dissipative forces of any of its elements. These forces are nonlinear and depend on deformation Δ and/or the rate of deformation. Another sign of nonlinearity is nonlinear relationships between generalized coordinates and/or velocities, such as trigonometric, logarithmic, and exponential functions, as well as operations of division, multiplication, etc. There is a significant difference between nonlinear systems fluctuations and the linear ones. In this case, the first approach is to study the dynamic properties of nonlinear systems with one degree of freedom. The results obtained by numerical integration for systems with one degree of freedom must be compared with the known analytical solutions. The satisfactory convergence of calculation results allows to proceed to the study of systems with a finite number of degrees of freedom.

2 The Numerical Solution of the Vertical Fluctuations Under the Force Disturbance

The analytical solutions for a conservative system with one degree of freedom can be obtained on the basis of an approximate harmonic balance method [1]. These approximate solutions make it possible to establish the three types of such system fluctuations: fundamental, ultraharmonic, and subharmonic. If the main fluctuations occur with the disturbance frequency ω , the ultraharmonic oscillations occur with frequencies $2\omega, 3\omega$, etc., and with lower amplitudes than the amplitudes of the main fluctuations. At the same time, subharmonic fluctuations occur with frequencies $\omega/2, \omega/3$, etc., and with larger amplitudes than the amplitudes of the main fluctuations [2–10].

Let us perform the numerical solution of the vertical fluctuations equation of a system with one degree of freedom [11–17] under force disturbance (Fig. 1):

$$m\ddot{z} + \beta\dot{z} + F_{el} = Q(t), \tag{1}$$

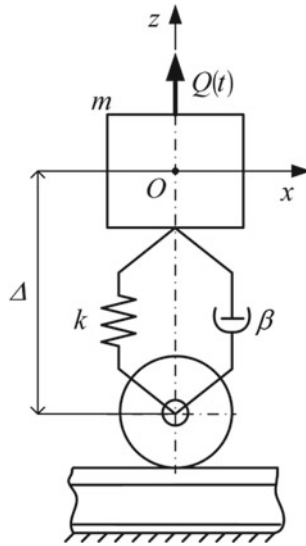


Fig. 1 Kinematic diagram of vertical fluctuations of a rail vehicle model as a system with one degree of freedom under force disturbance

In this equation, m —railway vehicle weight; β —damping coefficient; $Q(t)$ —force disturbance:

$$Q(t) = Q_m \sin 2\pi ft, \tag{2}$$

In this equation, f —frequency of disturbance.

The system also has a linear dissipation $\beta\dot{z}$ and a nonlinear restoring elastic force F_{el} (Fig. 2), determined by the equation:

$$F_{el} = kz + kz^3, \tag{3}$$

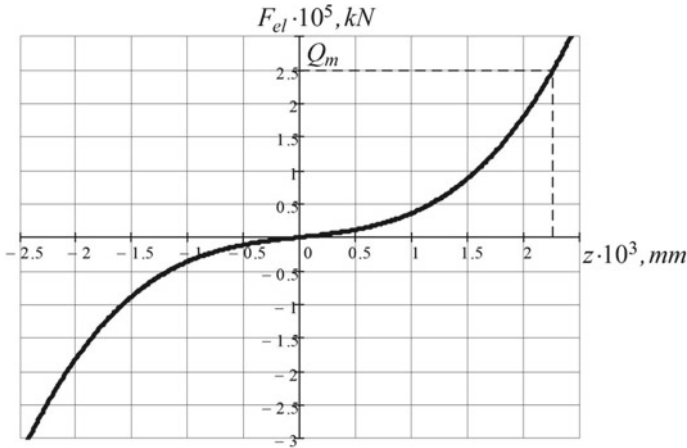


Fig. 2 Dependence of the nonlinear restoring elastic force on the coordinate

In this equation, k —spring stiffness.

The disturbance frequency is changed in the process of calculations. For each given value of the frequency, for example, f_1 , the amplitude was increased from 1 kN. The increase of the amplitude was continued until the ultra or subharmonic vibrations were appeared in the $z(t)$ system’s fluctuations in addition to the fundamental frequency. Then, the procedure was repeated for a new frequency value f_2 , etc.

The result of such calculations has the form

$$z(t) = \sum_i z_{mi-j}^{(n)} \sin(2\pi f_{i-j}^{(n)} t + \varphi_{i-j}^{(n)}), \tag{4}$$

In this equation, $f_{i-j}^{(n)}$, $z_{mi-j}^{(n)}$ и $\varphi_{i-j}^{(n)}$ —frequencies, amplitudes, and phases of harmonics, the first subscript in the denominator corresponds to the ordinal number of the disturbance frequency $i = 1, 2, \dots$, the subscript j —the frequency axis number f_1 or f_2 , the subscript n —the harmonic number.

3 The Results of Numerical Solution of the Vertical Fluctuations Equation

The graphs of the numerical solution results of Eq. (1) with the disturbance frequency $f_1 = 1$ Hz and $f_2 = 4$ Hz are shown in Fig. 3. The amplitude on the graphs is the normalized value:

$$A_{i-j}^{(n)} = z_{mi-j}^{(n)} / Q_m, \text{ mm/kN}, \tag{5}$$

The harmonic disturbance action (Fig. 3a, c) initiated the fluctuations of a nonlinear system (Fig. 3b, d) which, as expected, become periodic and significantly differing from harmonic ones. This difference can arise only due to the appearance of harmonic components in the fluctuations. The fluctuations processes were expanded in a Fourier

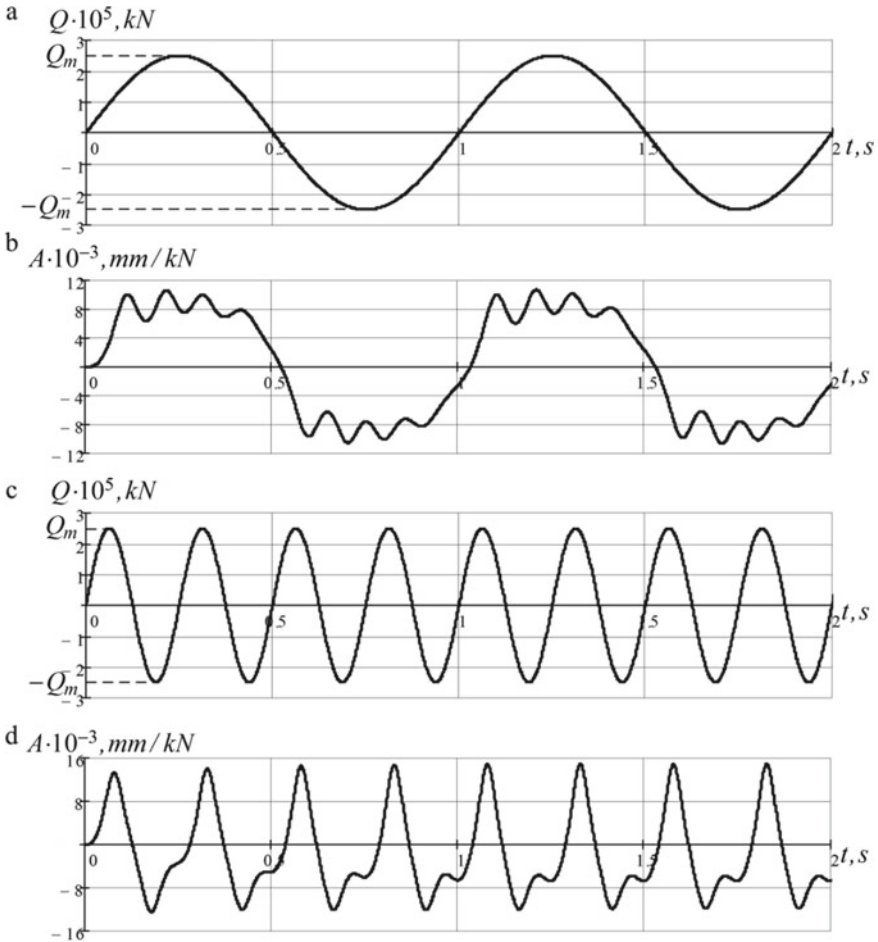


Fig. 3 Disturbance graphs **a, c** and the results of numerical solutions **b, d** of the fluctuation equation for a nonlinear system with one degree of freedom at disturbance frequencies of 1 Hz **a** and **b** and 4 Hz **c** and **d**

series to isolate these harmonics, and the amplitude spectrum of fluctuations was plotted. The results of the solution depend on the disturbance frequency (fundamental frequency of fluctuations), and therefore, the results of the spectral analysis were represented in 3D space. In this space, the results, plotted in the diagonal plane $[f = f_1 = f_2, A]$, correspond to the fundamental fluctuations occurring with the disturbance frequency, for example, f_1 and the relative amplitude A_1 (Fig. 4). The frequency values of the arising ultra and (or) subharmonic fluctuations were plotted on the axes f_1 and f_2 .

The values of f_i and A_i are given in Table 1. The ultraharmonic components were obtained in the processes of fluctuations. In addition, Table 1 contains the values of the frequencies and relative amplitudes of all harmonics $f_{i-j}^{(n)}$ and $A_{i-j}^{(n)}$ included in the solution (4).

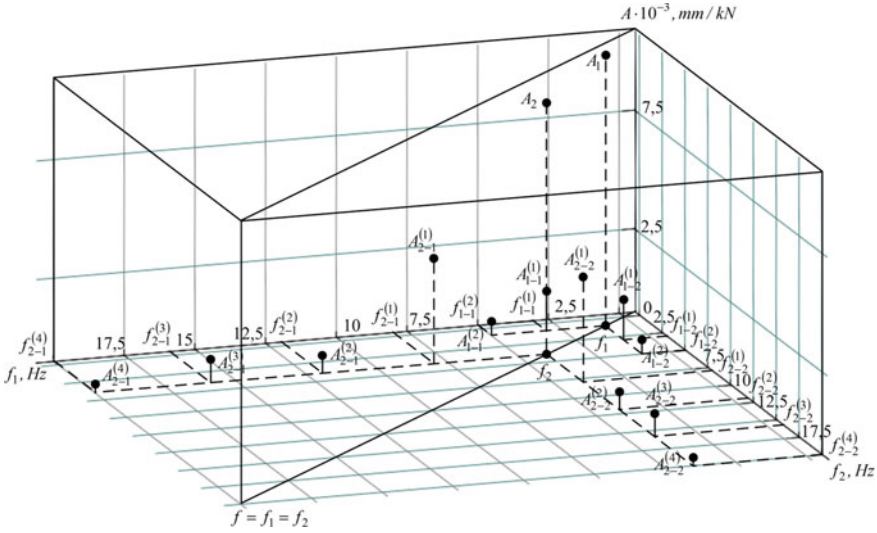


Fig. 4 Frequencies and relative fluctuation amplitudes

Table 1 shows that the first value of the fundamental frequency $f_1 = 1$ Hz corresponds to the fundamental harmonic with an fluctuation amplitude $A_1 = 9.58 \times 10^{-3}$ mm/kN, as well as two ultraharmonics with frequencies: $f_{1-1}^{(1)} = f_{1-2}^{(1)} = 3f_1 = 3$ Hz and $f_{1-1}^{(2)} = f_{1-2}^{(2)} = 5f_1 = 5$ Hz and amplitudes $A_{1-1}^{(1)} = A_{1-2}^{(1)} = 1,41 \cdot 10^{-3}$ mm/kN and $A_{1-1}^{(2)} = A_{1-2}^{(2)} = 0,46 \cdot 10^{-3}$ mm/kN.

The next value of the fundamental frequency $f_2 = 4$ Hz corresponds to the fundamental harmonic with amplitude $A_2 = 8,9 \cdot 10^{-3}$ mm/kN, as well as four ultraharmonics with frequencies: $f_{2-1}^{(1)} = f_{2-2}^{(1)} = 2f_2 = 8$ Hz, $f_{2-1}^{(2)} = f_{2-2}^{(2)} = 3f_2 = 12$ Hz, $f_{2-1}^{(3)} = f_{2-2}^{(3)} = 4f_2 = 16$ Hz, and $f_{2-1}^{(4)} = f_{2-2}^{(4)} = 5f_2 = 20$ Hz and amplitudes: $A_{2-1}^{(1)} = A_{2-2}^{(1)} = 3,73 \cdot 10^{-3}$ mm/kN, $A_{2-1}^{(2)} = A_{2-2}^{(2)} = 0,62 \cdot 10^{-3}$ mm/kN, $A_{2-1}^{(3)} = A_{2-2}^{(3)} = 0,82 \cdot 10^{-3}$ mm/kN, and $A_{2-1}^{(4)} = A_{2-2}^{(4)} = 0,29 \cdot 10^{-3}$ mm/kN.

4 Results

The performed numerical solutions of the vertical fluctuations equation of a system with one degree of freedom with nonlinear stiffness and linear dissipation confirmed the correctness of the known approximate analytical solutions and made it possible to establish the frequencies and amplitudes of the ultraharmonic components included in the solution of such system. The considered approach and, in particular, the method of graphical representation of the obtained solutions can be used to solve problems of random fluctuations of railway rolling stock with nonlinear characteristics of spring suspension.

Table 1 Frequencies and amplitudes of ultraharmonic fluctuations

No.	Types of harmonics	Frequencies and amplitudes	Values
1	First fundamental harmonic	f_1 , Hz	1
		A_1 , mm/kN	$9,58 \cdot 10^{-3}$
2	The first ultraharmonic	$f_{1-1}^{(1)} = f_{1-2}^{(1)}$, Hz	3
		$A_{1-1}^{(1)} = A_{1-2}^{(1)}$, mm/kN	$1,41 \cdot 10^{-3}$
3	The second ultraharmonic	$f_{1-1}^{(2)} = f_{1-2}^{(2)}$, Hz	5
		$A_{1-1}^{(2)} = A_{1-2}^{(2)}$, mm/kN	$0,46 \cdot 10^{-3}$
4	Second fundamental harmonic	f_2 , Hz	4
		A_2 , mm/kN	$8,9 \cdot 10^{-3}$
5	The first ultraharmonic	$f_{2-1}^{(1)} = f_{2-2}^{(1)}$, Hz	8
		$A_{2-1}^{(1)} = A_{2-2}^{(1)}$, mm/kN	$3,73 \cdot 10^{-3}$
6	The second ultraharmonic	$f_{2-1}^{(2)} = f_{2-2}^{(2)}$, Hz	12
		$A_{2-1}^{(2)} = A_{2-2}^{(2)}$, mm/kN	$0,62 \cdot 10^{-3}$
7	The third ultraharmonic	$f_{2-1}^{(3)} = f_{2-2}^{(3)}$, Hz	16
		$A_{2-1}^{(3)} = A_{2-2}^{(3)}$, mm/kN	$0,82 \cdot 10^{-3}$
8	The fourth ultraharmonic	$f_{2-1}^{(4)} = f_{2-2}^{(4)}$, Hz	20
		$A_{2-1}^{(4)} = A_{2-2}^{(4)}$, mm/kN	$0,29 \cdot 10^{-3}$

References

1. Panovko YaG (1980) Vvedeniye v teoriyu kolebaniy: ucheb. posobiye, 2-ye izd., pererab (Introduction to oscillation theory, 2nd ed, revised). Nauka (The Science), Moscow, p 272
2. Andronov AA, Vitt AA, Khaikin SE (1959) Teoriya kolebaniy (Theory of oscillations). State publishing house physical. mat. Literature, Moscow, p 916
3. Babakov IM (1965) Teoriya kolebaniy (Theory of oscillations). Nauka (The Science), Moscow, p 560
4. Butenin NV (1962) Elementy teorii nelineynykh kolebaniy (Elements of the theory of nonlinear oscillations). Sudpromgiz, Leningrad
5. Den-Gartok Dzh P (1960) Mekhanicheskiye kolebaniya (Mechanical vibrations). State publishing house physical. mat. Literature, Moscow, p 580
6. Blekhman II (1979) Kolebaniya nelineynykh mekhanicheskikh sistem. Vibratsii v tekhnike. V 6-ti tomakh. Tom 2. (Oscillations of nonlinear mechanical systems. Vibrations in technology. In 6 volumes. Vol. 2.): under the editorship of Dr. Phys.-Math. Science Blekhman II. Mashinostroyeniye (Mechanical Engineering), Moscow, p 352
7. Kochin NYe (1934) O krutyl'nykh kolebaniyakh kolenchatykh valov. Prikladnaya ma-tematika i mekhanika, II (On torsional vibrations of crankshafts. Applied Mathematics and Mechanics, II). No. 1

8. Obmoryshev AN (1965) *Vvedeniye v teoriyu kolebaniy* (Introduction to the theory of oscillations). Nauka (The Science), Moscow, p 276
9. YaG P (1976) *Osnovy prikladnoy teorii kolebaniy i udara* (Foundations of the applied theory of vibrations and impact). Mashinostroyeniye (Mechanical Engineering), Leningrad, p 320
10. Timoshenko SP (1967) *Kolebaniya v inzhenerenom dele* (Oscillations in engineering). Nauka (The Science), Moscow
11. Lazaryan VA (1964) *Dinamika vagonov* (Dynamics of railway cars). Transport, Moscow, p 255
12. Garg VK, Dukkipati RV: under the editorship of Pan'kin NA (1988) *Dinamika podvizhnogo sostava* (Rolling stock dynamics): trans. from English. Transport, Moscow, p 392
13. Vershinskiy SV, Danilov VN, Chelnokov II (1979) *Dinamika vagona* (Railway car dynamics). Transport, Moscow, p 352
14. Medel' VB (1974) *Podvizhnoy sostav elektricheskikh zheleznikh dorog. Konstruktsiya i dinamika* (Rolling stock of electric railways. Design and dynamics.). Transport, Moscow, p 232
15. Kamayev AA, Kamayev AA (eds) (1981) *Konstruktsiya, raschet i proyektirovaniye lokomotivov* (Construction, calculation and design of locomotives). Mashinostroyeniye, Moscow, p 351
16. Chelnokov II, Vishnyakov BI, Garbuzov VM, Estling AA (1963) *Gasiteli kolebaniy vagonov* (Railway cars vibration dampers). Transzheldorizdat, Moscow, p 176
17. Biryukov IV, Savos'kin AN, Burchak GP and etc.: under the editorship of Biryukov IV (1992) *Mekhanicheskaya chast' tyagovogo podvizhnogo sostava: Uchebnik dlya vuzov zh.-d. transporta* (The mechanical part of the traction rolling stock: textbook for universities of railway transport). Transport, Moscow, p 440



Evaluation of the Main Indicators of Piston Engine with an Improved Gas Exchange System by Modeling

L. V. Plotnikov^(✉), Yu. M. Brodov, and L. E. Osipov

Ural Federal University named after the first President of Russia B.N. Yeltsin, 19, ul. Mira, Ekaterinburg 620002, Russia

Abstract. Reciprocating engines are actively used in small-scale power engineering for heat and power supply to various consumers. Reciprocating engines are also used as emergency energy sources in critical facilities and organizations. Therefore, improving the working process and design of the engine gas exchange system is an urgent task in the development of power engineering. The article is based on mathematical modeling of the working process of a reciprocating engine with a piston diameter of 82 mm and a stroke of 71 mm. The main idea of the article was to modernize (by changing the design) the gas exchange system (intake and exhaust systems) of the engine in order to improve the technical and economic indicators. A brief overview of modern scientific and technical results on this topic is presented. A description of the technical characteristics of the engine under study is given. Mathematical modeling was carried out in the Diesel-RK software (Moscow State Technical University). The main methods (algorithms) of modeling are discussed in the article. The influence of the geometric configuration of the intake and exhaust systems on the quality indicators of gas exchange and engine performance is shown. For example, it is possible to increase power up to 11% with an increase in specific fuel consumption by only 0.5–1.5% by changing the configuration of the engine gas exchange system.

Keywords: Reciprocating engine · Cycle modeling · Gas exchange system · Filling coefficient · Residual gas coefficient · Technical and economic indicators

1 Introduction

It is known that the technical and economic indicators of reciprocating internal combustion engines (ICE) significantly depend on the geometric dimensions of the main elements of gas exchange systems [1, 2]. The development of optimal configurations of the intake and exhaust systems of the engine predetermines obtaining high output indicators of the ICE. At the same time, it is known that fine-tuning the gas exchange systems of engines is a rather complicated and laborious process [3–5]. There is a large number of scientific and technical works to improve the processes in gas exchange systems, as well as to fine-tune the design of these systems in order to improve the technical and economic indicators of engines. Let us take a quick look at some of the current

publications on this topic. Attention is drawn to the articles in which, on the basis of mathematical modeling of processes, the modernization of intake or exhaust systems is carried out in order to improve fuel efficiency [6, 7], environmental friendliness [8, 9], noise [10, 11] and reliability [12]. The intensive development of computer technology and calculation programs greatly simplifies the task of modernizing engines at the stage of preliminary design. Both ready-made (standard) software and the author's mathematical models are used for modeling. Mathematical modeling makes it possible to predict the main parameters of the engine before manufacturing a prototype. At the same time, there are articles in which the authors seek to improve the main indicators of the engine on the basis of experimental studies of the processes in the gas exchange system and the engine cylinder [13–16]. Research is of the greatest interest when the simulation results are confirmed by experimental research data [17, 18].

This article presents some results of mathematical modeling of the working cycle of a piston engine with a cylinder diameter of 82 mm and a piston stroke of 71 mm. The simulation was carried out in the Diesel-RK program (the developer was the Moscow State Technical University). The purpose of the study was to increase the power of the ICE by fine-tuning the design of the intake and exhaust systems.

2 Description of the Mathematical Model and Object of Research

Mathematical modeling was carried out using the Diesel-RK program (Russia). The features of a mathematical model for modeling processes in engine gas exchange systems are considered. The calculation of gas parameters in Diesel-RK is carried out with the assumption that all cylinders work identically. Therefore, only one cylinder is calculated, and the work of the rest is taken into account by the phase shift of the mass and energy flows in accordance with the engine operation order. In this case, the order of work is assumed to be uniform. The real interaction of impulses has a positive effect on some cylinders and negatively on others. The gas flow in the channels of the blockhead and in the valve channels is considered unsteady and one-dimensional. It is calculated by the method of A.S. Orlin, based on the integration of the equation of impulses over the channel length and time.

The Diesel-RK mathematical model contains the equation of motion for a one-dimensional, unsteady flow, the law of conservation of mass and energy of the flow, the first law of thermodynamics and the Boyle–Mariotte law. The solution of systems of equations based on these physical and mathematical approaches makes it possible to calculate the processes in the systems of gas exchange of engines with sufficient accuracy. Based on these data, it is possible to predict the values of the main indicators of engines, namely power and specific fuel consumption.

The engine from the Russian VAZ-OKA car was chosen as the base engine. In the calculations, the following basic design parameters were set: a four-stroke engine, two cylinders and an in-line arrangement, a blockhead with two valves per cylinder, a liquid cooling system, fuel–gasoline, a cylinder diameter of 82 mm, a piston stroke of 71 mm and a compression ratio of 9.9. Environmental parameters are barometric pressure $p_o = 0.1$ MPa and temperature $t_o = 20$ °C. The valve timing was set in accordance with the standard engine parameters of the VAZ-OKA car. The geometric characteristics (length

and inner diameter) of the intake (IS) and exhaust (ES) systems were also set according to these indicators for the base engine (VAZ-OKA). Thus, the inner diameter of the base intake pipe was 32 mm, and the inner diameter of the exhaust pipe was 30 mm. The length of the intake pipe for the basic ICE was set equal to 350 mm, and the length of the exhaust pipe—600 mm. The intake channel in the blockhead for the base engine had the following dimensions: inner diameter—31 mm and length—150 mm; the exhaust channel in the blockhead had the following dimensions: inner diameter—29 mm and length—130 mm.

In the course of numerical modeling, the geometric dimensions of the IS and ES were varied in order to improve the gas exchange indicators and the main indicators of the engine. The main hypothesis (idea) of the scientific research was to select such geometric dimensions of channels to improve the gas-dynamic perfection of gas exchange systems (reduce aerodynamic drag, level out reverse waves and vortex flows, and optimize heat exchange).

Two parameters were chosen as criteria for the perfection of the gas exchange system design: the filling coefficient η_v and the residual gas coefficient γ . The filling coefficient was defined as the ratio of the actual amount of air entering the cylinder to the theoretical amount of air that could enter the cylinder. The residual gas coefficient was defined as the ratio of the amount of residual gases in the cylinder to the actual amount of air entering the cylinder. The Diesel-RK program calculates these indicators for a single engine cycle.

3 Analysis and Discussion of Engine Operating Cycle Simulation Results

First, the results of fine-tuning the intake system and the effect of the design on the technical and economic indicators of the engine are considered. It was found that changes in the geometric dimensions (diameter and length) of the intake manifold and the channel in the cylinder head lead to an increase in the filling factor η_v in the range from 2.5 to 10.5% in comparison with the base engine (Fig. 1).

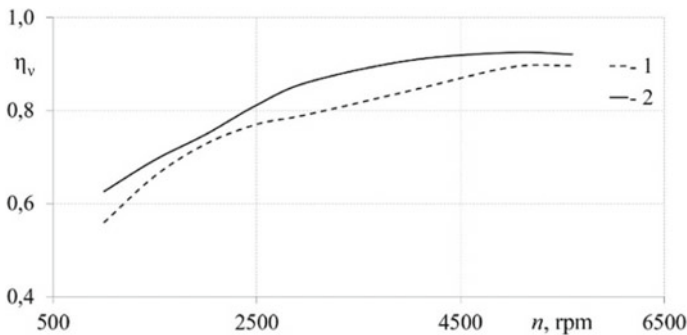


Fig. 1 Dependence of the filling ratio η_v on the crankshaft speed n for an engine with a basic (1) and modernized (2) IS

This indicates that the filling of the cylinder with the working fluid increases and favorable conditions for mixture formation and fuel combustion are created. As a result, such an increase in the coefficient η_v led to an increase in the power of the piston internal combustion engine by 2.5–11.0%, depending on the mode of its operation (Fig. 2). The maximum increase in power occurs at a crankshaft speed of more than 2500 rpm.

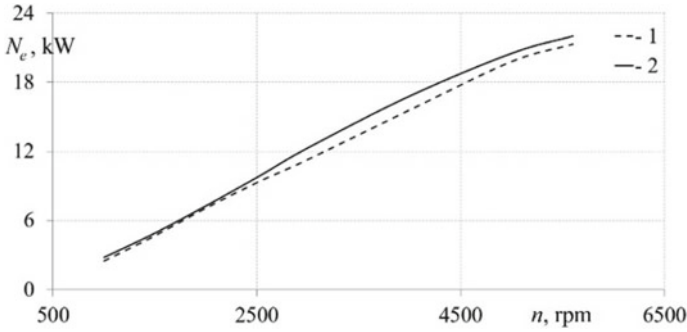


Fig. 2 Dependence of power N_e on the crankshaft speed n for an engine with a basic (1) and modernized (2) IS

It should be noted that the specific effective fuel consumption does not actually change in this case (Fig. 3). This indicates that the efficiency of the engine remains practically unchanged.

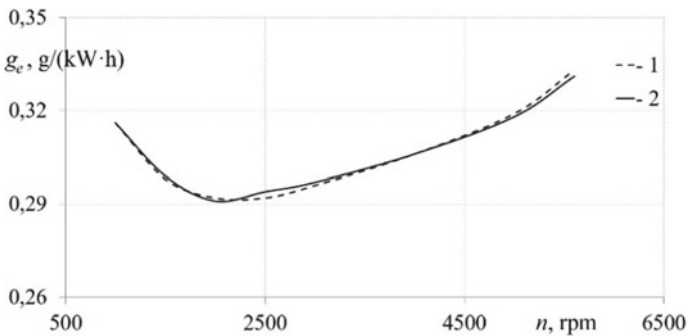


Fig. 3 Dependence of specific fuel consumption g_e on the crankshaft speed n for an engine with a basic (1) and modernized (2) IS

Further, the geometric dimensions of the exhaust system were upgraded in order to reduce the coefficient of residual gases γ . As a result, the optimal diameters and lengths of the main elements of the exhaust system were determined, at which the coefficient γ decreased in the range from 0.5 to 11.0% (Fig. 4).

However, it should be emphasized that this did not have a significant effect on the engine power. It can be seen that the increase in engine power is no more than 5.5%

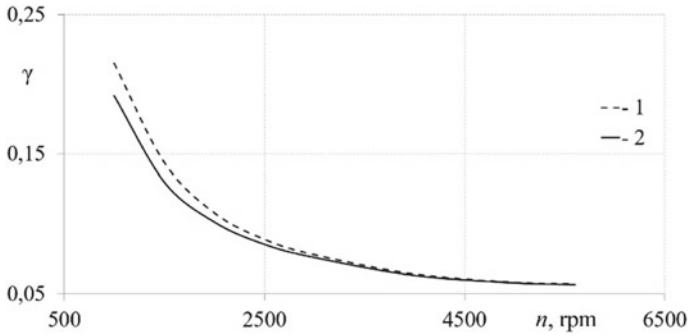


Fig. 4 Dependence of the coefficient of residual gases γ on the crankshaft speed n for an engine with a basic (1) and modernized (2) ES

when the design of the exhaust system is fine-tuned, and in most modes, the increase in power does not exceed 2%.

At the same time, the specific effective fuel consumption increases by an average of 0.5% (Fig. 5). In other words, the efficiency of the engine decreases slightly.

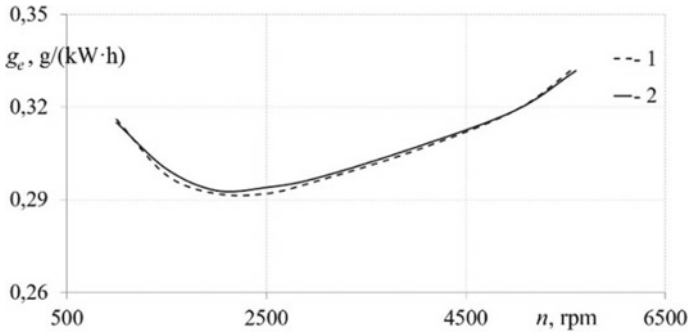


Fig. 5 Dependence of specific fuel consumption g_e on the crankshaft speed n for an engine with a basic (1) and modernized (2) ES

Thus, we can conclude that improving the design of the intake system (IS) is a more effective way to improve the technical and economic performance of engines in comparison with the exhaust system (ES).

At the final stage of the research, the impact of the simultaneous refinement of the intake and exhaust systems on the main engine parameters was evaluated. As expected, the joint design of the intake and exhaust systems provides a synergistic effect in terms of improving the quality of gas exchange. It is found that in this case, the filling coefficient increases to 25% compared to the base engine. In turn, the coefficient of residual gases in an engine with an upgraded gas exchange system has decreased by up to 25% compared to the basic ICE.

Figure 6 shows the dependence of power on the crankshaft speed after fine-tuning the engine gas exchange system. It can be seen that in this case the increase in power

is from 3.0 to 12.0%, depending on the operating mode of the engine (Fig. 6). It was revealed that the most sensitive gain is observed at high values of the crankshaft rotation frequency.

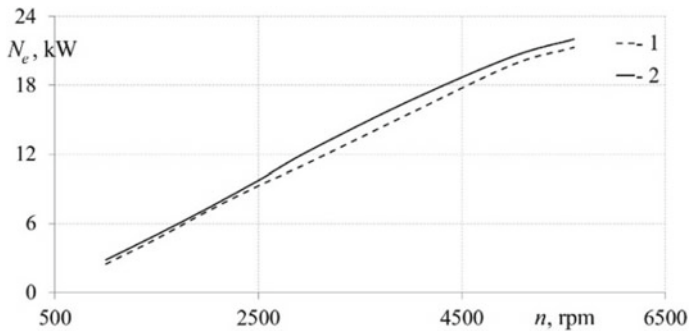


Fig. 6 Dependence of power N_e on the crankshaft speed n for an engine with a basic (1) and modernized (2) gas exchange system

It is possible to trace the change in specific fuel consumption in an engine with an upgraded gas exchange system according to the dependencies in Fig. 7. Figure 7 shows that fuel consumption increases by 0.55% on average.

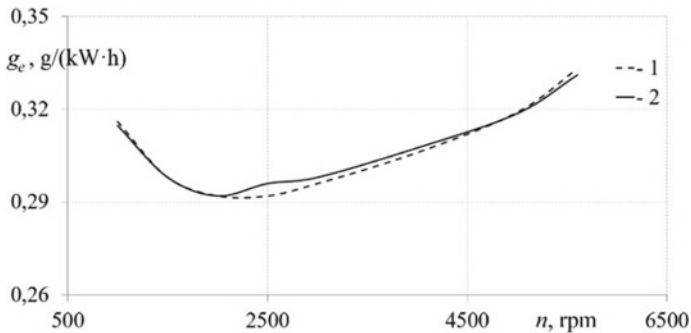


Fig. 7 Dependence of specific fuel consumption g_e on the crankshaft speed n for an engine with a basic (1) and modernized (2) gas exchange system

Thus, it can be noted that the joint fine-tuning of the intake and exhaust systems leads to the most noticeable increase in the main indicators of the engine.

4 Conclusion

The following main conclusions can be drawn from the research:

1. Optimization of the design of intake and exhaust systems of engines is an effective way to improve the technical and economic indicators of piston ICEs.

2. It is possible to achieve an increase in engine power up to 11% with a change in specific fuel consumption by $\pm 1.0\%$ by fine-tuning the gas exchange system.
3. Basic knowledge in the field of the theory of operating cycles and the design of engines is required for the practical use of the results of numerical modeling of gas exchange processes in ICEs.
4. The results of mathematical modeling must be confirmed by experimental research before their implementation in practice. It is also important to take into account the gas-dynamic non-stationarity in modeling and experimental research of processes in the systems of gas exchange of piston engines [19].

References

1. Sajith V, Shijo T (2017) Internal combustion engines. Oxford University Press, India
2. Mollenhauer K, Tschöke H (2010) Handbook of diesel engines. Springer Science & Business Media, London
3. Hiereth H, Prenninger P (2007) Charging the internal combustion engine. Springer Science & Business Media, London
4. Ganesan V (2012) Internal combustion engines. McGraw Hill Education, India
5. Plotnikov LV, Zhilkin BP, Brodov YM (2020) Thermomechanical improvement of gas-air systems of turbocharged piston internal-combustion engines. *J Eng Phys Thermophys* 93(6):1557–1566. <https://doi.org/10.1007/s10891-020-02260-y>
6. Kozarac D, Bozic M, Vucetic A, Krajinovic J, Sjeric M (2019) Experimental and numerical analysis of a dual fuel operation of turbocharged engine at mid-high load. *SAE Technical Papers*. September, pp 1–5. <https://doi.org/10.4271/2019-24-0122>
7. Yang S, Deng K, Cui Y, Gu H (2010) A study on an automatically variable intake exhaust injection timing turbocharging system for diesel engines. *J Eng Gas Turbines Power* 132(5):052803. <https://doi.org/10.1115/1.4000146>
8. Zhao H, Stone R, Zhou L (2010) Analysis of the particulate emissions and combustion performance of a direct injection spark ignition engine using hydrogen and gasoline mixtures. *Int J Hydrogen Energ* 35(10):4676–4686. <https://doi.org/10.1016/j.ijhydene.2010.02.087>
9. Wang Z, Jiao X (2017) ADRC-based transient air/fuel ratio control with time-varying transport delay consideration for gasoline engines. *IEEJ Trans Electr Electron Eng* 12(1):S117–S124. <https://doi.org/10.1002/tee.22444>
10. Selamet A, Kothamasu V, Novak JM (2001) Insertion loss of a Helmholtz resonator in the intake system of internal combustion engines: an experimental and computational investigation. *Appl Acoust* 62(4):381–409. [https://doi.org/10.1016/S0003-682X\(00\)00042-6](https://doi.org/10.1016/S0003-682X(00)00042-6)
11. Chiavola O (2002) Multi-dimensional CFD-transmission matrix modelling of IC engine intake and exhaust systems. *J Sound Vibr* 256(5):835–848. <https://doi.org/10.1006/jsvi.2002.5022>
12. Plotnikov LV, Zhilkin BP, Brodov YM (2020) Physical and numerical modeling of thermo-mechanical processes in gas-air systems of piston engines under gasdynamic-nonstationarity conditions. *J Eng Phys Thermophys* 93(3):594–604. <https://doi.org/10.1007/s10891-020-02157-w>
13. Liu C, Pan X, Zheng X, Yan Y, Li W (2016) An experimental study of a novel prototype for two-stage thermoelectric generator from vehicle exhaust. *J Energ Inst* 89(2):271–281. <https://doi.org/10.1016/j.joei.2015.01.019>
14. Nielsen KV, Blanke M, Eriksson L (2018) Adaptive observer for nonlinearly parameterized Hammerstein system with sensor delay—applied to ship emissions reduction. *IEEE Trans Control Syst Technol* 26(4):1508–1515. <https://doi.org/10.1109/TCST.2017.2715004>

15. Aly WIA, Abdo M, Hassaneen AE, Bedair G (2017) Thermal performance of a diffusion absorption refrigeration system driven by waste heat from diesel engine exhaust gases. *Appl Therm Eng* 114:621–630. <https://doi.org/10.1016/j.applthermaleng.2016.12.019>
16. Plotnikov LV, Bernasconi S, Brodov YM (2017) The effects of the intake pipe configuration on gas exchange, and technical and economic indicators of diesel engine with the 21/21 dimension. *Procedia Eng* 206:140–145. <https://doi.org/10.1016/j.proeng.2017.10.450>
17. Xu Z, Ji F, Ding S, Zhao Y, Zhang X, Zhou Y, Zhang Q, Du F (2020) High-altitude performance and improvement methods of poppet valves 2-stroke aircraft diesel engine. *Appl Energ* 276:115471. <https://doi.org/10.1016/j.apenergy.2020.115471>
18. Guan C, Ma Q, Huang Z, Han D (2020) Application of active subspace method in gas exchange strategy calibration on a variable valve timing gasoline engine. *J Eng Gas Turbines Power* 142(7). <https://doi.org/10.1115/1.4047126>
19. Plotnikov LV, Zhilkin BP (2018) Influence of gas-dynamical nonstationarity on local heat transfer in the gas–air passages of piston internal-combustion engines. *J Eng Phys Thermophys* 91(6):1444–1451. <https://doi.org/10.1007/s10891-018-1879-8>



Energy-Efficient Vertical Kiln for the Firing of Ceramic

I. V. Dolotovskij^(✉)

Saratov State Technical University named after Gagarin Yu.A, 77, Politekhnikeskaya, Saratov
410054, Russia

Abstract. The article proposes the design of a vertical kiln for firing ceramic products with microflame combustion of gas fuel and quasi-continuous processes of moving products. It is shown that the reduction in specific fuel costs is achieved by utilizing the heat of heated air in the elements of the loading mechanism and reducing heat losses in the air ducts. The increase in the energy efficiency of the kiln is provided by constructive solutions for the thermal insulation of the loading mechanism and the combination of the dryer with the kiln. The description of the operating modes of the kiln from the stage of loading to the stage of the finished product is given. The results of a comparative analysis of the current and proposed energy-efficient kiln for firing 24 million bricks per year are presented. Shown that by reducing the operating costs for fuel gas, the cost of brick production during the introduction of the kiln reduced by 23–25%.

Keywords: Kiln · Ceramic products · Combination of processes · Energy efficiency · Economic indicators

1 Introduction

Rationalization of the use of fuel, in particular, natural gas, at energy-intensive enterprises of the industrial sector gives the greatest energy–ecological–economic effect in the technological chain, including facilities for gas production, its preparation, processing, and transportation to consumers [1, 2]. At enterprises producing ceramic bricks and other building ceramics, the most energy-intensive processes are the heat treatment of raw materials and the processes of firing products, which consume more than 80% of the consumed fuel gas. In the works on energy saving in kilns for firing ceramic products, the main technically feasible areas are noted, which make it possible to optimize the fuel balance of the enterprise as a whole at various stages of the kiln's life cycle. The main technical solutions include modernization of the refractory layer and thermal insulation; solutions for energy recovery both in the kiln itself and for the utilization of waste gas heat for the needs of the enterprise; new burners and types of fuels, including the use of renewable energy sources; monitoring and control systems [3–7]. At the same time, it is noted that there is a high degree of uncertainty about the possible consequences of integrating new solutions not only in kilns, but also in the previous processes of preparing raw materials and subsequent conditioning processes for finished products [6]. In this

regard, an integrated approach to the design of the structural and parametric characteristics of the system is required, taking into account the prospects for the development of the enterprise and multi-criteria assessments of efficiency [7–9].

In the context of solving the important issue of the rational combination of the processes of firing and drying ceramic products with the effective use of the potential of secondary resources, the relevance and prospects of the vertical kiln design are developed by the authors obvious [10].

2 Scheme and Design Features of the Kiln

The concept of the developed design of a vertical kiln for firing bricks and other ceramic products [10] is based on the technological combination of drying and firing processes, which ensures a decrease in heat losses of equipment and fuel gas consumption. Figure 1 shows a diagram of the furnace (view from the side of the loading mechanism and view one of its sections). It should be noted that the kiln can be operated in thermal waste disposal systems, which are supplied to the kiln in special standards containers.

The kiln operates as follows. First, in the vertical firing channels one by one, using a special loading device (not shown in Fig. 1), the pre-prepared (remaining from the previous launch) commercial (fired) ceramic products (or empty special standards containers) are loaded. It is possible to load raw bricks after a semi-dry pressing press. In the following, all raw materials are supplied to the furnace and the resulting product is called "products."

Then, the air supply fan 26 is turned on, and the air ducts 5 and 7, the heat-insulated bodies 12 and 13, and the flue gas channels 6 are purged.

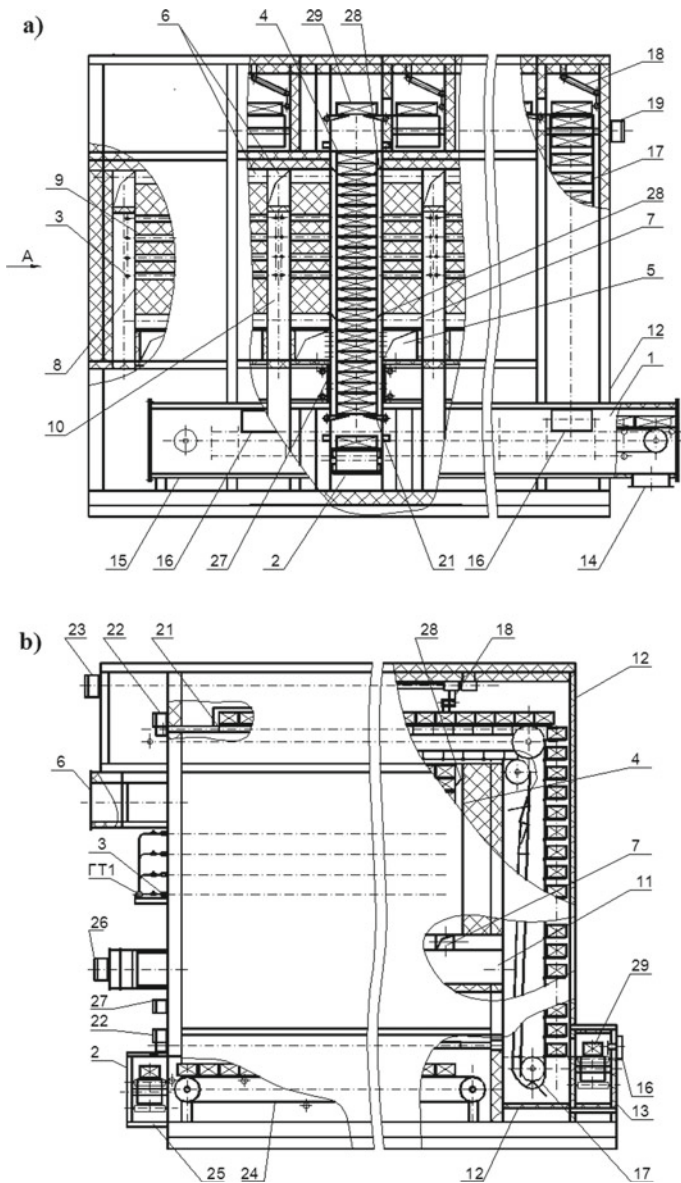
The required airflow rate and pressure in the firing channels are set. After filling the fuel supply lines in front of the furnace, one by one (from bottom to top), the burners 3 is put into operation.

After reaching the operating temperature, products 29 is fed from the preparatory compartment to the 15 transporter of the loading mechanism. Each product is transported along the transporter to the firing channel, which is included in the operation, and the transfer 16 moves to the ascending branch of the escalator 17.

During the operation of escalators, the products move to the upper, horizontal section, from which the end-shifter 18 moves to the upper swivel frames 21 located above the entrance to the vertical firing channel 4, which is in operation.

When moving products inside the heat-insulated bodies 13 and 12 of the transporter 15 and each of the escalators 17 of the loading mechanism, the raw product is dried. The drying process takes place with countercurrent contact of the raw product with heated air that comes out of the channels 11 for removing heated air from the kiln.

Moving raw materials and, at the same time, unloading the bottom row of finished products are performed as follows. The support plates of the retainers 27 move and take the load of the products located above. The lower swivel frames 21 smoothly rotate to the lower vertical position and are loaded onto the unloading transporter 24 for the lower row of finished products. The transporter 24 moves the finished products out of the oven onto the marketable transporter 25. Then, the lower swivel frames 21 return to their original horizontal position, the support plates of the retainer 27 move apart, and the



products move smoothly (under their own weight) down to a height equal to the height of one product.

With further movement from top to bottom in the firing channels, the products enter the firing zone located at the level of the burner tunnels 9.

Firing of products occurs under the influence of thermal radiation of the following elements of the kiln:

◀**Fig. 1** Scheme of vertical kiln: **a** view from the side of the loading mechanism and **b** view A. 1, 2—loading and unloading mechanisms; 3—burners; 4—vertical firing channels; 5—channels for supplying combustion air and for cooling products; 6—channels for ducts flue gas; 7—channels for the removal of heated air; 8—walls of firing channel; 9—burner tunnels; 10—gaps between the walls of the firing channels; 11—channels for removing heated air from the kiln; 12—heat-insulated housing of loading mechanism escalator; 13—heat-insulated housing of loading mechanism transporter; 14—branch pipe for exhaust heated air; 15—transporter for loading mechanism; 16—transfer; 17—escalator; 18—end-shifter; 19—escalator drive; 20—reinforcement block of burners; 21—swivel frame; 22—swivel frame drive; 23—end-shifter drive; 24—transporter for unloading; 25—transporter for commercial products; 26—air supply fan; 27—retainer (clamping) of loading products; 28—rotary self-adjusting flaps; 29—products (bricks or heat-resistant containers)

- burner tunnels;
- sections of walls of eight burning channels adjacent to the burner tunnels.

and also due to convective heat exchange with flue gases coming out of the tunnels 9.

Due to the micro-flare radiation convective mode of heat transfer, the firing of products carried out is not only uniformly, but also with a higher thermal efficiency, since less heat is lost through the kiln fences.

The zone of end-temperature holding of products is located below the firing zone (from the lower row of burner tunnels to channels 7 for the removal of heated air). In this zone, the temperature field is leveled in the products that have passed the firing.

The cooling zone is located along the height of the firing channel 4: from the outlet channels 7 to the air distributors of the channels 5 for supplying cooling air. In this zone, there is a counter-current movement of products and air flow. The supply of a part of the airflow for cooling was also provided through the holes at the bottom of the channels 5 and through the perforations in the base plates of the retainers 27. Thus, three zones of optimal cooling intensity were formed along the height. This provides a soft, defect-free mode of cooling products and a deeper recuperation of their heat.

During operation of a vertical furnace for firing products, the fuel coming out of the nozzles of the burners 3 was mixed with heated air and burned in the burner tunnels 9, which are coaxial with the nozzles. The kiln provides an energy efficient (without heat loss) micro-flame firing mode with the ability to regulate the heat supply. An optimum temperature profile in height is also ensured in the firing zone. Flue gases from the preheating zone were fed into series-connected channels 6. The upper rotary self-aligning dampers 28 carry out reducing air leaks from the heat-insulated housing 12 of the escalator 17 into the channels 6.

Channels 6 can be connected outside the kiln to one or more heat-insulated gas ducts connecting the kiln to the flue gas heat recovery system.

The proposed design solutions for all of the listed elements of the roasting kiln made it possible to solve two main tasks of increasing the efficiency of the furnace: to create a quasi-continuity mode for the combined processes of drying and roasting and to reduce losses due to the utilization of heat from technological streams.

3 Energy and Technical and Economic Efficiency of the Kiln

The energy efficiency of the proposed vertical kiln for firing ceramic products increased due to the following components:

- heat recovery of the cooled brick;
- elimination of fuel costs for drying raw brick;
- reduction of heat losses to the environment.

The economic effect of the introduction of a vertical kiln for firing ceramic products is to reduce the cost of production by reducing the main component of operating costs—the cost of fuel gas.

The values of the unit costs (per unit of production) C_i of two variants of the ceramic brick kiln with a capacity of 24 million pieces/year are shown in Fig. 2.

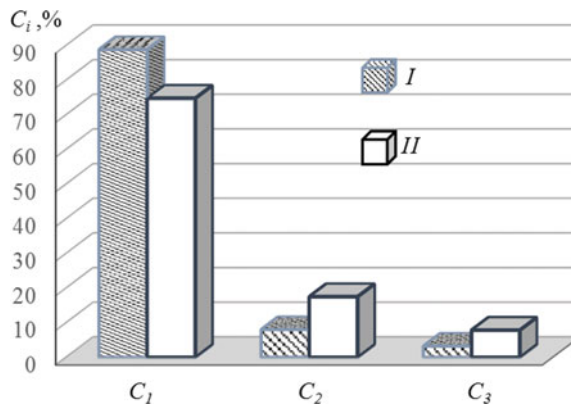


Fig. 2 Unit operating costs for two types of ceramic brick kiln (I—basic and II—effective)

To solve the problem of comparative energy–ecological–economic analysis, the software of the information-analytical system for the regulation and optimization of the production and consumption of fuel and energy carriers at the enterprise was used [9].

Furnace versions (I—basic version, tunnel kiln and II—efficient version and new vertical kiln) compared according to the following components:

- C_1 —fuel costs;
- C_2 —electricity costs;
- C_3 —maintenance, repair, and amortization costs of equipment (capital cost function).

It should be noted that fuel costs are 88.7 and 74.7% of the total operating costs for options I and II, respectively.

Figure 3 shows the change in the main three components of the annual costs for firing ceramic bricks and their sums ($\Delta C_\Sigma = \sum_1^3 C_i$) when introducing an efficient vertical kiln with a combination of processes in one unit.

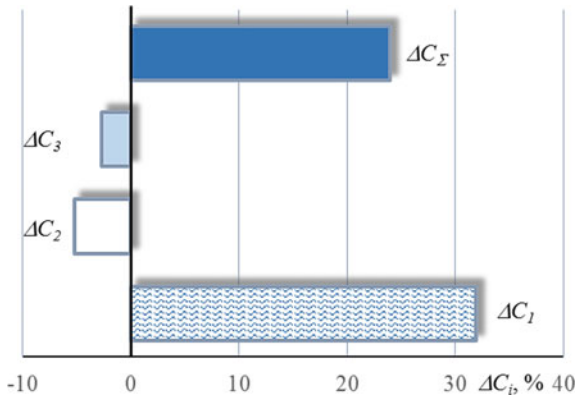


Fig. 3 Difference in annual operating costs in the compared variants of the ceramic brick-firing kiln

Analysis of the data shown in Fig. 3 shows that in the new vertical kiln with a combination of drying and firing processes, fuel costs have decreased by about 32%. At the same time, electricity costs increased (by about 5.6%) due to the use of additional movement mechanisms. The costs of maintenance, repair, and amortization of the kiln also increased (by 2.7% in total).

The overall efficiency of the introduction of a vertical kiln for firing ceramic products with a combination of processes and utilization of heat resources is determined by the cost of production, which will decrease by about 23–25% compared to the version of the existing kiln.

With the current ratio of prices for equipment and tariffs for energy carriers in the Russian Federation, the approximate payback period of the kiln, taking into account the time of construction and commissioning, will not exceed three years. This period is quite acceptable for new equipment projects.

4 Conclusion

In an efficient vertical kiln for firing ceramic products, constructive solutions have been proposed for the execution of heat-insulated bodies of escalators and a conveyor of the loading mechanism, in which the heat of the heated air removed from the kiln is utilized. The kiln was used not only for firing ceramic products, but also in other industries for heat treatment of products and materials in standards containers. By combining processes, reducing heat losses, and utilizing the heat of technological streams, operating costs for fuel gas reduced and the cost of heat treatment of products with the introduction of a vertical kiln reduced by about 23%.

References

1. Abdelaziz EA, Saidur R, Mekhilef S (2011) A review on energy saving strategies in industrial sector. *Renew Sustain Energ Rev* 15(1):150–168

2. Hasanuzzaman M, Rahim NA, Hosenuzzaman M et al (2012) Energy savings in the combustion based process heating in industrial sector. *Renew Sustain Energ Rev* 16(7):4527–4536
3. Mezquita A, Boix J, Monfort E, Mallol G (2014) Energy saving in ceramic tile kilns: cooling gas heat recovery. *Appl Therm Eng* 65:102–110
4. Sharapov AI, Arzamastsev AG, Peshkova AV, Neklyudov MN (2020) Enhanced energy efficiency of ceramics manufacturing due to heat recovery from secondary energy sources. *Int Trans J Eng Manag Appl Sci Technol* 11(13):11A13E
5. Shkarovskiy AL, Birulya VB (2017) Modernizatsiya tunnel'nykh pechey dlya proizvodstva stroy keramiki s tsel'yu snizheniya raskhoda teplonositeley (Modernization of tunnel kilns for the production of ceramics in order to reduce the consumption of heat carriers). *Vestnik grazhdanskikh inzhenerov* 6(65):206–212
6. Arnal AJ, Díaz-Ramírez M, Acevedo L et al (2020) Multicriteria analysis for retrofitting of natural gas melting and heating furnaces for sustainable manufacturing and industry 4.0. *J Energ Resour Technol Trans ASME* 142(2):022203
7. Massimo M, Luca M, Matteo S et al (2017) Numerical analysis of an entire ceramic kiln under actual operating conditions for the energy efficiency improvement. *J Environ Manag* 1:1–12
8. Ferrer S, Mezquita A, Monfort E, Aguilera VM (2019) Beyond the energy balance: exergy analysis of an industrial roller kiln firing porcelain tiles. *Appl Therm Eng* 1:1002–1015
9. Dolotovskij IV (2012) Informatsionno-analiticheskaya sistema normirovaniya i optimizatsii vyrabotki i potrebleniya topliva i energonositeley na predpriyatii (Information and analytical system for the regulation and optimization of the production and consumption of fuel and energy at the enterprise). RU Patent 2,465,639, 27 okt 2012
10. Dolotovskij IV (2015) Vertikal'naya pech' dlya obzhiga keramicheskikh izdeliy (Vertical kiln for firing of ceramic). RU Patent 151,374, 2 March 2015



Identification of Parameters of a Sub-Rail Base in the Computer System “Wheel-Railway Track”

E. S. Evtukh and G. A. Neklyudova^(✉)

Bryansk State Technical University, 7, Bulvar 50 Let Oktyabrya, Bryansk 241035, Russia

Abstract. The article describes a developed laboratory setup for studying vibrations in the “wheel-railway track” system. With its use, the rigidity of the ballast layer and the vibration damping coefficient is determined. A dry friction model can be applied in the experiment, where railway ballast is a free-flowing medium. In the calculations, it is replaced by a model of a viscous friction medium, so this model provides equivalent energy dissipation in the ballast layer. Identification of the vibration damping coefficient was carried out by comparing the oscillation waveforms obtained experimentally and using a computer model of the setup. The suggested scheme of a laboratory setup for determining the elastic and dissipative characteristics of the ballast layer provides conditions for applying a load to the ballast layer close to real (full-scale) conditions. The obtained values of the vibration damping coefficient and the stiffness of the ballast layer fall into the corresponding ranges given in the literature for various states of the ballast layer.

Keywords: Ballast layer · Elastic characteristics · Dissipative characteristics · Rigidity · Damping coefficient · Laboratory setup · Computer model · Parameter identification

1 Introduction

In the modern world, most processes and phenomena are usually investigated using computer simulation. However, important parameters of computer models can often be determined only experimentally. This article is devoted to finding the parameters of damping vibrations of a sub-rail base in computer simulation of the passage of a car wheel on a railway rail. In the computer model, the car is represented by masses, moments of inertia of the masses of wheel pairs, bogie frames, a body and the characteristics of the connections between them. A number of these values are quantified, and identifying the values of the rest is not as difficult as identifying the path parameters. There are significant difficulties with simulation of a sub-rail base. One of the most difficult tasks is to determine the elastic-dissipative properties of the ballast layer. This complexity is due to the fact that it is a bulk medium for which a dry friction model can be applied. However, the use of such a model in calculations is inconvenient, so it is replaced by a model of a medium with viscous friction, and then there is a need to determine the coefficient of viscous friction for this model to provide equivalent energy dissipation in

the ballast layer. The article presents the results of identification of the characteristics of rigidity and the coefficient of viscous friction of the ballast layer obtained using the developed laboratory setup.

1.1 Data Provided in Literature

One of the difficulties of accounting for the ballast layer in simulation is that its elastic-dissipative properties strongly depend on the time of year, weather conditions and the degree of contamination of the ballast. This explains quite a large variation in the quantitative assessment obtained by various authors. So, in the works of Kogan [1, 2], the coefficient of viscous friction has the value of 60 kN s/m, and in the works of Vinogradov V. A., Gasanov A. I., Burchak G. P., its value is set in a wide range from 200 to 800 kN s/m.

In the works of foreign scientists [3, 4], you can find the frequency dependence of the ratio of the rail deflection w to the amplitude of the periodic disturbing force P applied to the rail at a point located above the sleeper and in the middle between the sleepers. In the frequency range from 0 to 100 Hz, it varies little and is 1.52×10^{-8} m/N.

1.2 Problem Statement

In this study, the problem of determining the elastic-dissipative properties of the ballast layer is set and solved. In addition to taking into account the influence of weather conditions on the characteristics of a sub-rail base, it is necessary to take into account that railway ballast is a bulk medium for which a dry friction model can be applied. However, the use of such a model in calculations is inconvenient, so it is replaced by a model of a medium with viscous friction, and then there is a need to determine the coefficient of viscous friction for this model to provide equivalent energy dissipation in the ballast layer.

In this article, to identify the characteristics of a sub-rail base, a laboratory setup was developed and used, which allows conducting experimental studies of oscillation processes at operating frequencies of the order of 15 Hz.

2 Experimental Studies of the Characteristics of a Sub-Rail Base

To identify the characteristics of a sub-rail base, a laboratory setup was developed and used. This setup allows you to conduct experimental studies of oscillation processes at frequencies of the order of 15 Hz. The analysis of scientific research suggests that the results obtained with its use will be valid in the range up to 100 Hz. The diagram of the setup is shown in Fig. 1.

For simulation of a sub-rail base, cylindrical shell 1 was used. It is installed on chipboard 2, located on metal plate 3 with T-shaped grooves. Layer of sand 4 and crushed stone 5 is filled inside the shell. The load on the ballast layer is transmitted through package of steel and rubber gaskets 6, punch 7 and roller 8. The force on the roller is applied using lever 9. The lever is pivotally attached to rod 10. The rod at one end has eye 11, by means of which it is attached to the lever, and at the other end it has

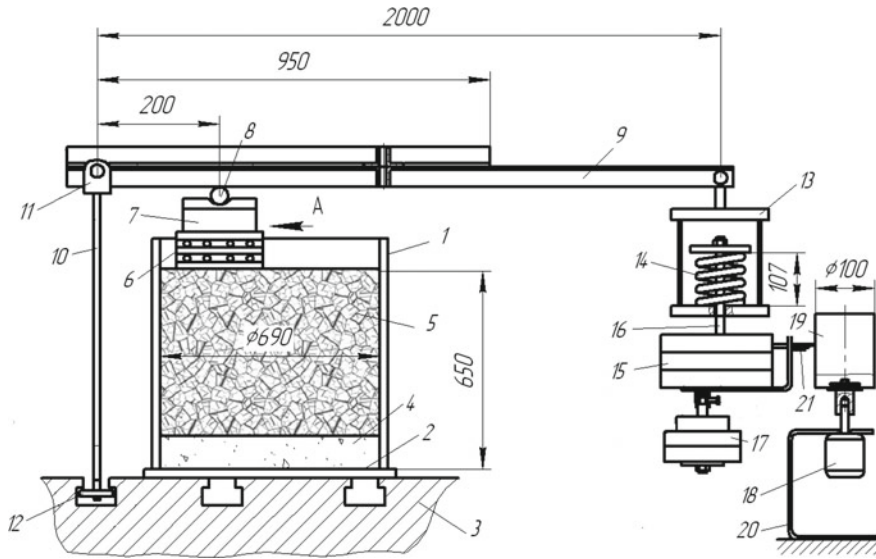


Fig. 1 Scheme of the experimental setup

plate 12, which enters the T-shaped groove of plate 3. The arms of the lever are selected in such a way that the force transmitted to the set of gaskets is 10 times the weight of the loads suspended from the other end of the lever. Frame 13 is attached to this end of the lever, on the lower plate of which spring 14 is installed. The load on the spring is created by the weight of loads 15, which are placed on upper suspension 16. The spring has a rigidity of $C_n = 2.5 \times 10^4$ N/m, so that its draught under the weight of 500 N loads is 20 mm. The rod of the lower suspension with an annular recess goes into the hole of the lower cylindrical part of the upper suspension, which is locked with a bolt. Loads 17 with a total weight of 250 N are placed on the lower suspension.

When developing the setup scheme, the goal was to determine the rigidity of the ballast layer, and the ballast layer together with a set of gaskets, as well as the damping coefficient of the ballast layer. The latter goal is achieved by recording the free vibrations of the mass of loads 15 on spring 14. The force equal to 5 kN is created due to the use of the lever. The force acts directly on the ballast layer or through a set of gaskets. To determine the elastic and dissipative properties of a single ballast layer, tests are carried out without a set of gaskets. In this case, punch 7 rests directly on the ballast layer. The area of the support surface of the punch is selected so that the specific pressure is the same as from the sleeper to the ballast layer.

The setup allows you to get the mass vibrations of loads 15 on the spring with a sufficiently large amplitude, which facilitates the recording of the oscillogram using the simplest equipment. Free vibrations are initiated in the system as follows. Loads 15 and 17 are placed on the suspensions, whilst the lower suspension is fixed from falling out with a bolt. The spring deflection is 30 mm. Then, the bolt turns away, loads 17 with the lower suspension fall down, and loads 15 make free damped vibrations relative to

the equilibrium position corresponding to the static deflection of the spring under their weight.

To record the vibrations, the authors used a device consisting of gear motor 18, drum 19 mounted on stand 20 and pen 21. The drum is mounted on the shaft of the gearbox with a hub. A paper tape is attached to the drum. The pen attached to the lower cup of suspension 16 is pressed against the paper tape by a spring. During the tests, electric motor 18 is turned on, which rotates the drum at a speed of 8.76 rpm.

3 Computer Model of the Experimental Setup

The dynamic model of the laboratory setup is shown in Fig. 2. The ballast layer is represented by an elastic bond with the rigidity C_6 and a viscous friction damper with the damping coefficient β . Loads 15 are represented by the mass m , suspended from lever 9 on an elastic bond with the rigidity C_n . The lever is considered as an elastic element (elastic beam) with the rigidity EJ_1 on the section of the length d and the rigidity EJ_2 on the sections of the lengths a and b . Rod 10 is also considered as an elastic element. The displacements y_1 of the mass m and y_2 of the point B in the support of the punch on the ballast layer are taken as generalized coordinates. In this scheme, a set of gaskets was not considered. The position of the lever when hanging loads 15 with the mass m to it is shown in figure of the curve $A_1B_1D_1$. The points B and D in this case receive the static displacements y_{1cm} and y_{2cm} . The line $A_2B_2D_2$ shows the position of the lever for the moment when the system is in a state of free vibrations.

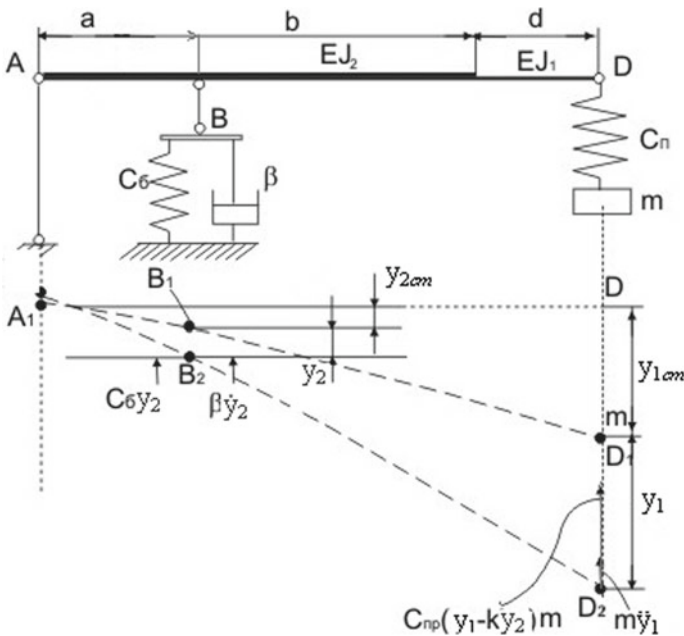


Fig. 2 Dynamic model of the experimental setup

The force occurring in the elastic bond $C_{np}(y_1 - ky_2)$ acts on the mass m , where k is the gear ratio of the lever; C_{np} is the reduced rigidity, taking into account the rigidity of the spring C_n , the lever arm and the rod C_p , and the force of inertia $m\ddot{y}_1$.

The response of the ballast layer which is equal to the sum of the forces $C_{\delta}y_2$, arising in the elastic connection and $\beta\dot{y}_2$, arising in the damper is applied at point B.

Free vibrations of the mass m are represented by differential equations:

$$\begin{cases} m\ddot{y}_1 + c_{np}(y_1 - ky_2) = 0, \\ kc_{np}(y_1 - ky_2) = c_{\delta}y_2 + \beta\dot{y}_2. \end{cases} \tag{1}$$

The second equation expresses the condition when the reaction of the ballast layer is equal to the force transmitted to it from the lever.

The values included in differential Eq. (1) have the following values: the gear ratio of the lever $k = 10$; the spring rigidity $C_n = 2.5 \times 10^4$ N/m; the rigidity due to the elastic properties of lever 9 and rod 10, $C_p = 4.68 \times 10^4$ N/m; the reduced rigidity of the lever and the spring is $C_{np} = \frac{C_n C_p}{C_n + C_p}$, $C_{np} = 1.63 \times 10^4$ N/m. Solving Eq. (1) with respect to y_1 , we obtain

$$\frac{\beta m}{kc_{np}} \ddot{y} + \left(\frac{mc_{\delta}}{kc_{np}} + km \right) \dot{y}_1 + \frac{\beta}{k} y_1 + \frac{c_{\delta}}{k} y_1 = 0. \tag{2}$$

The characteristic equation for Eq. (2) has the form:

$$\lambda^3 + A\lambda^2 + B\lambda + D = 0, \tag{3}$$

where

$$A = \frac{k^2 c_{np}}{\beta} + \frac{c_{\delta}}{\beta}; \quad B = \frac{c_{np}}{m}; \quad D = \frac{c_{np} c_{\delta}}{\beta m}.$$

To determine the rigidity of the ballast, the movements of the suspension point D are measured depending on the weight of the loads. Their values are shown in Table 1.

Table 1 The movements of the suspension point D are measured depending on the weight of the loads

Load on crushed stone, kN	1	2	3	4	5	6	7	7.5
Movements of the suspension point, mm	8	16	24	32	40.2	47.8	57.2	61.5
Crushed stone draught, mm	0.118	0.373	0.56	0.75	0.952	1.1	1.42	1.55

A linear dependence of the ballast draught on the applied force is practically obtained. The static movement of the suspension point is

$$\Delta_{cm} = \frac{kmg}{c_{\delta}} k + \frac{mg}{c_{np}}.$$

Substituting the values of $mg = 500$ N and $\Delta_{cm} = 40.2$ mm in this dependence, we obtain the rigidity of the ballast layer $C_{\delta} = 5.25 \times 10^6$ N/m.

4 Identification of Vibration Damping Parameters in the “wheel-Railway Track” System

With the help of the developed laboratory setup, free vibrations of the mass m , suspended from lever 9 through spring 14 were studied (Fig. 1). The tests were carried out without the use of rubber and metal gaskets. Loads 15 were used as the vibrating mass. The initial conditions were created by deviating them from the equilibrium position. The lower suspension with weights 17 was attached to them from below. The deviation from the equilibrium position $y_{01} = 18 \text{ mm}$ was obtained.

Suspension 16 was released from loads 17, and loads 15 made free damping vibrations. The oscillation waveform was recorded on a paper tape attached to drum 19. It is shown in Fig. 3a. This figure shows vividly expressed damping vibrations. Before the system came to a state of rest, it made 14 vibrations.

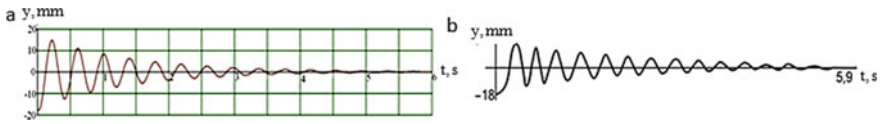


Fig. 3 Oscillograms of cargo vibrations: **a** in the experiment; **b** theoretical solution

10 total vibrations are taken as the calculated ones. The time of ten vibrations on the oscillogram corresponds to the segment of the length $L = 192 \text{ mm}$ along the abscissa axis. The time of ten vibrations is

$$t = \frac{L}{\omega R} = 3.96 \text{ s,}$$

where $\omega = \frac{\pi n}{30} = 0.917 \text{ rad/s}$; $n = 8.76 \text{ rpm}$ is the rotation speed of the drum; $R = 50 \text{ mm}$ is the radius of the drum.

Then, the vibration frequency is

$$f = \frac{10}{t} = 2.525 \text{ Hz,}$$

and the circular frequency is

$$k = 2\pi f = 15.87 \text{ rad/s.}$$

The parameter of vibration damping in the ballast layer is determined by selection. Equation (2) was solved by the Runge-Kutt method using standard Mathcad programmes. The initial conditions were: $y_{10} = 0.018 \text{ m}$; $\dot{y}_{10} = 0$; $\ddot{y}_{10} = 0$.

The parameter β varied in such a way as to obtain a vibration oscillogram close to the experimental one. The best approximation is achieved at $\beta = 14 \times 10^4 \text{ N/s.m}$. The oscillogram is shown in Fig. 3b.

The frequency of free vibrations $k = 15.99 \text{ rad/s}$ was obtained from the solution of characteristic Eq. (3). As in the experiment, before the transition to the equilibrium position, the system made 14 complete vibrations.

5 Conclusion

The experimental studies made it possible to draw the following conclusions:

- Using the developed setup, the value of the rigidity coefficient of the ballast layer of 5.25×10^6 N/m was obtained. The pressure on the ballast was transmitted through a rectangular plate with an effective area of 0.024 M^2 . Since here, we considered the vertical rigidity that connects the force applied to the half of the sleeper and the ballast draught, and it must be proportional to the area of support on the ballast layer. The effective area of support of the sleeper is 0.3 m^2 . Then, the rigidity of the ballast layer, due to the support of half of the sleeper on it, is 65.6×10^6 N/m. In [5], this value is 50×10^6 N/m.
- The value of the vibration damping coefficient of 14×10^4 N s/m was obtained. In [6], the value of the attenuation coefficient of 6×10^4 N s/m is given. The value of the vibration damping coefficient obtained using the laboratory setup exceeds the value given in Kogan's work [6–16], but does not contradict the results given in [5]. The overestimated rigidity values of the ballast layer and vibration damping obtained during the experimental research using the laboratory setup can be related to the fact that the ballast was located in a closed volume in a rigid cylindrical shell.

References

1. Kogan AY (1997) Dinamika puti i ego vzaimodejstvie s podvizhnym sostavom (The dynamics of the way and its interaction with the rolling stock). Transport, Moscow
2. Kogan A, Peich YL, Poleshchuk IV (2003) Raschety dinamiki udara v yelementah konstrukcii puti (Calculations of the impact dynamics in the elements of the path construction). In: Problems of track facilities of Eastern Siberia: coll. of sc. pap. IrGUPS, Irkutsk, p 17–29
3. Nielsen J, Lunden R, Johansso A (2003) Train-track interaction and mechanisms of irregular wear on wheel and rail surfaces. Veh Syst Dyn 40:3–54
4. Ripke B, Knothe K (1991) Die unendlich lange Schiene auf diskreten Schwellen bei harmonischer Einzellasterregung. VDI-Verl., Dusseldorf, p 54
5. Verigo MF, Kogan AY (1986) Vzaimodeistvie puti i podvizhnogo sostava (Interaction of the track and rolling stock). Transport, Moscow
6. Kogan AY, Pejch YL (2000) Raschet napryazhenno-deformirovannogo sostoyaniya elementov konstrukcii puti v zone styka rel'sov (Calculation of the stress-strain state of railway track structural elements in the rail junction zone). Bull All-Russ Res Inst Transp Eng 2:31–39
7. Evtukh ES et al (2009) Vlijanie prosadki ballasta na dinamicheskie usilija, voznikayushie mezhdru kolesom i rel'som pri prohozhdenii styka (Effect of ballast subsidence on the dynamic forces that arise between the wheel and the rail during the passage of the joint). Transp Urals Ekaterinburg 23:32–34
8. Sakalo V et al (2019) Computer modeling of processes of wear and accumulation of rolling contact fatigue damage in railway wheels using combined criterion. Wear 432–433
9. Sakalo VI, Sakalo AV (2019) Kriterii dlya prognozirovaniya vozniknoveniya kontaktno-ustalostnyh povrezhdenij v kolesah zheleznodorozhnogo podvizhnogo sostava i rel'sah (Criteria for predicting the occurrence of contact fatigue damages in railway wheels and rails). Bull All-Russ Res Inst Transp Eng 78(3):141–148

10. Evtukh ES (2011) Napryazhyonno-deformirovannoe sostoyanie v oblasti kontakta koleasa i rel'sa pri naezde koleasa na styk (Stress-strain state in the contact area of wheel and rail when hitting the wheel on the joint). Bull Bryansk State Tech Univ 3:74–79
11. Evtukh ES, Sakalo VI (2013) Vliyaniye rel'sovykh stykov na nakopleniye kontaktno-ustalostnykh povrezhdeniy v koleсах podvizhnogo sostava (The influence of rail joints on the accumulation of contact fatigue damages in railway wheels). Bull Bryansk State Tech Univ 4:9–17
12. Evtukh E, Neklyudova G (2016) Accumulation of contact fatigue damages in car wheels when raiing over rail joints. In: XVII Scientific-expert conference on railways. Mechanical Engineering Faculty of the University of Niš., Serbia, p 161–165
13. Evtukh ES, Neklyudova GA (2012) Computer simulation of the process of passing the wheel through the joint to solve the contact problem. Visnik Volodymyr Dahl East Ukrainian Nat Univ 176(2):7–11
14. Evtukh ES, Neklyudova GA (2013) Decision of the contact problem for wheels for freight cars passing rail joints. Visnik Volodymyr Dahl East Ukrainian Nat Univ 207(1):19–22
15. Evtukh ES, Neklyudova GA (2017) Analiz problemy vzaimodeystviya zheleznodorozhnogo koleasa s rel'sovym stykom (Analysis of the problem of interaction of a railway wheel with a rail joint). In: VI International scientific seminar “Dynamic deformation and contact interaction of thin-walled structures under the influence of fields of different physical nature” Moskva, p 46–48
16. Evtukh ES, Neklyudova GA (2019) Sozdaniye komp'yuternoy modeli dvizheniya zheleznodorozhnogo koleasa cherez rel'sovyy styk dlya resheniya kontaktnoy zadachi (Creation of a computer model of the movement of a railway wheel through a rail joint to solve a contact problem). In: Obratsov IF, Yanovsky YG (eds) 8th All-Russian scientific conference “Mechanics of Composite Materials and Structures, Complex and Heterogeneous Media” with international participation. Moskva, p 254–257



Aerodynamic and Numerical Studies of the Flow in the Relief Surface Seals

G. E. Evtukh^(✉), A. Yu. Androsov, and V. V. Gorbachev

Bryansk State Technical University, 7, Bulvar 50 Let Oktyabrya, Bryansk 241035, Russia

Abstract. In turbomachines, a significant influence on efficiency is represented by the leaks in the labyrinth seals (end diaphragm, peripheral ones above the rotor blades). Losses from internal leaks are very significant in the percentage. The number of sealing sectors sometimes (in steam turbines) takes up to 40% of the shaft length. A greater reserve for increasing the turbomachine efficiency is improving the seal flow path to reduce the leaks or their localization in the case of using aggressive harmful media. Intensifying vortex flows on relief surfaces, affecting the main leakage flow in slot seals, was studied in a number of experimental works. The results of physical and numerical modeling of relief surface seals are presented. The physical study of the flow was carried out on an experimental stand, and the numerical study was fulfilled using the ANSYS CFXv.19 software package. The studies of honeycomb-hole seal were implemented at various operating parameters (pressure drops) and gap sizes with determining the flow rate characteristics.

Keywords: Turbomachines · Labyrinth seal · Honeycomb surfaces · Hole surfaces · Flow rate · Working fluid

1 Introduction

The analysis of the practical improvement of the profile surfaces of the seals is carried out, both from the point of view of the highest aerodynamic efficiency and the formation of stable vortex structures, and the possible effects of flow pulsation in the seal, which not only intensify the sealing effect, but can also be a source of aerodynamic excitation of oscillations of turbomachine rotors. The use of honeycomb-hole compaction is aimed at increasing the sealing effect using the mutual influence of vortex structures in the space of honeycomb cells and holes, revealing the main design parameters of profile surfaces that affect the effectiveness of combined seals.

1.1 Literature Review

In [1, 2], numerous studies of effecting vortex flow in honeycomb seal cells on the flow in the flat slot space are presented. It is noted, in particular, the vortices interaction intensification in “shallow” honeycomb cells ($h_c/d_c \approx 0.3/0.5$) with a leakage flow,

leading to the flow rate decrease by 10–15% in comparison with a smooth slot, depending on the gap size and pressure drops.

Tornado-like or whirlwind vortex jet structures are known [3]. They are formed by flowing around “shallow” holes ($h_h/d_h \approx 0.06/0.1$) on the plane, and they reduce the flow rate in a flat slot by about 5% [2, 3].

A characteristic feature of influencing “shallow” holes on the flow is a moderate increase in hydraulic resistance compared to a significant increase in the heat transfer.

Using hole assemblies with the appropriate parameters made it possible to significantly improve the functional, technical, and economic characteristics of uranium fuel rods, heat exchange equipment for gas turbine engines, etc. [4].

In [5–7], the substantiation of the physical essence of the effectiveness of the sealing effect is given using the spatial structure of the flow in the cells of the seals and their influence on the leakage flow.

The literature [8–10] presents the results of experimental studies of turbine stages with honeycomb seals in a wide range of design and operating parameters.

On the other hand, there is a sufficient number of literary sources that note the resonant disturbance of the flow in channels with profiled surfaces, which affect both the flow characteristics of the seals, heat exchange [11–14], and the vibration activity of the shafts of turbomachines [15–17].

1.2 Problem Statement

Creating vortex generators, which would have minimum hydrodynamic resistance and would generate artificial vortex systems with the given kinematic and dynamic parameters, is of great practical importance.

Seal channels of complex shape are proposed; methods of sealing leaks, optimizing the design and operating parameters, taking into account reliability factors, are improved.

This paper presents one of such devices, namely a combined honeycomb-hole seal [2, 18], which implies the mutual influence of vortex structures in honeycomb cells on one of the flat slot walls and a two-cell vortex structure in holes on the opposite surface.

2 Test Procedure and Models

For comparison, a slotted seal with straight smooth walls was taken as the initial test option. The flow path is made in the form of a slot with a width of $b = 58$ mm and a length of $l = 175$ mm. The height was determined by the size of the gap $\delta = 1, 2, 3$ mm. The layout of the experimental stand is shown in Fig. 1. Variants of plates with different reliefs are shown in Fig. 2. The studies were carried out in air at pressure drops $P_{in}^*/P_{out} = 1.14/1.38$.

The method of the flow numerical investigation takes into account the design and operating parameters of the flow in the seals.

The element of the flow path is considered (flat slot is 58 mm wide, 175 mm long, clearance $\delta = 1$ mm, pressure drop is $P_{in}^*/P_{out} = 1.2$).

The computational grid was made in such a way that about 10 cells could fit in the gap $\delta = 1$ mm. The final computational grid consisted of 3.5 million computational cells.

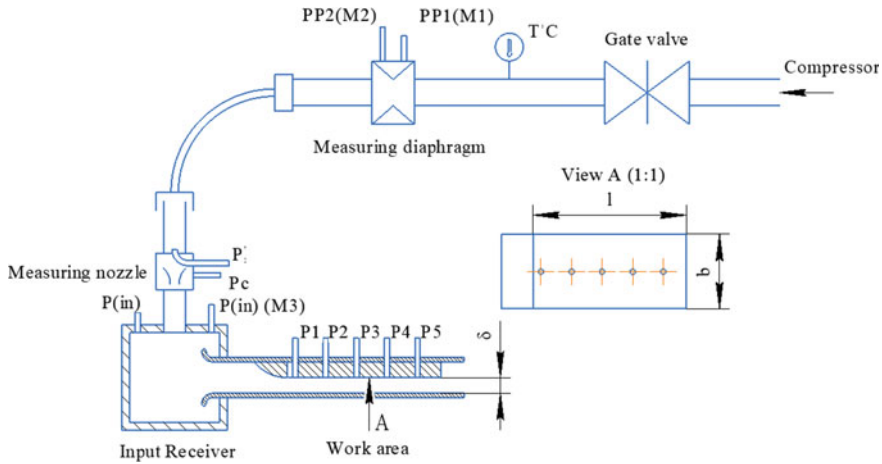


Fig. 1 Experimental stand

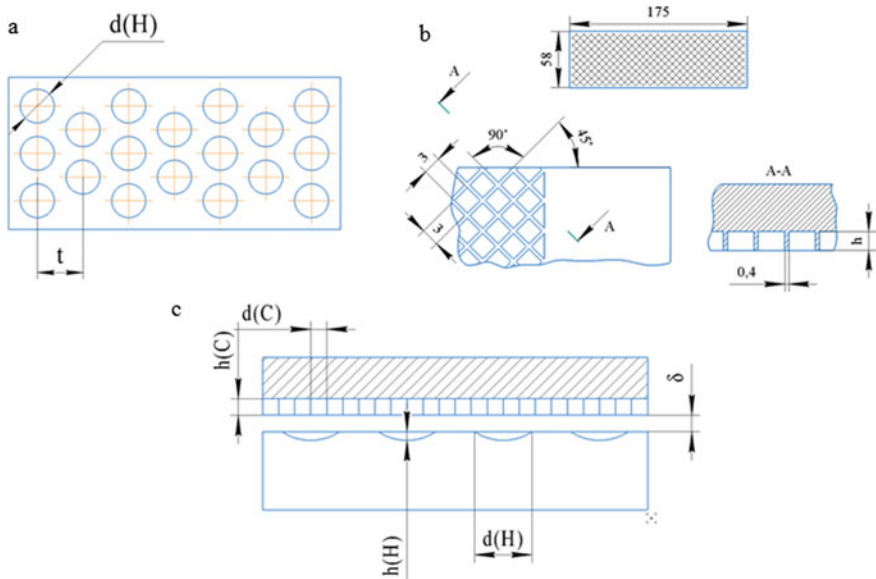


Fig. 2 Variants of plates with different reliefs: **a** hole surface; **b** cell surface; **c** cell + hole seal

The standard $k - \epsilon$ turbulence model was chosen, which is typical for such problems. The working medium (air-perfect gas) was completely compressible; the time step was initially set equal to 0, 1 of the flight time. The static pressure and temperature were taken as input boundary conditions. The absence of large oscillations in the values of the input and output parameters was taken as a criterion for convergence.

2.1 Experimental Results

The results of studying the seal characteristics are shown in Fig. 3 in the form of dependences of the flow rate ratio in a channel with relief surfaces \bar{G} and a smooth slot \bar{G}_{sm} , depending on the gap size and the pressure drop in the seal. Note that the greatest influence of the surface relief is noticeable at the increased pressure drops P_{in}^*/P_{out} .

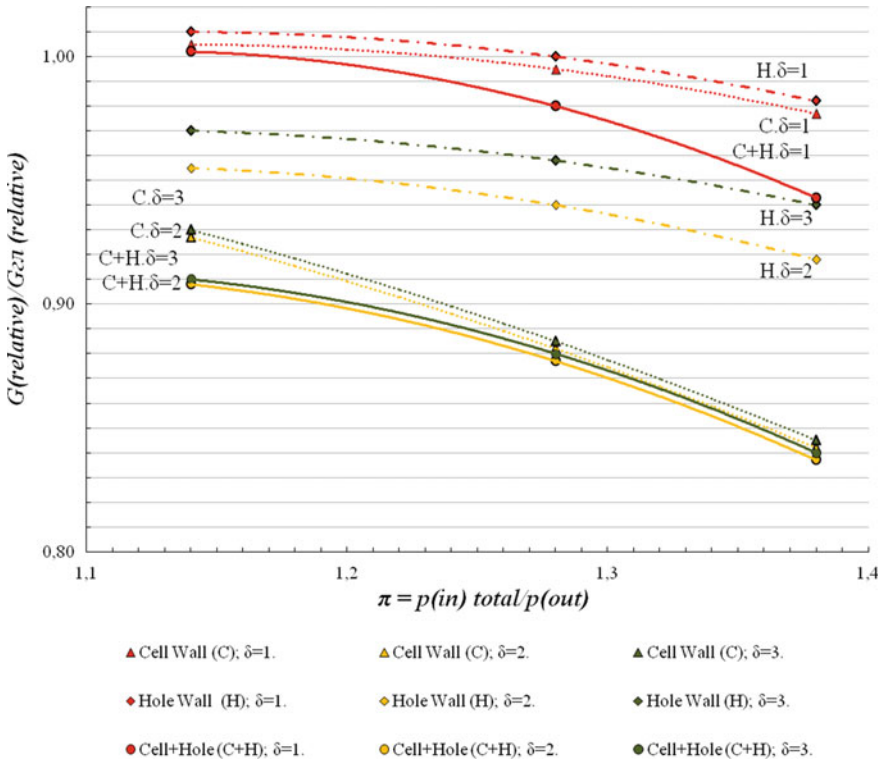


Fig. 3 Comparison of seal performance at different clearances and pressure drops

With a gap of $\delta = 1$ mm, the influence of individual honeycomb and hole surfaces is insignificant (approximately 2% at $P_{in}^*/P_{out} = 1.38$). Honeycomb-hole seal shows a 6% effect.

A honeycomb seal on one of the walls (the opposite wall is smooth) reduces the leakage rate (at $\delta = 2/3$ mm) by 16% at $P_{in}^*/P_{out} = 1.38$ and 7% at $P_{in}^*/P_{out} = 1.14$.

Accordingly, the hole seal reduces \bar{G}/\bar{G}_{sm} by 7 and 4%.

The advantage of honeycomb-hole seal ($h_c + h$) over honeycomb (h_c) is noticeable at low pressure drops ($P_{in}^*/P_{out} = 1.2$) and amounts of about 1%, and over a hole (h), it amounts of about 6%.

The total effect of honeycomb-hole seal against a smooth gap in the investigated pressure drop at gaps of 2–3 mm is 9–16%.

The honeycomb surface makes the greatest contribution to the sealing effect. However, the influence of the hole surface is noticeable at small pressure drops ($P_{in}^*/P_{out} \approx 1.14$).

It should be noted that the experimental data are given only for one standard size of the relief surfaces (honeycomb and hole).

2.2 Numerical Results

The results of studying the seal flow structure are shown in Figs. 4 and 5. The flow structure in conjunction with the operating and geometric parameters provides a basis for understanding the features of the working process in the labyrinth seal and its consumption characteristics and creates the prerequisites for their improvement.

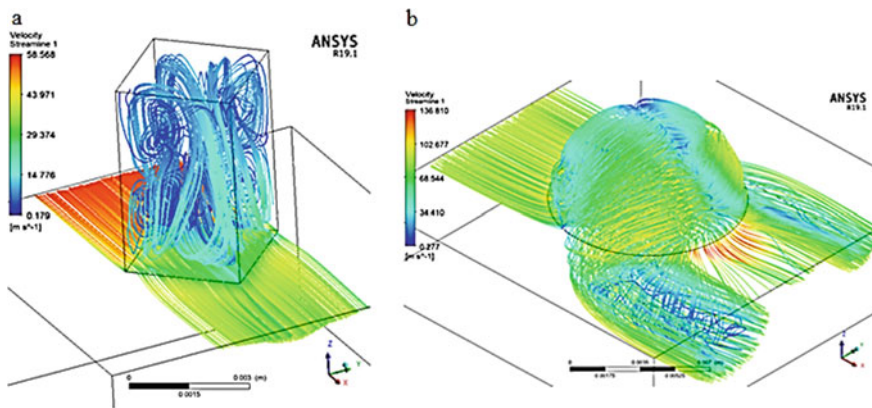


Fig. 4 Detail view of streamlines in **a** a cell and **b** a hole

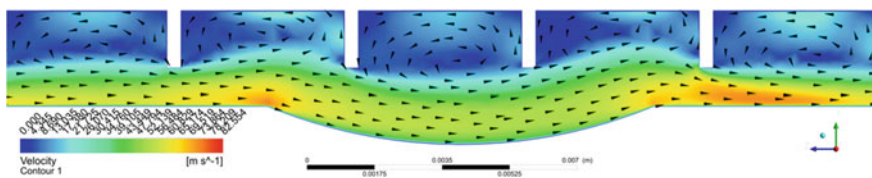


Fig. 5 The interaction of cells and holes

The research results are presented by visualizations in the form of vector fields and velocity isolines.

The logic of the research was lined up from studying the flow of individual honeycomb cells and holes to a honeycomb seal, consisting of an ensemble of relief surfaces.

Figure 4 shows the flow visualization in the individual honeycomb cells (a) and holes (b).

A peculiarity of the considered vortex flows in the holes is the ejection of vortices into the main leakage flow, interaction with it, and the boundary layer on the relief surfaces.

Visualizing the flow in a smooth slot revealed an insignificant effect of the boundary layers at the walls.

Figure 5 shows the flow visualization in a honeycomb-hole seal with a distinct influence of the vortex structures on the honeycomb surface and the vortex bifurcation in the holes and their mutual influence.

3 Conclusion

The analysis of the flow structure made it possible to explain the significant decrease in the leakage rate in the honeycomb-hole seal not only in comparison with a smooth slot, but also in the individual honeycomb and hole surfaces, which is confirmed by the experimental studies.

Experimental studies of the vortex flow in the space of hexagonal or diamond-shaped honeycomb cells indicate the formation of flows reflected from the side faces, which is not only circulate in the space of the cells, but also capable of affecting the main leakage flow in the seal gap. The discovered effect [1] of interaction of flows is especially manifested in shallow cells ($h_c/d_c = 0.3/0.5$).

The visualization of the flow in seals with holes also provides grounds for practical optimization of the design parameters of the hole surface in order to localize the leakage rate in the seals of turbomachines [19–21].

References

1. Buglaev VT, Perevezentsev VT, Perevezentsev SV et al (2006) Sotovye uplotneniya v turbomashinah (Honeycomb seals in turbomachines). Publishing house of Bryansk State Technical University
2. Nikitin I, Sazonov K, Perevezentsev V (2020) Combined seal in turbomachines. In: VIII International multidisciplinary conference “Recent Scientific Investigation”. USA Primedia E-launch LLC, Shawnee, p 60
3. Alekseev VV, Gagechiladze IA, Kiknadze IA, Oleinikov VG (1998) Smerchevoj energoobmen na trekhmernoj rel'efnoj strukture samoorganizuyushchihsysya techenij, ih vizualizaciya i mekhanizmy obtekaniya poverhnostej (Tornado energy exchange on a three-dimensional concave relief structure of self-organizing flows, their visualization and mechanisms of flow past surfaces). Publishing house of Moscow, p 37–42
4. Nagoga GP (1996) Effektivnye sposoby ohlazhdeniya lopatok vysokotemperaturnyh gazovyh turbin (Effective methods of cooling the blades of high-temperature gas turbines). Publishing house of Moscow Aviation Institute, p 100
5. Buglaev VT, Perevezentsev SV, Gerke VG et al (1996) O fizicheskoj sushchnosti techeniya rabochej sredy v kamerah labirintnyh uplotnenij turboustanovok (On the physical essence of the flow of the working medium in the chambers of the labyrinth seals of turbine plants). Atomic Energ Med 2:52–55
6. Buglaev VT, Perevezentsev SV, Klimtsov AA (1999) Issledovanie elementov teploenergeticheskikh ustanovok. (Study of the spatial structure of the flow in honeycomb seals). Publishing house of Bryansk State Technical University, p 68–78

7. Ivanov VA, Zharky MS (1985) K raschyotu protechek v labirintovykh uplotneniyaх pri perekhodnykh rezhimakh raboty turbomashin (Calculation of leaks in labyrinth seals during transient operating modes of turbomachines). Publishing House Univ Energ Med 10:81–84
8. Klimtsov AA, Zakharenko VA, Tsybin AG (1987) Ispytanie turbinnoj stupeni s sotovym radial'nym uplotneniem (Honeycomb radial seal turbine stage test). Publishing House Univ Energ Med 95–98
9. Perelman RG, Nesterenko VG, Lyubogurov AM (1983) Issledovanie gazodinamicheskoy effektivnosti labirintnykh uplotnenij GTD s profil'noj stenкой statora (Investigation of the gas-dynamic efficiency of labyrinth seals of a GTE with a stator profile wall). Publishing House Univ Aviat Technol Med 1:105–108
10. Buglaev VT, Perevezentsev SV (2002) K metodike optimizatsii sotovykh uplotnenij (On the method of optimizing honeycomb seals). Publishing House Univ Energ Med 2:45–50
11. Buznik VM (1969) Intensifikatsiya teploobmena v sudovykh ustanovkakh (Heat transfer intensification in ship installations). Sudostroenie, p 364
12. Nazmeev YuG, Olimpiev VV, Konakhin AM et al (1994) Rezonansnoe vozmushchenie potoka v kanalah s diskretnymi vystupami (Resonant flow disturbance in channels with discrete protrusions). Publishing House Univ Aviat Technol Med 1:79–82
13. Kostyuk AG (1986) Analiz nestacionarnogo techeniya v labirintnykh uplotneniyaх turbo-mashin (Analysis of unsteady flow in labyrinth seals of turbomachines). Teploenergetika 12:31–36
14. Rechnoblit AY, Avdeenko OV (1985) Issledovanie vliyaniya razmerov sotovykh yacheek na effektivnost' uplotnitel'nykh ustrojstv s razlichnymi vrashchayushchimisya elementami (Investigation of the influence of the size of honeycomb cells on the efficiency of sealing devices with various rotating elements). Trudy CIAM Med 11(56):11
15. Kostyuk AG, Serkov SA, Urev EV, Petrushin BN (1991) Vliyanie diafragmennykh uplotnenij parovoy turbiny na aerodinamicheskoe vozbuzhdenie kolebanij rotora (Influence of diaphragm seals of a steam turbine on aerodynamic excitation of rotor vibrations). Teploenergetika 11:43–47
16. Bondarenko GA, Pshik VR (1982) Eksperimental'noe issledovanie vibroaktivnosti uplotnenij valov turbomashin Energomashinostroenie (Experimental study of vibration activity of shaft seals of turbomachines). 4:5–8
17. Marcinkovski VA (2005) Shchelevoj uplotneniya: teoriya i praktika (Throat seals: theory and practice). Publishin house of SumSU, p 416
18. Perevezentsev VT, Nikitin IA, Chukhnov VS, Kolchanov AV (2020) Kombinirovannoe uplotnenie v turbomashinakh (Combined seal in turbomachines). RU Patent 196232, Jan 2020
19. Gorelov YG, Kopylov NS (2003) Formirovanie effektivnosti konvektivnogo ohlazhdeniya rabochih lopatok turbin s vihrevymi skhemami techeniya ohladitelya (Problems of gas dynamics and heat and mass transfer in power plants). Publishing house of Moscow Energetic Institute, p 406
20. Isaev SA, Leontev AI, Baranov PA (2000) Identifikatsiya samoorganizuyushchih-sya smercheobraznykh struktur pri chislennom modelirovanii turbulentnogo obtekaniya lunki na ploskosti potokom neszhimaemoj zhidkosti (Identification of self-organizing tornado-like structures in the numerical simulation of turbulent flow around a hole on a plane by an incompressible fluid flow). Lett JTF Med 1:28–35
21. Isaev SA, Leontev AI, Baranov PA, Pyshny IA (2003) Chislennyj analiz vliyaniya na turbulentnyj teploobmen glubiny sfericheskoy lunki na ploskoj stenke (Numerical analysis of the effect of the depth of a spherical dimple on a flat wall on turbulent exchange). IFJ Med 1:52–59



A Mathematical Model for the Asynchronous Drive of the Overhead Traveling Crane

V. A. Krutova^(✉) and I. A. Yaitskov

Rostov State Transport University, 2, Lenin Ave, Rostov-on-Don 344038, Russia
nikarostov@bk.ru

Abstract. This article aims to research the generation of a vibration field and noise by the reduction gear to find opportunities to reduce vibration, calculate noise levels, and develop engineering practices for the calculation of noise levels. The dynamic systems of machinery power trains usually have low dissipation, and their links are elastic or, in some cases, quasi-elastic. This means that the model must be based on an elastic-inertia core system of differential equations. Dissipation factors, in this case, are seen as additional parameters of the core. Asynchronous electric motors of varying output and rotor speeds act as the source of energy for hoisting and movement mechanisms of overhead traveling cranes. They are also the first components of the respective crane drives.

Keywords: Drive · Reduction gear · Asynchronous electric motor · Overhead traveling crane · Vibration · Noise · Gearset force

1 Introduction

This article deals with mathematical modeling of such drives as a system of quintic differential equations [1–19]:

$$\begin{aligned} \frac{d\Psi_{1x}}{dt} &= U_{1x} - \frac{r_1 \cdot L'_2 \cdot \Psi_{1x}}{\Delta} + \frac{r_1 \cdot L_0 \cdot \Psi_{2x}}{\Delta} + \Omega_0 \cdot \Psi_{1y}; \\ \frac{d\Psi_{1y}}{dt} &= U_{1y} - \frac{r_1 \cdot L'_2 \cdot \Psi_{1y}}{\Delta} + \frac{r_1 \cdot L_0 \cdot \Psi_{2y}}{\Delta} - \Omega_0 \cdot \Psi_{1x}; \\ \frac{d\Psi_{2x}}{dt} &= -\frac{r'_2 \cdot L_1 \cdot \Psi_{2x}}{\Delta} + \frac{r'_2 \cdot L_0 \cdot \Psi_{1x}}{\Delta} + (\Omega_0 - \Omega) \cdot \Psi_{2y}; \\ \frac{d\Psi_{2y}}{dt} &= -\frac{r'_2 \cdot L_1 \cdot \Psi_{2y}}{\Delta} + \frac{r'_2 \cdot L_0 \cdot \Psi_{1y}}{\Delta} - (\Omega_0 - \Omega) \cdot \Psi_{2x}. \end{aligned} \quad (1)$$

$$\frac{d\omega}{dt} = \frac{3 \cdot Z_p}{2} \cdot \frac{L_0}{J \cdot \Delta} \cdot (\Psi_{2x} \cdot \Psi_{1y} - \Psi_{2y} \cdot \Psi_{1x}) - \frac{1}{J} \cdot M_C, \quad (2)$$

where $U_{1x} = \sqrt{2} \cdot U_m \cdot \cos \omega_p \cdot t$; $U_{1y} = \sqrt{2} \cdot U_m \cdot \sin \omega_p \cdot t$; $M_{dv} = \frac{L_0}{\Delta} \cdot (\Psi_{2x} \cdot \Psi_{1y} - \Psi_{2y} \cdot \Psi_{1x})$; $\Psi = \frac{N^2}{Z_M} \cdot i = L \cdot i$ are the armature flux linkage; $\Delta = L_1 \cdot L'_2 - L_0^2$ is the coefficient; r_1 is the active resistance of the stator; r'_2 is the active resistance of the rotor; L_1 is the self-inductance of the stator; L'_2 is the self-inductance of the rotor; L_0 is the mutual inductance of the stator, and the rotor; ω_p is the mains frequency (50 Hz).

2 A Model of the Joint Box Located Between the Electric Motor and the Input Shaft of the Reduction Gear

According to multiple research works on machine dynamics [3], flexible joints can be seen as piecewise-linear components. Let us assume that the joints used in the drive have no hard deformation limiters. This is typical of joints featuring elastic elements, i.e., pin bush and coil ones [3].

If we take $\gamma_k = \varphi_k - \varphi_{k+1}$ and $U(\gamma)$ is the elastic response of the joint, the typical characteristic of this component can be expressed as a piecewise-linear function in Fig. 1:

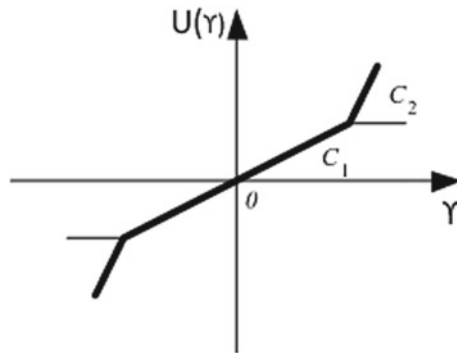


Fig. 1 Typical elastic characteristic of the joint

Let us assume that this characteristic can be expressed as a sum of two characteristics:

- a straight line crossing the zero, whose slope ratio is equal to rigidity C_1 ;
- the second characteristic has a slope ratio equal to rigidity $C_2 - C_1$ and it looks like in Fig. 2:

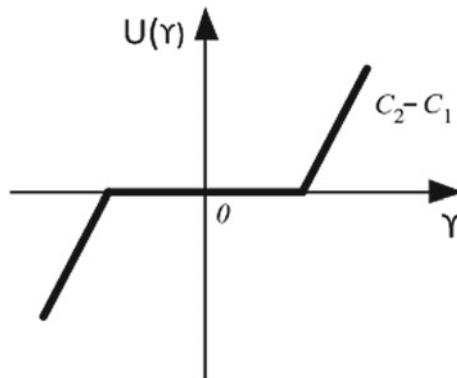


Fig. 2 Nonlinear component of the elastic joint characteristic

Let us assume the following: the section of the shaft between the electric motor and the first half-joint, as well as the section of the reduction gear input shaft between the second half-joint and the cogwheel, do not allow us to ignore their torsional rigidity as compared to the joint rigidity.

According to literature, joints with metal elastic components, as well as those with rubber blocks and balls can be classified as low-friction joints [1, 2]. It must be noted that strictly speaking, all elastic joints are nonlinear due to their nonlinear elastic and dissipation properties. Normally, joints are seen as “built into the body.” In this case, the piecewise-constant rigidity values for the characteristic shown in Fig. 1 represent an angular function relative to the half-joint shift.

We can try to express this characteristic as a sum of two: the linear and the nonlinear one with a dead zone as in Fig. 2.

The nonlinear behaviors of the elastic characteristic of the joint can be accounted for through the introduction of additional components into the vector of the right-hand members of the matrix equation of the system in question.

In this case, we get the following system of equations for the joint:

$$\begin{aligned}
J_{dv} \frac{d\Omega_{dv}}{dt} + \beta_{dv} \Omega_{dv} &= M_{dv} - M_{1M}; \\
J_{1M} \frac{d\Omega_{1M}}{dt} + \beta_{1M} \Omega_{1M} &= M_{1M} - M_M; \\
J_{2M} \frac{d\Omega_{2M}}{dt} + \beta_{2M} \Omega_{2M} &= M_M - M_V; \\
\frac{dM_{1M}}{dt} &= C_{1M} (\Omega_{dv} - \Omega_{1M}) + \beta_{1M} \left(\frac{d\Omega_{dv}}{dt} - \frac{d\Omega_{1M}}{dt} \right); \\
\frac{dM_M}{dt} &= C_M (\Omega_{1M} - \Omega_{2M}) + \beta_M \left(\frac{d\Omega_{1M}}{dt} - \frac{d\Omega_{2M}}{dt} \right),
\end{aligned} \tag{3}$$

where Ω_{M1} is the angular speed of the first half-joint; Ω_{M2} is the angular speed of the second half-joint; C_M is the joint rigidity; β_M is the joint damping factor; M_M is the torque transferred by the joint.

To account for the nonlinear dependence between the joint rigidity and the difference of the turning angles of the first and the second half-joints, we introduce an additional coordinate equal to their difference:

$$\gamma_M = \varphi_{1M} - \varphi_{2M}; \quad \frac{d\gamma_M}{dt} = \Omega_{1M} - \Omega_{2M}, \tag{4}$$

where γ_M is the difference of the generalized coordinates from the two half-joints.

The system of equations that describe the changes in torques can be written down as the following more accessible matrix:

$$\begin{aligned}
\frac{d\Omega_{dv}}{dt} &= \frac{1}{J_{dv}} M_{dv} - \frac{1}{J_{dv}} M_{1M} - \frac{\beta_{dv} \Omega_{dv}}{J_{dv}} \\
\frac{d\Omega_{1M}}{dt} &= \frac{1}{J_{1M}} M_{1M} - \frac{1}{J_{1M}} M_M - \frac{\beta_{1M} \Omega_{1M}}{J_{1M}}
\end{aligned}$$

$$\begin{aligned}
\frac{d\Omega_{2M}}{dt} &= \frac{1}{J_{2M}}M_M - \frac{1}{J_{2M}}M_V - \frac{\beta_{2M}\Omega_{2M}}{J_{2M}} \\
\frac{d\Omega_1}{dt} &= \frac{1}{J_1}M_{2M} - \frac{1}{J_1}M_{12} - \frac{\beta_1 \cdot \Omega_1}{J_1} \\
\frac{d\Omega_2}{dt} &= \frac{1}{i_{12}J_2}M_{12} - \frac{1}{J_2}M_{23} - \frac{\beta_2 \cdot \Omega_2}{J_2} \\
\frac{d\Omega_3}{dt} &= \frac{1}{J_3}M_{23} - \frac{1}{J_3}M_{34} - \frac{\beta_3 \cdot \Omega_3}{J_3} \\
\frac{d\Omega_4}{dt} &= \frac{1}{i_{34}J_4}M_{34} - \frac{1}{J_4}M_{45} - \frac{\beta_4 \cdot \Omega_4}{J_4} \\
\frac{d\Omega_5}{dt} &= \frac{1}{J_5}M_{45} - \frac{1}{J_5}M_{56} - \frac{\beta_5 \cdot \Omega_5}{J_5} \\
\frac{d\Omega_6}{dt} &= \frac{1}{i_{56}J_6}M_{56} - \frac{1}{J_6}M_C - \frac{\beta_6 \cdot \Omega_6}{J_6} \\
\frac{dM_{1M}}{dt} &= \left(C_{1M} - \frac{\beta_{1M}\beta_{dv}}{J_{dv}} \right) \Omega_{dv} - \left(C_{1M} - \frac{\beta_{1M}^2}{J_{1M}} \right) \Omega_{1M} \\
&\quad - \left(\frac{\beta_{1M}}{J_{dv}} + \frac{\beta_{1M}}{J_{1M}} \right) M_{1M} + \frac{\beta_{1M}}{J_{1M}} M_M + \frac{\beta_{1M}}{J_{dv}} M_{dv} \\
\frac{dM_M}{dt} &= \left(C_M - \frac{\beta_{1M}\beta_M}{J_{1M}} \right) \Omega_{1M} - \left(C_{1M} - \frac{\beta_{1M}\beta_M}{J_{2M}} \right) \Omega_{2M} \\
&\quad - \left(\frac{\beta_M}{J_{1M}} + \frac{\beta_M}{J_{2M}} \right) M_M + \frac{\beta_M}{J_{2M}} M_{2M} + \frac{\beta_M}{J_{1M}} M_{1M} \\
\frac{dM_{2M}}{dt} &= \left(C_{2M} - \frac{\beta_{2M}^2}{J_{2M}} \right) \Omega_{2M} - \left(C_{2M} - \frac{\beta_{2M}\beta_1}{J_1} \right) \Omega_1 \\
&\quad - \left(\frac{\beta_{2M}}{J_{2M}} + \frac{\beta_{2M}}{J_1} \right) M_{2M} + \frac{\beta_{2M}}{J_1} M_{12} + \frac{\beta_{2M}}{J_{2M}} M_M \\
\frac{dM_{12}}{dt} &= \left(C_{12} - \frac{\beta_{12}\beta_1}{J_1} \right) \Omega_1 - \left(C_{12} - \frac{\beta_{12}\beta_2}{i_{12}J_2} \right) \Omega_2 \\
&\quad - \left(\frac{\beta_{12}}{J_1} + \frac{\beta_{12}}{i_{12}^2 J_2} \right) M_{12} + \frac{\beta_{12}}{i_{12}J_2} M_{23} + \frac{\beta_{12}}{J_1} M_{2M} \\
\frac{dM_{23}}{dt} &= \left(C_{23} - \frac{\beta_{23}\beta_2}{J_2} \right) \Omega_2 - \left(C_{23} - \frac{\beta_{23}\beta_3}{J_3} \right) \Omega_3 \\
&\quad - \left(\frac{\beta_{23}}{J_2} + \frac{\beta_{23}}{J_3} \right) M_{23} + \frac{\beta_{23}}{J_3} M_{34} + \frac{\beta_{23}}{i_{12}J_1} M_{12} \\
\frac{dM_{34}}{dt} &= \left(C_{34} - \frac{\beta_{34}\beta_3}{J_3} \right) \Omega_3 - \left(C_{34} - \frac{\beta_{34}\beta_4}{i_{34}J_4} \right) \Omega_4
\end{aligned}$$

$$\begin{aligned}
 & - \left(\frac{\beta_{34}}{J_3} + \frac{\beta_{34}}{i_{34}^2 J_4} \right) M_{34} + \frac{\beta_{34}}{i_{34} J_4} M_{45} + \frac{\beta_{34}}{J_3} M_{23} \\
 \frac{dM_{45}}{dt} &= \left(C_{45} - \frac{\beta_{45} \beta_4}{J_4} \right) \Omega_4 - \left(C_{45} - \frac{\beta_{45} \beta_5}{J_5} \right) \Omega_5 \\
 & - \left(\frac{\beta_{45}}{J_4} + \frac{\beta_{45}}{J_5} \right) M_{45} + \frac{\beta_{45}}{J_5} M_{56} + \frac{\beta_{45}}{i_{34} J_4} M_{34} \\
 \frac{dM_{56}}{dt} &= \left(C_{56} - \frac{\beta_{56} \beta_5}{J_5} \right) \Omega_5 - \left(C_{56} - \frac{\beta_{56} \beta_6}{i_{56} J_6} \right) \Omega_6 \\
 & - \left(\frac{\beta_{56}}{J_5} + \frac{\beta_{56}}{i_{56}^2 J_6} \right) M_{56} + \frac{\beta_{56}}{i_{56} J_6} M_C + \frac{\beta_{56}}{J_5} M_{45}
 \end{aligned} \tag{5}$$

The equation system obtained has the order of $n = 25$. Besides, the proper operator for MATLAB modeling can be expressed as a block matrix. The vector of the right-hand part of the differential equation system can also be conveniently expressed as a block vector that we do not include in this article for the sake of brevity.

3 System Component Movement with an Allowance for the Clearance

In this case, it is necessary to speak about movement with and without the clearance. If the clearance is “set,” the system dynamics is defined by the values of rigidity and damping ratios reviewed above.

To construct the vector of the right-hand side of the mechanical component of the drive when reviewing forced vibration of mechanisms, we need to account for the clearances that inevitably appear in kinematic pairs and rigid connections. For mechanisms employing gear drives, angular clearance is used [5]:

- \bar{c}_τ is the average tangential clearance value in the gears;
- ε_τ is the maximum deviation from the average tangential clearance.

These values for gear sets are normally calculated using empirical formulae:

$$\bar{c}_\tau = 0.68(\Delta_M h_1 + \Delta_M h_2) + 0.34(\delta h_1 + \delta h_2), \tag{6}$$

$$\varepsilon_\tau = 0.1(\delta h_1 + \delta h_2) + 0.4 \cdot \delta A + 0.13(E_{01} + E_{02}), \tag{7}$$

where $\Delta_M h_1, \Delta_M h_2$ is the least profile shift; $\delta h_1, \delta h_2$ is the profile shift tolerance; δA is the axle base tolerance; E_{01}, E_{02} is the radial motion variation for the gear rim.

Thus, the clearance in the gear pair can be expressed as follows:

$$\Delta\varphi = \bar{c}_\tau \pm \varepsilon_\tau. \tag{8}$$

All of the values listed are subject to GOST standards for gearwheel production [2–5]. Clearances impact the collision of mechanism components, which results in dynamic loads. The appearance of this effect is not subject to any particular behavior. Thus, if the instantaneous torque is below the average for the specified component, the kinematic train is not broken [5].

When modeling the reduction gear in question, we shall only focus on the impacts of clearances in great sets. The dynamic characteristic of the nonlinear component can be expressed as follows [3]:

$$\rho_k \cdot \gamma_{k,k+1} = a_k, \tag{9}$$

where $\gamma_{k,k+1} = \varphi_{k+1} - \varphi_k$ is a generalized coordinate; a_k is the piecewise-constant function; ρ_k is the ratio.

When the components do not interact, i.e., when moving within the clearance (open-clearance movement stops when the difference between the turning angles of the first and the second mass equals half of the clearance). In this case, $\rho_k = 0$, otherwise $\rho_k = 1$. Numerous research works [2–4] confirm that the strikes during the clearance movement are non-elastic and that elastic forces usually exceed the dissipation ones by large.

If the clearance is open, the movement stops when the following condition is satisfied:

$$\varphi_k - \varphi_{k+1} = \frac{\delta}{2} = \frac{\Delta\varphi_{k,k+1}}{2}. \tag{10}$$

In this case, the dependence between the transferred torque and turning angle differences for two linked inertia mass looks as follows:

$$\begin{cases} M_{k,k+1} = C_{k,k+1} \cdot \left(\varphi_k - \varphi_{k+1} \mp \frac{\Delta\varphi_{k,k+1}}{2} \right), & |\varphi_k - \varphi_{k+1}| > \frac{\Delta\varphi_{k,k+1}}{2} \\ M_{k,k+1} = 0, & |\varphi_k - \varphi_{k+1}| < \frac{\Delta\varphi_{k,k+1}}{2}. \end{cases} \tag{11}$$

The structure chart for this phenomenon can be expressed as follows (Fig. 3).

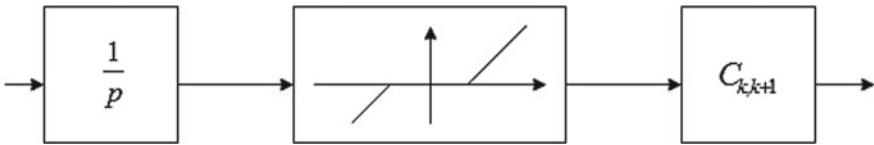


Fig. 3 Structure chart for movement model with the clearance

The final right-hand vector of the equation system analyzed can be expressed as a block one:

$$P = \begin{bmatrix} P1 \\ P2 \\ P3 \end{bmatrix}. \tag{12}$$

4 Conclusions

The obtained mathematical model for the forced movement of the system is required for the study of the excitable vibration field. To this end, the system of equations was formed, respectively, to the rotation torques appearing at the startup and during the basic operation to assess the vibration capacity.

The gear set forces were determined based on the obtained torque expressions while taking into account the mentioned features of drive kinematics.

References

1. Veits VL (1969) Machine assembly dynamics. Mashinostroyeniye, Moscow, p 368
2. Kreynina GV (ed) (1988) Machine dynamics and management. Mashinostroyeniye, Moscow, p 239
3. Rivin EI (1966) Machine drive dynamics. Mashinostroyeniye, Moscow
4. Veits VL, Kolovsky MZ, Kochura AE (1984) The dynamics of controlled machine assemblies. Nauka, Moscow, p 352
5. Meshcheryakov VN, Usov SV (2010) The mathematical characterization of the group electric drive for a thin steel strip. Electr Units Manage Syst 1
6. Ivovich VA (1969) Transfer matrices in elastic system dynamics. Mashinostroyeniye, Moscow
7. Kudinov VA (1968) Machine dynamics. Mashinostroyeniye, Moscow
8. Levin AI (1978) Mathematic modeling in machine research and development. Mashinostroyeniye, Moscow
9. Miroshnichenko VG (1996) Some problems of the system theory. RGASKhM, Rostov-on-Don
10. Mikhailov OP (1989) The dynamics of electromechanical drive in metal-cutting machines. Mashinostroyeniye, Moscow
11. Mikhailov OP (1990) Automated electric drive for machines and robots. Mashinostroyeniye, Moscow
12. Murashkin LS, Murashkin SL (1977) Applied non-linear machine mechanics. Mashinostroyeniye, Leningrad
13. Orlikov ML (1980) Machine dynamics. Vysshaya shkola, Kyiv
14. Popov VI, Loktev VI (1975) Machine dynamics. Tekhnika, Kyiv
15. Svetlitsky VA (1976) Accidental vibrations in mechanical systems. Mashinostroyeniye, Moscow
16. Sigorsky VP (1975) The mathematical tools of an engineer. Tekhnika, Kyiv
17. Andreyenko SN, Voroshilov MS, Petrov BA (1975) Design of manipulator drives. Mechanical engineering, Leningrad, p 312
18. Butenin NV, Neymark YI, Fufayev NA (1976) Introduction to the theory of non-linear vibrations. Nauka, Moscow
19. Veits VL, Kochura AE (1979) Vibration systems in machine assemblies. Leningrad University Press, Leningrad



Study of Asphalt Milling Workflow Dynamics

D. V. Furmanov^(✉), N. E. Lysakov, and L. M. Shamahov

Yaroslavl State Technical University, 88, Moskovsky prospect, Yaroslavl 150023, Russia

Abstract. During milling asphalt, there are inevitable pulsating loads that impact the cutting element of the working unit, the nature and magnitude of which depends on a number of factors. This, in turn, causes shock loads on road machine drive elements and premature failure of drive units and welded joints of a drum. The paper presents the main directions in the research of asphalt concrete milling processes. In addition, it contains the results of experimental studies of asphalt concrete cutting with a single cutting element. The paper also includes a description of the experiment. It contains oscillograms of cutting resistance forces obtained while cutting asphalt concrete of grades SMA-16, SMA-20, A1, B2, B3 and MZP. It also presents calculations of dynamic coefficients and amplitude-frequency parameters of cutting force impulses. It is noted that the pulsation amplitudes of cutting resistance forces greatly exceed the averages for cutting resistance forces. Based on the study results, the paper offers substantial solutions aimed to increase the reliability of elements of a working unit and a drive of milling machines.

Keywords: Asphalt concrete · Asphalt concrete milling · Cutting resistance forces · Cutting element · Dynamic factor · Road machine

1 Introduction

Asphalt milling is a highly important and expensive technological operation [1]. As a dispersion-filled composite [2, 3], asphalt concrete exhibits a set of complex strength properties both during operation and destruction by road milling machines [4, 5]. This, among other things, is the reason why milling is so energy-intensive. In order to ensure the required productivity, it is necessary to use machines equipped with powerful internal combustion engines that consume a sufficiently large amount of fuel. Obviously, these machines not only require large initial and operating costs, but also cause environmental pollution.

Solving these problems requires improving the design of the working units installed on milling machines, but this is impossible without a thorough study of the workflow.

There are several ways to improve the design of milling machines. One of them is identifying the cutting resistance forces for different cutting element designs, material types and feed values. In practice, these loads are determined using experimental [6, 7] and numerical methods [8, 9]. Based on some machine models with a way to determine the forces of cutting resistance, researchers calculate the parameters of the machine as a whole [10], as well as provide a rationale for the parameters of the control systems of these machines [11, 12].

A separate group of works ensures the required quality of asphalt concrete surface after milling [13], as well as assesses the strength of asphalt concrete located below the milling surface [14]. Since the milled asphalt concrete is frequently reused, certain researchers study the milling modes aimed at preserving the integral structure of the filler [15]. Another group of papers is devoted to the study of abrasive wear of cutting tools by material [16].

Thus, given the continuing interest of researchers, cold milling is still far from perfect despite more than half a century of history of asphalt milling machines.

2 Study Problems

Almost all of the problems discussed above cannot be solved without understanding the contact interaction between the material and the cutting element. To design a full scheme of asphalt concrete cutting, it is necessary to know derivative laws of cutting resistance forces, energy costs imposed on the cutting element, as well as average and maximum forces of cutting resistance, frequency of pulsations of these forces and cutting force direction.

These questions can be partially researched by using a pendulum stand. Such structures are successfully used to determine the brittle fracture energy when testing metals [17] and polymers [18], to determine the energy intensity of the cutting natural materials—wood waste and peat [19]. These structures have also been successfully used to determine the energy intensity of cutting with a single cutting element of a milling machine [20].

This method can be used to determine the energy intensity of cutting and the average tangential component of the cutting force. Studying the samples on the pendulum stand makes it possible to determine the energy in the process and, consequently, the required drive power and the average loads on the elements of the drive and the drum. Another indisputable advantage of such equipment is that we can simulate the work of the cutting element on the cutter drum as accurately as possible, achieving the required cutting speeds using real (not scaled) cutting elements.

However, this method does not allow estimating the cutting resistance force impulses, the maximum cutting resistance forces and the direction of the cutting resistance force on the cutting element.

Since the vast majority of milling drum designs are welded, determining the pulse frequency and maximum cutting force during interaction of material with the cutting element is a particularly important task in order to ensure guaranteed durability. The main objective of this study is to determine these patterns.

3 Study Methods

Experimental problems of asphalt concrete cutting dynamics cannot be solved without data obtained with maximum similarity of the experimental conditions to the real object. To do this, we have developed an experimental bench with a mechanical drive (Fig. 1). The bench is a table that can be moved by a motor with a screw gear 1 relative to the base. Plate 3 is installed on the table. It has a horizontal degree of freedom and a sample 4 of a

material fixed on it. On the other side, the plate is held by force sensor 8. When moving the table, a stationary cutter 7 interacts with the material and transmits its reaction to the force sensor 5 through the parallelogram suspension 6. Thus, the horizontal component of the cutting resistance force is monitored by sensor 8, and the vertical component is monitored by sensor 6. These strain gauges are powered from strain gauge recorder 9; the signal from the sensors is also transmitted to it. The processed digital signal is transmitted in real time to a personal computer and saved on the device.

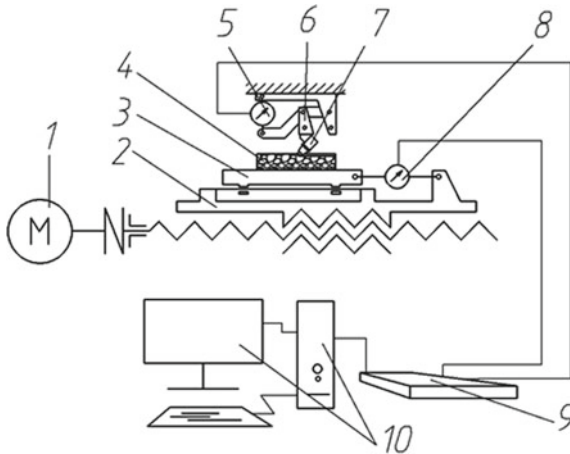


Fig. 1 Schematics of the bench for determining the forces of resistance to cutting asphalt concrete with a single cutting element of a road milling machine

A universal vertical milling machine 6R12P is the base of the bench (Fig. 2). Under this solution, the system is highly rigid, and the feed rate and thickness of the cutting chips can be adjusted precisely. The specified method makes it possible to determine the specifics of cutting resistance force pulsations, vertical and horizontal components of cutting force.

Sensors of vertical and horizontal components of cutting resistance forces were calibrated directly on the stand with an electronic dynamometer.

As a result of the study, we have obtained the oscillograms of the components of the cutting resistance forces (Fig. 3) for different grades of asphalt concrete.

The samples selected corresponded to the most commonly used grades of asphalt concrete in the road construction in the central part of Russia. Grades A1, B2, B3, MZP [21], SMA-20 [22] and SMA-16 [23] were chosen as samples. The experiment was conducted at an asphalt concrete temperature of 22 °C.

The obtained oscillograms undergo filtering, and then we select the active areas that characterize the cutting process of asphalt concrete. The selected areas are then processed (Fig. 4).

There are several notable areas. Area 1 corresponds to the zero cutting resistance force component; Area 2 represents the voltage spike in the force sensor circuit resulting from large starting currents in the table feed motor circuit. Area 3 corresponds to the steady



Fig. 2 Experimental bench to study asphalt concrete cutting with a single cutting element of a road milling machine

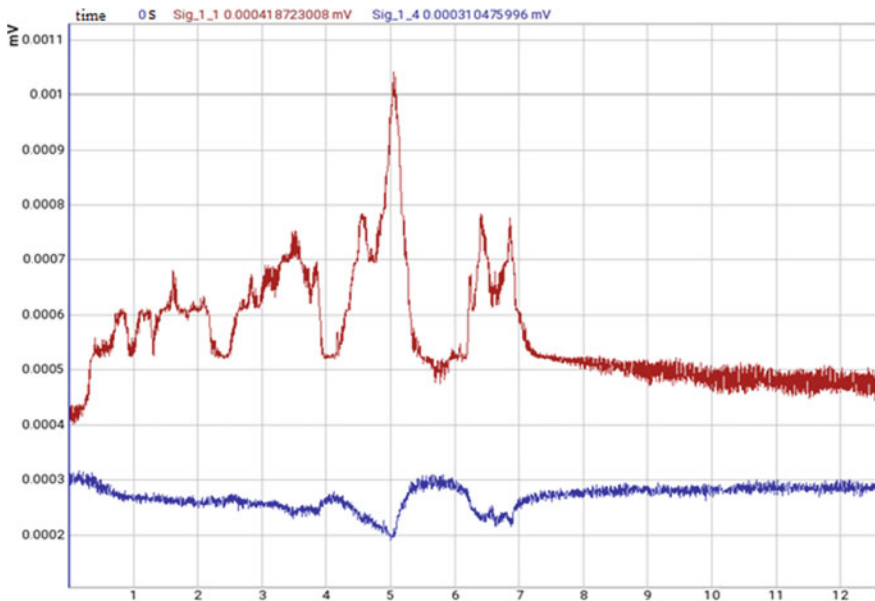


Fig. 3 Oscillogram of horizontal and vertical components of cutting resistance forces of asphalt concrete grade B3 [21]

motion of the table during asphalt cutting. There are several maximum components of cutting resistance that form Peaks 4 considered in this area. Area 5 is caused by the motor turning off and a voltage spike, which happens similarly to Area 2 of the oscillogram.

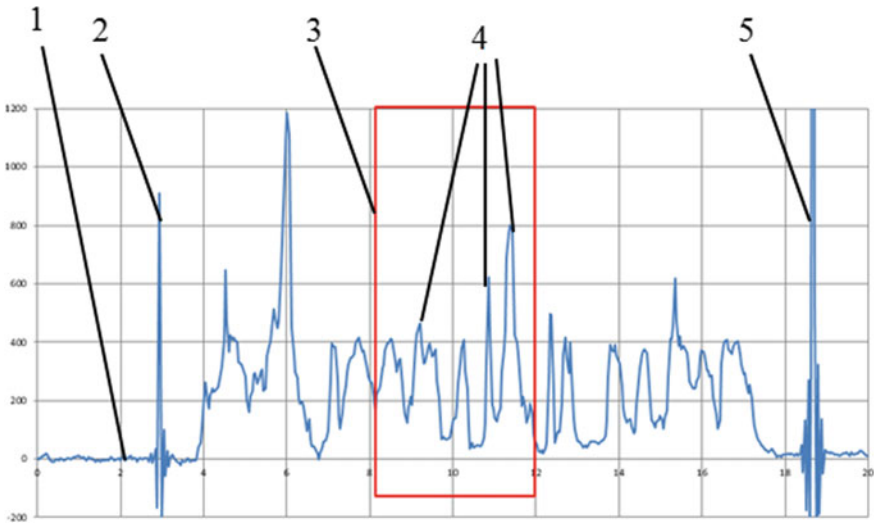


Fig. 4 Notable areas of the oscillogram analysed after the experiment

As a result of data processing, it is necessary to determine the dynamic factor which, in turn, determines calculated loads on the elements of milling drum and drive for strength calculation.

To do this, the dynamic factors K_{di} are specified for the observed peak load values:

$$K_{di} = F_{\max i} / F \tag{1}$$

where $F_{\max i}$ —maximum observed cutting resistance force, F —average cutting resistance force within the monitored oscillogram area.

The obtained dynamic factors are used to calculate its average K_d and standard deviation in a set sample $\sigma(K_d)$.

The maximum dynamic factor should be considered in the design of new machines. It is determined by this dependence:

$$K_{d \max} = K_d + 3s(K_d). \tag{2}$$

The calculated dynamic factor relies on the assumption that it is highly improbable for the dynamic factor to exceed its mean value by more than 300% of the standard deviation [24].

4 Study Results

The cross-plot of cutting resistance of asphalt concrete and thickness of a cutting chip presented in Fig. 5 shows an average horizontal component of cutting resistance force, as well as its maximum and an average of five largest pulses.

At the same time, it was not possible to establish any sufficiently reliable correlation of the dynamic coefficient to the thickness of the cutting chip (Fig. 6); although it can be

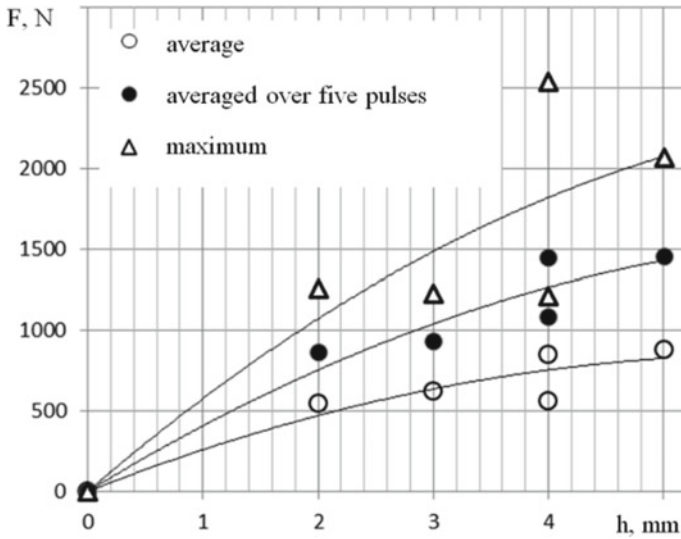


Fig. 5 Dependences of the total average, maximum and an average over five pulses of the components of the cutting resistance force obtained when testing a B3 grade asphalt concrete sample on the test bench

seen that for granular asphalt concretes with higher stone fraction strength, this value is higher. Obviously, this figure is a random variable that depends on the structure of the asphalt concrete.

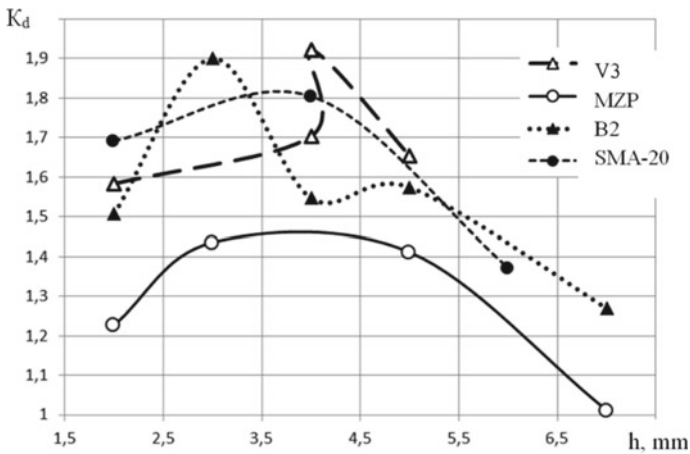


Fig. 6 Dynamic factors obtained at different cutting depths

In order to use the dynamic factors in the practical calculations of the equipment, they must be separated into two types. Considering the distribution density of any random

dynamic factor obtained during the analysis of the experimental results, we can distinguish two important values—the first value K_d corresponds to the mean probable excess of cutting resistance forces. The second value K_{dmax} corresponds to the maximum value of cutting resistance forces, which can represent dangerous loads. The calculated values of K_d and K_{dmax} are presented in Table 1 for all the asphalt concretes listed above.

Table 1 Results of statistical analysis and calculation of dynamic factors of cutting resistance forces for asphalt concrete of some grades

Asphalt concrete grade	Results of statistical processing		
	Average dynamic factor	Standard deviation	Maximum dynamic factor
A1	1.445	0.260	2.228
B2	1.567	0.372	2.674
C3	1.673	0.478	3.106
MZP	1.340	0.505	2.854
SMA-20	1.622	0.655	3.587
SMA-16	1.542	0.572	3.258

The obtained factors may be recommended for strength calculation of milling drum elements. Since a road milling machine can work with various grades of asphalt concrete, we should assume the largest values of the dynamic factors.

5 Conclusion

Asphalt concrete is a complex composite material, and its disposal is accompanied by extremely high operating costs. Therefore, even small reduction in milling energy consumption leads to an increased equipment efficiency. When designing new machines, however, it is impossible to avoid the dynamic loads that inevitably occur on the cutting elements of the milling drum.

It has been experimentally established that to design new equipment, the dynamic factors should be 2.2–3.6 approximately depending on the type and grade of asphalt concrete. Despite these recommendations, the choice of safety margins in equipment design is left to the engineer, keeping in mind possible new materials and cutting elements over the lifetime of the machine.

References

1. Wisdom B (2013) The power of milling. Better Roads. Retrieved 29 Nov 2013
2. Bazhenov SL (2014) *Mekhanika i tekhnologiya kompozitsionnykh materialov: Nauchnoe izdanie* (Mechanics and technology of composite materials: scientific edition). Publishing House Intellect, Dolgoprudny, p 328

3. Matthew FL, Rawlings RD (2004) Composite materials: engineering and science. Technosphere, Moscow, p 408
4. Gezenzvey LB (1976) Dorozhnyi asfaltobeton. (Road asphalt). Transport publ. house, Moscow, p 336
5. Rybyeve IA (1978) Stroitelnye materiali na osnove vyazhushchih veschestv (Construction materials based on binders). Vysshaya Shkola, Moscow, p 309
6. Kulepov VF (1983) Eksperimentalnoe issledovanie nagruzok na diskofrezernom rabochem organe pri vskrytii asfaltobetonnyh pokrytii (Experimental study of loads on disc cutting working member during the opening of asphalt concrete pavements). In: Primenenie EVM v proektirovanii i ispytanii mashin i oborudovaniya: reports proceedings. Gorky regional scientific and technical conference, Gorky, p 27
7. Baratashvili MP Opredelenie vliyayushih faktorov na rezhimi raboti mashini i ih znachenie dlya razrusheniya poverhnostnih sloev asfaltobetonnyh pokrytii (Determination of factors influencing the operation modes of a machine and their importance for destruction of the surface asphalt layers). Scientific digital archive. <http://econf.rae.ru/article/6606>. Access date 11 Feb 2019 (in Russian)
8. Zhou LQ (2010) Computer simulation for the orthogonal milling process of asphalt concrete. Adv Mater Res 139–141:1014–1017
9. Sherstnev NS, Ignatov SD (2014) Raschet moshchnosti silovoi ustanovki dorozhnoi frezy (Calculation of the power unit of a road milling machine). Razvitiye dorozhno-transportnogo i stroitel'nogo kompleksov i osvoenie strategicheskoi vazhnykh territorii Sibiri i Arktiki: vklad nauki: International conference proceedings (in Russian), SibADI, Omsk, Book 2, p 79–81
10. Wong JY (2001) Theory of ground vehicles. Wiley, New York, pp 301–309
11. (1984) Povyshenie effektivnosti rabochikh organov i agregatov dorozhno-stroitel'nykh mashin (Improvement of efficiency of working bodies and units of road-building machines: MADI works compilation). Moscow, p 126
12. Kochetkov AV, Yankovskii LV, Volkov GN, Kokodeeva NE, Zhunusov DI (2013) Upravlenie dorozhnoi frezoi pri remonte kolei (Control of a road milling machine during gauge repair). Stroitel'nye i dorozhnye mashiny 3:39–41 (in Russian)
13. Gao L, de Fortier Smit A, Prozzi JA, Buddhavarapu P, Murphy M, Song L (2015) Milled pavement texturing to optimize skid improvements. Constr Build Mater 101(1):602–610. <https://doi.org/10.1016/j.conbuildmat.2015.10.077>
14. Diouri K, Bousselham R, De A, Hera A, El-Korchi T, Mallick RB (2020) A study on the effect of milling on stress distributions in asphalt pavements. In: Raab C (ed) Proceedings of the 9th international conference on maintenance and rehabilitation of pavements—Mairepav 9. Lecture notes in civil engineering, vol 76. Springer, Cham. https://doi.org/10.1007/978-3-030-48679-2_89
15. Jianmin W, Li D, Zhu B, Chunsheng W (2018) Milling process simulation of old asphalt mixture by discrete element. Constr Build Mater 186:996–1004. <https://doi.org/10.1016/j.conbuildmat.2018.08.015>
16. Bibikov VN, Tarbaev NN, Kulepov VF (1975) Vliyanie mekhanicheskikh svoystv asfaltovogo betona na iznos rezhushchego instrumenta pri ego frezerovanii (The impact of mechanical properties of asphalt concrete on the wear of the cutting tool during milling) Works of Gorky Polytechnic Institute. Gorky 31(8):11–14
17. GOST 4647–2015 (2017) Plastics. Method for determination of Charpy impact strength. Standardinform, Moscow. Active since 20 Nov 2015
18. GOST 9454–78 (1994) Metals. Method for testing the impact strength at the low, room and high temperature. Standards Publ. House, Moscow. Active since 17 April 78
19. Samsonov LN (1985) Frezerovaniye torfjanoi zalezhi (Milling peat deposits). Nedra, Moscow, p 211

20. Furmanov DV, Chizhov VS, Lysakov NE (2020) Eksperimental'noe opredelenie sil soprotivleniya rezaniyu pri razrushenii asfal'tobetona edinichnym rezhushchim elementom (Experimental determination of cutting resistance forces at destruction of asphalt concrete by a single cutting element). *SibADI Bull* 17(2):196–207 (in Russian)
21. GOST 9128–2009 (2010) Asphaltic concrete mixtures for roads and aerodromes and asphaltic concrete. Specifications. Standartinform, Moscow. Introduced from 1 Jan 2009
22. GOST 31015–2002 (2003) Bituminous stone mastic mixtures and stone mastic asphalt. Specifications. Gosstroj Rossii, Tsentri Proektnoi Produktsii, Moscow. Introduced 01 May 2003
23. GOST 58406.2–2020 (2020) Automobile roads of general use. Hot asphalt mixtures and asphalt concrete. Technical conditions. Standartinform, Moscow, p 53
24. Vlasov KP (2013) *Metody issledovaniya i organizatsiya eksperimentov* (Research methods and organization of experiments). Gumanitarnii Tsentri Publishing House, Kharkov, p 412 (in Russian)



Environmental Properties Evaluation of Spark-Ignition Engines Running on Water/Fuel Mix

S. Plotnikov¹, Sh. Buzikov¹ (✉), and A. Birukov²

¹ Vyatka State University, 36, Moskovskaya str, Kirov 610000, Russia

² Vologda State Dairy Farming Academy by N.V. Vereshchagin, 2, Schmidt str., Vologda region, Vologda city district, Molochnoye village 160555, Russia

Abstract. The relevance of the given study is based upon the need to evaluate the feasibility of water/fuel mixes (WFM) in electronically controlled spark-ignition engines. The objective of the study is to evaluate the VAZ-21114 engine's environmental properties when run on marketable gasoline as well as when run on WFM with 10, 15, and 20% of water content. The study resulted in the evaluation of the environmental properties of the VAZ-21114 electronically controlled spark-ignition engine when run on marketable gasoline as well as when run on WFM with 10, 15, and 20% of water content. The analysis demonstrated general drop in the toxicity of the exhaust gases (EG), once the engine was tested in full-load mode and two modes under load. The maximum drop in the concentration of toxic components in the EG was registered for: nitrogen oxide (NO_x) from 119 to 38 ppm at 20% water content in the WFM at RPM $n = 2000 \text{ min}^{-1}$, and at $n = 4000 \text{ min}^{-1}$ —from 142 to 113 ppm, respectively; carbon monoxide (CO) at 10% water content in the WFM at $n = 2000 \text{ min}^{-1}$ —from 3.6 to 1.7%, at $n = 4000 \text{ min}^{-1}$ —from 8.5 to 6.0%; unburnt hydrocarbons (CH) at 10% water content in the WFM at $n = 2000 \text{ min}^{-1}$ —from 221 to 181 ppm, at $n = 4000 \text{ min}^{-1}$ —from 214 to 173 ppm. The obtained results proved the feasibility of water/fuel mixes (WFM) in electronically controlled spark-ignition engines in improving the aforesaid engines environmental characteristics.

Keywords: Water/fuel mix · Gasoline · Exhaust gases · Engine · Bench test · Environmental characteristics

1 Introduction

As of today, there is no universal way to simultaneously improve both the performance and ecological characteristics of internal combustion engines. It is only logical to solve the problem of improving the engines' performance along with the issue of scarcity and finite nature of conventional fuel sources. The application of pure alternative fuels poses quite a number of challenges and problems, such as deterioration of engines' environmental, performance, and efficient properties. Other points to consider are significant complication of the engines' designs and the difference of physical and chemical

properties of alternative fuels. Besides, the existing fuel-distributing market is not infra-structurally ready to switch to a new kind of fuel. Thus, the use of fuel mixes containing not only conventional fuel components but also some additives of not petroleum origin seems to be feasible.

Such fuel mixes can be used as alternative fuel in both diesel and spark-ignition internal combustion engines. The research into the use of water/fuel mixes (emulsions) (WFM) is two-pronged: (1) induction of water into the combustion chamber immediately prior to the fuel combustion; (2) preparation of a ready water/fuel emulsion with an optimal water-to-fuel ratio [1–26]. Emulsions are kinetically stabilized mixtures of two or more immiscible liquids. These mixtures are nothing else but thermodynamically unstable systems possessing increased internal energy [2]. Surfactants or surface-active agents (SAA) can be effective stabilizers [3]. Mechanical mixing is the most common way to make emulsions [4].

The use of water/fuel emulsions in internal combustion engines results in the reduction of nitrogen oxides (NO_x) total emission. This phenomenon is easily explained by the fact that water has higher both the specific heat capacity and the latent heat of vaporization of 2256 kJ/kg, which approximately six times that of gasoline at regular air pressure and temperature [5]. The cooling effect caused by the presence of water in the combustion chamber improves both the fuel's spraying and combustion, which, in its turn, reduces the combustion delay and affects soot-generating chemical reactions [6–10]. Addition of water-to-fuel can reduce the combustion peak temperature, which, evidently, reduces the amount of heat-generated NO_x [5, 11]. The use of emulsions to reduce the NO_x emission has been studied for quite some time. There are three directions in the research [12, 13] into the reduction of NO_x emission: exhaust gases recirculation, water induction, and WFM use. Multi-zone simulation modeling has resulted in the conclusion that the use of emulsions is optimal in order to minimize fuel consumption and the exhaust gases toxicity.

At present, the use of WFM seems to be the most efficient way to improve environmental properties of diesel engines [5, 12, 14–18]. The use of water/fuel emulsion yields good results with diesel engines, in whose case the issue of good fuel spraying is of crucial importance [15]. The use of emulsions containing various additives improving their properties is a simple, cheap, and easily available method. This method makes it possible to cut diesel fuel consumption without any significant changes in the engine's design.

At 18–20% water content in the WFM, the tests [15] demonstrated no loss of pressure in the diesel engine's cylinders [19], while the efficiency of combustion grew noticeably. At the same time, there was recorded a decrease in the carbon depositing rate on the engine's parts. The tests also showed a drop in the heat flow, lower temperature, and heat load on the parts of the combustion chamber [20], as well as less soot and NO_x in the exhaust gases.

Tests run on a single-cylinder diesel engine at RPM $n = 1200\text{--}3300 \text{ min}^{-1}$ on 5, 10, 15, and 20% water content WFM demonstrated that the higher the WFM water content was the higher the combustion efficiency, thermal efficiency, torque, and the engine's power output were, while the exhaust gas temperature and fuel consumption dropped [21].

The use of WFM in automobile diesel engines without any significant adjustments or modifications to the engine's design resulted in the decrease in the exhaust gases toxicity, averaging 32% [6]: carbon (soot) by 50%, NO_x content by 40%, and three times less solid particles as compared to the combustion of pure diesel fuel [7].

Based on the comparative analysis of the toxicity of exhaust gases in a number of water induction tests [22], it became possible to conclude that the use of water/fuel emulsions led to the reduction of NO_x and carbon concentration in the EG without any adverse effects upon the engine's operation. The lowest concentration of NO_x and C was reached at 40% water content in the total volume of diesel fuel [23–25].

Addition of rapeseed-oil methyl ester (20%) and water (up to 2.5%) to diesel fuel was not reported to worsen the fuel's physical and chemical properties, while lowering the toxicity of exhaust gases by up to 60% [14, 26].

The after-test analysis of water/gasoline mix, either as liquid or vapor, induction proved general lowering of combustion rate, shortening of the ignition delay period and certain changes to the duration of combustion phases [24–26].

A 125 cc 4-stroke direct-injection electronically controlled spark-ignition engine running at $n = 2000\text{--}7000 \text{ min}^{-1}$ RPM range (idling to fully open throttle) demonstrated decrease in carbon monoxide (CO) and total nitrogen oxides (NO_x) values, once the water percentage in the emulsion was raised [13, 26]. The engine was fed 5, 10, and 15% water content WFM. However, the volume of unburnt hydrocarbons (CH) rose proportionally to the amount of added water. The reason for that phenomenon might be significant emulsion-induced cooling of the combustion chamber [17, 26]. Certain increase in torque and decrease in fuel consumption was observed at 5 and 10% water content in the water/fuel emulsion. However, at 15% water content in the emulsion, we registered some drop in torque, and increase in both the fuel consumption and the exhaust temperature due to slower combustion process [5].

Tests of 5, 10, and 15% water content water/gasoline emulsion in a 376 cc single-cylinder four-stroke spark-ignition engine demonstrated gradual decrease in CO, NO_x, and CH proportionally to the increase in water content in the fuel. When fed 5–15% water content emulsion, the engine's power rose by 3.8–14% [25, 26].

Tests have demonstrated that feeding WFM to electronically controlled spark-ignition engines is currently quite a promising venue.

2 Research Objectives

The objective of the study is quantitative evaluation of the VAZ-21114 engine's environmental properties when run on gasoline as well as on 10, 15, and 20% of water content WFM.

3 Materials and Methods

The study's subject was the VAZ-21114 gasoline four-stroke multi-point fuel injection spark-ignition engine. The engine was fitted with WFM feed system. The test bench included the KI-2139 electric-brake test bench, balance-beam pendulum tester, the VAZ-21114 modernized-fuel-feed spark-ignition engine, and various sensing equipment.

A closed-circuit forced-circulation cooling system was used to keep the cooling liquid temperature within the required temperature range (93...95 °C). No changes were introduced into the engine's lubricating system. An MT-type A-class 1.0 MPa-upper limit pressure gauge was used to monitor the in-system oil pressure.

In Fig. 1, one can see the diagram and the general view of the test bench. The engine test bench includes: fuel tank 1 (contains regular fuel), water tank 2, fuel pump 3 (feeds the fuel to the internal combustion engine), graduated tank 4 (measures the amount of added water), filters 5, 6 (filter solids out of water and fuel), fuel pressure control 7, mixer 8 (in it water and fuel are mixed), scales 9 (measures fuel consumption), gasoline tank 10 (flushes and cleans the fuel-feed system), loading brake 11 (brakes the engine), engine control unit 12, computer 13 (the installed Electronic Engine Management System (EEMS) software monitors and controls the tested parameters, AVTOTEST-02.03 multi-component gas analyzer 14, exhaust gas temperature sensor (EGTS) 15, UKT-38SchCh EGTS gauge 16.

The engine was tested in the full-load mode and two modes under load (at $n = 2000 \text{ min}^{-1}$ and $n = 3000 \text{ min}^{-1}$). The effect of the WFM composition on the engine's environmental characteristics was evaluated in the study.

The following parameters were measured: the RPM, the torque, the brake horsepower, specific and hourly fuel and water consumption, hourly air consumption. The EG was tested for carbon monoxide, unburnt hydrocarbons and aggregate amount of nitrogen oxides.

The J5 On-line Tuner software suite, installed onto the PC connected to the diagnostic circuit of the electronic engine management system, monitored the RPMs, mass air consumption, coolant temperature, and the throttle position. Water consumption was evaluated through the volumetric technique. The AVTOTEST-02.03 multi-component gas analyzer was used to measure the concentrations of carbon monoxide, unburnt hydrocarbons, and aggregate amount of nitrogen oxides. The 3NF/F nitric oxide CITIcel sensor was used to quantify aggregate nitric oxides amounts.

During the tests, the exhaust manifold temperature was measured. To do so, the DTPK 135-0314.250 thermocouple combined with the UKT 38-Sch4-TP sensor was used. Based on the obtained results, a comparative analysis was run to establish the correlation between the amounts of carbon monoxide CO (%), unburnt hydrocarbons CH (ppm), nitric oxides NO_x (ppm) in the exhaust gas, and the temperature of the exhaust gas itself on the WFM supply parameters under various loads and RPM operating modes.

During the tests, there was continuous recording of the monitored parameters to ensure high quality of obtained information. The values of error limit at a single measurement and the greatest possible statistical error of the arithmetic mean deviation at multiple measurements were calculated based on well-known techniques.

4 Results and Discussion

The study resulted in the authors' establishing correlation between the concentrations of various toxic components in the engine's exhaust and the fuel type: conventional gasoline of WFM. The tested engine was an electronically controlled spark-ignition one run in full-load mode or under two different loads at RPM $n = 2000 \text{ min}^{-1}$ and $n = 3000 \text{ min}^{-1}$.

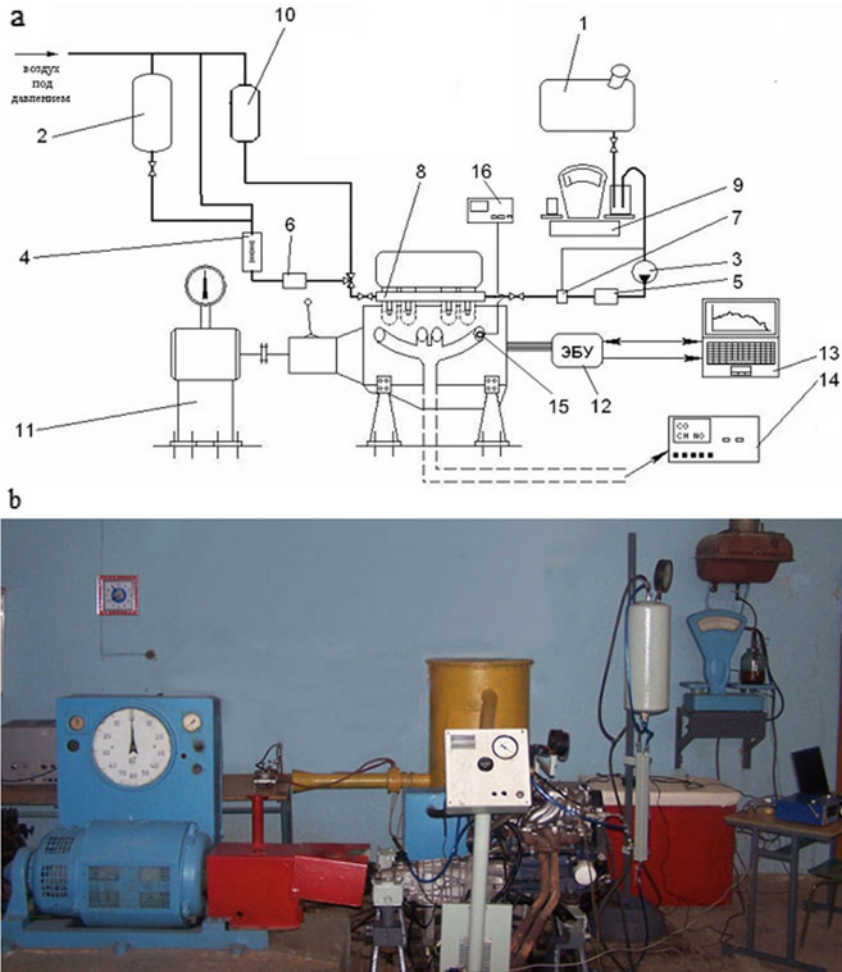


Fig. 1 The test bench diagram (a) and general view (b): 1—fuel tank; 2—water tank; 3—pump; 4—graduated tank; 5, 6—filters; 7—pressure control; 8—mixer; 9—scales; 10—cleaning gasoline tank; 11—loading brake; 12—engine control unit; 13—real-time electronic engine management system; 14—AVTOTEST-02.03 multi-component gas analyzer; 15—exhaust gas temperature sensor (EGTS); 16—UKT-38SchCh EGTS gauge

Figure 2 demonstrates the variations in the concentration of toxic EG components, when the engine is run in full-load mode. Analysis of the obtained correlations demonstrated a significant drop in the quantities of toxic components in the exhaust gases. The drop in NO_x concentration in the EG was registered throughout the complete RPM range. The lowest NO_x emission was observed at 20% water content of the total fuel amount at $\text{RPM } n = 2000 \text{ min}^{-1}$ (from 119 to 38 ppm). At $\text{RPM } n = 4000 \text{ min}^{-1}$ and 20% water content WFM, the drop in the NO_x concentration was less pronounced—from 142 to 113 ppm, while for the 15% water content WFM it went down from 142 to 108 ppm.

With the increase in water content in the WFM, the lessening of NO_x concentration in the EG was registered throughout the entire range. That was due to the decrease in the work cycle temperature because of the cooling effect produced by the water contained in the WFM charge [5, 6].

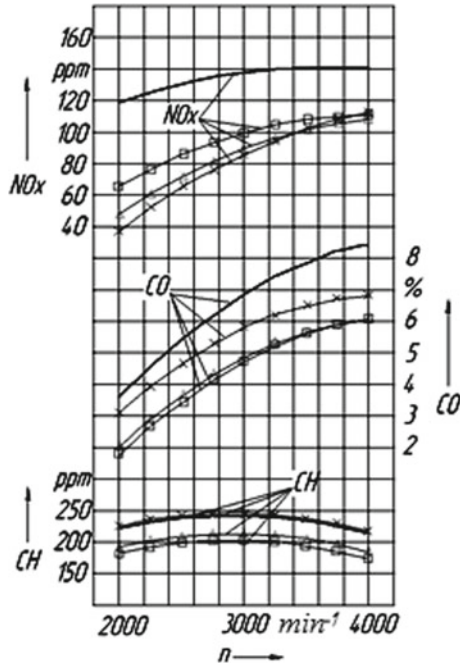


Fig. 2 Variations in the concentration of toxic EG when the engine is fed either conventional fuel or WFM, while in full-load mode: — conventional fuel; 10% water content WFM; Δ 15% water content WFM; \times 20% water content WFM

There was also registered a sizable drop in CO concentration in EG. Most pronounced the effect was for 10% water content WFM at RPM $n = 2000 \text{ min}^{-1}$ —from 3.6 to 1.7%; at RPM $n = 4000 \text{ min}^{-1}$ —from 8.5 to 6.0%. That was explained by more complete combustion through mix turbulization due to WFM water evaporation and the effect produced by active H^+ and OH^- radicals [5–11]. In general, all the tested water/fuel mixes demonstrated drop in CO concentration in EG; however, in cases when WFM water content exceeded 10...15%, there was a rise in CO concentration due to incomplete combustion [5].

The effect of WFM on unburnt hydrocarbons (CH) concentration in the engine's exhaust gases was somewhat ambiguous. When run on 10% water content WFM the CH concentration went down practically equally throughout the RPM range: at $n = 2000 \text{ min}^{-1}$ —from 221 to 181 ppm; at $n = 3000 \text{ min}^{-1}$ —from 242 to 202 ppm; at $n = 4000 \text{ min}^{-1}$ —from 214 to 173 ppm.

When the engine was run on 15% water content WFM, the CH concentration went down less noticeably, and it made at $n = 2000 \text{ min}^{-1}$ —28 ppm; and at $n = 4000 \text{ min}^{-1}$ —30 ppm. That can be explained by more complete combustion through better mixture formation due to water evaporation [17, 25]. However, once the WFM water content exceeded 20%, the CH content rose above that of the engine run on pure conventional fuel, through the RPM range. It was explained by the fact water cooled the near-the-wall layers of the mix inside the cylinder of the internal combustion engine, which hinders the complete combustion [26].

Figure 3a represents the variations in toxicity of exhaust gases when the engine was fed pure conventional fuel or WFM and run under load at RPM of $n = 2000 \text{ min}^{-1}$. A significant drop in nitric oxides emission once the engine was WFM fed was noted as compared to engine's operation on pure conventional fuel. The lowest NO_x emission was observed at 20% water content of the total fuel amount. The recorded emission was: at engine's power of $N_e = 10 \text{ kW}$ —from 473 to 382 ppm; at 15 kW—from 399 to 310 ppm; and at 20 kW—from 300 to 213 ppm. When used 15% water content WFM, the NO_x concentration went down at power outputs: $N_e = 10 \text{ kW}$ —to 395 ppm; at 15 kW—to 323 ppm; and at 20 kW—to 225 ppm. Burning 10% water content WFM affected the NO_x concentration somewhat less. Thus, at the power output of $N_e = 10 \text{ kW}$, there was a dip to 414 ppm; at 15 kW—to 342 ppm; and at 20 kW—to 244 ppm.

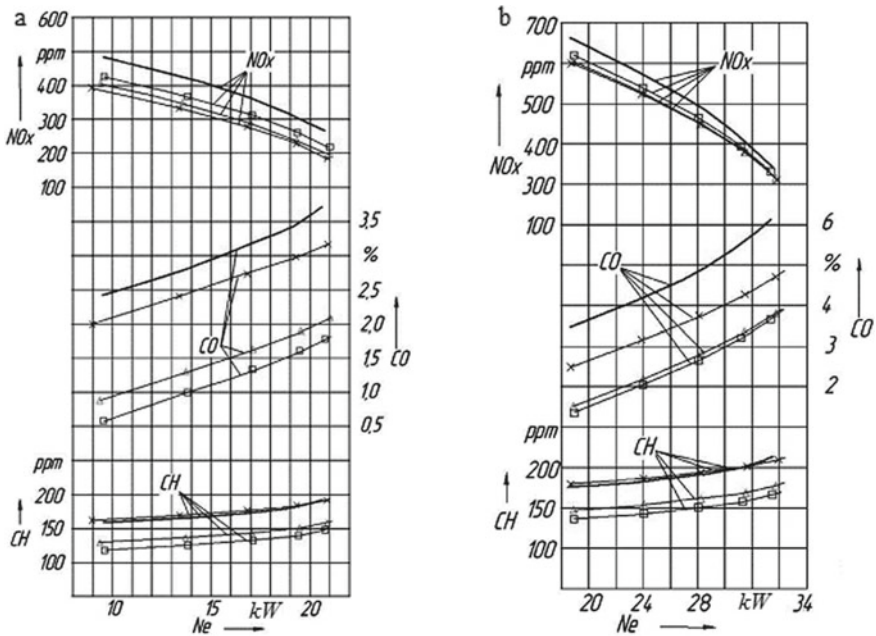


Fig. 3 Variations in the concentration of toxic EG when the engine is fed either conventional fuel or WFM, while run under load: **a** at RPM $n = 2000 \text{ min}^{-1}$, **b** at RPM $n = 3000 \text{ min}^{-1}$: — conventional fuel; 10% water content WFM; Δ 15% water content WFM; \times 20% water content WFM

Upon having analyzed the changes in the carbon monoxide (CO) concentration in the EG, it was noted that lowest values were registered when 10% water content WFM was used. In that case, the CO concentration went down from 2.44 to 0.65% at the output power of $N_e = 10$ kW; from 2.93 to 0.14%—at 15 kW; from 3.46 to 1.65% at 20 kW. When WFM used had water content of 15%, the decrease was by 1.48; 1.5 and 1.52%, respectively, at 10; 15 and 20 kW power output. When WFM used had water content of 20%, the decrease was not so pronounced and made it by 0.36; 0.38 and 0.41%, respectively, at 10; 15 and 20 kW power output.

Also, as it was demonstrated under full-load, the effect of WFM under partial load at $n = 2000 \text{ min}^{-1}$ upon the CH concentration was controversial. When the engine was fed 20% water content WFM, the exhaust gases CH concentration exceeded that when fed pure conventional fuel, by 4.1 ppm at 10 kW power output and by 5 ppm at 15 kW. However, when 10% water content WFM was used, there was registered a significant decrease in CH concentration: from 158.9 to 119.2 ppm; from 167.9 to 127.8 ppm; from 186.7 to 142.5 ppm at 10; 15 and 20 kW, respectively.

Figure 3b represents the variations in toxicity of exhaust gases when the engine was fed pure conventional fuel or WFM and run under load at RPM of $n = 3000 \text{ min}^{-1}$. In general, the correlations' nature was similar to that obtained when the engine was tested under load at RPM $n = 2000 \text{ min}^{-1}$. With the increase in water content in the WFM, the NO_x concentration went down.

The lowest NO_x emission was observed at 20% water content in the WFM: from 637 to 578 ppm at $N_e = 20$ kW power output. The lowest CO concentration in the EG was registered at 10% water content in the WFM: from 5.24 to 2.97% (1.76 times less) at $N_e = 30$ kW power output. The CH concentration in the EG at 10% water content WFM of the total fuel amount went down by 42.6 ppm (from 197.5 to 154.9 ppm).

5 Conclusion

1. The study resulted in the evaluation of the environmental properties of the VAZ-21114 electronically controlled spark-ignition engine when run on marketable gasoline as well as when run on WFM with 10, 15, and 20% of water content.
2. The greatest drop in the NO_x emission was registered, when the engine was fed 20% water content WFM at RPM $n = 2000 \text{ min}^{-1}$ (from 119 to 38 ppm), while at $N_e = 10$ kW output power it dropped from 473 to 382 ppm; at 15 kW—from 399 to 310 ppm; and at 20 kW—from 300 to 213 ppm.
3. The lowest CO concentration in the EG was observed at 10% water content of the total fuel amount at RPM $n = 2000 \text{ min}^{-1}$ from 3.6 to 1.7%; at $n = 4000 \text{ min}^{-1}$ —from 8.5 to 6.0%; and at $N_e = 10$ kW power output from 2.93 to 0.14%—at 15 kW; from 3.46 to 1.65% at 20 kW.
4. When run on 10% water content WFM the CH concentration went down practically equally throughout the RPM range: at $n = 2000 \text{ min}^{-1}$ —from 221 to 181 ppm; at $n = 3000 \text{ min}^{-1}$ —from 242 to 202 ppm; at $n = 4000 \text{ min}^{-1}$ —from 214 to 173 ppm; and at 10; 15 and 20 kW power output from 158.9 to 119.2 ppm; from 167.9 to 127.8 ppm; from 186.7 to 142.5 ppm, respectively.

5. The obtained results proved the feasibility of water/fuel mixes (WFM) in electronically controlled spark-ignition engines in improving the aforesaid engines' environmental characteristics.

Acknowledgements. This article is part of thesis research conducted in the framework of the project "The use of alternative fuels in power plants". The authors would like to thank the rector of the Federal State Budgetary Educational Institution of Higher Education "Vologda State Dairy Farming Academy by N. V. Vereshchagin" for assistance in conducting experimental research.

References

1. Dłuska E, Hubacz R, Wroński S, Kamiński J, Dyląg M, Wójtowicz R (2007) The influence of helical flow on water fuel emulsion preparation. *Chem Eng Commun* 194(10):1271–1286. <https://doi.org/10.1080/00986440701293959>
2. Deepti K, Rahul G (2020) Effects of silicon dioxide nanoparticles on the performance and emission features at different injection timings using water diesel emulsified fuel. *Energy Convers Manage* 205:112379. <https://doi.org/10.1016/j.enconman.2019.112379>
3. Piaseczny L, Zadrag R (2005) Researches of influence of water delivery to cylinder on parameters of combustion process and toxicity of CI engine. In: *Proceeding of polish congress-PTNSS*. Bielsko Biala=Szczyrk., Poland, p 1301–1312
4. Piaseczny L, Zadrag R (2006) Water fuel emulsions properties for naval diesel engines. In: *Proceeding of polish conference on gas engines*. Czestochowa, Poland, p 1240–1249
5. Wu YY, Chen BC, Hwang JJ, Chen CY (2009) Performance and emissions of motorcycle engines using water-fuel emulsions. *Int J Veh Des* 49(1–3):91–110
6. Farfaletti A, Astorga C, Martini G (2005) Effect of water/fuel emulsions and a cerium-based combustion improver additive on HD and LD diesel exhaust emissions. *Environ Sci Technol* 39(17):6792–6799
7. Marchitto L, Calabria R, Tornatore C, Bellettre J, Massoli P, Montillet A, Valentino G (2018) Optical investigations in a CI engine fueled with water in diesel emulsion produced through microchannels. *Exp Thermal Fluid Sci* 95:96–103. <https://doi.org/10.1016/j.expthermflusci.2018.02.008>
8. Abstracts (2011) *Fuel and energy abstracts* 52(1):2–64. <https://doi.org/10.1016/j.fueleneab.2010.12.002>
9. Osama AE, Murari MR, Manpreet SS (2017) Experimental investigation on a diesel engine fueled by diesel-biodiesel blends and their emulsions at various engine operating conditions. *Appl Energy* 203:582–593. <https://doi.org/10.1016/j.apenergy.2017.06.052>
10. Xavier T, Alain M, Samiur RS (2010) Experimental study of inlet manifold water injection on combustion and emissions of an automotive direct injection diesel engine. *Energy* 35(9):3628–3639. <https://doi.org/10.1016/j.energy.2010.05.007>
11. Ozcan H, Soylemez MS (2005) Experimental investigation of the effects of water addition on the exhaust emissions of a naturally aspirated, liquefied-petroleum-gas-fueled engine. *Energy Fuels* 19:1468–1472
12. Hountalas DT, Mavropoulos GC, Zannis TC, Mamalis SD (2006) Use of water emulsion and intake water injection as NO_x reduction techniques for heavy duty diesel engines. *SAE technical papers—SAE world congress*. Detroit, MI, United States. Code 90162. <https://doi.org/10.4271/2006-01-1414>

13. Hountalas DT, Mavropoulos GC, Zannis TC (2007) Comparative evaluation of EGR, intake water injection and fuel/water emulsion as NO_x reduction techniques for heavy duty diesel engines. SAE Paper No 2007-01-0120. <https://doi.org/10.4271/2007-01-0120>
14. Klyus O, Bezyukov O (2017) Use of water-fuel mixture in diesel engines at fishing vessels. *Manage Syst Prod Eng* 25(2):105–109. <https://doi.org/10.1515/mspe-2017-0016>
15. Ivanov A, Chikishev E (2017) Level recession of emissions release by motor-and-tractor diesel engines through the application of water-fuel emulsions. Ecology and safety in the technosphere: current problems and solutions. IOP Conf Ser Earth Environ Sci 50:01200. <https://doi.org/10.1088/1755-1315/50/1/012005>
16. Leng L, Yuan X, Zeng G, Wang H, Huang H, Chen X (2015) The comparison of oxidative thermokinetics between emulsion and microemulsion diesel fuel. *Energy Convers Manage* 101:364–370. <https://doi.org/10.1016/j.enconman.2015.05.071>
17. Lif A, Holmberg K (2006) Water-in-diesel emulsions and related systems. *Adv Colloid Interface Sci* 123–126:231–239. <https://doi.org/10.1016/j.cis.2006.05.004>
18. Misra M, Chen S, Grimes P (2005) Water-fuel emulsions for energy application. In: Proceedings of the Jan D. Miller symposium—innovations in natural resource processing, p 329–336
19. Vigneswaran R, Balasubramanian D, Sabari Sastha BD (2021) Performance, emission and combustion characteristics of unmodified diesel engine with titanium dioxide (TiO₂) nano particle along with water-in-diesel emulsion fuel. *Fuel* 285:119115. <https://doi.org/10.1016/j.fuel.2020.119115>
20. Claxton LD (2015) The history, genotoxicity, and carcinogenicity of carbon-based fuels and their emissions. Part 3: diesel and gasoline. *Mutat Res/Rev Mutat Res* 763:30–85. <https://doi.org/10.1016/j.mrrev.2014.09.002>
21. Abdollahi M, Ghobadian B, Najafi G, Hoseini SS, Mofijur M, Mazlan M (2020) Impact of water—biodiesel—diesel nano-emulsion fuel on performance parameters and diesel engine emission. *Fuel* 280:118576. <https://doi.org/10.1016/j.fuel.2020.118576>
22. Subramanian KA (2011) A comparison of water–diesel emulsion and timed injection of water into the intake manifold of a diesel engine for simultaneous control of NO and smoke emissions. *Energy Convers Manage* 52(2):849–857. <https://doi.org/10.1016/j.enconman.2010.08.010>
23. EL-Seesy AI, Kayatas Z, Takayama R, He Z, Kandasamy S, Kosaka H (2020) Combustion and emission characteristics of RCEM and common rail diesel engine working with diesel fuel and ethanol/hydroxy ethanol injected in the intake and exhaust port: assessment and comparison. *Energy Convers Manage* 205:112453. <https://doi.org/10.1016/j.enconman.2019.112453>
24. Vellaiyan S (2020) Combustion, performance and emission evaluation of a diesel engine fueled with soybean biodiesel and its water blends. *Energy* 201:117633. <https://doi.org/10.1016/j.energy.2020.117633>
25. Venkanna BK, Reddy CV (2013) Effect of injector opening pressure on performance, emission and combustion characteristics of DI diesel engine fueled with diesel and honne oil methyl ester. *Environ Prog Sustain Energy* 32:148–155. <https://doi.org/10.1002/ep.10607>
26. Lin CY, Lin SA (2007) Effects of emulsification variables on fuel properties of two- and three-phase biodiesel emulsions. *Fuel* 86:210–217



Trinkler Cycle Analysis with Maximum Pressure Limitation

A. Malozemov¹(✉), A. Naumov¹, and A. Shavlov²

¹ South Ural State University, 76, Lenin Avenue, Chelyabinsk 454080, Russia
malozemovaa@susu.ru

² Branch of Air Force Academy named after N.Ye. Zhukovsky and Yu.A. Gagarin, 1, 11-town,
Chelyabinsk 454015, Russia

Abstract. In the course of the theoretical study, a mathematical model for the Trinkler (Sabathe) cycle thermodynamic analysis was developed, taking into account the mutual influence of the parameters included in the thermal efficiency equation and the need to limit the maximum gas pressure in the cylinder, which includes new equation for determining the dependence of the Trinkler cycle thermal efficiency on the cylinder and the compressor compression ratios, taking into account the limitation of the maximum cycle pressure and new equation to determine the cylinder and the compressor compression ratios at which the maximum thermal efficiency is achieved for the relative maximum cycle pressure various values. Using the developed model, combinations of the compression ratio in the combined engine cylinder and compressor that implements the Trinkler cycle have been identified, which provide the thermal efficiency maximum value under the given maximum cycle pressure limitations. The range of the preliminary and subsequent expansion ratios limiting values was determined from the condition of increasing the thermal efficiency maximum possible value with a decrease in the cylinder compression ratio.

Keywords: Reciprocating engine · Working process · Trinkler cycle · Thermodynamic analysis · Compression ratio · Thermal efficiency

1 Introduction

Reciprocating internal combustion engines are still the main source of energy for mankind. The problems of increasing their efficiency are important for the world economy. The engine fuel efficiency is determined by the combustion chamber working processes efficiency and mechanical losses in mechanisms. The thermal and mechanical loading of the engine parts and its life time depend on the dynamics of changes in the values of pressures and temperatures in cylinder. One of the effective ways to improve the engine fuel economy is to increase the air density in cylinder by increasing the compression ratio and boost pressure. However, in this case, the maximum combustion pressure values can increase significantly, which will negatively affect the engine reliability. Therefore, at the engine conceptual development stage, it is necessary, among

other things, to assess the thermodynamic effect of the compression ratio and boost pressure on the working cycle indicators, taking into account the limitations on the maximum allowable pressure in the cylinder.

2 Problem

The closest to the real supercharged diesel engine working cycle is the Trinkler (Sabathe) ideal cycle with a mixed heat supply [1]. The average Trinkler cycle pressure without cooling the air supplied by the compressor is determined by the known expression:

$$P_t = P_a \cdot \frac{\varepsilon_0^k}{\varepsilon_0 - 1} \cdot \frac{\lambda - 1 + k \cdot \lambda \cdot (\rho - 1)}{k - 1} \cdot \eta_t, \quad (1)$$

here ε_0 —total compression ratio in the cylinder and compressor; k —adiabatic index; λ —pressure increase ratio; ρ —preliminary expansion ratio; P_a —initial cycle pressure.

Pressure increase ratio:

$$\lambda = \frac{P_z}{P_c}, \quad (2)$$

here P_z —maximum cycle pressure; P_c —compression pressure.

Preliminary expansion ratio:

$$\rho = \frac{V_z}{V_c}, \quad (3)$$

here V_z, V_c —gas volume corresponding to P_z and P_c .

Thermal efficiency of Trinkler cycle:

$$\eta_t = 1 - \frac{1}{\varepsilon_0^{k-1}} \cdot \frac{\rho^k \cdot \lambda - 1}{\lambda - 1 + k \cdot \lambda \cdot (\rho - 1)}. \quad (4)$$

The total compression ratio, depended from the cylinder ε and the compressor ε_c compression ratio:

$$\varepsilon_0 = \varepsilon \cdot \varepsilon_c. \quad (5)$$

According to Eq. 4, an increase in the total compression ratio entails an increase in the thermal cycle efficiency. However, many experimental data show that the influence of the compression ratio on the fuel efficiency of an internal combustion engine is not so unambiguous. For example, in [2] shown that for 1CHN8/12 engine the minimum specific fuel consumption in the range of compression ratios 15...18 in almost the entire range of loads is provided at $\varepsilon = 16...17$. Similar data are given in [3, 4] and many other works, as well as obtained in the course of various types diesel engines experimental studies at SUSU. Of course, thermal and effective efficiency are not directly proportional values; however, thermodynamic analysis of an ideal operating cycle can reveal the reasons for the ambiguous influence of the compression ratio on the real internal

combustion engine fuel consumption. The “classical” Eq. 4 does not take into account the complex nature of the mutual influence of the geometric compression ratio, boost pressure, pressure rise ratio, preliminary ratio and initial cycle pressure, that is, all the parameters included in these equation.

The works of scientists Demidov [5], Khutsiev [6], Zlenko [7], Ter-Mkrtichyan [8], Yamanin [9], Sharoglazov et al. [10], Tumoney [11], Hariram et al. [12], Balian [13], Iliev [14], and many others are devoted to the compression ratio and boost pressure influence on the processes in the diesel engine combustion chamber. The main direction of researches is the substantiation of the compression ratio optimal value choice according to the criterion of minimum fuel consumption. For example, GG Ter-Mkrtichyan obtained a formula for determining the effective efficiency maximum value:

$$\eta_{e \max} = k_i \cdot \left(1 - \frac{2 \cdot n - 1}{n}\right) \cdot \frac{1}{\left(\frac{n-1}{n} \cdot \frac{k_i}{k_m}\right)^{\frac{n-1}{2n-1}}}, \quad (6)$$

here n —compression polytropic index; k_i —coefficient taking into account the difference between the real engine cycle and the thermodynamic one; k_m —coefficient that takes into account mechanical losses.

Compression ratio for maximum efficiency:

$$\varepsilon = \left(\frac{n-1}{n} \cdot \frac{k_i}{k_m}\right)^{\frac{1}{2n-1}}. \quad (7)$$

However, these works do not take into account the need to limit the maximum gas pressure in the combustion chamber and do not solve the problem of choosing geometric compression ratio and boost pressure rational combinations from the position of ensuring the minimum fuel consumption while maintaining the reliability indicators. Most often, to select the compression ratio optimal value, not analytical dependences (like the Eq. 7) are used, but universal methods of multicriterial search for the optimum. For example, in the works [15, 16] the gray relational analysis (GRA) method [17] was used, in the book [18]—the Broyden–Fletcher–Goldfarb–Shanno (BFGS) methods [19], genetic algorithms (MOGA—multiobjective genetic algorithm, NSGA—non-dominated sorting genetic algorithm, ARMOGA—adaptive range multiobjective genetic algorithm, etc.) [20, 21].

The study purpose, the brief results of which are given in this article, is to develop a mathematical model for thermodynamic analysis of the Trinkler cycle, taking into account the mutual influence of the parameters included in the equation of thermal efficiency (Eq. 4) and the need to limit the maximum gas pressure in the cylinder.

3 Mathematical Model

Let us take the initial compression pressure P_a in Eq. 4 equal to the gas pressure after the compressor and proportional to the compressor compression ratio ε_c , then the compression pressure P_c :

$$P_c = P_a \cdot \varepsilon^k = P_0 \cdot \varepsilon_c \cdot \varepsilon^k, \quad (8)$$

here P_0 —gas pressure before the compressor.

The pressure increase ratio in Eq. 4:

$$\lambda = \frac{P_z}{P_0 \cdot \varepsilon_c \cdot \varepsilon^k} = \frac{P'_z}{\varepsilon_c \cdot \varepsilon^k}, \tag{9}$$

here $P'_z = P_z/P_0$ —relative cycle maximum pressure (relative to the gas pressure before the compressor).

The preliminary expansion ratio ρ is a value proportional to the compression ratio in the cylinder:

$$\rho = \frac{V_z}{V_c} = \frac{\varepsilon}{\delta}, \tag{10}$$

here δ —subsequent expansion ratio.

Substituting Eq. 9 and Eq. 10 into Eq. 4 and performing transformations, we get:

$$\eta_t = 1 - \frac{\varepsilon \cdot \left(\frac{\varepsilon_c^{1-k}}{\delta^k} - \frac{\varepsilon_c^{2-k}}{P'_z} \right)}{k \cdot \left(\frac{\varepsilon}{\delta} - 1 \right) - \frac{\varepsilon^k \cdot \varepsilon_c}{P'_z} + 1}. \tag{11}$$

To determine the cylinder compression ratio, at which the thermal efficiency maximum value is reached at $\varepsilon_c = \text{const}$, it is necessary to solve the equation $\partial \eta_t / \partial \varepsilon = 0$. The solution (omitting intermediate calculations) is a system of two equations:

$$\varepsilon_c = \frac{P'_z}{\delta^k}. \tag{12}$$

$$\varepsilon_c = \frac{P'_z}{\varepsilon^k}. \tag{13}$$

Equation 12 does not contain the cylinder compression ratio value. With $\varepsilon = 11 \dots 18$, the value of δ^k varies in the range $14 \dots 44$ (here $\delta = \varepsilon/\rho$, for diesel engines $\rho = 1.2 \dots 1.7$); therefore, Eq. 12 corresponds to technically unrealizable design and operating parameters of a real low- or medium-powered diesel engines. For example, for a 4CHN15/20.5 engine, the compressor compression ratio, which ensures the maximum thermal efficiency, should be 3.9 units. Therefore, further we will consider only Eq. 13. Substituting Eq. 13 into Eq. 11, we obtain (omitting intermediate calculations) an expression for determining the maximum possible Trinkler cycle thermal efficiency:

$$\eta_{t \max} = 1 - \left(\frac{P'_z}{\varepsilon^{k-1}} \right)^{1-k} \cdot \frac{\left(\frac{\varepsilon}{\delta} \right)^k - 1}{k \cdot \left(\frac{\varepsilon}{\delta} - 1 \right)}. \tag{14}$$

The growth of the thermal efficiency maximum possible value with a decrease in the cylinder compression ratio, which is important from the reducing mechanical loads on engine parts point of view, is achieved when the condition $\partial \eta_{t \max} / \partial \varepsilon \leq 0$ is met. After substituting Eq. 14 in this condition:

$$\left(A - \frac{B}{\delta} \cdot \varepsilon^k \right) \cdot \left(k \cdot \left(\frac{\varepsilon}{\delta} - 1 \right) \right) + \varepsilon \cdot \left(\frac{\varepsilon^k}{\delta} - 1 \right) \cdot \frac{k}{\delta} \leq 0, \tag{15}$$

$$A = 2 \cdot (k + 1) \cdot (k - 1)^2 \approx 0.768, \tag{16}$$

$$B = (k^2 - k + 1) \cdot (2 \cdot k - 1) \approx 2.808. \tag{17}$$

4 Results and Discussion

For fixed value of P'_z (i.e., when the conditions for limiting mechanical loads on the engine are met) and δ (i.e., for the same law of heat release), the graphs of the thermal efficiency dependence on the compression ratio in the engine cylinder and compressor have the form shown in Fig. 1. As can be seen from Fig. 1, at ε_c low value, an increase in the cylinder compression ratio leads to an increase in thermal efficiency; however, when the ε_c value reaches some values, the thermal efficiency begins to decrease with increasing ε_c . And the higher the relative maximum cycle pressure and the lower the subsequent expansion ratio, the higher the compressor pressure corresponding to the maximum thermal efficiency.

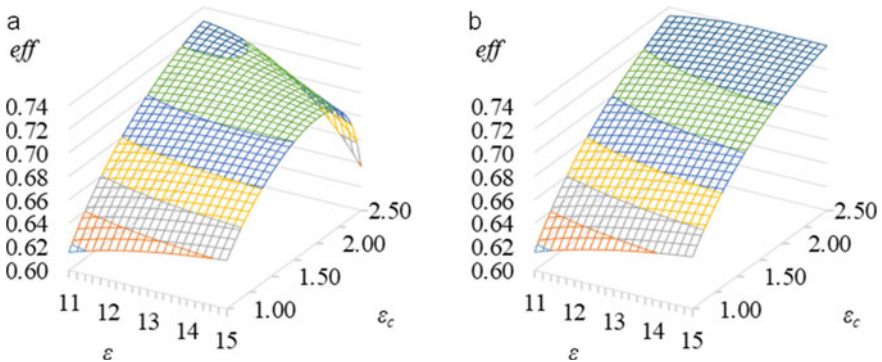


Fig. 1 Dependence of thermal efficiency on the compression ratio in the engine cylinder and compressor ($\delta = 10$): **a** $P'_z = 70$; **b** $P'_z = 100$ (eff—thermal efficiency)

Based on the results of the calculation using Eq. 11, graphs are created (Fig. 2), which show the ε_c and ε combination, at which the thermal efficiency maximum value is achieved for the relative maximum cycle pressure various values. The higher the compressor compression ratio, the lower the engine cylinder compression ratio is necessary to ensure the maximum thermal efficiency at a constant value of the relative maximum cycle pressure. For example, for $\varepsilon = 14.5$ and $P'_z = 90$ (which approximately corresponds to the 4CHN15/20.5 engine maximum power), the highest thermal cycle efficiency is achieved at a compressor compression ratio $\varepsilon_c = 2.1$, which corresponds to the experimental data. According to Eq. 13, the position of the maximum thermal efficiency lines does not depend on the magnitude of the subsequent expansion ratio, or (for the real diesel engine working cycle) on the heat release rate form.

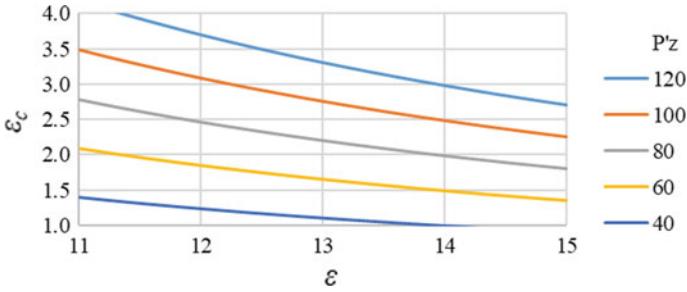


Fig. 2 Combination of ϵ_c and ϵ , at which the maximum thermal efficiency value is achieved for various values of the relative maximum cycle pressure

Figure 3 shows the dependence of the maximum possible thermal efficiency on the cylinder compression ratio and the relative maximum cycle pressure, obtained using Eq. 14. The nature of the thermal efficiency dependence on ϵ at $\epsilon_c = \text{const}$, $\rho = \text{const}$, $\lambda = \text{const}$ fully corresponds to the theory of internal combustion engines (the greater the compression ratio, the higher the thermal efficiency). However, in this case, there is a significant change in the cycle maximum pressure value with an increase in the compression ratio.

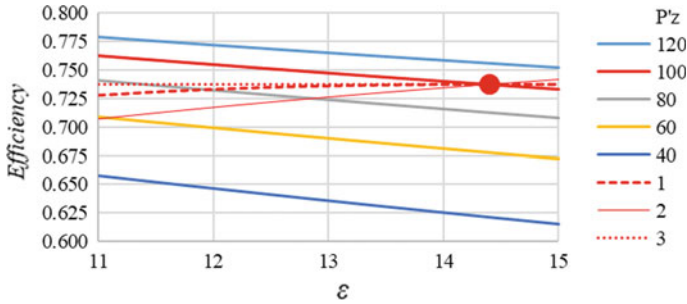


Fig. 3 Maximum possible thermal efficiency ($\delta = 10$) with an ϵ_c and ϵ optimal combination: 1—for $\epsilon_c = \text{const}$, $\rho = \text{var}$, $\lambda = \text{var}$; 2—for $\epsilon_c = \text{const}$, $\rho = \text{const}$, $\lambda = \text{const}$; 3—limiting condition $\partial\eta_{l \max}/\partial\epsilon \leq 0$

5 Conclusion

Thus, in the course of the performed theoretical study, a mathematical model was developed for thermodynamic analysis of the Trinkler cycle, taking into account the mutual influence of the parameters included in the thermal efficiency equation and the need to limit the maximum gases pressure in the cylinder, which includes new equations for determining the dependence of the Trinkler cycle thermal efficiency on the cylinder and compressor compression ratio, taking into account the maximum cycle pressure limitation and to determine the cylinder and the compressor compression ratio, at which

the thermal efficiency maximum value is achieved for relative maximum cycle pressure various values.

Using the developed model, combinations of the cylinder and compressor compression ratio of a supercharged engine that implements the Trinkler cycle have been identified, which provide the thermal efficiency maximum value at the given maximum cycle pressure limits. The range of the preliminary and subsequent expansion ratios limiting values is determined from the condition of increasing the thermal efficiency maximum possible value with a decrease of cylinder compression ratio.

This work results can find application in the thermodynamic optimization of supercharged diesel engine designs at the stage of their conceptual development, as well as in theoretical research related to the thermodynamic analysis of the Trinkler (Sabathe) cycle.

References

1. Vyubov DN, Ivaschenko NA, Ivin VI (1983) Internal combustion engines: theory of piston and combined engines. Mashinostroyeniye, Moscow
2. Mathur YB, Poonia MP, Jethoo AS, Singh R (2012) Optimization of compression ratio of diesel fueled variable compression ratio engine. *Int J Energy Eng* 2(3):99–101
3. Pesic RB, Milojevic ST, Vecinovic SP (2010) Benefits and challenges of variable compression ratio at diesel engines. *J Therm Sci* 4:1063–1073
4. Raol NS, Babu NH, Rao BV (2015) Experimental investigations of a variable compression ratio diesel engine fueled with neem methyl ester (NeME). *Int J Eng Res Technol* 4(4):141–145
5. Demidov VP (1978) Engines with variable compression ratio. Mashinostroyeniye, Moscow
6. Khutsiev AI (1986) Internal combustion engines with variable compression process. Mashinostroyeniye, Moscow
7. Zlenko MA (2005) Theory and practice of creating internal combustion engines with variable displacement and compression ratio. Thesis of doctoral dissertations, Moscow
8. Ter-Mkrtychyan GG (2004) Scientific basis for creating engines with controlled compression ratio. Thesis of doctoral dissertations, Moscow
9. Yamanin IA (2011) Research of vibrodynamic characteristics of engines with variable compression ratio. Thesis of candidate dissertations, Yaroslavl
10. Sharoglazov BA, Farafontov MF, Klementyev VV (2006) Internal combustion engines: theory, modeling and calculation of processes. SUSU Publishing House, Chelyabinsk
11. Tumoney SG (1971) Variable compression ratio diesel engine. In: Proceeding of engineering conference, Boston, p 356–363
12. Hariram V, Vagesh Shangar R (2015) Influence of compression ratio on combustion and performance characteristics of direct injection compression ignition engine. *Alex Eng J* 54:807–814
13. Balian RA (1990) The effect of compression ratio on the performance of a direct injection diesel engine: a thesis submitted for the degree of doctor of philosophy. Brunel University, Uxbridge
14. Iliiev S (2014) Simulation on single cylinder diesel engine and effect of compression ratio and EGR on engine performance and emission. In: Scientific proceedings XXII international scientific-technical conference. “Trans and Motauto—14”, vol 1, pp 48–50
15. Kartheek GK, Lakshmi Prasad K, Viswanadh KV et al (2019) Multi-response optimization of variable compression ratio CI engine using Grey-Taguchi method. In: Recent advances in material sciences. Springer Nature Switzerland AG, p 425–436

16. Wilson VH, Udayakumar M (2012) Optimization of diesel engine parameters using Taguchi method and design of evolution. *J Braz Soc Mech Sci Eng* 34:423–428
17. Zhang J, Wu D, Olson D (2005) The method of grey related analysis to multiple attribute decision making problems with interval numbers. *Math Comput Model* 991–998
18. Shi Y, Ge HW, Reitz RD (2011) *Computational optimization of internal combustion engines*. Springer-Verlag, London
19. Broyden CG (1970) The convergence of a class of double-rank minimization algorithms. *J Inst Math Appl* 6:76–90
20. Holland JH (1975) *Adaptation in natural and artificial systems*. MIT press, Cambridge
21. Genzale CL, Reitz RD, Wickman DD (2007) A computational investigation into the effects of spray targeting, bowl geometry and swirl ratio for low-temperature combustion in a heavy duty diesel engine. *SAE Paper* 2007-01-0119



Simulation of Different Vibration Modes of a Drum in Continuous Compaction Control Systems of Soil by Vibratory Rollers

I. S. Tyuremnov and A. S. Morev^(✉)

Yaroslavl State Technical University, 88, Moskovsky prospect, Yaroslavl 150023, Russia
asmorev@bk.ru

Abstract. Modern vibratory rollers are equipped with systems of continuous compaction control to quickly monitor the quality of soil compaction by vibratory rollers not only at individual points of sampling, but over the whole compaction area. The operation of the continuous compaction control systems of vibratory rollers is based on the calculation of CMV, RMV, CCV, and other indicators. The paper presents the results of a computational experiment on the comparative performance of CMV, RMV, and CCV compared to the newly proposed compaction value. As a result of computational experiment on the three-mass rheological model, it was found that this CV, with a reasonable choice of influencing factors, has a high sensitivity to changing the properties of soil during compaction by vibratory drum in partial uplift mode and indicates the transition of vibrations in the undesirable double jump mode. At the same time, CV is insensitive to changes in soil properties in constant contact mode, as are CMV, RMV, and CCV. Further studies should clarify the values of factors influencing the calculated CV for various types of soil compacted by different vibratory rollers, conduct field experiments, as well as improve the simulation of interaction between vibratory roller and the compacted soil.

Keywords: Soil · Compaction · Vibration · Vibratory roller · Compaction criterion · Continuous compaction control

1 Introduction

Soil compaction is one of the most effective technologies for increasing its durability and resistance to climatic factors and mechanical loads. The technological process of constructing soil structures on compacted soils includes backfilling with a layer of a specified thickness, layer compaction by vibrating rollers, and surface profiling by motor graders. In this case, the vibratory rollers compact soil by driving over its layer, putting their own weight on it, and generating vibrations. The required number of passes to compact each layer depends on the type of soil, layer thickness, required density (strength) of soil, and the roller properties (weight, drum size, frequency, vibration force, and speed). It usually ranges from 6 to 20 passes. Soil compaction is perfect to automate and robotize due to its comparative simplicity, repeatability, rather large size of the construction site and

its isolation. However, ensuring the quality of soil compaction depends on the correct choice of roller weight, vibration parameters, and speed. The change in soil properties at each pass causes the vibratory roller to operate in different oscillation modes as the soil density increases. The oscillation is in constant contact during the first passes (the roller keeps constant contact with the ground in each oscillation cycle). This mode is commonly referred to as continuous contact [1–3] (Fig. 1). After several passes, the drum goes into partial uplift mode, in which the drum lifts off the ground and is put back on each oscillation cycle. The oscillation amplitude of the drum is the same each oscillation cycle (Fig. 1). As the soil is being compacted, the oscillation can progress to the undesirable double jump mode. In this mode, the amplitudes of successive drum jumps are not equal, and the peak loads on the drum elements increase (Fig. 1). Soil properties can vary randomly along and across the roller’s travel lane within a single pass, as the type and moisture can vary within a single layer. Under certain soil conditions, due to asymmetric driving force of the exciter relative to the center of gravity of the drum, as well as during motion with partial overlapping of the trace from the previous pass, when the right and left edges of the drum are on the ground with different degrees of compaction, a rocking motion mode may occur with undesirable transverse oscillation [1–4]. These features have led to the development of continuous compaction control (CCC) systems [2, 5, 6], which detect changes in soil properties in real time during compaction and can also signal when the vibratory roller enters undesirable double jump or rocking motion oscillation modes.

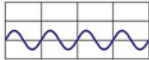
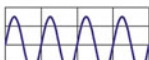


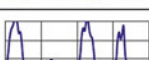
drum motion	Interaction drum-soil	operating condition	soil contact force	application of CCC	soil stiffness	roller speed	drum amplitude
periodic	continuous contact	CONT. CONTACT		yes	low ↓ ↑ high	fast ↑ ↓ slow	small ↓ ↑ large
	periodic loss of contact	PARTIAL UPLIFT		yes			
		DOUBLE JUMP		yes			
		ROCKING MOTION		no			
chaotic	non-periodic loss of contact	CHAOTIC MOTION		no	high	slow	large

Fig. 1 Influence of soil properties and roller operation mode on the used vibration modes of the drum [1]

Continuous control compaction systems (CCC) also document the compaction results. If a roller is equipped with a high-precision positioning system, overlaying the current state of the material on the roller path can be used to create a density map of the

work area to detect undercompacted areas, ensuring 100% control of the entire area and documenting the result [5–7].

2 Problem Statement

Various manufacturers of vibratory rollers use CCC systems that work differently [2, 3, 5, 6, 8–12].

The most widespread are the systems based on spectral analysis of the vertical component of the roller acceleration and calculation of some indicators by the amplitudes of different harmonics of the spectrum that appear by recording vertical accelerations of the vibratory roller (Fig. 2).

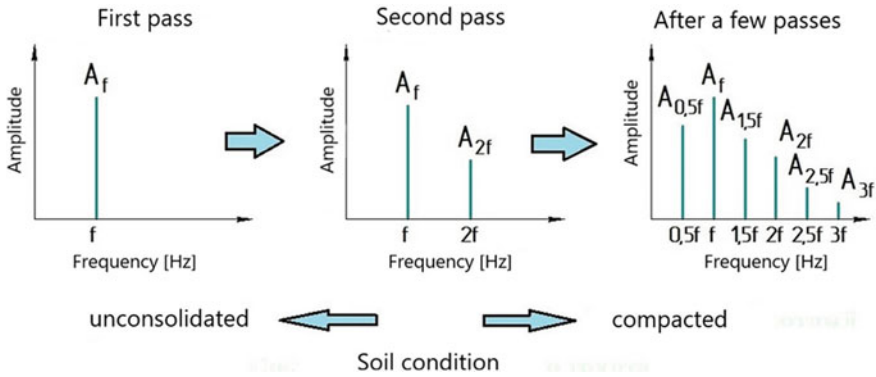


Fig. 2 Change of the vertical acceleration spectrum of the vibratory roller drum during compaction [12]

DYNAPAC, VOLVO, and some other companies install CCC systems on their vibratory rollers, which function using CMV and RMV calculation [5–7]. SAKAI uses the CCV parameter [5, 6]:

$$CMV = C \cdot \frac{A_{2f}}{A_f}, \tag{1}$$

$$RMV = BV = C \cdot \frac{A_{0.5f}}{A_f}, \tag{2}$$

$$CCV = \frac{A_{0.5f} + A_{1.5f} + A_{2f} + A_{2.5f} + A_{3f}}{A_{0.5f} + A_f} \cdot 100\%, \tag{3}$$

where $A_{0.5f}$, A_f , $A_{1.5f}$, A_{2f} , $A_{2.5f}$, A_{3f} —respectively, the amplitude of the harmonic spectrum of vertical accelerations of the vibratory roller at frequencies $0.5f, f, 1.5f, 2f, 2.5f, 3f$ (Fig. 2); f —vibration frequency of the vibrating roller, Hz.

CCC systems should be as sensitive as possible to changes in soil properties in partial uplift, which is the main operation mode during compaction, and respond to the transition of vibrations into undesirable double jump [1–3].

To improve the existing CCC indicators based on the analysis of the vertical acceleration spectrum, we propose the CV indicator, which is a modification of CMV, RMV, and CCV indicators [13]:

$$CV = K \cdot \frac{(K_{0.5f} \cdot A_{0.5f} + K_{1.5f} \cdot A_{1.5f} + K_{2f} \cdot A_{2f} + K_{2.5f} \cdot A_{2.5f} + K_{3f} \cdot A_{3f})}{(K_{0.5f} \cdot A_{0.5f} + K_f \cdot A_f)} \quad (4)$$

where K is the total calibration constant; $K_{0.5f}, K_f, K_{1.5f}, K_{2f}, K_{2.5f}, K_{3f}$ are the significance ratios of harmonic amplitudes of vertical acceleration spectrum of vibratory drum at frequencies $0.5f, f, 1.5f, 2f, 2.5f, 3f$, respectively.

To preliminary verify the effectiveness of the proposed CV indicator compared to the existing ones (CMV, RMV, and CCV), it is necessary to simulate the interaction of a vibratory drum with the soil and to conduct computational and live experiments.

To analyze the comparative effectiveness of the CV indicator, we have developed a mathematical model of interaction between vibratory roller and compacted soil and conducted a computational experiment. We used a three-mass rheological model [14] (Fig. 3) containing a drum frame, weight m_f , a vibratory drum, weight m_d , a harmonically varying impact force $P \sin(\omega t)$ applied to the drum, and an apparent mass m_s .

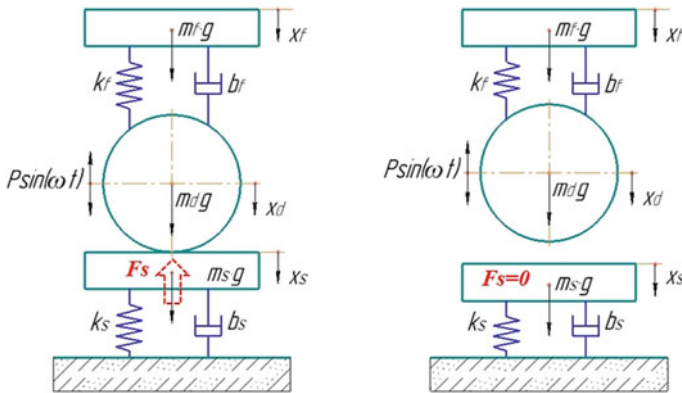


Fig. 3 Three-mass rheological model of interaction between a vibratory roller and soil [14]

Shock absorbers of the drum were modeled with elastic resistance elements (k_f factor) and viscous resistance elements (b_f factor). When calculating the resistance of soil to deformation, we considered the elastic and viscous resistance forces depending on the elastic k_s and viscous b_s resistance factors in soil along with the apparent mass.

One specific aspect of this simulation [14] is being able to simulate not only the continuous contact (Fig. 3a), which is what is usually considered in similar studies (e.g., [15–17]), but also the modes of repeated drum uplift off the ground (partial uplift and double jump) (Fig. 3b). To simulate the motion of each element of the frame-roller-soil system during continuous contact and uplift modes, we have formulated the differential equations of motion for all elements of the system for the phase of contact of the drum with soil and uplift from soil, as well as conditions for the start of uplift and the subsequent

return to contact [14]. Numerical solution of the differential equations was performed in MATLAB–Simulink.

3 Results and Discussion

We used a DM-614 roller produced by Road Machinery Factory (Russia) with the following parameters: $m_d = 4000$ kg; $m_f = 4000$ kg; $P = 215$ kN; $k_f = 7.240$ MN/m (for twenty U150.030 shock absorbers [18]); $b_f = 6.148$ kN s/m [19]; $\omega = 188.4$ rad/s. The apparent mass of soil was $m_d = 0.2$ md [19, 20]. The viscous resistance factor was assumed constant, $b_s = 212$ kN s/m [19].

We have verified the simulation results of DM-614 vibratory drum movement and accelerations along with the results of field experimental studies [20]. They showed that the model properly simulated the oscillations of the drum attached to the roller.

After assessing the correctness of the values of vertical accelerations and spectra of vertical accelerations simulated by the mathematical model and considering the results of field studies [20], we have conducted a computational experiment—we have calculated CMV, RMV, CCV, and CV parameters in the simulation model (Fig. 4).

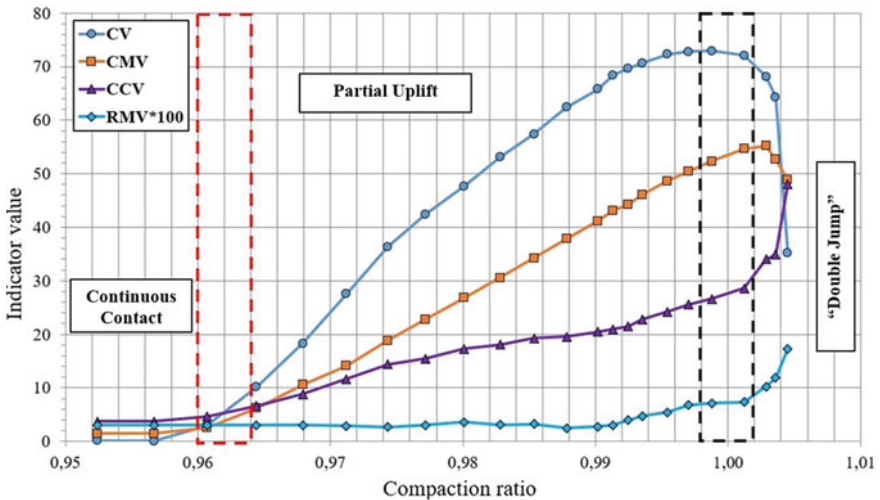


Fig. 4 Calculation results of CV, CMV, RMV, and CCV during vibratory roller operation in different modes

As a result of the computational experiment, it was found that the CV indicator proposed for CCC systems has a high sensitivity to changing the properties of soil during compaction in partial uplift mode, which is the main operation mode of modern vibratory rollers. At the same time, CV reacts to the transition of the roller oscillation to the double jump mode (Fig. 4). At the same time, CV is not sensitive to changes in ground properties as are CMV and CCV in the constant contact mode. This is because there is only one harmonic in the acceleration spectrum (at a frequency f) in constant

contact, and the results of calculations (1)–(4) do not lead to changes in the values of CV, CMV, RMV, and CCV.

It should be noted that the results of CV calculation essentially depend on the justification of numerical values of the factors K , $K_{0.5f}$, K_f , $K_{1.5f}$, K_{2f} , $K_{2.5f}$, K_{3f} included in formula (4). Justification of values of these factors for different roller models and types of soil requires further research.

The developed simulation model makes it possible not only to simulate the operation of the CCC system for vibratory rollers, but also to solve the problems of design and upgrade of vibratory rollers, for example, to justify the properties and number of shock absorbers in the mounting of the vibratory drum to the frame [21]. At the same time, the rheological model used in the study does not consider the accumulation of irreversible soil deformations and, therefore, can be further improved.

4 Conclusions

To improve soil compaction with vibrating rollers, it is necessary to improve the CCC systems, vibratory drum designs, and mode selection algorithms, considering the changing properties of soil and operating conditions.

The developed CV indicator for CCC systems for vibratory rollers has a high sensitivity to the change of soil properties in the partial uplift mode and lets the operator detect the change in oscillations into the undesirable double jump mode. However, in constant contact mode, the CV is insensitive to changes in ground properties.

The simulation model and the CV can be further improved in the CCC systems for vibratory rollers by adding to the rheological model new elements that consider accumulation of irreversible soil deformation during compaction as well as adjustment of factors K , $K_{0.5f}$, K_f , $K_{1.5f}$, K_{2f} , $K_{2.5f}$, K_{3f} used in calculation of CV during compaction of different soil by different vibratory rollers.

Acknowledgements. The authors are grateful to Professor Evgeniy Fyodorovich Skurygin, YSTU, for advice and assistance in developing the mathematical model.

References

1. Adam D, Kopf F (2004) Operational devices for compaction optimization and quality control (continuous compaction control and light falling weight device). In: Proceedings of the international seminar on geotechnics in pavement and railway design and construction, Athens, Greece, p 97–106
2. Mooney MA, Adam D (2007) Vibratory roller integrated measurement of earthwork compaction: an overview. In: Seventh international symposium on field measurements in geomechanics. [https://doi.org/10.1061/40940\(307\)80](https://doi.org/10.1061/40940(307)80)
3. Tyuremnov IS (2016) The review of systems of continuous control of soil compaction for vibratory rollers Part 3. The specifics of the functioning and “intelligent compaction”. Bull PNU 2(41):115–122
4. Norman WF, Van Susante P, Mooney MA (2009) Influence of rocking motion on vibratory roller-based measurement of soil stiffness. J Eng Mech ASCE 136(7):898–905. [https://doi.org/10.1061/\(ASCE\)EM.1943-7889.0000132](https://doi.org/10.1061/(ASCE)EM.1943-7889.0000132)

5. Mooney MA, Rinehart RV, Facas NW, Musimbi OM (2010) Intelligent soil compaction systems. National cooperative highway research program 676. <https://doi.org/10.17226/22922>
6. Tyuremnov IS, Morev AS (2015) The review of systems of continuous control of soil compaction for vibratory rollers. Part 1. Bull PNU 4(39):99–108
7. Dynapac Documentation System. Soil Compaction 3492 0033 01. <http://www.dynapac.com/en-us/-Products/?product=663&cat=36>. Accessed 04 Dec 2014
8. Tyuremnov IS, Morev AS (2015) The review of systems of continuous control of soil compaction for vibratory rollers. Part 2. Bull PNU 1(40):69–76
9. Thurner HF, Sandstrom A (2000) Continuous compaction control. CCC. European workshop compaction of soils and granular materials. Paris, p 237–246, 19 May 2000
10. Pavana KRV, White DJ, Morris MD (2010) Geostatistical analysis for spatially referenced roller-integrated compaction measurements. J Geotech Geoenvironmental Eng 136(6):813–822. [https://doi.org/10.1061/\(ASCE\)GT.1943-5606.0000285](https://doi.org/10.1061/(ASCE)GT.1943-5606.0000285)
11. White DJ, Pavana KRV (2010) A review of roller-integrated compaction monitoring technologies for earthworks. Final Report ER10–04. Earthworks Engineering Research Center (EERC), Iowa State University
12. Scherocman J, Rakowski S, Uchiyama K (2007) Intelligent compaction, does it exist? Proceedings of the annual conference—Canadian technical asphalt association
13. Tyuremnov IS, Morev AS (2020) New criterion for continuous compaction control systems by soil vibratory rollers. In: Radionov A, Kravchenko O, Guzeev V, Rozhdestvenskiy Y (eds) Proceedings of the 5th International Conference on Industrial Engineering (ICIE 2019). ICIE 2019. Lecture Notes in Mechanical Engineering. Springer, Cham. https://doi.org/10.1007/978-3-030-22063-1_62
14. Tyuremnov IS, Morev AS (2019) Sistemy nepreryvnogo kontrolya uplotneniya grunta vibratsionnymi katkami (Continuous soil compaction control systems for vibrating rollers). Publishing House of YSTU, Yaroslavl
15. Yoo TS, Selig ET (1979) Dynamics of vibratory-roller compaction. J Geotech Eng Div ASCE 105(GT10):1211–1231
16. Saveliev SV, Buriy GG (2015) Metodika obosnovaniya rezhimov raboty dorozhnykh katkov s uchetom massy uplotnyaemogo grunta v zone aktivnogo deistviya vibratsii (A method for substantiating the operating regimes of road rollers, taking into account the mass of the compacted soil in the zone of active vibration). Stroitel'nye i dorozhnye mashiny, Moscow
17. Tarasov VN, Boyarkina IV, Boyarkin GN, Serebrennikov VS (2019) Vliyanie massy vertikal'nogo prigruga na kolebaniya vibroval'tsa pri uplotnenii materialov (The influence of the vertical loader mass on the vibrations of the vibrating tumbler during compaction of materials). Dinamika sistem, mekhanizmov i mashin, Omsk
18. Tyuremnov IS, Fyodorova DV, Morev AS, Tarasova NE (2017) Eksperimental'noe opredelenie chislennykh znachenii koeffitsienta uprugogo soprotivleniya sdvigu amortizatorov U150.030 dlya vibratsionnykh katkov (Experimental determination of numerical values of the elastic shear resistance rate of the shock absorbers U150.030 for vibrating rollers). Mechanizatsiya stroitel'stva, Moscow
19. Van Susante PJ, Mooney MA (2008) Capturing nonlinear vibratory roller compactor behavior through lumped parameter modeling. J Eng Mech-ASCE 134:684–693. [https://doi.org/10.1061/\(ASCE\)0733-9399\(2008\)134:8\(684\)](https://doi.org/10.1061/(ASCE)0733-9399(2008)134:8(684))
20. Tyuremnov IS, Morev AS, Furmanov DV (2019) On the justification of the value of the apparent mass of soil in rheological modeling of the process of soil compaction by a vibrating roller. J Phys: Conf Ser 1260:112033. <https://doi.org/10.1088/1742-6596/1260/11/112033>
21. Tyuremnov IS, Fyodorova DV, Morev AS (2019) Study of impact of amount of shock absorbers on parameters of vibrations of drum and frame of vibrating roller. In: Radionov

A, Kravchenko O, Guzeev V, Rozhdestvenskiy Y (eds) Proceedings of the 5th International Conference on Industrial Engineering (ICIE 2019). ICIE 2019. Lecture notes in mechanical engineering. Springer, Cham. https://doi.org/10.1007/978-3-030-22063-1_82



The Dynamic Model of Unbalanced Grinding Wheel

E. N. Kashirskaya^(✉), S. V. Antonov, and I. A. Ganichev

MIREA—Russian Technological University, 78, Vernadsky Avenue, Moscow 119454, Russia

Abstract. Today, the problem of ensuring a quality objective of manufactured products during abrasive processing using grinding wheels is still relevant. Experimental studies carried out by the authors of this work showed that the grinding wheel during its operating is changeable under the influence of cutting forces. The centrifugal force is created by an unbalanced mass rotating and dynamic forces that cause fluctuations in the relative distance between the tool and the workpiece. Based on this conclusion, a dynamic model of an unbalanced grinding wheel was proposed. This model is characterized by the description of the cutting point motion path of the grinding wheel based on the functional relation with the grinding modes. An analytical study of the problem of grinding with an unbalanced grinding wheel was carried out using a mathematical apparatus based on known physical relationships. First, the projections of the cutting forces on the coordinate axes were obtained. Further, the problem was solved for flat grinding, and the formula that describes the functional relation of the cutting force with the actual amount of ground material was obtained. The obtained calculation scheme allows it to be used for future research in the direction of technological process monitoring and analysis of grinding technological operations and allows theoretically investigating the behaviour of an unbalanced grinding wheel during operation, taking into account the abrasive elastic properties.

Keywords: Dynamic model · Grinding wheel · Unbalanced systems · Manufacturing · Abrasive · Mechanical engineering

1 Introduction

One of the tasks of modern machine-building enterprises is to ensure the quality of products specified by the production manager [1, 2], which is solved at all stages of its life cycle [3].

The grinding process, widely used in modern enterprises, is characterized by the fact that the task of ensuring the quality of the processed surface remains important due to the high requirements make demands on the product by the production manager in the way of close size tolerance in the technological process development [4, 5].

Despite the tendencies towards the implementation of Industry 4.0 concept, accompanied by the digitalization and intellectualization of production processes under grinding [6]. The problem of ensuring a quality objective of manufactured products in the process of abrasive processing remains urgent. Despite the achievements of scientific

and technical progress connected with high-precision grinding machines implementation, the problems of negative effects of the system parameters on the cutting process, which lead to a decrease in the quality of the processed surfaces, remain not completely resolved. Among such problems are the masses imbalance of rotating machine elements [7], vibration in the «workpiece-cutting tool» system [8], temperature effects [5] and others.

We can find different approaches for ensuring a quality objective at grinding process in scientific publications. The main difference between these approaches is the set of conditions under consideration that affect the cutting process [9, 10]. Such external influences need compensation in the general control system of processing, for example, as it is solved in [11, 12].

Thus, we can talk about the necessity of applying the modelling method to solve the problem of ensuring a quality objective of products [13], since using this method, it is possible to describe sufficiently close the process under consideration and in the future to design and configure the abrasive processing control system. This conclusion is confirmed by the practice of using modelling methods to solve problems in the field of mechanical engineering [14], where we can find examples of using mathematical [15] and simulation [16, 17] models. Future projected systems are built based on the technological processes monitoring systems [18, 19] using intelligent processing [20] and the concept of digital twins of processes and objects [21, 22].

A special place in the scientific practice is occupied by the study of oscillatory non-stationary processes at grinding processes [12, 23, 24] due to the complexity of their study and analysis. Scientific advances in this area apply to the problem of ensuring a quality objective of abrasive processing, which is solved in this work.

Previously, it has already studied the effects of an unbalanced grinding wheel on the machining process [8]. The vibration effect at the grinding process on the roughness and strength of the product after processing was considered in [25, 26]. Relations were established between the dynamic characteristics of a cutting process, and the laws for controlling the workpiece quality by regulating the grinding parameters were formed in papers [17, 27]. On the other hand [8, 28], the topology of the grinding wheel and the used abrasive grain were considered in [15]. The result of many works is the development of a self-balancing system for grinding wheels [12, 29, 30].

The scientific goal of this article is to develop a dynamic model of an unbalanced grinding wheel, taking into account the elastic properties of the abrasive.

2 The Experiment Data

The influence of vibrations at finishing grinding was studied experimentally according to the geometric accuracy of the surface workpiece. Compressor piston pins with a diameter of 50 mm and a length of 140 mm were chosen as samples. Grinding was carried out on an RSM 500 B CNC machine. Profilograms were taken from the surface of sixty machined parts. All of them indicated the presence of oscillations in the frequency range up to 100 Hz. Harmonic analysis of these profilograms made it possible to draw a frequency diagram of the oscillations (Fig. 1).

The histogram clearly shows two frequency ranges: 15–50 Hz and 85–110 Hz. The natural frequencies of the main elements of the machine are known:

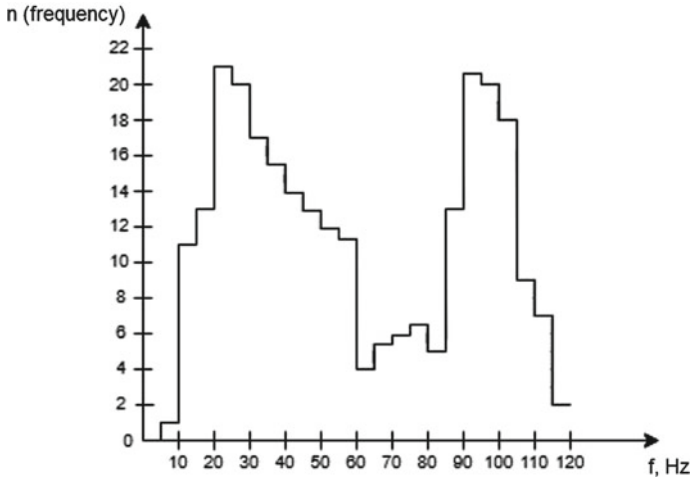


Fig. 1 Frequency diagram of the oscillations

- 25 Hz—the grinding wheel frequency,
- 30–45 Hz—the grinding wheel head frequency,
- 85–100 Hz—the spindle frequency,
- 100 Hz—the cutting knife frequency.

Consequently, the natural vibrations of the machine elements affect the shaping of the workpiece surface with the main effect being the vibrations of the grinding wheel and its spindle.

In the processing, the grinding wheel is exposed to several force factors: cutting forces, centrifugal force generated by a rotating unbalanced mass and dynamic forces that cause fluctuations in the relative distance between the tool and the workpiece.

3 The Dynamic Model Development

Let us consider the effect of cutting force. The cutting force can be represented by a power-law relation (1), which is most convenient for us since it provides a functional relation with the grinding modes, which allows carrying out analytical studies:

$$P = C_p V^{a_x} S^{a_s} t^{a_t}, \tag{1}$$

where

- V is the speed of the main cutting movement, m/min,
- S the longitudinal feed both for flat and circular grinding, mm/rev,
- t the cutting depth, mm,
- C_p the proportionality factor.

The projections of the cutting forces on the coordinate axes can be expressed by the following formulas:

$$\begin{aligned}
 P_x &= C_{P_x} V^{a_{v_x}} S^{a_{s_x}} t^{a_{t_x}} \\
 P_y &= C_{P_y} V^{a_{v_y}} S^{a_{s_y}} t^{a_{t_y}} \\
 P_z &= C_{P_z} V^{a_{v_z}} S^{a_{s_z}} t^{a_{t_z}}
 \end{aligned}
 \tag{2}$$

Considering further only the process of flat grinding, which cannot affect the generality of the solution to the problem, we note that the cutting force is functional to the actual thickness of the removed layer. To determine this value, we consider the grinding process in the presence of relative oscillations of the grinding wheel and the workpiece, leading to an error on the surface of the part. The vertical size of a processed part on a flat grinder is determined by a complex parametric relation [12] (3):

$$\begin{cases}
 X = V\tau + B \sin(\omega\tau + \varphi) + \frac{RA \cos \omega\tau}{\sqrt{A^2 \omega^2 \cos^2 \omega\tau + [V + B\omega \cos(\omega\tau + \varphi)]^2}} \\
 Y = A \sin \omega\tau - \frac{P[V + B\omega \cos(\omega\tau + \varphi)]}{\sqrt{A^2 \omega^2 \cos^2 \omega\tau + [V + B\omega \cos(\omega\tau + \varphi)]^2}}
 \end{cases},
 \tag{3}$$

where X is the horizontal coordinate of the point at which the vertical dimension of the part is determined,

- Y the vertical dimension of the part,
- V the longitudinal feed speed (machine table speed),
- τ the time parameter,
- A the vertical component of the vibration amplitude,
- B the horizontal component of the vibration amplitude,
- ω the frequency of the relative vibrations (rotation frequency of the grinding wheel),
- φ the initial phase of oscillations,
- R the radius of the grinding wheel.

This parametric relation can be replaced by an explicit function Y of X , having the same extreme points that gave the same waviness height:

$$Y = h - t_0 - A + H \left[1 - \left| \cos \left(\frac{\omega X}{2V} + \frac{\pi}{4} \right) \right| \right],
 \tag{4}$$

where

- t_0 is the specified cutting depth,
- h the initial height of the workpiece,
- H the height of the waviness of the processed surface [12].

In the absence of relative vibrations between the tool and the workpiece, the machined flat is located at a distance $Y = h - t_0$ from the table surface of the surface grinding machine (Fig. 2). With the presence of relative fluctuations between the grinding wheel and the workpiece, the actual cutting depth, which is one of the factors affecting the grinding accuracy, differs from the specified cutting depth.

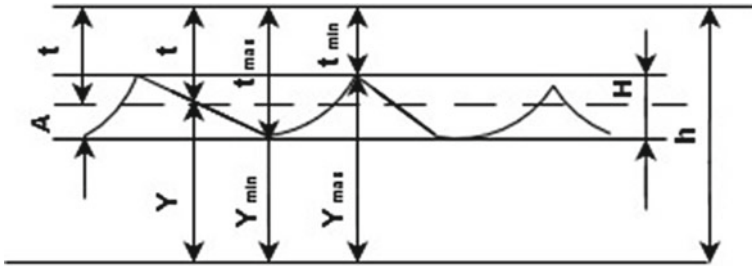


Fig. 2 Formation of waviness at the grinding process

Studies of the real surface formed on the part make it possible to determine the value of the actual cutting depth t , that is, the thickness of the removed layer, taking into account the fluctuations:

$$t = h - y_0 = t_0 + A - H \left[1 - \left| \cos \left(\frac{\omega x}{2V} + \frac{\pi}{4} \right) \right| \right], \quad (5)$$

The rotation of an unbalanced grinding wheel leads to the appearance of centrifugal force, which the projections on the coordinate axes are written as follows:

$$\begin{aligned} P_x &= D\omega^2 \sin \omega\tau + m\omega^2 X_0 \\ P_y &= D\omega^2 \cos \omega\tau + m\omega^2 Y_0, \\ P_z &= 0 \end{aligned} \quad (6)$$

where D is the value of the imbalance of the wheel, equal to the product of the grinding wheel mass by the distance between the gravity centre and the geometric wheel centre (in statics),

- ω the angular velocity of the circle,
- m the mass of the grinding wheel,
- τ the time,
- X_0, Y_0 coordinates of the relative movement of the grinding wheel and workpiece, restricted on time.

The dynamic forces that cause relative oscillations of the tool and the workpiece can be expressed by various functions depending on the selected rated model of the grinding wheel. The representation of the grinding wheel as a single-mass model leads to obtaining projections of dynamic forces in the following form:

$$\begin{aligned} P_x &= m \frac{d^2 X_0}{d\tau^2} \\ P_y &= m \frac{d^2 Y_0}{d\tau^2}, \\ P_z &= m \frac{d^2 Z_0}{d\tau^2} \end{aligned} \quad (7)$$

We consider that we can get the following equations with relative vibrations of the tool and workpiece:

$$X_0 = V\tau + B \sin(\omega\tau + \varphi)$$

$$\begin{aligned} Y_0 &= A + \sin \omega \tau \\ Z_0 &= C \sin \alpha \tau \end{aligned} \tag{8}$$

Then, we obtain expressions for the projection of the total force effect on the grinding wheel:

$$\begin{aligned} P_x &= C_{P_x} V^{av_x} S^{as_x} t^{at_x} + D\omega^2 \sin \omega \tau + m\omega^2 x_0 - mB\omega^2 \sin(\omega \tau + \varphi) \\ P_y &= C_{P_y} V^{av_y} S^{as_y} t^{at_y} + D\omega^2 \cos \omega \tau + m\omega^2 y_0 - mA\omega^2 \sin \omega \tau \\ P_z &= C_{P_z} V^{av_z} S^{as_z} - mC\alpha^2 \sin \alpha \tau \end{aligned} \tag{9}$$

A model of a grinding wheel with a random three-dimensional distribution of cutting edges can be investigated only by methods of mathematical statistics, and a model of a grinding wheel with lumped or uniformly distributed parameters can be investigated by methods of vibration theory.

4 The Elastic Properties of the Grinding Wheel

If we consider the grinding wheel as a single-mass model, we do not take into account the natural elastic properties of the grinding wheel. The elastic properties of the grinding wheel should be expressed by the elastic constant of fixing the abrasive grains since each grain is under load and moves almost independently in the grinding machine site. In this point of view, a model of a grinding wheel in the form of a two-mass system is proposed (Fig. 3), where m is the mass of the grinding wheel reduced to two positions: $\frac{m}{2}$ is concentrated in the centre of the circle, and $\frac{m}{2}$ is distributed along the periphery ($m_{per} = \frac{m}{4\pi R}$),

- C the hardness of the grinding wheel,
- K the vibration damping coefficient,
- P_{dis} the force from unbalance, determined by (6),
- P_{cut} the cutting force determined by (2).

The equation of motion of an unbalanced grinding wheel during operation is written as follows:

$$\begin{cases} \frac{m}{2} Y_0 + K(Y_0 - Y) + C(Y_0 - Y) = -P_{dis} \\ \frac{4\pi REY}{m} \frac{\partial^4(Y - Y_0)}{\partial X^4} + \frac{\partial^2 Y}{\partial t^2} = P_y \end{cases} \tag{10}$$

where

$$\begin{aligned} P_{dis} &= D\omega^2 \cos \omega t + m\omega^2 y_0, \\ P_y &= C_{P_y} V^{av_y} S^{as_y} t^{at_y}. \end{aligned}$$

The solution is sought in the form:

$$Y(x, \tau) = x(x)T(\tau).$$

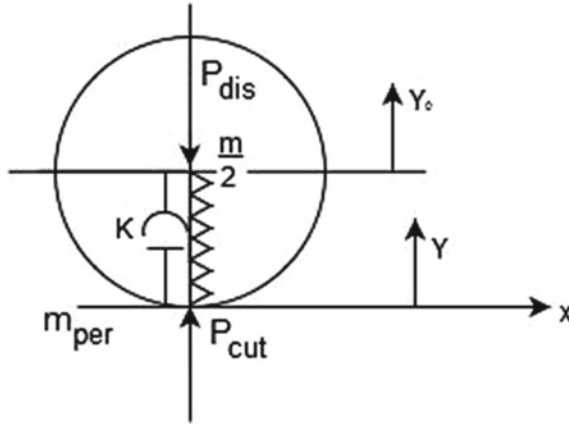


Fig. 3 Two-mass model of the grinding wheel

Boundary conditions with $x = 0$:

$$x'' = 0, 4\pi REYX'' = cX.$$

The solution looks like this:

$$\begin{aligned} X_K(x) &= C_{1K}K_1(\beta X) + C_{2K}K_2(\beta X) + C_{3K}K_3(\beta X) + C_{4K}K_4(\beta X) \\ T_K(\tau) &= C_{5K} \sin(P_K \tau + \psi_K) \\ \beta &= \sqrt[4]{\frac{mP^2}{4\pi REY}} \end{aligned}$$

The system of Eqs. (10) is solved numerically by the finite difference method. The found function Y describes the vertical movement of the cutting point of the grinding wheel.

5 Conclusions

No matter how accurate the machines are, the grinding process is always accompanied by different disturbances. Therefore, further improving the grinding accuracy is possible only with the use of automatic control and diagnostics, which determines the relevance of this study. To diagnose the process, a calculation scheme was proposed, which allowed investigating theoretically the behaviour of an unbalanced grinding wheel taking into account the elastic properties of the abrasive.

The proposed dynamic model takes into account not only cutting parameters but also system vibration parameters. The simulation results can be used to solve the problems of optimizing the grinding process, predicting the quality of manufactured products and auto-balancing systems development.

Acknowledgements. The reported study was funded by RFBR, project number 19-37-90053.

References

- Hou YL, Li CH, Lu BH (2009) Study on the surface quality of finished by abrasive jet with grinding wheel as restraint. In: 2009 International conference on measuring technology and mechatronics automation. IEEE, p 322–325. <https://doi.org/10.1109/ICMTMA.2009.306>
- Kashirskaya EN, Kurnasov EV, Kholopov VA et al (2017) Methodology for assessing the implementation of the production process. In: 2017 IEEE II international conference on Control in Technical Systems (CTS). IEEE, p 232–235. <https://doi.org/10.1109/CTSYS.2017.8109533>
- Okita T, Kawabata T, Murayama H et al (2019) A new concept of digital twin of artifact systems: synthesizing monitoring/inspections, physical/numerical models, and social system models. *Procedia CIRP* 79:667–672. <https://doi.org/10.1016/j.procir.2019.02.048>
- Chen H-G, Shen J-Y, Chen W-H et al (2019) Grinding chatter detection and identification based on BEMD and LSSVM. *Chin J Mech Eng* 32:1. <https://doi.org/10.1186/s10033-018-0313-7>
- Panaioti VA, Meshkov VV, Kurnasov EV (2020) Lowering the temperature in grinding high-speed steel. *Russ Eng Res* 40:308–312. <https://doi.org/10.3103/S1068798X20040140>
- Byrne G, Ahearne E, Cotterell M et al (2016) High performance cutting (HPC) in the new era of digital manufacturing—a roadmap. *Procedia CIRP* 46:1–6. <https://doi.org/10.1016/j.procir.2016.05.038>
- Pan X, Lu J, Huo J et al (2020) A review on self-recovery regulation (SR) technique for unbalance vibration of high-end equipment. *Chin J Mech Eng* 33:89. <https://doi.org/10.1186/s10033-020-00514-7>
- Cao Y, Guan J, Li B et al (2013) Modeling and simulation of grinding surface topography considering wheel vibration. *Int J Adv Manuf Technol* 66:937–945. <https://doi.org/10.1007/s00170-012-4378-7>
- Zhang M, Yao Z (2015) Force characteristics in continuous path controlled crankpin grinding. *Chin J Mech Eng* 28:331–337. <https://doi.org/10.3901/CJME.2015.0107.007>
- Liu Y, Fan J, Miao W (2013) Soft compensation for CNC crankshaft grinding machine tool. *Adv Mech Eng* 5:254709. <https://doi.org/10.1155/2013/254709>
- Wang L, Wang D, Wang B et al (2020) Development of an oscillating grinding machine tool based on error analysis. *Sci China Technol Sci* 63:912–922. <https://doi.org/10.1007/s11431-019-1481-8>
- Kashirskaya EN, Kholopov VA, Antonov SV et al (2020) Transient oscillatory processes at the balancing device operation of abrasive wheel grinder. *J Phys Conf Ser* 1679:022070. <https://doi.org/10.1088/1742-6596/1679/2/022070>
- Peng K, Wang B, Dong J (2017) An efficient quality-related fault diagnosis method for real-time multimode industrial process. *J Control Sci Eng* 2017. <https://doi.org/10.1155/2017/9560206>
- Kholopov VA, Kashirskaya EN, Gusev MV (2018) Optimization of configuration of industrial ethernet networks during design of the automated production management system. *Russ Technol J* 6(2):20–31. <https://doi.org/10.32362/2500-316X-2018-6-2-20-31>
- Chen Y, Chen X, Xu X et al (2018) Quantitative impacts of regenerative vibration and abrasive wheel eccentricity on surface grinding dynamic performance. *Int J Adv Manuf Technol* 96:2271–2283. <https://doi.org/10.1007/s00170-018-1778-3>
- Kashirskaya EN, Kholopov VA, Shmeleva AG et al (2017) Simulation model for monitoring the execution of technological processes. In: 2017 IEEE II International conference on control in technical systems (CTS). IEEE, p 307–310. <https://doi.org/10.1109/CTSYS.2017.8109553>
- Sun C, Niu Y, Liu Z et al (2017) Study on the surface topography considering grinding chatter based on dynamics and reliability. *Int J Adv Manuf Technol* 92:3273–3286. <https://doi.org/10.1007/s00170-017-0385-z>

18. Ragavanantham S, Sampathkumar S, Kumar SS (2016) Optimisation of grinding parameters for wheel loading and dressing. In: 2016 International conference on electrical, electronics, and optimization techniques (ICEEOT). IEEE, p 2341–2343. <https://doi.org/10.1109/ICEEOT.2016.7755112>
19. Lin Y-K, Wu B-F, Chen C-M (2018) Characterization of grinding wheel condition by acoustic emission signals. In: 2018 International conference on system science and engineering (ICSSE). IEEE, p 1–6. <https://doi.org/10.1109/ICSSE.2018.8520249>
20. Lee C-H, Jwo J-S, Hsieh H-Y et al (2020) An intelligent system for grinding wheel condition monitoring based on machining sound and deep learning. *IEEE Access* 8:58279–58289. <https://doi.org/10.1109/ACCESS.2020.2982800>
21. Kholopov VA, Antonov SV, Kashirskaya EN (2019) Application of the digital twin concept to solve the monitoring task of machine-building technological process. In: 2019 International Russian automation conference (RusAutoCon). IEEE, p 1–5. <https://doi.org/10.1109/RUSAUTOCON.2019.8867800>
22. Kholopov VA, Antonov SV, Kurnasov EV et al (2019) Digital twins in manufacturing. *Russ Eng Res* 39:1014–1020. <https://doi.org/10.3103/S1068798X19120104>
23. Berdnikov VP (2017) Algorithm of determination of non-stationary nonlinear systems full stability areas. *Russ Technol J* 5(6):55–72. <https://doi.org/10.32362/2500-316X-2017-5-6-55-72>
24. Jung D, DeSmidt H (2011) Hybrid adaptive rotor imbalance vibration control via passive autobalancer and active bearing actuation. In: 23rd Biennial conference on mechanical vibration and noise, parts A and B. ASMEDE, vol 1, p 1045–1052. <https://doi.org/10.1115/DETC2011-48629>
25. Sun C, Duan J, Lan D et al (2018) Prediction about ground hardening layers distribution on grinding chatter by contact stiffness. *Arch Civ Mech Eng* 18:1626–2164. <https://doi.org/10.1016/j.acme.2018.06.010>
26. Ma Y, Yang J, Li B et al (2017) An analytical model of grinding force based on time-varying dynamic behavior. *Int J Adv Manuf Technol* 89:2883–2891. <https://doi.org/10.1007/s00170-016-9751-5>
27. Guo M, Jiang X, Ding Z et al (2018) A frequency domain dynamic response approach to optimize the dynamic performance of grinding machine spindles. *Int J Adv Manuf Technol* 98:2737–2745. <https://doi.org/10.1007/s00170-018-2444-5>
28. Zhang L, Kang M, Tang W (2019) Effect analysis of grinding wheel under different dressing parameters on surface grinding quality. In: 2019 IEEE International conference on computation, communication and engineering (ICCCCE). IEEE, 113–116. <https://doi.org/10.1109/ICCCCE48422.2019.9010888>
29. Chen S-P, Wang Z-Z, Yu H et al (2018) Research on automatic compensation technology for eccentricity of grinding wheel. *Int J Precis Eng Manuf* 19:1201–1209. <https://doi.org/10.1007/s12541-018-0141-9>
30. Zhang X, Liu X, Zhao H (2018) New active online balancing method for grinding wheel using liquid injection and free dripping. *J Vib Acoust* 140. <https://doi.org/10.1115/1.4037955>



Combined Extraction of Liquid from Wet Leather Semifinished Products

A. M. Nabiev^(✉)

Institute of Mechanics and Seismic Stability of Structures Academy of Sciences of the Republic of Uzbekistan, 33, Durmon yuli street, Tashkent, Uzbekistan

Abstract. The article provided the experimental pressing of moisture leather semifinished products after chrome tanning was conducted in combination with fibrous materials put between them. The technological process of pressing a semifinished leather product to the bend on the base plate along the vertical plane between the roller pair is considered. The regularity of the pressure change between the squeezing rolls during the processing of semifinished leather on the stand of a vertical roller machine is studied experimentally. Bend on the base plate, the factors acting on the processed material in the contact zone with the roller pair of the roller machine for processing leather are investigated. The experimental studies were conducted on a specially designed and manufactured stand using modern electronic measuring equipment aimed to apply the results in further theoretical calculations. The methods of mathematical statistics were used to process experimental results. The mathematical dependences of the amount of liquid removed for each semifinished leather product on the feeding speed and the pressing force of the pressing rollers were obtained. The use of the results obtained will increase the productivity of the technological process of extracting moisture from the leather semifinished product, taking into account its physical and mechanical properties. The results of the experiment can be used in design, research, and development institutions and at enterprises of the leather industry.

Keywords: Roll pair · Leather semifinished product · Two-layer pressing · Moisture-extracting material · Pressing force · Feeding speed · Planning of experiment

1 Introduction

In the leather industry, the defects in semifinished or finished leather products depend on the technical level of the equipment. As the geometric dimensions, weight and physical and mechanical properties of each piece of the processed semifinished leather product are different and non-uniform. In modern leather production, both new and outdated designs of technological machines are used for processing semifinished leather products.

The pressing roller machines used in the leather industry are expensive and designed to process certain types of semifinished leather products. Therefore, they do not always meet the requirements of domestic manufacturers of leather products and are not free from shortcomings.

To improve the design of the pressing machines, it developed a new design of the roller machine for the mechanical processing of the semifinished leather products.

To perfect the technological process of extracting excess liquid from semifinished products, it developed a method of multilayer liquid removal in the form of a package [1]. The latter consists of alternating layers of moisture-removing wet cloths and leather semifinished products. It should be noted that this method can be used in various combinations. The purpose of this work is to determine rational parameters for intensifying the technological process of pressing wet semi-finished leather products [2–5].

Improvement of existing designs and implementation of new technological equipment are the directions of innovative development of enterprises (finished products manufacturers). They have to be adapted to modern requirements of consumers and ensure the competitiveness of leather products. In solving these issues, it is necessary to strive to improve the quality of processing of leather raw materials [6–15].

2 Research Methodology

The experiment was conducted on a special stand, where the pair of rollers was installed horizontally, and the base plate was made of a metal sheet 0.005 m thick, 0.1 m wide and 0.30 m long (Fig. 1).

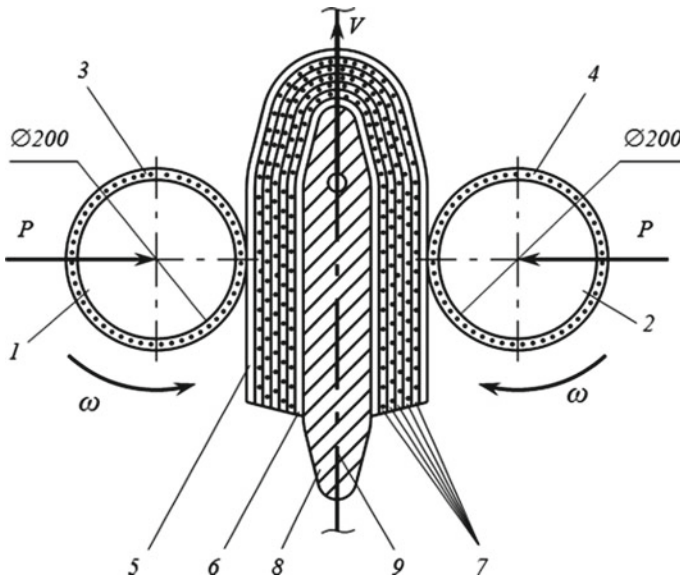


Fig. 1 Scheme of a multilayer package feeding between the pressing rollers: 1, 2—pressing rollers; 3, 4—moisture-removing material; 5—the first layer of the semifinished leather product; 6—the second layer of the semifinished leather product; 7—moisture-removing material of the LASCH brand; 8—base plate; 9—traction chain

The material of the semifinished leather product for the experiment was a medium-weight slow hide after chrome tanning and splitting. According to the International

Standards ISO 2588-85, the required number of samples of the semifinished leather product was determined according to the following formula:

$$n = 0.2\sqrt{x} \quad (1)$$

where x is the number of the semifinished leather products for the experiment, 2500 pieces, $n = 10$ pieces. The strips 0.05×0.25 m from these ten semifinished leather products were cut out with a cutter across the spine line and numbered. The strips were assembled into groups of five pieces according to the scheme given in [16]. The experiment was conducted as follows: A semifinished leather product was laid on a metal base plate, then came five layers of LASCH fiber cloth of a total thickness of 0.02 m. Afterward a layer of the semifinished product is delivered. After that, the stand was turned on, and the compression of the springs was calibrated to the desired pressure. The speed was controlled by an autotransformer, and the rotational speed of the rollers was regulated by the clock-type tachometer TCh10P. Preliminarily, control samples of the semifinished leather product were fed, and then the compression of the springs was measured, i.e., the deviation from the set values. In case if the deviation exceeded 3%, the compression of the springs was adjusted by tightening the nuts. Samples were weighed on VLTE-500 laboratory scales before and after pressing with the resolution 0.01 g (ISO-9001).

Processing the experimental results, the method of D-optimal planning of the second order was used by applying the K. Kano design matrix, which provides the highest accuracy in the estimates of the regression coefficients [17]. It was taken into account that Kano's design matrix provides for a variation of factors at three levels: lower (–), zero (0) and upper (+) levels, which is appropriate for this study. Considering the abovementioned, the process of liquid removal was studied taking into account two factors: x_1 —the pressure intensity P , kN/m; x_2 —the feeding speed, V , m/s. The range of pressure change was from 32 to 96 kN/m. The speed of pressing rollers is from 0.17 to 0.34 m/s obtained in the analysis of roller pressing machines from different sources. In the study, the diameter of the pressing rollers was 0.2 m, and the coating from BM cloth was 0.01 m thick.

The required number of measurements (the number of replicates) was selected before the experiment, using the methods of mathematical statistics, which provided the required accuracy.

The working matrix was drawn up according to the K. Kano design matrix for a two-factor experiment. Factors were encoded according to the following formula:

$$x_i = \frac{c_i - c_{i0}}{t_0} \quad (2)$$

where x_i is the encoding of the factor value; c_i , c_{i0} are the natural values of the factor at the current and zero levels; t_0 is the natural value of the factor variation range. The levels and ranges of variation of the experimental factors are given in Table 1.

The chain function is approximated by the polynomial

$$y = b_0 + \sum_{i=1}^k b_i x_i + \sum_{i,j=1}^k b_{ij} x_i \cdot x_j + \sum_{i=1}^k b_{ii} x_i^2 \quad (3)$$

Table 1 Levels and intervals of variation of experimental factors

Index	Factor values encoding	Natural values of factors	
		x_1 , kN/m;	x_2 , m/s
Upper level	+	96	0.340
Basic level	0	64	0.255
Lower level	-	32	0.170
Variation range		32	0.085

where y is the amount of moisture removed in coded form; b_0, b_i, b_{ij} and b_{ii} are the regression coefficients.

After the working matrix implementation, the arithmetic mean values were obtained (Table 2). The homogeneity of variance was checked using the Cochran test with a probability $\alpha = 0.95$. Knowing the total number of variance estimates N and the number of degrees of freedom $f = n - 1$, we determine $G_T = 0.358$ according to the table given in [17].

$$G_{cal1} = \frac{S_{max}^2}{\sum_1^N S_i} = \frac{7.685}{49.265} = 0.156 < G_T = 0.358 \tag{4}$$

$$G_{cal2} = \frac{8.58}{51.73} = 0.166 < G_T = 0.358 \tag{5}$$

3 Experiment Results

First of all, it determined the regression coefficients b_0, b_i, b_{ij} and b_{ii} from the table given in [17] and Table 2.

For the first layer of the semifinished leather product, the coefficients are $b_0 = 23.9545; b_{11} = 0.1501; b_{22} = -0.5501; b_1 = 2.9657; b_2 = -2.7510; b_{12} = -0.775$.

For the second layer of the semifinished leather product, the coefficients are $b_0 = 22.9182; b_{11} = 0.3186; b_{22} = -0.66686; b_1 = 3.0530; b_2 = -2.7362; b_{12} = -0.85$.

The regression equation in a coded form is as follows.

For the first layer of the semi-finished leather product

$$y_1 = 23.9545 + 0.1501x_1^2 + 0.5501x_2^2 + 2.9657x_1 - 2.7510x_2 - 0.775x_1x_2 \tag{6}$$

For the second layer of the semi-finished leather product

$$y_2 = 22.9182 + 0.3186x_1^2 + 0.6686x_2^2 + 3.0530x_1 - 2.7362x_2 - 0.85x_1x_2 \tag{7}$$

substituting $x_1 = \frac{P-64}{32}$, where P is the pressing force of the pressing rollers and $x_2 = \frac{V-0.255}{0.085}$, where V is the feeding speed of wet leather semifinished products between the

Table 2 Experiment design matrix

No.	P, x_1	V, x_2	No. of leather product	Measurement results, %							$\sum_1^n (y - \bar{y})^2$	S_{er}^2	\hat{y}_{cal}	$\bar{y} - \hat{y}_{cal}$	$(\bar{y} - \hat{y}_{cal})^2$
				y_1	y_2	y_3	y_4	y_5	y_6	\bar{y}					
1	0	0	1	22.1	23.8	24.5	21.8	24.8	23.4	11.18	2.795	23.95	0.5	0.25	
			2	22.6	23.8	25.0	20.3	20.8	22.5	15.68	3.29	22.9	0.4	0.16	
2	+	+	1	20.8	23.6	23.2	26.8	25.6	24.0	21.44	5.36	24.1	0.1	0.01	
			2	20.4	22.1	25.8	23.3	25.9	23.5	23.26	5.815	23.4	0.01	0.01	
3	-	+	1	18.4	20.5	18.2	22.6	16.8	19.3	20.6	5.15	19.7	0.4	0.16	
			2	21.5	17.2	19.0	20.6	16.2	18.9	32.55	8.138	19.0	0.1	0.01	
4	-	-	1	24.8	22.0	21.8	23.8	25.1	23.5	9.48	2.37	23.7	0.2	0.04	
			2	24.6	20.7	24.2	18.2	24.8	22.5	34.32	8.58	22.7	0.2	0.04	
5	+	-	1	34.5	28.0	30.4	30.5	33.4	31.3	27.62	6.91	31.1	0.02	0.04	
			2	28.8	30.0	32.5	28.5	32.7	30.5	15.98	3.955	30.5	0	0	
6	+	0	1	30.6	26.4	25.4	24.0	29.1	27.1	29.24	7.31	27.1	0	0	
			2	25.1	25.0	28.8	25.8	26.3	26.2	9.58	2.395	26.3	0.1	0.01	
7	0	+	1	22.4	22.8	18.1	20.0	24.2	21.5	23.6	5.9	21.8	0.03	0.09	
			2	23.5	18.0	18.8	19.3	23.6	20.7	29.11	7.278	20.9	0.2	0.04	
8	-	0	1	18.1	23.4	23.4	24.0	18.1	21.6	30.74	7.685	21.1	0.5	0.25	
			2	22.1	18.0	18.6	24.1	21.2	20.8	25.24	6.355	20.2	0.6	0.36	
9	0	-	1	24.1	27.3	29.1	30.0	29.5	28.0	23.16	5.79	27.3	0.7	0.49	

(continued)

Table 2 (continued)

No.	P, x_1	V, x_2	No. of leather product	Measurement results, %						$\sum_1^n (y - \bar{y})^2$	S_{er}^2	\hat{y}^{cal}	$\bar{y} - \hat{y}^{cal}$	$(\bar{y} - \hat{y}^{cal})^2$
				y_1	y_2	y_3	y_4	y_5	\bar{y}					
			2	24.4	27.2	25.0	29.8	28.6	27.0	21.2	5.3	26.3	0.7	0.049
			1							$\Sigma 197.06$	$\Sigma 49.265$			$\Sigma 1.33$
			2							$\Sigma 206.92$	$\Sigma 51.730$			$\Sigma 1.12$

rotating pressing rollers, we obtain the equations of the amount of moisture removed from wet leather semifinished products between the rotating pressing rollers in natural form.

The hypothesis about the adequacy of the equations obtained was tested using the Fisher criterion at a confidence level of $\alpha = 0.95$ [17–20].

$$F_{\text{cal}} = \frac{S_{\text{ad}}^2}{S_{\{y\}}^2} < F_T \quad (8)$$

where S_{ad}^2 is the residual variance or the variance of adequacy; $S_{\{y\}}^2$ is the variance reproducibility.

S_{ad}^2 and $S_{\{y\}}^2$ were determined from Tables 1 and 2 as follows:

$$S_{\text{ad}}^2 = \frac{\sum_1^N n(\bar{y} - \hat{y})^2}{\frac{N-(x+2)(x+1)}{2}} \quad (9)$$

$$S_{\{y\}}^2 = \frac{\sum_1^N \sum_1^n (y - \bar{y})^2}{N(n-1)} \quad (10)$$

where N is the total number of experiments; k is the number of factors; n is the number of replicates in the experiment; y is the result of a separate observation; \bar{y} are the arithmetic mean values of the results of experiment; \hat{y} are the calculated values of the criterion according to the regression equation.

For the first layer of the semifinished leather product

$$S_{\text{ad}1}^2 = \frac{5 \cdot 1.33}{3} = 2.217; S_{\{y\}1}^2 = \frac{197.06}{36} = 5.474;$$

$$F_{\text{cal}1} = \frac{2.217}{5.474} = 0.405; F_{\text{cal}2} = 0.405 < F_T = 2.88.$$

For the second layer of the semifinished leather product

$$S_{\text{ad}2}^2 = \frac{5 \cdot 1.12}{3} = 1.86; S_{\{y\}2}^2 = \frac{206.92}{36} = 5.748;$$

$$F_{\text{cal}2} = \frac{1.86}{5.748} = 0.324; F_{\text{cal}2} = 0.324 < F_T = 2.88.$$

4 Discussion of Results

As the regression equation can be considered suitable with a 95% confidence level, which in the named form after decoding, it has the following form.

For the first layer of the semi-finished leather product

$$\begin{aligned} \Delta W_1 = & 27.1778 + 0.0001466P^2 + 76.1384V^2 \\ & + 0.1512P - 52.9623V - 0.2849PV, \end{aligned} \quad (11)$$

For the second layer of the semi-finished leather product

$$\Delta W_2 = 27.2126 + 0.0003111P^2 + 92.5398V^2 + 0.1353P - 59.3859V - 0.3125PV. \tag{12}$$

A graph of the dependence of the amount (in %) of removed moisture ΔW from two layers of wet leather semifinished products at different feeding speeds V and pressing forces P (Fig. 2) is plotted.

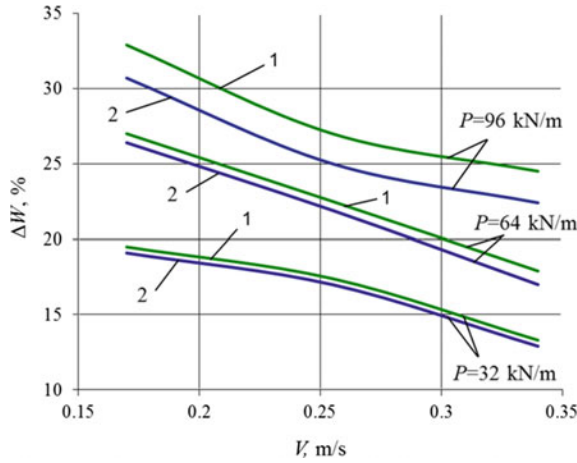


Fig. 2 Dependence of the amount of removed moisture ΔW on the feeding speed V of the leather semifinished products under the pressure of the pressing rollers: $P = 32$ kN/m; $P = 64$ kN/m; $P = 96$ kN/m. 1—the first layer of the semifinished leather product; 2—the second layer of the semifinished leather product

The regression equations were obtained for the first layer of a semifinished leather product (11) and for the second layer of a semifinished leather product (12) in the named form. The minimum extraction of excess liquid in the experiment was approximately 18.9%. The maximum moisture content of a semifinished leather product from the bovine hide of average weight was 73%. The required residual moisture was 60%, so, it was necessary to remove 13%, but more than 18.9% was removed in the experiment. This means that it is possible to remove excess liquid from wet leather semifinished products with a pressing force of the pressing rollers of 32 kN/m and a feeding speed of 0.2 m/s. This made it possible to increase for more than 3 times the productivity of the technological process of moisture removal from wet leather semifinished products. It should be noted that the samples cut from the bovine hide of medium weight for leather of the shoe upper, compared with existing pressing roller machines.

5 Conclusions

The results of experiments (Fig. 2) showed that with an increase in the thickness of the moisture-removing material between two wet leather semifinished products, the

efficiency of removing excess liquid significantly increases. For example, in contrast to a two-layer moisture-removing material, in a five-layer moisture-removing material put between two wet leather semifinished products, the maximum amount of liquid extracted during pressing increases by 7%. The possibility of pressing out excess liquid from two leather semifinished products (fed by layers) on a base plate in one pass between rotating pressing rollers has been experimentally confirmed. That will increase the productivity of the pressing roller machines by 2 times or more. The experimental results are also suitable for use in real production since the tests were performed as close as possible to industrial conditions. The obtained results of the experimental study will be used in projecting new industrial designs of the pressing roller machine. In the future, it will be tested at small business enterprises specialized in the leather tannery.

References

1. Amanov TY, Bahadirov GA, Tsoy GN, Nabiev AM (2011) Method of extracting moisture from wet leather. Patent RUz for invention No. IAP 04451, Published in Patent Bulletin No. 12. <http://baza.ima.uz/home/bulletin>
2. Sokolovsky AR (2010) Development of methods and improvement of means for studying the physical and mechanical properties of fiber-porous materials of light industry. Dissertation, Moscow. <https://www.dissercat.com/content/razvitie-metodov-i-sovershenstvovanie-sredstv-issledovaniya-fiziko-mekhanicheskikh-svoistv-v>
3. Amanov AT, Bahadirov GA, Amanov TY, Tsoy GN, Nabiev AM (2019) Determination of strain properties of the leather semi-finished product and moisture-removing materials of compression rolls. *J Mater*. <https://doi.org/10.3390/ma12213620>
4. Bahadirov G, Tsoy G, Nabiev A, Umarov A (2020) Experiments on moisture pressing from a leather semi-finished product. *IJRTE*. <https://doi.org/10.35940/ijrte.E6125.018520>
5. Danylkovych A, Bilinskiy S, Potakh Y (2018) Plasticification of leather semifinished chrome tanning using biocatalytic modifier. *EUREKA: Phys Eng*. <https://doi.org/10.21303/2461-4262.2018.00527>
6. Bahadirov GA, Sultanov TZ, Abdurkarimov A (2020) Comparative analysis of two gear-lever differential inter-roller transmission mechanisms. *IOP Conf Ser: Earth Environ Sci* 614:012102. <https://doi.org/10.1088/1755-1315/614/1/012102>
7. Bahadirov GA, Sultanov TZ, Abdurkarimov A (2020) Kinematic analysis of tooth-lever differential transmission mechanisms. *IOP Conf Ser: Earth Environ Sci* 614:012101. <https://doi.org/10.1088/1755-1315/614/1/012101>
8. Bahadirov G, Sultanov T, Umarov B, Bakhadirov K (2020) Advanced machine for sorting potatoes tubers. *IOP Conf Ser: Mater Sci Eng* 883:012132. <https://doi.org/10.1088/1757-899X/883/1/012132>
9. Mavlonov T, Akhmedov A, Saidakhmedov R, Bakhadirov K (2020) Simulation modelling of cold rolled metal strip by asymmetric technology. *IOP Conf Ser Mater Sci Eng* <https://doi.org/10.1088/1757-899X/883/1/012194>
10. Covington AD, Wise WR (2020) Current trends in leather science. *J Leather Sci Eng* 2:28. <https://doi.org/10.1186/s42825-020-00041-0>
11. Rigueto CVT, Rosseto M, Krein DDC et al (2020) Alternative uses for tannery wastes: a review of environmental, sustainability, and science. *J Leather Sci Eng* 2:21. <https://doi.org/10.1186/s42825-020-00034-z>
12. Navarro D, Wu J, Lin W et al (2020) Life cycle assessment and leather production. *J Leather Sci Eng* 2:26. <https://doi.org/10.1186/s42825-020-00035-y>

13. Appiah-Brempong M, Essandoh HMK, Asiedu NY et al (2020) An insight into artisanal leather making in Ghana. *J Leather Sci Eng* 2:25. <https://doi.org/10.1186/s42825-020-00039-8>
14. Ershov SV (2013) Dynamic loading of the roller pair to intensify the spinning process. Dissertation, Ivanovo. <https://www.dissercat.com/content/dinamicheskoe-nagruzhenie-vaikovoi-pary-dlya-intensifikatsii-protsesta-otzhima>
15. Darda IV (2004) Development of theoretical foundations for improving the technological equipment of leather and fur production. Dissertation, Moscow. https://rusneb.ru/catalog/000199_000009_002770921/
16. Golovteeva AA, Kutsidi DA, Sankin LB (1982) Laboratory workshop on chemistry and technology of leather and fur. Moscow. <https://www.twirpx.com/file/2792823/>
17. Tikhomirov VA (1974) Experiment planning and analysis. Moscow. <https://www.twirpx.com/file/236275/>
18. Wu CFJ, Hamada MS (2009) Experiments: planning, analysis, and optimization, 2nd edn. USA. <https://www.twirpx.com/file/895683/>
19. Beghetto V (2013) The leather industry: a chemistry insight part I: an overview of the industrial process. *Sciences at Ca' Foscari* 12–22. <https://doi.org/10.7361/SciCF-448>
20. Farooq MA, Nóvoa, H, Araújo A, Tavares SMO (2016) An innovative approach for planning and execution of pre-experimental runs for design of experiments. *Eur Res Manage Bus Econ*. <https://doi.org/10.1016/j.iedee.2014.12.003>



Experimental Determination of the Influence of Fibrous Material on the Dehydration of Wet Semifinished Leather Product

G. N. Tsoy^(✉)

Institute of Mechanics and Seismic Stability of Structures of the Academy of Sciences of the Republic of Uzbekistan, 33, Durmon yuli str., Tashkent, Uzbekistan100125

Abstract. The article provides the results of test studies to determine the influence of parameters such as the feed velocity, the specific pressing force of squeezing rollers, and the use of capillary-porous materials on the squeezing process of wet semifinished leather products. Moisture removal tests were carried out using BM-grade fibrous materials with a guide bar instead of a metal base plate with or without a fibrous coating. The package consists of one layer of wet skin and a capillary-porous material, bent over the guide bar with vertical feed to the squeezing rollers. To conduct the test, the D-optimal method of processing test results was used with the Kano planning matrix for the tests. As a result of the study, a mathematical model of the process of squeezing out liquid from a wet skin, depending on the feed rate, the specific pressing force of the squeezing rollers, was obtained. For the experiment, we used squeezing rollers with a diameter of 0.2 m made of porous BM fabric with a guide bar instead of metal base plates. The analysis of the results of the pilot study showed that the moisture removal efficiency is higher with a guide rod than with a metal base plate. At that, it is possible to reduce the dimensions and weight of the squeezing machine. This study empirically revealed the advantage of the proposed technological process for extracting moisture from wet skin.

Keywords: Squeezing pair · Moisture squeezing · Semifinished leather product · Capillary-porous material · Test bench · Guide rod

1 Introduction

In references [1–13], studies of the physical and mechanical properties and characteristics of fibrous materials, for example, semifinished leather products, are considered. The skin structure is a complex of properties of a hide, which depends on physical and mechanical parameters such as weight, size, thickness, as well as on the conditions of animal care. Leather is the skin of an animal chemically, physically, and mechanically treated. After treating, the hide is used for the manufacture of clothing and footwear and as a building material for the dwellings of northern peoples, to protect them from heat and cold. Let us take a closer look at the skin structure. The quality of the hide depends

on physical and mechanical parameters and biological conditions of the animal care. It consists of two layers: upper and lower layers.

The condition of the lower layer determines the strength of the skin due to the density of the collagen content in the fibers; the upper layer is loose; it provides surface protection. More details about the animal skin structure can be found in [3, 4]. The study of literary sources allows a more correct approach to solving the problem of squeezing out liquid from a wet semifinished leather product. This article presents studies of the dependence of the skin parameters on the technological process of squeezing out moisture using new materials and technologies. It is possible to correctly produce high-quality leather and choose the optimal way of its processing knowing the structure of a hide, its upper and lower layers, physical parameters, and biological conditions of animal care.

The tasks of improving technological processes and technological machines for pressing wet skin are considered in [5–8, 13, 14]. The quality of the finished leather is influenced by all stages of technological processing. Therefore, after completing each stage, it is necessary to analyze the condition of the leather semifinished product. Experimental research in the tanning industry is aimed at solving complex multi-parameter problems, the result of which is determined by the rational modes of technological processes for treating leather raw materials. The physical and mechanical properties of semifinished leathers vary depending on their moisture content. Consequently, the technological operation of squeezing out excess moisture from a water-saturated leather semifinished product after its liquid processing significantly affects the quality of subsequent technological processes of treating, for example, planning, splitting, and drying. It is important to study physical and mechanical properties of the skin, its reticulate-fibrous structure, different types of skin, and their topographic sections. This pilot study demonstrates the advantage of using a capillary-porous material mounted on a porous fibrous material BM with a metal guide rod underneath. Wet skin is bent over this guide bar. The feeding chains move the skin vertically onto the squeezing rollers, covered with one layer of the capillary-porous material BM [9–11]. Currently, there are many designs of squeezing roller machines for removing liquid from moisture-saturated leather semifinished products. Their main drawback is low productivity. Therefore, we have developed a method in which a capillary-porous material is used; it is installed bent on a guide rod, to which a wet semi-finished leather product is fed; it is fed to processing zone vertically by chains between squeezing rollers, covered with one layer of capillary-porous material of BM brand.

2 Test Procedure and Research Results

The tests were conducted on a special bench, where the working elements were installed horizontally in a row. A conveying block consists of a capillary-porous material BM 0.01 m thick, fed to a metal guide rod. The rod is attached at both ends to the feeding chains (Fig. 1). The sample for squeezing consists of one layer of semifinished leather product with one layer of capillary-porous material made of BM brand cloth. For tests, tanned samples were taken from bovine hide of medium weight, after liquid treatment.

The sample for squeezing consists of one layer of semifinished leather product with one layer of capillary-porous material made of BM brand cloth. For tests, tanned samples



Fig. 1 Test bench for moisture squeezing out of semifinished leather products

were taken from bovine hide of medium weight, after liquid treatment. According to the established standards, the required amount of semi-finished leather was selected according to the following formula

$$n = 0.2\sqrt{x} \quad (1)$$

where x —is the number of samples of semifinished leather product for the test; 2500 pieces were taken from the batch, so $n = 10$ pieces. From these ten samples, strips were cut out with a cutter across the backbone line, 0.05×0.25 m in size, and the numbered samples were grouped in five pieces.

To conduct the tests, the topographic sections of the skin of medium samples were selected using the method of asymmetric fringe [15] in this case, and the effect of various parameters of the skin can be compared with the data obtained. During the test with BM monchon, a 0.01-m-thick capillary-porous material was mounted on a metal guide rod, followed by a wet semifinished product 0.004 m thick. The samples were weighed before and after squeezing on a VLTE-500 laboratory balance with a resolution of 0.01 g (ISO-9001).

In the study and processing of the results obtained, the method of test planning was used [16]. In the tests, two parameters were taken into account: x_1 —pressure intensity P , kN/m; x_2 —feed velocity V , m/s. The specific pressing force was taken in the range from 32 to 96 kN/m, the rotation speed of the squeezing rollers from 0.17 to 0.34 m/s for one semifinished leather product; the values were defined based on the analysis of the designs of various squeezing machines.

The selected diameter of the squeezing rollers was 0.2 m coated with 0.01-m-thick capillary-porous material made of BM brand cloth. Prior to the main test, the required number of parallel tests was selected by the method of mathematical statistics.

The test matrix was built in the following coded form

$$x_i = \frac{c_i - c_{i0}}{t_0} \tag{2}$$

where x_i is the encoding of parameter values; c_i, c_{i0} are the real values of parameters at the current and average levels; t_0 is the real value of the parameter variation interval.

Target functions are approximated by the following polynomial

$$y = b_0 + \sum_{i=1}^k b_i x_i + \sum_{i,j=1}^k b_{ij} x_i x_j + \sum_{i=1}^k b_{ii} x_i^2 \tag{3}$$

where y is the amount of removed moisture in coded form; b_0, b_i, b_{ij} , and b_{ii} are the regression coefficients.

The planning matrix was built in the following coded form. In tests, when assessing the influence of various parameters on the comparability of the data obtained, it is necessary to eliminate the dependence on the topographic sections of semifinished leather products.

To do so, the asymmetric fringe method was used in the selection of average samples. The levels and ranges of variation of test parameters are given in Table 1.

Table 1 Levels and ranges of variation of test parameters

Index	Coded value of parameters	Real values of parameters	
		x_1 , kN/m	x_2 , m/s
The highest level of parameters	+	96	0.340
The average level of parameters	0	64	0.255
The least level of parameters	-	32	0.170
Parameter variation interval		32	0.085

The homogeneity of the variance was checked using the Cochran test [15–17] with a probable error $\alpha = 0.95$. The number of variance estimates N and the number of degrees of freedom $f = k - 1$ are determined from [16], and $G_T = 0.358$ is calculated at $N = 9$; $f = 5 - 1 = 4$.

k is the number of the test replication.

$$S_{er}^2 = \frac{\sum_1^n (y - \bar{y})^2}{n - 1} \tag{4}$$

$$\sum_1^N S_i^2 = \frac{\sum_1^N \sum_1^n (y - \bar{y})^2}{N(n - 1)} \tag{5}$$

$$G_{cal} = \frac{S_{max}^2}{\sum_1^N S_i^2} = \frac{20.06}{74} = 0.278 < G_T = 0.358 \tag{6}$$

Consequently, the results of the experiments are reproducible. Determine the regression coefficients b_0, b_i, b_{ij} , and b_{ii} from Table 4 given in [15].

For a semi-finished leather product in coded form, they are $b_0 = 28.1764; b_{11} = -0.005592; b_{22} = 2.2444; b_1 = 2.4784; b_2 = 5.7364; b_{12} = 1.025$.

We obtain the following regression equations in coded form for the leather semifinished product

$$y = 28.1764 - 0.005592x_1^2 + 2.2444x_2^2 + 2.4784x_1 - 5.7336x_2 - 1.025x_1x_2 \quad (7)$$

Substituting $x_1 = \frac{P-64}{32}$, where P is the specific pressing force of the squeezing rollers and $x_2 = \frac{V-0.255}{0.085}$, where V is the feed velocity of wet leather semifinished products between the rotating squeezing rollers, we obtain in natural form the equations of the amount of moisture removed from wet leather semifinished products between rotating squeezing rollers.

The initial and final weights of semifinished leather products before and after the test are given in Table 2 at different values of the pressing force $x_1 (P)$ and velocity $x_2 (V)$.

Table 2 Weight of leather semifinished product before and after moisture extraction

No.	P, x_1	V, x_2	y_1, g_r		y_2, g_r		y_3, g_r		y_4, g_r		y_5, g_r	
			y_{st1}	y_{fin1}	y_{st2}	y_{fin2}	y_{st3}	y_{fin3}	y_{st4}	y_{fin4}	y_{st5}	y_{fin5}
1	0	0	84.5	56.1	97.4	66.6	69.0	50.3	70.7	51.3	88.8	60.8
2	+	+	88.4	64.5	80.1	59.0	98.2	67.7	72.9	51.8	98.0	72.2
3	-	+	77.7	61.6	79.5	40.3	80.0	61.8	82.7	65.2	91.5	69.5
4	-	-	81.6	56.7	87.5	63.3	76.5	49.3	75.0	46.9	84.9	56.6
5	+	-	88.3	54.2	93.9	59.1	79.6	38.3	61.8	35.2	87.7	52.7
6	+	0	70.1	45.7	76.1	53.6	75.8	55.8	87.5	61.6	94.2	63.9
7	0	+	72.7	54.1	65.0	49.6	95.5	69.6	73.2	56.4	86.1	65.3
8	-	0	87.0	62.7	95.5	73.3	71.8	55.6	62.0	44.3	80.2	60.3
9	0	-	85.1	28.1	91.0	54.1	90.1	64.0	78.0	48.2	92.6	61.4

y_{st} is the weight of a sample before the test; y_{fin} is the weight of a sample after moisture extraction.

After mathematical processing of the test results, the average values of the amount of extracted liquid (in %) were obtained (Table 3).

3 Analysis of the Results

The coincidence of the obtained equations was checked using the Fisher criterion with error $\alpha = 0.05$ [16–20]

$$F_{cal} = \frac{S_{ad}^2}{S_{\{y\}}^2} < F_T \quad (8)$$

Table 3 Test planning matrix

No.	P, x ₁	V, x ₂	Measurements results, %							Σ ₁ ⁿ (y - \bar{y}) ²	S _{er} ²	y _{cal}	$\bar{y} - y_{cal}$	($\bar{y} - y_{cal}$) ²
			y ₁	y ₂	y ₃	y ₄	y ₅	\bar{y}						
1	0	0	27.3	31.6	26.5	27.5	31.5	28.8	24.36	6.09	28.2	0	0	
2	+	+	27	26.4	31.1	29.0	26.3	26.1	34.35	8.59	26.1	0	0	
3	-	+	20.7	25.9	22.7	21.2	24.0	23.1	18.02	4.55	24.0	0.9	0.81	
4	-	-	30.5	27.7	35.6	37.4	33.3	32.9	60.5	15.03	32.6	0.3	0.09	
5	+	-	38.6	37.1	41.3	43.0	40.0	40.0	21.06	5.27	39.7	0.3	0.09	
6	+	0	34.4	29.6	30.3	29.6	30.3	30.2	18.38	4.60	30.6	0.4	0.16	
7	0	+	25.0	23.7	27.1	23.0	24.6	25	10.26	2.60	24.7	0.3	0.09	
8	-	0	27.9	23.2	22.6	28.5	24.8	25.4	28.9	7.23	25.7	0.3	0.09	
9	0	-	34.0	40.6	29.0	38.2	33.7	35.1	80.24	20.06	36.2	1.1	1.21	
									Σ 296.07	Σ 74.0			Σ 2.72	

where S_{ad}² is the residual variance; S_{y}² is the error of tests reproducibility (Table 4).

Table 4 Determination of tests regression coefficients

No.	P, x ₁	V, x ₂	Coefficients factors						
			b ₀	b ₁₁	b ₂₂	b ₁	b ₂	b ₁₂	\bar{y}
1	0	0	0.5772	-0.3234	-0.3234	0	0	0	28.8
2	+	+	-0.1057	0.1691	0.1691	0.1961	0.1961	0.25	26.1
3	-	+	-0.1057	0.1691	0.1691	-0.1961	0.1961	-0.25	23.1
4	-	-	-0.1057	0.1691	0.1691	-0.1961	-0.1961	0.25	32.9
5	+	-	-0.1057	0.1691	0.1691	0.1961	-0.1961	-0.25	40.0
6	+	0	0.2114	0.1617	-0.3383	0.1078	0	0	30.2
7	0	+	0.2114	-0.3383	0.1617	0	0.1078	0	25.0
8	-	0	0.2114	0.1617	-0.3383	-0.1078	0	0	25.4
9	0	-	0.2114	-0.3383	0.1617	0	-0.1078	0	35.1

S_{ad}² and S_{y}² are determined from Tables 1, 2, and 3.
 Forth semi-finished leather product:

$$S_{ad}^2 = \frac{\sum_1^N n(\bar{y} - \hat{y})^2}{\frac{N-(x+2)(x+1)}{2}} = \frac{5 \cdot 2.72}{3} = 4.53 \tag{9}$$

$$S_{\{y\}}^2 = \frac{\sum_1^N \sum_1^n (y - \bar{y})^2}{N(n - 1)} = \frac{296.07}{36} = 8.22 \tag{10}$$

Fisher’s criterion for reproducibility of the model is

$$F_{\text{cal}} = \frac{S_{\text{ad}}^2}{S_{\{y\}}^2} = \frac{4.53}{8.22} = 0.551 < F_T = 2.880 \tag{11}$$

where N is the number of tests; k is the number of parameters; n is the test replication; y_i are the data points of each measurement in the test; \bar{y} is the average result of the test; y_p are the calculated values according to the regression equation.

The regression Eq. (7) is obtained with error of 5%, which in the named form after decoding has the form:

For the leather semifinished product:

$$\Delta W = 54.2466 - 0.000005461P^2 + 310.640V^2 + 0.1742P - 201.7668V - 0.3768PV \tag{12}$$

A graph of the function of the amount of removed moisture ΔW from wet leather semifinished products in percentage in the range of feed velocities V from 0.17 to 0.34 m/s and specific pressing force P from 32 to 96 kN/m is plotted (Fig. 2).

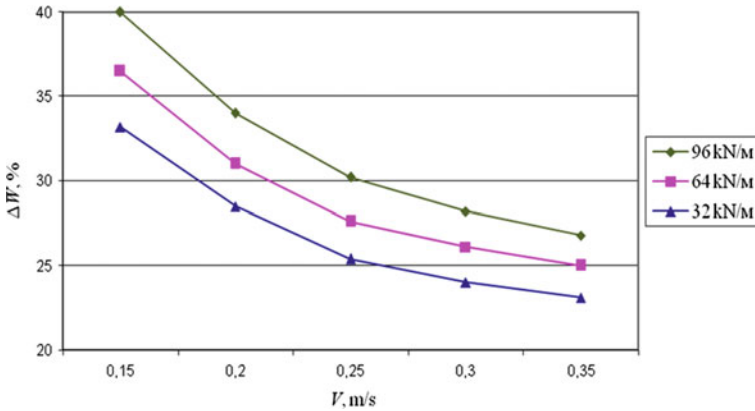


Fig. 2 Dependence of the amount of removed moisture ΔW on the feed velocity V of a semifinished leather product at a specific pressing force of squeezing rollers: $P = 32$ kN/m, $P = 64$ kN/m, $P = 96$ kN/m

4 Conclusions

The test results obtained show that it is possible to increase the productivity of the technological process of liquid extraction from the moisture-saturated leather semifinished products. It is possible to increase the moisture squeezing velocity by replacing

the base metal plate with a guide rod covered with a capillary-porous material. The moisture-removing material consists of wool and nylon of BM brand.

The test results show that the highest values of moisture removed under specific pressure of the squeezing rollers $P = 96$ kN/m and the feed velocity $V = 0.17$ m/s amount approximately to 40% of the initial weight of the leather semifinished product samples. The least values of moisture removed under specific pressure of the rollers $P = 32$ kN/m and the feed velocity of the semi-finished products $V = 0.34$ m/s amount to 23.1% of the initial weight of semifinished leather samples. In our case, in the tests, the residual moisture after squeezing is approximately 60%. Therefore, when extracting moisture in a roller machine, it is required to remove a maximum of 13% of the fluid. The test showed that moisture removed in excess of the required 13% is 10–16% of the initial weight of semifinished leather products. Consequently, it is possible to squeeze out moisture from wet leather semifinished products at a velocity of more than 0.34 m/s under the specific pressing force of the squeezing rollers from 32 to 96 kN/m.

In the future, the maximum velocity of moisture squeezing (more than 0.34 m/s) from semifinished leather products will be determined by experimental studies using the proposed design of a chain conveyor in the form of a metal guide bar with a moisture-extracting device made of a cloth of BM brand, attached to the chain conveyor. The use of the proposed design as a conveying unit, which consists of a metal guide rod covered by the moisture-removing fibrous cloth of BM brand, shows its effectiveness in squeezing out liquid from semifinished leather products. An analysis of the design of squeezing roller machines for extracting moisture from a semifinished leather product showed that a metal base plate for hanging a semifinished leather product (for example) has large dimensions and leads to a high metal consumption of the machine. Therefore, the test on moisture extraction was performed under a vertical feed of a semifinished leather product to a metal guide rod covered with a moisture-extracting material made of monchon cloth of BM or LASCHE brands. The use of a metal guide rod with moisture-removing material in the vertical squeezing machine reduces the metal consumption of the design. It eliminates the bulkiness and reduces energy consumption in conveying and moisture squeezing out of a leather semifinished product. Therefore, it is advisable to use a squeezing roller machine with a vertical feed on a guide metal rod with moisture-removing material.

References

1. Sokolovsky AR (2010) Development of method and improvement of means for studying the physical and mechanical properties of fibrous-porous materials in light industry. Dissertation, Moscow
2. Amanov AT, Bahadirov GA, Amanov TY, Tsoy GN, Nabiev AM (2019) Determination of strain properties of the leather semi-finished product and moisture-removing materials of compression rolls. *J Mater.* <https://doi.org/10.3390/ma12213620>
3. Chernov NV, Aronina YN, Gaidarov LP et al (1952) *Leather processing technology.* Gizlegprom, Moscow, p 680
4. Mikaelyan II (1978) The influence of biological and technological factors on the properties of leather raw materials and the quality of leather. *Light industry, Moscow*, p 168

5. Bahadirov GA, Sultanov TZ, Abdukarimov A (2020) Comparative analysis of two gear-lever differential inter-roller transmission mechanisms. IOP Conf Ser: Earth Environ Sci 614:012102. <https://doi.org/10.1088/1755-1315/614/1/012102>
6. Bahadirov GA, Sultanov TZ, Abdukarimov A (2020) Kinematic analysis of tooth-lever differential transmission mechanisms. IOP Conf Ser: Earth Environ Sci 614:012101. <https://doi.org/10.1088/1755-1315/614/1/012101>
7. Bahadirov G, Sultanov T, Umarov B, Bakhadirov K (2020) Advanced machine for sorting potatoes tubers. IOP Conf Ser: Mater Sci Eng 883:012132. <https://doi.org/10.1088/1757-899X/883/1/012132>
8. Mavlonov T, Akhmedov A, Saidakhmedov R, Bakhadirov K (2020) Simulation modelling of cold rolled metal strip by asymmetric technology. IOP Conf Ser Mater Sci Eng <https://doi.org/10.1088/1757-899X/883/1/012194>
9. Amanov TY, Bahadirov GA, Tsoy GN, Nabiev AM (2011) Method of extracting moisture from wet leather. Patent RUz for invention No. IAP 04451, Published in Patent Bulletin 12
10. Bahadirov G, Tsoy G, Nabiev A, Umarov A (2020) Experiments on moisture squeezing from a leather semi-finished product. IJRTE. <https://doi.org/10.35940/ijrte.E6125.018520>
11. Bahadirov G, Tsoy G, Nabiev A (2020) Wringing of wet leather semi-finished product using moisture-removing cloth. International collection of scientific papers “Progressive technologies and systems of mechanical engineering”. Donetsk 4(71). <http://ptsm.donntu.org/arhiv%20nambe/pdf%20-71/index.htm>
12. Wright DM (1996) Deformation, yield, relaxation and recovery in partially processed leather. Dissertation, University of Leicester. <http://nectar.northampton.ac.uk/2660/>
13. Kagunyu AW, Matiri F, Ngari E (2013) Camel hides: production, marketing and utilization in pastoral regions of northern Kenya. Pastoralism 3:25. <https://doi.org/10.1186/2041-7136-3-25>
14. Burmistrov AG et al (1981) Equipment of enterprises for the production of leather and fur. Textbook. Light and Food Industry, Moscow, p 416. <https://lib26.ru/index.php?id=78150>
15. Golovteeva AA, Kutsidi DA, Sankin LB (1982) Laboratory workshop on chemistry and technology of leather and fur. Moscow
16. Tikhomirov VA (1974) Experiment planning and analysis. Moscow
17. Wu CFJ, Hamada MS (2009) Experiments: planning, analysis, and optimization, 2nd edn. USA
18. Constales D, Yablonsky GS, D’hooge DR, Thybaut JW, Marin GB (2017) Chapter 9—Experimental data analysis: data processing and regression. <https://doi.org/10.1016/B978-0-444-59485-3.00009-6>
19. Fávero LP, Belfiore P (2019) Data science for business and decision making. Des Anal Exp. <https://doi.org/10.1016/B978-0-12-811216-8.00021-5>
20. Farooq MA, Nóvoa H, Araújo A, Tavares SMO (2016) An innovative approach for planning and execution of pre-experimental runs for design of experiments



Modeling Nonlinear Oscillations for the Wall of a Narrow Channel Interacting with Viscous Liquid

A. V. Christoforova¹, V. S. Popov^{2,3} (✉), and A. A. Popova²

- ¹ Saratov State University, 83 Astrakhanskaya Street, Saratov 410012, Russia
² Yuri Gagarin State Technical University of Saratov, 77, Politechnicheskaya street, Saratov 410054, Russia
vic_p@bk.ru
³ Institute of Precision Mechanics and Control of the Russian Academy of Sciences, 24, Rabochaya street, Saratov 410028, Russia

Abstract. In this paper, we considered nonlinear vibrations of a rigid plate induced by pulsating liquid pressure. The rigid plate is supported by a spring and is the top wall of a narrow parallel-walled channel filled with viscous liquid. We assumed the opposite channel wall is motionless, and the law of liquid pressure change at the channel ends is given as harmonic one, as well as the supporting spring possesses a hardening cubic nonlinearity. The plane coupled problem of hydroelasticity consisting of the dynamics equations for a viscous incompressible liquid and the channel wall motion equation as a spring-mass system, as well as the boundary conditions for the pressure at the channel ends and the liquid velocity at the channel walls, was formulated for the channel under consideration. Due to the narrowness of the channel, the liquid motion in it was studied as a creeping one. The hydrodynamic parameters of the liquid layer in the channel were determined, which made it possible to find the driving force acting on the channel wall, as well as the damping coefficient due to the liquid squeezing by the channel wall. As a result, the Duffing equation was obtained for the study of the channel wall nonlinear oscillations. Using the harmonic balance method, a solution to this equation was found and the study of the channel wall hydroelastic response for the case of anharmonic vibrations was carried out.

Keywords: Nonlinear oscillations · Hydroelasticity · Parallel-walled channel · Viscous fluid · Mathematical modeling

1 Introduction

Nowadays, hydroelasticity problems are of great importance for modern mechanical engineering, instrument making, civil engineering, and other industries, since in practice it is often necessary to deal with fluid–structure interactions [1]. It should be noted studies devoted to the interaction dynamics of a liquid with solids and elastic elements in the form of beams and plates. For instance, in reference [2] the hydroelastic vibrations of

circular plate interacting with an ideal liquid were considered based on the coupled hydroelasticity problem solution. The hydroelastic stability problem for a rectangular plate forming the wall of a narrow channel through which the ideal liquid flow moves is studied in [3]. Reference [4] is devoted to the determination of the added masses in the interaction of rigid and elastic plates of various shapes and sizes with an infinite ideal liquid volume. Studies of vibrations and stability for plates that are part of the channel wall or installed on its end are carried out in [5, 6]. Reference [7] deals with the study of the post-divergence behavior of circular cross-sectional pipe conveying fluid and supported at both its ends. The nonlinear flutter of a spring-mounted cantilevered flexible plate interacting with a uniform flow of an ideal liquid was studied in [8]. Reference [9] is considered dynamics and stability of fluid-conveying pipe supported at both ends by linear translational and rotational springs.

Besides, we can note the following papers deal with the interaction problems of solid and elastic bodies with a viscous liquid. Mathematical modeling of longitudinal vibrations of spring-mounted rigid walls of a narrow annular channel with a viscous pulsating liquid was carried out in [10]. Reference [11] deals with the study of longitudinal oscillations of a rectangular plate supported at its ends by linear springs in a viscous incompressible fluid flow in a channel with parallel walls. Longitudinal and transverse vibrations of a spring-mounted rigid wall of a narrow tapering channel of finite length, induced by vibrations of its foundation, were studied in [12]. The dynamic stability problem for a plate which is a part of a rigid boundary separating regions filled with various viscous incompressible fluids was investigated in [13]. Modeling on bending vibrations of the outer flexible wall of an annular channel filled with a viscous liquid and surrounded by an elastic medium due to vibration of its inner rigid wall based on a spring-mass system are carried out in [14]. The interaction dynamics of solids with a thin layer of viscous incompressible fluid surrounding them for gyroscopic navigation devices were considered in [15, 16]. Reference [17] devoted to the numerical simulation of the interaction rigid disk supported by a linear spring with a viscous compressible liquid to study the behavior of the disk of the spring-type safety valve. The mathematical modeling of the hydroelastic response of a flexible end seal for a narrow parallel-walled channel filled with viscous liquid was done in [18, 19]. However, the above papers did not consider the interaction dynamics of the channel wall supported by a spring with a hardening nonlinearity with a layer of pulsating viscous liquid filling this channel. In this paper, we formulate and solve the hydroelasticity problem for the narrow parallel-walled channel, one of the walls of which is supported by a hardening spring with cubic nonlinearity.

2 Statement of the Nonlinear Oscillations Problem

Let us consider a narrow parallel-walled channel as shown in Fig. 1. We introduce the Cartesian coordinate system, the origin of which coincides with the channel bottom center. The upper channel wall is absolutely rigid plate elastically supported by a nonlinear spring. We assume the spring with hardening cubic nonlinearity. The bottom channel is a clamped rigid plate. The clearance between channel walls is filled with a viscous incompressible liquid. Channel wall sizes in the plan view are $2\ell \times b$. Further, we study

the plane problem; i.e., we accept $b \gg 2\ell$. There are cavities filled with the same liquid at the channel ends; i.e., the liquid can flow freely from the narrow channel into these cavities. We assume that the liquid pressure p^* at all points in the end cavities is pulsed according to a harmonic law. As a result, the upper channel wall oscillates along the z -axis under the pulsating liquid action. In the unperturbed state, the clearance between the channel walls is δ_0 , and due to the channel narrowness $\delta_0 \ll 2\ell$. We denote the amplitude of the upper wall oscillations as z_m and consider it to be significantly smaller than δ_0 , i.e., $z_m \ll \delta_0$. Next, we will focus on studying the nonlinear steady-state periodic forced response of the upper channel wall, i.e., anharmonic channel wall vibrations [20, 21].

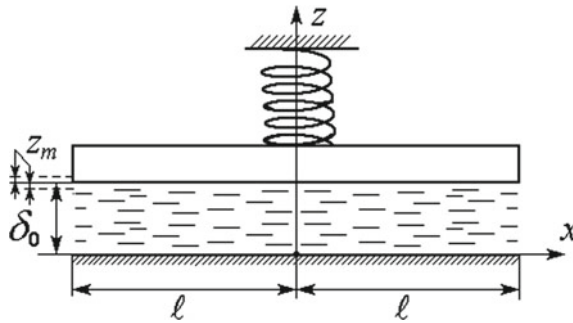


Fig. 1 A narrow channel with upper wall having supporting spring with hardening cubic nonlinearity

3 The Theory and Solution

The movement of the upper channel wall is considered in the framework of the spring-mass system with hardening cubic nonlinearity; i.e., its dynamics equation is written as

$$m \frac{d^2z}{dt^2} + n_1z + n_3z^3 = b \int_{-\ell}^{\ell} p dx \tag{1}$$

where m is the upper channel wall mass, n_1 is the linear stiffness of the supporting spring, n_3 is the cubic stiffness of the supporting spring, p is the liquid pressure in the channel, t is the time.

The liquid movement in the narrow parallel-walled channel can be considered as creeping one [22]; i.e., the motion equations for viscous incompressible liquid between the channel’s walls are the Navier–Stokes equations with the omitted inertial terms, supplemented by the continuity equation

$$v \left(\frac{\partial^2 u_x}{\partial x^2} + \frac{\partial^2 u_x}{\partial z^2} \right) - \frac{1}{\rho} \frac{\partial p}{\partial x} = 0, \quad v \left(\frac{\partial^2 u_z}{\partial x^2} + \frac{\partial^2 u_z}{\partial z^2} \right) - \frac{1}{\rho} \frac{\partial p}{\partial z} = 0, \quad \frac{\partial u_x}{\partial x} + \frac{\partial u_z}{\partial z} = 0. \tag{2}$$

where u_x, u_z are the fluid velocity vector projections on the coordinate axis, ρ is the fluid density, ν is the kinematic viscosity coefficient of the fluid.

The motion equations for the viscous incompressible liquid must be supplemented with appropriate boundary conditions. We formulate the boundary conditions of Eqs. (2) as conditions for the coincidence of the velocities of the liquid and the channel walls limiting it, i.e., the non-slip conditions

$$u_x = 0, u_z = 0 \text{ at } z = 0, \quad u_x = 0, u_z = \frac{dz}{dt} \text{ at } z = \delta_0 + z_m f(\eta t) \quad (3)$$

where $z_m f(\eta t)$ is the upper channel wall law motion, η is the channel wall vibrations frequency.

Additionally, we formulate the boundary conditions for liquid pressure at the channel edge cross sections

$$p = p^*(\omega t) \text{ at } x = \pm \ell \quad (4)$$

where $p^*(\omega t) = p_m \sin(\omega t)$ is the pressure pulsating harmonic law in the end cavities, ω is the pressure pulsating frequency.

Let us introduce dimensionless variables of the problem under consideration

$$\xi = \frac{x}{\ell}, \quad \zeta = \frac{z}{\delta_0}, \quad u_x = \frac{z_m \eta}{\psi} U_\xi, \quad u_z = z_m \eta U_\zeta, \quad p = p^*(\omega t) + \frac{\rho \nu z_m \eta}{\delta_0 \psi^2} P \quad (5)$$

moreover, taking into account the above problem statement we introduce into consideration the small parameters

$$\psi = \delta_0 / \ell \ll 1, \quad \lambda = z_m / \delta_0 \ll 1. \quad (6)$$

Substituting (5), (6) into Eqs. (1), (2) and boundary conditions (3), we obtain

$$m \frac{d^2 z}{dt^2} + n_1 z + n_3 z^3 = 2b\ell p^*(\omega t) + b\ell^3 \frac{\rho \nu z_m \eta}{\delta_0^3} \int_{-1}^1 P d\xi. \quad (7)$$

$$\frac{\partial P}{\partial \xi} = \frac{\partial^2 U_\xi}{\partial \zeta^2} + \psi^2 \frac{\partial^2 U_\xi}{\partial \xi^2}; \quad \frac{\partial P}{\partial \zeta} = \psi^2 \left[\psi^2 \frac{\partial^2 U_\zeta}{\partial \xi^2} + \frac{\partial^2 U_\zeta}{\partial \zeta^2} \right], \quad \frac{\partial U_\xi}{\partial \xi} + \frac{\partial U_\zeta}{\partial \zeta} = 0. \quad (8)$$

$$U_\xi = 0, U_\zeta = 0 \text{ at } \zeta = 0, \quad U_\xi = 0, U_\zeta = \frac{1}{\eta} \frac{df}{dt} \text{ at } \zeta = 1 + \lambda f(\eta t). \quad (9)$$

Neglecting the small terms [23] in (8), (9), we write the dimensionless equations for viscous liquid

$$\frac{\partial^2 U_\xi}{\partial \zeta^2} - \frac{\partial P}{\partial \xi} = 0, \quad \frac{\partial P}{\partial \zeta} = 0, \quad \frac{\partial U_\xi}{\partial \xi} + \frac{\partial U_\zeta}{\partial \zeta} = 0 \quad (10)$$

and the boundary conditions for them

$$U_\xi = U_\zeta = 0 \text{ at } \zeta = 0, U_\xi = 0, U_\zeta = \frac{1}{\eta} \frac{df}{dt} \text{ at } \zeta = 1, P = 0 \text{ at } \xi = \pm 1. \tag{11}$$

Here we take into account boundary conditions for pressure (4) which are written in dimensionless variables (5).

Solving Eqs. (10) with boundary conditions (11), we find

$$U_\xi = \frac{\zeta(\zeta - 1)}{2} \frac{\partial P}{\partial \xi}, U_\zeta = \frac{3\zeta^2 - 2\zeta^3}{12} \frac{\partial^2 P}{\partial \xi^2}, P = \frac{6(\xi^2 - 1)}{\eta} \frac{df}{dt} \tag{12}$$

Substituting (12) in Eq. (7) we write

$$m \frac{d^2 z}{dt^2} + K \frac{dz}{dt} + n_1 z + n_3 z^3 = 2blp^*(\omega t), \tag{13}$$

where $K = 8\ell^3 b\rho\nu(\delta_0)^{-3}$ is the viscous liquid damping coefficient due to it squeezing by the upper channel wall.

Equation (13) is the Duffing oscillator equation. It is known [20, 24] that for small oscillations amplitude and damping coefficient under the periodic driving force, the Duffing oscillator equation solution is anharmonic vibrations or nonlinear oscillations. To solve this equation, we use the harmonic balance method [21, 25]. According to this method, the forced oscillations frequency is assumed to be equal to the driving force frequency, and the solution is represented as a harmonic one, i.e., $\eta \approx \omega$ and $z = z_m \sin(\omega t + \phi)$. The nonlinear term is linearized by decomposing it into a Fourier series and holding the first decomposition term. After that, the primary response of the oscillatory system is studied. Thus, performing the linearization procedure of Eq. (13) by the harmonic balance method [25], we obtain

$$m \frac{d^2 z}{dt^2} + K \frac{dz}{dt} + n_1 z + \frac{3}{4} z_m^2 n_3 z = 2blp_m \sin(\omega t). \tag{14}$$

The solution of this equation for steady-state forced oscillations has the form

$$z = z_m \sin(\omega t + \phi), z_m = \frac{2lb p_m / m}{\sqrt{(\omega_*^2 - \omega^2)^2 + (K\omega/m)^2}}, \text{tg } \phi = \frac{K\omega/m}{\omega_*^2 - \omega^2} \tag{15}$$

where $\omega_*^2(z_m) = (n_1/m) + (3/4)z_m^2 n_3/m$.

It can be noted for the case of the linear spring, i.e., $n_3 \rightarrow 0$, we get a well-known frequency response of the channel wall

$$z_m = 2lb p_m / \sqrt{(n_1 - m\omega^2)^2 + (K\omega)^2}, \tag{16}$$

According to (15) from the expression for z_m , we obtain

$$z_m^2 ((\omega_*^2 - \omega^2)^2 + (K\omega/m)^2) = (2lb p_m / m)^2, \tag{17}$$

Solving Eq. (17) with respect to the oscillations frequency ω , we obtain the nonlinear frequency response for the primary resonance study

$$\omega^2 = \Omega^*(z_m) \pm \sqrt{\left(\frac{2\ell b p_m}{m z_m}\right)^2 - \left(\frac{K}{m}\right)^2 \omega_*^2(z_m) + \frac{1}{4}\left(\frac{K}{m}\right)^2}, \tag{18}$$

where $\Omega^*(z_m) = \omega_*^2(z_m) - (1/2)(K/m)^2$.

4 Calculation Results

In order to illustrate the mathematical model for the channel under consideration, we gave an example of calculating its nonlinear frequency response for the primary resonance. In our calculations, we used the following data: $\ell = 0.1$ m, $\delta_0 = 0.05$ m, $b = 0.5$ m, $m = 2$ kg, $n_1 = 10^7$ kg/s², $n_3 = 10^{12}$ kg/(s²m²), $\rho = 1.84 \cdot 10^3$ kg/m³, $\nu = 2.53 \cdot 10^{-4}$ m²/s, $p_m = 10^4$ Pa. The calculations result of the nonlinear frequency response (18) is shown in Fig. 2 for cases of successive increase in the amplitude pressure pulsation. The calculations result of the linear frequency response (16) is shown in Fig. 3.

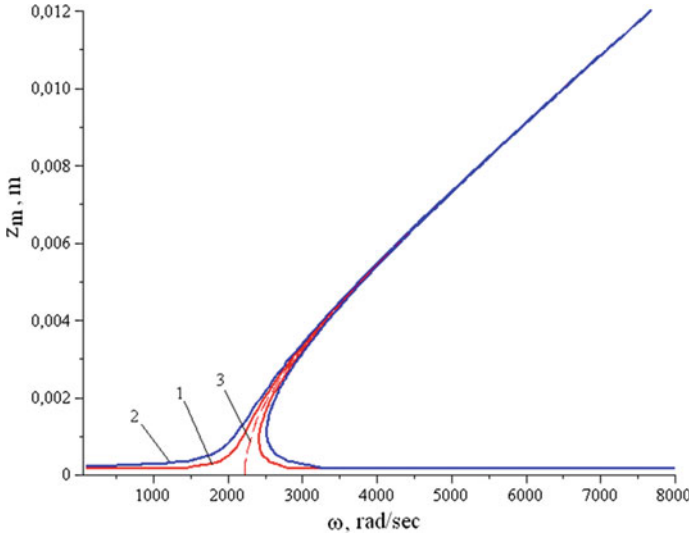


Fig. 2 Charts of the nonlinear frequency response Eq. (18) for cases: (1) $p_m = 10^4$ Pa, (2) $p_m = 2 \cdot 10^4$ Pa, (3) the line of Ω^*

5 Summary and Conclusion

We have formulated and solved the plane coupled hydroelasticity problem for the channel wall supported by hardening spring with cubic nonlinearity. It is shown that the study

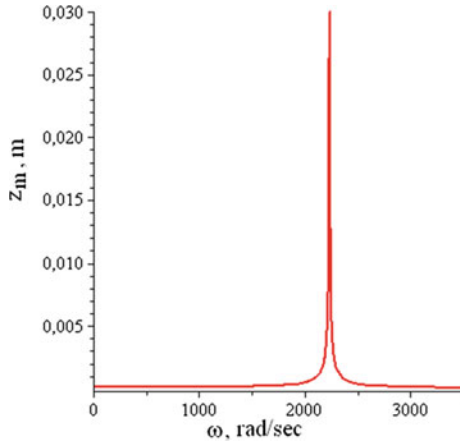


Fig. 3 Charts of the linear frequency response Eq. (16)

of nonlinear oscillations of the channel wall, induced by a pulsating liquid pressure at channel ends, is reduced to the study of the Duffing equation. Using the harmonic balance method to solve this equation, we obtained the expression for the primary response of the oscillatory system under consideration. Calculations of the primary response for channel wall supported by hardening nonlinear spring showed a strong effect of liquid viscosity and the distance between the channel walls on the vibration amplitudes. The plotted graphs of the nonlinear frequency response for the channel wall make it possible to determine the frequency range of its unstable oscillations. In this range, a jump-like change in the amplitudes of the channel wall oscillations is observed. For example, for the frequency response shown in Fig. 2, this range is from 2400 to 7600 rad/s. In addition, the calculations showed that for the influence of the cubic nonlinear term, the corresponding stiffness coefficient should be significantly greater than the stiffness coefficient for the linear term, but under the condition that $z_m^2 n_3 / n_1 = O(1)$. The results obtained can be used to simulate dynamic processes in hydraulic drive systems, devices, and machines with nonlinear elastic elements interacting with a viscous liquid, as well as to develop methods for their non-destructive testing by the forced vibration parameters of these elements.

Acknowledgements. The study was funded by Russian Science Foundation (RSF) according to the project No 22-29-00173.

References

1. Païdoussis MP, Price SJ, De Langre E (2010) Fluid-structure interactions: cross-flow-induced instabilities. Cambridge University Press
2. Amabili M, Kwak MK (1996) Free vibrations of circular plates coupled with liquids: revising the lamb problem. *J Fluids Struct* 10(7):743–761. <https://doi.org/10.1006/jfls.1996.0051>

3. Bochkarev SA, Lekomtsev SV, Matveenkov VP (2016) Hydroelastic stability of a rectangular plate interacting with a layer of ideal flowing fluid. *Fluid Dyn* 51(6):821–833. <https://doi.org/10.1134/S0015462816060132>
4. Morozov D, Indeitsev D, Michailov A (2019) Added mass study of plane structures at their various motions. *Mater Phys Mech* 41(1):116–124. https://doi.org/10.18720/MPM.4112019_19
5. Velmisov PA, Ankilov AV (2015) Mathematical modelling of dynamics and stability of elastic elements of vibration devices. *IFAC-PapersOnLine* 48(11):970–975. <https://doi.org/10.1016/j.ifacol.2015.09.318>
6. Velmisov PA, Pokladova YV (2019) Mathematical modelling of the “Pipeline—pressure sensor” system. *J Phys: Conf Ser* 1353(1):012085. <https://doi.org/10.1088/1742-6596/1353/1/012085>
7. Modarres-Sadeghi Y, Païdoussis MP (2009) Nonlinear dynamics of extensible fluid-conveying pipes, supported at both ends. *J Fluids Struct* 25(3):535–543. <https://doi.org/10.1016/j.jfluidstructs.2008.09.005>
8. Howell RM, Lucey AD (2019) Non-linear spring-mounted flexible plates in axial flow. In: *Fluid-structure-sound interactions and control. Lecture notes in mechanical engineering*, pp 287–292. https://doi.org/10.1007/978-981-10-7542-1_44
9. Kheiri M, Païdoussis MP, Del Pozo GC, Amabili M (2014) Dynamics of a pipe conveying fluid flexibly restrained at the ends. *J Fluids Struct* 49:360–385. <https://doi.org/10.1016/j.jfluidstructs.2013.11.023>
10. Kondratov DV, Popov VS, Popova AA (2019) Longitudinal walls oscillations of an annular channel filled with pulsating viscous fluid. *IOP Conf Ser: Earth Environ Sci* 272(3):032253. <https://doi.org/10.1088/1755-1315/272/3/032253>
11. Kurzin VB (2011) Streamwise vibrations of a plate in a viscous fluid flow in a channel, induced by forced transverse vibrations of the plate. *J Appl Mech Tech Phys* 52(3):459–463. <https://doi.org/10.1134/S0021894411030163>
12. Mogilevich LI, Popov VS, Popova AA (2018) Longitudinal and transverse oscillations of an elastically fixed wall of a wedge-shaped channel installed on a vibrating foundation. *J Mach Manuf Reliab* 47(3):227–234. <https://doi.org/10.3103/S1052618818030093>
13. Velmisov PA, Ankilov AV (2017) Dynamic stability of plate interacting with viscous fluid. *Cybernet Phys* 6(4):262–270
14. Mogilevich LI, Popov VS, Kondratov DV, Rabinskiy LN (2017) Bending oscillations of a cylinder, surrounded by an elastic medium and containing a viscous liquid and an oscillator. *J Vibroeng* 19(8):5758–5766. <https://doi.org/10.21595/jve.2017.18179>
15. Antsiferov SA, Kondratov DV, Mogilevich LI (2009) Perturbing moments in a floating gyroscope with elastic device housing on a vibrating base in the case of a nonsymmetric end outflow. *Mech Solids* 44(3):352–360. <https://doi.org/10.3103/S0025654409030030>
16. Andreichenko KP, Smarun AB (2011) Simulation of the axial hydromechanical effect in gyroscopes with a spherical hydrodynamic suspension. *J Mach Manuf Reliab* 40(3):216–221. <https://doi.org/10.3103/S1052618811020038>
17. Koroleva MR, Mishenkova OV, Raeder T, Tenenev VA, Chernova AA (2018) Numerical simulation of the process of activation of the safety valve. *Comput Res Modeling* 10(4):495–509. <https://doi.org/10.20537/2076-7633-2018-10-4-495-509>
18. Popov VS, Popova AA, Christoforova AV (2020) Hydroelastic response of an end wall interacting with a vibrating stamp via a viscous liquid layer. *J Phys: Conf Ser* 1441(1):012108. <https://doi.org/10.1088/1742-6596/1441/1/012108>
19. Popov VS, Popova AA (2020) Modeling of a channel wall interaction with an end seal flexibly restrained at the edge. *Comput Res Model* 12(2):387–400. <https://doi.org/10.20537/2076-7633-2020-12-2-387-400>

20. Nayfeh AH, Mook DT (1979) Nonlinear oscillations. Wiley, New York
21. Magnus K (1976) Schwingungen. Teubner, Stuttgart
22. Loitsyanskii LG (1966) Mechanics of liquids and gases. Pergamon Press, Oxford
23. Van Dyke M (1975) Perturbation methods in fluid mechanics. Parabolic Press, Stanford, CA
24. Korsch HJ, Jodl H-J, Hartmann T (2008) Chaos: a program collection for the PC: third revised and, Enlarged. Springer, Berlin, Heidelberg
25. Krack M, Gross J (2019) Harmonic balance for nonlinear vibration problems. Springer, New York



Study of the Base Plate Motion Between the Pairs of Shafts

Z. A. Rakhimova^(✉)

Tashkent Chemical—Technological Institute, 32, A.Navoiy street, Tashkent 100011, Uzbekistan

Abstract. The vertical motion of a flat material bent in a fold on a base plate between rotating pairs of shafts is investigated in the article. Roller pairs are located one above the other, and the distance between them is equal to the height of the base plate. The technological process is analytically considered to determine the energy consumption for the stable operation of the roller machine. Four cases of the state of the base plate during its movement between the pairs of shafts are considered. According to the conditions of the technological process, the positions of the base plate at the entrance between the bottom roller pair, between two pairs of shafts, at the exit between the bottom roller pair and the upper roller pair were studied. In the study, Newton's second law was used, and differential equations describing the technological process were obtained. Based on the solutions obtained, graphs of the dependence of the base plate velocity on the force of gravity and the friction coefficient were built. Graphical results were analyzed. Based on the results of calculations and graphs, the base plate motion at constant velocity was theoretically substantiated in the four cases considered.

Keywords: Pair of shafts · Flat material · Base plate · Gravity · Coefficient of friction · External pressure · Reaction force · Grip zone · Velocity · Time

1 Introduction

Currently, certain studies are conducted in Uzbekistan concerning the deep processing of leather raw materials in order to expand the volumes and types of export-oriented finished products and to provide the population with high-quality and cheap shoes and leather goods of local production. Much attention is paid to the introduction of advanced technologies at enterprises, to modernization and technical re-equipment of enterprises in leather production.

Dozens of types of roller machines are used in modern tanneries. The development of theoretical and applied aspects of improving the roller machines in the tanning, which increase the quality of the resulting product, is a relevant issue. A significant number of non-mechanized operations remain in the leather industry. The level of mechanization in our republic is 50–75%, while at advanced foreign enterprises, it approaches 80%. Even during mechanized operations, the worker has to perform heavy and monotonous manual tasks. Most of the technical operations of the tanning industry are machine-manual ones. Along with the advantages of roller machines, there are significant disadvantages such

as low quality, defects of the processed material, and the fragility of some units and parts, caused by the inconsistency with technological requirements.

In [1], a method of pulling-in the sheet material bend over a base plate between rotating shafts was studied.

In [2], the classification of the support plates of the roller machine was compiled, their advantages and disadvantages were determined, and new designs were proposed.

The deformation properties of a semi-finished leather product were experimentally determined by its topographic sections. The squeezing out of a two-layer moisture-saturated leather semi-finished product on a base plate between the squeezing rollers was studied in [3–10].

The factors influencing the shape of the coated surfaces and existing methods of its modeling were investigated, and a new model of the contact zone surface of the roller pair was proposed. The deformation zone between the roller pair was studied in [11, 12].

The belt motion of the conveying device was investigated in [12, 13].

Programs and dynamic models for roller machines used in industry were developed in [14–19]. The design of the technological line for conveying and machining of flat material was developed. The technological line consists of three main working areas, in which various technological processes are realized using working pairs of shafts and base plates [20].

Tsoi [21] conducted research on the use of moisture-permeable working shafts made of cermet materials. As a result of the experiments, it was found that for the effective extraction of moisture from the skin between the squeezing rollers, the upper roller should be covered with a moisture-extracting material, and the lower roller should be made of the cermet.

Shukurov [22] considered the issues of technological reliability of machines and devices in the textile industry in order to increase the vibration-resistant system and the features of the interaction of the processed product with the working bodies.

2 Research Methods

In order to study the interaction of the pairs of shafts and the base plate in the working process of the technological line, we consider four special cases using analytical methods. The base plate with flat material in the system is assumed to move at a constant velocity.

I—is a particular case. From the conditions of the technological process, consider the position of the base plate with flat material at the entrance between the bottom roller pair (Fig. 1). Based on Newton's second law, we define the following:

$$m\ddot{y} = G + 2F_{ishq} \cos \alpha - 2N \sin \alpha - P \quad (1)$$

According to the Colon-Amonton friction law, the friction force is

$$F_{ishq} = f \cdot N \quad (2)$$

where G —is the pulling-in force of the chain, Q —is the external pressure force, P —is the gravity of the base plate and flat material, N —is the reaction force, and F_{ishq} —is

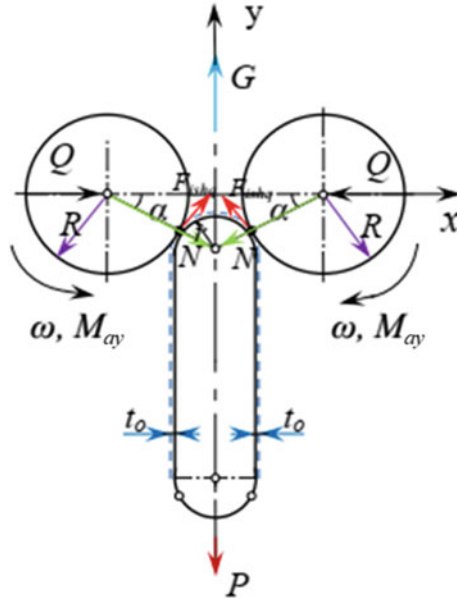


Fig. 1 Gripping the base plate by the working shafts

the friction force. According to the condition of the problem, we take the radii of the shafts and their gravities as equal. Expression (1) is written in the form of a differential equation. If equal to $\ddot{y} = \frac{d\dot{y}}{dt}$ (3), then we substitute it into differential Eq. (1) and obtain the following expression:

$$m \frac{d\dot{y}}{dt} = G + 2F_{ishq} \cos \alpha - 2N \sin \alpha - P \tag{4}$$

We integrate the resulting Eq. (4) taking into account the initial boundary conditions and obtain the following expression.

$$m \int_{\dot{y}_0}^{\dot{y}} d\dot{y} = \int_0^t (G + 2F_{ishq} \cos \alpha - 2N \sin \alpha - P) dt \tag{5}$$

Considering given condition $\dot{y}_0 = \vartheta_0 = 0.17 - 0.34 \text{ m/s}$, integrating Eq. (5), we determine the velocity of the base plate, which satisfies the condition for the first particular case under consideration.

$$m\vartheta = Gt + 2F_{ishq} \sin \alpha + 2N \cos \alpha - Pt - 2N + m\vartheta_0 \tag{6}$$

Simplifying Eq. (6), we reduce it to the following form:

$$\vartheta = \frac{1}{m} (Gt + 2F_{ishq} \sin \alpha + 2N \cos \alpha - Pt - 2N) + \vartheta_0 \tag{7}$$

Further, taking into account expression (2), Eq. (7) can be written in the following form:

$$\vartheta = \frac{1}{m}(Gt + 2N(f \sin \alpha + \cos \alpha - 1) - Pt) + \vartheta_0 \tag{8}$$

II—is a particular case. Consider the base plate motion at the exit from the grip zone between the working shafts (Fig. 2).

$$mw = G - 2F_{ishq} \cos \alpha + 2N \sin \alpha - P \tag{9}$$

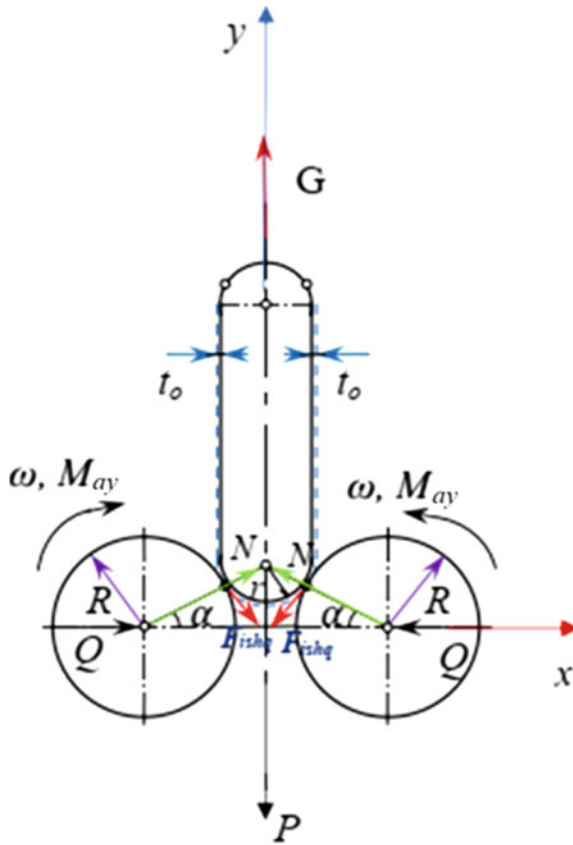


Fig. 2 Exit of the base plate from the grip zone between the working shafts

We integrate Eq. (9) similar to the first particular case.

$$m \int_{\dot{y}_0}^{\dot{y}} d\dot{y} = \int_0^t (G - 2F_{ishq} \cos \alpha + 2N \sin \alpha - P) dt \tag{10}$$

By integrating expression (10), we determine the velocity of the base plate for the second particular case:

$$\vartheta = \frac{1}{m}(Gt - 2F_{ishq} \sin \alpha - 2N \cos \alpha - Pt + 2N) + \vartheta_0 \tag{11}$$

With expression (2), Eq. (11) can be written as:

$$\vartheta = \frac{1}{m}(Gt - 2N(f \sin \alpha + \cos \alpha - 1) - Pt) + \vartheta_0 \tag{12}$$

III—is a particular case. The base plate is at an equal distance from the bottom and upper roller pairs at $\alpha = \psi$ (Fig. 3). In this case, the equation of motion for the base plate is:

$$mw = G + 4F_{ishq} \cos \alpha - 4N \sin \alpha - P \tag{13}$$

Equation (13) is integrated similar to the two particular cases given above.

$$m \int_{\dot{y}_0}^{\dot{y}} d\dot{y} = \int_0^t (G + 4F_{ishq} \cos \alpha - 4N \sin \alpha - P) dt \tag{14}$$

By integrating expression (14), we determine the velocity of the base plate that meets the condition of the third particular case:

$$\vartheta = \frac{1}{m}(Gt + 4N(f \sin \alpha + \cos \alpha - 1) - Pt) + \vartheta_0 \tag{15}$$

IV—is a particular case. Let the base plate be located between the roller pairs at a distance under condition $\alpha \neq \psi$ (Fig. 3). In this case, the equation of motion for the base plate is:

$$mw = G + F_{ishq} \cos \alpha - 2N \sin \alpha - 2N \sin \psi + 2F_{ishq} \cos \psi - P \tag{16}$$

Similar to the three particular cases considered above, integrating (16), we obtain the following equation:

$$m \int_{\dot{y}_0}^{\dot{y}} d\dot{y} = \int_0^t (G + F_{ishq} \cos \alpha - 2N \sin \alpha - 2N \sin \psi + 2F_{ishq} \cos \psi - P) dt \tag{17}$$

Therefore, by integrating expression (17), we determine the velocity of the base plate that satisfies the condition of the fourth particular case:

$$\vartheta = \frac{1}{m}(Gt + 2F_{ishq} \sin \alpha + 2N \cos \alpha + 2N \cos \psi + 2F_{ishq} \sin \psi - Pt) + \vartheta_0 \tag{18}$$

Here, considering expression (2), Eq. (18) can be written in the following form:

$$\vartheta = \frac{1}{m}(Gt + 2N(f \sin \alpha + \cos \alpha) + 2N(\cos \psi + f \sin \psi) - Pt) + \vartheta_0 \tag{19}$$

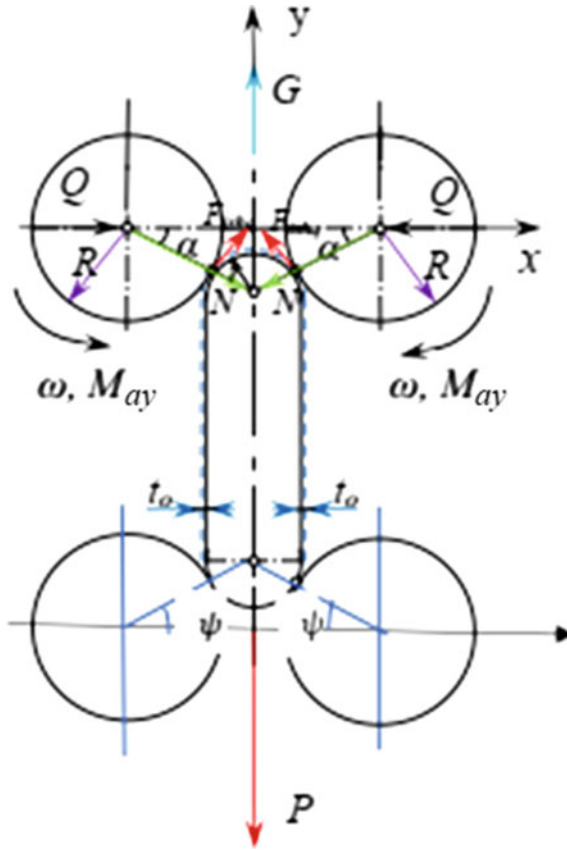


Fig. 3 Position of the base plate between the lower and upper roller pairs

3 Discussion of Results

The conditions for ensuring a constant velocity of motion of the base plate were substantiated on the basis of the obtained Eqs. (8), (12), (15), and (19); the graphs were plotted (Figs. 4, 5 and 6).

With an account of the initial boundary conditions, the results of the graphs obtained for four particular cases coincide. In all cases, a constant velocity of the base plate between the roller pairs can be observed. Even if the numerical values of pulling-in force of the chain, gravity, friction coefficient, or other parameters change, the constant velocity of the base plate is not disturbed. Figure 4 shows a graph of the dependence of the velocity of the base plate on the pulling-in force of the chain.

From Fig. 4, it can be seen that with an increase in the values of the pulling-in force of the chain, the velocity of the base plate remains unchanged. In Fig. 5, a graph of the dependence of the velocity of the base plate on the gravity of the latter is plotted. From Fig. 5, it can be seen that with an increase in the gravity of the base plate, its velocity also remains unchanged. Figure 6 shows a graph of the dependence of the velocity of the

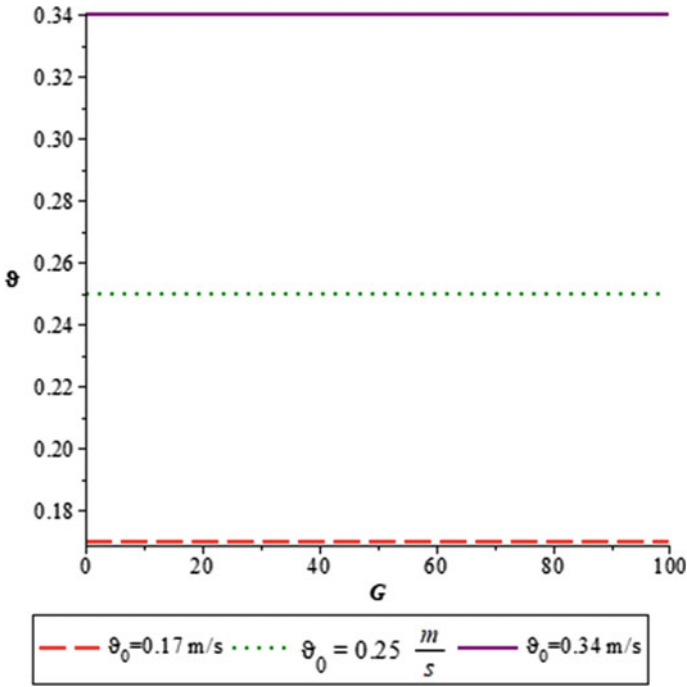


Fig. 4 Graph of the dependence of the velocity of the base plate on the pulling-in force of the chain

base plate on the coefficient of friction. From Fig. 6, it is seen that the friction coefficient does not significantly affect the constancy of the base plate velocity.

4 Conclusions

Based on the calculation of the differential Eqs. (8), (12), (15), and (19) obtained and the analysis of the plotted graphs (Figs. 4, 5 and 6), the following conclusion can be drawn. To meet the technological requirements of the process of machining flat material, the transporting base plate must move between the working roller pairs at a constant velocity. Only in this case, the processing of flat material will be uniform over its entire area.

So, using the example of four particular cases, the conditions for ensuring a constant velocity of the base plate between roller pairs located one above the other were substantiated by theoretical calculations.

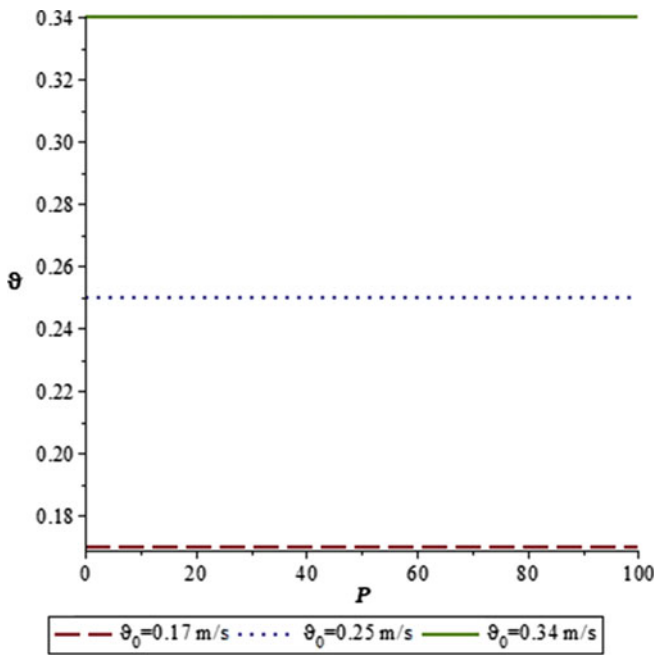


Fig. 5 Graph of the dependence of the velocity of the base plate on the force of its gravity

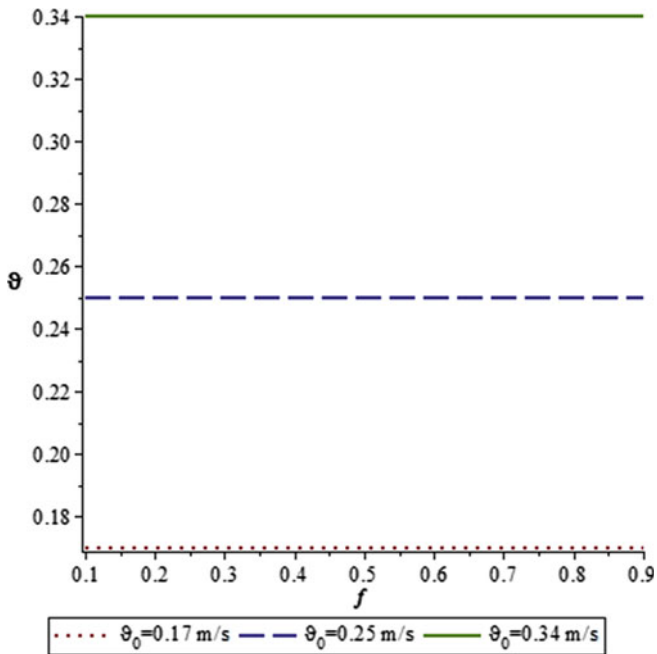


Fig. 6 Graph of the dependence of the velocity of the base plate on the friction coefficient

References

1. Amanov TY (2016) Design features and operating conditions of the vertical-type squeezing machine. *Uzbek J “Problems of Mechan”* 4:67–69
2. Bahadirov GA, Sultanov TZ, Abdurkarimov A (2020) Kinematic analysis of tooth-lever differential transmission mechanisms. *IOP Conf Ser: Earth Environ Sci* 614:012101. <https://doi.org/10.1088/1755-1315/614/1/012101>
3. Amanov AT, Bahadirov GA, Amanov TY, Tsoy GN, Nabiev AM (2019) Determination of strain properties of the leather semi-finished product and moisture-removing materials of compression rolls. *J Mater*. <https://doi.org/10.3390/ma12213620>
4. Mavlonov T, Akhmedov A, Saidakhmedov R, Bakhadirov K (2020) Simulation modelling of cold rolled metal strip by asymmetric technology. *IOP Conf Ser Mater Sci Eng* <https://doi.org/10.1088/1757-899X/883/1/012194>
5. Bahadirov G, Tsoy G, Nabiev A, Umarov A (2020) Experiments on moisture squeezing from a leather semi-finished product. *IJRTE*. <https://doi.org/10.35940/ijrte.E6125.018520>
6. Bahadirov G, Sultanov T, Umarov B, Bakhadirov K (2020) Advanced machine for sorting potatoes tubers. *IOP Conf Ser: Mater Sci Eng* 883:012132. <https://doi.org/10.1088/1757-899X/883/1/012132>
7. Zakharov NM, Kuts SM (2020) The approach to determine the elastic characteristic of the contact of rough surfaces. *Int J Mech Eng Robot Res* 9(7):937–942. <https://doi.org/10.18178>
8. Bahadirov GA, Sultanov TZ, Abdurkarimov A (2020) Comparative analysis of two gear-lever differential inter-roller transmission mechanisms. *IOP Conf Ser: Earth Environ Sci*. 614:012102. <https://doi.org/10.1088/1755-1315/614/1/012102>
9. Liu J (2020) A dynamic modelling method of a rotor-roller bearing-housing system with a localized fault including the additional excitation zone. *J Sound Vibrat* 469 / 11514. www.elsevier.com/locate/isv
10. Covington AD, Wise WR (2020) Current trends in leather science. *J Leather Sci Eng* 2:28. <https://doi.org/10.1186/s42825-020-00041-0>
11. Djurayev A, Jumaev A (2020) Providing the development of new designs for the design of the roller mechanism transmitting rotational motion in belt conveyors. *IJETER* 8(9):6609–6617
12. Rigueto CVT, Rosseto M, Krein DDC et al (2020) Alternative uses for tannery wastes: a review of environmental, sustainability, and science. *J Leather Sci Eng* 2:21. <https://doi.org/10.1186/s42825-020-00034-z>
13. Navarro D, Wu J, Lin W et al (2020) Life cycle assessment and leather production. *J Leather Sci Eng* 2:26. <https://doi.org/10.1186/s42825-020-00035-y>
14. Appiah-Brempong M, Essandoh HMK, Asiedu NY et al (2020) An insight into artisanal leather making in Ghana. *J Leather Sci En* 2:25. <https://doi.org/10.1186/s42825-020-00039-8>
15. Ershov SV (2013) Dynamic loading of the roller pair to intensify the spinning process. Dissertation, Ivanovo
16. Bahadirov G, Tsoy G, Nabiev A (2021) Study of the efficiency of squeezing moisture-saturated products. *Eureka: Phys Eng* 1:86–96. <https://doi.org/10.21303/2461-4262.2021.001606>
17. Souza MLR, Hoch AL, Gasparino E (2016) Compositional analysis and physicochemical and mechanical testing of tanned rabbit skins. *World rabbit science*. 24(3):233–238
18. Yeh C, Perng DA (2005) Reference standard of defect compensation for leather transactions. *Int J Adv Manuf Technol* 25(11):1197–1204
19. Failli F, Dini G (2004) An innovative approach to the automated stacking and grasping of leather. *Plies CIRP Annals-Manuf Technol* 53(1):31–34
20. Bahadirov GA, Amanov TY, Tsoy GN, Nabiev AM (2012) Line for transportation and mechanical processing of semi-finished leather products. Patent RUz No. FAP 00686, Of. Bull. No. 1(129)

21. Tsoy GN (1989) On the removal of moisture from the leather half factory on roller pressing machines. Mechanics from "flat media": Representative Conference-Tashkent, April 24–26, pp 51
22. Shukurov MM (2004) Scientific bases of design and calculation of working bodies of spinning machines. Dis Doct Techn Sciences. Tashkent, pp 324



Study of the Influence of Body Roll on Lateral Stability When Maneuvering and Cornering

Tint Naing Win^(✉) and V. M. Alakin

Wheeled Vehicles and Applied Mechanics, Bauman Moscow State Technical University, Kaluga Branch, 2, Bazhenova Str, Kaluga 248000, Russia

Abstract. The lateral stability of a modern car during heavy traffic is mainly determined by the roll angle of the sprung mass. The roll arm of the sprung mass, the angular stiffness of the elastic elements of the suspension and anti-roll bar, as well as the magnitude of the lateral inertia force, have a significant effect on the roll angle and, accordingly, the lateral stability of the vehicle. Knowledge of the theory of motion and the development of vehicle lateral stability is important for the development of vehicle lateral stability systems, which should provide improved road safety. This article describes a study of the effect of body roll on the lateral stability of a vehicle in a combined mode of high-speed cornering or during intensive maneuvering. The lateral forces and body roll angle were determined under the combined modes of heavy traffic on turns and when maneuvering a van-type vehicle, taking into account the angular stiffness of the suspension. The obtained results of the lateral forces and the body roll angle in the combined mode of high-speed cornering or during intensive maneuvering are compared, tested, and proposed for the modernization of lateral stabilization systems of the serial van-type vehicle, as well as for future research on the creation of controlled stabilizers.

Keywords: Lateral force · Centrifugal force · Roll angle · Anti-roll bars · Vehicle rollover · Roll stability · Suspension stiffness

1 Introduction

The lateral stability of vehicles such as a van-type in the process of heavy traffic and maneuvering largely determines the safety of traffic and the safety of the human property. Rollover or sliding of high-speed vehicle is one of the main forms of road traffic accidents [1]. Therefore, the development of technical solutions to stabilize the longitudinal stability of vehicles during intensive maneuvering becomes very important. In cars produced by domestic and especially foreign companies, numerous systems of mechanical and automatic control of the position of the body relative to the suspension are used in order to restore the vertical position of the car in motion. The issues of studying the lateral stability of a car are considered in numerous works of Russian and foreign scientists [1–12]. It has been established that the roll of the sprung mass has a significant effect on the lateral stability of the vehicle, especially in the combined mode of high-speed

movement when cornering and during intensive maneuvering. Under the action of a lateral force, the loads on the elastic elements of the suspension and tires of the left and right sides of the car change, as a result of which the body tilts in the transverse direction [13]. Therefore, driving comfort, handling, and road stability in high-speed cornering and intensive maneuvering should be ensured by more modern technical solutions. The anti-roll bar improves the vehicle's handling by increasing stability when cornering and when maneuvering, but it has several disadvantages. So, the stabilizer does not imply the use of an automatic body position control system during maneuvering and cornering. Therefore, for good vehicle stability and tire grip, it is necessary to develop lateral stabilization devices in the direction of developing systems adapted to combined modes of heavy traffic, both when cornering and maneuvering [14].

Improvement in vehicle stabilization and control solutions is possible when the dynamic and power parameters of the vehicle are known in the combined heavy traffic mode, both when cornering and maneuvering, such as average operating speed, lateral forces, body roll angle, and reaction on wheels associated with the roll arm, mass, and height of the vehicle, and its center of gravity. The resulting lateral and vertical tire load will determine the vehicle's stability when cornering and maneuvering, which in turn determines its stability.

Therefore, at the stage of studies of lateral stability of a modernized serial van-type car, the lateral forces, the value of the roll angle, and the reaction of the wheel bearings when turning and when maneuvering on a horizontal road were determined, taking into account the real values of the structure of the modernized vehicle, speed, and turning radius.

2 Determination of Lateral Forces and Body Roll Angle for a Van-type Vehicle When Cornering

Determination and analysis of the roll angle for serial van-type GAZelle NEXT when vehicle cornering. To determine the roll angle, the balance of the body was considered, on which the forces G_s , F_y and suspension reactions act during curvilinear motion and lateral roll (Fig. 1). The roll angle can be determined as follows [15, 16]:

$$\psi = \frac{F_y h_r}{(K_{\phi 1} + K_{\phi 2}) - G_s h_r}, \quad (1)$$

where $K_{\phi 1}$, $K_{\phi 2}$ is the angular stiffness of the front and rear suspension of the vehicle, h_r is the roll arm, G_s is the sprung mass of the vehicle, and F_y is the lateral force of the sprung masses of the vehicle.

From the formula, we see that the lateral stability of the machine and the roll body during curvilinear motion are significantly affected by inertial forces arising from the turn. As a result of a significant roll of the center of gravity, the body is displaced in the direction of the lateral force, as a result of which the outer wheels are additionally loaded, and the inner wheels are further unloaded. Therefore, to calculate the roll angle, the lateral force F_y was determined taking into account the real operational values of

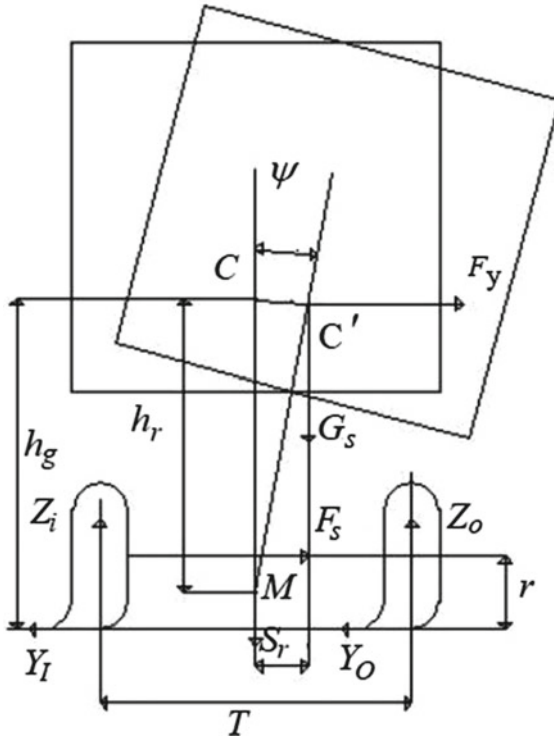


Fig. 1 Scheme for determining the lateral force of inertia and body roll angle in the study of lateral stability

the speed and turning radius for the investigated production car. The lateral force was determined by the well-known formula [15–17]:

$$F_y = \frac{Mv^2}{R}, \tag{2}$$

where M is the mass of the cargo van body, v is the vehicle speed, and R is the turning radius of the vehicle.

The roll arm of the car body h_r was determined by calculation from the technical data of the load distribution over the axles and the calculation of the parameters of the location of the center of gravity of a fully loaded production vehicle [15–18].

$$h_r = h_g - \frac{ah_2 - bh_1}{L}, \tag{3}$$

where h_1 and h_2 are, respectively, the distance from the road surface to the front and rear roll center, a is the distance from the center of mass to the front axle, and b is the distance from the center of mass to the rear axle.

The angular stiffness of the suspension for a modernized production car is determined by the following equations [16–20]:

- for coil spring suspension:

$$K_{\phi 1} = 0.5 s^2 K_s, \tag{4}$$

- for leaf spring suspension:

$$K_{\phi 2} = 0.5 s_l^2 K'_s \eta, \tag{5}$$

where K_s —normal stiffness of the front coil spring suspension; s —the distance between the centers of the coil springs; s_l —the distance between the centers of the leaf springs, m ; K'_s —normal stiffness of the rear leaf spring suspension; η —the coefficient taking into account the increase in the stiffness of the springs when twisting in the transverse direction = 1.05–1.25 (Table 1).

Table 1 Initial data of van-type vehicle

N ^o	Parameter	Value
1	The sprung mass of the vehicle, G_s (kg)	3216
2	Wheelbase L , m	3.145
3	Distance from center of mass to the front axle, a (m)	2.126
4	Distance from center of mass to rear axle, b (m)	1.019
5	The car’s center of gravity height, h_g (m)	1.6
6	Normal front suspension stiffness, K_s (N/m)	66,280
7	Normal rear suspension stiffness, K'_s (N/m)	36,640
8	Distance between the centers of the coil springs, s (m)	1.2
9	Distance between the centers of leaf springs, s_l (m)	1.25
10	Coefficient taking into account the increase in the stiffness of the leaf springs when twisting in the transverse direction	1.05–1.25
11	Rear axle roll center height, h_2 (m)	0.4
12	Roll arm h_r (m)	1.3

An example of calculating the roll angle of the body of a serial van-type vehicle taking into account the lateral force of inertia F_y at a speed of $v = 40$ km/h and a turning radius of the car $R = 70$ m. The roll angle is determined from Eq. (1):

$$\psi = \frac{F_y h_r}{(K_{\phi 1} + K_{\phi 2}) - G_s h_r} = \frac{5660.1.3}{(47000 + 34350) - 32160.1.3} = 0.186 \text{ rad} = 10.65 \text{ deg} .$$

As a result of the study, the roll angle ψ increases with an increase in the lateral force F_y and the roll arm h_r and fits with an increase in the angular stiffness of the car’s suspension. The roll angle usually does not exceed 10 degrees [15, 16]. According to safety requirements, the roll angle should not exceed 10 degrees. As a result of the

determination, at a speed (50 km/h) and a turning radius from 60 to 80 m, the roll angle of the researched vehicle will be more than 10 degrees (Table 2). In this case, a dangerous rollover condition starts to occur, and the vehicle will rollover.

Table 2 Results of calculating the body roll angle at different speeds and turning radius for a modernized of van-type vehicle GAZelle NEXT

Vehicle turning radius (m)	Vehicle speed (km/h)			
	50 (km/h)	40 (km/h)	30 (km/h)	20 (km/h)
80	0.25 rad	0.162 rad	0.091 rad	0.04 rad
70	0.29 rad	0.186 rad	0.01 rad	0.045 rad
60	0.34 rad	0.217 rad	0.121 rad	0.053 rad

3 Determination of Lateral Forces and Body Roll Angle for a Van-type Vehicle During Maneuvering

Determination and analysis of the roll angle for serial van-type GAZelle NEXT during intensive maneuvering. To determine the roll angle, we also considered the balance of the body, on which the forces F_y (F_{cl} , F_c) act during the transverse roll (Fig. 2). The roll angle is also determined during intensive maneuvering [15, 16]:

The transverse component of the centrifugal force Fig. 2:

$$F_y = F_c \cos \gamma \approx \frac{Mv^2\theta}{L}, \quad (6)$$

When driving on the transition curve on the car acts as the force caused by the change of curvature of the trajectory.

The transverse component of the lateral force (Fig. 2):

$$F'_y = \frac{Mvb}{L}\omega_{yk}, \quad (7)$$

Thus, the total centrifugal force acting on the car during (Fig. 2):

$$F = F_y + F'_y = \frac{M}{L} \left(v^2\theta + vb\omega_{yk} \right), \quad (8)$$

where b is the distance from the center of gravity of the vehicle to the rear axle in m, ω_{yk} is the angular velocity of the steered wheels in rad/s, θ is the steering angle steerable wheel (Fig. 2), and L is the wheelbase.

Force F_y always occurs in curvilinear motion. It is proportional to the square of the speed v^2 and the angle θ . The force F'_y only acts when the steering wheel is turned, i.e.,

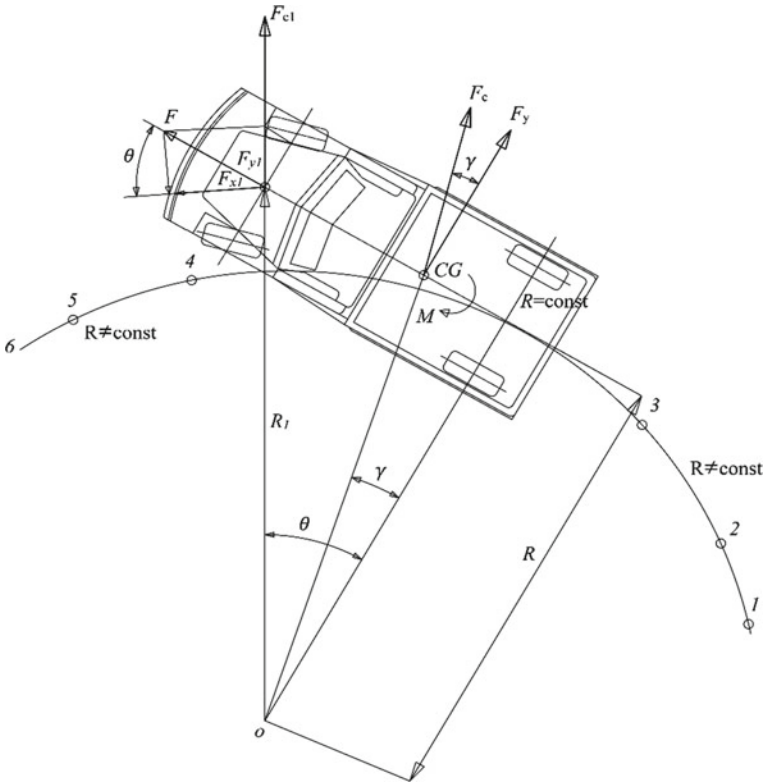


Fig. 2 Scheme for determining the lateral inertia force and body roll angle during intensive maneuvering

when the vehicle is moving along the transition curves when maneuvering (Fig. 2). It is proportional to the vehicle speed and angular velocity of the front wheels. When the car enters the turns during maneuvering, the angle Θ increases, and the angular velocity ω_{yk} is positive; therefore, the force F'_y , adding up with the force F_y , increases the risk of skidding and overturning the car. When the car exits a corner, the angular velocity is negative, and the car can move at a higher speed without losing stability.

Force F'_y arises when the vehicle moves unevenly when maneuvering. This force increases with a sharp increase in the angle and acceleration of the vehicle.

An example of calculating the total centrifugal force acting on a car:

$$L = 3.145 \text{ m}, b = 1.019 \text{ m}, M = 3216 \text{ kg}, \omega_{yk} = 0.03 \text{ rad}, v = 11.1 \text{ m/s}.$$

At the initial moment of movement along the transition curve, i.e., at $t = 0$, the angle $\Theta = 0$, therefore, the first term on the right-hand side of the expression (Eq. 9) is also equal to zero.

Therefore,

$$F = F'_y = \frac{Mvb}{L} \omega_{yk} = \frac{3216 \times 11.1 \times 1.019}{3.145} 0.03 = 347 \text{ N}$$

In 2 s after the start of the turn, the steered wheels will be turned by an angle.

$$\begin{aligned} \theta &= \omega_{yk}t = 0.03 \times 2 = 0.06 \text{ rad} \\ F &= F_y + F'_y = \frac{3216}{3.145} \left(11.1^2 \times 0.06 + 11.1 \times 1.019 \times 0.03 \right) \\ &= 8021 + 347 = 8368N \end{aligned}$$

An example of calculating the roll angle of the body of a laden serial van taking into account the lateral force of inertia at a speed of $v = 40 \text{ km/h}$ and the angular velocity of the front wheels $\omega_{yk} = 0.03$ when maneuvering.

The roll angle is also determined during intensive maneuvering [15, 16];

$$\psi = \frac{F_y h_r}{(K_{\phi 1} + K_{\phi 2}) - G_s h_r} = \frac{8368 \times 1.3}{(47000 + 34350) - 32160 \times 1.3} = 0.27 \text{ rad} = 15.4 \text{ deg}.$$

As a result of the study, the roll angle ψ increases with an increase in the lateral force F_y and decreases with an increase in the angular stiffness of the car’s suspension. The roll angle of a vehicle should usually not exceed 10 degrees [15, 16]. The results of determining and analyzing the roll angle for a serial van-type of the vehicle GAZelle NEXT during intensive maneuvering at a speed (40 km/h) and an angular velocity ($\omega_{yk} = 0.03 \text{ rad/s}$) of the front wheels during maneuvering will be more than 10 degrees (Table 3), and a dangerous rollover condition starts to occur. In this case, a more dangerous condition than at a turn begins when the angular speed of the front wheels = 0.04 rad/s.

Table 3 Results of calculating the body roll angle at various speeds and angular velocity ω_{yk} of the steered wheels when maneuvering for the modernized of van-type vehicle GAZelle NEXT

Angular velocity ω_{yk} (rad/s)	Vehicle speed (km/h)			
	50(km/h)	40(km/h)	30(km/h)	20(km/h)
0.02	0.274 rad	0.17 rad	0.1 rad	0.048 rad
0.03	0.4 rad	0.27 rad	0.15 rad	0.07 rad
0.04	0.54 rad	0.36 rad	0.2 rad	0.09 rad

4 Conclusions

In this article, we proposed the results of body roll research and determined the values of the roll angle for a modernized production van-type vehicle when cornering and maneuvering on a horizontal road, taking into account the real values of the structure of the modernized car, speed, and turning radius. Anti-roll bars are used to increase lateral stability and reduce the roll angle of the vehicle. But recently in cars, anti-roll bars of individual action with automatic control of hydraulic and electric-type are used. During the research, an excess of the roll angle was found for a modernized production

van-type vehicle when maneuvering on a horizontal road of view in comparison with cornering. Therefore, it is proposed to investigate and develop controlled electromagnetic stabilizers, individually on the left and right sides of the axle, to increase the stability and controllability of van-type vehicle of the GAZelle NEXT when maneuvering and cornering.

References

1. Aparicio F, Paez J, Moreno F, Jimenez F, Lopez A (2005) Discussion of a new adaptive speed control system incorporating the geometric characteristics of the roadway. *Int J Veh Auton Syst* 3(1):47–64. <https://doi.org/10.1504/IJVAS.2005.007037>
2. Zhou GXM, Lan FC, Chen JQ et al (2010) Research on analysis and optimization design of coach roll-over based on FEM technology. *Modern Manuf Eng* 5:115
3. Doumiati M, Victorino A, Charara A, Lechner, (2009) Lateral load transfer and normal forces estimation for vehicle safety: experimental test. *Veh Syst Dyn* 47(12):1511–1533
4. Kamnik R, Boettiger F, Hunt K (2003) Roll dynamics and lateral load transfer estimation in articulated heavy freight vehicles. *Proc Inst Mech Eng D, J Automob Eng* 217(11):985–997. <https://doi.org/10.1243/095440703770383884>
5. Verma MK, Gillespie TD (1980) Roll dynamics of commercial vehicles. *Veh. System Dynam* 9(1):1–17. <https://doi.org/10.1080/00423118008968612>
6. Liu PJ, Rakheja S, Ahmed AKW (1997) Detection of dynamic roll instability of heavy vehicles for open-loop rollover control. In: *Proceedings of the 1997 international truck and bus meeting*. SAE Special Publications 1308, Cleveland, Ohio, SAE paper 973263:105–112. <https://doi.org/10.4271/973263>
7. Blow PW, Woodrooffe JHF, Sweatman PF (1998) Vehicle stability and control research for US comprehensive truck size and weight study. *SAE Trans* 107(982819):617–623. <https://doi.org/10.4271/982819>
8. Arnaud JPM, David C (2005) Optimal roll control of an articulated vehicle: theory and model validation 43(12):867–893. <https://doi.org/10.1080/00423110500217167>
9. Nalez AG, Bindemann AC, Brewer HK (1989) Dynamic analysis of vehicle rollover. In: *Proceedings of the 12th international technical conference on experimental safety vehicles*, Gottenburg, Sweden
10. Lund YI, Bernard JE (1995) Analysis of simple rollover metrics. *SAE Technical paper* 950306:23–30. <https://doi.org/10.4271/950306>
11. Garrott RW, Heydinger GJ (1992) An investigation, via simulation, of vehicle characteristics that contribute to steering maneuver induced rollover. *SAE Technical paper* 920585:151–166. <https://doi.org/10.4271/920585>
12. Kutkov GM (2004) *Traktory i avtomobili: Teorija i tehnologicheskie svojstva (Theory and technological properties)*. Izdatel'stvo Kolos, Moscow
13. Polivaev OI, Kostikov OM (2013) *Povysheniye ekspluatatsionnykh svoystv mobil'nykh energeticheskikh sredstv za schet sovershenstvovaniya privodov vedushchikh koles (Improving the operational properties of mobile power facilities by improving the drives of the driving wheels)*. Voronezh
14. Kelvin Hubert Spartan chassis (2005) "Anti-Roll Stability Suspension Technology" SAE PP. 2005-01-3522
15. Artamonov MD, Ilarionov VA, Morin MM (1974) *Osnovy teorii i konstrukcii avtomobilja (Fundamentals of the theory and design of automobiles)*. Uchebnik dlja tehnikumov "Mashinostroenie". Moscow

16. Ilarionov VA (1966) *Ekspluatatsionnyye svoystva avtomobilya* (The operational properties of the car). Uchebnik dlya studentov avtomobil'no-dorozhnykh vtuzov i fakul'tetov. Izd. 3-ye, pererab "Mashinostroyeniye", Moscow
17. Rakheja S, Piche A (1990) Development of directional stability criteria for an early warning safety device. SAE Technical paper 902265:1–16. <https://doi.org/10.4271/902265>
18. Verzhbickij AN (2009) *Pokazateli mass avtomobilej: metod ukazaniya k vypolneniju laboratornyh rabot i domashnego zadaniya po kursam "Osnovy nauchnyh issledovaniy i ispytaniy avtomobilej" i "Osnovy nauchnyh issledovaniy i ispytaniy kolesnyh mashin"* (Fundamentals of research and testing of wheeled vehicles). Izdatel'stvo BMSTU im. N. Je. Baumana, Moscow
19. Kuznetsov VA, Dyakov IF (2003) *Konstruirovaniye i raschet avtomobilya* (Vehicle design and calculation). *Podveska avtomobilya: Uchebnoye posobiye*. Ulyanovsk
20. Khocheva AM, Chichekina IV (2011) *Konstruirovaniye i raschet shassi avtomobilya* (Design and calculation of a car chassis). MSIU, Moscow



Improvement of Turbocharger Aeroacoustic Performance When Opening Wastegate

R. I. Rakhmatov^(✉), V. E. Krutolapov, and A. G. Vetoshnikov

FSUE “NAMI” State Research Center of the Russian Federation, 2, Avtomotornaya Street,
Moscow 125438, Russia

rakhmatjon.rakhmatov@nami.ru

Abstract. The paper addresses the results of calculation studies of turbocharger aeroacoustic performance when opening the wastegate. The modern methods of computational aeroacoustics (CAA) are considered, allowing reduction of the noise level and including the turbocharger, when the wastegate is opened. The finite element model of the internal volume of the wastegate with the turbocharger “cold” end was developed. The hybrid approach with Mohring’s analogy was chosen for the aeroacoustic noise calculation when opening the turbocharger wastegate. The aeroacoustic noise of the turbocharger when opening the wastegate was calculated, and the noise source density areas were localized according to Mohring. Experimental validation of the calculation was performed on the engine and vehicle test bench. Parametric optimization was performed in order to reduce the noise when opening the turbocharger wastegate. Aeroacoustic noise reduction when opening the turbocharger wastegate was confirmed experimentally on the engine test bench and within the road tests. Based on the results of the optimization research, the 5 dBA reduction in the noise of the turbocharger at opening was registered.

Keywords: Computational aeroacoustics · Turbocharger noise · Finite element modeling · Aeroacoustic noise calculation · Mohring’s analogy · Experimental validation of calculation · Parametric optimization · Engine tests · Road tests

1 Introduction

A turbocharger is the main actuator of any turbocharging system applied in internal combustion gasoline or diesel engines in order to increase their power and efficiency factor. A turbocharger is a generic colloquial name of any energy machine, which function is the use of kinetic energy of exhaust gases of an internal combustion engine for air compression for its further use in this engine for its operation. Structurally, it always consists of two impeller (vane) machines—a gas turbine and a rotary (vane) compressor—connected by a common shaft. A turbocharger principle of operation is as follows: The flow of the exhaust gases with high temperature and pressure passes through the impeller machine of the gas turbine and rotates it by means of its kinetic energy. The turbine transfers the rotation energy through the shaft to the impeller machine of the

vane compressor, which compresses the air. The compressed air is transferred to the engine combustion chamber, where it is mixed with liquid fuel. In the chamber, due to thermochemical processes, the potential energy of compressed air and fuel turns into kinetic energy; the volume of the mixture and its temperature increase simultaneously; due to that, both engine operation and impact on the turbocharger turbine are somehow performed.

This article examines the mode of pressure relief in the turbocharger compressor-part circuit by means of the wastegate, which results in the observed increase of the overall sound pressure of the vehicle by 10 dBA. In order to reduce the aeroacoustic noise, calculation and optimization works were performed; the result of which allowed reducing the noise by 5 dBA. The experimental validation has also been performed.

2 Computational Aeroacoustics (CAA)

It is known that aeroacoustics is a branch of physics at the borderline of aerodynamics and acoustics that studies the issues of aerodynamic sound generation, sound propagation in a moving medium, interaction between sound and an unsteady flow, as well as methods of aerodynamic (wind) noise reduction.

Presently, computational aeroacoustics (CAA) capable to solve a wide range of aeroacoustic issues is developing at a swift rate. In this connection, it is expedient to consider and examine modern methods of computational aeroacoustics (Fig. 1), which will help to reduce noise including that of a turbocharger when opening the wastegate [1–20].

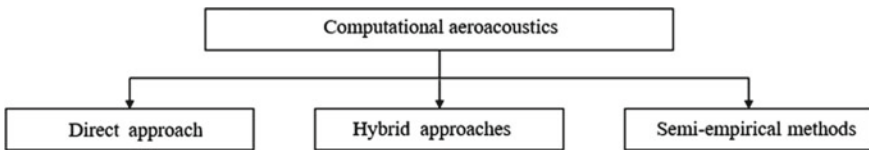


Fig. 1 Methods of computational aeroacoustics

Direct approach It is the most consuming in terms of computational resources. Related or coupled issues of vibroacoustics, absorption in sound-absorbing materials, etc. are impossible to solve.

1. It provides the highest calculation accuracy. In theory, it can be applied to any type of flow. It assumes solving full Navier–Stokes equations across all turbulence scales. No empirical dependences. All arising physical effects (reflection, diffraction, dispersion or scattering of waves, etc.) are taken into account.
2. Computational performance:

- The turbulence is being defined by two factors or components:
- Eddy length (characterized by the Kolmogorov length scale): $l_v = \frac{L}{\sqrt[4]{Re_{LF}^3}} \approx$

$$\frac{L}{\sqrt[4]{Re^3}}$$

- Time (related to the Kolmogorov structure): $\tau_v = \frac{l_v}{u_v} \approx \frac{l_v}{U}$
 - The acoustic wave propagation is determined by two components:
 - Wave length: $\lambda = \frac{c_0}{f} = \frac{c_0}{St} \cdot \frac{L}{M} = \frac{L}{St \cdot M}$, therefore: $\frac{\lambda}{L} \sim \frac{1}{M}$
 - Time: $T = \frac{1}{f} = \frac{L}{St \cdot U}$, therefore: $T \sim \frac{L}{U}$
3. The higher the Reynolds number is, the better the grid quality shall be. Respectively, increase in the Reynolds number is inversely proportional to the eddy length l_v .
 4. Computational inputs for direct solutions of Navier–Stokes equation for aeroacoustics

- The memory requirements are related to discretization of space:

$$\left(\frac{\lambda}{l_v}\right)^3 \sim \frac{\sqrt[4]{\text{Re}^9}}{M^3}$$

- The calculation time is related to time discretization:

$$\frac{T}{\tau_v} \sim \frac{L/U}{l_v/U} = \frac{L}{l_v} \approx \frac{\sqrt[4]{\text{Re}^3}}{M}$$

- General computational resources: (calculation time) \times (memory requirements):

$$\left(\frac{\lambda}{l_v}\right)^3 \cdot \left(\frac{T}{\tau_v}\right) = \frac{\text{Re}^3}{M^4}$$

Hybrid approach This method is developed for calculation of generation and propagation of noise with “acceptable” computational inputs, with possibility to solve related problems, also considering “all” acoustic effects.

1. Assumption:

- Acoustic sources are related to the turbulent flow;
- The acoustic field does not affect the flow.

2. Calculation sequence:

- Calculation of an unsteady flow by means of DES, LES, U-RANS, etc.;
- Unsteady Reynolds-averaged Navier–Stokes equations (for an unsteady flow):
 - Using Reynolds averaging procedure;
 - Application of Reynolds averaging to Navier–Stokes equations leads to obtain Reynolds equations, which are incomplete or non-closed;
 - Closing or completing Reynolds equations (determination of turbulent shear stresses) is made by means of semi-empirical turbulence models. All turbulent eddies are simulated;

- Detached eddy simulation (DES) method:
 - Combination of the classical RANS formulation with the LES method elements;
 - Accurate prediction of the turbulent boundary layer up to the separation or detachment point;
 - The computational inputs for the flows with high Re values are by orders less.
- Large eddy simulation (LES) method:
 - The transfer equations are solved relative to “solvable scales”;
 - The large eddies are resolved; the small ones are simulated;
 - The solution is by definition unsteady; Δt is determined by the smallest resolved eddies.
- Derivation of noise sources from the gas-dynamic (CFD) calculation;
- Interpolation of the gas-dynamic grid with the derived flow data to the acoustic grid;
- Calculation of noise propagation from the source.

3. Types of calculation methods:

- Analogy concept: Goldstein’s, Lighthill’s and Mohring’s analogies are intended for calculation of all aeroacoustics problem types;
- Goldstein’s analogy is used to calculate the fan’s tonal noise. The fundamental idea of Goldstein’s analogy is replacing the rotating blades of the fan with an equivalent set of sources in the form of monopoles ($\rho_0 V_n$), dipoles (F_i) and quadrupoles (T_{ij}) shown below:

$$\begin{aligned}
 p(x, t) = & - \int_{-T}^T \int_{S(\tau)} \left(\rho_0 V_n \frac{\partial G}{\partial T} + F_i \frac{\partial G}{\partial T} \right) dS(y) d\tau \\
 & + \int_{-T}^T \int_{v(\tau)} \left(T_{ij} \frac{\partial^2 G}{\partial y_i \partial y_j} \right) dv(y) d\tau
 \end{aligned}$$

- Lighthill’s analogy is used to calculate noise at flow speeds up to 0.2 Mach. The fundamental idea of Lighthill’s analogy is as follows:
 - Sound is generated by the flow through moment-of-momentum fluctuation during the interaction between the flow and a solid boundary, which constitutes its fundamental difference from active radiation (foreground emission) in the classic sense;
 - The medium in which sound propagates is considered non-convective;
 - The main variable of the acoustic source is density;

Therefore, this analogy is based on the assumption that density fluctuation in the turbulent region shall behave similarly to acoustic waves. The equation describing sound generation under such assumptions is as follows:

$$\frac{\partial^2 \rho}{\partial t^2} - c_0^2 \nabla^2 \rho = \frac{\partial^2 T_{ij}}{\partial x_i \partial x_j}$$

where T_{ij} is the Reynolds (turbulence) stress tensor defined as stated below:

$$T_{ij} = \partial \rho v_i v_j + \delta_{ij} (p - p_0 - c_0^2 (\rho - \rho_0)) - e_{ij}$$

where e_{ij} is the viscous stress tensor defined as stated below:

$$e_{ij} = \left(\frac{\partial v_i}{\partial y_j} + \frac{\partial v_j}{\partial y_i} - \frac{2}{3} \delta_{ij} \frac{\partial v_k}{\partial y_k} \right)$$

- Mohring’s analogy. This analogy allows calculation of noise at flow speeds up to 0.9 Mach, including calculation in a convective medium. The fundamental idea of Mohring’s analogy:

- Includes using scalar equations, which are best suited to describe sound propagation in an inhomogeneous medium;
- Requires average flow thermodynamic parameter values;
- Acoustic simulation requires refinement in certain areas of the acoustic domain in order to exclude parasite noise sources;

The equation describing sound generation and propagation is as follows:

$$\begin{aligned} & \frac{\partial}{\partial t} \left(\frac{\rho}{\rho_T^2 c^2} \frac{\partial b}{\partial t} + \frac{\rho v_i}{\rho_T^2 c^2} \frac{\partial b}{\partial x_i} \right) + \frac{\partial}{\partial x_i} \left(\frac{\rho v_i}{\rho_T^2 c^2} \left(\frac{\partial b}{\partial t} + v_i \frac{\partial b}{\partial x_i} \right) - \frac{\rho}{\rho_T^2} \frac{\partial b}{\partial x_i} \right) \\ &= - \frac{\partial}{\partial x_i} \left(\frac{\rho}{\rho_T} (\vec{v} \cdot \vec{\omega})_i - \frac{\partial \tau_{ij}}{\partial x_j} \right) + \frac{\partial}{\partial x_i} \left(\frac{v_i}{\rho_T} \left(\frac{\partial \rho}{\partial S} \right)_p \frac{\partial S}{\partial t} - \frac{\rho T}{\rho_T} \frac{\partial S}{\partial x_i} \right) \\ &+ \frac{\partial}{\partial t} \left(\frac{1}{\rho_T} \left(\frac{\partial \rho}{\partial S} \right)_p \frac{\partial S}{\partial t} - \frac{\rho v_i}{\rho_T^2} \frac{\partial \rho_T}{\partial x_i} \right) \end{aligned}$$

Classification based on similarity with a canonical monopole, dipole, quadrupole;

$$p - p_0 = \frac{1}{4\pi c_0^2} \frac{\partial^2}{\partial x_i \partial x_j} \int_V \frac{T_{ij}(y, t - \frac{r}{c_0})}{r} dy - \frac{1}{4\pi c_0^2} \frac{\partial}{\partial x_i} \int_S \frac{P_i(y, t - \frac{r}{c_0})}{r} dS(y)$$

Therefore, the surface integral of Lighthill’s theory modification is the acoustic impact created by dipole source distribution through or by force P_i per unit of area.equivalent set of sources in

- Lighthill’s integral method is based on the assumption that density fluctuation $p - p_0$ in the turbulent region shall behave similarly to acoustic waves.

The complete calculation history shall be saved in the time domain;
This method uses the volume integral.

- Ffowcs Williams-Hawkings integral method describes distribution of each separate source type.

$$\left(\frac{\partial^2 \rho}{\partial t^2} - c_0^2 \frac{\partial^2}{\partial x_i^2} \right) (p - p_0) H(f) = \frac{\partial^2 (T_0 H(f))}{\partial x_i \partial x_j} - \frac{\partial F_i}{\partial x_i} \delta(f) + \frac{\partial Q_i}{\partial t} \delta(f)$$

The first element on the right hand side of the equation represents the quadrupole source distribution; the second one represents the dipole source distribution; the third one represents the monopole source distribution determined by volume displacement.

The sound pressure calculation in the far (long range) field is based on the near (short range) field surface radiation;

Semi-empirical methods These methods are developed for calculation of noise generation and propagation in case of accidental exposure or impact. Discontinuous Galerkin method can be qualified as a semi-empirical method:

1. Sound propagation in an acoustic medium is considered in linear setup taking the following into account:
 - Fields of average velocity of medium flow;
 - Impedance boundary conditions;
 - Conditions of non-attenuation at the boundaries of the calculated area;
 - Wide range of external influences.
2. Linearized Euler equations are solved;
3. Discontinuous Galerkin method is used:
 - P-adaptive sampling;
 - Expansion in basis functions;
 - Explicit time integration scheme;
 - Automatic time step adjustment based on the Courant criterion;

Based on the above, it can be concluded that:

1. The direct approach is the most demanding in terms of computational performance and capability; it can be implemented only with supercomputers in actual practice; it is hardly applicable to engineering tasks and does not allow solving the problems regarding vibroacoustics, taking absorption into account, etc.;
2. The hybrid approaches are the most suitable for engineering tasks; they require less computing machine resources, take all acoustic effects into account and provide solutions to related tasks and problems;
3. The semi-empirical methods are the most suitable for gas turbine engine noise analysis including analysis with regard to vibrating surfaces and sound-absorbing materials.

The hybrid approach with Mohring's analogy was chosen for aeroacoustic noise calculation when opening the turbocharger wastegate.

3 Calculation Studies and Optimization

The three-dimensional model of the inner volume of the wastegate with the turbocharger "cold" end is shown in Fig. 2a, and the finite element model according to [20–22] is shown in Fig. 2b, respectively. The gas-dynamic (CFD) calculation was performed in the Siemens Star CCM + software.

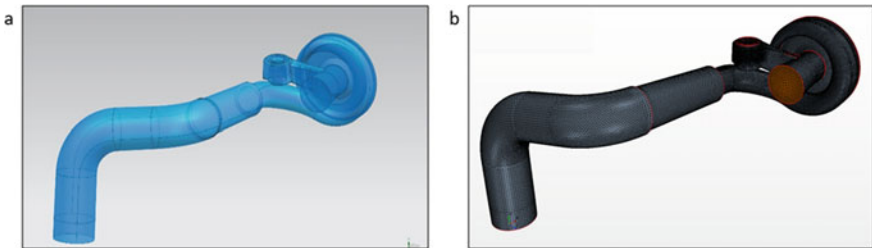


Fig. 2 a Three-dimensional model; b Finite element model

Figure 3 provides the result of noise source density calculation according to Mohring performed in the Actran (Hexagon/FFT) software suite.

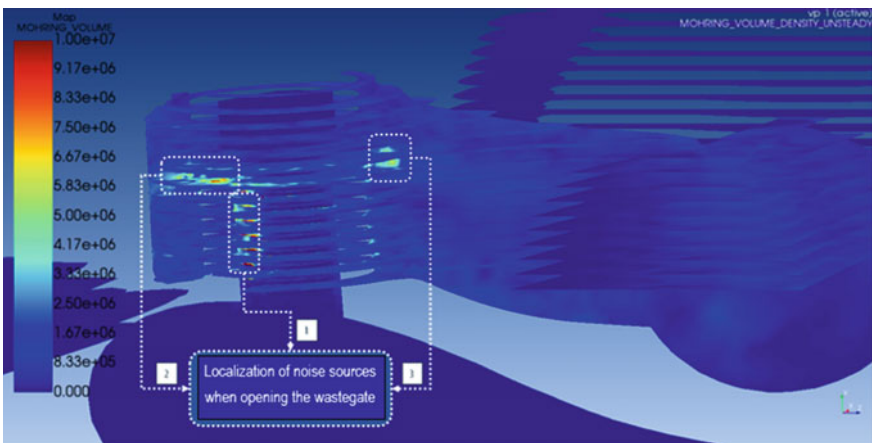


Fig. 3 Mohring noise source density

Figure 4 shows distribution of sound pressure over volume at frequencies of 500 (a) and 1500 (b) Hz.

Figure 5 shows distribution of sound pressure over volume at frequencies of 2500 (a) and 3500 (b).

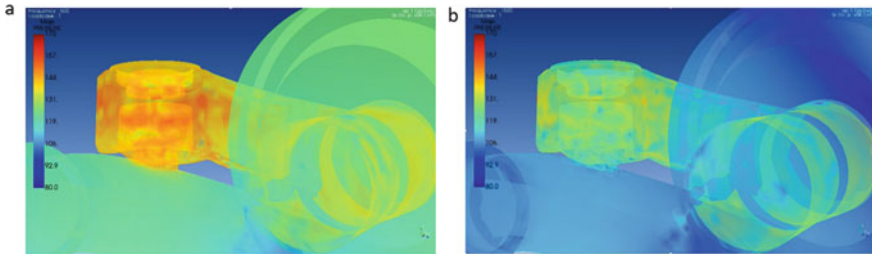


Fig. 4 **a** Sound pressure distribution over volume at 500 Hz; **b** Sound pressure distribution over volume at 1500 Hz

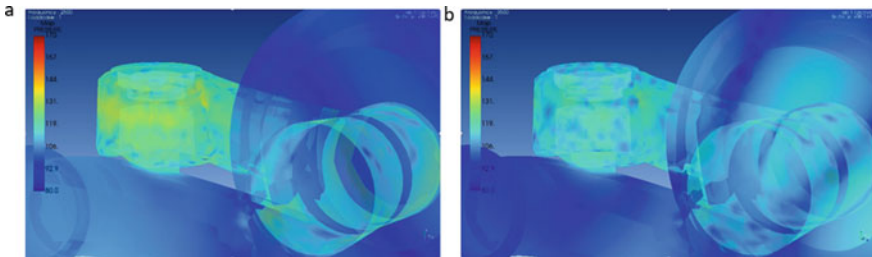


Fig. 5 **a** Sound pressure distribution over volume at 2500 Hz; **b** Sound pressure distribution over volume at 3500 Hz

There were three noise source localization areas registered when opening the wastegate (Fig. 3). In order to reduce aeroacoustic noise, a parametric optimizer was used with the following variables:

1. Rounding-off radius of the wastegate mounting seat edge (R_{out});
2. Relative diameter of the wastegate channel (ΔD);
3. Rounding-off radius of the wastegate channel base edge (R_{in}).

And the target function: reduction of the turbulent flow viscosity.

180 variants have been analyzed. The best design with the minimum value of turbulent viscosity with designated boundary conditions is the design of the wastegate channel with the following parameters: $R_{out} = 5.44$ mm, $\Delta D = 0.1$ mm, $R_{in} = 0.1$ mm.

Then, comparison aeroacoustic calculations were performed, and the measurement point was inside the intake pipe at the distance of 300 mm from the wastegate. The comparison diagram is shown in Fig. 6.

4 Experimental Validation

In order to assess adequacy of the calculation studies and optimizing works, experimental studies were performed. The tests were performed on the engine test bench, and the microphone was arranged at the distance of 300 mm from the intake system mouth (Fig. 7). Test mode: acceleration to 4000 rpm and tip-out, 600 N/m load.

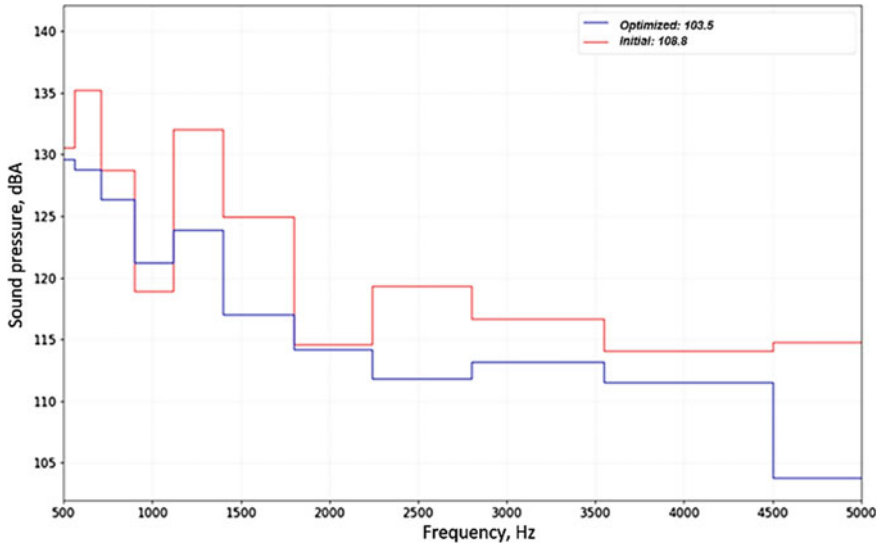


Fig. 6 Comparison diagram of A-scale sound pressures of the initial and optimized turbocharger designs

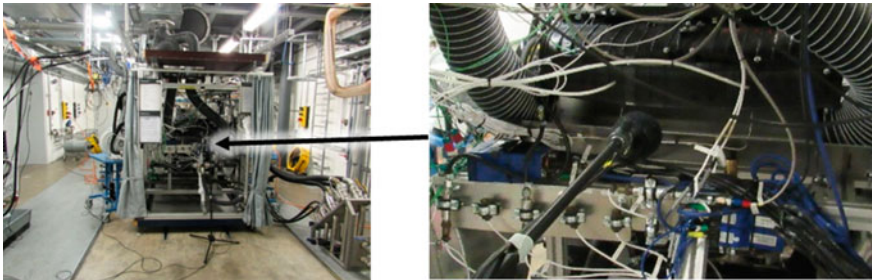


Fig. 7 Microphone position on the engine test bench

The results of the experimental research are shown in Fig. 8 (a—waterfall diagram and b—sound pressures over time diagram).

From the cascade diagram (Fig. 8a), it follows that the maximum sound pressure when opening the wastegate is within the frequency band of 200–2000 Hz. And, the diagram in Fig. 8b shows that the optimized design of the wastegate channel reduces noise by 5 dBA.

It is worth pointing out that the sound pressure spectra in the calculation and experimental studies are well-correlated with one another, but due to different microphone positions, the levels differ. It is not reasonable to simulate the microphone arrangement as in the experiment because solving this issue will demand unreasonably high computational resources due to simulating the whole intake system. In addition, there is no possibility to spatially arrange the microphone as in the calculation case due to physical

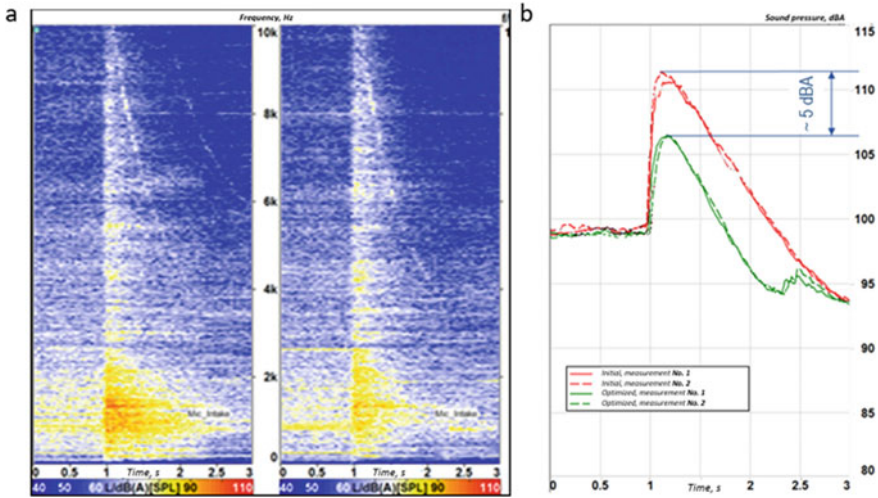


Fig. 8 a Waterfall diagram of sound pressures of initial and optimized designs of the turbocharger; b Sound pressures level diagram of initial and optimized designs of the turbocharger

impact of the flow on the microphone membrane. Notwithstanding the above, the registered difference in sound pressures of 5 dBA between the initial turbocharger design and the optimized one is confirmed by the experimental and calculation studies. The comparison study shows adequacy of the calculation studies.

In addition to that, the experimental validation of the calculation was performed on the vehicle. Testing mode: acceleration in third gear and slowing down. The microphone shown in Fig. 9 was arranged 50 mm away from the intake mouth.

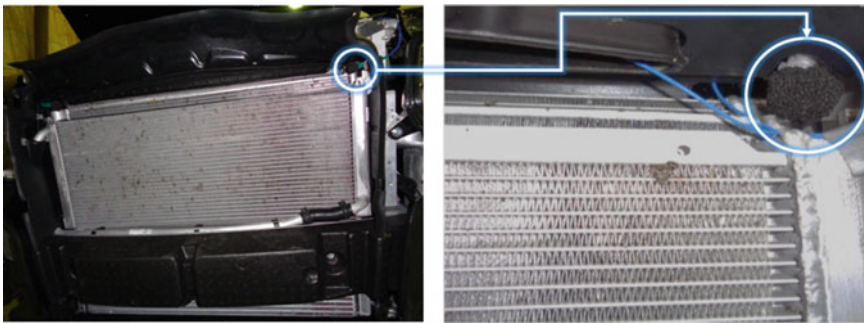


Fig. 9 Microphone position on the vehicle

The results of the experimental studies on the vehicle are shown in Fig. 10.

A 5 dBA sound pressure difference between the initial and optimized turbocharger designs was detected, which proves the adequacy of the calculation studies. Due to the optimization works, 5 dBA noise reduction when opening the wastegate has been achieved.

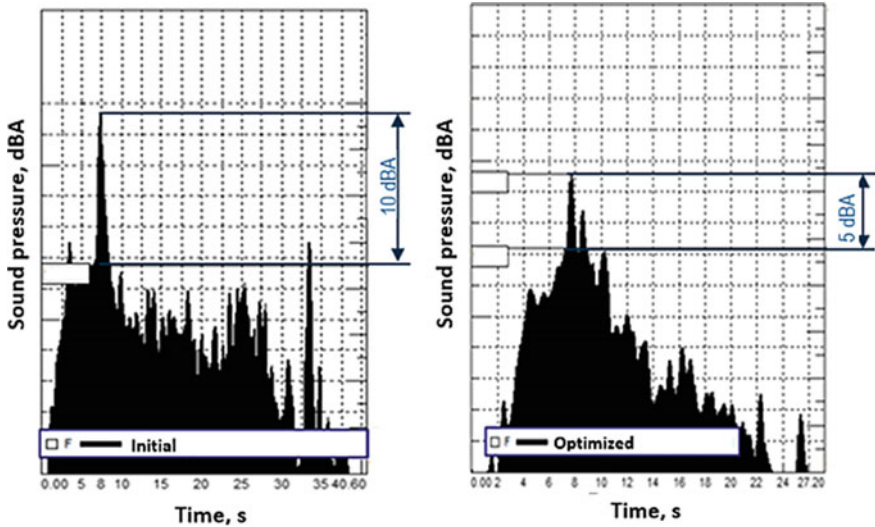


Fig. 10 Results of experimental studies on the vehicle

5 Conclusion

1. The aeroacoustic noise of the turbocharger when opening the wastegate was calculated, and the noise source density areas were localized according to Mohring.
2. The parametric optimization was performed, which allowed reduction of the noise by 5 dBA.
3. The experimental validation of the calculation confirming the adequacy of the calculation studies was performed.
4. The reduction of the turbocharger noise by 5 dBA was registered when opening the wastegate.

References

1. Blokhintsev DI (1981) In: Acoustics of inhomogeneous moving medium. Science, Moscow, pp 208
2. Howe MS (1975) Contribution to the theory of aerodynamic sound, with application to excess jet noise and the theory of the flute. *J Fluid Mech* 71(4):625–673
3. Crighton DJ (1981) Acoustics as a branch of fluid mechanics. *J Fluid Mech* 106:261–298
4. Hardin JC, Pope DS (1994) An acoustic splitting technique for computational aeroacoustics. *Theor Comput Fluid Dyn* 6:334–340
5. Goldstein M (1981) In: Aeroacoustics. Mashinostroenie, Moscow, pp 296
6. Lighthill MJ (1952) On sound generated aerodynamically: I. general theory. *Proc Royal Soc London Ser A* 211(1107):564–587
7. Lighthill MJ (1954) On sound generated aerodynamically: II. turbulence as a source of sound. *Proc Royal Soc London, Ser A* 222(1148):1–32

8. Mohring W (1979) Modeling low mach number noise. In: Proceedings symposium mechanics sound generation in flow. Springer, Berlin, pp 85–96
9. Curle N (1955) The influence of solid boundaries upon aerodynamic sound. Proc Royal Soc A: Math Phys Eng Sci 231(1187):505–510
10. Williams JEF, Hawkings DL (1969) Sound generated by turbulence and surfaces in unsteady motion. Philos Trans R Soc A264(1151):321–342
11. Bewley TR, Moin P, Temam R (2001) DNS-based predictive control of turbulence: an optimal benchmark for feedback algorithms. J Fluid Mech 447:179–225
12. Collis SS, Ghayour K, Heinkenschloss M, Ulbrich M, Ulbrich S (2000) Numerical solution of optimal control problems governed by the compressible Navier–Stokes equations. In: Leugering G, Sprekels J, Troltzsch F (eds), Proceedings of the international conference on optimal control of complex structures, Birkhauser
13. Jameson A, Pierce NA, Martinelli L (1997) Optimum aerodynamic design using the Navier-Stokes equations. AIAA paper 97–0101
14. Holmes P, Lumley JL, Berkooz G (1996) In: Turbulence, coherent structures, dynamical systems and symmetry. Cambridge University Press, Cambridge
15. Bodony DJ, Lele SK (2005) On using large-eddy simulation for the prediction of noise from cold and heated turbulent jets. Phys Fluids 17:085103
16. Huff DK (2001) Proceedings of the jet noise workshop, Technical Report NASA CP–2001–211152, NASA, Cleveland, Ohio
17. Cockburn B, Shu C-W (1998) The local discontinuous Galerkin method for time-dependent convection-diffusion systems. SIAM J Numer Anal 35(6):2440–2463
18. Chevaugeon N, Remacle J-F, Gallez X, Ploumans P, Caro S (2005) Efficient discontinuous Galerkin methods for solving acoustic problems. In: 11th AIAA/CEAS aeroacoustics conference, AIAA 2005–2823
19. Schiltz B, Leneveu R, Caro S, Druon Y, Mosson A (2009) Exhaust noise reduction of realistic 3D lined turbofans submitted to strong shear layers. In: 15th AIAA/CEAS aeroacoustics conference. AIAA 2009–3416
20. Rakhmatov RI, Krutolapov VE, Zuzov VN (2019) Development of calculation research method for exhaust system main elements acoustic characteristics / IOP conference series: materials science and engineering, vol 819. International Automobile Scientific Forum (IASF-2019) “Technologies and Components of Land Intelligent Transport Systems” 16–18 October 2019 Moscow, Russian Federation
21. Rakhmatov RI, Zuzov VN (2019) Development of a design method for determining the attachment of the exhaust mounting mounts. AKUSTIKA 34:141–147
22. Rakhmatov RI (2019) Modern Vehicle exhaust system design dynamic analysis. AKUSTIKA 32:351–354



Cooling System Axial Fan Design Calculation and Optimization in Terms of Tonal Noise

R. I. Rakhmatov^(✉), V. E. Krutolapov, and R. H. Kurmaev

FSUE “NAMI” State Research Center of the Russian Federation, 2, Automotornaya street,
Moscow 125438, Russia
rakhmatjon.rakhmatov@nami.ru

Abstract. The paper provides methods of axial fan noise reduction and considers the results of calculation studies of the fan tonal noise. The tonal noise related to the rotational and interaction noise has 15–20 dB higher levels than the broadband turbulent and vortex noises, and therefore, it has the most annoying impact. A finite element model of the cooling system fan has been developed. The noise was calculated with the microphone located in the near field and the speed of the cooling fan being 2142 rpm. Goldstein analogy was used for modeling and further optimization in terms of tonal noise. Parametric optimization for tonal noise reduction was performed. The number of blades and the angles between blades were chosen as variables. More than 20 options of the cooling system fans were considered. The best design in terms of the tonal noise of the blade among the ones included in this article is the seven-blade fan.

Keywords: Computational aeroacoustics (CAA) · Fan noise · Finite element modeling · Aeroacoustic noise calculation, Goldstein analogy · Parametric optimization

1 Introduction

The efficiency factor of modern internal combustion engines does not exceed 40%, and thus, more than 60% of energy turns into heat which needs to be removed. This problem is solved by a liquid cooling system of an internal combustion engine with an axial fan (the fan), but the fan itself is one of the main sources of noise and vibration of the vehicle. Sound or acoustic radiation during the fan operation appears basically because of aerodynamic processes. As we know from [1–3], aerodynamic or wind noises can be caused by different types of sources (monopole, dipole, quadrupole, etc.) with different origins, while they can be divided into two groups:

1. Sources causing tonal (discrete) noise:

- Noise connected with rotation of blades:
 - Load noise—caused by the influence of the flow on the fan blades;

- Displacement noise—caused by the displacement of certain air volume by the rotating blades;
- Interaction noise—connected with the interaction of the airflow with fixed parts of the fan (electric motor housing), the inlet guide vanes (casing), and the outlet straightener.

2. Sources causing broadband noise:

- Turbulent boundary layer noise connected with separation or shedding of turbulent boundary layer eddies from the rear or trailing edge of the blades when blown over by the airflow;
- Vortex noise connected with pressure pulsations (lifting force) on the blades;

Figure 1 is an illustration of two types of aerodynamic sources, the first receiver “perceives” broadband noise, and the second one perceives tonal noise, respectively.

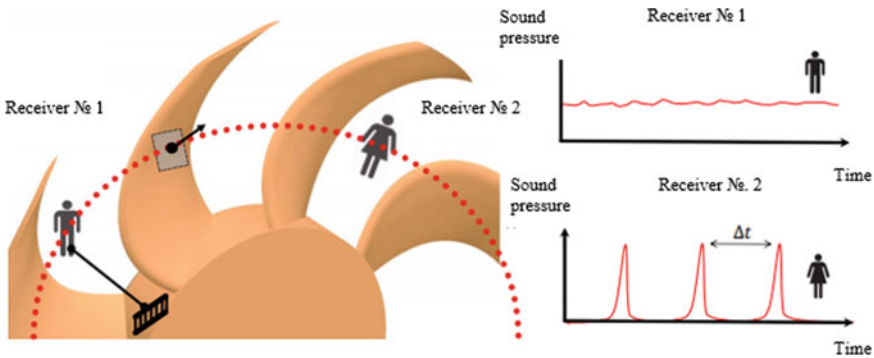


Fig. 1 Types of noise sources

Additionally, receiver No. 2 will “perceive” a periodic impulse in the course of time Δt . This impulse is final and proportional to the gas-dynamic pressure at frequencies f and its harmonics $2f, 3f, \dots, nf$. Frequency f is determined by the following Eq. 1.

$$f = \frac{n}{60} \cdot i \tag{1}$$

where n is the fan rpm and i is the number of blades.

It should be noted that this paper does not consider the noise connected with unbalance of the impeller and electromechanical noise of the fan motor making a contribution to the general noise of the fan.

2 Methods of Fan Noise Reduction

The methods of fan noise reduction by changing the fan design and organizing the airflow correspondingly are given in papers [4–17] according to which the recommendations are as follows:

- Fan impeller peripheral speed reduction—as sound power of the following noise sources is proportional to the fan impeller peripheral speed (v):
 - Turbulent noise (quadrupole source) $\sim v^8$
 - Vortex noise (dipole source) $\sim v^6$;
 - Load noise (dipole source) $\sim v^6$;
 - Displacement noise (monopole source) $\sim v^4$.
- Increasing the number of impeller blades and simultaneously lowering aerodynamic forces occurring on the blade profile;
- Shaping its elements blown over by the airflow to be well-streamlined;
- Reducing obstacles in the flow at the impeller inlet and ensuring smooth inlet to the impeller without swirling or eddying.
- The number of the blades of the guide vanes Z_n and impeller Z_n shall comply with Eq. 2:

$$\frac{k_m m}{i Z_\kappa} > \frac{M_v}{\sqrt{1 - M_{ca}^2}} \quad (2)$$

where $M_v = v_k/c_0$; $M_{ca} = c_a/c_0$; v_k is the peripheral speed of the blade tips or ends; c_a is the axial speed; k_m is the wave parameter; $m = |iZ_{pk} + kZ_{AH}|$; k is the coefficient ranging over the values of all integers; i is the harmonic number.

- Optimization of the blade shape in order to ensure flow without separation (attached airflow) throughout the length of the blade—in paper, there is an example of a non-optimal aerodynamic shape of the fan blade where the boundary layer noise generates tonal noise. To solve this task, paper suggests using the fan blades with the serrated shape of the trailing edge;
- Use of the impeller blade with the curved axis of profile alignment—Fig. 2 shows the blade and signals of rotational noise from its different sections (with different phases because of the spatial shape of the blade). On the right, the vector chart of the signal sum is shown, from which it is apparent that the correct combination of phases and amplitudes of the signals can significantly reduce the rotational noise. The idea of forming the phase shift of acoustic waves from different sections of the impeller blades by changing the profile alignment axis shape.
- Use of the impeller with an irregular pitch of the blades—in case of an irregular pitch (uneven spacing), each blade will radiate a sequence of sound pressure impulses in uneven intervals, which leads to lowering and “blurring” of tonal noise. Figure 3 shows noise reduction depending on relative grid spacing unevenness. It is worth pointing out that this effect decreases as the number of cooling system fan blades becomes higher.
- Connecting the impeller blades peripherally using a ring.
- Increasing the fan casing stiffness in order to reduce the noise generated by the casing surfaces.

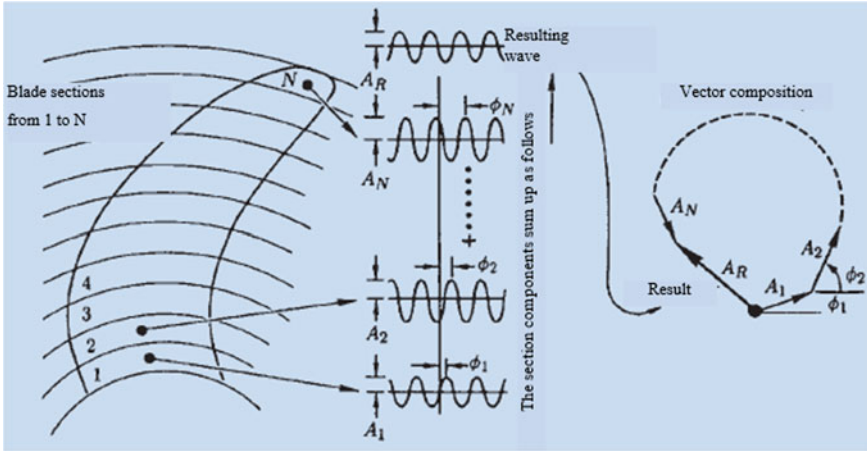


Fig. 2 Scheme of interference of excitations from individual areas of the fan blade

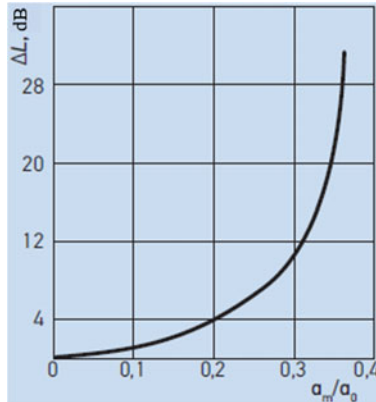


Fig. 3 Noise reduction depending on relative grid spacing unevenness

3 Calculation Research

The tonal noise related to the rotational and interaction noise has 15–20 dB higher levels than the broadband turbulent and vortex noises, and therefore, it has the most annoying impact.

To model and further optimize in terms of noise, we will use Goldstein’s analogy [18], and the formula of which is given below:

$$p(x, t) = - \int_{-T}^T \int_{S(\tau)} \left(\rho_0 V_n \frac{\partial G}{\partial T} + F_i \frac{\partial G}{\partial T} \right) dS(y) d\tau + \int_{-T}^T \int_{V(\tau)} \left(T_{ij} \frac{\partial^2 G}{\partial y_i \partial y_j} \right) dv(y) d\tau \quad (3)$$

where ρ_0 is the average flow density and G is the Green’s function.

It follows from the formula that the sources can be divided into three types:

- Monopole— $\rho_0 V_0$;
- Dipole— F_i ;
- Quadrupole— T_{ij} .

Figure 4 shows as follows:

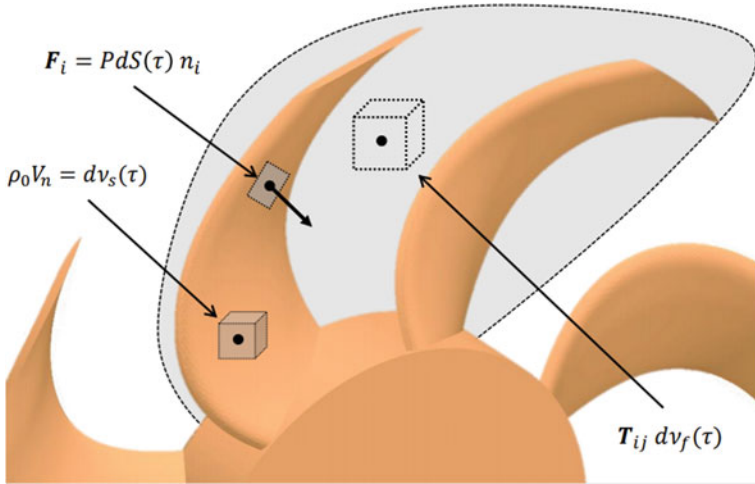


Fig. 4 Noise sources used in Goldstein's analogy in Actran software

- In differential area dS , force per area unit is applied, which corresponds to gas-dynamic pressure P multiplied by normal vector n_i ;
- Solid body differential volume dv_s generates mass oscillations (monopole source) due to the rotor motion;
- Differential gas volume dv_f defines tensor stresses or quadrupole sources.

Based on this analogy, for the calculation of the fan tonal noise, it is enough to obtain the monopole and dipole sources from the gas-dynamic calculation and then calculate the propagation of the sound wave. For this purpose, a finite element model of the cooling system fan [19, 20] has been developed. Extraction of thermodynamic fields from the gas-dynamic flow and calculation of the sound wave propagation were conducted in the FFT/Hexagon Actran software suite. Boundary conditions for the gas-dynamic problem: operating speed of the cooling system fan—2142 rpm.

Figure 5 provides the finite element model of the cooling system fan and blade profile sections with the maximum, medium, and minimum radii.

The surface noise sources derived from a—impulse (F_i) input and b—mass input $\rho_0 V_0$ are given in Fig. 6.

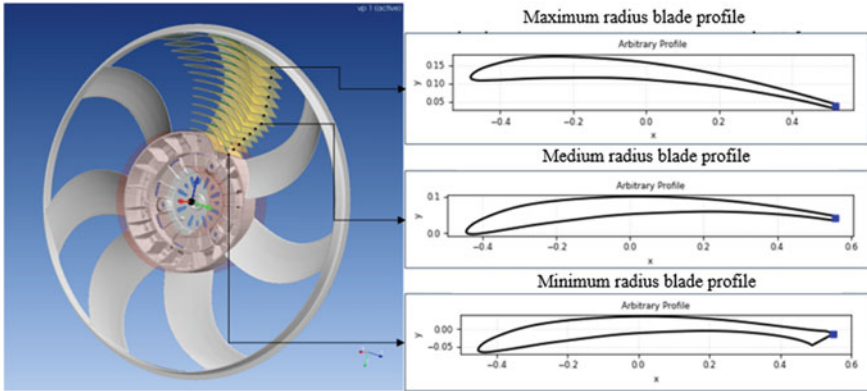


Fig. 5 Finite element model of the fan, fan blade profiles with different radii

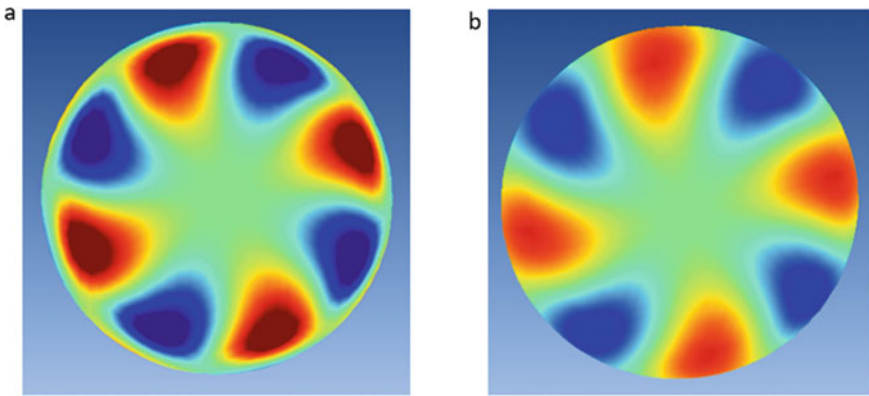


Fig. 6 Noise sources derived from gas-dynamic calculation

The sound pressures of the cooling system fans with 7, 8, and 9 identically located blades have been calculated; the calculation results as well as sound pressure distributions are given in Fig. 7.

The microphone was located 1 m away from the fan center. It follows from Fig. 7 that the least amount of noise is generated by the fan with 9 blades. It is worth noting that the maximum sound pressure amplitudes correspond to frequencies 249 Hz—7 blades, 285.6 Hz—8 blades, and 321.3 Hz—9 blades, which are the blade passing frequencies.

Parametric optimization in terms of noise was performed. The number of blades and angles between the blades are taken as variables. Over 20 variants of the cooling system fans have been considered, and the best result in comparison is shown in Fig. 8 (the design with 7 blades).

The fan design with 9 blades and with blade position angles 0, 45, 90, 125, 160, 205, 250, 290, 325 has the maximum sound pressure amplitude at the frequency of 321 Hz corresponding to 46.4 dB. The optimized fan design with 7 blades and with blade position angles 0, 51.47, 102.86, 154.29, 205.71, 257.14, 308.57 generates the

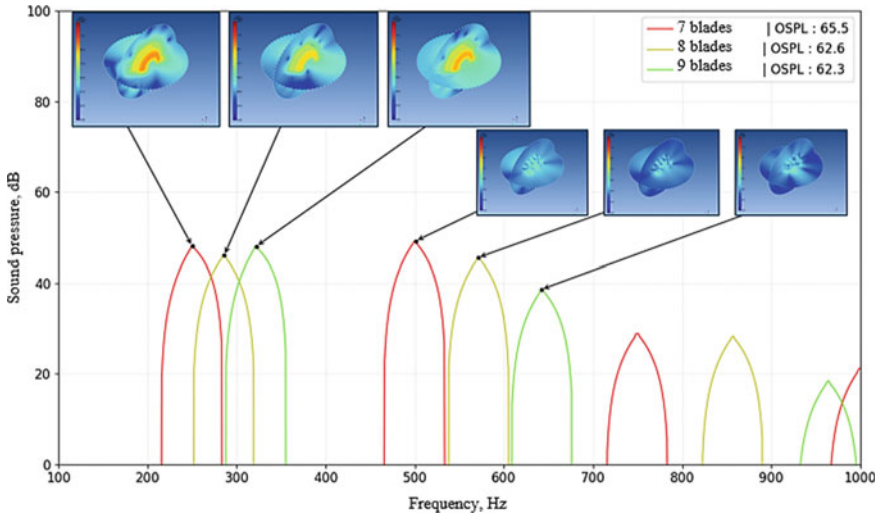


Fig. 7 Calculation study results

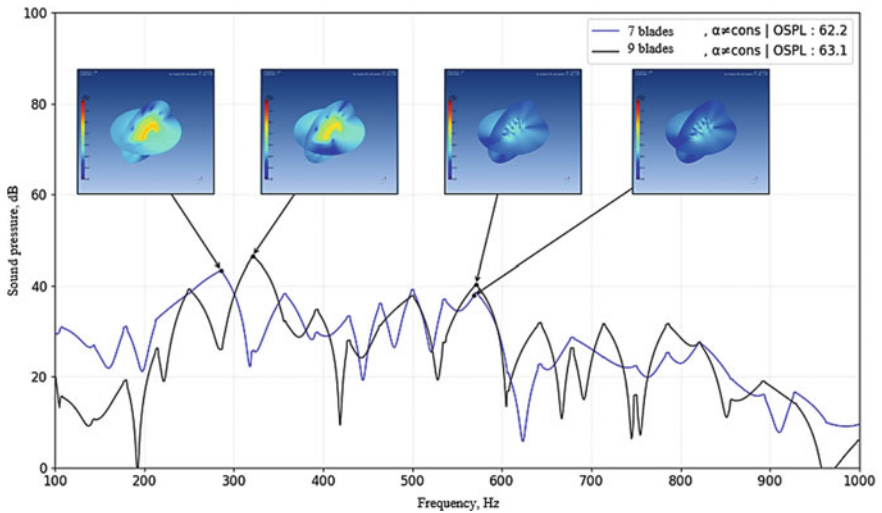


Fig. 8 Calculation study results for optimized design

least amount of noise among the considered variants. The maximum sound pressure falls at the frequency of 286 Hz and amounts to 43.3 dB.

4 Conclusion

1. The calculation of the vehicle cooling system fan tonal noise was carried out using Goldstein's analogy.

2. Parametric optimization was performed, which allowed obtaining the cooling system fan design with the lowest level of tonal noise.
3. The best design in terms of tonal noise is the fan design with 7 blades and the following position angles: 0, 51.47, 102.86, 154.29, 205.71, 257.14, and 308.57.

References

1. Lighthill, MJ (1952) On sound generated aerodynamically: I. general theory. *Proc Royal Soc London Ser A* 211(1107):564–587
2. Lighthill MJ (1954) On sound generated aerodynamically: II. turbulence as a source of sound. In: *Proceedings Royality Social London, Series A* 222(1148):1–32
3. Goldstein ME (1981) *Aeroacoustics*. Mashinostroenie, Moscow, p 296
4. Yudin EYa (1958) Study of the noise of fan installations and methods of dealing with it: scientific publication. Oborongiz, Moscow, pp 227 (*TsAGI Sci J*; Issue 713)
5. Yudin EY (1964) *Combating noise*. Collected papers under general editorship of Professor. Stroiizdat, Moscow, pp 700
6. Khoroshev GA, Petrov YI, Egorov NF (1981) *Struggle against fans' noise*. M.: Energoizdat, pp 143
7. Hickling R (ed) (1977) *Aerodynamic noise in engineering*, p 332
8. Jay Patel, Kingston NY (1978) United States Patent, 4,089,618, May 16, 1978
9. Belamri T, Kouidri S, Fedala D and Rey R (2005) Comparative study of the aeroacoustic behavior of two axial flow fans with different sweep angles. Paper FEDSM2005–77242, *Proceedings of ASME FEDSM'05, 2005 ASME Fluid Engineering Summer Conference Houston, TX, USA, June 16–23*
10. Lu J, Wei X, Li Y (2010) Research on aerodynamics and exit flow field of skewed fan-rotors. In: *Power and Energy Engineering Conference (APPEEC), Asia-Pacific*, pp 1–4
11. Konrad, Thomas BC (2012) Optimization of axial fans with highly swept blades with respect to losses and noise reduction. *Fan 2012, Senlis (France)*, 18–20 April 2012, pp 12
12. Khoroshev GA, Petrov YuI, Egorov NF (1981) *Struggle against fans' noise*. Energoizdat, Moscow, p 143
13. Brusilovsky IV (2004) *Aerodynamics and acoustics of axial fans*. *TsAGI Sci J* 2650, Moscow, pp 275
14. Lee J, Nam K (2008) Development of low-noise cooling fan using uneven fan blade spacing, *SAE Technical Paper* 2008–01–0569
15. Lu HZ, Huang L, So RMC, Wang J (2007) A computational study of the interaction noise from a small axial-flow fan. *J Acoust Soc Am* 122(3):1404–1415
16. Sawyer S, Nallasamy M, Hixon R, Dyson RW, Koch LD (2003) Computational aeroacoustic prediction of discrete-frequency noise generated by a rotor-stator interaction. In: *9th AIAA/CEAS aeroacoustics conference and exhibit*, pp 18
17. Woodward RP, Elliott DM, Hughes CE, Berton JJ (1999) Benefits of swept and leaned stators for fan noise reduction *AIAA-99-0479*, pp 12
18. Actran (2021) *User's Guide Vol. 1*
19. Rakhmatov RI, Krutolapov VE, Zuzov VN (2019) Development of calculation research method for exhaust system main elements acoustic characteristics / IOP conference series: materials science and engineering. vol 819. *International Automobile Scientific Forum (IASF-2019) "Technologies and Components of Land Intelligent Transport Systems"* 16–18 October 2019 Moscow, Russian Federation
20. Rakhmatov RI, Krutolapov VE ZVN (2019) Development of a design method for determining the attachment of the exhaust mounting mounts. *AKUSTIKA* 34:141–147



Research and Improvement of Muffler Acoustic Characteristics with Regard to Thermodynamic Characteristics of Exhaust Gas Flow with Aeroacoustic Sources

R. I. Rakhmatov^(✉), V. E. Krutolapov, and G. G. Nadareishvili

FSUE “NAMI” State Research Center of the Russian Federation, 2, Automotornaya Street,
Moscow 125438, Russia

rakhmatjon.rakhmatov@nami.ru

Abstract. The paper describes the physical and mathematical basis of the research of the acoustic characteristics of the mufflers with due consideration to thermodynamic characteristics of the exhaust gas flow with the aeroacoustic sources. Also, the paper describes the results of calculation studies of aeroacoustic characteristics of the muffler. The finite element model of the muffler has been developed. Since hybrid methods are less computationally expensive and more accurate than other methods, since the flow rate at maximum crankshaft speed of the internal combustion engine exceeds Mach 0.6, Mohring’s analogy is used. Calculation of sound pressures from aeroacoustic sources is performed. The calculation is performed with regard to transmission losses, transmission losses taking into account thermodynamic characteristics of the flow, as well as transmission losses taking into account thermodynamic characteristics of the flow and aeroacoustic sources. A new muffler is developed based on the analysis of the aeroacoustic characteristics of the series muffler. The acoustic characteristics of the developed design are better than those of the series design. Experimental validation of the calculation is performed.

Keywords: Computational aeroacoustics (CAA) · Muffler · Finite element modeling · Transmission losses · Aeroacoustic noise calculation · Mohring’s analogy

1 Introduction

At present, a vehicle exhaust system is a complicated system that shall provide performance of a whole set of tasks with many variables that shall be found according to the optimizing procedures taking into account that each variable can have a multidirectional influence on each output parameter: reduction of the gas flow area in the muffler increases acoustic efficiency, but also increases the backpressure of the exhaust system, reduction of cell density in the catalysts reduces the backpressure, but also reduces efficiency in terms of toxicity, etc. In this connection, this paper is devoted to improvement of the exhaust system transmission loss calculation method in order to define the exhaust gas

flow influence on the acoustic characteristics of the system by the example of the main muffler.

As we know from [1–6], the parameter of transmission loss (TL) is often used for assessment of the performance of both the exhaust system as a whole and its separate elements as it is unambiguous and does not depend on acoustic conditions at the inlet and outlet of the exhaust system by definition:

$$TL = 10 \lg(W_{in}/W_{out}) \quad (1)$$

where W_{in} and W_{out} are the sound wave power values at the inlet and outlet of the muffler when the inlet and outlet loads are matched.

In order to take into account the thermodynamic characteristics of the flow with aeroacoustic sources, we will use the hybrid method for aeroacoustics calculation. As we know from [7–20], hybrid methods are less consuming in terms of computational resources and more precise compared to other methods; so, since the flow speed at maximum rpm of the internal combustion engine crankshaft exceeds 0.6 Mach, we will use Mohring's analogy.

2 Physicomathematical Basis

Any oscillating body causes a corresponding change of pressure or displacement of air particles which in the form of a wavefront are capable of propagation and reaching the listener. The Navier–Stokes equation not only describes a fluid flow, but can also slightly describe an acoustic pressure wave movement. Acoustic waves are pressure oscillations, which can exist within a compressible fluid. The pressure changes that occur there when the fluid contracts or expands create restoring forces responsible for acoustic wave propagation. These restoring forces are forces, which the fluid body uses to resist deformation, and they can be considered similar to the restoring forces in a spring. We will use the equation of state for the analysis of sound waves propagating in a fluid. The equation of state for a fluid connects internal restoring forces with the corresponding deformations. The equation of state for a fluid medium shall connect physical quantities describing thermodynamic behavior of the fluid. Gas state equation (law):

$$p_i = \rho \cdot R \cdot T \quad (2)$$

where p_i is the dynamic pressure; ρ is the density; R is the gas constant; T is the absolute temperature.

Acoustic processes are almost isentropic (adiabatic and reversible). That is due to the fact that heat diffusion is much slower than acoustic oscillations, which means that fluid thermal conductivity and thermal gradients are rather small, so there is no significant thermal energy transmission between the neighboring fluid elements. Therefore, fluid or liquid entropy remains almost constant, and acoustic behavior can be described using the adiabatic equation:

$$\frac{p_i}{p_0} = \left(\frac{\rho_i}{\rho_0} \right)^\gamma \quad (3)$$

where p_0 is the pressure of the medium, ρ_0 is the density of the medium, and γ is the adiabatic index (the ratio of the heat capacity at constant pressure C_P to heat capacity at constant volume C_V).

For the fluids other than an ideal gas, the adiabatic relation in (3) becomes more complicated. However, the connection between pressure and density oscillations can be expressed through the Taylor polynomial:

$$p_i = p_0 + \left(\frac{\partial p_i}{\partial \rho}\right)_{\rho_0} \cdot (\rho - \rho_0) + \frac{1}{2} \cdot \left(\frac{\partial^2 p_i}{\partial \rho^2}\right)_{\rho_0} \cdot (\rho - \rho_0)^2 + \dots \quad (4)$$

In Eq. 4, partial derivatives are determined for isentropic compression and expansion of the fluid in relation to its steady-state (equilibrium) density. When these oscillations are small, it is necessary to preserve only the term of the lowest order, which provides a linear dependence between pressure oscillation and density.

$$p_i - p_0 \approx \beta(\rho - \rho_0)/\rho_0 \quad (5)$$

where β is the adiabatic volume modulus which is determined as $\rho_0 \left(\frac{\partial p_i}{\partial \rho}\right)_{\rho_0}$.

The following dependence can be written from the acoustic pressure $p = p_i - p_0$ and density standpoint:

$$p = \beta(\rho - \rho_0)/\rho_0 \quad (6)$$

The Navier–Stokes equation expresses two core or fundamental principles of mechanics—conservation of mass on the one hand and Newton’s second law on the other hand ($\vec{F} = m \cdot \vec{a}$). For the first case—conservation of mass—let us consider the infinitesimal rectangular parallelepiped-shaped volume of the medium with the following sides: $AD = EF = BC = GH = dx$, $AE = DF = BG = CH = dy$, and $AB = DC = FH = EG = dz$ (Fig. 1). Increasing the volume mass in the course of time dt leads to the corresponding increase in density.

Let us examine side $dx dz$ perpendicular to the Y axis. The flow of matter coming into the volume from this side in the course of time dt is written as follows:

$$\rho \vartheta_y dx dz dt \quad (7)$$

Considering the change of density and speed between the two parallel sides of the control volume, the flow of matter coming out through the opposite side during the same period of time can be described using the following formula:

$$\left(\rho + \frac{\partial \rho}{\partial y} dy\right) \left(\vartheta_y + \frac{\partial \vartheta_y}{\partial y} dy\right) dx dz dt \quad (8)$$

Taking only the first derivative of Eq. 8 into consideration, the net flow of matter through the two sides of the parallelepiped is expressed as follows:

$$-\frac{\partial(\rho \vartheta_y)}{\partial y} dx dy dz dt \quad (9)$$

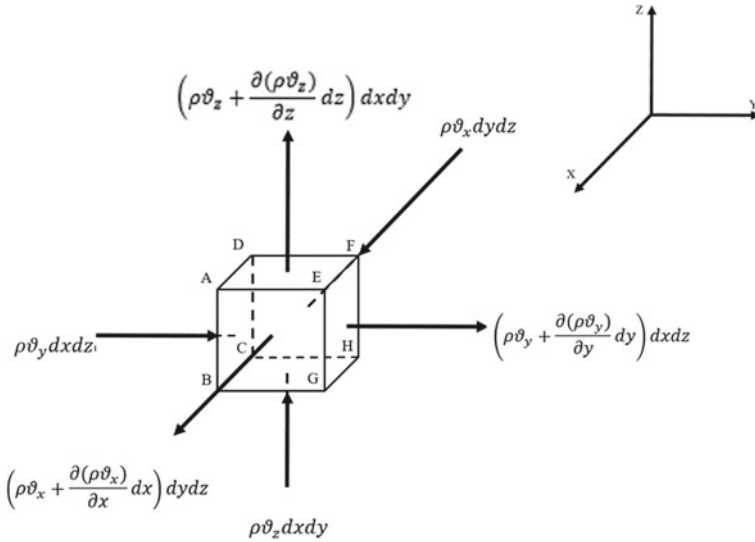


Fig. 1 Continuity equation

Having performed similar calculations for the other two pairs of parallelepiped sides, we will obtain the following expression for the flow of matter coming through the control volume during period dt :

$$-\left(\frac{\partial(\rho\vartheta_x)}{\partial x} + \frac{\partial(\rho\vartheta_y)}{\partial y} + \frac{\partial(\rho\vartheta_z)}{\partial z}\right) dx dy dz dt \tag{10}$$

Let us consider the distributed source of mass $m(x, y, z, t)[kg/(m^3 \cdot s)]$. The total mass produced by this source in the rectangular parallelepiped volume during period dt is.

$$m dx dy dz dt \tag{11}$$

We can also evaluate the increase of mass in the volume considering the density change:

$$\left(\rho + \frac{\partial\rho}{\partial t} dt\right) dx dy dz - \rho dx dy dz = \frac{\partial\rho}{\partial t} dx dy dz dt \tag{12}$$

Conservation of mass requires that the sum of (10) and (11) shall be equal to (12). This ratio is called the continuity equation.

$$\frac{\partial\rho}{\partial t} = m - \left(\frac{\partial(\rho\vartheta_x)}{\partial x} + \frac{\partial(\rho\vartheta_y)}{\partial y} + \frac{\partial(\rho\vartheta_z)}{\partial z}\right) \tag{13}$$

or

$$m = \frac{\partial\rho}{\partial t} + \left(\frac{\partial(\rho\vartheta_x)}{\partial x} + \frac{\partial(\rho\vartheta_y)}{\partial y} + \frac{\partial(\rho\vartheta_z)}{\partial z}\right) \tag{14}$$

If we replace letters x , y , and z of the Cartesian reference system space axes with x_1 , x_2 , and x_3 , and velocity vectors directed along these axes, ϑ_x , ϑ_y , and ϑ_z , with ϑ_1 , ϑ_2 and ϑ_3 , Eq. 14 will be as follows:

$$m = \frac{\partial \rho}{\partial t} + \sum_{i=1,3} \frac{\partial(\rho \vartheta_i)}{\partial x_i} \tag{15}$$

The time derivative of function f may be written as $\partial_t f$, and the x_i -derivative may be written as $\partial_i f$, then the continuity equation will be as follows:

$$m = \partial_t \rho + \sum_{i=1,3} \partial_i(\rho \vartheta_i) \tag{16}$$

Equation 16 can be additionally simplified using the Einstein’s assumption. When repeating the index (which is called an unnamed index) while summing, there is no need to save the summation symbol, provided that:

1. The index cannot be written more than twice in one equation;
2. Except for the unnamed index, other equation terms shall contain the same homogeneous indices.

In view of the above, we shall write the addend of the right part of the continuity equation without the summation symbol:

$$m = \partial_t \rho + \partial_i(\rho \vartheta_i) \tag{17}$$

According to the Crocco’s theorem, the momentum conservation equation will be written as follows:

$$\rho \frac{\partial \vartheta_i}{\partial t} + \rho \frac{\partial h_t}{\partial x_j} = \rho T \frac{\partial s}{\partial x_i} + \rho \delta_{ijk} \vartheta_j \omega_k - \frac{\partial \tau_{ij}}{\partial x_j} \tag{18}$$

where h is the enthalpy; τ is the viscous stress tensor; $h_T = h + \frac{\vartheta_i \vartheta_i}{2}$ is the total enthalpy; $\delta_{ijk} \vartheta_j \omega_k = \left(\vec{\vartheta} \cdot \vec{\omega} \right)_i$, $\vec{\omega} = \nabla \cdot \vec{\vartheta}$ is the vorticity or eddying.

And the energy conservation equation:

$$\rho \frac{\partial h_t}{\partial t} + \rho \vartheta_i \frac{\partial h_t}{\partial x_i} - \frac{\partial \rho}{\partial t} = \frac{\partial q_j}{\partial x_j} - \frac{\partial \vartheta_i \tau_{ij}}{\partial x_j} \tag{19}$$

without taking into account, the dissipation power due to viscous forces and heat will be as follows:

$$\rho \frac{\partial h_t}{\partial t} + \rho \vartheta_i \frac{\partial h_t}{\partial x_i} = \frac{\partial \rho}{\partial t} \tag{20}$$

Having combined the mass and energy conservation equations taking into account the acoustic velocity $c^2 = \left(\frac{\partial p}{\partial \rho} \right)_{s=\text{cons}}$, we will obtain:

$$\rho \frac{\partial \vartheta_i}{\partial t} = \frac{\partial \rho \vartheta_i}{\partial t} - \frac{\rho \vartheta_i}{c^2} \frac{\partial h_t}{\partial t} - \frac{\rho \vartheta_i \vartheta_j}{c^2} \frac{\partial h_t}{\partial x_j} - \left(\frac{\partial \rho}{\partial s} \right)_p \vartheta_i \frac{\partial s}{\partial t} \tag{21}$$

Let us rewrite Eq. 20 taking into account the 18 one:

$$\frac{\partial \rho v_i}{\partial t} - \frac{\rho v_i}{c^2} \frac{\partial h_t}{\partial t} - \frac{\rho v_i v_j}{c^2} \frac{\partial h_t}{\partial x_j} - \left(\frac{\partial \rho}{\partial s} \right)_p v_i \frac{\partial s}{\partial t} + \rho \frac{\partial h_t}{\partial x_j} = \rho T \frac{\partial s}{\partial x_i} + \rho (\vec{v} \cdot \vec{\omega})_i - \frac{\partial \tau_{ij}}{\partial x_j} \tag{22}$$

Let us also rewrite Eq. 21 but taking into account the scaled enthalpy (ρ_T -total density):

$$\frac{\partial b}{\partial t} + v_i \frac{\partial b}{\partial x_i} = \rho_T \frac{\partial h_t}{\partial t} + \rho_T v_i \frac{\partial h_t}{\partial x_i} \tag{23}$$

Based on the above, let us write Mohring’s equation.

$$\begin{aligned} & \frac{\partial}{\partial t} \left(\frac{\rho}{\rho_T^2 c^2} \frac{\partial b}{\partial t} + \frac{\rho v_i}{\rho_T^2 c^2} \frac{\partial b}{\partial x_i} \right) + \frac{\partial}{\partial x_i} \left(\frac{\rho v_i}{\rho_T^2 c^2} \left(\frac{\partial b}{\partial t} + v_i \frac{\partial b}{\partial x_i} \right) - \frac{\rho}{\rho_T} \frac{\partial b}{\partial x_i} \right) \\ &= - \frac{\partial}{\partial x_i} \left(\frac{\rho}{\rho_T} (\vec{v} \cdot \vec{\omega})_i - \frac{\partial \tau_{ij}}{\partial x_j} \right) \\ &+ \frac{\partial}{\partial x_i} \left(\frac{v_i}{\rho_T} \left(\frac{\partial \rho}{\partial s} \right)_p \frac{\partial S}{\partial t} - \frac{\rho T}{\rho_T} \frac{\partial S}{\partial x_i} \right) \\ &+ \frac{\partial}{\partial t} \left(\frac{1}{\rho_T} \left(\frac{\partial \rho}{\partial s} \right)_p \frac{\partial S}{\partial t} - \frac{\rho v_i}{\rho_T^2} \frac{\partial \rho_T}{\partial x_i} \right) \end{aligned} \tag{24}$$

where the left part of the equation is the acoustic wave operator. The first expression of the right part of the equation is the turbulence noise.

In the frequency domain and in the finite element arrangement, Eq. 24 will be as follows:

$$\begin{aligned} & -\omega^2 \int_V N_a \frac{\rho b}{\rho_T^2 c^2} dV + i\omega \int_V N_a \frac{\rho v_i}{\rho_T^2 c^2} \frac{\partial b}{\partial x_i} - \int \frac{\partial N_a}{\partial x_i} \left(i\omega \frac{\rho v_i b}{\rho_T^2 c^2} + \frac{\rho v_i v_j}{\rho_T^2 c^2} \frac{\partial b}{\partial x_j} - \frac{\rho}{\rho_T} \frac{\partial b}{\partial x_i} \right) dV \\ &= \int \frac{\partial N_a}{\partial x_i} FT \left(\frac{\rho}{\rho_T} (\vec{v} \cdot \vec{\omega})_i - \frac{\partial \tau_{ij}}{\partial x_j} - \frac{v_i}{\rho_T} \left(\frac{\partial \rho}{\partial s} \right)_p \frac{\partial S}{\partial t} - \frac{\rho T}{\rho_T} \frac{\partial S}{\partial x_i} \right) dV \\ &+ i\omega FT \left(\int_V \frac{N_a}{\rho_T} \left(\frac{\partial \rho}{\partial s} \right)_p \frac{\partial S}{\partial t} - \frac{\rho v_i N_a}{\rho_T^2} \frac{\partial \rho_T}{\partial x_i} dV \right) + i\omega FT \left(\oint_S N_a \frac{\rho v_i n_i}{\rho_T} dS \right) \end{aligned} \tag{25}$$

where the left part of the equation describes propagation of the acoustic wave. The first and second expression of the right part of the equation is the spatial (volume) source, and the third expression is the surface source.

As a result, the spatial turbulent source without taking into account the viscous effects $\frac{\partial \tau_{ij}}{\partial x_j}$, entropy-related sources $\left(\frac{\partial S}{\partial t} \right)_p$ and $\frac{\partial S}{\partial x_i}$ and total density fluctuations $\left(\frac{\partial \rho_T}{\partial x_i} \right)$ will be calculated according to the following formula:

$$\int \frac{\partial N_a}{\partial x_i} FT \left(\frac{\rho}{\rho_T} (\vec{v} \cdot \vec{\omega})_i \right) dV \tag{26}$$

Consequently, the surface source will be calculated according to Eq. 27:

$$i\omega FT \left(\oint_S N_a \frac{\rho v_i n_i}{\rho T} dS \right) \quad (27)$$

3 Calculation Research

The three-dimensional model of the muffler inner volume is given in Fig. 2. The gas-dynamic (CFD) calculation was performed in the Siemens Star CCM + software. Boundary conditions for the gas-dynamic calculation: at the inlet of the muffler inlet branch, the exhaust gas flow is 0.24 kg/s, the temperature is 900 K, there is atmospheric pressure on the sphere surface around the muffler outlet branch, the temperature is 300 K, and there are adiabatic conditions on all the muffler surfaces.

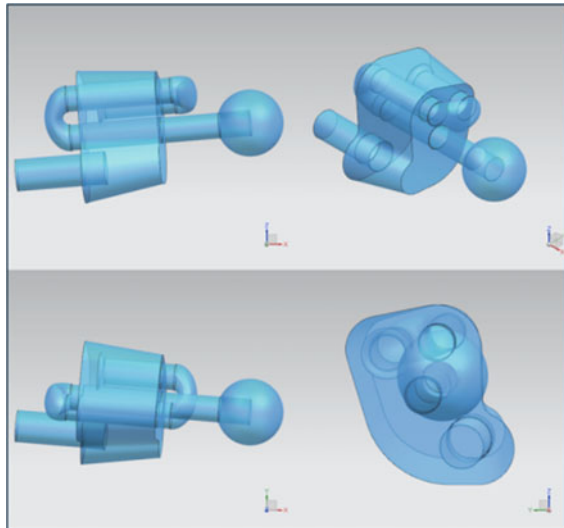


Fig. 2 Three-dimensional model of series muffler

According to the Kotelnikov (Nyquist–Shannon) sampling theorem, the frequency sampling is determined by the maximum time interval ($\Delta f = \frac{1}{T}$), and the maximum frequency is determined by the time step ($f_{\max} = \frac{1}{2T_e}$). Based on the above, the gas-dynamic calculation has been performed for the aeroacoustic problem with the maximum frequency of 5000 Hz with the 5 Hz step, with the maximum calculation time of 0.2 s and the step of 0.0001 s with autosaving of data of the velocity vector value and the following scalar values: temperature, pressure, density, and kinetic energy of the turbulent flow and acoustic velocity.

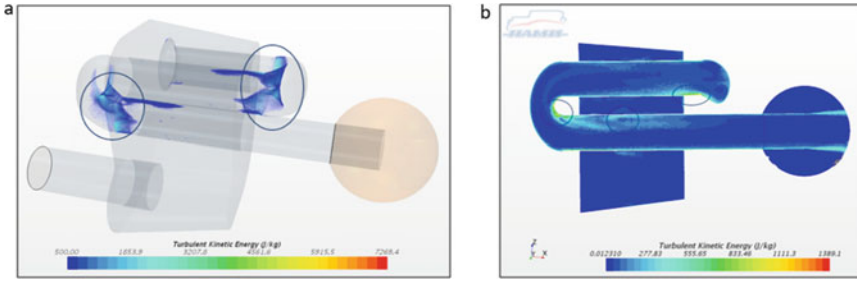


Fig. 3 a Distribution of turbulent flow kinetic energy over volume; b distribution of turbulent flow kinetic energy over section

Figure 3 provides the gas-dynamic calculation result, distribution of the turbulent flow kinetic energy over volume (a) and over the section (b). The areas of the maximum values of the turbulent flow kinetic energy are pointed out.

The turbulent flow kinetic energy (Fig. 3) is concentrated in the first bend of the inlet as well as in the second bend of the outlet pipe of the muffler. Furthermore, it is pronounced at the junction in the outlet of the straight outlet pipe (pipe connection point). Separation areas are also detected after the first and second bends of the muffler outlet pipe inlet.

The finite element model of the muffler inner volume is given in Fig. 4. The model composition is as follows: number of nodes—804,459, number of elements—560,503, element type—tetrahedral second-order. The acoustic calculation was performed in Actran software (Hexagon/FFT). Boundary conditions: at the inlet—channel modes without acoustic excitation, the matched (anechoic) load is directed inside the muffler inlet pipe, at the outlet—free channel modes directed away from the muffler outlet pipe.

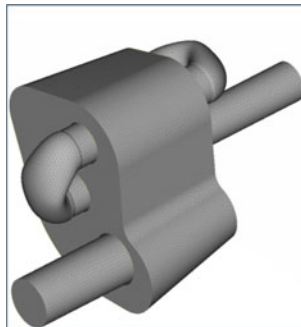


Fig. 4 Finite element model of series muffler

The results of calculation of the muffler sound pressures from the aeroacoustic sources according to Mohring’s analogy are shown in Fig. 5.

The overall (integral) level is 115.4 dB (Fig. 5). The maximum amplitudes of the muffler sound pressures are found at the first bend of the inlet section and amount to 99 dB at 500 Hz, 96.2 dB at 370 Hz, and 92.9 dB at 235 Hz.

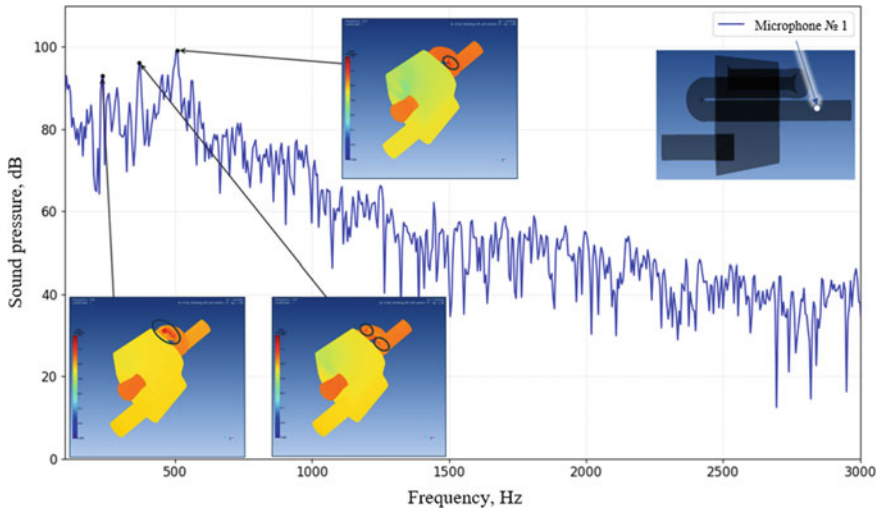


Fig. 5 Sound pressure measured along the outlet pipe axis 50 mm away from the end of the outlet pipe and distribution of the sound pressures over the volume of the series muffler

Then, the muffler transmission losses were calculated. The calculation results are shown in Fig. 6.

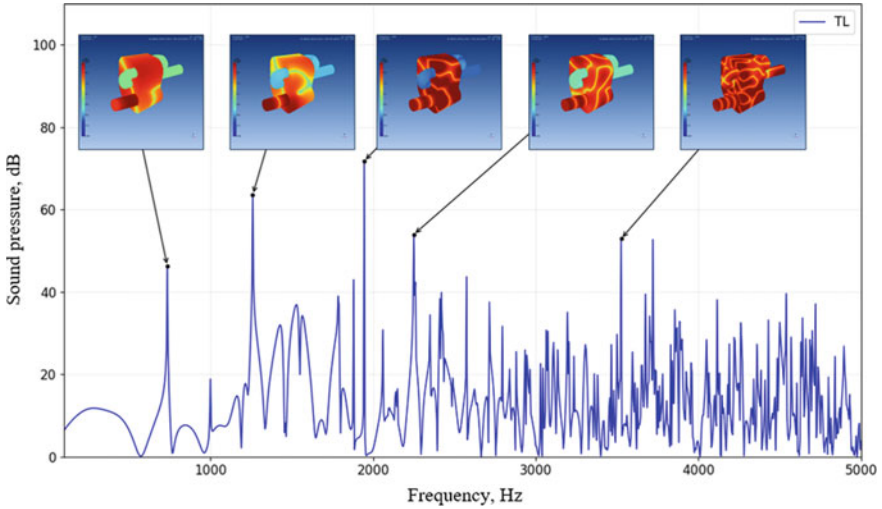


Fig. 6 Muffler transmission losses, distribution of sound pressures over the muffler volume

The calculation results for the transmission losses taking into account thermodynamic characteristics of the exhaust gas flow are shown in Fig. 7.

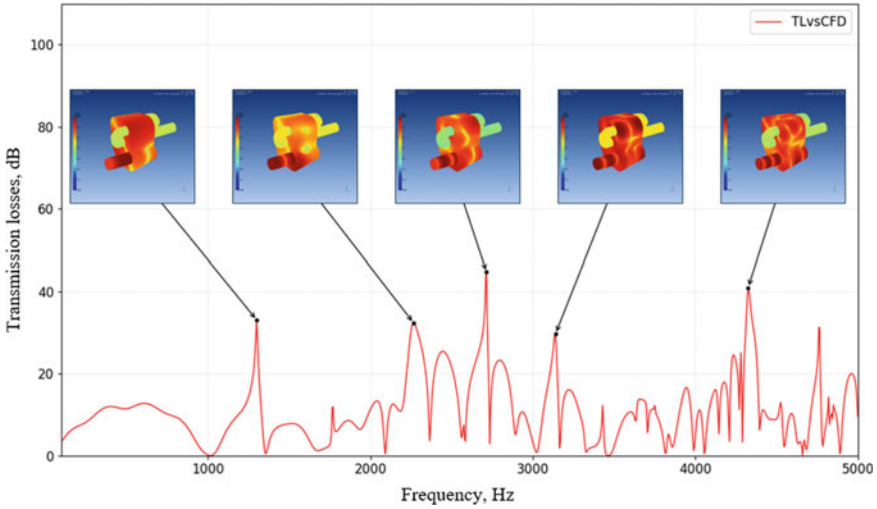


Fig. 7 Muffler transmission losses taking into account thermodynamic characteristics of the flow, distribution of sound pressures over the muffler volume

The calculation results for the transmission losses taking into account thermodynamic characteristics of the exhaust gas flow and the aeroacoustic sources are shown in Fig. 8.

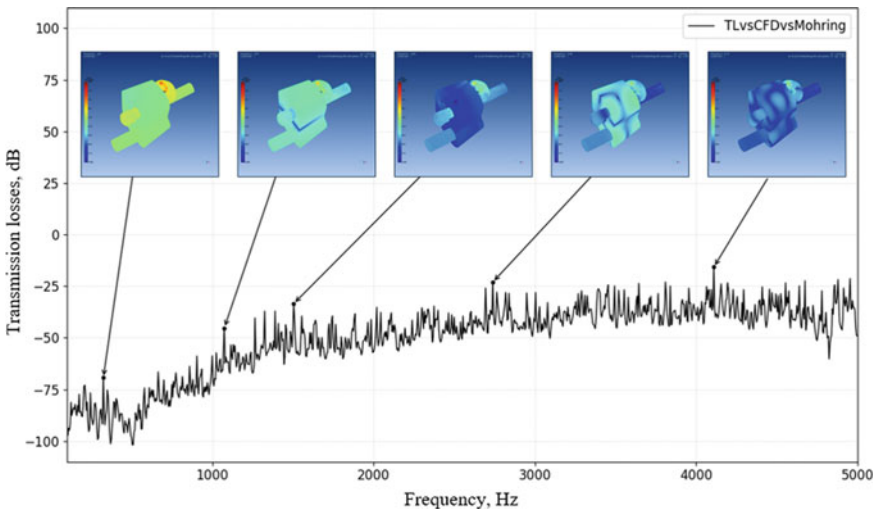


Fig. 8 Muffler transmission losses taking into account thermodynamic characteristics of the flow and aeroacoustic sources, distribution of sound pressures over the muffler volume

The transmission losses comparative diagram is shown in Fig. 9.

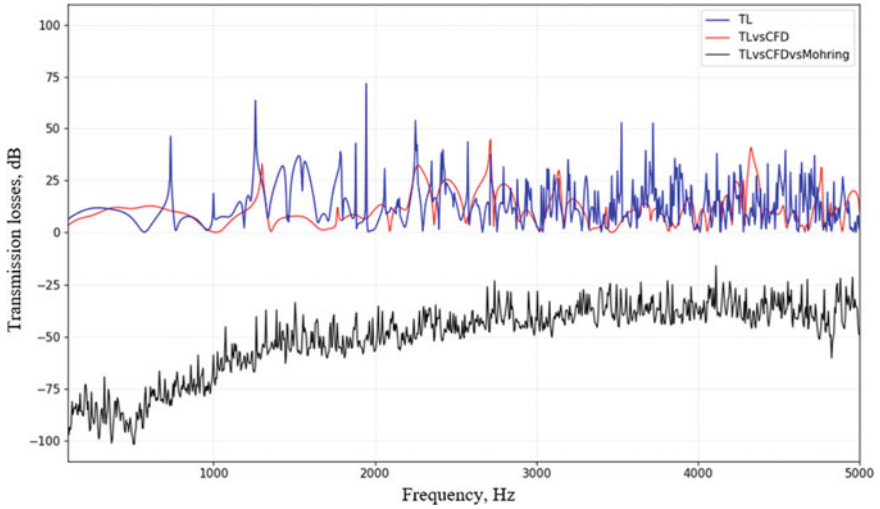


Fig. 9 Muffler transmission losses comparative diagram

As it appears from Fig. 9, thermodynamic characteristics of the flow, especially with aeroacoustic sources, have a significant impact on the transmission losses.

In order to improve the acoustic characteristics of the muffler based on the aeroacoustic calculation studies, the diameter of the bends was increased. The three-dimensional model of the muffler prototype (a) and the results of the gas-dynamic calculations of the turbulent flow kinetic energy are given in Fig. 10.

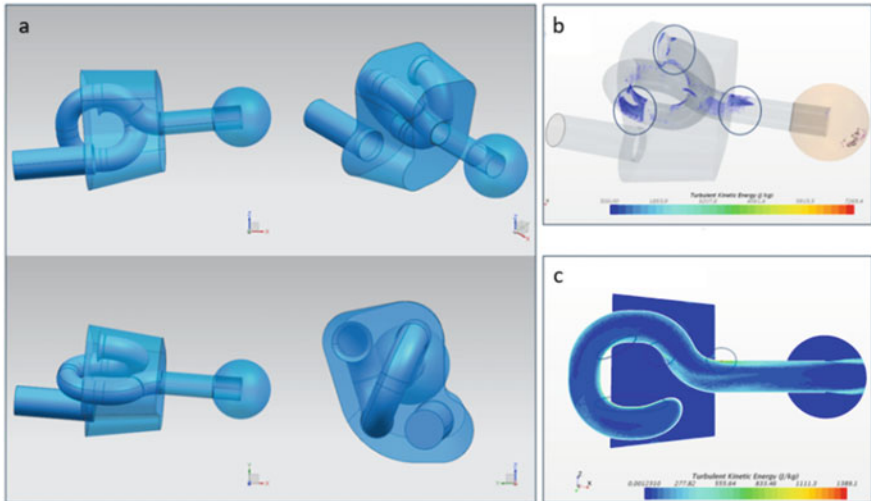


Fig. 10 **a** Three-dimensional model of muffler prototype; **b** distribution of turbulent flow kinetic energy over volume; **c** distribution of turbulent flow kinetic energy over section

The calculation results for the sound pressures from the aeroacoustic sources are shown in Fig. 11.

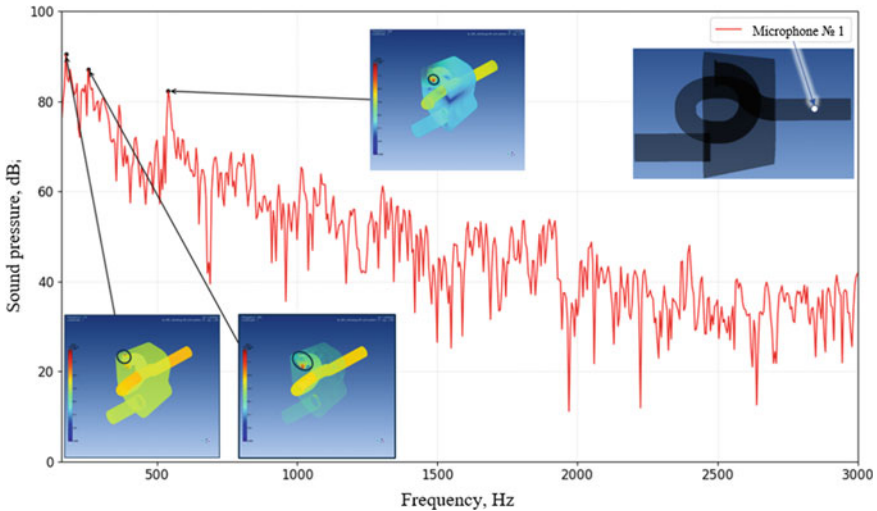


Fig. 11 Sound pressure measured along the outlet pipe axis 50 mm away from the end of the outlet pipe and distribution of sound pressures over the volume of the muffler prototype

The overall (integral) level of the muffler prototype is 105.8 dB (Fig. 11). The maximum sound pressure is found at the volute inlet and amounts to 90.4 dB at 175 Hz, 87.1 dB at 255 Hz, and 82.3 dB at 540 Hz.

Figure 12 shows the comparative diagram of the sound pressures from aeroacoustic sources.

The overall level of the muffler prototype is ~ 10 dB lower than that of the series muffler. Within the frequency range of 250–500 Hz, reduction of sound pressure amplitudes up to 30 dB is observed. On the whole, reduction of sound pressure amplitudes is observed almost across the whole frequency range.

4 Experimental Validation

In order to assess the adequacy of the calculation studies, experimental studies were performed. The tests were performed on the horizontal straight road, and the microphone was located at the distance of 150 mm away from the exhaust pipe mouth at the 45° angle. Test mode: internal combustion engine crankshaft speed—5500 rpm, neutral mode of the gearbox. The position of the microphones and test results are shown in Fig. 13.

A 10 dB sound pressure difference between the series and prototype muffler design was detected, which proves the adequacy of the calculation studies. Due to the optimization works, reduction of the aeroacoustic sources noise by 10 dB was achieved.

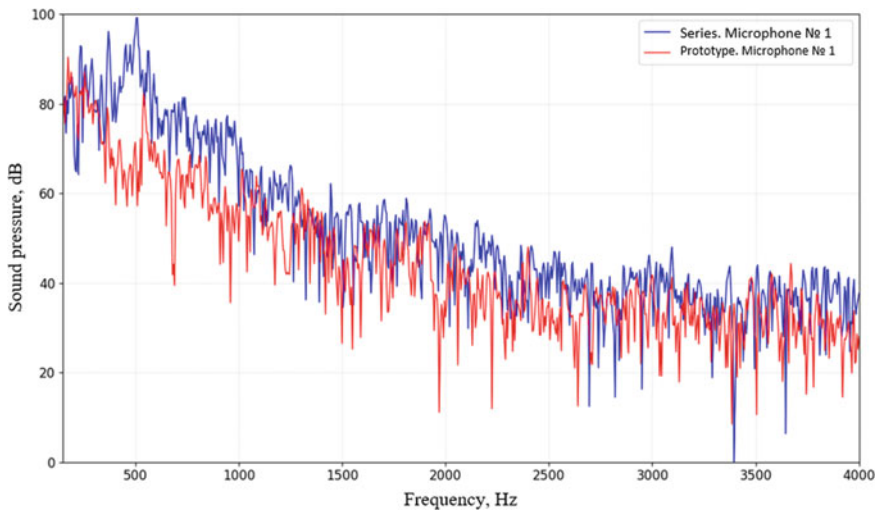


Fig. 12 Sound pressure comparative diagram

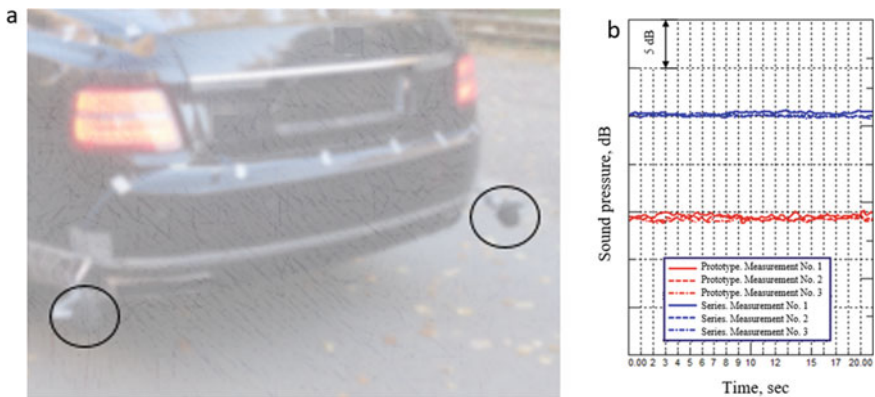


Fig. 13 **a** microphone position on the vehicle, **b** experimental research results

5 Conclusion

1. The muffler aeroacoustic noise was calculated, and the areas with the maximum sound pressure amplitudes were traced and localized.
2. The new muffler design providing noise decrease by 10 dB was developed.
3. The transmission losses, transmission losses with thermodynamic characteristics, and transmission losses with thermodynamic characteristics and aeroacoustic sources were calculated.
4. The significant impact of thermodynamic characteristics of the flow with aeroacoustic sources on the transmission losses was detected.
5. Experimental validation of the calculation confirming the adequacy of the calculation studies was performed.

References

1. Rakhmatov RI, Krutolapov VE, Zuzov VN (2019) Development of calculation research method for exhaust system main elements acoustic characteristics. IOP conference series: materials science and engineering, vol 819. International Automobile Scientific Forum (IASF-2019) “Technologies and Components of Land Intelligent Transport Systems” 16–18 October 2019 Moscow, Russian Federation
2. Nadareishvili GG, Rakhmatov RI, Galevko VV (2019) Improvement of acoustic characteristics of motor vehicle intake system based on calculation and experimental research. Lecture Notes in Mech Eng 9783319956299:2311–2322
3. Nadareishvili GG, Yudin SI (2012) Development of vehicle exhaust systems using finite element modeling calculation methods. In: Abstracts of VI international scientific-practical conference: “information and communication technology in education, science and manufacture”, Protvino, Moscow Region, 3–5 July 2012
4. Galevko V, Rakhmatov R, Khodosevich K, Yudin S, Nadareishvili G (2014) Acoustic characteristics of catalytic units of exhaust system. In: Proceedings of the 1st international sciences conference «science and education in Australia, America and Eurasia: Fundamental and Applied Science, International Agency for the Development of Culture, and Science, Australia, Melbourne, pp 139–143
5. Galevko VV, Rakhmatov RI (2015) Development of finite element models and computational and experimental investigation of exhaust gas processing systems. *Sci Rev* 22:129–135
6. Galevko VV, Rakhmatov RI (2017) Computational and experimental research of exhaust gas treatment systems. *Vestnik of Samara University Aerospace Mech Eng* 6(3):145–154
7. Blokhintsev DI (1981) Acoustic of a moving inhomogeneous medium. Nauka, Moscow, p 206
8. Howe MS (1975) Contribution to the theory of aerodynamic sound, with application to excess jet noise and the theory of the flute. *J Fluid Mech* 71(4):625–673
9. Crighton DJ (1981) Acoustics as a branch of fluid mechanics. *J Fluid Mech* 106:261–298
10. Hardin JC, Pope DS (1994) An acoustic splitting technique for computational aeroacoustics. *Theor Comput Fluid Dyn* 6:334–340
11. Goldstein ME (1981) Aeroacoustics. Mashinostroenie, Moscow, p 296
12. Lighthill, MJ (1952) On sound generated aerodynamically: I. general theory. *Proc Royal Soc London Ser A* 211(1107):564–587
13. Lighthill MJ (1954) On sound generated aerodynamically: II. turbulence as a source of sound. *Proc Royal Soc London Ser A* 222(1148):1–32
14. Mohring W (1979) Modeling low Mach number noise. In: Proceedings symposium mechanics sound generation in flow. Springer, Berlin, pp 85–96
15. Curle N (1955) The influence of solid boundaries upon aerodynamic sound. *Proc Royal Soc A: Math Phys Eng Sci* 231(1187):505–510
16. Ffowcs Williams JE, Hawkings DL (1969) Sound generated by turbulence and surfaces in unsteady motion. *Philos Trans R Soc A* 264(1151):321–342
17. Friedmann A (1922) An essay on hydrodynamics of compressible fluid. Petrograd, pp 516. Reprinted Archived 2016-03-03 at the wayback machine in 1934 under the editorship of Nikolai Kochin (see the first formula on page 198 of the reprint)
18. Crocco L (1937) Eine neue Stromfunktion für die Erforschung der bewegung der gase mit rotation. *ZAMM* 17(1):1–7. <https://doi.org/10.1002/zamm.19370170103>
19. Shapiro Ascher H (1969) National committee for fluid mechanics films film notes for ‘vorticity. Encyclopædia Britannica Educational Corporation, Chicago, Illinois. <http://web.mit.edu/hml/ncfmf/09VOR.pdf> (14/01/2020)
20. Liepmann HW, Roshko A (2001) Elements of gasdynamics. Dover Publications, Mineola, NY



System Views on the Features of the Dynamics of Elements of Oscillatory Structures

A. V. Eliseev^{1,2}(✉), N. K. Kuznetsov¹, and A. S. Mironov²

¹ Irkutsk National Research Technical University, 83, Lermontov Str., Irkutsk 664074, Russia
eavsh@ya.ru

² Irkutsk State Transport University, 15, Chernyshevsky Str., Irkutsk 664074, Russia

Abstract. An approach to the formation of a methodological basis for the system analysis of the dynamics of mechanical oscillatory structures based on frequency functions and damping functions is being developed. The argument of the functions is the coefficient of connectivity of the forms of motion of mass-inertia elements. The connectivity coefficient reflects the lever relationship of the parameters of the generalized coordinates. Mechanical oscillatory systems that are not connected to the support surfaces are considered. Mechanical oscillatory systems are formed by two mass-inertia elements, a spring and a damper. The aim of the study is to develop a method for constructing frequency functions and damping functions. The method is based on the use of an energy ratio that relates the kinetic, potential energy and the values of the energy dissipation function. The Lagrange formalism is used for composing differential equations. To determine the forms of frequency functions and damping functions, the so-called parametrizing function is used. Frequency functions and damping functions for mechanical oscillatory systems performing free movements are constructed. The graph-analytic evaluation of the extreme properties of frequency functions and damping functions is carried out. The possibility of the existence of four extreme values for frequency functions is shown. A topological criterion for classifying the forms of graphs of frequency functions and damping functions is proposed. The developed method can be used to display the dynamic features of mechanical oscillatory systems that include devices for converting movements.

Keywords: Mechanical system · Dynamics · Frequency function · Damping function · Connectivity of movement · Extreme properties · Oscillation · Viscous friction

1 Introduction

Mechanical vibration systems are actively used as design schemes for technical objects operating under conditions of intense vibration loads [1–8]. Well-known approaches to the evaluation of the dynamic properties of mechanical oscillatory systems include methods based on energy relations [9, 10]. In particular, the concept of the so-called frequency function was developed. The argument of the frequency function is a dimensionless coefficient equal to the ratio of the amplitudes of the generalized coordinates of

mechanical oscillatory systems [11–15]. The consideration of connectivity coefficients finds application in the possibility of tincture and correction of vibration fields of transport and technological machines [16, 17]. The physical interpretation of the coefficient of connectivity of the forms of motion is the lever connection between the elements of mechanical oscillatory systems.

At the same time, the methods for estimating the dynamic properties of mechanical oscillatory systems, taking into account the forces of viscous friction, based on the frequency function, require detailed consideration. In particular, the so-called damping function can be introduced to account for viscous friction.

The proposed work is devoted to the development of methods for evaluating the properties of mechanical oscillatory systems with viscous friction using the frequency function and the damping function, which reflect the significant dynamic characteristics of the system in extreme values.

2 Generalities. Problem Statement

A mechanical elastic-dissipative system with two degrees of freedom is considered. The schematic diagram is shown in Fig. 1. It is assumed that the elements m_1 and m_2 make small movements, taking into account the presence of three elastic elements $k_0, k_1,$ and k_2 and three dampers $b_0, b_1,$ and b_2 .

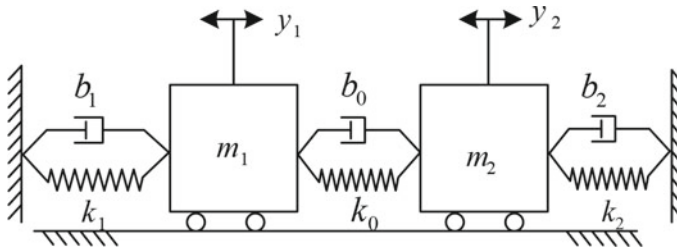


Fig. 1 Mechanical oscillatory system taking into account viscous friction

Generalized coordinates y_1 and y_2 denote the displacements of mass-inertial elements m_1 and m_2 relative to the positions of static equilibrium. The kinetic energy T , potential energy Π , and scattering function F have the form:

$$T = \frac{1}{2}m_1\dot{y}_1^2 + \frac{1}{2}m_2\dot{y}_2^2, \tag{1}$$

$$\Pi = \frac{1}{2}k_1y_1^2 + \frac{1}{2}k_2y_2^2 + \frac{1}{2}k_0(y_2 - y_1)^2, \tag{2}$$

$$F = \frac{1}{2}b_1\dot{y}_1^2 + \frac{1}{2}b_0(\dot{y}_2 - \dot{y}_1)^2 + \frac{1}{2}b_2\dot{y}_2^2. \tag{3}$$

The system of Lagrange equations of the second kind for functions (1–3) takes the form:

$$\begin{cases} m_1\ddot{y}_1 + (b_0 + b_1)\dot{y}_1 - b_0\dot{y}_2 + (k_0 + k_1)y_1 - k_0y_2 = 0; \\ m_2\ddot{y}_2 + (b_0 + b_2)\dot{y}_2 - b_0\dot{y}_1 + (k_0 + k_2)y_2 - k_0y_1 = 0. \end{cases} \quad (4)$$

Along with the solution of the system, we consider the movement $y_1 = y_1(t), y_2 = y_2(t)$ in the form:

$$\vec{y} = \vec{Y}e^{pt}, \quad (5)$$

where $\vec{y} = \begin{bmatrix} y_1(t) \\ y_2(t) \end{bmatrix}$ is the vector-function, $\vec{Y} = \begin{bmatrix} Y_1 \\ Y_2 \end{bmatrix}$ is the displacement vector, $p = \sigma + j\omega$ is the complex parameter, and t is the time variable. It is assumed that for the initial conditions:

$$\vec{y}(0) = \vec{Y}, \dot{\vec{y}}(0) = p\vec{Y}. \quad (6)$$

The task is to develop a method for constructing the frequency function and the damping function for evaluating the dynamic properties of mechanical oscillatory systems, taking into account the forces of viscous friction on the basis of extreme properties.

3 Determination of the Frequency Function and Damping Function Based on the Energy Ratio

The system (4) in the notation (5) has the form:

$$\begin{bmatrix} m_1p^2 + (b_0 + b_1)p + k_0 + k_1 & -b_0p - k_0 \\ -b_0p - k_0 & m_2p^2 + (b_0 + b_2)p + k_0 + k_2 \end{bmatrix} \begin{bmatrix} Y_1 \\ Y_2 \end{bmatrix} = 0 \quad (7)$$

Consider the matrices A , B , and C :

$$A = \begin{bmatrix} m_1 & 0 \\ 0 & m_2 \end{bmatrix}, B = \begin{bmatrix} b_0 + b_1 & -b_0 \\ -b_0 & b_0 + b_2 \end{bmatrix}, C = \begin{bmatrix} k_0 + k_1 & -k_0 \\ -k_0 & k_0 + k_2 \end{bmatrix} \quad (8)$$

In the notation (8), the system (4) can be represented as:

$$(p^2A + pB + C)\vec{Y} = 0. \quad (9)$$

Multiply the equality (9) scalar by the vector:

$$p^2\langle A\vec{Y}, \vec{Y} \rangle + p\langle B\vec{Y}, \vec{Y} \rangle + \langle C\vec{Y}, \vec{Y} \rangle = 0. \quad (10)$$

After substitution, $p = \sigma + j\omega$ (10) will take the form of the energy ratio:

$$(\sigma^2 - \omega^2 + 2j\sigma\omega)\langle A\vec{Y}, \vec{Y} \rangle + (\sigma + j\omega)\langle B\vec{Y}, \vec{Y} \rangle + \langle C\vec{Y}, \vec{Y} \rangle = 0. \quad (11)$$

We introduce a coefficient α that reflects the lever nature of the relationship between the generalized coordinates of the system:

$$Y_2 = \alpha Y_1. \tag{12}$$

The vector \vec{Y} can be represented as:

$$\vec{Y} = Y_1 \vec{\alpha}, \tag{13}$$

where $\vec{\alpha} = \begin{bmatrix} 1 \\ \alpha \end{bmatrix}$. After substituting (13), expression (11) takes the form of a complex expression:

$$(\sigma^2 - \omega^2 + 2j\sigma\omega)A_\alpha + (\sigma + j\omega)B_\alpha + C_\alpha = 0, \tag{14}$$

where $A_\alpha = \langle A\vec{\alpha}, \vec{\alpha} \rangle$, $B_\alpha = \langle B\vec{\alpha}, \vec{\alpha} \rangle$ and $C_\alpha = \langle C\vec{\alpha}, \vec{\alpha} \rangle$ are real functions of the argument of coefficient α . Equality (14) can be represented as two expressions for the imaginary and complex parts:

$$\begin{cases} \omega^2 A_\alpha = \sigma^2 A_\alpha + \sigma B_\alpha + C_\alpha; \\ 2\sigma\omega A_\alpha + \omega B_\alpha = 0. \end{cases} \tag{15}$$

System (15) is considered as a form of determining the real frequency function $\omega(\alpha)$ and the real damping function $\sigma(\alpha)$ of the argument α .

If the friction forces are «small»:

$$B_\alpha^2 < 4A_\alpha C_\alpha, \tag{16}$$

the solution of the system (15) can be represented as:

$$\begin{cases} \omega^2 = \frac{C_\alpha}{A_\alpha} - \left(\frac{B_\alpha}{2A_\alpha}\right)^2; \\ \sigma = -\frac{B_\alpha}{2A_\alpha}. \end{cases} \tag{17}$$

Under the condition of «large» viscous friction forces:

$$B_\alpha^2 > 4A_\alpha C_\alpha, \tag{18}$$

the solution of the system (15) can be represented as:

$$\omega = 0, \tag{19}$$

$$\sigma_1(\alpha) = -\frac{B_\alpha}{2A_\alpha} - \sqrt{\left(\frac{B_\alpha}{2A_\alpha}\right)^2 - \frac{C_\alpha}{A_\alpha}}, \tag{20}$$

$$\sigma_2(\alpha) = -\frac{B_\alpha}{2A_\alpha} + \sqrt{\left(\frac{B_\alpha}{2A_\alpha}\right)^2 - \frac{C_\alpha}{A_\alpha}}. \quad (21)$$

Specific analytical expressions of the frequency function and the damping function are determined by the parameters of the mechanical oscillatory system. The choice of specific values of mass-inertia coefficients, stiffness coefficients, and coefficients of viscous friction forces determines the extreme values of the frequency function ω^2 and the damping function $\sigma(\alpha)$.

4 Forms of Frequency Functions and Damping Functions

To evaluate the extreme properties of the frequency function and the damping function, a family of systems with parameters $b_1 = 0, b_2 = 0, k_1 = 0, k_2 = 0$ is considered. The schematic diagram of the mechanical system is shown in Fig. 2. The peculiarity of the system under consideration is the absence of connection of mass-inertia elements with the support surfaces, provided that the mass-inertia elements are connected by an elastic element and a damper (dyad).

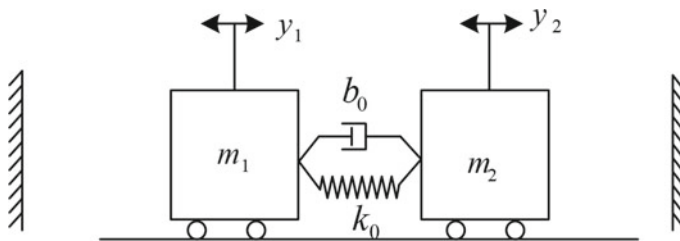


Fig. 2 Schematic diagram of the dyad

The corresponding values $A_\alpha, B_\alpha,$ and C_α have the form:

$$A_\alpha = m_1 + m_2\alpha^2, \quad (22)$$

$$B_\alpha = b_0(\alpha - 1)^2, \quad (23)$$

$$C_\alpha = k_0(\alpha - 1)^2. \quad (24)$$

The critical values of the parameters separating the regions of “small” and “large” viscous friction forces can be represented by the expression:

$$\frac{1}{4} \cdot \left(\frac{b_0(\alpha - 1)^2}{m_1 + m_2\alpha^2}\right)^2 = \frac{k_0(\alpha - 1)^2}{m_1 + m_2\alpha^2}. \quad (25)$$

For each value b_0 , the subgraph domain defines a set of coefficients α for which the condition of «small» of the friction forces is satisfied:

$$\frac{1}{4} \cdot \left(\frac{b_0(\alpha - 1)^2}{m_1 + m_2\alpha^2}\right)^2 < \frac{k_0(\alpha - 1)^2}{m_1 + m_2\alpha^2}. \quad (26)$$

The condition of “small” frictional forces can be transformed to the inequality:

$$\gamma_0 < M(\alpha), \tag{27}$$

where the value $\gamma_0 = \frac{b_0^2}{4k_0}$ reflects the given characteristics of the system, and the value $M(\alpha) = \frac{m_1 + m_2 \alpha^2}{(\alpha - 1)^2}$ depends on the coefficient α and is called a parametrizing function. The frequency function and the attenuation functions depend essentially on the fulfillment of the condition of smallness of the friction forces, which divide the areas of determination of the corresponding functions into sets of coefficients of forms.

The icons shown in Fig. 3b–l, plotted on the function graphs in Fig. 3m–x, reflect the topological features of the graphs of frequency functions and damping functions. The characteristic forms include representations in the form of a single continuous smooth curve with only one zero value, the presence of bifurcation points of one curve into two curves, two disjoint curves or «rings», the graphs touching the boundary points of the region (the function is equal to zero at a point or on an interval), etc.

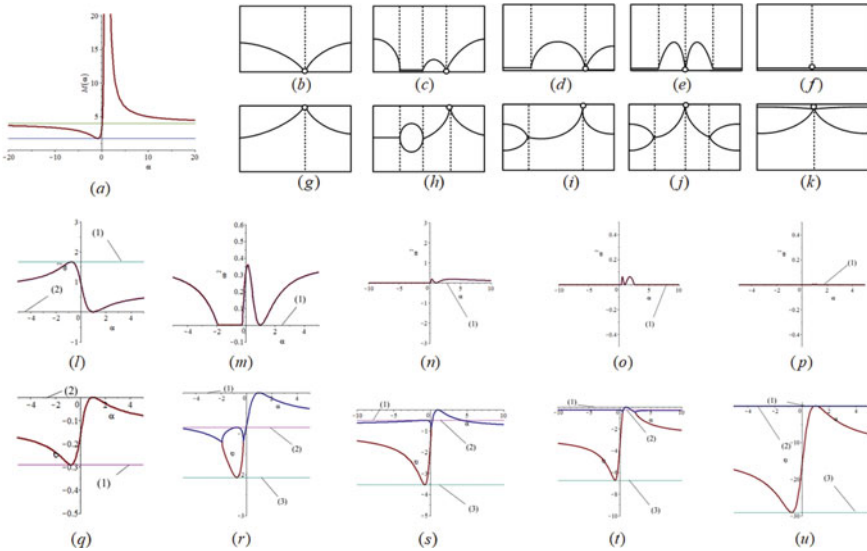


Fig. 3 Features of frequency functions and damping functions: **a**—graph of the parametrizing function; **b–f**—pictograms of frequency functions **l–p**; **g–k**—pictograms of damping functions **q–u**; **l–p**—graphs of frequency functions; **q–u**—graphs of damping functions

Thus, the forms of the frequency function and the damping function, in particular, extreme values and zero values, are determined by the features of the natural frequencies and dissipative coefficients of damped movements of a mechanical oscillatory system formed by two mass-inertial elements connected by a spring taking into account the forces of viscous friction.

5 Conclusion

Based on the results of the conducted research, a number of conclusions can be drawn.

1. A method for constructing the frequency function and the damping function for mechanical oscillatory systems of the chain type with two degrees of freedom, taking into account the forces of viscous friction, is developed. It is shown that the forms of the graphs of frequency functions and damping reflect in extreme values the natural frequencies and dissipative coefficients of the forms of motion of mass-inertia elements.
2. It is shown that the frequency function and the damping function can be represented in two forms, for “small” and “large” viscous friction forces, respectively. In particular, for “small” viscous friction forces, the frequency function takes positive values and the damping function has one negative component, while for “large” viscous friction forces, the frequency function takes zero values and the damping function has two negative components.
3. To determine the variants of the forms of frequency functions and damping functions corresponding to the family of mechanical systems of a given structure, the method of parametrizing functions is proposed, which compares the system parameters with the forms of frequency functions and damping functions that have topological features, which are a classification criterion for mechanical oscillatory systems.
4. It is shown that the forms of frequency functions and damping functions reflect the structural features of mechanical oscillatory systems.

References

1. de Silva CW (2000) *Vibration*. CRC Press, Boca Raton, London, New York, Washington, D.C, Fundamentals and Practice
2. Simon I (2006) *Handbook of railway vehicle dynamics*. CRC Press Taylor & Francis Group, Boca Raton
3. Banakh L, Kempner M (2010) *Vibrations of mechanical systems with regular structure*. Springer, Berlin, Heidelberg
4. Karnovsky IA, Lebed E (2016) *Theory of vibration protection*. Springer International Publishing, Switzerland
5. Eliseev SV, Eliseev AV (2020) *Theory of oscillations*. In: *Structural mathematical modeling in problems of dynamics of technical objects*. Springer International Publishing, Cham
6. Eliseev SV, Lukyanov AV, Reznik YuN, Khomenko AP (2006) *Dynamics of mechanical systems with additional ties*. Publishing Irkutsk State University, Irkutsk
7. Rocard Y (1949) *General Dynamics of Vibrations*. Masson, Paris
8. Eliseev AV, Kuznecov NK, Moskovskih AO (2019) *Dinamika mashin. Sistemnye predstavlenija, strukturnye shemy i svjazi jelementov (Dynamics of machines. System representations, structural schemes and connections of elements)*. Innovacionnoe mashinostroenie, Moscow
9. Eliseev SV, Artjunin AI (2016) *Prikladnaja teorija kolebanij v zadachah dinamiki linejnyh mehanicheskikh sistem (Applied theory of oscillations in problems of dynamics of linear mechanical systems)*. Nauka, Novosibirsk

10. Strett JV (1955) *Teorija zvuka (Theory of sound. Vol.1)*. Izdatel'stvo fiziko-matematičeskoj i tehničeskoj literatury, Moscow
11. Eliseev SV (2018) *Prikladnoj sistemnyj analiz i strukturnoe matematičeskoe modelirovanie. Dinamika transportnyh i tehnologičeskih mashin: svjaznost' dvizhenij, vibracionnye vzaimodejstvija, rynchazhnye svjazi (Applied system analysis and structural mathematical modeling. Dynamics of transport and technological machines: connectivity of movements, vibration interactions, lever connections)*. IrGUPS, Irkutsk
12. Khomenko AP, Eliseev SV (2016) *Razvitie jenergetičeskogo metoda opredelenija častot svobodnyh kolebanij mehaničeskih sistem (Development of the energy method for determining the frequencies of free vibrations of mechanical systems)*. *Sovremennye tehnologii. Sistemnyj analiz. Modelirovanie (Modern technologies. System analysis. Modeling)* 1(49):8–19
13. Eliseev SV, Kuznetsov NK, Bolshakov RS, Nguyen DH (2016) *O vozmožnostjah ispol'zovanija dopolnitel'nyh svjazej inercionnogo tipa v zadachah dinamiki tehničeskih sistem (On the possibilities of using additional inertial-type connections in problems of dynamics of technical systems)*. *Vestnik Irkutskogo gosudarstvennogo tehničeskogo universiteta (Bulletin of the Irkutsk State Technical University)* 112:19–36. <https://doi.org/10.21285/1814-3520-2016-5-19-36>
14. Eliseev SV, Bolshakov RS, Nguyen DH, Vyong KC (2016) *Opredelenie častot sobstvennyh kolebanij mehaničeskih kolebatel'nyh sistem: osobennosti ispol'zovanija častotnoj jenergetičeskoj funkcii. Čast' I. (Determination of natural oscillation frequencies of mechanical oscillatory systems: features of using the frequency energy function. Part I)*. *Vestnik Irkutskogo gosudarstvennogo tehničeskogo universiteta (Bulletin of the Irkutsk State Technical University)* 113:26–33. <https://doi.org/10.21285/1814-3520-2016-6-26-33>
15. Eliseev SV, Bolshakov RS, Nguyen DH, Vyong KC (2016) *Opredelenie častot sobstvennyh kolebanij mehaničeskih kolebatel'nyh sistem: osobennosti ispol'zovanija častotnoj jenergetičeskoj funkcii. Čast' II. (Determination of natural oscillation frequencies of mechanical oscillatory systems: features of using the frequency energy function. Part II)*. *Vestnik Irkutskogo gosudarstvennogo tehničeskogo universiteta (Bulletin of the Irkutsk State Technical University)* 114:10–23. <https://doi.org/10.21285/1814-3520-2016-7-10-23>
16. Eliseev A, Kuznetsov N, Eliseev S, Vuong Q (2020) *Possibilities for regulation of distribution of oscillation amplitudes points of working bodies of technological machines*. *IOP Conf Ser: Mater Sci Eng* 843:012017. <https://doi.org/10.1088/1757-899X/843/1/012017>
17. Mironov AS, Eliseev AV (2020) *System bases of formation of a set of standard links in structural applications of mathematical modeling methods to problems of dynamics of technological and transport machines*. *J Adv Res Techn Sci* 21:5–14. <https://doi.org/10.26160/2474-5901-2020-21-5-14>



Study of the Vibration Separation of Mineral Raw Materials

A. D. Bardovsky^(✉), I. I. Basyrov, and L. M. Valeeva

National University of Science and Technology “MISiS”, 4, Leninsky Prospekt, Moscow 119049, Russia

Abstract. The paper presents the results of studying the process of separating mineral raw materials into fractions in a vibration pneumatic gravitational separator containing a number of series-connected sections through which the classified material passes. Based on the results of theoretical research confirmed by experimental studies, we established that the separation efficiency of mineral raw materials increases exponentially with an increase in the frequency and amplitude of vibration effect on the pneumatic separator body. With an increase in the amplitude and frequency of vibrations of the separator body walls, there is a decrease in the particle settling rate in the near-wall area, which increases the separation efficiency, with the greatest effect achieved when the vibrator is installed on the separator front wall. We found that the maximum separation efficiency of limestone waste from the Khomyakovskoye deposit by the limit size of 1 mm is achieved with the following combinations of the separator body vibration parameters: vibration amplitude $A = 2.5$ mm; vibration frequency $\omega = 250$ s⁻¹.

Keywords: Pneumatic separator · Mineral raw material · Turbulent pulsations · Separator body · Vibration amplitude · Frequency

1 Introduction

It is known that processing mineral raw materials is impossible without generation of a significant amount of waste, amounting to 20...30% of the total volume of mined rock mass, which generally is sent to dumps, e.g., the dumps of carbonate quarries contain from 30 to 50% of a valuable product that could be used by processing industries as fillers for building materials and for other purposes [1–8]. Promising equipment for separating dispersed materials by particle size, in terms of versatility, reliability, and quality of the resulting products, is a machine containing a vibration pneumatic gravitational separator [9].

The performance of such a machine depends, first of all, on the design of the pneumatic separator, the physical and mechanical properties of the material separated, the relationship between the machine parameters, and other factors. A promising trend in the separation technology is cascade separation in one apparatus consisting of several series-connected sections through which the classified material passes [9]. This design of a pneumatic separator allows for achieving greater separation efficiency due to the repeated classification process in each of the individual sections of the machine.

The machine that implements the above scheme of switching on the separation sections is a zigzag separator [10]. Its high separation efficiency is ensured through many repetitions of the separation process in series-connected sections.

A further development of the zigzag classifier is a pneumatic separator with a cascade of solid inclined shelves installed alternately in height on two opposite sides of a section [10]. Figure 1 shows the layout of a single section of the shelf pneumatic separator in space. The raw material inside the section is blown from the bottom by a stream of air “*B*”. In this case, large pieces of “*K*” slide down the inclined shelves under the action of gravity and settle on the separator bottom, whereas fine product “*M*” is carried upward by the air flow. It was established that the separation efficiency in turbulent air flows is increased by 8% [11]. The drawbacks of such machines include high aerodynamic resistance (1...2 kPa) and adhesion of wet separable material under the shelves.



Fig. 1 Layout of an individual section of the pneumatic separator in space

One of the ways to optimize the classification process in a pneumatic separator is applying vibration effect on the separated bulk material (Fig. 2) [10], as it was implemented in the vibro-pneumatic classifier by the Alpine company (Germany). The raw polydisperse material “*I*” is fed into the separator through pipe 1 and falls on vibrating screen 2. The material is blown by an upward air stream “*B*” and is simultaneously exposed to vibration. Under the action of the upward flow, small particles passing through the battery of zigzag Sects. 4 are carried upward by air “*B + M*” to pipe 5. Large particles “*K*”, on which gravity acts more strongly, fall down into pipe 3. Vibration effect on the distribution grid 2 of the pneumatic classifier, along with simultaneous blowing with air, allows for creating a suspended vibrating layer of material where an intensive loosening of small and wet particles occurs, the hydraulic resistance of the system is sharply reduced, the structure of the layer boiling improves, and good conditions are created for sorting and separating dust particles.

Studies show that, in the separation chamber of a pneumatic separator, at air flow rates that are sufficient to carry away fine particles, some fine particles fall down, against the flow direction. Particle settling occurs mainly in the near-wall area of the chamber. This effect is enhanced and constantly maintained by the radial movement of particles in the ascending air flow, which is facilitated by turbulent pulsations, local pressure

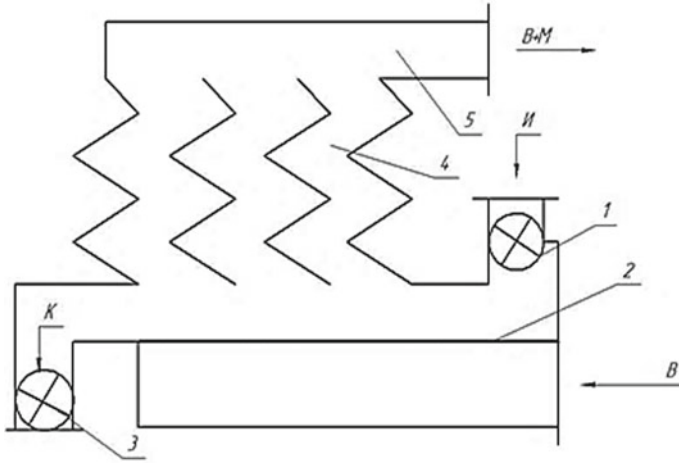


Fig. 2 Layout of the Alpine vibro-pneumatic separator (Germany): 1—raw material pipe; 2—vibrating screen; 3—large product pipe; 4—battery of zigzag sections; 5—air outlet

irregularities, rotation of particles, and their mutual collision. In [12–17], it is noted that a particle in the near-wall area can be longitudinally displaced along the walls without leaving this area. It was established that such a displacement is short in time with an upward motion of the particle and long in time with its downward motion. Fine fractions settling in the near-wall area provide their abundant ingress into the large-sized product and a decrease in the separation efficiency.

In the above papers, the authors suggest switching the two-phase flow into unsteady modes of movement in the separator's separation chamber in order to increase the classification efficiency of bulk materials in a gravitational pneumatic separator. It is noted that such unsteady two-phase flow movement mode can be obtained in different ways: by sharp deceleration, by turning the flow, or by introducing obstacles into the flow. In this way, vortex formation and transition to a turbulent flow mode are initiated in the separation chamber. Favorable conditions for separating bulk material are created in flows with the following parameters of their turbulent structure: turbulence must be of high intensity, because this provides the greatest difference in the speed of small and large fractions; turbulent vortices must have a minimum transverse dimension, because large vortices cause mixing of particles, which deteriorates the separation conditions.

In terms of theory of liquids and gases, the vortex size in a turbulent flow of a continuous medium is usually called the turbulence scale. To optimize the separation process, every possible reduction in the two-phase flow turbulence scale is required, which is achieved by minimizing the geometric dimensions of separation chambers. It has been proved that inclined shelves installed in a cascade separation chamber equalize the particle concentration profile due to their multiple removals from the near-wall area to the flow center. The scale of turbulent pulsations is minimized by reducing the geometric dimensions of cascade sections.

Therefore, we can argue that an increase in the particle settling rate of a two-phase flow in the near-wall area is provided by a decrease in the gas pulsation rates due to an

increased concentration of particles in this area. An increase in the particle concentration near the walls limiting the two-phase flow is due to migration flows of particles and a decrease in the diffusion qualities of the turbulent two-phase flow in the near-wall area. Ascending and turbulent migration flows are due to the Magnus effect and the gradient distribution of the transverse component of the carrier gas flow pulsating velocity, respectively [10].

In [18–22], the authors study separation of limestone quarry waste by the limit separation size of 0.63–1 mm. They note that, the upper limit of the range in pneumatic separators reaches 1 mm. The foregoing allows us to conclude that all fine product of limestone quarry waste separation, moving in a separation chamber, acquires a pulsating velocity and, accordingly, performs a migration movement toward the chamber walls. It is stated that the main hydrodynamic factor affecting the concentration distribution of separated particles in the cross section of the pneumatic separator channel is the migration movement of particles. As applied to cascade separators with transfer shelves, the author believes that, in the presence of such transfer shelves, particle movement patterns become much more complex; therefore, it is possible to consider the dynamics of a two-phase flow with sufficient accuracy only in equilibrium gravitational pneumatic separators.

The studies aimed at assessing the benefits of vibration exposure during pneumatic separation were limited to the study of vibration of the distribution grid, disregarding the possible positive effects of the separator body vibration. The lack of research in this field prevents their widespread use at enterprises processing mineral raw materials; therefore, assessing the nature of changes in the pneumatic separation effectiveness when vibrations are applied to the separator walls to prevent fine particles settling in the near-wall area of the separation chamber is of interest.

2 Researches Objects and Methods

To determine the separation efficiency on a vibration pneumatic separator, we used the Hancock's Formula [11]:

$$E = \gamma_M \cdot \left(\frac{\beta}{\alpha} - \frac{b}{a} \right), \quad (1)$$

where γ_M is the fine product yield, %; β is the content of fine fractions in a fine product sample, %; α is the content of fine fractions in a raw material sample, %; b is the content of coarse fractions in a fine product sample, %; a is the content of coarse fractions in a raw material sample, %.

As a result of solving the problems posed using the apparatus for researching two-phase flows in closed channels [22–38], we have formulated the dependence of the separation efficiency of fine fractions of mineral raw materials on some parameters of vibration pneumatic separation [18]:

$$E = \frac{D_1 + D_2 A^2 u_m \sqrt{\omega} \exp\{D_3 \sqrt{\omega}\}}{1 + c}, \quad (2)$$

where A is the vibration amplitude of the body walls, m ; ω is the vibration frequency of the body walls, s^{-1} ; u_m is the air flow rate, m/s ; c is the weight concentration of material in the separation chamber, kg/m^3 ; D_1 , D_2 , and D_3 are coefficients, the values of which are determined depending on the particle size distribution and physical and chemical properties of the mineral raw materials being separated.

To check the results of theoretical studies in assessing the effect of the pneumatic separator body wall vibrations on the ascending finely dispersed turbulent flow, we created an experimental machine for separating mineral raw materials, including a pneumatic separator with inclined shelves (Fig. 3).

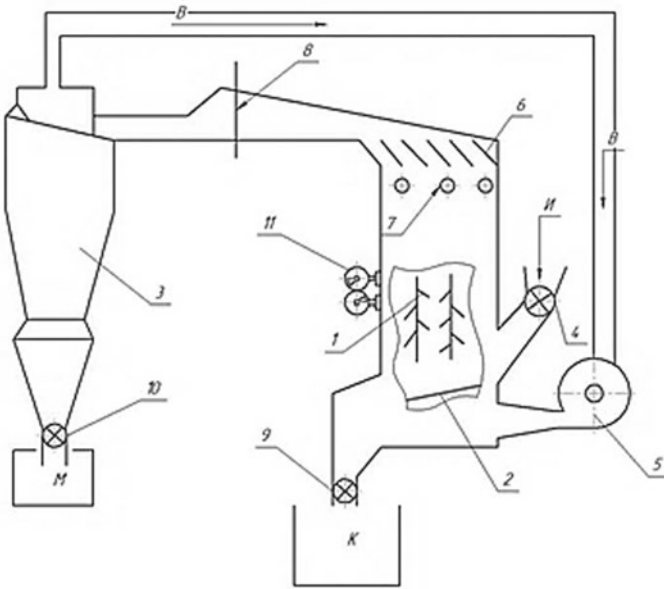


Fig. 3 Schematic diagram of a cascade shelf pneumatic separator

As mineral raw material, we used limestone waste from the Khomyakovskoye deposit with a particle size of 0...10 mm, a bulk density of 2.4 tons/ m^3 , and a moisture content of 2...4%.

Raw material “ M ” is fed from feeder 4 to distribution grid 2. Large particles move to hopper “ K ”, whereas small and part of large particles, being caught by the air flow penetrating through the grid cells from air blower 5, are carried upward into the separation chamber to battery of separation sections 1. Under the effect of the separator body walls vibration from self-balanced vibrator 11, oscillatory motion of a two-phase flow is generated, which provides an additional classification of particles. Large particles along the walls are sent to hopper “ K ”, whereas fine particles with air are sent through throttle valves 6 into cyclone 3 and further into hopper “ M ”. Coarse product gate 9 and fine product gate 10, that are installed on the outlet pipes, as well as common gate 8, allow for maintaining the required air flow parameters in the separator. Additional control is ensured through inspection windows 7.

We changed the following parameters, the range of which was determined based on the results of preliminary studies: vibration amplitude $A = 0.5 \dots 3$ mm and vibration frequency $\omega = 100 \dots 300$ s⁻¹. The air flow rate and the material weight concentration in the separation chamber have been determined based on the results of preliminary studies, being equal to $u_m = 5.44$ m/s and $c = 1.5$ kg/m³, respectively.

As a result of our research, we obtained a regression equation that describes the dependence of the separation efficiency on the above parameters:

$$E = -1,58 \cdot 10^{-4} \omega^2 + 0,1147 \omega + 2,16 \cdot 10^6 A^2 + 841,8A + 9,417c^2 - 55,16c - 3,03u_m^2 + 33,93u_m + 28,26. \quad (3)$$

The coefficients used to determine the theoretical values of the separation efficiency are: $D_1 = 196.3$; $D_2 = 3.101 \cdot 10^4$; $D_3 = 9 \cdot 10^{-2}$, respectively.

As a result of designing a simplex experiment, we have established the most rational values of the vibration amplitude and frequency of the separator body walls: $A = 2.5$ mm and $\omega = 250$ s⁻¹.

It is obvious that, with an increase in the vibration amplitude and frequency of the separator body walls, the particles settling rate in the near-wall area decreases, which enhances the separation efficiency, with the maximum effect achieved when installing the vibrator on the separator front wall. This can be explained by the turbulent movement of the carrying gas flow in the near-wall area due to the vibration effect from the front wall. Vibration of the pneumatic separator walls equalizes the particle concentration over the channel cross section and, consequently, reduces the amount of settled fine particles.

3 Conclusions

1. Our analysis of the process of turbulent pulsations of a two-phase flow in the separation chamber of a shelf pneumatic separator allows us to identify the nature of changes in the particles velocities in the near-wall space and to find that vibration effect on the separator body decreases the rate of particles settling on its walls.
2. The maximum separation efficiency of limestone waste from the Khomyakovskoye deposit by the limit size of 1 mm is achieved with the following combinations of vibration parameters of the separator body: vibration amplitude $A = 2.5$ mm; vibration frequency $\omega = 250$ s⁻¹.

References

1. Federal target program "Waste". Section 1.17: Technical policy on mining waste (1994), Moscow
2. Bardovsky AD, Gerasimova AA, Bibikov PY (2020) Principles of improvement of milling equipment. *Gornyi Zhurnal* 3:56–59. <https://doi.org/10.17580/gzh.2020.03.10>
3. Kokun'ko VV (1994) Creation and development of a new raw material base of building materials on the basis of simultaneously extracted rocks and waste of mining enterprises. *Building Mater* 4:4–6

4. Kartavy NG (2009) The prospect of developing highly efficient classification-grinding equipment for the production of waste non-metallic building materials. Problems of complex development of deposits of solid minerals: Coll. Scientific. Papers MGI. Nedra, Moscow, p 115–128
5. Basyrov II, Bardovsky AD (2020) Innovative crushing technique and vertical roll crusher design. *Mining Info Analy Bullet* 2:121–129. <https://doi.org/10.25018/0236-1493-2020-2-0-121-129>
6. Goncharov YuA (1988) Pneumogravitational separator. Nedra, Moscow, pp 1–12
7. Bardovsky AD, Gerasimova AA, Basyrov II (2019) Study of oscillating process of harp screens. In: *Lecture notes in mechanical engineering* 0(9783319956299), pp 133–139. https://doi.org/10.1007/978-3-319-95630-5_14
8. Eron'ko SP, Oshovskaya EV, Yushchenko MV, Starodubtsev BI (2014) Screw systems for supplying slag-forming mixture to the molds of continuous-casting machines. *Steel in Transl* 44(9):640–645. <https://doi.org/10.3103/S0967091214090071>
9. Bardovsky AD, Valeeva LM, Basyrov II (2020) A plant with a rotary jet grinder to produce small fractions of mineral raw material. *IOP Conf Ser: Mater Sci Eng* 971(5):052004. <https://doi.org/10.1088/1757-899X/971/5/052004>
10. Gerasimova AA, Keropyan AM, Girya AM (2018) Study of the wheel-rail system of open-pit locomotives in traction mode. *J Mach Manuf Reliab* 47(1):35–38. <https://doi.org/10.3103/S1052618818010065>
11. Mednikov EP (1981) Turbulent transfer and deposition of aerosols. Nauka, Moscow
12. Bardovskii AD, Gerasimova AA, Keropyan AM, Bibikow PY (2018) Influence of the mechanical characteristics of harp screen material on screening process. *Izvestiya. Ferrous Metallurgy* 61(9):678–682. <https://doi.org/10.17073/0368-0797-2018-9-678-682>
13. Gamin YV, Romantsev BA, Pashkov AN, Patrin PV, Bystrov IA, Fomin AV, Kadach MV (2020) Obtaining hollow semifinished products based on copper alloys for electrical purposes by means of screw rolling. *Russian J Non-Ferrous Metals* 61(2):162–171. <https://doi.org/10.3103/S1067821220020054>
14. Kukhar V, Kurpe O, Klimov E, Balalayeva E, Dragobetskii V (2018) Improvement of the method for calculating the metal temperature loss on a Coilbox unit at the rolling on hot strip mills. *Int J Eng Technol (UAE)* 7(4):35–39. <https://doi.org/10.14419/ijet.v7i4.3.19548>
15. Karelin IN, Sedykh VD, Sedykh LV (2013) Modernization of a sharply bending elbow in a steel pipeline. *Chem Pet Eng* 49(5–6):351–354. <https://doi.org/10.1007/s10556-013-9754-0>
16. Kondratenko VE, Sedykh LV, Surkova RY (2020) Effective design features of rotor shafts. *IOP Conf Ser: Mater Sci Eng* 971(4):042010. <https://doi.org/10.1088/1757-899X/971/4/042010>
17. Chichenev NA, Gorbatyuk SM, Naumova MG, Morozova IG (2020) Using the similarity theory for description of laser hardening processes. *CIS Iron and Steel Rev* 19:44–47. <https://doi.org/10.17580/cisirs.2020.01.09>
18. Goncharov YA (1992) Substantiation of the main parameters of vibropneumoseparators for the classification of waste from carbonate quarries. Dissertation, Moscow MGI
19. Sedykh LV, Albul SV, Efremov DB, Sukhorukova MA (2020) Application of additive technologies for manufacturing a wear-resistant steel pipe outlet. *IOP Conf. Ser.: Mater. Sci. Eng.* 971(2):022002. <https://doi.org/10.1088/1757-899X/971/2/022002>
20. Nikolaev VA, Rusakov AD, Chichenev NA (1996) Forecasting a multiroll mills rolls hardness. *Stal'* 9:58–60
21. Gerasimova AA, Radyuk AG, Glukhov LM (2014) Applying coatings to the narrow walls of continuous-caster molds to improve the quality of the surface of slabs. *Metallurgist* 58(5–6):397–400. <https://doi.org/10.1007/s11015-014-9922-2>
22. Durelli AJ, Chichenev NA, Clark JA (1972) Developments in the optical spatial filtering of superposed crossed gratings—Spatial-filtering techniques are used to obtain individually, as

- separate patterns in a simple and precise manner, the whole field of displacement components and of their time and space derivatives. *Exp Mech* 12(11):496–501. <https://doi.org/10.1007/BF02320745>
23. Kobelev OA, Zinov'ev AV, Tsepin MA (2009) Effective production of large pipe blanks. *Steel in Transl* 39(6):501–505. <https://doi.org/10.3103/S0967091209060163>
 24. Artiukh V, Mazur V, Adamtsevich A (2017) Priority influence of horizontal forces at rolling on operation of main sheet rolling equipment. *MATEC Web of Conf* 106:04001. <https://doi.org/10.1051/mateconf/201710604001>
 25. Albagachiev AY, Keropyan AM, Gerasimova AA, Kobelev OA (2020) Determination of rational friction temperature in lengthwise rolling. *CIS Iron and Steel Rev* 19:33–36. <https://doi.org/10.17580/cisr.2020.01.07>
 26. Zagirnyak M, Zagirnyak V, Moloshtan D, Drahobetskiy V, Shapoval A (2019) A search for technologies implementing a high fighting efficiency of the multilayered elements of military equipment. *Eastern-European J Enterprise Technol* 6(1–102):33–40. <https://doi.org/10.15587/1729-4061.2019.183269>
 27. Solomonov KN, Tishchuk LI (2019) Simulation of deformation processes in upsetting. *J Phys: Conf Ser* 1348(1):012020. <https://doi.org/10.1088/1742-6596/1348/1/012020>
 28. Kulikova EY, Ivannikov AL (2020) The terms of soils removal from the defects of the underground structures' lining. *J Phys: Conf Ser* 1425(1):012062. <https://doi.org/10.1088/1742-6596/1425/1/012062>
 29. Kondratenko VV, Sedykh LV, Mirzakarimov A, Aleksakhin A (2020) Static analysis and strength calculation of drive shaft of large-scale cone crusher. *E3S Web of Conf* 193:01038. <https://doi.org/10.1051/e3sconf/202019301038>
 30. Tarasov YS, Kobelev OA, Sayfullayev SD (2020) Improving the heat insulation efficiency of the blast furnace tuyere. *IOP Conf Ser: Mater Sci Eng* 971(3):03203. <https://doi.org/10.1088/1757-899X/971/3/032033>
 31. Naumova MG, Morozova IG, Borisov PV (2020) Study of metal surface with color image obtained with laser marking. *Solid State Phenomena* 299SSP:943–948. <https://doi.org/10.4028/www.scientific.net/SSP.299.943>
 32. Karfidova AO, Vasilyev MV, Morozova IG (2020) Modernization of an industrial passive exoskeleton prototype for lower extremities using rapid prototyping technologies. *IOP Conf Ser: Mater Sci Eng* 971(5):052049. <https://doi.org/10.1088/1757-899X/971/5/052049>
 33. Keropyan A, Albul S, Zarapin A (2020) Problem of increasing tractive effort of railway locomotives in conditions of arctic and continental shelf regions. In: *Lecture notes in mechanical engineering*, pp 651–658. https://doi.org/10.1007/978-3-030-22063-1_69
 34. Kondratenko VE, Devyatiarova VV, Albul SV, Kartyshev DS (2020) Improving methodology for calculating scaffolding formwork of monolithic slabs in building constructions. *IOP Conf Ser: Mater Sci Eng* 971(5):052037. <https://doi.org/10.1088/1757-899X/971/5/052037>
 35. Bibikov PY, Bardovskiy AD, Keropyan AM (2019) Investigation of press classification process of weak rocks. *Mater Today: Proceed* 19:2552–2554. <https://doi.org/10.1016/j.matpr.2019.08.207>
 36. Kondratenko VE, Devyatiarova VV, Albul SV, Valeeva LM (2020) Method of calculating volumetric scaffold of monolithic slab formwork. *IOP Conf Ser: Mater Sci Eng* 971(5):052036. <https://doi.org/10.1088/1757-899X/971/5/052036>
 37. Kobelev OA, Tyurin VA (2007) Production of large plates. *Steel in Transl* 37(9):727–729. <https://doi.org/10.3103/S096709120709001X>
 38. Keropyan AM, Kantovich LI, Voronin BV, Kuziev DA, Zotov VV (2017) Influence of uneven distribution of coupling mass on locomotive wheel pairs, its tractive power, straight and curved sections of industrial rail tracks. *IOP Conf Ser: Earth Environ Sci* 87(6):062005. <https://doi.org/10.1088/1755-1315/87/6/062005>



Influence of the Incoming Flow Velocity to the Error of the Orientation Angle of a Horizontal-Axial Wind Turbine

A. Terekhin^(✉), A. Martyanov, and D. Ismagilov

South Ural State University, 76, Lenin Av., Chelyabinsk 454000, Russia

Abstract. Due to the increasing use of renewable sources for generating electricity and the large-scale operation of wind power plants, the problem of efficient use of wind energy arises. An analysis of the most common horizontal-axial wind turbines (HAWT) shows that this type of installation has some disadvantages. One of these disadvantages is the need to ensure the collinearity of the rotor axis of the WT and the wind direction. Failure to comply with this requirement in the operation of WT leads to a decrease in efficiency due to inadequate use of wind potential. To ensure the alignment of the wind direction and the rotor, the WT uses a yaw control system based on an anemorumbometer. However, when the WT rotor rotates, there is a deviation of the air flow due to the bending of the moving WT blade. As a result, the anemorumbometer located in the upper part of the WT nacelle behind the rotating rotor determines the wind direction with some error, which is why the yaw control system turns the wind turbine rotor with some deviation from the optimal direction, which leads to a decrease in the efficiency of wind energy conversion. The aim of the presented work is to study the flow of air flow behind the rotor to determine the magnitude of the resulting error in various modes of operation of the WT.

Keywords: Wind power · Weather vane · Blade · Anemorumbometer · Aerodynamic profile · Vortex

1 Analytical Description of the Problem

WT require the orientation of the rotor in the wind direction in order to obtain the greatest power generation. The orientation is either passive (due to the presence of a weather vane rigidly connected to the nacelle), but for large turbines this approach is not acceptable due to the large mass of the rotor. In this regard, active orientation is used with the help of an anemometer located at most turbines on the back of the nacelle. The turbine power can be expressed using the following system of equations:

$$P_{\max} = 0.5 \cdot \rho \cdot A_r \cdot C_p \cdot V_p^3; \quad (1)$$

$$V_p = V_0 \cdot \cos \theta_E. \quad (2)$$

Equation (1) shows that the maximum power (P_{\max}) that can be captured by the turbine depends on the wind speed perpendicular to the swept area of the rotor (V_p), taking into account the air density (ρ), the rotor area (A_r), and the power factor of the wind turbine (C_p). In Eq. (2), the perpendicular component of the wind speed is expressed in terms of the wind speed of the free flow (V_0) and the cosine of the yaw error angle (θ_E) between the exposed direction of the turbine and the direction of the wind flow vector. Combining these two equations means that if there is a yaw error, the power decreases by the cube of the cosine of the yaw error.

To clarify the cosine dependence, field tests were conducted with LIDAR systems [1–3]. LIDAR equipment was installed on a rotating rotor to measure wind flow parameters before installation. An alternative measurement of wind speed and direction was carried out using an anemometer mounted on the nacelle and additionally a rumba anemometer mounted on a free-standing weather mast (met mast). The results of processing empirical data [4–6] generally showed that in any case, the orientation mismatch reduces the power of the wind turbine, but the relationship can be cosine-squared. However, it was not reliably found out how accurate the orientation of the rotor was, how the incoming flow deviates from the main direction, how much the wind speed decreases under the influence of the installations in front of the wind farm, etc.

2 Results of Experimental Studies

To confirm whether LIDAR improved the rotor orientation, a comparison was made between the rotor position and the wind flow direction. However, since the wind direction is not explicitly known, comparisons were made with wind direction measurements using three instruments: LIDAR, a rumba anemometer on the nacelle, and an anemometer on the weather mast to determine the overall trend. Figure 1 shows the mismatch of the rotor orientation compared to the wind direction measurement using LIDAR, as well as the met rumba anemometer. masts as a function of the turbine rotor speed.

The left diagram shows the orientation mismatch when measuring LIDAR. The right diagram shows the orientation mismatch when measuring the rumba anemometer on a weather mast. For the anemometer controller on the nacelle, the orientation offset correction function was not applied (if the orientation correction function had been applied, the reading deviation would have been lower).

The graphs show an orientation error when using the anemometer on the nacelle in almost all cases around 20° , while LIDAR operates with an error close to zero.

Moreover, the orientation error from the anemometer on the nacelle does not depend on the speed of rotation of the rotor. This result contradicts many other experiments [7].

An analysis of the efficiency of LIDAR measurements with registration of the wind turbine output power is shown in Fig. 2.

It can be seen that in the case of LIDAR measurements, the orientation at pre-nominal wind speeds is better and, accordingly, the power of the wind turbine is higher. At higher wind speeds, the situation is uncertain due to the smaller number of measurement data.

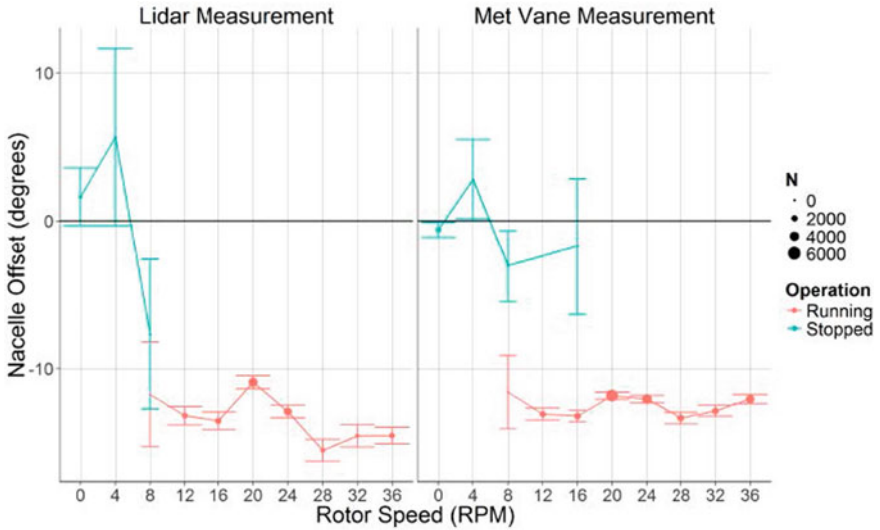


Fig. 1 Plot of the rotor orientation mismatch depending on the rotor speed: for the anemorumbometer controller on the nacelle (red) and for the LIDAR controller (blue)

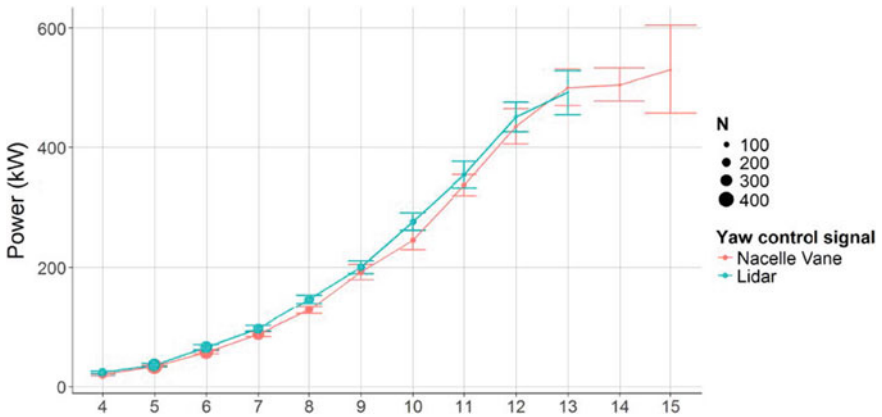


Fig. 2 WT power graph for different wind speeds: when oriented with the anemorumbometer controller on the nacelle (red) and when oriented with the LIDAR controller (blue)

3 Modeling of Aerodynamic Flows

The main technical characteristics of the Siemens HAWT: SWT-3.6–120 with the blade profile B52 [8], given in Table 1, are used as the basis for constructing computer models for conducting research.

The following factors served as a justification for the choice of this WT:

Table 1 Main technical characteristics of WT Siemens: SWT-3.6–120

Rotor		Blade		Operational data	
Parameter	Data	Parameter	Data	Parameter	Data
Type	3-bladed, horizontal axis	Type	B52	Cut-in wind speed	3–5 m/s
Position	Upwind	Length	58.5 m	Nominal power	at 12–13 m/s
Diameter	120 m	Chord in comle	4.2 m	Cut-out wind speed	25 m/s
Swept area	11,300 m ²	Aerodynamic profile	NACA63.xxx, FFAxxx	Maximum 2 s gust	70 m/s (IEC version)
Speed range	5–13 rpm	Material	GRE	Tip speed ratio	5 modules
Power regulation	Pitch regulation with variable speed	Coverage	Semi-matt, < 30 / ISO2813		
Rotor tilt	6 degrees	Color	Light gray, RAL 7035		

- the most common unit capacity of wind power plants in wind farms, which make the main contribution to the generation of electricity by the global wind industry is 2–4 MW;
- the typical location of the anemorumbometer is on the conventionally horizontal surface of the nacelle, in its rear part (the inclination of the nacelle in relation to the rotor axis is usually 0...120 degrees);
- characteristic structure of the blades (in the analysis, only the blade stack, which has a cylindrical cross section is involved).

Figure 3 shows the location of the anemorumbometer on the nacelle to determine the direction and speed of the wind, as well as the level of location of the devices relative to the blade.

In studies, the location of the anemorumbometer based on the manufacturer's technical data and clarifying measurements is taken as follows:

- the distance from the rotor (blade) to the anemorumbometer is 13 m (along the X-axis, as will be accepted in the future);
- height above the nacelle—3 m (on the Y-axis, as will be accepted in the future).

However, these are conditional values intended for modeling only. In practice, these values will be different for different wind turbines.



Fig. 3 Location of the wind speed and direction sensor (anemorumbometer) at a distance of 13 m from the rotor and at a height of 3 m (data taken for modeling)

The model of the HAWT based on a serial product manufactured by Siemens SWT-3.6–120 with a blade profile B52 is built in the SolidWorks 3D software package. The three-dimensional geometric model is shown in Fig. 4. The adequacy of the model is confirmed by comparing the overall characteristics of the model and the prototype SWT-3.6–120 manufactured by Siemens.

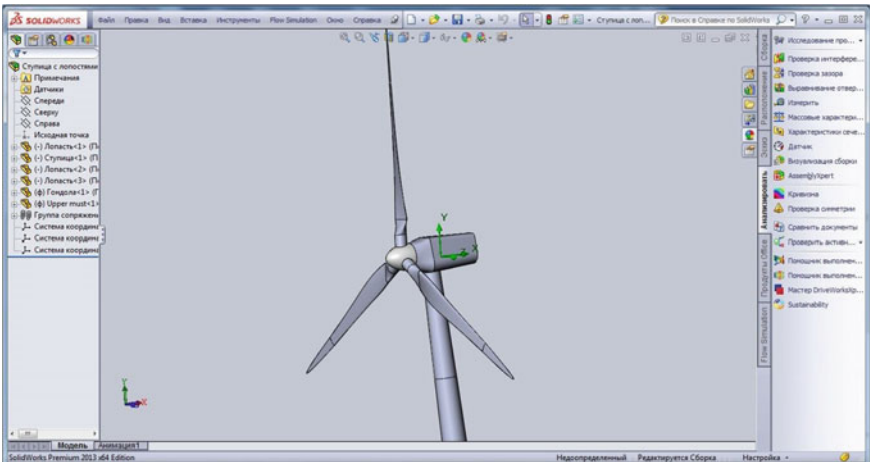


Fig. 4 HAWT model SWT-3.6–120 in solidworks flow simulation

Mathematical modeling of the gas movement in the region of the wind turbine power plant in accordance with [9–24].

4 Investigation of Air Flow Disturbance by the Rotor of a Wind Power Plant

The conditions for blowing are defined as follows: the rotor moves at a constant speed, the value of which is determined on the basis of the main reference points of wind speed—pre-start speed of 3 m/s, starting speed of 5 m/s, nominal speed of 12 m/s, and post-nominal speed of 25 m/s. Speed (the ratio of the linear speed of the end of the blade to the wind speed) is assumed to be $Z = 5$ based on the manufacturer's information. The parameters are taken from [3]. The mast of the HAWT is stationary, the rotor rotates counterclockwise when viewed from the front. The nominal angular rotor speed ω corresponds to the rated wind speed of $V_w = 12$ m/s at specific speed $Z = 5$ modules, which corresponds to the best characteristics of contemporary wind turbines and represents the ratio of the linear velocity of the end of the blade to the wind speed (rotor radius R was taken equal to the length of the blade):

$$\omega = \frac{Z \cdot V_w}{R} = \frac{5 \cdot 12}{58.5} = 1.03 \left[\frac{\text{rad}}{\text{s}} \right]. \quad (3)$$

The obtained angular velocity corresponds to a rotation frequency of 9.7 rpm, which in turn satisfies the operating range of the rotor speed of the studied HAWT of 5–13 rpm. Thus, the choice of speed $Z = 5$ modules can be considered reasonable. The wind speed for blowing the rotor is selected based on the characteristics of the HAWT. The nominal speed of rotation of this WT is taken 12 m/s.

5 Conclusions

The result of the study is the degree of deviation of the wind flow Θ from the vertical plane passing through the axis of symmetry of the rotor, the axis of the mast and the anemorumbometer. Figure 5 shows comparisons of simulation results at wind speeds of 7 and 12 m/s.

The theoretical analysis of the analytical dependences of the wind power plant performance showed the presence of a significant influence of the wind flow direction on the amount of generated power—an orientation error can lead to a decrease in power in cubic dependence on the cosine of the yaw error.

There are no published studies on how accurate you want the orientation of the rotor the velocity vector of the incoming flow as deflected velocity vector from the mainstream and how decreases the module of the velocity vector under the influence of the front facing in wind farms installations.

There are some published research results that suggest that the orientation error from the anemorumbometer on the nacelle does not depend on the speed of rotation of the rotor. However, these results contradict many other experiments. Thus, there is uncertainty in the issue under study, which justifies the need for additional research.

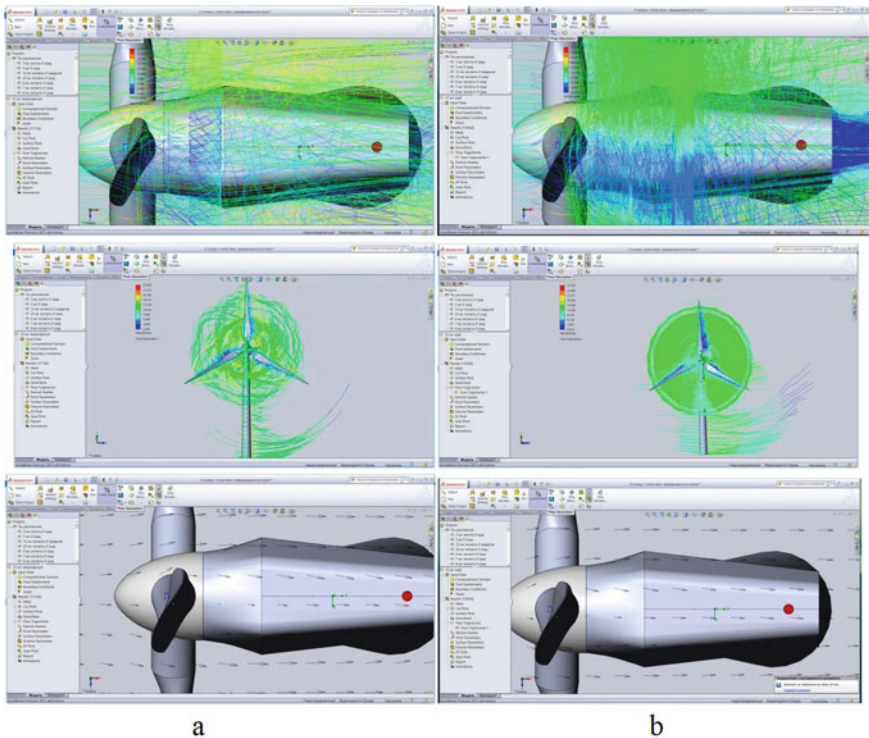


Fig. 5 Simulation results at 7 m/s (a) and 12 m/s (b)

Other published data suggest that when using an anemumbometer on a nacelle, the orientation error is about 20° , while LIDAR shows a smaller error. However, there is no reliable data on the magnitude of this error due to the lack of measurements of the actual values of the air flow parameters.

Preliminary numerical simulation of the air flow showed that the main mass of air passing near the nacelle has a significant effect only on the part of the swept area, which is a circle with a radius $r \leq 0.25 R$, where R is the length of the blade. The result of preliminary modeling allowed us to narrow the study area and reduce the requirements for computing resources while reducing the calculation time.

As a result of detailed modeling of the air flow around the nacelle, the dependences of the angle of deviation of the air flow velocity vector in the vertical plane passing through the axis of symmetry of the rotor, the mast axis and the anemumbometer for different wind speeds are obtained. The results showed that, despite the large number of different vectors, the main direction of flow at the location of anemumbometer diverges by 5° to 20° , depending on wind speed and rotor speed wind turbine.

For further studies of the air flow near the anemumbometer, it is planned to consider cases with other wind speeds, including limit ones, as well as with different values of the rotor speed, as well as to obtain results using more complex numerical models and compare them with each other to confirm the reliability of the results.

Acknowledgements. The presented material was supported by Russian Foundation for Basic Research, Agreement RFBR #19-08-00070 on the base of Project Training at South Ural State University (National research university), Russian Federation.

References

- Scholbrock A, Fleming P, Wright A, Slinger C, Medley J, and Harris M (2015) Field test results from lidar measured yaw control for improved yaw alignment with the NREL controls advanced research turbine. In: National renewable energy laboratory. <https://www.nrel.gov/docs/fy15osti/63202.pdf>. Accessed 10 Jan 2021
- Schlipf D, Bischoff O, Hofsaß M, Rettenmeier A, Trujillo JJ and Kuhn M (2004) Lidars and wind turbine control. In: Endowed chair of wind energy, institute of aircraft design. <https://www.researchgate.net/publication/279381610>. Accessed 10 Jan 2021
- Scholbrock A, Fleming P, Wright A, and Wang Na (2016) Lidar-enhanced wind turbine control: past, present, and future. In: American control conference Boston, Massachusetts. <https://www.nrel.gov/docs/fy16osti/65879.pdf>. 10 Jan 2021
- Solomin E, Kirpichnikova I, Martyanov A (2015) Iterative approach in design and development of vertical axis wind turbines. In: Applied mechanics and materials, vol. 792. Energy Systems, Materials and Designing in Mechanical
- Volovich GI, Solomin EV, Topolskaya IG, Topolsky DV, Topolsky ND (2015) Modelling and calculation of adaptive devices of automation, control and protection for intellectual electric grid in SCILAB freeware computer mathematic package. In: Bulletin of South Ural State University. Section “Mathematic modeling and programming”, Chelyabinsk, vol. 8(4)
- Sirotkin EA, Solomin EV, Gandzha SA, Kirpichnikova IM (2018) Backup mechanical brake system of the wind turbine. *J Phys Conf Ser* 944(1)
- Kragh KA and Fleming PA (2012) Rotor Speed Dependent Yaw Control of Wind Turbines Based on Empirical Data. In: Proceedings of the 51st AIAA aerospace sciences meetings and exhibit, American Institute of Aeronautics and Astronautics, Nashville, TN
- Wind power plant Siemens: SWT—3.6—120, Technical documentation. <https://pdf.archie.xpo.com/pdf/siemens-gamesa/swt-36-120/88089-134487.html>. Accessed 10 Jan 2021
- Wesseling P (2001) In: Principles of computational fluid dynamics. Springer, Berlin, Heidelberg, pp 644
- Bensow RE, Fureby C, Liefvendahl M, Persson T (2006) Numerical investigation of the flow over an axisymmetric hill using LES, DES and RANS. *J Turbul* 7(4):1–17
- Pope SB (2000) Turbulent flows. Cambridge University Press
- Ferziger JH and Perić M (2002) In: Computational methods for fluid dynamics. 3rd edn. Springer
- Daily JW, Pitz RW (1983) Combustion in a turbulent mixing layer formed at a rearwardfacing step. *AIAA J* 21(11):1565–1570
- Krajnović S (2008) Large eddy simulation of the flow over a three-dimensional hill. *Flow Turbulence Combust* 81:189–204
- Baldwin BS, Barth TJ (1990) A one-equation turbulence transport model for high-Reynolds number wall-bounded flows. NASA TM-102847
- Abdulridha ZS, Martyanov AS, Martyanov NA (2020) Simulation model of hybrid renewable energy system. In: Proceedings—2020 international conference on industrial engineering, applications and manufacturing, ICIEAM 2020, 9111998
- Martyanov A, Martyanov N, Sirotkin E (2018) State observer for variable speed wind turbine. In: Proceedings—2018 international ural conference on green energy, UralCon 2018, pp 97–100, 8544344

18. Martyanov AS, Troickiy AO, Korobotov DV (2018) Performance assessment of perturbation and observation algorithm for wind turbine. In: Proceedings—2018 International conference on industrial engineering, applications and manufacturing, ICIEAM 2018, 8728559
19. Martyanov AS, Martyanov NA, Anikin AS (2015) Comparative analysis of wind turbine control strategies. *Proc Eng* 129:607–614
20. Terekhin AA, Mertemyanova VA, Kovalyov AA (2021) Mathematical models of turbulence for the wake vortex parameters determination. In: Proceedings—2020 International conference on industrial engineering, applications and manufacturing, ICIEAM 2020
21. Bradshaw P, Ferriss DH, Atwell NP (1967) Calculation of boundary layer development using the turbulent energy equations. *Fluid Mech* 23:31–64
22. Gatski TB (1993) Speziale CG (1993) On the explicit algebraic stress models for complex turbulent flows. *Fluid Mech* 254:59–78
23. Lumley JL (1978) Computational modeling of turbulent flows. *Appl Mech* 18:124–176
24. Rahman MM, Siikonen T (2001) An artificial compressibility method for incompressible flows. *Numer Heat Transfer, Part B* 40:391–409



Some Features of Measurements of Dynamic Characteristics of Heavy Machinery Objects During Operation in the Far North

M. O. Sinita^(✉), E. V. Tumakova, and A. S. Komshin

Bauman Moscow State Technical University, 5, p. 1, 2-ya Baumanskaya str., Moscow 105005, Russia

sinmaria@yandex.ru

Abstract. Since 2019, arctic studies are actively developing in Russia and the world. It is obvious that the development of technologies to create and implement not just renewable energy sources, namely renewable energy sources capable of operating in the Arctic, is becoming particularly relevant today. Space weather is a significant factor that can have a negative impact on renewable energy, in addition to the harsh climate. The paper provides an analysis of the impact of geinduced currents on the operation of traditional power plants and wind farms. It has conducted a correlation analysis of experimental data obtained from one of the turbines of Surgut GRES-1 and data on the AE index, characterizing the intensity of Auroral currents, to establish the relationship between the functioning of electromechanical systems and geomagnetic disturbances. The factors leading to malfunctions at renewable energy facilities, as well as at traditional electricity facilities, have been analyzed.

Keywords: Renewable energy sources · Geinduced currents · The measuring complex · Heavy engineering

1 Introduction

Since 2019, arctic studies are actively developing in Russia and the world. It should be mentioned Arctic Strategy Congress Department of Defense, Sustainable Development in the Arctic, Arctic Contamination Action Program, etc.

Russia adopted the state energy development program in 2019, with the implementation period expected to be completed by 2024. The aim of the program is two aspects:

1. Maximizing assistance to the country's socioeconomic development, which plays a significant role in the formation of revenues of the Russian budget;
2. Strengthening and maintaining the Russian Federation's position in the world energy sector.

Achieving this goal requires an accelerated transition to more efficient, flexible and sustainable energy [1].

In addition to the above-mentioned program, in 2020, the Russian President's Decree of October 26, 2020, № 645 approved the strategy for the development of the Arctic zone of the Russian Federation and national security for the period up to 2035. This strategy, among other things, highlights a high proportion of local electricity generation based on the use of economically inefficient and environmentally unsafe diesel fuels as the main dangers, challenges, and threats that pose risks to the development of the Arctic zone and national security.

It is obvious that the development of technologies to create and implement not just renewable energy sources, namely renewable energy sources capable of operating in the Arctic, is becoming particularly relevant today.

The issue of GWEC¹ Global Wind Report [2]:

- The total capacity of all wind farms in the world now exceeds 651 GW;
- The share of offshore wind power from the total number of new installations also became a record and amounted to 10% [3].

On this background, the need for innovative solutions in the field of information and metrological support and measuring technologies that contribute to the transition from monitoring to forecasting the assessment of the technical condition of basic and auxiliary equipment in the field of heavy engineering in the process of operation and energy is growing sharply [4, 5].

At the present stage of scientific and technological development, all conditions have been created for the implementation at a new metrological level of intelligent measuring complexes to support the life cycle of complex technical systems using intelligent measuring learning systems and artificial intelligence, taking into account not only technological factors (internal), but also external (heliogeophysical, geomagnetic, ionospheric, and seismic measurements). In such conditions, it becomes necessary to achieve a level of information and metrological support of the technosphere that meets the requirements of its development in the context of the fourth industrial revolution.

In the last decade, a new phase of studying the impact of space on various human activities has begun. Space weather, which refers to a set of processes occurring in the sun and in space, poses direct risks to the normal functioning of natural, technological, and biological systems located on Earth and in near-Earth space.

On the one hand, the Arctic regions of Russia have significant potential for the development of wind turbines. The average wind speed in many regions is about 6–7 m/s, which contributes to the development, in particular, of wind energy. However, on the other hand, there are the harsh climatic conditions of the Arctic, which characterized by very low temperatures, gusty winds, and, as a consequence, a minimum of maintenance [6, 7].

¹ GWEC—Global Wind Energy Council, <https://gwec.net/gwec-over-60gw-of-wind-energy-capacity-installed-in-2019-the-second-biggest-year-in-history/>.

Space weather is another significant factor that can have a negative impact on renewable energy sources. The study of its influence on the technosphere is one of the developing directions in science. Until now, the consequences that can lead to changes in the Earth's magnetic field in relation to electromechanical systems have not been studied.

The territory of the Arctic is located in the so-called auroral zone. The auroral zone is a strip of latitudes where the most powerful magnetic disturbances and the brightest auroras recorded. The auroral zone in Russia and Northern Europe mainly passes over the Arctic Ocean [8].

The solar wind is the source of geomagnetic storms. It is formed by charging particles emitted by the sun. During a storm in space weather, the magnetosphere-ionosphere system becomes severely disturbed, containing intense and rapidly changing flows. The so-called auroral zone (auroral electrojet) arises—an electric current in the area of the auroral oval, directed westward at night and morning hours, and eastward—at evening hours and according to Faraday's law of induction, a geoelectric field is induced on the surface of the Earth. This geoelectric field creates geinduced currents (GIC) in ground technological networks [9]. The GIT is a quasi-constant current. The duration of the flow through the power grids ever recorded by GIT ranges from hundreds of seconds to tens of hours and the highest recorded value of GIT is 320 A [10]. Such currents can lead to negative consequences for electric power facilities. The works [11–15] provide descriptions of the recorded accidents on electrical networks that occurred due to the occurrence of GIT in them.

2 The State of Wind Power

The paper [16] presents an analysis of the development of the field of wind power and hydropower in the Russian Federation and substantiates the possibility of using measuring phase-chronometric technology for renewable energy facilities, such as wind turbines and hydroelectric units.

According to studies of wind turbines and their downtime (more than 24,000 wind turbines were investigated, the results published by Durham University) found that the failure rate per wind turbine is between 0.2 and 0.5, and the greatest number of failures observed in responsible structural parts, among them should be noted [16, 17]:

- Electric systems;
- Control systems;
- Hydraulic systems;
- A weathervane control system;
- Wind turbine blades;
- Gearboxes;
- Generator, etc.

From the results of the study, it should be noted that electrical systems have the greatest frequency of failure, failure of transmissions leads to the longest downtime, at the same time gearbox failures, broken blades, and transmission failures lead to 95% of equipment outages.

3 The Measuring Technology to Monitor the Technical Condition of Gearboxes and Rolling Bearings During Operation

As noted in [16], the results of experimental studies are presented depending on the type of wear of gear wheels and the results of measuring the magnitude of wear in polar coordinates.

The accuracy of measuring the wear of the teeth is within $\pm 0.15\%$. At the same time, it is obvious that the changes in the EMF value during natural wear of the working surface of the tooth will be smooth, and all volumetric changes such as chipping or tooth breakage will give abrupt changes in the EMF of the sensor. Figure 1c shows an example of diagnosing a breakdown of the 15th tooth of a gear.

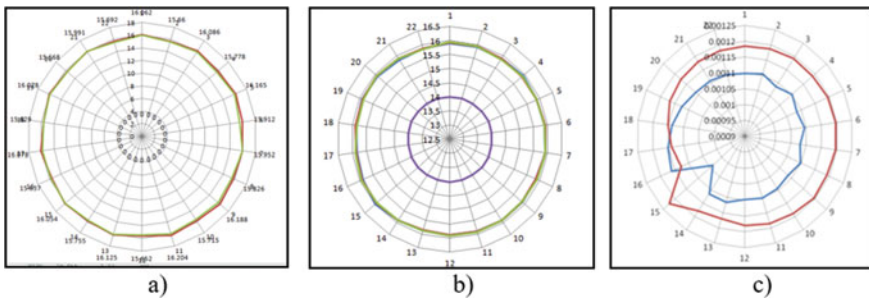


Fig. 1 Results of measurements of the respective teeth of the serrated wheels, depending on the type of wear in the polar coordinates: the circumference—the number of the tooth, the axis of the residents—the result of measuring the size of the tooth by the dividing circle

Figure 2 shows a graph of the change in the measuring signal of the transmitter coil of the induction sensor over time, depending on the wear of the tooth.

Measuring information phase-chronometric technologies allow solving the following tasks:

- Control of the parameters of natural abrasive wear of the working surfaces of the teeth, their possible chipping;
- Control of tooth breakage;
- Measurement of tooth wear during operation;
- Evaluation of the parameters of the gearing;
- Evaluation of the gearbox (gearbox, etc.).

To obtain reliable information about the operation of a bearing, a systematic approach is required, including:

- Development of test methods based on common scientific principles for all stages of the object's life cycle;
- Application of the minimum nomenclature of measured physical quantities;
- Creation of a unified methodological approach to assessing the current technical condition of rolling bearings.

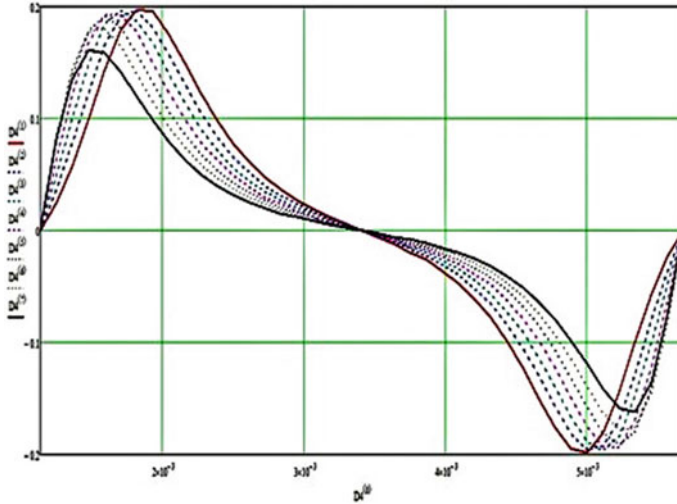


Fig. 2 Graph of the change in the measuring signal of the transmitter coil of the induction sensor in time depending on the wear of the tooth

Expensive bearing testing is a problem, especially for large ones from a commercial batch. In this regard, the task is to develop methods for researching bearings and accelerated test procedures. Tests accompany all stages of the bearing life cycle, and the current unsatisfactory situation in the development of structures is associated with a lack of scientific knowledge and a low metrological level of traditional methods and diagnostic tools.

The generalized function of changing the time intervals of a roller bearing is presented by introducing for all rollers the connection between the changes in the angle of rotation with the corresponding change in the time interval:

$$\Delta T_n = f(\Delta\varphi_1, \Delta\varphi_2, \Delta\varphi_3, \dots, \Delta\varphi_n, \Delta N_n, \Delta F_n), \tag{1}$$

where n —the number of rolling elements, $\Delta\varphi$ —the angle of the center of the rolling bodies relative to the center of the bearing rings, and ΔN —an additional load associated with the functioning of the rolling bearing (e.g., for the tow bearing impact when passing the arrow wheeled pair).

4 Implementation of Metrological Support for Heavy Engineering Facilities in the Far North

To establish the relationship between the functioning of electromechanical systems and geomagnetic disturbances, a correlation analysis of the experimental data obtained at one of the turbine units of the Surgutskaya GRES-1 and data on the AE-index characterizing the intensity of auroral currents was carried out. The AE-index is used in the study of geomagnetic activity at high latitudes and is widely used as a characteristic of changes in the geomagnetic environment in general [18, 19].

Table 1 Periods of time under consideration

Date	Time
15.06.2010	02:00 – 02:50
15.06.2010	16:00 – 16:50
15.06.2010	22:00 – 22:50
16.06.2010	00:00 – 00:50
16.06.2010	02:00 – 02:50
16.06.2010	04:00 – 04:50
16.06.2010	14:00 – 14:50
16.06.2010	16:00 – 16:50
17.06.2010	08:00 – 08:50
17.06.2010	12:00 – 12:50
17.06.2010	14:00 – 14:50

For consideration were selected data in the periods presented in Table 1.

The experimental data obtained at one of the turbine units of the Surgutskaya GRES-1 are the time intervals obtained using the phase-chronometric system developed at the Moscow State Technical University. N.E. Bauman.

The World Center in Japan stores and processes the AE index values [18]. In Fig. 3 is shown a view of the data from this center:

DATE	TIME	DOY	AE	AU	AL	A0	
16,06,2010	0:01:00	167	443,00	198,00	-245,00	-24,00	
16,06,2010	0:02:00	167	437,00	184,00	-253,00	-35,00	
16,06,2010	0:03:00	167	446,00	182,00	-264,00	-41,00	
16,06,2010	0:04:00	167	469,00	188,00	-281,00	-47,00	
16,06,2010	0:05:00	167	457,00	181,00	-276,00	-48,00	
16,06,2010	0:06:00	167	430,00	170,00	-260,00	-45,00	
16,06,2010	0:07:00	167	437,00	165,00	-272,00	-54,00	
16,06,2010	0:08:00	167	468,00	164,00	-304,00	-70,00	

Fig. 3 Data from the World center in Kyoto, Japan

The criterion of Pearson, Kendall, Fechner, etc., is used as criteria for the correlation analysis. One of the key limitations when using this or that correlation coefficient is the need for the set of values of all factorial and effective indicators to obey the multivariate normal distribution.

In this paper, the correlation coefficients of Spearman and Kendall were considered. It was found that the correlation for both Spearman and Kendall is observed on 06/16/2010 in the time period from 02:00 to 02:50, and on 06/17/2010 in the time period from 14:00 to 14:50. The values of the correlation coefficients are given in Table 2.

Table 2 Correlation ratios

16.06.2010, 02:00 to 02:50		17.06.2010, 14:00 to 14:50	
Spearman’s correlation coefficient	Confidence probability	Spearman’s correlation coefficient	Confidence probability
-0.383	$P = 0.994$	-0.387	$P = 0.994$
16.06.2010, 02:00 to 02:50		17.06.2010, 14:00 to 14:50	
Kendall’s correlation coefficient	Confidence probability	Kendall’s correlation coefficient	Confidence probability
-0,252	$P = 0.990$	-0.267	$P = 0.993$

When designing renewable energy for the Arctic zone, it is necessary to take into account all the main factors leading to malfunctions at the electricity facilities at present. To do this, an analysis of accidents at thermal power plants for 2019—on the one hand, and analysis of accidents at wind farms between 1980 and 2013—on the other hand was carried out.

The choice of thermal power plants as a facility for analysis is conditioned by the fact that the share of thermal power plants in 2019 accounted for about 70% of all electricity generated in the Russian Federation. Because of this analysis, it was found that all accidents could be divided between three groups of factors [20]. These groups included:

- Errors of service personnel;
- Defects in the electrical part;
- Defects in the mechanical part.

Table 3 shows faults identified during the analysis of accidents at thermal power plants.

During the analysis of accidents at wind farms, it was found that all accidents can be divided into the following categories [21]:

- The accidents that occurred due to non-compliance with safety regulations when servicing the wind generator;
- The accidents related to natural phenomena. Such accidents can be caused by natural disasters:
 - Lightning
 - Typhoons
 - Hurricanes
 - Icing
 - Erosion, etc.
- The accidents caused by poor control and installation at the production site.

Table 3 Malfunctions in the operation of thermal power plants

Mistakes of service personnel	Defects in the electrical part	Defects in the mechanical part
Wrong connection of stator winding turns (the winding is connected not by a star, but by a triangle)	The voltage on the engine clamps is below par, so the engine is overloaded with electric power at nominal power	Rotor defects (sudden change in the vibration of the turbo generator bearing supports due to the break of the blade of the feather)
The contacts of the same phase are incorrectly connected; one or more coils "inverted"	A break in one phase of the network or an internal precipice in the winding of the stator	Break of the stud of the horizontal connector of the medium-pressure cylinder case
The mechanical imbalance of the turbine after the replacement of the blades and defect in the assembly of the clutch (the cause belongs to two groups)	Short circuit in the winding of the stator	The mechanical imbalance of the turbine after the replacement of the blades and defect in the assembly of the clutch (the cause belongs to two groups)

Thus, the extensive study and measurement of GIT parameters is one of the promising and key areas of metrological support for the functioning of objects in the Arctic and the Far North.

5 The Implementation of a Measuring Complex for Heavy Engineering Objects in the Far North

Consider in more detail all levels of implementation of such a system. The main elements of building such a system should be:

- A unified approach and concept within the industry sector and typical design solutions (thermal power, hydropower, railway transport, aviation, metallurgy, oil and gas production, etc.);
- Implementation of the measuring (instrumental part of the system), providing the required level of accuracy, depending on the object under study and the processes in it;
- Implementation of an integrated approach to information metrological support of facilities at the level of one production link (section-shop-plant, hydraulic unit-machine room-station, etc.) with the transfer of information to analytical decision-making centers;
- Implementation of the unified centralized system for monitoring and diagnostics of support for mechanical engineering facilities in the digital economy.

According to the results obtained, a common factor leading to malfunctions, both at the facilities of the traditional electric power industry and renewable energy sources, is

personnel errors that occur during the maintenance of power plants. For the conditions of the Arctic zone—this factor is especially important, due to the minimum maintenance by personnel.

Figure 4 shows an example of the implementation of the measuring complex of heavy engineering facilities in the Far North.

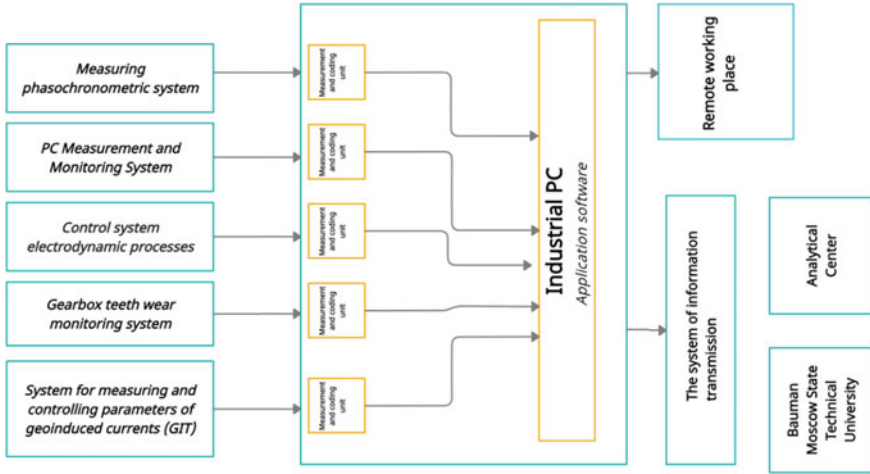


Fig. 4 Scheme of a measuring complex for heavy engineering facilities in the Far North

The measuring complex contains a measuring phase-chronometric system, a system for measuring and monitoring a rolling bearing, a system for monitoring electrodynamic processes, a system for monitoring the wear of gear teeth, and a system for measuring and monitoring parameters of geinduced currents (GIC). Figure 5 shows a dynamic diagram of the measured characteristics of a wind generator using the systems included in the measuring complex.

Important components are the implementation of the transmission of measurement information to both a remote workplace at the station, the scientific processing center (Bauman Moscow State Technical University) and the analytical decision-making center [22, 23].

6 Conclusion

During designing new renewable energy for the Arctic zone, it is necessary to take into account the features of this zone. The main features of the Arctic zone include severe climate and geomagnetic disturbances. After analyzing the accidents and their causes at traditional power plants and wind farms, it was found that there was no official cause of geomagnetic storms or their private manifestation—GIT.

According to the results obtained, a common factor leading to malfunctions, both at the facilities of the traditional electric power industry and renewable energy sources, are personnel errors that occur during the maintenance of power plants. For the conditions

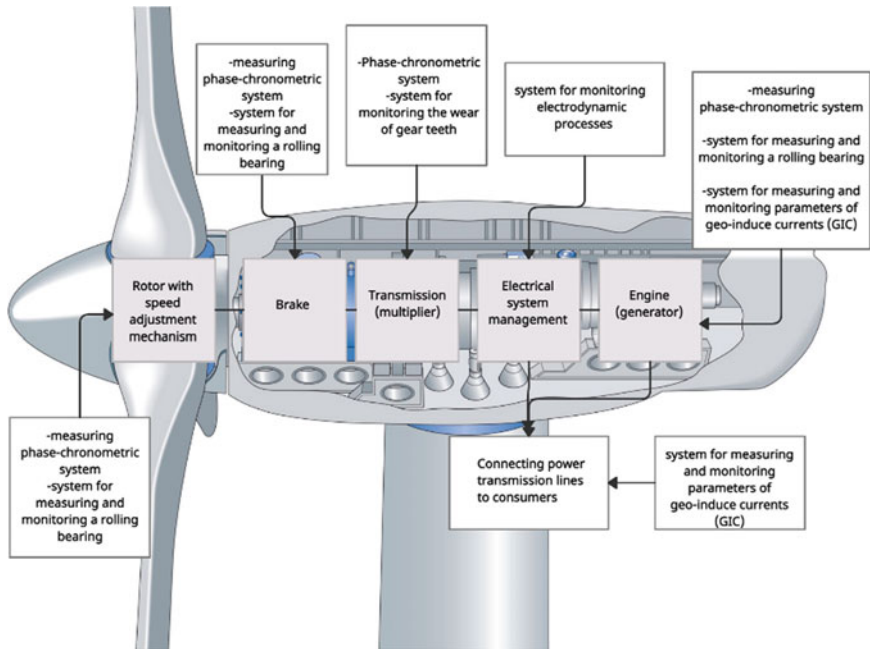


Fig. 5 Dynamic scheme of measured characteristics of the wind generator

of the Arctic zone—this factor is especially important, due to the minimum maintenance by personnel.

Acknowledgements. This work was supported by a grant from the President of the Russian Federation for state support of young Russian scientists, doctors of sciences MD-1209.2020.8. Separate results supported in the framework of the state task №0705-2020-0046 in the field of scientific activity.

References

1. State Program of the Russian Federation “Energy Development” (2020). <https://minenergo.gov.ru>. Accessed 13 September 2020
2. <https://gwec.net/gwec-over-60gw-of-wind-energy-capacity-installed-in-2019-the-second-biggest-year-in-history/>. Accessed 01 February 2021
3. Burtsev SA, Komshin AS (2019) Challenges in development of wind energy in Russia. In: 2019 International conference on industrial engineering, applications and manufacturing (ICIEAM), pp 1–5
4. Kiselev MI, Pronyakin VI, Tulekbaeva AK (2018) Technical diagnostics functioning machines and mechanisms. IOP Conf. Ser.: Mater. Sci. Eng. 312(1):012012
5. Boldasov DD, Komshin AS, Syritskii AB (2020) Method of lathe tool condition monitoring based on the phasechronometric approach. In: Radionov A, Karandaev A (eds) Advances in automation. RusAutoCon 2019. Lecture Notes in Electrical Engineering, vol 641

6. Minaev V, Starozuk Y, Stepanov R, Faddeev A (2020) Oil-and-gas-bearing territories in the arctic: new models for finding and clarifying boundaries. *IOP Conf. Ser.: Earth Environ Sci* 539(1):012147
7. Lazutin L (2012) Influence of magnetic storms on the technosphere and the effect of displacement of the north magnetic pole. <https://trv-science.ru/2012/07/17/vozdejjstvie-magnitnykh-bur-na-tekhnosferu-i-ehffekt-smeshheniya-severnogo-magnitnogo-polyusa/>
8. Romash ME, Varaksin AY, Protasov MV (2021) A new passive-active method of protection from dynamic vortex atmospheric structures: physical foundations, technical and economic advantages. *Int J Eng Res Technol* 13(12):4134–4138
9. Pirjola R, Viljanen A, Pulkkinen A et al (2004) Space weather effects on electric power transmission grids and pipelines. *Amm. Geo Forschungs Zentrum Potsdam. D-14473, Germany. Effect of space weather on technology infrastructure*, pp 235–256
10. Tumakova EV (2020) Development of a system for monitoring the state of Electromechanical objects taking into account the influence of magnetic storms. *IOP Conf Ser: Mater Sci Eng* 747(1):012133. <https://doi.org/10.1088/1757-899X/747/1/012133>
11. Potapov KG, Tumakova EV, Ummanova OV (2020) The computational models of measurement parameters for electromechanical energy systems with the application of neurodiagnostics. *IOP Conf Ser: Mater Sci Eng* 971. <https://doi.org/10.1088/1757-899X/971/4/042038>
12. Avakyan SV, Voronin NA (2011) The role of space factors in energy and environmental safety. *Academy of Energy* 6(44):28–35
13. Kuznetsov VA (2014) Detection of geinduced currents and their monitoring in power supply systems. Dissertation, Vitaly Kuznetsov, Tolyatti, p 148
14. Pulkkinen A, Pirjola R, Viljanen (2008) *A Space Weather* 6
15. Vorobyev AV, Pilipenko VA, Sakharov YA, Selivanov VN (2019) Statistical relationships of variations of the geomagnetic field, auroral electrojet, and geinduced currents 5(1):48–58
16. Komshin AS, Potapov KG, Syrisky AB, Fomin AE (2020) Monitoring system of hydro and wind power equipment based on intelligent measuring complexes and Neurodiagnostics. *IOP Conf Ser: Mater Sci Eng* 971:022055. <https://doi.org/10.1088/1757-899X/971/2/022055>
17. Anishchanka YV, Loktionov EY, Telekh VD (2018) Investigation of minimum laser ignition energies of combustible gas mixtures. *J Phys: Conf Ser* 1115(4):042020
18. <http://wdc.kugi.kyoto-u.ac.jp/aedir>. Accessed January 28 2011
19. Gavrilov BG, Ryakhovsky IA, Markovich IE, Lyakhov AN, Egorov DV (2016) On the applicability of planetary and station indices of geomagnetic activity. *Heliogeophys Res* 15:42–48
20. Buzoverov EA, Varaksin AY, Denshchikov KK (2019) Ensuring the quality of power supply to industrial enterprises using universal power converters. *Int J Eng Res Technol* 12(12):2683–2686
21. Wind Turbine Accident Compilation (2020) <https://fliphtml5.com/dqsm/kcam/basic>. Accessed 25 Oct 2020
22. Komshin AS, Medvedeva OV (2014) Measurement control of the degradation of the properties of the structural materials of shaft lines. *Meas Tech* 57:526–532. <https://doi.org/10.1007/s11018-014-0491-3/>
23. Kiselev MI, Komshin AS, Matveev VA (2017) The system of information and metrological support of the country's energy facilities based on satellite grouping. *Sci Intens Technol* 18(6):68–72



Dynamic Coupling Between Links of Articulated Transport Systems

E. Bazhenov¹, A. Zelenin¹, and D. Chernyshev²(✉)

¹ Ural State Agrarian University, 42, Karl Liebknecht Street, Ekaterinburg 620075, Russia

² Ural State Forest Engineering University, 37, Siberian Highway, Ekaterinburg 620100, Russia

Abstract. The issues of improving the operational properties of transport systems are considered. Various ways to improve productivity, economic and environmental performance, operational reliability, as well as improve and automate the transport system controls are shown. One of the most important issues in the theory of movement, i.e., the effective distribution of the power flow between the drive axles and sections is considered. The coupling between the transport system links is estimated. The coupling between the links of active articulated multi-section machines has been analyzed based on various variants of the kinematic misalignment in the drive. The state graph of a two-section active articulated transport and production machine is considered. The coupling between the links of the articulated transport system is considered and formalized for the pole trailer supported simultaneously by two or more machine sections. The areas of further link coupling analysis based on the state graph of a two-section active articulated transport system are determined.

Keywords: Articulated systems · Transport systems · Kinematic misalignment · Coupling of links · Energy section · Articulated link · Operational properties · State graph

1 Introduction

The emergence of new, more powerful multi-operational machines allows mechanizing most of the work in forestry, agriculture, oil and gas and mining, and other sectors of the national economy. The all-wheel-drive transport systems based on the active trailer train and articulated transport and production machines are among the promising ways to solve many problems of operating the transport and production complexes on snow or dirt roads during the mud period and in other specific conditions.

The concept of an articulated transport system (ATS) is very broad and comprises a range of machines with at least two sections coupled by an articulated link with one or more degrees of freedom. Also, some ATs have a specific steering design. As a special but rather widespread case of an ATS, road trains with active trailers (RTAT) should be considered. If the thrusters of not only the power link (tractor—TT) but also the trailed ones (trailers—TL) are driven, then such an ATS is an active articulated transport system (AATS).

The use of AATSS in mining and other raw material economy branches and the defense complex allows building a wide range of production and transport systems [1, 2].

Thus, improving the operational properties of transport systems are among the main mechanical engineering problems, which should be solved in various ways: improving productivity, economic and environmental performance, operational reliability, as well as improving and automating the transport system controls and a whole range of other theoretical and experimental studies.

The solution of one of the most important issues in the ATS movement theory—the effective distribution of the power flow between the drive axles and sections implies estimating the coupling between the transport system links.

2 Experimental Results

In general, the adhesion and resistance condition of the transport system movement (with a deterministic approach) is expressed by the inequality:

$$P_{\psi} \leq P_{\kappa} \leq P_{\varphi} \tag{1}$$

Non-satisfaction of the left-hand inequality part is a full loss of passage.

Non-satisfaction of the right-hand inequality part is a partial loss of passage (see Fig. 1).

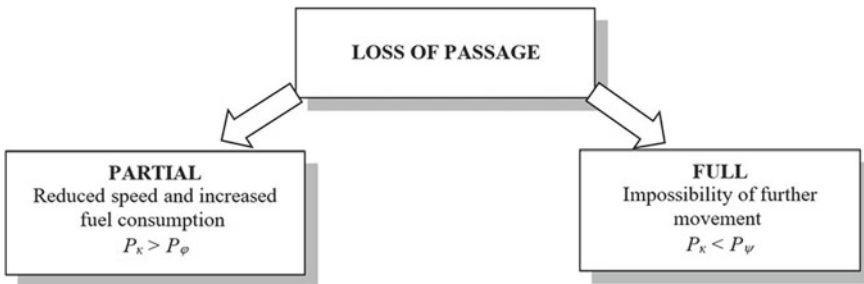


Fig. 1 Loss of passage

The articulated transport system specificity is determined, in particular, by the variety of road conditions in which it performs its functions. As a result, depending on the operating modes, there are different variants of the transport system link coupling and the loss of passage [3, 4].

Various states of the articulated transport system movement and loss of passage can be analyzed based on a directed graph [5, 6]. The graph peaks characterize the articulated transport system state at a given time instant, and the edges describe the transition between states, depending on the movement mode. A directed state graph of an articulated transport system with an active first section and a passive trailer (e.g., a road train consisting of a tractor and a passive trailer) is shown (see Fig. 2).

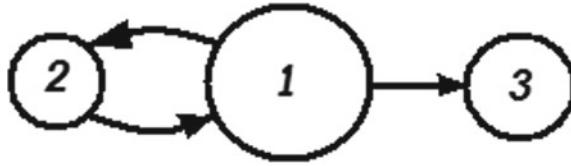


Fig. 2 State graph of an ATS with passive trailed section

In this, Fig. 1 is the articulated transport system state characterized by movement due to the tractive effort of the first section (tractor). In this case, the adhesion and resistance conditions are met. 2 is the state of a partial loss of passage (non-fulfillment of the right-hand part of inequality (1)). The transport system can exit this state in various ways (antiskid chains, reduction of air pressure in tires, etc.). 3 indicates the overtaking transport system state. In this case, the left-hand part of inequality (1) is not fulfilled, and the transport system can leave this state only with the help of an additional external energy source.

Figure 3 shows a directed state graph of a two-section AATS.

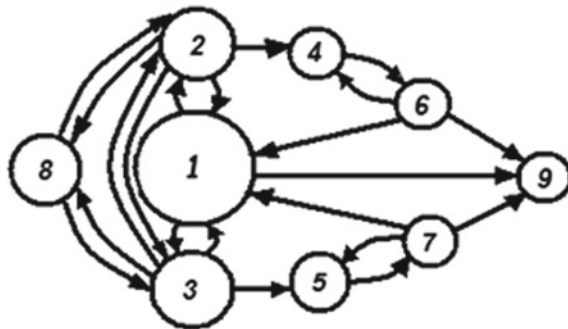


Fig. 3 State graph of a two-section AATS: 1—the state when the AATS moves due to the traction forces of the first and second sections (inequality (1) is fulfilled); 2—the AATS is moved by the second section wheels. The first section wheels slip (depending on the kinematic misalignment sign, this is sliding or skidding); 3—the AATS is moved by the first section wheels; wheels of the second section slip; 4—loss of passage: the first section wheels skid, and the traction force of the second section is not enough for movement. From this state, the AATS cannot independently return to state 2; 5—loss of passage: the traction force of the first section is not enough to move the AATS; the second section wheels skid. The AATS can independently return from state 5 to state 3; 6—the AATS is moved by the first section wheels; the second section wheels do not create a traction force (or it is not enough to overcome the AATS movement resistance force); 7—the AATS is moved by the second section wheels; the tangential traction force of the first section wheels is less than its total movement resistance force. The movement is possible only if the second section traction force exceeds the AATS movement resistance force; 8—loss of passage due to slipping first and second section wheels; 9—loss of passage: insufficient traction force of the first and second section wheels. This is an overtaking state. Independent exit from this state is impossible

The AATS state graph allows formalizing various movement modes when the kinematic misalignment between sections, road conditions, etc., change. The state graph will further be used to analyze the coupling between the AATS sections in different movement modes.

The active trailed AATS section inevitably causes cyclic coupling in the articulation assembly when driving in various road conditions, and for the pole trailer transport system when the load rests simultaneously on the first and second section supporting devices, through these supporting devices.

2.1 Coupling of the Passive AATS Links at the Straight-Line Movement

To move a passive trailer (TL), the tractor (TT) should apply a force, the value of which should not be less than the sum of all the movement resistance forces. The force applied to the trailer, i.e., the link coupling force, should not exceed the force of the load package friction against the tractor’s supporting device (see Fig. 4).

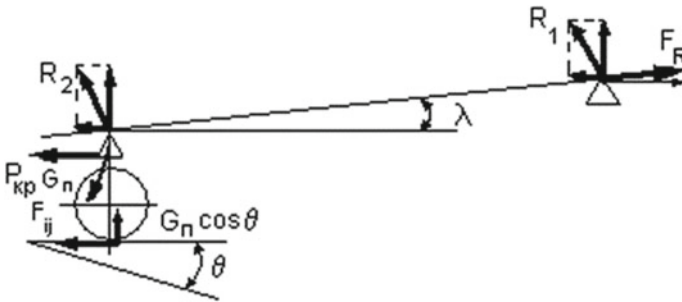


Fig. 4 Forces acting on a passive ATS trailer

According to Fig. 4, the coupling force:

$$F_R = \frac{\sum_{i=4}^5 \sum_{j=1}^2 F_{ij} + (R_1 + R_2) \sin \lambda + G_{\Pi} \cdot \sin \theta}{\cos \lambda}. \tag{2}$$

For the TL and the TT, the F_R force will be positive and negative, respectively.

2.2 Coupling of the AATS Links at the Uniform Straight-Line Movement

When the active TL moves (Fig. 5), the force of its action on the TT is determined as follows:

$$F_R = \frac{\sum_{i=4}^5 \sum_{j=1}^2 \operatorname{sgn} \dot{\psi}_{ij} F_{ij} - (R_1 + R_2) \sin \lambda - G_{\Pi} \cdot \sin \theta - P_{kp}}{\cos \lambda}, \tag{3}$$

where the $\operatorname{sgn} \dot{\psi}_{ij}$ function means that not all the active TL wheels may be driven; therefore, the force sign will depend on whether the TL axis is active or not.

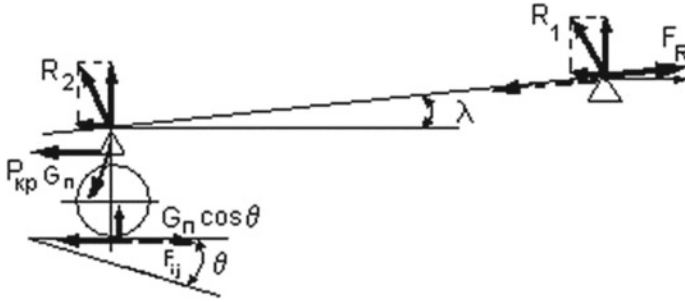


Fig. 5 Forces acting on the active AATS trailer

In this case, the force of the load package friction against the bolsters also serves as a limitation:

$$F_R \leq R_1 \cdot \nu. \tag{4}$$

These considerations are valid for negative closed-loop misalignment when the adhesion passage condition is met, i.e., when the resulting tangential reaction does not exceed the maximum possible traction creepage in the given road conditions.

Otherwise, the coupling will be reduced to the passive trailer case. In this case, the $\sum_{i=4}^5 \sum_{j=1}^2 \text{sgn} \dot{\psi}_{ij} F_{ij}$ force will be defined as the slip resistance force (the slide resistance force for a positive misalignment and the skid resistance force for a negative misalignment).

The total passive road train traction force is defined as the total tangential traction force of the TT wheels and the total TT movement resistance force minus the RTAT link coupling force:

$$F_T = \sum_{i=1}^3 \sum_{j=1}^2 \text{sgn} \dot{\psi}_{ij} F_{ij} - G_T \cdot \sin \theta - F_R \cdot \cos \lambda. \tag{5}$$

For a positive misalignment, the total RTAT traction force will be the sum of the total TT traction force and the TL pushing force, considering the resistance to movement from the slope:

$$F_T = \sum_{i=1}^3 \sum_{j=1}^2 \text{sgn} \dot{\psi}_{ij} F_{ij} - G_T \cdot \sin \theta + F_R \cdot \cos \lambda. \tag{6}$$

For different misalignment variants and the TT and TL wheel adhesion coefficients, the sign of the link coupling force F_R will change, and when determining these forces, the slip (slide or skid) resistance force will be considered.

To solve the systems of equations for the AATS-RTAT movement, the limiting movement parameter values should be used in the link coupling force equations. For a passive trailer, the maximum force that can be applied to the TL is determined by the dynamic

TT parameters and its coupling capabilities:

$$F_T = \sum_{i=1}^3 \sum_{j=1}^2 \operatorname{sgn} \dot{\psi}_{ij} F_{ij} = \frac{M_{\Delta T} \cdot c_{ij}}{r_{ij}} \leq G_{\text{CHT}} \cdot \varphi_T. \quad (7)$$

Instead of the force F_R , the total value of the resultant elementary tangential reactions of the ij th TT wheel is used in the system of equations for the TL movement.

For the AATS, when substituting values (Eq. 6) into the TL movement system of equations, the misalignment magnitude and the movement mode should be considered, which will affect the F_R force sign.

The movement of the AATS without differential (locked) TL wheel drive is accompanied by an elastic moment emerging in the ‘transmission—drive TT wheels—drive TL wheels—support surface’ closed loop, which depends on the difference in the twist angles of the end loop elements (kinematic misalignment).

The kinematic misalignment magnitude is estimated by a dimensionless coefficient, defined as the ratio of the difference between the peripheral TT and TL wheel speeds for a certain period and the peripheral TT wheel speed:

$$\xi = \left(1 - \frac{V_{\omega 2}}{V_{\omega 1}} \right) 100 \quad (8)$$

where ξ is the kinematic misalignment coefficient, $V_{\omega 2}$ is the peripheral TL wheel speed, $V_{\omega 1}$ is the peripheral TT wheel speed.

In the analysis, we will consider only the interaxle and intersectional misalignment since the interwheel differential excludes the possibility of forming a closed loop if neglect the effect of friction in the differential. The total misalignment will be the sum of the individual group misalignments.

2.3 Constructive Kinematic Misalignment

The constructive kinematic misalignment between the TT and the TL is caused by:

- the difference between the rolling radii within the tire manufacture tolerance (for the same TT and TL tires),
- change in tire pressure,
- mass distribution over the AATS links,
- dynamic vertical loads.

In some cases, the misalignment varies within 1–7% and may reach 12% in total.

For the RTAT, misalignment may reach 7% due to the different TT and TL tire types. The change in tire pressure is 1–1.5%. The difference in the mass distribution over the links is up to 1.5%. The total misalignment may reach 14–15%.

Kinematic Misalignment Due to Curvilinear Movement.

Three modes of the curvilinear AATS movement are possible:

- input transition trajectory,

- circular trajectory,
- output transition trajectory.

In each of these cases, there are different ratios of the TT and TL turning radii and, therefore, different kinematic misalignments.

2.4 Kinematic Misalignment Due to the Coarse Track Irregularities

Kinematic misalignment due to vertical coarse irregularities arises from different paths of the AATS links when one link moves up or down, while the second one continues moving along the horizontal track section.

For practical calculations, it is advisable to use the following equation:

$$\xi = \left(1 - \frac{1}{\cos \theta} \right), \tag{9}$$

where θ is the track ascent or descent angle.

When expressing the kinematic parameters of one AATS link through another (e.g., the shaft rotation frequency or the TL wheel turning angle through the TT wheel rotation frequency) using the coefficient ξ and substituting the dependences obtained into the system of equations for the AATS movement, the effect of the kinematic misalignment between the TT and the TL on the dynamic AATS movement parameters can be studied or the effective misalignment determined by the criterion of the maximum AATS hook traction force, which, taken together, characterize the traction capabilities of the transport system.

Depending on the road conditions in which the AATS moves and the kinematic misalignment, the positive and negative slip of the TT and TL wheels may occur. In this case, the sliding wheels will resist the AATS movement. The movement resistance coefficient will be determined without considering the horizontal gravity component as follows [7, 8]:

- (1) at a positive slip of the driving wheels (skidding):

$$\delta > 0, f_k = f_0 \cdot \left(\frac{r_{k0}}{r_{k \min}} \right)^2 + \varphi \left(\frac{r_{k0}}{r_{k \min}} - 1 \right) \tag{10}$$

where f_0 —is the rolling resistance coefficient of the wheels in the absence of slipping, r_{k0} is the wheel rolling radius, m , $r_{k \min}$ is the wheel rolling radius when skidding, m .

$$r_{k \min} \cong r_{k0} \left(1 - \lambda_k \cdot \varphi \cdot 10^{-3} \right), \tag{11}$$

where λ_k —is the tangential tire elasticity, m/Nm, φ —is the wheel adhesion coefficient.

(2) at a negative slip (sliding):

$$c_{\max} = \varphi \left(r_D - r_{k0} + G_k \cdot \varphi \cdot \lambda_k \cdot 10^{-3} \right). \quad (12)$$

The tangential elasticity of the driving wheels causes a change in the dynamic radius of the wheel, depending on the torque applied [9, 10]:

$$r_D = r_{k0} - \lambda_k \cdot M_k. \quad (13)$$

Thus, the dynamic radius of the driving wheels will change depending on the gear ratio in the AATS transmission.

3 Conclusion

Different road conditions in which the AATS has to work affect its movement nature, and as a result, the AATS link coupling may vary. Various link coupling cases have been analyzed and represented in the form of a directed AATS state graph shown in Figs. 1 and 2. Using the state graph built, each of the possible AATS movement cases has been formalized, i.e., a different combination of road conditions, misalignments, etc. As a result, the graph becomes directed and marked out. This allows simulating all the possible AATS link coupling variants and determining both the dynamic AATS performance and the strength characteristics of the articulator elements at the design stage.

References

1. Bazhenov EE, Vyukhin AV (2010) Possibility of application of articulated transport systems in the extractive industries. Truck, Moscow, pp 18–21
2. Bazhenov EE, Chernyshev DO, Bazhenova LV (2019) Use of articulated transport systems in the mining industry. In: IOP conference series: materials science and engineering, UK, p 1–5
3. YaS A, Vol'skaya NS (2008) Theory of automobiles: a tutorial. MGIU, Moscow, p 318
4. Platonov VF (1989) All-wheel drive cars. In: Mechanical engineering. Moscow, p 312
5. Bazhenov EE (2009) Articulated transport and technological systems: monograph. USTU–UPI, Ekaterinburg, p 174
6. Setinc M, Gradisar M, Tomat L (2015) Optimization of a highway project planning using a modified genetic algorithm. UK, pp 687–707
7. Veits VL (1969) Dynamics of engine aggregates with internal combustion engines. In: Mechanical engineering. Leningrad, p 370
8. Tarasik VP (1998) Mathematical modeling of technical systems. Design-Pro, Moscow, pp 204–640
9. Chelomey VN (1980) Vibration in engineering: a handbook. In: Mechanical engineering. Moscow, p 544
10. Dhir A, Sankar S (1997) Analytical model for dynamic simulation of off-road Tracked Vehicles. Veh Syst Dyn 27:37–63



Comparative Evaluation of the Compressor-Ejector Unit's Designs for Gas Evacuation During Repair of the Main Gas Pipeline

A. R. Buranshin^(✉), D. A. Godovskiy, and A. P. Tokarev

Ufa State Petroleum Technological University, 8/3, Cosmonauts, Ufa 450062, Russia

Abstract. In the process of main gas transportation, repair work is periodically necessary. In some cases, it includes a long length section's isolation and emptying the internal space of the pipeline. According to established practice, in order to reduce the total duration of repair work, gas from the isolated section is blew out to the atmosphere. This leads to losses of significant volumes of natural gas. In order to save resources, ejectors can be used to pump gas into a parallel gas pipeline. They provide deeper vacuum. Due to the pressure decrease in the isolated section, it is necessary to provide a high efficiency of the pumping unit. A comparison of versions with the gas blowing to the vent stack and evacuation to a parallel gas pipeline by various designs of the compressor-ejector unit is proposed (standalone ejector, ejector with different compressor positions). The unit operating parameters are determined using Schlumberger OLGA. A graph of the change in time of the evacuated volume of gas, reduced to standard conditions, and the pressure for various parameters of the compressor and its location relative to the ejector is plotted.

Keywords: Ejector · Compressor · Natural gas · Gas pipeline · Energy saving · Computer modeling

1 Introduction

The world's largest gas transmission system (GTS) is operated by PJSC Gazprom. It includes the Unified Gas Supply System (UGSS) of Russia. Due to the large scale of the system, the issues of reliability, energy saving and energy efficiency of individual elements have high practical importance. A small, at first glance, cost reduction is able to lead to a visible energy-saving effect.

The maximum realization of the available energy saving potential is necessary due to the high costs of transporting gas over long distances [1].

The most efficient ways in terms of saving natural gas in fraction of the total amount of savings under the executing Energy Saving Program of PJSC Gazprom [2, 3] in gas transportation are:

- reduction of costs during repairs and routine maintenance at compressor stations (CS), linear part (LP) and gas distribution stations (GDS)—38.6%;
- gas compressor unit's repairs to improve their technical condition—17.0%;
- equipment modernization or replacement at CS, LP and GDS—16.4%;
- improving quality of dispatch control to provide rational modes of main gas transportation using calculation and optimization complexes—13.6%;
- realization of resource-saving procedures during repairs and elimination of gas leaks at CS, LP and GDS—11.7%.

Let's consider in detail the first direction according to the greatest potential in terms of saving natural gas [4, 5].

Repair work is periodically performed on the main gas pipeline's linear sections to prevent accidents and maintain high efficiency.

According to the established practice of operation hot and gas hazardous works on gas transmission systems, in order to reduce the total duration of work, gas is blew out to the atmosphere from the pipeline's repaired section with a full emission loss [6, 7].

The yearly average number of repairs is in the range from 12 to 15 for every 1000 km of the gas pipeline route [8, 9]. Nodes with linear valves and crossovers between the gas pipelines (for a multiline gas pipeline) are located every 25–30 km of the gas pipeline route. The average amount of gas emitted during only one repair, depending on the size of the pipeline section being repaired and the gas pressure in it, can reach 3–4 million m³ [10].

With the duration increase of main gas pipeline's operation, the need for repairs and gas losses to the atmosphere due to emissions are going to increase. In addition to the natural gas losses during emission, the gas transmission company pays for the emissions of pollutants, the IV hazard class of which includes methane.

2 Urgency of the Problem

With the aging of the operated main gas pipelines and the need to maintain the energy efficiency of gas transportation, the problem of reducing natural gas emissions into the atmosphere is urgent.

To reduce natural gas emissions into the atmosphere during main gas pipeline's repair, it is required to evacuate out, collect and then utilize gas.

The gas evacuating process must meet certain requirements:

1. short duration—due to an increase in the cost of transporting gas in the technological corridor when the repaired section is isolated [11] (for a pipeline with a diameter of 1420 mm, a length of 30 km with an initial pressure of 7.5 MPa and a final pressure of 1.0 MPa, the evacuating time should be no more than 100 h);
2. high mobility of equipment—due to field conditions (transportation and deployment at LP).

For these purposes, some schemes have been proposed for both single-line and multi-line gas pipelines. (Fig. 1). One of the main elements in these schemes is the jet pump—ejector [12–17].

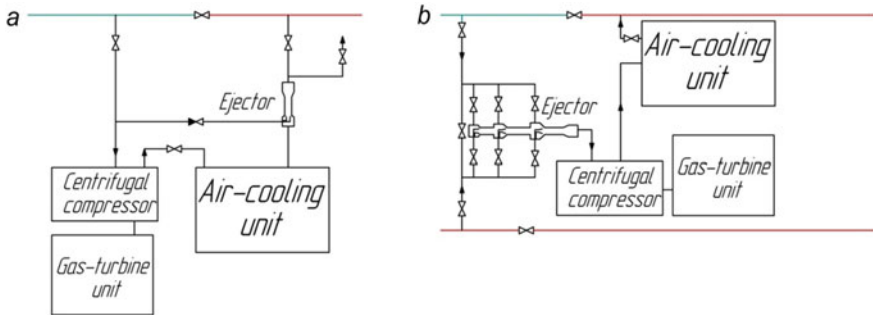


Fig. 1 Schematic diagrams of gas utilization during the repair of a section of a single-line (a) and multi-line gas pipelines (b)

In the scheme for a single-line gas pipeline, the source of both active and passive gas is an isolated section of the gas pipeline. Gas pressure will drop on the suction line of the ejector and centrifugal compressor. As a result, it will be necessary at the final stage of evacuating to use several compression stages of centrifugal compressor. Cases of repairs a section of a main gas pipeline lying in the same technological corridor with one or more gas pipelines are more common. In gas evacuating schemes, the source of the active gas is the nearby gas pipeline, the pressure in which remains at the same level.

Due to the gas pressure decrease in the cut-off section [18–20], it is necessary to compare the evacuating efficiency of the including an ejector unit's various configurations.

The calculation of gas evacuating from the pipeline section was performed in the Schlumberger OLGA software package with obtaining flow parameters in the technological corridor.

3 Problem Formulation

A technological corridor of two main gas pipelines between two compressor stations is being considered. The length of each gas pipeline is 125 km. The gas source is the section of the gas pipeline in front of the isolated section. The length of the disconnected section is 25 km. The disconnection of the section from 75 to 100 km of the route is simulated for repair work.

The main evacuating schemes under consideration (Fig. 2):

- design 1—blowing to the atmosphere with one vent stack;
- design 2—evacuating by standalone ejector;
- design 3—evacuating by ejector and compressor on the high-pressure gas line;
- design 4—evacuating by ejector and compressor on the low-pressure gas line;
- design 5—evacuating by ejector and compressor on the mix gas line.

The key evacuating parameters are the change in the evacuated gas volume and the pressure in the isolated section over time. To simplify calculations, we will accept the following initial data:

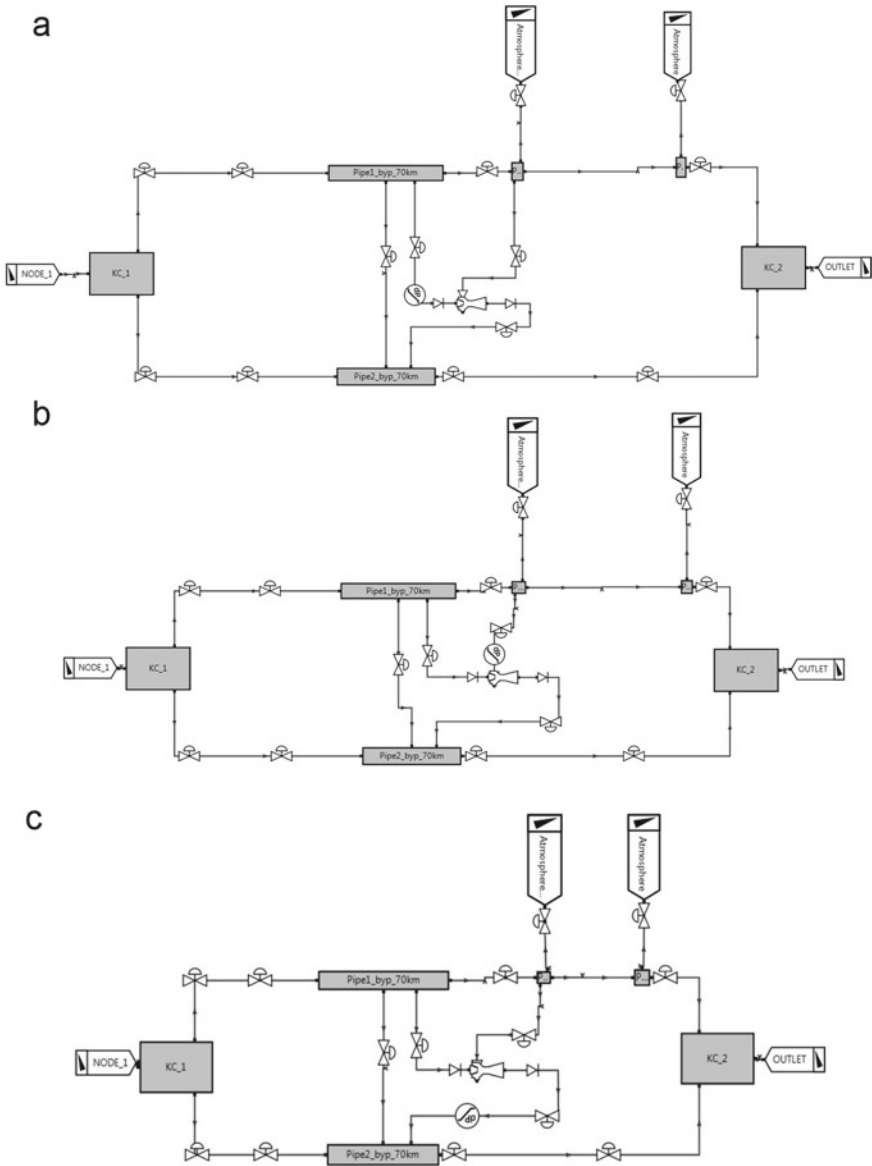


Fig. 2 Model circuits in OLGA with a compressor in the high-pressure (a), low-pressure (b) and mixed (c) gas lines

- constant pressure is maintained at the compressor station ($P_H = 7.5$ MPa, $P_K = 5.1$ MPa);
- temperature at the outlet of the first CS—25 °C;
- temperature at the inlet of the second CS—8 °C;
- ejector nozzle diameter—30 mm;

- ejector mixing chamber diameter—40 mm;
- inner diameter of the pipeline—1400 mm;
- the relief influence is not considered—the pipelines are horizontal;
- fluid—methane;
- the ejector is considered as ideal—zero friction pressure losses along the ejector elements (nozzle, suction chamber, mixing chamber, diffuser);
- the compressor in the unit increases the gas pressure by a fixed value (0.5 и 1.2 MPa).

4 Computer Simulation's Results

Based on the results of the simulated model's calculations in OLGA with changed parameters, graphs were built (flow rates under standard conditions and pressure and over time) (Figs. 3, 4 and 5) and a summary table was drawn up (Table 1).

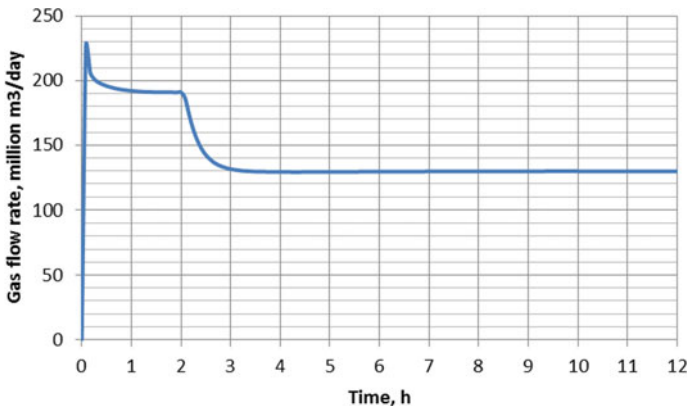


Fig. 3 Gas flow rate change in the technological corridor when one section is isolated

As a result of the one section isolation in the technological corridor of the main gas pipeline between the two compressor stations, gas flow rate at standard conditions decreases from 190 million m³/day to 130 million m³/day. Initial fluctuations of parameters in the calculation are associated with the deviation of the initial conditions from the stabilized regime.

Estimated gas volume in the isolated section when converted to standard conditions—2.4 million m³. The geometric volume of the isolated area is about 38000 m³.

Analysis of the obtained results confirms that the fastest option is to blow gas through the vent stack to the atmosphere. It is also noticeable that the most prolonged options are evacuating out by standalone ejector and ejector with a compressor on the high-pressure gas line.

When the pressure is increased by 0.5 MPa, the unit with compressor on the mixed gas line will pump out 0.75 million m³ more quickly, but if the pressure is increased by a compressor by 1.2 MPa, evacuating out by unit with a compressor on the low-pressure gas line will be faster.

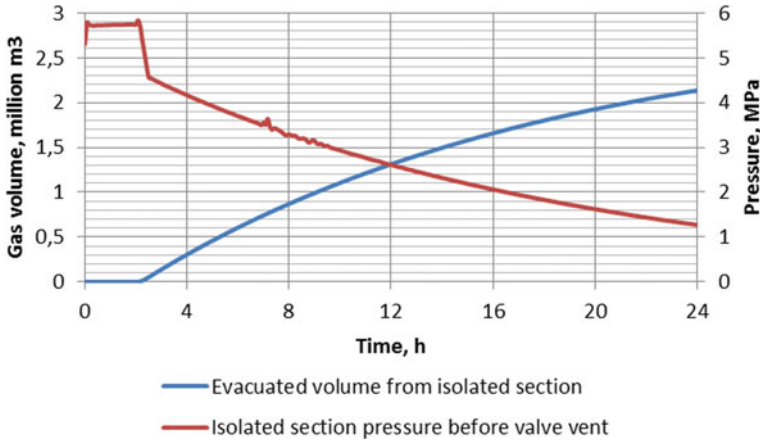


Fig. 4 Pressure change in front of the vent stack and gas volume according to design 1

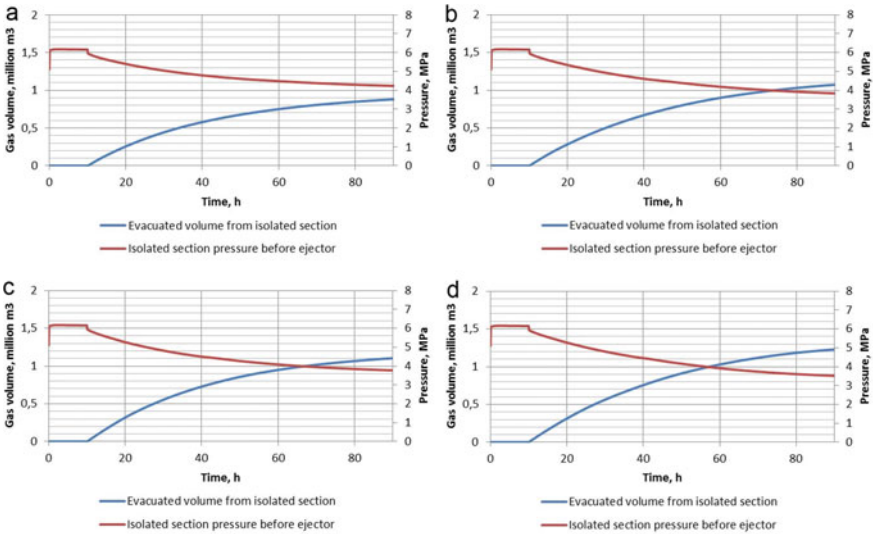


Fig. 5 Pressure change in front of the ejector and gas volume by $dP_{compressor} = 0.5$ MPa and various designs. **a** design 2. **b** design 3. **c** design 4. **d** design 5

5 Conclusions

Units used for process gas evacuating in order to save resources should provide, other things being equal, the shortest preparation time for a repair work pipeline section.

Comparison, based on the results of computer simulation in OLGA, of gas evacuation unit's various designs from an isolated section (blowing to atmosphere, standalone ejector, ejector with different compressor positions) showed that the second-longest duration

Table 1 Duration of evacuating a fixed volume from the isolated section by various designs

Design	Duration of evacuating 0.5 million m ³ , h	Duration of evacuating 0.75 million m ³ , h
blowing to the atmosphere with one vent stack	3.3	5.1
evacuating by standalone ejector	23.9	50.2
evacuating by ejector and compressor on the high-pressure gas line (dP _{compressor} = 0.5 MPa)	19.9	35.9
evacuating by ejector and compressor on the high-pressure gas line (dP _{compressor} = 1.2 MPa)	18.2	31.3
evacuating by ejector and compressor on the low-pressure gas line (dP _{compressor} = 0.5 MPa)	17.4	31.6
evacuating by ejector and compressor on the low-pressure gas line (dP _{compressor} = 1.2 MPa)	13.8	22.5
evacuating by ejector and compressor on the mix gas line (dP _{compressor} = 0.5 MPa)	17.2	29.7
evacuating by ejector and compressor on the mix gas line (dP _{compressor} = 1.2 MPa)	15.9	25.5

after blowing gas to the atmosphere will be evacuating by an ejector with a compressor on the low-pressure gas line in case increasing compressor pressure.

In the first approximation, in connection with the simplified representation of the compressor, the design with a compressor on the low-pressure gas line looks promising, despite the fact that the scheme with a compressor on the mixed gas line showed rather similar results. The rationale for this is the multiple increase in the gas flow rate through the compressor in the latter design and the expected increase in energy expenses for the compressor drive.

Further development of the comparison of units for evacuating process gas is associated with the refinement of the mobile compressor parameters according to each of the unit designs. The development and assessment of a complex process of evacuating

a certain gas volume with subsequent blowing to the atmosphere at the final stage are also promising to provide the preparing standard time for gas pipeline repair.

References

1. Russia's Energy Strategy 2035
2. GAZPROM PJSC. Program for power saving and improvement of Gazprom energy efficiency in 2018–2020
3. Gadelshina AR, Kitaev SV, Galikeev AR (2015) Current state and prospects for development of resource saving technologies Gazprom Public Company Territorija "NEFTEGAZ" Oil and Gas Territory 12:136–139
4. Khvorov GA (2017) Analysis of power saving potential realization in 2011–2016 for Gazprom PJSC gas mains Vesti Gazovoy Nauki. Moscow: Gazprom VNIIGAZ LLC, 2017, spec. iss.: Environmental protection, power saving and labor protection in oil-gas industry, pp 50–60
5. Aksyutin OE, Ishkov AG, Khvorov GA, Akopova GS (2017) Realization of the energy saving potential in the main gas transportation of PJSC Gazprom. Gas Ind S1(750):52–58
6. Maslovsky VV, Kaptsov II, Sokruto IV (2004) Fundamentals of technology for repairing gas equipment and pipeline systems. Higher school, Moscow, p 319
7. Sobolev AA, Sedunin VA (2016) Development of mobile compressor station Proceedings of the first scientific and technical conference of young scientists of the Ural Power Engineering Institute. Ural Federal University, Yekaterinburg, pp 103–106
8. Harris NA (2011) Resource-saving technologies of pump and compressor station equipment operation. Ufa State Petroleum Technological University, Ufa, p 255
9. Ostrovskaya AV 2017 Environmental safety of gas compressor stations. Part 2. The impact of the gas transport system on the environment. Ural University Publishing House, Yekaterinburg, p 151
10. STO Gazprom 3.3-2-024-2011. Procedure for rationing natural gas consumption for own technological needs and technological losses of gas main transport
11. Ivanov ES, Kitayev SV (2015) Resource saving technology of the main gas pipeline section shutdown for repair with gas generation by the compressor station for GPU and consumer via gas distribution plant Territorija "NEFTEGAZ" Oil and Gas Territory 6:40–46
12. Patent RU 2167343 C1 Method of pumping gas from a disconnected section of a gas pipeline
13. Patent RU 2108489 C1 Mobile unit for pumping gas from disconnected section of main gas pipeline (versions)
14. Patent RU 2386862 C1 Processing of gas from repaired section of gas pipeline
15. Patent RU 2576951 C2 Method for pumping gas from a disconnected section of a gas pipeline
16. Patent RU 2601912 C1 Device for pumping gas from a disconnected section of a multi-line gas pipeline
17. Patent RU 160555 U1 Main gas pipeline
18. Buranshin AR, Godovskiy DA, Tokarev AP (2019) Regulation of the operation of ejector systems under unsteady gas Pipage IOP conference series: earth and environmental science, vol 459, no 2, 14 April 2020. 2019 International science and technology conference on earth science, ISTC earth science 2019; Russky Island; Russian Federation; 10–12 December 2019. <https://doi.org/10.1088/1755-1315/459/2/022076>
19. Buranshin AP, Godovsky DA, Tokarev AP (2019) Ejector installations in resource-saving at the main gas transport Pipeline transport-2019. USPTU, Ufa, pp 389–390
20. Yumagulov RD, Godovsky DA (2018) Application of the ejector to pumping-out gas from the emptying gas pipeline Pipeline transport-2018. USPTU, Ufa, pp 424–425



The Algorithm of Calculation of the Four-Stroke Turbocharged Diesel Engine Cycle Using the Compressor Efficiency Map

A. Yu. Abalyaev^(✉), A. A. Gavrilov, and A. N. Gots

Vladimir State University Named After Alexander and Nikolai Stoletovs, 87, Gorkiy str,
Vladimir 600000, Russia
ice_aya@bk.ru

Annotation. The analysis of the intake manifold and the cylinder gas exchange of the four-stroke turbocharged diesel engine is carried out. It is necessary to account for influence of pressure pulsation and air flow rate through a compressor on the parameters of the four-stroke turbocharged engine. The compressor efficiency map is used for calculation of the engine cycle. A mathematical model, an algorithm and operating procedure are delivered. A two-stage heat release model of combustion process of atomized fuel is provided. It comprises kinetic combustion of vaporized fuel at the ignition delay and diffusion combustion of the main fuel delivery. The accuracy of the provided model is confirmed by the results of computational and experimental study of the four-stroke two-cylinder turbocharged diesel engine 2CHN10.5/12.

Keywords: Cylinder · Intake manifold · Diesel engine · Turbocharger · Compressor efficiency map

1 Introduction

Strict requirements to the power, economic and environmental parameters of internal combustion engines affect the design of new engines and the improvement of the present ones [1, 2]. The most useful improvement is supercharged cycle usage that enables to increase the engine efficiency significantly with minimal change of the engine design [3–5]. This might be achieved by the compressor and turbine of the turbocharger unit efficiency map and the reciprocating engine flow math [6].

The results of the study [7–9] demonstrate that the accuracy of the turbocharger and the reciprocating engine math is very responsive to pulsation of air flow rate G_k and boost pressure ratio π_k that influence the efficiency of the compressor η_k and the entire supercharged engine parameters by:

- the total volume of intercooler, the intake manifold and intake ports;
- the number of cylinders, that aggregate the intake manifold;
- valve timings, valve train and other valve parameters;

- the turbocharger operation;
- the engine operation, duty cycle, etc.

The intake manifold pressure (p_s) change mostly affects p_k and G_k pulsation. Pressure pulsation is determined by the intake flow into the cylinder. To reduce negative effect of pressure pulsation on the parameters of the supercharged engine, it is recommended to choose the intake manifold volume V_s which at least three times exceeds the cylinder displacement V_h . However, as mentioned in [10, 11], such recommendation is not universal.

The zero-dimensional numerical simulation of the diesel engine cycle has sufficient accuracy and versatility. A state change of gases in the combustion chamber, i.e., pressure, is decomposed into independent terms, each of them describes heat and mass exchange between the intake manifold, the cylinder and exhaust manifold gases, as mentioned in [8].

The heat release calculation in the combustion chamber of the diesel engine is a complex task being solved on the base of the works [12, 13]. The main drawback of Razleitsev's method [13] is the widespread use of empirical and semi-empirical data describing both geometric parameters of the diesel engine and physical properties of the fuel, gas-dynamic phenomena in the combustion chamber, etc. Vibe's method [12] describes the heat release in both gasoline and diesel engines, and in engines running on alternative fuels, i.e., biofuels, gaseous fuels including methane and generator gas, heavy fuels including fuel oil, emulsions, etc. Its main disadvantage is inability to take a heat release of vapors combustion of atomized fuel vaporized through ignition delay [14]. However, a number of papers are devoted to implementation of two-stage Vibe combustion, i.e., determination of biofuel diesel combustion [15] and two-stage Vibe diesel combustion parameters [16].

In most computational models of the turbocharged engine, a simplified representation of the turbocharger is used. A turbine is presented as constant restriction with predetermined efficiency, the turbocharger rotor maintains constant rotation speed and the compressor maintains constant pressure boost and efficiency [17]. This approach is acceptable in most cases, but in case of pulsed flow rate and pressure through compressor, it is not applicable. However, this problem can be solved using the compressor efficiency map. The compressor map has been used for the engine cycle calculation implemented in [18], but it caused the excessive data input leaving out the compressor map features. As a result, there is the demand for applying the complex approximation methods that adversely affect the speed and complexity of the engine cycle calculation. The representation of the compressor map mentioned in [7, 8, 19, 20] and continued in this paper provides high accuracy, simplicity and good performance.

2 Relevance of the Research Topic

Evaluation of the effect of pressure pulsation in the intake manifold on the turbocharged engine cycle will allow to improve accuracy of cycle computation and fuel efficiency of the supercharged diesel engine.

3 Problem Statement and Research Method

The description of the simulation method for the zero-dimension supercharged diesel engine cycle is considered. It includes thermodynamics calculations with the intake manifold pressure pulsation using the compressor efficiency map.

The enthalpy I_c or internal energy U_c of the combustion chamber gases depends on the heat released during combustion Q_x , thermodynamic work of cylinder volume change V , a mass M_c and heat Q_w transfer between gases and cylinder wall.

Through the reciprocating engine cycle, the change of in-cylinder pressure p_c , volume V , temperature T_c and mass of fluid M_c is observed. The p_c , T_c and M_c values are determined by the in-cylinder processes and state of fluids in the intake and exhaust manifolds of the turbocharged diesel engine. This can be denoted by function $p_c = f(Q_x, V, M_c, Q_w)$ [20], the time derivative of which is:

$$\frac{dp}{dt} = \frac{\partial p_c}{\partial Q_x} \frac{dQ_x}{dt} + \frac{\partial p_c}{\partial V} \frac{dV}{dt} + \frac{\partial p_c}{\partial M_c} \frac{dM_c}{dt} + \frac{\partial p_c}{\partial Q_w} \frac{dQ_w}{dt}. \quad (1)$$

The terms of (1) can be defined as

$$\begin{aligned} \frac{\partial p_c}{\partial Q_x} \frac{dQ_x}{dt} &= (Q_z + U_c - U_x) \frac{1}{V} \frac{dx}{dt}; \\ \frac{\partial p_c}{\partial V} \frac{dV}{dt} &= -k\omega F_p \frac{p_c}{V} \left(R_k \sin \phi + \frac{L}{2} \sin 2\phi - \lambda e \cos \phi \right); \\ \frac{\partial p_c}{\partial M_c} \frac{dM_c}{dt} &= \frac{R}{(c_p)_c} \\ &\left[-(c_p)_c T_c G_{cp} + (c_p)_p T_p G_{pc} + (c_p)_s T_s (G_{sc} + G_{1sc}) - (c_p)_c T_c (G_{cs} + G_{1cs}) \right]; \\ \frac{\partial p_c}{\partial Q_w} \frac{dQ_w}{dt} &= -\frac{k-1}{V} Q_w; \\ \frac{dT_c}{dt} &= \frac{1}{\rho_c R} \frac{dp_c}{dt}, \end{aligned}$$

where p , T , M —pressure, temperature and mass of the fluid; V , dV/dt —volume of the cylinder and its rate of change; k —heat capacity ratio; R —gas constant, J/(kg·K); G_{cp} , G_{pc} —mass flow rate from the cylinder into the exhaust manifold and their possible discharge into the cylinder; G_{cs} , G_{sc} —mass flow rate from the cylinder to the intake manifold and returned to the cylinder with valve overlap; G_{1sc} , G_{1cs} —charge mass flow rate when the fluid is admitted and re-ejected from the cylinder into the intake manifold; c_p —isobaric specific heat capacity; dx/dt —the rate of heat release during combustion; $Q_z = H_u g_c$ —the amount of heat supplied in the cycle; H_u —the lowest calorific value of the fuel; g_c —the cyclic fuel supply; U_c , U_x —the internal energy of the working fluid at the beginning and during the combustion process; ω —the angular speed of rotation of the crankshaft; F_p —the area of the piston; R_k —the radius of the crank; L —the length of the connecting rod; e —piston pin offset; ϕ —the crankshaft angle; ρ_c —density of

the fluid in the cylinder; indices: c —cylinder; s —intake manifold; p —exhaust manifold; k —compressor; t —turbine; k_x —value determined by the compressor map.

The results of the diesel engine 4CH10.5/12 pressure trace treatment [21] denote that the relative heat release rate curve has two peaks. This characteristic of the curve is a consequence of two different processes that determine the combustion of the atomized fuel in the diesel engine [22]: kinetic combustion—the process of burning out a homogeneous mixture of fuel vapors and air formed during the ignition delay, the duration and intensity of which is determined by the chemical reaction rate and diffusion combustion—a relatively slow combustion process of a heterogeneous mixture of the atomized fuel and air. Its speed is limited by the processes of droplets evaporation and diffusion of fuel vapor and air oxygen into the reaction zone. Therefore, the rate of relative heat release $dx/d\tau$ at each specific moment of combustion time will be defined as the sum of the relative heat release rates of kinetic $dx_k/d\tau$ and diffusive $dx_d/d\tau$ combustion.

Simulation of each of these processes is possible using a fairly simple and universal technique proposed in [12]. In accordance with it, the relative heat release rate and the relative heat, released to a certain moment of combustion, are calculated as

$$\frac{dx}{d\tau} = a(m+1)\tau^m e^{-a\tau^{m+1}}$$

and

$$x = 1 - e^{-a\tau^{m+1}},$$

where $a = \ln(1-x_z)$ —completeness of combustion coefficient, considering x_z —fraction of fuel reacted to the end of the active heat release, for $x_z = 0.999$ coefficient $a = 6.908$; $\tau = \varphi_0/\varphi_z$ —relative time of heat release; φ_0 —turn off crank angle (CA) from the start of combustion; φ_z —combustion duration; m is the shape parameter, selected based on the mixture formation characteristics, mainly the vortex formation in the combustion chamber of the diesel engine. For the combustion process of the heterogeneous mixture $m = 0 \dots 1.2$, and in case of the prepared, homogeneous, fuel–air mixture $m = 3 \dots 4$ [12].

The shape parameter can be determined by the value of the maximum rate of relative heat release [12]

$$\left(\frac{dx}{d\tau}\right)_{\max} = a(m+1) \left[\frac{m}{a(m+1)e} \right]^{\frac{m}{m+1}}$$

or by the relative position of the maximum rate of relative heat release

$$\tau_m = \left[\frac{m}{a(m+1)} \right]^{\frac{1}{m+1}}.$$

The method for calculating the heat release process as a superposition of kinetic and diffusion combustion is known and described, i.e., in [23]. The rate of relative heat release in accordance with it can be written as

$$\frac{dx}{d\tau} = \frac{dx_k}{d\tau} + \frac{dx_d}{d\tau} = \sigma_k a(m_k + 1) \tau_k^{m_k} e^{-a\tau_k m_k + 1} + (1 - \sigma_k) a(m_d + 1) \tau^{m_d} e^{-a\tau^{m_d + 1}}, \quad (2)$$

where $\tau_k = \varphi/\varphi_k$ is the relative time of kinetic combustion; m_k is a shape parameter of kinetic combustion; m_d is a shape parameter of diffusion combustion; σ_k is the share fuel weight burned during kinetic combustion.

Integrating (2), we get the expressions for the relative heat release

$$x = x_k + x_d = \sigma_k \left(1 - e^{-a\tau_k m_k + 1}\right) + (1 - \sigma_k) \left(1 - e^{-a\tau^{m_d + 1}}\right).$$

The duration of combustion can be determined experimentally, as a result of processing the indicator diagram for heat release, or by calculation, i.e., following the method [13]:

$$\varphi_z = \varphi_{inj} - \Delta\varphi_i + 6nt_{vap},$$

where φ_{inj} is the injection duration; $\Delta\varphi_i$ is the ignition delay period, for diesel 2CH10.5/12 can be determined by the [24, 25]; n is the engine speed, min^{-1} ; t_{vap} is the evaporation and combustion time of large fuel droplets.

The time of evaporation and combustion of large fuel droplets can be determined using the method [24], or by any other method that has been confirmed for the studied diesel engine. Sufficient accuracy for practical purposes is provided by the methodology described in [13], according to which

$$t_{vap} = \frac{A_z}{\alpha^{0,5}} \frac{p_c d_{32}^2}{y},$$

where α is the excess air ratio; $A_z = 4.6, \text{s}^{-1}$ is the evaporation time constant; y is a coefficient considered the combustion chamber geometry, the intensity of the axial and radial vortices, etc.; p_c is the pressure in the cylinder at the time of the start of fuel delivery, MPa; d_{32} is the Sauter mean diameter of the drops, microns.

The fraction of the fuel vaporized during the ignition delay period σ_k participating in kinetic combustion can be calculated by numerical integration, or by any other method from the relative evaporation rate of the atomized fuel within the auto-ignition delay [13] using relative injection trace.

The duration of kinetic combustion can be calculated from the results of processing the indicator diagram for heat release. In the absence of experimental data, its approximate value can be determined as half of the self-ignition delay period $\varphi_k \approx 0,5\Delta\varphi_i$.

The calculation of the heat flux Q_w is performed by the expression [26]

$$Q_w = \alpha_w \left[\pi D S_p (T_c - T_{cc}) + \frac{\pi D^2}{4} (2T_c - T_{cp} - T_{ck}) \right],$$

where S_p is the piston displacement, m; D is the cylinder diameter, m; T_{cc} , T_{cp} and T_{ck} are the average surface temperatures of the cylinder liner, piston and cylinder head.

The heat transfer coefficient is determined by the Woschni formula [27]. The processes in the exhaust and intake manifolds described by the equations

$$\frac{dp_p}{dt} = \frac{R}{V_p} \left\{ \sum_{j=1}^i \left[\frac{(c_p)_c}{(c_p)_p} G_{cp} T_c \right] - \sum_{j=1}^i (G_{pc} T_p) - G_{po} T_p + \frac{E_p}{(c_p)_p} \right\};$$

$$\frac{dT_p}{dt} = \frac{1}{\rho_p R} \frac{dp_p}{dt};$$

$$\frac{dp_s}{dt} = \frac{R}{V_s} \left\{ G_k T_k - \sum_{j=1}^i (G_{1sc} + G_{sc}) T_s + \sum_{j=1}^i \left[\frac{(c_p)_c}{(c_p)_s} (G_{1cs} + G_{cs}) T_c \right] + \frac{E_s}{(c_p)_s} \right\};$$

$$\frac{dT_s}{dt} = \frac{1}{\rho_s R} \frac{dp_s}{dt},$$

where V_p , V_s are the volumes of the exhaust and intake manifolds; G_k , T_k are the mass flow rate and temperature of air outgoing from the compressor; G_{po} is the mass flow rate through of the bypassed trough the turbine gas; E_p , E_s is the kinetic energy of the fluids in the exhaust and intake manifolds; ρ_p , ρ_s are the density of the fluid in the exhaust and intake manifolds; i is a number of cylinders.

The air flow rate through the compressor G_k , the efficiency of the compressor η_k , and the rotor speed n_{tk} are determined by the compressor efficiency map. For the selected value of π_{kx} , a series of ratios G_{kx}/η_{kx} is calculated. The physical meaning of the last one is the mass flow of ideal gas through the compressor without resistances. The important property of the function $G_{kx} = f(G_{kx}/\eta_{kx})$ is its increase in the entire range of values of η_{kx} and G_{kx} . Approximation of the dependence $G_{kx} = f(G_{kx}/\eta_{kx})$ by the fourth-order polynomial denotes satisfactory accuracy in determining the parameters of the tight air and compressor performance. The value of G_k for intermediate values of π_k can be determined by interpolation, i.e. linear.

4 Results of the Study

The influence of air pressure pulsation in the intake manifold on the performance of the turbocharged engine was studied on 2CHN10,5/12 diesel engine with TD03-06G turbocharger by Mitsubishi [7].

According to the initial assumptions, to increase the effective power from 22.1 kW to 30 kW with the excess air ratio $\alpha = 1.7$, the pressure ratio is required to be at least $\pi_k = 1.6$, when the air flow rate is $G_k \approx 0.049$ kg/s (0.0412 m³/s), which corresponds to the efficiency of the compressor $\eta_k = 0.73$ and the compressor speed $n_{tk} = 129500$ min⁻¹ on the compressor efficiency map.

Tests of a diesel engine with the volume of the intake manifold approx. $V_s \approx 1$ dm³ gave insufficient results: the effective power increased by less than 10% to $N_e = 24$ kW, at the increasing the specific effective fuel consumption to $g_e = 290$ g/(kW h).

Computational studies using elements of the proposed mathematical model displayed the demand for increasing the volume of the intake manifold V_s up to 6.5 dm³. As a result, the effective power increased to $N_e = 30$ kW and the specific effective fuel consumption reduced to $g_e = 230$ g/(kW h).

5 Conclusions

1. The calculation of the heat release with direct diesel fuel injection by the modified Vibe method allows us to take into account the two-stage combustion, including both kinetic and diffusion stages.
2. The calculation of the variable air flow rate through a compressor using the compressor efficiency map can take into account the change of the turbocharger operation parameters within the engine cycle.
3. The developed mathematical model enables to calculate the turbocharged diesel engine cycle with high accuracy. It can be used for high precision calculation of the turbocharger and the reciprocating diesel engine.

References

1. Markov VA, Bashirov RM, Gabitov II (2002) Toxicity of diesel exhaust gases. Moscow State Technical University n.a. N. E. Bauman, Moscow
2. Chernetsov DA (2010) Toxicity of diesel exhaust gases and their impact on humans. *J Questions Mod Sci Pract* 10–12(31):54–59
3. Matievsky GD, Svistula AE, Bryakotin ME and Nekrasova MA (2016) Reduction of fuel consumption and harmful emissions of tractor diesel. LAPLAMBERT, Saarbrücken
4. Khanin NS, Aboltin EV, Lyamtsev BF (1991) Automobile engines with turbocharging. Mechanical engineering Press, Moscow
5. Hak G (2003) Turbomotors and compressors: reference. Manual. LLC “Astrel Publishing House” and LLC “AST Publishing House”, Moscow
6. Gavrilov AA (2016) Supercharging units. Publishing House of Vladimir State University, Vladimir
7. Gavrilov AA and Efros VV (1997) Pulsed boost system of four-stroke low-voltage diesel engines. *J Tractors Agric Mach* 10(6–18)11:24–27
8. Gavrilov AA, Gots AN (2013) Turbocharging model in the engine cycle with variable air pressure at the inlet. *J Fundam Res* 8(1):24–28
9. Gavrilov AA, Ignatov MS (2009) Design of turbochargers for supercharging of Porsche internal combustion engines: training manual. Publishing House of Vladimir State University, Vladimir
10. Abalyaev AYU (1999) Improvement of the intake process of a two-cylinder diesel engine with gas turbine supercharging. Dissertation, Vladimir State University, Vladimir
11. Gavrilov AA (1999) Turbocharging of four-stroke diesels with the number of cylinders up to three. Dissertation, Moscow State Technical University n.a. N. E. Bauman
12. Vibe II (1962) New about the working cycle of the engine. MASHGIZ Press, Sverdlovsk
13. Razleitsev NF (1980) Modeling and optimization of the combustion process in diesel engines. Higher School Publishing House, Kharkiv
14. Bolshakova AV (2009) Calculation of fuel burnout in a diesel cylinder. In: Actual problems of operation of motor vehicles. Materials of the XIII International Scientific and Practical Conference dedicated to the 40th anniversary of the Faculty of Motor Transport, Vladimir State University Press, Vladimir, pp 262–265
15. Peshis RB (2010) Experimental determination of double vibe function parameters in diesel engines with biodiesel. *J Therm Sci* 14:S197–S208

16. Lazarev EA (2010) Physical concepts and mathematical models of the fuel combustion process in diesel. *J Bull SUSU* 10:32–39
17. Ivanchenko NN, Krasovsky OG, Sokolov SS (1983) High supercharging of diesels. Mechanical engineering Press, Leningrad
18. BOOST Application Examples (2020) Compression Ignited. AVL, Graz 2020:10
19. Gavrilov AA, Gotz AN (2013) Influence of external factors on the pressure of the working fluid in the cycle of a piston engine. In: Materials of the V-th All-Ukrainian scientific and technical conference with international participation “Modern problems of engine building: state, ideas and solutions”, Pervomaysk, pp 52–59
20. Gavrilov AA, Gots AN (2014) Modified mathematical model of the piston engine cycle. Modern mechanical engineering. In: Radkevich MM, Evgrafov AN (eds) Science and education: proceedings of the 4th international scientific and practical conference. Publishing house of Polytechnical Institute. St. Petersburg, pp 1239–1249
21. Abalyaev AYU, Basurov VM, Guskov VF (2011) Influence of nanocomposite additive to Mg/MoO₃ fuel on the working cycle of diesel. In: Materials of the IV international scientific and practical conference “science-technology-resource saving”: collection of scientific works. Vyatka State Agricultural Academy, Kirov, pp 3–4
22. Vzorov BA, Adamovich AV et al (1981) Tractor diesel engines. In: Vzorov BA (ed) Mechanical engineering Press, Moscow
23. The Experimental VCR Diesel Engine and Determination of Double Vibe Function Parameters. Pesic Radivoje, Milojevic Sasa, Davinic Aleksandar, Veinovic Stevan, Virgiliu Dan Negrea, Pop Gheorghe, CAR 2005 The International Congress on Automotive Pitesti, Romania, 2–4 November 2005
24. Spalding DB (1985) Combustion and mass transfer. Mechanical engineering Press, Moscow
25. Gavrilov AA, Gots AN (2014) Duration of ignition delay of fuel-air mixture in piston engines. *J. Fundam Res* 6(4):703–708
26. Kavtaradze RZ (2008) Theory of piston engines. a special chapter. Textbook for higher education. Publishing House of Bauman Moscow State Technical University, Moscow
27. Kavtaradze RZ (2007) Local heat exchange in piston engines, 2nd edn. Publishing House of the Bauman Moscow State Technical University, Moscow



Analysis of the Possibility and Feasibility of Using the Clocking Effect in the Design of Compressors and Turbines of Gas Turbine Engines

I. A. Krivosheev, N. B. Simonov^(✉), and K. E. Rozhkov

Ufa State Aviation Technical University, 12, K. Marksa, Ufa 450008, Russia

Abstract. A method for analyzing the effect of the blades number and the mutual circumferential position of the stator (and rotor) blade rows on the efficiency is considered. This mutual position is ensured when designing and assembling compressors and turbines. The method of equivalent channels proposed by the authors is used for the analysis. The geometry of such channels is built from the results of traditional 3DCAD/CAE-modeling of compressors and turbines with a rotating rotor. The utmost variants of the mutual circumferential position of the blade rows in the stator (and in the rotor) are considered—optimal and non-optimal. In 3DCAD/CAE modeling of a stationary equivalent channel for the stator (and for the rotor), for each of the options, the values of the total pressure recovery ratio σ are determined for the equivalent channels and their sections. From their values and from the values of the reduced speed λ , the values of the speed coefficients φ (for the turbine) and the coefficients $K\lambda$ for the compressor are determined. For each option, the values of these indicators are different. With their use, the σ values of the blade rows (for each of the variants) and the σ values for the compressor or turbine as a whole are determined. According to these values, according to the expressions, proposed by the authors, the values of the compressor or turbine efficiency are determined for the optimal or non-optimal mutual position of the blade rows in the stator (in the rotor).

Keywords: Engine · Compressor · Turbine · Rotor · Stator · Blade row · Equivalent channel · Total pressure · Recovery ratio · Efficiency · Clocking effect

1 Introduction

At present, when designing blade machines (BM)—compressors and turbines, the solidity of the blade rows (BR) is determined, then their width is determined, and this makes it possible to determine the number of blades z . However, not enough attention is paid to the mutual circumferential position of the stator blades of adjacent stages. Similarly, the influence of the mutual circumferential position of the rotor blades of adjacent stages is not taken into account. At the same time, it is known [1–6] that optimization of the blades number in the stator (and in the rotor) of adjacent stages and their mutual position

allows increasing (by 1–2%) the efficiency of a compressor or turbine. In modern conditions, this is a significant result. However, the methods used for analyzing the clocking effect are either empirical or 3DCAD/CAE-modeling in a non-stationary mode, which requires a lot of computational resources.

2 Proposed Solution

To analyze the possibility and feasibility of using the clocking effect [7–12] in the design and assembly of compressors and turbines, the following technique is proposed.

1. 3DCAD/CAE-calculation of BM is carried out using a CAE-system (for example Ansys CFX). For this, a sector with an angle φ along the flow part (FP) or the entire FP is selected. In this case, in the compressor, the mass flow averaged values of the total pressure recovery ratio σ are determined for IGW (inlet guide vane), RB (rotor blade) and GV (guide vane). Accordingly, these indicators are determined in the turbine for the NA (nozzle apparatus) and the RB. In this case, along any streamline, the dependences of the change in the total pressure P^* and the ideal pressure $P_{ID}^* = P_0^*(T^*/T_0^*)^{\frac{k}{k-1}}$ are plotted, along which the current value of the parameter $\sigma = \frac{P^*}{P_{ID}^*}$. The value of σ for each blade row (BR) is determined by the expression $\sigma_{BR} = \frac{\sigma_i}{\sigma_{i-1}}$. Here the indicator σ_{i-1} is for the section from the entrance to the BM to the entrance to the given BR or stage, σ_i - for the section from the entrance to the BM to the exit from the given BR or stage. In modern CAE systems (in the calculator) [13–18], it is possible to display the average integral over the circumference and along the height of the FP (flow path) of the entire BR value $\langle \sigma \rangle$ by area or by mass flow rate (i.e., mass average—taking into account the current density distribution around the circumference and along the height FP). In this case, averaging over the flow rate (by mass) $\langle \sigma \rangle_G$ is required. It is more correct to determine $\langle \sigma \rangle^{\frac{k-1}{k}} > G$. It determines $\langle T_S^* \rangle > G$. In this case, separately along the surfaces of the current “shr”, “mid” and “hub”, it is possible to perform averaging in finite differences over a circle in a simplified manner $\langle \sigma \rangle \approx (1/4)(\sigma_{SS} + \sigma_{PS}) + \sigma_C/2$. Here, the value of the parameter SS is along the blade suction side, σ_{PS} is along the blade pressure side, and σ_C is along the flow core, it is assumed that the current density is the same in the circumferential direction along the front of the grating. If in this way the mean integral values in the sections “shr”, “mid” and “hub” are determined, then according to the same scheme, it is possible to simplify the σ parameter over the FP height for the entire blade row (for IGW, RB, GV, respectively) over all stages. In this case, the efficiency of each blade row, stage, BM as a whole is determined by the formula proposed by the authors, the value of the efficiency in the compressor $\eta = 1 - (1 - \sigma^{\frac{k-1}{k}}) (cp T_1^*/\bar{H}_T + 1)$ in the turbine $\eta = 1/[1 + (1 - \sigma^{\frac{k-1}{k}}) (cp T_o^*/\bar{L}_u - 1)]$. In this case, for the BM as a whole $\sigma = \Pi \sigma_i$. Here σ_i —is the parameter value for the stages. Compressor stage value is $\sigma = \sigma_{IGV} \sqrt{\sigma_{wAG1} \sigma_{AG1}} \sigma_{wRB} \sqrt{\sigma_{wAG2} \sigma_{AG2}} \sigma_{GV}$ and for the turbine stage is $\sigma = \sigma_{NA} \sqrt{\sigma_{wAG1} \sigma_{AG1}} \sigma_{wRB}$.
2. According to the results of 3DCAD/CAE-modeling, along each flow surface, along suction and pressure sides of every BR, trajectories and streamlines are identified

(Fig. 1). At the same time, such streamlines are additionally constructed in the RB for absolute motion, and in the GV, respectively, for relative motion. This allows you to build “equivalent canals” (EC) (Figs. 2 and 3) using elements of the IBC type (interblade canal).

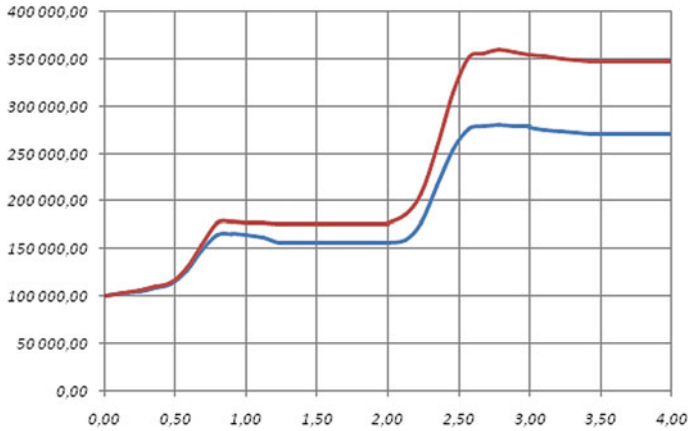


Fig. 1 Change in total pressure P^* (blue) and ideal total pressure (red) $P_{ID}^* = P_0^* (T^*/T_1^*)^{\frac{k}{k-1}}$ along the stage flow path according to the results of 3DCAD/CAE simulation

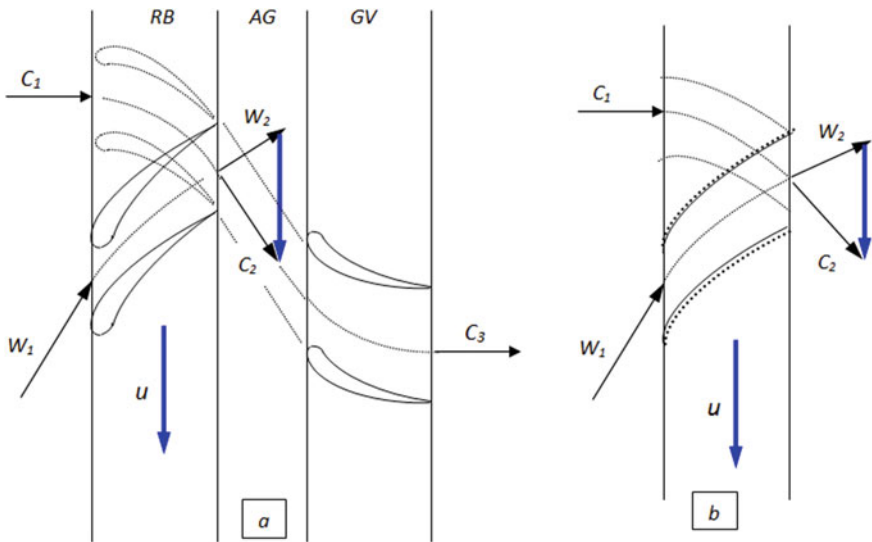


Fig. 2 Scheme of an equivalent channel (EC) for a stage of a compressor cascade. **a** scheme of a stage with an “equivalent channel”. **b** A diagram of an interblade and an “equivalent” channel in the RB

3. Taking this into account, 3DCAD models of the EC for the rotor and stator of the BM are formed. 3DCAD/CAE-modeling of the flow in stationary EC of the rotor

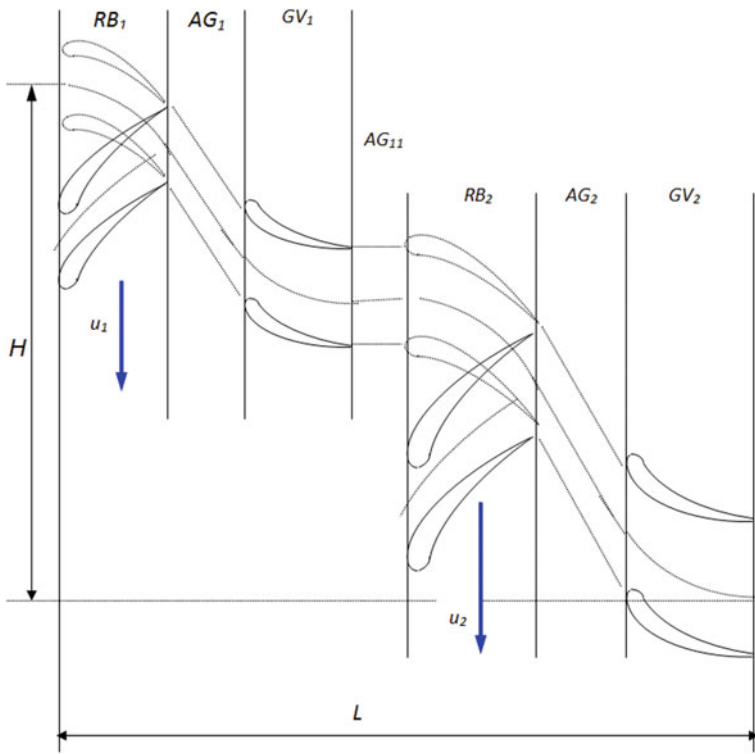


Fig. 3 Scheme of the “equivalent” channel for the stator, composed of elements of the “IBC” and EC type, allowing to analyze the flow in the compressor in absolute and relative motion simultaneously

and stator is performed. In this case, two options are considered. For the stator EC, options are considered with the best (optimal) mutual circumferential position of the stator BR (IGV and GV—in the compressor, NA—in the turbine) and with their worst mutual position. In this case, instead of the blades of the RB, curved surfaces (boundaries) are installed in the EC of the rotor. Similarly, for the EC of the rotor, options are considered with the best (optimal) mutual position of the BR of the rotor (and the RB) and with their worst mutual circumferential position. Instead of blades IGV and GV (in the compressor) and NA (in the turbine), curved surfaces (boundaries) are installed in the rotor EC.

4. 3DCAD/CAE-modeling of the flow in stationary EC of the rotor and stator (with the best and worst relative positions of the BR) allows determining the values of σ for each BR in its composition. Accordingly, the results of simulation of flow in the stationary stator compressor EC indicator values σ are determined for each GV and IGV and the turbine for each NA in each such position.

From the expression proposed by the authors for the BR compressor $\sigma \approx \pi(K_\lambda \lambda)$, the value of the parameter is determined $K_\lambda = \sqrt{[(k + 1)/(k - 1)][1 - \sigma^{(k-1)/k}]/\lambda}$. Here, λ is the reduced speed at the inlet to the compressor GV. For a turbine, the

same indicator can be used, but for λ at the outlet from the NA or the traditionally used indicator φ from the condition $\sigma \approx \pi(\lambda/\varphi)/\pi(\lambda)$.

Similarly, based on the simulation results of the flow in the stationary EC of the compressor and turbine rotor, the values of the parameter σ_w for the RB are determined for each such position. From the expression proposed by the authors for the compressor BR $\sigma \approx \pi(K\lambda\lambda)$ the value of the parameter is determined $K\lambda = \sqrt{[(k+1)/(k-1)][1 - \sigma^{(k-1)/k}]/\lambda}$ [19–23]. Here, λ is the reduced speed at the compressor inlet to the RB. For the turbine, the same parameter can be used, but for λ at the outlet from the RB or the traditionally used indicator φ from the condition $\sigma \approx \pi(\lambda/\varphi)/\pi(\lambda)$. In the case of the optimal relative position of the BR in the stator and, accordingly, in the rotor, the corresponding values of the BRK_λ less than a φ are greater than at a non-optimal mutual circumferential position.

5. Using the values of the reduced speed at the inlet to the BR of the compressor and at the outlet from the RB of the turbine (according to the results of 3DCAD/CAE-modeling of the BR when the rotor rotates according to claim 1) and defined in item 4. Indicators K_λ and φ , already for the case with rotor rotation, the values of parameters σ of the BR are determined by the expressions $\sigma \approx \pi(K_\lambda\lambda)$ or $\sigma \approx \pi(\lambda/\varphi)/\pi(\lambda)$ —for the turbine BR (and for the IGV in the compressor). This allows using the expressions $\sigma = \Pi\sigma_i$ to determine the efficiency values for the BM of the optimal and non-optimal relative positions of the BR—in the rotor and in the stator, respectively. These values are in the first case 1 ... 2% higher than in the second.
6. Based on the simulation results, it is determined at what angle θ with respect to the first blade row in the stator (and in the rotor) in the circumferential direction, the following BRs should be displaced during assembly so that the efficiency of the BM is maximized. When constructing the EC (Fig. 4), it is used that the distance between the trajectories of the same particle in the circumferential direction in absolute and relative motion $\Delta H = \int \frac{ds}{\bar{c}_a} \approx \frac{\Delta s}{(\bar{c}_a)_{cp}}$, where Δs is the interval along the BM axis (BR width). A simplified construction of the trajectory of the flow core at $\bar{c}_a \approx \text{const}$ within each BR, taking into account the rays at the entrance to each BR in absolute and relative motion, is shown in Fig. 5. Figure 6 shows how the boundaries (current surfaces for the flow core) are constructed. It can be seen that the optimal mutual position of the stator blades (and, accordingly, the rotor) is when the surfaces (boundaries) of the flow core coincide. The worst mutual position of the stator BR (and accordingly the rotor) is when the mixing is half a step. Due to the difference in the number of blades Z , the equivalent channel is built not for one but for several IBC (interblade channels) at the inlet (Figs. 5, 6). When calculating in Ansys, the equivalent channel is built up gradually. First, for the first BR, σ and λ at the inlet are determined; for them, K_λ is determined. Then a fragment of the equivalent channel for the next BR (stator and rotor, respectively) is added. The total value of σ is determined. It is divided by the same indicator for the equivalent channel (EC) in the previous form. This gives the σ value for the added fragment.

In the given example, for a two-stage LPC, $H_T = cp(T_2^* - T_1^*) = 115085 \text{ J/kg}$ and efficiency $\eta^* = 1 - (1 - \sigma_{st}^{0,286})(cp T_1^*/H_T + 1) = 0,84$. With an optimized circumferential position of the rotor and stator BR in this two-stage compressor, the σ values are

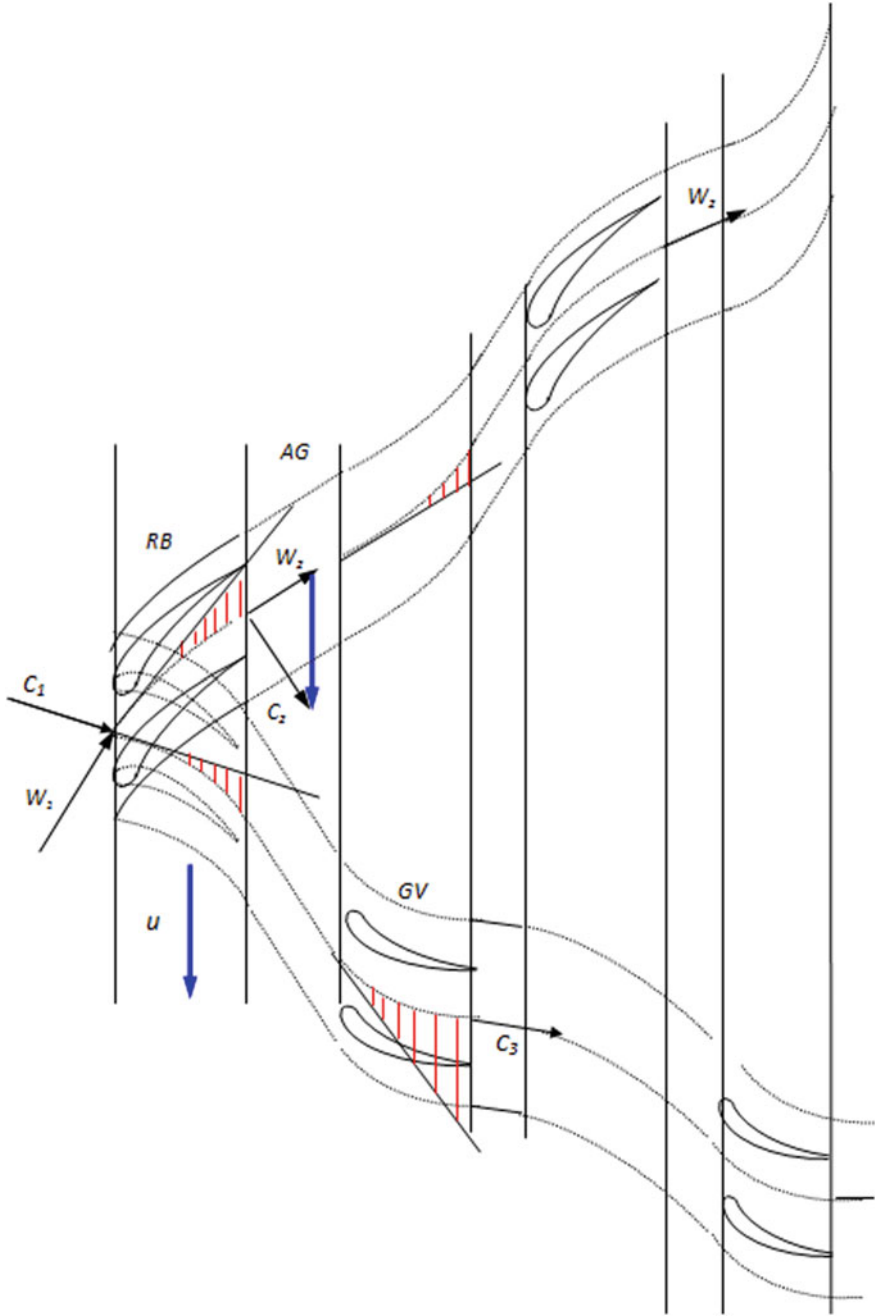


Fig. 4 Scheme for constructing an EC taking into account the flow paths in the compressor in absolute and relative motion

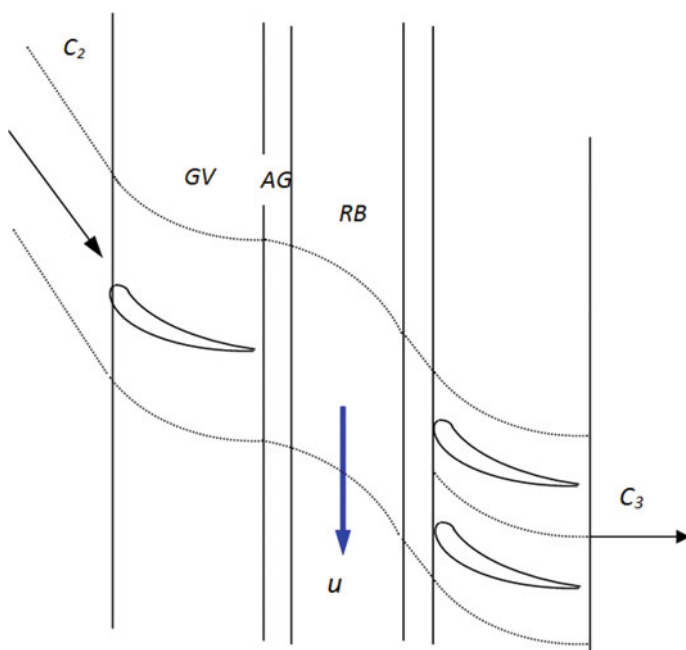


Fig. 5 Scheme for constructing an EC for a stator, taking into account the difference in the number of blades Z (shown is the optimal relative position grids in the stator)

1.5% higher. Taking this into account, the obtained values for K_λ for the optimal and non-optimal mutual positions of the stator BR (and, accordingly, the rotor) differ. The values of λ at the inlet to each RB and GV during the rotation of the rotor (from the usual 2D calculation or calculation in Ansys) are used to calculate the σ of all BRs and σ for the compressor as a whole (for the optimal and non-optimal relative positions of the BRs of the stator and, accordingly, the rotor) made it possible to determine the efficiency of the compressor 0.85 and 0.84, respectively, for the optimal and non-optimal variant of the relative circumferential position of the BR in the stator). This is the efficiency in the design mode (at the calculated value at the input. This allows us to determine the displacement (Fig. 7) of the curves $\eta(\bar{c}a)$ for each of the variants of the relative position of the stator blades (and, accordingly, the rotor).

3 Conclusion

Thus, it has been shown that the proposed method for analyzing the possibility and feasibility of using the clocking effect in the design and assembly of compressors and turbines (including birotative ones) allows solving the problem with minimal resource consumption for 3DCAD/CAE modeling. The proposed use of equivalent channels and methods for determining the efficiency of turbines and compressors at the optimal and non-optimal mutual circumferential position of the BR in the stator (and in the rotor) allows increasing the degree of adequacy of the result obtained. This allows you to set

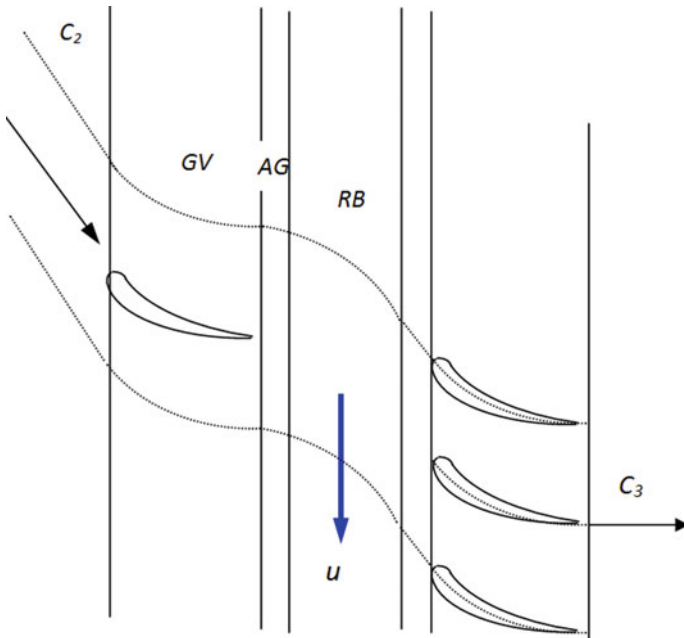


Fig. 6 Scheme of constructing an EC for a stator, taking into account the difference in the number of blades Z (shown is a non-optimal relative position grids in the stator)

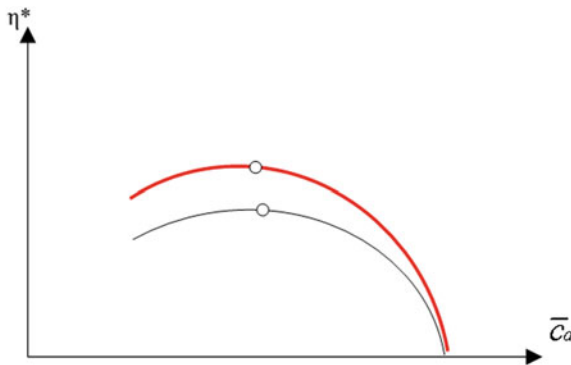


Fig. 7 Dependencies η (\bar{c}_a) for the optimal and non-optimal mutual position of the stator blades (and, accordingly, the rotor)

the conditions for the relative position of the blade rows when assembling stators (and rotor) of a compressor or turbine.

References

1. Krivosheev IA (2007) Ispolzovanie imitacionnogo modelirovaniya i podderjki prinyatia reshenii pri sistemnom proektirovanii avionicnogo dvigatelya (The use of simulation modeling

- and decision support in the system design of an aircraft engine as part of an aircraft). *Aerospace Engineering Technology* 6:63–81
2. Savin NM, Saren VE (2006) Effects of stator clocking in system of rows stator-rotor-stator of the subsonic axial compressor. In: *Unsteady aerodynamics, aeroacoustics and aeroelasticity of turbomachines*, pp 581–601
 3. Savin NM, Saren VE (2006) Gasdynamic effects of tangential bowing of stator vanes in a subsonic stage of axial compressor. In: *Turbo machines aero elasticity aero acoustics unsteady aerodynamics*, pp 201–214
 4. Barankiewicz W, Hathaway M (1997) Effects of stator indexing on performance in a low speed multistage axial compressor. In: *Proceedings of ASME TURBO EXPO 97-GT-496*
 5. Hsu ST, Wo AM (1997) Reduction of unsteady blade loading by beneficial use of vortical and potential disturbances in an axial compressor with rotor clocking. In: *Proceedings of ASME TURBO EXPO 97-GT-86*
 6. He L, Chen T, Wells RG, Li YS, Ning W (2002) Analysis of rotor-rotor and stator-stator interferences in multi-stage turbomachines. In: *Proceedings of ASME TURBO EXPO GT-2002-30355*
 7. Key N, Lawless P, Fleeter S (2008) An experimental study of vane clocking effects on embedded compressor stage performance. In: *Proceedings of ASME TURBO EXPO GT2008-51087*
 8. Key N, Lawless P, Fleeter S (2008) An investigation of the flow physics of vane clocking using unsteady flow measurements. In: *Proceedings of ASME TURBO EXPO GT2008-51091*
 9. Mileschin VI, Braillko IA, Savin NM, Kozhemyako PG (2013) Numerical and experimental analysis of rotor and stator clocking effect by example of model high loaded two stage compressor on $\pi^*C = 3.7$. In: *Proceedings of ISABE conference ISABE-2013-1131*
 10. Kato D, Imanari K (2003) Effects of airfoil clocking on aero-performance and unsteady blade loading in a high-speed axial compressor. In: *Proceedings of the international gas turbine congress IGTS2003, Paper TS-058*
 11. Mileschin VI, Savin NM, Kozhemyako PG, Druzhinin YaM (2014) Numerical and experimental analysis of radial tip clearance influence on rotor and stator clocking effect by example of model high loaded two stage compressor. In: *Proceedings of ASME TURBO EXPO GT2014-26345*
 12. Mileschin VI, Kozhemyako PG, Orekhov IK, Fateev VA (2012) Experimental and numerical study of two first highly-loaded stages of compressors as a part of HPC and separate test unit. In: *Proceedings of ICAS congress ICAS 2012-474*
 13. Saren VE, Savin NM, Smirnov SA, Krupa VG, Yudin VA (2006) Hydrodynamic interaction of axial turbomachine cascades. *J Eng Math* 1–4:9–39
 14. Hirsch Ch (2012) Non-deterministic methodologies for uncertainty quantification in turbomachinery CFD, Numeca international, Brussels. Pannelsession. In: *Proceedings of ASME TURBO EXPO*
 15. Hirsch Ch (1990) *Numerical computation of internal and external flows*, vol 2. John Wiley & Sons
 16. Yang Z and Shih TH (1993) A $k-\epsilon$ model for turbulence and transitional boundary layer. In: So RMC, Speziale CG, Launder BE (eds) *Near-wall turbulent flows*. Elsevier-Science Publishers B. V., pp 165–175
 17. Jameson A (1991) Time dependent calculations using multigrid, with applications to unsteady flows past airfoils and wings. *AIAA-91-1596*
 18. CFD Open Series Essentials of Turbo-Machinery in CFD. Ideen Sadreghighi, Ph.D. ANNAPOLIS, MD. See discussions, stats, and author profiles for this publication at: <https://www.researchgate.net/publication/318456872>

19. Krivosheev IA, Rozhkov KE, Simonov NB (2019) Optimizatsiya chisla stupeney i raspredeleniya parametrov v protochnoy chasti pri proyektirovanii kompressorov i turbin GTD (Stages number optimization and parameters distribution in flow parts at compressor and turbines designing GTE). *Aviation Technol* 2:124–132
20. Krivosheev IA, Rozhkov KE (2013) Analiz rabochnykh protsessov i kharakteristik lopatochnykh mashin (Analysis of working processes and characteristics of blade machines). *Vestnik UGATU* 5(40):3–10
21. Krivosheev IA, Rozhkov KE, Simonov NB (2018) Optimizatsiya geometrii i rezhimov raboty lopatochnykh ventsov pri proyektirovanii kompressorov GTD (Optimization of geometry and modes of operation of blade crowns in the design of GTE compressors). *Vestnik PNRPU* 55:90–103
22. Krivosheev IA, Rozhkov KE, Simonov NB, Bagautdinov MZ (2019) Metod ucheta poter' v elementakh protochnoy chasti gazoturbinykh dvigateley (Method for accounting losses in the elements of flowing part of gas turbine engines). *Vestnik UGATU* 1(83):40–48
23. Krivosheev IA, Rozhkov KE, Simonov NB (2019) Vybor uglovatki pri proyektirovanii lopatochnykh ventsov v sostave kompressorov GTD (Choice of angle attack on design blade row in the composition of gte compressors). *Vestnik UGATU* 3(85):62–71



Analysis of the Smooth Running of Wheeled Suspensionless Vehicles in Various Operating Conditions

A. V. Pozdeev^(✉), I. M. Ryabov, and N. V. Timoshin

Volgograd State Technical University, 28 Lenin Ave., Volgograd 400005, Russia

Abstract. This article is devoted to the analysis of the smooth running of wheeled suspensionless vehicles (WSV) in various operating conditions based on experimental studies obtained by Scientific Research Tractor Institute (NATI) and other research organizations. The graphs of the dependences of the root mean square (RMS) vertical and horizontal accelerations are given for three levels of norms according to the ISO 2631–1:1997 standard. It was revealed that the vibration-protective properties of pneumatic tires are very low due to a narrow frequency zone in width and a very steep resonance located in the low-frequency region. To analyze the smooth running of WSV, the RMS-levels of the vibration accelerations in 1/3-octave frequency bands for tractors YuMZ, MTZ-50, K-700, T-150 K, and T-40 are given, as well as the experimental values of the natural frequencies of their vertical oscillations. It was revealed that domestic wheeled tractors in all considered operating conditions can perform resonant vibrations on pneumatic tires. Therefore, the smooth running of domestic wheeled tractors is unsatisfactory, RMS of the vertical accelerations of the skeletons of domestic tractors is up to 4.5 times higher than the permissible level.

Keywords: Wheeled suspensionless vehicle · Operating conditions · Smooth running · Vibration frequency

1 Introduction

Research by the authors [1–5] shows that wheeled suspensionless vehicles (WSV) have a low running smoothness. Many potential built-in operating characteristics of these vehicles (speed, efficiency, stability, controllability of movement, fuel efficiency) are not fully realized in various operating conditions. When driving, these vehicles experience significant vibrations, they swing and vibrations damp very slowly. Therefore, even having sprung seats and driving at a speed lower than the design one, the operator's vibration load is not provided, both when performing basic technological operations in the fields and when performing transport operations on the roads [6–11]. To reduce the vibration, as well as to ensure traffic safety, the operator has to lower the vehicle's speed which worsens fuel efficiency and reduces productivity and efficiency of using the vehicle. Vibrations of agricultural machinery working in the fields increase the tire pressure on the soil, which reduces yields. With long-term exposure to vibration, machine

operators often suffer from occupational diseases—spinal deformities, gastroptosis, etc., which reduces the prestige of their profession. It is noted in the study [12] that during the transition to the first stage of increasing, the operating speeds of machine-tractor aggregates (up to 6–9 km/h), the working conditions on the wheeled tractors MTZ-50, T-40, T-74, etc., have significantly deteriorated, and tractor drivers could not fully realize the capacity of these machines without harm to their health. Clinical examinations of machine operators carried out by medical organizations have shown that about 50% of machine operators suffer from diseases causally related to working with vehicles.

2 Analysis of the Smooth Running of Wheeled Suspensionless Vehicles in Various Operating Conditions

In the study [13], it is noted that it is unacceptable to use vibration-hazardous machines and perform work if the vibration acting on a person during an 8 h working day exceeds the specified norms. Nowadays, root mean square (RMS) acceleration is a generally accepted parameter for evaluating the smooth running of vehicles. It is measured in absolute units (m/s^2) and in relative units of decibels (dB). For the last variant, the following dependency is used:

$$L = 20 \lg(\ddot{z}_{\text{RMS}}/\ddot{z}_0), \quad (1)$$

where $\ddot{z}_0 = 0.000314 \text{ m/s}^2$ is the acceleration of the sensitivity threshold.

For a more accurate assessment of the dependence of the permissible values of vibration velocities and vibration accelerations on the vibration frequencies, the octave bands are divided into 1/3-octave bands. For this purpose, the octave frequency range is divided into three components, and the geometric mean values of each one-third octave frequency band are rounded off.

The standard [14] gives the permissible values of vibration accelerations for the level of maximum permissible tiredness, exceeding which is dangerous to health (with the duration of 8 h vibration), because it leads to occupational diseases.

To obtain a given norm for the level of permissible operator tiredness which does not lead to a decrease in labor productivity, the values of the norm for the level of maximum permissible tiredness are reduced twice or by 6 dB. To obtain the norm of comfort level that provides the ability to read, write, and eat while driving, the standard RMS acceleration of the maximum permissible level of tiredness is reduced by 6.3 times or by 16 dB. Currently, the norm of comfort level for WSV is desirable, but not applied, due to the lack of technical capabilities to comply with it.

Data analysis from [14] shows that the most dangerous frequency band is from 4 to 8 Hz. The minimum acceleration value for the tiredness level is 0.315 m/s^2 or 0.032 g .

Over time, exposure to vibration and human tiredness accumulates; therefore, if the operator is exposed to the vibration of the same level with intervals during the working day, then the total exposure time is determined as the sum of separate periods [15].

With the integral frequency assessment of WSV smooth running, the permissible levels of vibration of the II level (ensuring productive work) are used with the duration

of exposure during the working day (480 min): $[\ddot{z}_{RMS}] = 0.54 \text{ m/s}^2$; $[\ddot{x}_{RMS}] = [\ddot{y}_{RMS}] = 0.38 \text{ m/s}^2$ [13].

To determine the degree of permissible accelerations, $[\ddot{z}_T]$ increases with a decrease in the duration of exposure to vibrations T relative to 8 h, and it is convenient to use the formula:

$$[\ddot{z}_T] = \delta[\ddot{z}_{8h}], \tag{2}$$

where δ is the coefficient of permissible accelerations increases with a decrease in the duration of exposure to vibrations starting from 8 h.

The dependence of the coefficient of permissible accelerations increases with a decrease in the duration of exposure to vibrations starting from 8 h according to the ISO 2631-1:1997 standard is shown in [16].

Since the only elements of WSV that protect its body from vibration (resulting from wheel collisions on uneven roads) are pneumatic tires, then experimental studies that reveal the features of its vibration-protective properties are of particular interest. The study [2] contains vibration tests for a BELARUS tractor tire with a load of 700 kg installed on a vibrating platform of a dynamic test stand [17, 18]. The stand drive allowed the vibrating platform to perform harmonic vibrations with different frequencies in the range of 1–5 Hz and an amplitude of 15 mm (Fig. 1a). As a result of wheel tests, the amplitude-frequency characteristics (AFCs) of the load swing on the tire were obtained at different initial air pressure in the tire (Fig. 1b).

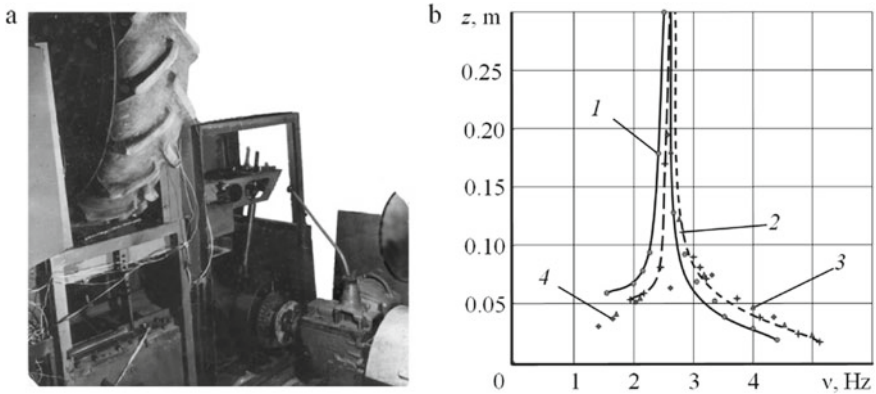


Fig. 1 **a** View of the tire of the BELARUS tractor on the dynamic stand. **b** the frequency response of the oscillations of a load weighing 700 kg on the tire at various pressures: 1— $p_0 = 0.1 \text{ MPa}$; 2— $p_0 = 0.15 \text{ MPa}$; 3— $p_0 = 0.20 \text{ MPa}$; 4— $p_0 = 0.26 \text{ MPa}$

Analysis of AFC of load swing on the tire (Fig. 1b) allows to draw the following conclusions about the features of the vibration-protective properties of the pneumatic tire:

- load swing on the tire when the vibration frequency of the vibration platform approaches the resonance zone sharply increases (more than 10 times), the tire breaks

away from the vibration platform during vibrations due to low damping properties in the tire material and the lack of damping properties of compressed air inside the tire;

- the resonance zone is very narrow, its width is about 0.5 Hz, it depends little on the pressure in the tire, and all the AFC are shifted to the right with pressure increasing;
- AFC displacement at pressure change is very small, for example, when the pressure in the tire decreases by 2.6 times (from 0.26 to 0.10 MPa), the AFC shifts to the left only by 8%, i.e., lowering the pressure in the tire to an acceptable level does not give the necessary reduction in its rigidity and the natural vibration frequency of the WSV body.

One more feature of the tire behavior, when tested on the test stand, is also noted in the study [2]: the intensity of growth and the magnitude of the load swing on the tire increase with pressure increasing in it. Therefore, to obtain the superresonance part of the AFC at high pressure in the tire (0.20–0.26 MPa), they used the method of the fast passage of the disturbance frequency corresponding to the resonance zone to exclude the stand breakdown.

Thus, the vibration-protective properties of pneumatic tires are very low due to the narrow width of the zone and very steep resonance; therefore, when analyzing WSV smooth running, it is of interest to assess the probability of this phenomenon under various operating conditions. To do this, we will compare the frequency effect of the track irregularity with the natural frequencies of WSV body vibration on tires when carrying out transport work on the roads and basic technological operations in the fields.

It is noted in the study [19] that the smooth running of domestic and foreign wheeled tractors is unsatisfactory, since RMS of the vertical accelerations of domestic tractor bodies is 0.25 g, i.e., 4.5 times higher than the permissible level. Foreign wheeled tractors have an even lower smooth running. RMS of the vertical accelerations at their seats is 0.30 g, i.e., 5.5 times higher than the permissible level. These data are confirmed by the results of vertical accelerations measurements of the serial seat and on the cabin floor of MTZ-50, MTZ-52, MTZ-82, T-40, and T-150 K tractors, carried out at a speed of 10–12 km/h on the same agricultural background [20]. The measurement results are shown in Table 1. Data analysis in Table 1 indicates that for MTZ-50, MTZ-52, MTZ-82, T-40, and T-150 K tractors, RMS acceleration on the seats is 15–25% higher than on the cabin floor. The norms of operator's vibration load are exceeded by 209.3–518.5%; therefore, the time of permissible operation of these tractors is within 0.5–2.0 h (according to the dependence of the coefficient of permissible accelerations increases with a decrease in the duration of exposure to vibrations starting from 8 h according to the ISO 2631-1:1997 standard in [16]).

To determine the frequencies at which the levels of vertical RMS vibration accelerations in 1/3-octave frequency bands exceed the norm, and to find the excess value, it is convenient to use the AFC of tractors obtained in [21] (Fig. 2).

When receiving the AFC (Fig. 2a-e), measurements of vertical accelerations on the serial seat and on the cabin floor were carried out in the process of performing the following main technological operations: sowing winter crops (speed 12 km/h); disking (6–8 km/h); plowing (8–10 km/h); driving on asphalt (speed 25 km/h).

Analysis of the diagrams in Fig. 2 shows that the experimental characteristics of vertical vibrations obtained (both on the seat and on the body) have a prominent peak

Table 1 Experimental data on vibration loading of wheeled tractors at a travel speed of 10 ... 12 km/h on one agricultural agrophone

Tractor	Vibration measuring point	RMS of vertical accelerations σ , «g»	RMS of vertical accelerations σ , m/s ²	Excess of the norm $\Delta = (\sigma - \sigma_n) / \sigma_n$, %	Dynamism factor $K = \sigma_{\text{seat}} / \sigma_{\text{body}}$
MTZ-50	seat	0.34	3.34	518.5	1.21
	cabin floor	0.28	2.75	409.3	
MTZ-52	seat	0.32	3.14	481.5	1.23
	cabin floor	0.26	2.55	372.2	
MTZ-82	seat	0.26	2.55	372.2	1.13
	cabin floor	0.23	2.26	318.5	
T-40	seat	0.25	2.45	353.7	1.25
	cabin floor	0.20	1.96	263.0	
T-150 K	seat	0.21	2.06	281.5	1.23
	cabin floor	0.17	1.67	209.3	

caused by resonance for almost all tractors. YuMZ and MTZ-50 tractors have resonance in the frequency range of 2.5–3.0 Hz. K-700 and T-150 K tractors have shock absorbers; therefore, the resonance is in a lower frequency range of 1.8–2.0 Hz, respectively. T-40 tractor has two resonance peaks at frequencies of 2.5 Hz and 5.0 Hz, due to the presence of a spring suspension on the front axle. It follows from Fig. 2f that the integral norm of operator's vibration load at MTZ-80 tractor by vertical vibrations (0.54 m/s²) when carrying out transport work at speeds above 7.5 km/h is also not provided, and even is exceeded at speeds above 14–16 km/h.

Figure 3 shows RMS of vibration accelerations on the tractor driver's seat when T-150 K tractor moves in various gears with the 1-PTS-9 semi-trailer on a field road.

Analysis of Fig. 3 shows that HTZ seat has higher vibration-protective properties than the sprung seats of other manufacturers; however, the operator's vibration load rate (straight line 5) is not provided for this seat too in the low-frequency resonance zone, and the deviation from the norm increases almost linearly with movement speed increasing.

The experimental and calculated values of the natural vibration frequencies of the front and rear parts of wheeled tractors are given in (Table 2) [19].

Analysis of Table 2 shows that the calculated frequencies are lower than the experimental ones. It happens due to the nonlinearity of the elastic characteristics of the tire. To analyze the smooth running of the considered wheeled tractors, it is necessary to use the experimental values of the natural vibration frequencies of their rear part on the tires (since the cabin is located there), which are in the range of 2.89–3.43 Hz. The frequency of the end of the resonance zone can be found by multiplying the value of the natural frequencies by 1.41.

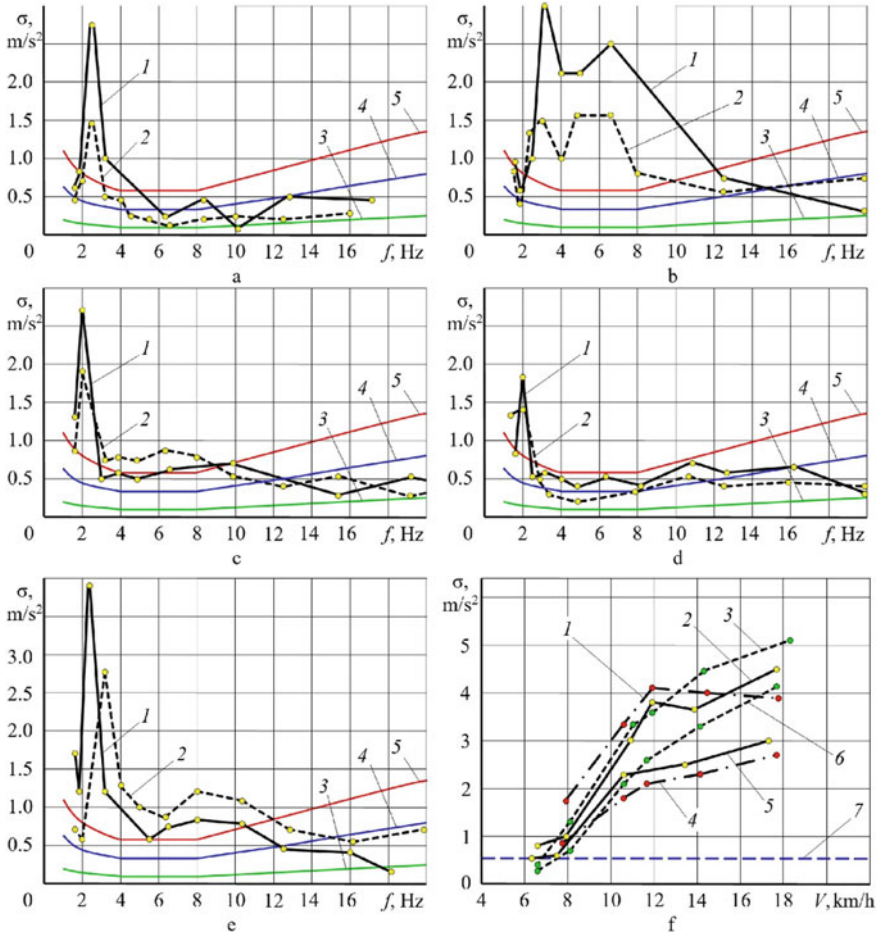


Fig. 2 Experimental vertical vibration acceleration of wheeled tractors. **a** YuMZ. **b** T-40. **c** K-700. **d** T-150 K. **e** MTZ-50 (1—on the frame; 2—on the seat; 3—comfort level; 4—level of permissible fatigue; 5—level of maximum permissible fatigue) **f** MTZ-80 (1, 2, 3—on the seat; 4, 5, 6—on the floor of the cabin; 1, 4—movement with the I-PTS-4 semi-trailer; 2, 5—movement with the mounted plow PN-3- 35; 3, 6—transport mode; 7—integral norm of vibration loading of the operator): $[\ddot{z}_{RMS}] = 0.54 \text{ m/s}^2$)

Data on the irregularities lengths in the study [22] were taken to obtain the frequencies of the disturbing effect of a dirt road and various fields when WSV moved at different speeds (Table 3).

To determine the presence and number of resonant modes of tractor movement in Table 3, there are highlighted (in bold) values of the frequencies of the disturbing effect of the dirt road and various fields, which are included in the resonance zone of the rear suspension of the tractors (Table 2). As a result, it was found that in all considered operating conditions, YuMZ, MTZ-50, MTZ-7 M, and T-40 domestic wheeled tractors

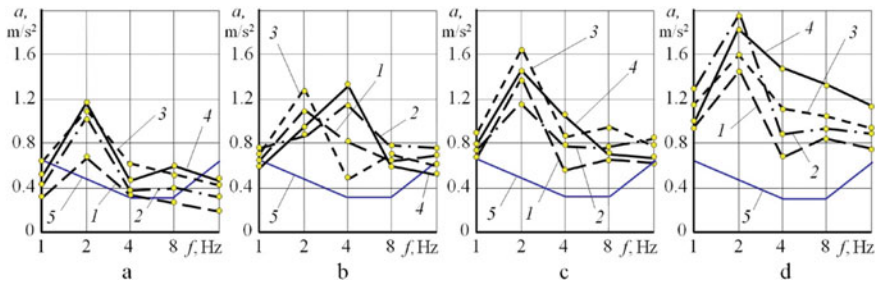


Fig. 3 Root mean square values of vertical accelerations on the driver’s seat when the T-150 K tractor moves in different gears with the 1-PTS-9 semi-trailer on a dirt road. **a** in 5th gear. **b** in 6th gear. **c** in 7th gear. **d** in 8th gear; 1—HTZ seat; 2—seat by Bustrem; 3—serial seat; 4—Grammer seat; 5—level of permissible fatigue

Table 2 Experimental data on vibration loading of wheeled tractors at a travel speed of 10 ... 12 km/h on one agricultural agrophone

Tractor brand	Springs stiffness, kgf/cm	Front suspension			Rear suspension		
		Frequency, Hz					
		Calculated	Experimental	Difference, %	Calculated	Experimental	Difference, %
T-40 rel. 1962	600	3.9	4.1	5	2.9	3.27/4.6	11.3
	∞	–	–	–	2.9	3.19/4.5	9.1
T-40 rel. 1963	600	4.21	4.51	6.7	3.02	3.43/4.8	11.6
MTZ-7M	1500	3.24	3.43	5.6	–	–	–
MTZ-50	580	2.74	2.9	5.5	2.6	3.02/4.3	13.9
MTZ-50	395 (experim.)	2.48	2.65	6.4	2.6	2.89/4.1	10

Note the frequency of the end of the resonance zone is indicated through a fraction

can make resonant vibrations on the rear tires when performing various works in the following ranges of travel speeds:

- 12–30 km/h—when performing transport work on dirt roads;
- 5–7 km/h—when performing agricultural operations in the field for sugar beets;
- 5–9 km/h—when performing agricultural operations in the field for sunflowers;
- 6–12 km/—when performing agricultural operations in the field for potatoes;
- 8–15 km/h—when performing agricultural operations in the field for sweet corns.

K-700 and T-150 K tractors are not WSV since they have spring suspension. Suspension complicates the design, but makes tractors more suitable for transport work on dirt roads and agricultural operations in the fields, since they have a lower natural frequency (in the range of 1.8–2.0 Hz). When performing transport work, they have resonant vibrations on dirt roads only when driving at low speed in the range of 9–12 km/h.

Table 3 Experimental data on vibration loading of wheeled tractors at a travel speed of 10 ... 12 km/h on one agricultural agrophone

Travel speed, km/h (m/s)	Disturbance frequency, Hz						
	Soil background						
	Dirt road	Sugar beet field	Sunflower field	Potato field	Corn field	Cross-furrow travel	Stubble of spikes
4 (1.1)	0.55–1.1	2.4	1.8	1.57	1.2	3.14–3.66	7.2
5 (1.4)	0.7–1.4	3.1	2.3	2	1.5	4–4.7	9.4
6 (1.66)	0.8–1.7	3.7	2.8	2.4	1.85	4.7–5.5	11
7 (1.94)	0.97–1.9	4.3	3.2	2.8	2.16	5.5–6.48	12.5
8 (2.2)	1.1–2.2	4.9	3.7	3.17	2.47	6.3–7.4	14.8
9 (2.5)	1.25–2.5	5.5	4.16	3.57	2.77	7.14–8.33	16.5
12 (3.3)	1.6–3.3	7.4	5.5	4.7	3.7	9.5–11.1	22
15 (4.2)	02-Apr	9.3	7	6	4.7	Dec-14	28
30 (8.4)	04-Aug	18.6	14	12	9.4	24–28	56
45 (12.6)	06-Dec	27.9	21	18	14.1	36–42	84

Note the frequencies of the disturbing effect of a dirt road and various fields, included in the resonance zone of the rear suspension of tractors, are shown in bold

Since transport work is performed at speeds 2–3 times higher, then resonant vibrations will be unlikely, and the higher the speed, the lower the probability of resonance. When performing agricultural operations in the fields, resonant vibrations of these tractors can also occur only at speeds below 7 km/h, and at higher speeds, they are also unlikely. However, the experience of operating and studying the smooth running of various vehicles on various roads shows that the accelerations affecting the driver become bigger with an increase in the driving speed and can exceed the standard values.

3 Conclusions

Analysis of the smooth running of WSV (YuMZ, MTZ-50, MTZ-7 M, T-40, K-700, and T-150 K), which was based on experimental studies obtained by NATI and other research organizations, showed the following:

- the vibration damping properties of tires are very low due to their narrow width and very steep resonance;
- YUMZ, MTZ-50, MTZ-7 M, and T-40 domestic wheeled tractors can perform resonant vibrations on tires in all considered operating conditions;
- the smooth running of YuMZ, MTZ-50, MTZ-7 M, and T-40 domestic wheeled tractors is unsatisfactory, and RMS of the vertical accelerations of domestic tractors bodies is up to 4.5 times higher than the permissible level;

- K-700 and T-150 K tractors are not WSV since they have a spring suspension, which complicates the design, but makes them more suitable for performing transport operations on dirt roads and agricultural operations in the fields.

References

1. Ryabov IM, Pozdeev AV et al (2014) Vibrozashchitnye svojstva pnevmaticheskikh shin bespodvesochnyh mashin i puti ih povysheniya (Vibration-protective properties of pneumatic tires of suspensionless vehicles and ways to improve them). *Avtomobil'naya promyshlennost'* (Automotive Industry) 8:20–22
2. Sokolov AYü (2014) Povyshenie vibrozashchitnykh svojstv shin za schet vnutrennej pnevmaticheskoy dempfirmuyushchej sistemy (Improvement of vibroprotective properties of tires due to internal pneumatic damping system) Dissertation of Candidate of technical sciences, Volgograd State Technical University, p 149
3. Ryabov IM, Pozdeev AV et al (2015) Rezul'taty issledovaniy vibrozashchitnykh svojstv shiny s vnutrennej pnevmaticheskoy dempfirmuyushchej sistemoy (Research results of vibration-protective properties of a tire with an internal pneumatic damping system). *Shina Plus* (Ukraine) 3:8–10
4. Pozdeev AV et al (2019) Theoretical research of impact of the changed elastic and damping parameters of vehicle tyres and loading on the wheels breakaway time from the cobblestone road. In: IOP conference series: materials science and engineering, vol 632. International conference on innovations in automotive and aerospace engineering: proceedings, Irkutsk National Research Technical University. IOP Publishing, p 7. <https://doi.org/10.1088/1757-899X/632/1/012059>
5. Pozdeev AV et al (2020) Perspectives of increasing smooth ride of wheeled vehicles without suspension with pneumatic damping system. In: IOP conference series: materials science and engineering, vol 820. Design Technologies for Wheeled and Tracked Vehicles (MMBC) 2019, Moscow, Russian Federation, IOP Publishing, p 8. <https://doi.org/10.1088/1757-899X/820/1/012036>. <https://iopscience.iop.org/issue/1757-899X/820/1>
6. Brundza IA (1975) Issledovanie nizkochastotnykh kolebaniy traktora T-25 pri vypolnenii s/h rabot i razrabotka meropriyatij po snizheniyu vozdejstviya kolebaniy na voditelya (Study of low-frequency vibrations of the T-25 tractor during agricultural work and the development of measures to reduce the impact of vibrations on the driver) Dissertation of Candidate of technical sciences, Kaunas, p 150
7. Arutyunyan VS (1983) Obosnovanie parametrov i razrabotka konstrukcij tipovogo treka dlya ispytaniy kolesnyh sel'skohozyajstvennykh traktorov po ocenke vibracii (Substantiation of parameters and development of designs of a typical track for testing wheeled agricultural tractors for vibration assessment). Dissertation abstract of Candidate of technical sciences, Moscow, p 24
8. Biblyuk NI et al (1986) Vliyanie parametrov sistemy podressorivaniya na plavnost' hoda transportnoj mashiny na baze traktora T-150K (Influence of the parameters of the suspension system on the smooth running of the transport vehicle based on the T-150K tractor). *Mashiny i orudiya dlya mekhanizacii lesozagotovok i lesnogo hozyajstva* (Machines and tools for the mechanization of logging and forestry). Interuniversity collection of scientific papers, LTA, pp 23–28
9. Kalchenko BI et al (1987) Kompleksnaya ocenka dinamicheskoy ustojchivosti i plavnosti hoda kolesnykh traktorov (Comprehensive assessment of the dynamic stability and smooth running of wheeled tractors). *Traktory i sel'hozmashiny* (Tractors and agricultural machines) 7:6–10

10. Korobeinikov AT, Likhachev VS, Sholokhov VF (1985) Ispytaniya sel'skohozyajstvennykh traktorov (Agricultural tractor testing). Mashinostroenie Publ., Moscow, p 239
11. Khudorjokov SI (1998) Puti povysheniya effektivnosti kolesnykh traktorov maloj moshchnosti (Ways to Improve the efficiency of low power wheeled tractors). Dissertation of Doctor of technical sciences, Kurgan, p 316
12. Vliyanie vibracij na organizm cheloveka (The influence of vibrations on the human body) (1977) Academy of Sciences of the USSR. State Scientific Research Institute of Mechanical Engineering named after Academician A.A. Blagonravova. Nauka, Moscow, p 447
13. Vibracii v tekhnike. Tom 6. Zashchita ot vibracij i udarov (Vibrations in technology. Volume 6. Protection against vibrations and shocks) (1981). In: Frolov KV (ed). Mashinostroenie Publ., Moscow, p 456
14. GOST 31191.1-2004 (ISO 2631-1:1997) Vibraciya i udar. Izmerenie obshchej vibracii i ocenka ee vozdejstviya na cheloveka. Chast' 1. Obshchie trebovaniya (Vibration and shock. Measurement of general vibration and assessment of its impact on humans. Part 1. General requirements)
15. Vibracii v tekhnike. Tom 3. Zashchita ot vibracij i udarov (Vibrations in technology. Volume 3. Protection against vibrations and shocks) (1980). In: Frolov KV (ed). Mashinostroenie Publ., Moscow, p 544
16. Pevzner Ya M et al (1979) Vehicle vibrations: Tests and research. In: Pevzner Ya M (ed) Mechanical Engineering, Moscow, p 208
17. Novikov VV et al (2013) Stendy dlya ispytaniya podvesok nazemnykh transportnykh sredstv (Rigs for testing of suspensions of land vehicles). Volgograd State Technical University, Volgograd, p 114
18. Novikov VV, Pozdeev AV, Diyakov AS (2015) Research and testing complex for analysis of vehicle suspension units. In: Radionov AA (ed) Procedia engineering, international conference on industrial engineering (ICIE-2015), Elsevier publishing 129:465–470. <https://doi.org/10.1016/j.proeng.2015.12.153>
19. Popov DA et al (1974) Sistemy podressorivaniya sovremennykh traktorov (Suspension systems for modern tractors). Mashinostroenie Publ, Moscow, p 176
20. Zayac YaI et al (1974) Vibronagruzhennost' rabochih mest traktoristov kolesnykh sel'skohozyajstvennykh mashin pri vozdejstvii NSK (Vibration loading of workplaces of tractor drivers of wheeled agricultural machines under the influence of NSC). Vliyanie vibracii na organizm cheloveka i problemy vibrozashchity (The influence of vibration on the human body and the problems of vibration protection). Nauka, Moscow, pp 37–43
21. Chernyshev VI (1994) Uluchshenie uslovij truda operatorov transportnykh sredstv putem razrabotki i realizacii vibrozashchitnykh sistem s impul'snym upravleniem (Improving the working conditions of vehicle operators through the development and implementation of vibration protection systems with impulse control). Dissertation of Doctor of technical sciences, St. Petersburg, p 458
22. Pobedin AV (1994) Proektirovanie vibroshumoizolyacii traktornoj kabiny (Design of vibration and noise isolation of a tractor cab). VSTU, Volgograd, p 92



Improvement of the Performance Properties of the Wheel with a Pneumatic Tire Due to the Internal Elastic Damping System

I. M. Ryabov, A. V. Pozdeev^(✉), and V. V. Erontaeв

Volgograd State Technical University, 28, Lenin Ave., Volgograd 400005, Russia

Abstract. This article is devoted to improving the performance of a wheel with a pneumatic tire due to the internal elastic damping system. Pneumatic tires have low vibration resistance due to high rigidity and low damping. The solution to this scientific problem is of great interest, especially for wheeled suspensionless vehicles. The ways of increasing the vibration protective properties of pneumatic tires are considered. The description of a wheel with an internal pneumatic elastic damping system is presented. The principle of operation of a wheel with a mechanism with negative stiffness is shown, its elastic characteristics are given, including at elevated pressure. A formula for calculating the stiffness of the elastic characteristic is obtained. On the basis of calculations, it has been proved that for the proposed pneumatic wheel, the rigidity of the elastic characteristic decreases 2.28 times at a pressure suspended by 20%.

Keywords: Wheel · Pneumatic tire · Elastic characteristic · Mechanism with negative stiffness

1 Introduction

Pneumatic tires for suspensionless machines (SM) such as wheeled tractors, combines, agricultural, road-building, and other special machines, are the only elements that protect the frame from vibration, resulting from the interaction of wheels with irregularities of fields and roads. However, pneumatic tires have low vibration protective properties due to their high stiffness and poor damping [1–5]. Operating experience of SM [6–11] and the studies carried out [12–20] show, that when performing transportation and technological operations, SM have insufficient smoothness of the ride, because they do not ensure compliance with the norms of vibration loading of the operator, even when driving on low worn roads. Vibrations of agricultural machinery in the fields increase the tire pressure on the soil, which reduces yields. Long-term vibration action on machine operators causes occupational diseases, which reduces their quality of life and the prestige of their profession. Due to the low vibration protective properties of tires, SM move at a low speed and create road congestions, which reduce their throughput, lead to an increase in the risk of accidents and deterioration of the functioning of transport. In this regard, an increase in the vibration protective properties of a wheel with a pneumatic tire for SM due to an internal elastic damping system is of great interest.

2 Ways to Increase the Vibration Properties of Tires

One of the ways to improve the vibration protective properties of a wheel with a pneumatic tire is to reduce the pressure in the tire to reduce its rigidity [21–28]. Figure 1 shows the dependence of the resonance amplitudes of displacements and accelerations of the rear part of the frame of the T-40 tractor on the stiffness of the tires of the driving wheels. Analysis of Fig. 1 shows that a decrease in the tire stiffness of the driving wheels of the T-40 tractor leads to a decrease in the resonance amplitudes of displacements (curve 1) and accelerations (curve 2). However, the range of change in tire stiffness with the allowable change in tire pressure (shaded area) is very narrow.

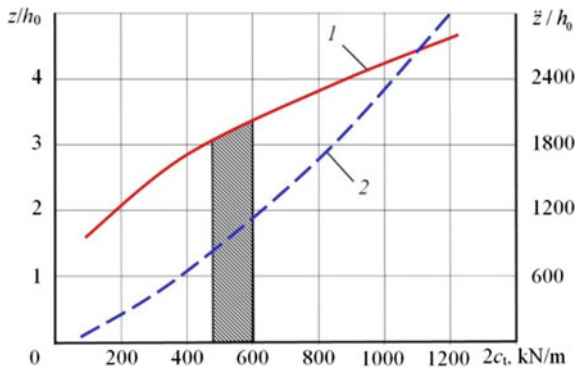


Fig. 1 Dependences of the resonance amplitudes of displacements (curve 1) and accelerations (curve 2) of the rear part of the frame of the T-40 tractor on the stiffness of the tires of the driving wheels (the shaded area is the range of changes in tire stiffness with an allowable change in tire pressure)

Thus, due to decrease in the pressure in the tires, it is impossible to solve the problem of increasing the vibration protective properties of wheels with a pneumatic tire. Therefore, the authors of the article proposed another way to solve it.

On the basis of the patent [29], a wheel with an internal elastic damping system (IEDS) was developed, with a mechanism with negative stiffness (MNS) [30] (Fig. 2).

A wheel with IEDS (Fig. 2) contains a rim 1 and a pneumatic tire 2, in the cavity of which an elastic shell 3, which does not rotate relative to the car, is installed, truncated in the lower part 4. It rests on the rim by means of rollers 5, fixed on it, and divides the tire cavity into two cavities: *A*—shell cavity 3 and *B*—annular working cavity of the tire 2. In the lower part, the shell 4 has a lock 6, which facilitates its installation into the tire.

The elastic shell is a pneumatic damping system and has valves with orifice holes 7 through which cavities *A* and *B* communicate. In the lower part of the elastic shell, a bracket 8 is fixed with two levers 9, which have rollers 10 at the ends, and a hydraulic absorber 11 and rods 12 are hinged between the levers, forming a rhombic four-link mechanism with the levers—a mechanism with negative stiffness (MNS). It presses the rollers 10 to the side surfaces of the tire by means of a tension spring 13, connecting the hinge between the rods 12 with a bracket 14, fixed to the shell. To reduce stresses at

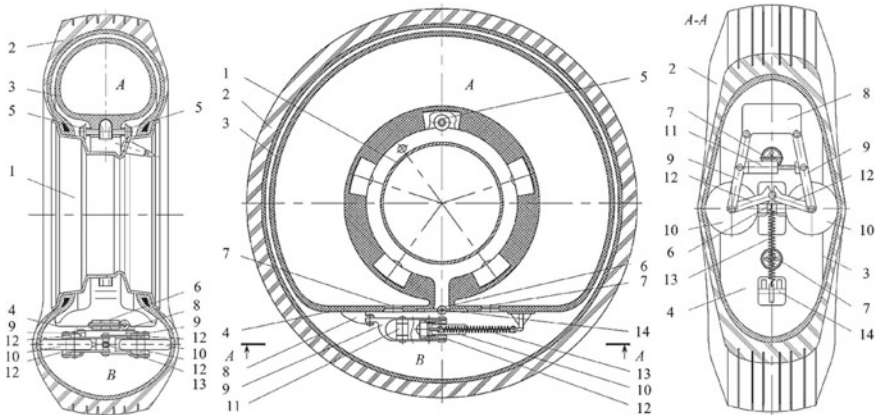


Fig. 2 Wheel with an internal elastic damping system (IEDS) containing a mechanism with negative stiffness (RF patent No. 179290): A—shell cavity; B—annular working cavity of the tire; 1—rim; 2—pneumatic tire; 3—elastic shell; 4—truncated part of the elastic shell; 5—rollers; 6—lock; 7—throttling hole; 8—bracket; 9—lever; 10—roller; 11—hydraulic shock absorber; 12—thrust; 13—tension spring; 14—bracket

the place of contact between the rollers 10 and the sidewalls of the tire 2, the working surface of the rollers 10 is made in the form of a torus part and has a coating with a low friction coefficient.

When the weight of the vehicle is applied to the wheel, the sidewalls of the tire 2 are deformed, forming concave surfaces inside the tire. When the wheel rolls, the rollers 10, pressed by the spring to the side surfaces of the tire, turn the shell together with the tire. The rollers, being at the bottom, go into the deformed sidewalls of the tire under the action of the spring and provide a stable holding of the shell in position with the truncated part 4 downward when the wheel rolls. This is due to the fact that when deviating from this position, the rollers 10 move into the zone of lesser deformation of the tire sidewalls and tend to return to the area of maximum deformation.

To calculate the mechanism with negative stiffness, the design scheme, shown in Fig. 3, was used.

The balance of forces in Fig. 3 implies

$$F_r \sin \gamma = F_{spr1} \cos \gamma; \tag{1}$$

$$F_r d = F_{spr1} e; \tag{2}$$

$$F_r (d_0 - z) = F_{spr1} (e_0 + x); \tag{3}$$

$$F_r (d_0 - z) = (F_{spr10} + k_{spr1z})(e_0 + x); \tag{4}$$

$$F_{r0} d_0 = F_{spr10} e_0. \tag{5}$$

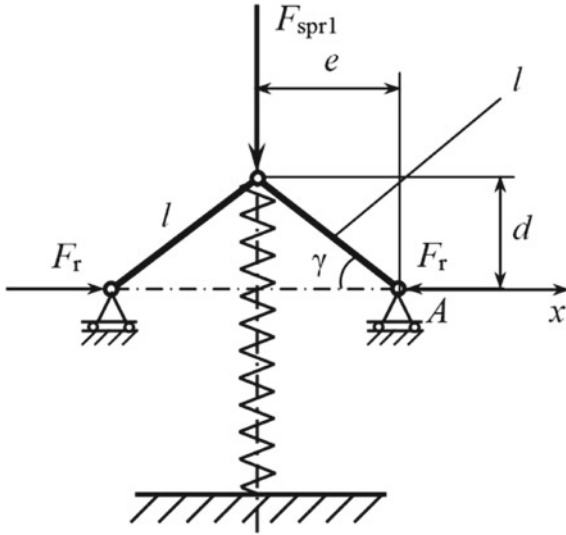


Fig. 3 Design diagram of mechanism with negative stiffness: l —length of the lever on which the roller is installed; γ —angle of inclination of the roller lever of length l relative to the x -axis; x —axis along which the rollers expand; F_{spr1} —current force of the rollers expansion caused by the tension spring; F_r —current force from the action of the roller on the inner surface of the tire; d —vertical projection of the distance from point A of the roller action to the connection point of the two roller arms in the current position; e —horizontal projection of the distance from point A of the roller action to the point of connection of two roller arms in the current position

where z —axis along which the tension spring acts; F_{spr10} —static force of the rollers expansion caused by the tension spring; F_r —static force from the action of the roller on the inner surface of the tire; k_{spr1} —stiffness of the tension spring; d_0 —vertical projection of the distance from the point A of the roller action to the connection point of the two roller arms in a static position; e_0 —horizontal projection of the distance from point A of the roller action to the connection point of the two roller arms in a static position.

Let us set

$$d_0 - z = \sqrt{l^2 - (e_0 + x)^2}, \tag{6}$$

$$z = d_0 - \sqrt{l^2 - (e_0 + x)^2}. \tag{7}$$

Then, the force of the rollers can be determined by the formula

$$F_r = \frac{(F_{spr10} + k_{spr1}z)(e_0 + x)}{d_0 - z}. \tag{8}$$

The design scheme of the tire is presented in the form of a four-link hinge mechanism, inscribed in it (Fig. 4).

The balance of forces in Fig. 4 implies

$$F_r b = F c; \tag{9}$$

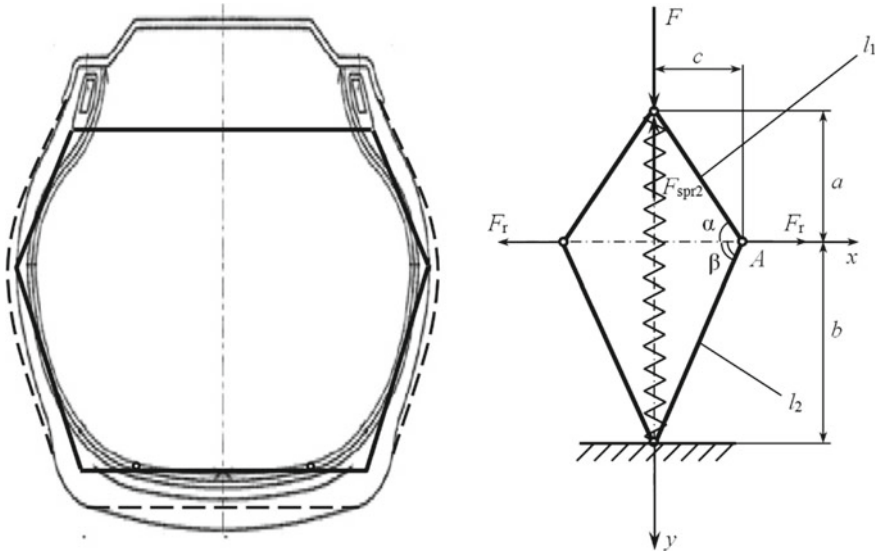


Fig. 4 Design diagram of the tire in the form of a four-link hinge mechanism inscribed in it: a —vertical projection of the distance from point A of the roller action to the wheel rim in the current position; b —vertical projection of the distance from point A of the roller action to the supporting surface (or to the tread) in the current position; c —horizontal projection of the distance from point A of the roller action to the vertical axis in the current position; y —vertical axis along which the pneumatic tire is compressed; α, β —the angles of inclination of the sides of the hexagon of length l_1 and l_2 relative to the x -axis; l_1, l_2 —the lengths of the sides of the hexagon; F_{spr2} —current wheel compression force caused by the air pressure in the tire under load; F —external load on the tire; F_r —current force from the action of the roller on the inner surface of the tire

$$F_r(a_0 - y_1) = (F_{spr2} - F)(c_0 + x); \tag{10}$$

$$F_r(a_0 - y_1) = (F_{spr20} + k_{spr2}y - F)(c_0 + x); \tag{11}$$

$$y = a_0 + b_0 - \sqrt{l_1^2 - (c_0 + x)^2} - \sqrt{l_2^2 - (c_0 + x)^2}, \tag{12}$$

where a_0 —vertical projection of the distance from point A of the roller action to the wheel rim in a static position; b_0 —vertical projection of the distance from the point A of the roller action to the supporting surface (or to the protector) in a static position; c_0 —horizontal projection of the distance from point A of the roller action to the vertical axis in a static position; F_{spr20} —static force of compression of the wheel caused by the air pressure in the tire under load; F_{r0} —static force from the action of the roller on the inner surface of the tire; k_{spr2} —stiffness of the pneumatic tire in the current position.

After transformations, we get

$$F = F_{spr20} + k_{spr2}y - \frac{(F_{spr10} + k_{spr1}(d_0 - \sqrt{l^2 - (e_0 + x)^2}))(e_0 + x)}{(c_0 + x)\sqrt{l^2 - (e_0 + x)^2}} \cdot \left(a_0 - \frac{2b_0y - y^2}{2(a_0 + b_0 - y)}\right) \tag{13}$$

$$F(y) = F_{spr10} \frac{a_0 e_0}{c_0 d_0} + k_{spr2}y - \frac{(F_{spr10} + k_{spr1}(d_0 - \sqrt{l^2 - (e_0 + x)^2}))(e_0 + x)}{(c_0 + x)\sqrt{l^2 - (e_0 + x)^2}} \cdot \left(a_0 - \frac{2b_0y - y^2}{2(a_0 + b_0 - y)}\right), \tag{14}$$

where $x = \sqrt{l^2 - (a_0 - y)^2} - d_0$.

The elastic characteristics of a wheel with IEDS and MNS are shown in Fig. 5.

Elastic characteristic 1 corresponds to a tire pressure of 1.8 atm., and elastic characteristic 2 corresponds to a higher (by 20%) tire pressure. Both elastic characteristics (Fig. 5) in the area of static deformation of the tire have a section of reduced stiffness: 1' and 2', respectively. Below the x -axis, the elastic characteristic of the MNS is plotted for the standard tire pressure (curve 3) and increased pressure (curve 3').

The stiffness of the linear elastic characteristic of a tire can be calculated by the formula

$$c_t = 10000\pi^2 / \lambda_{st}, \tag{15}$$

where c_t —stiffness of the tire; λ_{st} —reduced static deformation of the tire.

From Formula (15), it follows that the ratio of the stiffnesses of linear elastic characteristics is inversely proportional to the ratio of their reduced static dips. Then, after performing the measurements in Fig. 5 of reduced dips of elastic characteristic 2 with and without a soft section, we get the ratio

$$\lambda'_{st} / \lambda_{st} = 2.28 \tag{16}$$

Thus, IEDS with MNS in the soft section reduces the stiffness of the elastic characteristics of the tire by 2.28 times, and this result was obtained for a tire with a 20% increased pressure, i.e., with less static deformation and rolling resistance.

3 Conclusions

Thus, the proposed wheel with IEDS allows to improve the following performance properties of tires and SM:

- to increase the vibration protective properties of the tire by reducing the stiffness and combined air and hydraulic damping, which improves the smoothness of the ride of the SM;
- to reduce the rolling resistance of the tire, by reducing its static deformation, which improves the fuel efficiency of the SM.

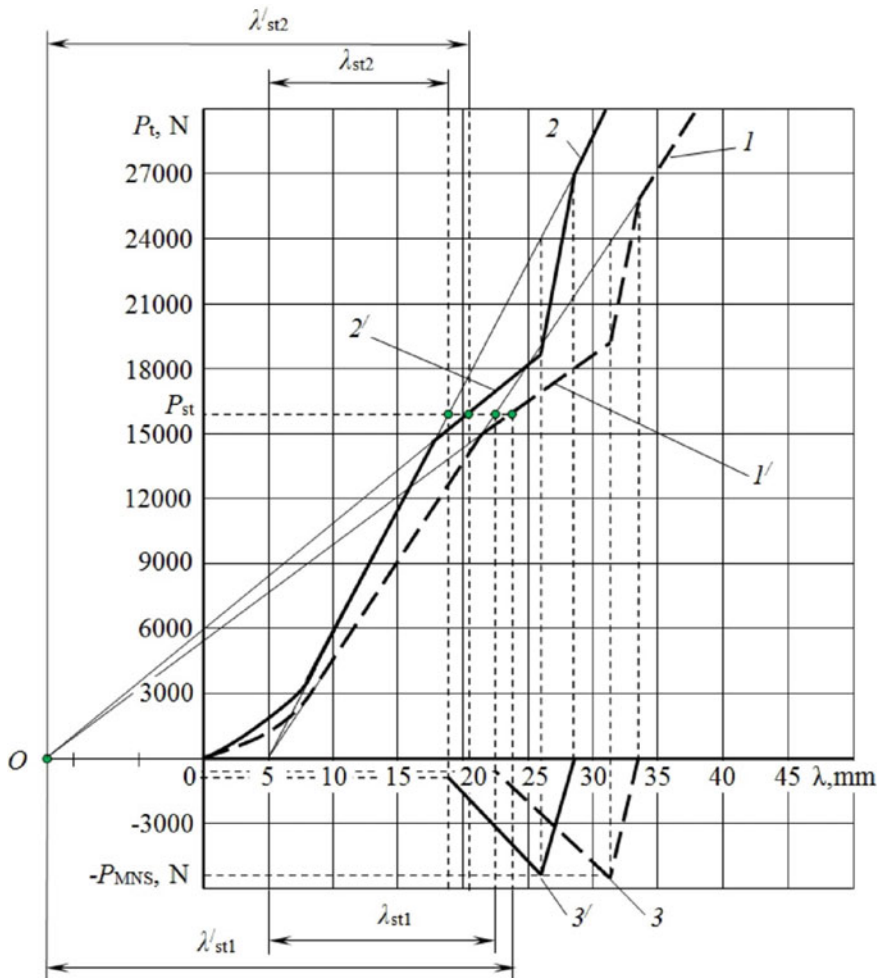


Fig. 5 Elastic characteristics of the rear wheel of the T-40 tractor with IEDS and MNS: 1, 2—elastic characteristics of the tire at standard (1.8 atm.) pressure and increased by 20% (2.16 atm.) pressure; 1', 2'—areas of reduced rigidity; 3, 3'—elastic characteristics of MNS; λ_{st1} and λ'_{st1} —reduced static deformations of a classic tire; λ_{st2} and λ'_{st2} —reduced static deformations of the tire with MNS; P_{st} —static load on the tire

References

1. Yatsenko NN, Prutchikov OK (1969) Plavnost' hoda gruzovyh avtomobilej (Smoothness of the course of trucks). Mashinostroenie Publ., Moscow, p 219
2. Rotenberg RV (1972) Podveska avtomobilya (Car suspension). Mashinostroenie Publ., Moscow, p 392
3. Khachaturov AA et al (1976) Dinamika sistemy doroga—shina—avtomobil'—voditel' (System dynamics road—tire—vehicle—driver). In: Khachaturov AA (ed). Mashinostroenie Publ., Moscow, p 535

4. Yatsenko NN (1978) Pogloshchayushchaya i sglazhivayushchaya sposobnost' shin (Tire absorption and smoothing capacity). Mashinostroenie Publ., Moscow, p 133
5. Knoroz VI et al (1976) Rabota avtomobil'noj shiny (Car tire operation). Transport, Moscow, p 238
6. Brundza IA (1975) Issledovanie nizkochastotnyh kolebanij traktora T-25 pri vypolnenii s/h rabot i razrabotka meropriyatij po snizheniyu vozdeystviya kolebanij na voditelya (Study of low-frequency vibrations of the T-25 tractor during agricultural work and the development of measures to reduce the impact of vibrations on the driver). Dissertation of Candidate of technical sciences, Kaunas, p 150
7. Arutyunyan VS (1983) Obosnovanie parametrov i razrabotka konstrukcij tipovogo treka dlya ispytaniy kolesnyh sel'skohozyajstvennyh traktorov po ocenke vibracii (Substantiation of parameters and development of designs of a typical track for testing wheeled agricultural tractors for vibration assessment). Dissertation abstract of Candidate of technical sciences, Moscow, p 24
8. Biblyuk NI et al (1986) Vliyanie parametrov sistemy podressorivaniya na plavnost' hoda transportnoj mashiny na baze traktora T-150K (Influence of the parameters of the suspension system on the smooth running of the transport vehicle based on the T-150K tractor). Mashiny i orudiya dlya mekhanizacii lesozagotovok i lesnogo hozyajstva (Machines and tools for the mechanization of logging and forestry). Interuniversity collection of scientific papers, LTA, p 23–28
9. Kalchenko BI et al (1987) Kompleksnaya ocenka dinamicheskoy ustojchivosti i plavnosti hoda kolesnyh traktorov (Comprehensive assessment of the dynamic stability and smooth running of wheeled tractors). Traktory i sel'hozmashiny (Tractors Agric Mach) 7:6–10
10. Korobeinikov AT, Likhachev VS, Sholokhov VF (1985) Ispytaniya sel'skohozyajstvennyh traktorov (Agricultural tractor testing). Mashinostroenie Publ., Moscow, p 239
11. Khudorjokov SI (1998) Puti povysheniya effektivnosti kolesnyh traktorov maloj moshchnosti (Ways to Improve the efficiency of low power wheeled tractors). Dissertation of Doctor of technical sciences, Kurgan, p 316
12. Ryabov IM, Chernyshov KV, Sokolov AYu (2007) Matematicheskaya model' koleasa s pnevmaticheskoy dempfiroyushchej sistemoy dlya bespodvesochnyh mashin (Mathematical model of a wheel with a pneumatic damping system for suspensionless machines). Izvestia VolgGTU, Series "Ground transport systems" 2(8):51–53
13. Ryabov IM, Pozdeev AV et al (2014) Koleso s vnutrennej pnevmaticheskoy dempfiroyushchej sistemoy i issledovanie ego dinamicheskogo gasitelya (A wheel with an internal pneumatic damping system and a study of its dynamic damper). Izvestia VolgGTU, Series "Ground transport systems" 3(130):37–41
14. Ryabov IM, Pozdeev AV et al (2014) Effektivnaya ploshchad' pnevmaticheskoy shiny i metodika opredeleniya zakona ee izmeneniya pri vertikal'noj deformacii (Effective area of a pneumatic tire and a method for determining the law of its change in vertical deformation). Gruzovik (Truck) 6:29–33
15. Ryabov IM, Pozdeev AV et al (2014) Vibrozashchitnye svoystva pnevmaticheskikh shin bespodvesochnyh mashin i puti ih povysheniya (Vibration-protective properties of pneumatic tires of suspensionless vehicles and ways to improve them). Avtomobil'naya promyshlennost' (Auto Ind) 8:20–22
16. Sokolov AYu (2014) Povyshenie vibrozashchitnyh svoystv shin za schet vnutrennej pnevmaticheskoy dempfiroyushchej sistemy (Improvement of vibroprotective properties of tires due to internal pneumatic damping system). Dissertation of Candidate of technical sciences, Volgograd State Technical University, p 149

17. Ryabov IM, Pozdeev AV et al (2015) Rezul'taty issledovaniy vibrozashchitnyh svoystv shiny s vnutrennej pnevmaticheskoy dempfiruyushchej sistemoy (Research results of vibration-protective properties of a tire with an internal pneumatic damping system). *Shina Plus (Ukraine)* 3:8–10
18. Ryabov IM, Pozdeev AV et al (2019) Razrabotka metoda polucheniya uchastka ponizhennoj zhestkosti na uprugoj karakteristike avtomobil'noj shiny (Development of a method for obtaining a site of reduced stiffness on the elastic characteristic of an automobile tire). *Traktory i sel'hozmashiny (Tractors Agric Mach)* 6:36–47
19. Pozdeev AV et al (2019) Theoretical research of impact of the changed elastic and damping parameters of vehicle tyres and loading on the wheels breakaway time from the cobblestone road. In: *IOP conference series: materials science and engineering*, vol 632. International conference on innovations in automotive and aerospace engineering: proceedings, irkutsk national research technical university. IOP Publishing, p 7. <https://doi.org/10.1088/1757-899X/632/1/012059>
20. Pozdeev AV et al (2020) Perspectives of increasing smooth ride of wheeled vehicles without suspension with pneumatic damping system. In: *iop conference series: materials science and engineering*, vol 820. Design technologies for wheeled and tracked vehicles (MMBC) 2019. IOP Publishing, Moscow, Russian Federation, p 8. <https://doi.org/10.1088/1757-899X/820/1/012036>
21. Balabin IV, Chabunin IS, Gruzdev AS (2014) Vliyaniye vnutrennego davleniya vozduha v shinah na ih nagruzochnyy rezhim (Influence of internal air pressure in tires on their loading conditions). *Zhurnal avtomobil'nyh inzhenerov (J Automot Eng)* 2(85):32–35
22. Evzovich VE, Raibman PG (2010) *Avtomobil'nye shiny, diski i obod'ya (Car tires, wheels and rims)*. Avtopolis-plus, Moscow, p 144
23. Klennikov EV (1979) *Shiny legkovykh avtomobilej (Passenger car tires)*. Transport, Moscow, p 48
24. Damzen VA (2009) *Povysheniye bezopasnosti i resursa avtomobil'nykh shin (Improving the safety and resource of car tires)* Dissertation of Candidate of technical sciences, Saratov State Technical University, p 152
25. Biderman VL, Guslitsler RL (1963) *Avtomobil'nye shiny (konstrukciya, raschet, ispytaniya, ekspluatatsiya) (Car tires (design, calculation, testing, operation))*. Goskhimizdat Publ., Moscow, p 384
26. Mityanin PI (1974) *Issledovaniye pogloshchayushchej i sglazhivayushchej sposobnosti shiny pri kolebaniyakh gruzovykh avtomobilej (Investigation of the absorbing and smoothing capacity of a tire during vibrations of trucks)*. Dissertation of Candidate of technical sciences, Moscow, p 154
27. Popov DA et al (1974) *Sistemy podressorivaniya sovremennykh traktorov (Suspension systems for modern tractors)*. Mashinostroenie Publ., Moscow, p 176
28. Zayac YaI et al (1974) *Vibronagruzhennost' rabochih mest traktoristov kolesnykh sel'skohozyajstvennykh mashin pri vozdejstvii NSK (Vibration loading of workplaces of tractor drivers of wheeled agricultural machines under the influence of NSK)*. Vliyaniye vibratsii na organizm cheloveka i problemy vibrozashchity (The influence of vibration on the human body and the problems of vibration protection). Nauka, Moscow, p 37–43
29. Ryabov IM (1998) *Koleso transportnogo sredstva (Vehicle wheel)*. RF Patent for invention 2,108,240, 1998
30. Ryabov IM, Pozdeev AV (2018) *Koleso transportnogo sredstva (Vehicle wheel)*. RF Utility model patent 179,290, 2018



Drive Axle of Vehicle and Environment Impact

A. Yu. Barykin¹(✉), M. M. Mukhametdinov², and R. Kh. Takhaviev¹

¹ Naberezhnye Chelny Institute (Branch) of Kazan (Volga Region) Federal University, 68/19, Prospekt Mira, Naberezhnye Chelny 423812, Russia

² Individual Entrepreneur, Naberezhnye Chelny 423800, Russia

Abstract. An automated blocking of inter-axial or inter-wheel differentials eliminates any chance of power circulation occurrence or additional loading of transmission units, which makes part service lives longer. To reduce the expenses which multiply as the operation and maintenance stages of vehicle units and systems approximate, it is necessary to take into account a whole set of driver's influence options, environmental influence, power, and chassis devices influences already at the design of advanced structures. The simplest option of a discrete differential represents a self-blocking small friction differential equipped with a forced manual blocking device. The conducted research allows speaking about a small probability of power circulation under high aggregate resistance towards motion, irregular distribution of weight, and rotation torque on the axes. The most complex cases of the drive-axle part loading are operating modes during winter at the action of extremely low temperatures as well as the operation in summer and action of high temperatures, dust, and other environmental factors.

Keywords: Drive axle · Differential · Blocking · Transmission oil · Winter conditions · Operating temperature

1 Introduction

Assessment of the influence of external factors of operation of wheeled vehicles should be based on a systematic approach. In particular, the main factors of the truck operating mode should be taken into account:

- Blocking coefficient of differential mechanisms of drive axles. Its value is closely related to the criteria for the operational properties of the car, which leads to a change in operating efficiency in difficult conditions [1].
- Current gear oil temperature. A change in temperature can lead to a decrease in the operational properties of the oil, which will lead to a reduction in the resource of parts [2].

The application of a systematic approach allows taking into account the influence of the following significant factors: control module, driver, power unit, transmission, road, and environment. This technique allows us to establish new significant relationships in the operational process of the drive axle [3–5]. The paper [6] proposed a classification for

external influences in a system taking into account a third-party influence on the operation conditions of a truck drive axle. In particular, the authors conducted bench tests of truck units and obtained important experimental data facilitating the specification of the links in the considered system. It is extremely important to evaluate the current condition and the residual life of such components by means of on-board controls and continuous monitoring of operating parameters [2].

The influence of the elements of the system of interaction of the car with the road and the environment is complex and mutual [6].

- Increasing the cross-country ability of the car by blocking the differentials can lead to additional loading of the transmission components [7]. This phenomenon is called power circulation. Significant losses in a locked transmission occur when driving on a road with a high grip coefficient.
- Untimely or improper replacement of gear oil can shorten the life of parts [6]. A similar phenomenon will occur with deviations of the gaps or preliminary forces in the joints when exposed to low temperatures. The most negative effect is to reduce the stiffness of the main gear.
- The factor that complicates the operation of the system is the influence of the driver. For example, abrupt engagement of the clutch leads to dynamic loading of the gearbox. Increased torque can also be transmitted to the cardan gear. Untimely gear changes can also have a negative impact on the operation of the drive axle. The drive-axle control in automatic mode must be carried out taking into account these factors. [8].
- In summer, the drive-axle parts often fail due to the elevated oil temperature and poor lubricating properties. Oil leakage through seals is also possible due to a significant decrease in viscosity. In the winter time of operation, there is an increase in the viscosity of the oil, which is the cause of large friction losses. It is necessary to take into account the negative effect of snow cover on the road and on the surface of transmission units. For example, see Fig. 1.

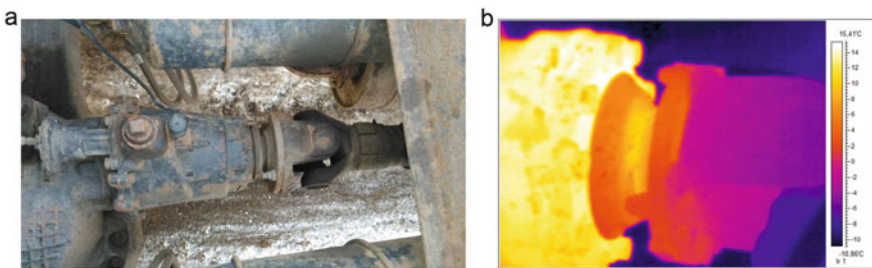


Fig. 1 a Transmission in winter operation. b Thermogram of transmission units

2 Methods

The factor complicating the operation of a performance automated control system is a driver's influence. An automated blocking of inter-axial or inter-wheel differentials eliminates any chance of power circulation occurrence or additional loading of transmission units which makes part service lives longer:

$$k_{\text{bvar}} = \frac{R_{z1}\varphi_1 r_{d1} + R_{z1}f_1 r_{d1}}{R_{z2}\varphi_2 r_{d2} + R_{z2}f_1 r_{d2}} \quad (1)$$

k_{bvar} —variable blocking coefficient; R_{z1} —vertical reaction on the lagging wheel; φ_1 —traction coefficient on the lagging wheel; r_{d1} —dynamic radius of the lagging wheel; f_1 —rolling resistance coefficient on the lagging wheel; R_{z2} —vertical reaction on a running wheel; φ_2 —traction coefficient on the running wheel; r_{d2} —dynamic radius of the running wheel; f_1 —rolling resistance coefficient on the running wheel.

A possibility of forced manual blocking means an increase in the cost of a blocking mechanism for an automated differential [10]. Additionally, untimely blocking can cause significant expenses due to unscheduled repair and transmission part replacement.

To reduce the expenses which multiply as the operation and maintenance stages of vehicle units and systems approximate, it is necessary to take into account a whole set of driver's influence options, environmental influence, power, and chassis devices influences already at the design of advanced structures [11–15]. In this case, one shall take a method of a mutual influence of weighty external and internal factors influencing a vehicle as a research basis [1].

The information space of a control system of differential is determined by external (environment, the road) and internal (engine, drive) objects of influence, each of which is possible to characterize by final number of the factors. It is necessary to relate the factors of the automobile, road, environments, duration, character, and amplitude of influence and other factors to them.

The given factors are powerful in a various degrees depending on the influence of a necessary degree of blocking of inter-wheel (inter-axial) contours and from influence against each other. The part of such interrelations is investigated in a sufficient degree, and some of them are groundless neglected. It also relates to the basic restrictions on size of blocking influence for the basic (controllable) groups of the operational properties:

- On a difference of revolutions of wheels of one bridge, turn of a steering wheel, and dynamic course of a suspension bracket (restriction for turn, sliding of wheels, branch of wheels from a basic surface).
- On speed of the automobile, corners of a lateral withdrawal of trunks, turn of a steering wheel, and condition of a road covering (restriction on a condition of safe passage of turn on high speed).
- On speed and amplitude of change of redistribution of the twisting moments, turn of a steering wheel, and condition of a road covering (restriction on a condition of safe passage of turn on a slippery covering).
- On speed and amplitude of change of redistribution of the twisting moments, influence of an environment, and condition of a road covering (restriction of an opportunity of an emergency).

- On presence of the negative twisting moments on conducting wheels (restriction for cases of braking, circulation of parasitic capacity).
- On size of the twisting moments on wheels, total forces of resistance and properties of a basic surface (restriction on a condition of realization of passableness).
- On size and duration of action of the twisting moments on couplings, conditions of work of coupling (differential), and influence of an environment (restriction on a condition of maintenance of effective work of the mechanism of distribution).

The complexity of load redistribution by the road turn passing criteria consists in the fact that a fast change of rotation torques only by the criteria of wheel rotation frequency difference can induce significant change of the rotational capacity, while slow (smooth) change of torques may be inefficient and lead to wheel slipping [9, 10]. Besides, the intensity of such redistribution shall be connected with a specific motion mode and road surface properties which can be additionally influenced by other factors, for example, environmental influence [1]:

$$k_{\text{con}} \leq \frac{M_{\text{res}}}{M_{g \text{ max}}} k_{\text{bcon}} \quad (2)$$

k_{con} —turning criterion; M_{res} —bending moment; k_{bcon} —rational blocking coefficient; $M_{g \text{ max}}$ —maximum friction moment of gear differential.

The simplest option of a discrete differential represents a self-blocking small friction differential equipped with a forced manual blocking device [16]. This option is the most cost-efficient as it is established that a sufficiently small internal friction provides for passability virtually in all cases except for explicitly extreme situations.

The conducted research allows speaking about a small probability of power circulation under high aggregate resistance towards motion, irregular distribution of weight, and rotation torque on the axes [1, 5]:

$$M_z = 0.02 \frac{\chi_i r_k}{\gamma_{pr} (\gamma_1 / \gamma_2 + 1)} - r_k \left(G_a f + G_a \sin \alpha r_k + 0, 5 c_x \rho_v F v_\omega^2 r_k + G_a \delta_{vr} j r_k / g \right) \frac{\gamma_1 / \gamma_2 - 1}{\gamma_1 / \gamma_2 + 1} \quad (3)$$

M_z —circulation moment; χ_i —kinematic mismatch; r_k —wheel radius; G_a —car weight; f —rolling resistance coefficient; α —vehicle angle; c_x —air resistance coefficient; ρ_v —air density; F —car frontal area; v_ω —air speed; δ_{vr} —rotational mass accounting factor; j —car acceleration; g —acceleration of gravity; γ_1 —coefficient of tangential elasticity of the first bridge; γ_2 —coefficient of tangential elasticity of the second bridge; γ_{pr} —reduced tangential elasticity coefficient.

Friction clutch with a program control provides for a fast and accurate change of a friction torque but is a relatively complex and expensive mechanism. Besides, one should take into account that a fact redistribution of rotation torques only by the criteria of rotation frequency difference can cause a significant change in the vehicle cornering ability, while slow redistribution can cause wheel slippage.

The operation mode of a power plant and transmission unit also has a higher value for anective estimation of a drive-axle technical state.

A relative time of gearbox operation at various transmissions defines the value of an equivalent rotation torque transmitted by the main gearing and corresponding reactions in the bearings. This problem has been quite widely covered in scientific papers [17–24]. Suspension dynamic deflection causes the change of the angle between cardan drive shafts and, correspondingly, influences the transmitted rotation torque. If the friction of the wheel with the road is close to zero, it is necessary to fulfill the condition [1]:

$$\begin{cases} M_{e \max} i_{tr} \leq P_{\text{res}} r_k \\ M_{\text{lag}} \leq G_{ki} \varphi_i r_k \end{cases} \quad (4)$$

$M_{e \max}$ —maximum engine torque; i_{tr} —gear ratio from gearbox to wheels; P_{res} —total force of resistance to movement; r_k —wheel rolling radius; M_{lag} —lagging wheel torque; G_{ki} —vertical reaction on the wheel; φ_i —traction coefficient on the lagging wheel.

In this case, the maximum degree of blocking is found by the formula:

$$k_{b \max} \leq \frac{G_{ki} \varphi_i r_k^2 S_{pr}}{I_k (\omega_0 r_k - v_{a \min}) v_a} \quad (5)$$

S_{pr} —length of area where grip is zero; I_k —moment of inertia of the wheel; ω_0 —differential housing speed; $v_{a \min}$ —minimum steady car speed, v_a —current car speed.

A number of parameters of this model shall be specified in the basis of the experimental research data [25]. For example, see Fig. 1.

Further, the authors are going to research the mechanical load influence and evaluate the resulting action of operating conditions onto the wear extent and the main gearing parts' failure probability [26, 27].

Many regions of the Russian Federation (Russia) quite often need vehicle transportation under extremely low ambient temperatures [28, 29]. This problem has been quite widely covered in technical papers [3, 5, 12, 20–23]. In addition, heating under starting conditions does not provide for a rational temperature mode over the whole route [30].

The causes of failures and breakdowns should be sought in the unsatisfactory condition of the parts of the main gear and differential, partially losing strength properties during subcooling [25, 30].

Heating with the heat emitted by burned gases is an efficient and admissible way to warm a vehicle, while it is moving as well. This method is applied for a local heating of certain vehicle units and parts, for example, a damper body. However, a drive-axle heating by this method seems to be a very complex process. In addition, it will be difficult to automatically adjust an operating temperature. Oil level in the drive-axle crankcase adjusted for rotation-induced spattering. The oil volume also has to be adjusted for heating or cooling against the baseline.

Aside from these main parameters, it is imperative to take into account the location of noise/vibration/heat sources in the adopted coordinates.

3 Results and Discussion

The optimum distribution of capacity in an automobile drive represents a rather difficult task. It is determined by a large number of external and internal factors influencing and limiting the choice of the distributing units rational characteristics for construction, cost, and other reasons [1]. The most complex cases of the drive-axle part loading are operating modes during winter at the action of extremely low temperatures as well as the operation in summer and action of high temperatures, dust, and other environmental factors. In both cases, the transmission oil operating condition is far from a proper one causing a whole number of consequences. Apparently, reliable evaluation of the adjustments made by the automatic transmission-process control system requires objective data on the intensity of heat transfer in the drive-axle—environment system [2].

Let us enumerate the wheel drive cold start consequences related to inappropriate condition of transmission oil:

- Significant dynamic loads on the parts and their possible damage caused by an increased fragility and direct interaction of contact surfaces at the semi-dry friction sections;
- Intensive wear of the parts due to high oil viscosity, improper oil mix and distribution on the contact surfaces, oil film damage, and increase in friction forces because of semi-dry friction sections' occurrence;
- An increased fuel consumption caused by the increase of the motion resistance in the drive, both due to additional hydraulic resistances of a more viscous oil and additional mechanical resistances due to inappropriate lubrication and decrease of the mechanical performance factor.

References

1. Barykin AYu (2001) Basics of modern differentials theory. KamPI, Naberezhnye Chelny
2. Barykin AYu, Mukhametdinov MM, Takhaviyev RKh, Samigullin AD (2019) Studying the effects of mechanical loads and environmental conditions on the Drive-Axle performance. In: IOP conference series: materials science and engineering 570:012010. <https://doi.org/10.1007/s001090000086>
3. YeS K, Boldin AP, Vlasov VM et al (2001) Car technical operation: manual for higher education institutions, 4th edn. Nauka, Moscow
4. Lyandenburskiy VV et al (2015) Diagnostics of truck axle drive gears. In: Problems of quality and operation of motor vehicles: operation and development of motor vehicles: Materials of the Xth International virtual scientific and technical conference. PGUAS, Penza, 15 May 2015, pp 199–205
5. Aksenov PV (1989) Multi-axis cars. Mashinostroyeniye, Moscow
6. Barykin AYu, Basyrov RR, Mukhametdinov MM (2014) To issue of system analysis of operating conditions of wheel drives of KAMAZ. Sci Tech Bull Povolzhye 6:74–76
7. Barykin AYu (2004) Self-locking differential gear: probability and methods of the use of road grip of tyre. Avtomobil'naya Promyshlennost 9:17–21
8. Barykin AYu (2002) Dimensionless characteristic of automatic differential. Avtomobil'naya Promyshlennost 9:20–21
9. Barykin AYu, Takhaviev RKh, Samigullin AD (2018) The research of thermal processes of the automobile chassis. Int J Mech Prod Eng Res Develop 8(8):458–464

10. Barykin AYu (2005) Comparative characteristics of inter-wheel differentials of various types. *Avtomobil'naya Promyshlennost* 5:15–19
11. Barykin AYu (2001) Criterion of efficiency of application of automobile differential gear. *Avtomobil'naya Promyshlennost* 7:18–19
12. Barykin AYu, Basyrov RR, Mukhametdinov MM (2015) On influence of external factors on performance characteristics of truck wheel drive. In: *Materials of the Xth International virtual scientific and technical conference*, Penza, pp 50–55
13. Mukhametdinov MM (2012) Researching intensity of starting torque drop in rolling-contact bearings of axle drive of Kam AZ. In: *Mechanical engineering: design, engineering, calculation and repair & production technology. Materials of All-Russian scientific and practical conference*. IzhGTU, Izhevsk, pp 113–114
14. Barykin AYu, Basyrov RR, Mukhametdinov MM (2016) Evaluation of factors determining wheel drive operation conditions. In: *Architectural, constructional and road complexes: problems, prospects, innovations. Materials of international research-to-practice conference*, SibADI, Omsk, 7–9 December 2016
15. Barykin AYu (2000) Automatic differential: synthesis of structure of blocking properties. In: *International conference MSTU MAMI*, 27–28 Sept 2000, pp 35–36
16. Barykin AYu (2013) Evaluation of performance characteristics influence on blocking properties of small friction differentials. In: *Materials of international scientific and technical conference “Innovative mechanical engineering technology, equipment and materials—2013” and the Forum “Increasing competitiveness and energy efficiency of mechanical engineering companies under WTO conditions”*, Kazan, 2013, pp 34–36
17. Kulakov AT, Gafiyatullin AA, Barylnikova EP (2014) Providing normal conditions of lubricating of diesel engine during its operation. *IOP Conf Ser: Mater Sci Eng* 69:1012027
18. Kulakov A, Gattarov I, Frolov A (2015) Provision of gas engine bus performance with air-fuel mixture. *J Environ Manage Tourism* 6(1):91–100
19. Maretzke J, Richter B (1986) Traction and directional control of 4WD passenger cars—Part 1. *ATZ* 9:463–470
20. Platonov VF (1989) All-wheel drive cars. *Mechanical engineering*, Moscow
21. Bakurevich YL, Tolkachev SS, Shevelyov FN (1973) Operation of cars in the north. *Transport*, Moscow
22. Semyonov NV (1993) Operation of cars in the conditions of low temperatures. *Transport*, Moscow
23. Mavleev IR, Salakhov II, Nuretdinov DI (2018) Modular heavy-duty truck transmission. *IOP Conf Ser: Mater Sci Eng* 386(1):012018
24. Gusakov NV, Zverev IN et al (2000) Car design. Chassis. MAMI, Moscow
25. Barykin AYu, Takhaviev RKh, Samigullin AD (2019) Evaluation of the heat balance of driving Axle in winter conditions. *HELIX* 9(5):5350–5353. <https://doi.org/10.29042/2019-5350-5353>
26. Barykin AYu, Takhaviyev RKh (2017) Evaluation of energy consumption during winter operation of truck drive axle. In: Israfilov IKh (ed) *Energy saving. Science and education*, Naberezhnye Chelny Institute K(P)FU, Naberezhnye Chelny, pp 52–57
27. Barykin AYu, Takhaviyev RKh (2017) Peculiarities of transmission oil operation in wheel drive. In: *Final scientific conference of professors and academics*, Naberezhnye Chelny Institute K(P)FU, Naberezhnye Chelny, 3 February, pp 61–68
28. Minimum air temperature (2019) *Geography of Russia*. <https://geographyofrussia.com/minimalnaya-temperatura-vozduxa/>. Accessed 29 Nov 2019
29. Weather files (2019) *Weather and Climate*. <http://www.pogodaiklimat.ru/archive.php>. Accessed 29 Nov 2019
30. Klamann D (1988) *Lubricants and other related products. Synthesis. Properties. Application. Chemistry*, Moscow



Numerical and Experimental Research of Intentional Mistuning of an Academic Bladed Disk Using Sensitivity Analysis

O. V. Repetckii¹, V. V. Nguyen^{1(✉)}, and Bernd Beirow²

¹ Irkutsk State Agrarian University N. a. A. A. Ezhevsky, 1/1, Molodezhny Settlement, Irkutsk 664038, Russia

² Brandenburg University of Technology, 1, Platz Der Deutschen Einheit, 03046 Cottbus, Germany

Abstract. For analyzing dynamic characteristics and predicting the resource of the turbomachine bladed disk, experimental and numerical researches are often carried out in parallel. This paper presents numerical and experimental studies of forced vibrations of the rotor's blades with an intentional mistuning parameter and considers the effects of the mistuning parameter on the vibrational behavior of the bladed disk. With a small value of mistuning blades, we can significantly increase amplitude, displacement or stresses of the bladed structures. This article analyzes the effect of the intentional mistuning of an axial academic bladed disk in order to reduce forced response. The finite element method (FEM) and other program systems are chosen as the basic research methods in the article. In this regard, the development of high-precision mathematical models based on the FEM, effective algorithm for studying the influence of the mistuning parameter of the turbomachine rotor on their resource using sensitivity analysis is an urgent task.

Keywords: Dynamic · Turbomachine · Vibration · Intentional mistuning · Sensitivity

1 Introduction

Turbine rotors always work under difficult conditions (high temperature, high speed, gas load) and must satisfy the strict standard for the level of resonant vibration frequencies. The mistuning parameter of the rotor is one of the important factors which has a significant impact not only on the work level, but also on the durability of the entire design of turbomachine. The reason for the mistuning parameter of the rotor depends on several factors:

- technological tolerances in the production of blades or disks;
- changing damping between the blades or on the surfaces of bandage;
- non-uniform distribution of aerodynamic loads over the blades;
- heterogeneous characteristics of material of the blades, etc.

One of the important directions in the study of vibrations of mistuned rotors is the question about the effect of mistuning on the dynamic characteristics as well as on their fatigue strength and durability. The effect of mistuning has been researched for a long time in these works [1–17]. Bladed mistuning is small differences between the blades in terms of mass, geometry, material, etc., which violate the cyclic symmetry of rotor. The values of the mistuning parameter of the blades are determined in the form [18, 19]:

$$\Delta f_i = \frac{f_{j,i} - \bar{f}_j}{\bar{f}_j} \quad (1)$$

where \bar{f}_j —the arithmetic mean of the fundamental frequencies; $f_{j,i}$ —the value of the frequency j th mode blades, $i = 1, \dots, N$ (N —the blade number). The degree mistuning as a measure of the magnitude or severity mistuning in a given rotor is defined as:

$$S_k = \frac{1}{\bar{f}_j} \sqrt{\frac{1}{N} \sum_1^N (f_{i,j} - \bar{f}_j)^2} \quad (2)$$

A significant effect in the vibration of tuned system is an increase of the amplitude and stresses compared to the ideal system. For a quantitative assessment the maximum increase amplitude factor γ is introduced, which connects the maximum amplitude of mistuned system with the maximum amplitude of tuned system

$$\gamma = \frac{u_{\text{mistuned(max)}}}{u_{\text{tuned(max)}}} \quad (3)$$

where amplitude is understood as the maximum displacement or maximum dynamic stress during forced vibrations. The amplitude amplification factor substantially depends on the degree of mistuning and the rule of mistuned distribution. In theoretical calculations Ewins simulates the influence of different distributions mistuning on the maximum amplitude vibrations, which can vary from 130 to 210% [8–10]. Whitehead shows an approach to estimating the maximum overshoot amplitude [11, 12]. He establishes the following empirical relationship between maximum value of γ and blade number of rotor (N):

$$\gamma_{\text{max}} = \frac{1}{2} (1 + \sqrt{N}) \quad (4)$$

Many numerical, experimental and theoretical studies show that problems of the rotor's mistuning have been known for a long time. From earlier works Ewins shows the result of experimental studies of the vibrations in mistuned systems. From 2001 to present time, Repetckii O.V., Beirow B., Kuehhorn A. and other authors have used the finite element method (FEM) to analyze free vibrations of rotors with mistuning [4, 5, 13, 14, 20, 21]. Afterward, they analyzed the influence of the mistuning parameter on the rotor's resource of power and transport turbomachine using the program BLADIS + [2] and other programs.

2 Numerical Research of Forced Vibration of the Bladed Disk with Mistuning

Many studies by different authors have shown that the phenomenon of mistuning parameter can have a significant effect on the resource of power and transport turbine engines due to the fact that during forced vibrations of turbomachine rotor with mistuning, the amplitude and dynamic stresses can sharply increase. An academic bladed disk with 10 blades, which is manufactured at Brandenburg University of Technology, was chosen as the object of study. The material of the bladed disk is Steel, Young's modulus— $2.1 \cdot 10^5$ MPa, density— 7850 kg/m^3 , Poisson's ratio—0.3. The general view of the rotor and one sector is shown in Fig. 1a and b. Numerical studies in this work were carried out using the ANSYS and ABAQUS software packages and supported by experimental data. Figure 1c shows a finite element model of one sector, which uses TET10 triangular finite elements from the ANSYS WORKBENCH program, each having 3 degrees of freedom in one node with a total of 2515 finite elements and 14,616 degrees of freedom. The designated model was rigidly fixed to the rim of the disk.

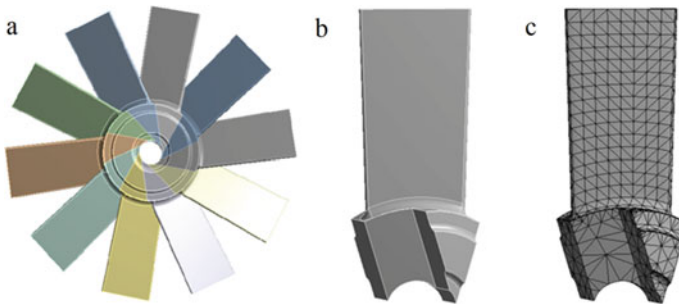


Fig. 1 Academic bladed disk with 10 blades (blisk). **a** Full disk. **b** One sector. **c** Sector finite element model

The natural frequency and vibrational mode represent dynamic properties of the rotor's blade and determine the oscillatory processes of the blades. Thus, the study of natural frequencies and vibrational mode of the blades is an important task in the design of the turbomachine. Figure 2 shows the types of low vibrational mode (mode 2) and more high vibrational modes (modes 5, 7, 8, 10) of one sector. Figure 3 shows the eigenvalue of the cyclic symmetry model (CSM) bladed disk for the first mode. The calculation of natural frequencies of one sector with experimental data and obtained results in the ANSYS and ABAQUS software packages are shown in Table 1.

The results of calculating forced vibrational characteristics of the academic bladed disk with mistuning parameter under the impact of exciting load, at which there are maximum value of amplitude displacement and stress depending on the frequency of exciting force, shown in Figs. 4 and 5.

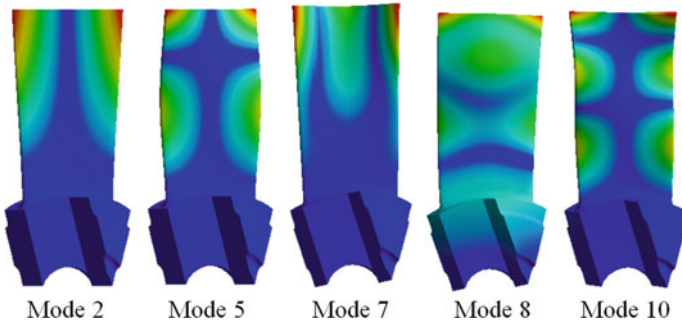


Fig. 2 Vibrational modes of disk's one sector

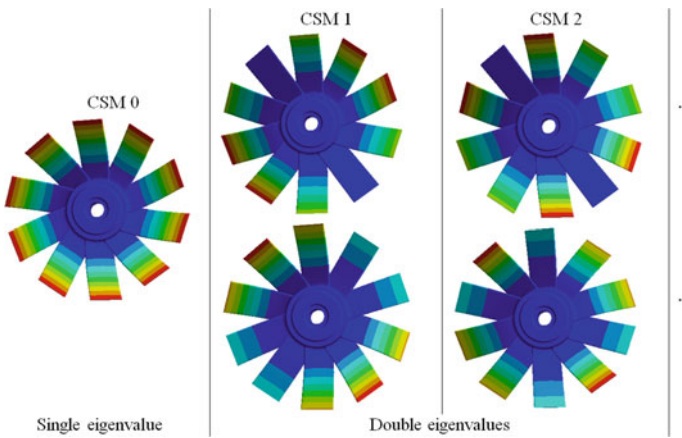


Fig. 3 Characterization by CSM lines of the bladed disk for the first mode

3 Experimental Research and Analysis of the Effects of Mistuning with Appropriate Sensitivity

The values of mistuning are random values. Using experimental method to assess the effect of mistuning on the dynamics of rotor is a difficult task because it is necessary to analyze a large number of options for mistuning during the experiment. In these cases, such numerical method as the Monte Carlo method can be used to study random processes. Sensitivity function has been investigated to control and improve the efficiency of mistuning. Some authors [2, 19] show that sensitivity analysis of the blades can help determine the location of mistuning zone and be useful for the design of increased reliability blades and new design of structures. Besides, sensitivity analysis allows one to create effective model of mistuning and reduce stress level in the blade, and therefore, increase its resource. An effective technique for analyzing the sensitivity blades of a bladed disk to determine the locations of the mistuning zone with additional mass and maximum effect on the dynamic response of the structure is considered in this work. The sensitivity analysis of free and forced vibration blades is performed in work [2] (Fig. 6).

Table 1 Natural frequencies of bladed disk’s one sector (Hz)

Modes	Frequency in ABAQUS	Frequency in ANSYS	Experimental data
1	264.49	260.57	–
2	923.46	905.4	919.69
3	1361.5	1342.1	–
4	1958.0	1937.3	–
5	2857.1	2748.0	2752.50
6	3745.7	3689.0	–
7	4957.6	4510.5	4489.84
8	5422.9	4915.2	5319.30
9	5628.6	5348.2	–
10	7204.2	7036.2	6914.84

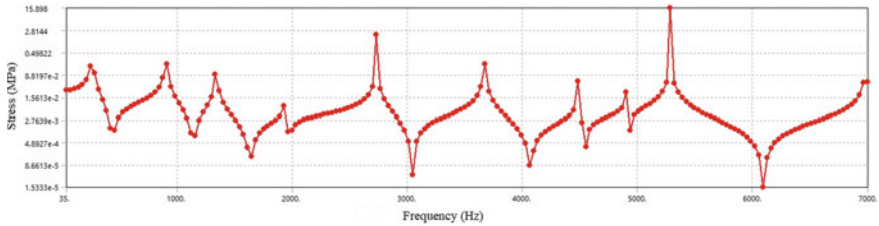


Fig. 4 The value of stress depending on the vibration frequency

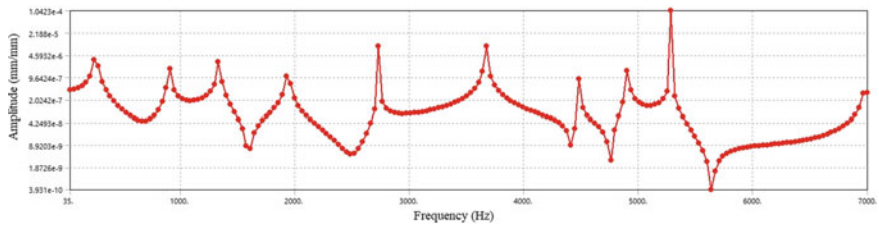


Fig. 5 The value of amplitude displacement depending on the vibration frequency

The measurement system for analyzing excitation of disk vibration (laser scanning vibrometer) is shown in Fig. 7a. The experimental setup of the laser scanning vibrometer system consists of a bladed disk, control device, laser vibrometer, modal hammer, additional mass and foam pad [5]. Table 2 shows experimental calculation of the academic bladed disk vibration frequencies.

At the next stage of the research, a block mistuning model No.1 with additional mass 5.0 g is considered, which consists of 5 mistuning blocks (Fig. 7b). Here, one group includes one tuned blade and one mistuned blade (with mass). Figure 8 shows

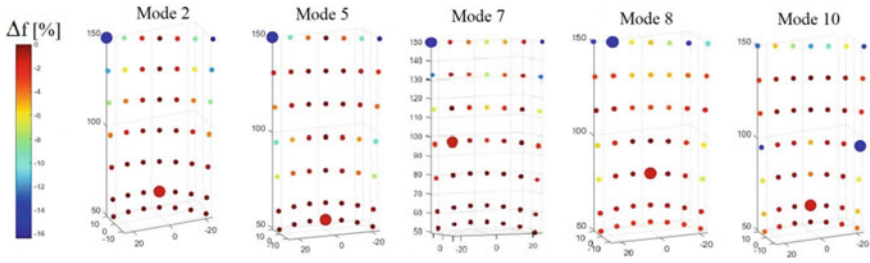


Fig. 6 Sensitivity analysis for academic bladed disk

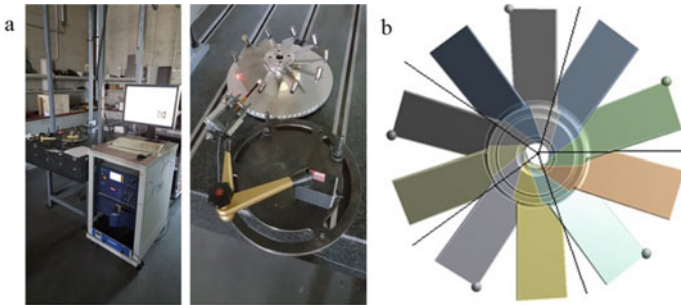


Fig. 7 a Experimental setup. b Block mistuning model No.1 with additional mass 5.0 g

Table 2 Experimental calculation of bladed disk’s vibration frequencies (Hz)

Blade number	Mode 2	Mode 5	Mode 7	Mode 8	Mode 10
1	919.69	2752.50	4489.84	5319.30	6914.84
2	920.08	2756.72	4498.98	5324.61	6923.83
3	921.48	2757.34	4501.02	5328.91	6930.23
4	920.08	2753.98	4491.88	5322.27	6918.83
5	920.63	2757.50	4499.84	5327.11	6924.22
6	921.33	2756.41	4494.30	5326.48	6924.38
7	922.58	2758.44	4502.50	5329.69	6934.53
8	922.03	2758.52	4500.55	5330.00	6927.11
9	922.34	2759.14	4503.98	5332.97	6933.91
10	921.17	2757.27	4497.57	5328.35	6925.03

the values of mistuning of the blade’s vibration frequencies for the block mistuning model No.1. The value of amplitude magnification was less than the blade’s maximum displacement amplification depending on the blade number according to Whitehead ($\gamma_{\max} = 2.08$), see Eq. (3).

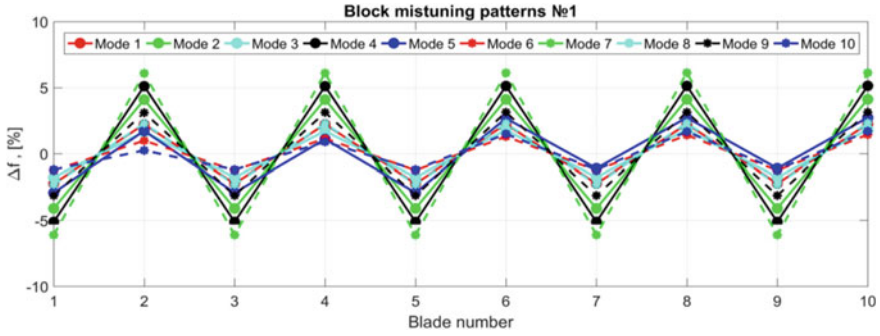


Fig. 8 The values of mistuning for the block mistuning model No.1

Figure 9 illustrates that almost the same maximum values of displacement amplification were obtained for all blades of the academic bladed disk during vibrational modes 2 and 3, vibrational mode 8 has high maximum value of the bladed displacement amplification $\gamma_{max} = 1.84$ (reduces by 11.5% over the result of Whitehead’s maximum displacement amplification). The maximum bladed displacement amplification for vibrational modes 1 and 4 ($\gamma_{max} = 1.41$) shows that the most effective result is obtained for the block mistuning model No.1 (reduces by 32.2%).

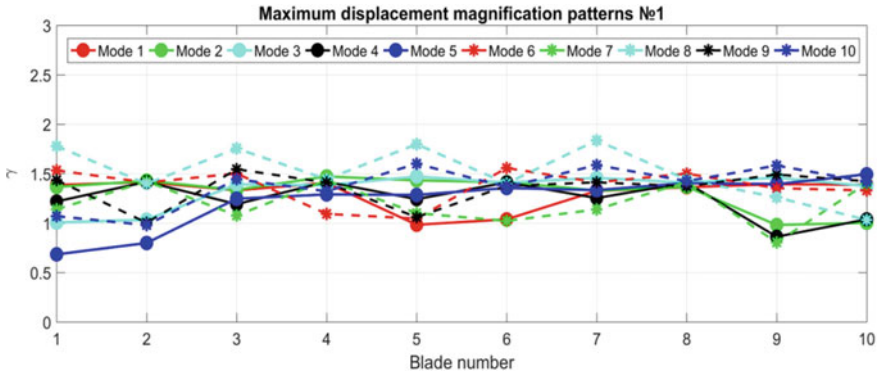


Fig. 9 The maximum displacement amplification for the block mistuning model No.1

4 Conclusions

This article presents the results of sensitivity analysis and optimal location mistuning with additional mass for rotor blades. The information presented in this article shows the main results of numerical and experimental researches of the effect of mistuning parameter on the blade’s dynamic characteristics of the academic rotor, taking into account the sensitivity analysis based on the FEM. Intentional mistuning is obtained by optimizing the algorithms and implemented using small geometric changes in the

blade with additional mass 5.0 g on the periphery bladed feather. The results of this study show reliability and effectiveness using block intentional mistuning in bladed disk model, which is reduced the maximum value of the displacement amplification of the blade by 33%.

Acknowledgements. The authors wish to express their gratitude to apl. Prof. Dr.-Ing. habil. Bernd Beirow for research assistance and internships at Brandenburg University of Technology, Cottbus, Germany.

References

1. Petrov EP, Ewins DJ (2003) Analysis of the worst mistuning patterns in bladed disk assemblies. *ASME J Turbomach* 125(4):623–631
2. Repetski O, Rygikov I, Springer H (1999) Numerical analysis of rotating flexible blade-disk-shaft systems. In: *Proceedings of the ASME Turbo Expo* 4(3):317
3. Afolabi DH (1982) Vibration of mistuning bladed disk assemblies. Dissertation, Imperial College of Science & Technology, London
4. Beirow B (2009) Grundlegende Untersuchungen zum Schwingungsverhalten von Verdichtertaufrädern in Integralbauweise. Shaker Verlag, 1 Dec 2009, p 172
5. Beirow B, Kühhorn A (2008) Method for determining blade mistuning on integrally manufactured rotor wheels. US Patent 8024137, Sep 2011
6. Bah MT et al (2003) Forced response statistics of mistuned bladed disks: a stochastic reduced basis approach. *J Sound Vib* 263(2):377–397
7. Bayoumy LE (1975) Influence of mistuning on rotor blade vibrations. *J AIAA* 13(3):460–464
8. Ewins DJ (1969) Effects of mistuning upon forced vibrations of disks. *J Sound Vib* 9(1):65–79
9. Ewins DJ (1973) Vibration characteristics of bladed disk assemblies. *J Mech Eng Sci* 12(5):165–186
10. Ewins DJ (1976) Vibration modes of mistuned bladed disks. *ASME J Eng Power* 98(3):349–355
11. Whitehead DS (1976) Effect of mistuning on forced vibration of blades with mechanical coupling. *J Mech Sci* 18(6):306–307
12. Whitehead DS (1966) Effect of mistuning on the vibration of turbomachine blades induced by wakes. *J Mech Eng Sci* 8(1):15–21
13. Beirow B, Giersch T, Kuehhorn A et al (2015) Optimization-aided forced response analysis of a mistuned compressor Blik. *J Eng Gas Turbines power* 137(1):012504
14. Beirow B, Kuehhorn A, Figashevsky F, Bornhorn A, Repetckii O (2019) Forced response reduction of a blisk by means of intentional mistuning. *J Eng Gas Turbines Power* 141(1):011008
15. Han Y, Murthy R, Mignolet MP, Lentz J (2014) Optimization of intentional mistuning patterns for the mitigation of effects of random mistuning. *J Eng Gas Turbines Power* 136(6):1–9
16. Chan YJ (2009) Variability of blade vibration in mistuned bladed discs. Dissertation, Imperial College, London
17. Petrov EP (2010) Reduction of forced response levels for bladed discs by mistuning: overview of the phenomenon. *J Eng Gas Turbines Power* 133(7):072501. <https://doi.org/10.1115/GT2010-23299>
18. Griffin JH, Hoosac TM (1984) Model development and statistical investigation of turbine blade mistuning. *ASME J Vib, Acoust, Stress, Reliab Des* 106(2):204–210

19. Repetski O, Zainchkovski K (1997) The sensitivity analysis for life estimation of turbine blades. In: Proceedings of the ASME Turbo Expo 1(10):136
20. Beirow B, Kuehhorn A, Figashevsky F, Bornhorn A (2019) Vibration analysis of a mistuned axial turbine blisk. J ASME Turbo Expo 7:92047. <https://doi.org/10.1115/GT2019-92047>
21. Repetckii O, Ryzhikov I, Nguyen TQ (2018) Investigation of mistuning impact on vibration of rotor bladed disks. J Phys: Conf Ser 944(1):012096



Reducing Fuel Consumption During Diesel Engine Operation on Idle Mode

A. N. Gots^(✉) and V. F. Guskov

Vladimir State University Named After Alexander and Nikolai Stoletovs, 87, Gorky str,
Vladimir 600000, Russia

Abstract. We have analyzed previously conducted studies on improving the fuel efficiency of automobile and tractor diesels when idling with a disconnected part of the cylinders by stopping the fuel supply to them as a result of closing the intake and exhaust valves or without them closing. The well-known calculation methods considered by us are based on the use of experimental characteristics and empirical dependencies that are valid only for specific diesel engines and their operating modes. At the same time, the calculated assessment of fuel efficiency when diesels operate in partial modes with some cylinders switched off by stopping the fuel supply is carried out without experimental confirmation. The results of such computational studies differ qualitatively from the results of experimental studies. The paper proposes a method for evaluating fuel efficiency based on the use of the load characteristic of a full-size diesel engine. This makes it possible to calculate the indicator efficiency and hourly fuel consumption of a diesel engine when it is running at idle with a part of the cylinders turned off. The results are presented of experimental and computational studies of changes in the fuel efficiency of a $4 \times 10.5/12$ diesel engine when operating in partial modes and at idle, if some of the cylinders are disconnected by stopping the fuel supply with simultaneous closing of the intake and exhaust valves, as well as without affecting their drive, are presented.

Keywords: Cylinder · Shutdown · Fuel efficiency · Partial modes · Idling · Excess air · Indicator coefficient efficiency

1 Introduction

Diesel engines installed on agricultural or transport vehicles run at idle for a long time during some operations in operation. Research has established [1–3] that as a percentage of the total operating time in operation, diesel engines operate at idle: on transport vehicles—15–30%; on agricultural machines—4 ... 29%; on combine harvesters—5–16%. At the same time, the diesel fuel consumption when operating at idle is from 7 to 17%, respectively, of the total fuel consumption. In this mode, the work obtained from fuel combustion is spent on overcoming mechanical losses in the diesel engine. For these purposes, require a small cyclic feed of fuel, the injection of which into the cylinder are carried out at low pressures. This leads to a deterioration of the mixing and combustion

processes and, as a result, a decrease in the indicator efficiency at high values of the excess air coefficient [4–6].

If part-load mode or the idle speed requires changing the cycle fuel feed in [7–9] it is recommended to organize the work of the diesel so that it was possible to turn off the fuel supply to some cylinders when you decrease load and increase fuel delivery by increasing the frequency of rotation of the crankshaft of diesel engine [10–12]. In diesel locomotives, some sections of the fuel pump are switched off when running at idle. A method for disconnecting part of the cylinders was developed, which was first implemented in 1981 on engines with forced ignition of Cadillac cars [13]. Possible ways to disable the cylinder of the engine is to stop the fuel supply to it, while closing the gas distribution organs or without it.

The method of disconnecting a part of the cylinders has been successfully implemented on many modern engines with forced ignition, since it reduces not only the losses associated with throttling a fresh charge, and heat losses to the cylinder wall, but also pumping losses, and also provides conditions for the operation of the lambda probe of the electronic control unit. Thus, 4-cylinder TSI engine capacity of 1.4 L and an effective power output of 103 kW, part of a series of engines EA211 company Volkswagen, equipped with an original system ACT (active cylinder technology) disable half of the cylinders, reducing fuel consumption by the engine in the NEFZ cycle by 0.4 L per 100 km of mileage [14].

This system not only stops the fuel supply to the 2nd and 3rd cylinders and closes the intake and exhaust valves in them in the range of crankshaft speeds of 1250...4000 min⁻¹ when the engine torque is limited to 85 N*m, but also eliminated sparking between the spark plug electrodes in these cylinders.

On transport diesels and agricultural machinery diesels, the cylinder shutdown method has not yet found practical application due to the complexity of its design in the fuel supply system and gas distribution mechanism. However, the results of studies [2–4] indicate the feasibility of its use.

Since these methods differ in the complexity of implementation, it is advisable to make a reasonable choice of one of them to perform a comparative assessment of the fuel efficiency of a diesel engine in full-size idling modes, as well as when the fuel supply to a part of the cylinders stops while the intake and exhaust valves are closed, or to limit only the fuel supply.

In [10–12], a computational and experimental method is proposed for evaluating fuel efficiency when a part of the cylinders is disconnected based on an experimental universal (combined, multi-parameter) map of a full-size engine for a specific operating mode. This method is widely used for calculating changes in the specific effective fuel consumption when a part of the cylinders is switched off by stopping the fuel supply not only in automobile and tractor diesels [8–10], but also in four-stroke gasoline and gas engines with forced ignition [11–13] in partial modes of their operation. It should be noted that the results of computational studies [10] for 2H10.5/12 diesel using this method contradict the results of experimental studies [7]. With regard to idle modes, it is not possible to use the universal map represented by the lines of effective power and specific effective fuel consumption [7, 8] to assess fuel efficiency and fuel consumption when a part of the diesel cylinders is switched off [14].

In [4–6], a method for determining diesel fuel consumption in idle mode when a part of the cylinders is switched off is proposed, based on the assumptions that mechanical losses when the fuel supply to some cylinders is stopped are constant, and the speed of the crankshaft is also constant. In this case, the average indicator pressure in the combustion cylinders increases in direct proportion to the ratio of the number of diesel cylinders to the number of cylinders with fuel supply. For calculating fuel efficiency, it is recommended [5, 6] to use the parabolic dependence of the relative value of the indicator efficiency as a function of the relative middle indicator pressure. The coefficients in this relationship are the experimental values of the maximum and minimum indicator efficiency at idle. In their conclusions, the authors [5–7] note that in the absence of a maximum relative indicator efficiency in this dependence, it is impossible to improve the fuel efficiency of a diesel engine as a result of disabling some cylinders by stopping the fuel supply in them. In this regard, we should note the works [3, 4], which found that the reduction of hourly fuel consumption by the engine when the cylinder part is disconnected by stopping the fuel supply while closing the valve timing at idle is not only due to the increase in indicator efficiency, but also due to a decrease in mechanical losses.

The method proposed in [3, 4], as in [5–7], is based on the empirical dependence of the indicator efficiency as a function of the average indicator pressure, obtained by approximating experimental data from the results of tests of a full-size engine. However, such dependencies are formal, valid for specific engines and their operating modes, since it is known that the indicator efficiency is determined primarily by the excess air coefficient, and the size middle indicator pressure is the ratio of the indicator efficiency to the excess air coefficient.

2 Relevance of the Research Topic

Increasing the fuel efficiency of diesel engines when operating in partial modes is an urgent task. The paper evaluates the fuel efficiency of a diesel engine at idle with the shutdown of a part of the cylinders by stopping the fuel supply to them with the simultaneous closing of the intake and exhaust valves or without closing them.

3 Problem Statement and Research Method

Based on the analysis of studies on changes in fuel efficiency indicators when a part of the cylinders is switched off in different ways at idle, we carry out an analytical calculation and compare the calculated data with experimental results.

A review of studies on the fuel efficiency of diesel engines when a part of the cylinders is switched off showed [14–16]:

- design and experimental studies were performed for known diesel engines with significant restrictions on their operating modes; some results of design studies are not confirmed by the results of motor tests [17];
- the basis for using the developed methods are experimental characteristics, empirical dependencies, and other experimental data that are valid for specific diesel engines and their operating modes.

In order to reduce the complexity and increase the reliability of the results of computational studies to assess the fuel efficiency of diesels with cylinders disconnected in various ways, it is necessary to develop a methodology based on the use of a minimum volume of test results for a full-size engine, with the following assumptions:

- mechanical losses are determined only by the speed of the crankshaft;
- there is no unevenness in the indicator specific cycle operation for cylinders with fuel supply;
- the distribution of fresh charge across the cylinders of the engine, regardless of whether there is a fuel supply in them, with or without closing the gas distribution organs, is uniform;
- the degree to which the cylinder is filled with fresh charge (cycle feed) does not depend on the load at a constant speed of the crankshaft (filling coefficient $\eta_v = \text{cons}$).

From the first assumption, it follows that the work of mechanical losses of the engine with disconnected cylinders, equal to the sum of the work of mechanical losses of the cylinders with the fuel supply and disconnected cylinders, is formalized by the equation [18]

$$p_{m,i-z}V_h(i-z) = p_{m,i}V_h(i-z) + p_{m,i}V_hzk_m, \tag{1}$$

where $p_{m,i}$, $p_{m,i-z}$ —the average pressure mechanical losses of the full-sized engine with the number of cylinders i and engine partially disabled the cylinders number z ; V_h —cylinder capacity; k_m —coefficient of reduction of mechanical losses in the disabled cylinder.

In General, mechanical losses per cylinder are reduced when the cylinder is switched off due to reduced power to drive the fuel pump and gas distribution organs and transfer air when the intake and exhaust valves are closed. Assuming that the total share of these losses is δ_m [14, 19, 20] in the power of mechanical losses, the coefficient k_m will be equal to

$$k_m = 1 - \delta_m. \tag{2}$$

Then the average pressure of mechanical losses of the engine with disconnected cylinders in the amount of z , taking into account (1) and (2), is equal to

$$p_{m,i-z} = p_{m,i} \left(\frac{i - z\delta_m}{i - z} \right). \tag{3}$$

From the second assumption and equality of works indicated and mechanical losses at a constant frequency of crankshaft rotation, just for idle speed of the engine, taking into account (3) we get the following dependence of relative changes of average indicator pressure engine for full-size and disabled z cylinders [14, 21]

$$p_{i,i-z}/p_{i,i} = (i - z\delta_m)/(i - z), \tag{4}$$

where $p_{i,i}$ and $p_{i,i-z}$ are the average indicator pressures of engines: full-size and with z cylinders disconnected.

For a special case, corresponding to the disconnection of a part of the cylinders only by cutting off the fuel supply, from (4) at $\delta_m = 0$ follows

$$p_{i,i-z}/p_{i,i} = i/(i - z) \tag{5}$$

In order to establish the relationship between changes in the average indicator pressure and the indicator efficiency of the engine when some cylinders are turned off, we consider the well-known formula for the average indicator pressure p_i [18]

$$p_i = (H_u \eta_i \eta_v \rho_0) / (l_0 \alpha), \tag{6}$$

where H_u is the lowest heat of combustion of the fuel; η_i is the indicator efficiency; η_v is the filling coefficient; ρ_0 is the intake air density; l_0 is the theoretically necessary amount of air sufficient for the complete combustion of 1 kg of fuel and calculated from stoichiometric ratios; α is the excess air coefficient.

Taking into account Formula (6), the third and fourth assumptions, and the condition $\rho_0 = \text{const}$, we obtain that the relative change in the average indicator pressure with a decrease in the number of cylinders with fuel supply determined by the relative change in the ratio of the indicator efficiency η_i to the excess air coefficient α :

$$p_{i,i-z}/p_{i,i} = (\eta_{i,i-z}/\alpha_{i-z}) / (\eta_{i,i}/\alpha_i), \tag{7}$$

where α_i and α_{i-z} are the excess air coefficients of a full-size engine (with the number of cylinders i) and an engine with disconnected cylinders (with the number of cylinders $i-z$), respectively.

According to the experimental dependence of η_i/α from the excess air ratio set according to the results of testing of the engine 4Ч10,5/12, the relative change in the relationship η_i/α when the load changes and engine speed and, consequently, the relative change of the average indicator pressure when you disconnect a part of cylinders is approximated by a function [19, 20]

$$p_{i,i-z}/p_{i,i} = \alpha_i^{1-\frac{1}{\alpha_i}} / \alpha_{i-z}^{1-\frac{1}{\alpha_{i-z}}}. \tag{8}$$

Using (7) and (8) for known values of α_i and α_{i-z} is defined as

$$\eta_{i,i-z}/\eta_{i,i} = \alpha_{i-z}^{\frac{1}{\alpha_{i-z}}} / \alpha_i^{\frac{1}{\alpha_i}}. \tag{9}$$

The relative change in hourly fuel consumption is calculated using the formula

$$\frac{G_{t,i-z}}{G_{t,i}} = \frac{\eta_{i,i}}{\eta_{i,i-z}} \left(1 - \frac{z\delta_m}{i} \right) \tag{10}$$

For a special case, the corresponding disconnection of a part of the cylinders only by stopping the fuel supply at $\delta_m = 0$ from (9) follows

$$G_{t,i-z}/G_{t,i} = \eta_{i,i}/\eta_{i,i-z}. \tag{11}$$

The joint solution of Eqs. (4) or (5), (8), (9), (10) or (11) allows you to evaluate the fuel efficiency of a diesel engine by the value of the relative change in the hourly flow rate when a part of the cylinders is switched off in different ways at idle for known values $\eta_i, \alpha_i, \delta m$.

Experimental studies of the fuel efficiency of diesel when the fuel supply to a part of the cylinders is stopped were conducted in the engine laboratory of the Department of "Heat engines and power plants" of the VISU.

During bench tests of the 4ch10,5/12 air-cooled diesel engine, the load characteristics were removed for the crankshaft rotation speeds $n = 1100, 1300, 1500 \text{ min}^{-1}$ in the effective power range 0–12 kW for a full-size diesel engine, as well as when one and two cylinders were switched off. During bench tests, mechanical losses were also determined by the engine cranking the crankshaft.

Stopping the fuel supply to the disconnected cylinders was provided by disconnecting the discharge pipeline from the nozzle and connecting it to the measuring tank for determining fuel consumption by weight.

4 Results of Experimental Studies

Based on the results of experimental studies, it can be concluded that an increase in the number of disconnected cylinders by stopping fuel supply in the studied range of rotation speeds and loads causes an increase in the specific effective fuel consumption g_e (see Formulas (9–10)). This is due to a reduction in the excess air ratio due to an increase in the cycle fuel feed and a corresponding decrease in the indicator efficiency. In this case, the air flow rate G_v diesel does not depend on the number of disconnected cylinders for $n = \text{const}$ (Fig. 1, curve 4).

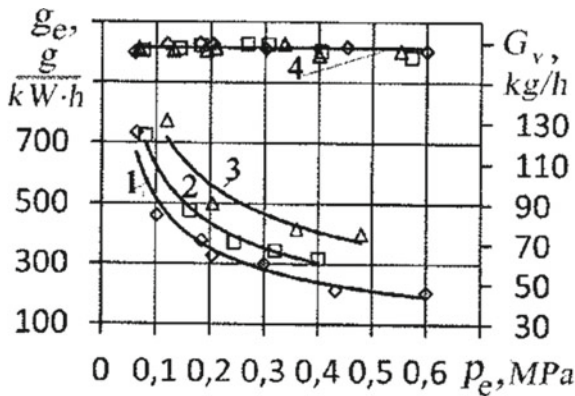


Fig. 1 Load characteristic of the 4h10,5/12 diesel engine at the speed of the crankshaft $n = 1500 \text{ min}^{-1}$: 1-full-size diesel engine; 2-one cylinder is disconnected ($z = 1$); 3- $z = 2$; 4-air consumption $G_v, \text{ kg/h}$

The change in the indicated efficiency at idle $\eta_{i,i-z}/\eta_{i,i}$ depending on the number of disconnected cylinders z by stopping the fuel supply is shown in Fig. 2, from which it

follows that an increase in the number of disconnected cylinders z leads to an increase in the indicated efficiency due to improved fuel atomization due when the cyclic fuel supply is increasing.

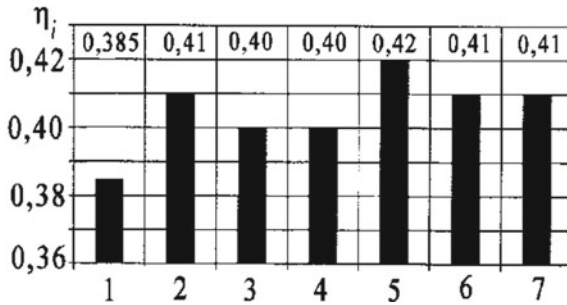


Fig. 2 Change in the indicator efficiency of a diesel engine at a speed of rotation of the crankshaft $n = 1500 \text{ min}^{-1}$ at idle: 1-full-size diesel engine, experiment; 2-1 cylinder disabled ($z = 1$), experiment, $\delta m = 0$; 3- $z = 1$, calculation, $\delta m = 0$; 4- $z = 1$, calculation of $\delta m = 0.14$; 5- $z = 2$, experiment, $\delta m = 0$; 6- $z = 2$, calculation of $\delta m = 0$; 7- $z = 2$, calculation of $\delta m = 0.14$

The initial data for comparative calculation estimation of diesel fuel efficiency indicators at idle when a part of the cylinders is disconnected was formed using various methods based on the load characteristics of a full-size engine. The average pressure of mechanical losses for calculating indicator indicators was determined based on the dependence obtained by approximating experimental data $p_{m,i} = 0,111 = 0,0158c_p$, where c_p is the average piston speed.

Figure 3 shows the change in the attitude of Ni/α from α , which with sufficient accuracy in the range of $\alpha = 1,4 \dots 7$ and $n = 1100 \dots 1500 \text{ min}^{-1}$ describes the above dependence (9).

The selection of the coefficient of reduction of mechanical losses in the disconnecting cylinder was made on the basis of the distribution of mechanical losses in each systems of diesel 4 CH 10,5/12 [14]. There are also experimental data on mechanical losses determined by the method of cold cranking the crankshaft.

The calculated change in the relative hourly fuel consumption of a diesel engine when a part of the cylinders is switched off in different ways is shown in Fig. 4. The Results obtained indicate a significant reduction in fuel consumption at idle when two cylinders in diesel 4CH10.5/12 are switched off by stopping the fuel supply to them while simultaneously closing the gas distribution organs.

According to [3, 4], the relative value of pumping losses for the D-240 diesel engine is 14%. Taking into account the method of stopping the fuel supply to the disconnected cylinders, for example, using special devices [4, 21], and relatively insignificant losses on the fuel pump drive, their influence on mechanical losses when disconnecting a part of the cylinders can be ignored.

The latter also applies to the reduction of mechanical losses on the drive of the gas distribution mechanism, due to the lack of a drive of the gas distribution organs in the disconnected cylinders of the engine. Therefore, the calculations took $\delta m = 0.14$.

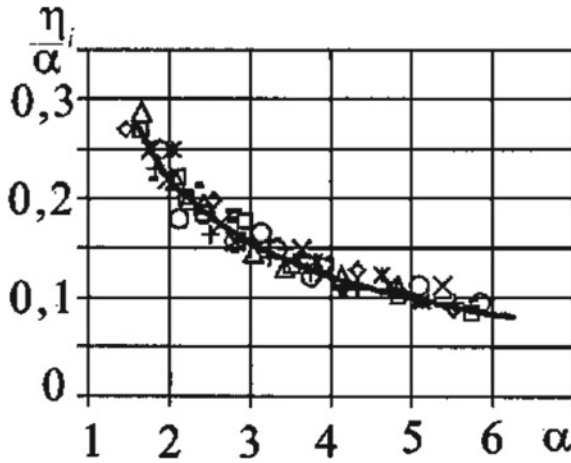


Fig. 3 Dependence of η_i/α on the excess air coefficient of diesel 4CH10,5/12 in the range of crankshaft speeds 1100...1500 min^{-1} : \square — $n = 1100 \text{ min}^{-1}$; Δ — $n = 1100 \text{ min}^{-1}$ ($z = 1$ —one cylinder is disabled); \circ — $n = 1100 \text{ min}^{-1}$ ($z = 2$); \times — $n = 1300 \text{ min}^{-1}$; \blacksquare — $n = 1300 \text{ min}^{-1}$ ($z = 1$); $+$ — $n = 1300 \text{ min}^{-1}$ ($z = 2$); K — $n = 1500 \text{ min}^{-1}$; $-$ — $n = 1500 \text{ min}^{-1}$ ($z = 1$); \diamond — $n = 1500 \text{ min}^{-1}$ ($z = 2$)

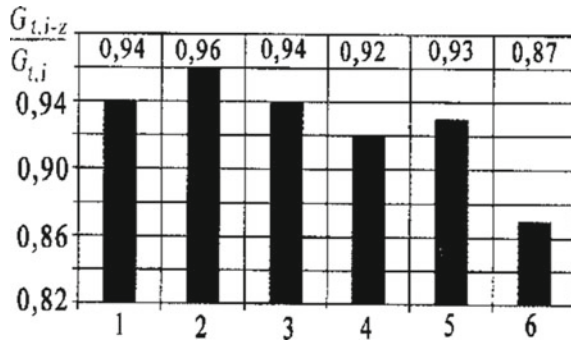


Fig. 4 Relative change in hourly fuel consumption at the speed of the crankshaft $n = 1500 \text{ min}^{-1}$ at idle when a part of the cylinders is disconnected: 1-one cylinder is disconnected $z = 1$, experiment, $\delta_m = 0$; 2- $z = 1$, calculation, $\delta_m = 0$; 3- $z = 1$, calculation, $\delta_m = 0.14$; 4- $z = 1$, calculation, $\delta_m = 0$; 5- $z = 2$, calculation, $\delta_m = 0$; 6- $z = 2$, calculation, $\delta_m = 0.14$

A comparison of the results of calculated and experimental studies (Fig. 2) shows their satisfactory convergence, as well as the absence of a noticeable effect of the method why cylinders become disconnected on the change in the indicator efficiency of the diesel engine when it is running at idle.

5 Conclusions

The research results allow us to draw the following conclusions:

1. The proposed method for evaluating the fuel efficiency of a diesel engine with the shutdown of some cylinders at idle is based on experimental data determined from the standard load characteristics of a full-size engine.
2. The determination of changes in the indicator indicators of transport diesels at partial modes and idle speeds, including with the disconnection of part of the cylinders, should be carried out according to the experimental dependence of the ratio η_i/α of the indicator efficiency to the excess air coefficient, depending on the excess air coefficient α
3. It is established that when the fuel supply to a part of the cylinders is discontinued for a 4CH10,5/12 diesel engine (in the amount of up to $z = 2$), then in the range of crankshaft speeds $n = 1100 \dots 1500 \text{ min}^{-1}$ and loads $N_e = 2 \dots 12 \text{ kW}$, fuel efficiency deteriorates, and at idle slightly improves.
4. It is determined that in idle mode, the method of disconnecting a part of the cylinders of the 4CH10.5/12 diesel in the frequency range of the crankshaft $n = 1100 \dots 1500 \text{ min}^{-1}$ does not have a noticeable effect on the change in the indicator efficiency. The greatest possible reduction in hourly fuel consumption in these modes is provided when the cylinder parts are switched off by stopping the fuel supply and simultaneously closing the intake and exhaust valves by reducing the power of mechanical losses and is about 13% when two cylinders are switched off.

References

1. Ukhanov DA (2009) Improvement of performance indicators of automotive equipment with the improvement of engine operation at idle: abstract of the dissertation on competition of a scientific degree of doctor of technical Sciences, Saratov State Technical University named after Yu. A. Gagarinro Saratov, p 32
2. Otradnov AV (2007) Improvement of performance indicators of agricultural vehicles in idle mode: abstract of the dissertation on competition of a scientific degree of candidate of technical sciences. RUDN University, Moscow, p 16
3. Surkin VI, Petelin AA, Fedoseev SY (2012) Reducing the opacity of exhaust gases of a diesel engine by disabling part of the cylinder. *J South Ural State Univer* 33:69–74
4. Fedoseev SYu (2015) Increasing fuel efficiency of the tractor-transport unit by disconnecting part of the engine cylinders: abstract of the dissertation on competition of a scientific degree of candidate of technical sciences. South Ural State University, Chelyabinsk, p 23
5. Dragunov GD, Medvedev AN (2007) Method for evaluating the efficiency of switching off the cylinders of an automobile. *J Engine Constr* 4:2–22
6. Medvedev AN (2008) Improving fuel efficiency of automobile diesels by disconnecting part of cylinders: abstract of the dissertation on competition of a scientific degree of candidate of technical Sciences. South Ural State University, Chelyabinsk, p 16
7. Khusainov VN (2010) Justification of the methodology and development of technical means for investigating the efficiency of converting diesels to regulate operating modes by skipping the working strokes of pistons: abstract of the dissertation on competition of a scientific degree of candidate of technical Sciences. Saint Petersburg state Agrarian University, Saint Petersburg-Pushkin, p 20
8. Strashnov SV (2017) Regulation of the 6CH11/12.5 diesel engine by changing the number of operating cylinders or cycles: abstract of the dissertation on competition of a scientific degree

- of candidate of technical Sciences. Moscow State University of Mechanical Engineering, Moscow, p 18
9. Anoshina TS (2014) Improving the economic and environmental qualities of transport diesel when operating under low load and idle modes: abstract of the dissertation on competition of a scientific degree of candidate of technical sciences. Moscow State University of Mechanical Engineering, Moscow, p 18
 10. Kamyshnikov RO (2017) Improving the performance of motor-tractor diesels by regulating their active working volumes at low load modes: abstract of the dissertation on competition of a scientific degree of candidate of technical sciences. Moscow State University of Mechanical Engineering, Moscow, p 16
 11. Savastenko EA (2016) Regulation of an engine with spark ignition by changing its working volume: abstract of the dissertation on competition of a scientific degree of candidate of technical Sciences. Moscow State University of Mechanical Engineering, Moscow, p 15
 12. Lotfullin ShR (2019) Improving energy efficiency and environmental friendliness of the automobile gas engine by changing its active volume: abstract of the dissertation on competition of a scientific degree of candidate of technical Sciences. RUDN, Moscow, p 16
 13. Volkswagen Technical Site. <http://volkswagen.msk.ru>
 14. Gots AN, Guskov VF, Fomin VM (2020) Estimation of fuel efficiency of automobile and tractor diesel engines, operating with the shutdown of part of the cylinders. *J Tractors Agric Mach* 3:19–27
 15. Gaisin EM (2009) Improving the fuel efficiency of tractor diesels by regulating their operation modes by skipping the fuel supply: abstract of the dissertation on competition of a scientific degree of candidate of technical sciences. RUDN University, Moscow, p 16
 16. Dragunov GD, Medvedev AN (2007) Method for evaluating the efficiency of switching off the cylinders of an automobile. *J Engine Constr* 4:20–22
 17. Vyruhov DN, Ivashchenko NA, Ivin VI et al (1983) Theory of piston and combined engines, 4th edn. Engineering Publ., Moscow, p 372
 18. Portnov DA (1963) High-Speed engines with compression ignition. Engineering Publ., Moscow, p 639
 19. Baykov BP, Bordukov GV, Ivanov PV, Deitch RS (1975) Turbochargers to boost diesel engines. Engineering Publ., Leningrad, p 200
 20. Putintsev SV (2011) Mechanical losses in piston engines. Special chapters for design, calculation, and testing. Electronic educational publication, Bauman Moscow State Technical University, Moscow, p 288
 21. Patrakhaltsev NN, Kamyshnikov OV, Emil MV, Djuri P (1988). Diesel power system. A. S. of the USSR No. 1408092. M. KL. F 02V17102, pub. 07.07.88. Bull. No. pp 25–27



Numerical Analysis of Dynamics and Fatigue Life of the Turbomachine Impeller with Mistuning

I. N. Ryzhikov¹(✉), O. V. Repetckii², and V. V. Nguyen²

¹ Irkutsk National Research Technical University, 83, Lermontov Str., Irkutsk 664074, Russia
rin111@list.ru

² Irkutsk State Agrarian University Named After A.A. Ezhevsky, Irkutsk Region, Irkutsk
Distrikt, Molodezhny Settlement 664038, Russia

Abstract. In real designs of impellers, the blades differ in size and shape from each other within the tolerances for their manufacture. These differences are called mistuning and, as numerous studies have shown, can have a significant impact on the values of the vibration frequencies, their shape, as well as on the level of dynamic stresses in the blade material. The article presents the developed mathematical models of impeller vibration with mistuning and the results of calculations of free and forced vibration of a real impeller in the developed Ocs_Rotor software package in comparison with the experiment, as well as the calculation of its fatigue life in the ANSYS software package. The results of the calculations are in good agreement with the experimental data. Recommendations have been developed for the distribution of blades with a mistuning along the rim of the impeller in order to increase its fatigue life.

Keywords: Turbomachine · Impeller · Vibration · Mistuning · Fatigue life

1 Introduction

The impellers of aviation gas turbine engines operate under high static and dynamic loads: These are centrifugal forces at high temperatures, as well as large variable loads from gas flow pulsations, leading to fluctuations. During vibrations, the dynamic stresses that occur in the blade material can reach significant values, which negatively affects the strength and durability of the blades.

When designing the impellers of aircraft gas turbine engines, they are usually modeled as cyclically symmetric systems. However, the derangement of the parameters, which is inevitably present in the design of a real wheel as a result of imperfect manufacturing technology, can have a significant impact on the vibrations, stress state and durability of the impeller. So, the disorder can cause such a harmful phenomenon as the localization of vibrations, in which the amplitude of vibrations of one or more blades in the wheel increases significantly.

The literature coverage of the problem of mistuning began with the work [1]. In it, Whitehead describes this effect by using the coefficient of maximum increase in the amplitude of vibrations as a function of the number of blades in bladed disk N :

$$\gamma = \frac{u_{\max(\text{mistuned})}}{u_{\max(\text{tuned})}} = \frac{1}{2} \left(1 + \sqrt{N} \right), \tag{1}$$

where γ is the coefficient of the maximum increase in the amplitude; $u_{\max(\text{mistuned})}$ — the maximum amplitude of vibrations of the bladed disk with mistuning; $u_{\max(\text{tuned})}$ — maximum vibration amplitude of the impellers without mistuning; N — number of blades in bladed disk. The mistuning effect was studied in [2–20].

This article presents mathematical models for vibration analysis of the impellers of aircraft gas turbine engines. The results of calculations of natural vibrations (modal analysis) of the impeller, its forced vibrations and fatigue life, performed in the developed Ocs_Rotor program and in the ANSYS package, are also presented.

2 The Calculation of Free Vibration of the Impeller Without Mistuning

The equation of free vibrations, which can be used to find the eigenvalues for a cyclically symmetric system without mistuning, has the form:

$$M \ddot{\delta} + K \delta = O, \tag{2}$$

while

$$\delta = \delta_0 \cos(\omega t - \beta), \tag{3}$$

where M — mass matrix; K — stiffness matrix; δ — node accelerations; δ — node displacements; δ_0 — amplitudes; ω — circular frequency; β — oscillation phase.

After the transformations, we get:

$$\left(K - \omega^2 M \right) \delta_0 = 0. \tag{4}$$

The general view of the impeller and the results of calculations of the first forms of impeller vibrations without mistuning in accordance with this algorithm are shown in Fig. 1.

3 The Calculation of Free Vibration of the Impeller with Mistuning

The mistuning was simulated by adding additional masses to the blades (Fig. 2). Table 1 shows the values of the additional masses attached to the blades.

The results of calculating the frequencies in comparison with the experiment are shown in Table 2. The results of the calculation in the developed Ocs_Rotor program are in good agreement with the experimental data.

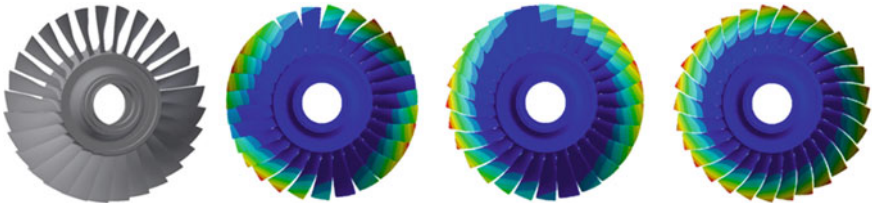


Fig. 1 General view of the impeller and free vibration modes without mistuning

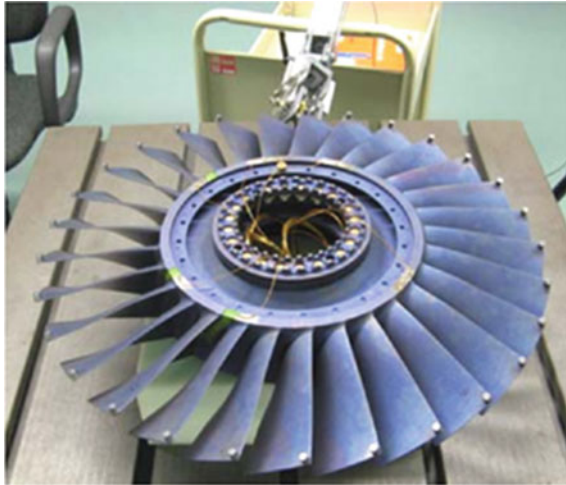


Fig. 2 Impeller with additional masses

Table 1 Values of additional masses m

Blade number	m (κg)	Blade number	m (κg)	Blade number	m (κg)
1	0.001251440	11	0.001451640	21	0.001356856
2	0.001302147	12	0.001302100	22	0.001125158
3	0.000025486	13	0.000065488	23	0.000085489
4	0.001102156	14	0.001502634	24	0.001402132
5	0.001305234	15	0.001600680	25	0.001202183
6	0.001205214	16	0.001166480	26	0.001102121
7	0.000802923	17	0.000735542	27	0.001302524
8	0.001100598	18	0.001553548	28	0.000356542
9	0.001302003	19	0.001135789	29	0.001205558
10	0.001202100	20	0.001257365	21	0.001356856

Table 2 Results of calculating the eigenfrequencies of the blades with mistuning

No. of blade	Mode 1 (Hz)		Mode 2 (Hz)		Mode 3 (Hz)	
	Exp	Ocs	Exp	Ocs	Exp	Ocs
1	403.8	416.3	1255	1304.5	1766	1843.3
2	404.4	416.3	1256.4	1305.5	1767	1843.3
3	405	416.4	1257.3	1305.5	1768	1843.3
4	403.7	416.4	1254.7	1307.3	1766.6	1843.5
5	403	416.4	1251.9	1307.3	1765.6	1843.5
6	403	416.4	1251.8	1308.6	1764.6	1844
7	403.4	416.6	1252.8	1308.6	1763.8	1844
8	404.5	416.6	1255.8	1309.4	1766.6	1844.5
9	405	416.7	1256.1	1309.4	1766.3	1844.5
10	404.5	416.8	1256.8	1310.2	1766.7	1844.8
11	404	416.8	1254.6	1310.2	1764.5	1844.8
12	404.8	417.3	1256.7	1311.1	1769.2	1845
13	403.1	417.4	1252	1311.1	1764.9	1845
14	402.6	417.9	1250.3	1312.1	1764.6	1845.1
15	403.5	417.9	1252.9	1312.2	1765.5	1845.1
16	404.4	418.5	1254.8	1313.2	1765.4	1845.2
17	405	418.5	1256.6	1313.2	1766.7	1845.2
18	404.5	419.1	1256	1314.2	1766.6	1845.3
19	403.7	419.1	1254	1314.2	1767.5	1845.3
20	403	419.5	1251	1315.2	1766.6	1845.4
21	403.7	419.5	1253.4	1315.2	1766.9	1845.4
22	405.3	419.9	1256.8	1315.9	1768.5	1845.5
23	404.8	419.9	1256.4	1315.9	1768.3	1845.5
24	404.2	420.2	1255	1316.5	1767.2	1845.6
25	404	420.2	1254	1316.5	1765.9	1845.6
26	402.4	420.3	1250.6	1316.9	1761.4	1845.6
27	402.6	420.3	1250.4	1316.9	1760.4	1845.6
28	402.3	420.4	1250.2	1317.1	1760.1	1845.7
29	402.8	420.4	1252.4	1317.1	1761.3	1845.7

The value of mistuning was determined in accordance with the formula:

$$\Delta f_{r,n} = \frac{(f_{r,n}^2 - f_{r,0}^2)}{f_{r,0}^2}, \quad (5)$$

where $f_{r,n}^2$ is the natural frequency of the n th blade, $f_{r,0}^2$ is the natural frequency of the tuned blade.

A block diagram of the algorithm for determining the values of mistuning when the mass of the blades changes is shown in Fig. 3.

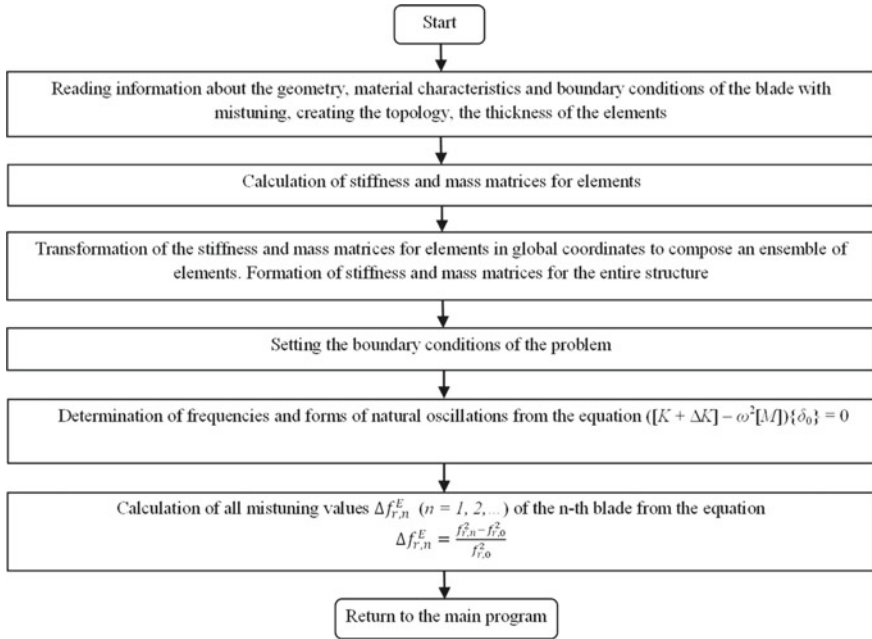


Fig. 3 Block diagram of the algorithm for determining the values of the blade mistuning

The values of the mistuning of the blades in the disk, calculated by the (5), are shown in the graph of Fig. 4.

4 Calculation of Forced Vibrations of the Impeller with Mistuning

The excitation of forced vibrations of the blades was carried out through 20 nozzle blades. The variable force was determined using a Fourier series:

$$P(t) = L_0(1 + 0.5 \cos \varphi + 0.025 \cos 2\varphi), \tag{6}$$

where L_0 is the static component of the load [5].

The results of the calculation of stresses under forced vibrations of the mistuned impeller are shown in Fig. 5.

5 Calculating the Fatigue Life of the Impeller

The next step of the research was to calculate the fatigue life of the impeller with different variants of mistuning. The calculation was carried out in the ANSYS software package.

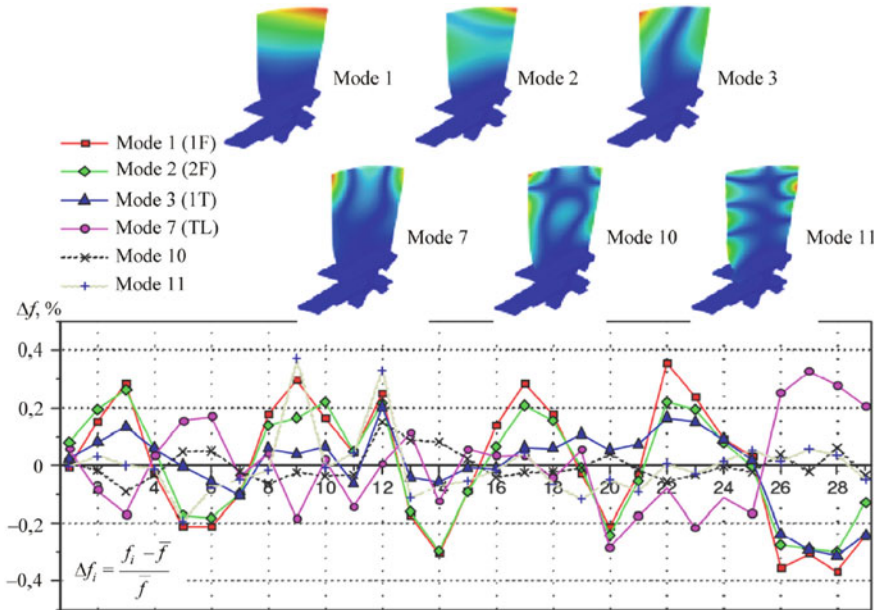


Fig. 4 Values of blade mistuning for some modes

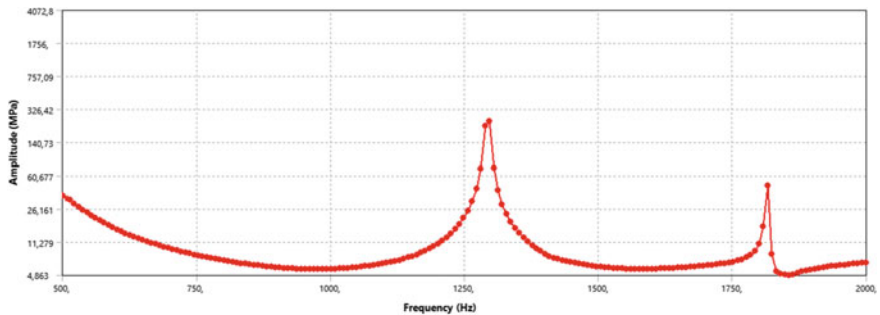


Fig. 5 Stresses under forced vibrations of the mistuned impeller

Mistuning was modeled by attaching additional masses to the periphery of the blades. Three variants of the distribution of additional masses were investigated:

- Variant 1: Masses were attached to the periphery of all the blades in accordance with Table 1.
- Variant 2: Same masses (0.00211 kg) were attached to the periphery of 28 blades. The 29th blade was without additional mass.
- Variant 3: Same masses (0.005 kg) were attached to the periphery of 28 blades. The 29th blade was without additional mass.

The results of calculating the fatigue life of the impeller are shown in Fig. 6 and in Table 3.

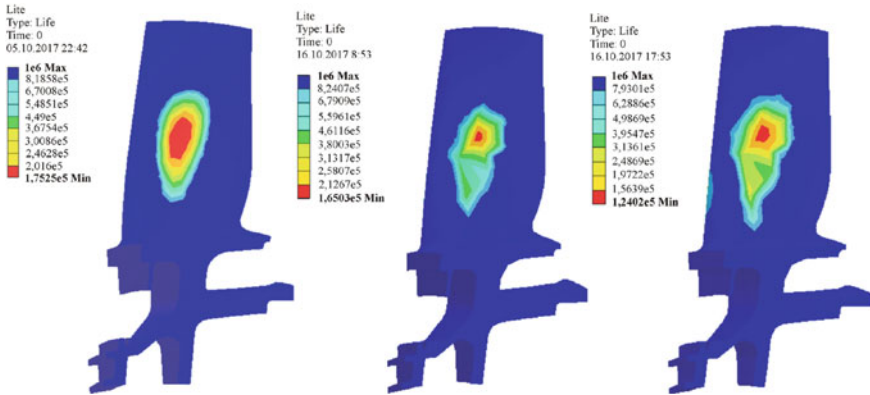


Fig. 6 Results of impeller fatigue life calculating

Table 3 Results of impeller fatigue life calculating

Mode number	Variant 1		Variant 2		Variant 3	
	Natural frequency, Hz					
	FEM	Exp	FEM	Exp	FEM	Exp
1	416.3864	403.8574	403.3854	397.8125	410.3864	402.9375
2	1304.5584	1255.0780	1296.5417	1261.000	1300.2214	1252.6875
3	1843.3258	1766.0640	1803.3784	1766.3125	1826.6854	1765.6750
Fatigue life, hour	1.7525E + 5		1.6503E + 5		1.2402E + 5	

As the results show, the bladed disk with additional masses attached to all the blades has the greatest fatigue life (variant 1). The decrease in fatigue life occurs with an increase in the mass value and in cases where there is a large discrepancy in the mass of the adjacent blades (variants 2 and 3).

Acknowledgements. The authors wish to express their gratitude to Prof. A. Kuehnhorn and Dr. Bernd Beirrow for research assistance.

References

1. Whitehead D (1966) Effect of mistuning on the vibration of turbomachine blades induced by wakes. *J Mech Eng Sci* 8(1):15–21
2. Irretier H (1983) Spectral analysis of mistuned bladed disk assemblies by component mode synthesis. In: *Vibrations of bladed disk assemblies*. ASME, pp 115–125
3. Irretier H, Schmidt K (1982) Mistuned bladed disks—dynamical behaviour and computation. In: *Proceedings IFToMM conference of rotordynamics problems in power plants*. Rome, Italy, pp 215–226
4. Repetskii O (1990) Use of the FEM to solve the thermoelasticity problem of turbine blades. *Strength Mater* 22(12):1848–1854
5. Repetskii O (1995) *Proceedings of Higher educational institutions*. Machine building 1–3:45–53
6. Repetskiy OV, Cuong BM (2011) Fatigue life prediction of modern gas turbomachine blades. In: *Incorporating sustainable practice in mechanics of structures and materials*. Proceedings of the 21st Australian conference on the mechanics of structures and materials, pp 275–280
7. Bladh J, Castanier M, Pierre C (2001) Component mode based reduced order modeling techniques for mistuned bladed disks—Part I: theoretical models. *J Eng Gas Turbines Power* 123(1):100–108. <https://doi.org/10.1115/1.1338947>
8. Bladh R, Castanier M, Pierre C (1999) Reduced order modelling and vibration analysis of mistuned bladed disk assemblies with shrouds. *J Eng Gas Turbines Power* 121(3):515–522
9. Ewins D, Han Z (1984) Resonant vibration levels of a mistuned bladed disk. *J Vib Acoust Stress Reliab* 106(2):211–217
10. Beirow B, Kühhorn A, Figaschewsky F et al (2018) Forced response reduction of a blisk by means of intentional mistuning. In: *Proceedings of the ASME Turbo Expo*. Turbomachinery technical conference and exposition. “ASME Turbo Expo 2018: turbomachinery technical conference and exposition GT2018”.
11. Figaschewsky F, Kühhorn A (2015) Analysis of mistuned blade vibrations based on normally distributed blade individual natural frequencies. In: *Proceedings of ASME Turbo Expo*, GT2015–43121
12. Wagner J (1967) Coupling of turbomachine blade vibrations through the rotor. *J Eng Gas Turbines Power* 89(4):502–512
13. Wagner M (2010) Model reduction methods for rotor dynamic analysis: a survey and review. *Int J Rotating Mach*, p 17
14. Sinha A (1986) Calculating the statistics of forced response of a mistuned bladed disk assembly. *J AIAA* 24(11):1797–1801
15. Happawana G, Nwokah O, Bajaj A et al (1998) Free and forced response of mistuned linear cyclic systems: a singular perturbation approach. *J Sound Vib* 211(5):761–789
16. Griffin J, Hoosac T (1984) Model development and statistical investigation of turbine blade mistuning. *J Vib Acoust Stress Reliab* 106(2):204–210
17. Griffin J, Sinha A (1985) The interaction between mistuning and friction in the forced response of bladed disk assemblies. *J Eng Gas Turbines Power* 107(1):205–211
18. Pierre C, Murthy D (1989) Aeroelastic modal characteristics of mistuned bladed assemblies: mode localization and loss of eigenstructure. *J AIAA* 30(10):2036–2050
19. Beirow B (2009) *Grundlegende Untersuchungen zum Schwingungsverhalten von Verdichters-lauffrädern in Integralbauweise*. Dissertation, Cottbus, p 172
20. Beirow B, Giersch T, Kuehhorn A et al (2015) Optimization-aided forced response analysis of a mistuned compressor blisk. *J Eng Gas Turbines Power* 137(1):012504



Fatigue Crack Growth Estimation in Low-Alloy Steel Under Random Loading in Middle Section of Fatigue Diagram

A. N. Savkin, A. A. Sedov, and K. A. Badikov(✉)

Volgograd State Technical University (VSTU), 28, Lenina St, Volgograd 400005, Russian Federation

Abstract. The fatigue crack growth kinetics were studied under regular and irregular cyclic loading with different asymmetry ratios, as well as spectral loading typical for the operation of various structural objects, in the middle section of the fatigue crack growth diagram on $C(T)$ type specimens cut from low-alloy steel used in the automotive industry. The R -ratio of different levels influence and irregular loading character on the fatigue crack growth duration at different values of maximum loading is shown. A model of the crack growth duration is proposed on the basis of considering the “crack closure,” and for irregular cyclic loading, in addition, the character of variable amplitude loading with its reduction to an equivalent regular loading. This made it possible to reduce the fatigue crack growth diagrams group with different asymmetry ratios to one equivalent curve. The forecasting of the fatigue crack growth duration was carried out by the cyclic calculation method (“cycle-by-cycle”) and by the proposed empirical dependence.

Keywords: Regular and irregular cyclic loading · Low-alloy steel · Crack growth life model

1 Introduction

While in operation, vehicles experience variable loads from various types of road surfaces, maneuvering during movement, changes in temperature conditions, impact action in the obstacle crossing process. It leads to fatigue damage accumulation in the load-bearing design elements, leading to the fatigue cracks growth. Microcracks are formed in stress raiser of a part, and it is often difficult to detect them without special equipment. Gradually, this process takes on the character of an avalanche effect, and the part may be destroyed.

To prevent such a scenario, it is necessary, knowing where such fatigue cracks can occur, to check the maintenance inspection to detect them. To establish the examination of such rates, it is necessary to know the crack growth kinetics so that the emerging crack can be detect before its critical growth.

In the suggested work, on the low-alloy steel specimens used in the automotive components production, and the fatigue crack kinetics growth analysis under regular

and irregular loading is carried out, considering the effect on of different asymmetry ratio R and maximum loading P_{max} . Irregular loading is modeled based on standard random spectra using in the engineering design of automotive load-bearing structural elements.

2 Material, Research Technique

The compact specimens $60 \times 62.5 \times 5$ mm in size with an edge crack are investigated, cut from low-alloy steel, close to the analog Russian steel—09G2. This alloy is used in the automotive industry, concretely for the manufacture of front suspension for passenger cars [1–5].

The thickness of this material specimen is 5 mm that give it possible to assert that the fatigue crack propagation under a plane stress condition. The drawing is shown in Fig. 1.

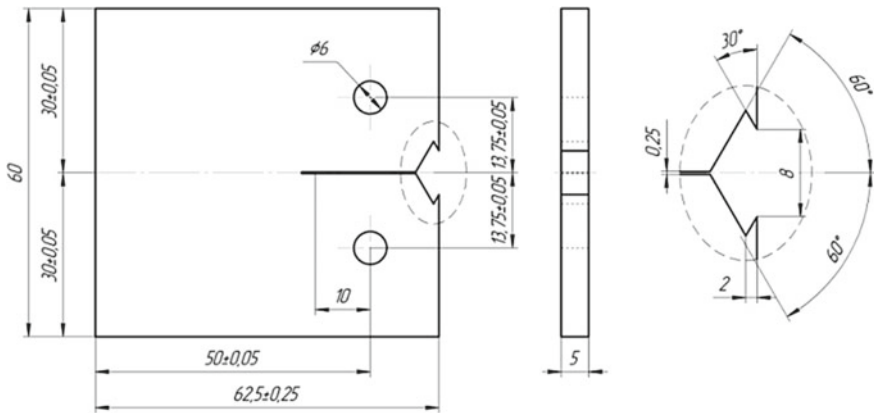


Fig. 1 Geometry of test specimen

Chemical composition of the alloy % (mass): Fe 98.7; C 0.078; Cr 0.1; Cu 0.016; Mn 0.96; Nb 0.04; Si 0.1; Ti 0.016; Al 0.036. Mechanical properties of alloy: ultimate strength $\sigma_u = 496$ MPa, conditional yield strength $\sigma_y = 345$ MPa, modulus of elongation $E = 210$ GPa.

Experimental studies were carried out using specialized software MTL-32, controls the test under load control mode. VAFCP (Variable Amplitude Fatigue Crack Propagation) software, which allows testing under various loading conditions in automatic mode, including loading level control to provide a set value of K , as well as automatic recording of the crack length and other test results. The compliance method was used to measure crack length, using the BISS Bi-06–201 Crack Opening Displacement (COD) gauge, which measures distance between edges of the specimen. The tests were carried out in air under normal ambient conditions, and the frequency of the main type of loading was 10 Hz. The test procedure conforms to the specification of ASTM E 647–08. The crack growth kinetics were recorded depending on the number of cycles during the test.

The crack resistance testing program consists of testing at constant amplitude (CAL) and variable amplitude loading (VAL) with different asymmetry ratio R from 0 to 0.75 and a maximum load of 3.5–7 kN. For variable amplitude tests, spectra of a quasi-random nature are formed on the basis of standard loading spectra typical for variable loading of various technical objects and contractual elements [6–10]. Figure 2 shows examples of normalized loading spectra.

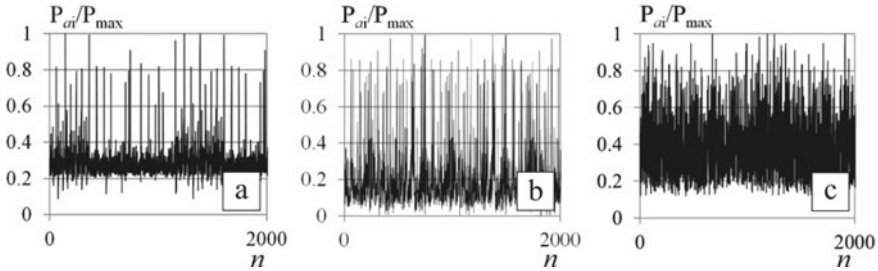


Fig. 2 Examples of selection from normalized loading spectrums: **a**—SAESUS; **b**—SAE-TRANS; **c**—SAEBRACKET

SAESUS, SAEBRACKET, SAETRANS spectra—shortened load front suspension spectrums, brake gear and transmission of a passenger car. Model spectra A and C are formed on the basis of an autocorrelation approach for the Rayleigh distribution, which is most typical for failures of technical objects and constructions fatigue-prone and wear [11–13]. The test schedule is shown in Table 1. Before testing, the fatigue crack was performed by precracking to a value of $a_0 = 15$ mm under constant amplitude loading with a nominal load at $R = 0, P = 0.6 \cdot P_{max}$ from the subsequent test. The critical size, of the crack length corresponding to the specimen failure at the provided tests, is $a_{cr} = 31–34$ mm.

3 Research Results

Figure 3 shows the test results (Fig. 3a). Based on the dependences of the crack growth kinetics $a\text{-lg}N$, obtained using a crack opening displacement gauge, the testing machine software automatically estimates the growth rate da/dN and the amplitude of the stress intensity factor (SIF) ΔK at the crack mouth. These results make it possible to plot the fatigue diagrams. Item numbers in Fig. 3 correspond to those numbers in Table 1.

Test results at different types of loading and different values of the asymmetry ratio of the loading block $R = 0–0.75$ show that all fatigue diagram curves have tendency to parallelism in logarithmical coordinates ($\lg(da/dN)\text{-}\lg(\Delta K)$). Comparison of tests under constant amplitude loading is carried out with the same P_{max} but different R , and show that an asymmetry ratio increasing leads to an increase in crack growth life, because of a decrease in the range of the ΔK . In Fig. 3a, it can be seen that at a constant $P_{max} = 5$ kN and $R \leq 0.5$ for a given material, the rate hardly exceeds 300 thousand cycles, and at $R \geq 0.7$ the durability essentially increases to million cycles.

Table 1 Test schedule

Loading	P_{max} , kN	R	V	K	N_{EXP} million cycles	N_{VAL} , million cycles	N_{CYC} , million cycles	Position in Fig. 3
CAL	5	0	1	1	0.080	-	0.063	1
	5	0.1	1	1	0.062	-	0.073	2
	5	0.3	1	1	0.118	-	0.112	3
	5	0.5	1	1	0.310	-	0.235	4
	5	0.7	1	1	1.090	-	0.911	5
	5	0.75	1	1	1.701	-	1.553	6
SAETRANS	3.5	0.1	0.381	20	5.300	4.815	7.258	7
	5	0	0.381	20	1.770	1.821	1.733	8
	7	0.1	0.381	20	0.553	0.616	0.627	9
SAEBRACKET	3.5	0.1	0.401	18	3.404	4.319	6.068	10
	5	0	0.401	18	1.277	1.633	1.450	11
	7	0.1	0.401	18	0.488	0.522	0.525	12
SAESUS	3.5	0.1	0.277	32	14.317	8.474	6.289	13
	5	0	0.277	32	5.325	3.204	5.281	14
	7	0.1	0.277	32	1.957	1.083	1.907	15
Spectrum A	7	0.1	0.391	19	0.641	0.583	0.573	16
Spectrum C	7	0.1	0.296	30	1.523	0.977	1.512	17

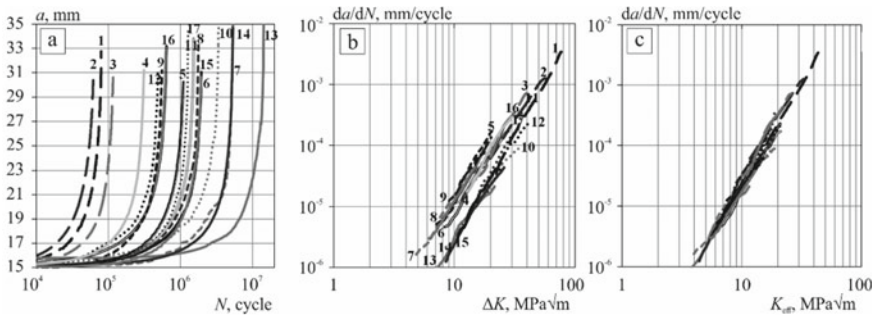


Fig.3 Curves of crack growth (a), experimental (b) and effective SIF (c)

The asymmetry ratio is also influencing on the fatigue diagram position. In Fig. 3b, it is clearly seen that at increase asymmetry ratio, the curves from 1 to 6 are located lower and more to the left. At a constant value P_{max} and regular loading, the range of coefficient ΔK decreases and the duration of crack growth increases. Growth curves and KDFC 5 and 6 in Fig. 3 correspond to tests at asymmetry of 0.7 and 0.75. It is

assumed that at such asymmetries R , the crack closure effect is not observed [14–16], which effects on the crack growth kinetics.

The difference between variable and constant amplitude loading is estimated with measuring of irregularity (completeness). The loading completeness ratio V for the presented tests is shown in Table 1, for constant amplitude loading the completeness ratio is equal to one.

$$V = \left[\frac{1}{v_b} \left[\sum_{i=1}^{v_b} v_{ai} \left(\frac{\Delta P_{ai}}{P_{\max}} \right)^n \right] \right]^{\frac{1}{n}} \tag{1}$$

where v_b, v_a —number of cycles of the sample and block of variable loading with load ΔP_{ai} ; $\Delta P_{ai}/P_{\max}$ —is the normalized i loading amplitude. This approach corresponds to the replacement of variable amplitude loading with equivalent constant ones, corresponding to irregular random loading in terms of the damaged ability. The calculated V ratio is shown in Table 1. It is clearly seen from the position of the initial part of fatigue diagram for different spectra, where, at a decrease V ratio in the SAESUS spectrum, fatigue diagram settle regardless of R and P_{\max} that crack growth life reduces, but retains parallelism in these coordinates, as and fatigue diagrams at CAL. On the fatigue diagram, position of VAL is influenced by the value of the maximum load P_{\max} . At the increase the load from 3.5 to 7 kN and maintaining a low asymmetry $R = 0\text{--}0.1$, the fatigue diagram curves shift toward the region of increased crack growth rates. This is clearly seen in the SAESUS spectrum (13–15 curves) and the SAETRANS spectrum (7–9 curves).

Analytical fatigue diagram curves in the middle zone are described by the Paris equation [5]:

$$\frac{da}{dN} = C \cdot \Delta K^n \tag{2}$$

where da/dN is the crack growth rate during the loading cycle; ΔK is the range of SIF; C and n are empirically determined coefficients that are the cyclic crack resistance characteristics of the material. In the present work, for the steel under study, the values $C = 5 \cdot 10^{-14}$ and $n = 3.5$ are obtained to estimate the speed da/dN (mm / cycle) and ΔK in $\text{MPa}\sqrt{\text{mm}}$.

Because the position of the fatigue diagram curves at CAL block (Fig. 3b) significantly depends on the asymmetry ratio R , and the position of the curves at VAL, accept asymmetry, is influenced by the irregularity ratio V ; therefore, in this article, the approach of the effective SIF ΔK_{eff} is used, which makes it possible to approximate these curves to a single curve specific at $R = 0$, which is shown in Fig. 3c.

To consider the phenomenon of “crack closure” [17–21], which occurs when the cycle asymmetry ratio R is less than 0.6–0.7, and which reduces the crack growth rate by reducing the range ΔK , the parameter U is introduced to describe crack closure with an asymmetry of $0.1 \leq R \leq 0.7$ for steels according to the equation in the form of a polynomial dependence:

$$U = 0.57 + 0.16 \cdot R + 0.53 \cdot R^2 - 0.43 \cdot R^3 - 2.58 \cdot R^4 + 6.15 \cdot R^5 - 3.13 \cdot R^6 \tag{3}$$

Thus, in our calculation, the effective SIF at the crack mouth for different types of loading is taken as:

$$\Delta K_{eff} = \Delta K \cdot U \cdot V \tag{4}$$

In this expression, the effect of “crack closure” and the loading cycle asymmetry on the crack growth rate is estimated through the asymmetry ratio R .

4 Results and Discussion

The crack propagation process largely depends on the sequence of loads, which is random. So, the prediction of crack growth is carried out by integration, by the cycle-by-cycle method in the order of the cycles in a random process, starting from the minimum crack length, at which its detection is possible, according to the formula:

$$N_{CYC} = \int_{a_0}^{a_{cr}} \frac{1}{C \cdot \Delta K_{eff}^n} \tag{5}$$

where N_{CYC} —estimated of crack growth life under CAL and VAL by the cycle-by-cycle method; ΔK_{eff} —the effective SIF, determined by Eq. (4); a_0 ; a_{cr} —initial and critical crack length.

Another approach for estimating of crack growth life at VAL N_{VAL} is based on the proposal to consider the crack growth kinetics on the basis of its growth at CAL N_{CAL} and taking into account the nature of variable loading through the irregularity coefficient V at the same force parameters P_{max} and R without taking into account the interaction of amplitudes in the loading spectrum (6):

$$\begin{aligned} N_{VAL} &= N_{CAL} \cdot K \\ K &= 10^{(1+A \lg n) \cdot (1-V)} \end{aligned} \tag{6}$$

where A —scaling parameter equal to 2 for the studied steel, K —the coefficient of increasing the fatigue crack growth life at VAL compared to CAL with the same loading parameters P_{max} and R .

The calculation results using the methods describe above are shown in Fig. 4 in the form of the calculated values dependence N_{CYC} or N_{VAL} from the experimental N_{EXP} . Comparison of the durability gives good enough agreement between the calculated and experimental data [9, 10].

5 Conclusions

Thus, it has been established that the growth rate and the position of curves on fatigue diagram under VAL are influenced not only by the asymmetry ratio R , as in the case of CAL, but also by the irregularity ratio V , which takes into account the irregularity of random loading.

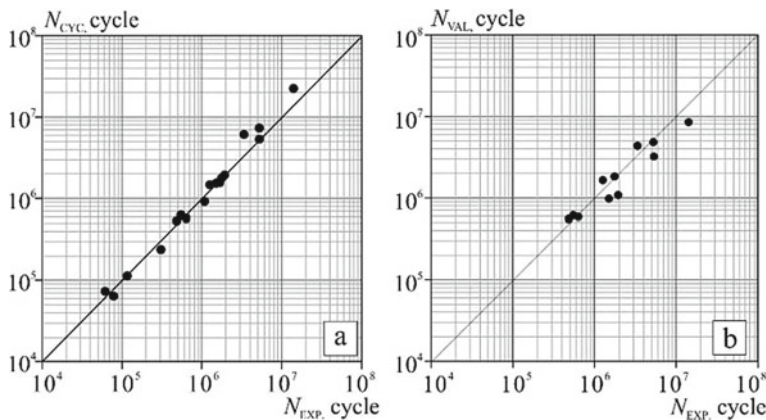


Fig. 4 Calculation of the crack growth life by the cycle method **a** and by formula (6) **b** in comparison with the experiment

The cycle-by-cycle method for predicting the fatigue crack life in steels, considering the effective SIF, show a high convergence of the calculated and experimental values, as well as the approach based on the use of an equivalent constant amplitude loading to predict irregular loading. The correlation coefficient for the first and second methods is $r_2 = 0.99$ and $r_2 = 0.91$, respectively.

References

1. Gouth HJ (1926) The fatigue of metals. Scott, Greenwood, London
2. Furuya Y (2019) Gigacycle fatigue in high strength steels. *Sci Technol Adv Mater* 20(1):643–656
3. Schijve J (2009) Fatigue of structures and materials. Springer, Delft, pp 623
4. Barsom JM (1976) Fatigue crack growth under variable amplitude loading in various bridge steels. In: Fatigue crack growth under spectrum loads, pp 217–232. <https://doi.org/10.1520/STP33374S>
5. Paris PC (1964) The fracture mechanics approach to fatigue, fatigue an interdisciplinary approach. Syracuse University Press, Syracuse, N.Y., pp 107–132
6. Savkin AN, Sedov AA, Denisevich DS, Badikov KA (2018) Crack-tip stress distributions under variable amplitude loading. AIP conference proceedings, pp 2051
7. Johnson HU, Paris PC (1968) The growth of fatigue cracks due to variations in load. *Jorn Fract Mech* 1:1–45
8. Sunder R (2012) Unraveling the science of variable amplitude fatigue. *J ASTM Int* 9(1):32
9. Savkin AN, Denisevich DS, Badikov KA, Sedov AA (2019) A new semi-analytical approach for obtaining crack-tip stress distributions under variable-amplitude loading. *Procedia Structural Integrity*, pp 684–687. <https://doi.org/10.1016/j.prostr.2019.05.085>
10. Savkin AN, Sunder R, Badikov KA, Sedov AA (2018) Fatigue crack growth kinetic on steels under variable amplitude loading. *PNRPU Mech Bull* 3:61–70. <https://doi.org/10.15593/perm.mech/2018.3.07>
11. Skorupa M (1998) Load interaction effects during fatigue crack growth under variable amplitude loading, a literature review. Part I .empirical trends. *Fatigue Fract Eng Mater Struct* 987–1006

12. Savkin AN, Sunder R, Denisevich DS, Sedov AA, Badikov KA (2018) Load interaction effects during near-threshold fatigue crack growth under variable amplitude: theory, model, experiment. *PNRPU Mech Bull* 4:246–255. <https://doi.org/10.15593/perm.mech/2018.4.22>
13. Bekal S (2013) Calculation growth on variable amplitude loading: master thesis. Manipal Institute of Technology, India, pp 112
14. Irwin GR (1957) Analysis of stresses and strain near the end of a crack traversing a plate. *J Appl Mech-Trans ASME* 24:351–369
15. Antunes FV, Souda T, Branco R, Corrieis L (2015) Effect of crack closure on non-linear crack tip parameters. *Int J Fatigue* 71:53–63
16. Arijit R, Manna I, Tarafder S, Sivaprasad S, Paswan S, Chattoraj I (2013) Hydrogen enhanced fatigue crack growth in an HSLA steel. *Mater Sci Eng* 588:86–96
17. Yang Y, Zhang W, Yongming L (2014) Existence and insufficiency of the crack closure for fatigue crack growth analysis. *Int J Fatigue* 62:144–153
18. Savkin AN, Sunder R, Andronik AV, Sedov AA (2018) Effect of overload on the near-threshold fatigue crack growth rate in a 2024–T3 aluminum alloy: I. effect of the character, the magnitude, and the sequence of overload on the fatigue crack growth rate. *Russ Metallurgy (Metally)* 11:1094–1099. <https://doi.org/10.1134/S0036029518110113>
19. Willenborg J, Engle RH, Wood HA (1971) A crack growth retardation model based on effective stress concepts. report AFFEL-TM-71-1- FBR, Dayton (OH): air force flight dynamics laboratory, wright-patterson air force base 9:15
20. Manjunatha CM (2008) Fatigue crack growth prediction under spectrum load sequence in an aluminum alloy by K^* -RMS approach. *Int J Damage Mech* 17:477–492
21. Carpinteri A, Spagnoli A, Terzano M (2019) Crack morphology models for fracture toughness and fatigue strength analysis. *Fatigue Fract Eng Mater Struct* 42(9):1965–1979. <https://doi.org/10.1111/ffe.13064>



Mathematical Simulation of Car Dynamics with Account of Air Conditioning System

M. Yu. Elagin and R. N. Khmelev(✉)

Tula State University, 92, Lenin Ave, Tula 300012, Russia

Abstract. A refined simulation dynamic model of a car has been developed, which takes into account the influence of the air conditioning system on the process of car functioning. This model allows making joint research and calculations for the engine and the car both in steady-state and non-steady-state modes. The refined simulation dynamic model is based on the theory of bond graphs, which is the basis of many high-level CAE products used in the aviation industry, heavy machine building and robotics. The change in the state of the working fluid in the intake manifold and in each cylinder is described by the differential equations of the laws of mass and energy conservation. These equations are supplemented by known dependencies for determining the indicators related to the working fluid, gas exchange, combustion and heat exchange processes. The developed software allows establishing the regularities of the influence of the air conditioning system on the traction and speed indicators and fuel efficiency of cars, to select the refrigeration compressor and other elements of the air conditioning system to the vehicle based on its structural features and operating conditions. The dynamic simulation car model is designed in view of the air conditioning system. It can be used for research and design calculations related to assessing influence of the applied air conditioning system on the dynamic characteristic of the car. The results of the car dynamics simulation when the air conditioning compressor is being turned on/off are presented.

Keywords: Car · Air conditioning system · Simulation dynamic model

1 Introduction

Contemporary theoretical research is characterized by the extensive use of simulation models to reproduce the functioning of complex dynamical systems. In particular, computational experiments in the development of new and refinement of the existing structures of vehicles can be conducted using a simulation car which takes into account the most significant interconnections between its elements [1–13]. Simulation is evolving now. The models become more detailed and natural. At the same time, computational model experiments can be an alternative to full-scale tests.

2 Development of a Dynamic Car Simulation Model

The purpose of this research work is to develop and study a refined dynamic model of the car, which takes into account the influence of the air conditioning system on the process of car functioning. The compressor of the operating air conditioning system consumes approximately 5–10% of the generated power of the car engine which significantly affects the dynamic characteristics of the car and the safety of its operation.

The refined simulation dynamic model is based on the theory of bond graphs [11–14], which is fundamental to many high-level CAE products used in the aviation industry, heavy engineering and robotics.

Bond graphs are characterized by clarity and relative simplicity of providing system information. Bond graphs are based on the analysis of power flows transmitted in technical systems. In bond graphs theory, energy effects take the main part in any process except for the informational one. The value of these effects is determined by the properties of the both interacting systems. In addition, the transmitted power flow is always defined by the product of two model values, called fundamental (current and voltage for electrical, force and speed for mechanical, pressure and volume flow for hydraulic, specific exergy and mass flow for gas systems), one of which is determined by the first system, and another—by the second.

The car bond graphs are based on the process of power exchange of the various car subsystems with the environment and with each other. We get a model of the system as a whole by connecting the models of subsystems with the relevant connections. If necessary, the model may become more complex to account for important physical effects. The causality of each added element is defined, and the value of added effects is assessed.

Bond graphs of individual elements and, therefore, of the whole system are detailed, indicating:

- The direction of the transmitted power flow (marked with a semi-arrow);
- An argument, i.e. an independent input value for the element, and a function, i.e. a dependent output in the transmitted power flow. This action is done for establishing the causality of the graph. It is marked with a bar on the bond. It means that the power flow depends on the properties of the interacting elements (systems). Moreover, one of the fundamental parameters that define the flow of power or energy is set by the first element and is the output for it, and the other is the second element and the input for the first one.

Showing the direction of the power flow and causality on the graph allows making a consistent description of the individual system elements.

Thus, the elements of bond graphs are the simplest devices that implement the operations of accumulation, dissipation, transformation and transfer of power, i.e. power basic links.

Figure 1 shows a generalized bond graph [11–13] of a car.

The common notation was used during the graph building, in particular: *Se*—force source; *R*—scattering element reflecting energy losses; *I*, *C*—accumulating inductive

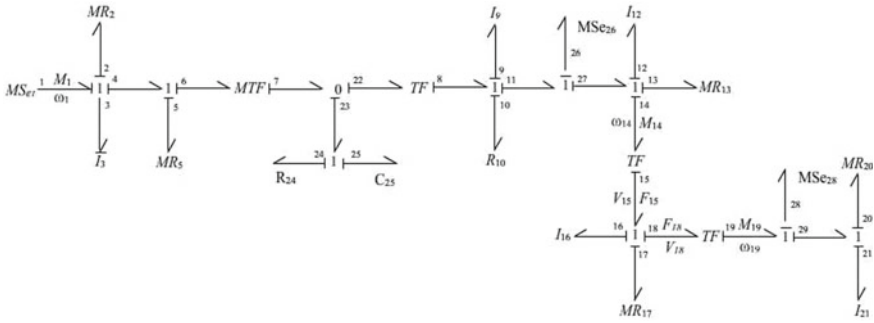


Fig. 1 Generalized bond graph of a car

and capacitive elements, respectively; TF—transforming element; MSe, MR, MTF—modulating elements (elements with varying characteristics); 1—general flow node, 0—general force node. The characteristics of the energy base units included in the graph are shown in Table 1.

Table 1 Characteristics of energy base units

Energy base units	Name of the unit (node) of the car
Se1, MR2, I3	Engine
MR5, MTF7	Clutch disc
R24,C25	Torsional vibration dampener
TF8,I9,R10	Gear box, gimbal and main gear
MSe26, (MSe28)	Brake mechanisms of driving (driven wheels)
I12,MR13, TF15 (I21,MR20,TF19)	Driving (driven) wheels
I16,MR17	Car body

The air conditioning system is an integral part of the MR₂ element. It is a dissipating element that reflects energy losses in a car internal combustion engine (ICE).

The mathematical description of a car with a four-cylinder internal combustion engine and a manual transmission includes fifteen ordinary differential equations [11–13], of which twelve equations describe the process of engine operation.

In particular, the change in the state of the working fluid in the intake manifold and in each cylinder is described by differential equations of the laws of conservation of mass and energy [11, 15, 16], which are supplemented by known dependencies for determining indicators related to the working fluid, gas exchange, combustion and heat exchange processes.

The angular velocity and angle of rotation of the crankshaft are determined from the differential equations of the piston and crankshaft motion [11, 17].

The known dependencies of the car theory are used to make a mathematical description for the operation of the transmission units (clutch, gearbox), driving and driven

wheels [18]. The operation of the torsional vibration damper is described by two differential equations. The speed of car motion when the clutch is turned off is determined by the differential equation of car motion [11].

A multicyclic calculation of the car transient state is made by this model, and the steady state is considered as a special case of the transient state. Thus, the model allows conducting calculations both for car static and dynamic characteristics.

This model is open, so it is possible to connect models of processes, occurring in specific car systems.

The design and operational parameters of the VAZ 21,114 car are used as initial data for mathematical simulation.

The compressor DY5V16 with a variable cylinder volume is used as an example of the air conditioning system [19–21].

Compressor characteristics:

- The volume of cylinders, 10–160 cm³;
- Number of cylinders, 5;
- DC voltage, 12 V;
- Refrigerant, R134a;
- Lubricating oil, PAG 100, PAG 150, PB 100;
- Oil volume, 150 cm³;
- Maximum permissible speed of the compressor shaft rotation, 8000 rpm;
- Maximum continuous rotation speed of the compressor shaft, 6500 rpm;
- cooling capacity Q_0 , from 3.8 to 9.6 kW;
- Power consumption N , from 3.3 to 7.0 kW at the speed of rotation of the compressor shaft, 1000–3000 rpm.

The calculation of cooling capacity (Q_0 , kW) and power consumption (N , kW) is made using the equations:

$$Q_0 = 5, 8 \left(\frac{n}{2000} + 0, 5 \right) - 2,$$

$$N = 3, 7 \left(\frac{n}{2000} + 0, 5 \right) - 0, 4,$$

n is the rotation speed of the compressor shaft, rpm.

3 Mathematical Model Testing

Figures 2, 3 and 4 show the main results of simulating the process of car motion with the air conditioning system being turned off/on. The car acceleration was carried out with a sequential gear switching on (from the first to the fourth one). The air conditioner was turned on at the 20th second. At the same time, the fuel supply characteristic and the gearshift algorithm were unchanged for the two calculation options.

4 Conclusion

Thus, the use of bond graphs for mathematical simulation of car dynamics allows:

- Revealing the structural features of a complex dynamic system;

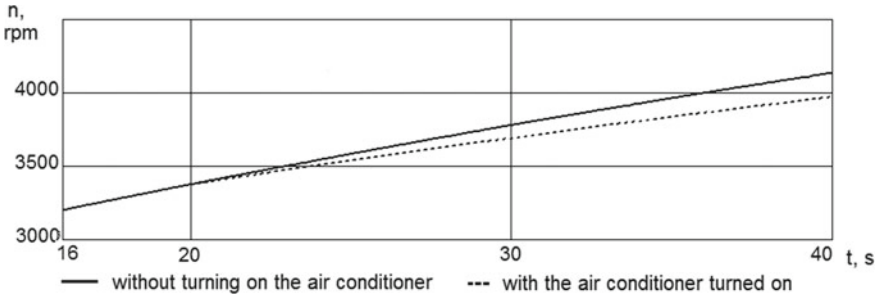


Fig. 2 Graphs of the change in the crankshaft rotation frequency in the internal combustion engine with the air conditioning system turned on and off

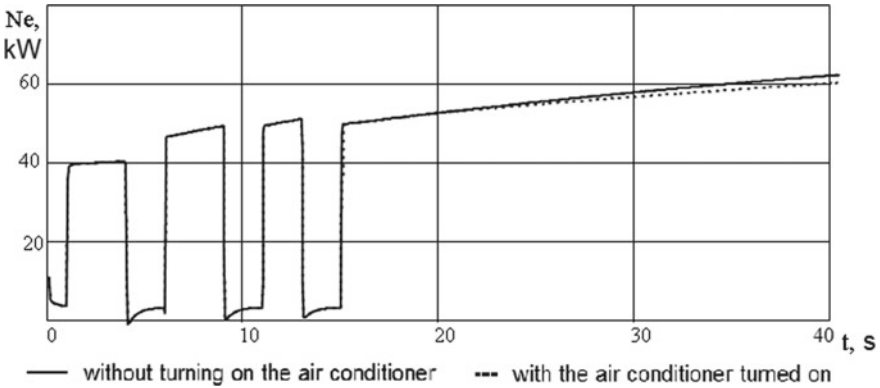


Fig. 3 Graphs of changes in the effective power of the car engine

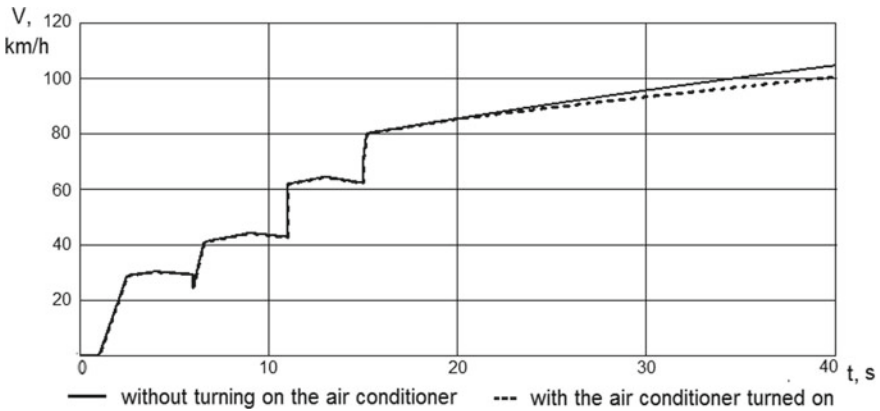


Fig. 4 Graphs of speed changes the air conditioning system turned on and off

- Determining the cause-and-effect relations that establish the input–output for specific elements of the car and the car as a whole system;

- Implementing a unified approach to the formulation of conditions at the boundaries of interacting car subsystems to jointly apply existing mathematical models in car design systems.

The results presented in Figs. 2, 3 and 4 allow us to draw a conclusion about the wide possibilities of the developed model for describing the joint operation of the car and the air conditioning system in real operating conditions.

The developed software allows setting the regularities of the impact the air conditioning system has on the traction and speed indicators and car fuel efficiency. The mathematical description and software also allow selecting the refrigeration compressor and other elements of the conditioning system for the vehicle based on its design features and operating conditions. A simulation dynamic model of the car developed with the air conditioning system can be used in research conduct and design calculations related to the assessment of the influence the condition systems have on the dynamic car figures.

References

1. Shibakov VG, Karabtsev VS, Valeev ID (2009) Optimization of car design parameters using computer simulation. *Gruzovik* 6:16–19
2. Basyrov RR, Shaikhullin EF (2012) Technologies for modeling parameters at car design. *Russ forests econ* 1–2(42–43):8–9
3. Bakhmutov SE, Akhmedov AA (2010) Multi-criteria optimization of automotive equipment during its creation and development. *Automot Ind* 10:14–16
4. Belousov NB (2012) Complex mathematical model as the basis for creating the PTS of the future. *Automot Ind* 8:8–12
5. Radionova LV, Chernyshev AD (2015) Mathematical model of the vehicle in MATLAB Simulink. *Procedia Eng* 129:825–831
6. Zhang P, He L, Liu X, Xia Q (2013) Study on computer simulation for car handling dynamics with 8 DOF. *Adv Mater Res* 655–657:1136–1140
7. Grabowski L, Pietrykowski K, Wendeker M (2012) AVL simulation tools practical applications. *Politechnika Lubelska Graz. Lublin*, pp 96
8. Venture G, Gautier M, Khali W, Bodson P (2003) Parametric identification of the car dynamics. *IFAC Proc Volumes (IFAC-PapersOnline)* 36(16):285–290
9. Terzo A, Gobatto P, Masi M, Rossi A (2016) An engine vehicle model to assess the theoretical increase of car safety by using the spark ignition engine to support the conventional braking system. *Int J Thermodyn* 19(4):187–196
10. Wang C, Yin C, Chen L (2010) A study on engine modeling with BOOST and BOOST-CRUISE co-simulation. *Qiche Gongcheng/Automot Eng* 32(1):26–30
11. Maliovanov MV, Khmelev RN (2013) Development and research of car dynamic model. In: *Modernization and research in the transport complex*. Perm, pp 207–216
12. Grunichev AV, Maliovanov MV, Khmelev RN (2013) Development of car simulation model. In: *Progress of transport and systems*, Volgograd, pp 47–46
13. Maliovanov MV, Radko AE, Khmelev RN (2014) Software-based complex “Simulation car dynamic model”. Certificate of state registration of the computer program No. 2014617074, registration date 10 June 2014
14. Kernop D, Rozenberg R (1974) Application of bond graphs theory in engineering. Mir, Moscow, p 95

15. Elagin MYu (1995) Mathematical modeling of non-stationary processes in open thermodynamic systems. Tula, TulSU, pp 86
16. Elagin MYu (2013) Thermodynamics of open systems. Tula, TulSU, pp 400
17. Agureev IE, Elagin MYu, Khmelev RN, Platonov KYu, Pyshnyi VA (2020) Using experience of the dynamic models of piston internal combustion engines. IOP Conf Ser: Mater Sci Eng 786(1):012080. https://doi.org/10.1007/978-3-030-22063-1_29
18. Safullin RN, Bashkardin AG (2010) Cars. Operational properties. vol. 2. SPb, SPbGASU, pp 244
19. Elagin MYu, Alekseyev IE, Tishin SA (2017) Air conditioning systems in automobile transport. Tula, TulSU, pp 75
20. Elagin MYu (2020) Thermodynamics of open systems. Practical application Tula. TulSU, pp 482
21. Elagin MYu, Chukanova EM (2002) Mathematical modeling of working processes of axial piston compressors. News of TulSU. Series "Road transport" 6:103–108



Determination of the Hydrodynamic Vibration Frequencies in the Main Pump Pippings

A. P. Tokarev^(✉), S. E. Spirin, and A. R. Valeev

Ufa State Petroleum Technological University, 1, Kosmonavtov Street, Ufa 450062, Russia

Abstract. Oscillations of pump pippings can be caused by both hydrodynamic reasons and vortex formation at local resistances and resonance with the natural frequencies of the piping. In some cases, the vibration of pipelines exceeds the permissible norms by 1.5–2 times. The range of vibration frequencies of a hydrodynamic nature directly depends on the flow rate of the working medium. As the latter decreases, the range also decreases. In any elbow of the pipeline, with a sufficient flow rate of the liquid, vortex formation occurs, which is the cause of forced vibrations. The article is devoted to experimental studies of the dependence of the vortex formation frequencies on the local resistances of the pump pippings of the main pumping units on the mode of their operation and to the determination of the possibility of predicting such phenomena. At the same time, the values of the Strouhal number characterizing hydrodynamic phenomena in unsteady flow regimes for the flow of liquids in local resistances of pipelines have been studied very little.

Keywords: Vibration · Vortex formation · Hydrodynamics · Process pipelines · Pump piping · Strouhal number

1 Introduction

Vibration of pumping units is one of the most important reasons for their failures. Swirling flow arising in the pump piping affects its operation. If the range of excitation frequencies of vortex formation in the pipeline coincides with the excitation frequencies of the pump, it will be possible to observe a beat—a process of increasing the amplitude of stationary harmonic oscillations [1, 2]. In some cases, the vibration of pipelines exceeds the permissible norms by 1.5–2 times and, being transmitted to the pumping unit, can serve as one of the most important reasons for its increased vibration [2–6].

Determination of the conditions for the occurrence and the possibility of predicting the hydrodynamic vibration of pipelines for piping of pumping units is an urgent task for pipeline transportation of oil and oil products.

2 Experimental Study of Vortex Formation Frequencies for Vibrations Arising in the Pipe Bend

The main causes of vibration in a pipeline are of a hydrodynamic nature. In bent pipelines, bends, tees due to a change in the flow velocity vector, centrifugal forces arise, directed

from the center of curvature to the outer wall of the pipeline. This process is accompanied by an increase in pressure at the outer wall and a decrease on the inner one, which leads to a diffuser effect near the inner wall and a confuser effect near the outer one (when passing from a curved section to a straight one, the opposite picture is observed, Fig. 1). The appearance of centrifugal forces and the presence of a boundary layer at the walls explains the appearance of a secondary cross-flow in a bent pipe, i.e., the formation of a paired vortex, which is superimposed on the main flow, parallel to the channel axis, and gives the lines a helical shape [7–9]. This effect is accompanied by the appearance of an impulse of force on the body, which leads to the formation of vibration, as well as noise.

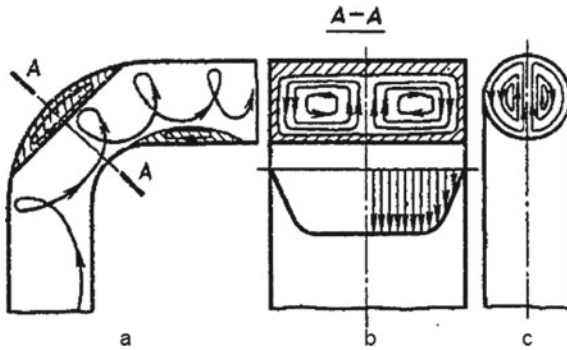


Fig. 1 Paired vortex in the pipe bend: **a**—longitudinal section; **b**—cross section (rectangular channel); **c**—cross section (round pipe)

The object of research (Fig. 2) for analyzing the hydrodynamic causes of vibration for vortex formation is a section of a pipeline with a diameter of 108 mm and a wall thickness of 3.5 mm with a bend with a 90° rotation angle. To study the emerging vibration, the water supply Q in the pipeline was varied from 165 to $15 \text{ m}^3/\text{h}$ with a step of $15 \text{ m}^3/\text{h}$. The vibration analyzer “Diana-8” was used as a device, and the software “Atlant” was used for data processing. Before the turn, the section has a length of 4.4 m and the pipeline is freely fixed at the ends. This leads to additional noise on the readings. At the same time, the site is in almost complete isolation from vibrations caused by a running pump. Analysis of hydrodynamic vibrations is reduced to the analysis of vortex formation, since it is the main cause of vibrations in this case. The most important in this case will be the readings from horizontal sensors 1 and 2 (Fig. 2), since the vortex is observed precisely in these places in the fluid flow, which is confirmed by works [2, 3, 9]. Consider the results of the experiment using the example of flow rate of $165 \text{ m}^3/\text{h}$ (Fig. 3).

For all the measurements carried out according to the obtained peak values for vertically located sensors, three values of the natural frequencies of the pipeline vibrations can be distinguished, which are repeated regardless of the pipeline supply: 11.921 Hz, 28.610 Hz and 59.604 Hz.

In general, with a decrease in supply, the frequency range becomes narrower and smaller in value (the first range is in the range of 16.7–47.7 Hz), which indicates the

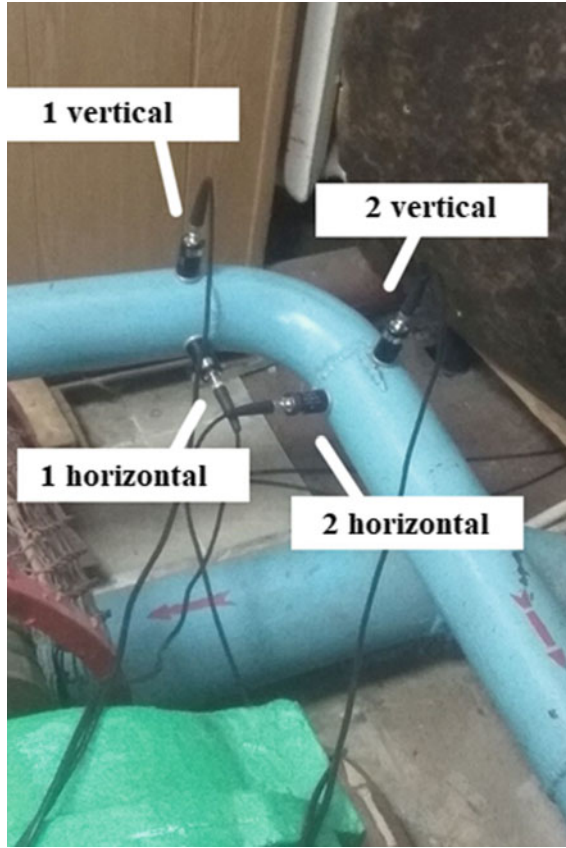


Fig. 2 Location of vibration sensors at the experimental site

hydrodynamic frequencies in the pipeline. This range also includes two natural frequencies of 11.921 Hz and 28.610 Hz, which have a significant effect on the amplitude of oscillations.

3 Dependence of the Frequencies of Hydrodynamic Vibration in Process Pipelines from the Flow and Pipeline Parameters

It is known that the frequencies of vortex formation depend on the velocity v of the liquid and the diameter of the pipeline D . Based on the experimental data, in the first approximation, we find the Strouhal number Sh , which characterizes the process of the arising vibration:

$$Sh = \frac{f \cdot D}{v} = \frac{f \cdot \pi \cdot D^3}{4 \cdot Q} = \frac{11.921 \cdot 3.14 \cdot 0.101^3 \cdot 3600}{4 \cdot 165} = 0.210 \quad (1)$$

where f is the frequency of vortex formation, Hz.

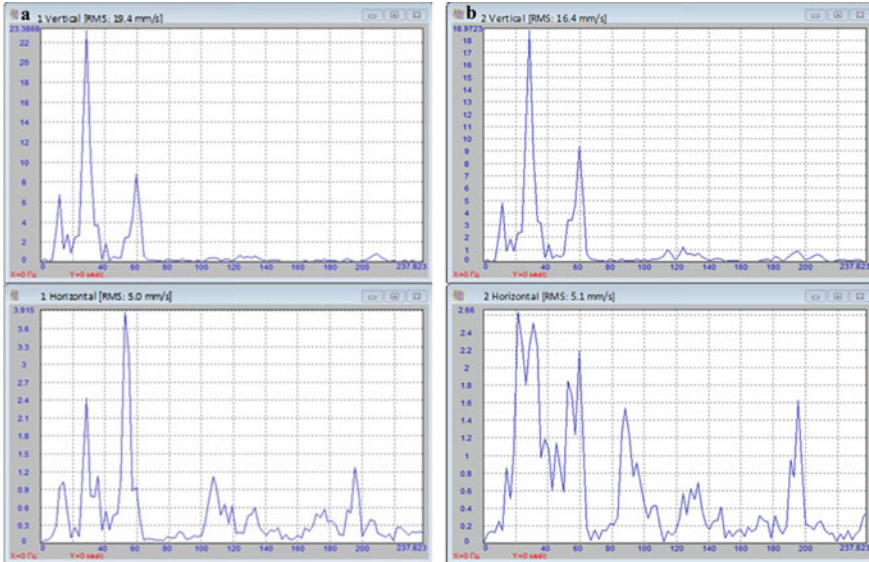


Fig. 3 Obtained results of measurements of vibration velocity at $Q = 165 \text{ m}^3/\text{h}$ from, **a** first sensor and, **b** second sensor

Reynolds number:

$$Re = \frac{v \cdot D}{\nu} = \frac{4 \cdot Q}{\pi \cdot D \cdot \nu} = \frac{4 \cdot 165}{3600 \cdot 3.14 \cdot 0.101 \cdot 1 \cdot 10^{-6}} = 578083 \quad (2)$$

where ν is the kinematic coefficient of viscosity of the working fluid.

The resulting range of Strouhal numbers depending on the Reynolds number is shown in Fig. 4.

4 Determination of the Probable Vibration Frequencies of the Pump Pipings of the Main Pumping Unit NM 10,000–210

To project the obtained results to the main pump pipings, we will find the characteristic parameters of the process under consideration—the Reynolds number within the working area of the pumping unit NM 10,000–210 and the Strouhal number.

To find the possible frequencies of vortex formation, we will take the following: the nominal diameter of the pipeline is 900 mm, the viscosity of the pumped oil is $\nu = 35 \cdot 10^{-6} \text{ m}^2/\text{s}$. Using Eq. 2 let’s find the Reynolds numbers in the pump working area, which, according to [10], is in the range of $7500\text{--}11,000 \text{ m}^3/\text{h}$:

at $Q = 7500 \text{ m}^3/\text{h}$, $Re = 84,211$,

at $Q = 11,000 \text{ m}^3/\text{h}$, $Re = 123,510$.

According to the data obtained as a result of the experiment (Fig. 4), in the obtained range of Reynolds numbers, the Strouhal number is between 1.3 and 4.1.

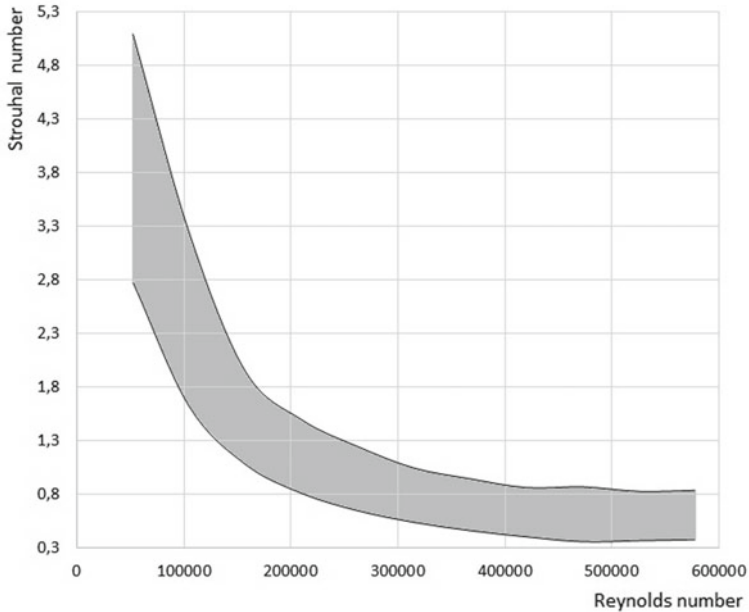


Fig. 4 Dependence of the Strouhal number on the Reynolds number

To find the possible frequencies of vortex formation for pipings of NM 10,000–210, we will find the Sh in the frequency range from 2.384 to 50.000 Hz (Table 1). The characteristic frequencies of vortex formation are highlighted.

It can be seen from the table that the characteristic frequencies of vortex formation in the piping of the pump NM 10,000–210 will lie in the range of 4.768–23.842 Hz.

5 Summary

The hydrodynamic causes of vibration in the pipeline are currently poorly studied. This is a vast area that requires research, since the range of their frequencies may be within the range of frequencies of disturbing forces, the source of which is the pumping-power unit. In this case, beating of both the pumping and power plant and the pipeline in the supports may occur, since this is a mutually communicating system.

For the pipings of the main pump HM 10,000–210, the Strouhal number at the Reynolds number from 84,000 to 123,500 is in the range from 1.3 to 4.1, the assumed range of excitation frequencies of vortex formation lies in the range of 4.768–23.842 Hz (depending on the fluid flow rate).

Table 1 Results of finding possible vortex formation frequencies for pipings of NM 10,000–210

Q, m ³ /h	7500	8000	8500	9000	9500	10000	10500	11000
Re	84211	89826	95440	101054	106668	112282	117896	123510
f, Hz	Sh							
2,384	0,655	0,614	0,578	0,546	0,517	0,491	0,468	0,447
4,768	1,310	1,228	1,156	1,092	1,035	0,983	0,936	0,893
7,153	1,966	1,843	1,735	1,638	1,552	1,474	1,404	1,340
9,537	2,621	2,457	2,313	2,184	2,069	1,966	1,872	1,787
11,921	3,276	3,071	2,891	2,730	2,586	2,457	2,340	2,234
14,305	3,931	3,686	3,469	3,276	3,104	2,949	2,808	2,681
16,689	4,587	3,985	4,047	3,822	3,621	3,440	3,276	3,127
19,074	5,242	4,914	4,625	4,068	4,088	3,931	3,744	3,574
21,458	5,897	5,529	5,203	4,914	4,656	4,090	4,102	4,021
23,842	6,552	6,143	5,782	5,460	5,173	4,914	4,680	4,108
26,226	7,208	6,757	6,360	6,006	5,690	5,406	5,148	4,914
28,610	7,863	7,371	6,938	6,552	6,208	5,897	5,616	5,361
30,994	8,518	7,986	7,516	7,098	6,725	6,389	6,084	5,808
33,379	9,173	8,600	8,094	7,644	7,242	6,880	6,552	6,255
35,763	9,829	9,214	8,672	8,190	7,759	7,371	7,020	6,701
38,147	10,484	9,829	9,250	8,737	8,277	7,863	7,488	7,148
40,531	11,139	10,443	9,829	9,283	8,794	8,354	7,956	7,595
45,300	12,450	11,671	10,985	10,375	9,829	9,337	8,893	8,488
47,684	13,105	12,286	11,563	10,921	10,346	9,829	9,361	8,935
50,000	13,760	12,900	12,141	11,467	10,863	10,320	9,829	9,382

References

- Gumerov AG, Gumerov RS, Akberdin AM (2001) Eksploatatsiya oborudovaniya nefte-perekachivayushchikh stantsiy (Operation of pumping stations equipment). Nedra, Moscow
- Gumerov AG, Gumerov RA, Iskhakov RG (2008) Vibroizoliruyuschaya kompensiruyuschaya sistema nasosno-energeticheskikh agregatov (Vibration-isolating compensation system of pump-power units). SUE "IPITER", Ufa
- Samarin AA (1979) Vibratsii truboprovodov energeticheskikh ustanovok i metody ih ustraneniya (The vibrations of pipelines of power equipment and methods of their elimination). Energia, Moscow
- Tokarev A, Zotov A, Valeev A (2017) Study of application of vibration isolators with Quasi-zero stiffness for reducing dynamics loads on the foundation. *Procedia Eng* 176:137–143. <https://doi.org/10.1016/J.PROENG.2017.02.281>
- Tokarev A, Zotov A, Valeev A (2017) The application of passive vibroprotective systems having power characteristics with hysteresis loops of rectangular shape for the main pumping units. *Procedia Eng* 176:118–127. <https://doi.org/10.1016/J.PROENG.2017.02.279>
- Tokarev A, Valeev A, Zotov A (2019) Use of vibration isolation systems with negative stiffness on the basis of special shaped guides to reduce pump piping vibration. In: Proceedings of the 5th international conference on industrial engineering (ICIE 2019), lecture notes in mechanical engineering, pp 913–920. https://doi.org/10.1007/978-3-030-22041-9_97
- GOST 32388–2013 (2013) Technological pipelines. Norms and methods of strength analysis, vibration and seismic effects. Standartinform, Moscow
- Drozyner P (2011) Determining the limits of piping vibration. *Sci probl mach oper maintenance* 1:97–103

9. Idelchik IE (1992) Spravochnik po gidravlicheskim soprotivleniyam (Handbook of hydraulic resistances). Mashinostroenie, Moscow
10. Catalog, (1973) Tsentrobezhnyye neftyanye magistral'nyye i podpornyye nasosy (Centrifugal oil main and booster pumps). Tsintikhimneftemash, Moscow



Mathematical Planning of the Experiment in Product Design

K. V. Zhegera^(✉), N. A. Petuhova, and E. A. Samigullina

Penza State University of Architecture and Construction, 28, Titova St., Penza 440028, Russia

Abstract. The foundations of the theory of experiment play a large role in the modern world. An experiment is a procedure for choosing the number and conditions for conducting experiments necessary and sufficient for solving the problem with the required accuracy. Along with the control of products, it is often necessary to control the parameters of technological processes. This task can be solved by testing statistical hypotheses. However, the greatest effect can be achieved not by controlling the quality parameters, but by such an organization of production processes in which the products are not discarded. The task of the experiment is to establish the minimum required number of experiments and the conditions for their conduct, the choice of methods for mathematical processing of results and decision-making. The object of study must be managed and must meet the requirements of reproducibility. The article discusses the use of methods of mathematical planning of the experiment on the example of asphalt mix. Strength is selected as the optimization parameter.

Keywords: Experiment · Experiment planning · Asphalt concrete mix · Strength

1 Introduction

Since its inception, science is looking for ways to learn the laws of the world. Making one discovery after another, scientists climb higher and higher up the ladder of knowledge, erasing the boundary of uncertainty and entering new frontiers of science. This path is through experiment. By consciously limiting the infinite diversity of nature to the artificial framework of scientific experience, we turn it into a picture of the world understandable for the human mind.

Experiment as a scientific research is the form in which and through which science exists and develops. The experiment requires careful preparation before conducting it. In biomedical research, the planning of the experimental part of research is particularly important because of the wide variability of properties characteristic of biological objects. This feature is a major cause of difficulty in interpreting results, which can vary significantly from experience to experience.

Statistical problems justify the need to choose an experimental scheme that would minimize the effect of variability on a scientist's conclusions. Therefore, the goal of experiment planning is to create a scheme that is necessary to obtain as much information as possible at the lowest cost to complete the study. More precisely, experiment planning

can be defined as a procedure for choosing the number and conditions for conducting experiments that are necessary and sufficient to solve the problem with the required accuracy.

The problem of planning the experiment involved many scientists [1–10].

Thus, experiment planning is a procedure for choosing the number and conditions for conducting experiments that are necessary and sufficient to solve the problem with the required accuracy. In this case, the following is significant:

- Striving to minimize the total number of experiments;
- Simultaneous variation of all variables determining the process according to special algorithms;
- The use of a mathematical apparatus that formalizes many actions of the experimenter;
- The choice of a clear strategy to obtain adequate data and make informed decisions after each series of experiments.

Consider the use of experimental design on the example of the design of asphalt concrete mix.

When planning an experiment, the choice of the optimization parameter is decisive.

When choosing an optimization parameter, it is necessary to take into account a number of requirements [11–15]:

1. The optimization parameter must be quantitative, set by a number. The set of values that an optimization parameter can take is called its scope. Definitions can be continuous and discrete, limited and unlimited.
2. The optimization parameter must be a single number. In most cases, this is obtained naturally, as the registration of the instrument reading. More often, it is necessary to make some calculations.
3. Uniqueness in a statistical sense. The set of values of the factors should correspond to one with the accuracy of the experiment parameter value.
4. The effectiveness of the evaluation system. To successfully achieve the goal of the study, it is necessary that the optimization parameter evaluate the efficiency of the system in a pre-selected sense. This requirement is the main, determining the correctness of the formulation of the problem.
5. The effectiveness of the parameter optimization in a statistical sense. In fact, this requirement is reduced to the choice of the optimization parameter, which is determined with the greatest possible accuracy.
6. The next requirement for the optimization parameter is the requirement of universality or completeness. The universality of the optimization parameter is understood as its ability to comprehensively characterize an object. In particular, the technological parameters of optimization are not universal enough: They do not take into account the economy.
7. The optimization parameter should have a physical meaning, be simple and easily calculated.

To select the most significant optimization parameters at the stage of preliminary study of the object of study with the formalization of a priori information, we can conduct

a psychological experiment, consisting in the objective processing of data obtained as a result of a survey of experts or as a result of studies published in the literature. This kind of experiment allows us to design the object of study more correctly, accept or reject some preliminary hypotheses, correctly select the parameters for the subsequent active experiment, justifiably excluding some of them from further consideration.

2 Methods

The number of factors is large, so we use an a priori ranking of factors, since it is necessary to select the most important from a large number of factors. This method consists in evaluating each factor by assigning it a certain rank. Moreover, the factors are ranked in descending order of their contribution. The prior method is based on the expert method [16].

First, the sum of the ranks is determined by factors $\left(\sum_1^n a_{ij}\right)$ and then the difference (Δi) between the sum of each factor and the average sum of ranks and the sum of squared deviations (s) (Eqs. 1 and 2):

$$\Delta i = \sum_1^n a_{ij} - \frac{\sum_1^m \sum_1^n a_{ij}}{m} = \sum_1^n a_{ij} - T, \tag{1}$$

$$S = \sum_1^m (\Delta i)^2 \tag{2}$$

where a_{ij} —is the rank of each i th factor of the j th explorer;
 n —is the number of researchers;
 m —is the number of factors;
 T —the average sum of ranks.

The consistency of expert opinion is checked by Eq. 3.

$$\omega = \frac{12S}{m^2(k^3 - k) - m \sum_1^m T_j}, \tag{3}$$

The hypothesis of the consent of the researchers can be accepted if, for a given number of degrees of freedom, the tabular χ^2 value is less than the calculated value for the 5% level (Eq. 4).

$$\chi^2 = \frac{12S}{mk(k + 1) - \frac{1}{k-1} \sum_1^m T_j} \tag{4}$$

The coefficient of pair correlation is calculated by Eq. 5 [17]

$$r_{xy} = \frac{\overline{xy} - \bar{x}\bar{y}}{S(x)S(y)}, \tag{5}$$

The assessment of the significance of the pair correlation coefficient is carried out using student's criterion (Eq. 6).

$$t_{\text{calc}} = r_{xy} \frac{\sqrt{n-2}}{\sqrt{1-r_{xy}^2}}, \tag{6}$$

The regression equation is a form of static relationship between variables (Eq. 7) [18].

$$y = b_0 + b_1x_1 + b_2x_2 + b_3x_3 + \dots + b_nx_n, \tag{7}$$

Parameter b is the regression coefficient. It shows how much the value of feature y changes when x changes by one. The value and sign of the coefficient indicates the contribution of this factor to the overall result in the transition from zero to the upper or lower level of the factor.

Coefficients of the regression equation are calculated by Eq. 8–9 [19, 20]:

$$b_0 = \frac{\sum y \sum x^2 - \sum xy \sum x}{n \sum x^2 - (\sum x)^2}, \tag{8}$$

$$b_1 = \frac{n \sum xy - \sum x \sum y}{n \sum x^2 - (\sum x)^2}, \tag{9}$$

The uniformity of the dispersion is checked by Eq. 10.

$$S_B^2 = \frac{\sum y^2 - (\frac{1}{n})(\sum y)^2}{n-1}, \tag{10}$$

The adequacy of the model is checked by Eq. 11–12.

$$S_a^2 = \frac{\sum (y - \hat{y})^2}{n-2}, \tag{11}$$

$$F = \frac{S^2}{S_B^2}, \tag{12}$$

The model is considered adequate if $F_{\text{calc}} < F_{\text{tabl}}$.

Testing the significance of the coefficients is carried out by the criterion of Student (Eq. 13).

$$t = \frac{|b_j|}{S_{\{y\}}} \tag{13}$$

The coefficient is considered significant if it is greater than the table value of the student's criterion. $F_{\text{calc}} < F_{\text{tabl}}$.

3 Results

Four specialists ($m = 4$) were interviewed during the preliminary study of reinforced concrete. These surveys were used for a priori ranking of parameters in order to identify the most significant of them. The survey was conducted using a questionnaire containing seven parameters: (x_1 -shear stability, x_2 -shear adhesion, x_3 -crack resistance, x_4 -compressive strength, x_5 -porosity, x_6 -water resistance, x_7 -water saturation), which had to be ranked according to the degree of their influence on asphalt concrete.

The main quality indicator of asphalt concrete mix compressive strength was chosen as an optimization parameter. When optimizing this indicator, the most important task is solved, the competitiveness of products in the market.

The strength of concrete is influenced by a number of factors:

- Quality of preparation of asphalt concrete mix;
- Observance of a temperature mode;
- Quality of asphalt concrete mix laying;
- Compliance with the recommendations according to the scheme of sealing rollers.

We construct an average chart of ranks for the factors under consideration (Table 1).

Table 1 Rank matrix

Researchers, m	Factors ($k = 7$)							T_j
	x_1	x_2	x_3	x_4	x_5	x_6	x_7	
1	4	2	5	7	2	2	7	30
2	3	1	3	7	3	1	5	30
3	5	2	5	7	2	3	6	12
4	5	4	5	7	3	3	7	18
$\sum_1^m a_j$	17	9	18	28	10	9	25	$\sum T_j = 90$
Δ_j	0.4	-7.6	1.4	11.4	-6.6	-7.6	8.4	
$(\Delta_j)^2$	0.16	57.76	1.96	129.96	43.56	57.76	70.56	$S = 361.72$

Let us estimate the degree of consistency of opinions of all researchers using the concordance coefficient ω by Eq. 3:

$$\omega = \frac{12 \cdot 361.72}{4^2 \cdot (7^3 - 7) - 4 \cdot 90} = 0.87$$

Estimate the significance of the coefficient of concordance by Eq. 4.

$$\chi^2 = \frac{12 \cdot 361.72}{4 \cdot 7(7 + 1) - \frac{1}{7-1}90} = 20.8$$

Due to the fact that the tabular value of the χ^2 criterion is less than the calculated one, it can be stated with a 95% confidence level that the researchers' opinion on the degree of influence of factors is consistent in accordance with the concordance coefficient $\omega = 0.87$. This allows us to construct an average rank chart for the factors under consideration (Fig. 1).

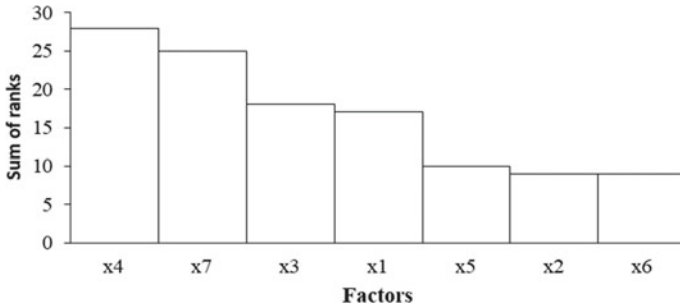


Fig. 1 Rank chart

The diagram shows that the distribution is uniform, the decrease is non-monotonic. The factors X_4 and X_7 are significant because they stand out most in the constructed diagram.

The main factors affecting the water saturation of the samples is strength. Thus, it is advisable to determine the dependence of water saturation (x , %) on strength (y , MPa), which will allow us to find the optimum strength. Baseline data are presented in Table 2.

To establish the relationship between the variables being studied, we calculate the pair correlation coefficient.

$$r_{xy} = \frac{13069.857 - 62.571 \cdot 208.714}{2.195 \cdot 4.861} = 0.966$$

We will assess the significance of the pair correlation coefficient using student's criterion.

$$t_{\text{calc}} = 0.966 \cdot \frac{\sqrt{5}}{\sqrt{1 - 0.966^2}} = 8.356$$

Let us compare the obtained value with the critical value of the t-criterion, which is determined by the student's distribution table, the significance level $\alpha = 0.05$ and the degrees of freedom $k = 5$; we find t_{crit} :

$$t_{\text{crit}}(n - m - 1; \alpha/2) = (5; 0.025) = 2.571$$

Because $t_{\text{tabl}} = 8.356$ and $t_{\text{calc}} > t_{\text{tabl}}$, the correlation coefficient is significant.

Make a regression equation. To do this, we find the coefficients of the regression Eq. 8:

$$b_0 = \frac{1461 \cdot 27440 - 91489 \cdot 438}{7 \cdot 27440 - (438)^2} = 74.82$$

Table 2 Experimental results

Nº	x	y	x ²	y ²	xy
1	63	211	3969	44 521	13 293
2	63	209	3969	43 681	13 167
3	58	200	3364	40 000	11 600
4	65	215	4225	46 225	13 975
5	65	214	4225	45 796	13 910
6	62	207	3844	42 849	12 834
7	62	205	3844	42 025	12 710
∑	438	1461	27 440	305 097	91 489

$$b_1 = \frac{7 \cdot 91489 - 438 \cdot 1461}{7 \cdot 27440 - (438)^2} = 2.14$$

The regression equation will be as follows:

$$y = 74.82 + 2.14x$$

Using the coefficients, we can find out the strength of the influence of factors. The greater the magnitude of the coefficient, the greater the influence of the factor. In this case, the coefficient has a plus sign. This means that as the value of the factor increases, the value of the optimization parameter increases.

When compiling the regression equation, it is necessary to take into account the homogeneity of the variance, the adequacy of the compiled model and the significance of the regression coefficients.

Check the dispersion uniformity. Dispersion characterizes the experiment error. Reproducibility is a characteristic of the test results, determined by the proximity of the results of the object re-tests.

$$S_B^2 = \frac{305097 - \frac{1}{7} \cdot (1461)^2}{7 - 1} = 27.6$$

Calculate the adequacy of the model

$$S_a^2 = \frac{11.05}{5} = 2.21$$

$$F = \frac{2.21}{27.6} = 0.08$$

The table value $F = 3.79$ is more than calculated, and then, the model is adequate. Check the significance of the coefficients

$$t_1 = \frac{2.14}{4.67} = 0.46 \leq t_{\text{krit}}$$

Thus, the model is adequate, the coefficients are significant, and so, we can build the dependence of water saturation on the strength (Fig. 2).

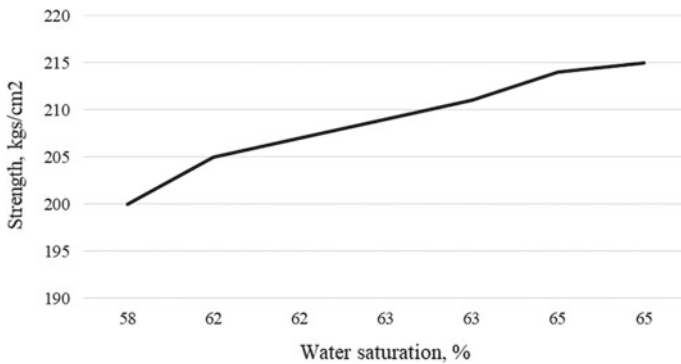


Fig. 2 Dependence of water saturation on the strength

4 Summary

Thus, during the course of the work, the degree of influence of factors on the optimization parameter (strength) was established and a function was obtained relating the factors and the optimization parameter. The resulting relationship between the factors and the response is called the response surface, the equation relating the factors and the response are called the regression equation, and the definition of the coefficients of this equation is the estimate of the coefficients.

A regression equation for the effect of water absorption on the strength of the asphalt concrete mix is compiled. It has been established that there is a linear relationship between water absorption and the strength of the asphalt concrete mix. A graphical dependency model has been built.

References

1. Kassandraova ON, Lebedev VV (1970) Processing the results of observations. Science, Moscow

2. Trusov VS (1983) The theory of experiment planning. Tutorial. Tomsk publishing house, Un-ta, Tomsk
3. Zaitsev VS (1990) System analysis of operator activity. Radio and Communication, Moscow
4. Hartman K (1977) Planning an experiment in research and technological processes. World, Moscow
5. Fisher RA (1951) The design of experiments. 6th edn. Oliver and Boyd, London
6. Krasovsky GI, Filaretov GF Planning an experiment. Publishing house BSU, Minsk
7. Ermakov SM (1983) Mathematical theory of experiment planning. Science, Moscow
8. Grigoriev YuD (2015) Methods for optimal experiment planning: linear models: study guide. Lan publishing house, Saint Petersburg
9. Fisher RA (1958) Statistical methods for researchers. Gosstatizdat, Moscow
10. Snedecor GW (1989) Statistical Method. Ames. Blackwell Publishing Professional, Iowa
11. Tarasov RV, Makarova LV, Zhegera KV (2017) Basics of scientific research. Organization and planning of the experiment. PGUAS, Penza
12. Ermolaeva VI (2007) The choice of the optimization parameter in the mathematical modeling of the object. Bull Ulyanovsk State Agric Acad 2(5):41–42
13. Adler YuP (1968) Introduction to experiment planning. Metallurgy, Moscow
14. Montgomery DK (1980) Experiment planning and data analysis. Shipbuilding, London
15. Dekhterinsky LV (1979) Technology of car repair. Transport, Moscow
16. Shchekin AV (2004) A priori ranking of factors. Guidelines for laboratory work for students of the specialty 110400 ‘Foundry production of ferrous and non-ferrous metals’. Habar.gos.tekh.un-ta, Khabarovsk
17. YaR M, Katyshev PK, Peresetsky AA (1998) Econometrics. The initial course. Rev. Delo, Moscow, pp 17–42
18. Efimova MR, Petrova EV, Rumyantseva VN (2000) General theory of statistics: textbook, 2nd edn. INFRA-M, Moscow
19. Belenky VZ (2012) Analysis and modeling of economic processes. CEMI RAS, Moscow
20. Gavrillets YN (2012) Mathematical and computer modeling of socio-economic processes. CEMI Russian Academy of Sciences, Moscow



Modeling the Laying Material Trajectory on the Technological Mandrel Surface Specified by an Irregular Spatial Point Set

E. Ustinova^(✉)

Platov South-Russian State Polytechnic University (NPI), 132, Prosveshcheniya st, Novocherkassk 346428, Russia

Abstract. The paper deals with the design of the material laying trajectory on the technological mandrel surface and the complex geometric shape mandrel surface model representation in automated systems for preparing control programs for winding composite materials products. The technological mandrel surface model can be represented as an irregular spatial point set. It is proposed to use an approach based on small surface segment approximation and modification of the differential equations system intended for integration laying material trajectories over an analytically given surface. The developed mathematical apparatus for constructing curves on surfaces given by irregular spatial point set makes it possible to construct smooth class-second curves without the need to first obtain the complete surface model. The proposed solutions adequacy are confirmed by the numerical experiments carried out on modeling the filament laying trajectory on various complex-profile mandrels given by an irregular point set and by the results of winding prepared control programs running out on a real multiaxis machine.

Keywords: Winding · Mandrel surface · Point cloud · Composite material product · CNC winding machine · Laying material trajectory

1 Introduction

The most common and one of the most effective manufacturing composite materials products methods is the continuous winding method. During winding, the impregnated material fibers are fed under tension and placed on the mandrel surface. Winding is carried out on machines with numerical control (CNC). The machine working bodies' control is carried out according to pre-compiled control programs. Automated programming systems for machine are used to prepare control programs [1].

The material laying trajectory designing on the technological mandrel surface is one of the preparing stages of the winding control programs. The mandrel surface model in the winding control programs preparing systems can be represented in various ways. Usually, an analytical surface description, for which various material laying trajectories mathematical models have been developed, is used [2–9]. However, this description surface method significantly complicates the complex geometric shape mandrel models

description and construction. For such surfaces, the analytical description obtaining task is very difficult and sometimes not feasible.

The presence of complex geometric shape mandrel model which is not revolution body in the winding control programs preparation system is especially important. This makes it possible to automate the programs preparation especially for the complex-profile mandrel surfaces, which significantly expands the products range manufactured by the winding method from composite materials.

A description of a complex surface is possible in the simpler surface set form, with clearly defined boundaries and local coordinates, and the rules for moving from the one simple surface coordinates to the another coordinates [10]. In this case, for any complex surface, you will have to define many simple surfaces and describe the transitions between them.

An alternative way to describe the technological mandrel surface model can be a description by spatial points' irregular set (point cloud). Such a set of points can be obtained, for example, as a result of scanning real mandrels with special devices, i.e., in the mandrel surface digital model reverse engineering process. Also, set of points can be obtained as a result of mandrel surface data import from various modern CAD systems in the form of a triangulated surface defined by a point cloud through the standard data exchange format—STL. However, in the specifying a surface by a cloud of points case, it is necessary to develop a mathematical apparatus that allows you to build the laying trajectory on such surfaces.

To solve material laying trajectory constructing problem on the technological mandrel surface set by a cloud of three-dimensional points, it is proposed to use an approach based on the surface small segment approximation and modifying the known differential equation system designated for calculating material laying trajectory on an analytically specified surface by integration.

2 The Laying Trajectory Constructing on the Point Cloud

In case modeling the laying trajectory on the mandrel surface, described by a regular surface in a parametric form $r = r(u, v) = [x(u, v), y(u, v), z(u, v)]$ $r = r(u, v) = [x(u, v), y(u, v), z(u, v)]$. [11], where u and v —independent parameters (superficial curvilinear coordinates), known differential equation system can be used [12]:

$$\begin{cases} \frac{du}{ds} = u' \\ \frac{dv}{ds} = v' \\ \frac{du'}{ds} = -\frac{N_d(r_V \times m - (\tau r_U) \text{tg}\theta m)}{mm} \\ \frac{dv'}{ds} = \frac{N_d(r_U \times m - (\tau r_V) \text{tg}\theta m)}{mm} \end{cases} \quad (1)$$

where s —natural parameter of the laying trajectory; $N_d = r_{UU}u'^2 + r_{VV}v'^2 + 2r_{UV}u'v'$; $r_U = \frac{\partial r(u,v)}{\partial u}$; $r_V = \frac{\partial r(u,v)}{\partial v}$; $r_{UU} = \frac{\partial^2 r(u,v)}{\partial u^2}$; $r_{VV} = \frac{\partial^2 r(u,v)}{\partial v^2}$; $r_{UV} = \frac{\partial^2 r(u,v)}{\partial u \partial v}$; $m = [r_U \times r_V]$; $\tau = \frac{dr(u,v)}{ds} = r_U u' + r_V v'$, $\text{tg}\theta$ —geodetic deviation angle tangent.

To use this system in the case of specifying the mandrel surface by a point cloud, it is necessary to bring the point cloud fragment description to $r = r(u, v)$ and modify (1) accordingly.

A surface point cloud is represented by a radius vector set $r = [x, y, z]$, which lies in some global coordinate system. Let us define the surface point set r' nearby to the starting point, located in the sphere vicinity with a R_{sphere} radius and satisfying the condition:

$$(x - x_0)^2 + (y - y_0)^2 + (z - z_0)^2 \leq R_{\text{sphere}}$$

At the initial point r_0 a vector tripod τ , b , and m is defined such that τ and b lie in the surface tangent plane at point r_0 , and the vector m is the surface normal vector at the same point. Together they represent the orthonormal right vector tripod (Fig. 1).

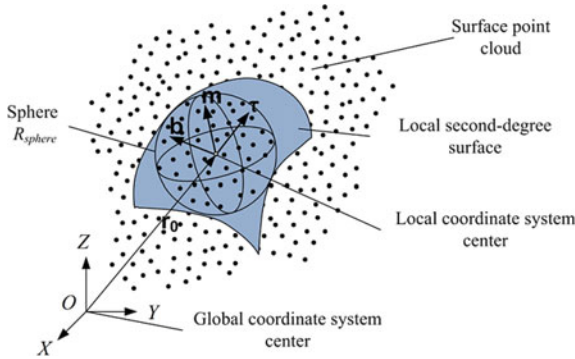


Fig. 1 Surface defined by point cloud

With a small sphere radius value, the selected point set can be approximated by a second-degree surface [13]:

$$a_{xx}x^2 + a_{yy}y^2 + a_{zz}z^2 + 2a_{xy}xy + 2a_{xz}xz + 2a_{yz}yz + 2b_x x + 2b_y y + 2b_z z + c = 0 \tag{2}$$

Equation (2) contains ten unknown coefficients. Let us reduce the unknown number and pass to an $z = f(x, y)$ equation.

Let us determine the new local coordinate system center at the point r_0 , through which the approximate surface fragment is guaranteed to pass, then the coefficient c will be zero.

The coefficients (b_x, b_y, b_z) of (2) are responsible for the direction of the normal surface vector $m = [b_x, b_y, b_z]$ at the point $[0, 0, 0]$. If we perform an additional coordinates transformation so that the surface normal vector at a point (in the global coordinate system it is a vector m) coincides with the local coordinate system z vector, then the coefficients b_x and b_y become equal to zero. In this case, the coefficient b_z can be equal to any positive number, for convenience we will take b_z equal to 1. The well-known transformation formulas express the point's radius vector old coordinates through the new ones:

$$\begin{bmatrix} x \\ y \\ z \end{bmatrix} = \begin{bmatrix} x_0 \\ y_0 \\ z_0 \end{bmatrix} + C \begin{bmatrix} x' \\ y' \\ z' \end{bmatrix} \quad \text{or, } \begin{cases} x = x_0 + c_{11}x' + c_{12}y' + c_{13}z' \\ y = y_0 + c_{21}x' + c_{22}y' + c_{23}z' \\ z = z_0 + c_{31}x' + c_{32}y' + c_{33}z' \end{cases}$$

where C —matrix of transition from the global coordinate system basis to the τ , b , and m basis (Fig. 2):

$$C = \begin{bmatrix} \tau_x & \tau_y & \tau_z \\ b_x & b_y & b_z \\ m_x & m_y & m_z \end{bmatrix}$$

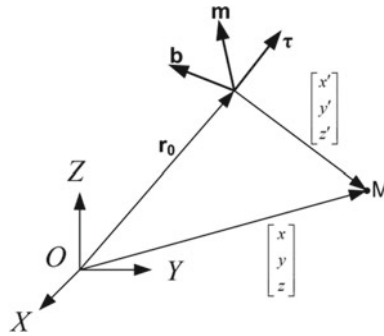


Fig. 2 Point’s radius vector coordinates in different coordinate systems

The new coordinates can be obtained through the old ones using the expression:

$$\begin{bmatrix} x' \\ y' \\ z' \end{bmatrix} = C^{-1} \left(\begin{bmatrix} x \\ y \\ z \end{bmatrix} - \begin{bmatrix} x_0 \\ y_0 \\ z_0 \end{bmatrix} \right)$$

Equation (2) for the transformed points is reduced to:

$$a_{xx}x^2 + a_{yy}y^2 + a_{zz}z^2 + 2a_{xy}xy + 2a_{xz}xz + 2a_{yz}yz + 2z = 0$$

To determine six unknown coefficients of surface passing through a given point set, we use the least squares method [14]. As the functional to be minimized, we choose the $f(x, y, z)^2$:

$$S = \sum_{i=1}^n \left(a_{xx}x_i^2 + a_{yy}y_i^2 + a_{zz}z_i^2 + 2a_{xy}x_iy_i + 2a_{xz}x_iz_i + 2a_{yz}y_iz_i + 2z_i \right)^2$$

Let us differentiate the last equation with respect to each unknown coefficient and reduce the resulting equations into the [A|B] matrix [15]. The terms related to b_z are transferred to the matrix right side:

$$\left[\begin{array}{ccc|c} a_{11} & \cdots & a_{16} & b_1 \\ \vdots & \ddots & \vdots & \vdots \\ a_{61} & \cdots & a_{66} & b_6 \end{array} \right] \tag{3}$$

where $a_{11} = \sum_{i=1}^n x_i^4, a_{12} = a_{21} = \sum_{i=1}^n x_i^2 y_i^2, a_{13} = a_{31} = \sum_{i=1}^n x_i^2 z_i^2, a_{14} = 2 \sum_{i=1}^n x_i^3 y_i, a_{15} = 2 \sum_{i=1}^n x_i^3 z_i, a_{16} = a_{45} = a_{54} = 2 \sum_{i=1}^n x_i^2 y_i z_i, b_1 = -2 \sum_{i=1}^n x_i^2 z_i, a_{22} = \sum_{i=1}^n y_i^4, a_{23} = a_{32} = \sum_{i=1}^n y_i^2 z_i^2, a_{24} = 2 \sum_{i=1}^n x_i y_i^3, a_{25} = a_{46} = a_{64} = 2 \sum_{i=1}^n x_i y_i^2 z_i, a_{26} = 2 \sum_{i=1}^n y_i^3 z_i, b_2 = -2 \sum_{i=1}^n y_i^2 z_i, a_{33} = \sum_{i=1}^n z_i^4, a_{34} = a_{56} = a_{65} = 2 \sum_{i=1}^n x_i y_i z_i^2, a_{35} = 2 \sum_{i=1}^n x_i z_i^3, a_{36} = 2 \sum_{i=1}^n y_i z_i^3, b_3 = -2 \sum_{i=1}^n z_i^3, a_{41} = \sum_{i=1}^n x_i^3 y_i, a_{42} = \sum_{i=1}^n x_i y_i^3, a_{43} = \sum_{i=1}^n x_i y_i z_i^2, a_{44} = 2 \sum_{i=1}^n x_i^2 y_i^2, b_4 = -2 \sum_{i=1}^n x_i y_i z_i, a_{51} = \sum_{i=1}^n x_i^3 z_i, a_{52} = \sum_{i=1}^n x_i y_i^2 z_i, a_{53} = \sum_{i=1}^n x_i z_i^3, a_{55} = 2 \sum_{i=1}^n x_i^2 z_i^2, b_5 = -2 \sum_{i=1}^n x_i z_i^2, a_{61} = \sum_{i=1}^n x_i^2 y_i z_i, a_{62} = \sum_{i=1}^n y_i^3 z_i, a_{63} = \sum_{i=1}^n y_i z_i^3, a_{66} = 2 \sum_{i=1}^n y_i^2 z_i^2, b_6 = -2 \sum_{i=1}^n y_i z_i^2.$

The second-order local surface equation is reduced to $z = f(x, y)$:

$$z(x, y) = \frac{1}{a_{zz}} \left(-a_{xz}x - a_{yz}y - 1 \pm \sqrt{(a_{xz}x + a_{yz}y + 1)^2 - a_{zz}(a_{xx}x^2 + a_{yy}y^2 + 2a_{xy}xy)} \right)$$

Passing to the surface representation as a vector function of two scalar arguments, we get:

$$r(x, y) = [x; y; f(x, y)]$$

System (1) can be written as follows:

$$\begin{cases} \frac{dx}{ds} = x' \\ \frac{dx'}{ds} = -\frac{N_d(r_Y \times m - (\tau r_Y)tg\theta m)}{mm} \\ \frac{dy}{ds} = y' \\ \frac{dy'}{ds} = \frac{N_d(r_X \times m - (\tau r_X)tg\theta m)}{mm} \end{cases} \tag{4}$$

where $N_d = r_{XX}x'^2 + r_{YY}y'^2 + 2r_{XY}x'y'$.

Let's define $r(x, y), r_X(x, y), r_Y(x, y), r_{XX}(x, y), r_{YY}(x, y)$ and $r_{XY}(x, y)$ functions:

$$\begin{aligned} r(x, y) &= \left[x; y; \frac{1}{a_{zz}} \left(-a_{xz}x - a_{yz}y - 1 \pm \sqrt{(a_{xz}x + a_{yz}y + 1)^2 - a_{zz}(a_{xx}x^2 + a_{yy}y^2 + 2a_{xy}xy)} \right) \right]; \\ r_X(x, y) &= \left[1; 0; \frac{1}{a_{zz}} \left(-a_{xz} \pm \frac{(a_{xz}x + a_{yz}y + 1)a_{xz} - a_{zz}(a_{xx}x + a_{xy}y)}{\sqrt{(a_{xz}x + a_{yz}y + 1)^2 - a_{zz}(a_{xx}x^2 + a_{yy}y^2 + 2a_{xy}xy)}} \right) \right]; \\ r_Y(x, y) &= \left[0; 1; \frac{1}{a_{zz}} \left(-a_{yz} \pm \frac{(a_{xz}x + a_{yz}y + 1)a_{yz} - a_{zz}(a_{yy}y + a_{xy}x)}{\sqrt{(a_{xz}x + a_{yz}y + 1)^2 - a_{zz}(a_{xx}x^2 + a_{yy}y^2 + 2a_{xy}xy)}} \right) \right]; \\ r_{XX}(x, y) &= \left[\begin{aligned} &\left(\pm(a_{xz}^2 - a_{zz}a_{xx}) \cdot \sqrt{(a_{xz}x + a_{yz}y + 1)^2 - a_{zz}(a_{xx}x^2 + a_{yy}y^2 + 2a_{xy}xy)} \right. \\ &\quad \mp \frac{(a_{xz}x + a_{yz}y + 1)a_{xz} - a_{zz}(a_{xx}x + a_{xy}y)^2}{\sqrt{(a_{xz}x + a_{yz}y + 1)^2 - a_{zz}(a_{xx}x^2 + a_{yy}y^2 + 2a_{xy}xy)}} \end{aligned} \right]; \\ &0; 0; \frac{a_{zz}((a_{xz}x + a_{yz}y + 1)^2 - a_{zz}(a_{xx}x^2 + a_{yy}y^2 + 2a_{xy}xy))}{a_{zz}((a_{xz}x + a_{yz}y + 1)^2 - a_{zz}(a_{xx}x^2 + a_{yy}y^2 + 2a_{xy}xy))} \\ r_{YY}(x, y) &= \left[\begin{aligned} &\left(\pm(a_{yz}^2 - a_{zz}a_{yy}) \cdot \sqrt{(a_{xz}x + a_{yz}y + 1)^2 - a_{zz}(a_{xx}x^2 + a_{yy}y^2 + 2a_{xy}xy)} \right. \\ &\quad \mp \frac{((a_{xz}x + a_{yz}y + 1)a_{yz} - a_{zz}(a_{yy}y + a_{xy}x))^2}{\sqrt{(a_{xz}x + a_{yz}y + 1)^2 - a_{zz}(a_{xx}x^2 + a_{yy}y^2 + 2a_{xy}xy)}} \end{aligned} \right]; \\ &0; 0; \frac{a_{zz}((a_{xz}x + a_{yz}y + 1)^2 - a_{zz}(a_{xx}x^2 + a_{yy}y^2 + 2a_{xy}xy))}{a_{zz}((a_{xz}x + a_{yz}y + 1)^2 - a_{zz}(a_{xx}x^2 + a_{yy}y^2 + 2a_{xy}xy))} \end{aligned}$$

$$r_{XY}(x, y) = \begin{bmatrix} \left(\begin{array}{c} \pm (a_{yz}a_{xz} - a_{zz}a_{xy}) \cdot \sqrt{(a_{xz}x + a_{yz}y + 1)^2 - a_{zz}(a_{xx}x^2 + a_{yy}y^2 + 2a_{xy}xy)} \\ \mp \frac{(a_{xz}x + a_{yz}y + 1)a_{xz} - a_{zz}(a_{xx}x + a_{xy}y)((a_{xz}x + a_{yz}y + 1)a_{yz} - a_{zz}(a_{yy}y + a_{xy}x))}{\sqrt{(a_{xz}x + a_{yz}y + 1)^2 - a_{zz}(a_{xx}x^2 + a_{yy}y^2 + 2a_{xy}xy)}} \end{array} \right) \\ 0; 0; \frac{a_{zz}((a_{xz}x + a_{yz}y + 1)^2 - a_{zz}(a_{xx}x^2 + a_{yy}y^2 + 2a_{xy}xy))}{a_{zz}((a_{xz}x + a_{yz}y + 1)^2 - a_{zz}(a_{xx}x^2 + a_{yy}y^2 + 2a_{xy}xy))} \end{bmatrix}$$

The laying trajectory new point integration occurs in the τ vector direction, which is represented by the local coordinate system x vector. The x' and y' increments are determined by the formulas:

$$x' = \frac{(\tau \times r_Y)m}{mm}; \quad y' = \frac{(\tau \times r_X)m}{mm}$$

After integrating (3), we obtain the x_0 and y_0 values of the new point and the x' and y' increments.

Let us define a new orthonormal vectors triple at this point:

$$\tau_1 = r_X(x_1, y_1)x' + r_Y(x_1, y_1)y'; \quad m_1 = \frac{r_X(x_1, y_1) \times r_Y(x_1, y_1)}{\|r_X(x_1, y_1) \times r_Y(x_1, y_1)\|};$$

$$b_1 = m_1 \times \tau_1$$

We transform the coordinates of the resulting radius vector the point and the vectors triple to the global coordinate system:

$$r_1^{GCS} = r_0 + C \cdot r(x_1, y_1); \quad \tau_1^{GCS} = C \cdot \tau_1; \quad b_1^{GCS} = C \cdot b_1; \quad m_1^{GCS} = C \cdot m_1$$

Next, a new point set in a sphere vicinity centered at a r_1^{GCS} point is determined, a new surface approximation is constructed, and the laying trajectory next point is integrated, according to the approach described above. The laying trajectory design on a surface defined by a point cloud is shown in Fig. 3 schematically.

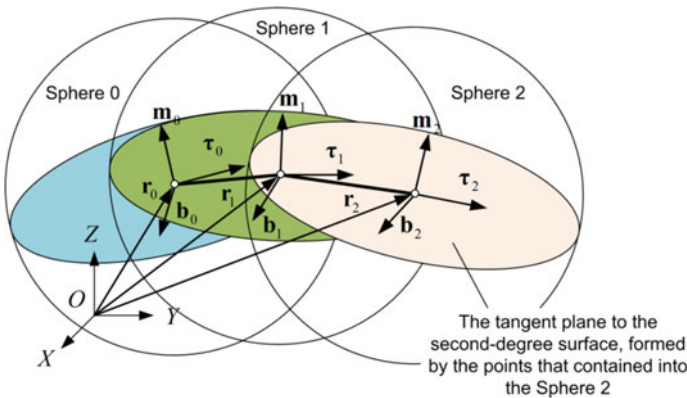


Fig. 3 Laying trajectory

In the numerical experiments course, the described approach has shown itself well at integration steps not exceeding the sphere radius. When using larger values, problems arise associated with the deviation of the points obtained as a system (4) integration result from the initial irregular point set.

The condition for the local surface passage through local coordinate system origin at a new point is violated. In this case, the c coefficient for the new local surface becomes nonzero. Therefore, when passing to large integration step values, it is necessary to additionally determine the c coefficient value. Thus, the c coefficient is a new point belonging indicator to a new surface defined in this point vicinity. Then, instead of a six equations system, we will use a similar system, but of seven equations:

$$\left[\begin{array}{ccc|c} a_{11} & \cdots & a_{17} & b_1 \\ \vdots & \ddots & \vdots & \vdots \\ a_{71} & \cdots & a_{77} & b_7 \end{array} \right] \tag{5}$$

where $a_{17} = a_{71} = \sum_{i=1}^n x_i^2$, $a_{27} = a_{72} = \sum_{i=1}^n y_i^2$, $a_{37} = a_{73} = \sum_{i=1}^n z_i^2$, $a_{47} = \sum_{i=1}^n x_i y_i$, $a_{57} = \sum_{i=1}^n x_i z_i$, $a_{67} = \sum_{i=1}^n y_i z_i$, $a_{74} = 2 \sum_{i=1}^n x_i y_i$, $a_{75} = 2 \sum_{i=1}^n x_i z_i$, $a_{76} = 2 \sum_{i=1}^n y_i z_i$, $a_{77} = n$, $b_7 = -2 \sum_{i=1}^n z_i$.

If, after solving (5), the c coefficient is nonzero, i.e., the new point does not belong to the surface, measures should be taken to return the laying trajectory new points to the source point cloud. Figure 4 illustrates the deviation that occurs.

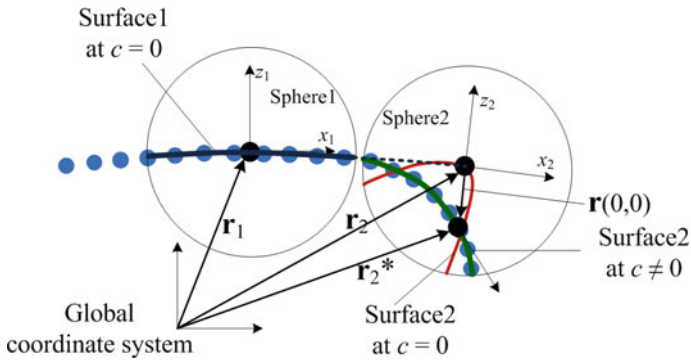


Fig. 4 Point deviation from surface

Surface1 is built on the original irregular point set located in Sphere1 and within Sphere1 coincides with the original surface. From point 1, point 2 is integrated in the specified direction by a distance greater than the sphere radius. If point 2 does not belong to the original surface, then Surface2 obtained in the Sphere2 vicinity as a solving system (3) result, i.e., at $c = 0$, it will be strongly deformed. When using system (5), the surface will not be distorted, but will not pass through the coordinate system center defined at the calculated point. The calculated point data will be used to define the point $\mathbf{r}(x, y)$

belonging to Surface2. The calculated point will be projected onto Surface2 if substitute the values [0;0] into the vector $\mathbf{r}(0, 0) = [0, 0, f(0, 0)]$.

Thus, as an integrating system (4), result of the laying trajectory points will be obtained that belongs to irregular point original set.

3 Experimental Results

Figure 5 shows a laying trajectory built on a revolution surface (ballon and ellipsoid) defined as a point cloud. Figure 6 shows the calculated laying trajectory constructed on a complex geometry surfaces (round tee and round cross) also represented by a point cloud.

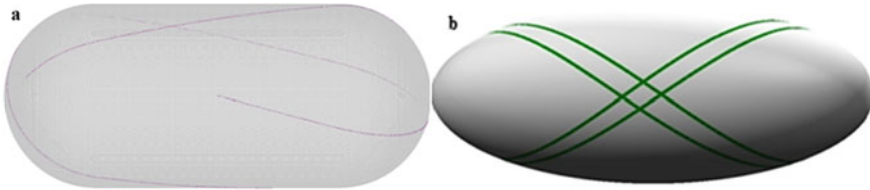


Fig. 5 Laying trajectory on a revolution surface: **a** ballon, **b** ellipsoid

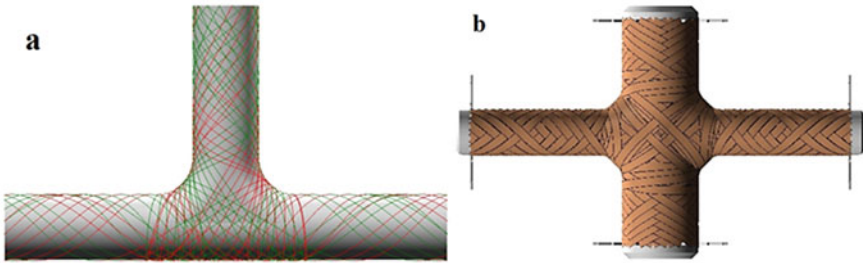


Fig. 6 Laying trajectory on a complex geometry surfaces: **a** round tee, **b** round cross

4 Conclusion

The developed mathematical apparatus for constructing curves on surfaces given by irregular spatial point set makes it possible to construct smoothness class second curves without the need to first obtain the complete surface model.

The described approach is universal and applicable to a wide class of surfaces that can be represented by an irregular point set.

The proposed solutions' adequacy is confirmed by the numerical experiments carried out on modeling the filament laying trajectory on various complex-profile mandrels given by an irregular point set (Fig. 6) and by the results of winding prepared control programs running out on a real multiaxis machine (Fig. 7).

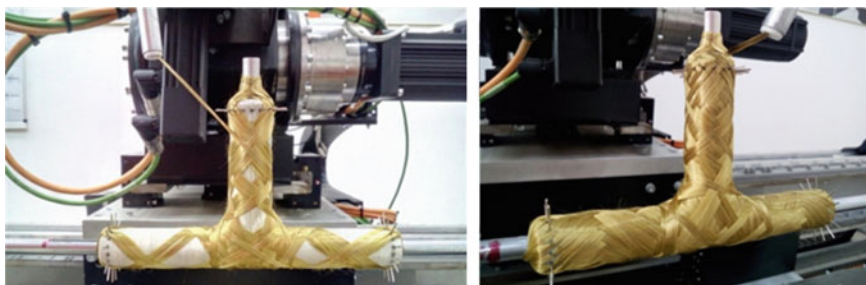


Fig. 7 Product winding result on a CNC machine according to the calculated laying trajectories on the tee surface

References

1. Savin AG (2017) Mathematical and software for modeling of the equipment kinematics and the forming products process by the winding and laying out method in an automated system for technological production preparation. Dissertation, Platov South-Russian State Polytechnic University (NPI)
2. Scholliers J (1992) Robotic filament winding of asymmetric composite parts. Dissertation, Leuven University
3. Koussios S (2004) Filament winding: a unified approach. DUP Science, Delft
4. Aleksejchik VV, Ershov VK, CHikildin JJ (1979) Optimal reinforcement and rational forms selection of composite materials structures. In: Process control systems, pp 44–50
5. Ayusheev TV (2006) Three-dimensional modeling and control methods of the manufacturing processes parts from composite materials by the winding method. Dissertation, East Siberian State Technological University
6. Bitjukov UI (2010) The winding and laying out fibrous composite materials structures technological processes geometric modeling. Dissertation, Moscow Aviation Institute (State Technical University)
7. Vasilev VV, Mitkevich AB, Protasov VD (1981) The optimal design of pressure vessels in the revolution shells form formed from composite materials by the winding method. Mekhanika polimerov, Moscowformed from composite materials by the winding method. Mekhanika polimerov, Moscow
8. Ivanchenko AN (2000) The constructing a curve on a surface problem. News of Higher Educational Institutions. North Caucasian region. Tech Sci 4:28–31
9. Kalinin VA (1997) Theoretical foundations of the winding and laying out fibrous composite materials structures processes geometric modeling. Dissertation, Moscow State University of Food Production
10. Marinin VI, Shvarc AB (2001) Building a filament winding trajectory on freeform surfaces. News of higher educational institutions. North Caucasian reg. Tech Sci 3:34–38
11. Onoprijko MD (2003) Geometric models surfaces reconstruction represented by a digital data discrete set. Nizhny Novgorod State University of Architecture and Civil Engineering, Dissrtation abstract
12. Korn G, Korn T (1978) Mathematics reference book (for mathematicians and engineers). In: The “Nauka” publishing house main physical and mathematical literature editorial office, Moscow
13. Shvarc AB (2002) Mathematical and software for geometric modeling of the winding process composite materials products. Dissertation, South-Russian State Technical University (NPI)

14. Ilin VA, Kim GD (2008) Linear algebra and analytic geometry: tutorial. TK Velbi, Moscow
15. Piskunov NS (1978) Differential and integral calculus, vol 1. Nauka, Moscow



Estimation of the Total Road Load Coefficient for a Road Train

D. N. Dem'yanov^(✉) and I. M. Hazipov

Kazan Federal University, 18, Kremlevskaya St., Kazan 420008, Russia

Abstract. The problem of estimating the coefficient of total road load for a rectilinear moving vehicle is considered. A linearized mathematical model of vehicle motion is designed in the form of a state-space representation. A mathematical model of an extended object is obtained, which includes a description of vehicle dynamics and unmeasured external disturbance. The principal solvability of the problem of estimating the unmeasured state variable of the extended object is verified. State observers of full and reduced order are synthesized, allowing us to estimate the coefficient of total road load with the estimation error asymptotically tending to zero. A computer model of the rectilinear movement of a truck on a highway with a changing value of the total road load coefficient is developed. A computer simulation of the observers' work was carried out, which confirmed the correctness of the results obtained. A comparative analysis of the effectiveness of using an observer of full and reduced order for solving the problem is made.

Keywords: Road train · Total road load coefficient · Asymptotic state observer

1 Introduction

In the modern world, the automotive industry is one of the most important and dynamically developing industries. The requirements for handling, fuel efficiency, environmental friendliness, reliability, and safety of the car are growing every year [1, 2]. In this regard, new engineering and technical solutions appear to improve the efficiency of the vehicle [3].

One of the most common ways to improve the efficiency of automotive technology today is the implementation of advanced driver-assistance systems (ADAS). According to the most common classification, 6 levels of ADAS are defined (from 0 to 5): level 0 means no automation, and level 5 means full automation (no driver required) [4]. At the same time, high-level ADAS requires the collection of a large amount of information about the current state of the vehicle, external conditions, and the behavior of other road users [5]. Most often, a complex of various sensors is used for this purpose. However, for any sensor, there is always a nonzero probability of failure or significant distortion of readings. In addition, in some cases, the required values cannot be measured directly for a number of technical and economic reasons. Therefore, along with direct measurement methods, indirect methods of estimating the condition of the vehicle and its driving conditions are widely used [6–8].

We can specify many factors that determine the driving conditions of the vehicle, but one of the most important indicators in this list will be the coefficient of total road load [9]. It is a generalized metric that includes the rolling resistance of the vehicle and the lifting resistance. This coefficient significantly affects the dynamic properties of the vehicle, its maximum speed, and fuel efficiency. However, the direct determination of this coefficient is extremely difficult: if the slope of the road can still be measured with some degree of accuracy using modern telematics, then the rolling resistance on a production vehicle cannot be measured directly, it can only be estimated by indirect methods [10, 11].

Thus, the development of methods for estimating the coefficient of total road load is an urgent task, the solution of which is of great practical importance. This task is of particular importance when creating ADAS trucks that carry out long-term movement along the route, the characteristics of which can vary significantly in different sections.

2 Mathematical Model

Consider a vehicle driving rectilinearly on a flat road with a homogeneous surface. It is known [9], that such a motion can be described with a sufficiently high degree of accuracy by the following differential equation:

$$\dot{v}_x = \frac{1}{\sigma m} \left[\frac{M(1-k)u\eta}{r} - mg\psi - 0,5 c_x \rho S v_x^2 \right]. \quad (1)$$

Here it is indicated: v_x —is velocity of longitudinal movement of the center of inertia; σ —is rotational inertia coefficient; m —is vehicle weight; M —is engine torque; k —is power take-off factor for auxiliary equipment drive; u —is transmission ratio; η —is transmission efficiency; r —is rolling radius; g —is acceleration of gravity; ψ —is total road load coefficient; c_x —is streamline coefficient (drag coefficient) of the vehicle in the longitudinal direction; ρ —is the air density; and S —is vehicle frontal projection area.

In the steady state, we obtain the following equation:

$$\frac{M_0(1-k)u\eta}{r} - mg\psi_0 - 0,5 c_x \rho S v_{x0}^2 = 0. \quad (2)$$

Here, the symbols M_0 , ψ_0 , v_{x0} denote, respectively, the engine torque, the total road load coefficient, and the speed of the longitudinal displacement of the vehicle's center of inertia in the steady mode.

We linearize model (1) in the vicinity of the steady mode (2), assuming that the values of the variable quantities change little, and there is no gear change or change in the coefficients k , σ , η . To do this, we represent the variables as the sum of the steady mode value and the deviation:

$$M = M_0 + \Delta M; \quad \psi = \psi_0 + \Delta\psi; \quad v_x = v_{x0} + \Delta v_x. \quad (3)$$

Taking into account formulas (2) and (3), Eq. (1) takes the following form:

$$\Delta \dot{v}_x = \frac{1}{\sigma m} \left[\frac{\Delta M(1-k)u\eta}{r} - mg\Delta\psi - c_x \rho S v_{x0}\Delta v_x - 0,5 c_x \rho S (\Delta v_x)^2 \right]. \quad (4)$$

Assuming that the speed deviations will be much less than its steady mode value, we discard the last term on the right side of Eq. (4) and get a linearized equation of the vehicle’s motion in the vicinity of the steady mode:

$$\Delta \dot{v}_x = \frac{1}{\sigma m} \left[\frac{\Delta M (1 - k) u \eta}{r} - mg \Delta \psi - c_x \rho S v_{x0} \Delta v_x \right]. \tag{5}$$

Consider the movement of a vehicle along a highway, the angle of the longitudinal slope which changes so slowly that it can be approximated with high accuracy by segments of straight lines. Since it was previously assumed that the road surface is homogeneous, in this case, the coefficient of total road load is a piecewise constant function.

Taking into account all the assumptions made, model (5) can be represented as a system of equations in the state space:

$$\dot{X} = AX + BU; \quad Y = CX. \tag{6}$$

In model (6), the variables are defined as follows:

$$X = \begin{pmatrix} \Delta v_x \\ \Delta \psi \end{pmatrix}; \quad U = \Delta M; \quad Y = \Delta v_x. \tag{7}$$

Coefficient matrices of model (6) are given by the following expressions:

$$A = \begin{bmatrix} -\frac{c_x \rho S v_{x0}}{\sigma m} & -\frac{g}{\sigma} \\ 0 & 0 \end{bmatrix}; \quad B = \begin{bmatrix} \frac{(1-k) u \eta}{\sigma m r} \\ 0 \end{bmatrix}; \quad C = [1 \ 0]. \tag{8}$$

The resulting model (6–8) can be used to design linear state observer using one of the known methods [12–14].

3 Full-Order Observer

First of all, let us estimate the solvability of the observer synthesis problem. To do this, we estimate observability per Kalman of the model (6–8). The observability matrix is defined as follows [15]:

$$Q = [C^T \ (CA)^T] = \begin{bmatrix} 1 & -\frac{c_x \rho S v_{x0}}{\sigma m} \\ 0 & -\frac{g}{\sigma} \end{bmatrix}. \tag{9}$$

Obviously, the matrix Q defined by expression (9) is non-degenerate, its rank is 2. Hence, the model (6–8) is entirely observable per Kalman, and it is possible to construct an asymptotic state observer.

We form a full-order asymptotic state observer for object (6) using feedback on the estimation error [16]. Then the observer’s equation will have the form:

$$\dot{\tilde{X}} = (A - LC)\tilde{X} + BU + LY. \tag{10}$$

In this case, the estimation error will be determined by the following expressions:

$$\varepsilon = \tilde{X} - X; \quad \dot{\varepsilon} = (A - LC)\varepsilon. \tag{11}$$

In formulas (10) and (11), it is indicated: \tilde{X} —is estimation of the vector X ; ε —is estimation error; and L —is numeric matrix called observation matrix.

We set the matrix L such that the dynamics of the estimation error (11) is asymptotically stable. Then the estimation vector (10) will asymptotically tend to the true value of the state vector over time [16].

It is known that the calculation of the coefficients of a full-order observer can be reduced to a modal control problem using the following relation:

$$|A - LC - \lambda I| = |A^T - C^T L^T - \lambda I|$$

Denoting $A^T = \tilde{A}$, $C^T = \tilde{B}$, $L^T = K$, we obtain the classical modal control problem, for the solution of which one of the standard algorithms [17] can be used.

Let us set the desired position of the poles of the closed system using the Newton distribution:

$$\alpha_c(s) = s^2 + 2\omega_0 s + \omega_0^2.$$

Parameter ω_0 sets the speed of the transient process and is defined as the ratio of the setting time for the model with $\omega_0 = 1$ to the desired setting time.

To calculate the coefficients of the modal regulator, we use the Ackermann formula [17]:

$$K = [0 \ 1] [\tilde{B} \ \tilde{A}\tilde{B}]^{-1} \alpha_c(\tilde{A}). \tag{12}$$

Here $\alpha_c(\tilde{A})$ —is the matrix polynomial formed on the basis of the desired characteristic polynomial $\alpha_c(s)$:

$$\alpha_c(\tilde{A}) = \tilde{A}^2 + 2\omega_0 \tilde{A} + \omega_0^2 I. \tag{13}$$

We define the matrix of coefficients of the modal controller using relations (12) and (13):

$$K = \left[-\frac{c_x \rho S v_{x0}}{\sigma m} + 2\omega_0 \quad -\frac{\sigma \omega_0^2}{g} \right]. \tag{14}$$

The corresponding coefficients of the observer are obtained by transposing the expression (14):

$$L = \begin{bmatrix} -\frac{c_x \rho S v_{x0}}{\sigma m} + 2\omega_0 \\ -\frac{\sigma \omega_0^2}{g} \end{bmatrix}. \tag{15}$$

Substituting into the formula (15), the parameters of the vehicle, the desired value of the response speed, and the value of the reference speed v_{x0} , it is possible to obtain the numerical values of the observation matrix corresponding to the given operating mode.

4 Reduced-Order Observer

Full-order observers are characterized by a certain degree of redundancy, since they form the entire vector of estimates of state variables, even if part of this vector is determined by the measurement of the output signal [18, 19]. In our case, this redundancy is manifested in the fact that the value of the longitudinal velocity is estimated, which in practice can be directly measured with a sufficiently high degree of accuracy.

This redundancy can be eliminated by using a reduced-order observer (Luenberger observer). The basic idea of such an observer is that only state variables that cannot be directly measured are evaluated. In our case, there is only one such variable—this is the deviation from the nominal value of the total road load coefficient. Accordingly, a first-order observer can be used to estimate it. This reduction in the observer dimension reduces the amount of computations required. This can be quite important in the practical implementation of estimation algorithms in conditions of limited resources of the on-board information and control system of a vehicle.

Let us form an asymptotic observer of reduced order for object (6). Let the following relations be valid for the matrix coefficients of the model:

$$A = \begin{bmatrix} A_{11} & A_{12} \\ A_{21} & A_{22} \end{bmatrix}; \quad B = \begin{bmatrix} B_1 \\ B_2 \end{bmatrix}; \quad C = [I \ 0]. \tag{16}$$

Then the vector of state variables will consist of two components: the vector of measured output signals $X_1 \equiv Y$ and the vector of unmeasured variables X_2 . In this case, the equation of the reduced-order observer will have the form:

$$\dot{\tilde{X}}_2 = (A_{22} - LA_{12})\tilde{X}_2 + (A_{21} - LA_{11})Y + (B_2 - LB_1)U + LY. \tag{17}$$

In this case, the estimation error will be determined by the following expressions:

$$\varepsilon = \tilde{X}_2 - X_2; \quad \dot{\varepsilon} = (A_{22} - LA_{12})\varepsilon. \tag{18}$$

In practice, the differentiation of the output signal often leads to large modulo computational errors. To eliminate this drawback, the calculation scheme (17–18) can be transformed by introducing an auxiliary vector Z :

$$\begin{cases} \dot{Z} = (A_{22} - LA_{12})Z + (A_{22}L - LA_{12}L + A_{21} - LA_{11})Y + (B_2 - LB_1)U; \\ \tilde{X}_2 = Z + LY. \end{cases} \tag{19}$$

Analysis of relations (18) and (19) shows that by specifying the matrix L it is possible to provide the required rate of tending to zero of the estimation error. To calculate the matrix L , modal control methods can also be used.

Model (6–8) satisfies the conditions described above; therefore, formulas (16) and (19) can be used to construct an observer of the reduced order. In this case, the following relations will be fulfilled:

$$\begin{bmatrix} A_{11} & A_{12} \\ A_{21} & A_{22} \end{bmatrix} = \begin{bmatrix} -\frac{c_x \rho S v_{x0}}{\sigma m} & -\frac{g}{\sigma} \\ 0 & 0 \end{bmatrix}; \quad \begin{bmatrix} B_1 \\ B_2 \end{bmatrix} = \begin{bmatrix} \frac{(1-k)u\eta}{\sigma m r} \\ 0 \end{bmatrix}.$$

Since in the case under consideration, the Luenberger observer has the first order, the corresponding characteristic polynomial has the form:

$$\alpha_c(s) = s + \omega_0 .$$

Applying the formula (12), we find the observer gain:

$$L = -\frac{\omega_0 \sigma}{g} . \tag{20}$$

By substituting the desired value of ω_0 into formula (20), we can get the numerical value of the desired observation coefficient and form the observer (19). It should be noted that in this case L does not depend on the value of the reference speed of the vehicle.

5 Results of Computer Simulation

The effectiveness of the formed observers was assessed by means of computer modeling. In the Simulink environment of the MATLAB computer mathematics system, a model was created that describes the rectilinear motion of a vehicle with variable values of torque and the coefficient of total road load. The numerical values of the model coefficients were taken from open sources describing the design and dynamic features of the vehicle KAMAZ-5490–68 (T5) [20]. The values of a number of coefficients describing the external conditions and driving modes of the vehicle were selected from reference books [9].

Table 1 shows the numerical values of the coefficients included in the Eq. (1). Table 2 shows the main engine and transmission parameters used in the simulation. It should be noted that the developed model does not provide for the possibility of reversing the vehicle; therefore, the corresponding parameters of the gearbox are not indicated.

Table 1 Values of model coefficients

$m, \text{ kg}$	c_x	$\rho, \text{ kg/m}^3$	$S, \text{ m}^2$	η	$r, \text{ m}$
18,600	1.5	1.25	9.36	0.92	0.48

Within the framework of this work, a series of computational experiments was carried out, in which the behavior of the full-order observer and the Luenberger observer at different values of v_{x0} and ω_0 was considered. To ensure the effective work of observers at the entire permissible range of vehicle speeds, an array of coefficients was formed for models (10) and (19) at different values of u and v_{x0} . The calculation of the coefficients was carried out for each gear value and for a number of longitudinal speed values possible in the current gear, with a step of 2 m/s. The choice of specific values of the observer coefficients was carried out depending on the values of u and v_{x0} (the reference value of the speed in reality can come, for example, from the cruise control subsystem).

Table 2 Main parameters of engine and transmission

Parameter name	Parameter value
Maximum net torque, N*m	2100
The crankshaft speed corresponding to the maximum torque, rpm	1100
Maximum net power, kW	315
The crankshaft speed corresponding to the maximum power, rpm	1900
Final drive ratio	3.077
Number of transmission gears	16
Gear ratios on the gears	1: 13.86–11.56; 2: 9.52–7.96; 3: 6.56–5.48; 4: 4.58–3.83; 5: 3.02–2.53; 6: 2.08–1.74; 7: 1.43–1.20; 8: 1.00–0.84
Maximum speed, km/h	110
Gradeability, % (deg)	18 (10)

As an example, let us consider the results of one of the computational experiments. Initial values: $v_{x0} = 26$ m/s; $\omega_0 = 10$; $\Delta\psi$ varies uniformly from 0 to 0.01 in the interval from 1 to 6 s of the model time; the speed stabilization system is active.

In Fig. 1a, the red line shows the actual change in the total road load coefficient, the green line shows the value of the estimate obtained using the full-order observer, and the blue line shows the value of the estimate obtained using the Luenberger observer.

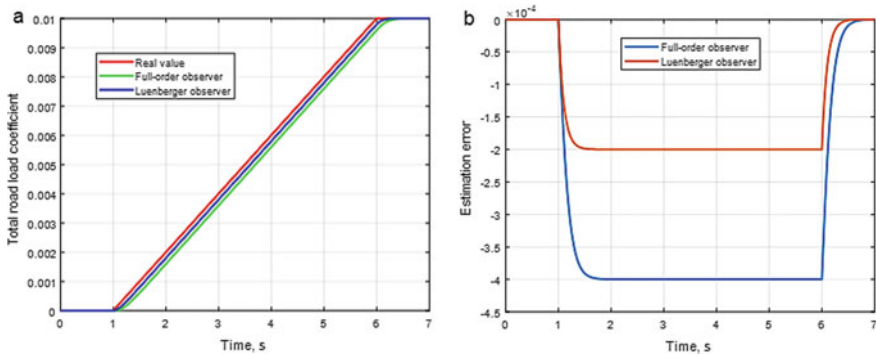


Fig. 1 a True value and estimate of $\Delta\psi$ and **b** change in the estimation error

Figure 1b shows graphs of changes in the estimation error for the full-order observer (blue line) and the Luenberger observer (red line). As can be seen in the graphs, for observers of both types, the maximum value of the estimation error does not exceed 5%

of the steady-state value $\Delta\psi$. In this case, a nonzero estimation error occurs only in the transient mode; at constant $\Delta\psi$, the estimation error asymptotically tends to zero.

It should be noted that according to the results of the computational experiments, the Luenberger observer showed a higher efficiency: the maximum and root mean square values of the estimation error were less than for a full-order observer. In addition, the model (19) used for its implementation has a lower dimension, which means that it will require less computing system resources for implementation.

6 Conclusion

This paper describes the construction of asymptotic observers of various types to estimate the coefficient of total road load for a rectilinearly moving vehicle. A computer model describing the dynamics of a truck with a changing coefficient of total road load is developed. A model of a multimode state observer is developed, the values of the coefficients of which depend on the selected gear and the current value of the reference speed of the vehicle. A comparative analysis of the efficiency of the full-order observer and the Luenberger observer is carried out. It is shown that the Luenberger observer provides a lower value of the estimation error, and its implementation requires less computing system resources.

As part of further research, it is proposed to build a discrete model of the estimation process and analyze the effectiveness of various types of observers, taking into account the discrete nature of the data on the current speed value coming from the CAN bus. It is also planned to conduct more detailed studies of the robustness of the resulting observer, to assess the dependence of its characteristics on changes in the model parameters. In addition, it is necessary to study in more detail the issue of determining the optimal number of reference speeds for each gear used in the formation of the array of observer coefficients.

After the research is completed, it is planned to use the developed algorithms to improve the efficiency of the automatic speed control system for trucks.

References

1. Yuan PX, Cai Y (2021) Forecasting the development trend of low emission vehicle technologies: based on patent data. *Technol Forecast Soc Change* 166:120651. <https://doi.org/10.1016/j.techfore.2021.120651>
2. Zhang Y, He W, Chen H, An P (2020) Patent analysis review of automated driving vehicle safety technology. *Scientia Sinica Informationis* 50(11):1732–1755. <https://doi.org/10.1360/SSI-2020-0004>
3. Classen S, Jeghers M, Morgan-Daniel J, Winter S, King L, Struckmeyer L (2019) Smart In-vehicle technologies and older drivers: a scoping review. *OTJR Occup Participation Health* 39(2):97–107. <https://doi.org/10.1177/1539449219830376>
4. Novakazi F, Orlovska J, Bligård L-O, Wickman C (2020) Stepping over the threshold linking understanding and usage of automated driver assistance systems. *Transp Res Interdiscip Persp* 8:100252. <https://doi.org/10.1016/j.trip.2020.100252>
5. Kukkala VK, Tunnell J, Pasricha S, Bradley T (2018) Advanced driver-assistance systems: a path toward autonomous vehicles. *IEEE Consum Electron Mag* 7(5):18–25. <https://doi.org/10.1109/MCE.2018.2828440>

6. Qu Y, Xu F, Yu S-Y, Chen H, Li Z-L (2020) Model predictive control based on extended state observer for vehicle yaw stability. *Control Theory Appl* 37(5):941–949. <https://doi.org/10.7641/CTA.2019.19018>
7. Feng P, Zhang J, Yang W (2020) Observer-based state-feedback robust control for path following of autonomous ground vehicles. *Proceedings of the Institution of Mechanical Engineers. Part I: J Syst Control Eng* 234(2):222–239. <https://doi.org/10.1177/0959651819851676>
8. Volkov VG, Dem'yanov DN (2017) Designing physically realizable state observer for estimating the kinematic parameters of the road train. *IOP Conf Series: Mater Sci Eng* 240:012067. <https://doi.org/10.1088/1757-899X/240/1/012067>
9. Jazar RN (2014) *Vehicle dynamics: theory and application*. Springer, New York
10. Na G, Park G, Turri V, Johansson KH, Shim H, Eun Y (2020) Disturbance observer approach for fuel-efficient heavy-duty vehicle platooning. *Veh Syst Dyn* 58(5):748–767. <https://doi.org/10.1080/00423114.2019.1704803>
11. Kim S, Bang JS, Kim S, Lee H (2020) Robust vehicle speed control using disturbance observer in hybrid electric vehicles. *Int J Automot Technol* 21(4):931–942. <https://doi.org/10.1007/s12239-020-0089-5>
12. Gu D-K, Liu L-W, Duan G-R (2019) A parametric method of linear functional observers for linear time-varying systems. *Int J Control Autom Syst* 17(3):647–656. <https://doi.org/10.1007/s12555-018-0155-1>
13. Asanov AZ, Dem'yanov DN, (2015) Estimation of directly unmeasurable external perturbations using functional observers. *Optoelectron Instrum Data Process* 51(5):449–455. <https://doi.org/10.3103/S8756699015050039>
14. Aloui R, Braïek NB (2018) Synthesis of a minimum functional state observer approach for unperturbed/perturbed dynamical systems. *Int J Control Autom Syst* 16(4):1736–1745. <https://doi.org/10.1007/s12555-017-0144-9>
15. Luenberger DG (1966) Observers for multivariable systems. *IEEE Trans Autom Control* 11:190–197. <https://doi.org/10.1109/TAC.1966.1098323>
16. Isermann R, Munchhof M (2011) *Identification of dynamic systems*. Springer-Verlag, Berlin-Heidelberg, An Introduction with Applications
17. Antsaklis PJ, Michel AN (1997) *Linear systems*. McGraw-Hill, New York
18. Gu D-K, Liu L-W, Duan G-R (2018) Functional interval observer for the linear systems with disturbances. *IET Control Theory Appl* 12(8):2562–2568. <https://doi.org/10.1049/iet-cta.2018.5113>
19. Asanov AZ, Dem'yanov DN, (2015) Analytical synthesis of functional low-order observers. *J Comput Syst Sci Int* 54(4):505–513. <https://doi.org/10.1134/S1064230715040048>
20. KAMAZ PTC (2021) KAMAZ-5490–68 (T5). <https://kamaz.ru/production/serial/sedelnye-tyagachi/kamaz-5490/>. Accessed 10 Jan 2021



Artificial Intelligence in the Problems of Organizational Control and Planning of Electric Power Consumption in Oil Pipeline Transportation

N. Gabdrakhmanova(✉)

Peoples Friendship University of Russia, (RUDN University), 6, Miklukho-Maklaya str., Moscow 117198, Russia

Abstract. Oil pipeline transportation is one of the significant power consumers. Currently, a single electric power market has been formed, which ensures strict control over its consumption. Any excess in or underdrawal of the actual power consumption compared to the planned figure is punished with fines. In this connection, the accuracy of planning the power consumption for oil transportation is a relevant problem. Artificial intelligence allows promptly and effectively solve complex problems in various areas. In this paper, the problem of building a neural network identification model for oil pipeline transportation has been considered. Solving problems using neural networks proceeds in several stages. First, identification models of the object under study are built, and then, the object's behavior is studied and analyzed using the models built. Using the neural network model, the problems of organizational control and planning of electric power consumption in oil pipeline transportation have been considered. The models have been built and tested based on actual data.

Keywords: Electricity · Neural network · Control · Mathematical model

1 Introduction

Oil pipeline transportation is one of the significant power consumers. Currently, a single electric power market has been formed, which ensures strict control over its consumption [1, 2]. Any excess in or underdrawal of the actual power consumption compared to the planned figure is punished with fines. In this connection, the accuracy of planning the power consumption for oil transportation is a relevant problem. Power consumption is an item of expenditure that may change significantly in the course of pipeline operation due to the practical implementation of pipeline loading modes; it is affected by the reliability of the key pumping and power equipment, well-coordinated work of oil suppliers and consumers, the quality of planning, and the efficiency of the power equipment used. Planning the work of oil trunk pipelines is associated with solving many problems, e.g., the problems of determining the optimal oil pumping schedules, calculating

power consumption to implement the schedules obtained, forecasting power consumption, etc., should be solved. Under current conditions, only practical experience is not enough to solve these problems. In many studies, mathematical methods are used to plan the operation of pipeline systems. They comprise analytical, probabilistic, logical, and game-theoretic methods. The neural network (NN) models have a number of advantages over the previously developed ones. The NN models are adaptive; neural networks allow extracting hidden information from the source data; the NN noise immunity has been proven [3]. The NN models have previously been developed to solve planning problems [4–6]. According to the study results, despite the high accuracy of forecasting, at individual points, the calculations gave unacceptable errors. Also, new problems have arisen related to arranging the control over the oil pipeline operating modes. In this regard, a new model specification has been determined and new studies have been performed on the use of the NN models in solving organizational control problems.

2 Formulation of the Mathematical Simulation Problem

Let us consider an oil pipeline as a dynamic system. Let \mathbb{S} is a dynamic system, X is input variables (input actions on the object), Y is the object's reaction to the input actions (in this case, the reaction is the power consumption at given X), and P is the object of the study. To introduce the class of problems under consideration [7, 8], let us introduce $\mathbb{S} = X, P, Y$. Let us assign three main problems:

- X, P, Y —identifying the dynamic system (find P by X and Y);
- X, P, Y —analyzing the dynamic system behavior (find Y by X and P);
- X, P, Y —synthesizing the dynamic system control (find X by Y and P).

Problem 2 belongs to the class of direct problems, and problems 1 and 3—to the class of inverse ones.

2.1 Formulation of Problem 1

An oil linepipe is given. It is adopted that pumping oil from the tank farm of the start point to that of the endpoint is a complete process. Under these conditions, the power consumption is determined for the entire oil pipeline considering all objects and recorded hourly for each pump. At the start pipeline point, the instantaneous rheological oil properties are measured. At the endpoint, a system to measure the pumped oil flow rate is provided. It is required to build an identification model of the object based on the measurement data to assess the impact of the factors chosen on power consumption.

2.2 Formulation of Problem 2

An identification model of pumping oil through a pipeline is given in the form of an NN mapping $\hat{F}(\cdot)$. For the developed pumping plan, forecasted power consumption should be found for pumping by Tp moves ahead.

2.3 Formulation of Problem 3

An identification model of pumping oil through a pipeline is given in the form of an NN mapping $\hat{F}(\cdot)$. Using the $\hat{F}(\cdot)$ mapping, the efficiency of the chosen control from the standpoint of minimizing the power consumption for pumping a given volume of oil should be evaluated over the entire planning period.

3 Solving Problems

At the first stage, the use of artificial intelligence in a particular area supposes solving the model specification problem. The choice of simulation variables depends on the object structure. For a single linepipe, the number of simulation variables can be reduced. The parameters characterizing the properties of a specific oil linepipe and equipment installed on it are relatively constant values and remain unchanged over a long period. These are the pipeline length, the pipeline route layout, the difference in the pipeline start and end elevations, the datasheet characteristics, etc. The main changing parameters are physical and chemical properties of the pumped oil, volumes of oil supplied and received for the planned period, the number and actual characteristics of main and booster pumping units, the restrictions on power systems and the peak capacity declared, and the oil pipeline operating modes. The oil pipeline operating mode is most susceptible to changes and to the maximum extent affects the power consumption value and efficiency.

3.1 The Model Specification

As an output N_N variable, the Y value—the power consumption (kW·day), and as input variables, X_1 —temperature, X_2 —oil density (kg/m³), X_3 —oil viscosity (cSt), X_4 —daily volume of oil pumped (t), X_5 —the tank farm utilization rate, X_6 —the pipeline utilization rate, X_7 —the oil pipeline outage hours, X_8 —a categorical variable (introduced to split the area), and X_9 —the rate of the pumped volume change (t) are taken.

To consider the availability of oil and free capacity (tank farm (TF)), the X_5 value is introduced, i.e., the tank farm utilization rate, which is defined as the ratio of the oil volume (V_{prod}) to the total TF volume (V_{TF}):

$X_5 = V_{\text{prod}}/V_{\text{TF}}$; X_9 allows evaluating the impact of switching pumping modes on power consumption; X_8 is a categorical variable, and it splits the entire simulation area into two ones: the accident-free oil pipeline operation area and the oil pipeline emergency operation area. Numerical experiments have shown that introducing the X_8 variable allows reducing the error in the NN calculations. This is explained as follows. To describe the process in the entire area, all the areal variables should be used. When describing a system in a small area, some variables are constant, and we can use fewer variables for simulation. The categorical variable was introduced to find low-mode areas [9, 10]. One of the most important reasons for the low efficiency of conventional NN models in problems associated with complex technical systems is forming a purely empirical model, which should cover all the dynamic system behavior nuances. By introducing categorical variables, we split the entire simulation area into those described by a small number of variables.

3.2 Mathematical Formulation of Problem 1

Let N observations over the \mathbb{S} system was performed $\{y_i\} = F(X_i), i = 1, \dots, N$.

In each observation, the current value of the controlled input action $X_i = X(t_i)$ and the corresponding output $y_i = y(t_i)$ were recorded. The results of these observations form a s:

$$\{y_i, X_i\} \dots, \dots X_i \in Dy_i \in U, i = 1, \dots, N \tag{1}$$

Using the data (1), such an approximation $\hat{F}(\cdot)$ should be found for the $F(\cdot)$ mapping implemented by the \mathbb{S} system, at which the below condition is true:

$$\hat{F}(X(t)) - F(X(t)) \leq \varepsilon, \forall X(t_i) \in D \tag{2}$$

The $\hat{F}(\cdot)$ mapping is built using neural networks [9].
 ε results of building the models are given in Sect. 3.3.

3.3 The Results of Solving Problem 1

For the chosen source data of the problem, a matrix of sample pair correlation coefficients was built. Analysis of estimates of paired correlation coefficients has shown that the introduced new variables have a significant correlation with the y variable (power consumption). In Table 1, significant correlation coefficients are highlighted in red.

Table 1 Pairwise correlation matrix

	X ₁	X ₂	X ₃	X ₄	X ₅	X ₆	X ₇	X ₈	X ₉
X ₁	1.0	-0.7	-0.8	0.0	0.0	0.1	0.0	0.1	-0.0
X ₂	-0.7	1.0	0.8	-0.1	-0.1	-0.1	-0.0	-0.1	0.0
X ₃	-0.8	0.8	1.0	-0.1	-0.1	-0.1	-0.1	-0.1	0.0
X ₄	0.0	-0.1	-0.1	1.0	0.1	0.1	-0.5	-0.4	0.5
X ₅	0.0	-0.1	-0.1	0.1	1.0	0.1	0.1	0.1	0.1
X ₆	0.1	-0.1	-0.1	0.1	0.1	1.0	0.0	0.0	-0.1
X ₇	0.0	-0.0	-0.1	-0.5	0.1	0.0	1.0	0.8	-0.3
X ₈	0.1	-0.1	-0.1	-0.4	0.1	0.0	0.8	1.0	-0.2
X ₉	-0.0	0.0	0.0	0.5	0.1	-0.1	-0.3	-0.2	1.0
y	0.0	-0.1	-0.1	0.5	0.0	0.1	-0.2	-0.1	0.3

Figure 1a shows a plot of approximation by the data in the space of variables y, X_4, X_9 . The plot shape allows concluding that the X_9 values affect the resulting indicator y . Figure 2b shows the scatter diagram in the space y, X_4, X_8 . The scatter diagram shows the result of splitting the observation points into two clusters according to the X_8 parameter:

$$X_8 = \begin{cases} 0, \text{ no accident} \\ 1, \text{ accident} \end{cases}$$

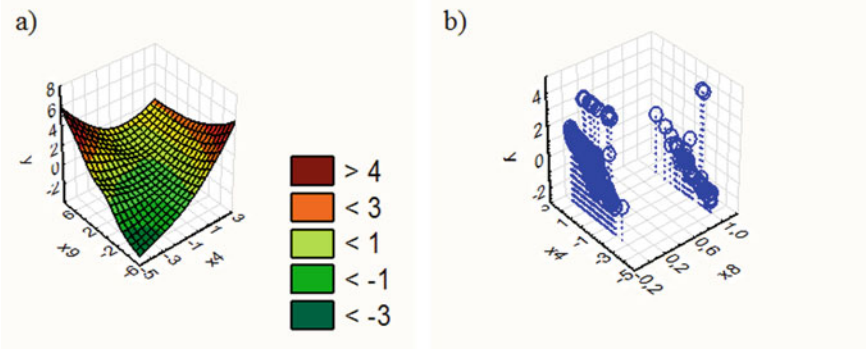


Fig. 1 a Surface plot approximated by the data (y, X_4, X_9); b scatter diagram in the space y, X_4, X_8

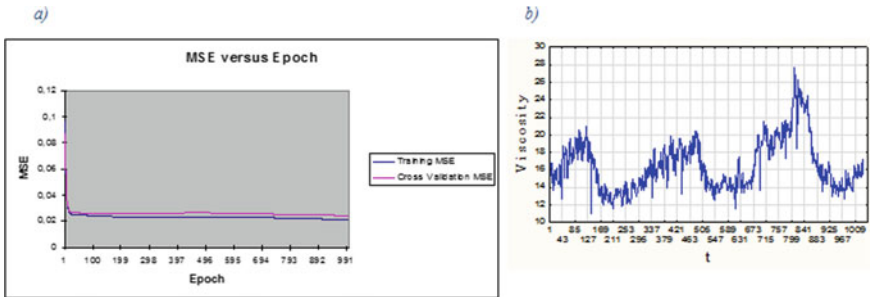


Fig. 2 a Plot of the change in the training MSE and Cross-Validation MSE (Y-direction) versus the number of training epochs (X-direction); b viscosity dynamics over the observation period

To evaluate the neural network method for solving the problem, a parallel model was built based on the same data using nonlinear regression [10–12] in the Statistica 10 environment (Table 2, column 5).

Table 2 Comparative analysis of computational errors for models 1, 2, 3, 4

	Model 1	Model 2	Model 3	Model 4
1	2	3	4	5
NMSE	0.091	0.086	0.073	0.13
Min Abs Error	0.005	0.004	0.002	0.031
r	0.89	0.91	0.99	0.79

Experiments on the analysis of the NN models built [13–16] have been performed with different ways of model specification. Table 2 gives estimates of the quality of building the NN models.

Let the areas $D_1, D_2, D_3, D_1 \subset R^7, D_2 \subset R^8, D_3 \subset R^9$ be defined. Let the set of input data belong to the area D_1, D_2, D_3 , and the set of output data is $y \in U, U \subset R$,

$$(X_1, X_2, X_3, X_4, X_5, X_6, X_7) \in D_1$$

$$(X_1, X_2, X_3, X_4, X_5, X_6, X_7, X_8) \in D_2$$

$$(X_1, X_2, X_3, X_4, X_5, X_6, X_7, X_8, X_9) \in D_3$$

Model 1. The NN model: $\hat{F}_1 : D_1 \rightarrow U$.

Model 2. The NN model: $\hat{F}_2 : D_2 \rightarrow U$.

Model 3. The NN model: $\hat{F}_3 : D_3 \rightarrow U$.

Model 4. Nonlinear regression model.

In Table 2, the following notations are used:

$$NMSE \text{ is the mean square error of testing, } NMSE = \left(\frac{\sum_{i=1}^{n_1} (y_i - \hat{y}_i)^2}{n_1} \right)^{1/2},$$

where n_1 is the number of test points, y_i is the model output value, **Min Abs Error** \hat{y}_i is minimum absolute error, r is the coefficient of correlation between two columns: the columns of calculated and declared output values.

These results indicate a good approximation degree.

The table shows that after introducing new variables, the model accuracy has increased. Figure 2a shows a plot of the change in the Training MSE and Cross-Validation MSE (Y-direction) versus the number of training Epochs (X-direction). The plot shows the successful training of the neural network.

To solve problem 2, a submodel has been developed. The submodel developed is aimed at improving the accuracy of solving problem 2. When using a trained NN model, e.g., to solve the problem of planning power consumption.

For a T_p period, vector X is fed to the input and vector Y is obtained at the output. Therefore, the more accurate the vector X value, the more accurate the Y value. We have noticed that the vector X variables can be conditionally divided into two groups. The first one comprises variables that are known with sufficient accuracy, e.g., the difference between the geodetic marks of the pipe end and start for the linear section considered, the pipe length, diameter, etc. The second group comprises variables whose value is affected by the environment, e.g., the air temperature affects the pumped oil temperature, viscosity, and density. Figure 2b shows the viscosity dynamics. The ordinate and the abscissa show the viscosity and the observation point number, respectively. Observation points are taken for three years. On the plot, the upper peaks and the lower points correspond to the winter and summer periods, respectively (fluctuations in oil viscosity at constant air temperature are insignificant). Therefore, even if the pumped oil characteristics for the given period are known, the change in the air temperature for the forecasted period should be considered.

Conclusion: when using an identification model to forecast power consumption, predictive models of time series of input variables should be developed considering the environmental effect. For the problem being solved, models have been built to correct (for the air temperature effect) the values of the time series of rheological properties.

Table 3 shows a fragment of the normalized source data on the rheological properties of the oil. The density and viscosity are given at the specified air temperature.

Table 3 Fragment of normalized source data on the rheological properties of oil

Measurement	Measurement	Air temperature	Viscosity	Density
Start (Date; time)	End (Date; time)	1	2	3
31.01; 0:00	31.01; 8:00	-1.2	0.3	-0.9
31.01; 8:00	31.01; 16:00	-1.2	1.1	-0.4
31.01; 16:00	01.02; 0:00	-1.2	1.1	-0.5
01.02; 0:00	01.02; 8:00	-1.2	0.5	-1.4
01.02; 8:00	01.02; 16:00	-1.1	0.2	-0.8
01.02; 16:00	02.02; 0:00	-1.1	0.2	-0.5
02.02; 0:00	02.02; 8:00	-1.0	0.7	0.7
02.02; 8:00	02.02; 16:00	-1.0	0.8	1.0

Currently, the planned pipeline performance is calculated based on the pumping volume scheduled for the calculation period, oil density, and the scheduled pipeline operating time [3]. The kinematic viscosity (m²/s) and density (kg/m³) at the average oil temperature are determined empirically or calculated by formulas. The average oil temperature is calculated based on the available temperature data for the same period of the previous 2–3 years. The studies of the time series of atmospheric temperature and oil density and viscosity have shown that these data have a fractal structure. From the mathematical point of view, a fractal object has a fractional dimension. Another important property of almost all fractals is their self-similarity (scale invariance). The main statistical data of the following indicators have been calculated [17]: the coefficient of sample correlation between temperature and viscosity $r = -0.66251$; between air temperature and density: $r = -0.72369$; between density and viscosity: $r = 0.591$. To study the self-similarity in the process studied, the Hurst exponent H has been calculated (using the Fraktan 4.4 software package). It is known that a continuous stochastic process is considered self-similar if $0, 5 \leq H \leq 1$. Calculations have shown that for oil viscosity, the Hurst exponent $H = 0.8857$, the fractal dimension $D = 2 - H = 1.1143$, and the correlation dimension $C = 3$. The autocorrelation function and Hurst exponent calculation results testify to a self-similar nature of the time series of the rheological oil properties. This result is confirmed by a high coefficient of correlation between the rheological properties and temperature. It is known that it was the study of the temperature time series that led to the discovery of self-similarity in similar processes. The study results provided have been further used to choose simulation techniques and the model structure.

Based on the viscosity time series data, a neural network model of the multilayer perceptron (MLP) type has been built to make a forecast n moves ahead. The MLP

architecture has been chosen using nonlinear dynamics. For our predictive neural network model of the viscosity time series, the prediction window p has been chosen by the formula [17]: $p = [2C] + 1$, where C is the correlation dimension and $[.]$ is the integer part of a number.

Further studies have shown that the identification model built can be used to solve some other management problems, e.g., those associated with the design of new linear pipeline sections or a change in the well of the pumped oil. The results of solving another problem are given below.

Assume that to make managerial decisions, the effect of rheological properties, e.g., the pumped oil viscosity, on the power consumption should be evaluated. The following algorithm is proposed. An array of input data should be created with the column data, which correspond to the viscosity, changing from the minimum to the maximum with some constant step (but remaining within the admissible problem solution domain), and constant values assigned to all other input values, e.g., those equal to the average value over some interval. This array is fed to the input of the neural network, and then the corresponding power consumption is calculated. The calculation results are shown in Fig. 3. On the plot (Fig. 3), the abscissa and the ordinate show the viscosity and the power consumption, respectively.

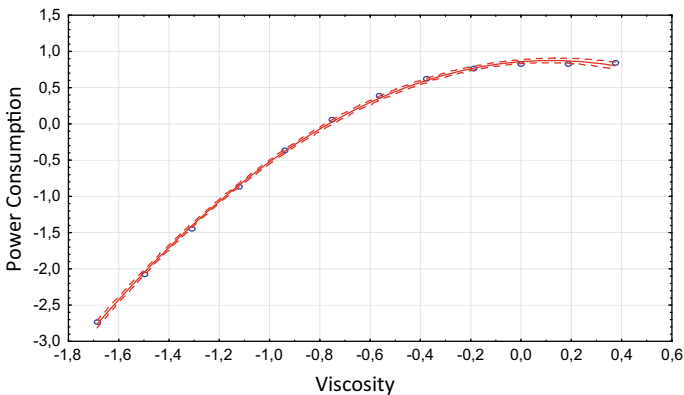


Fig. 3 Dependence of power consumption on viscosity

The plot can be used to solve management problems.

The NN models built can be used to forecast the power consumption for pumping oil through newly designed linear pipeline sections. To unify the models developed, the input data vector should be supplemented with such indicators as the pipe diameter, the length of the linear oil pipeline section, and the difference between the geodetic marks of the pipe end and start for the linear section considered. The computational experiments have shown positive NN model unification results for planning power consumption for pumping oil. Conclusion: the developed mathematical models allow the automation of planning power consumption, which will improve the efficiency of the main oil pipeline maintenance.

3.4 The Results of Solving Problem 2

Let the vectors $X(t)$, $t \in T_p$ be defined. When taking the planned values of the input variables as the model inputs, we obtain the forecasted daily power consumption values: $\hat{y}(t) = \hat{F}_3(X(t))$, $t \in T_p$.

The solution to the retro-forecasting problem has shown that the error in the NN calculations for the monthly data is mainly 2%, and two observations only have a 3% error (Table 4).

Table 4 Fragment of the comparison of the declared and calculated NN output values

t	$y(t)$	$\hat{y}(t)$	$ y - \hat{y} $	$\left \frac{y - \hat{y}}{y} \right $
1	-0.35754	-0.33215	0.02538	-0.071
2	-0.35754	-0.35442	0.00312	-0.00872
3	-0.35327	-0.32921	0.02407	-0.06812
4	1.01766	1.01044	-0.00723	-0.0071

3.5 The Results of Solving Problem 3

Let us perform the following experiment. Let us select data for a certain month from the source file; rename t , assume that $t = 1, 2, \dots, 30$; calculate $V = \sum_{i=1}^{30} y_i$. The input variables of the chosen interval will be the same, except for X_4 and X_9 . Let us assume that at all inputs within the interval, these variables $X_4 = V/30$, $X_9 = 0$. Let us enter the transformed data into the NN model and calculate \hat{y} , and then compare them with the observed y values for this period. Calculations have shown that the actual consumption is much higher. This model experiment allows roughly compare the power consumption at frequently switching pumping modes with the oil pipeline operation when the modes change occasionally. In the experiments performed, the energy savings amounted to 75,666 (kW·day).

4 Conclusions

The studies performed allow drawing the below conclusions.

- The accuracy of building NN identification models can be improved by the model specification. In particular, it is shown that introducing new variables X8 and X9, directly related to the control quality, may improve the accuracy of building the NN model.
- The retro-forecast using the NN models built showed that the problem of planning power consumption can be solved with the required accuracy.

- The numerical experiments performed using the NN model have shown that frequently switching pumping modes increase the power consumption for pumping oil. This conclusion is consistent with practical observations and the theory. The experimental algorithms with the use of the NN models described can be used to solve organizational control problems.
- Herein, the NN models are built and the solutions to problems are obtained based on actual data, and however, the quality of solving problems can be improved through additional studies.

Currently, the capabilities of mathematical and computer simulation tools lag behind the needs of many complex production process control problems, including the oil transportation control processes.

Acknowledgements. This research is funded by RFFI, grant 19-08-00261.

References

1. Methodology for calculating electricity consumption for oil transportation through oil trunk pipelines. (2004) "IPTEP", Ufa
2. Regulations for the development of technological maps, calculation of operating modes of main oil pipelines of OAO AK Transneft (2008) Moscow
3. Gorban A (1984) A generalized approximation theorem and the computational capabilities of neural networks. *Sib J Calc Math Siberian* 1(1):11–24
4. Shammazov I et al (2009) Application of neural networks for predicting electricity consumption in oil transportation. *J Probl Collect Prep Transp Oil Oil Prod* 150:89–95
5. Kozachuk BA et al (2010) Algorithm for solving the problem of predicting electricity consumption in pipeline transport of oil using neural networks. *J Oil Gas Bus* 2010(3). <http://www.ogbus.ru/authors/Shammazov-2.pdf>
6. Makarenko OA, Shiriazdanova LF (2011) Basic aspects of building a neural predictive model of electricity consumption on developing oil pipelines. *J Oil and Gas Bus* 2011(3):94–102. <http://www.ogbus.ru/authors/Shammazov-2>
7. Tyumentsev Yu (2017) Neural network identification of characteristics of nonlinear controlled dynamic systems. In: XIX international scientific and technical conference "neuroinformatics—2017", Moscow
8. Malinetskiy G, Potapov A (2001) Channels and jokers: on new methods for predicting the behavior of complex systems. Preprint IMP II M.V. Keldysh RAS
9. Gorbakov SA, Gabdrakhmanova NT (2001) Ways to improve the associative properties of neural network mathematical models in the tax control and management system. *Inf technol* 4:7–12
10. Yakushev AA, Gorbakov SA, Gabdrakhmanova NT (2000) Multidimensional statistical methods and neural network models in economic analysis. BTIPB, Ufa
11. Borovikov VP, Ivchenko GI (2006) Forecasting in the STATISTICA system in the WINDOWS environment. Finance and statistics, Moscow
12. Ayvazyan SA, Enyukov IS, Meshalkin LD (1983) Applied statistics. In: Basics of modeling and primary data processing. Finance and Statistics, Moscow
13. Gorban AN, Rossiev DA (1996) Neural networks on a personal computer. Science (Siberian Branch. Science (Siberian Branch), Novosibirsk

14. Wasserman F (1992) Neurocomputer technology: theory and practice. Mir, Moscow
15. Russel SJ, Norvig P (2007) Artificial intelligence. A Modern Approach. Publishing house "Williams", Moscow
16. Hajkin S (2006) Nejrionnye seti: polnyj kurs. Izdatel'skij dom "Vil'jams", Moscow
17. Gabdrakhmanova N, Gabdrakhmanov A (2016) Neural network models of time series of network traffic intensities. In: Procedia Computer Science 103:483–488. XIIth International symposium "intelligent systems". INTELS'16. 5–7 October



Control of a Mobile Cart with Two Traction Rear Wheels and a Free Front Wheel

S. Kochetkov^(✉)

Institute of Control Sciences of RAS, 65, Profsoyuznaya Str., Moscow 117997, Russia
kos@ipu.ru

Abstract. The problem of control for the mobile cart with two traction rear wheels and free front wheel is considered in the paper. The traction wheels are governed by two mechanically independent direct current drive motor. The free wheel can turn around your mounting point. The problem of the desired path following with given linear velocity is stated in the paper under assumption that mobile robot is interfered by external perturbations, which physically represent the external force actions, wind blowing, friction force and so on. Due to this aim, the combined control law, which consists of continuous and discontinuous components, is synthesized in the paper. The discontinuous term provides oscillation mode of the transient process in the closed system, and continuous component leads to decaying of the oscillation amplitude of the output variables asymptotically to zero. The simulation results depict the efficiency of the designed algorithm.

Keywords: Mobile cart · Vortex algorithm · External perturbations · Path following problem · Decomposition

1 Introduction

Nowadays, nonholonomic electrically driven vehicles attract a lot of attention of the designers due to its controllability, fast control inputs response and high efficiency of the traction systems on the base of alternative current or direct current electric drives [1–3]. In contrast to vehicles with combustion engine, there are two great advantages of the electric vehicles (EV), because they can be made with independently controlled wheels and EV has much smaller ratio between the size and the power of the traction system.

In this paper, the full model with actuators dynamics of the mobile cart is considered [4] to avoid simplification of the control algorithm synthesis procedure caused by reduced mathematical description like in [3, 5–7]. Moreover, as it was mentioned above, the electric drives are used as actuators, and the real control inputs correspond to the electrical voltages applied to the stators windings, so the control amplitude limitation (maximum voltages) must be introduced during problem statement and further control law synthesis [8].

One of the main challenges concerned with the electric mobile vehicles, robots control is the desired path following problem [5, 9, 10]. The task can be complicated

by consideration the parametric and external disturbances in the mathematical model of the plant [7, 11, 12]. According to these issues in this paper, the problem is extended by treatment, that mobile cart must track trajectory with the given function of the linear motion velocity. Mobile cart under absence of wheels sliding belongs to the class of nonholonomic systems, which attract attention from the control point of view during last three decades [13].

There are many approaches based on the achievements of modern control theory, which help to solve the discussed problem. Lee et al. [8] developed linear feedback control law, which globally provides robot motion convergence to the path specified by straight line, a circle or a path approaching the origin. Boukens et al. [12] designed the intelligent controller on the base of neural network approach. However, only global stability is guaranteed in the sense, that all trajectory tracking errors are bounded under influence of the parametric and external perturbations. The nonlinear predictive approach is used by Mirzaeinejad [7] to design the controller for the trajectory tracking of a nonholonomic mobile robot in the presence of model uncertainties and disturbances. After analysis, it was shown that the tracking errors are remarkably decreased by the proposed control system in the presence of model uncertainties and disturbances. Klancar used linearized tracking-error dynamics for prediction the system behavior. Further, the quadratic cost function around the system tracking error is utilized for control law derivation [9].

In this paper, the new approach is developed for disturbances rejection in the problem of the desired path following for the mobile cart. In contrast to the classical methods of perturbations compensation on the base of the known disturbances excitation model and linear feedback synthesis [14, 15], the combined nonlinear discontinuous control is proposed. The main idea consists in organizing the transient oscillation process in the closed loop system with decaying amplitude [16, 17], so the tracking errors tend to zero asymptotically in time. It is necessary to note that proposed approach provides invariance property with respect to unmatched external perturbations, which does not belong to control space [18].

The paper is organized as follows. In Sect. 2, the mathematical model of the plant is introduced, and its control structure and the problem statement are considered. Further, the hierarchical procedure of the control inputs synthesis is developed in the next section. The formal relations for the choice of the feedback loop parameters are derived. The simulation results of the designed control scheme are presented in Sect. 4. Finally, the main results are discussed in the conclusion section.

2 Problem Statement

The kinematic model of the mobile cart is considered in the form [1] (see Fig. 1):

$$\dot{x}_1 = v \cos x_3; \quad \dot{x}_2 = v \sin x_3; \quad \dot{x}_3 = \omega, \quad (1)$$

where x_1, x_2, x_3 are planar coordinates in [m] and angle position of the mobile robot in [rad] in stationary coordinate system X_1OX_2 , $v = \frac{\omega_1 + \omega_2}{2} r$ is linear velocity of the center of the mass of the mobile robot in [m/sec]; $\omega = \frac{\omega_1 - \omega_2}{D} r$ is angular velocity of

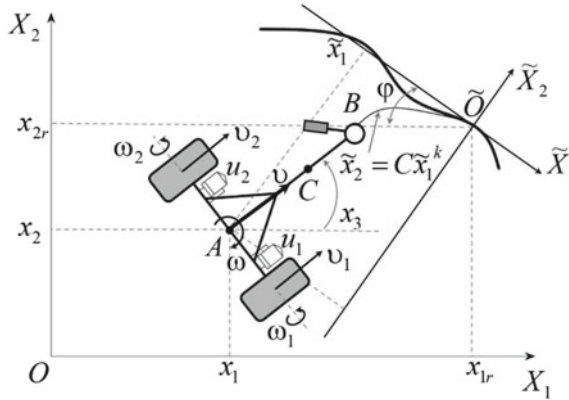


Fig. 1 Coordinate systems of the mobile robot

the mobile robot around the center of the mass in [rad/s], r, D are known wheel radius and distance between driving wheels in [m].

The control torques is implemented with the help of direct current motors with permanent excitation. Combining the drive model with the equations for linear v and angular ω velocities, leads to the system [4]

$$\begin{aligned}
 J\dot{\omega} &= \frac{c_i D}{r} (I_1 - I_2) - m_1 a v \omega + \xi_1(t), \\
 \dot{I}_1 &= -\frac{R}{L} I_1 - \frac{c_i}{rL} (v + D\omega) + \frac{u_1}{L}; \\
 m\dot{v} &= -\frac{c_i}{L} (I_1 + I_2) + m_1 a \omega^2 + \xi_2(t), \\
 \dot{I}_2 &= -\frac{R}{L} I_2 - \frac{c_i}{rL} (v - D\omega) + \frac{u_2}{L},
 \end{aligned} \tag{2}$$

where I_1, I_2 are stator currents of DC drives in [A], $\xi_1(t)$ is external perturbation torque in [$N \cdot m$], $J, [\text{kg} \cdot \text{m}^2], m, [\text{kg}]$ are generalized moments of inertia and mass of a mobile robot, which are known values, $\xi_2(t)$ is perturbation force in [N]; the perturbations are bounded functions with two first bounded derivatives: $|\xi_i(t)| \leq \Sigma_i, |\dot{\xi}_i(t)| \leq \bar{\Sigma}_i, |\ddot{\xi}_i(t)| \leq \bar{\Sigma}_i, i = 1, 2; R$ is rotor resistance in [Ohm], $c_i [N \cdot m \cdot A^{-1}], c_\omega, [V \cdot s \cdot \text{rad}^{-1}]$ are known torque constant and back electric motion force constant, $|u_i| \leq U_i = \text{const}, i = 1, 2$ are the bounded control inputs (the stators voltages) in [V], L is the stator inductance in [H], the point A is the center of the rear shaft, the center of the mass of the cart is in the point $C, a = AC, [\text{m}]$.

Further, the systems of Eqs. (1) and (2) are considered as models of the control object under the assumption that the components of their state space vectors are available for measurement. The task is to stabilize the movement of a mobile robot relative to a given trajectory.

The program trajectory or path can be defined as some function of the parameter on the plain

$$x_{1r} = h_1(s), x_{2r} = h_2(s), \tag{3}$$

where $h_i(s) \in C^4$, $i = 1, 2$, x_{1r}, x_{2r} are the coordinates of the center of the mass, which correspond to the desired position in the global coordinate systems in [m], s is the path parameter.

The task of the desired trajectory (3) tracking with the prescribed speed can be formulated on the base of some reference model, like that

$$\begin{aligned} \dot{s} &= \frac{v_r}{\sqrt{[(h_1)'_s]^2 + [(h_2)'_s]^2}}, \\ \dot{x}_{1r} &= v_r(t) \cos x_{3r}, \quad \dot{x}_{2r} = v_r(t) \sin x_{3r}, \\ \dot{x}_{3r} &= \omega_r(t) = \frac{(h_2)''_s (h_1)'_s - (h_1)''_s (h_2)'_s}{([(h_1)'_s]^2 + [(h_2)'_s]^2)^{(3/2)}} v_r, \\ \dot{v}_r &= a_r, \\ \dot{a}_r &= -\frac{R}{L} \left[a_r - \frac{m_1 a}{m} \omega_r \right] - \frac{2c_i^2}{mr^2 L} v_r + \frac{c_i}{mrL} u_r, \end{aligned} \tag{4}$$

where x_{1r}, x_{2r}, x_{3r} are the desired position in [m] and angle coordinate in [rad], $\omega_r(t), v_r(t)$ are the reference linear and angular velocities in [rad/s] and [m/s], a_r is the reference acceleration in [m/s²], u_r ([V]) is the bounded correction input of the reference model, $|u_r| \leq U_1 + U_2$; $(h_i)'_s, (h_i)''_s$ ($i = 1, 2$) are the two first partial derivatives of the functions (3) with respect to the parameter s .

The equation for the errors $\bar{x}_i = x_i - x_{ri}$, $i = \overline{1, 3}$ according to (1), (4) is

$$\begin{aligned} \dot{\bar{x}}_1 &= v \cos(\bar{x}_3 + x_{r3}) - v_r(t) \cos x_{3r}, \\ \dot{\bar{x}}_2 &= v \sin(\bar{x}_3 + x_{r3}) - v_r(t) \sin x_{3r}, \\ \dot{\bar{x}}_3 &= \omega - \omega_r(t). \end{aligned} \tag{5}$$

For the feedback synthesis purpose, the coordinates concerned with the reference model (4) are introduced:

$$\tilde{x} = H\bar{x}, \quad H = \begin{pmatrix} \cos x_{3r} & \sin x_{3r} & 0 \\ -\sin x_{3r} & \cos x_{3r} & 0 \\ 0 & 0 & 1 \end{pmatrix}. \tag{6}$$

Using (4–6), the equations for the errors in the coordinate system $\tilde{X}_1 \tilde{O} \tilde{X}_2$ can be derived (see Fig. 1) (the axis $\tilde{O} \tilde{X}_1$ is tangent to the desired path trajectory)

$$\begin{aligned} \dot{\tilde{x}}_1 &= v \cos \tilde{x}_3 - v_r + \omega_r \tilde{x}_2; \\ \dot{\tilde{x}}_2 &= -\omega_r \tilde{x}_1 + v \sin \tilde{x}_3; \\ \dot{\tilde{x}}_3 &= \omega - \omega_r. \end{aligned} \tag{7}$$

The problem of the state space vector of the system (7) stabilization is stated in the paper

$$\lim_{t \rightarrow +\infty} \|\tilde{x}(t)\| = 0. \quad (8)$$

3 Control Algorithm Synthesis

The solution of the control inputs synthesis problem in the systems (1) and (2) is based on two-level decomposition. First, we consider the kinematic model (1), for which the linear and angular velocities are formed to provide movement along the desired trajectory (3) with the given trajectory speed. At the second stage, control inputs are synthesized in the electromechanical system (2), which ensures the maintenance of the linear and angular velocities obtained at the first step.

3.1 The Kinematic Subsystem Stabilization

It is necessary to note that some initial point P of the mobile cart trajectory can be situated far away from the point \tilde{O} , corresponding to the reference point motion concerned with the reference system (4) trajectory. So, the convergence path or convergence trajectory must be considered for the feedback synthesis. With this aim, some neighborhood or δ -vicinity of the origin \tilde{O} is introduced, which has the following sense. If the distance between the two points P and \tilde{O} is sufficiently large, then the desired convergence path is the straight line (the minimal distance between two points on the plane). In other case, when the trajectories of the mobile cart belong to δ -vicinity of the point \tilde{O} , the convergence is chosen, for example, in the form [19]:

$$\tilde{x}_2 = C\tilde{x}_1^\alpha, \alpha > 1. \quad (9)$$

The derivative of the function (9) in the point $\tilde{x}_1 = 0$ is

$$\frac{d\tilde{x}_2}{d\tilde{x}_1} = C\tilde{x}_1^{\alpha-1} \Rightarrow \left. \frac{d\tilde{x}_2}{d\tilde{x}_1} \right|_{\tilde{x}_1=0} = 0, \quad (10)$$

where C is the constant, depending on the initial conditions. It is obviously from (10) that the tangent to the function (9) in the point $\tilde{x}_1 = 0$ coincide with the axis $\tilde{O}\tilde{X}_1$ of the reference system or the tangent to the desired path trajectory.

From (9), the following equation can be derived

$$\frac{d\tilde{x}_2}{d\tilde{x}_1} = \alpha \operatorname{tg}\phi, \tag{11}$$

where $\operatorname{tg}\phi = \frac{\tilde{x}_2}{\tilde{x}_1}$, $\phi = \begin{cases} \operatorname{arctg}(\tilde{x}_2/\tilde{x}_1), & \tilde{x}_1 \geq 0; \\ \pi + \operatorname{arctg}(\tilde{x}_2/\tilde{x}_1), & \tilde{x}_1 < 0. \end{cases}$

By choosing the different value for the parameter α in (9), the convergence path shape can be adjusted. With $\alpha = 1$ in (9), the straight line is achieved, and the value of α must be chosen greater than one to provide smooth convergence to the point \tilde{O} of the reference system. According to this reasons, the desired relationship between the variables of the system (7) according to (11) can be introduced in the form

$$\operatorname{tg}\tilde{x}_3 = k(e_{11})\operatorname{tg}\phi, \tag{12}$$

where $k(e_{11}) = \begin{cases} 1, & e_{11} \geq \delta; \\ \frac{\alpha - 1}{\delta^4} e_{11}^4 - 4\frac{\alpha - 1}{\delta^3} e_{11}^3 + 6\frac{\alpha - 1}{\delta^2} e_{11}^2 - 4\frac{\alpha - 1}{\delta} e_{11} + \alpha, & e_{11} < \delta, \end{cases}$
 $\phi = \begin{cases} \operatorname{arctg}(\tilde{x}_2/\tilde{x}_1), & \tilde{x}_1 \geq 0; \\ \pi + \operatorname{arctg}(\tilde{x}_2/\tilde{x}_1), & \tilde{x}_1 < 0, \end{cases} \quad e_{11} = \frac{\tilde{x}_1^2 + \tilde{x}_2^2}{2}.$

Further, the control law synthesis is considered on the base of step-by-step decomposition, corresponding to the block approach methodology [20, 21]. So, in the kinematic subsystem the variables v, ω of the kinematic subsystem (7) are considered as fictitious control inputs. Equation (7) can be written in the new variables into account (12):

$$\begin{aligned} \dot{e}_{11} &= \sqrt{2e_{11}}(v\cos(\tilde{x}_3 - \phi) - v_r\cos\phi); \\ \frac{d}{dt}(\operatorname{tg}\phi) &= (v/\sqrt{2e_{11}})(1 + \operatorname{tg}^2\phi)\sin(\tilde{x}_3 - \phi) - \omega_r(1 + \operatorname{tg}^2\phi) + (v_r/\sqrt{2e_{11}}) \\ &\times \operatorname{tg}\phi\sqrt{1 + \operatorname{tg}^2\phi}; \\ \frac{d}{dt}(\operatorname{tg}\tilde{x}_3) &= (1 + \operatorname{tg}^2\tilde{x}_3)(\omega - \omega_r). \end{aligned} \tag{13}$$

It is required to choose v, ω in such a way to provide relation (12) and to stabilize the variable e_{11} in (13). With this goal, the variable $e_{12} = \operatorname{tg}\tilde{x}_3 - k(e_{11})\operatorname{tg}\phi$ is considered according to the equation

$$\dot{e}_{12} = (1 + \operatorname{tg}^2\tilde{x}_3)(\omega - \omega_r) + b(\phi, \tilde{x}_3, e_{11})v + f_1(\omega_r, \phi, \tilde{x}_3, e_{11}), \tag{14}$$

where

$$f_1 = -k(e_{11})[-\omega_r(1 + tg^2\phi) + (v_r/\sqrt{2e_{11}})tg\phi\sqrt{1 + tg^2\phi}] + (dk/de_{11})\sqrt{2e_{11}}v_r \sin \phi;$$

$$b = -k(e_{11}) \cdot (1 + tg^2\phi)\sin(\tilde{x}_3 - \phi)/\sqrt{2e_{11}} - (dk/de_{11})tg\phi\sqrt{2e_{11}}\cos(\tilde{x}_3 - \phi).$$

As a result, the fictitious control inputs are chosen in the form

$$\omega = \omega_r - \frac{f_1 + l_{12}e_{12}}{1 + tg^2\tilde{x}_3} - \frac{b(e_{11}, \phi, \tilde{x}_3)[-l_{11}\sqrt{e_{11}} + v_r \cos \phi]}{(1 + tg^2\tilde{x}_3)\cos(\tilde{x}_3 - \phi)}, \quad (15)$$

$$v = \frac{-l_{11}\sqrt{e_{11}} + v_r \cos \phi}{\cos(\tilde{x}_3 - \phi)}, \quad l_{11} > 0, l_{12} > 0, \quad (16)$$

and closed loop system looks like the following

$$\dot{e}_{12} = -l_{12}e_{12}, \dot{e}_{11} = -\sqrt{2}l_{11}e_{11}.$$

According to this result, the relation (12) is provided, the variable e_{11} is stabilized asymptotically and the motion trajectory of the mobile robot converges to the desired trajectory.

3.2 Step-by-step Control Inputs Synthesis in the Electrical Subsystem

In this subsection, a step-by-step procedure is developed to provide desired fictitious control inputs according to the angular (15) and linear (16) speeds in the electromechanical subsystem (2).

Step 1. In the first equations of the subsystems (2), the difference $c_i(I_1 - I_2)$ and the sum $c_i(I_1 + I_2)$ of the electromagnetic torque of the electric drives are considered as fictitious controls. The following variables must be stabilized

$$e_{21} = v + \frac{l_{11}\sqrt{e_{11}} - v_r \cos \phi}{\cos(\tilde{x}_3 - \phi)};$$

$$e_{22} = \omega - \omega_r + \frac{f_1 + l_{12}e_{12}}{1 + tg^2\tilde{x}_3} + \frac{(-l_{11}\sqrt{e_{11}} + v_r \cos \phi)b(\phi, \tilde{x}_3, e_{11})}{(1 + tg^2\tilde{x}_3)\cos(\tilde{x}_3 - \phi)}.$$

According to (2), (13–14) the equations with respect to these variables are

$$\dot{e}_{21} = \frac{c_i}{mr}(I_1 + I_2) + \frac{m_1 a}{m}\omega^2 + f_{21}(\phi, \tilde{x}_3, v, v_r, \omega, \omega_r, \dot{v}_r, e_{11}),$$

$$\dot{e}_{22} = \frac{c_i D}{Jr}(I_1 - I_2) - \frac{m_1 a}{J}v\omega + f_{22}(\phi, \tilde{x}_3, v, \omega, v_r, \omega_r, \dot{v}_r, \dot{\omega}_r, e_{11}, e_{12}), \quad (17)$$

the full analytical expression of the functions $f_{21}(\cdot), f_{22}(\cdot)$ are:

$$\begin{aligned}
 f_{21} &= \frac{(l_{11}[1/(2\sqrt{e_{11}})]\dot{e}_{11} - \dot{v}_r \cos \phi + v_r \sin \phi \dot{\phi}) \cos(\tilde{x}_3 - \phi)}{\cos^2(\tilde{x}_3 - \phi)} \\
 &+ \frac{l_{11}\sqrt{e_{11}} \sin(\tilde{x}_3 - \phi)(\dot{\tilde{x}}_3 - \dot{\phi}) - v_r \cos \phi \sin(\tilde{x}_3 - \phi)(\dot{\tilde{x}}_3 - \dot{\phi})}{\cos^2(\tilde{x}_3 - \phi)} \\
 f_{22} &= -\dot{\omega}_r + \frac{(\dot{f}_1 + l_{12}\dot{e}_{12})}{1 + tg^2\tilde{x}_3} - \frac{2tg\tilde{x}_3 \frac{d(tg\tilde{x}_3)}{dt}(f_1 + l_{12}e_{12})}{(1 + tg^2\tilde{x}_3)^2} \\
 &+ \frac{b(-l_{11}\frac{\dot{e}_{11}}{2\sqrt{e_{11}}} + \dot{v}_r \cos \phi - v_r \sin \phi \dot{\phi}) + \dot{b}(-l_{11}\sqrt{e_{11}} + v_r \cos \phi)}{(1 + tg^2\tilde{x}_3) \cos(\tilde{x}_3 - \phi)} - \\
 &- \frac{2tg\tilde{x}_3 \frac{d(tg\tilde{x}_3)}{dt} \cos(\tilde{x}_3 - \phi) - (1 + tg^2\tilde{x}_3) \sin(\tilde{x}_3 - \phi)(\dot{\tilde{x}}_3 - \dot{\phi})}{(1 + tg^2\tilde{x}_3)^2 \cos^2(\tilde{x}_3 - \phi)} \\
 &(-l_{11}\sqrt{e_{11}} + v_r \cos \phi)b(\phi, \tilde{x}_3, e_{11}), \\
 \dot{b} &= -\left[\frac{dk}{de_{11}} \frac{\dot{e}_{11}}{\sqrt{2e_{11}}} - \frac{\dot{e}_{11}}{2\sqrt{2}e_{11}^{3/2}}k(e_{11}) \right] \\
 &(1 + tg^2\phi) \sin(\tilde{x}_3 - \phi) - 2\frac{k(e_{11})}{\sqrt{2e_{11}}}tg\phi \frac{d(tg\phi)}{dt} \sin(\tilde{x}_3 - \phi) - \\
 &- \frac{k(e_{11})}{\sqrt{2e_{11}}}(1 + tg^2\phi) \cos(\tilde{x}_3 - \phi)(\dot{\tilde{x}}_3 - \dot{\phi}) \\
 &- \frac{d^2k}{de_{11}^2}\dot{e}_{11}tg\phi\sqrt{2e_{11}} \cos(\tilde{x}_3 - \phi) - \frac{dk}{de_{11}} \frac{d(tg\phi)}{dt} \sqrt{2e_{11}} \cos(\tilde{x}_3 - \phi) - \\
 &- \frac{dk}{de_{11}}tg\phi \left[\frac{\dot{e}_{11}}{\sqrt{2e_{11}}} \cos(\tilde{x}_3 - \phi) + \sqrt{2e_{11}} \sin(\tilde{x}_3 - \phi)(\dot{\tilde{x}}_3 - \dot{\phi}) \right], \\
 \dot{f}_1 &= -\frac{dk}{de_{11}}\dot{e}_{11} \left[-\omega_r(1 + tg^2\phi) + \frac{v_r}{\sqrt{2e_{11}}}tg\phi\sqrt{1 + tg^2\phi} \right] \\
 &- k(e_{11}) \left[-\dot{\omega}_r(1 + tg^2\phi) - 2\omega_rtg\phi \frac{d(tg\phi)}{dt} + \right. \\
 &+ \left. \left(\frac{\dot{v}_r}{\sqrt{2e_{11}}} - \frac{\dot{e}_{11}v_r}{2\sqrt{2}e_{11}^{3/2}} \right) tg\phi\sqrt{1 + tg^2\phi} \right. \\
 &+ \left. \frac{v_r}{\sqrt{2e_{11}}} \frac{d(tg\phi)}{dt} \sqrt{1 + tg^2\phi} + \frac{v_r}{\sqrt{2e_{11}}}tg^2\phi \frac{d(tg\phi)}{dt} \sqrt{1 + tg^2\phi} \right] + \\
 &+ \frac{d^2k}{de_{11}^2}\sqrt{2e_{11}}\dot{e}_{11}v_r \sin \phi + \frac{dk}{de_{11}} \frac{\dot{e}_{11}}{\sqrt{2e_{11}}}v_r \sin \phi \\
 &+ \frac{dk}{de_{11}}\sqrt{2e_{11}}\dot{v}_r \sin \phi + \frac{dk}{de_{11}}\sqrt{2e_{11}}v_r\dot{\phi} \cos \phi
 \end{aligned}$$

In contrast to feedback with perturbations estimations on the base of the observer [22], to ensure invariance to perturbations f_{21}, f_{22} in the system (17), we choose fictitious

control stator currents based on the static feedback in the form [5]:

$$\begin{aligned} \frac{c_i}{mr}(I_1 + I_2) + \frac{m_1 a}{m}\omega^2 = \bar{I}_1; \quad \frac{c_i D}{Jr}(I_1 - I_2) - \frac{m_1 a}{J}v\omega = \bar{I}_2; \\ \dot{\bar{I}}_1 = -\text{sat}_1(\bar{I}_1) - M_1 \text{sign}(e_{21}); \quad \dot{\bar{I}}_2 = -\text{sat}_2(\bar{I}_2) - M_2 \text{sign}(e_{22}), \end{aligned} \quad (18)$$

where $\text{sat}_i(\bar{I}_i) = \begin{cases} \alpha_i \bar{I}_i, & |\alpha_i \bar{I}_i| \leq M_i; \\ M_i, & |\alpha_i \bar{I}_i| > M_i, \end{cases}$ $\alpha_i = \text{const} > 0$, $M_i = \text{const} > 0$, the initial conditions for the variables \bar{I}_i can be chosen in arbitrary manner, for example, equal to zero.

Step 2. The relations (18) can be provided by organizing the sliding mode on the hyper-surface

$$S = \begin{pmatrix} s_1 \\ s_2 \end{pmatrix} = \begin{pmatrix} I_1 \\ I_2 \end{pmatrix} - H^{-1} \begin{pmatrix} \bar{I}_1 - \frac{m_1 a}{m}\omega^2 \\ \bar{I}_2 + \frac{m_1 a}{J}v\omega \end{pmatrix} = 0, \quad (19)$$

where $H = \begin{pmatrix} \frac{c_i}{mr} & \frac{c_i}{mr} \\ \frac{c_i D}{Jr} & -\frac{c_i D}{Jr} \end{pmatrix}$.

In practice, the maximal velocities and acceleration for the plant (2) and the reference system (4) are bounded. Taking into account the class of the external perturbation (2), the following inequalities can be written

$$|f_{2i}| \leq F_{2i}, \quad |\dot{f}_{2i}| \leq \bar{F}_{2i}, \quad |\ddot{f}_{2i}| \leq \tilde{F}_{2i}, \quad i = 1, 2, \quad (20)$$

where $F_{2i}, \bar{F}_{2i}, \tilde{F}_{2i}$ are some positive constants.

According to (2) and (19), the expressions for the components of the vector S can be written

$$\begin{aligned} \dot{s}_1 = & -\frac{R}{L}I_1 - \frac{c_i}{rL}(v + D\omega) + \frac{u_1}{L} - h_{11}^{-1} \left[\dot{\bar{I}}_1 - \frac{2m_1 a}{m}\omega \left(\frac{c_i D}{Jr}(I_1 - I_2) - \frac{m_1 a}{J}v\omega \right) \right] - \\ & - h_{12}^{-1} \left[\dot{\bar{I}}_2 + \frac{m_1 a}{J} \left(\frac{c_i D}{Jr}(I_1 - I_2)v - \frac{m_1 a}{J}v^2\omega + \frac{c_i r}{m}(I_1 + I_2)\omega + \frac{m_1 a}{m}\omega^3 \right) \right]; \\ \dot{s}_2 = & -\frac{R}{L}I_2 - \frac{c_i}{rL}(v - D\omega) + \frac{u_2}{L} - h_{21}^{-1} \left[\dot{\bar{I}}_1 - \frac{2m_1 a}{m}\omega \left(\frac{c_i D}{Jr}(I_1 - I_2) - \frac{m_1 a}{J}v\omega \right) \right] - \\ & - h_{22}^{-1} \left[\dot{\bar{I}}_2 + \frac{m_1 a}{J} \left(\frac{c_i D}{Jr}(I_1 - I_2)v - \frac{m_1 a}{J}v^2\omega + \frac{c_i r}{m}(I_1 + I_2)\omega + \frac{m_1 a}{m}\omega^3 \right) \right], \end{aligned} \quad (21)$$

where $h_{ij}^{-1}, \dot{h}_{ij}^{-1}$ ($i = 1, 2; j = 1, 2$) are elements of the matrices $H^{-1}(\Psi) \dot{H}^{-1}(\Psi)$.

The real control inputs are chosen in the form of discontinuous functions

$$u_i = -U_i \text{sign}(s_i), \quad i = 1, 2, \quad (22)$$

Taking into account the physical restrictions on the phase coordinates and the relations (18), (20), one can choose the voltage amplitudes in the system (21) according to the inequalities

$$\begin{aligned}
 U_1 &> \left| -RI_1 - \frac{c_i}{r}(v + D\omega) - L\Psi_1 \right|, \quad U_2 > \left| -RI_2 - \frac{c_i}{r}(v - D\omega) - L\Psi_2 \right|, \\
 \Psi_j &= h_{j1}^{-1} \left[\dot{I}_1 - \frac{2m_1 a}{m} \omega \left(\frac{c_i D}{Jr} (I_1 - I_2) - \frac{m_1 a}{J} v \omega \right) \right] + \\
 &+ h_{j2}^{-1} \left[\dot{I}_2 + \frac{m_1 a}{J} \left(\frac{c_i D}{Jr} (I_1 - I_2) v - \frac{m_1 a}{J} v^2 \omega + \right. \right. \\
 &\left. \left. + \frac{c_i r}{m} (I_1 + I_2) \omega + \frac{m_1 a}{m} \omega^3 \right) \right], \quad j = 1, 2.
 \end{aligned}$$

to provide sliding mode [23] existence on the manifold (19).

The parameters α_i, M_i of the inner controller (18) are chosen according to the inequalities (20) and the conditions of Theorem 2 from [16, 17]

$$M_i > \alpha_i F_{2i} + \bar{F}_{2i}, \alpha_i (M_i - \alpha_i F_{2i} - \bar{F}_{2i}) > \tilde{F}_{2i}. \tag{23}$$

4 Simulation Results

The following parameters are used for the numerical simulation of the designed control law: $J = 1$ [kg · m²], $m = 1$ kg, $m_1 = 0.5$ [kg], $R = 0.1$ [Ohm], $L = 0.01$ [H], $a = 1$ [m], $c_i = 1$ [N · m · A⁻¹], $c_\omega = 1$ [V · s · rad⁻¹], $D = 1$ [m], $r = 1$ [m], $\xi_1(t) = \sin(t)$ [N · m], $\xi_2(t) = 2 \sin(2t)$ [N].

The desired trajectory of movement can be depicted as a flower with four petals (the length of the each petal is fifty meters), and with the reference linear velocity $v_r = 10$ [m/s], it can be described according to (4) by the following mathematical model

$$\begin{aligned}
 \dot{s} &= \frac{1}{5\sqrt{2.5 + 1.5 \cos(4s)}}, \quad \dot{x}_{1r} = 10 \cos x_{3r}, \quad \dot{x}_{2r} = 10 \sin x_{3r}, \\
 \dot{x}_{3r} &= \frac{6.5 + 1.5 \cos(4s)}{5[2.5 + 1.5 \cos(4s)]^{3/2}}.
 \end{aligned}$$

During numerical experiment, the following bounds were estimated for the functions from (20)

$$\begin{aligned}
 |f_{21}| &\leq 14 \text{ [N]}, \quad |f_{22}| \leq 2 \text{ [N · m]}, \quad |\dot{f}_{21}| \leq 10 \text{ [N/s]}, \\
 |\dot{f}_{22}| &\leq 2 \text{ [N · m/s]}, \quad \ddot{f}_{21} \leq 200 \text{ [N/s}^2\text{]}, \quad |\ddot{f}_{22}| \leq 150 \text{ [N · m/s}^2\text{]}.
 \end{aligned}$$

Using this inequalities, the parameters of the inner loop controller from (18) are chosen according to (23)

$$\alpha_1 = 200, M_1 = 15, 000, \alpha_2 = 1000, M_2 = 15, 800.$$

The real control inputs (22) are chosen with the amplitudes $U_1 = 200$ [V], $U_2 = 200$ [V].

The simulation results of the real sliding mode [24] with the fundamental integration step $t_s = 10^{-4}$ s are depicted on the Figs. 2, 3 and 4.

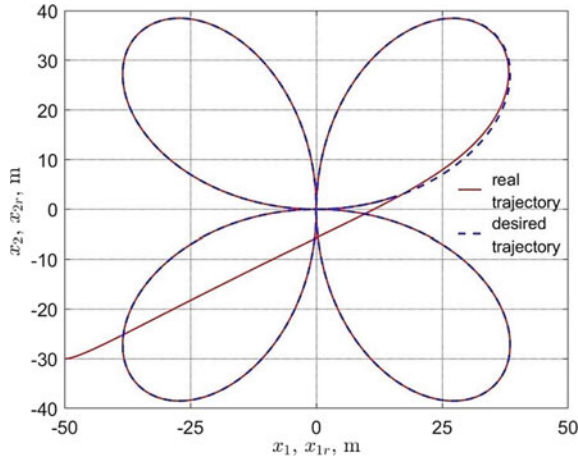


Fig. 2 Phase portrait of the reference and control object systems

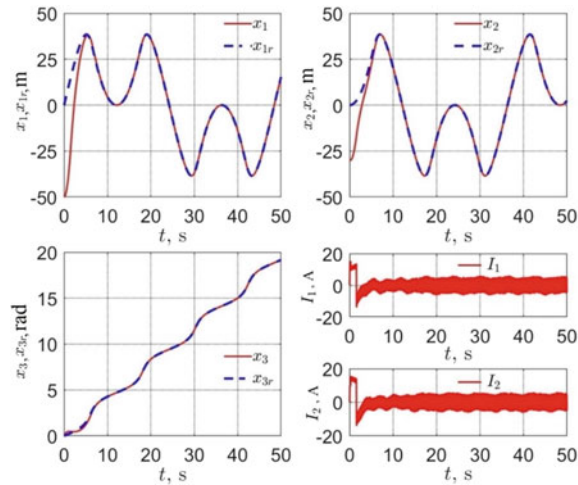


Fig. 3 Transient processes for the kinematic and electrical subsystems

5 Conclusions

The problem of the desired path following problem was considered in the paper for the mobile cart with independent rear wheels drives. The static feedback control law was derived. It was shown that designed algorithm provides asymptotical convergence of the tracking errors to zero. The situation with unknown parameters of the mobile cart, such as masses of the cart parts, inertia, position of the center of the mass, must be considered in the future research.

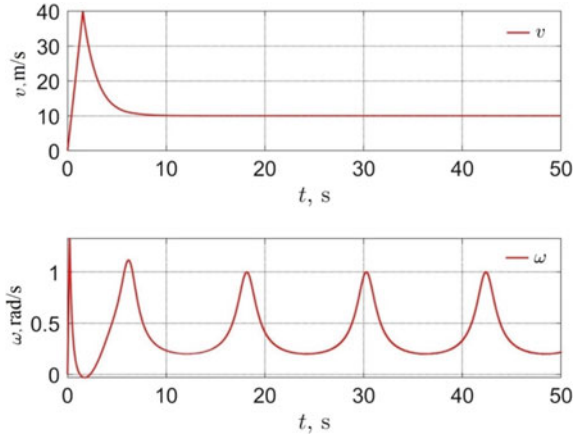


Fig. 4 Transient processes for the linear and angular velocities

Acknowledgements. The work was partially supported by the Russian Foundation for Basic Research under project no. 20-01-00363A.

References

1. Burdakov SF, Miroshnik IV, Stelmakov RE (2001) Motion control systems of wheeled mobile robots. Science, Saint-Petersburg
2. Klancar G, Zdesar A, Blazic S, Skrjanc I (2017) Wheeled mobile robotics. Butterworth-Heinemann, Oxford
3. Dixon W, Dawson DM, Zergeroglu E, Behal A (2001) Nonlinear control of wheeled mobile robots (in series Lecture notes in control and information sciences). Springer-Verlag, Berlin
4. Martynenko YuG (2007) Motion control of mobile wheeled robots. *J Math Sci* 147(2):6569–6606
5. Pesterev AV, Rapoport LB, Tkachev SB (2015) Canonical representation of a nonstationary path following problem. *J Comput Syst Sci Int* 54(4):656–670
6. Budanov VM, YeAD (2003) The motion of wheeled robots. *J Appl Math Mech* 67(2):215–225
7. Mirzaeinejad H (2019) Optimization-based nonlinear control laws with in-creased robustness for trajectory tracking of non-holonomic wheeled mobile robots. *Transp Res Part C* 101:1–17
8. Ti-Ch L, Song K-T, Lee C-H, Teng C-C (2001) Tracking control of unicycle-modeled mobile robots using a saturation feedback controller. *IEEE Trans Contr Sys Tech* 9(2):305–318
9. Klancar G, Skrjanc I (2007) Tracking-error model-based predictive control for mobile robots in real time. *Robot Auton Syst* 55:460–469
10. Andrianova OG, Korol'kova MA, Kochetkov SA, Krasnova SA (2010) Kinematic control of the mobile robot motion on range while avoiding obstacles. In: Proc. control in technical systems conference, Saint-Petersburg, pp 356–359
11. Shojaei KH, Shahri AM, Tarakameh A (2011) Adaptive feedback linearizing control of non-holonomic wheeled mobile robots in presence of parametric and nonparametric uncertainties. *Robot Comput-Integr Manuf* 27:194–204
12. Boukens M, Boukabou A, Chadli M (2017) Robust adaptive neural network-based trajectory tracking control approach for nonholonomic electrically driven mobile robots. *Robot Auton Syst* 92:30–40

13. Kolmanovsky VB, McClamroch NH (1995) Developments in nonholonomic control problem. *IEEE Trans Contr Sys* 15(6):20–36
14. Khlebnikov MV (2016) Control of linear systems subjected to exogenous disturbances: combined feedback. *Autom Remote Control* 77(7):1141–1151
15. Han J (2009) From PID to active disturbance rejection control. *IEEE Trans Ind Electron* 56(3):900–906
16. Kochetkov SA, Utkin VA (2013) Providing the invariance property on the basis on oscillation modes. *Dokl Math* 88(2):618–623
17. Kochetkov SA, Utkin VA (2013) Invariance in systems with un-matched perturbations. *Autom Remote Control* 74(7):1097–1127
18. Wonham WM (1985) *Linear multivariable control*. Springer-Verlag, Berlin, A geometric approach
19. Kochetkov SA, Utkin VA (2011) Method of decomposition in mobile robot control. *Autom Remote Control* 72(10):2084–2099
20. Drakunov SV, Izosimov DB, Lukyanov AG, Utkin VA (1990) Block control principle. *Autom Remote Control* 51(5):601–608
21. Utkin VA (2001) Invariance and independence in systems with separable motion. *Autom Remote Control* 62(11):1825–1843
22. Krasnova SA, Utkin AV (2016) Analysis and synthesis of minimum phase nonlinear SISO systems under external unmatched perturbations. *Autom. and Remote Control* 77(9):1665–1675
23. Utkin VI, Shi J, Guldner J (2009) *Sliding mode control in electromechanical systems*. Taylor and Francis, London
24. Kochetkov SA, Utkin VA (2012) The invariance property of control systems with imperfect relay elements. *Autom Remote Control* 73(6):1085–1115



Predictive Algorithm for Tuyere Areas' Parameters and Control Over the Distribution of Blast Parameters Around a Blast Furnace

I. A. Gurin^(✉), N. A. Spirin, and V. V. Lavrov

Ural Federal University, 19, Mira street, Ekaterinburg 620002, Russia
ivan.gurin@urfu.ru

Abstract. In the article, one has presented a mathematical description and an algorithm for prediction of tuyere areas' parameters and control over the distribution of blast parameters around a blast furnace based on the application of patterns of heat transfer between the hot blast and cooling water for tuyere elements. The algorithm has been designed to align the thermal condition of the tuyere areas of a blast furnace along the circumference. It entails the calculation of the following parameters for each tuyere: output and composition of the hearth gas, heat removal from a tuyere, hot blast blowout velocity from a tuyere, kinetic energy of the hot blast, total mechanical energy of the blast flow, length of circulation and oxidation zones, and theoretical combustion temperature. One calculates the mean values of parameters, the area of oxidation zones, and the relative area of tuyere areas. It has been shown that, in case of the non-uniform distribution of the hot blast to tuyeres, to stabilize the thermal state of tuyere areas and to align the gas distribution along the furnace circumference, one is required to adjust the natural gas flow rate to each tuyere to maintain the theoretical combustion temperature at a target level.

Keywords: Blast furnace · Tuyere area · Numerical simulation · Control algorithm · Prediction · Blast distribution

1 Introduction

When operating a blast furnace, the actual distribution of the hot blast to tuyeres is far from uniform: differences in blast flow rate at individual tuyeres, ranging from 5 to 50%, are observed [1–9]. Uneven distribution of the hot blast to tuyeres leads to different lengths of tuyere areas. This causes a difference in the speed of material descent in the individual sections of the furnace and concurrently a distorted gas flow along the furnace cross section [7–10]. In case of uncontrolled distribution of the blast to tuyeres, gas temperature in tuyere areas will vary and maintaining the theoretical combustion temperature within the optimal range will become impossible without the redistribution of natural gas between tuyeres of the furnace.

Several published papers [2–4, 7–10] describe methods and ways of controlling blast flow rate through blast furnace tuyeres. However, they are extremely short-lived and unsustainable due to elevated temperatures and aggressiveness of the hot blast. In

recent years, systems for control over the hot blast flow rate to tuyeres, based on the application of patterns of heat exchange between the blast and cooling water of tuyere elements, have been developed [9–14].

2 A Mathematical Computational Model and a Calculation Algorithm

In this paper, authors employed the method of determining the blast flow rate to tuyeres, based on numerical simulation of the heat power of the flow passing through a tuyere and the value of heat taking off from this tuyere. Block diagram of the algorithm for prediction of tuyere areas' parameters and control over blast parameters distribution around the blast furnace is shown in Fig. 1.

In numerical simulation, it is assumed that when the blast passes through the tuyere, part of the heat flow is transferred to the water cooling the tuyere, and to a greater extent, the higher is the heat power of the passed heat. This assumption is reasonable, since the design of all tuyere installed in the furnace is the same, the wall thickness of all tuyeres is the same, the coefficients of heat transfer from blast to tuyere and from tuyere to cooling water are also constant; the heat transfer coefficient of tuyere walls is assumed constant.

To calculate the blast distribution to each tuyere, one determines the mean value of the heat flow of the blast passing through tuyeres based on the average performance indices of a blast furnace as a whole:

$$q_{\partial} = \frac{Q \cdot C_B \cdot t_B}{n} + \frac{V_{N.G.} \cdot P \cdot C_{N.G.} \cdot t_{N.G.}}{1440 \cdot n}, \tag{1}$$

where n is the number of tuyeres, pcs.; Q —a blast flow rate, m^3/min . C_B —a hot blast heat capacity, $kJ/(m^3 \cdot K)$; t_B —a hot blast temperature, $^{\circ}C$; $C_{N.G.}$ —a heat capacity of natural gas, $kJ/(m^3 \cdot K)$; $V_{N.G.}$ —a specific natural gas flow rate, m^3/t of molten iron; $t_{N.G.}$ —a natural gas temperature, $^{\circ}C$; P —a furnace production rate; t —molten iron/day.

When this heat flow passes through a tuyere, part of it is transferred through the walls of the tuyere to the cooling water and heats the latter. The numerical value of such heating determines the heat removal from a tuyere:

$$q_b = m \cdot C_{H2O} \cdot \Delta t, \tag{2}$$

where m is a water flow rate for tuyere cooling, kg/min ; C_{H2O} —a heat capacity of cooling water, $kJ/(kg \cdot K)$; Δt —a temperature difference of water when passing the tuyere, $^{\circ}C$.

The average fraction of heat transferred from the heat flow of the blast going through the tuyere to the cooling water will be equal to:

$$\alpha = \frac{(m \cdot C_{H2O} \cdot \Delta t)_{av}}{q_b} \tag{3}$$

It is assumed that the value of α is constant for all tuyeres and is determined by the averaged performance indices of the blast furnace as a whole. Then the blast flow rate to the individual i th tuyere is determined from the equation:

$$\alpha = \frac{(m \cdot C_{H2O} \cdot \Delta t)_i}{Q_B^i \cdot C_B \cdot t_B + V_{N.G.}^i \cdot C_{N.G.} \cdot \frac{t_{N.G.}}{60}} \tag{4}$$

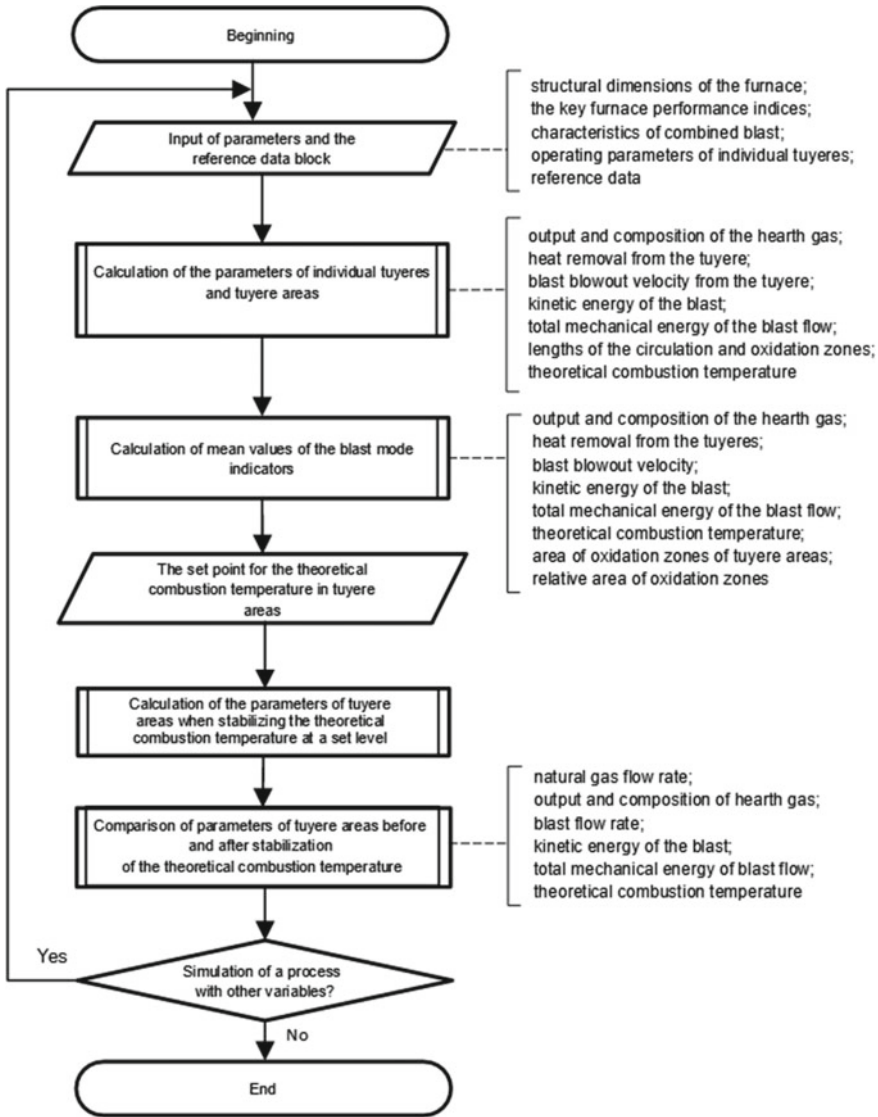


Fig. 1 Block diagram of the algorithm for prediction of tuyere areas' parameters and control over blast parameters distribution around the blast furnace

where $(m \cdot C_{H2O} \cdot \Delta t)_i$ is the value of heat removal from the i th tuyere, kJ/min; Q_B^i —a blast flow rate through the i th tuyere, m^3/min ; $V_{N.G.}^i$ —a set flow rate of natural gas through the i th tuyere, m^3/h .

From this equation, with a known value of the α coefficient, one calculates the estimated value of blast flow rate to the i th tuyere:

$$Q_B^i = \frac{(m \cdot C_{H_2O} \cdot \Delta t)_i - \alpha \cdot V_{N.G.}^i \cdot C_{N.G.} \cdot \frac{t_{N.G.}}{60}}{\alpha \cdot C_B \cdot t_B} \tag{5}$$

In the employed calculation algorithm, with known characteristics of the blast at tuyeres (flow rate, temperature, pressure, humidity, oxygen content in the blast, and natural gas flow rate) and tuyere diameter, one calculates blast blowout velocity, value of kinetic energy, and total mechanical energy of the blast flow at each air tuyere. The values of kinetic and total mechanical energy of the blast flow determine the length of the circulation zone, the numerical value of which corresponds to the oxygen content in the gaseous phase of the tuyere area equal to 2% and the length of the oxidation zone of the tuyere area (corresponds to CO₂ content in the gaseous phase equal to 2%) [15–19]. Subsequently, one determines the area of the oxidation zone of each tuyere area and the total area of these zones, related to the cross section of the hearth [20]. Based on the blast flow rate and the output of hearth gas at the found values of the heat content of the hearth gas and the known flow rate of natural gas for each tuyere, one calculates the theoretical combustion temperature in the tuyere areas according to the procedure presented in the papers [19–21].

With uneven distribution of the blast and supplied natural gas to tuyeres, one has observed significant variations in the theoretical combustion temperature along the circumference of the furnace in the tuyere areas. To eliminate the existing unevenness of tuyere areas' heating, it is necessary to redistribute the natural gas flow rate to tuyeres, focusing on the established unevenness of blast distribution.

For this purpose, at the first stage, one sets the value of the theoretical combustion temperature in the tuyere areas. At each tuyere at a known blast flow rate, one calculates the natural gas flow rate, which is necessary to stabilize the theoretical combustion temperature at known temperature, moisture, and oxygen content of the hot blast. Further, one calculates the parameters of tuyere areas when the theoretical combustion temperature has been stabilized at a predetermined level.

A complete list of initial data for calculating the distribution of hot blast over blast furnace tuyeres is presented in Tables 1, 2, and 3. It includes the design dimensions of the blast furnace, the technological parameters of blast furnace process, and the parameters of each tuyere.

Table 4 presents some performance indices of the blast furnace process and calculated data pertinent to the parameters of individual tuyere areas at blast furnace No. 2 at PAO MMK (PJSC Magnitogorsk Iron and Steel Works).

The histogram of the measured and required natural gas flow rates for the blast furnace tuyeres is shown in Fig. 2.

The estimated blast distribution to tuyeres is uneven: the maximum value of blast flow rate has been observed at tuyeres No 13 and 14 (152 and 148 m³/min, respectively) and the minimum—at tuyeres No 3 and 6—108 and 102 m³/min, respectively. Calculated value of tuyere areas' circulation zone length varies from 1.19 m (tuyere No 6) and reaches the maximum of 1.69 m at air tuyere No 13. Values of the theoretical combustion temperature for separate tuyere areas vary from 1958 °C at tuyere No. 6 to 2088 °C at

Table 1 Blast furnace dimensions

Parameter name	Symbol	Unit
Useful volume	V_0	m^3
Diameter of the hearth	D_{top}	m
Number of tuyeres	n	pcs
Tuyere diameter	d_ϕ	mm
Tuyere projection	H_ϕ	mm

Table 2 Parameters of individual tuyeres

Parameter name	Symbol	Unit
Natural gas flow rate	$V_{N.G}^i$	m^3/min
Water flow rate for tuyere cooling	m_i	kg/min
Temperature difference of water when passing the tuyere	Δt_i	$^\circ\text{C}$
The required value of the theoretical combustion temperature	T_i^i	$^\circ\text{C}$

Table 3 Blast furnace process parameters

Parameter name	Symbol	Unit
Furnace production rate	P	t of molten iron/day
Blast flow rate	Q	m^3/min
Blast pressure	P_B	atmosphere
Hot blast temperature	t_B	$^\circ\text{C}$
Blast humidity	f_B	g/m^3
Oxygen content in blast	ω	%
Blast losses in the air path	γ	%
Specific coke consumption	k	kg/t of molten iron
Reactivity of coke	CRI	%

Table 4 Blast furnace performance indices and estimated tuyere parameters for blast furnace No. 2 at PAO MMK (PJSC Magnitogorsk Iron and Steel Works)

Air tuyere number	Blast furnace process indices			Calculated parameters				Required gas flow rate to maintain t_t , m^3/h	
	Measured gas flow rate per tuyere, m^3/h	Water flow rate per tuyere, m^3/h	Temperature difference of water at the tuyere, $^{\circ}C$	Heat removal from the tuyere, kW	Calculated blast flow rate through the tuyere, m^3/min	Theoretical combustion temperature, $^{\circ}C$	Blast blowout velocity from the tuyeres, m/s		Length of the oxidation zone, m
1	908.5	11.41	11.25	149.1	132.9	2019	222.4	1.49	832
2	908.5	12.11	9.44	132.7	118.3	1975	200.6	1.34	741
3	917.6	12.83	8.17	121.7	108.5	1938	186.2	1.26	679
4	920.8	12.62	8.96	131.3	117.1	1966	199.1	1.33	733
5	921.4	12.26	9.60	136.6	121.8	1981	206.2	1.38	763
6	822.3	11.59	8.53	114.8	102.3	1958	174.5	1.19	641
7	925.3	12.50	10.59	153.7	137.1	2023	229.0	1.54	858
8	926.8	12.33	10.40	148.8	132.7	2011	222.6	1.49	831
9	921.8	11.81	9.56	131.1	116.9	1965	198.8	1.33	732
10	918.7	11.40	11.10	146.9	131.0	2009	219.8	1.47	820
11	920.7	13.41	10.33	160.9	143.4	2041	238.4	1.60	898
12	918.4	12.71	10.48	154.6	137.9	2028	230.0	1.54	863
13	854.0	13.25	11.09	170.7	152.2	2088	249.6	1.69	953

(continued)

Table 4 (continued)

Air tuyere number	Blast furnace process indices			Calculated parameters				Required gas flow rate to maintain t_r , m^3/h	
	Measured gas flow rate per tuyere, m^3/h	Water flow rate per tuyere, m^3/h	Temperature difference of water at the tuyere, $^{\circ}C$	Heat removal from the tuyere, kW	Calculated blast flow rate through the tuyere, m^3/min	Theoretical combustion temperature, $^{\circ}C$	Blast blowout velocity from the tuyeres, m/s		Length of the oxidation zone, m
14	914.2	14.45	9.88	165.7	147.8	2054	244.7	1.65	925
15	830.0	13.62	8.47	133.9	119.4	2012	200.1	1.34	748
16	904.5	11.31	12.21	160.4	143.0	2046	237.3	1.60	896
17	910.5	13.63	8.58	135.8	121.1	1983	204.8	1.37	758
18	905.3	12.57	10.34	150.9	134.5	2024	224.7	1.51	842
19	921.6	11.68	9.75	132.3	117.9	1968	200.4	1.34	738
20	910.6	11.52	10.97	146.8	130.9	2012	219.4	1.47	819

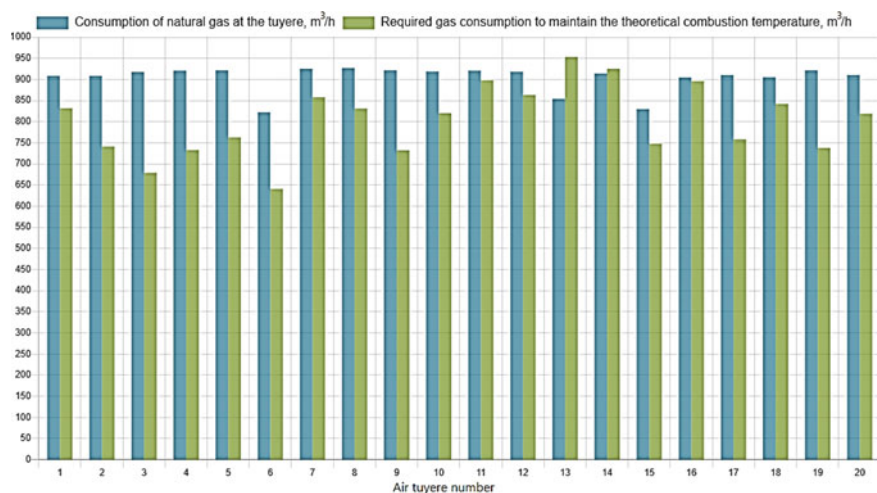


Fig. 2 Histogram of the measured and required natural gas flow rates for the blast furnace tuyeres

tuyere No. 13. Increase in the natural gas flow rate, required to stabilize the theoretical combustion temperature at a target level of 2050 °C, will contribute to the alignment of gas distribution around the furnace.

3 Conclusion

Therefore, the distribution of hot blast to the blast furnace tuyeres is uneven, and it is determined by the blast furnace operation practice and the design of the air supply ductwork. It has been shown that when the blast is unevenly distributed to the tuyeres, to stabilize the thermal state in the tuyere areas and to align the gas distribution around the furnace, one is required to adjust the natural gas flow rate to each tuyere to maintain the theoretical combustion temperature at a set target level.

References

1. Bol'shakov VI (2007) Technology of highly efficient energy-saving blast-furnace smelting. Naukova Dumka, Kiev, pp 411
2. Tovarovskii IG (2009) Blast furnace smelting. Porogi, Dnepropetrovsk, pp 768
3. Geerdes M, Chaigneau R, Lingardi O et al (2020) Modern blast furnace ironmaking: an introduction (4th edn), pp 274
4. Kurunov IF (2015) Modern state of blast-furnace production in China, Japan, South Korea, Western Europe, North and South America. Metallurg 7:12–22
5. Peacey JG, Davenport WG (1979) The iron blast furnace: theory and practice. Pergamon Press, pp 266
6. Ertem ME, Gurgun S (2006) Energy balance analysis for Erdemir blast furnace number one. Appl Therm Eng 26:1139–1148

7. Shirshov MYu, Druzhkov VG, Pavlov AV, Prokhorov IE (2014) Results of evaluation of the uniformity of distribution of the blast over the tuyeres of blast furnaces. In: Theory and technology of metallurgical production, Magnitogorsk State Technical University, Magnitogorsk, vol 2, pp 27–31
8. Nakajima R, Kishimoto S, Hotta H, Ishii K (1990) New technology of blast-furnace smelting with the use of regulating valves of hot blast in the tuyere devices. *NKK Tech Rev* 59:1–7
9. Mozharensko NM, Paranosenkov AA, Negoda VI (2005) Development of the systems of monitoring and regulation of the hot blast flow rate in air tuyeres of the blast furnace. In: Fundamental and applied problems in ferrous metallurgy, Institute of Ferrous Metallurgy, vol 10. Ukrainian NAS, Dnipropetrovs'k, pp 71–78
10. Mozharensko NM, Kanaev VV, Paranosenkov AA et al (2005) Automated system of monitoring of the blast flow rate in air tuyeres of the blast furnace. In: Fundamental and applied problems of ferrous metallurgy, Institute of Ferrous Metallurgy, vol 11. Ukrainian NAS, Dnipropetrovs'k, pp 34–42
11. Kanaev VV, Kobeza II, Buzoverya MT, Shuliko ST (1995) Monitoring of the distribution of blast over the air tuyeres of a blast furnace. *Metallurg. Gorno-Rudn Promysh* 2:69–71
12. Bugaev KM, Antonov VM, Varshavskii GV et al (1987) Vliyanie raspredelenija dut'ja po furmam na gazovyj potok v domennoj pechi (Influence of the distribution of blast by tuyeres on the gas flow in a blast furnace). *Steel* 2:17–22
13. Polinov AA, Pavlov AV, Onorin OP et al (2018) Blast distribution over the air Tuyeres of a blast furnace. *Metallurgist* 62(5–6):418–424
14. Andronov VN, Belov YuA (2002) Estimation of the efficiency of distributions of blast and natural gas over the tuyeres. *Steel* 9:15–17
15. Lyalyuk VP, Tarakanov AK, Kassim DA, Riznickii IG (2018) Increasing uniformity of blast distribution along BF circumference. *Metallurg* 2:30–34
16. Lyalyuk VP, Kassim DA, Tovarovskii IG (2018) Uniformity of blast-furnace parameters over the perimeter. *Steel Translation* 48(3):179–184
17. Lyalyuk VP, Tovarovskii IG (2003) Vybor rezhimov domennoj plavki na kombinirovannom dut'e s ocenok parametrov furmennoj zony (Selection of modes of blast-furnace smelting on combined blast with estimation of the parameters of tuyere zones). *Chernye Metally* 11:13–16
18. Lyalyuk VP (2020) Analysis of the blast furnace operations with a volume of 5000 m³ on tuyeres of different diameters from the positions of full mechanical energies of flows of combined blow and hearth gas. *Ferrous Metallurgy. Bull Sci Tech Econ Inf* 76(7):691–699
19. Onorin OP, Spirin NA, Terent'ev VL et al (2005) Komp'yuternye metody modelirovanija domennogo processa (Computer methods of simulation of the blast-furnace process). USTU-UPI, Ekaterinburg, pp 301
20. Spirin NA, Lavrov VV, Rybolovlev VYu et al (2011) Model'nye sistemy podderzhki prinyatija reshenij v ASU TP domennoj plavki metallurgii (Model systems for the support of decision making in automatic systems of control over the technological process of blast-furnace smelting in metallurgy). UrFU, Ekaterinburg, pp 462
21. Spirin NA, Lavrov VV, Rybolovlev VYu et al (2014) Matematicheskoe modelirovanie metallurgicheskikh processov v ASU TP (Mathematical modeling of metallurgical processes in automated process control systems). UrFU, Ekaterinburg, pp 558



Research of a Nonlinear Vibration Isolation System with a Controlled Magnetorheological Damper

D. Randin^(✉), A. Abakumov, and A. Goryachkin

Samara State Technical University, 244, Molodogvardeyskaya street, Samara 443100, Russia
em@samgtu.ru

Abstract. The article dwells upon the study of the properties of a passive vibration isolation system with a nonlinear characteristic of a controlled damper. The existing problems in the field of research and the objectives of the research are indicated. As an actuator, a magnetorheological vibration damper is used, the design of which is similar to serial samples. The design diagram of an oscillatory system with a nonlinear element of viscous resistance is presented. The characteristics of the nonlinear element depend on the linear speed of the damper piston as well as on the control current. To study the characteristics of the vibration isolation system, the MATLAB program was used. With the help of a special block of two variables for the specified program, a simulation model of the damper is set, based on which a simulation model of the vibration isolation system is built. The mechanism of formation for the damper nonlinear temporal characteristics is studied. Based on equivalent frequency characteristics, the dynamics of the vibration isolation system with the damper nonlinear and linearized characteristics is investigated. The calculation results are confirmed by experiments on the developed bench. The satisfactory adequacy of the developed model to the real vibration isolation system is shown. The obtained results are analyzed, and conclusions on the work done are formulated.

Keywords: Magnetorheological damper · Nonlinearity · Vibration isolation system · Linearization · Amplitude frequency response

1 Introduction

A review of research on vibration isolation systems with controlled magnetorheological dampers shows a broad interest in this field. One can highlight several major directions in this area. Simplistically, they can be divided into the following: (a) damper design development [1–3]; (b) damper improving [4–6]; (c) development of control algorithms [7–9], etc. In the latter area, simulation modeling is of particular relevance [10, 11]. As the analysis of publications shows, the dynamics of vibration isolation systems, taking into account the nonlinear properties of the magnetorheological damper used, is not fully studied. In this regard, this article considers the impact of the nonlinearities of the magnetorheological damper characteristics on its dynamic characteristics of the vibration isolation system.

2 Development of a Mathematical Model of the Vibration Isolation System

A single-mass vibration isolation system with a controlled viscous resistance element in the form of a magnetorheological damper is considered, the design model of which is shown in Fig. 1.

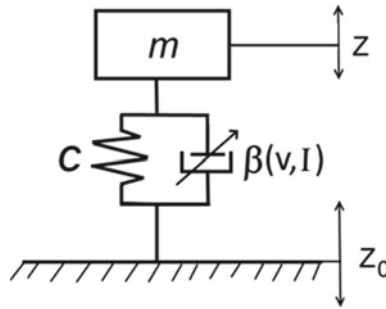


Fig. 1 Design scheme of a single-mass vibration isolation system: m —mass of the protected object; C —stiffness of the elastic element; $\beta(v, I)$ —hydraulic resistance coefficient as a function of the damper speed and control current

The dynamics of the system according to Fig. 1 is described by the differential equation

$$m \frac{d^2 Z}{dt^2} + \beta(v, I) \frac{d(Z - Z_0)}{dt} + C(Z - Z_0) = 0. \tag{1}$$

The characteristics of the viscous drag elements used in road transport have a nonlinear form, and controlled magnetorheological dampers depend both on the linear speed v of the rod movement and on the control signal (current I) value.

The dynamic characteristics of the system under consideration, taking into account the nonlinear dependence of the coefficient β on the damper control current and speed

$$v(t) = \frac{d(Z - Z_0)}{dt} \tag{2}$$

in the operator form, they are described by the expression

$$mp^2 Z(p) + \beta(v, I)p[Z(p) - Z_0(p)] + C[Z(p) - Z_0(p)]. \tag{3}$$

The given expression corresponds to the block diagram shown in Fig. 2.

It is of interest to study the dynamic characteristics of a vibration isolation system with a damper model, taking into account the nonlinearity of its characteristics. The study was conducted using the “Lookup Table 2-D” block of two input variables in the MATLAB application software package (Fig. 3).

A simulation model for studying the properties of a vibration isolation system with a controlled element of viscous resistance, taking into account the nonlinearity of its characteristics, is shown in Fig. 4.

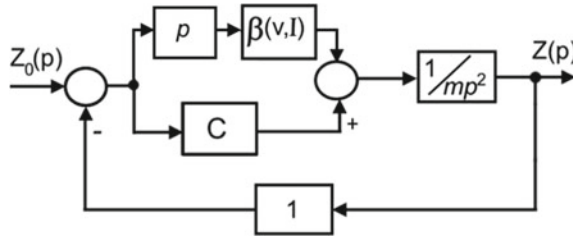


Fig. 2 Block diagram of the vibration isolation system

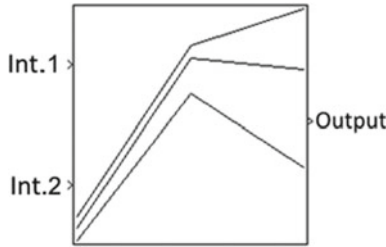


Fig. 3 Icon of the block of two variables in the MATLAB program

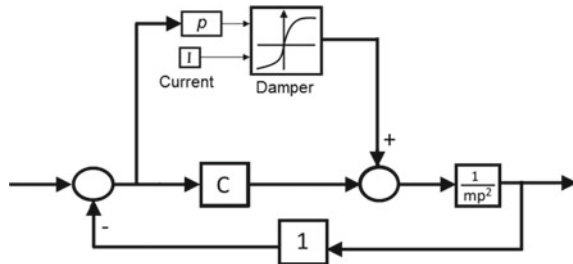


Fig. 4 Simulation model for the study of the active vibration isolation system

3 Specifying the Properties of a Model for a Controlled Magnetorheological Damper

The magnetorheological vibration damper is a promising electrical actuating device with a relatively simple design (Fig. 5).

A similar structure has a controlled magnetorheological damper, developed by Delphi Corporation, the characteristics of which were filmed on the automated diagnostic system for suspension shock absorbers of motor vehicles “Centurion.”

The dependences of the maximum resistance force F on the damper rod on the corresponding maximum linear velocity v of its moving part, obtained for the “compression” stroke (first quadrant) and the “rebound” stroke (third quadrant) at different values of the current I flowing through the electromagnet winding, are studied experimentally.

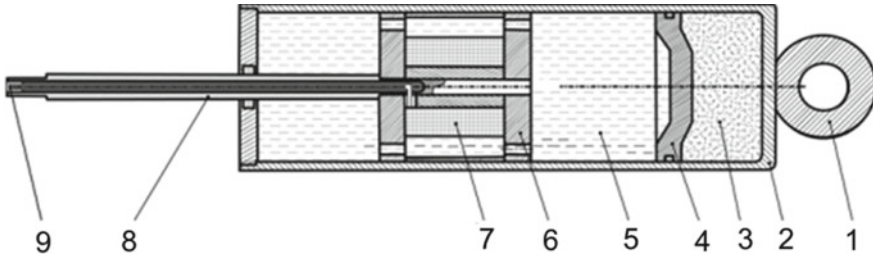


Fig. 5 Magnetorheological damper: 1—lower damper mount; 2—body; 3—gas; 4—the dividing piston; 5—magnetorheological fluid; 6—the core of the electromagnet; 7—the winding of the electromagnet; 8—stock; and 9—contact

The characteristics of the damper shown in Table 2 are obtained for six fixed values of the rotational speed ω of the test bench crank mechanism. The corresponding graphs are shown in Fig. 3.

The graphs corresponding to Tables 1 and 2 are shown in Fig. 6.

Table 1 Characteristics of the damper for stroke “Rebound”

F , kH for $I = 0$ A	F , kH for $I = 0.5$ A	F , kH for $I = 1$ A	v , m/s
0	0	0	0
305	423	434	0,013
387	487	545	0,05
400	502	606	0,103
413	557	684	0,24
423	570	710	0,31
436	574	736	0,39

Data from Table 2 was loaded into the “Lookup Table 2-D” block, as shown in Fig. 7.

The method of processing the data entered in the “Lookup Table 2-D” block, if the input parameters differ from the table parameters, is set to “Interpolation-extrapolation,” which assumes linear interpolation between the two elements proximate to it. If the input signal goes beyond the boundaries of the vector of input values, then, according to the method used, a linear extrapolation is performed over the two extreme elements.

4 Time Characteristics of the Controlled Damper

Since the damper has nonlinear elastic characteristics, it is of interest to study its equivalent frequency characteristics. Figure 8 shows a simulation scheme for studying the characteristics.

Table 2 Characteristics of the damper for stroke “Compression”

F , kH for $I = 0$ A	F , kH for $I = 0.5$ A	F , kH for $I = 1$ A	v , m/s
0	0	0	0
430Л	547	552	0,013
493	592	673	0,05
516	603	689	0,103
553	653	721	0,24
569	671	752	0,31
576	695	835	0,39

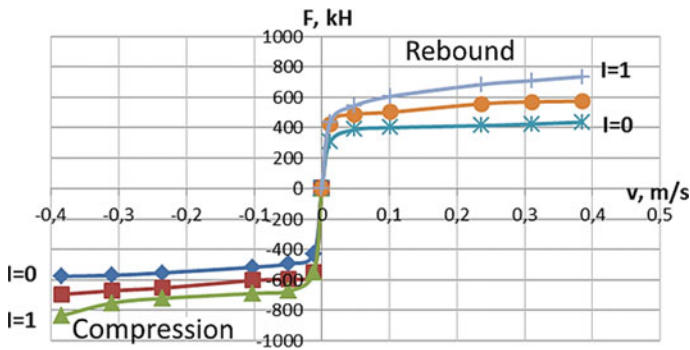


Fig. 6 Graphs of the dependence of the force F on the linear velocity v for different current values

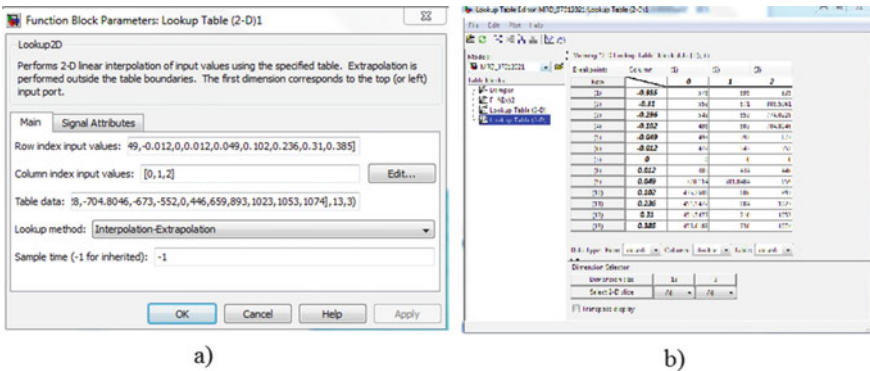


Fig. 7 a) Dialog box for entering an array of data. b) Dialog box for adding data to a table

Figure 9 shows the process of forming the dependence of the elastic force as a function of time for the zero value of the control current and the input speed signal,

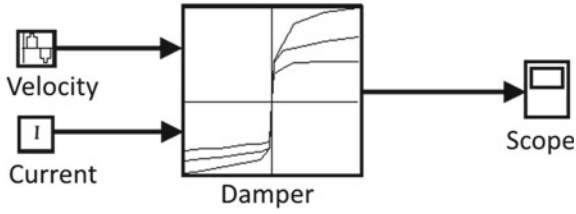


Fig. 8 Simulation scheme for studying the characteristics

which changes according to the harmonic law (sine) with an amplitude of 1 cm and an angular frequency of 1 rad/s.

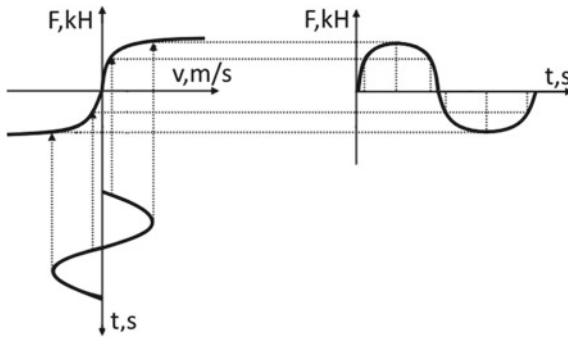


Fig. 9 Formation of the output signal of the damper

Figure 10 shows a graph calculated using the MATLAB program.

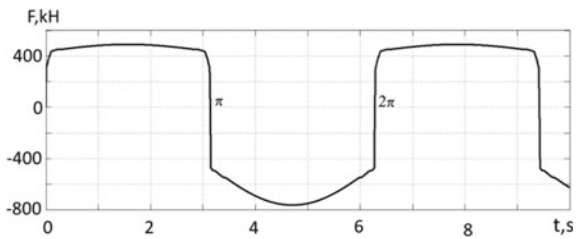


Fig. 10 Calculated graph of the elastic characteristic of the damper under harmonic input action

The resulting dependence of the force on time is asymmetric: the amplitude of the force change in the area from zero to π differs from the amplitude in the area from π to 2π . The output signal contains a constant component.

5 Frequency Characteristics of the Vibration Isolation System

Figure 11 shows the graph of changes in the output variable of the vibration isolation system (movement of the protected object) calculated in the MATLAB program when a input harmonic signal with an amplitude of 1 cm and an angular frequency of 10 rad/s is applied, for the mass of the protected object of 80 kg and the stiffness of the elastic element $C = 30 \text{ kN/m}$.

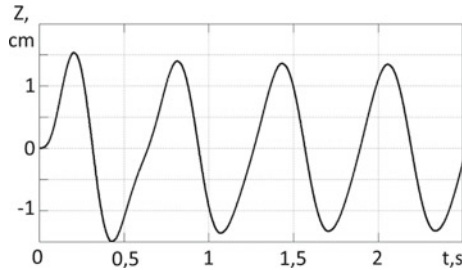


Fig. 11 Graph of changes in the output variable of the vibration isolation system

The analysis of the graph in Fig. 11 shows that due to the presence of an inertial link in the system, there is a harmonic linearization of the nonlinearity, but the output signal has higher harmonics in its composition.

To define a spectral composition of the output signal, the MATLAB fast Fourier transform device was used. Figure 12 shows the spectrum for the graph in Fig. 11.

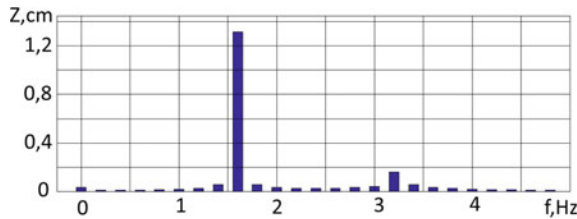


Fig. 12 Spectrum of the output signal of the vibration isolation system for the input harmonic effect with an amplitude of 1 cm and an angular frequency of 10 rad/s

As follows from Fig. 12, the main harmonic (1.6 Hz, which corresponds to an angular frequency of 10 rad/s) of the output signal has the largest amplitude of other harmonics.

The amplitudes of the spectra for other angular frequencies of the input signal and the damper control currents are calculated in a similar way.

The results of calculating the amplitude of the first harmonic are presented in Tables 3, 4, and 5.

According to the results of calculations, the equivalent frequency response is determined as the ratio of the amplitude of the first harmonic of the output signal A_{z1} to the amplitude A_{z0} of the input harmonic effect:

$$A_e(A_{z0}, I) = \frac{A_{z1}}{A_{z0}} \tag{4}$$

Table 3 Calculation results equivalent to the frequency response in the absence of a damper current

$\omega_{in}, \text{ rad/s}$	0,1	1	10	20	30	40	50
$A_{Z0}, \text{ cm}$	1						
$A_{Z1}, \text{ cm}$	1	1	1.2	1,8	0.8	0.41	0.26
$Ae(A_{Z0}, I), r.u$	1	1	1.2	2	0.8	0.41	0.26

Table 4 Calculation results equivalent to the frequency response for the current of the damper 0.5 A

$\omega_{in}, \text{ rad/s}$	0,1	1	10	20	30	40	50
$A_{Z0}, \text{ cm}$	1						
$A_{Z1}, \text{ cm}$	1	1	1.2	1.6	0.8	0.45	0.3
$Ae(A_{Z0}, I), r.u$	1	1	1.2	1.6	0.8	0.45	0.3

Table 5 Calculation results equivalent to the frequency response for the current of the damper 1 A

$\omega_{in}, \text{ rad/s}$	0,1	1	10	20	30	40	50
$A_{Z0}, \text{ cm}$	1						
$A_{Z1}, \text{ cm}$	1	1	1.1	1.1	0.7	0.47	0.28
$Ae(A_{Z0}, I), r.u$	1	1	1.1	1.1	0.7	0.47	0.28

Figure 13 shows the graphs of the equivalent frequency response $Ae(A_{Z0}, I)$ for the vibration isolation system constructed according to Tables 3, 4, and 5 with numerical values of the parameters $C = 30\text{kH/m}$, $m = 80 \text{ kg}$.

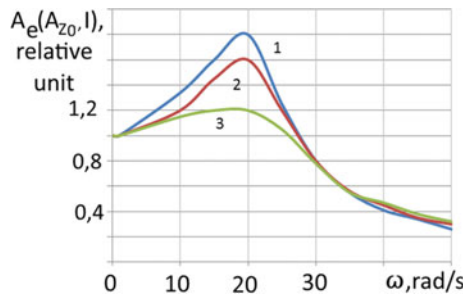


Fig. 13 Estimated graph of equivalent frequency response for different current values: 1—in the absence of current; 2—at a current of 0.5 A; and 3—at a current of 1 A

As follows from Fig. 13, with an increase in the value of the current set in the damper winding, the relative amplitude of the movements of the protected object decreases from 2 *r.u.* (in the absence of current) to 1.1 *r.u.* (at a current of 1 A). At the same time, the resonant frequency is 20 rad/s or 3.2 Hz.

Additionally, the influence of the linearization of the damper characteristics on the properties of the vibration isolation system is investigated.

When studying the linearized model of the vibration isolation system, a fixed average value of the coefficient β for the value of the damper current is equal to zero. For this purpose, the value of β at the current $I = 0A$ in the linearized model is assumed to be equal to the ratio of the maximum measured force F_{max} (according to Table 2) to the corresponding velocity, i.e., $\beta = F_{max}/v = 436/0.4 = 1132 \text{ kPa s m}$.

In this case, based on the block diagram (Fig. 2), the transfer function of the system for the output variable—the movement of the vibration-protected object and the input—the movement of the base has the form

$$W_{Z_0,Z}(p) = \frac{Z(p)}{Z_0(p)} = \frac{\beta p + C}{mp^2 + \beta p + C} \tag{5}$$

The frequency response graph for the linearized model is shown in Fig. 14 (curve 2). It also shows the equivalent frequency response of the system in the absence of current and taking into account the nonlinearity of the damper characteristics (curve 1).

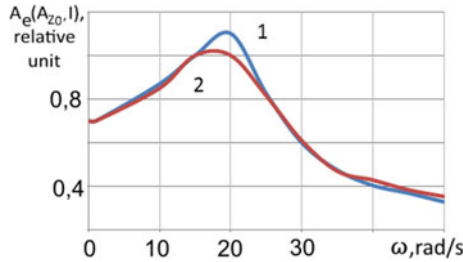


Fig. 14 Graphs of the frequency characteristics of the vibration isolation system: 1—equivalent frequency response taking into account the nonlinearity; 2—frequency response of the linearized model

The results of calculating the maximum value of the frequency response amplitude are presented in Table 6.

Table 6 Results of calculating the maximum value of the frequency response amplitude

Maximum amplitude of the frequency response of the vibration isolation system	Parameter value
linearized damper model	1.81
Nonlinear damper model	1.65

Divergence between the frequency response of the vibration isolation system with linearized and nonlinear properties of the damper is due to the fact that the constant value of β is higher than the nonlinear value at resonant and resonant frequencies.

6 Experimental Study of the Dynamic Properties of a Vibration Isolation System with a Magnetorheological Damper

For experimental studies of the characteristics of a vibration isolation system with a controlled magnetorheological damper, a bench shown in Fig. 15 has been developed.

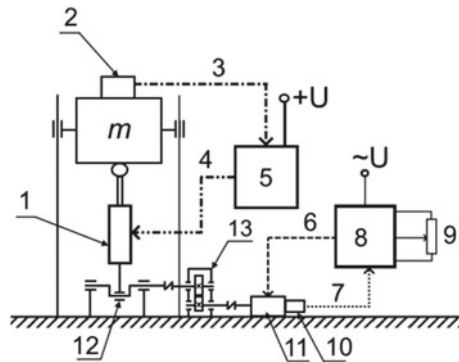


Fig. 15 Bench for studying the characteristics of an active vibration isolation system with linear DC motor: 1—magnetorheological damper; 2—acceleration sensor; 3—acceleration feedback signal; 4—controlled voltage; 5—regulator; 6—voltage signal for the drive DC motor; 7—voltage feedback signal from the tachometer; 8—controlled rectifier; 9—adjustment; 10—tachometer; 11—drive DC motor; 12—crank mechanism; and 13—reductor

Figure 12 shows the previously obtained calculated graphs of the equivalent frequency response for a vibration isolation system with a controlled magnetorheological damper, on which the experimental values are additionally marked. At the same time, the discrepancy between the theoretical data and the experimental data does not exceed 15%.

7 Conclusions

The developed simulation model of the vibration isolation system, taking into account the nonlinearity of the properties of the controlled magnetorheological damper, is adequately consistent with the experimental data obtained. In particular, the discrepancy between the theoretical and experimental data does not exceed 15% and is explained by the deviation of the properties of the functional elements in the experimental bench from their nominal values, as well as not taking into account the dry friction in the system. The nonlinearities of the magnetorheological damper characteristics significantly affect the system dynamics.

References

1. Kazakov YuB, Morozov NA, Nesterov SA (2017) Development of models of the magnetorheological fluid damper. *J Magn Magn Mater* 431:269–272
2. Guoliang HU, Yun LU, Sun S, Li W (2017) Development of a self-sensing magnetorheological damper with magnets in-line coil mechanism. *Sens Actuators A* 255:71–78
3. Yanga J, Ningb D, Suna SS, Zhengc J, Luc H, Nakanoa M, Zhangd S, Dub H, Li WH (2021) A semi-active suspension using a magnetorheological damper with nonlinear negative-stiffness component. *Author Links Open Overlay Mech Syst Signal Process* 147
4. Hemmatian M, Sedaghati R, Rakheja S (2020) Temperature dependency of magnetorheological fluids' properties under varying strain amplitude and rate. *J Magn Magn Mater* 498
5. Yoon D-S, Park Y-J, Choi S-B (2019) An eddy current effect on the response time of a magnetorheological damper: Analysis and experimental validation. *Author Links Open Overlay Mech Syst Signal Process* 127:136–158
6. Potter Jack N, Neild Simon A, Wagg David J (2011) Quasi-active suspension design using magnetorheological dampers. *J Sound Vib* 330(10):2201–2219
7. Jian WU, Zhou H, Liu Z, Mingqin GU (2019) A load-dependent PWA- H_∞ controller for semi-active suspensions to exploit the performance of MR dampers. *Mech Syst Signal Process* 127:441–462
8. Kopylov S, Chen ZB, Abdelkareem MA (2020) Acceleration based ground-hook control of an electromagnetic regenerative tuned mass damper for automotive application. *Alexandria Eng J* 59(6):4933–4946
9. Li J, Liu Z, Liu Z, Huang L, Zhou C, Liu X, Zhu W (2018) Electromechanical characteristics and numerical simulation of a new smaller magnetorheological fluid damper. *Mech Res Commun* 92:81–86
10. Elsaady W, Oyadiji SO, Nasser A (2020) Evaluation of nonlinear dynamic phenomena in the hysteretic behaviour of magnetorheological dampers. *Appl Eng Sci* 3
11. Abakumov AM, Antropov VE and Randin DG (2017) Electrotechnical vibration isolation system with a magnetorheological damper. *International Conference on Industrial Engineering. Appl Manuf (ICIEAM)* 1–4



Estimating the Level of Friction and Wear in Gas-Powered Diesel Engines

A. V. Muratov and V. V. Lyashenko^(✉)

Samara State Transport University, 2 V, Svoboda street, Samara 443066, Russia
lyashenko@samgups.ru

Abstract. The paper considers the impact of natural gas as a motor fuel on diesel engine friction and wear. According to the state energy strategy, the expansion of using NGVs is a very important area in the development of engine building. To implement the priority directions of the strategy, modernizing the existing diesel engines is proposed to switch them to gas–diesel cycle. The paper discusses the results of theoretical studies on the impact of using natural gas as a motor fuel on friction and wear of the D242 gas-powered diesel engine parts. A comparative analysis of mechanical losses and wear of the main friction members of the cylinder–piston assembly and the crank mechanism of the D242 diesel engine operating according to the gas and diesel cycle has been performed. Based on the study results and computational experiments, it has been found that the use of gas fuel in diesel engines effects positively on the friction and wear of gas-powered diesel engines.

Keywords: Diesel engine D242 · Gas–diesel cycle · Gas engine fuel · Natural gas · Methane · Friction · Wear · Mechanical losses · Cylinder–piston assembly

1 Introduction

The development of the energy sector in the Russian Federation is aimed at, on the one hand, maximally promoting the socio-economic development of the country and, on the other hand, strengthening and maintaining the position of the Russian Federation in the global energy sector, at least for the period until 2035. The priorities of the State Energy Strategy of the Russian Federation are, among other things, the transition to environmentally friendly and resource-saving energy, rational use of natural resources, energy efficiency, etc. [1, 2].

Based on the priority areas of the considered strategy, it can be concluded that using NGVs and switching the existing diesel engines to the gas–diesel cycle is advisable.

The gas–diesel operation involves the gas-powered diesel engine using diesel fuel to ignite the gas–air mixture in the cylinder.

One of the most promising types of gas motor fuel for vehicles is natural gas, the energy and physical characteristics of which allow obtaining sufficiently high economic, environmental, and resource performance of a diesel engine [3, 4].

2 Problem Statement

Natural gas (methane) is most suitable for a diesel engine. Its energy and physical parameters are higher as compared to diesel fuel by about 10% of the mass calorific value: reduction in emissions of toxic combustion products by 1.5–2.0 times and a 30–40% decrease in the impact on lubricating oils, leading to their aging, allow obtaining higher economic, environmental, and resource performance of vehicles using heat engines as a power source [5, 6].

The design of friction units of internal combustion engines (ICEs) should maximally meet the requirements for increasing the service life, reliability, efficiency of fuel and oil consumption, and the specific aggregate capacity, improving the ease of maintenance, environmental safety, etc. Despite the specifics of engines of cars and trucks, railway locomotives, tractors, marine, and other engines of various modifications, the main friction assemblies have a common design and characteristic tribotechnical indicators [7–9].

The main tribotechnical indicators characterizing the friction in the mechanism are the friction horsepower and mechanical efficiency [10, 11].

Mechanical losses are inextricably linked with the operation of the internal combustion engine junction nodes and are the part of the power spent on overcoming the friction and resistance forces in them.

On average, mechanical losses account for 15–33% of engine power and ultimately lead to increased fuel consumption.

The greatest friction and resistance forces arise in the engine's cylinder–piston assembly (CPA) and crank mechanism (CM).

About 40 and 23% of the friction horsepower come on CPA and CM, respectively [11, 12].

3 Research Questions

The studies use an estimative analysis that allows characterizing the impact of switching to the gas–diesel cycle on mechanical losses and mechanical efficiency that in turn are an indicator of friction in the engine.

The operation of two engines was simulated based on the D242 diesel engine in the Diesel-RK software [13, 14]. The first one was operated on diesel fuel and the second one on gas. The mathematical model was tuned in the Diesel-RK software according to the actual D242 diesel engine indicators. This approach allowed forecasting the real diesel engine behavior when switching the operation mode from diesel to gas.

4 Theoretical Section

Computational studies gave the mechanical efficiency values η_{mech} for the D242 diesel engine operation in the entire range of power modes on diesel fuel and methane (Table 1).

The computational study results show an improvement of the mechanical efficiency over the entire range of the D242 diesel engine power characteristics from 0.025 to

Table 1 Results of computational and experimental studies

D242 diesel engine operating mode (percentage of power used)	0% (idle)	25%	50%	75%	100%
η_{mech} value, % (D242 diesel engine operation on diesel)	0.872	0.865	0.856	0.849	0.831
η_{mech} value, % (D242 diesel engine operation on gas)	0.897	0.894	0.893	0.890	0.884
Relative change of efficiency $\delta_{\eta_{\text{mech}}}^{\%}$, %	0.025	0.029	0.037	0.041	0.053

0.053% when operating on methane and, as a consequence, a decrease in the friction horsepower and an increase in the effective power of a diesel engine.

The highest relative change in the mechanical efficiency $\delta_{\eta_{\text{mech}}}^{\%}$ is observed at the rated power $\delta_{\eta_{\text{mech}}}^{\%} = 0.053\%$.

The study results unambiguously show a positive change in mechanical efficiency when switching diesel engines to a gas–diesel cycle over the entire power range and the use of natural gas as a motor fuel reduces friction.

The next study stage is estimating the impact of natural gas used as a motor fuel in the D242 gas-powered diesel engine on the wear.

The cylinder–piston assembly is the most wearable part of internal combustion engines, which is subject to abrasive, fatigue, and oxidative wear [15, 16].

Considering the impact of natural gas on the CPA wear, the composition of diesel fuel and natural gas should be analyzed by comparing the fuel components.

According to [17], sulfur is the main component in the fuel leading to increased wear.

The combustion comprises chains of chemical reactions of oxidation and interaction with water, as a result of which sulfur transforms into sulfurous and sulfuric acids that interact with the engine oil components—detergents, thereby negatively affecting the oil properties.

Also, the fuel sulfur causes deposits on the gas distribution mechanism parts and cylinder walls, which, in turn, significantly worsens the thermal operation mode and increases the likelihood of increased wear of the cylinder–piston assembly parts.

Due to this, the resource of the above diesel engine parts can be significantly reduced, more frequent replacement of engine oil will be required, and operating costs will grow.

Therefore, it can be concluded that the fuel sulfur negatively affects the wear of the diesel engine’s CPA, so decreasing the sulfur concentration in the fuel is one of the ways to reduce wear.

For clarity, let us perform a comparative analysis of the amount of sulfur supplied to the cylinders of the diesel- and gas-powered D242 diesel engine.

The sulfur content in diesel fuel meeting the EURO-5 requirements is 10 mg per kg of diesel fuel, and in natural gas (methane), the sulfur content is usually less than 0.2 mg per m³ of gas.

Using the fuel consumption at various D242 diesel engine operating modes and the sulfur content in it, let us compare the amount of sulfur supplied with fuel to the cylinders when switching from diesel fuel (DF) to natural gas (Table 2).

Table 2 Reduction in the amount of sulfur supplied to the D242 diesel engine cylinders for 12-h rated-mode operation

Diesel engine D242 operation	Fuel consumption in a rated mode for 12 h (DF/methane)	Amount of sulfur supplied to the cylinder with fuel (DF + methane), mg	Reduction in sulfur supplied when operating according to the gas–diesel cycle, mg
Diesel operation	150 kg/-	1500 mg	–
Gas–diesel operation (100% replacement of DF with methane)	– /179 m ³	36 mg	1464 mg

The data obtained show that for 12 h in rated operating mode, the reduction of sulfur supplied to diesel cylinders will be 1464 mg.

Obviously, the use of natural gas will significantly reduce harmful deposits on diesel engine parts due to a significant reduction in sulfur, which in turn will lead to reduced CPA wear and the engine oil replacement frequency, and, as a result, significantly reduced operating costs.

It should also be noted that the reduced content of sulfur compounds in diesel fuel decreases its lubricity, which negatively affects the wear of friction pairs in the environment of this fuel.

Obviously, the use of natural gas will significantly reduce harmful deposits on diesel engine parts due to a significant reduction in sulfur, which in turn will lead to reduced CPA wear and the engine oil replacement frequency, and, as a result, significantly reduced operating costs.

It should also be noted that the reduced content of sulfur compounds in diesel fuel decreases its lubricity, which negatively affects the wear of friction pairs in the environment of this fuel.

In diesel engines, fuel acts as a lubricant for plunger pumps, needle valves, pins, and other inaccessible parts of fuel supply and control equipment.

Bench and road testing the vehicle engines in the impact of low-sulfur diesel fuels on the fuel equipment durability have shown unacceptable losses in efficiency and severe mechanical damage to this equipment [18, 19].

The use of two types of fuel, diesel and natural gas, allows solving the issue of reducing sulfur compounds in the composition of diesel fuel, required to improve the environmental safety and operational efficiency of the vehicle diesel engines since in a gas-powered diesel engine, standard high-pressure fuel equipment is used to supply diesel fuel. Natural gas is used, as a rule, according to the external air-bleed principle and is mixed with air before entering the cylinder. This solves two important problems.

On the one hand, the amount of sulfur entering the cylinder reduces, increasing the wear resistance, efficiency, and environmental friendliness of the vehicle diesel engine; on the other hand, the equipment supplying and controlling the amount of diesel fuel operates in normal mode since diesel fuel is used, which contains sulfur compounds that allow lubrication.

5 Findings

The use of natural gas in diesel engines is associated with a change in the internal cylinder processes. The ignition and combustion of the air–fuel mixture change. Therefore, one of the wear estimation criteria is the dependence of wear on the internal cylinder parameters characterizing the engine operation.

To establish the relationship between the cylinder–piston assembly wear and changes in thermodynamic processes occurring in the cylinder of a gas-powered diesel engine, let us use the equation proposed in [20] for the CPA wear rate.

Equation (1) shows the dependence of the CPA wear rate on the average effective pressure of the diesel engine.

This equation has the form:

$$\vartheta_{\text{wear}} = \text{const.} \cdot (k_{fr} / P_e \cdot n)^3 \quad (1)$$

where ϑ_{wear} is wear rate, $\mu\text{m}/1000 \text{ h}$, k_{fr} is coefficient of friction, P_e is the average effective pressure, MPa, n is crankshaft rotation speed, 1/min, const is an empirical constant, 6.5×10^7 .

To compare the average effective pressure arising during operation according to the diesel and gas-diesel cycles, the computational data obtained in the Diesel-RK software have also been used [10, 11].

The results of these studies are given in Table 3.

Table 3 Computational data for the diesel- and gas-powered D242 diesel engine

Used D242 diesel power, %	0% (idle)	25%	50%	75%	100%
Crankshaft rotation speed, 1/min	780	1020	1270	1435	1800
Average effective pressure (diesel cycle), MPa	0.585	0.629	0.66	0.67	0.68
Average effective pressure (gas cycle), MPa	0.7	0.794	0.81	0.83	0.84

Table 2 shows that the average effective pressure grows over the entire range of the D242 diesel operating modes. The largest pressure difference is achieved at maximum operating modes. This behavior of the average effective pressure allows concluding that the cylinder–piston assembly wear decreases according to the dependence (1).

Thus, when operating according to the gas cycle at rated power, the wear rate can decrease by 15% or more.

6 Conclusion

As theoretical analysis shows, the use of natural gas having better component characteristics ensures the desired result in terms of reducing mechanical losses and wear.

This is achieved by reducing the sulfur content in the fuel and mechanical losses and increasing the average effective pressure.

Along with improved efficiency and environmental safety, vehicle diesel engines operating according to gas–diesel and gas cycles are less wearable and have better tribological indicators characterizing friction.

In general, for the gas-powered diesel engines, the efficiency of using energy resources and the service life increases.

References

1. Energy Strategy of the Russian Federation for the Period up to 2035, approved by the Order of the Government of the Russian Federation No. 1523-r dated 6/9/2020
2. Transport Strategy of the Russian Federation for the Period up to 2030, approved by the Order of the Government of the Russian Federation No. 1734-r dated November 22, 2008
3. Nosyrev DYa, Roslyakov AD, Muratov AV (2009) Prospects and problems of using alternative fuels in locomotive power units: monograph. SamGUPS, Samara, p 117
4. Prosvirov YuE, Nosyrev DYa, Muratov AV, Petukhov SA (2012) Innovative energy-saving technologies in the locomotive economy: monograph. SamGUPS, Samara, p 123
5. Furman VV et al (2013) Fuel supply systems for gas–diesel and gas engines. *Gruzovik* 4:38–45
6. Zheleznov DV, Lyashenko VV, Muratov AV (2016) Problems and prospects of switching the traction rolling stock of railways to gas engine fuel. *Bull Transp Volga Region* 1:16–20
7. Berkovich II, Gromakovskiy DG (2000) Tribology. Physical fundamentals, mechanics, and technical applications: textbook for Universities. Samara STU, Samara p 268
8. Nosyrev DYa, Petukhov SA, Muratov AV (2016) Problems and prospects of the use of lubricants in the locomotive economy: monograph. SamGUPS, Samara, p 183
9. Astashkevich BM (1995) Tribological aspects of wear of the cylinder–piston assembly parts of powerful internal combustion engines. *Friction Wear* 16(1):91–105
10. Sharov GI et al (2008) Friction reduction as a form of energy saving of a ship power unit. *Dvigatelaystryeniye* 4:29–31
11. Putintsev SV, Kuleshov AS, Ageev AG (2013) Estimating mechanical losses of modern piston engines. *Dvigatelaystryeniye* 2:15–20
12. Putintsev SV, Kuleshov AS, Ageev AG (2014) Empirical dependence for studying mechanical losses in four–stroke diesel engines. *Dvigatelaystryeniye*. 3:3–7
13. Diesel–RK Software Package. <http://www.diesel-rk.bmstu.ru>
14. Kuleshov AS (2004) DIESEL–RK Software for calculating and optimizing internal combustion engines. Description of mathematical models, solution of optimization problems. N.E. Bauman MSTU, Moscow, p 123
15. S.V. Putintsev (2018) Introduction to tribology of piston engines: textbook. Publishing House of N.E. Bauman MSTU, Moscow, p 183
16. Putintsev SV (2011) Mechanical losses in piston engines: special chapters of design, calculation, and testing. Electronic educational publication. Publishing House of the N.E. Bauman MSTU, Moscow, p 288

17. Kornev SV et al (2017) Impact of the diesel fuel quality on the engine performance. Omsk Sci Bull 2:13–16
18. Shevchenko GA, Krivtsova NI (2015) Impact of sulfur compounds on the lubricating capacity of diesel fuels. Bulletin of the Tomsk State University. Chemistry 2:45–58
19. Timokhova OM, Timokhov RS (2014) Impact of sulfur compounds of fuels on corrosive wear of machine parts. Voronezh Sci Tech Bull 3:122–126
20. Pogodaev LI, Kuzmin VN (2006) Structural and energy models of reliability of materials and machine parts. Academy of Transport of the Russian Federation, St. Petersburg, p 607



The Analysis of New Manufacturing Methods Dry Friction Powder Articles with Fe-Based Materials

Y. I. Krykhtin and V. I. Karlov^(✉)

Volgograd State Technical University, 28, Russia Lenin Prospect, Volgograd 400005, Russia
au@vstu.ru

Abstract. Technological indices of new manufacturing methods, as well as physical, mechanical, and tribotechnical properties of new dry friction articles made from Fe-based friction powder materials (PFM), are given by rolling and dynamic hot pressing methods compared to separate pressing and continuous sintering under pressure. The main factors affecting the properties of new friction products made by these methods taking into account their operating conditions have been identified. Approximate dependencies of effect of porosity of friction materials on their tribotechnical properties are obtained. A method of selecting tribotechnical indices (dynamic coefficient of friction, wear, and temperature) in a disk friction device depending on sliding speeds and specific pressures according to approximating equations of friction process parameters obtained from results of tribotechnical tests on a friction machine for a pair: friction powder material—countertelo—has been developed. Great prospects are shown for using the high-performance method of dynamic hot pressing (DHP-PFM) for making friction articles for dry friction from Fe-based powder materials made through a sublayer of carbonyl iron. The results of the work can be used in the creation of new and modernization of existing transmissions for light tracked vehicles with high specific capacity.

Keywords: Dry friction · Molding blank · Fe based · Framework · Pressing and agglomeration · Dynamic hot pressing · Rolling

1 Introduction

Wheeled transport vehicle transmissions with high specific capacity (more than 30 HP/t) are usually equipped with belt brakes, cheek brakes and disk brakes, coupling, and other friction assemblies working in the conditions of dry friction. Friction parts of such assemblies, such as disks, flat sector plates, and curved cheeks, represent structures consisting of a nickel–steel frame with a sintered layer of PFM. The friction material is made by the powder metallurgy method and is a multi-component alloy containing metallic and non-metallic components. Depending on the purpose and operating conditions, sintered PFMs are made on the basis of iron or bronze. For heavily loaded disk brakes, belt brakes, cheek brakes, clutches, and other friction units operating in dry friction as a part

of transmissions of transport vehicles with high specific capacity, mainly Fe-based PFMs are used that allow heating to 1000–1100 °C. The operational properties of such friction products are specified by their design together with PFM, manufacturing technology, and working conditions, as well as by the composition and structure of the PFM layer.

2 Significance, Scientific Relevance, and a Brief Review of the Literature

An analysis of publications [1–8] on the study of heavily loaded friction parts, locally deformable friction parts, and Fe-based friction parts with PFMs working under dry friction shows that a multivariate analysis of the properties of both PFMs and methods for manufacturing friction products with such materials is relevant for further study to improve their efficiency, reliability, and durability, to determine their capabilities, justify the prospects for use, to identify promising options, and to determine the ways of targeting perfection. For this purpose, first of all, it is necessary to identify the essential features, parameters, and dependencies that determine the properties and development prospects of modern PFMs and methods for manufacturing friction products with PFMs in order to compare them with each other.

3 Targeting

The purpose of the study is to substantiate the choice of the most promising method for manufacturing new Fe-based powder dry friction products with respect to transmissions of transport machines with high specific power.

4 Theory and Experiment

When developing PFM for the manufacture of dry friction linings with Fe-based material, three (tested new) methods were considered.

The known method of separate pressing and prolonged sintering under pressure of friction materials is widely known. Using this method, such modern sintered Fe-based friction powder materials as CMK-80, CMK-I37, CMK-I37II, and others [2] are obtained, which have high frictional and operational characteristics and heat resistance under various operating conditions.

The disadvantages of this method include baking instability, laboriousness, low productivity of the manual operation of assembling the sintering bag, the impossibility of mechanizing the package assembly process due to the low strength of the pressed linings, the difficulty of preventing spoilage due to the displacement of the lining on the carrier substrate, the use of low-performance mine thermal in practice furnaces that do not provide stability of high-temperature sintering. In addition, the impossibility of pressing thin friction linings, which leads to increased thickness, which, in turn, leads to an increase in the volume of machining.

The new technology for the manufacture of friction linings using a sublayer between the framework and PFM of carboxylic Ni, rolling, and short-term sintering without

pressure and the use of high-performance thermal equipment available for production for short-term sintering in a continuous furnace provide an increase in productivity and a decrease in labor intensity, but it requires significant material costs for organizing specialized production.

It was tested in the manufacture of powder friction material based on Fe-type МПФ 1005-I. It was found that during the formation of a composite material on a steel substrate with large rolling forces, delamination occurs.

At normal pressure of 0.08–0.12 GPa, a satisfactory mechanical adhesion of the friction layer is achieved, while porosity is 25–30%. With an increase in the pressing pressure, the mechanical strength of the friction material increases. The dependences of the porosity Π , density γ , and height h of the compacts on the pressing pressure p are shown in Fig. 1. The dependence of the strength p' of the friction layer and its adhesion to the intermediate layer on the pressure p is shown in Fig. 2.

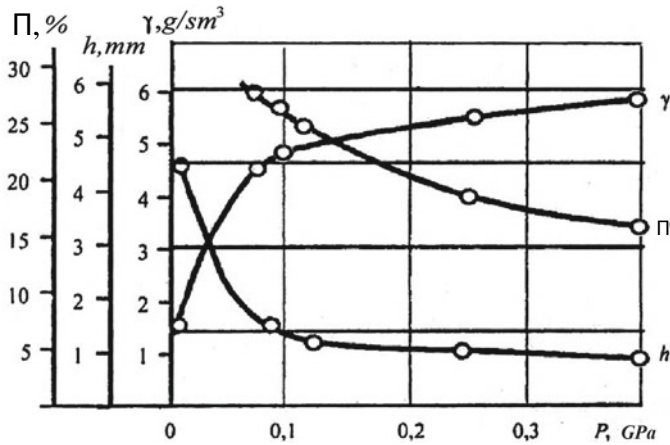


Fig. 1 Dependences of porosity Π , density γ , and height h of compacts on pressing pressure p

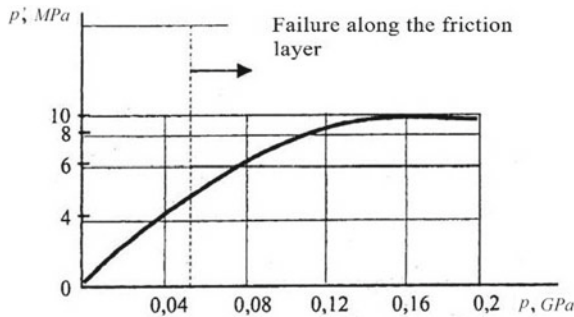


Fig. 2 Dependence of the strength p' of the friction layer and its adhesion to the intermediate layer on the pressure p

The microstructures of the new Fe-based friction powder materials obtained by rolling are shown in Fig. 3.

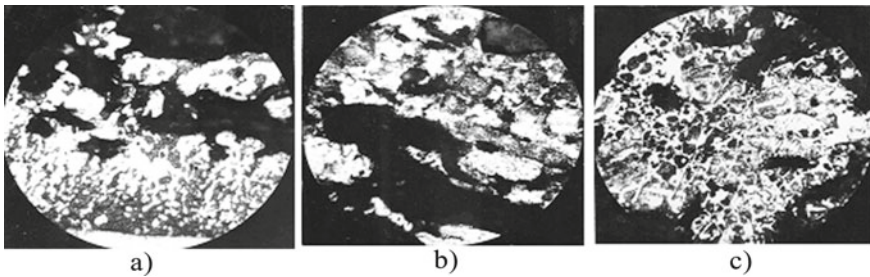


Fig. 3 Microstructures of new Fe-based friction powder materials obtained using rolling: **a** a substrate, a transition layer, and a friction layer; **b** friction layer sintered without pressure; and **c** friction layer sintered under pressure

A new technology for the manufacture of friction linings using rolled materials in a mixture and sintering a mixture under pressure involves preliminary rolling of a portion of the mixture granules. The technology provides a reduction in labor costs and uses sintering equipment available in production. Using this technology, PFM based on Fe-type МПФ 1005-0 is obtained, which has high frictional and operational characteristics.

It is known that structural products from powders have low mechanical properties, mainly due to increased porosity. To improve the mechanical properties with respect to structural products, the hot pressing method, i.e., hot stamping or dynamic hot pressing (DHP) of powder blanks, is used.

Based on this method, a new method is proposed for obtaining PFM dry friction on Fe based on the use of a sublayer between the framework and PFM from carbonyl Fe, called the DHP-PFM method [7, 8]. This method uses dynamic (impact) loading of preheated friction material.

When DHP-PFM requires rapid heating of the pre-sintered billet, for example, high-frequency currents in the quenching inductor to a temperature of 1000–1100 °C. DHP-PFM is produced in a stamp for hot stamping heated in a quenching inductor of a lining (pad) under a pressure of 500–700 MPa using a special stamping unit mounted on a press. In this case, DHP-PFM should create such stresses in the workpieces that are greater than the elastic limit, but less than the tensile strength.

This is a high-performance mobile low-cost method for creating PFM on Fe base with low porosity and high hardness of both flat plates and curved blocks with a reduction in labor costs due to the simplification of the manufacturing method.

The dependences of the limiting loads of setting, wear resistance, and coefficient of friction of PFM on its porosity are shown, shown in Fig. 4, obtained on an MT-66 friction machine at a sliding speed of 6 m/s, with a specific pressure of 3.5 MPa under conditions of limited lubricant supply.

The dependences of the coefficient of friction, temperature, and the rate of wear of the friction pair on the sliding speed and specific pressure for the friction pair CMK-137—steel 40X at a specific pressure $q = 1.5$ MPa—shown in Fig. 5. The experiment

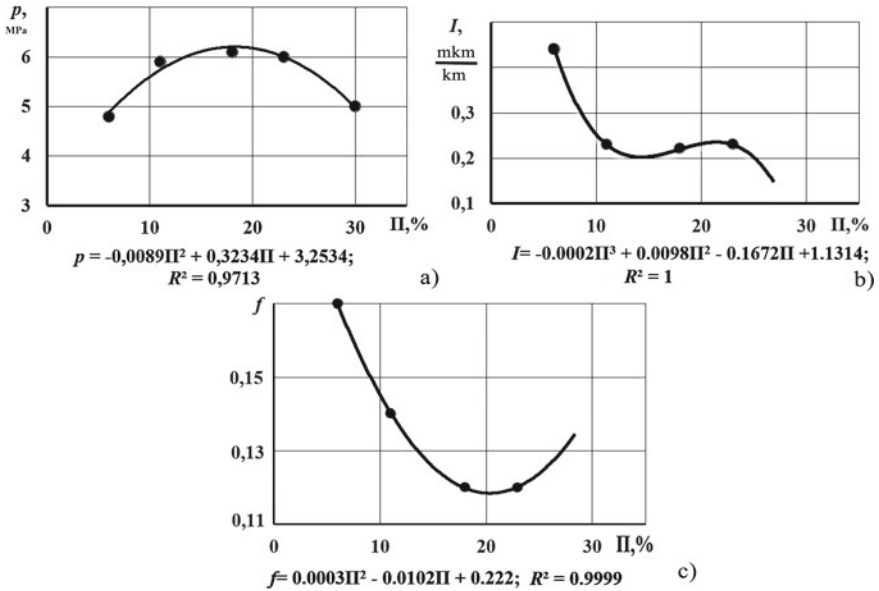


Fig. 4 Dependence graphs of the investigated friction parameters PFM based on steel 40X13 with a counterbody made of steel 20X2H4A, HRC = 58: **a** $p = F_1(\Pi)$; **b** $I = F_2(\Pi)$; **c** $f = F_3(\Pi)$

was carried out on an MT-68 friction machine under continuous friction loading at a constant sliding speed and constant load in a steady state.

The microstructures of new materials based on Fe based, obtained by X-ray diffraction analysis, were studied. Microstructures of friction materials: CMK-80, CMK-137—metal base made of ferrite and perlite alloyed with Mo and Mn, FeB, MnS, solid solution of Mn and Fe in Cu; CMK-137Π—metal base of doped Mn ferrite—perlite (granular perlite is not less than 30% and Cu with a uniform distribution of graphite, electrocorundum, Mo concentrate, and pores); MΠΦ 1005-0 inclusion of granules of graphite and electrocorundum in the metal matrix of Fe particles doped with Cu and Cu; MΠΦ 1005-1 for inclusion of graphite and electrocorundum granules in a Fe-based metal matrix, at the grain boundaries of which a phase of a low-melting Cu-based component is visible; ΦMK-79 DHP, MKB-50A DHP is a pearlite–ferrite mixture with inclusions of Cu, graphite, sulfides, with non-metallic inclusions (carbides), inclusions of cementite and sections of ledeburite are allowed.

The manufacturing technological parameters and the physicomachanical and tribotechnical properties of the new PFM based on Fe, the basis for dry friction made by different methods, revealed as a result of the study, are summarized in Tables 1 and 2, respectively [9–16].

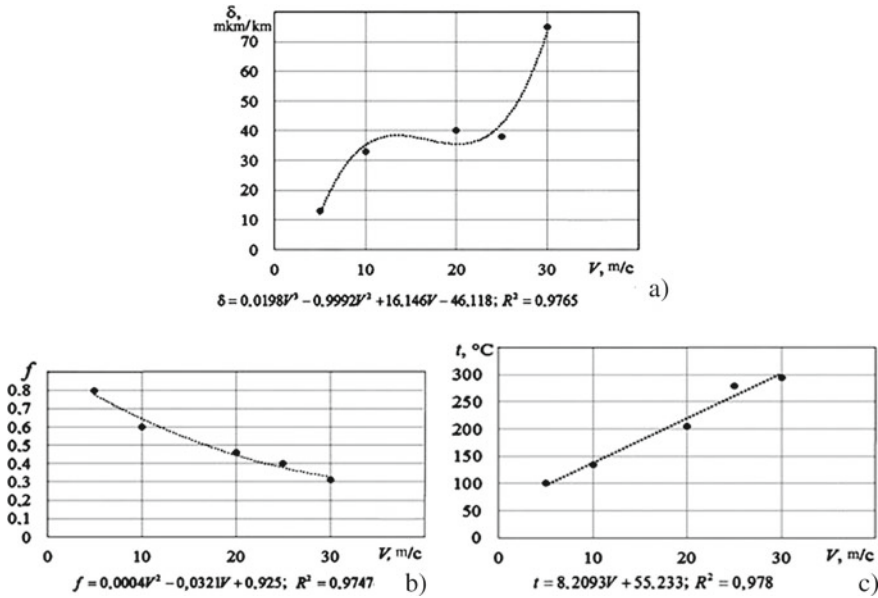


Fig. 5 Dependences of the investigated parameters of the friction pair CMK-137—steel 40X at a specific pressure $q = 1.5$ MPa versus sliding speed: **a** the rate of wear; **b** coefficient of friction; and **c** temperature

5 Practical Relevance and the Conclusion

Based on a comparative analysis of manufacturing technological parameters, physico-mechanical, and tribotechnical properties of dry friction products made from PFM on a Fe basis [17, 18] in accordance with modern requirements for friction materials [19–22] for the creation and modernization of friction units for transmissions of transport vehicles with large specific power, as well as for its further development, as the most promising proposed a new method of DHP-PFM and friction products manufactured by this method with PFM Φ МК-79 DHP. The proposed development improves the reliability of the adhesion of the pressing with the frame density and mechanical strength, manufacturability and productivity of the manufacture of friction products and simplifies the thermal equipment for their manufacture.

Table 1 Technological indicators for the manufacture of new PFM

PFM	Chemical composition, (%)	^a Formation p_{Π} , (MPa)	^b Sintering: t_s , ($^{\circ}$ C); p_s , (MPa); T_s , (h) or ^c baking: t_b , ($^{\circ}$ C); T_b , (h)
CMK-80	Mn = 6,5–10; Cu = 9–25; molybdenum disulfide (MoS ₂) = 2–5; boron nitride (BN) = 6–12; boron carbide (B ₄ C) = 8–15; silicon carbide (SiC) = 1–6; Fe– the rest	By pressing $p_{\Pi} = 491\text{--}589$	Sintering in a chamber furnace: $t_s = 990$, $p_s = 4.9\text{--}5.3$, $T_s = 4$
CMK-137	Mn = 3–10; Cu = 9–30; C = 7–16; electrocorundum = 2.5–8; molybdenum disulfide (MoS ₂) = 2–5; Fe– the rest	The same	The same
CMK-137II	C = 11–13; FeMg = 6–8; Cu = 20–22; molybdenum concentrate = 2–4; electrocorundum = 3–5; Fe = 42–44; urea ((NH ₂) ₂ CO) = 9–11	By pressing $p_p = 350\text{--}450$	Sintering in a chamber furnace: $T_s = 890$ in H ₂ ; $p_s = 1\text{--}1.5$; $T_s = 3$
МПФ 1005–1	Powder Fe = 54.9 ± 0.5 ; Cu powder = 34.0 ± 0.5 ; graphite 8.9 ± 0.5 ; electrocorundum = 1.8 ± 0.1 ; tin powder 0.4 ± 0.1	By rolling (rolls) $\emptyset 170$, [min])	Continuous oven baking: $T_b = 1100$; $T_b = 3\text{--}5$, [min]
МПФ 1005–0	The same + rolled charge granulas	By pressing $p_p = 250\text{--}300$	Sintering in a chamber furnace: $t_s = 980$; $p_s = 2\text{--}2.5$; $T_s = 4$
ФМК -79 DHP	C = 6; S = 0.7; Cu = 10; B = 1.6; Si = 3.0; Fe– the rest	By pressing $p_p = 450\text{--}500$	Continuous oven baking: $t_b = 900\text{--}950$ in H ₂ ; $T_b = 1\text{--}2$ then quickly heat up to $1000\text{--}1100$, [$^{\circ}$ C] and DHP with pressure $500\text{--}700$, [MPa]

(continued)

Table 1 (continued)

PFM	Chemical composition, (%)	^a Formation p_{Π} , (MPa)	^b Sintering: t_s , ($^{\circ}$ C); p_s , (МПа); T_s , (h) or ^c baking: t_b , ($^{\circ}$ C); T_b , (h)
MKB-50A DHP	C = 9.5–9.8; S = 1.0–1.2; Cu = 9.8–9.9; B = 3.5–3.7; Si = 3.5–3.7; asbestos = 3.1–3.3; Fe— the rest	The same	The same

Note ^aForming: p_p —pressing pressure before sintering (baking). ^bSintering: t_s —temperature, p_s —pressure, T_s —holding time; ^cBaking: t_b —temperature; T_b —holding time

Table 2 Properties of the new PFM

PFM	Physical and mechanical properties			Counterbody	Tribological properties				
	Hardness, (MPa)	Porosity P (%)	Density, (g/cm^3)		P_{per} (MPa)	f	α	$\Delta_{\text{FM}}/\Delta_{\text{КТ}}$	Test bench
СМК-80	539–932	15–20	5.9	Steel 30ХГСА	1.2	0.22	0.68	0.15/0.08	МИФИ-1
СМК-137	350–500	15	5.7	Steel 40X	1.2	0.33	0.65	0.9/1.1	МИФИ-1
СМК-137П	200–300	20–25	5.2	Steel 45X	1.2	0.36	0.65	1.2/0.9	МИФИ-1
МПФ 1005-1	320–600	15–20	6.57	Steel 40X	1.4	0.3	0.65	1/1	МИФИ-1
МПФ 1005-0	400–650	12–17	6.57	Steel 40X	1.4	0.3	0.65	1/1	МИФИ-1
ФМК -79 DHP	80–105 HRF	5–8	5.2–5.6	Steel 30ХГСА	1.4	≥ 0.25	≥ 0.7	0.75/0.3 not more	У-37
МКВ-50А DHP	60–80 HRF	5–8	5–5.1	Steel 30ХГСА	1.4	0.31	≥ 0.7	0.65/0.75	У-37

Note p_{per} —permissible pressure; f —the coefficient of friction; α —the stability of the coefficient of friction; Δ_{FM} —wear of the friction material in microns for one braking; $\Delta_{\text{КТ}}$ —counterbody wear in microns for one braking

Acknowledgements. The work was carried out with the support of RFFI and the Administration of the Volgograd Region on project no. 19-48-340021.

References

1. Aleksandrov MP (ed) (1985) Tormoznye ustroystva (Brake devices). Mashinostroyeniye, Moscow
2. Fedorchenko IM, Kryachek VM, Panaioti II (1975) Sovremennyye friktsionnyye materialy (Modern friction materials). Naukova dumka, Kiev
3. Panaioti II, Ivanova II, Karpets MV (2009) Kinetika tribosinteza struktur v zone friktsionnogo kontakta materialov friktsionnoj pary, rabotayushchey v usloviyakh teploimpulsnogo nagruzheniya (Kinetics of the tribosynthesis of structures in the area of frictional

- contact of materials of a friction pair operating under heat-impulse loading). *Trenie i smazka v mashinah i mekhanizmah* 4:40–43
4. Drozdov YuN, Pavlov VG, Puchkov VN (1986) *Trenie i iznos v ekstremalnykh usloviyakh* (Friction and wear under extreme conditions). Spravochnik, Mashinostroenie, Moscow
 5. Trukhanov VM, Zubkov VF, Krykhtin YuI, Zheltobryukhov VF (2001) *Transmissii gusenichnykh i kolesnykh mashin* (Transmissions of tracked and wheeled vehicles). Mashinostroenie, Moscow
 6. Fedorchenko IM, Frantsevich IN, Rodomyselskiy ID (1985) *Poroshkovaya metallurgiya, materialy, tekhnologii, svoystva, oblasti primeneniya* (Powder metallurgy, materials, technologies, properties, applications). Naukova dumka, Kiev
 7. Krykhtin YuI, Karlov VI (2019) *K razrabotke tekhnologicheskikh osnov izgotovleniya novykh friktsionnykh izdeliy sukhogo treniya na Fe – osnove metodom dinamicheskogo goryachego pressovaniya* (The development of technological foundations for the manufacture of new dry friction products based on Fe: a method of dynamic hot pressing). *Izvestiya VolgGTU* 9:35–39
 8. Krykhtin YuI, Karlov VI (2019) *Ispytaniya novykh friktsionnykh izdeliy sukhogo treniya na Fe – osnove dlya povysheniya nadezhnosti i dolgovechnosti raboty transmissiy legkikh gusenichnykh mashin* (Testing of new friction products of dry friction on a Fe basis to increase the reliability and durability of the transmission of light tracked vehicles). *Izvestiya VolgGTU* 9:39–42
 9. Kragelsky IV, Alisin VV (eds) (1978) *Trenie, iznashivanie i smazka* (Friction, Wear and Lubrication). Mashinostroenie, Kniga 1, Moscow
 10. Krykhtin YuI, Karlov VI (2018) *Razrabotka glavnykh friktsionov s metallokeramicheskimi diskami s novymi materialami treniya v transmissiyakh gusenichnykh mashin i matematicheskoy modeli nagruzheniya friktsionnogo materiala* (Development of the main friction clutches with ceramic-metal disks with new friction materials in the transmissions of tracked vehicles and a mathematical model of friction material loading). *Sbornik v mashinostroenii, priborostroenii* 19(11):497–502
 11. Krykhtin YuI, Karlov VI (2018) *Razrabotka diskovykh ostanovochnykh tormozov s metallokeramicheskimi diskami v transmissiyakh gusenichnykh mashin i matematicheskaya model nagruzheniya friktsionnogo materiala* (Development of disc brake brakes with cermet disks in transmissions of tracked vehicles and a mathematical model of friction material loading). *Sbornik v mashinostroenii, priborostroenii* 20(1):12–17
 12. Krykhtin YuI, Karlov VI (2019) *K voprosu razrabotki bortovykh friktsionov s metallokeramicheskimi diskami s novymi materialami treniya v transmissiyakh gusenichnykh mashin i matematicheskoy modeli nagruzheniya friktsionnogo materiala* (On the issue of developing on-board friction clutches with cermet disks with new friction materials in transmissions of tracked vehicles and a mathematical model of friction material loading), *Spravochnik. Inzhenernyy zhurnal* 1:36–41
 13. Krykhtin YuI, Karlov VI (2019) *K voprosu razrabotki lentochnogo ostanovochnogo tormoza s metallokeramicheskimi kolodkami s novymi materialami treniya v transmissiyakh gusenichnykh mashin i matematicheskoy modeli nagruzheniya friktsionnogo materiala* (On the issue of developing a tape brake brake with ceramic-metal pads with new friction materials in transmissions of tracked vehicles and a mathematical model of friction material loading), *Spravochnik. Inzhenernyy zhurnal* 2:9–15
 14. Mur D (1978) Principles and application of tribology. In: Kharlamov SA (tr), Krachelskogo IV, Troyanovskoy GI (eds) *Mir*
 15. Krykhtin YuI, Shabalin AV (1999) *Novye poroshkovye materialy v diskakh sukhogo treniya ostanovochnykh tormozov* (New powder materials in dry friction discs of brakes). *Traktory i selskokhozyaystvennyye mashiny* 10:6–8

16. Shol NR, Lyuosov VD, Ikonnikov LYa, Prokhorov VYu (2004) Primeneniye sovremennykh materialov dlya izgotovleniye i remonta detaley mashin (Application of modern materials for producing and repairing machine parts, Ukhta. Student's book
17. Shapovalov VV, Koropets PA, Shub MB (2000) Matematicheskoye modelirovaniye dinamicheskikh sistem Ekipazh Put (Mathematical modeling if dynamic system Ekipazh Put). Vestnik RGUPS 2:130–131
18. Kucherov VG, Tuzhikov OI, Tuzhikov OO, Khanov GV (2004) Osnovy nauchnykh issledovaniy (Principles of scientific research). RPK Politehnik, Volgograd
19. Ozyabkin AL, Kolesnikov IV, Kharlamov PV (2012) Monitoring tribotermodynamiki friktsionnogo contacta mobilnoy tribosistemy (Monitoring of tribotic and thermal ynamics of friction contact of mobile trybotic system) Treniye i smazka v mashinakh i mekhanizmax 3:25–36
20. Krykhtin YuI (2014) Methods for improving operational properties, friction devices of mechanical transmissions of light tracked viechles with high specific power (Metody povysheniya ekspluatatsionnykh svoistv, friktsionnykh ekonomicheskikh transmissiy legkhkikh gusenechnikh mashin s bolshoy udelnoy moshchnostyu. Tekhnologiya kolesnykh i dvigatelnykh mashin 14(4):47–51
21. Belyi VA, Sviridenko AI (1986) Aktualnye napravleniya razvitiya issledovaniy v oblasti tribologii (Actual directions of development of research in the field of tribology). Trenie Iznos 4:593–603
22. Shapovalov VV, Sladkovski A, Erkenov ACh (2015) Aktualnye zadachi sovremennoy tribotekhniki i puti ikh resheniya (Actual problems of modern tribotechnology and ways to solve them). Izvestiya vysshih uchebnykh zavedenij, Mashinostroenie 1:64–75



Welding Technology in the Manufacture, Repair, and Restoration of Large Castings Made of High-Manganese Steel

A. Davydov¹ and V. Broido²(✉)

¹ IZTM-Engineering, LLC, 1, Oktyabrskoi Revolutsii Street, Irkutsk 664007, Russia

² Irkutsk National Research Technical University, 83, Lermontov Str., Irkutsk 664074, Russia

Abstract. The purpose of the R&D is the technology for welding high-manganese steel 110G13L in manufacturing and repairing large castings of dredging equipment. This steel in the quenched state has an austenitic structure and high plastic properties and a tendency to harden in the working area. Therefore, it is used to make large castings for dredge parts operating under conditions of intense water-jet abrasive wear and shock loads: scoops and the lower scooping drum (LSD). It is known that steel 110G13L has a limited weldability due to the tendency to form hot and cold cracks. But its use is necessary in the manufacture of casting for welding technological cracks and connecting LSD half-drums, as well as eliminating defects in large parts during operation for welding cracks and chips and welding visors (allotments) to restore the wear of dredge scoops. Materials: Alloying schemes were selected, and the chemical composition of the weld metal was determined. The results of the study were the development of a welding technology for large castings manufacture, as well as repair welding technology for the restoration of fast-wearing parts of dredges made of 110G13L steel. Conclusion: Technology variants have been developed, providing for better reliability and durability of operation of large castings made of 110G13L steel for dredges operated in the North.

Keywords: Dredge · Lower scoop drum · Scoops · Austenite · Carbides · Technological cracks · Welding · Repair · Restoration

1 Introduction

Hadfield 110G13L high-manganese steel has been successfully used in mechanical engineering for more than a hundred years. Due to the work surface hardening with a viscous core, 110G13L steel even now has virtually no alternative for the manufacture of products operating under the influence of shock, shock-abrasive loads, and high specific static pressures, for example lower scoop drums, dredge scoops, tractor tracks, rail crosspieces [1–3]. Alongside with its unique properties, steel has a fairly low cost, so its use has undeniable advantages.

Improving the operational stability of critical parts and structures of mining machines is a very urgent task. For gold mining dredgers and walking excavators operating in the

North, it is important to increase the durability of the parts of the scooping mechanism. The operation of powerful dredges shows that the reliability and durability of cast parts made of high-manganese steel 110G13L, from which their working bodies are made, are insufficient. Such details are the bottom of bucket drums and buckets of drag. They are parts or welded structures made of thick-walled large castings weighing up to $5 \div 10$ tons [4, 5]. The complex shape of castings determines their low manufacturability and tendency to form a number of technological defects. The most serious of them are hot and cold cracks. Intensive operation also leads to various defects, in particular, to intensive wear of the working area and cracks [6, 7].

When producing specified details, IZTM-Engineering, LLC eliminates technological defects of castings by welding. At the same time, gold mining enterprises carry out repair and restoration of parts and structures by welding and surfacing methods.

Castings made of high-manganese steel are quenched at the temperature of 1050–1100 °C, after which the metal acquires the structure of austenite and is characterized by a high level of mechanical and plastic properties, in particular, by a high level of impact strength and a tendency to harden at high impact loads. The hardening leads to increase in the hardness in the working area of the parts from 200–250 HB to 550–600 HB, which determines the high level of wear resistance of the parts under shock loads. It is believed that this steel has a unique combination of properties; i.e., it is not prone to brittle destruction, including at low negative temperatures [8].

2 Statement of the Problem

In order to meet the ever-increasing demand of gold mining enterprises for high-manganese steel parts, work is constantly being carried out to improve the welding technology for the repair of castings, welding in the manufacture of welded drums, and the use of welding in the restoration of these parts and structures during operation. The technology is changed by developing and using new technological techniques for identifying and cutting cracks for welding, surface preparation and improving welding performance through the use of mechanized welding at the stages of factory production and repair work on dredges.

3 Development of Welding Technology for the Repair of Castings and the Manufacture of Welded LSD

It is known that high-manganese steel has limited weldability [9, 10]. The reasons are the decay of austenite and the precipitation of carbides, as well as an increased tendency to form hot and cold cracks due to the low coefficient of thermal conductivity, high coefficient of linear expansion, and embrittlement of the metal in the thermal impact zone (TIZ).

The decay of austenite in the metal of the seam and TIZ occurs at an insufficiently high cooling rate, which is facilitated by a low thermal conductivity of steel. This leads to the formation of needle carbides $(\text{Fe, Mn})_3\text{C}$ in areas with a high carbon content along the grain boundaries and even inside the grains, and a high content of carbides is observed in local areas. In some cases, a solid ferrite–carbide mixture is formed [11–15].

The main problem of welding high-manganese austenitic steels is their tendency to form hot cracks. The reasons for this phenomenon are considered to be the presence of a number of internal defects (sweating and non-metallic inclusions) and a large length of grains, which is why the accumulation of low-melting eutectic at their border is pronounced. To reduce the probability of cracking, the welding zone is cooled immediately after welding and (or) a deposited metal having an austenitic–ferritic structure is used. While repairing operating dredges cooling by a water jet after melting of each electrode for welding of a site 150–200 mm long is done in IZTM-Engineering, LLC [16].

3.1 Welding Materials

The main materials used for welding and surfacing high-manganese steels are shown in Table 1.

All the materials listed in the table form austenitic corrosion-resistant steels of chromium–nickel or chromium–nickel–manganese composition in the deposited metal or austenitic manganese steel alloyed with up to 4% nickel and up to 2–3% molybdenum [17–20].

Low-carbon electrodes are mainly used with alloying systems based on Cr-Ni (OK 67.45, OK 67.15), Cr-Mn-Ni (OK 61.85; OK 61.80; OK 61.86).

In the manufacture of welded drums, mechanized welding in a mixture (Ar + CO₂) with wires CB-06X20H11M3T, CB-06X19H19T and OK Autrod 16.86 with a diameter of 1.2–1.6 mm is used. During the welding process, it is not allowed heating the metal in the adjacent zone above 60 °C, and to do that, it is periodically cooled with running water. Welding during the restoration of dredge scoops, welding of drum cracks is performed either by a mechanized method with powder wire OK Turbodur 15.65 or with austenitic electrodes НИИ-48Г (OK 67.45).

Unfortunately, currently in Russia, welding and surfacing materials based on manganese austenite are not produced. Their use would significantly reduce the cost of welding operations associated with the high cost of nickel-containing materials, so foreign analogs are used in production.

3.2 Preparation for Welding and Cracks Cutting

When repairing defects in large castings in the form of cold and hot cracks, the greatest difficulty is represented by: determination of the boundaries and depth of cracks. The use of reliable ultrasound and x-ray results is complicated by the complexity and/or impossibility of surface preparation and corrupted control readings due to the influence of defects characteristic of castings. The only thing available in most cases is visual inspection with metal etching and pre-cleaning. This method is used for the repair of cracks not only to determine their boundaries, but also to control the completeness of the sample by the crack depth when cutting the edges for crack welding. It is preferable to use mechanical processing on metal-cutting machines. However, the unsatisfactory machinability of high-manganese steel, the complexity of installing and fixing massive castings, the complex nonlinear shape of cracks in the plan, the inaccessibility for mechanical processing of a number of surfaces, the need to use in most cases only large boring machines, and carbide tools significantly complicate and make the cutting process

Table 1 Materials used for welding and surfacing high-manganese steels

Brand of material ESAB	Brand of material Russia	Chemical composition of the deposited metal (%)									
		C	Mn	Si	Cr	Ni	Mo	other			
OK 67.45	НИИ-48Г	<0.11	6	0.5	18.5	8.5	<0.5	Cu < 0.5			
OK 67.15	ОЗЛ-6	<0.12	<2.5	0.5	26	21	–	Cu < 0.5			
OK 61.85; OK 61.80; OK 61.86	ЭА 395/9	<0.07	1.7	0.3–0.7	19.5	10.0–22.0	<0.5	–			
OK 67.62	ОЗЛ-19	0.07	0.9	0.2–0.9	24	13	–	–			
OK Tigrod 347Si / OK Tigrod 347I	Св-06Х19Н9Т	max 0.08	1.00–2.50	0.4–1.0	19.0–21.0	9.00–11.00	–	Nb 10x%S-1.00			
OK Autrod 318 Si	Св-06Х20Н11М3ТБ	<0.08	1.7	0.8	19	12.5	2.7	Nb 0.6			
OK Autrod 2209		0.1	1.6	0.6	23	9	3	Nb 0.1			
OK 92.58	ПП-Нп-90Г13Н4	0.7–0.9	13.0–15.0	0.1–0.3	–	3.5–4.5					
OK 13Mn	ЦНИИИ-4	30.65	13	0.5	24,326.0	2.5–3.0					
OK 14MnNi; OK Turbodur 13Mn O/G	ЭНГ-13Н4	1.1	13	0.8	–	–					
OK Turbodur 15.65		0.8	14	<0.3	–	3.5					
		0.3	13.5	0.6	15.5	1.8	1.2	V 0.4			

expensive. The main method for cutting edges for welding remains air–arc gouging with graphite or graphite electrodes, followed by surface cleaning with grinding machines. At the same time, both mechanical processing with a metal-cutting tool and, especially, thermal cutting lead to metal hardening (up to 350–400 HB after machining), the occurrence of microcracks at the cut surface and the need for final cleaning with a grinding wheel, which is not always possible due to the shape and depth of the crack.

When cutting cracks on metal-cutting machines, pre-drilling is applied to the full depth (10–15 mm) from the edges of the crack and drilling to a certain depth with a step (1.1–1.2) d_{CB} along the entire length of the crack for entering the cutter at each pass. The number of passages is determined by the crack depth. In some cases, when the cutting is deepened, there is an expansion of the crack and the transition of the crack into the shrink shell. At the same time, the cutting depth is optimal, which provides the crack opening for the gap not exceeding the largest gap value during manual arc welding.

When selecting air–arc gouging modes, preference is given to graphite electrodes of circular cross section with a diameter of 8–9 mm and $I_p \leq 500$ A.

For cutting large cracks graphite, electrodes with a cross section of up to 15×25 mm are used with a specialized installation at currents up to 1500 A.

Arc gouging with 6.5*305 mm ESAB CARBON electrodes with a diameter of 6.5 mm is limited. Cleaning the cutting surface with a grinding wheel after thermal cutting is carried out to a depth of at least 1.5 mm and to a depth of up to 0.5 mm after mechanical processing (if possible). Cleaning down to clean metal is also performed on surfaces adjacent to the edges for a width of 20–30 mm.

3.3 Features of Welding, Repair, and Restoration of Some Castings

The lower dredge scoop drum (LSD) is a welded structure weighing up to 10 tons of two cast half-drums with ribs made of 110G13L steel, along the cylindrical part of which a chain with scoops moves (Fig. 1).

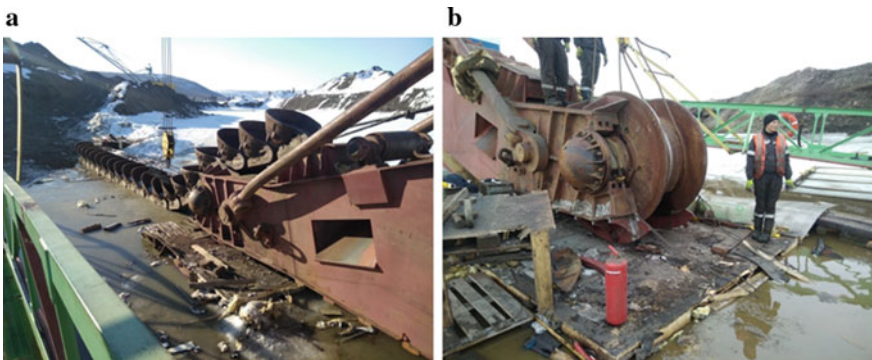


Fig. 1 **a** Scooping chain during mounting on the frame dredge 250 l and **b** lower scooping drum during mounting on the frame of the dredge 250 l

The drum works under conditions of waterjet wear with impacts that are mainly observed in the area of the edges. The breakaway of the edge can cause a scooping chain

consisting of several dozen scoops to descend into the pit. Attempts to use perlite steels 35L, 20GSL, and 35KhML with wear-resistant surfacing of the ribs as the base metal were mainly unsuccessful and ended up in the destruction and breakage of the ribs.

Figures 2 and 3 show the welded insert of the rib and the drawing of the LSD dredge 400 L:

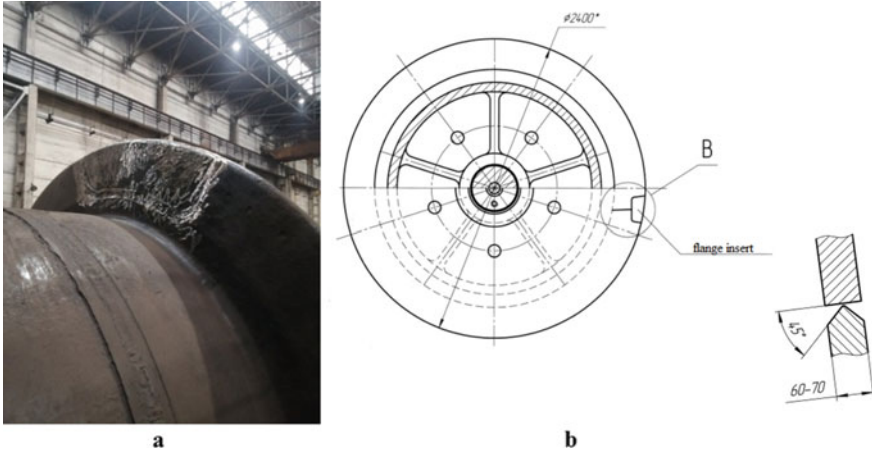


Fig. 2 a LSD dredge 400 l with an insert and b repair drawing of LSD

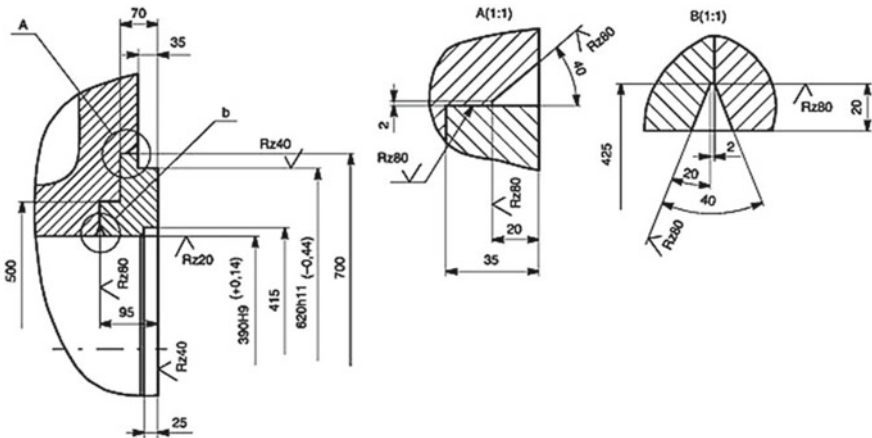


Fig. 3 Sketch of the repair connection with a 110G13L steel insert

Casting of semi-drums in a single sand mold is performed using the upper position of the end part of the casting. Four to six feeders are located on it for high-quality liquid metal supply. After heat treatment (quenching), the feeders are cut off at a height of 10–15 mm by oxygen cutting and cleaned by air-arc cutting. Cracks often occur in this part of the castings, the most dangerous of them being cracks in the central part and

those that are directed perpendicular to the edge of the hole. Welding of such cracks often led to the destruction of the welded drum when landing on the shaft after heating to a temperature of 350–400 °C.

Repair of such defects is carried out by welding the insert after removing the defective part of the casting by processing the upper part of the hole on a boring machine with a bevel of the edges for welding. The insert is made with a 110G13L steel casting, quenched with subsequent machining corresponding to the shape of the repair part of the hole. Figure 3 shows a sketch of the repair connection.

During operation, the drums are quite rarely repaired, and repair is associated with the occurrence of cracks in the end part or splinters in the bearing rib along the edge of the drum in emergency situations. Most often, cutting grinding wheels and arc gouging with a melting and non-melting electrode are used for cutting. Welding is performed with a self-protective powder wire ПП-АНВ2у or electrodes НИИ-48Г (OK 67.45).

Dredge scoops are the main working bodies of the dredge. Productivity depends on its condition. Cast scoops made of 110G13L steel with a capacity of 80–400 L are used on dredges, and the weight of the scoop is up to 3 tons. The welding of technological cracks in the manufacture of scoops is not allowed in the working area of the body and on the front and rear eyelets.

Over the years, attempts have been made to restore the height of the working edge by surfacing to preserve the design capacity of the scoop. A number of special materials and even methods of surfacing were developed, and some materials were characterized by high wear resistance. But the disadvantages of any methods and materials are the limited height of the restored layer along the working edge, and, most importantly, the need for additional repair stops for surfacing a large number of scoops. Due to the impossibility of long downtime of dredges during the washing season, surfacing during winter repairs did not provide for the restoration of seasonal wear, and the capacity of scoops decreased.

Currently, the restoration of scoops during the winter repair is carried out by welding special allotments—canopies. Visors are castings made of 110G13L steel in the form of a working part of the scoop body, which can be welded or mounted on a bolted connection to the body of a worn scoop (Fig. 4).



Fig. 4 **a** Visor used to restore the scoop; **b** dredge scoop (250 l) restored by welding

The visors in the lower part have a V-shaped cutting for welding. The repair and restoration of scoops after operation currently consist in fitting the edges of the scoop to the shape of the visor, with riveted and containing microcracks of metal removed by gas–oxygen cutting and stripping with a grinder down to pure metal, and then, the visor is attached and welded to the body. In addition, to eliminate the backlash in the front eyelets, the grinding machine is cleaned and the worn part of the eyelets is surfaced with НИИ-48Г electrodes (OK 67.45).

4 Conclusions

1. The article considers the development and implementation of the technology for welding large castings made of high-manganese steel 110G13L during the repair of castings in the process of manufacturing parts, as well as restoration during operation;
2. To perform welding work in the manufacture and repair of parts and welded structures of high-manganese steels, we recommend to use mechanized welding in shielding gas or self-shielded flux-cored wire and manual arc welding electrodes, providing a seam in the weld metal with chromium–nickel and chromium–nickel–manganese austenite;
3. It is advisable to develop and organize the production of welding materials that provide the production of manganese austenite in the weld metal;
4. It is advisable to improve the methods of non-destructive testing of castings made of high-manganese steel to determine the boundaries and depth of defects.

References

1. Vdovin KN, Feoktistov NA, Gorlenko DA, Koptseva NV (2018) Wear of high-manganese steel castings. *Chernye Metally* 9:48–53
2. Korotkov VA (2015) Wear resistance of carbon steel with different types of hardening. *J Friction Wear* 36(2):149–152
3. Chernyak SS, Broido VL (2001) Improvement of operation stability of crucial parts and constructions when repairing dredges and other mining machines exploited in conditions of North. Publishing house of Irkut. Gos University, Irkutsk
4. Gurevich LI (1986) Restoration of dredge ladles by welding a canopy made of 110G13L steel. *Autom Weld* 7:68–69
5. Broido VL, Krasnoshtanov SU (2018). Improvement of operation stability of crucial parts and constructions when repairing dredges and other mining machines exploited in conditions of North. In: IOP Conference Series: Materials Science and Engineering
6. Shishkina L (2020) Hardening features for high manganese steel cores of crosspieces along the way. E3S Web of Conferences, Topical Problems of Green Architecture, Civil and Environmental Engineering, TPACEE-2019. <https://doi.org/10.1051/e3sconf/202016414020>
7. Sinadskii NA, Turbina LA, Genkin IZ, Glyuzberg BE, Dusevich VM, Bogorskii NV, Goronkov ND (1994) Welding high-manganese and carbon steels. In: *Welding International*, pp 220–223
8. Berezovsky AV (2015) Improvement of high-manganese steel welding technology. Reasons for the formation of defects in welded joints. Ways to prevent them: monograph. LAP LAMBERT, Deutschland

9. Schmidova E, Hlavaty I, Hanus P (2016) The weldability of the steel with high manganese. *Tehnički vjesnik* 23(3):749–752
10. Mendez J, Ghoresly M, Mackay WBF, Smith TJN, Smith RW (2004) Weldability of austenitic manganese steel. *Mater Process Technol* 152–154:596–602
11. Zhang F, Lv Bo, Baitao Hu, Li Y (2007) Flach butt welding of high manganese steel crossing and carbon steel rail. *Mater Sci Eng A* 454–455:288–292
12. Bhavan Manak, Bahadur Shah Zafar Marg (2000) *Austenitic-Manganese steel castings—specification*, New Delhi, 110002
13. Khan PAA, Debroy T, David SA (1988) Laser beam welding of high-manganese stainless steels—examination of alloying element loss and microstructural changes. *Weld J* 67:75–76
14. Veit J, Wesling V, Schram A, Flugge W, Fritzsche Ch (2013) Resistance spot welding of high-manganese TWIP-steels without hot cracking. *Chernye Metally* 12:70–76
15. Kim J, Kim J, Pyo C (2020) A study on fiber laser welding of high-manganese steel for cryogenic tanks. *Processes* 8(12):1536
16. Broido VL (2015) Using welding in manufacture, repair and reconditioning of large castings of high manganese steels. In: *Welding International*, pp 650–653
17. ESAB Manuals User Manuals | ESAB Welding & Cutting
18. Hardfacing Alloys for Railroad Track Components Repair & Rebuilding. ESAB/esab.com 31c. Stoodly.com <https://www.esab.ru/shared/documents/litdownloads/8204>
19. Han I, Li B, Choi J, Park S (2013) Microstructure and mechanical properties of the weld metal of cryogenic high-manganese steel. *Int J Offshore Polar Eng* 27:348–352
20. Korotkov VA, Lipatov AG, Wesnin AM (2015) Innovative technologies of repair and reconstruction and extension of service life of parts and components of mining equipment. *Gornyi Zhurnal* 8:83–88



Influence of the Rate Composition for the Chemical Elements in the Steel Parts on the Serviceability of the Pairs of Friction

A. Esbulatova¹ and K. Voinov²(✉)

¹ West-Kazakhstan Agrarian-Technical University, 51, Zhangir khan street, Uralsk 090009, Kazakhstan

² University ITMO, 49 bldg. A, Kronverksky Pr., Saint-Petersburg 197101, Russia

Abstract. It is a common knowledge that there are too many different mechanical systems which have the wide range of the mobile pairs of friction which have wear and tear during the operation. The velocity of deterioration is very various as well. Many factors influence seriously upon this situation, namely structure of material, chemical composition, power factors, conditions of operations and others. Common instructions say that each part in the mechanical system must be manufactured with the definite chemical composition. Practically, there are not investigations with the statistical tests about the percentages for the chemical elements if the measurements have more meanings than two numerals after the point. As our practice shows, this problem plays the very important role to the normal operation. To answer the problem, several precise experiments/measurements are made, and computer calculations are presented too using the cover MathCad-15. To investigate the process of wear and endurance for each steel samples, several objects were taken. Reached improvements for investigated steels for wear and tensile strength usually were from 7 till 12%. In the unfavourable cases even if there are chemical elements correspond very exactly to the state standard, the real new design can be suddenly demolished although the applied loads were in the permissible limits (and even less at about 45–50%). That is why we recommend to learn this effect in the nearest future to get the very important information (as a reference book) which will be claimed at the process of the new projecting.

Keywords: Chemical compositions · Steel parts · Wear · Tensile strength

1 Introduction

It is a common knowledge that there are too many different mechanical systems which have the wide range of the mobile pairs of friction which have wear and tear during the operation. The velocity of deterioration is very various as well. Many factors influence seriously upon this situation, namely structure of material, chemical composition, power factors, conditions of operations and others. But, unfortunately, practically any designer does not take into account the next very important factor which is connected straight to the reliability of the new mechanical system. It is the influence of the precise amount of

the chemical elements into the structure of the part. It turns out that any designer must know those percentage compositions in the chemical elements which are not good for the operation though all parts were made in the official approved documents and demands. Many scientists work with these tasks [1–21], but this problem will be investigated and solved here on another level with the definite recommendations in detail.

2 Initial Positions

As usual, common instructions say that each part in the mechanical system must be manufactured with the definite chemical composition.

For example, steel 45 (in Russian classification) must have the next chemical main elements in the definite limits (%) with Fe \approx 97%:

- carbon (C = 0.42–0.50); silicon (Si = 0.17–0.37); manganese (Mn = 0.5–0.8);
- nickel (Ni < 0.25); sulphur (S < 0.04); phosphorus (P < 0.035);
- chromium (Cr < 0.25); copper (Cu < 0.25); arsenic (As < 0.08).

So then, practically in all cases there are definite limits “from...to”: 0.17–0.37 or 0–0.25. This is the real fact which takes place with the different materials.

Therefore, the important question is: Will it be indifferent for the reliability for the mobile joints in pairs of friction if there are such wide range of the different chemical elements and with their various combinations? And the next important question: Is it really enough for such small range connected with the accuracy of measurement for each chemical element (usually not more than two meanings after the point, namely after the whole number)?

Further let us try to get our preliminary answer because it is very strange if the new mechanical design cannot work very long, and after the short period of operation it has serious damages or even destructions.

Practically, there are not investigations with the statistical tests about the percentages for the chemical elements if the measurements have more meanings than two numerals after the point. As our practice shows, this problem plays the very important role to the normal operation.

To answer the problem, several precise experiments/measurements are made, and computer calculations are presented too using the cover MathCad-15.

3 Initial Preparations for Experiments and First Results

To investigate the process of wear and endurance for each steel samples, several objects were taken (in Russian classifications): steel 10, 65G, 40X, 45, 30XM, 14X17H2, 38XH3MFASH and 20X13. Each cylindrical pattern has diameter 10–0.02 mm and the length 60–1 mm with the same roughness. In this work, the next benches were applied: 3G71, 8B67, 6M12P and 1K62.

In a capacity of the equipment, the drilling bench (model B16RM, Hitachi) was used.

Process of friction was between our patterns and the abrasive emery paper (MIRKA P 100 WPF FINLAND). To weigh each sample model 1579, Digital Scale Professional-mini, capacity 200 g, graduation 0.01 g was applied (Made in Japan, Tanita Corporation).

The average way of friction each time was 520 m.

The wastes in the weight (g) for the patterns were the next:

- Sample №1 65G: 0.24 and 0.21;
- Sample №2 65G: 0.23 and 0.21;
- Steel 10 samples №3 and №4: 0.30 and 0.45;
- Steel 40X samples №5, №6 and №13: 0.24; 0.27 and 0.20;
- Steel 45 samples №7 and №8: 0.30 and 0.20;
- Steel 30XM samples №9 and №9a: 0.16 and 0.29; 0.20 and 0.11;
- Steel 14X17H2 samples №10 and 10a, №11, №12 and №15: 0.18; 0.19; 0.20; 0.21; 0.24 and 0.38; sample №16: 0.30 and 0.36;
- Steel 38XHMFASH sample №14: 0.31;
- Steel 20X13 sample №17: 0.27.

Further wear and tear (mm) for each pattern was the next:

- For steel 65G: 0.1 and 0.2;
- For steel 10: 0.2;
- For steel 40X: 0.1–0.2;
- For steel 45: 0.1;
- For steel 30XM: 0.16–0.28;
- For steel 14X17H2: 0.16; 0.25 and 0.36;
- For steel 38XHMFASH: 0.12;
- For steel 20X13: 0.28.

Measured hardness (by Brinell) for our samples had the next meanings: 110.5–113.5; 130–135; 166–178.5; 132; 148.5–156.0; 217.0; 151.5–173.0; 159–175; 187–193; 223–231; 255; 298–354; 368–373; 412–454.

Besides the pressing, the steel ball in our samples gave the next spots of diameter (mm) in the zone of contact: 2.87–3.01; 3.16–3.18; 3.24–3.52; 3.80; 3.98–4.05; 4.10–4.90; 4.34–4.40; 4.50–4.66; 4.74; 4.56–4.86; 5.18; 5.56–5.62.

The test bench for investigations is given here (Fig. 1).

High precise results of measurements for the chemical elements are in the steel patterns (Table 1).

Chemical compositions are given in the strict sequence: chemical elements, average meanings; chemical elements, average meanings; chemical elements, average meanings.

4 Results and Recommendations

1. For steel 10, the main qualitative indices (wear and tensile strength) were more good owing to the next chemical elements C, Mn, Si, Ni, Cr, Mo, Ti, Al, Nb, W, As, Sn, Pb, Zn, N and Fe which have more high meanings than another steel if elements P, S, Cu, Co, Sb and Ca had smaller % into the steel structure.

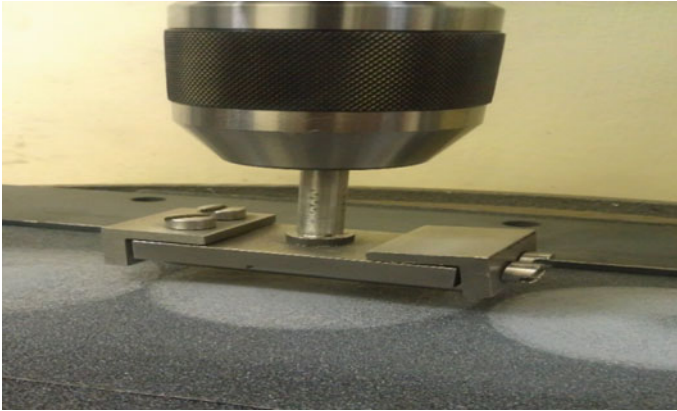


Fig. 1 For test investigations, the drilling bench was applied

2. For steel 65G, more good qualitative indices were if chemical elements Si, P, S, Ni, Cu, Ti, Nb, Pb, B, Sb and N had smaller meanings.

Table 1 High precise results of measurements for the chemical elements in the steel patterns Steel 65G/for springs/

C	Mn	Si	P	S	Ni	Cr	Cu
0.69172	1.00065	0.21534	0.01061	0.01809	0.152	0.18611	0.14713
Mo	V	Ti	Al	Nb	W	As	Sn
0.02252	0.00586	0.00279	0.02251	0.00039	0.00751	0.0052	0.0056
Co	Pb	B	Sb	Ca	Zn	N	Fe
0.01376	0.00091	0.00023	0.00055	0.00059	0.00036	0.00062	97.4913

Steel 65G

C	Mn	Si	P	S	Ni	Cr	Cu
0.66886	0.96685	0.25335	0.01202	0.02504	0.14686	0.21163	0.1929
Mo	V	Ti	Al	Nb	W	As	Sn
0.02237	0.00378	0.00532	0.0103	0.00045	0.00423	0.00223	0.00445
Co	Pb	B	Sb	Ca	Zn	N	Fe
0.0104	0.00149	0.000251	0.00073	0.00019	0.00024	0.01652	97.474

Steel 10 /for constructions high quality and carbonaceous/

C	Mn	Si	P	S	Ni	Cr	Cu
0.10043	0.41104	0.02356	0.01565	0.02594	0.02199	0.01169	0.03094
Mo	V	Ti	Al	Nb	W	As	Sn
0.00333	0.00378	0.00075	0.01819	0.00014	0.00112	0.00163	0.00156
Co	Pb	B	Sb	Ca	Zn	N	Fe

(continued)

Table 1 (continued)

<i>Steel 10 /for constructions high quality and carbonaceous/</i>							
0.00947	0.00105	0.0002	0.0007	0.00536	0.00256	0.00037	99.312
<i>Steel 10</i>							
C	Mn	Si	P	S	Ni	Cr	Cu
0.1361	0.47796	0.27179	0.00553	0.01059	0.07766	0.06946	0.20007
Mo	V	Ti	Al	Nb	W	As	Sn
0.01017	0.00316	0.00161	0.02096	0.00203	0.00451	0.00512	0.01146
Co	Pb	B	Sb	Ca	Zn	N	Fe
0.00842	0.004	0.00023	0.00026	0.00168	0.00081	0.03244	98.7088
<i>Steel 40X /for constructions with chrome and alloyed/</i>							
C	Mn	Si	P	S	Ni	Cr	Cu
0.52407	0.69503	0.28794	0.02157	0.02381	0.27996	1.00437	0.08913
Mo	V	Ti	Al	Nb	W	Sn	Co
0.03752	0.00523	0.0054	0.00444	0.00131	0.00623	0.00127	0.01144
Fe							
97.0013							
<i>Steel 40X</i>							
C	Mn	Si	P	S	Ni	Cr	Cu
0.43566	0.52924	0.21074	0.01291	0.01596	0.14144	0.79345	0.0563
Mo	V	Ti	Al	Nb	W	Sn	Co
0.0262	0.00084	0.00013	0.01678	0.00009	0.00483	0.00087	0.00902
Fe							
97.746							
<i>Steel 45 /for construction high quality and carbonaceous/</i>							
C	Mn	Si	P	S	Ni	Cr	Cu
0.52443	0.58207	0.25531	0.01399	0.03286	0.04421	0.06769	0.26103
Mo	V	Ti	Al	Nb	W	As	Sn
0.00569	0.00224	0.00156	0.00816	0.00043	0.00366	0.00775	0.00208
Co	Pb	B	Sb	Ca	Zn	N	Fe
0.02482	0.00109	0.0003	0.00137	0.00007	0.00063	0.02253	98.1811
<i>Steel 45</i>							
C	Mn	Si	P	S	Ni	Cr	Cu
0.45846	0.58103	0.24864	0.0131	0.00857	0.03933	0.05334	0.04765
Mo	V	Ti	Al	Nb	W	As	Sn
0.00583	0.00638	0.0019	0.01606	0.0003	0.00218	0.00194	0.002

(continued)

Table 1 (continued)

<i>Steel 45</i>							
Co	Pb	B	Sb	Ca	Zn	N	Fe
0.02742	0.00007	0.00016	0.0024	0.00049	0.0014	0.02731	98.5287
<i>Steel 30XM /heat resisting and alloyed/</i>							
C	Mn	Si	P	S	Ni	Cr	Cu
0.31092	0.5365	0.26462	0.01523	0.0066	0.15528	0.92214	0.13068
Mo	V	Ti	Al	Nb	W	Sn	Co
0.16445	0.00181	0.00049	0.01353	0.00051	0.00673	0.00455	0.01071
Fe							
97.4552							
<i>Steel 14X17H2 /heat-resisting chrome-nickel and stable against the corrosion/</i>							
C	Mn	Si	P	S	Ni	Cr	Cu
0.14171	0.41675	0.23439	0.02359	0.01716	2.00871	16.48899	0.14431
Mo	V	Ti	Al	Nb	W	As	Sn
0.11942	0.03121	0.00098	0.00223	0.00396	0.00646	0.00285	0.00787
Co	Pb	B	Sb	Ca	Zn	Fe	
0.04427	0.00026	0.00001	0.00891	0.00025	0.00267	80.3193	
<i>Steel 14X17H2 (10a)</i>							
C	Mn	Si	P	S	Ni	Cr	Cu
0.10451	0.26514	0.3073	0.02081	0.01251	1.63948	17.94223	0.08182
Mo	V	Ti	Al	Nb	W	As	Sn
0.06344	0.0292	0.00094	0.01024	0.00417	0.00231	0.00095	0.00331
Co	Pb	B	Sb	Ca	Zn	Fe	
0.01883	0.00029	0.00005	0.00846	0.00026	0.00363	79.5101	
<i>Steel 14X17H2</i>							
C	Mn	Si	P	S	Ni	Cr	Cu
0.17113	0.37292	0.36423	0.01873	0.00724	2.12371	16.56903	0.09514
Mo	V	Ti	Al	Nb	W	As	Sn
0.05213	0.00373	0.00074	–	–	–	0.00273	0.00581
Co	Pb	B	Sb	Ca	Zn	Fe	
0.01961	–	–	–	0.00033	0.00219	81.114	
<i>Steel 38XH3MFASH /for construction and alloyed/</i>							
C	Mn	Si	P	S	Ni	Cr	Cu
0.35338	0.32117	0.25551	0.00969	0.00258	3.00932	1.23127	0.13031

(continued)

Table 1 (continued)

<i>Steel 38XH3MFASH /for construction and alloyed/</i>							
Mo	V	Ti	Al	Nb	W	Sn	Co
0.36512	0.10317	0.00049	0.00917	0.00096	0.01426	0.00207	0.07956
Fe							
94.112							
<i>Steel 14X17H2</i>							
C	Mn	Si	P	S	Ni	Cr	Cu
0.17267	0.54987	0.29447	0.02418	0.01124	2.42096	16.6892	0.1038
Mo	V	Ti	Al	Nb	W	As	Sn
0.05195	0.02248	0.0019	0.00459	-0.00513	0.01481	0.0044	0.00476
Co	Pb	B	Sb	Ca	Zn	Fe	
0.04281	-0.00052	0.00002	-0.00506	0.00115	0.0042	79.5902	
<i>Steel 20X13 /heat resisting and high alloyed/ (and so on)</i>							
C	Mn	Si	P	S	Ni	Cr	Cu
0.20071	0.36805	0.30495	0.0262	0.01652	0.2148	12.49572	0.11561
Mo	V	Ti	Al	Nb	W	Sn	Co
0.04297	0.02906	0.0015	0.00293	0.0052	0.0444	0.00545	0.0289
Fe							
86.107							

- For steel 40X, better results were if chemical elements C, Mn, Si, P, S, Ni, Cr, Cu, Mo, V, Ti, Nb, W, Sn and Co had maximum (%), and at the same time % with the presence of Al and Fe was smaller.
- For steel 45, better results had the samples with high indices (%) Mo, V, Ti, Al, Co, Sb, Ca, Zn, N and Fe, and they had the less % for elements C, Mn, Si, P, S, Ni, Cr, Cu, Nb, W, As and Fe (the presence Sn was approximately the same for the two patterns).
- For steel 30XM, more good results were applied if chemical elements S, Mo, Ti and Fe had bigger meanings (%), but chemical elements C, Mn, Si, P, Ni, Cr, Cu, V, Al, Nb, W, Sn and Co had the smaller meanings (%).
- For steel 14X17H2 from positions of wear and tensile strength, the pattern number 10 had the better effect if the % composition for elements C, Mn, P, S, Ni, Cu, Mo, V, Ti, W, As, Sn, Co, Sb and Fe was bigger, but for elements Si, Cr, Al, Nb, Pb, B, Zn and Fe had a little bit less (%); Ca did not play some essential role.
- For steel 14X17H2, better results gave those patterns which had higher % of Mn, Ni, Cu and Mo.

Common conclusion: Reached improvements for investigated steels for wear and tensile strength usually were from 7 till 12%. In the unfavourable cases even if there are all chemical elements correspond very exactly to the state standard, the real new design

can be suddenly demolished although the applied loads were in the permissible limits (and even less at about 45–50%). That is why we recommend to learn this effect in the nearest future to get the very important information (as a reference book) which will be claimed at the process of the new projecting.

References

1. Shultz VV (2000) Optimization of the geometrical parameters for the drawing instrument. In: Proceedings of the International scientific-practical symposium, Saint-Petersburg, Slavyantribo-5, pp 37–39
2. Shultz VV (1990) The shape of the natural wear for the parts of machines and tools. Mechanical Engineering, Leningrad, p 208
3. Sizova OV (2000) Forming of the micro-structure for steel R6M5 during the thermo-processing and cutting. Proceedings of the International scientific-practical symposium. Saint-Petersburg, Slavyantribo-5, pp 144–146
4. Martirosyan RB, Afrikyan TG (1993) Working principles to form the abrasive instrument. Patent RF №315274
5. Gik LA, Ostashevicius V (2001) Machining of materials efficiency increasing method by alteration of traditional high-speed contact interaction principle of the tool. In: Proceedings of the III International conference on metal cutting and speed machining, Metz (France), June 27–29, 2001, pp 33–36
6. Bobrov VF (1975) The foundation of the theory to cut metals. Mechanical Engineering, Moscow, p 344
7. Voinov KN (2008) Modern methods of the edge machining and the another perspective processing of billets and parts. Educational supply, Saint-Petersburg, p 37
8. Chichinadze AV et al (2003) Friction, wear and lubricant (tribology and tribo-technic). Mechanical Engineering, Moscow, p 576
9. Voinov KN (2010) Tribology: International encyclopaedia, vol I, p 176
10. Voinov KN (2012) Tribology: International encyclopaedia, vol IV, p 423
11. Voinov KN (2015) Problems and answers in questions of friction/wear. SPb., Nestor-History, p 500
12. Kragel'skiy et al (1977) The foundation to calculate friction and wear. Mechanical Engineering, Moscow, p 526
13. Contact interaction and dry friction (2005) Proceedings of the International seminar. MG TU, Moscow, p 92
14. Myshkin NK, Petrokovets MI (2002) Tribology: principles and appendix. IMMS NANB, Gomel', p 310
15. Hiroki et al (2009) The effects of hydrogen on microstructural change and surface originated flaking in rolling contact fatigue. In: Proceeding of the world tribology congress in Kyoto, Japan
16. Filipowicz K, Kowal A (2006) Energy and environmental aspects of tribology. In: 7th international Symposium INSYCONT'06, Cracow, Poland, pp 73–81
17. Work Report 2000–2004 (2004) Centre for tribology technical diagnostics and hydraulics. Ljubljana, p 44
18. Gmurman VE (1975) Handbook to solve tasks in the theory of probability and mathematical statistics. High School, Moscow, p 333
19. Rumshiskiy LZ (1971) Mathematical analysis for the results of experiment. Science, Moscow, p 192
20. Rumshiskiy LZ (1976) Elements in a theory of probability. Science, Moscow, p 239
21. Voinov KN, Lutov DA (2020) Reliability, tribology and tribotechnica of systems. Textbook, Saint-Petersburg, GASU/ITMO: Nestor-History, p 72



The Influence of Agricultural Production Factors on the Rate of Changing the Radial Clearance in the Electric Motor Bearings When Working with V-belt Transmission

R. V. Banin¹(✉), V. A. Butorin¹, and I. B. Tsarev^{1,2}

¹ South Ural State Agrarian University, 13, Gagarin Str., Troitsk 457100, Russia

² South Ural University of Technology, 1, Kozhzhavodskaya Str., Chelyabinsk 454052, Russia

Abstract. The paper considers the regularity of changing the wear rate of asynchronous motor bearings under operating conditions which are typical for agricultural production premises. The radial clearance is selected as a parameter that determines the bearing performance; it is normalized in the reference literature for rolling bearings. Harsh environmental conditions and a high utilization rate of asynchronous motors in electrified processes of agro-industrial production result in an annual failure (about 20–25%) of the electric motor fleet. Bearing wear is noted to be the main cause of motor failure apart from damage to winding. As a result of the literature analysis and using the method of expert evaluations, the statistical characteristics of the deteriorating environmental factors for the main types of agricultural premises were specified. The authors have developed a bench that makes it possible to simulate the electric motor operation typical for agricultural production environments under laboratory conditions. Bench tests for studying the rate of changing the radial clearance were carried out using the asynchronous motor (the 6A80B2Y3 brand) which has a drive of a working machine with a V-belt transmission. The load value on the motor shaft was constant at the level of 10 kgf. Experimental studies were based on the theory of planning a multivariate experiment. The choice of a plan for a full three-factor factorial experiment has been substantiated. Relative air humidity, dust, and ammonia content were selected as wear factors. The result of the research was the polynomial dependence of the changing rate of the bearing radial clearance on the selected factors.

Keywords: Asynchronous motor · V-belt transmission · Bearing · Radial clearance · Bench tests

1 Introduction

A significant part of the technological processes occurring in agricultural production is carried out by an unregulated electric drive which includes an asynchronous motor. The harsh environmental conditions and the high utilization rate of asynchronous motors result in annual breaking down about 20–25% of the electric motor fleet [1–3]; this leads to losses in the agricultural sector. After the damage to the windings, bearing failure is the

second most common cause of motor failure. Up to 12% of asynchronous motor failures are caused by bearing destruction [2–5]. At the same time, the question related to the rate of bearings wear depending on the operating conditions of electric motors has not been sufficiently studied. The main parameter that determines the bearing performance is the radial clearance [6, 7]. In this regard, the question of the relationship between the rate of changing the bearing radial clearance and the wear factors seems to be relevant for agricultural production. An asynchronous motor of the 6A series, which is widely used in agricultural production, was selected as the object of research. To reduce the number of tests, the case of combining an electric motor and a working machine with a V-belt transmission was considered. The most reliable data about the bearings wear rate according to the operational factors can be obtained from operational observations. But this method is associated with great difficulties caused by many years of observation and collection of statistical data. We carried out bench tests based on the theory of active planning of an experiment [8–11], which helps to approximate the required functional dependence by a polynomial.

2 The Choice of Conditions for Bench Testing and Experiment Planning Matrix

After analyzing the literature [1–5] and using the method of expert evaluation, the statistical characteristics of the deteriorating environmental factors for the main types of agricultural premises were specified (Table 1).

Table 1 Statistical characteristics of environmental factors for the main types of agricultural premises

Type of premises	Statistical characteristics of environmental factors							
	Humidity, %		Hydrogen sulfide, g/m ³		Dust, g/m ³		Ammonia, g/m ³	
	\bar{W}	σ_W	\bar{S}	σ_S	\bar{C}	σ_C	\bar{A}	σ_A
Dry	60	2.3	0	0	0.0002	0.00007	0	0
Humid	67	2.6	0	0	0.0006	0.00004	0	0
Dusty	60	3.1	0	0	0.2	0.063	0	0
Damp	86	2.8	0.022	0.005	0.0045	0.001	0.036	0.012
Particularly damp with a chemically active medium	98	0.6	0.045	0.002	0.035	0.002	0.065	0.006

The obtained statistical characteristics made it possible to reveal the range of changes in the wear environmental factors inherent in the operating conditions of electric motors.

The factors that were maintained at a constant level during the experiment include the electric motor supply voltage and the radial load on its shaft equal to 10kGs (98 N) [13].

3 Designing a Bench for Experimental Studies

A bench for experimental studies has been designed [14] in order to conduct an experiment for studying the rate of changing the bearing clearance. It makes it possible to fully simulate the operating conditions of an electric motor under the conditions of agricultural production. The bench layout is shown in Fig. 1.

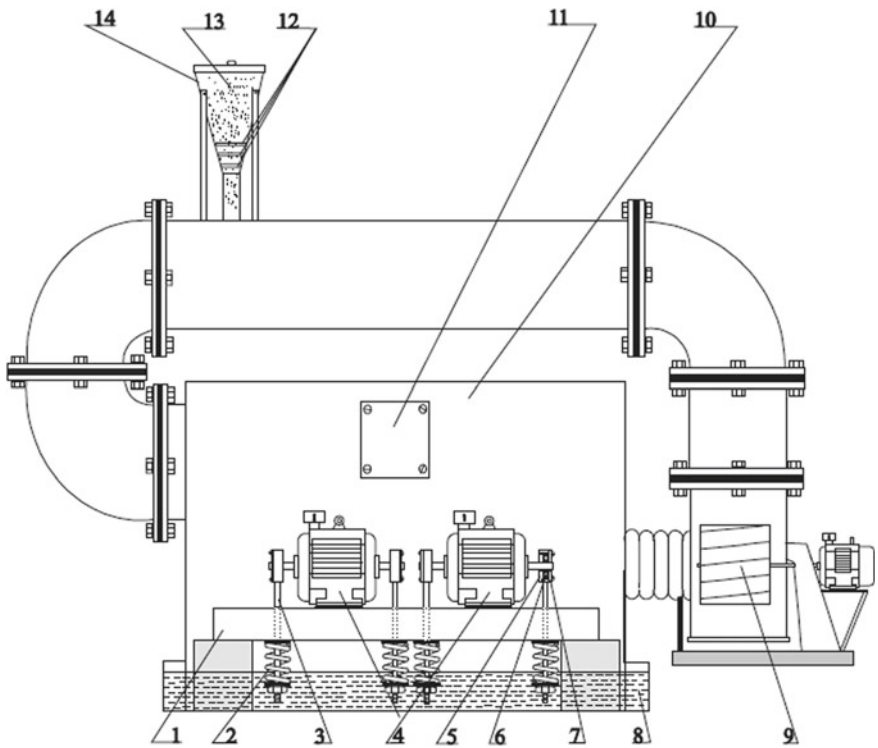


Fig. 1 Bench for studying the rate of increasing the radial clearance of electric motor bearings in agricultural premises: 1—frame; 2—spring; 3—stock; 4—electric motor; 5—brackets; 6—technological bearing; 7—washer; 8—tray; 9—fan; 10—chamber; 11—viewing window; 12—calibrated sieves; 13—dust; 14—funnel for dust delivery

The presented installation consists of a frame 1 where the tested electric motors (4) are installed. Their number is equal to two, thereby a fourfold repetition of each experiment is achieved. At the output ends of the electric motors shafts, the technological bearings (6) are installed. They are installed in the brackets (5) with washers (7) to which a given

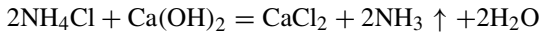
radial load is transferred through the stock (3) by means of springs (2) to the bearing units of the tested electric motors (4).

To create the necessary environmental conditions for testing, the entire installation is placed in a test chamber (10), with the tray (8) made of sheet iron. The dimensions of the chamber (10) along the perimeter of the base are slightly smaller than the dimensions of the tray (8) which ensures the constancy of the specified levels of factors during each experiment.

To supply a certain amount of dust (13), the chamber is equipped with a funnel (14), the lower part of which is covered with layers of calibrated sieves (12). The level of dust inside the test chamber (10) is controlled by a gas analyzer.

Maintaining a given relative air humidity around the tested engines is ensured by filling the tray (8) with water. The humidity level is controlled by a psychrometer.

The concentration of ammonia in the chamber is achieved by installation of an additional tank containing ammonium chloride (NH_4Cl) and slaked lime (CaOH). The number of reactants required to obtain the ammonia concentration specified under the experimental conditions is calculated by using the chemical reaction equation.



The reaction products are calcium chloride, free ammonia, and water. Monitoring of ammonia concentration in chamber (10) is carried out by a universal portable gas analyzer UG-2.

Visual observation of the installation operation and its parts is conducted through the viewing window (11).

An even distribution of environmental conditions inside the chamber is achieved by means of a fan (9) which is mounted in the test chamber (10).

The wires of the electric motors are connected through the branch pipe located on the side of the chamber (10).

4 The Results of Experimental Studies

The installation of four tension springs acting on the output ends of the shaft in two tested electric motors made it possible to achieve a fourfold repetition of the experiment. Bench test results are shown in Table 4.

Bench test data processing was carried out according to the methodology prevailing in the theory of experiment planning and included checking the reproducibility of experiments by the Cochran criterion, calculating the regression coefficients and assessing their significance by the Student's criterion, as well as checking the adequacy of the model by the Fisher criterion [15, 16]. We have found the dependence of the speed (V) of increasing the bearing radial clearance on the relative humidity of the air and the dust content in it. This dependence in encoded and decoded form, respectively, is as follows.

$$y = (0.940 + 0.32X_1 + 0.15X_2 + 0.175X_1X_2) \times 10^{-6}, \text{ mm/h}; \quad (1)$$

$$y = (0.355 + 0.0058W - 1.875C + 0.035WC) \times 10^{-6}, \text{ mm/h}; \quad (2)$$

Table 4 Bench test results

No. of experiment	Experiment planning matrix			The rate of changing the radial clearance, 10^{-6} mm/h			
	X_1	X_2	X_3	y_1	y_2	y_3	y_4
1	-1	-1	-1	0.39	0.77	0.52	0.61
2	1	-1	-1	0.61	0.77	0.99	1.34
3	-1	1	-1	0.58	0.51	0.64	0.78
4	1	1	-1	1.29	1.56	1.35	1.21
5	-1	-1	1	1.10	0.54	0.81	0.42
6	1	-1	1	1.10	0.97	0.72	0.98
7	-1	1	1	0.76	0.51	0.37	0.61
8	1	1	1	1.74	1.77	1.81	1.95

The value of the numerical coefficients in the coded expression (1) helps to estimate the relative contribution of each factor separately or as a result of their interaction to the wear process. It should be noted that in expression (1) according to the Student's criterion the regression coefficients for terms containing X_3 (ammonia) turned out to be insignificant. Therefore, the summands containing ammonia in the decoded dependence (2) are absent.

Decoded dependence (2) and the data in Table 5 make it possible to calculate the rate of increase in the radial clearance of bearings in asynchronous motors with V-belt transmission in the main types of agricultural premises (Table 5).

Table 5 Rate of changing the bearings radial clearance in asynchronous motors with V-belt transmission in the main types of agricultural premises

Type of premises	The rate of changing the radial clearance, 10^{-6} mm/h
Dry	0.703
Humid	0.744
Dusty	0.748
Damp	0.859
Particularly damp with a chemically active medium	0.978

5 Conclusion

1. The relative air humidity and dust content in it are the operational factors that have the greatest impact on bearings wear in asynchronous motors in agricultural premises.
2. Expressions (1) and (2) were obtained as a result of bench tests based on the theory of experiment planning. They describe the dependence of the rate of increasing the bearings radial clearance in an asynchronous motor (the 6A80B2Y3 brand) on the relative air humidity and the dust content in it when the electric motor and the working machine are coupled with a V-belt transmission.
3. Table 5 shows the rate of increase in the bearings radial clearance in asynchronous motors with V-belt transmission in the main types of agricultural premises.

References

1. Eroshenko GP, Medvedko YuA, Taranov MA (2001) *Ekspluatatsiya elektrooborudovaniya sel'skohozyajstvennykh predpriyatij* (Electrical equipment operation in agricultural enterprises). Terra, Rostov na Donu
2. Baharev AV, Umurzakova AD (2017) Analiz metodik ocenki tehnikeskogo sostoyaniya elektrodvigatelya (Analysing the methods for evaluating the technical condition of the electric motor). In: Lobur IA, Kashirskih VG (eds) *Proceedings of the III All-Russian scientific and practical conference Energy Saving: Theory and Practice*, Pavlodar
3. Banin RV (2010) Sovershenstvovanie sposoba povysheniya ekspluatatsionnoy nadezhnosti asinhronnykh elektrodvigatelye v sel'skom hozyajstve (Improving the method for improving the operational reliability of asynchronous motors in agriculture). *Dostizheniya nauki i tekhniki APK* 10:71–73
4. Butorin VA, Banin RV (1999) Okruzhayushchaya sreda i iznashivanie elementov sel'skohozyajstvennykh elektropriwodov (Environment and wear of elements of agricultural electric drives). *Mekhanizatsiya i elektrifikatsiya sel'skogo hozyajstva* 5:15–16
5. Butorin VA, Banin RV (2000) Issledovanie sprosa na zapasnye chasti dlya elektropriwodov v sel'skom hozyajstve (Demand researching of spare parts for electric drives in agriculture). *Vestnik chelyabinskogo agroinzhenerenogo universiteta* 30:85–90
6. Perel LY (1983) *Podshipniki kacheniya: Raschet, proektirovanie i obsluzhivanie opor: Spravochnik* (Roller bearings: calculation, design and maintenance of supports: reference guide). Mashinostroenie, Moscow
7. Russian State Standard GOST 24810–2013 (2013) *Podshipniki kacheniya. Vnutrennie zazory* (State Standard Specification 24810–2013. Rolling bearings. Internal clearances)
8. Hinkelmann K, Kempthorne O (2007) Design and analysis of experiments. In: *Introduction to experimental design*, 2nd edn., vol 1. Wiley, Hoboken
9. Hinkelmann K, Kempthorne O (2005) Design and analysis of experiments. In: *Advanced experimental design*, vol 2. Wiley, Hoboken
10. Hinkelmann K, Kempthorne O (2012) Design and analysis of experiments. In: *Special designs and applications*, vol 3. Wiley, Hoboken
11. Clarke GM, Kempson RE (2010) *Introduction to the design and analysis of experiments*. Wiley, New York
12. Evdokimov UA, Kolesnikov VI, Teterin AI (1988) *Planirovanie i analiz eksperimentov pri reshenii zadach treniya i iznosa* (Planning and analyzing the experiment for solving friction and wear problems). Nauka, Moscow

13. Aliev II (2002) Spravochnik po elektrotekhnike i elektrooborudovaniyu (Reference guide of electrical engineering and electrical equipment). Vysshaya shkola, Moscow
14. Banin RV, Butorin VA, Tsarev IB (2005) Stend dlya ispytaniya podshipnikov elektrodvigatelej na dolgovechnost (A lifetime testing bench for electric motor bearings). RF Patent 2,277,702, 16 Feb 2005
15. Tamhane AC (2012) Statistical analysis of designed experiments: theory and applications. Wiley, Hoboken
16. Easterling RG (2015) Fundamentals of statistical experimental design and analysis. Wiley, Chichester



The Influence of Structural Components of Diamond-Bearing Mineral Ceramic Abrasive Material on Its Cutting Ability and the Treated Surface Quality

A. Bolotov, O. Novikova, and V. Novikov^(✉)

Tver State Technical University, 22, A. Nikitin Emb., Tver 170026, Russia

Abstract. The use of known mineral ceramic tool materials is limited by their weak resistance to cyclic temperature changes, low bending strength. The authors propose a new abrasive mineral ceramic material with dispersed diamonds enclosed in a corundum matrix frame. The research includes assessing the influence of the composite material structural components on its cutting ability, the tool relief roughness characteristics, and the treated surface quality. The volumetric cutting ability of diamond-bearing samples is consistently high, exceeds the comparable traditional materials by 1.3–3 times, and increases nonlinearly with an increase in diamond grit. An increase in the diamond concentration in the abrasive material slightly reduces the grinding rate. The working surface morphology of a diamond-bearing abrasive tool does not change during operation. The ceramic matrix does not have wear marks, diamonds protrude significantly above the matrix surface, and the tool cutting surface retains the correct geometric shape. Abrasive tools made of the proposed material have good diamond retention, heat resistance, and goes into a self-sharpening mode during operation. It is found that the treated surface roughness increases when using diamonds of larger fractions. With an increase in the diamond concentration in a mineral ceramic material tool, the surface profile parameter Ra of a workpiece does not decrease linearly. An empirical dependence of Ra parameter is proposed. Grinding modes have a lesser effect on the surface morphology of the part treated with the mineral ceramic tool compared to the tool characteristics. The research results will be used in the design of new abrasive materials.

Keywords: Diamond-bearing ceramic material · Abrasive properties · Friction · Wear · Mineral ceramics

1 Introduction

Cutting tools made of mineral ceramic composite materials are widely used in modern mechanical engineering [1–3]. High hardness, heat and wear resistance, stable cutting properties make it possible to successfully use mineral ceramic alloy tools to turn and mill a wide class of materials. The existing disadvantages of mineral ceramics, such as

low bending strength, brittleness, low resistance to cyclic temperature changes, show a clear need for the development of new effective mineral ceramic materials [4–7].

We have made a research aimed at obtaining a new mineral ceramic material for manufacturing abrasive tools. The initial materials are microdispersed aluminum powder and synthetic copper-plated diamonds. By pressing, sintering, and microarc oxidation (MAO) [8, 9] of the working surface of a blank, we have obtained a composite material that is a refractory oxide matrix with embedded diamond particles. Preliminary tests have shown good abrasive properties of the developed material [9, 10]. But the problem of creating an abrasive tool from a diamond-bearing composite mineral ceramic material with a predetermined set of operational parameters, which are high grinding performance and the required quality of the treated surface, requires additional study [11–14].

The cutting ability and quality of the treated surface during abrasive processing (in addition to operating parameters) are affected by a large number of factors. However, the main contribution is made by grain size and concentration of diamonds, a combination of physical and mechanical properties of diamonds and a matrix [13–17].

The purpose of the study is to establish the influence of structural components of a new abrasive mineral ceramic composite material on its working properties: cutting ability, characteristics of the tool relief roughness, and the quality of the treated surface.

2 The Research Method

The abrasive properties of the developed mineral ceramic composite material were evaluated using an MT-2 friction machine [12]; its friction unit is implemented according to the finger-ring scheme. Its cutting surface structure and the treated surface morphology of the counter-sample was analyzed using a metallographic microscope and standard profilometry methods GOST 19,300-86 [18].

For comparative analysis, similar data were obtained for typically used tool diamond-bearing materials with metal (*M1*) and organic bakelite (*B1*) matrices. Industrial water was used as a lubricant. The counter-samples are made of BaO-SiO₂-Al₂O₃ ceramics (hardness 16 GPa). Contact pressure is 1 MPa, and the linear sliding speed is 30 m/s.

3 Results and Discussion

3.1 Influence of the Diamond-Bearing Tool Structure on its Performance

The grinding performance of diamond-bearing samples estimated as the volumetric cutting ability of a ceramic counter-sample is shown in Fig. 1. The cutting properties of abrasive materials correlate with the matrix material hardness. The ceramic matrix material has shown the best characteristics, which is explained by the highest resistance of the matrix to the abrasive effect of wear particles (Fig. 1a, b). A nonlinear increase in the cutting ability of abrasive materials with an increase in diamond grit does not depend on the matrix type; it is typical for all tested diamond-bearing materials (Fig. 1a). When the grit increases up to 100/80 μm, the prevailing factor is an increase in the protrusion of cutting grains above the matrix surface and, accordingly, an increase in the volume

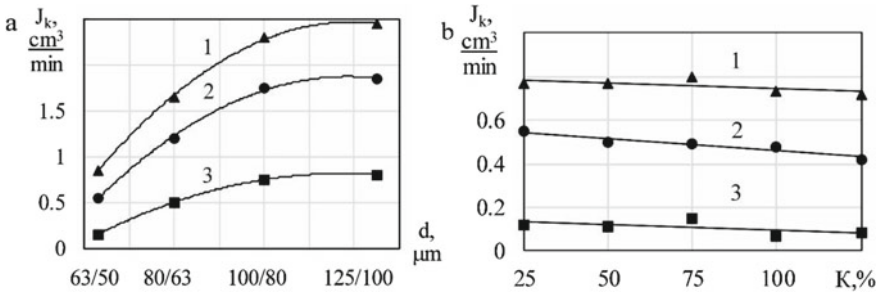


Fig. 1 Influence of diamond grit (a) and concentration (b) on the volumetric cutting ability of diamond-bearing materials. 1—a ceramic matrix, 2—M1 matrix, 3—B1matrix

of the wear material. A further increase in the diamond grain radii leads to a smoothing their cutting angles, rounded tops; there is no increase in the volumetric cutting ability.

An increase in the diamond concentration in the abrasive material somewhat reduces its volumetric cutting ability (Fig. 1b), which is related to the difficulties in removing wear particles from the friction zone.

The diamond-bearing material with the M1 matrix shows the cutting ability value most comparable to that of mineral ceramics. However, in order to maintain it at a high level, the tool requires periodic adjustment that removes the tool “grease” with wear products. It is established that diamond-bearing material samples with M1 and B1 matrices reduce their working capacity by about 2.6–6.7 times during 20 min of operation. For a mineral ceramic material, it almost does not change (decrease over a similar time by 4–6%). The consistently high cutting ability assumes that abrasive tools made from mineral ceramics operate in a self-sharpening mode.

3.2 Morphology Changes in the Working Surface of a Diamond-Bearing Abrasive Tool During Operation

The complex morphology of the cutting surface of an abrasive diamond-bearing mineral ceramic tool is the result of a three-dimensional internal structure, which is a refractory ceramic matrix of aluminum oxides with evenly distributed copper-metallized diamond grains (Fig. 2). The figures show the surfaces of samples with different diamond mass concentration K (Fig. 2a, b). The diamonds embedded in the matrix at different depths are clearly visible. After friction tests, the ceramic matrix has no signs of wear, the diamonds protrude significantly above the matrix surface, their cutting edges remain sharp.

Morphology comparison of the worn-out surfaces of the mineral ceramic material and the sample with the M1 matrix (Fig. 3) shows the significant advantages of the first one. The surface of the diamond-bearing M1 matrix material, which has shown a sufficiently high volumetric cutting ability, has significant traces of matrix plastic deformation, the diamond grains are “greasy” with wear particles.

The analysis of profilograms shows that the microgeometry of the mineral ceramic tool cutting surface almost does not change during operation (Fig. 4a, b). The height and pitch of microroughnesses have changed insignificantly, and the smoothing of the

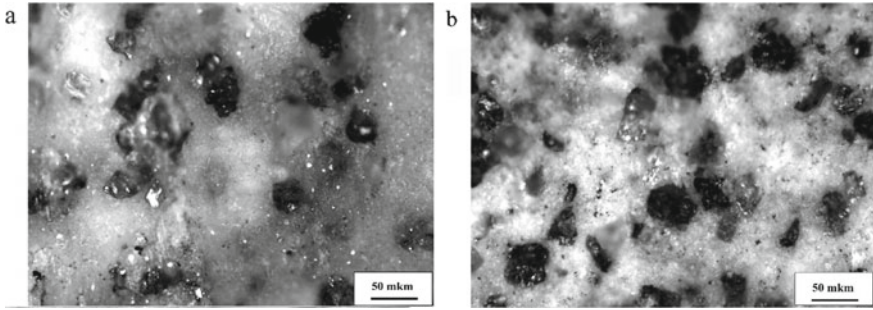


Fig. 2 Structure of the friction surface of mineral ceramics samples after testing **a** $d = 63/50$, $K = 75\%$, **b** $d = 63/50$, $K = 100\%$

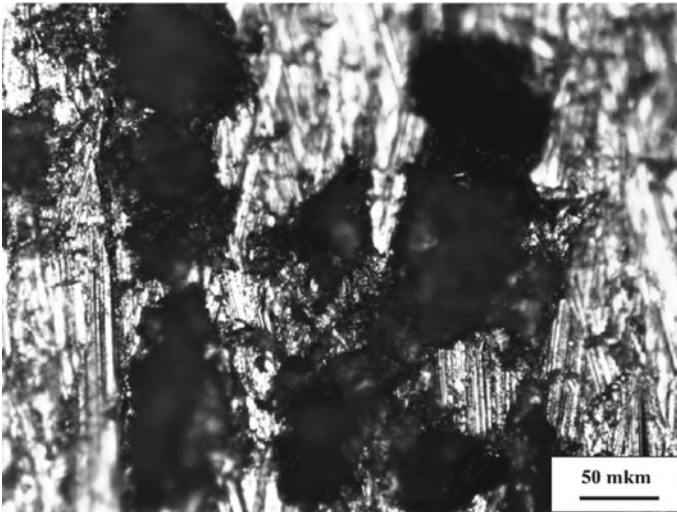


Fig. 3 Friction surface structure of the metal matrix samples after testing $d = 80/63$, $K = 75\%$

cutting tips is minimal. The geometric size of the periodically repeating irregularities (average microroughness pitch) corresponds to the average size of diamond grains in the sample. The waviness is minimal, and there is no deviation from the tool cylindricity: The sample surface retains the correct geometric shape.

As a comparison, we demonstrate a profilogram of a diamond-bearing material with *B1* matrix obtained after tests under similar conditions without additional tool adjustment (Fig. 4c). The initial profiles of the surfaces of mineral ceramics and *B1* samples had almost the same microgeometry parameters. After tribological action, they differ significantly (Fig. 4b, c). The *B1* sample profilogram shows a pronounced relief with deep depressions, which were probably left by diamonds removed from the surface together with a part of the matrix. There are randomly located horizontal areas formed by smoothing the soft surface of the matrix. On the working surface of the abrasive tool

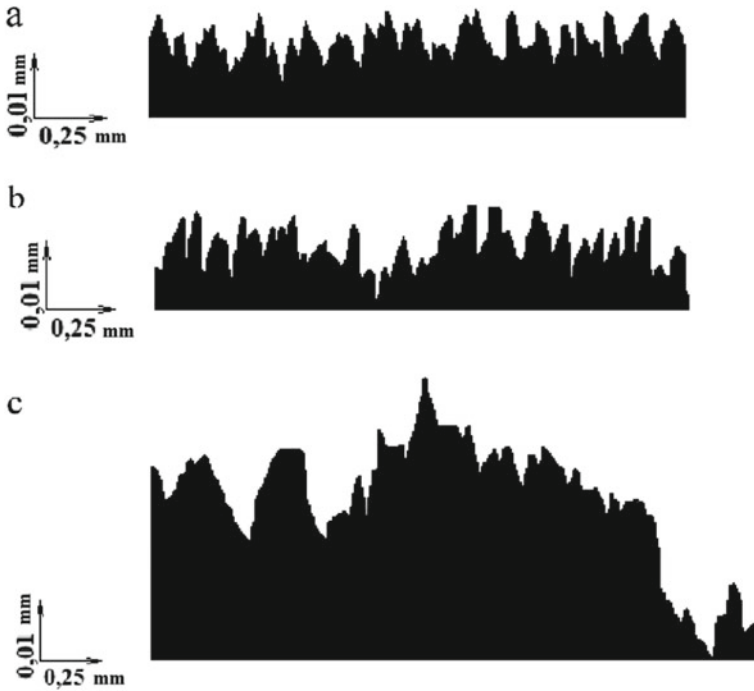


Fig. 4 Working surface profilograms of diamond-bearing tools with different types of matrices: **a** oxide ceramics before testing, **b** oxide ceramics after testing, **c** matrix B1 after testing

B1, the frictional action has formed a noticeable deviation from the tool cylindricity (barrel shape).

The stability of the cutting surface profile of a mineral ceramic tool, which determines its high performance, is an undoubted advantage over traditional materials. This is a consequence of the synergistic effect of improving the performance characteristics of a composite material formed by dispersed diamonds and an oxide matrix. High hardness and antifriction properties of these components [1–3, 19, 20] provide resistance to abrasive wear of the tool working surface. The corundum matrix has a high diamond retention and therefore provides a high overhang of cutting grains over the binder material and does not allow diamonds to be removed under the action of friction forces until complete wear out. At the same time, the contact area between the matrix and the processed material decreases, and the tool profile remains stable. Taking into account these facts and the close mechanical properties of the composite structural components, it can be assumed that worn diamonds are removed from the cutting surface together with a part of the surrounding matrix, exposing new grains and going into a self-sharpening mode. The high thermal conductivity of the aluminum substrate provides good heat removal from the friction zone, prevents unplanned graphitization of diamond grains, and a decrease in their cutting properties under high temperatures caused by frictional heating.

3.3 Influence of the Characteristics of Diamond-Bearing Abrasive Materials and Grinding Modes on the Treated Surface Morphology

The comparative tests have shown that the counter-sample roughness does not correlate inversely with the matrix material hardness (Table 1). The hardest mineral ceramic matrix provides average Ra parameter values between the softer matrices $M1$ and $B1$.

Table 1 Influence of the characteristics of diamond-bearing abrasive materials on the treated surface roughness

No	Matrix material	Grit	Roughness parameters Ra (μm)		
			Diamond concentration (%)		
			50	100	125
1	Oxide ceramics	100/80	1.05–0.90	0.85–0.70	0.72–0.60
		80/63	0.72–0.64	0.62–0.50	0.53–0.47
		63/40	0.56–0.44	0.48–0.40	0.40–0.32
2	$M1$	100/80	1.30–1.10	1.10–0.95	0.90–0.75
		80/63	0.95–0.85	0.80–0.70	0.65–0.55
		63/40	0.72–0.60	0.60–0.50	0.50–0.42
3	$B1$	100/80	0.70–0.58	0.63–0.50	0.40–0.32
		80/63	0.52–0.40	0.40–0.32	0.32–0.25
		63/40	0.42–0.30	0.32–0.25	0.25–0.20

The diamond grit provides the most significant influence on the formation of the treated surface morphology of the ceramic counter-sample: The roughness increases when using diamonds of larger fractions regardless of the matrix material (Table 1).

The effect of the diamond concentration in a mineral ceramic tool is more complex. When it changes in the ranges of 50–75% and 100–125%, the Ra parameter is quite stable. But in the range of 75–100% and with other factors unchanged, the workpiece surface roughness gradually decreases.

Grinding modes have less effect on the surface morphology of the part treated with a mineral ceramic tool, compared to the characteristics of the tool itself. The change in the normal pressure force in the contact zone of the abrasive wheel and the part almost does not affect the counter-sample roughness parameters.

The tests have shown that the increase in the linear sliding speed (rotation speed) of the abrasive mineral ceramic tool decreases the counter-sample surface roughness. In this case, a local change in the physical and mechanical properties of the counter-sample material due to the frictional heating of the surfaces in the contact zone plays the main role. To reduce roughness significantly, the speed must be very high (roughness is halved at a sliding speed of more than 100 m/s). However, due to structural considerations, the operation of diamond-bearing composite materials at speeds over 30 m/s is not advisable, since it leads to its destruction. The counter-sample roughness is essentially independent

of the abrasive processing speed in the recommended speed ranges and with good heat removal from the friction zone provided by the aluminum substrate of the mineral ceramic tool and a lubricant.

After processing the test results, we have obtained an empirical dependence of the surface profile parameter Ra of the workpiece in the form:

$$Ra = 8.81 \cdot 10^{-19} \cdot d^4 \cdot H_M^{0.67} \cdot H_K^{0.54} \cdot \left(\frac{10^{-4}K_V^2 + 1.25}{10^{-4}K_V^2 + 1} \right)$$

here d is the diamond grit in the mineral ceramic material indicated by the numbers of lower fraction (μm); H_M and H_K is microhardness of matrix and counter-sample materials (Pa); K_V is a volumetric concentration of diamonds (%). The calculated roughness values correlate with the experimental values for d from 20 to 200 μm , and K_V from 10 to 30%, with an error not exceeding 15%.

4 Conclusions

A new diamond-bearing mineral ceramic material has been obtained due to the synergy of the materials with unique physical and mechanical properties: diamond and corundum matrix. It has high triboengineering parameters. Abrasive tools made of it have a consistently high volumetric cutting ability, good diamond retention, heat resistance, and a self-sharpening mode during operation.

A relationship has been established between the working and structural components of diamond-bearing abrasive materials, the matrix hardness, and the characteristics of the treated surface relief roughness.

The research results obtained in a detailed study of the relationship between grit, diamond concentration, morphology of a diamond-bearing mineral ceramic tool, and the treated surface morphology will be used in the design of new abrasive materials.

References

1. Kumar GBV, Rao CSP, Selvaraj N, Bhagyashekar MS (2010) Studies on Al6061-SiC and Al7075-Al₂O₃ metal matrix composites. *J Miner Mater Charact Eng* 9(1):43–55. <https://doi.org/10.4236/jmmce.2010.91004>
2. Orlova LA, Chainikova AS, Popovich NV, Lebedeva YE (2013) Composites based on aluminum-silicate glass ceramic with discrete fillers. *Glass Ceram* 70(3–4):149–154. <https://doi.org/10.1007/s10717-013-9529-2>
3. Sweet GA, Brochu M, Hexemer RL, Donaldson IW, Bishop DP (2015) Consolidation of aluminum-based metal matrix composites via spark plasma sintering. *Mater Sci Eng: A* 648:123–133. <https://doi.org/10.1016/j.msea.2015.09.027>
4. Gadalov VN, Romanenko DN, Samoilov VV, Nikolaenko AV, Grigoriev SB (2010) Methods for assessing the surface roughness of an electrospark coating after smoothing with mineral ceramics. In: *Proceedings of higher schools. Powder metallurgy and functional coatings*, vol 4. pp 44–46
5. Popov AI, Mohammad NZ (2006) Increase of serviceability of cutting plates from mineral ceramics by ionic-vacuum processing. *Metalloobrabotka* 4(34):16–19

6. Vasilkov DV, Kochina TB (2011) Cutting forces during high-speed treatment of nickel-based alloys with mineral ceramics tools. *Metalloobrabotka* 4(64):11–14
7. Jessen T, Ustundag E (2000) 24th annual conf on composites, advanced ceramics, materials, and structures A. ceramic engineering and science proceedings, vol 21(3). American Ceramic Society, Westerville, OH. http://sk8es4mc2l.search.serialssolutions.com/?sid=sersol&SS_jc=TC0000715049&title=24th
8. Bolotov AN, Novikov VV, Novikova OO (2006) Application of microarc oxidation to obtain ceramic diamond-bearing material. *Strengthening Technologies Coatings* 3:13–16
9. Bolotov AN, Novikov VV, Novikova OO (2020) Synthesis of abrasive tools with diamond ceramic coating for precision micromachining of superhard materials. *All Materials Encyclopedic Reference* 4:30–37
10. Bolotov AN, Novikov VV, Novikova OO (2020) Mineral ceramic composite material: synthesis and frictional properties. *Metal Working Mater Sci* 22(3):59–68
11. Sudnik LV, Vityaz PA, Ilyushchenko AF (2012) Diamond-bearing abrasive nanocomposites. *Belaruskaya Navuka*, Minsk
12. Bolotov AN, Novikov VV, Novikova OO (2017) Wear dependence of a composite diamond-bearing material—ceramics friction pair. *Mechanics and Physics of Processes on the Surface and in Contact of Solids, Parts of Technol and Power Equipment* 10:153–157
13. Vityaz PA (2013) Detonation synthesis nanodiamonds: production and application. Monograph. *Belaruskaya Navuka*, Minsk
14. Polushin NI, Laptev AI, Sorokin MN, Tleuzhev AB, Kushkhabiev AS, Taov RV (2013) Dependence of the abrasive ability of diamond dressing tools on metal matrix mechanical properties. In: *Proceedings of Higher Schools. Powder metallurgy and functional coatings*, vol 3. pp 87–91
15. Yanyushkin AS, Lobanov DV, Skiba VYu, Gartfelder VA, Sekletina LS (2017) Improving the efficiency of metal-bonded diamond tools when grinding high-strength materials. *Metal Working Mater Sci* 3(76):17–27
16. Pereladov AB (2018) Determining the performance of modified bond diamond tools when grinding hard alloy. *Metalloobrabotka* 5(107):2–6
17. Shits EYu, Semenova ES, Koryakina VV (2010) Operational and mechanical properties of a diamond-abrasive composition based on ultra-high-molecular-weight polyethylene. *Mater Sci* 8:22–26
18. GOST 19300-86 (1986) Profilometry methods
19. Xu H, Yang Z, Li MK, Shi YL, Huang Y, Li HL (2005) Synthesis and properties of electroless Ni-P-Nanometer Diamond composite coatings. *Surf Coat Technol* 191(2–3):161–165. <https://doi.org/10.1016/j.surfcoat.2004.03.045>
20. Gubarevich AV, Usuba S, Kakudate Y, Tanaka A, Odawara O (2004) Diamond powders less than 100 nm in diameter as effective solid lubricants in vacuum. *Jpn J Appl Phys, Part 2: Letters* 43 7A. <https://doi.org/10.1143/JJAP.43.L920>



Mathematical Model of a Lubricant in a Bearing with a Fusible Coating on the Pilot and Irregular Slider Profile

M. A. Mukutadze and E. O. Lagunova^(✉)

Rostov State Transport University (FSBEIHE RSTU), 2 Rostovskogo Strelkovogo Polka
Narodnogo Opolcheniya sq., Rostov-on-Don 344038, Russia

Abstract. Using the well-known equation for a “thin layer” of fluid flow with truly viscous rheological properties, the continuity equation, as well as the equation defining the profile of the molten profile of the pilot taking into account the expression for the mechanical energy dissipation rate, an asymptotic solution is proposed for the system of differential equations in the form of series for parameter powers characterizing the melt of the surface coating. An exact automodeling solution for zero and first approximations was applied allowing to determine the lubricating layer’s velocity field and pressure taking into account melting of the coating as well as the adapted profile of the pilot’s support surface. This allows determining the main properties of the tribo-node, i.e., load capacity and friction force leading to specific hydrodynamic flow conditions in a pre-emergency situation. New multiparametric expressions have been developed for the main performance characteristics of a wedge-shaped sliding support with incomplete filling of the working gap, as well as taking into account the melt of the guide surface coated with a low-melting metal alloy. The resulting refined calculation models allow, as a result of varying the low-melting coating on the surface of the guide, to adjust the ratio of its bearing capacity and the coefficient of friction.

Keywords: Wedge-shaped support · Adapted profile · Hydrodynamic mode · Low-melting coating · Incomplete filling · Self-similar solution · Asymptotic solution · Zero approximation · First approximation

1 Introduction

Modern mechanical engineering mostly focuses on increasing the power and efficiency of manufactured units and machines, as well as on providing energy-saving technologies. A sufficient number of studies [1–22] are devoted to the development of a mathematical calculation model of sliding bearings with a fusible metal coating of movable and fixed contact surfaces. However, the surface melt based lubrication is not a self-sustaining process. To ensure a self-sustaining tribo-node lubrication process, fusible coatings shall be provided on one of the working contact surfaces, as well as permanent lubrication, which can be provided by a constant lubricant supply or an adapted support surface profile in the sliding bearing. This study provides a mathematical calculation model

of the hydrodynamic flow of the lubricant and the pilot’s coating surface melt, which have truly viscous rheological properties in the operating clearance of the wedge-shaped sliding support with the sliding support surface adapted to the friction conditions at incomplete filling (pre-emergency state) of the operating clearance.

2 Problem Definition

Let us consider the flow of lubricant and melt in the operating clearance. A support ring with a fusible coating moves at a speed u^* , while an inclined pilot with a support surface profile adapted to friction conditions is stationary (Fig. 1).

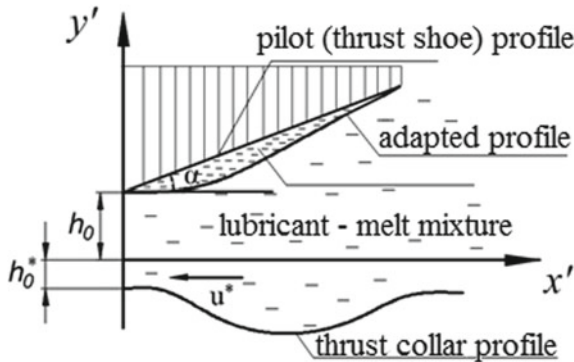


Fig. 1 Design diagram

The design diagram uses the Cartesian coordinate system. The tribo-system element profiles have the following designations: C_0 —linear pilot surface profile; C_1 —irregular slider surface profile; C_2 —pilot molten surface profile.

$$C_0 : y' = h_0 + x' tg \alpha; C_1 : y' = h_0 + x' tg \alpha - a' \sin \omega' x'; C_2 : y' = -\lambda' f'(x'). \quad (1)$$

Let us use the following notation: h_0 —lubricating film thickness in the initial section; h_0^* —molten layer thickness in the initial section; l —pilot’s surface length; α —pilot’s tilt against axis Ox' ; ω' —adapted pilot profile parameter; a' —disturbance amplitude.

This problem can be solved by using well-known equations for a “thin layer” of fluid flow with truly viscous properties, the continuity equation, as well as the equation describing the pilot’s surface molten profile.

3 Initial Equations and Boundary Conditions

In accordance with generally accepted simplifications and the associated boundary conditions, this system of equations will be written in the following form in the Cartesian coordinate system:

$$\frac{\partial^2 v}{\partial y^2} = \frac{dp}{dx}; \quad \frac{\partial v}{\partial x} + \frac{\partial u}{\partial y} = 0; \quad -\frac{d\Phi(x)}{dx} = K \int_{-\Phi(x)}^{h(x)} \left(\frac{\partial v}{\partial y} \right)^2 dy, \quad (2)$$

$$\begin{aligned}
 v = 0, \quad u = 0 \quad \text{at } y = h(x) = 1 + \eta x - \eta_1 \sin \omega x; \\
 v = -1, \quad u = 0 \quad \text{at } y = -\Phi(x); \Phi = -\frac{h_0^*}{l} \quad \text{at } x = 0; p(x_1) = p(x_2) = 0. \\
 \Phi(0) = 0,
 \end{aligned}
 \tag{3}$$

where

$$K = \frac{2\mu u^* l}{h_0 L^*}, \eta = \frac{tg\alpha}{h_0}, \eta_1 = \frac{a'}{h_0}.$$

Let us use the following notation: u, v —velocity vector components; p —lubricant pressure in the operating clearance; K —parameter describing the coating melt; L^* —specific heat of support ring coating melting; $\Phi(x)$ —function describing the molten-coating profile.

A conventional technique is used for conversion to the dimensionless quantities:

$$x' = lx; \quad y' = h_0 y; \quad v_{x'} = u^* v; \quad v_{y'} = \frac{h_0}{l} u^* u; \quad \omega = \omega' l; \quad p' = p^* p; \quad p^* = \frac{\mu u^* l}{h_0^2}.$$
(4)

Let us find the asymptotic solution (2)–(3) in the form of series:

$$\begin{aligned}
 v(x, y) &= v_0(x, y) + K v_1(x, y) + K^2 v_2(x, y) + \dots, \\
 u(x, y) &= u_0(x, y) + K u_1(x, y) + K^2 u_2(x, y) + \dots, \\
 p(x) &= p_0(x) + K p_1(x) + K^2 p_2(x) + K^3 p_3(x) + \dots, \\
 \Phi(x) &= 0 - K \Phi_1(x) - K^2 \Phi_2(x) - K^3 \Phi_3(x) - \dots
 \end{aligned}
 \tag{5}$$

Taking into account (5) in (2), we obtain a system of equations and associated boundary conditions.

- The following is true for zero approximation:

$$\frac{\partial^2 v_0}{\partial y^2} = \frac{dp_0}{dx}, \quad \frac{\partial v_0}{\partial x} + \frac{\partial u_0}{\partial y} = 0,$$
(6)

$$\begin{aligned}
 u_0 = 0, \quad v_0 = 0 \quad \text{at } y = 1 + \eta x - \eta_1 \sin \omega x + \Phi_0; \\
 v_0 = -1, \quad u_0 = 0 \quad \text{at } y = 0, \quad p_0(x_1) = p_0(x_2) = 0.
 \end{aligned}
 \tag{7}$$

- The following is true for the first approximation:

$$\frac{\partial^2 v_1}{\partial y^2} = \frac{dp_1}{dx}; \quad \frac{\partial v_1}{\partial x} + \frac{\partial u_1}{\partial y} = 0; \quad \frac{d\Phi_1(x)}{dx} = -K \int_0^{h(x)} \left(\frac{\partial v_0}{\partial y} \right)^2 dy,$$
(8)

$$u_1 = 0, \quad v_1 = 0 \quad \text{at } H(x) = 1 + \eta x - \eta_1 \sin \omega x + \Phi_1(x);$$

$$\begin{aligned}
 v_1 &= \left(\frac{\partial v_0}{\partial y} \right) \Big|_{y=0} \cdot \Phi_1(x); \\
 u_1 &= \left(\frac{\partial u_0}{\partial y} \right) \Big|_{y=0} \cdot \Phi_1(x); p_1(x_1) = p_1(x_2) = 0.
 \end{aligned}
 \tag{9}$$

Let us find the problem solution for the zero approximation in the form:

$$\begin{aligned}
 v_0(x, y) &= \frac{\partial \psi_0(x, y)}{\partial y} + V_0(x, y); \\
 u_0(x, y) &= -\frac{\partial \psi_0(x, y)}{\partial x} + U_0(x, y); \\
 \psi_0(x, y) &= \tilde{\psi}_0(\xi); \quad \xi = \frac{y + \Phi_0}{h(x) + \Phi_0}; \\
 V_0(x, y) &= \tilde{v}(\xi); \quad U_0(x, y) = \tilde{u}_0(\xi) \cdot h'(x).
 \end{aligned}
 \tag{10}$$

Taking into account (10) in (6)–(7), we obtain a system of equations and associated boundary conditions:

$$\tilde{\psi}_0'''(\xi) = \tilde{C}_2; \quad \tilde{v}_0''(\xi) = \tilde{C}_1; \quad \tilde{u}_0'(\xi) - \varepsilon \tilde{v}_0'(\xi) = 0; \quad \frac{dp_0}{dx} = \frac{C_1}{h^2(x)} + \frac{C_2}{h^3(x)}.
 \tag{11}$$

$$\begin{aligned}
 \tilde{\Psi}'_0(0) &= 0, \quad \tilde{\Psi}'_0(1) = 0; \\
 \tilde{u}_0(1) &= 0, \quad \tilde{v}_0(1) = 0; \\
 \tilde{u}_0(0) &= 0,
 \end{aligned}
 \tag{12}$$

$$\tilde{v}_0(0) = -1, \quad \int_0^1 \tilde{v}_0(\xi) d\xi = 0.$$

By solving the system of Eqs. (11)–(12), we obtain the following for the field of velocities and pressure:

$$\begin{aligned}
 \tilde{\Psi}'_0 &= \frac{\tilde{C}_2}{2} (\xi^2 - \xi), \quad \tilde{v}_0(\xi) = \tilde{C}_1 \frac{\xi^2}{2} - \left(\frac{\tilde{C}_1}{2} + 1 \right) \xi - 1; \\
 \tilde{C}_1 &= -6; \quad \tilde{C}_2 = 6(1 + \Phi_0) \left[1 + \frac{\eta}{2} (x_2 + x_1) + \frac{\eta_1}{\omega(x_2 - x_1)} (\cos \omega x_2 - \cos \omega x_1) \right]; \\
 p_0 &= \frac{6}{(1 + \Phi_0)^2} \left(\frac{\tilde{\eta}}{2} (x^2 - x_1^2) + \frac{\tilde{\eta}}{\omega} \sin \frac{\omega(x - x_1)}{2} \sin \frac{\omega(x + x_1)}{2} - \frac{\tilde{\eta}}{2} (x_2 + x_1)(x - x_1) - \right. \\
 &\quad \left. - \frac{2\tilde{\eta}_1(x - x_1)}{\omega(x_2 - x_1)} \sin \frac{\omega(x_2 - x_1)}{2} \sin \frac{\omega(x_2 + x_1)}{2} \right),
 \end{aligned}
 \tag{13}$$

where

$$\tilde{\eta} = \frac{\eta}{1 + \Phi_0}; \quad \tilde{\eta}_1 = \frac{\eta_1}{1 + \Phi_0}.$$

Taking into account (13), we obtain the following expression to determine the function describing the pilot’s molten profile:

$$\Phi_1(x) = \int_0^x \left(h(x) \int_0^1 \left(\frac{\tilde{\psi}_0''(\xi)}{h^2(x)} \right) + \frac{(\tilde{v}_0'(\xi))^2}{h(x)} d\xi \right) dx = x - \frac{\eta}{2}x^2 - \frac{\tilde{\eta}_1}{\omega} \cos \omega x + h_0^* \tag{14}$$

An automodeling solution of system (8) and (9) is found in the same way as for the zero approximation. This allows finding the following for the field of velocities and pressure:

$$\begin{aligned} \tilde{\psi}'_0 &= \frac{\tilde{C}_2}{2} (\xi^2 - \xi), \quad \tilde{v}_1(\xi) = \tilde{C}_1 \frac{\xi^2}{2} - \left(\frac{\tilde{C}_1}{2} + 1 \right) \xi + 1, \\ \tilde{C}_1 &= 6M, \quad \tilde{C}_2 = 6M \left(1 + \tilde{\Phi} \right) \left[1 + \frac{\tilde{\eta}}{2} (x_2 + x_1)^3 + \frac{\tilde{\eta}_1}{\omega(x_2 - x_1)} (\cos \omega x_2 - \cos \omega x_1) \right], \\ p_1 &= \frac{6M}{(1 + \tilde{\Phi})^2} \left(\frac{\tilde{\eta}}{2} (x_2^2 - x_1^2) - \frac{\tilde{\eta}_1}{\omega(x_2 - x_1)} (\cos \omega x_2 - \cos \omega x_1) - \right. \\ &\quad \left. - \frac{\tilde{\eta}}{2} (x_2 + x_1)(x_2 - x_1) - \frac{\tilde{\eta}_1(x_2 - x_1)}{\omega(x_2 - x_1)} (\cos \omega x_2 - \cos \omega x_1) \right) \end{aligned} \tag{15}$$

where

$$\tilde{\eta} = \frac{\eta}{1 - \tilde{\Phi}}; \quad \tilde{\eta}_1 = \frac{\eta_1}{1 - \tilde{\Phi}}; \quad \tilde{\Phi} = \sup_{x \in [x_1; x_2]} \Phi_1(x); \quad M = \sup_{x \in [x_1; x_2]} \left. \frac{\partial v_0}{\partial y} \right|_{y=0} \cdot \Phi_1(x).$$

Taking into account (6), (8), (13), and (15), we find the bearing capacity and friction force by the formulas:

$$W = p^* l \int_{x_1}^{x_2} (p_0 + K p_1) dx; \quad L_{TP} = \mu \int_{x_1}^{x_2} \left(\left. \frac{\partial v_0}{\partial y} \right|_{y=0} + K \left. \frac{\partial v_1}{\partial y} \right|_{y=0} \right) dy \tag{16}$$

4 Results and Discussion

The theoretical and experimental studies allowed to establish that the combination of the adapted profile of the pilot’s support surface and a fusible surface coating, which is optimal in terms of bearing capacity and friction force, allows increasing the bearing capacity by 15–17% and reducing the friction force by 10–12% (Table 1). Satisfactory convergence of theoretical and experimental results has been established, which confirms the reliability of the developed theoretical model. Technical tests using a friction machine showed a significant (up to 22%) reduction of the wear spot and longer life of lubricating film (up to 25%).

Table 1 Experimental study

Replicate experiments	Friction coefficient		
	Conventional	Fusible coating	Fusible coating and adapted profile
1	0.0048	0.0038	0.0024
2	0.0051	0.0040	0.0025
3	0.0057	0.0041	0.0024
4	0.0061	0.0044	0.0027
5	0.0067	0.0048	0.0028
Average	0.0052	0.0042	0.0025

References

- Zadorozhnaya E, Hudyakov V, Dolgushin I (2020) Evaluation of thermal condition of turbocharger rotor bearing. Lecture Notes in Mechanical Engineering, pp 1183–1193. https://doi.org/10.1007/978-3-030-22041-9_123
- Levanov IG, Zadorozhnaya EA, Mukhortov IV, Eschiganov MO (2020) Study of effect of metal oleates on mixed and boundary lubrication. Tribol Ind 42(3):461–467. <https://doi.org/10.24874/ti.708.06.19.08>
- Kandeva M, Rozhdstvensky YV, Svoboda P, Kalitchin Z, Zadorozhnaya E (2020) Influence of the size of silicon carbide nanoparticles on the abrasive wear of electroless nickel coatings. Part 2. J Environ Prot Ecol 21(1):222–233
- Zadorozhnaya E, Levanov I, Kandeva M (2019) Tribological research of biodegradable lubricants for friction units of machines and mechanisms: current state of research lecture notes in mechanical engineering 0(9783319956299), pp 939–947. https://doi.org/10.1007/978-3-319-95630-5_98
- Levanov I, Zadorozhnaya E, Vichnyakov D (2019) Influence of friction geo-modifiers on HTHS viscosity of motor oils. Lecture Notes in Mechanical Engineering 0(9783319956299):967–972. https://doi.org/10.1007/978-3-319-95630-5_101
- Mukhortov I, Zadorozhnaya E, Kandeva M, Levanov I (2019) Studying the possibility of using complex esters as AW/EP additives. Tribol Ind 41(3):355–364. <https://doi.org/10.24874/ti.2019.41.03.05>
- Levanov I, Zadorozhnaya E, Kandeva M, Kalitchin Z, Dolgushina N, Polyacko E (2019) Influence of friction geo-modifier on antiwear properties of plastic lubricants. J Environ Prot Ecol 20(3):1303–1309
- Zadorozhnaya E, Sibiryakov S, Hudyakov V (2017) Theoretical and experimental investigations of the rotor vibration amplitude of the turbocharger and bearings temperature. Tribol Ind 39(4):452–459. <https://doi.org/10.24874/ti.2017.39.04.04>
- Mukhortov IV, Pochkaylo KA, Zadorozhnaya EA (2016) The influence of anti-wear additives on the bearings hydro-mechanical characteristics. Procedia Eng 150:607–611. <https://doi.org/10.1016/j.proeng.2016.07.052>
- Akhverdiev KS, Mukutadze MA, Lagunova EO, Vasilenko VV (2017) Hydrodynamic calculation of a radial bearing lubricated with molten low-melting coating in the presence of a lubricant. Bull RSTU 2(66):129–135
- Akhverdiev KS, Lagunova EO, Vasilenko VV (2017) Calculation model of a radial bearing lubricated by the melt, taking into account the dependence of viscosity on pressure. Vestnik of DSTU 3(90):27–37

12. Vasilenko VV, Lagunova EO, Mukutadze MA (2017) Hydrodynamic calculation of a radial bearing lubricated by a melt of a fusible coating in the presence of a lubricant. Internet Magazine Naukovedenie 9(5). <https://naukovedenie.ru/PDF/20TVN517.pdf>
13. Lagunova EO (2017) Wedge-shaped sliding supports operating on viscoelastic lubricant material due to the melt, taking into account the dependence of viscosity and shear modulus on pressure. Int J Appl Eng Res 12(19):9120–9127
14. Lagunova EO (2017) Radial plain bearings operating on viscoelastic lubricant conditioned by the melt, taking into account the dependence of the viscosity of the lubricant and the shear modulus on the pressure. Int J Appl Eng Res 12(19):9128–9137
15. Vasilenko VV, Lagunova EO, Mukutadze MA, Prikhodko VM (2017) Calculation model of the radial bearing, caused by the melt, taking into account the dependence of viscosity on pressure. Int J Appl Eng Res 12(19):9138–9148
16. Akhverdiev KS, Mukutadze MA, Lagunova EO, Vasilenko VV (2017) Wedge-shaped sliding supports operating on a micropolar lubricant. Ensured by Melt Bull RSTU 3(67):8–15
17. Mukutadze MA, Lagunova EO, Vasilenko VV (2018) Development of the design model of a hydrodynamic lubricant formed during melting of the axial bearing in the presence of forced lubrication. Problems of Mechanical Engineering and Reliability of Machines 3:76–83
18. Lagunova EO (2018) Calculated model of the radial bearing lubricated by the melt in the turbulent friction mode taking into account viscosity dependence on pressure and temperature. Mech Eng Mach Sci 7(138):19–32
19. Lagunova EO (2018) Calculated model of sleeve bearing lubricated with melt in turbulent conditions of friction//science intensive technologies in mechanical. Engineering 7(85):38–45. https://doi.org/10.30987/article_5b31352a4c2976.03676284
20. Akhverdiev KS, Mukutadze MA, Lagunova EO, Vasilenko VV (2018) Simulation model of a wedge-shaped sliding support operating on a lubricant with a melt. Frict Wear 39(1):62–70
21. Akhverdiev KS, Mukutadze MA, Lagunova EO (2019) Wedge-shaped sliding support operating simultaneously on forced lubrication and that ensured by melting its surfaces. Bull Rostov State Transp Univ 2(74):8–14
22. Lagunova EO, Mukutadze MA (2019) Calculation of a radial slider bearing with a fusible coating. J Frict Wear 40(1):88–94



Micropolar Lubricants in a Bearing with a Low-Melting Base Ring Coating and a Porous Slider Surface Coating

A. M. Mukutadze, A. N. Opatskikh^(✉), and V. M. Prikhodko

Rostov State Transport University (RSTU), 2, Rostovskogo Strelkovogo Polka Narodnogo Opolcheniya sq., Rostov-on-Don 344038, Russia

Abstract. In the study, an asymptotic self-similar solution is found for the zero (without considering the melting) and first (considering the melting) approximation based on the equation describing the flow of a liquid lubricant and a molten coating in the running clearance of wedge-shaped sliding support with micropolar properties, the continuity equation, the Darcy equation describing the lubricant flow in the porous coating body, and the equation describing the profile of the molten contour of the guide surface. As a result, the fields of velocities and pressures in the lubricating and porous bodies are determined with and without considering the melting. Using the equation for the field of velocities and pressures, a function describing the molten guide coating contour, as well as the bearing capacity and friction force are determined. The impact of the molten guide coating parameters, the porous layer thickness, as well as N^2 и N_1 characterizing the micropolar lubricant properties are estimated.

Keywords: Sliding support · Hydrodynamics · Micropolar lubricant · Low-melting coating · Molten coating · Melt · Asymptotic solution · Asymptotic solution · Self-similar solution

1 Introduction

A sufficient number of publications [1–9] are dedicated to developing a mathematical model of the micropolar lubricant flow in the bearing running clearance. They provide simulation models of the hydrodynamic regime of lubrication with a micropolar lubricant in the absence of the low-melting metal coating melt on the working surfaces.

A feature of the existing simulation models for the considered bearing designs operating on micropolar lubricants and melts of low-melting metal coatings is the lack of self-sustaining lubrication [10–21]. To ensure the self-sustaining lubrication of journal bearings and damping properties, not only low-melting coating on one surface but also a porous layer on the another is needed. This study provides a calculation of the hydrodynamic flow of a lubricant and a molten coating with micropolar rheological properties in the running clearance and the porous coating body.

2 Research Objective

The flow of a liquid lubricant and a molten metal coating in the running clearance and porous coating of a thrust bearing is studied. In this case, the surface of the guide with a low-melting coating moves at a velocity u^* , and the inclined slider with a porous coating is fixed (Fig. 1).

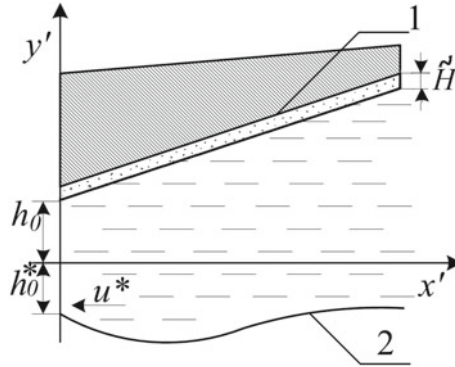


Fig. 1 Calculation scheme

The calculation scheme is built in the Cartesian coordinate system $x'o'y'$. The contour of the working slider surface is coated with a porous material, and the guide surface with a low-melting metal, the melt contour of which is described as follows:

$$y' = h_0 + x' \operatorname{tg} \alpha, \quad y' = -\eta' f'(x'). \tag{1}$$

3 Basic Equations and Boundary Conditions

To solve this problem, we use the well-known dimensionless flow equations of a micropolar liquid, the continuity equations, the Darcy equation, and the equation describing the profile of the molten contour of the guide surface:

$$\begin{aligned} \frac{\partial^2 u}{\partial y^2} + N^2 \frac{\partial v}{\partial y} &= \frac{1}{\mu} \frac{dp}{dx}, \\ \frac{\partial^2 v}{\partial y^2} &= \frac{v}{N_1} + \frac{1}{N_1} \frac{\partial u}{\partial y}, \\ \frac{\partial u}{\partial x} + \frac{\partial v}{\partial y} &= 0; \\ \frac{\partial^2 P}{\partial x^{*2}} + \frac{\partial P}{\partial y^{*2}} &= 0, \\ \frac{d\Phi(x)}{dx} &= K \int_{-\Phi(x)}^{h(x)} \left(\frac{\partial u}{\partial y} \right)^2 dy. \end{aligned} \tag{2}$$

Using the universally accepted simplifications, let us write down the boundary conditions for the system of equations in the lubricating and porous layer between the inclined slider and the guide as follows:

$$\begin{aligned}
 v &= 0, \quad v = 0, \quad u = 0, \quad \text{at } y = 1 + \eta x = h(x); \\
 v &= 0, \quad v = 0, \quad u = -1 \text{ at } y = -\Phi(x); \\
 p(0) &= p(1) = \frac{p_a}{p^*}; \quad p = P \text{ at } y^* = 1 + \eta x + \frac{\tilde{H}}{h_0}; \\
 u &= \tilde{M} \frac{\partial P}{\partial y^*} \text{ at } y^* = 1 + \eta x + \frac{\tilde{H}}{h_0}; \\
 \frac{\partial P}{\partial y^*} &= 0 \text{ at } y^* = 1 + \eta x;
 \end{aligned} \tag{3}$$

where

$$\tilde{M} = \frac{kl}{h_0^3}, \quad \eta = \frac{ltg\alpha}{h_0}, \quad K = \frac{2\mu_0 u^*}{h_0 L'}.$$

To pass to dimensionless variables, the standard technique is applied:

$$\begin{aligned}
 u' &= u^* u; \quad v' = u^* \varepsilon v; \quad v' = v^* v; \quad p' = p^* p; \quad y' = h_0 y; \quad N^2 = \frac{\kappa}{2\mu + \kappa}; \\
 N_1 &= \frac{2\mu l^2}{\kappa h_0^2}; \quad l^2 = \frac{\gamma}{4\mu}; \\
 \varepsilon &= \frac{h_0}{L}; \quad v^* = \frac{u^*}{2h_0}; \quad p^* = \frac{(2\mu + \kappa)Lu^*}{2h_0^2}; \quad x' = Lx.
 \end{aligned} \tag{4}$$

in a porous layer:

$$x' = Lx^*; \quad y' = Ly^*; \quad P' = p^* P. \tag{5}$$

In the further solution, we will consider the clearance smallness along with the equality $v = 0$ on both moving and fixed surfaces and average the second equation of system (2) over the lubricating layer thickness; as a result, from Eq. (2), we obtain:

$$\begin{aligned}
 \frac{\partial^2 u}{\partial y^2} + \frac{N^2}{2N_1 h(x)} (2y - h(x)) &= e^{\frac{1}{\mu}} \frac{dp}{dx}, \\
 v &= \frac{1}{2N_1 h(x)} (y^2 - h(x)y), \\
 \frac{\partial u}{\partial x} + \frac{\partial v}{\partial y} &= 0, \\
 \frac{\partial^2 P}{\partial x^{*2}} + \frac{\partial P}{\partial y^{*2}} &= 0 \\
 \frac{d\Phi(x)}{dx} &= K \int_{-\Phi(x)}^{h(x)} \left(\frac{\partial u}{\partial y} \right)^2 dy.
 \end{aligned} \tag{6}$$

Let us expand the function $\Phi(x)$ by the K parameter characterizing the molten surface coating:

$$\Phi(x) = -K\Phi_1(x) - K^2\Phi_2(x) - K^3\Phi_3(x) - \dots = H(x), \tag{7}$$

According to the universally accepted simplifications of the velocity components, the boundary conditions for the contour $y = -\Phi(x)$ will have the form:

$$\begin{aligned} v(0 - H(x)) &= v(0) - \left(\frac{\partial v}{\partial y}\right)\Big|_{y=0} H(x) - \left(\frac{\partial^2 v}{\partial y^2}\right)\Big|_{y=0} H^2(x) - \dots = 0; \\ u(0 - H(x)) &= u(0) - \left(\frac{\partial u}{\partial y}\right)\Big|_{y=0} H(x) - \left(\frac{\partial^2 u}{\partial y^2}\right)\Big|_{y=0} H^2(x) - \dots = -1. \end{aligned} \tag{8}$$

Considering (3) and (8), the asymptotic solution of system (6) will be written as follows:

$$\begin{aligned} v &= v_0(x, y) + Kv_1(x, y) + K^2v_2(x, y) + \dots \\ u &= u_0(x, y) + Ku_1(x, y) + K^2u_2(x, y) + \dots \\ \Phi(x) &= -K\Phi_1(x) - K^2\Phi_2(x) - K^3\Phi_3(x) - \dots \\ P(x) &= P_0 + KP_1(x) + K^2P_2(x) + K^3P_3(x) \dots \end{aligned} \tag{9}$$

Using (9), from (6), we obtain a system of equations and appropriate boundary conditions:

- for zero approximation:

$$\frac{\partial^2 u_0}{\partial y^2} + \frac{N^2}{2N_1 h(x)}(2y - h(x)) = \frac{1}{\mu} \frac{dz_0}{dx}, \quad \frac{\partial v_0}{\partial x} + \frac{\partial u_0}{\partial y} = 0, \quad \frac{\partial^2 P_0}{\partial x^{*2}} + \frac{\partial P_0}{\partial y^{*2}} = 0 \tag{10}$$

$$v_0 = 0, \quad v_0 = 0, \quad u_0 = 0, \quad \text{at } y = 1 + \eta x;$$

$$v_0 = 0, \quad u_0 = -1, \quad v_0 = 0, \quad \text{at } y = 0;$$

$$P_0(0) = P_0(1) = \frac{Pa}{p^*}$$

$$p_0 = P_0 \text{ at } y^* = 1 + \eta x + \frac{\tilde{H}}{h_0}; \tag{11}$$

$$u_0 = \tilde{M} \frac{\partial P_0}{\partial y^*} \text{ at } y^* = 1 + \eta x + \frac{\tilde{H}}{h_0};$$

$$\frac{\partial P_0}{\partial y^*} = 0 \text{ at } y^* = 1 + \eta x$$

- for the first approximation:

$$\begin{aligned} \frac{\partial^2 u_1}{\partial y^2} &= \frac{1}{\mu} \frac{dP_1}{dx}; \\ \frac{\partial v_1}{\partial x} + \frac{\partial u_1}{\partial y} &= 0; \\ \frac{d\Phi_1(x)}{dx} &= K \int_{-\Phi_0}^{1+\eta x} \left(\frac{\partial u_0}{\partial y} \right)^2 dy; \end{aligned} \tag{12}$$

$$\begin{aligned} \frac{\partial^2 P_1}{\partial x^{*2}} + \frac{\partial P_1}{\partial y^{*2}} &= 0 \\ v_1 &= \left(\frac{\partial v_0}{\partial y} \right) \Big|_{y=0} \cdot \Phi_1(x); \\ u_1 &= \left(\frac{\partial u_0}{\partial y} \right) \Big|_{y=0} \cdot \Phi_1(x); \end{aligned}$$

$$\begin{aligned} v_1 = 0, \quad v_1 = 0, \quad u_1 = 0 &\text{ at } y = 1 + \eta x; \\ P_1(0) = P_1(1) &= 0, \\ \Phi(0) = \Phi(1) &= h^*, \end{aligned}$$

$$p_1 = P_1 \text{ at } y^* = 1 + \eta x + \frac{\tilde{H}}{h_0}; \tag{13}$$

$$u_1 = \tilde{M} \frac{\partial P_1}{\partial y^*} \text{ at } y^* = 1 + \eta x + \frac{\tilde{H}}{h_0};$$

$$\frac{\partial P_1}{\partial y^*} = 0 \text{ at } y^* = 1 + \eta x;$$

The self-similar solution for the system of Eqs. (10) and (11) will have the form:

$$\begin{aligned} u_0(x, y) &= \frac{\partial \psi_0(x, y)}{\partial x} + U_0(x, y); \\ v_0(x, y) &= -\frac{\partial \psi_0(x, y)}{\partial y} + V_0(x, y); \\ \psi_0(x, y) &= \tilde{\psi}_0(\xi); \\ \xi &= \frac{y}{h(x)}; \\ V_0(x, y) &= -\tilde{v}(\xi) \cdot h'(x); \\ U_0(x, y) &= \tilde{u}_0(\xi); \\ \tilde{u}'_0(\xi) + \xi \tilde{v}'_0(\xi) &= 0. \end{aligned} \tag{14}$$

Substituting Eq. (14) into the system of (10) and (11), we obtain a system of equations and appropriate boundary conditions:

$$\begin{aligned} \psi'''_0(\xi) &= \tilde{C}_2; \\ \tilde{u}''_0(\xi) &= \tilde{C}_1 - \frac{N^2}{2N_1} (2\xi - 1); \\ \frac{dp_0}{dx} &= \left(\frac{\tilde{C}_1}{h^2(x)} + \frac{\tilde{C}_2}{h^3(x)} \right); \end{aligned} \tag{15}$$

$$\begin{aligned} \tilde{\psi}'_0(0) = 0, \quad \tilde{\psi}'_0(1) = 0; \quad \tilde{u}_0(1) = 0, \quad \tilde{v}_0(1) = 0; \quad v(0) = v(1) = 0, \\ \tilde{u}_0(0) = 1, \quad \tilde{v}_0(0) = 0, \quad \int_0^1 \tilde{u}_0(\xi) d\xi = 0, \quad p_0(0) = p_0(1) = e^{\frac{p_a}{p^*}}, \end{aligned} \tag{16}$$

$$u = \tilde{M} \frac{\partial P}{\partial y^*} \text{ at } y^* = 1 + \eta x;$$

Solving the problem (15) and (16), we obtain the calculation formulas:

$$\begin{aligned} \tilde{\psi}'_0(\xi) &= \frac{\tilde{C}_2}{2} (\xi^2 - \xi), \quad \tilde{C}_1 = 6, \\ \tilde{u}_0(\xi) &= \tilde{C}_1 \frac{\xi^2}{2} - \frac{N^2}{2N_1} \left(\frac{\xi^3}{3} - \frac{\xi^2}{2} \right) - \left(\frac{N^2}{12N_1} + \frac{\tilde{C}_1}{2} + 1 \right) \xi + 1. \\ \tilde{C}_2 &= -\tilde{C}_1 \left(1 + \frac{1}{2} \eta \right), \\ p_0 &= \tilde{C}_1 \frac{\eta}{2} (x - x^2) + \frac{p_a}{p^*} \end{aligned} \tag{17}$$

Considering (17), the Darcy equation is solved as follows:

$$P_0(x, y^*) = R_0(y^*) + \frac{\eta}{2} (x^2 - x) \tilde{C}_1 + \frac{p_a}{p^*} \tag{18}$$

Substituting Eq. (18) into the Darcy equation in the system (10) for the function $R(y^*)$, we obtain:

$$R''_0(y^*) + \frac{\eta}{2} \left(1 + \alpha \frac{p_a}{p^*} - \frac{\alpha^2}{2} \left(\frac{p_a}{p^*} \right)^2 \right) \tilde{C}_1 = 0 \tag{19}$$

$$R_0(0) = \frac{p_a}{p^*}; \quad \frac{\partial R}{\partial y^*} = 0 \text{ at } y^* = 1 + \eta x + \frac{\tilde{H}}{h_0} \tag{20}$$

Solving the problem (19) and (20), we obtain the calculation formula:

$$R(y^*) = -\tilde{C}_1 \eta \left(1 + \alpha \frac{p_a}{p^*} - \frac{\alpha^2}{2} \left(\frac{p_a}{p^*} \right)^2 \right) \left(\frac{y^*}{2} + \left(1 + \eta x + \frac{\tilde{H}}{h_0} \right) y^* \right) + \frac{p_a}{p^*} \tag{21}$$

Solving $\tilde{M} \frac{\partial P_0}{\partial y^*} \Big|_{y^*=1+\eta x+\frac{\tilde{H}}{h_0}} = \int_0^1 \tilde{u}_0(\xi) d\xi$, we get the following equation for \tilde{C}_1 :

$$\tilde{C}_1 = \frac{6}{-12\tilde{M}\eta\left(2 + \frac{\tilde{H}}{h_0}\right) + 1} \tag{22}$$

Then we obtain the calculation formula for pressure (zero approximation):

$$P_0 = \frac{3\eta(x^2 - x)}{-12\tilde{M}\eta\left(2 + \frac{H}{h_0}\right) + 1} + \frac{p_a}{P^*} \tag{23}$$

To determine the function of the molten guide contour considering (17), we obtain:

$$\frac{d\Phi_1(x)}{dx} = h(x) \int_0^1 \left(\frac{\psi_0''(\xi)}{h^2(x)} + \frac{\tilde{u}'_0(\xi)}{h(x)} \right)^2 d\xi. \tag{24}$$

Solving (24), we obtain the calculation formula:

$$\Phi_1(x) = \left[\frac{\tilde{C}_1^2}{12} \left(-x + \frac{\eta}{2}x^2\right) + \left(4 + \frac{N^4}{720N_1^2}\right) \left(x - \frac{\eta}{2}x^2\right) \right] + h^*. \tag{25}$$

The self-similar solution of the system of Eqs. (12) and (13) is sought in the same way as for the system of (10) and (11); as a result, for the field of velocities and pressures, we obtain the formulas:

$$\begin{aligned} \tilde{\psi}'_1(\xi) &= \frac{\tilde{C}_2}{2} (\xi^2 - \xi), \\ \tilde{u}_1(\xi) &= \tilde{C}_1 \frac{\xi^2}{2} - \left(\frac{\tilde{C}_2}{2} + M \right) \xi + M, \\ \tilde{C}_2 &= -\tilde{C}_1 \left(1 + \frac{1}{2}\eta \right), \\ P_1 &= \frac{3M\eta(x - x^2)}{12\tilde{M}\eta\left(2 + \frac{\tilde{H}}{h_0}\right) + 1}, \end{aligned} \tag{26}$$

where

$$M = \left| \sup_{x \in [0;1]} \left(\frac{\partial u_0}{\partial y} \right) \Big|_{y=0} \cdot \Phi_1(x) \right|$$

Considering (10), (12), (23), and (26), for the bearing capacity and friction force, we have:

$$W = p^* L \int_0^1 \left(p_0 + K p_1 - \frac{p_a}{p^*} \right) dx =$$

$$\frac{(2\mu_0 + \kappa_0)L^2 u^* \eta}{4h_0^2} \left[\frac{1}{12\tilde{M}\eta \left(2 + \frac{\tilde{H}}{h_0} \right) - 1} + \frac{KM}{12\tilde{M}\eta \left(2 + \frac{\tilde{H}}{h_0} \right) + 1} \right],$$

$$L_{mp} = \mu \int_0^1 \left[\frac{\partial u_0}{\partial y} \Big|_{y=0} + K \frac{\partial u_1}{\partial y} \Big|_{y=0} \right] dx = \mu \left[\left(1 - \frac{\eta}{2} \right) (1 + KM) - \frac{N^2}{12N_1} \left(1 + \frac{\eta}{2} \right) \right]. \tag{27}$$

For numerical analysis, the following ranges of parameters have been used:

$$\begin{aligned} \tilde{H} &= 0.00055 \div 0.003; \mu_0 = 0.001022 \text{ Ns/m}^2; \eta = 0.3 \dots 1 \text{ m}; \\ l &= 0.1256 \dots 0.1884 \text{ m}; u^* = 1 \dots 3 \text{ m/s}; \\ h_0 &= 10^{-7} \dots 2 \cdot 10^{-6} \text{ m}; K = 0.0000022 \dots 0.00052; \\ p_a &= 0.08 \div 0.101325 \text{ MPa}; L' = 35.33 \dots 38.1 \text{ N/m}^2 \end{aligned}$$

Based on the numerical calculation results (average values of the measuring range have been used to build the plots), the plots have been built shown in Fig. 2.

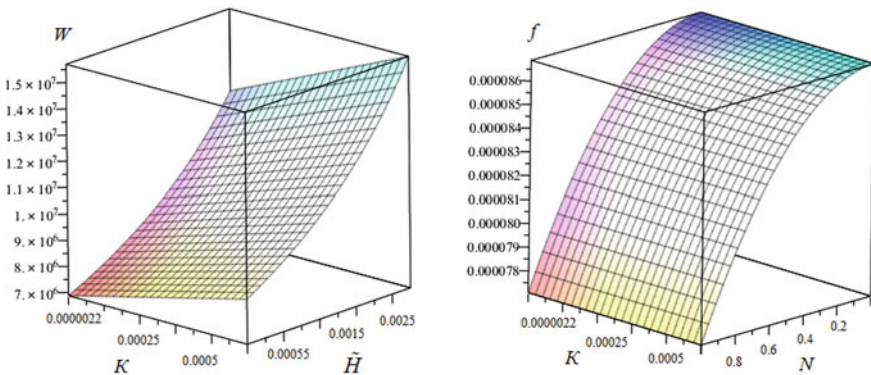


Fig. 2 Dependence of the bearing capacity and the friction factor on the parameter K characterizing the melt, the lubricating film thickness \tilde{H} , and the bond parameter N

4 Conclusions

1. A refined simulation model has been obtained for a wedge-shaped sliding bearing operating under hydrodynamic lubrication on a micropolar liquid lubricant, ensured by the molten low-melting guide surface coating.

2. A significant contribution of the K parameter characterizing the molten low-melting guide surface coating, the bond parameter N , and the lubricating film thickness \tilde{H} is shown.

References

1. Zadorozhnaya E, Hudyakov V, Dolgushin I (2020) Evaluation of thermal condition of turbocharger rotor bearing lecture notes in mechanical engineering, pp 1183–1193. https://doi.org/10.1007/978-3-030-22041-9_123
2. Levanov IG, Zadorozhnaya EA, Mukhortov IV, Eschiganov MO (2020) Study of the effect of metal oleates on mixed and boundary lubrication. *Tribol Ind* 42(3):461–467. <https://doi.org/10.24874/ti.708.06.19.08>
3. Kandeva M, Rozhdstvensky YV, Svoboda P, Kalitchin Z, Zadorozhnaya E (2020) Influence of the size of silicon carbide nanoparticles on the abrasive wear of electroless nickel coatings. Part 2. *J Environ Prot Ecol* 21(1):222–233
4. Zadorozhnaya E, Levanov I, Kandeva M (2019) Tribological research of biodegradable lubricants for friction units of machines and mechanisms: current state of research. *Lect Notes Mech Eng* 0(9783319956299):939–947. https://doi.org/10.1007/978-3-319-95630-5_98
5. Levanov I, Zadorozhnaya E, Vichnyakov D (2019) Influence of friction geo-modifiers on HTHS viscosity of motor oils. *Lect Notes Mech Eng* 0(9783319956299):967–972. https://doi.org/10.1007/978-3-319-95630-5_101
6. Mukhortov I, Zadorozhnaya E, Kandeva M, Levanov I (2019) Studying the possibility of using complex esters as AW/EP additives. *Tribol Ind* 41(3):355–364. <https://doi.org/10.24874/ti.2019.41.03.05>
7. Levanov I, Zadorozhnaya E, Kandeva M, Kalitchin Z, Dolgushina N, Polyacko E (2019) Influence of friction geo-modifier on antiwear properties of plastic lubricants. *J Environ Prot Ecol* 20(3):1303–1309
8. Zadorozhnaya E, Sibiryakov S, Hudyakov V (2017) Theoretical and experimental investigations of the rotor vibration amplitude of the turbocharger and bearings temperature. *Tribol Ind* 39(4):452–459. <https://doi.org/10.24874/ti.2017.39.04.04>
9. Mukhortov IV, Pochkaylo KA, Zadorozhnaya EA (2016) The influence of anti-wear additives on the bearings hydro-mechanical characteristics. *Procedia Eng* 150:607–611. <https://doi.org/10.1016/j.proeng.2016.07.052>
10. Akhverdiev KS, Mukutadze MA, Lagunova EO, Vasilenko VV (2017) Hydrodynamic calculation of a radial bearing lubricated with molten low-melting coating in the presence of a lubricant. *Bull RSTU* 2(66):129–135
11. Mukutadze MA, Mukutadze AM, Opatskikh AN (2019) V-shaped sliding bearings using micropolar lubricants caused by a melt accounting for the dependence of lubricant viscosity and porous layer permeability on pressure. *J Phys: Conf Ser. International conference high-tech and innovations in research and manufacturing, HIRM 2019*, p 01202
12. Mukutadze MA, Opatskikh AN, Morozova AV, Zadorozhnaya NS (2020) Mathematical model of wedge-shaped sliding support with a low melting metal-coated guide for partially filled working gap. *IOP Conf Ser: Mater Sci Eng* 941(1):012064
13. Kruchinina EV, Morozova AV, Mukutadze MA, Opatskikh AN (2020) Simulation model of a journal bearing with a low-melting and porous coating in the structure on different contact surfaces. In: *International multi-conference on industrial engineering and modern technologies, FarEastCon 2020*, p 9271268

14. Mukutadze MA, Vasilenko VV, Mukutadze AM, Opatskikh AN (2019) Mathematical model of a plain bearer lubricated with molten metal. IOP Conf Ser: Earth Environ Sci. International conference on innovations and prospects of development of mining machinery and electrical engineering 2019, p 012021
15. Vasilenko VV, Lagunova EO, Mukutadze MA, Prikhodko VM (2017) Calculation model of the radial bearing, caused by the melt, taking into account the dependence of viscosity on pressure. Int J Appl Eng Res 12(19):9138–9148
16. Akhverdiev KS, Mukutadze MA, Lagunova EO, Vasilenko VV (2017) Wedge-Shaped sliding supports operating on a micropolar lubricant. Ensured by Melt Bull RSTU 3(67):8–15
17. Mukutadze MA, Lagunova EO, Vasilenko VV (2018) Development of the design model of a hydrodynamic lubricant formed during melting of the axial bearing in the presence of forced lubrication. Problems of Mechanical Engineering and Reliability of Machines 3:76–83
18. Akhverdiev KS, Mukutadze MA, Lagunova EO, Vasilenko VV (2018) Simulation model of a wedge-shaped sliding support operating on a lubricant with a melt. Frict Wear 39(1):62–70
19. Akhverdiev KS, Mukutadze MA, Lagunova EO (2019) Wedge-Shaped sliding support operating simultaneously on forced lubrication and that ensured by melting its surfaces. Bull Rostov State Trans Univ 2(74):8–14
20. Mukutadze MA, Khasyanova DU, Mukutadze AM (2020) Hydrodynamic model of a wedge-shaped sliding support with a low-melting metal coating. Problems of Mechanical Engineering and Reliability of Machines 4:51–58
21. Mukutadze MA, Mukutadze AM, Vasilenko VV (2019) Simulation model of thrust bearing with a free-melting and porous coating of guide and slide surfaces. IOP Conf Ser: Mater Sci Eng, 012031



Experimental Evaluation of the Influence of Microgeometry on the Tribological Characteristics of a Radial Plain Bearing

K. Gavrilov^(✉), A. Doikin, and M. Izzatulloev

South Ural State University, 76, Lenin prospect, Chelyabinsk 454080, Russia
gavrilovkv@susu.ru

Abstract. One of the current trends in increasing the bearing capacity of plain bearings is the use of texturing of friction surfaces. To determine the influence of the parameters of the regular microgeometry of the friction surfaces on the hydromechanical characteristics of the “shaft-bearing” tribo-interface, experimental studies were carried out on an II 5018 friction machine II 5018. A model friction unit was developed that allows reproducing test conditions comparable to the real operating mode of sliding bearing of internal combustion engine. To assess the effect of texturing on the operation of plain bearings, three types of regular microgeometry were investigated. The study was based on the analysis of the Gersi-Striebeck diagrams for journal bearing, corresponding in its geometric characteristics to the connecting rod bearing of the crankshaft of the VAZ 21,083 engine. The results indicate that the texturing of the liners affects the operation of journal bearings. Of the three texturing samples under study, the option has been chosen that has the highest bearing capacity, and therefore makes it possible to achieve a change in the friction mode from liquid to boundary at higher loads than in other considered texturing samples. The work was carried out in the laboratory “Tribotechnics” named after V.N. Prokopyev, Department of Automobile Transport, South Ural State University (Chelyabinsk).

Keywords: Texturing surfaces · Friction machine · Bearing capacity · Hydromechanical characteristics

1 Introduction

In terms of energy losses due to friction, piston machines, including piston internal combustion engines, occupy leading positions in power engineering. Up to 30% of energy in such machines is lost to overcome friction losses [1, 2]. In terms of friction losses, the crankshaft sliding bearings take the second place after the “piston-cylinder” tribo-coupling (TC). Thus, reducing frictional losses in these key vehicles is one of the important goals in the design of piston machines. The main ways to reduce these losses include the use of coatings that reduce the coefficient of friction, improved surface treatment technologies, the use of energy-efficient lubricants, and a textured bearing surface. It should be noted that the selection of a lubricant is of great importance to

reduce friction losses in tribo-couplings. However, friction in the lubricated parts still accounts for about 25% of the power loss in reciprocating compressors and internal combustion engines [3].

The potential for taking into account microroughnesses in improving the tribological properties of friction units is one of the key points in ensuring the hydrodynamic friction regime of the vehicle. Microprofilng is designed to reduce friction in tribo-couplings, increase their bearing capacity, reduce wear, and improve the reliability and efficiency of friction units. So, the main types of microprofilng in the piston–cylinder interface include cylinder honing and piston skirt texturing.

Texturing of friction surfaces of hydrodynamic tribo-couplings is one of the promising methods of microprofilng and is the creation of a regular microprofile on the surface in the form of some kind of three-dimensional image texture (mesh or lines with certain geometric dimensions, depth, location) obtained with a laser (laser texturing) or in another way. Surface texturing promotes hydrodynamic effects. As the lubricant flow approaches the unevenness, the pressure increases, as a result of which an additional bearing capacity is created, which improves the working conditions of the tribo-interface and increases its resource.

A secondary lubricating effect acting in the mixed lubrication mode is also known. The liquid located in the lower part of the microrelief can be considered as a secondary source of lubrication resulting from the relative movement of surfaces, which reduces friction in contact [4]. The studies by Hamilton and Allen [5, 6] were the first to look at these phenomena. It has been established that microroughness by adding “irregularities” to one surface of a parallel mechanical seal of a rotating shaft can increase the bearing capacity of the support.

The use of textured surfaces to improve the characteristics of friction units of machines and mechanisms is not a new concept. Since 1965, more than 400 publications on surface texturing can be found, most of which have been published over the past two decades [7]. Among them, more than half of the studies are purely theoretical in nature and are based on various forms of the Reynolds, Navier–Stokes, or Stokes equations. Optimum parameters of surface texturing were found for basic friction units for various purposes, such as support bearings of rotary machines [8], mechanical seals [9], thrust bearings [10], and cylinder liners [11]. However, factors such as oil viscosity, density, and temperature, as well as surface deformation, were ignored in early models.

About a third of publications are related to experimental approaches. Most experiments were carried out with traditional tribometers (unidirectional pin-on-disc tests [12–16] or with piston friction rings [17–21]), while other studies were carried out on real components, including thrust bearings [22–25] and mechanical seals [26–28].

The wide spread of the practical application of texturing of friction surfaces of tribo-couplings is restrained due to insufficient knowledge of the mechanisms that provide an increase in the bearing capacity due to the presence of microtexture on friction surfaces.

The aim of this work is an experimental assessment of the tribotechnical parameters of hydrodynamic tribo-couplings, taking into account the regular microgeometry of the friction surfaces.

2 Description of Experimental Equipment

The experiment was carried out on an II 5018 machine. This machine is designed to test various friction, anti-friction, and lubricants for friction and wear in a wide range of loads and speeds. Measured parameters are friction moment, friction distance, and temperature. The standard friction unit designed for testing according to the “shaft-sleeve” scheme of the II5018 friction machine is not suitable for research for a number of reasons. Firstly, the roller and bushing running surfaces require additional processing. Secondly, the sleeve has no anti-friction coating. Thirdly, a large number of studies require the manufacture of a large number of bushings. In addition, there is no closed lubricant circulation system.

In this regard, for experimental research, the II 5018 friction machine has been modified—a model friction unit has been developed, a standard friction chamber has been modified, a system of continuous supply of lubricant to the bearing under pressure with the possibility of oil heating has been mounted. The scheme of the developed friction unit is shown in Fig. 1.

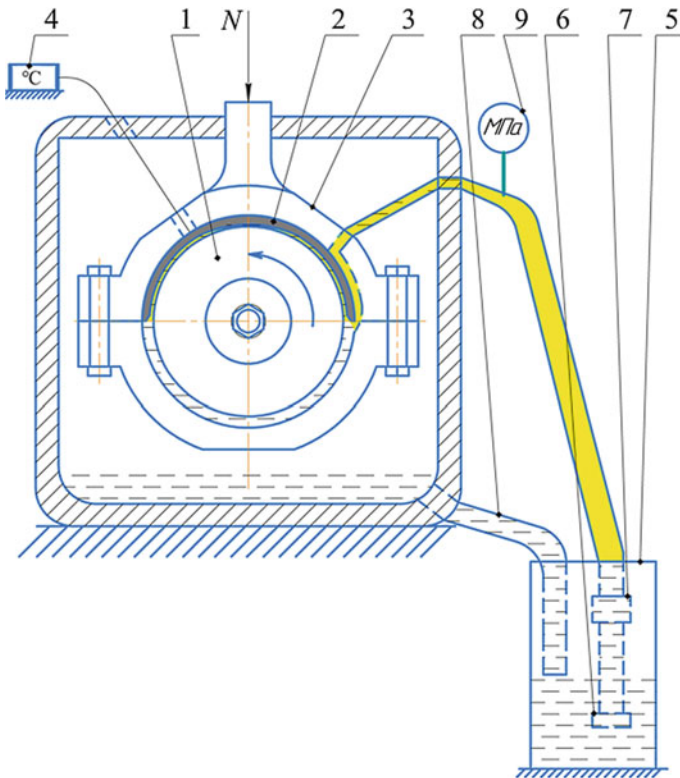


Fig. 1 Scheme of the developed experimental friction unit: 1—shaft; 2—bearing; 3—bearing housing; 4—temperature sensor; 5—reservoir for lubricant; 6—oil filter; 7—pump; 8—back drain; 9—manometer; N —load

Due to the beating of the lower sample, due to the design flaws of the friction machine, the model friction unit was assembled only with the upper journal bearing. This made it possible to achieve better repeatability of measurement results.

Before the experiment, the beat of the roller, simulating the crankshaft journal, was measured using an indicator. To measure the actual load, a BU 4263 measuring strain gauge was used. To measure the roughness of the friction surfaces, an ABRIS-PM7 contact profilometer was used. To analyze the effect of regular microgeometry of friction surfaces on the operation of plain bearings, the samples under study were textured by the drilling method. The texturing parameters of the friction surfaces were measured using a Coolingtec digital microscope. An MT-2.5 low pressure manometer was used to measure the oil supply pressure to the bearing. The temperature of the bearing housing and oil at the bearing inlet and in the reservoir were measured using thermocouples. Thermocouples for measuring the oil temperature were used in conjunction with two-channel OVEN 2TRM1 meter-regulators.

3 Problem Statement and Experiment Planning

For an experimental assessment of the influence of the parameters of regular microgeometry of friction surfaces on the hydromechanical characteristics of the “shaft-bearing” tribo-interface of the internal combustion engine (ICE), samples were prepared corresponding to the bearing—crankshaft journal (Fig. 2).

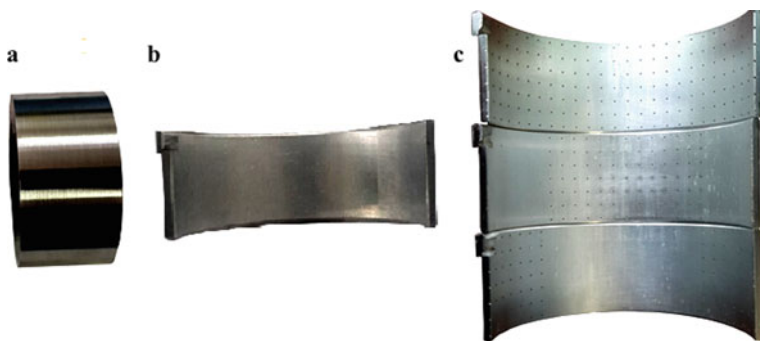


Fig. 2 Photographs of models: 1—roller; 2—liner without texturing; 3—liners with different surface texturing

The roller was made of alloy steel, which is closest to the material of the ICE crankshaft. Mechanical properties of steel: ultimate strength $\sigma_T = 590$ MPa, hardness $HB = 174 \dots 217$ MPa. For the experiment, liners of the standard size of the VAZ 21,083 engine were used (radial clearance $25 \mu\text{m}$, width $b = 20.5$ mm, diameter $d = 47.85$ mm). The roller geometry is shown in Fig. 3a, and the values of the roller and liner roughness parameters are given in Table 1.

To analyze the effect of regular microgeometry of friction surfaces on the operation of plain bearings, three types of regular microgeometry were applied to the liners by

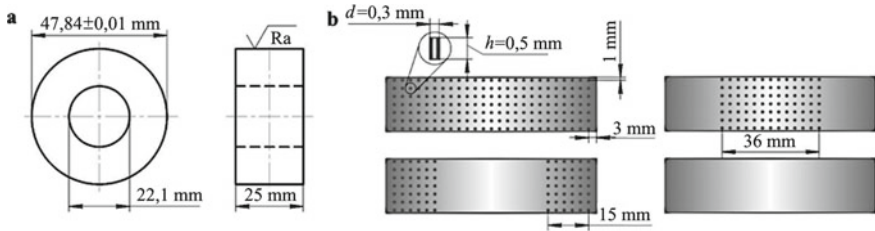


Fig. 3 a Roller; b liners with different surface texturing

Table 1 Roller and liner roughness parameters

Parameter	Value before experiment	
	Roller	Liner
Arithmetic mean deviation of the profile R_a , μm	0.044	0.116
Roughness height at ten points R_z , μm	0.039	0.398
Maximal profile height R_{max} , μm	0.224	0.798
The arithmetic mean of the microroughness step S_m , μm	59.302	37.57

drilling. Texturing parameters are shown in Fig. 3b and in Table 2. The appearance of the applied microdimples is shown in Fig. 4.

Table 2 Bearing surface texturing options

Type of texturing	Number of microdimples areas	Diameter (d , μm)	Depth (h , μm)
	1 (full texturing)	300	500
	2 ($\varphi_1 = 0 \dots 45$; $\varphi_2 = 135 \dots 180$)	300	500
	1 ($\varphi = 55 \dots 125$)	300	500

During the experiment, the axial load F was increased with a step of 250 N from 500 to 5000 N, the time of one step was 30 s. The lower and upper load limits were limited by the capabilities of the experimental setup. At each step, the friction torque and oil temperature were recorded.

Before the experiment, a set of controlled parameters was formed: the angular speed of rotation of the shaft, the axial load on the bearing, the type of roller surface treatment. The ranges of variation of the controlled parameters, determined by the capabilities of the experimental setup, are shown in Table 3.

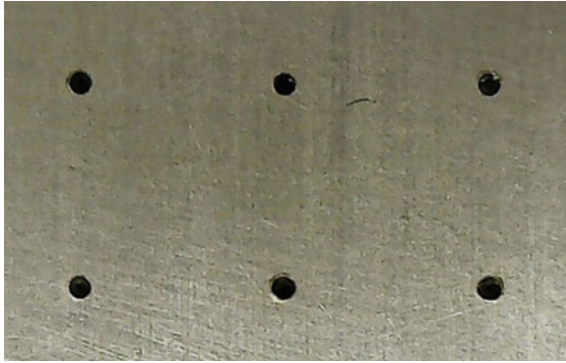


Fig. 4 Geometry of the microdimples under the microscope

Table 3 Bearing surface texturing options

N ^o	Controlled parameter	Change range	Number of levels L
1	Shaft speed n , min^{-1}	500	1
2	Roller surface finish (μm)	$R_a = 0.044$	1
3	Bearing loading cycle (N)	500...5000	1

In the course of experimental studies, a Gersi-Striebeck diagram was taken for each sample using the following procedure:

1. Measurement of the roughness parameters of the roller and liner surfaces before assembly.
2. Assembly of the plain bearing: installation of the upper liner in the bearing housing, installation of the roller on the shaft of the friction machine, connection of the oil supply, thermocouple, sealing the friction chamber by installing a transparent cover made of organic glass.
3. Warming up the oil in the tank to the required temperature.
4. Starting the friction machine and the friction unit without load, fixing the zero friction moment, which characterizes the friction loss in the spindle of the friction machine.
5. Running-in the bearing after warming up to the required temperature. It is carried out by stepwise loading of the bearing from 500 to 5000 N with a step of 250 N and subsequent reduction of the load in the reverse order. In this case, all friction parameters are recorded: friction moment, load, liner temperature, contact stress. The transition to the next step of loading is carried out after the stabilization of the friction torque at the current step. It should be noted that the maximum specific bearing load equal to 5.1 MPa corresponds to the real value of the load on the connecting rod bearings of the VAZ 21,083 engine.

6. Removing the Gersi-Striebeck diagram directly. In this case, the operating conditions of the bearing (load, angular velocity, and oil temperature) are selected in such a way as to fix the area of minimum friction coefficients on the diagram, indicating a change in the type of lubricant in the bearing from liquid to boundary. In our case, the speed of rotation of the roller was 500 rpm, and the load changed in steps similar to the running-in stage. After reaching the maximum load and fixing the friction parameters, the load was removed from the bearing and the value of the zero friction moment was again recorded. The diagram was fixed six times. The friction coefficient was recalculated using the obtained values of the friction moment and averaged over six measurements.

4 Processing of Experimental Research Results

The averaged results of measurements and recalculation of the friction coefficient for bearings with different texturing are shown in Fig. 5. The following designations are accepted in the figures: f_{mp} —friction coefficient, λ —Gersi number.

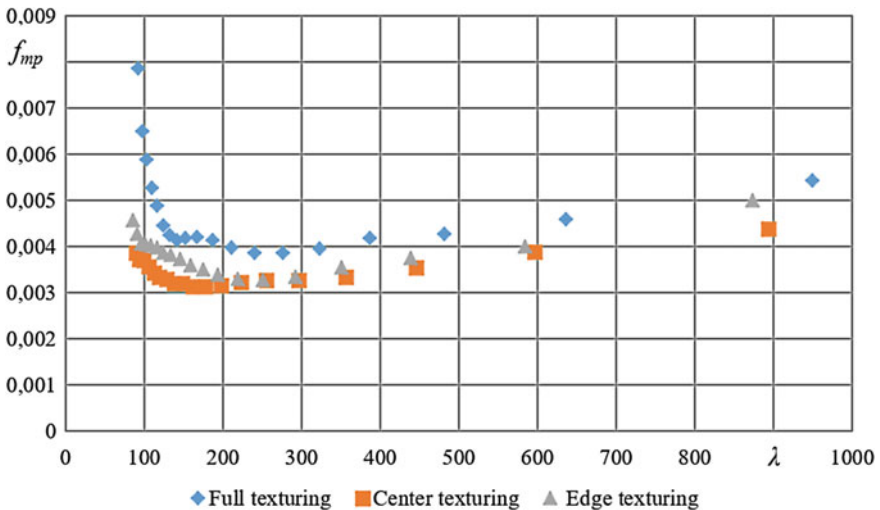


Fig. 5 Comparison of Gersi-Striebeck diagrams for bearings with different liner texturing

The obtained results indicate that the texturing of the liners affects the operation of the plain bearings. In this case, depending on the location of texturing on the surface of the liners, different values of the friction coefficients can be obtained. Of the considered options for texturing the bearing, the liner with center-texturing showed the best results. The diagram for this type of texturing has a minimum at values of the characteristic of the bearing operating mode λ in the range of 150...160. While for other options, the minimum coefficient of friction is achieved when the characteristic values of the operating mode of the bearing λ are in the region of 200...300. Thus, a bearing with a center-textured liner has a greater bearing capacity; the friction mode changes from

liquid to boundary mode at higher loads than in other considered texturing options. The results obtained are in good agreement with the results of other researchers.

5 Conclusion

For experimental research, the II 5018 friction machine was modified—a model friction unit was developed, a standard friction chamber was modified, a system of continuous supply of lubricant to the bearing under pressure with the possibility of oil heating was mounted. This made it possible to provide test conditions comparable to the actual operating mode of the bearing as part of a piston machine. The results of the experiment showed that a bearing with a partially textured liner has a higher bearing capacity compared to a fully textured and smooth bearing, and the friction changes from liquid to boundary friction for it at higher loads.

Acknowledgements. The research was funded by RFBR and Chelyabinsk Region, project number 20-48-740030.

References

1. Knauder C, Allmaier H, Knauder Sander DE et al (2015) Analysis of the journal bearing friction losses in a heavy-duty diesel engine. *Lub* 3:142–154
2. Holmberg K, Andersson P, Nylund NO et al (2014) Global energy consumption due to friction in trucks and buses. *Trib Int* 78:94–114
3. Ligier JL, Noel B (2015) Friction reduction and reliability for engines bearings. *Lub* 3:569–596
4. Ohue Y, Tanaka H (2013) Effect of surface texturing on lubricating condition under point contact using numerical analysis. *J Sci Res* 4:379–385
5. Hamilton D, Walowit J, Allen C (1966) A theory of lubrication by micro-irregularities. *J Bas Eng* 88(1):177–185
6. Anno JN, Walowit JA, Allen CM (1969) Load support and leakage from microasperity lubricated face seals. *Trans ASME J Bas Eng*:726–731
7. Gropper D, Wang L, Harvey T (2016) Hydrodynamic lubrication of textured surfaces: a review of modeling techniques and key findings. *J Trib Int* 94:509–529
8. Kango S, Sharma R, Pandey R (2014) Thermal analysis of microtextured journal bearing using non-Newtonian rheology of lubricant and JFO boundary conditions. *Trib Int* 69:19–29
9. Antoszewski B (2012) Mechanical seals with sliding surface texture—model fluid flow and some aspects of the laser forming of the texture. *Proc Eng* 39:51–62
10. Marian VG, Gabriel D, Knoll G et al (2011) Theoretical and experimental analysis of a laser textured thrust bearing. *Trib Let* 44(3):335–343
11. Zhou Y, Zhu H, Tang W et al (2012) Development of the theoretical model for the optimal design of surface texturing on cylinder liner. *Trib Int* 52:1–6
12. Kovalchenko A, Ajayi O, Erdemir A et al (2004) The effect of laser texturing of steel surfaces and speed–load parameters on the transition of lubrication regime from boundary to hydrodynamic. *Trib Trans* 47(2):299–307
13. Podgornik B, Vilhena L, Sedlaček M et al (2012) Effectiveness and design of surface texturing for different lubrication regimes. *Mec* 47(7):1613–1622

14. Scaraggi M, Mezzapesa FP, Carbone G et al (2013) Friction properties of lubricated laser-microtextured-surfaces: an experimental study from boundary-to hydrodynamic-lubrication. *Trib Let* 49(1):117–125
15. Braun D, Greiner C, Schneider J et al (2014) Efficiency of laser surface texturing in the reduction of friction under mixed lubrication. *Trib Int* 77:142–147
16. Profito FJ, Vlădescu S-C, Reddyhoff T et al (2017) Transient experimental and modelling studies of laser-textured micro-grooved surfaces with a focus on piston–ring–cylinder liner contacts. *Trib Int* 113:125–136
17. Vlădescu S-C, Medina S, Olver AV et al (2016) Lubricant film thickness and friction force measurements in a laser surface textured reciprocating line contact simulating the piston ring–liner pairing. *Trib Int* 98:317–329
18. Ronen A, Etsion I, Kligerman Y (2001) Friction-reducing surface-texturing in reciprocating automotive components. *Trib Int* 44(3):359–366
19. Ryk G, Kligerman Y, Etsion I (2002) Experimental investigation of laser surface texturing for reciprocating automotive components. *Trib Int* 45(4):444–449
20. Costa H, Hutchings I (2007) Hydrodynamic lubrication of textured steel surfaces under reciprocating sliding conditions. *Trib Int* 40(8):1227–1238
21. Morris N, Leighton M, De la Cruz M et al (2015) Combined numerical and experimental investigation of the micro-hydrodynamics of chevron-based textured patterns influencing conjunctive friction of sliding contacts. *Proc Inst Mec Eng, Part J: J Eng Trib* 229(4):316–335
22. Lu X, Khonsari M (2007) An experimental investigation of dimple effect on the stribeck curve of journal bearings. *Trib Let* 27(2):169–175
23. Etsion I, Halperin G, Brizmer V et al (2004) Experimental investigation of laser surface textured parallel thrust bearings. *Trib Let* 17(2):295–300
24. Qiu Y, Khonsari M (2011) Experimental investigation of tribological performance of laser textured stainless steel rings. *Trib Int* 44(5):635–644
25. Henry Y, Bouyer J, Fillon M (2015) An experimental analysis of the hydrodynamic contribution of textured thrust bearings during steady-state operation: a comparison with the untextured parallel surface configuration. *Proc Inst Mec Eng, Part J: J Eng Trib* 229(4):362–375
26. Yu X, He S, Cai R (2002) Frictional characteristics of mechanical seals with a laser-textured seal face. *J Mat Proc Tec* 129(1):463–466
27. Etsion I (2004) Improving tribological performance of mechanical components by laser surface texturing. *Trib Let* 17(4):733–737
28. Bai L, Bai S (2014) Frictional performance of a textured surface with elliptical dimples: geometric and distribution effects. *Trib Tran* 57(6):1122–1128



Modeling the Magnetorheological Fluid Flow Between Parallel Plates Under an External Magnetic Field

A. Fetisov^(✉), A. KornaeV, and V. Tyurin

Orel State University, 29, Naugorskoe Sh, Orel 302020, Russia

Abstract. The article presents the results of a computational experiment on the influence of volumetric electromagnetic forces on the characteristics of the flow of a magnetorheological fluid in a long channel between two parallel plates. A brief description of the new developed variational principle based on the generalized Lagrange equations for the case of a non-Newtonian fluid flow with allowance for electromagnetic forces is given. As a verification problem, the comparison of the calculation results based on the developed generalized variational Lagrange principle with the results of solving the hydrodynamic equations, that were obtained analytically, and the results of a computational experiment in Comsol Multiphysics and Ansys Fluent, is given. The results of the computational experiment showed that the developed generalized variational Lagrange principle is applicable for solving problems of the flow of non-Newtonian fluids taking into account volumetric forces. The results for the Lagrange variational principle, the analytical solution, and the simulation results in Comsol Multiphysics and Ansys Fluent are in good agreement and have little divergence.

Keywords: Lorenze force · Functional · Lagrange variational principle · Analytical solution · Computational fluid dynamics

1 Introduction

Currently, there are many approaches to solving problems of hydrodynamics that can be conditionally divided into classical and variational cases. The classical approach of mathematical modeling is based on solving a variety of differential equations taking into account a set of initial and boundary conditions [1–3]. The classical modeling approach includes many different methods of numerical modeling that give accurate results with small residuals. The greatest difficulty is the nonlinearity of the differential equations being solved [4–7]. For this work, the basic principle is the variational principle of J. Lagrange that is convenient to use for modeling stationary flows of viscous media. The justification of the Lagrange variational principle is described in sufficient detail in paper [8]. Justification of variational principles equivalent to solving systems of partial differential equations is usually performed using generalized Euler–Lagrange equations [9, 10].

2 Generalized Lagrange Equations for the Case of Viscous Incompressible Non-Newtonian Media Flow with Allowance for Mass Forces

Let the velocity field \vec{v} be the rotor of some auxiliary field $\vec{a} : \vec{v} = \nabla \times \vec{a}$. Thus, the generalized Lagrange functional takes the form:

$$J_L^*(a_m) = \int_{\Omega} \Pi_v d\Omega, \tag{1}$$

where $\Pi_v = \int TdH$ —viscoplastic potential.

Velocity components in Cartesian coordinates have the form:

$$v_i = \epsilon_{ijk} \partial a_k / \partial x_j, \tag{2}$$

where ϵ_{ijk} —Levi Civita symbol [11–14].

In scalar notation, functional (1), taking into account the Gershal–Bulkley model, takes the following form:

$$J_L^* = \int_{\Omega} \left[\frac{q_0}{2} (2\xi_{ij}\xi_{ji}) + \frac{q_1}{z+1} (2\xi_{ij}\xi_{ji})^{\frac{z+1}{2}} \right] d\Omega. \tag{3}$$

For the integrand, the Euler equations are written:

$$\nabla \cdot \vec{F}_r^m - \nabla \cdot (\nabla \cdot T_F^m) = F_y^m, \tag{4}$$

where $F_y^m = \frac{\partial F}{\partial y_m}$, $\vec{F}_r^m = \left[\left[F_{r_k^m} \right] \right] = \frac{\partial F}{\partial r_k^m}$, $T_F^m = \left[\left[F_{w_{ps}^m} \right] \right] = \frac{\partial F}{\partial w_{ps}^m}$, $\vec{r}^m = \left[\left[r_k^m \right] \right] = \nabla y_m$, $T_w^m = \left[\left[w_{ps}^m \right] \right] = \nabla \otimes \vec{r}^m = \nabla \otimes (\nabla y_m)$.

The following conditions must be met on the body surface S:

$$\begin{aligned} \left(\vec{n} \cdot \left(\vec{F}_r^m - \nabla \cdot T_F^m \right) \delta y_m \right) \Big|_s &= 0, \\ \left(\vec{n} \cdot \left(T_F^m \cdot \delta \vec{r}^m \right) \right) \Big|_s &= 0. \end{aligned} \tag{5}$$

Equation (5) is equivalent to boundary conditions. Euler–Lagrange Eqs. (4) for functions $y_m = a_m$ taking into account the Stokes formula $\xi_{ij} = (\partial v_i / \partial x_j + \partial v_j / \partial x_i) / 2$ take the form:

$$- \epsilon_{mjk} \frac{\partial}{\partial x_j} \left(\frac{\partial s_{pk}^m}{\partial x_p} \right) = 0. \tag{6}$$

By transformations, we obtain the following equation:

$$\nabla \times (\nabla \cdot D_{\sigma}) = 0. \tag{7}$$

Taking into account equality $\nabla \times (\nabla \cdot D_\sigma) = \nabla \times (\nabla \cdot T_\sigma)$ [8], it can be argued that the search for a stationary value of functional (1) is equivalent to solving the vorticity transport equation:

$$\nabla \times (\nabla \cdot T_\sigma) = 0. \tag{8}$$

Unknown functions must satisfy conditions (5), which are equivalent to boundary conditions. The fulfillment of these conditions can be achieved in several ways. The most common is to fix the values of unknown functions and their gradient components on the surface.

The vorticity transport equation for the case of taking into account the mass forces has the following form [15]:

$$\nabla \times (\nabla \cdot T_\sigma + \rho f) = 0, \tag{9}$$

where ρ —density and f —mass force.

To take into account the mass forces, it is necessary to supplement the integrand. For simplicity, we will further consider the additional term separately. The force of interaction between the magnetorheological fluid and the applied magnetic field (Lorentz force) was used as the mass force: $\vec{f} = \vec{H} \text{rot} \vec{H}$, where \vec{H} is the magnetic field strength. The Lorentz force \vec{f} has components $\vec{f} = [f_1 f_2 f_3]$. For the integrand, the additional term has the following form:

$$\int_{\Omega} (\rho \vec{f} \cdot \vec{v}) d\Omega = \int_{\Omega} (\rho \vec{f} (\nabla \times \vec{a})) d\Omega. \tag{10}$$

In Cartesian coordinates, the equation takes the following form:

$$\int_{\Omega} \left[\rho f_1 \left(\frac{\partial a_3}{\partial x_2} - \frac{\partial a_2}{\partial x_3} \right) + \rho f_2 \left(\frac{\partial a_1}{\partial x_3} - \frac{\partial a_3}{\partial x_1} \right) + \rho f_3 \left(\frac{\partial a_2}{\partial x_1} - \frac{\partial a_1}{\partial x_2} \right) \right] d\Omega \tag{11}$$

For the indicated integrand, the Euler–Lagrange equations are written. For $y = a_1$: $\rho \frac{\partial f_2}{\partial x_3} - \rho \frac{\partial f_3}{\partial x_2} = 0$. For $y = a_2$: $\rho \frac{\partial f_3}{\partial x_1} - \rho \frac{\partial f_1}{\partial x_3} = 0$. For $y = a_3$: $\rho \frac{\partial f_1}{\partial x_2} - \rho \frac{\partial f_2}{\partial x_1} = 0$.

The written expressions correspond to the differential operation of the rotor of the Lorentz force in the expression (11):

$$\nabla \times (\nabla \cdot T_\sigma + \rho f) = \nabla \times (\nabla \cdot T_\sigma) + \nabla \times (\rho f). \tag{12}$$

Thus, the modernized Lagrange functional taking into account the mass forces takes the form:

$$J_L^*(a_m) = \int_{\Omega} (\Pi_v + \rho \vec{f} (\nabla \times \vec{a})) d\Omega, \tag{13}$$

Finding the minimum of this functional is equivalent to solving the modernized vorticity transport Eq. (9).

3 The Magnetorheological Fluid Flow Between Two Parallel Plates

Simulation of fluid flow was also carried out with two programs: Comsol Multiphysics and Ansys Fluent. Both software have their own characteristics for calculating the flow of magnetic fluids [16, 17]. Comsol Multiphysics has difficulties with calculating the flow of magnetic fluids in thin layer that is associated with the meshing peculiarities. Ansys Fluent uses the built-in add-on model to calculate the flows of magnetorheological fluids that has features for calculating flows under the influence of strong magnetic fields that should significantly reduce the velocity profile over the channel section. In these cases, the presented model incorrectly considers the fluid flow profile. In this regard, highly stressed flows were not considered in this work.

The geometry of the flow of the magnetorheological fluid is identical for both programs. The fluid flow occurs in a limited volume $\Omega = L_1 \times 2L_2 \times L_3, L_3 = 1$. There is a pressure drop along the axis $x_1, p(0, x_2) = p_0, p(L_1, x_2) = p_1$ (Fig. 1). The main parameters of the flow area: $L_1 = 1 \text{ m}, L_2 = 75 \cdot 10^{-6} \text{ m}, p_0 = 1 \cdot 10^5 \text{ Pa}, p_1 = 1.5 \cdot 10^5 \text{ Pa}$. The problem is axisymmetric, and the height of the computational domain is half the height of the channel.

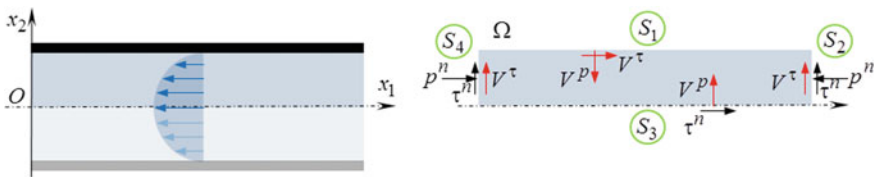


Fig. 1 Flow area and boundary conditions for a symmetric flow area

Ansys and Comsol Multiphysics use the equations of hydrodynamics typical for the classical formulation of the problem of fluid flow between parallel plates, which for this problem have the form:

$$\frac{\partial p}{\partial x_1} = \frac{\partial}{\partial x_2} \left(\mu \frac{\partial v_1}{\partial x_2} \right) + \rho f_1, \frac{\partial p}{\partial x_2} = 0, \frac{\partial v_1}{\partial x_1} = 0, \rho f_1 = \text{const.} \quad (14)$$

To solve the problem in both selected programs, a set of boundary and initial conditions is set for the equations of hydrodynamics and magnetic field. The solution in Comsol Multiphysics is made by the finite element method, in Ansys Fluent the solution was obtained by the method of control volumes.

In the solution process, Ansys took into account the K-Epsilon turbulence model [18, 19]. ANSYS CFX uses the Coupled Algebraic Multigrid technology solver [20]. The solution was made on a mesh that consisted of 100 mesh elements along the channel gap width and 100,000 mesh elements along the channel length. The solution process was carried out on the basis of achieving convergence criteria, which were chosen as root mean square residuals (RMS) equal to 10^{-6} . On average, the solution converged in 250–300 iterations.

The numerical solution of the variational problem can be conveniently obtained by one of the direct variational methods, for example, the Ritz method [10, 14]. The problem

of finding the optimal function that gives the minimum value to the functional is reduced to the problem of finding the extremum of a function of several variables. In this case, the stream function Ψ is specified using the orthonormal Legendre series $P_i(\tilde{x}_2)$ in the region with an interval $[-1, 1]$ in dimensionless coordinates [9]:

$$\Psi = \sum_{i=0}^N \alpha_i P_i(\tilde{x}_2) = \alpha_0 1 + \alpha_1 \tilde{x}_2 + \sum_{i=1}^N \alpha_{i+1} \left(\frac{2i+1}{i+1} \tilde{x}_2 P_i(\tilde{x}_2) - \frac{i}{i+1} P_{i-1}(\tilde{x}_2) \right) \quad (15)$$

where α_i —unknown coefficients and N —polynomial degree.

The solution of the variational problem is associated with the search for a set of values α_i ($i = 0 \dots N$) at which functional (1) takes a minimum value. The search for the minimum of a function of several variables was carried out using the built-in algorithm for finding the extremum in GNU Octave [21].

As a reference solution, we used an analytical solution for the classical setting, which can be defined as:

$$v_1 = \frac{1}{2\mu} \frac{p_0 - p_1}{L_1} (x_2^2 - L_2^2) - \frac{1}{2\mu} \rho f_1 (x_2^2 - L_2^2), \quad (16)$$

4 Results

In the course of the study, the simulation of the flow of a magnetorheological fluid in an applied external magnetic field was carried out. The magnetic field strength was varied in the range 0–15,000 A/m with 6 variations. The simulation results are shown in Fig. 2.

Figure 2 shows that the results of the analytical solution and the solutions obtained by other methods agree well. For zero strength of the applied magnetic field, the maximum error is no more than 1%. The velocity profile at zero strength corresponds to the Poiseuille flow. For the variational solution for all magnetic field strengths, the maximum error is no more than $1.5 \cdot 10^{-6}\%$. This indicates a high accuracy of the variational approach to modeling fluid flows.

The maximum error in the deviation of the analytical solution and the Comsol solution is about 40% at the magnetic field strength. A similar error value is created at the flow boundary in the near-wall region. This is due to the fact that a laminar flow model was used to simulate the fluid flow. Similar results were obtained using Ansys Fluent. This solution is characterized by a higher average calculation error in relation to the analytical solution. The average error was 1.4%. The maximum deviation of the velocity profile from the reference was obtained for an external magnetic field strength of 6000 A/m. The error in this fluid flow regime was 5.1%.

5 Conclusion

Within the framework of this study, the results of modeling the flow of a magnetorheological fluid under the action of an external magnetic field were obtained. The results

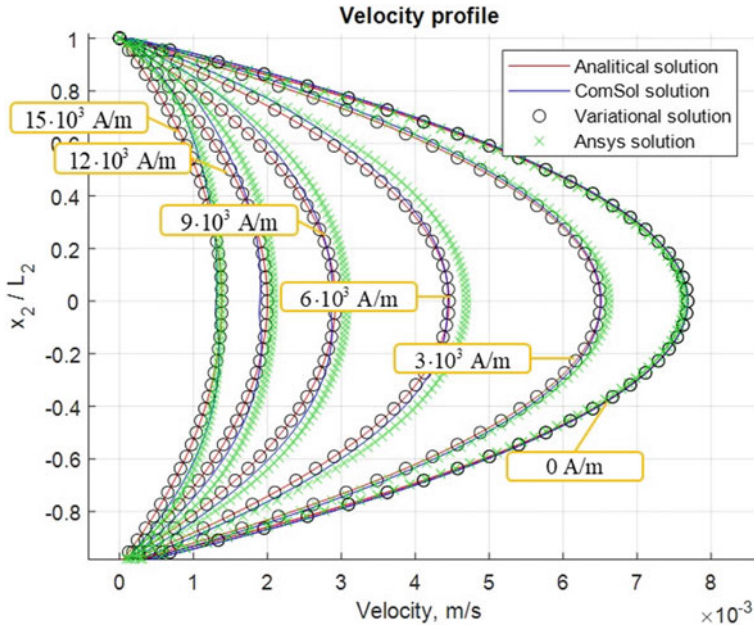


Fig. 2 Results of modeling the flow of magnetorheological fluid

obtained by the variational approach are in excellent agreement with the reference analytical flow. The results obtained by CFD programs agree quite well, with relatively small mean computational errors. The results obtained allow us to say that these software packages can be used for more complex cases of calculating the flow of magnetorheological fluids.

Acknowledgements. The reported study was funded by RFBR, project number 19-38-90259.

References

1. Polyakov R, Savin L, Fetisov A (2018) Analysis of the conditions for the occurrence of the effect of a minimum of friction in hybrid bearings based on the load separation principle. Part J: *J Eng Tribol* 233(2):271–280
2. Majorov S, Savin L, Babin A (2019) Estimation of energy efficiency of oscillations of rotors on radial fluid film bearings. *Lecture notes in mechanical engineering*, p 351–358
3. Babin A, Kornaev A, Rodichev A, Savin L (2020) Active thrust fluid-film bearings: Theoretical and experimental studies. Part J: *J Eng Tribol* 234(2):261–273
4. Roache P (1998) In: *Fundamentals of computational fluid dynamics*. Hermosa Pub, Socorro, New Mexico
5. Anderson J (1995) *Computational fluid dynamics. In: The basics with applications*. McGraw-Hill, New York
6. Hori Y (2006) In: *Hydrodynamic lubrication*. Yokendo Ltd, Tokyo
7. Dowson D (1962) A generalized Reynolds equation for fluid-film lubrication. *Int J Mech Sci* 4(2):159–170

8. Kucheryaev BV (2000) In: *Mekhanika sploshnyh sred (Continuum mechanics)*. MISIS, Moscow
9. Savin L, Kornaev A, Kornaeva E (2015) Variational principle in the hydrodynamic lubrication theory. *Int J Math Models Methods Appl Sci* 9:114–119
10. Schechter R (1967) *The variational method in engineering*. McGraw-Hill, New York
11. Kornaev A (2019) On proof of the generalized lagrange variational principle. *Lecture Notes in Mech Eng* 0:1071–1078
12. Fetisov AS, Kornaev AV, Bobyr MV (2020) Vliyanie massovyh sil na techenie nen'yutonovskikh zhidkostej v tonkih kanalah (Effect of mass forces on the fluid flow between parallel plates). *Fundamental'nyye i prikladnyye problemy tekhniki i tekhnologii* 1(339):103–107
13. Kornaev A, Kornaeva E, Savin L, Fetisov A (2019) Application of variational approach to non-Newtonian fluid flow modelling. In: *Proceedings of 10th international scientific conference BALTRIB 2019*, Vytautas Magnus University, Agriculture Academy, Kaunas, Lithuania, 14–16 November 2019
14. Korn G, Korn T (2000) *Mathematical handbook for scientists and engineers*, 2nd edn. Dover Publications, New York
15. Fetisov AS (2019) Variacionnyj podhod modelirovaniya gidrodinamicheskikh techenij sred s upravlyaemymi svojstvami (Variational approach for modeling hydrodynamic flows of media with controllable properties). In: *Materials of the XVII International conference energy and resource conservation - XXI century*, Orel State University, Orel, 2–4 December 2019
16. Yan Y, Smolentsev S, Abdou M (2017) Validation of COMSOL Multiphysics® for magneto-hydrodynamics (MHD) flows in fusion applications. In: *Materials of the comsol conference*, Boston, 4–6 October 2017
17. ANSYS, Inc. (2013) *16.ANSYS Fluent magnetohydrodynamics (MHD) module manual*. ANSYS, Inc., Canonsburg
18. Wilcox DC (2000) In: *Turbulence modelling for CFD*. DCW Ind., La Canada
19. Kato M, Launder BE (1993) The modelling of turbulent flow around stationary and vibrating square cylinders. In: *Proceedings of the 9th symposium on turbulent shear flows*, Kyoto, Japan, 16–18 August 1993
20. ANSYS, Inc. (2021). *Computational fluid dynamics (CFD) for software program solutions*. <https://www.ansys.com/products/fluids/ansys-cfx>. Accessed 28 Feb 2021
21. Eaton JW (2017) GNU Octave. <http://www.gnu.org/software/octave>. Accessed 30 Dec 2017



Surface Modification of AISI 321 Steel by Solid Lubricants

D. V. Tsukanov¹, G. S. Sevalnev¹, and N. N. Zubkov²(✉)

¹ Federal State Unitary Enterprise “VIAM”, 17, Radio Street, Moscow 105005, Russia

² Bauman Moscow State Technical University, 5/1, 2nd Baumanskaya Street, Moscow 105005, Russia

zoubkovn@bmstu.ru

Abstract. Deformational cutting is a method that permits to obtain microfinning on the surface of the steel parts. The main difference between conventional cutting process and deformational cutting is that the chips are cut from one side while being straightened up as fins which remain as a functional part of the workpiece. A tool cuts and deforms the surface layers, forming a finned structure since the undercut layers are connected to the main body of the workpiece. The width of the slot gaps between the fins can be from tens to hundreds of micrometers with a depth of gaps up to 1 mm. The article describes a method for increasing the wear resistance of stainless AISI 321 chrome-nickel steel via the creation of microfinning produced by deformational cutting and embedding two different solid lubricants into the slot gaps between fins. The results of the metallographic study have shown that the material of the created fins experienced severe plastic deformation, which was accompanied by a partial transformation of metastable austenite into martensite and a twofold increase in the surface layer hardness. The results of wear tests in the conditions of unlubricated sliding friction have shown that the application of microrelief with embedding solid lubricants substantially increased the surface wear resistance of stainless austenitic steel.

Keywords: Surface modification · Deformational cutting · Austenitic steel · Solid lubricants · Hardness · Sliding bearing · Wear rate

1 Introduction

The crucial task in the machine-building industry is increasing the product life cycle of sliding bearings. Low cost, high load capacity, and durability of sliding bearings are their major advantages. Sliding bearings are subjected to such damages as scuffing, plastic deformation within the contact zone, and wear resulting in the failure of the unit and machine as a whole [1].

Friction bearings operating in the conditions of a corrosion environment or high temperatures are manufactured from stainless austenitic chrome-nickel steel characterized by high corrosion resistance, good weldability, and technological effectiveness [2–4]. However, the low surface hardness limits the use of these steels in friction units due to the

low wear resistance characteristics. Increasing the wear resistance of corrosion-resistant austenitic steels is an urgent line of research.

The use of liquid lubricants increases the performance of plain bearings by reducing the coefficient of friction. As a result, the wear resistance of the sliding surfaces increases. In some friction units, the use of liquid lubricants is not applicable. This problem can be solved by applying solid lubricant materials (SLM) located inside the friction surface structure.

There are various methods for creating a system of small pockets in the friction surfaces [5–9]. The subsequent filling of these pockets with SLMs allows avoiding the application of liquid or grease lubricants.

As an advanced method for creating pockets for SLM filling, it is proposed to use the deformational cutting method (DCM), which makes it possible to create narrow vertical or inclined slotted splits on the surface. DCM is the cutting-deformational processing method, which makes it possible to create a macro- and microrelief structure on the surface in form of finning without chip formation [10]. Figure 1 demonstrates the principle of DCM.

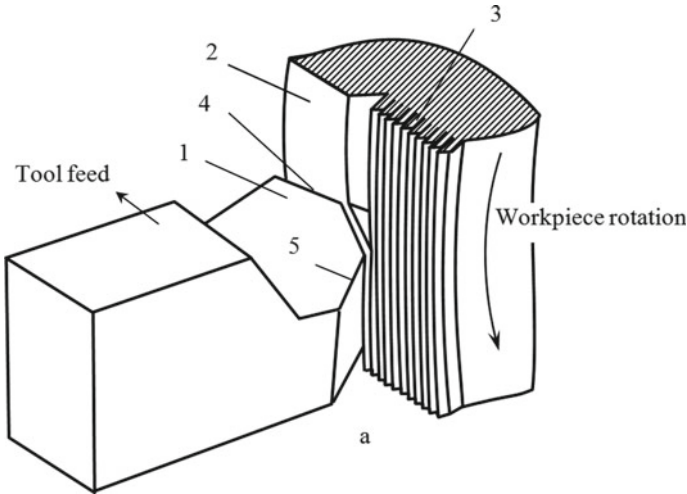


Fig. 1 Concept of deformational cutting method. 1—DCM tool, 2—treated surface, 3—finned surface, 4—cutting edge, and 5—deforming edge

Via varying the tool geometry and processing conditions, it is possible to obtain any necessary fin pitch, groove width, height, and fin angle [11]. Filling the surface relief with SLM makes it possible to decrease the friction factor and to increase the operational life of the product [12].

The DCM is not accompanied by chip formation, while the material of the created fins is subjected to severe plastic deformation [13], which increases the application effectiveness of steels with metastable austenitic structure subject to the transformation-induced plasticity effect [14, 15]. The combined austenite–martensite structure determines a high level of strength characteristics and plasticity [16–18].

2 Methods

The investigation was performed on Cr-Ni austenitic steel AISI 321 (18-8 Cr-Ni stainless steel, titanium stabilized).

Samples for the testing of the surface specific wear rate in unlubricated sliding friction were made in the form of disks with a diameter of 40 mm.

The sample surface preparation scheme is shown in Fig. 2.

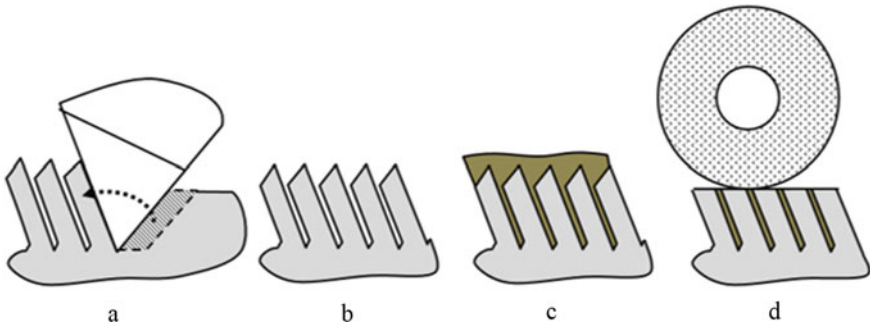


Fig. 2 Stages of surface preparation with the placement of solid lubricants in the friction surface structure. **a** Microfinishing by DCM, **b** Formed microfinning, **c** Filling of slot gaps with solid lubricant material, and **d** Grinding to remove sharp edge tips

A microrelief in the form of a spiral groove with a pitch of 0.2 mm was created by the DCM to the end surface of the disk. The cutter made of H10F cemented carbide (Sandvik Coromant) was used to create microfinning. The side cutting edge angle was $\varphi = 42^\circ$. Clearance angles: $\alpha = \alpha_1 = 3^\circ$ [19]. The depth of DCM was 0.2 mm, tool feed was 0.2 mm/rev. The dimensions of the created microfins are presented in Fig. 3a. Expanded graphite and Teflon thin sheets were pressed into the microrelief. The sharp fin tops were deleted after SLM embedding (Fig. 3b).

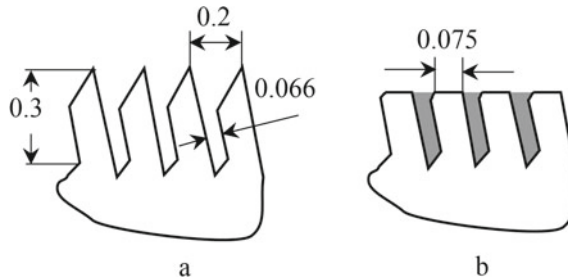


Fig. 3 Schematic drawing of surface microrelief; **a** After DCM; **b** After SLM embedding

Metallographic studies of the austenitic steel structure after DCM were performed using an Olympus GX-51 optical microscope (magnification of $\times 500$). For revealing the finned surface microstructure, etching in a 10% solution of oxalic acid was used.

Hardness was measured using a DuraScan 20 hardness tester under a load of 50 g. The qualitative structure was examined using a Hitachi SU8010 scanning electron microscope operating in the mode of secondary and back-scattered electrons (operational magnification of $\times 4500$ and an accelerating voltage of 15 kV), equipped with an attachment for carrying out micro X-ray spectral analysis with the AZtec software application.

Wear tests were carried out without liquid lubricants using the Nanovea T-50 tribometer using the “rod-disk” scheme. The sliding linear velocity was $V = 0.1$ m/s, and the rod loading was $F = 10$ N. Tribotechnical characteristics were evaluated based on the test results of three pairs of samples. In this arrangement, the tested samples were the disks, while the rod (counter face) had the ball-shaped end with a diameter of 6 mm made from AISI/ASTM 52100 chromium steel having the hardness of 64 HRC (Fig. 4).

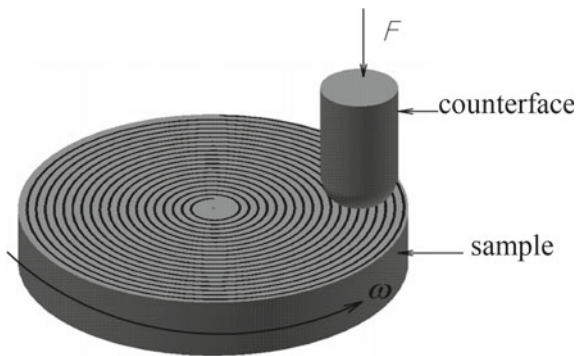


Fig. 4 Friction test diagram

3 Results and Discussion

The microstructure of the fin material after DCM is presented in Fig. 5.

Microhardness measurements, which were performed on the samples with the created fins, made it possible to establish that the severe plastic deformation occurred within the whole fin volume (Fig. 6). In the as-received condition (heat treatment: annealing), the hardness of the steel surface was 180 HV, while after deformational cutting, the hardness of the created microrelief was twice high: 375–410 HV.

The results of structure examination using a scanning electron microscope operating in the mode of secondary electrons demonstrated that the created microrelief contained traces of martensite, which was formed because of severe plastic deformation. Martensite plates appear under a microscope in the form of needles (Fig. 7).

A study of the specific wear rate during the wear test in the conditions of unlubricated sliding friction made it possible to find out that an increase in the hardness of the created microrelief surface resulted in a decrease in the specific wear rate by 1.9 times as compared with annealed samples (Fig. 8). Embedding SLM into the finned surface resulted in a decrease in the specific wear rate: After embedding Teflon into the splits,



Fig. 5 Microstructure of the fin material of AISI 321 steel, $\times 500$

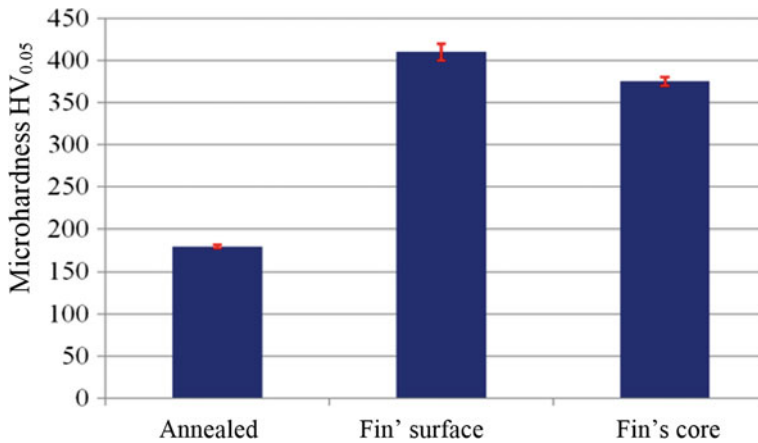


Fig. 6 Hardness of AISI 321 steel before and after deformational cutting

the wear rate decreased by 7.5 times as compared with annealed samples, while after embedding expanded graphite, the wear rate decreased by 22 times. The creation of microrelief and embedding SLM also made it possible to decrease the friction factor. The results illustrating changes in the friction factor are presented in Fig. 9.

4 Conclusion

Deformational cutting of Cr–Ni stainless steel with the structure of metastable austenite is an effective method for material hardening. Based on the results of microhardness

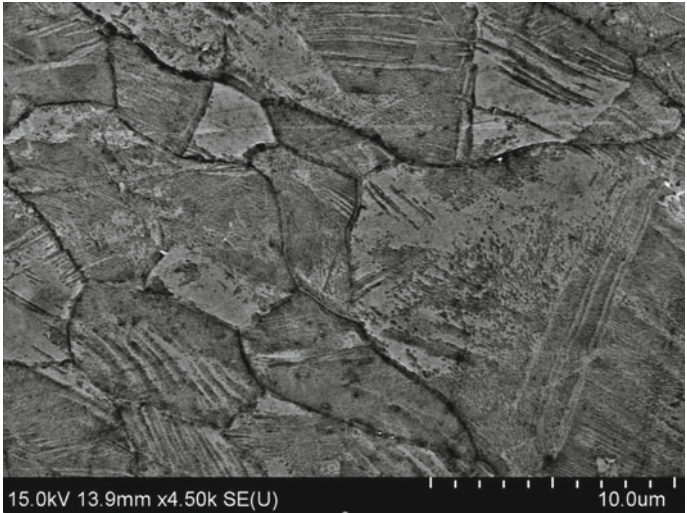


Fig. 7 Structure of the finned surface of AISI 321 steel, SEM, $\times 4500$

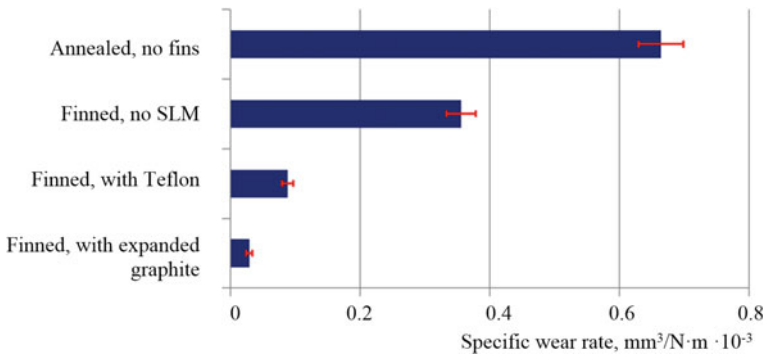


Fig. 8 Specific wear rate of AISI 321 steel after DCM and SLM embedding

measurements and microstructure studies, it was established that the DCM made it possible to increase the material hardness by more than two times, while martensite was contained in the fin structure.

The results of wear tests in the conditions of unlubricated sliding friction have demonstrated that DCM application makes it possible to decrease the specific wear rate of AISI 321 steel approximately by 1.9 times as compared with annealed samples. Embedding Teflon into the slotted structure of microrelief resulted in a decrease in the specific wear rate by 7.5 times as compared with annealed samples, while after embedding expanded graphite, the wear rate decreased by 22 times. Embedding SLMs also made it possible to decrease the friction factor for AISI 321 steel.

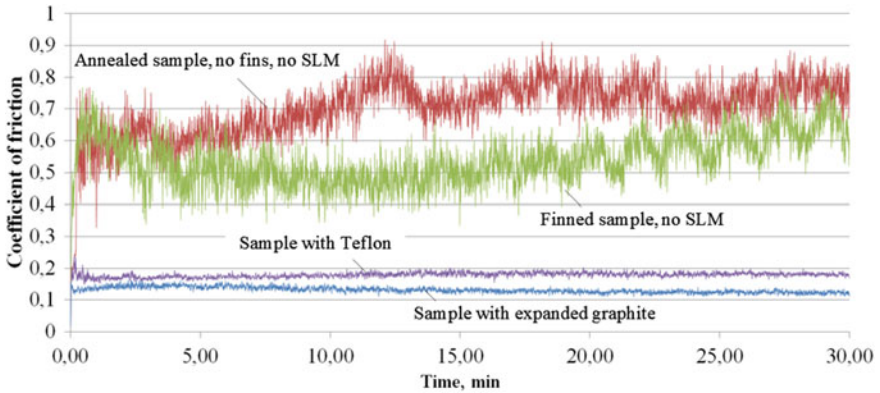


Fig. 9 Changes in the friction factor of steel AISI 321 after DCM and SLM embedding

References

1. Antunović R et al (2018) Diagnostics and failure of plain bearings. *IETI Trans Eng Res Pract* 2(2):9–18
2. Wang J et al (2012) Influence of time on the microstructure of AISI 321 austenitic stainless steel in salt bath nitriding. *Surf Coat Technol* 206(15):3399–3404
3. Tiarniyu AA et al (2016) A comparative study of the compressive behavior of AISI 321 austenitic stainless steel under quasi-static and dynamic shock loading. *Mater Des* 112:309–319
4. Fakhurtdinov RS et al (2020) Study of the structure and properties of high-chromium cast irons and stainless steels for chemical production pumps. *Met Sci Heat Treat* 62(1):145–151
5. Kitahara K et al (2007) US Patent 7234870B2. Plain bearing
6. Ono A et al (2000) US Patent 6059460A. Plain bearing
7. Mori S (1978) US Patent 4105267A. Bearing provided with oblique oil grooves and/or with a plurality of obliquely arranged rows of semicircular indentationsc
8. Niegel F et al (1997) US Patent 006095690A. Sliding bearing element with lubricating oil pockets
9. Porter M et al (2013) US Patent 20130287326A1. Spherical plain bearing with solid graphite lubricating plugs
10. Zoubkov NN, Ovchinnikov AI (1998) European Patent 0727269. Method of producing a surface with alternating ridges and depressions and a tool for carrying out the said method
11. Zubkov NN (2002) Combination of the processes of cutting and working by pressure in the novel method of forming improved surface structures. *Kuznechno-Shtampovochnoe Proizvodstvo (Obrabotka Metallov Davleniem)* 10:17–20
12. Zubkov NN, Vasil'ev SG (2013) Povyshenie iznosostojkosti detalej par treniya skol'zheniya na osnove metoda deformiruyushchego rezaniya (Wear resistance improvement based on deformational cutting method). *Uprochnyayushchie tekhnologii i pokrytiya* 8:3–9
13. Zhigalina OM et al (2020) Effect of carbon content on the structure and microhardness of steels under rapid action by deforming cutting. *Met Sci Heat Treat* 62(1):168–173
14. Terentev VF et al (2017) Influence of the tempering temperature on the mechanical properties and the phase composition of thin sheet trip steel. *Russian Metallurgy (Metally)* 10:867–870
15. Smaga M et al (2008) Deformation-induced martensitic transformation in metastable austenitic steels. *Mater Sci Eng* 48:394–397

16. Filippov AV et al (2018) *Izmeneniya v strukture i fazovom sostave stali 12H18N10T posle intensivnoj plasticheskoj deformacii i otzhiga (Changes in the structure and phase composition of steel 12H18N10T after intense plastic deformation and annealing)*. Tezisy dokladov mezhd. konf. "Perspektivnye materialy s ierarhicheskoj strukturoj dlya novyh tekhnologij i nadezhnyh konstrukcij", pp 306–306
17. Bubnov VA (2017) *Uprochnenie austenitnyh stalej holodnoj plasticheskoj deformaciej (Hardening of austenitic steels by cold plastic deformation)*. Vestnik Kurganskogo gosudarstvennogo universiteta 45(2):44–50
18. Karavaev DM et al (2020) *Wear resistance of composites based on expanded graphite and a steel base with structured macroscopic relief*. Russ Eng Res 40(10):867–869
19. Zubkov NN et al (2016) *Tool–workpiece interaction in deformational cutting*. Russ Eng Res 36(3):209–212



Technical Requirements for Lubricating Flanges Devices of Locomotive Wheelsets

I. A. Mayba(✉)

Rostov State Transport University, 2, Sq. Rostovskogo Strelkovogo Polka Narodnogo Opolcheniya, Rostov-on-Don 344038, Russia

Abstract. The work carried out extensive studies to date information environment in the field of development, implementation, and evaluation of the operational efficiency of the lubrication devices crests of wheel pairs locomotives and analyzed international practice and application features flanges lubrication devices and lubricants for contact “wheel-rail”. Among the topical issues that require appropriate design solutions are the issues of increasing the efficiency of the LDFL devices. Design work was carried out to develop technical specifications for lubrication devices for wheelset flanges of locomotives (hereinafter referred to as USGL devices) in accordance with GOST 15.902-2014 system of product development and launching into production. Railway rolling stock. The order of development and putting into operation. According to the results of tests, USGL devices were allowed to put into mass production and admission to use in the infrastructure of OJSC “Russian Railways”. The purpose of the work is to formulate normative indicators governing the main characteristics of effective devices for lubricating the flanges of wheel pairs of locomotives that meet the regulatory requirements for equipment that is installed on traction rolling stock.

Keywords: Project · Tests · Ridge lubrication device · Technical requirements · Project stages · Methodology

1 Introduction

In the course of the research publishing groups of foreign and Russian scientists were considered [1–17]. It is established that the considered subject “Systems, wheel flange lubricating device for lubricating materials for the contact ‘wheel-rail’” is of considerable interest. The variety of subjects of the presented patents indicates an active search for optimal solutions in the subject area under consideration. Nevertheless, the general analysis shows that, despite the large number of studies in the subject area of patent search, the optimal system for ridge lubrication of a locomotive wheel that meets all the requirements in accordance with the operating conditions has not been found yet. Based on this, the generalization of known approaches and the search for new ways to solve this problem seems important and promising.

2 Materials and Methods

The object of this research is devices for lubricating the flanges of locomotive wheelsets. The use of such devices on rolling stock allows you to obtain the following advantages:

- significantly reduce the wear rate of the wheel flanges (tires) and increase their resource;
- to reduce lateral wear of rails and increase their service life;
- to reduce resistance to movement and reduce the cost of electricity (diesel fuel) for traction;
- to reduce the probability of derailment by reducing the coefficient of friction;
- to reduce non-production costs associated with downtime of the rolling stock when replacing and turning wheels (tires) and grinding rails.

The purpose of the work is to formulate normative indicators governing the main characteristics of effective devices for lubricating the flanges of wheel pairs of locomotives that meet the regulatory requirements for equipment that is installed on traction rolling stock.

3 Results

The analysis performed allowed to formulate and define the main sections of the technical specification for the LDFL development devices and their content. The main results of the research are presented below.

1. Technical requirements

Product type.

LDFL devices must have a basic configuration with device options in various designs (modifications) with the ability to install on various types of locomotives and be a mechanical feed drive fixed on the bogie frame or on the axle box of the wheelset, oriented with its guide to the wheel crest at the point as far as possible from brake shoe brake linkage.

Requirements for the purpose.

The LDFL devices must apply a solid lubricating element (referred to as SLE) to the wheel flange using a rotaprint method and have a continuous feeding cycle and automatically apply SLE.

LDFL devices must comply with the main technical characteristics:

- maximum weight, kg, no more than 15;
- limiting dimensions, mm— $600 \times 600 \times 600$ (length \times width \times height);
- limiting dimensions of the feed mechanism guide, internal (for section), mm: 30×500 (diameter \times length) and/or $40 \times 60 \times 500$ (height \times width \times length);
- the force of the drive spring, N , in the range of 10–60.
- Mean time between failures must be at least 120 thousand operation cycles.

- the average service life must be at least 20 years.

Interoperability requirements.

The LDFL device must be functionally compatible with all types and series of locomotives on which it is installed. The overall installation and connection dimensions of LDFL should not change the overall dimensions of the locomotives.

Requirements for resistance to external influences and survivability.

LDFL devices must be manufactured in climatic version U category 1 in accordance with GOST 15,150. Limiting operating values of air temperature during operation are lower—minus 50 °C; upper—plus 45 °C.

When fastened in the elements of the first stage of spring suspension, it must remain operational and be resistant to mechanical influences in the form of dynamic loads arising from the movement of the locomotive from the superstructure of the track. If a wheelset is attached to the axle box, the LDFL must remain operational and be resistant to dynamic forces arising in contact between the wheel and the rail when the locomotive moves along uneven tracks.

Failure Criteria and Limit State.

The state of the LDFL, corresponding to the resource failure of its basic element, is the limit. Failure of LDFL is an event in which the device does not perform its basic functions or does not meet its basic characteristics.

General requirements for assessing reliability methods.

The compliance of the LDFL with the reliability requirements established in this technical specification at the development stage of the life cycle is assessed by the calculation method using data on the reliability of the components in accordance with GOST 27.301.

The compliance of LDFL with the reliability requirements at the stage of the life cycle “Operation” is assessed by the calculation and experimental method, according to the test program developed and agreed with the customer at the stage of development of working design documentation. The initial data for test planning (rejection level, customer risk, acceptance level, and supplier risk) should be defined in the reliability test program.

The developer must submit a product reliability report for approval with the customer, containing the following information: list of LDFL failures; analysis of the types of consequences; and criticality of failures in accordance with GOST27.310.

Ergonomic and technical aesthetics requirements.

LDFL devices must meet the requirements for ergonomics in accordance with GOST20.39.108.

Requirements for operation, maintenance, repair and storage.

The LDFL device must function normally and maintain its characteristics throughout the service life in conditions that meet the requirements of the technical specification.

LDFL should be installed on the elements of the bogie and/or axle box unit of the traction rolling stock. The installation procedure, installation diagram, installation and connection dimensions, and their deviations are carried out in accordance with the operating manual of the corresponding type of LDFL and the drawings of the design documentation.

USGL devices must ensure the possibility of changing the SLE at locomotive turnover points or their maintenance points in the amount and with frequency in accordance with the operating manual of the corresponding type of USGL device and drawings of design documentation.

The control of the pressing force of the SLE to the surface of the wheel flange should be carried out using an exemplary compression dynamometer of the third category in accordance with GOSTR 55,223 or its calibrated analogue.

Welded joints of UATL fasteners must be checked for compliance in accordance with GOST 3242. 3.7.6. The introduction of the UATL device into operation, its maintenance and repair should be carried out by persons who have passed the appropriate safety instructions for working on the rolling stock.

Repair of the LDFL device should be carried out at specialized enterprises by trained specialists. Documents containing data for carrying out repair work must be contained in the repair documentation.

The warranty period for the LDFL device is at least two years from the date of installation on the locomotive, or not more than 3 years from the date of manufacture and transfer to the customer.

LDFL devices must allow storage in a heated warehouse in a standard package for at least three years.

Transportation requirements.

LDFL devices in standard packaging must allow transportation by any type of transport, subject to the rules for the carriage of goods established for this type of transport in accordance with the requirements of GOST 15,150. The temperature range of the environment during transportation must correspond to the climatic version of the LDFL device.

Safety and health requirements.

LDFL devices must meet the requirements of GOST 34,394 for fire safety, be traumatic, its components must not contain toxic materials that emit harmful gases and other substances during combustion and during normal operation.

The production of the LDFL device must be carried out in accordance with GOST 2.2.2.1327-03 "Hygienic requirements for the organization of technological processes and requirements for production equipment".

Manufacturability requirements.

The design of the LDFL device must ensure its production using modern technologies, from modern materials in accordance with GOST14.201.

Environmental protection requirements.

During the production of the LDFL device, emissions into the atmosphere must be periodically monitored in accordance with GOST17.2.3.01.

Wastewater treatment should be monitored periodically in accordance with GOST17.1.4.01.

Disposal requirements.

The storage of the LDFL device taken out of service before their disposal must be carried out in accordance with the requirements of GOSTR 55,838. The LDFL device must be disposed of by the method of complex processing for secondary use.

2. Technical and economic requirements

The use of LDFL should increase the resource of locomotive wheelsets. Changes in technical and economic indicators should ensure the economic feasibility of using LDFL in comparison with analogues.

3. Requirements for types of collateral.
Metrological, diagnostic, and regulatory support of the LDFL device should be carried out in accordance with modern requirements and current regulatory documents GOSTR 51,672, GOST 27,518.
4. Requirements for raw materials, materials, and components.
As a raw material in the production of the LDFL device, commercially available metal products (high-quality metal products, shaped metal products, pipe metal products, sheet metal products, hardware and raw materials, high-quality steels, non-ferrous metals), mainly of domestic production, should be used.
5. Requirements for conservation, packaging, and labeling.
Conservation of the LDFL device must be carried out in accordance with the requirements of GOST9.014. The LDFL device must be packed in accordance with GOST 23,170.
The packaging of the LDFL device must ensure its integrity during loading and unloading operations, transportation, and storage. By agreement with the consumer, it can use various types of containers and packaging that ensure the safety of products. The LDFL device must be printed on the shipping container or label. Transport marking must be carried out in accordance with GOST 14,192.
6. Special requirements.
The patent purity of the developed LDFL device must be ensured in relation to the following countries: Russia, USA, EU countries, Japan, and Canada. Search depth is 10 years. By decision of the manufacturer, LDFL can be certified in any of the existing voluntary certification systems.
7. Requirements for documentation.
The UATL documentation set must contain:
 - (a) technical conditions;
 - (b) design documentation;
 - (c) operational documentation in accordance with GOSTR 2.601;
 - (d) a document on patent purity and non-copyright infringement.
 - (e) repair documentation in accordance with GOST2.602
8. The order of implementation and acceptance of the development stages work.
The work must be carried out in accordance with the requirements of GOST15.902. Place of preliminary and acceptance tests is a manufacturer, factory. Acceptance of work stages is carried out in accordance with the requirements of GOST15.902.
9. Stages of the device LDFL development (Table 1).

4 Discussion

The obtained research results represent the completed regulatory requirements for LDFL devices, which should be guided by the development of new and existing wheel-rail

Table 1 Stages for the development of the LDFL

Stage name	List of works
Development of technical specifications	Analysis of the latest achievements and prospects for the development of domestic and foreign science and technology in the field of activation of friction processes; conducting patent research. Coordination of technical specifications
Development of working design documentation	Development: <ul style="list-style-type: none"> ● design documentation for a prototype ● repair documentation for repair in accordance with ● operational documentation for operation in accordance with ● programs and methods for preliminary tests of a prototype in accordance
Manufacturing and acceptance tests of prototypes	Development of a prototype preparation of production for the manufacture of a prototype Manufacturing of a prototype conducting acceptance tests of a prototype. Preparation of a set of experimental equipment for installation on a locomotive
Preliminary tests of the prototype	Preliminary tests of prototypes during the trial run of the locomotive at the railway range. Consideration of the results of preliminary tests. Correction (if necessary) of design and operational documentation according to the results of preliminary tests of the prototype with the assignment of the letter “O”
Acceptance tests of prototypes and acceptance of R&D results	Acceptance tests. Correction of design and operational documentation (if necessary). Assignment of technical documentation of a prototype of the letter “O1 1” or “A”. Consideration of the acceptance test protocol. Consideration of the results of the ROC by the acceptance committee
Work results	Terms of reference for the development. A set of design, technological, repair, and operational documentation for LDFL devices

contact lubrication devices modernization. The presented material is instruction for the formation of technical specifications and technical conditions of lubrication devices created on scientifically based criteria for their operability and operational reliability. At the same time, it should be considered that the developed criteria are based on the regulations adopted by OJSC “Russian Railways”, which implies the possibility of expanding the

requirements depending on the specifics of the place of application of flange lubrication devices in a particular country.

5 Conclusion

During the research, a regulatory framework was created for design work in the field of creating devices for the flanges lubricating of wheel pairs of locomotives, which allows developers to operate effective devices for ridge lubrication that meet the current requirements of standards and regulatory documents of OJSC Russian Railways, which is the basis for increasing operational traction reliability of rolling stock.

References

1. Kokhanovskii VA, Maiba IA, Glazunov DV, Bol'shikh IV (2016) Lubricator casings for locomotive wheel rim. *Russ Eng Res* 36(5):364–365. <https://doi.org/10.3103/S1068798X16050099>
2. Kokhanovskii VA, Glazunov DV (2016) Selection of lubricant composition for open contact systems in rolling stock. *Russ Eng Res* 36(6):449–451. <https://doi.org/10.3103/S1068798X16060113>
3. Kochanowski VA, Maiba IA, Glazunov DV, Zoriev IA (2019) Powder bearings with polymer inserts. *J Friction Wear* 40(3):229–233. <https://doi.org/10.3103/S1068366619030048>
4. Kokhanovskii VA, Glazunov DV, Zoriev IA (2019) Macrocompositional polymer-powder bearings. *J Mach Manuf Reliab* 48(2):130–135. <https://doi.org/10.3103/S1052618819020080>
5. Kokhanovskii VA, Glazunov DV (2020) Velocity friction of fluoroplastic-containing coatings. *J Mach Manuf Reliab* 49(12):1096–1100. <https://doi.org/10.3103/S1052618820120067>
6. Kokhanovskii VA, Glazunov DV (2020) Multicriterial optimization of the composition of a lubricant. *J Mach Manuf Reliab* 7(49):624–632. <https://doi.org/10.3103/S1052618820070080>
7. Kokhanovskii VA, Glazunov DV (2020) A lubricant for rotaprint lubrication of the wheel-rail system. *J Frict Wear* 6(41):531–537. <https://doi.org/10.32864/0202-4977-2020-41-6-717-724>
8. Kolesnikov VI, Kudryakov OV, Zabiyaka IY, Novikov ES, Manturov DS (2020) Structural aspects of wear resistance of coatings deposited by physical vapor deposition. *Phys Mesomech* 6(23):570–583. <https://doi.org/10.1134/S1029959920060132>
9. Kudryakov OV, Varavka VN, Kolesnikov IV, Novikov ES, Zabiyaka IYu (2021) DLC coatings for tribotechnical purposes: Features of the structure and wear resistance. In: IOP conference series: materials science and engineering. International Workshop: Institute of Physics and IOP Publishing Limited. <https://doi.org/10.1088/1757-899X/1029/1/012061>
10. Maiba I, Glazunov DV, Maiba V (2020) Special purpose composite materials for wheel-rail contact. In: IOP conference series: materials science and engineering. International Workshop: Institute of Physics and IOP Publishing Limited. <https://doi.org/10.1088/1757-899X/709/3/033013>
11. Maiba IA, Glazunov DV (2020) Optimization of tribotechnical characteristics of wheel-rail friction modifiers. *J Frict. Wear* 6(41):517–520. <https://doi.org/10.3103/S1068366620060136>
12. Shapovalov VV, Ozyabkin AL, Kolesnikov IV, Kharlamov PV, Mischenko VB (2019) Tribological testing of MI-26T helicopter tail driver couplings. In: AIP conference proceedings. International Workshop: American Institute of Physics Inc. <https://doi.org/10.1088/1757-899X/1029/1/012043>

13. Shapovalov VV, Kolesnikov VI, Kharlamov PV, Kornienko RA, Petrik AM (2020) Improving the efficiency of the path. Rolling stock system based on the implementation of anisotropic frictional bonds. In: IOP conference series: materials science and engineering. International Workshop: Institute of Physics and IOP Publishing Limited. <https://doi.org/10.1088/1757-899X/1029/1/012034>
14. Shapovalov VV, Migal YuF, Ozyabkin AL, Burakova MA, Feizova VA, Korniyenko RA (2020) Metal cladding of friction surfaces in liquid media. In: IOP conference series: materials science and engineering international Workshop: Institute of Physics and IOP Publishing Limited. <https://doi.org/10.1088/1757-899X/900/1/012011>
15. Sidashov AV, Kozakov AT, Kolesnikov VI, Manturov DS, Yaresko SI (2020) Surface modification features of tool steels by laser radiation. *J Frict Wear* 6(41):549–553. <https://doi.org/10.1088/1757-899X/996/1/012022>
16. Shapovalov VV, Kharlamov PV, Gorin SL, Mischinenko VB, Kornienko RA, Zinovev VE (2021) Optimization of dynamically loaded nonlinear technical systems. In: IOP conference series: materials science and engineering. International Workshop: Institute of Physics and IOP Publishing Limited. <https://doi.org/10.1063/1.5138387/>
17. Shapovalov VV, Kolesnikov IV, Burakova MA, Kharlamov PV, Scherbak PN (2021) Thermo-metal-cladding of working surfaces of closed friction units of mobile systems. In: IOP conference series: materials science and engineering. International Workshop: Institute of Physics and IOP Publishing Limited. <https://doi.org/10.3103/S1068366620060185>



Improving the Reliability of the Sliding-Current Assembly for Electrical Machines by Using a Non-conductive Grinding Brush

A. Izotov^(✉), V. Timoshenko, and S. Izotov

Vyatka State University, 36, Moskovskaya street, Kirov 610000, Russia
izotov@vyatsu.ru

Abstract. Questions of guidance and erasure of the varnish (oxide-nitrous) film on the collectors and contact rings of electric machines are constantly in the field of view of specialists in electrical mechanics. The varnish film is a solid lubricant that reduces the coefficient of sliding friction in the unit of the sliding-current assembly (SCA) of electric machines, which in turn reduces the wear of standard brushes, collectors and slip rings. The absence of a polish film (the impossibility of formation) increases the wear of the brushes by hundreds of times. At the same time, too much thickness of the polish film can also lead to splitting of the brushes due to the occurrence of molecular coupling forces and even not starting the electric motor. Therefore, the control over the corrosion state of the polish film in the SCA is undoubtedly an urgent problem. This work is devoted to an attempt to apply an inexpensive solution for effective cleaning of metal contact surfaces of electric machines (EM) from negative formations using a talc-filled composite inserted in the form of a briquette in the standard window of the brush holder on the sliding track of high-power electric machines.

Keywords: Polishing film · Wear · Brushes · Collector and slip rings · Electrical machines · Talcum powder · Sanding block · Carbon deposits

1 Introduction

The reliability of electric machines that have a sliding-current assembly (SCA) unit in their composition largely depends on the wear rate of collectors and current-carrying brushes, which is determined by the presence of a surface polish film [1–3]. The polish film acts as a lubricant for the contact surfaces of the stationary electric brushes and the collector, as well as a protective cover film with a transient resistance, for the implementation of a stable electrical transfer. According to the regulatory regulations, the value of the transition resistance of the varnish film is not normalized due to its possible structural transformation, and the thickness is in the range of (5–100) nm. The polish film consists of the oxide component of the metal, which has a composition of oxides with different stoichiometry, and the carbonaceous brush material on top of it, and other components that are part of the brush product.

The presence of a “normal” polish film, as shown by the research, means that the resistance of the film passage is the most significant resistance of all possible resistances standing in the path of the current passage from the traverse to the collector metal. The polish film is in a dynamic equilibrium at which the process of its formation and its destruction occurs due to the grinding action of the brushes.

On the surface of the collector or contact ring of electric machines of direct and alternating current of general industrial use, even in conditions of acceptable switching, non-conductive spots—“carbon deposits,” which are thick oxide films, are often formed [4–6]. The appearance of spots-deposits of chemical origin is also noted [6, 7]. In addition, under certain atmospheric conditions and unfavorable switching modes of operation of an electric machine, often accompanied by increased sparking, the formation of an oxide-nitrous compound polish film of high thickness and resistance occurs [8–10]. These negative processes worsen the current distribution across parallel brushes. The concentration of the current load on individual brushes often leads to increased wear of standard carbon brush materials and in some cases even to their splitting. [11–13].

In DC motors, multi-brush units of a sliding-current collector with parallel working brushes designed to supply working currents to the rotating parts of an electric machine are widely used. As the experience of operating brush-collector units of rolling mill engines shows, in most cases, there are three acute problems: high wear of electric brushes, their sparking as a result of switching processes, as well as an unacceptably high temperature of the blade.

For the same reason, in the absence of preventive measures, electromechanical erosion of collectors and rings often occurs, while wear can go beyond the repair dimensions, followed by rejection of current-collecting rings and collectors [14–17]. On high-power electric machines (on turbo generators), this leads to large additional capital expenditures both for unscheduled repair activities due to the need to replace contact pairs with new ones, financial losses for the purchase of new complete sets, and time losses and increased labor intensity due to additional dismantling and installation activities.

Currently, the problem of eliminating the so-called carbon deposits which are tightly adhered oxide-acidic films and other salt deposits of chemical origin (impairing EM commutation) is solved by manual mechanical removal with abrasive skins or grinding stones. Depending on the design, they have versions with clamping handles (rings) and are marked 90602–90672 N, as well as additional designations of the grinding stone grain size (C, M, F, P). In this case, it is recommended to carry out processing first with a coarse-grained bar and then sequentially using several bars with a gradually decreasing grain size from C to P [16–18].

It is quite a difficult task. These devices have a significant drawback, which is determined by the subjective pressure effect of the maintenance and repair personnel. In addition, the hard grains of the abrasive component of the grinding stones saturate the material of the surface layer of the collector or ring, which leads to an increase in the intensity of electroerosive wear of the collector and brushes. Additionally, hard abrasive materials lead to the formation of blockages at the edges of the plates with a depth of 0.2–0.5 mm, reducing the contact area of the collector brush, ring-brush [19–21].

All these processes often lead to uneven wear of the metal surface and, as a result, to an increased level of arcing.

In some problematic cases, a laborious operation is required by milling the cylindrical rotating surface due to “carbon deposits” and “circular fire.” Using a turning tool with a cutting part made of tungsten-cobalt alloys of the VK-8 type for turning the working surface of the collector or slip ring often leads to the formation of burrs on the edges of the collector plates and rings, which worsen the mechanical connection between the brush and the ring or collector. The deburring operation is extremely time consuming and often done by hand [22–27].

1.1 Experimental Technique

The implementation of the technical solution was carried out on the basis of obtaining briquettes of powdered talcum powder on a bakelite bond varying the pressing pressure of the mixture. The pressing pressure was selected experimentally, allowing to achieve high strength indicators of the briquette, which was then normalized (heat-treated) at a certain temperature and time in the electrical box. The device for grinding the metal surface of the SCA was a non-conductive grinding brush made of a composite material, obtained by heat treatment with temperature mixing of a powder of a certain brand of talc and bakelite varnish, leading to the formation of a resin mixture due to the polymerization of the varnish (Figs. 1 and 2).



Fig. 1 Mixer for preparing a mixture of talc and binder

Subsequently, it was subjected to pressing in a mold (Fig. 3).

Vertical hydraulic top pressure press with a force of 60 tons (Fig. 4) without heating plates used directly for pressing briquettes. A feature of this press is the presence of an individual hydraulic drive and specialized equipment that allows to work in a semi-automatic mode.

To press out the finished briquettes, a vertical press with a force of 3 tons was used (Fig. 5).



Fig. 2 Bath with stirring Z-shaped paddles

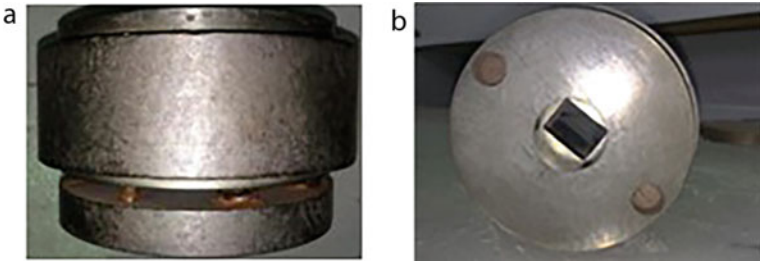


Fig. 3 **a** Side view talcum powder compression mold; **b** Top view

After pressing out the briquettes, a visual inspection is performed for the appearance of cracks. Past control the briquettes are in the process of heat treatment.

Heat treatment is the final stage of the technological process of manufacturing a semi-finished grinding brush, during which the compressed briquettes are subjected to heating and aging in order to give them the necessary properties. During the heat treatment, the binder is converted from a viscous state to a solid state, which gives the briquettes the required mechanical strength.

Dimensions of the contact surface of the grinding brush are equal to the current-collecting brushes. The grinding brush is installed on the slide track, instead of the standard brush. Each grinding brush is fastened with glue to a used standard brush and is spring-loaded in the brush holder with a standard brush spring.

Figure 6 shows a brush-collector unit, which includes: collector 1, collector brushes 2 in standard brush holders 3, grinding brush 4, bonded with glue with a used standard brush 5.



Fig. 4 Bath with stirring Z-shaped paddles



Fig. 5 Vertical press for extruding briquettes

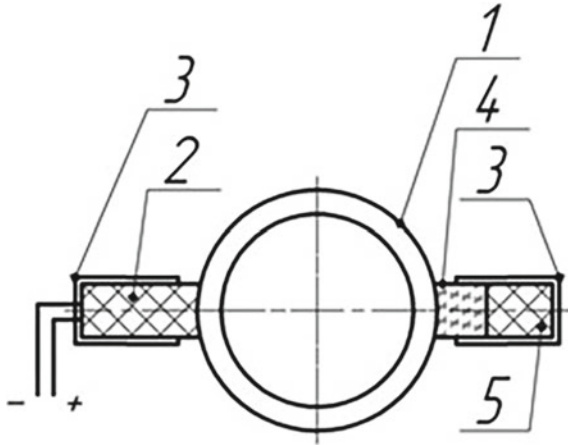


Fig. 6 Brush-collector unit with compound grinding brush

The work of the proposed technical solution in the brush-collector unit is carried out as follows. When the collector rotates, the grinding brushes clean the surface of the collector or slip ring where the collector brushes slide. Thickness of the polish film, in addition to visualization, was accessed by the value of its resistance.

The resistance of the polish film along the collector track was measured using a digital milliohm meter and silver-plated probes (Fig. 7).

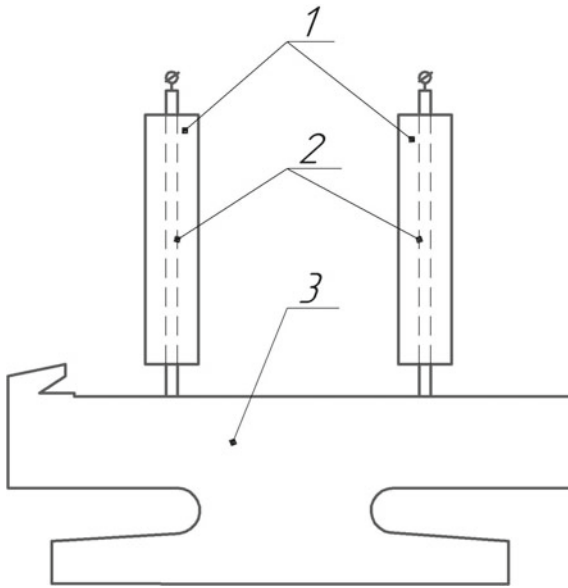


Fig. 7 Installing test leads for determining the resistance of the polish film. (1) false brush; (2) silvered probes; (3) collector plate

The assessment of the strength properties was carried out on a universal tensile testing machine of the R-5 type, which is used to check the compressive strength of the finished briquette. The method for checking the ultimate compressive strength is standardized by GOST 23,775-79. The briquettes recommended for use have hardness indicators within the permissible value, regulated by TU 1911-002-02,068,344-2017.

To assess the ultimate strength, we took 1 sample from a batch measuring $10 \times 10 \times 10$ mm. The tests are carried out on a universal tensile testing machine, type R-5. The load on the sample was applied in such a way that the direction of application of the force was parallel to the pressing plane, and the speed of movement of the moving part of the machine did not exceed 20 mm/min. The load increased continuously and uniformly until the sample was completely destroyed, with the force Q fixed at the moment of destruction. Knowing the initial area of the sample S^* , the compressive strength was calculated, which should be at least 4–5 MPa:

$$\sigma = \frac{Q}{S} \quad (1)$$

The thermal imager “Testo 875” was used to monitor the temperature of the processes associated with the heating of the composite mixture and the contact temperatures during grinding and switching (Fig. 8).

1.2 Discussion of Experimental Results

A preliminary assessment of the possibility of using a talc composite as a grinding agent was evaluated on grinding-universal machines (GUM), modernized for a test bench. These machines had an additional window where a spring-loaded talc-filled composite was inserted and then fixed with a rubber plug (Fig. 9).

The composite was located on the sliding track of standard brushes. The collector of the electric machine had “carbon deposits” on the surface obtained in non-optimal switching conditions. The results of experiments on removing the polish film with talcum powder are presented in Table 1.

In the case of using the proposed grinding brush, the surface of the copper collector is completely cleaned from the oxide-acidic film and carbon deposits. The accuracy of mating the grinding briquette with the surface to be cleaned is significantly increased. The productivity of the process is increased (10–15 min), and the labor intensity of the grinding operation is reduced.

Grinding brushes efficiently clean the surface of the collector or ring of an electric machine without disturbing the surface profile of the rings or the collector. Due to the low adhesion to the metal surface of talc, its grinding dust is easily blown out of the contact area.

The dimensions of the pilot-industrial mold make it possible to produce grinding briquettes corresponding to the geometric dimensions of standard industrial turbogenerators. In order to improve the material consumption of the process, it is possible to use used standard brushes as a carrier of the grinding briquette and allows you to easily adjust the size of the grinding briquette to the size of the standard brush. The proposed technical solution has priority in the Federal Institute of Industrial Property [28]. We offer deliveries of batches of non-conductive grinding brushes on high-power EMs to producers of electrical energy on contractual terms.



Fig. 8 Thermal imager machine Testo 875



Fig. 9 Test bench with a window for grinding composite

Table 1 Reducing the thickness of the polish film when grinding with a talc-filled composite of a copper collector

№	Resistance of the polished film (Ohm)			
	Time of the resistance measurement of the polished film (h)			
	Initial value	After 3 min of grinding	After 10 min of grinding	After 15 min of grinding
1	0.47	0.4	0.3	0.03
2	0.52	0.48	0.32	0.02
3	0.5	0.43	0.27	0.03
4	0.5	0.44	0.3	0.03

References

1. Shantarenko SG, Kuznetsov VF, Ponomarev EV, Taranenkov VA (2016) Improving the quality of current collection in the contact "brush-collector" of the traction electric motor of the electric locomotive 2 ES6. *Omsk Sci Bull* 5:77–80
2. Yu BD, Otradnoe AO (2013) Electrical discharge machining with jointed POS-ning of the electrodes relative to the surface number of the lecturer electric cars. *Omsk Sci Bull* 3:92–96
3. Kopylov IP (2000) *Electric cars*. Logos, Moscow, p 607
4. Stekolnikov YuA, Stekolnikova NM (2008) *Physical and chemical processes in mechanical engineering technology*. publishing house of the Elec-who state University named after I. A. Bunin, Moscow, Yelets, p 136
5. Kachin SI, Kachin OS (2011) A study of the influence of the fur-technical condition of collectors and bearings on the processes of wear in sliding contact electrical machines. *News of higher educational institutions. Electr Eng* 6:5–9
6. Samorodov YuN (2011) Risks of damage to turbo generators due to defects. *Electrical Engineering Library. NTF "Energoprogress"*, vol. 4, Moscow, p 64
7. Tsoпов GI, Ovsyannikov VN, Elshansky NA (2014) The mechanism of contacting a sliding contact from carbon-graphite materials. *Vestnik Transporta Povolzhya* 1(43):111–114
8. Safonov AL, Safonov LI (2009) Rectangular electric connectors. *Fretting-corrosion in electrical contacts. Technol Electr Ind* 3:48–54
9. Myshkin NK, Petrokovets MI (2007) *Friction, lubrication, wear. Physical bases and technical applications of tribology*. FIZMALIT, Moscow, p 368
10. Timoshenko VN (2018) *Reducing the wear of brushes in collector machines of direct and alternating current*. Dissertation, Moscow Power Engineering Institute
11. Fominykh AA (2015) *Assessment of the effect of solid lubricant on the tribo-characteristics of sliding current collection assemblies*. Dissertation, Moscow Power Engineering Institute
12. Samorodov YN (2011) Risks of damage to turbogenerators. *Lib Electr Eng* 3(1), Moscow, NTF "Energoprogress", "Energetik", p 80
13. Rostik GV (2008) *Evaluation of the technical condition of turbo generators: textbook*. - Prakt. manual. Agency for Education, Institute for Advanced Training of Civil Servants, Department "Operation of Power Grids. Facilities and energy sales activities", sector "Tech. re-armament, modernization and repair in the energy sector". PKI public service, Moscow, p 489
14. Kachin OS (2008) *Increasing the resource of the sliding contact of universal collector electric motors*. Dissertation. Tomsk Polytechnic University
15. Myshkin NK, Konchits VV, Brownovich MK (2008) *Electrical contacts*. Publishing house "Intellect", Moscow, p 560

16. GOST 6456-82. Sandpaper sanding paper. Technical conditions
17. GOST 9506.7-7 4. Brushes of electric machines
18. GOST 33534-2015. Grinding bars and segments
19. RD 34.45.502. Operating instructions for the contact ring assembly and the brush unit of the 165-300 MW turbogenerator
20. Azbukin YuA (1983) Improving the efficiency of operation of turbogenerators. Energeat-omizdat, Moscow, p 81
21. Petrochenko SV (2010) Improvement of technology of turning the working surface of the collectors traction motors. Transport of the Urals 2:53–55
22. Petrochenko SV, Fedorov AA (2014) Technology for improving the quality of the working surface of collectors of DC machines during mechanical processing. OMSK Sci Bull 1:113–117
23. Soldatkin AV (2013) Improving the switching stability of traction electric machines by improving the technology of collector repair. Dissertation, Omsk, p 22
24. Belan DYu, Luzin VM (2010) Improving the reliability of the tractor-brush assembly of traction electric motors. Izvestiya Transsib 4(4):6–11
25. Popov AYu, Belan D.Yu, Dyundin VV (2015) Improving the quality of repair of traction electric motor collectors by improving the geometry of the cutting tool. Omsk Sci Bull 3:38–41
26. Kharlamov VV, Popov DI, Baysadykov MF (2019) Determination wear intensity of electrical brushes in DC machines considering impact of collector's surface. J Phys Conf Ser 1260. <https://doi.org/10.1088/1742-6596/1260/5/052009>
27. Kharlamov VV, Shkodun PK, Ognevsky A (2018) Effect of transient processes on the switching stability of dc machines. MATEC Web Conf 239. <https://doi.org/10.1051/mateconf/201823901036>
28. Izotov AI, Izotov SA, Fominykh AA, Timoshenko VN (2020) Non-conductive grinding brush for current-removable rings and collectors of electric machines. RF Patent 2020142184/21 Dec 2020